The Geotechnical Characterisation of Christchurch Sands for Advanced Soil Modelling: Electronic Appendices

---

A thesis
submitted in partial fulfilment
of the requirements for the Degree
of
Doctor of Philosophy
by
Merrick L. Taylor

University of Canterbury
2015

Table of Contents

Chapter I

Introduction

This 'electronic appendix' document provides supplementary information to the main thesis, particularly plots of individual laboratory tests used to derive values and interpretations made in the study. It is not essential to the thesis, and has been provided in these electronic appendices as additional reference and supporting material.

Chapter II

Maps plans and sections

The electronic appendix contains the following:

- Digital Elevation Model and LiDAR ground movements at sites of interest.
- EQC Groundwater table levels at sites of interest.
- Conditional PGA Maps.
- Long Sections of CPT Interpretation at Kilmore Street.
- Long Sections of CPT Interpretation at Madras-Armagh Streets.

2.1 DEM and LiDAR ground movements

The following figures present extracts of LiDAR -based digital ground elevation model (DEM) and interpretation of ground settlements following 4 September 2010, 22 February 2011, and 13 June 2011 earthquakes. Base images obtained from the Canterbury geotechnical database.

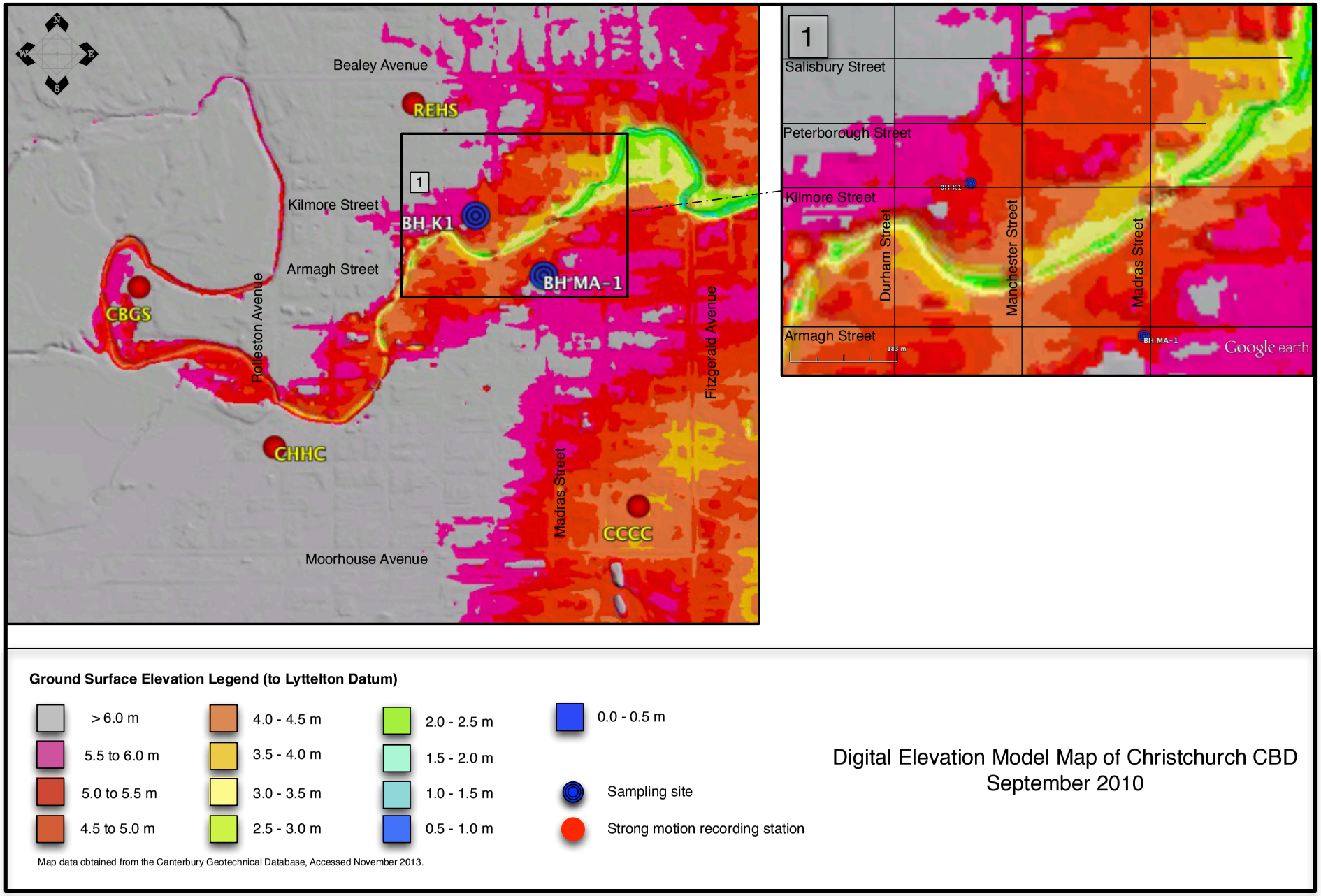

Figure 2.1: Digital Elevation Model of the Christchurch CBD for September 2010. Source: Canterbury Geotechnical Database 2013.

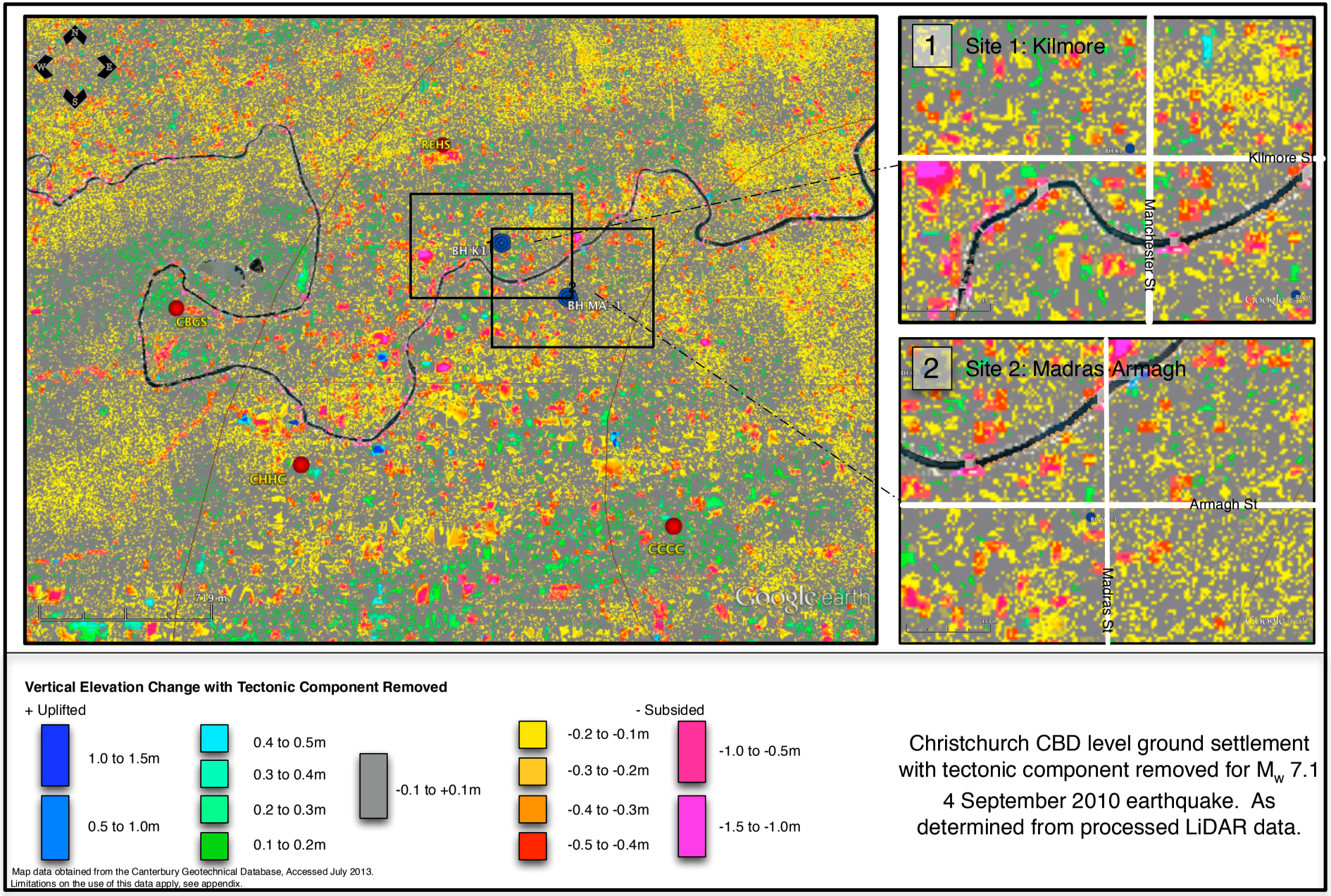

Figure 2.2: Vertical displacement of ground (less tectonic displacements) following 4 September 2010 earthquake estimated from LiDAR survey data in the CBD, with sites of interest at Kilmore and Madras-Armagh highlighted. Source data Canterbury Geotechnical Database 2013

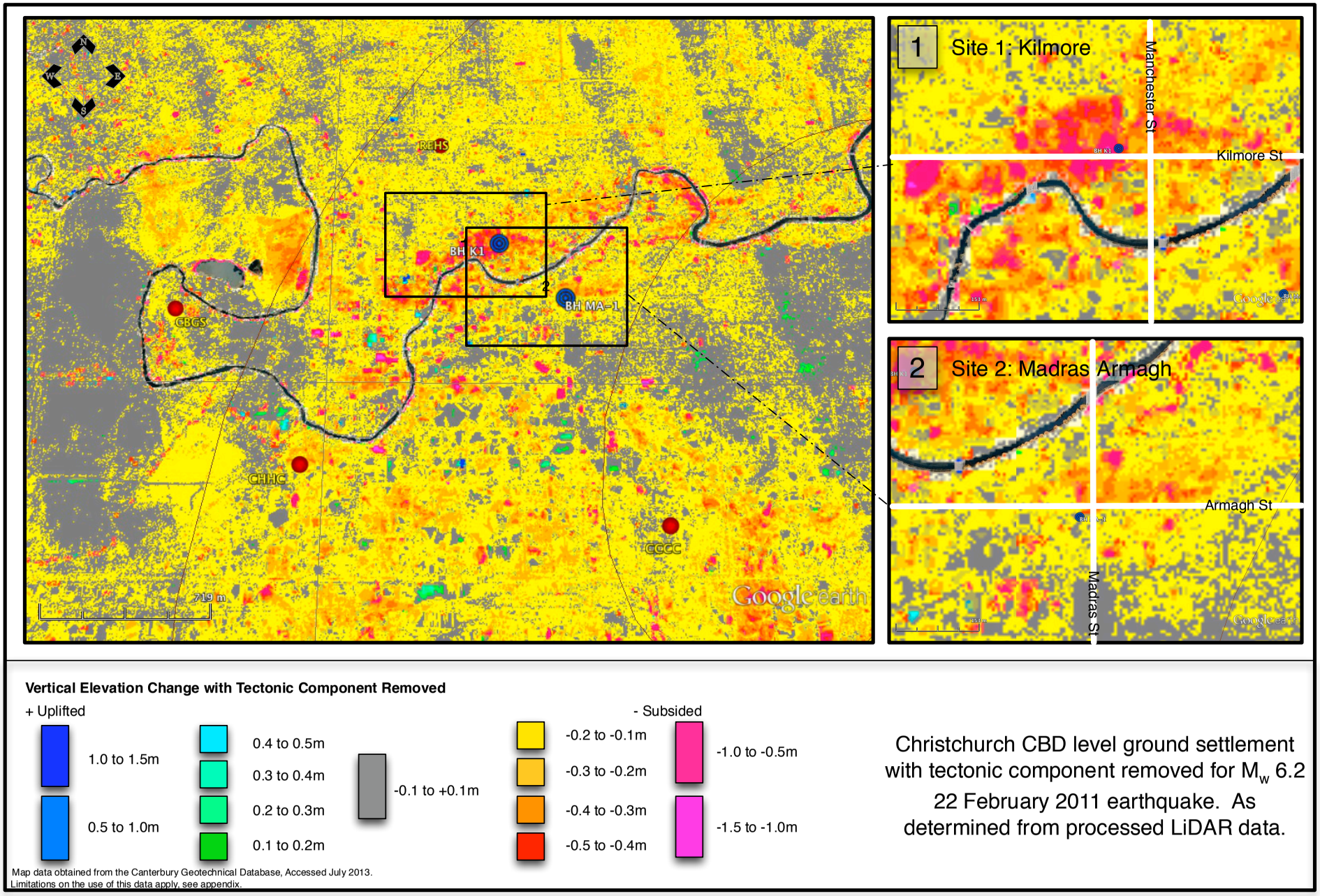

Figure 2.3: Vertical displacement of ground (less tectonic displacements) following 22 February 2011 earthquake estimated from LiDAR survey data in the CBD, with sites of interest at Kilmore and Madras-Armagh highlighted. Note that the largest displacements shown may indicate building collapses (e.g PGC building) and not liquefaction induced settlements. Source data Canterbury Geotechnical Database 2013.

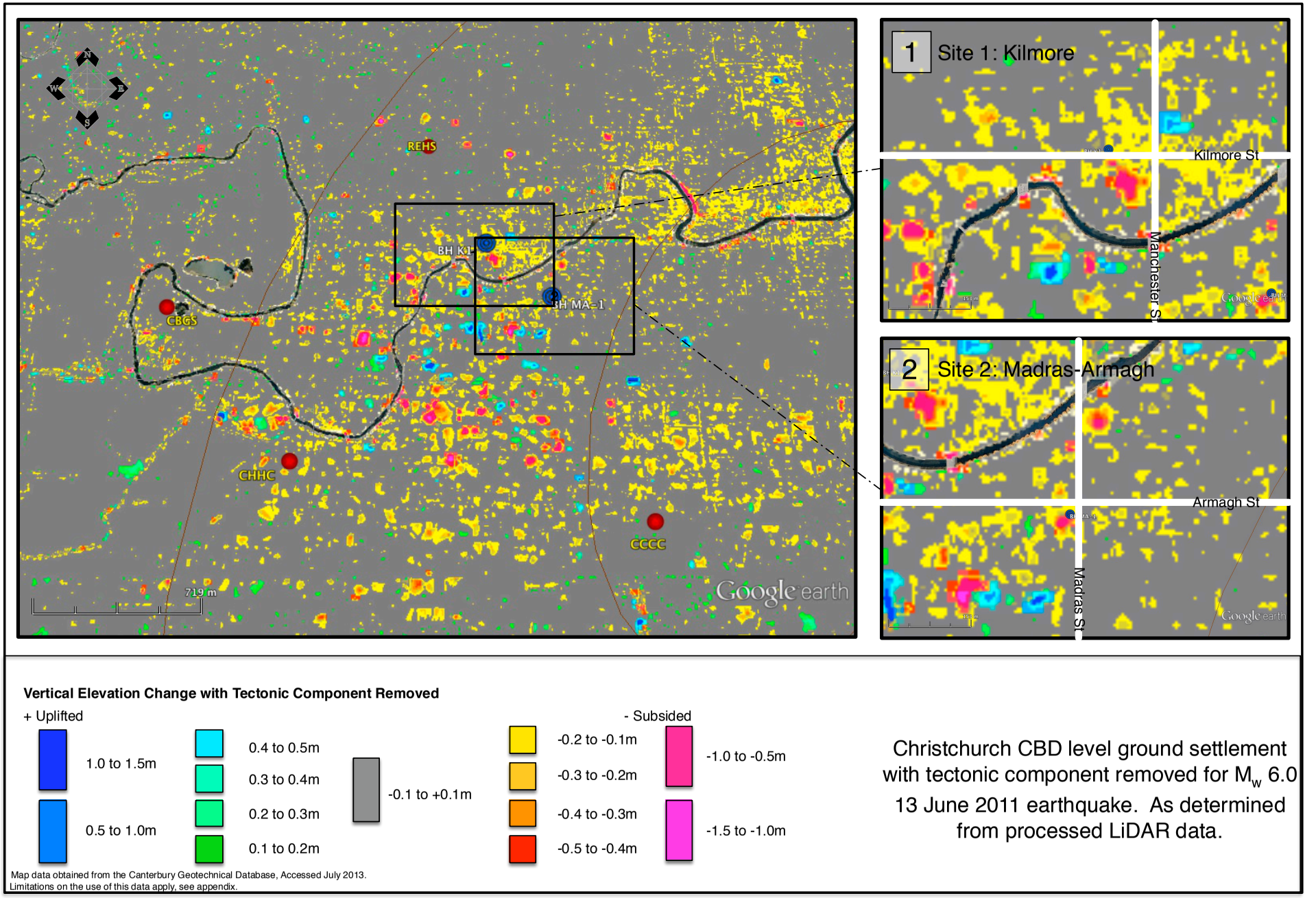

Figure 2.4: Vertical displacement of ground (less tectonic displacements) following 13 June 2011 earthquakes estimated from LiDAR survey data in the CBD, with sites of interest at Kilmore and Madras-Armagh highlighted. Source data Canterbury Geotechnical Database 2013

2.2 EQC Groundwater table levels

The following figures present extracts of Event Specific Groundwater table levels for 4 September 2010, 22 February 2011, and 13 June 2011 earthquakes developed for EQC by Tonkin & Taylor. Base images obtained from the Canterbury geotechnical database.

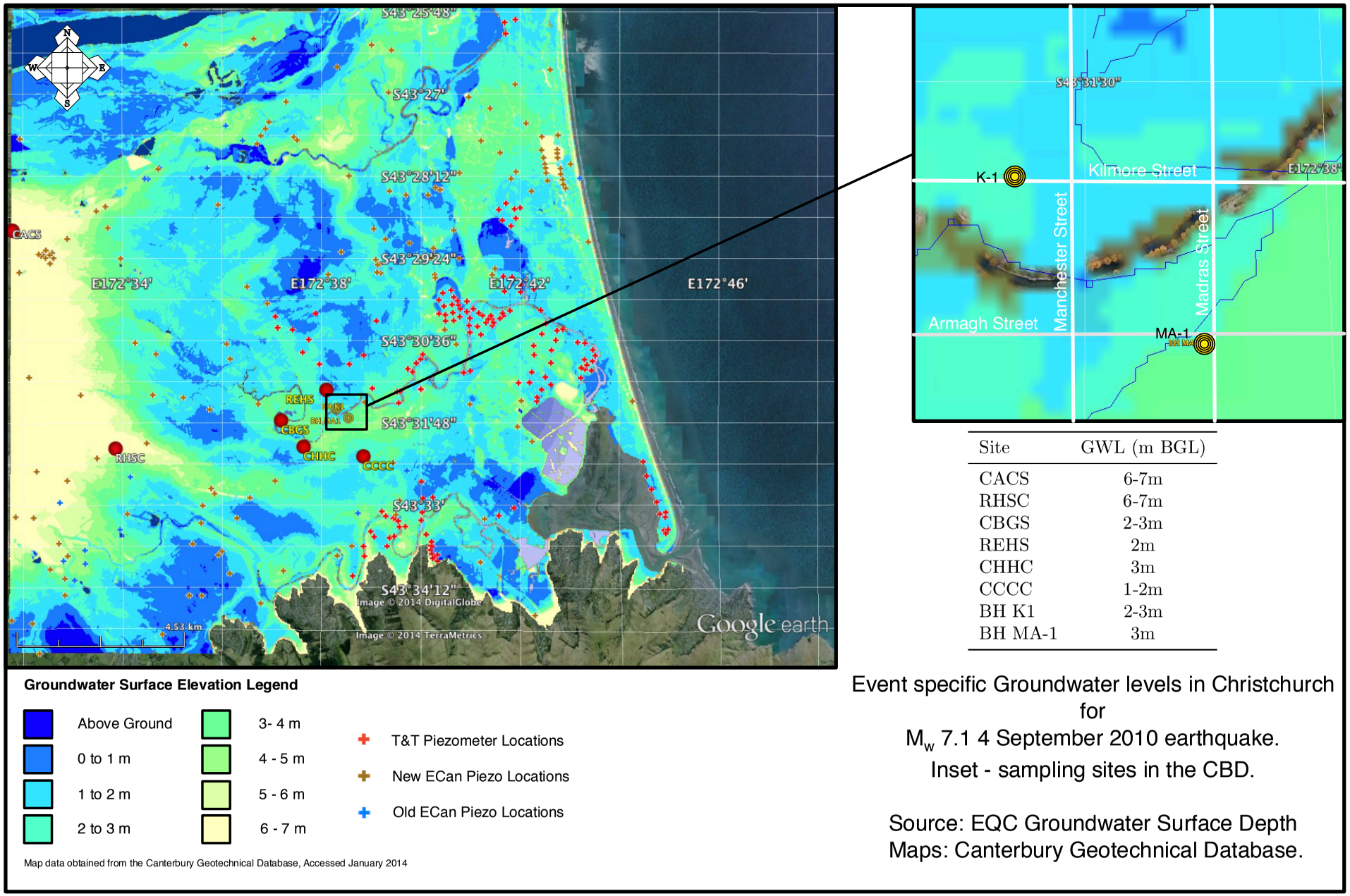

Site	GWL (m BGL)
CACS	6-7m
RHSC	6-7m
CBGS	2-3m
REHS	2m
CHHC	3m
CCCC	1-2m
BH K1	2-3m
BH MA-1	3m

Event specific Groundwater levels in Christchurch for M_w 7.1 4 September 2010 earthquake. Inset - sampling sites in the CBD.

Source: EQC Groundwater Surface Depth Maps: Canterbury Geotechnical Database.

Figure 2.5: Groundwater table levels (meters below ground level) during 4 September 2010 earthquake interpolated from installed piezometers, with sites of interest including Geonet Stations and sampling sites at Kilmore and Madras-Armagh highlighted. Source images: Canterbury Geotechnical Database 2013

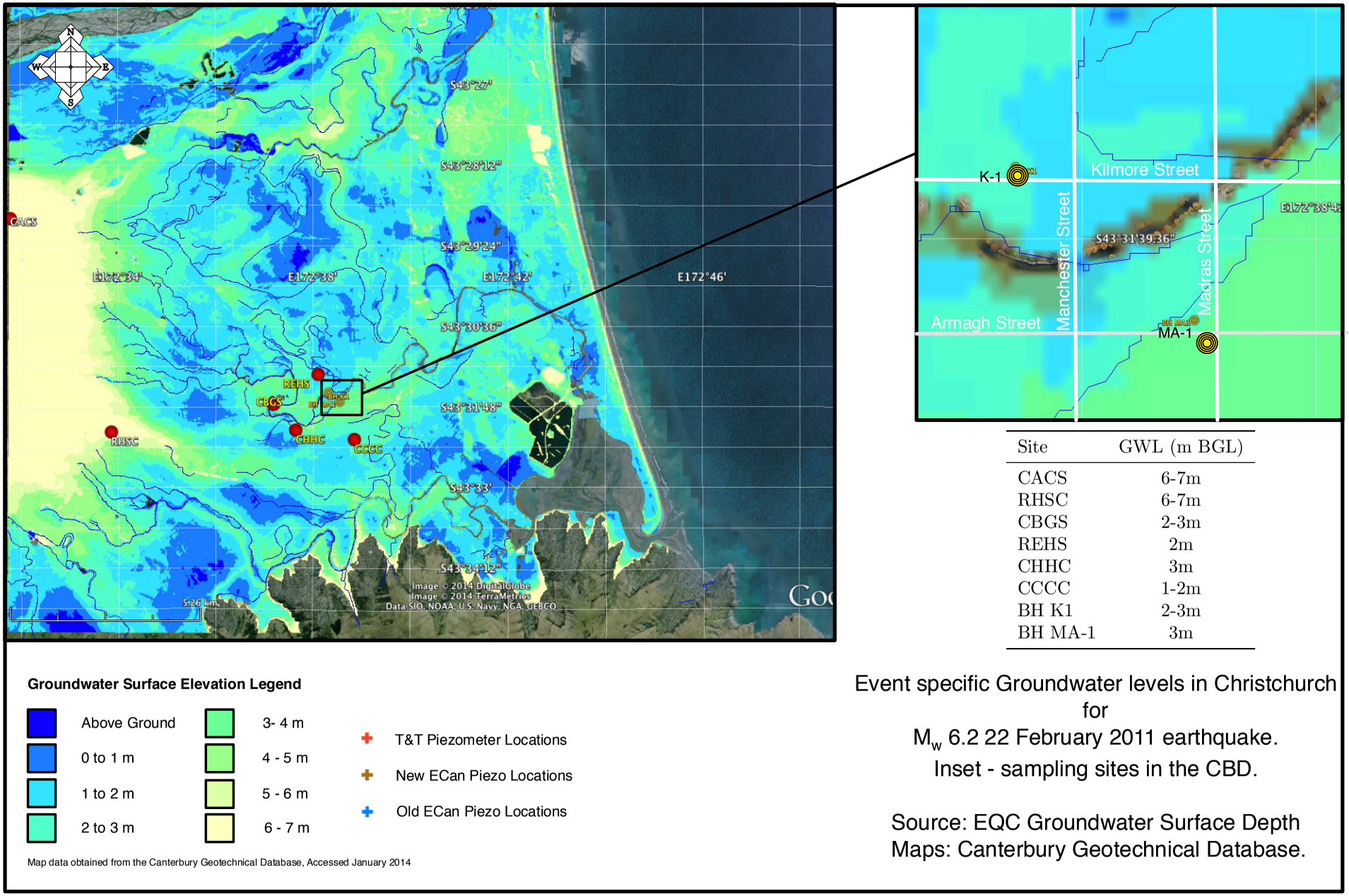

Site	GWL (m BGL)
CACS	6-7m
RHSC	6-7m
CBGS	2-3m
REHS	2m
CHHC	3m
CCCC	1-2m
BH K1	2-3m
BH MA-1	3m

Figure 2.6: Groundwater table levels (meters below ground level) during 22 February 2011 earthquake interpolated from installed piezometers, with sites of interest including Geonet Stations and sampling sites at Kilmore and Madras-Armagh highlighted. Source images: Canterbury Geotechnical Database 2013

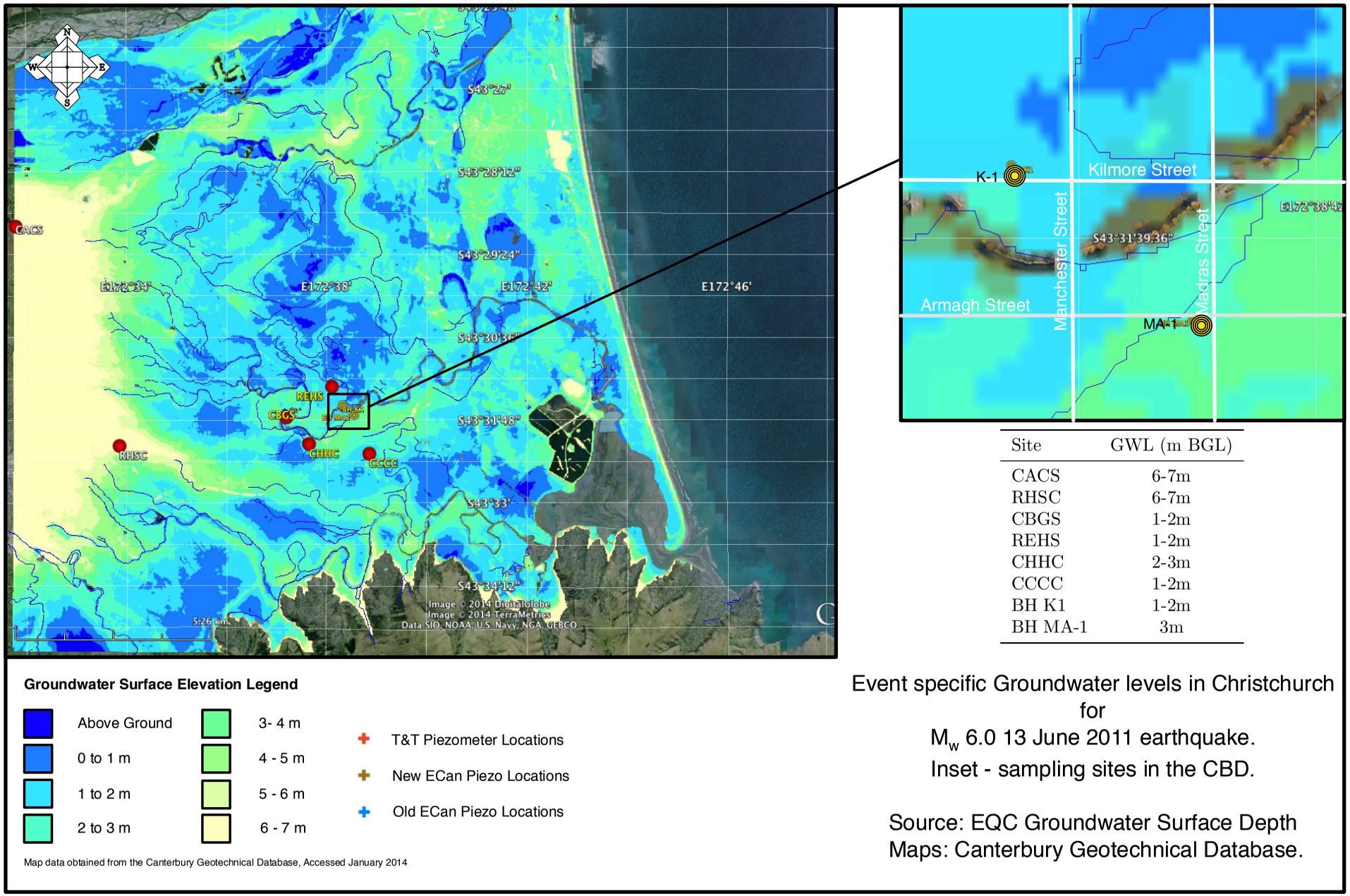

Site	GWL (m BGL)
CACS	6-7m
RHSC	6-7m
CBGS	1-2m
REHS	1-2m
CHHC	2-3m
CCCC	1-2m
BH K1	1-2m
BH MA-1	3m

Figure 2.7: Groundwater table levels (meters below ground level) during 13 June 2011 earthquake interpolated from installed piezometers, with sites of interest including Geonet Stations and sampling sites at Kilmore and Madras-Armagh highlighted. Source images: Canterbury Geotechnical Database 2013

2.3 Conditional PGA

The following figures present extracts of Conditional PGA for 4 September 2010, 22 February 2011, and 13 June 2011 earthquakes developed for the Department of Building and Housing (Ministry of Business, Innovation and Employment) by Bradley & Hughes (2012a)(2012b). Base images obtained from the Canterbury geotechnical database.

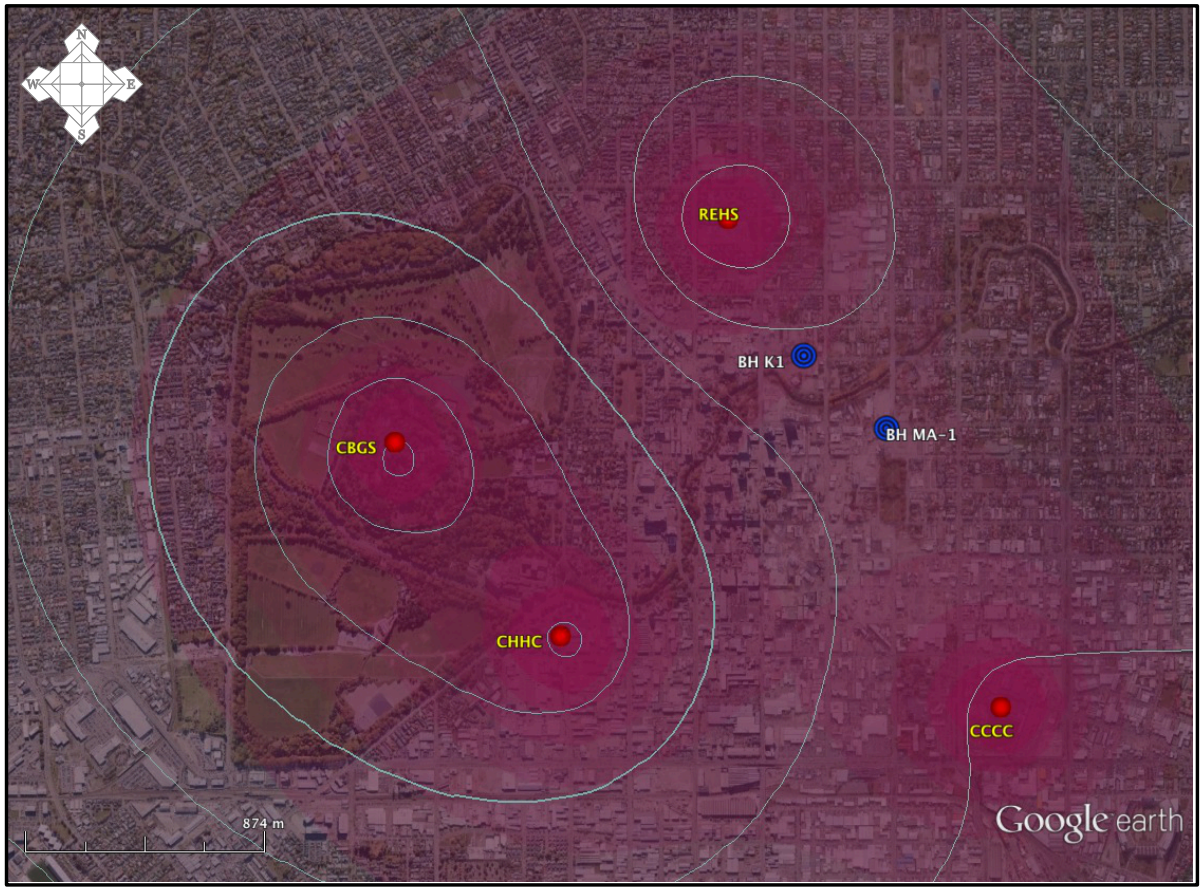

Site	PGA (g) Median	St-dev
CACS	0.2	-
RHSC	0.21	-
CBGS	0.16	-
REHS	0.25	-
CHHC	0.17	-
CCCC	0.22	-
BH K1	0.21	0.2425
BH MA-1	0.21	0.2625

Conditional Median PGA Contours:

0.8 g
0.7 g
0.6 g
0.5 g
0.4 g
0.3 g
0.2 g
0.1 g

Standard Deviation Bands

0.5
0.4
0.3
0.2

Spatially Distributed Conditional Median and Standard Deviation
Peak Ground Acceleration values in the Christchurch CBD.
M_w 7.1 4 September 2010 earthquake.

Source: Bradley & Hughes (2012a)
Maps: Canterbury Geotechnical Database.

Figure 2.8: Conditional PGA Maps of the CBD for 4 September 2010 earthquake

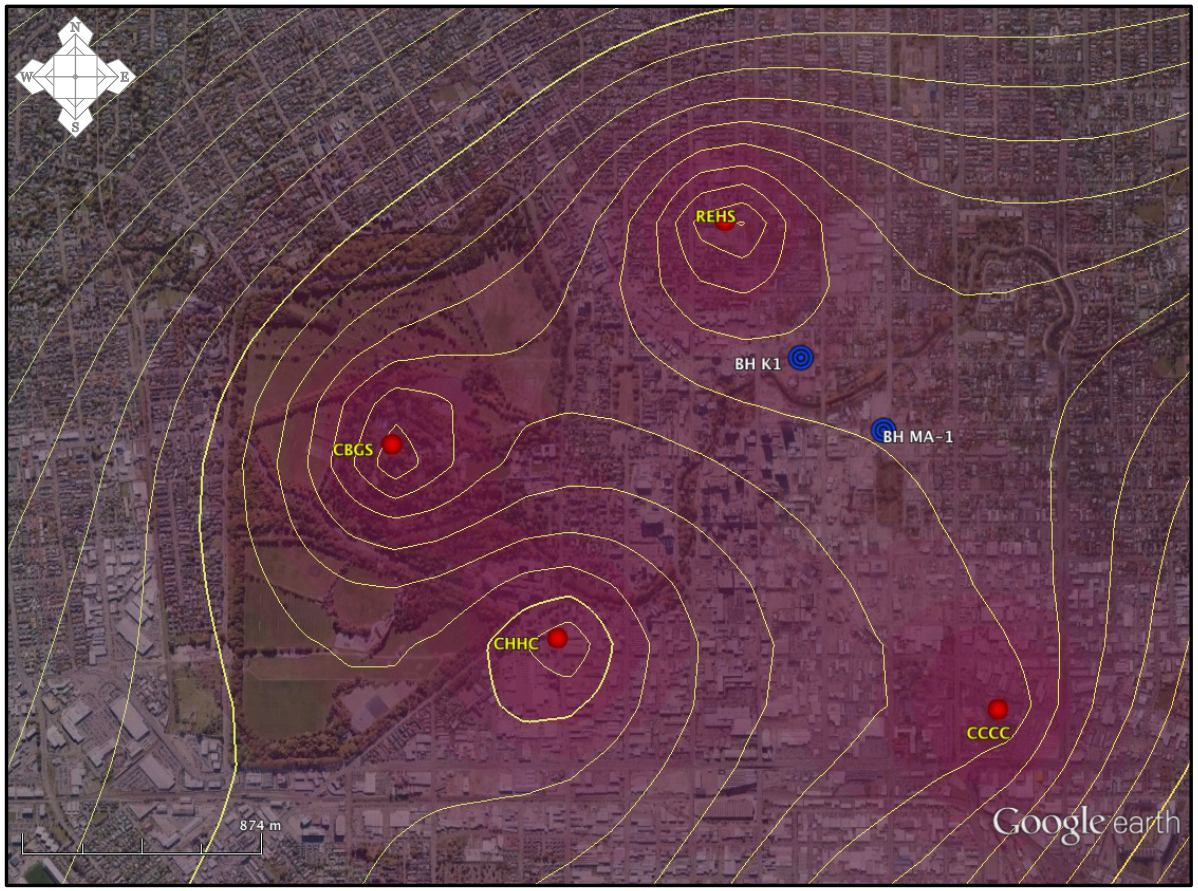

Site	PGA (g) Median	St-dev
CACS	0.21	-
RHSC	0.28	-
CBGS	0.5	-
REHS	0.52	-
CHHC	0.37	-
CCCC	0.43	-
BH K1	0.45	0.325
BH MA-1	0.45	0.2875

Conditional Median PGA Contours:

- 0.8 g
- 0.7 g
- 0.6 g
- 0.5 g
- 0.4 g
- 0.3 g
- 0.2 g
- 0.1 g

Standard Deviation Bands

- 0.5
- 0.4
- 0.3
- 0.2

Spatially Distributed Conditional Median and Standard Deviation
Peak Ground Acceleration values in the Christchurch CBD.
M_w 6.2 22 February 2011 earthquake.

Source: Bradley & Hughes (2012a)
Maps: Canterbury Geotechnical Database.

Figure 2.9: Conditional PGA Maps of the CBD for 22 February 2011 earthquake

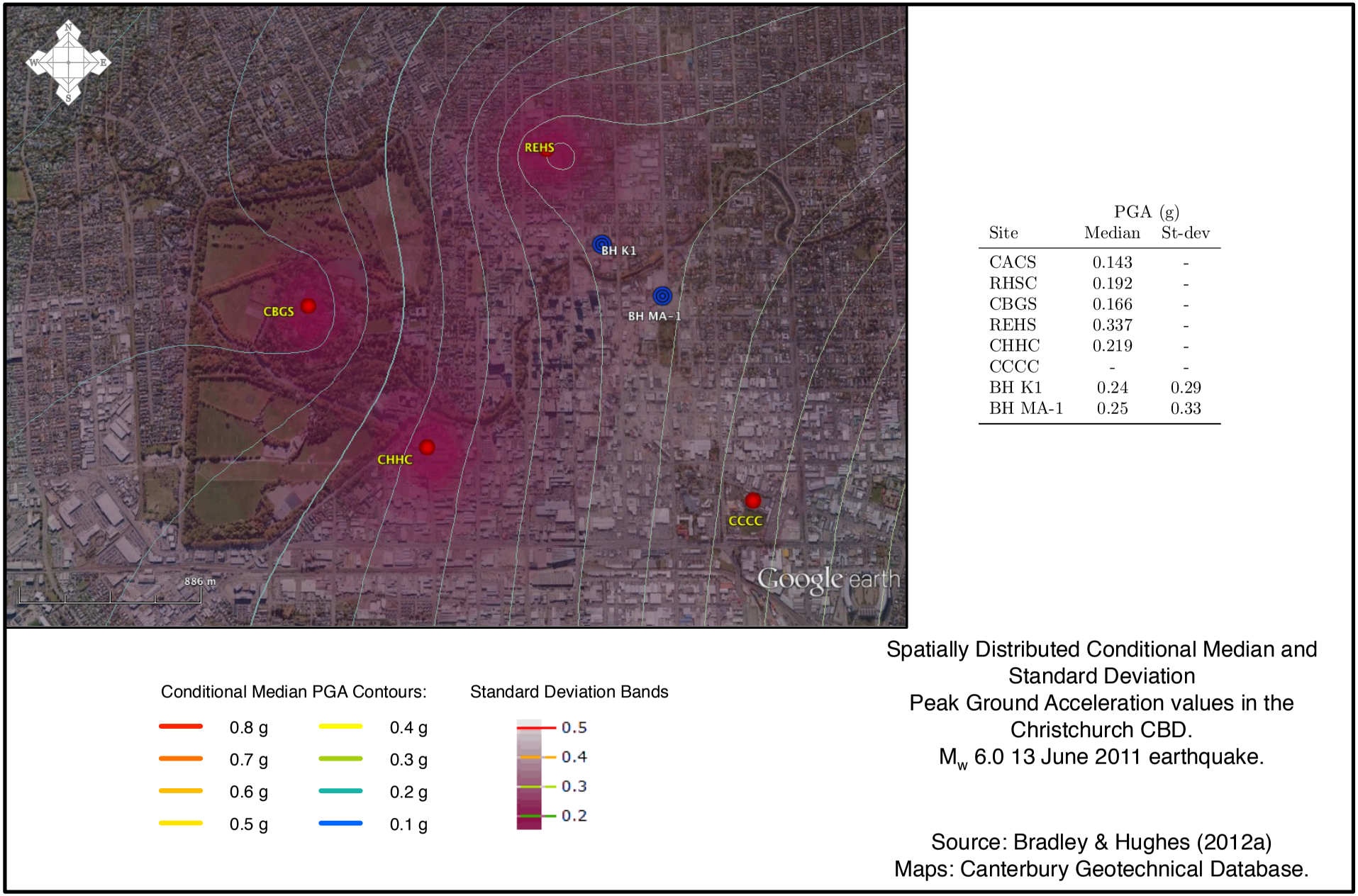

Site	PGA (g) Median	St-dev
CACS	0.143	-
RHSC	0.192	-
CBGS	0.166	-
REHS	0.337	-
CHHC	0.219	-
CCCC	-	-
BH K1	0.24	0.29
BH MA-1	0.25	0.33

Figure 2.10: Conditional PGA Maps of the CBD for 22 February 2011 earthquake

2.4 Interpretive Long Sections

The following plots and sections present the interpretation of geological profile, and geotechnical properties from the CPT test. There are three plots showing typical CPT profiles through the gravel channel, flood over-bank silty-sands, and distal silt-clay deposits in the Kilmore Street area north of the Avon River. There are two cross sections at Kilmore Site, and three for the Madras-Armagh Street site. The sections are labelled B through F. Note that Section A has not been included in this thesis as it refers to a cross section through boreholes in the centre-west of the CBD, crossing the gravel lobe, and not related to the sites of direct interest to this study.

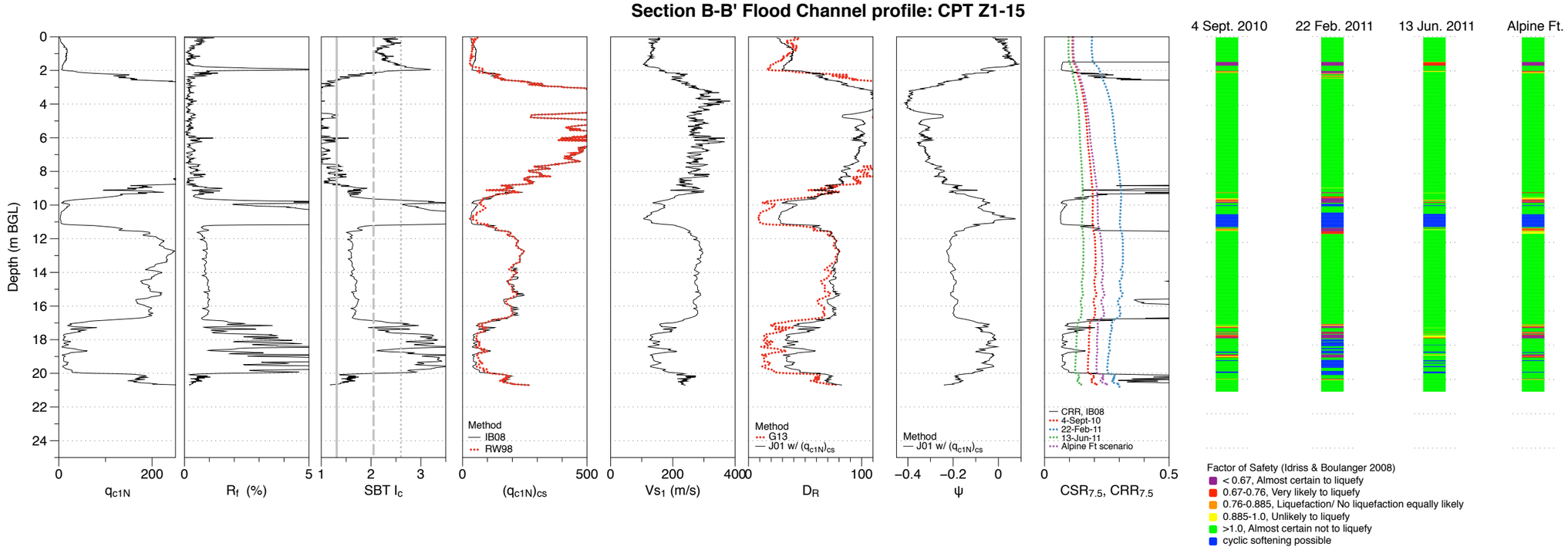

Figure 2.11: Typical 'Flood Channel' Soil Profiles from section B-B' as characterised by CPT interpretation including liquefaction hazard.

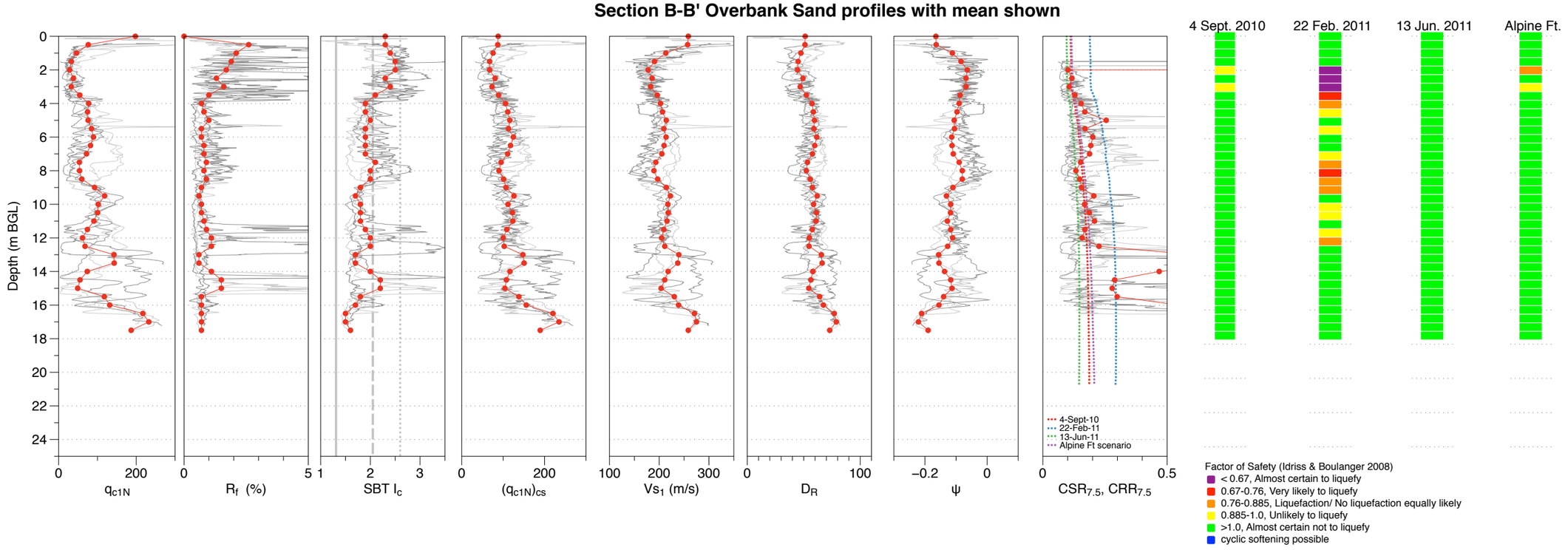

Figure 2.12: Typical 'Flood Overbank - Sand' Soil Profiles from section B-B' as characterised by CPT interpretation including liquefaction hazard. Geometric or arithmetic mean profiles derived from a number of CPTs within the zone have been used to represent the typical profile.

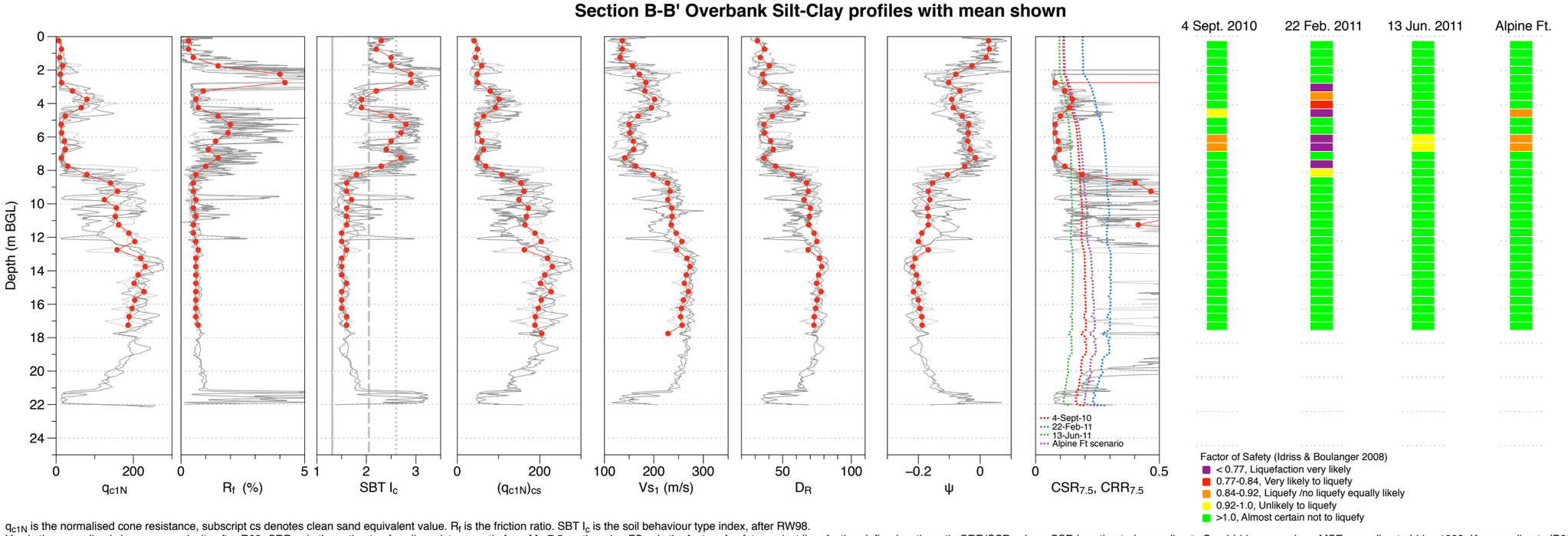

q_{c1N} is the normalised cone resistance, subscript cs denotes clean sand equivalent value. R_f is the friction ratio. SBT I_c is the soil behaviour type index, after RW98.
$V_{s,1}$ is the normalised shear wave velocity after R09. $CRR_{7.5}$ is the estimate of cyclic resistance ratio for a M_w 7.5 earthquake. FS_{Liq} is the factor of safety against liquefaction defined as the ratio CRR/CSR, where CSR is estimated according to Seed-Idriss procedure. MSF according to Idriss 1999, K_σ according to IB08.
IB08 = Idriss and Boulanger 2008. RW98 = Robertson & Wride 1998, R09 = Roberston 2009. Relative Density D_R by method of Jamiolkowski et al. 2001, with $q_{c1N,cs}$. Liquefiable soil cutoff criteria after RW98: SBT $I_c < 2.6$ & $R_f < 1\%$. Cyclic softening of soils with $I_c > 2.6$ determined according to Boulanger & Idriss 2007.

Figure 2.13: Typical 'Flood Overbank - Clay' Soil Profiles from section B-B' as characterised by CPT interpretation including liquefaction hazard. Geometric or arithmetic mean profiles derived from a number of CPTs within the zone have been used to represent the typical profile.

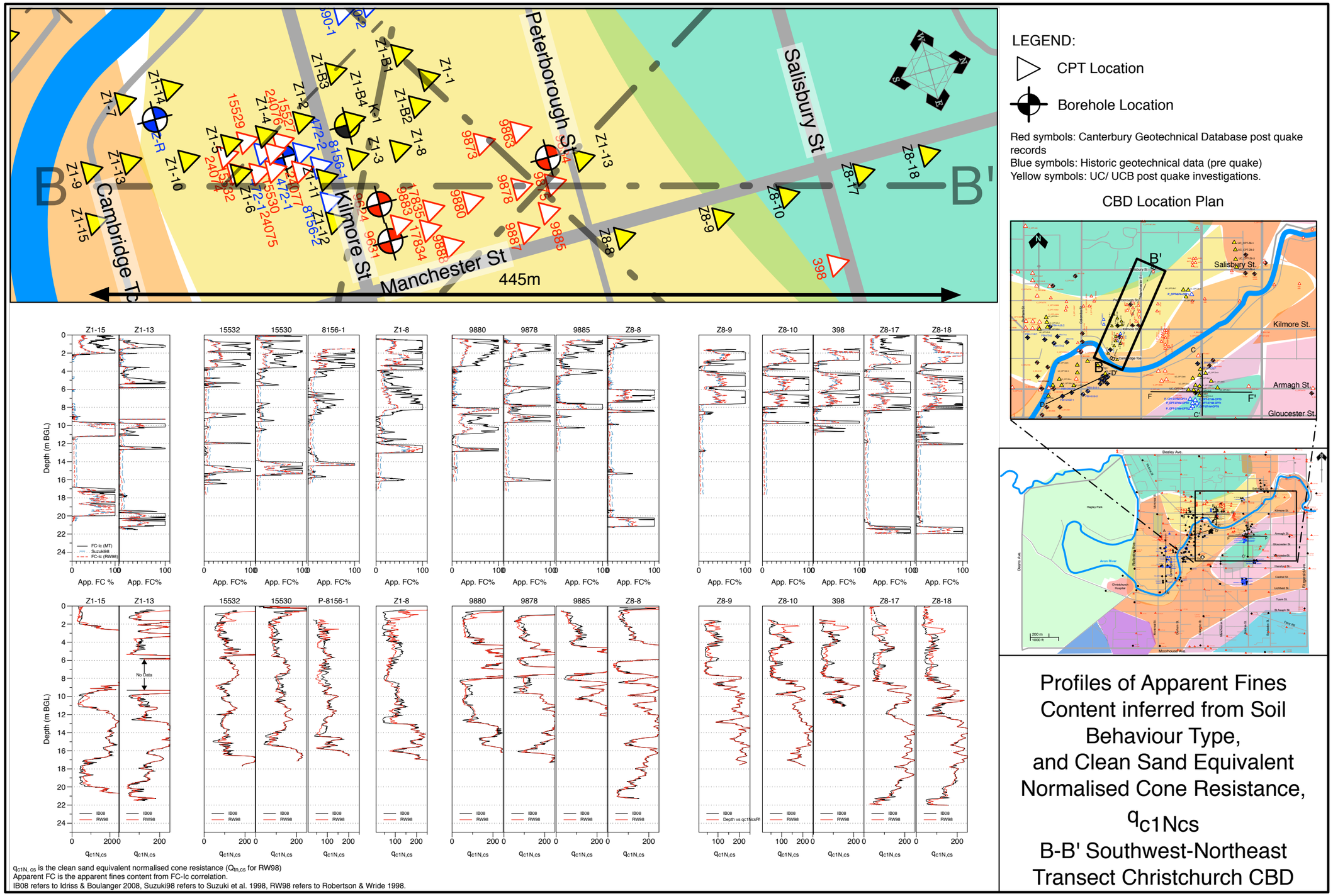

Figure 2.14: Section B-B', Kilmore Street Area. Interpreted fines content profiles, and 'clean sand equivalent' normalised cone resistance, q_{c1Ncs} profiles.

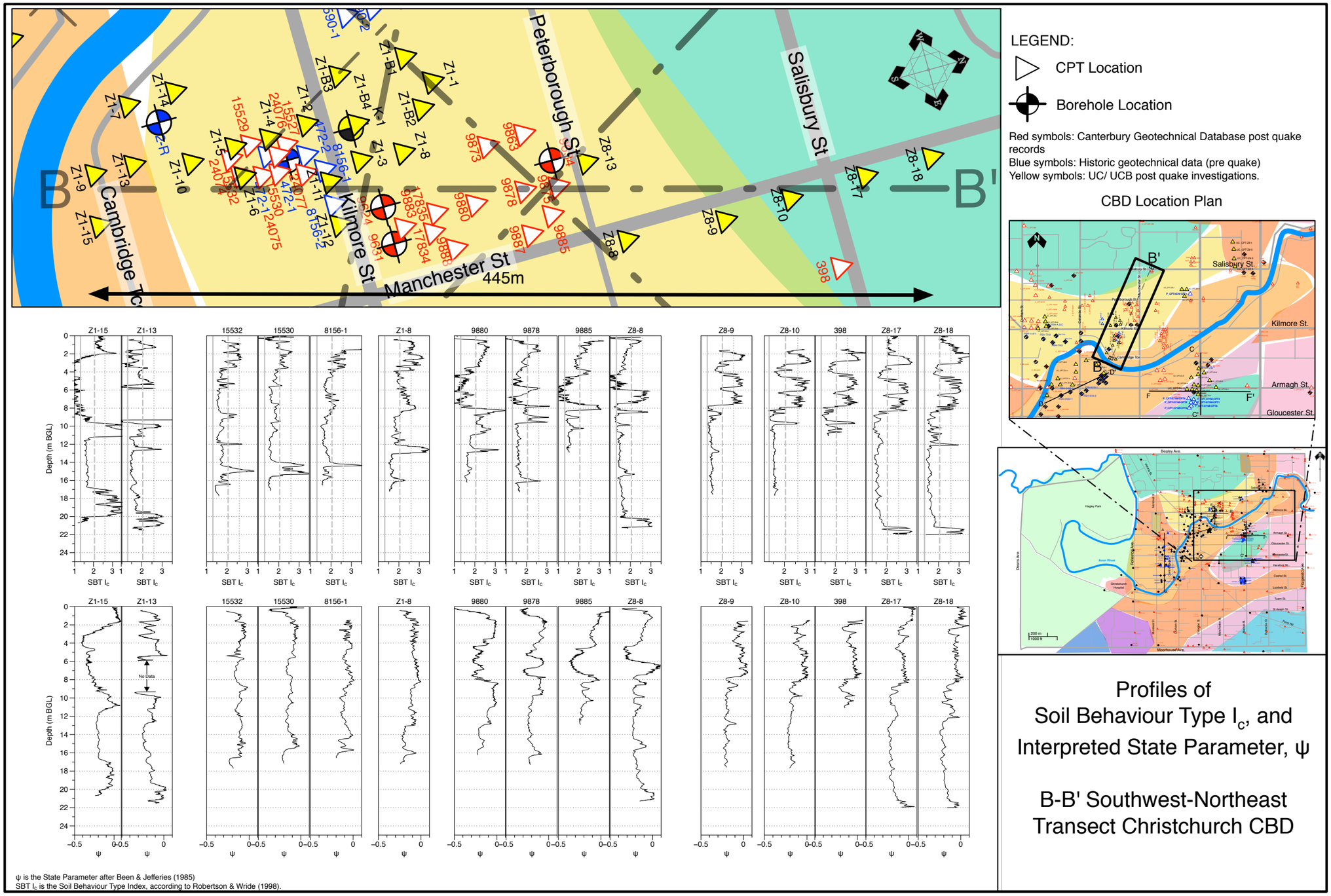

Figure 2.15: Section B-B', Kilmore Street Area. CPT-based Soil Behaviour Type Index I_c profile and State Parameter ψ interpreted from CPT.

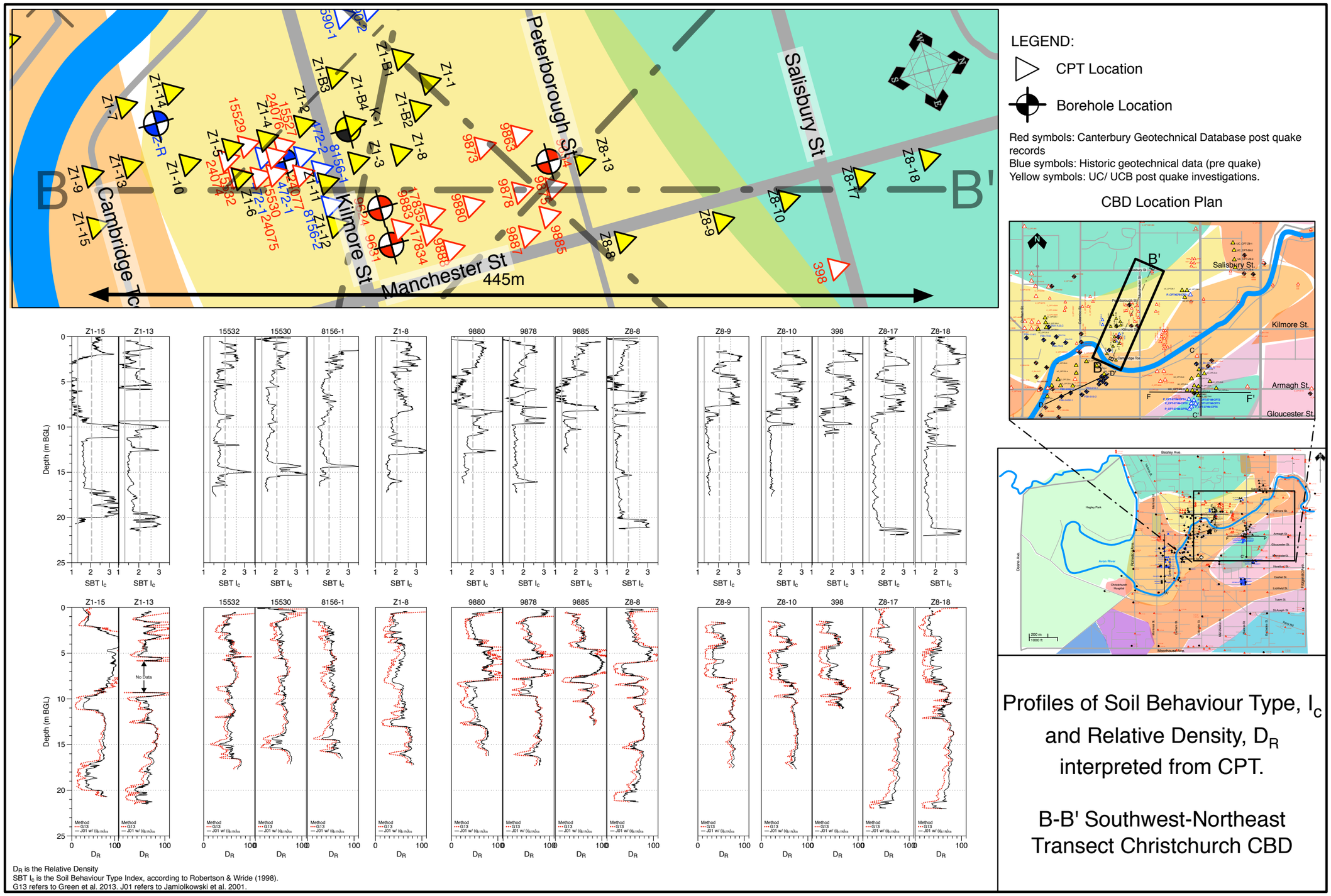

Figure 2.16: Section B-B', Kilmore Street Area. CPT-based Soil Behaviour Type Index I_c profile and Relative Density, D_R interpreted from CPT

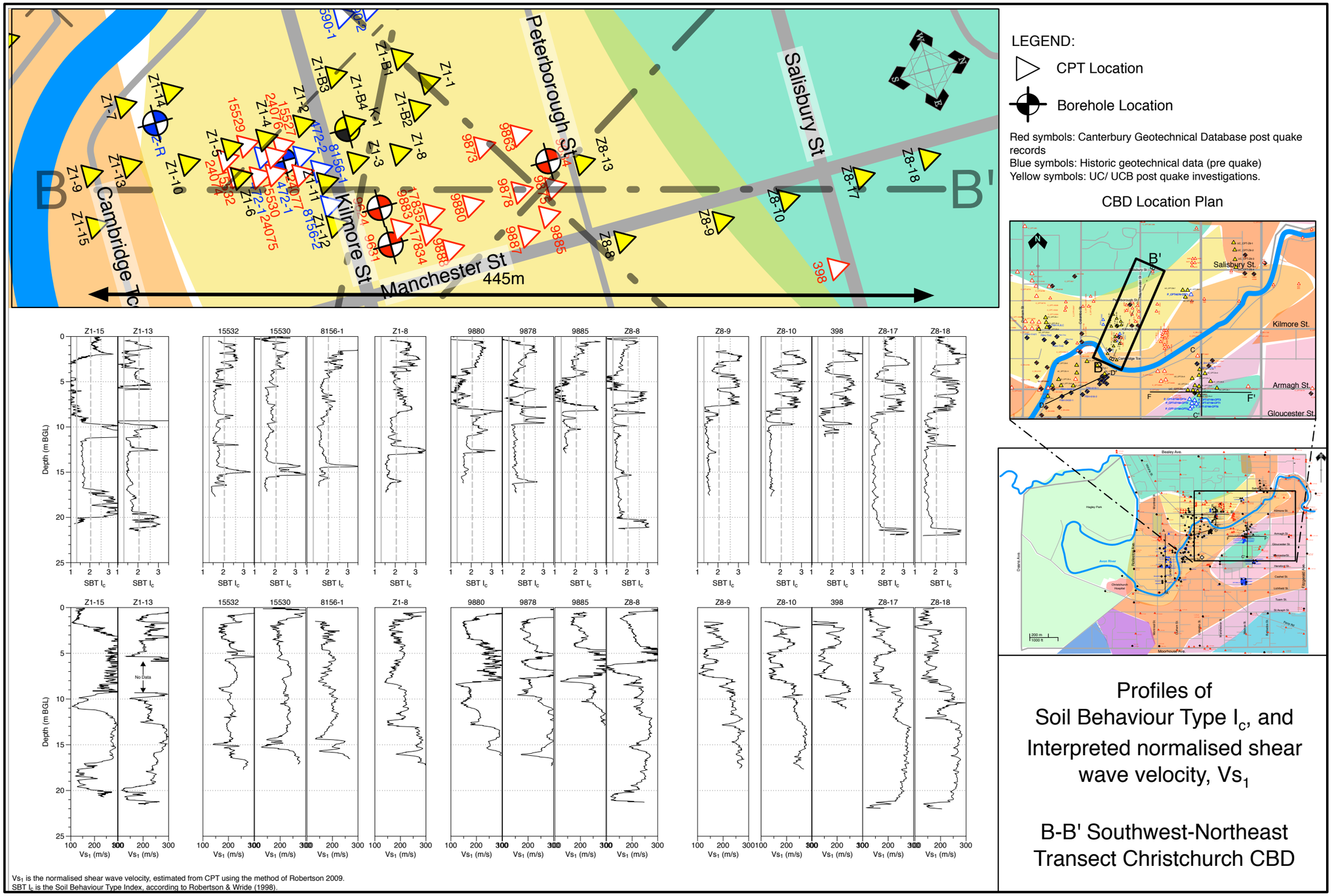

Vs_1 is the normalised shear wave velocity, estimated from CPT using the method of Robertson 2009.
SBT I_c is the Soil Behaviour Type Index, according to Robertson & Wride (1998).

Figure 2.17: Section B-B', Kilmore Street Area. CPT-based Soil Behaviour Type Index I_c profile and Shear Wave Velocity, V_s interpreted from CPT

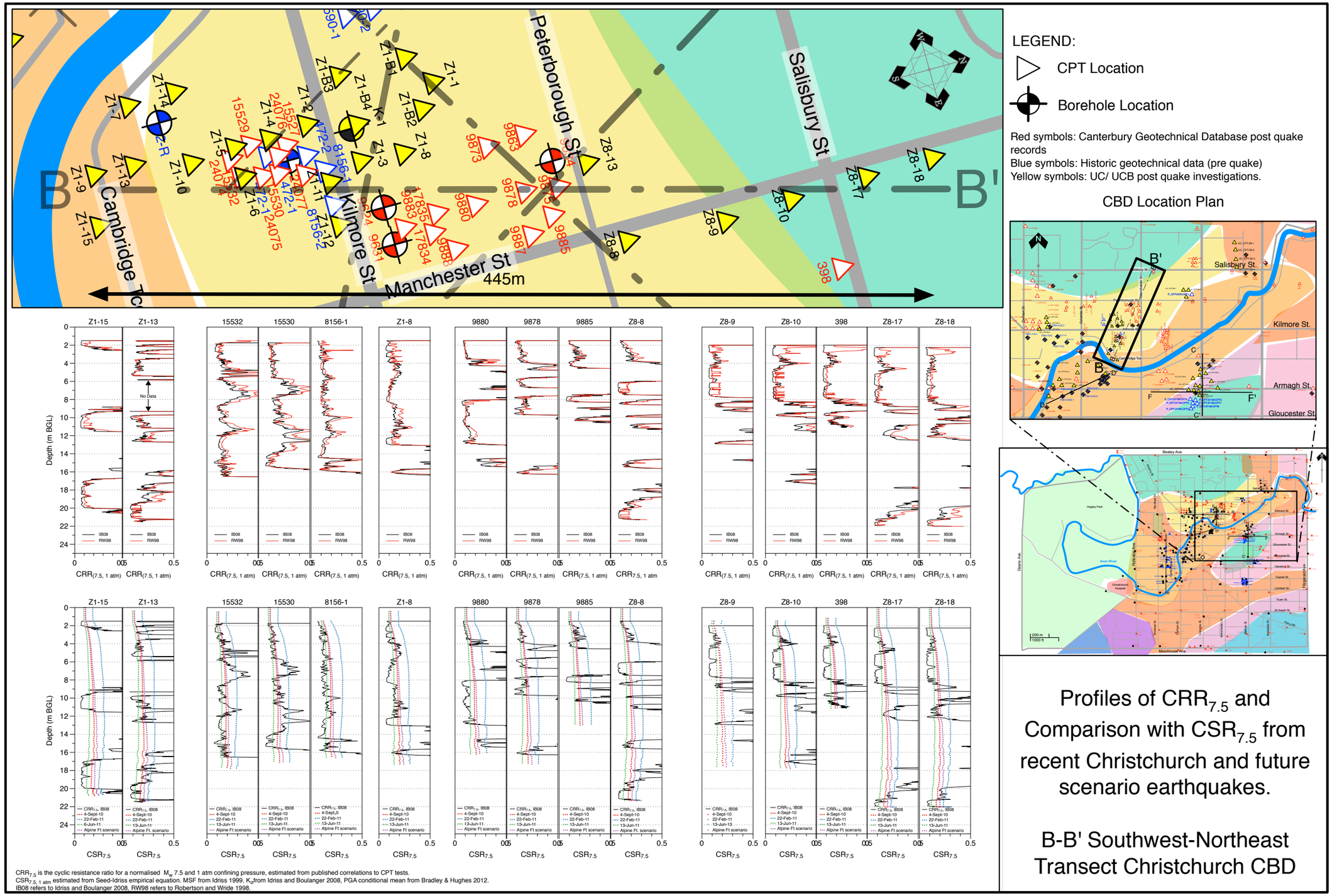

$CRR_{7.5}$ is the cyclic resistance ratio for a normalised M_w 7.5 and 1 atm confining pressure, estimated from published correlations to CPT tests.
$CSR_{7.5,\ 1\ atm}$ estimated from Seed-Idriss empirical equation. MSF from Idriss 1999, K_σ from Idriss and Boulanger 2008, PGA conditional mean from Bradley & Hughes 2012.
IB08 refers to Idriss and Boulanger 2008, RW98 refers to Robertson and Wride 1998.

Figure 2.18: Section B-B', Kilmore Street Area. CPT-based estimate of CRR, and comparison of CRR to CSR from significant earthquakes.

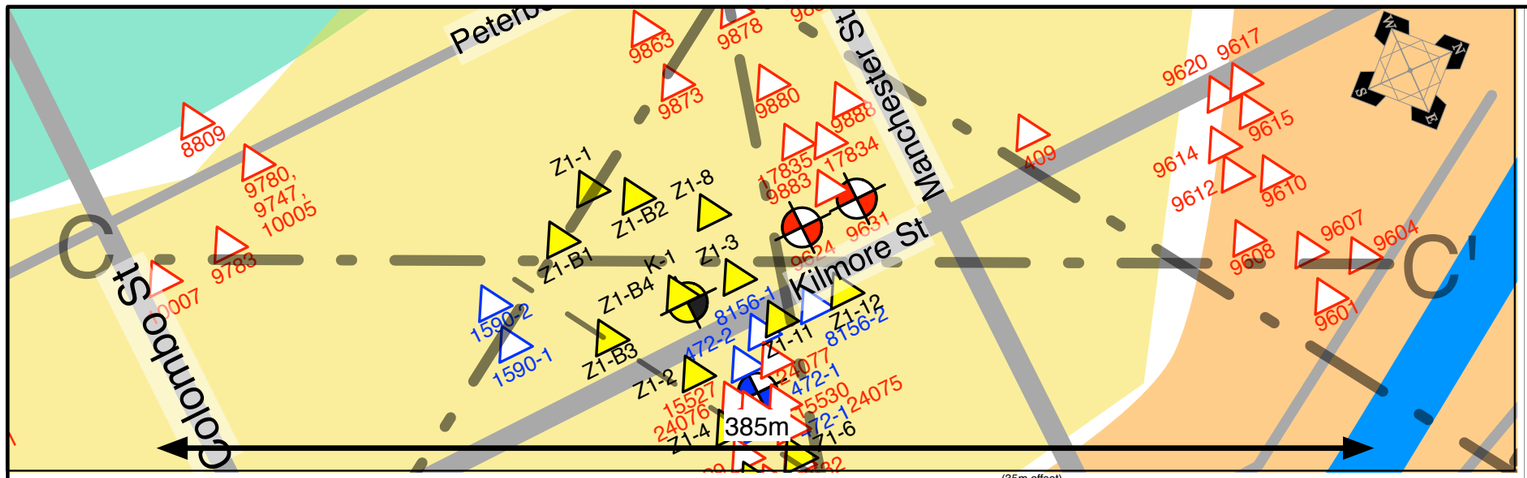

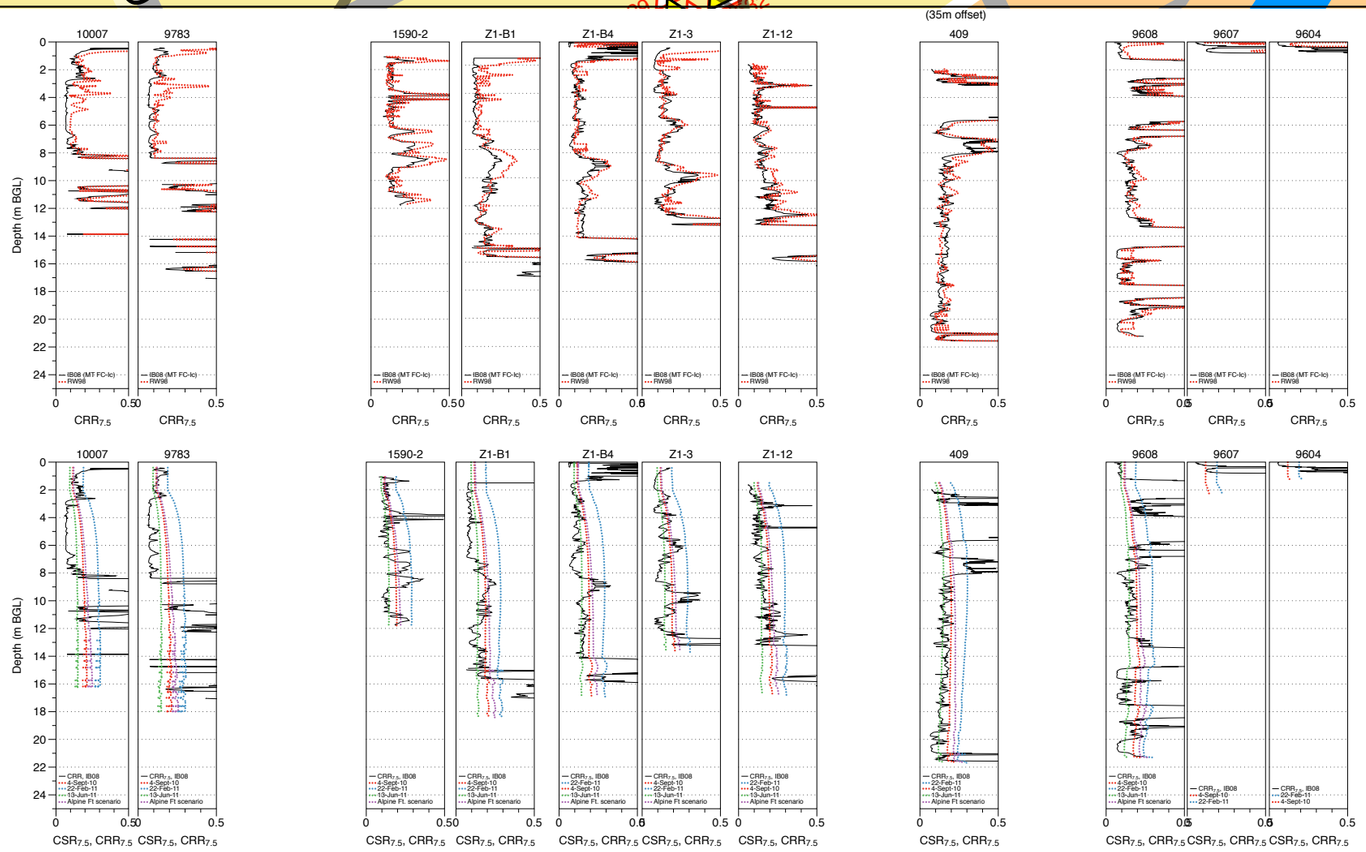

$CRR_{7.5}$ is the cyclic resistance ratio for a normalised M_w 7.5 and 1 atm confining pressure, estimated from published correlations to CPT tests.
$CSR_{7.5,\ 1\ atm}$ estimated from Seed-Idriss empirical equation. MSF from Idriss 1999, $K_\sigma$from Idriss and Boulanger 2008, PGA conditional mean from Bradley & Hughes 2012.
IB08 refers to Idriss and Boulanger 2008, RW98 refers to Robertson and Wride 1998.

LEGEND:

CPT Location

Borehole Location

Red symbols: Canterbury Geotechnical Database post quake records
Blue symbols: Historic geotechnical data (pre quake)
Yellow symbols: UC/ UCB post quake investigations.

CBD Location Plan

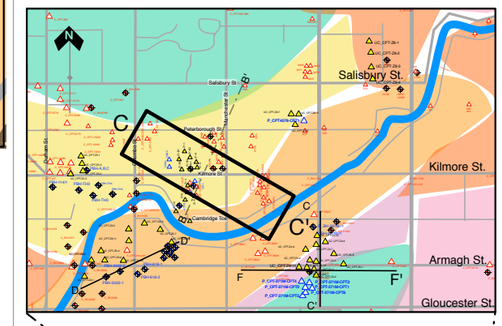

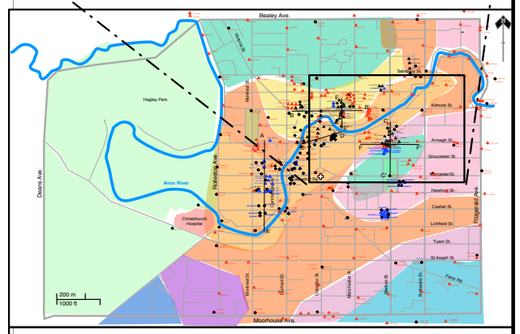

Profiles of $CRR_{7.5}$ and $CRR_{7.5}$ vs. $CSR_{7.5}$ from recent Christchurch and future scenario earthquakes.
Northwest-Southeast Transect
Christchurch CBD

Figure 2.19: Section C-C', Kilmore Street Area. CPT-based estimate of CRR, and comparison of CRR to CSR from significant earthquakes.

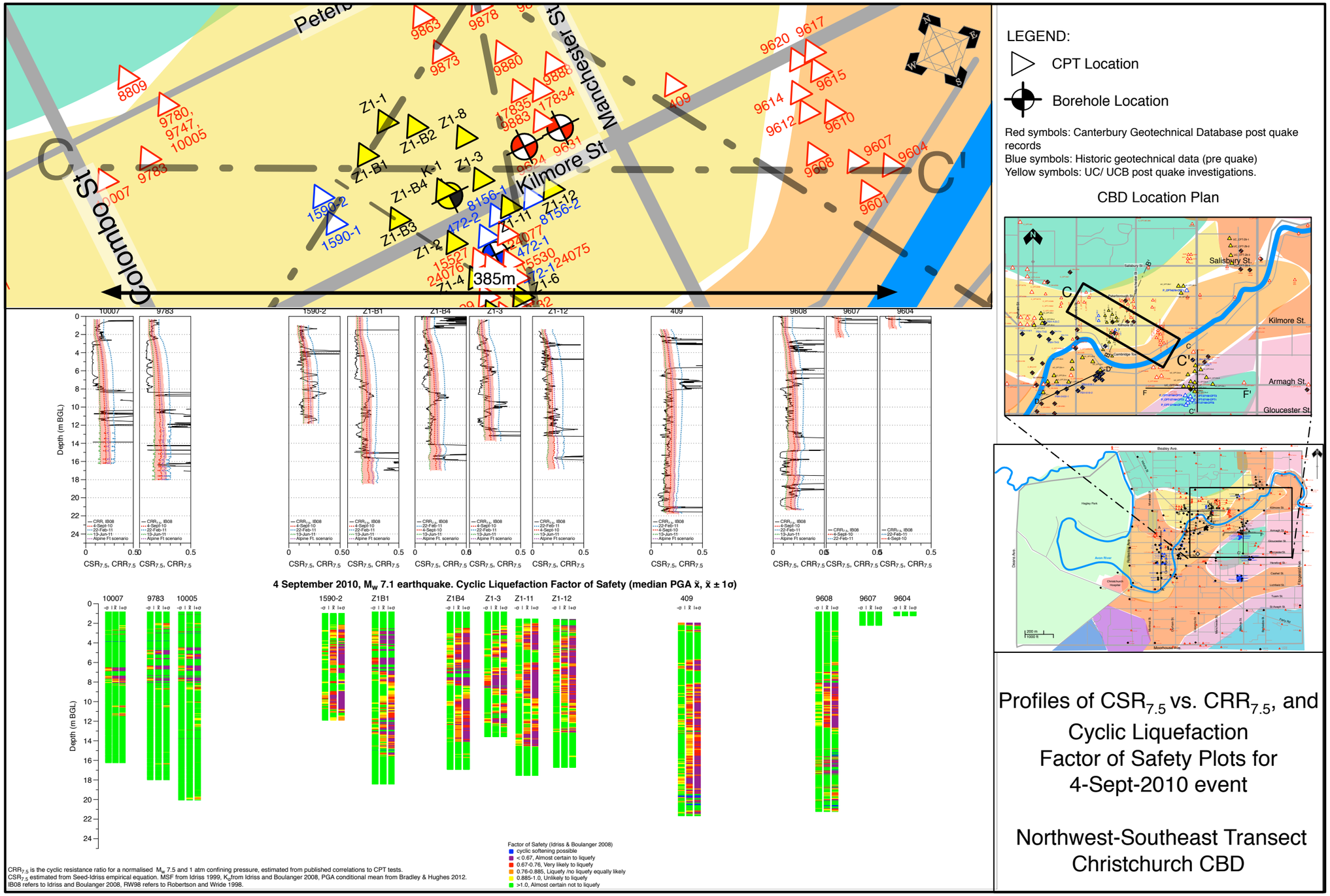

Figure 2.20: Section C-C', Kilmore Street Area. CPT-based estimate of CRR compared to CSR, and Factor of Safety plots for 4 September 2010 Event.

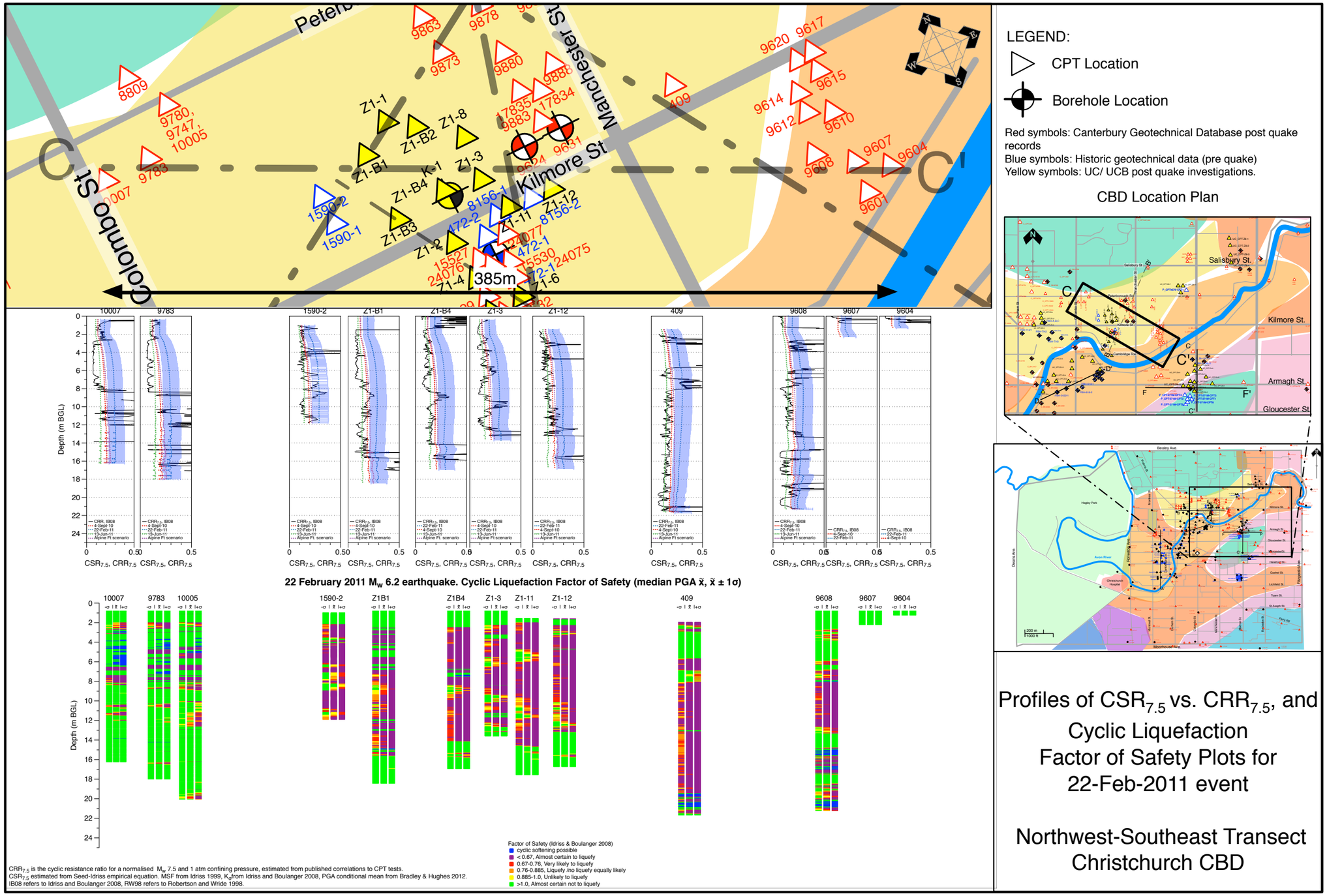

Figure 2.21: Section C-C', Kilmore Street Area. CPT-based estimate of CRR compared to CSR, and Factor of Safety plots for 22 February 2011 Event

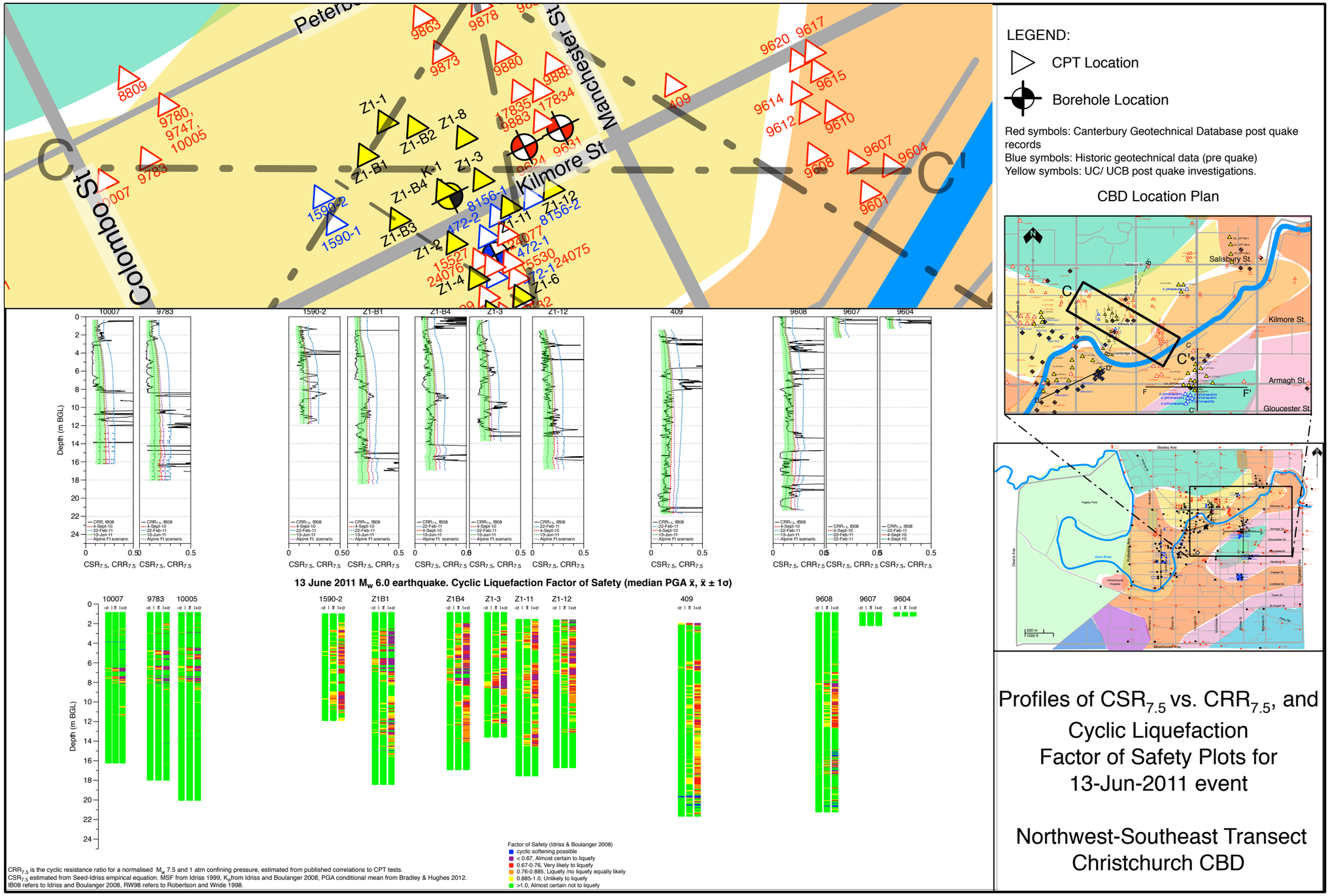

Figure 2.22: Section C-C', Kilmore Street Area. CPT-based estimate of CRR compared to CSR, and Factor of Safety plots for 13 June 2011 Event.

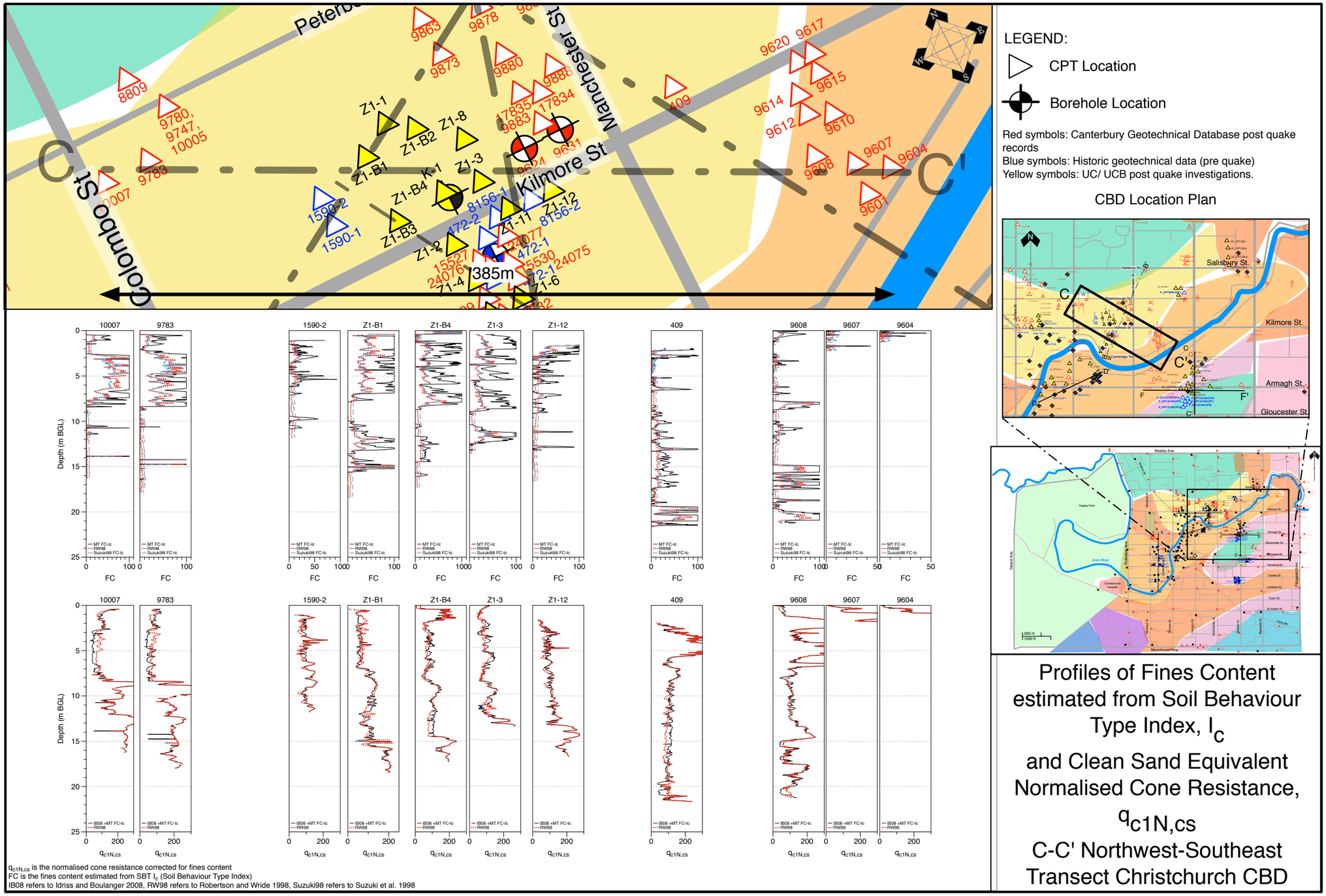

Figure 2.23: Section C-C', Kilmore Street Area. Interpreted fines content profiles, and 'clean sand equivalent' normalised cone resistance, q_{c1Ncs} profiles.

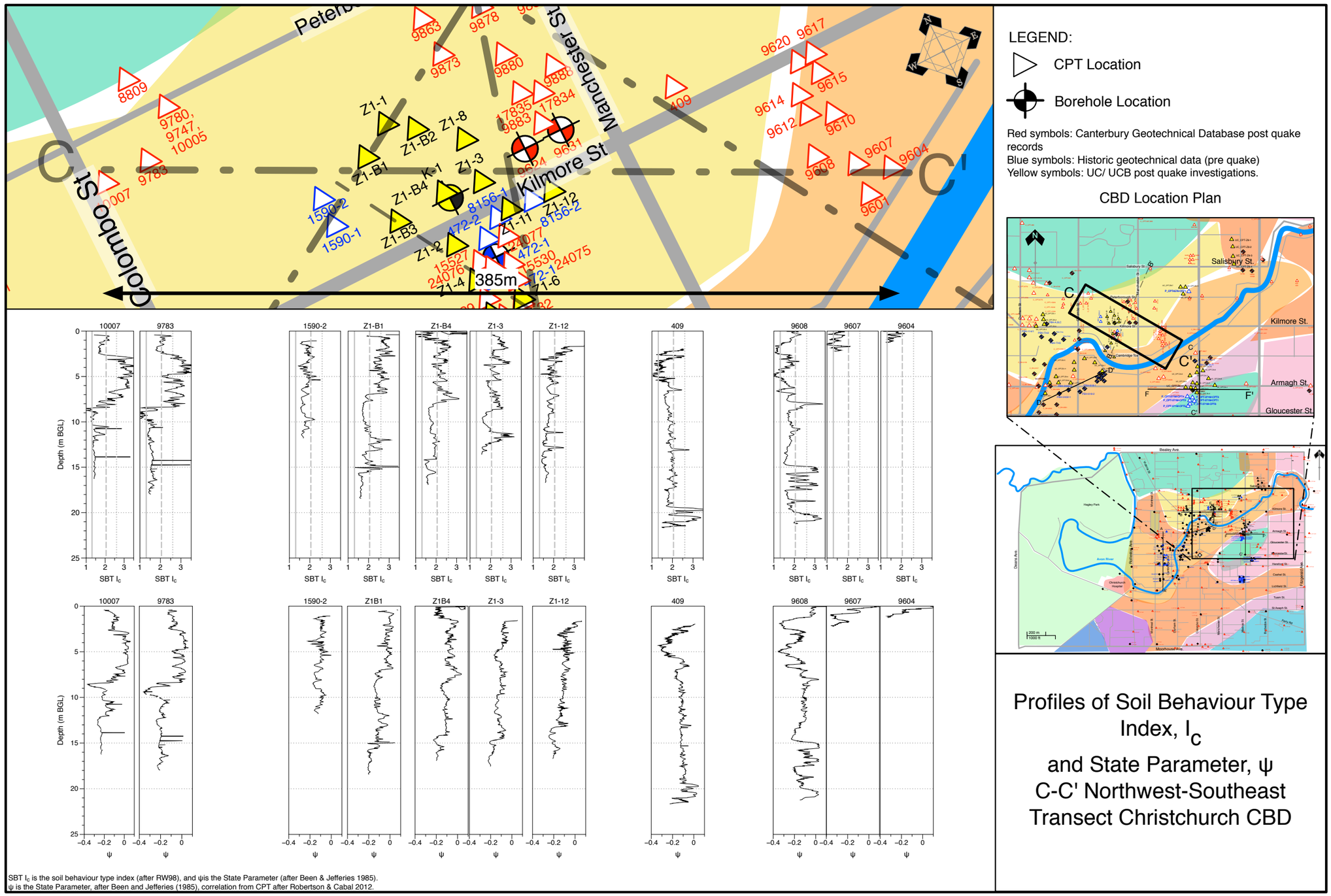

Figure 2.24: Section C-C', Kilmore Street Area. CPT-based Soil Behaviour Type Index I_c profile and State Parameter ψ interpreted from CPT.

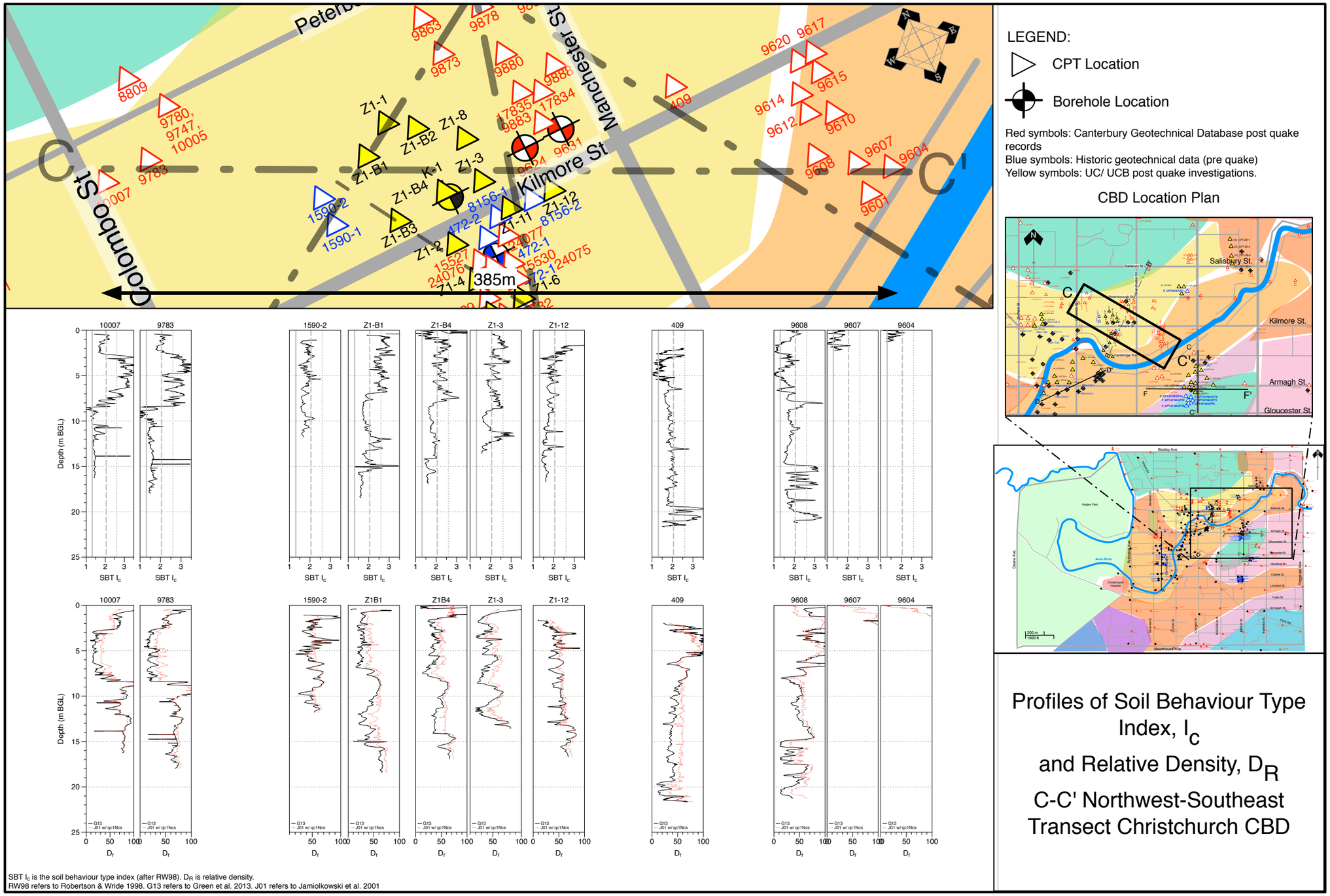

Figure 2.25: Section C-C', Kilmore Street Area. CPT-based Soil Behaviour Type Index I_c profile and Relative Density, D_R interpreted from CPT

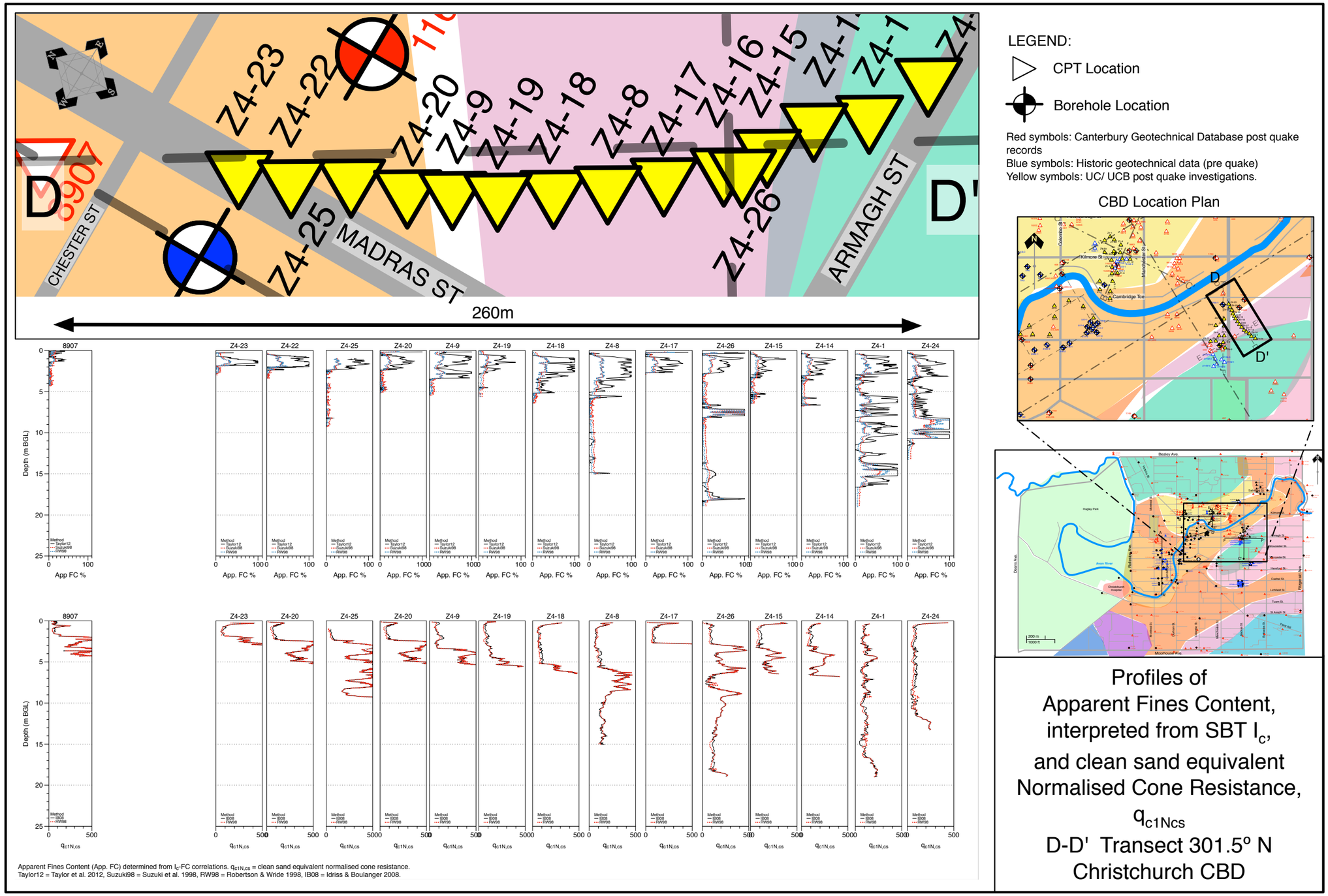

Apparent Fines Content (App. FC) determined from I_c-FC correlations. $q_{c1N,cs}$ = clean sand equivalent normalised cone resistance.
Taylor12 = Taylor et al. 2012, Suzuki98 = Suzuki et al. 1998, RW98 = Robertson & Wride 1998, IB08 = Idriss & Boulanger 2008.

Figure 2.27: Section D-D', Madras-Armagh Street Area. Interpreted fines content profiles, and 'clean sand equivalent' normalised cone resistance, q_{c1Ncs} profiles.

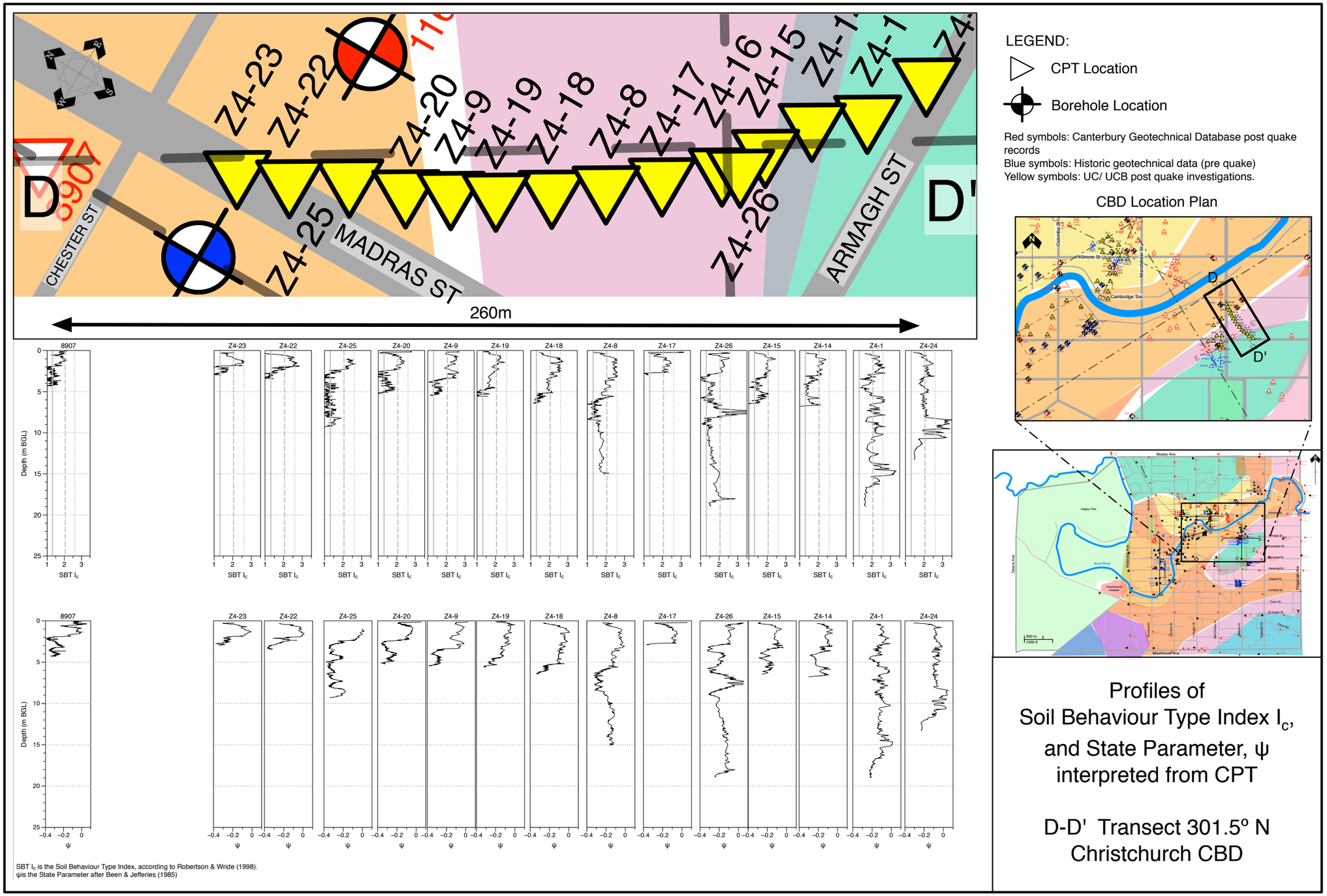

Figure 2.28: Section D-D', Madras-Armagh Street Area. CPT-based Soil Behaviour Type Index I_c profile and State Parameter ψ interpreted from CPT.

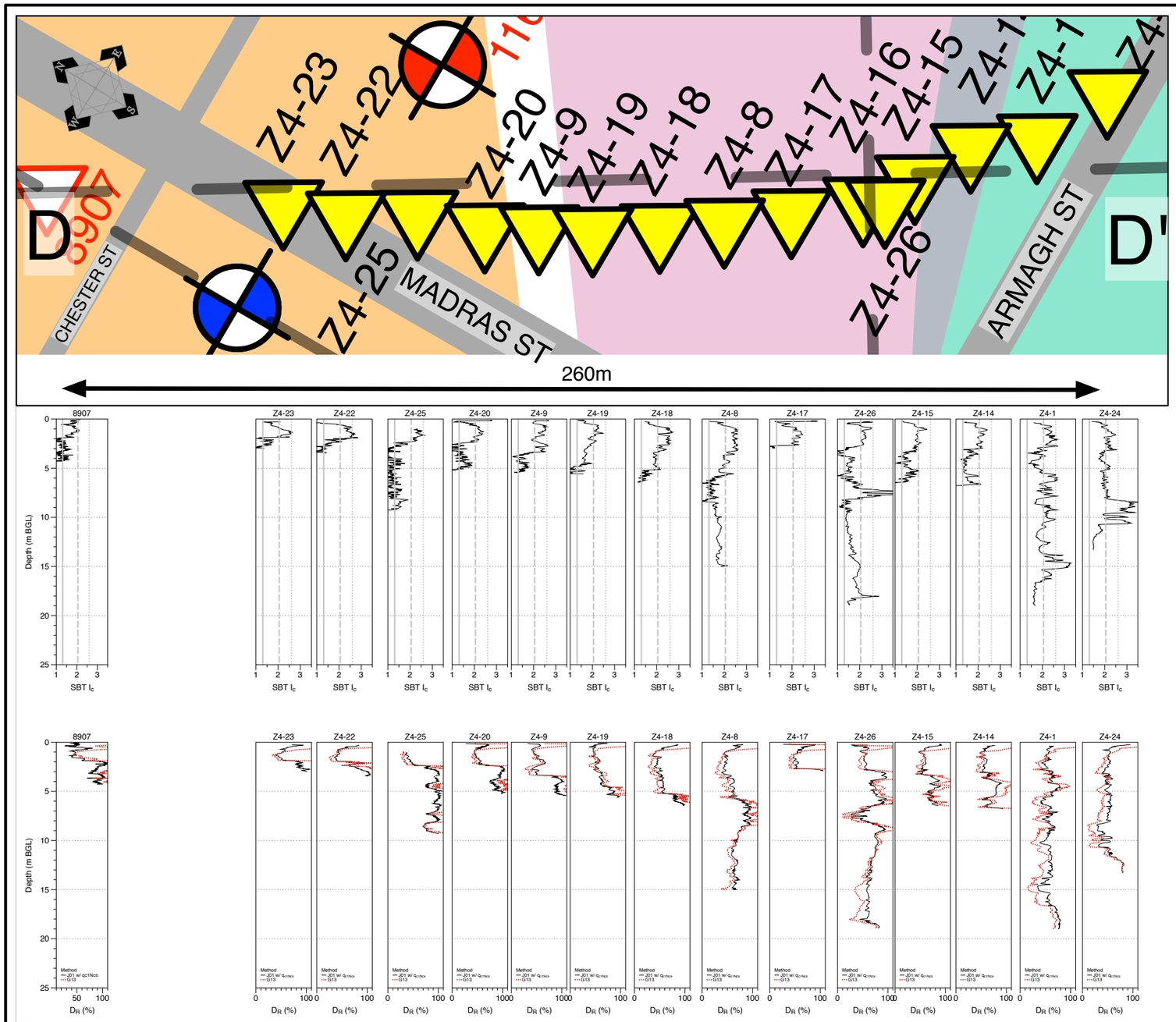

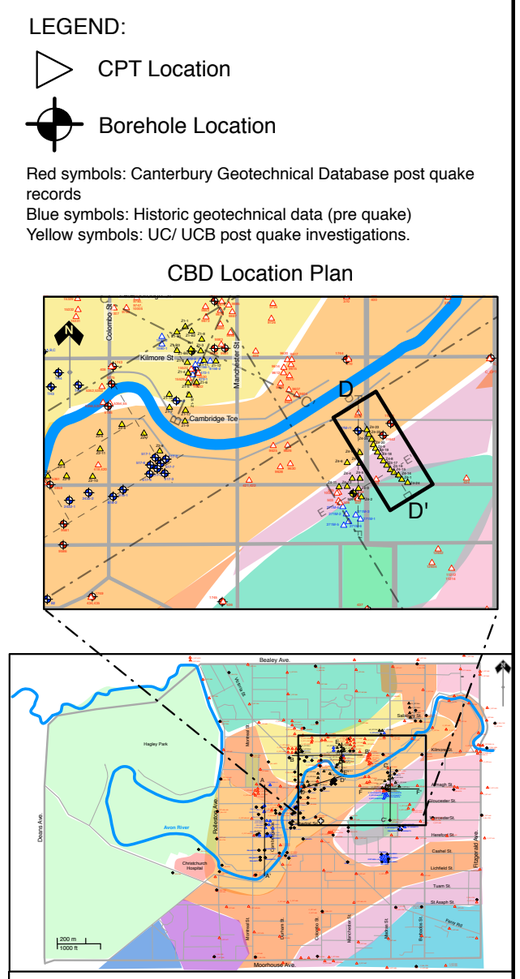

Figure 2.29: Section D-D', Madras-Armagh Street Area. CPT-based Soil Behaviour Type Index I_c profile and Relative Density, D_R interpreted from CPT

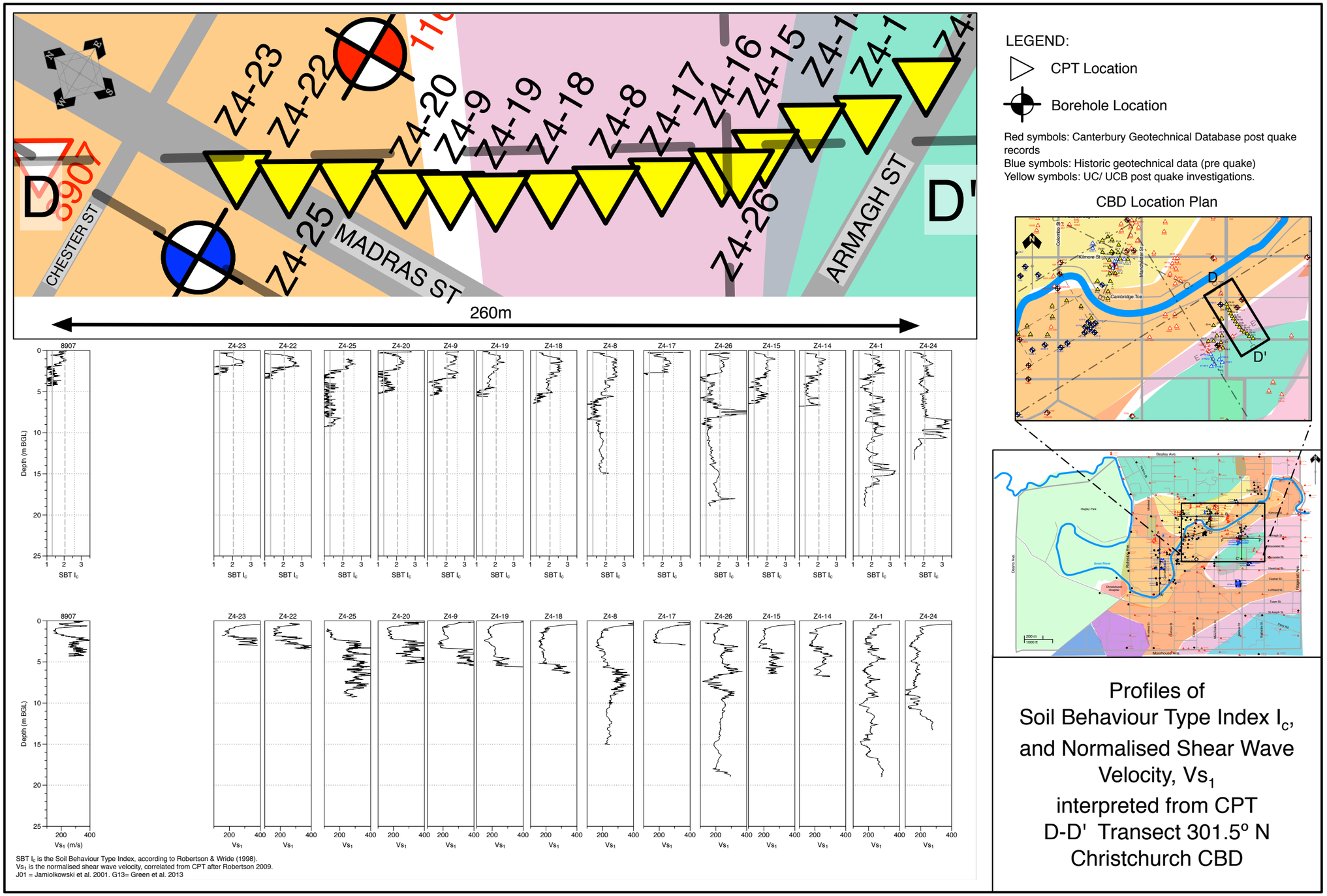

Figure 2.30: Section D-D', Madras-Armagh Street Area. CPT-based Soil Behaviour Type Index I_c profile and Shear Wave Velocity, V_s interpreted from CPT

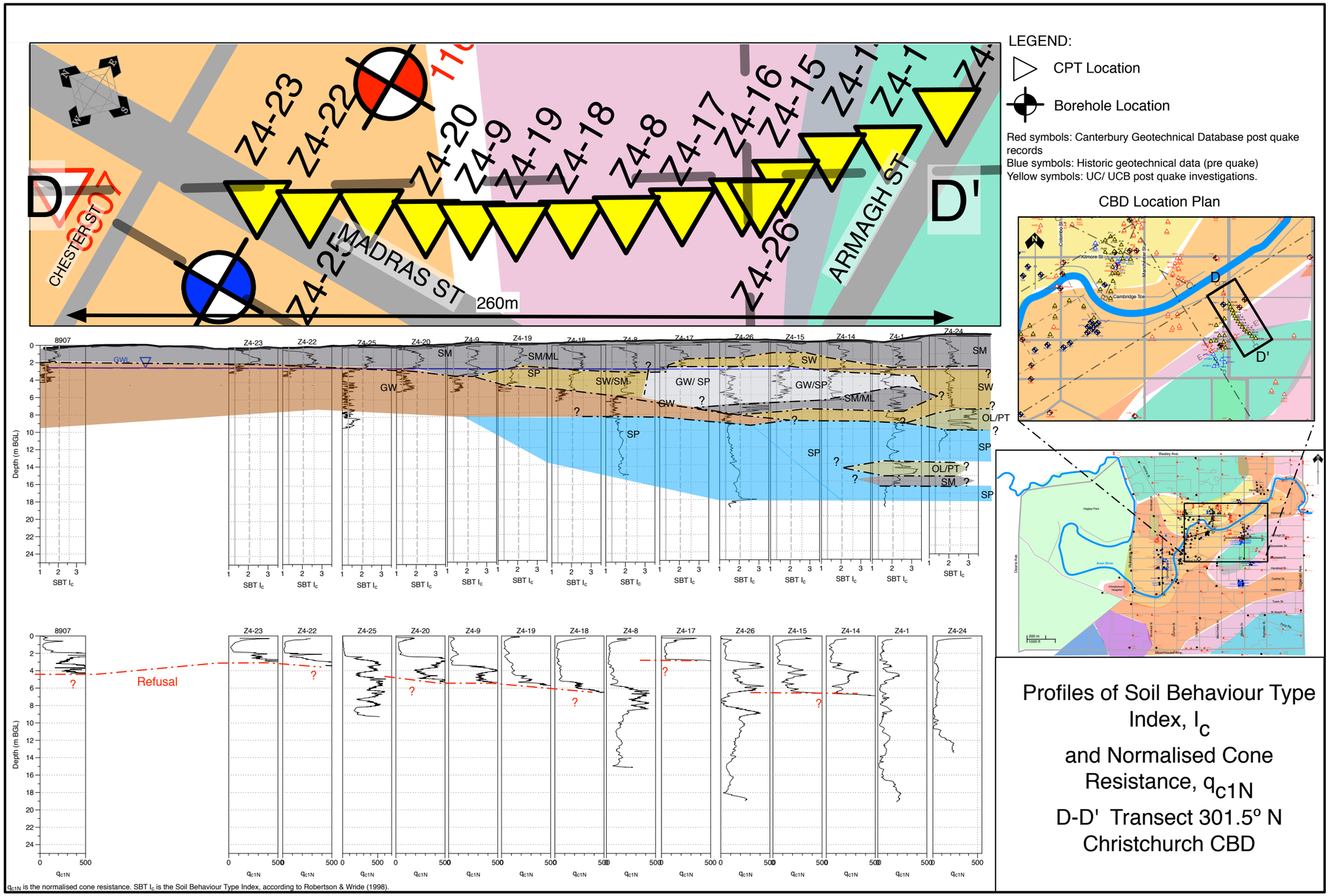

Figure 2.31: Section D-D', Madras-Armagh Street Area. Geological interpretation based on CPT-based Soil Behaviour Type Index I_c profiles (with shading).

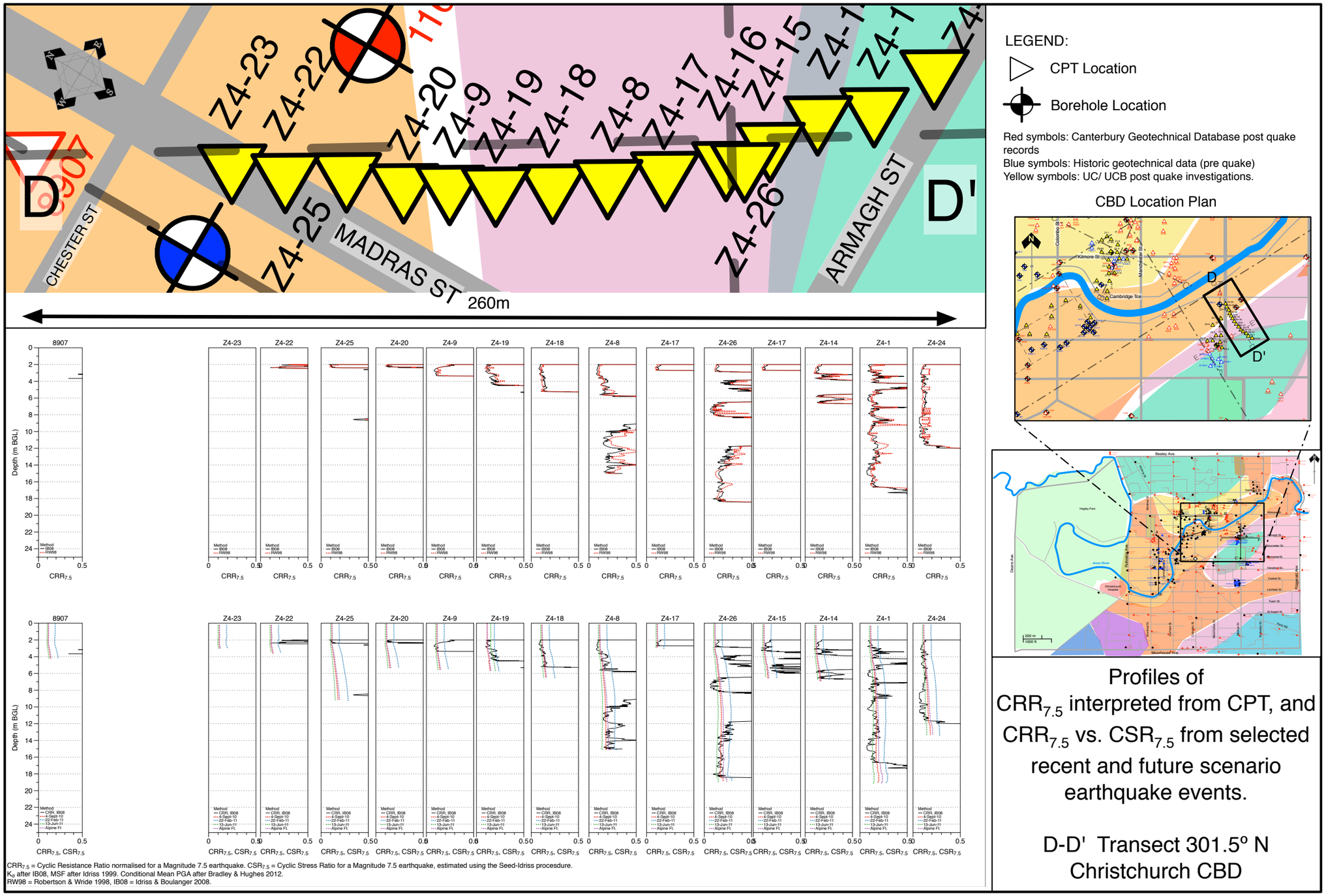

CRR$_{7.5}$ = Cyclic Resistance Ratio normalised for a Magnitude 7.5 earthquake. CSR$_{7.5}$ = Cyclic Stress Ratio for a Magnitude 7.5 earthquake, estimated using the Seed-Idriss procesdure.
K_σ after IB08, MSF after Idriss 1999. Conditional Mean PGA after Bradley & Hughes 2012.
RW98 = Robertson & Wride 1998, IB08 = Idriss & Boulanger 2008.

Figure 2.32: Section D-D', Madras-Armagh Street Area. CPT-based estimate of CRR, and comparison of CRR to CSR from significant earthquakes.

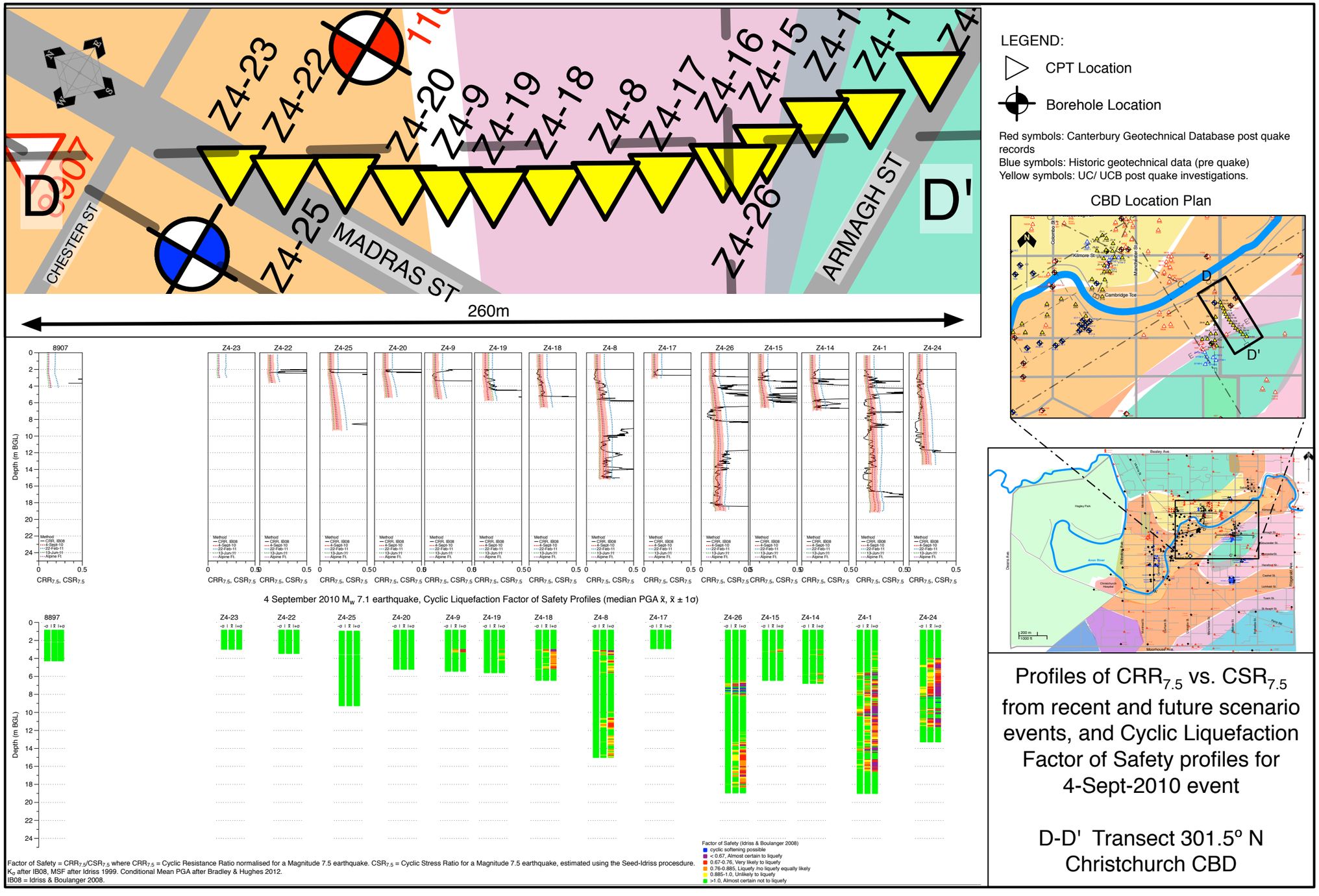

Figure 2.33: Section D-D', Madras-Armagh Street Area. CPT-based estimate of CRR compared to CSR, and Factor of Safety plots for 4 September 2010 Event

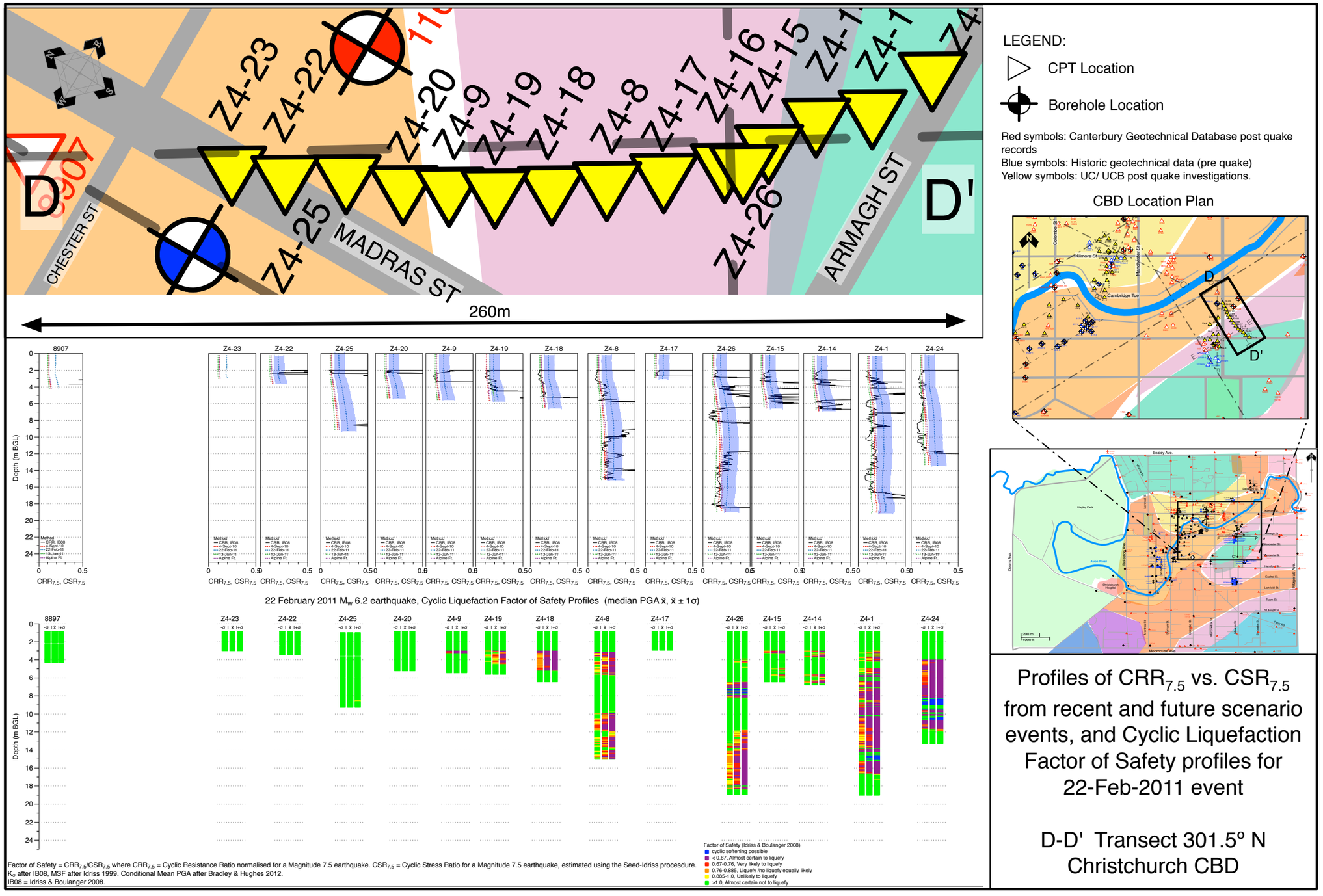

Figure 2.34: Section D-D', Kilmore Street Area. CPT-based estimate of CRR compared to CSR, and Factor of Safety plots for 22 February 2011 Event

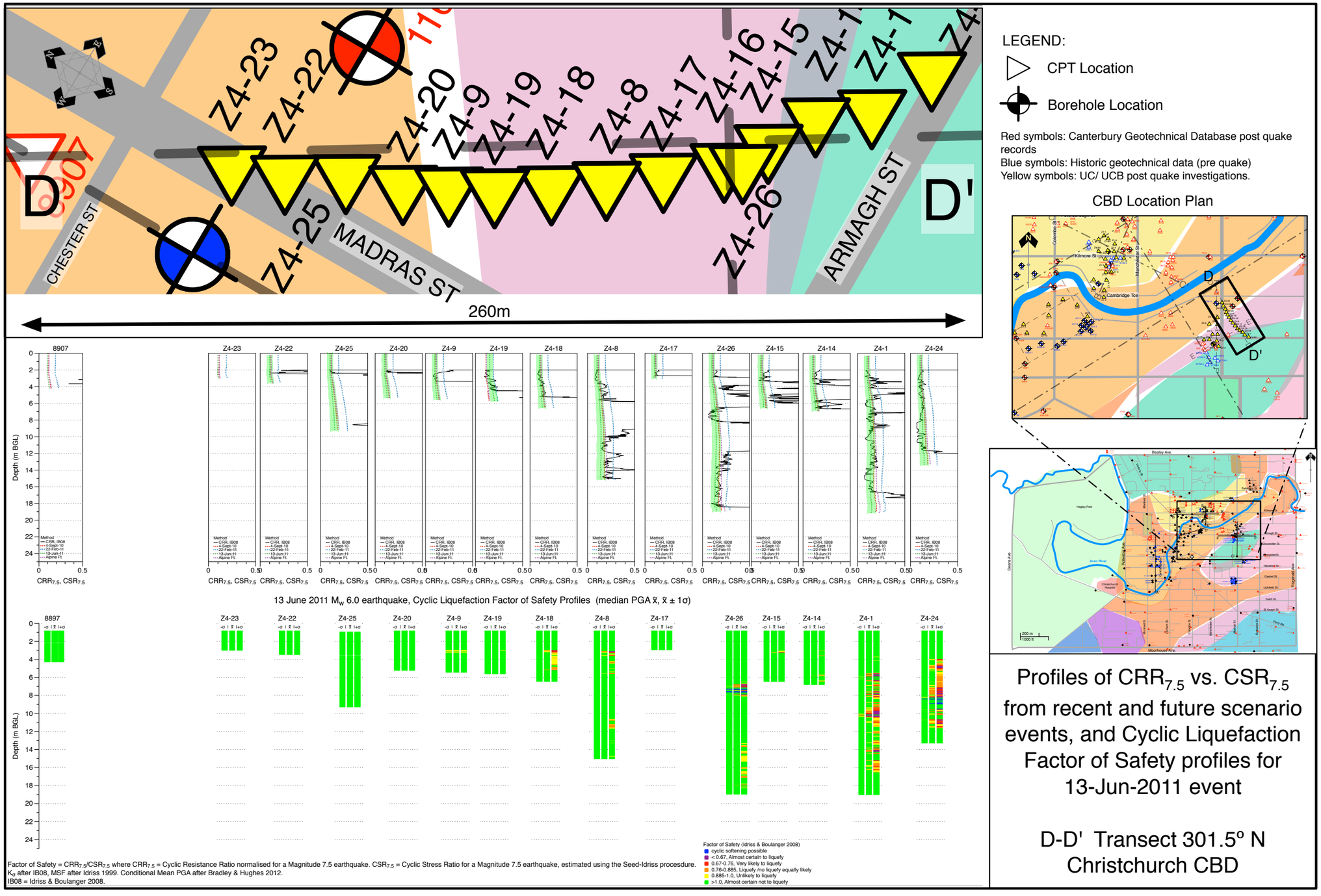

Figure 2.35: Section D-D', Kilmore Street Area. CPT-based estimate of CRR compared to CSR, and Factor of Safety plots for 13 June 2011 Event.

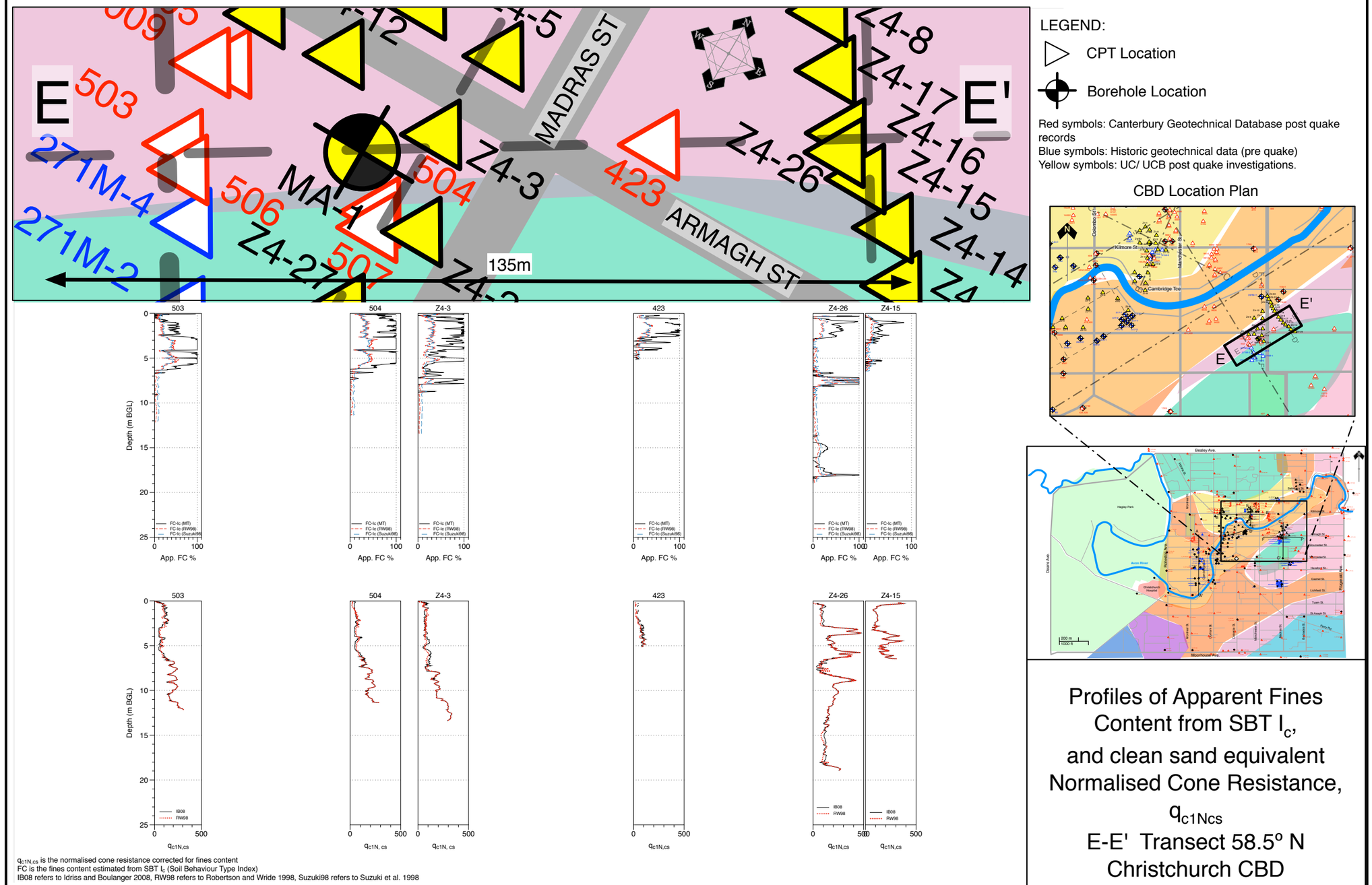

$q_{c1N,cs}$ is the normalised cone resistance corrected for fines content
FC is the fines content estimated from SBT I_c (Soil Behaviour Type Index)
IB08 refers to Idriss and Boulanger 2008, RW98 refers to Robertson and Wride 1998, Suzuki98 refers to Suzuki et al. 1998

Profiles of Apparent Fines Content from SBT I_c, and clean sand equivalent Normalised Cone Resistance, q_{c1Ncs}
E-E' Transect 58.5° N
Christchurch CBD

Figure 2.36: Section E-E', Madras-Armagh Street Area. Interpreted fines content profiles, and 'clean sand equivalent' normalised cone resistance, q_{c1Ncs} profiles.

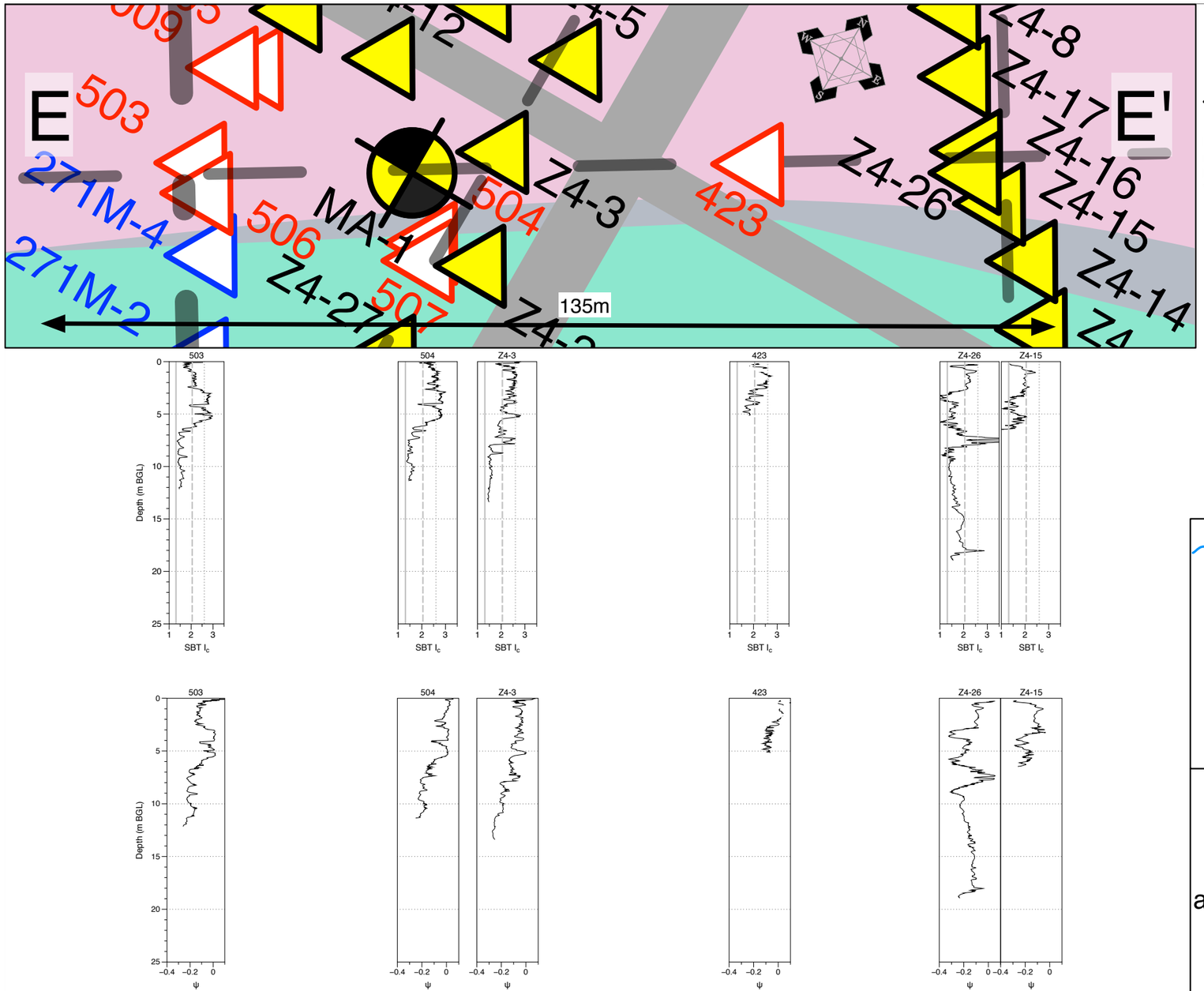

LEGEND:

CPT Location

Borehole Location

Red symbols: Canterbury Geotechnical Database post quake records
Blue symbols: Historic geotechnical data (pre quake)
Yellow symbols: UC/ UCB post quake investigations.

CBD Location Plan

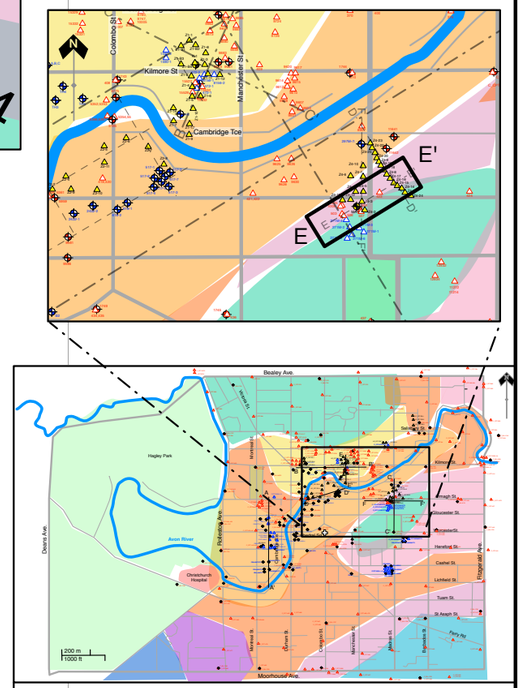

Profiles of Soil Behaviour Type Index, I_c
and State Parameter, ψ from CPT

E-E' Transect 58.5º N
Christchurch CBD

ψ is the State Parameter after Been & Jefferies (1985). Correlation from CPT after Robertson & Cabal 2012.
SBT I_c is the Soil Behaviour Type Index, according to Robertson & Wride (1998).

Figure 2.37: Section E-E', Madras-Armagh Street Area. CPT-based Soil Behaviour Type Index I_c profile and State Parameter ψ interpreted from CPT.

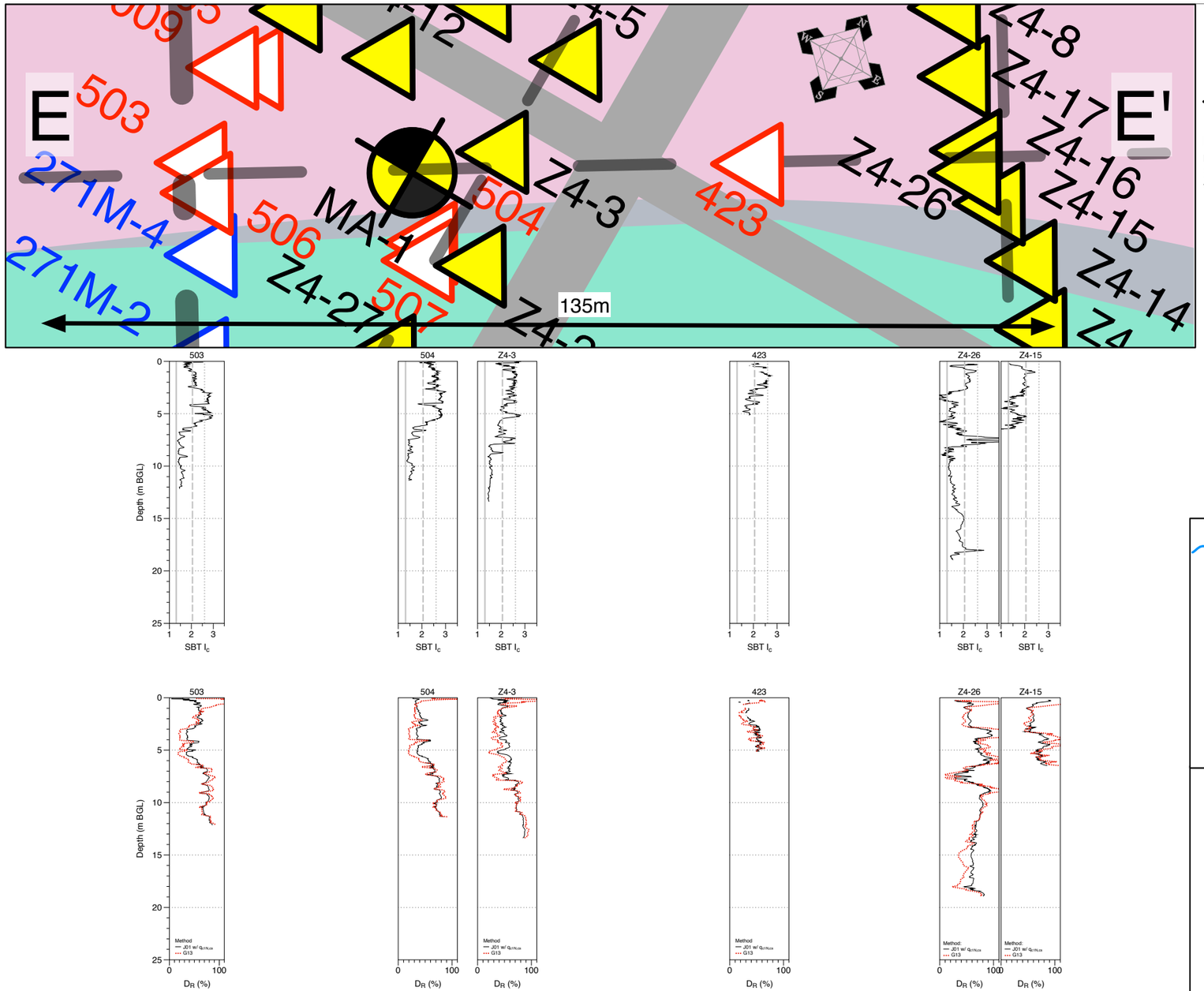

D_R is the relative density. J01 refers to Jamiolkowski et al. 2001. G13 refers to Green et al. 2013.
SBT I_c is the Soil Behaviour Type Index, according to Robertson & Wride (1998).

LEGEND:

CPT Location

Borehole Location

Red symbols: Canterbury Geotechnical Database post quake records
Blue symbols: Historic geotechnical data (pre quake)
Yellow symbols: UC/ UCB post quake investigations.

CBD Location Plan

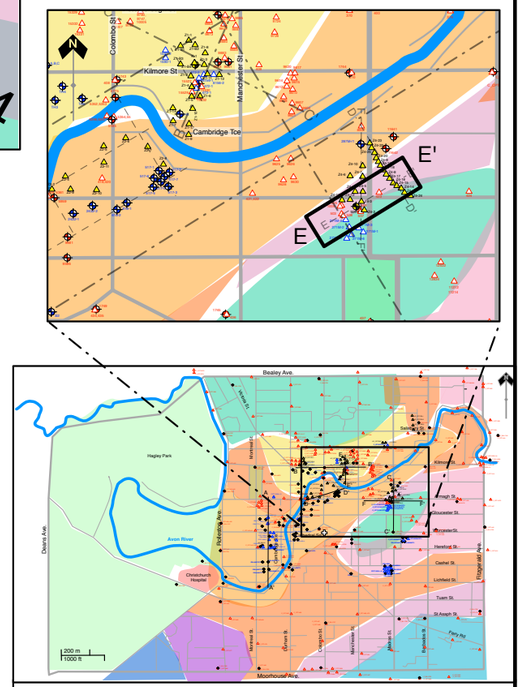

Profiles of Soil Behaviour Type Index, I_c, and Relative Density, D_R from CPT

E-E' Transect 58.5° N
Christchurch CBD

Figure 2.38: Section E-E', Madras-Armagh Street Area. CPT-based Soil Behaviour Type Index I_c profile and Relative Density, D_R interpreted from CPT

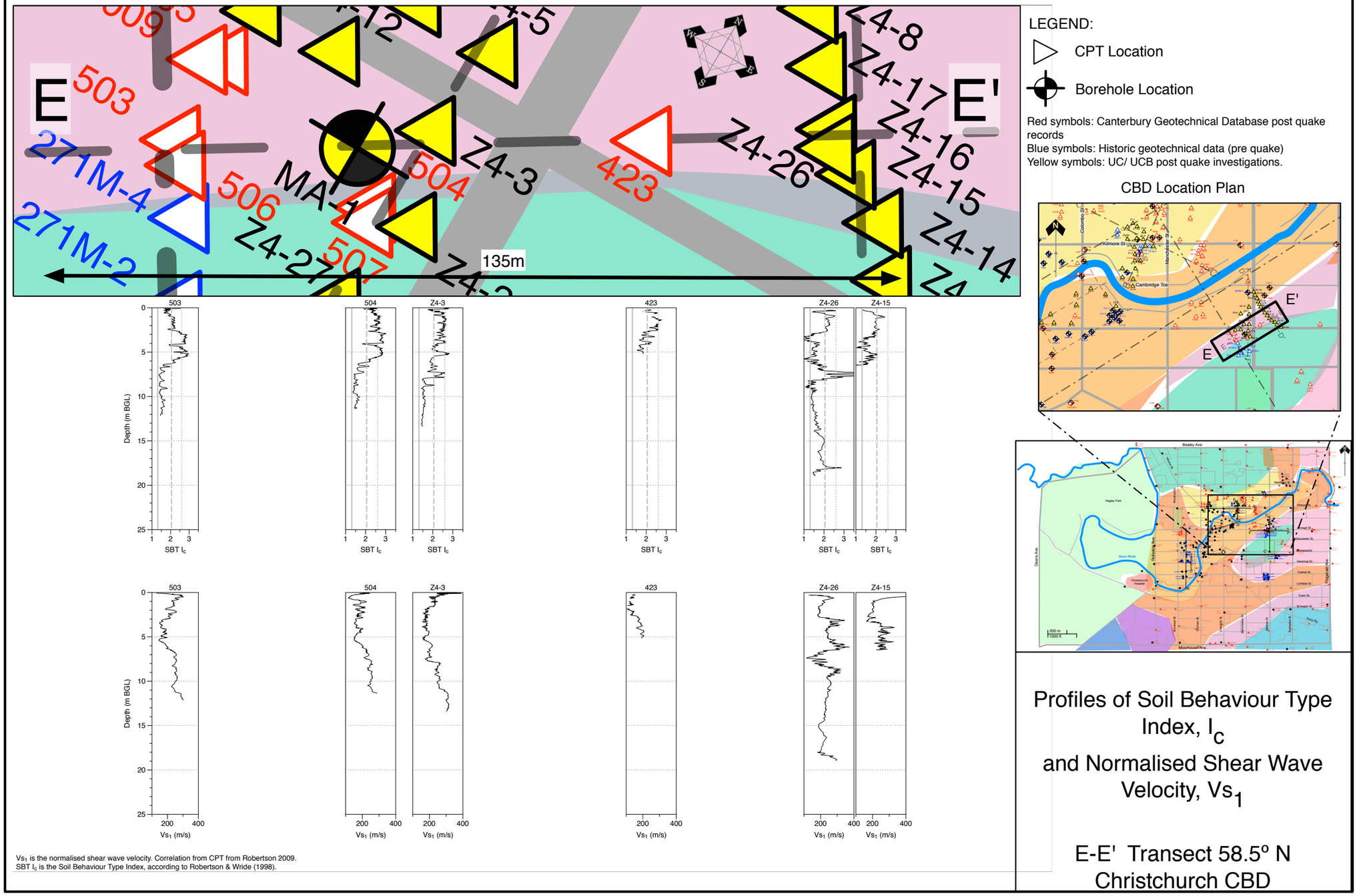

Figure 2.39: Section E-E', Madras-Armagh Street Area. CPT-based Soil Behaviour Type Index I_c profile and Shear Wave Velocity, V_s interpreted from CPT

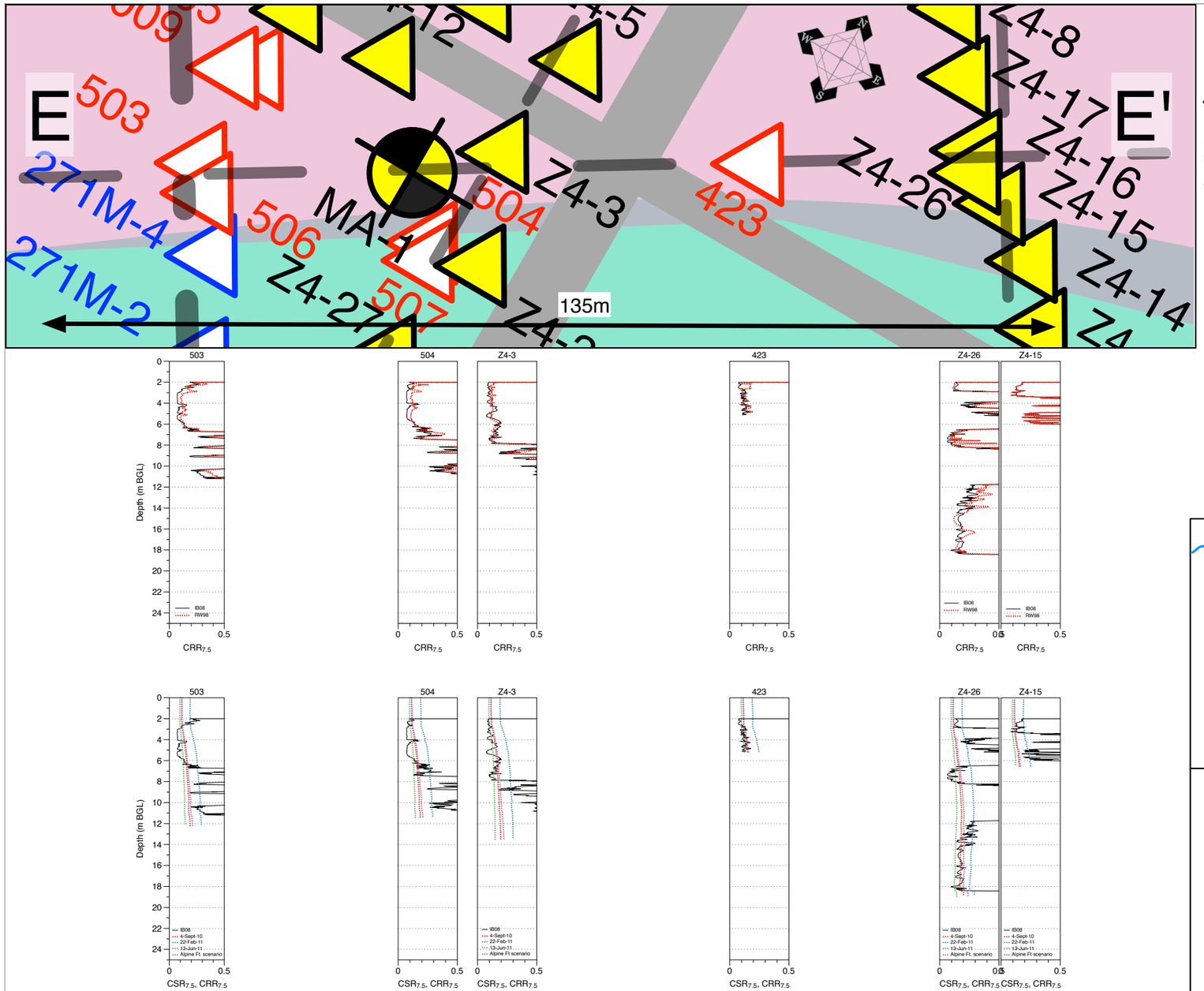

LEGEND:

CPT Location

Borehole Location

Red symbols: Canterbury Geotechnical Database post quake records
Blue symbols: Historic geotechnical data (pre quake)
Yellow symbols: UC/ UCB post quake investigations.

CBD Location Plan

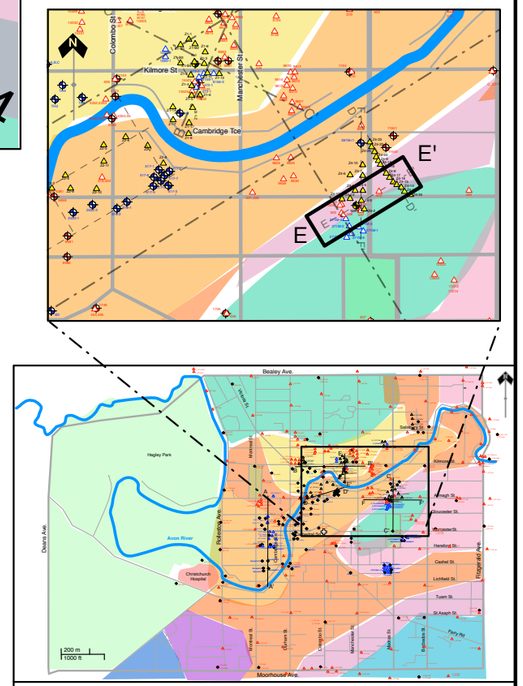

Profiles of $CRR_{7.5}$ from CPT, and $CRR_{7.5}$ vs. $CSR_{7.5}$ for scenario earthquake events.

E-E' Transect 58.5° N
Christchurch CBD

$CRR_{7.5}$ = Cyclic Resistance Ratio normalised for a Magnitude 7.5 earthquake. $CSR_{7.5}$ = Cyclic Stress Ratio for a Magnitude 7.5 earthquake, estimated using the Seed-Idriss procesdure.
K_σ after IB08, MSF after Idriss 1999. Conditional Mean PGA after Bradley & Hughes 2012.
RW98 = Robertson & Wride 1998, IB08 = Idriss & Boulanger 2008.

Figure 2.40: Section E-E', Madras-Armagh Street Area. CPT-based estimate of CRR, and comparison of CRR to CSR from significant earthquakes.

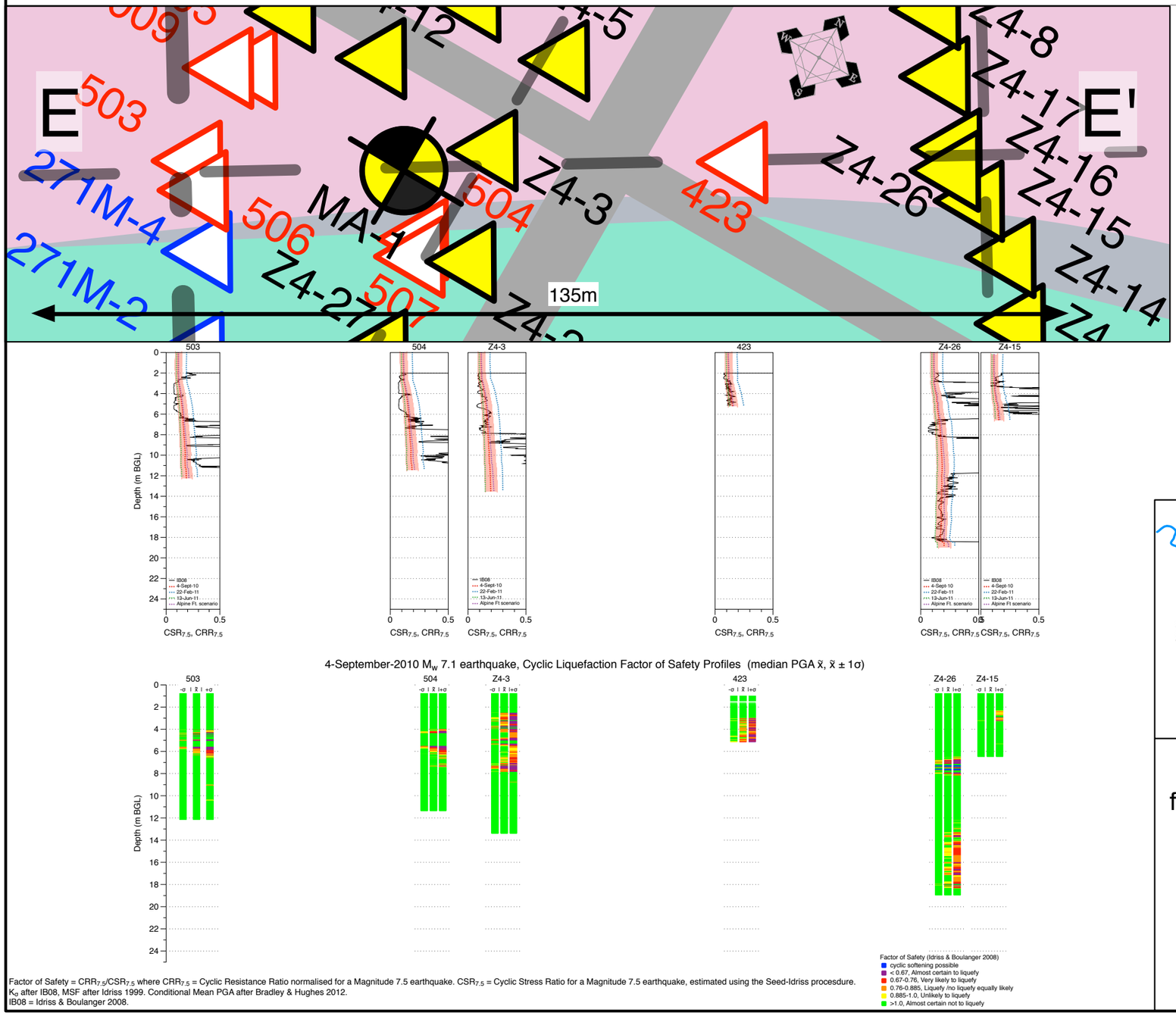

Factor of Safety = $CRR_{7.5}/CSR_{7.5}$ where $CRR_{7.5}$ = Cyclic Resistance Ratio normalised for a Magnitude 7.5 earthquake. $CSR_{7.5}$ = Cyclic Stress Ratio for a Magnitude 7.5 earthquake, estimated using the Seed-Idriss procesdure. K_σ after IB08, MSF after Idriss 1999. Conditional Mean PGA after Bradley & Hughes 2012.
IB08 = Idriss & Boulanger 2008.

LEGEND:

CPT Location

Borehole Location

Red symbols: Canterbury Geotechnical Database post quake records
Blue symbols: Historic geotechnical data (pre quake)
Yellow symbols: UC/ UCB post quake investigations.

CBD Location Plan

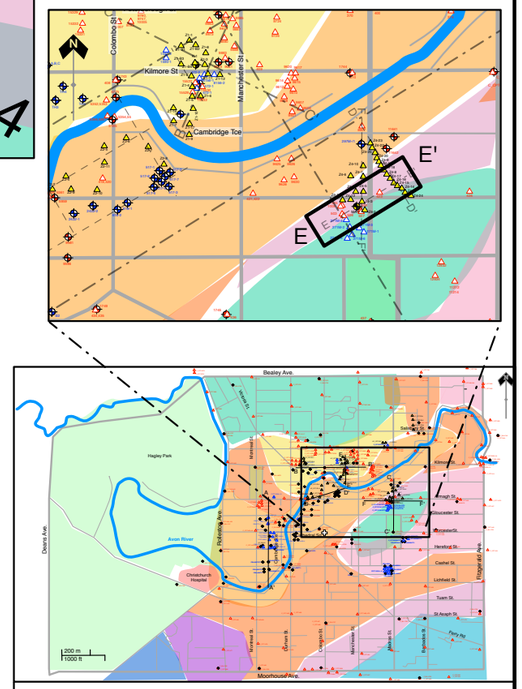

Profiles of $CRR_{7.5}$ vs. $CSR_{7.5}$ for scenario earthquake events, and Cyclic Liquefaction Factor of Safety for the 4-Sept-2010 event.

E-E' Transect 58.5° N
Christchurch CBD

Figure 2.41: Section E-E', Madras-Armagh Street Area. CPT-based estimate of CRR compared to CSR, and Factor of Safety plots for 4 September 2010 Event

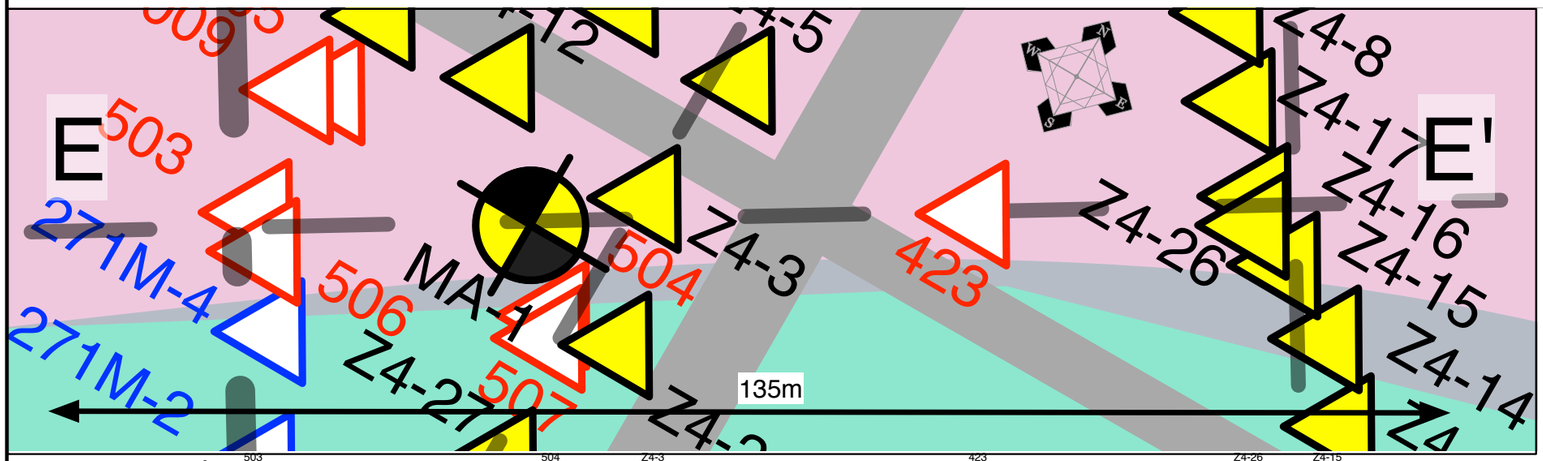

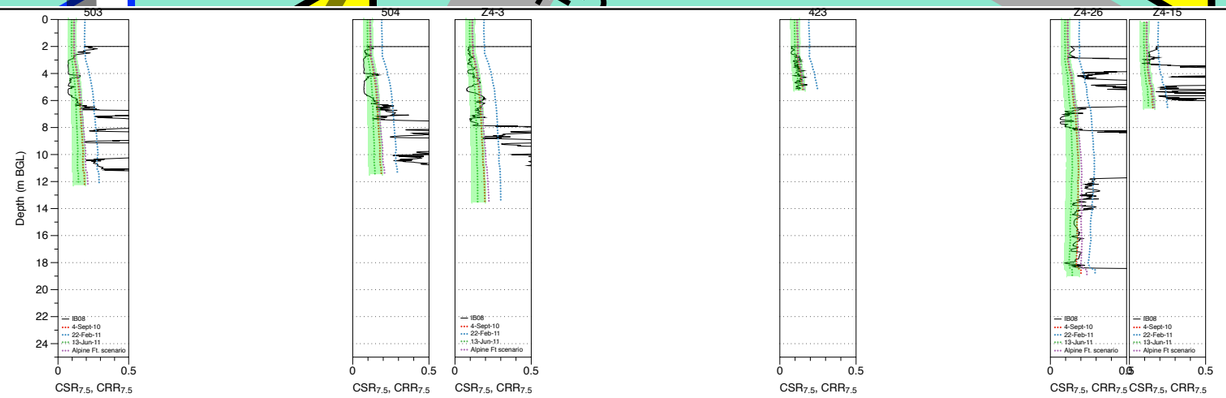

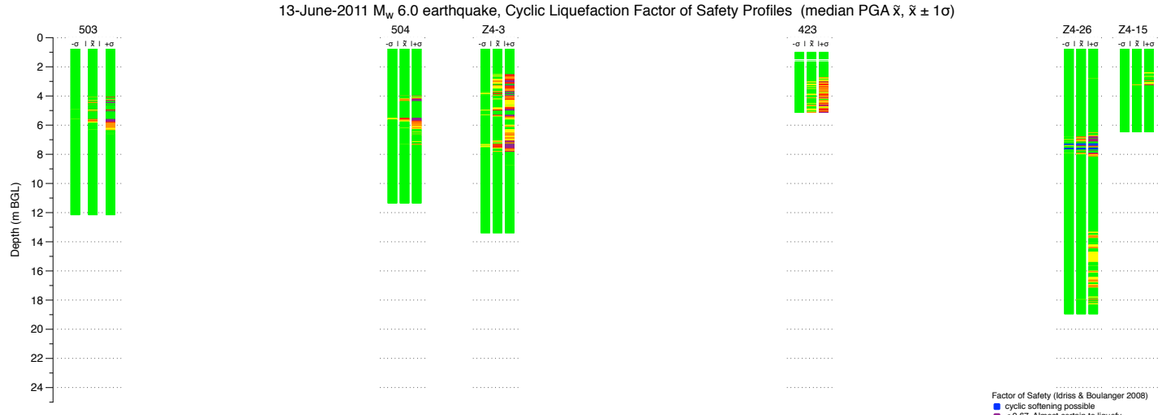

Factor of Safety = $CRR_{7.5}/CSR_{7.5}$ where $CRR_{7.5}$ = Cyclic Resistance Ratio normalised for a Magnitude 7.5 earthquake. $CSR_{7.5}$ = Cyclic Stress Ratio for a Magnitude 7.5 earthquake, estimated using the Seed-Idriss procesdure. K_σ after IB08, MSF after Idriss 1999. Conditional Mean PGA after Bradley & Hughes 2012.
IB08 = Idriss & Boulanger 2008.

LEGEND:

CPT Location

Borehole Location

Red symbols: Canterbury Geotechnical Database post quake records
Blue symbols: Historic geotechnical data (pre quake)
Yellow symbols: UC/ UCB post quake investigations.

CBD Location Plan

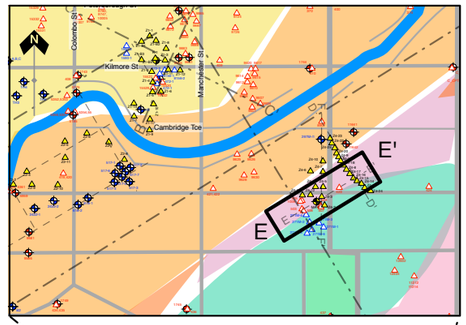

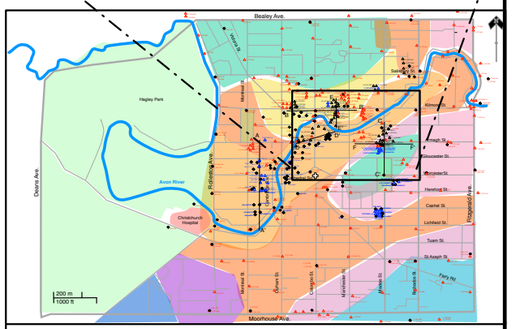

Profiles of $CRR_{7.5}$ vs. $CSR_{7.5}$ for scenario earthquake events, and Cyclic Liquefaction Factor of Safety for the 13-Jun-2011 event.

E-E' Transect 58.5° N
Christchurch CBD

Figure 2.42: Section E-E', Kilmore Street Area. CPT-based estimate of CRR compared to CSR, and Factor of Safety plots for 13 June 2011 Event.

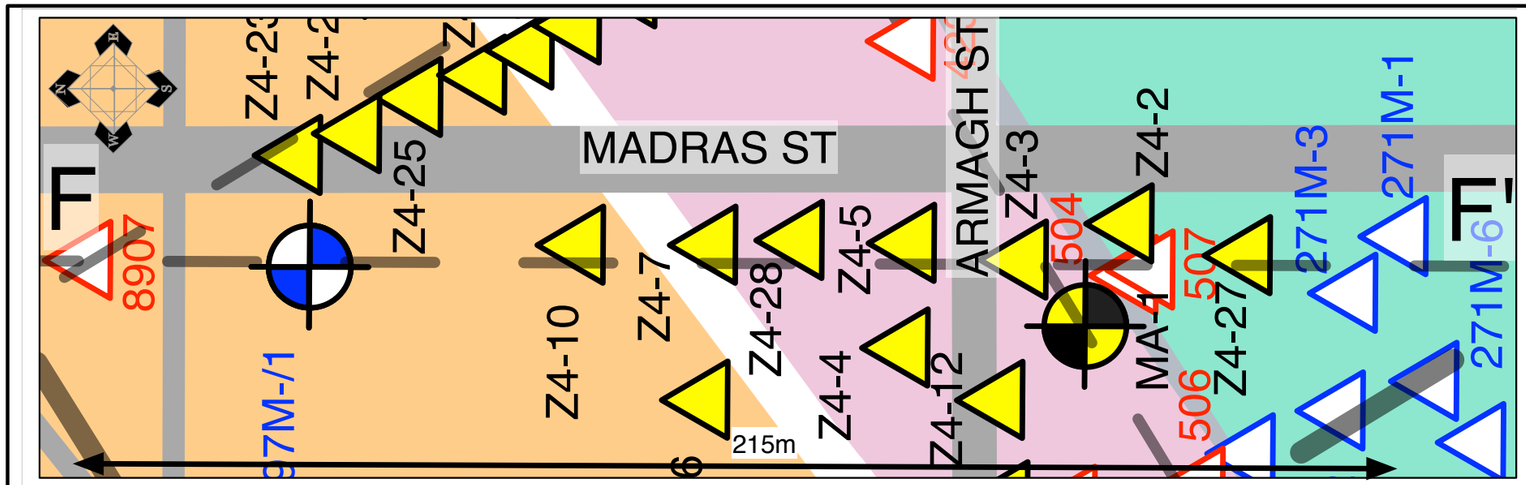

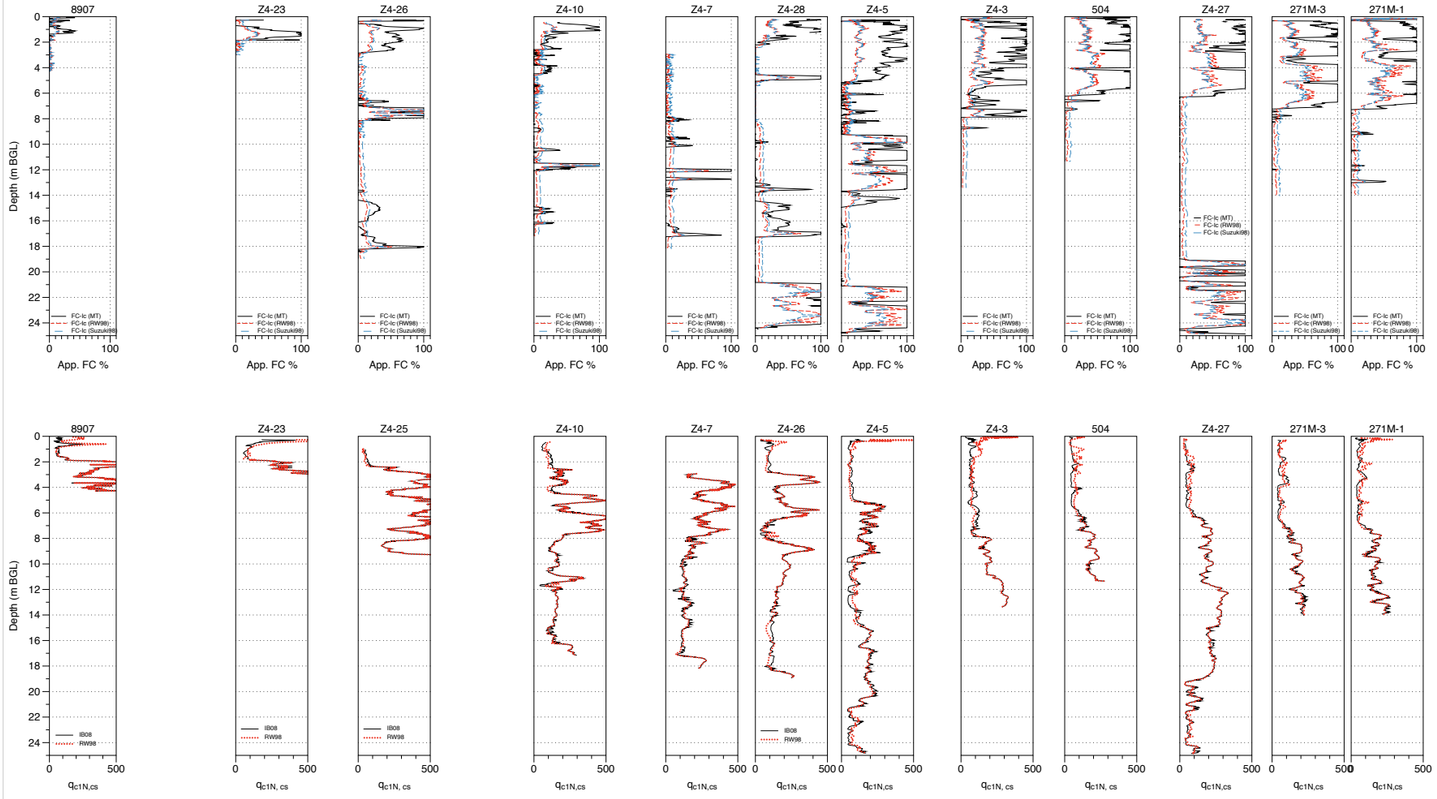

Apparent Fines Content (App. FC) determined from I_c-FC correlations. $q_{c1N,cs}$ = clean sand equivalent normalised cone resistance.
Taylor12 = Taylor et al. 2012, Suzuki98 = Suzuki et al. 1998, RW98 = Robertson & Wride 1998, IB08 = Idriss & Boulanger 2008.

LEGEND:

CPT Location

Borehole Location

Red symbols: Canterbury Geotechnical Database post quake records
Blue symbols: Historic geotechnical data (pre quake)
Yellow symbols: UC/ UCB post quake investigations.

CBD Location Plan

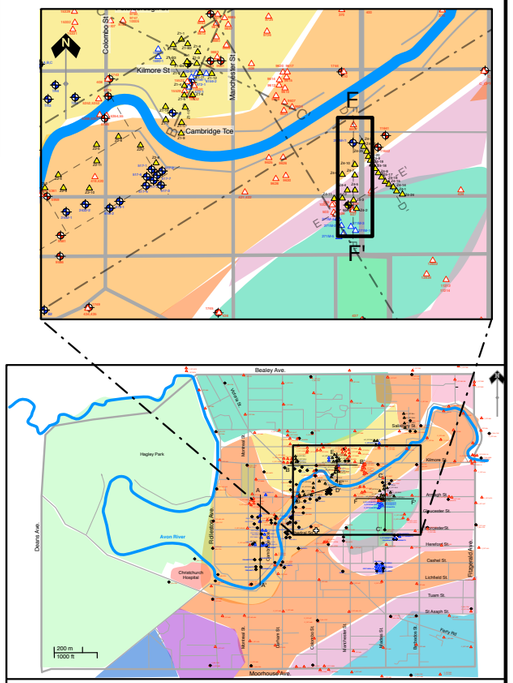

Profiles of Apparent Fines Content estimated from SBT, I_c and clean sand equivalent normalised cone resistance, q_{c1Ncs}
F-F' Transect N-S Christchurch CBD

Figure 2.43: Section F-F', Madras-Armagh Street Area. Interpreted fines content profiles, and 'clean sand equivalent' normalised cone resistance, q_{c1Ncs} profiles.

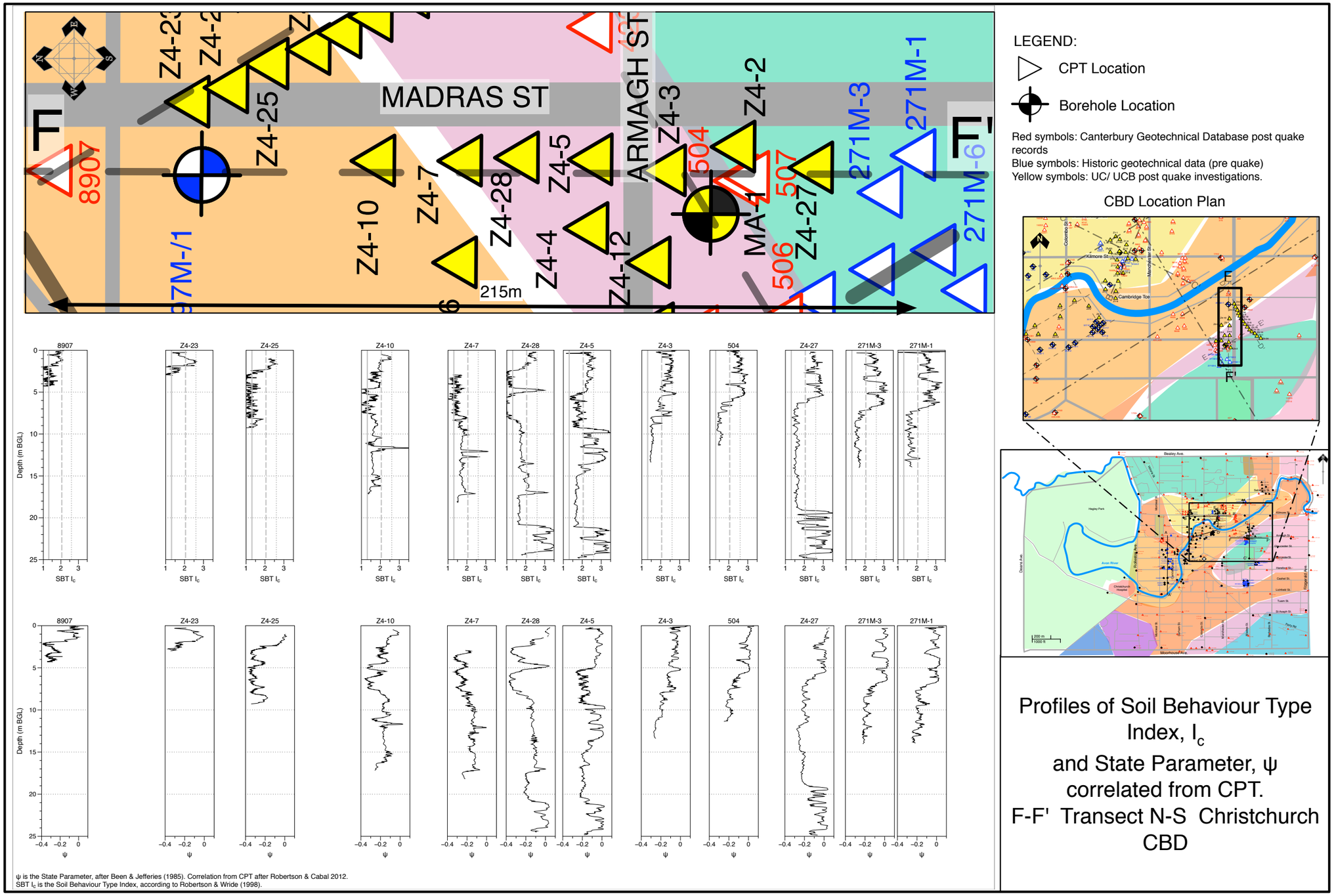

LEGEND:

CPT Location

Borehole Location

Red symbols: Canterbury Geotechnical Database post quake records
Blue symbols: Historic geotechnical data (pre quake)
Yellow symbols: UC/ UCB post quake investigations.

CBD Location Plan

Profiles of Soil Behaviour Type Index, I_c
and State Parameter, ψ
correlated from CPT.
F-F' Transect N-S Christchurch CBD

Figure 2.44: Section F-F', Madras-Armagh Street Area. CPT-based Soil Behaviour Type Index I_c profile and State Parameter ψ interpreted from CPT.

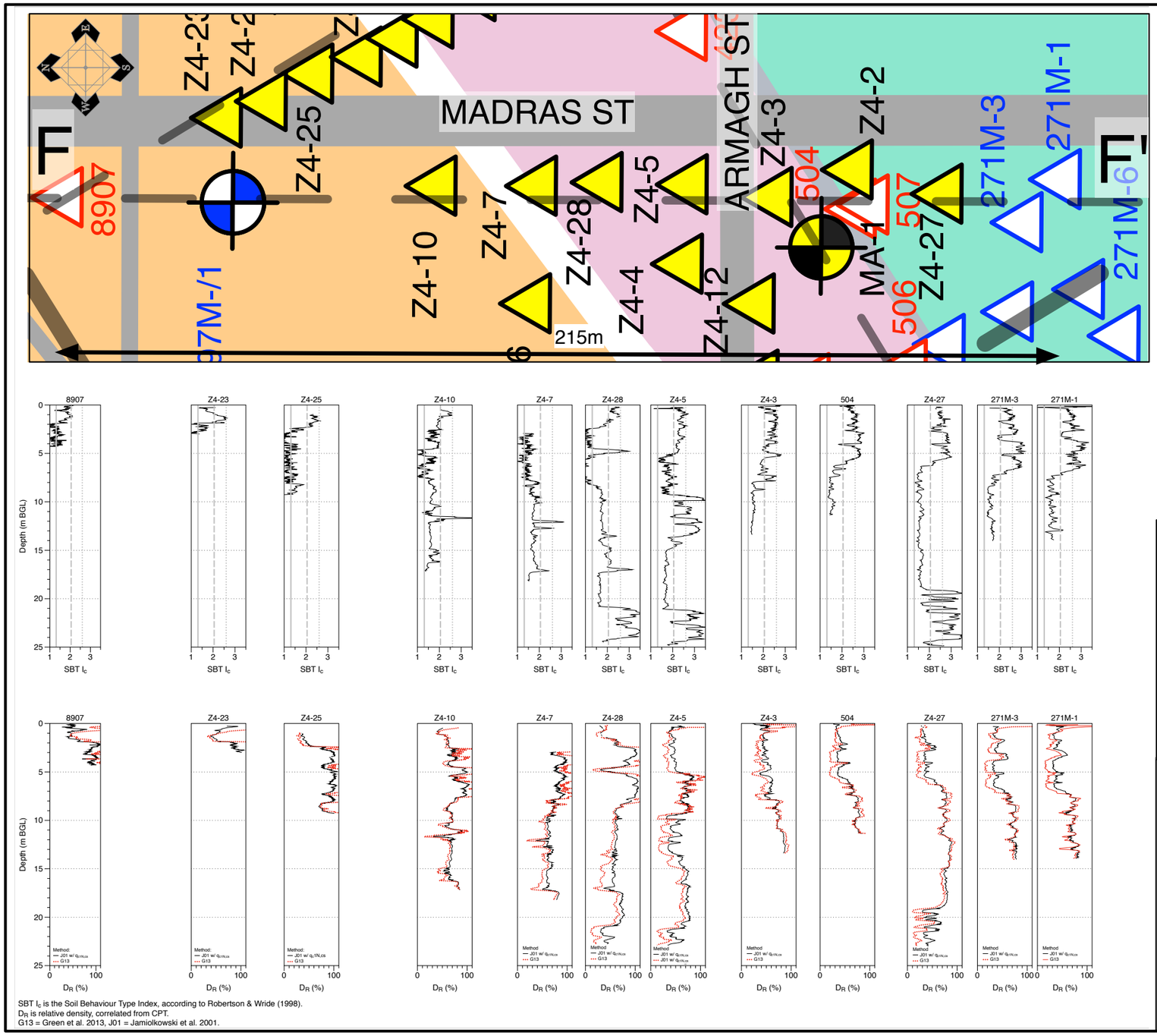

SBT I_c is the Soil Behaviour Type Index, according to Robertson & Wride (1998).
D_R is relative density, correlated from CPT.
G13 = Green et al. 2013, J01 = Jamiolkowski et al. 2001.

LEGEND:

CPT Location

Borehole Location

Red symbols: Canterbury Geotechnical Database post quake records
Blue symbols: Historic geotechnical data (pre quake)
Yellow symbols: UC/ UCB post quake investigations.

CBD Location Plan

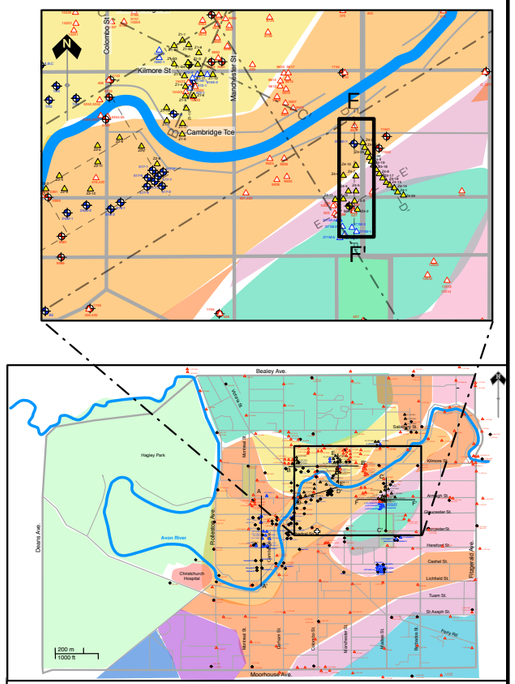

Profiles of Soil Behaviour Type Index, I_c and Relative Density, D_R correlated from CPT.
F-F' Transect N-S Christchurch CBD

Figure 2.45: Section F-F', Madras-Armagh Street Area. CPT-based Soil Behaviour Type Index I_c profile and Relative Density, D_R interpreted from CPT

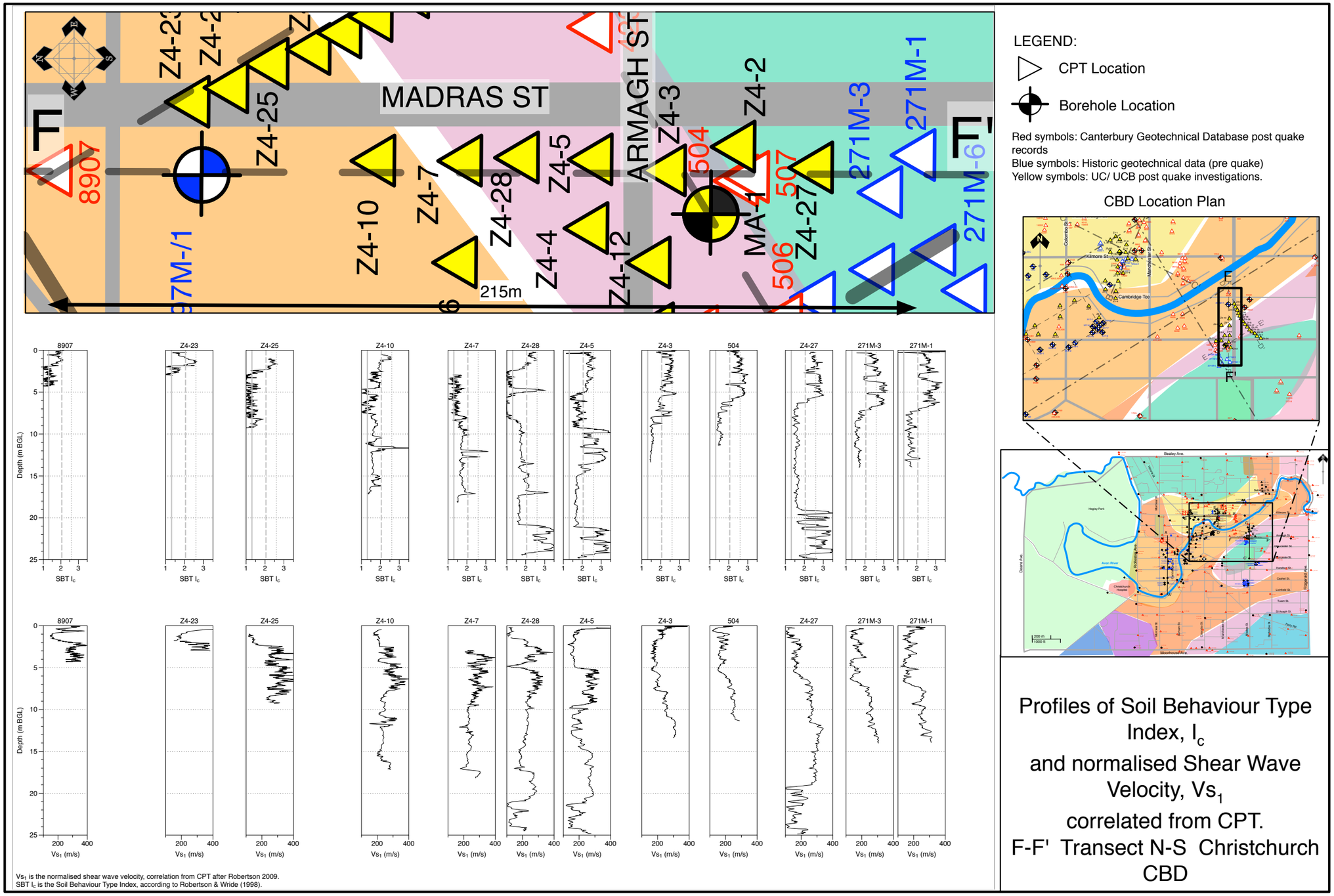

Figure 2.46: Section F-F', Madras-Armagh Street Area. CPT-based Soil Behaviour Type Index I_c profile and Shear Wave Velocity, V_s interpreted from CPT

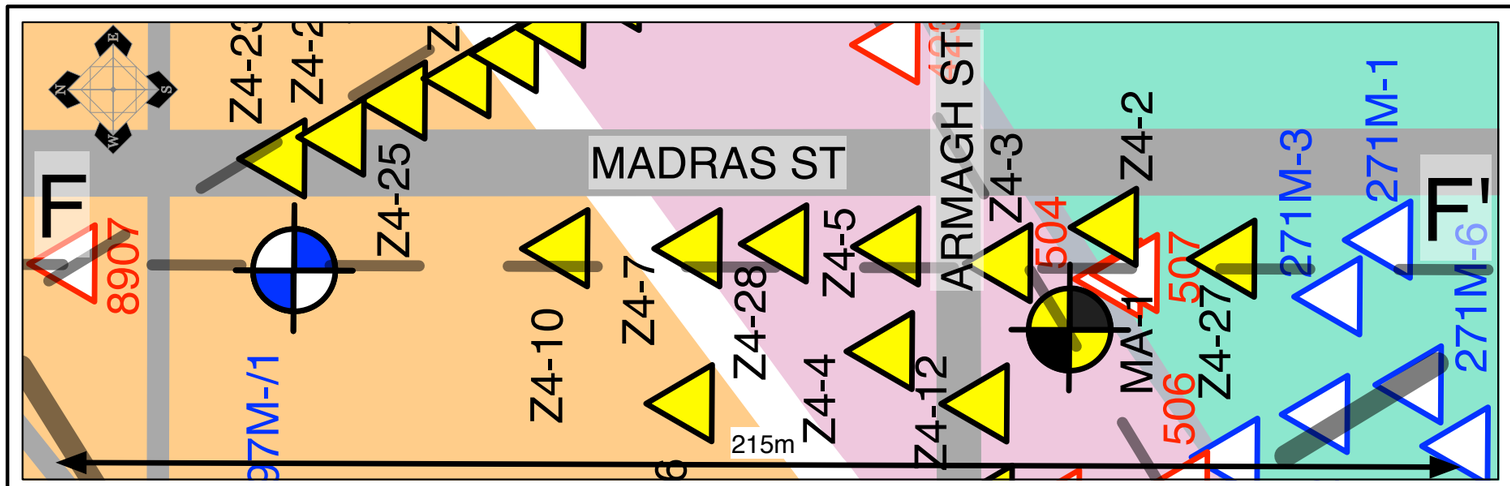

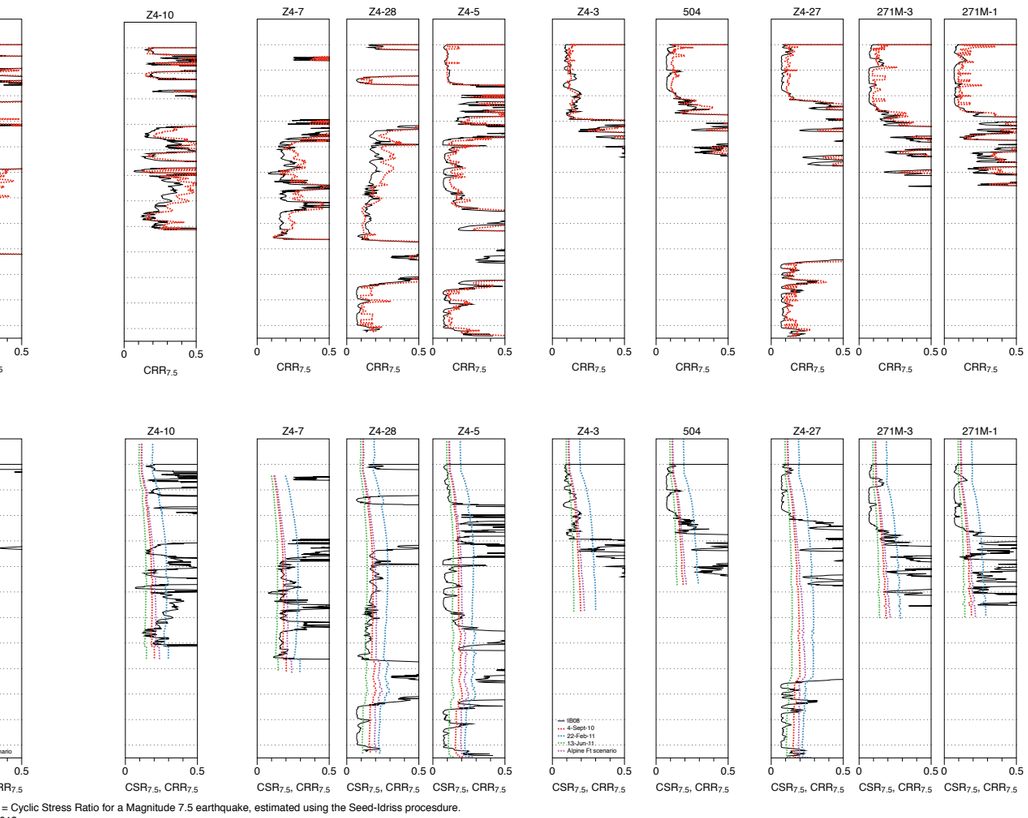

$CRR_{7.5}$ = Cyclic Resistance Ratio normalised for a Magnitude 7.5 earthquake. $CSR_{7.5}$ = Cyclic Stress Ratio for a Magnitude 7.5 earthquake, estimated using the Seed-Idriss procesdure.
K_σ after IB08, MSF after Idriss 1999. Conditional Mean PGA after Bradley & Hughes 2012.
RW98 = Robertson & Wride 1998, IB08 = Idriss & Boulanger 2008.

LEGEND:

CPT Location

Borehole Location

Red symbols: Canterbury Geotechnical Database post quake records
Blue symbols: Historic geotechnical data (pre quake)
Yellow symbols: UC/ UCB post quake investigations.

CBD Location Plan

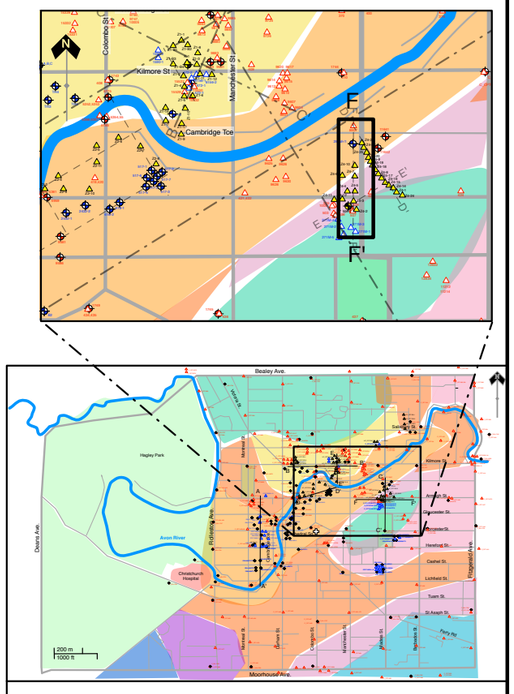

Profiles of $CRR_{7.5}$ correlated from CPT, and $CRR_{7.5}$ vs. $CSR_{7.5}$ for recent and future scenario earthquakes.

F-F' Transect N-S Christchurch CBD

Figure 2.47: Section F-F', Madras-Armagh Street Area. CPT-based estimate of CRR, and comparison of CRR to CSR from significant earthquakes.

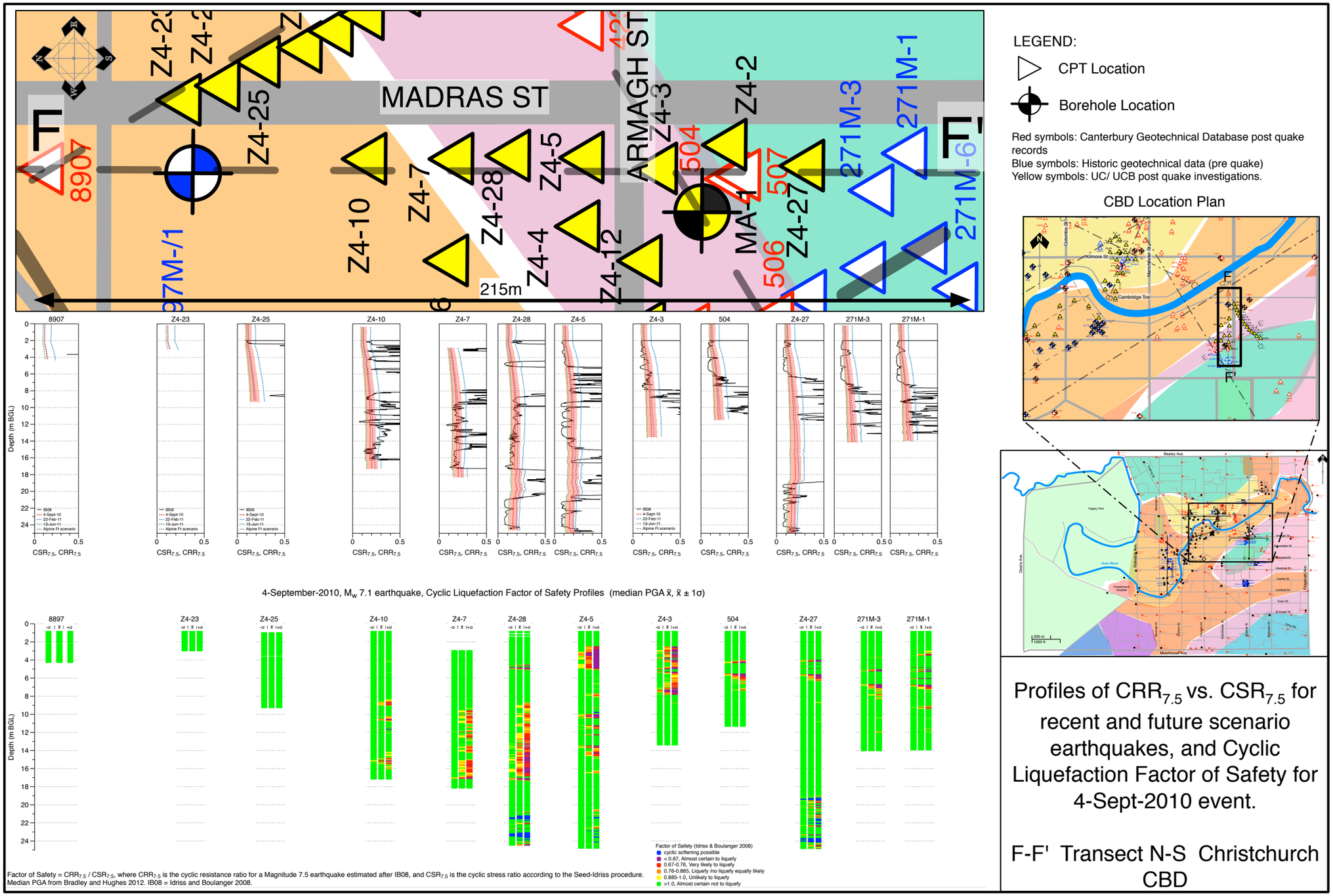

LEGEND:

CPT Location

Borehole Location

Red symbols: Canterbury Geotechnical Database post quake records
Blue symbols: Historic geotechnical data (pre quake)
Yellow symbols: UC/ UCB post quake investigations.

CBD Location Plan

Profiles of $CRR_{7.5}$ vs. $CSR_{7.5}$ for recent and future scenario earthquakes, and Cyclic Liquefaction Factor of Safety for 4-Sept-2010 event.

F-F' Transect N-S Christchurch CBD

Figure 2.48: Section F-F', Madras-Armagh Street Area. CPT-based estimate of CRR compared to CSR, and Factor of Safety plots for 4 September 2010 Event

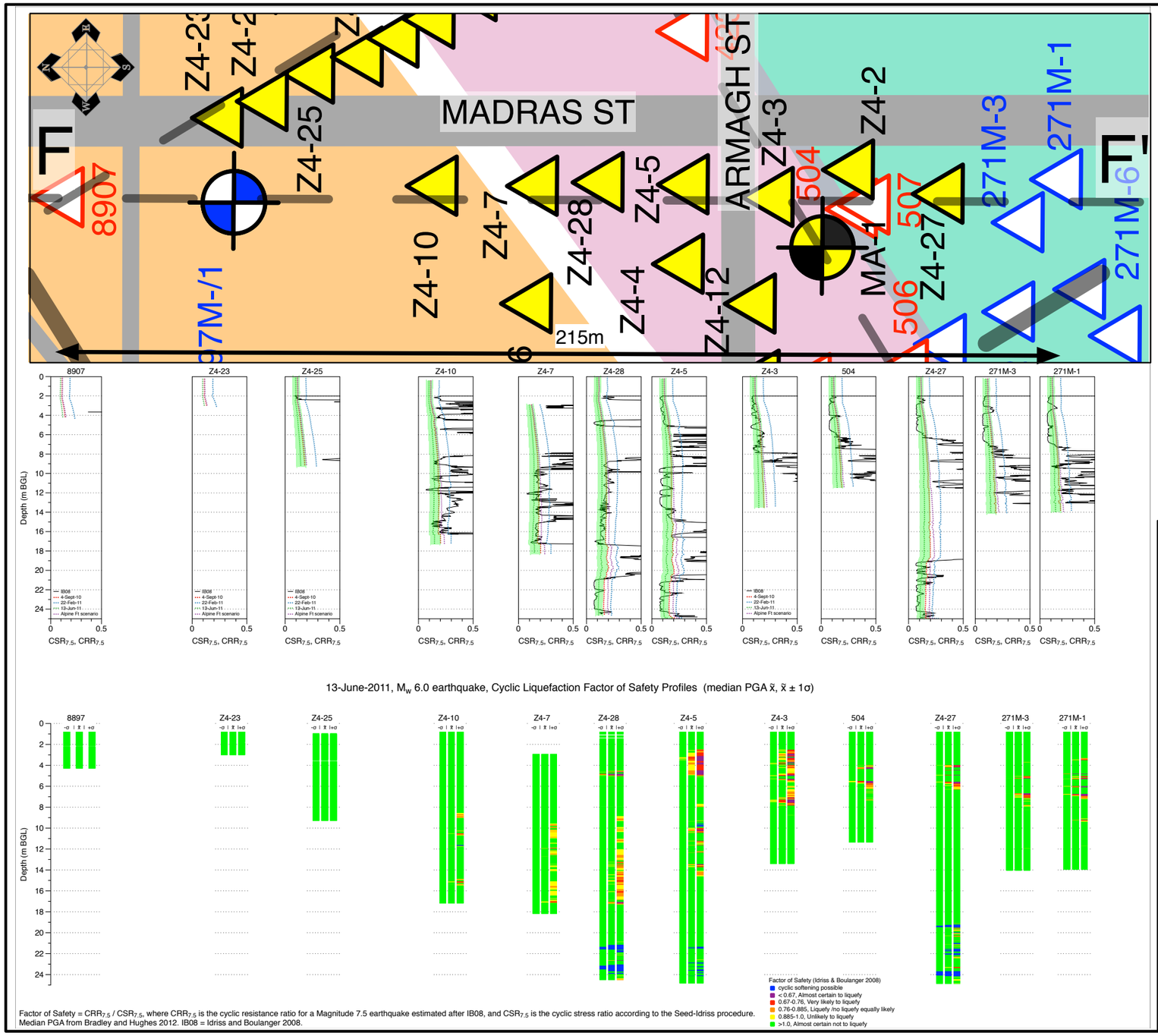

LEGEND:

CPT Location

Borehole Location

Red symbols: Canterbury Geotechnical Database post quake records
Blue symbols: Historic geotechnical data (pre quake)
Yellow symbols: UC/ UCB post quake investigations.

CBD Location Plan

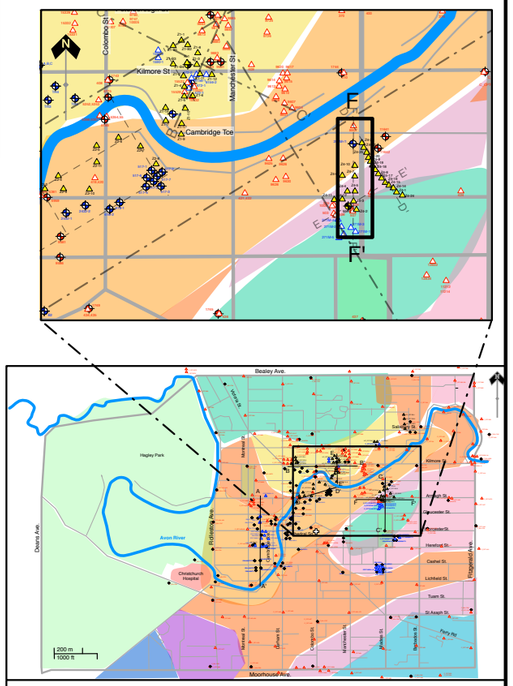

Profiles of $CRR_{7.5}$ vs. $CSR_{7.5}$ for recent and future scenario earthquakes, and Cyclic Liquefaction Factor of Safety for 13-Jun-2011 event.

F-F' Transect N-S Christchurch CBD

Figure 2.49: Section F-F', Kilmore Street Area. CPT-based estimate of CRR compared to CSR, and Factor of Safety plots for 13 June 2011 Event.

Chapter III

Laboratory testing supplementary information

The electronic appendix contains the following:

- Interpretation of Proximity Sensor strain data;
- Interpretation of Bender Elements - Plots;
- Interpretation of Bender elements - VBA code;
- Void Ratio measurement;
- Index data comparisons;
- Membrane Effects;

3.1 Interpretation of Proximity Sensor strain data

This section of Appendix C provides plots showing the interpretation of the small strain Young's Modulus from the stress-strain data below 0.01 % strain that was obtained by the high resolution proximity sensor, and the load cell in the testing of GP samples. The interpretation is carried for the initial loading, and for cyclic triaxial tests, also the first unloading cycle. For the tests conditions including sampling frequency of the data in each plot, confining stress, relative density, fines content of the samples, refer to the tables in the report. The tables also provide calculated small strain shear modulus and inferred shear wave velocity of the field condition from these interpreted stiffnesses.

3.1.1 K1 Drained Triaxial Tests

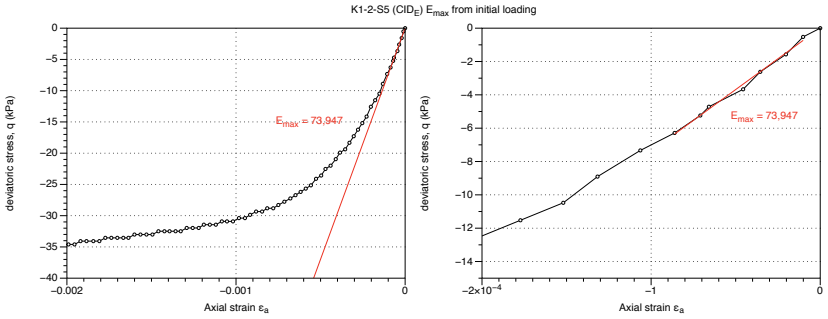

Figure 3.1: Young's Modulus as measured during initial loading. K1–2–S5 GP Sample CID extension test.

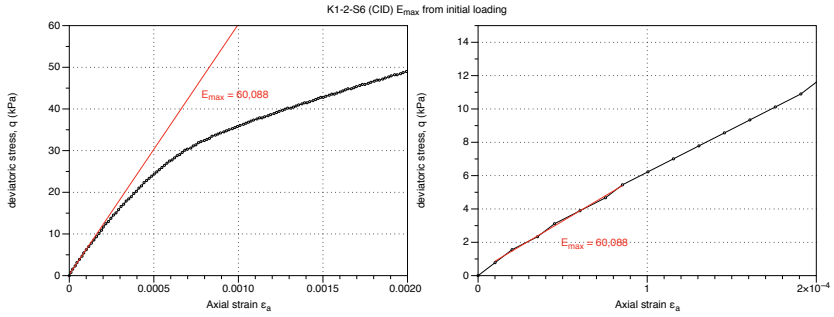

Figure 3.2: Young's Modulus as measured during initial loading. K1–2–S6 GP Sample CID compression test.

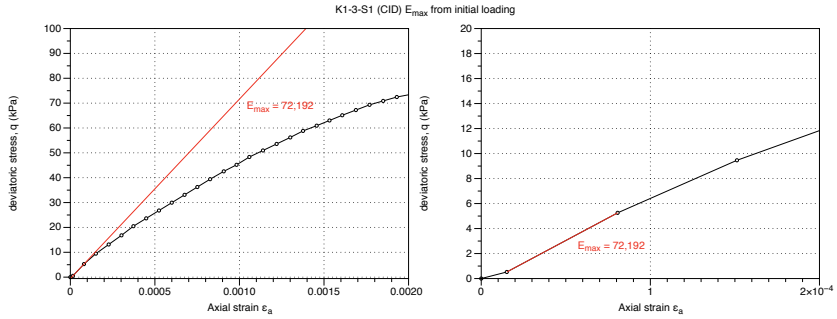

Figure 3.3: Young's Modulus as measured during initial loading. K1–3–S1 GP Sample CID compression test.

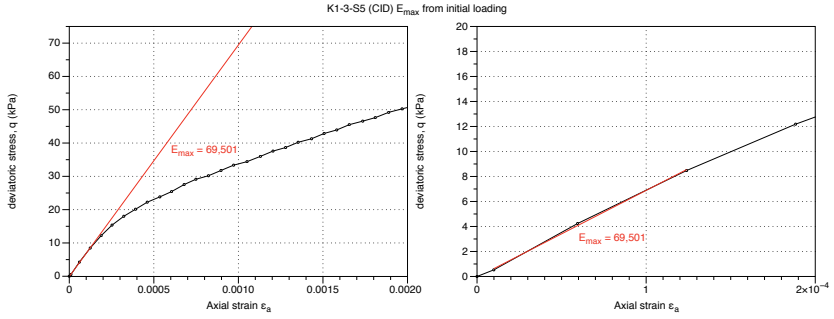

Figure 3.4: Young's Modulus as measured during initial loading. K1–3–S5 GP Sample CID compression test.

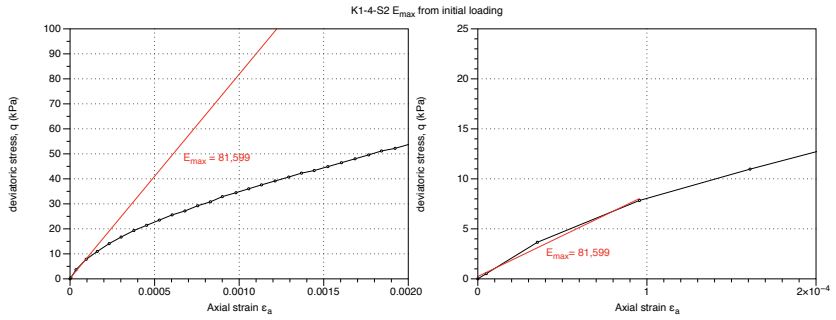

Figure 3.5: Young's Modulus as measured during initial loading. K1–4–S2 GP Sample CID compression test.

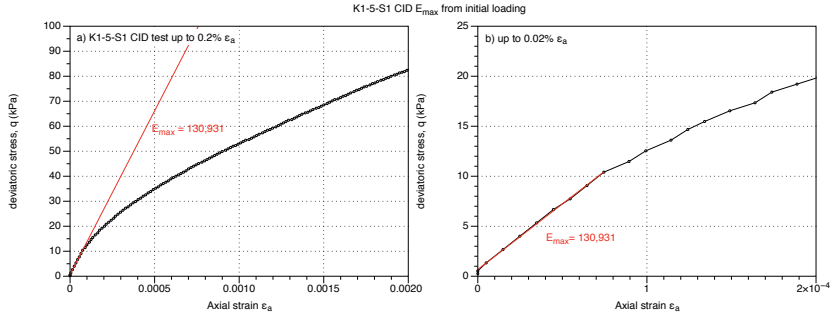

Figure 3.6: Young's Modulus as measured during initial loading. K1–5–S1 GP Sample CID compression test.

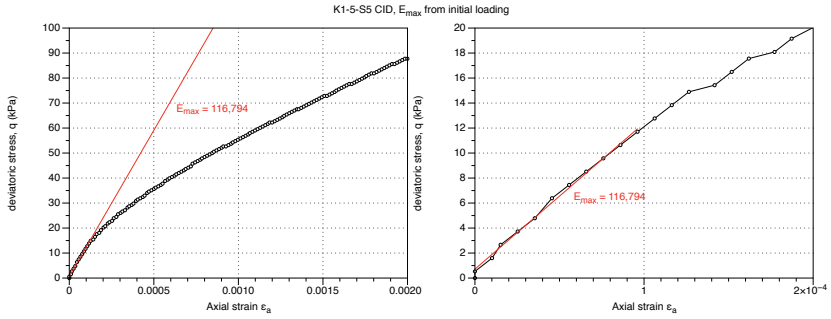

Figure 3.7: Young's Modulus as measured during initial loading. K1–5–S5 GP Sample CID compression test.

3.1.2 K1 Cyclic Triaxial Tests

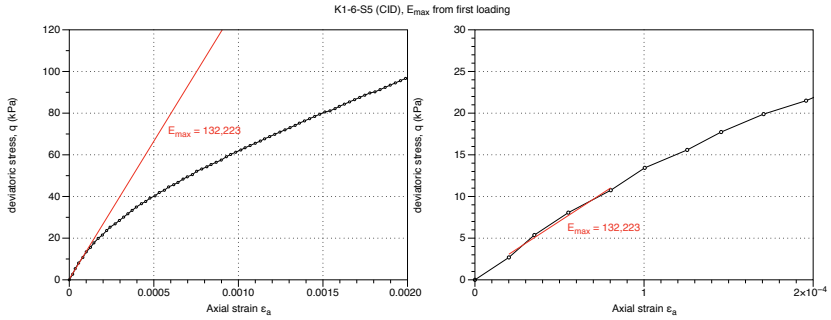

Figure 3.8: Young's Modulus as measured during initial loading. K1–6–S5 GP Sample CID compression test.

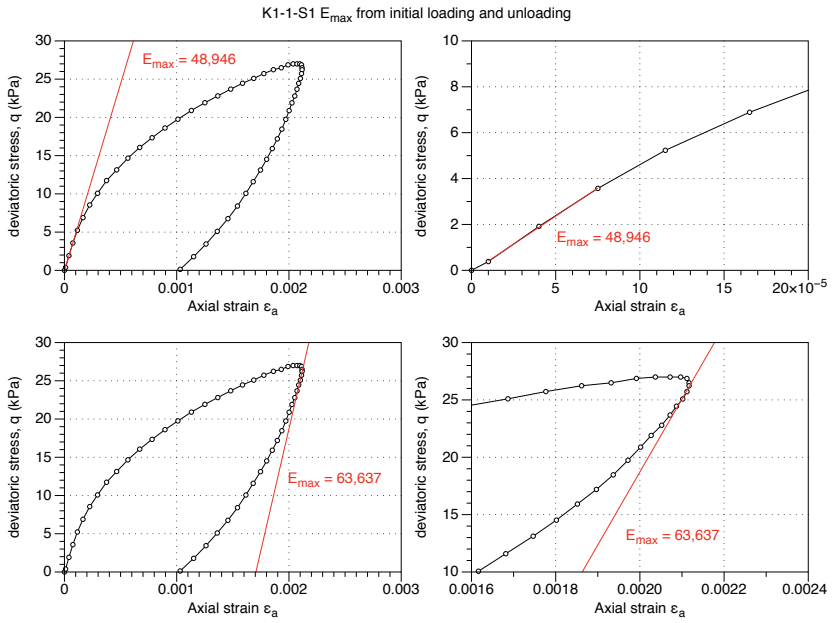

Figure 3.9: Young's Modulus as measured during initial loading and unloading. K1–1–S1 GP Sample Cyclic Triaxial Test

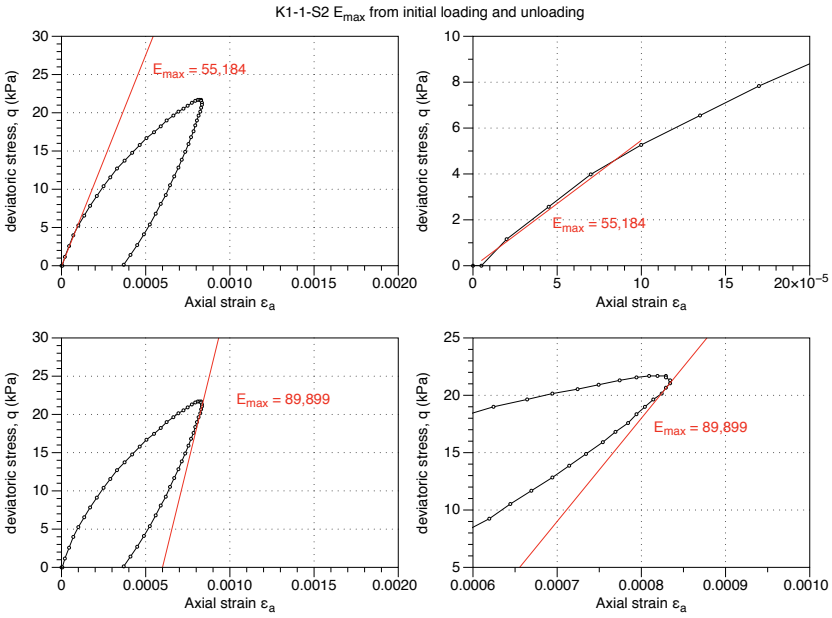

Figure 3.10: Young's Modulus as measured during initial loading and unloading. K1–1–S2 GP Sample Cyclic Triaxial Test

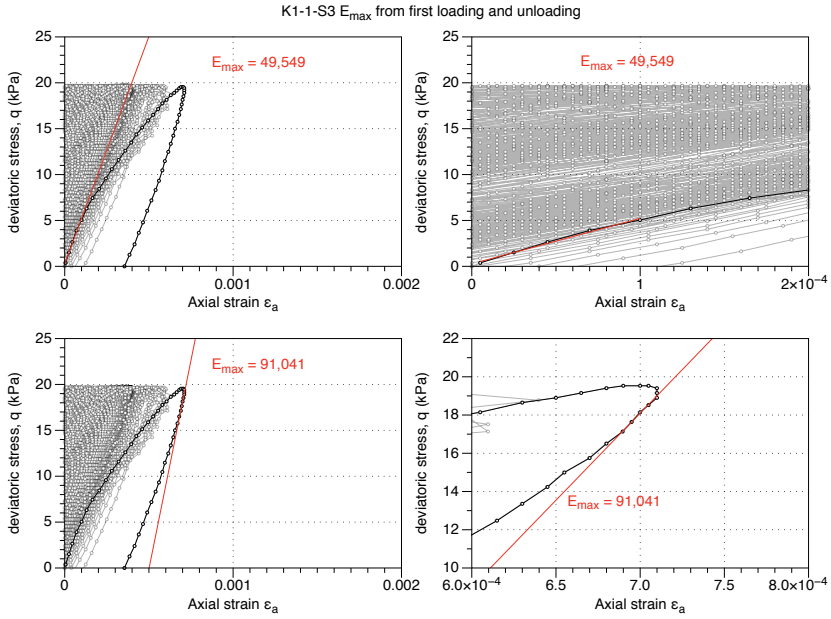

Figure 3.11: Young's Modulus as measured during initial loading and unloading. K1–1–S3 GP Sample Cyclic Triaxial Test

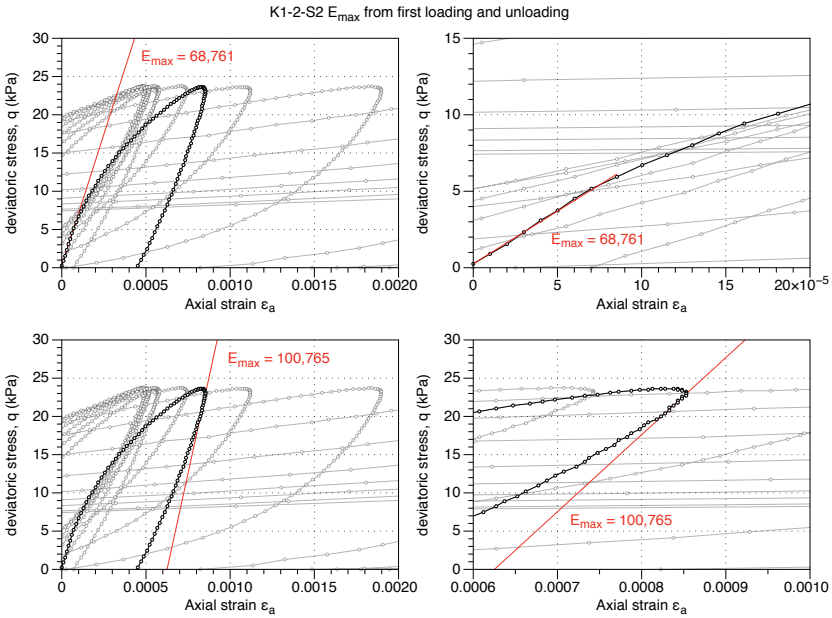

Figure 3.12: Young's Modulus as measured during initial loading and unloading. K1–2–S2 GP Sample Cyclic Triaxial Test

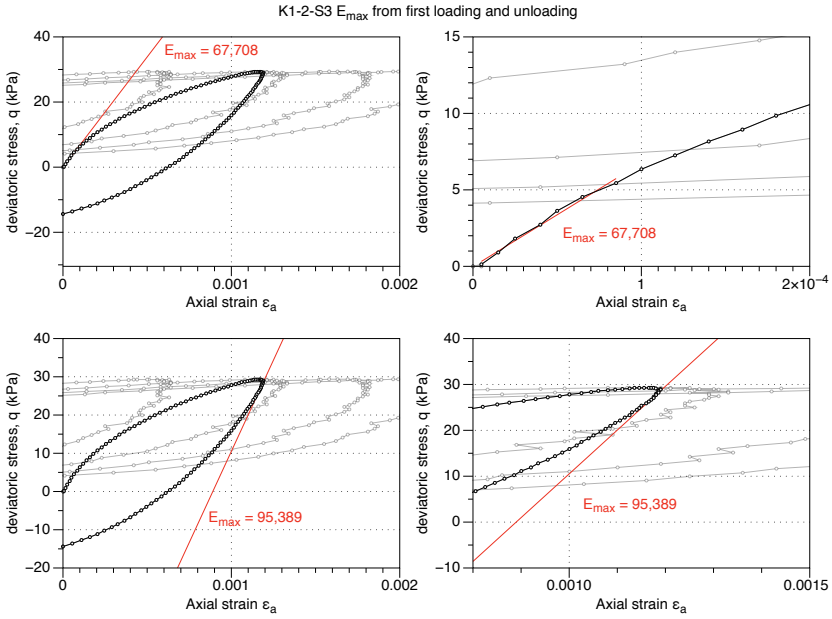

Figure 3.13: Young's Modulus as measured during initial loading and unloading. K1–2–S3 GP Sample Cyclic Triaxial Test

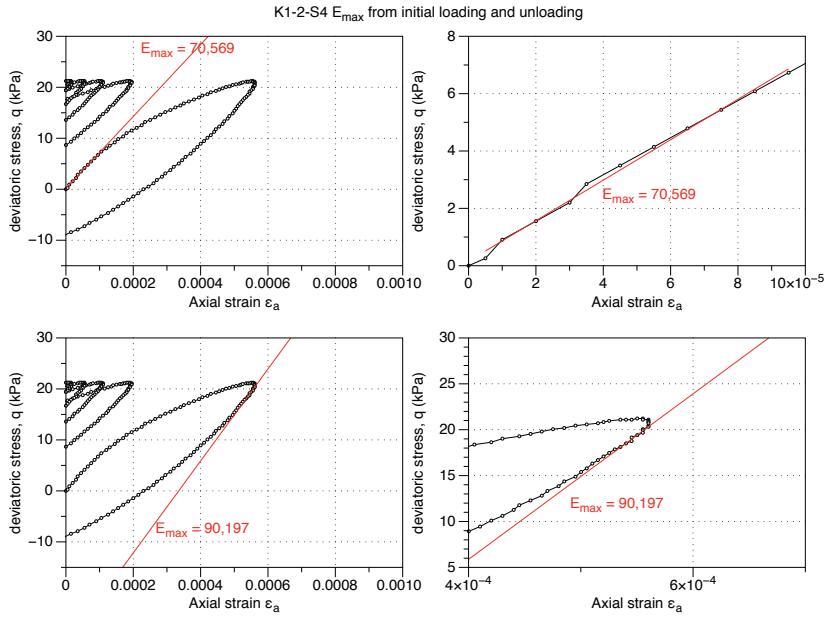

Figure 3.14: Young's Modulus as measured during initial loading and unloading. K1–2–S4 GP Sample Cyclic Triaxial Test

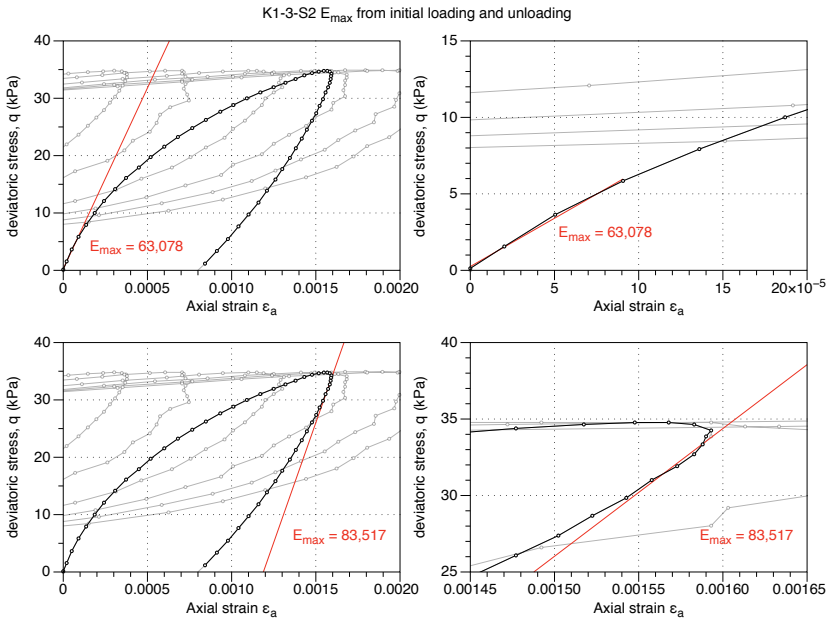

Figure 3.15: Young's Modulus as measured during initial loading and unloading. K1–3–S2 GP Sample Cyclic Triaxial Test

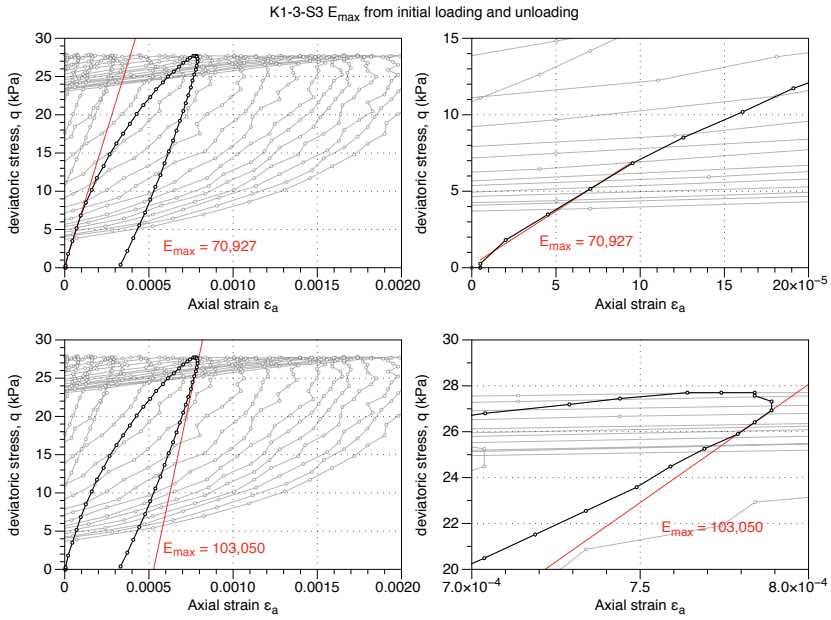

Figure 3.16: Young's Modulus as measured during initial loading and unloading. K1–3–S3 GP Sample Cyclic Triaxial Test

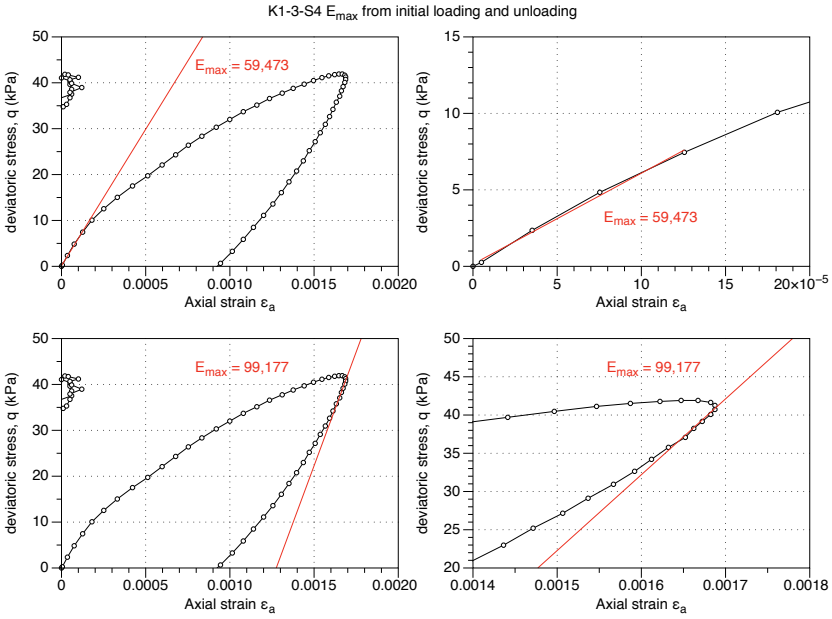

Figure 3.17: Young's Modulus as measured during initial loading and unloading. K1–3–S4 GP Sample Cyclic Triaxial Test

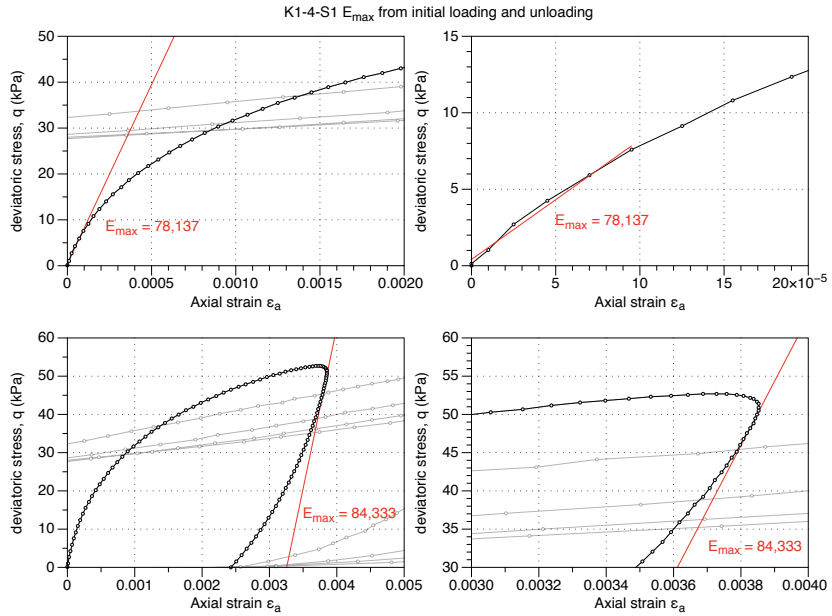

Figure 3.18: Young's Modulus as measured during initial loading and unloading. K1–4–S1 GP Sample Cyclic Triaxial Test

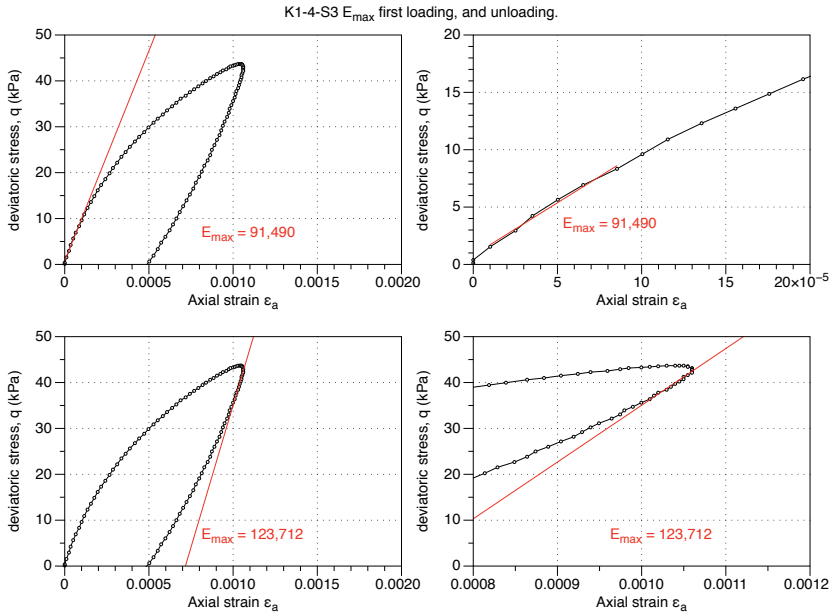

Figure 3.19: Young's Modulus as measured during initial loading and unloading. K1–4–S3 GP Sample Cyclic Triaxial Test.

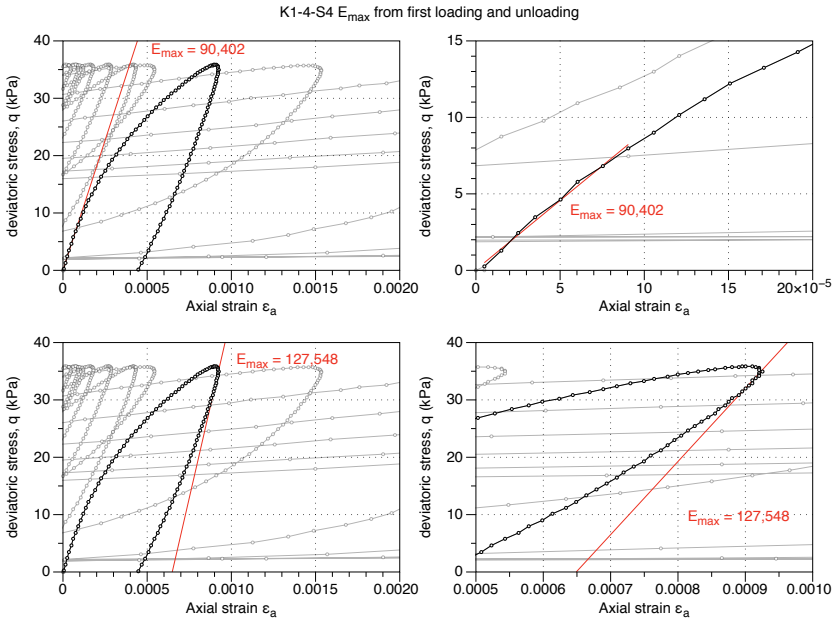

Figure 3.20: Young's Modulus as measured during initial loading and unloading. K1–4–S4 GP Sample Cyclic Triaxial Test

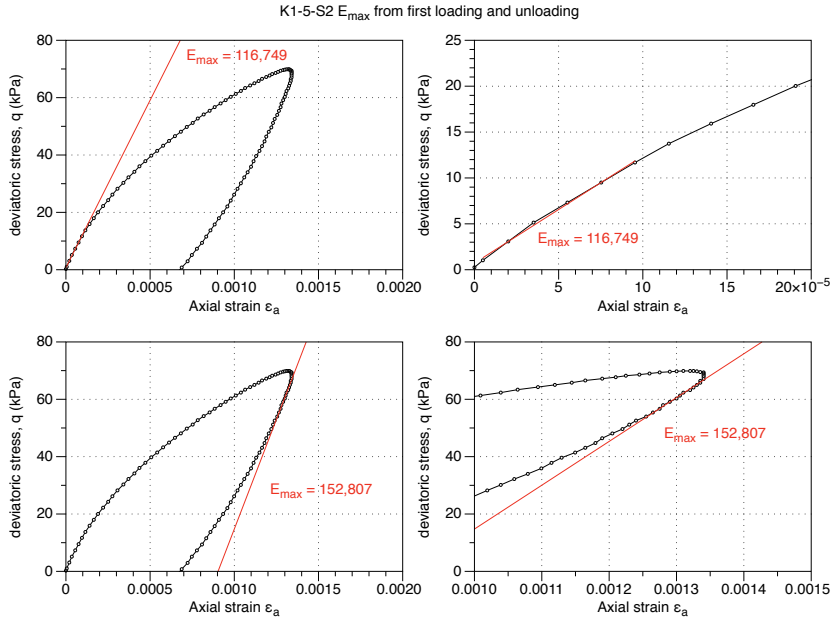

Figure 3.21: Young's Modulus as measured during initial loading and unloading. K1–5–S2 GP Sample Cyclic Triaxial Test

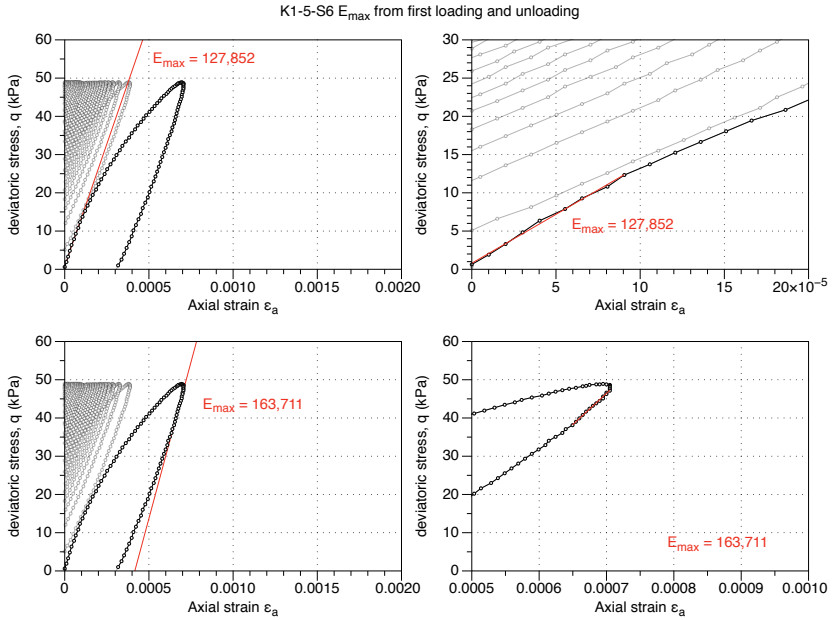

Figure 3.22: Young's Modulus as measured during initial loading and unloading. K1–5–S6 GP Sample Cyclic Triaxial Test

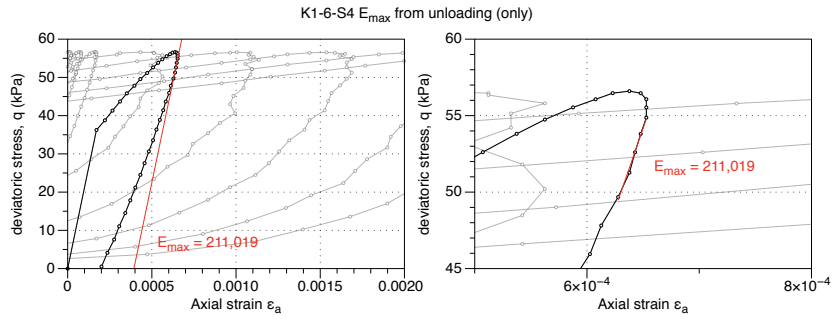

Figure 3.23: Young's Modulus as measured during initial loading and unloading. K1–6–S2 GP Sample Cyclic Triaxial Test

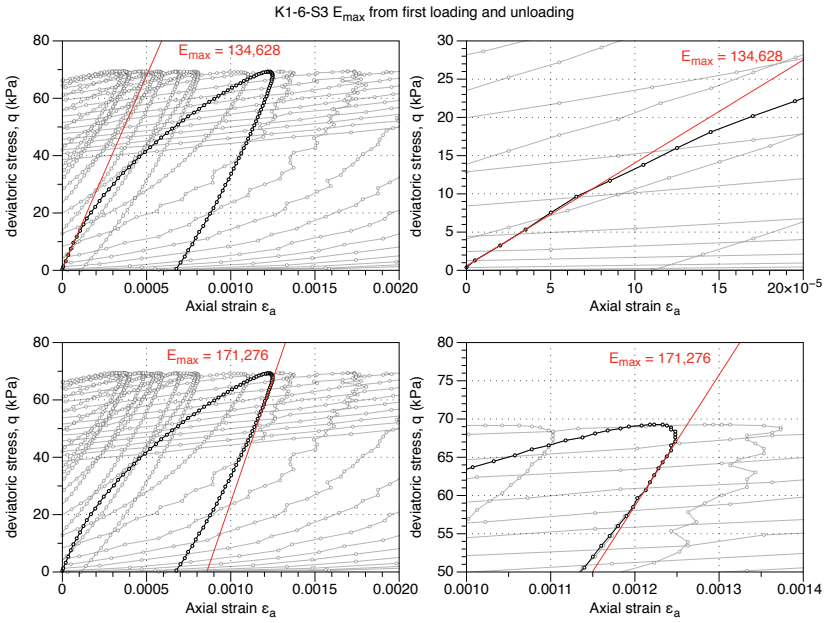

Figure 3.24: Young's Modulus as measured during initial loading and unloading. K1–6–S3 GP Sample Cyclic Triaxial Test

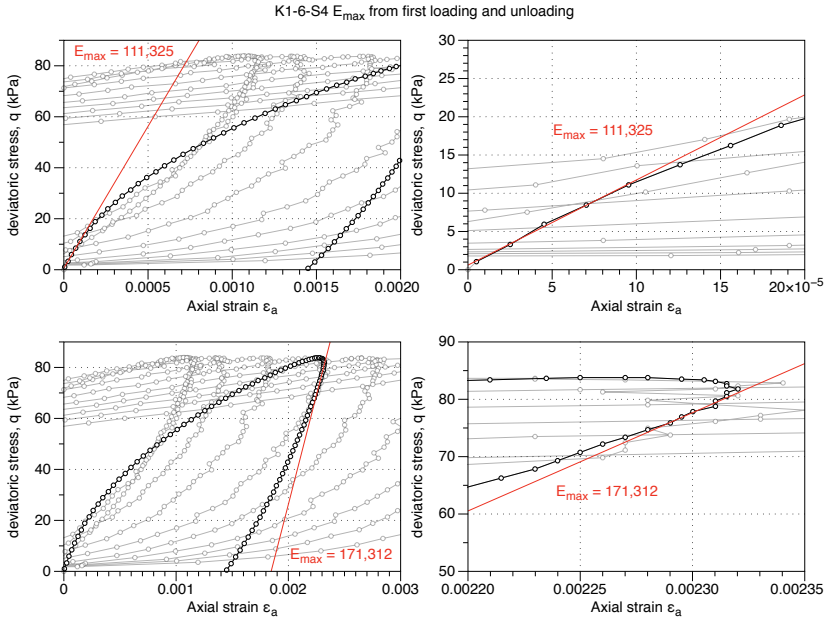

Figure 3.25: Young's Modulus as measured during initial loading and unloading. K1–6–S4 GP Sample Cyclic Triaxial Test

3.1.3 MA1 Drained Triaxial Tests

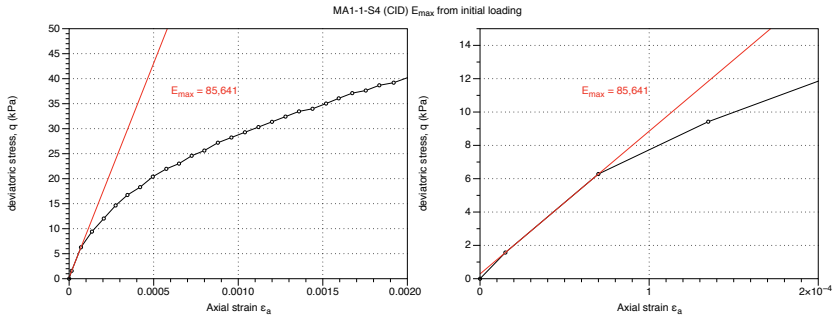

Figure 3.26: Young's Modulus as measured during initial loading. MA1–1–S4 GP Sample CID compression test.

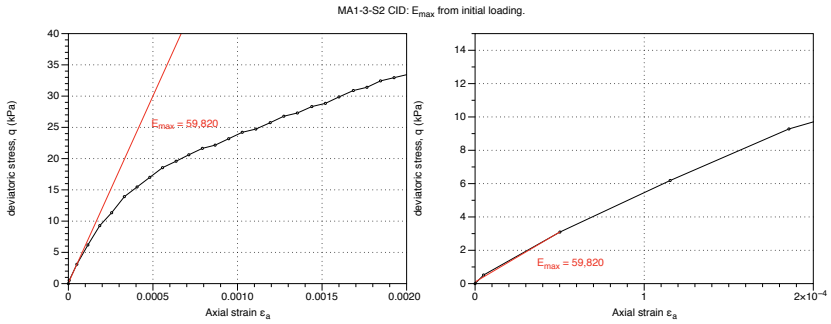

Figure 3.27: Young's Modulus as measured during initial loading. MA1–3–S2 GP Sample CID compression test.

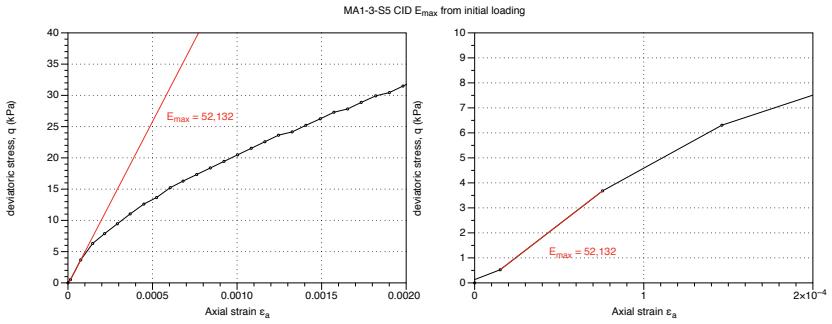

Figure 3.28: Young's Modulus as measured during initial loading. MA1–3–S5 GP Sample CID compression test.

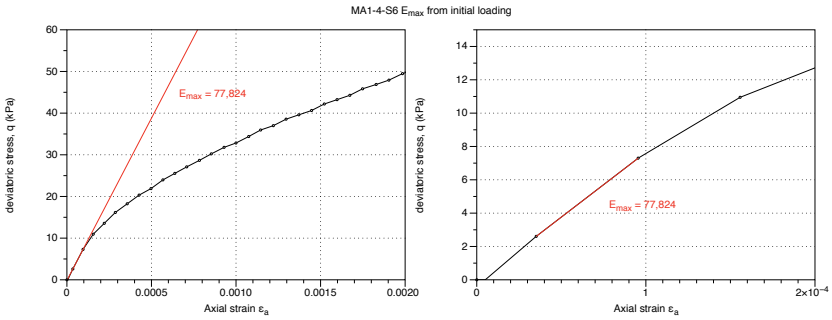

Figure 3.29: Young's Modulus as measured during initial loading. MA1–4–S6 GP Sample CID compression test.

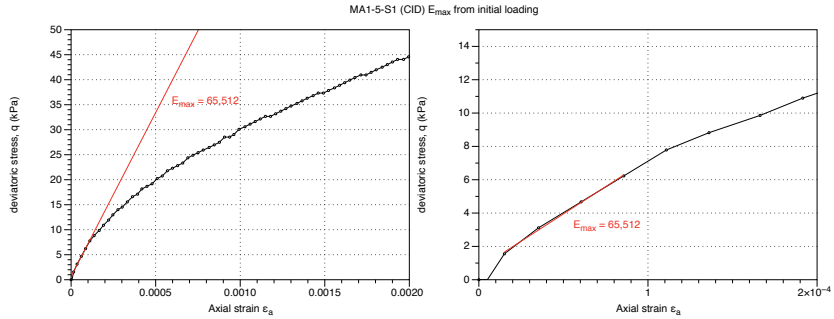

Figure 3.30: Young's Modulus as measured during initial loading. MA1–5–S1 GP Sample CID compression test.

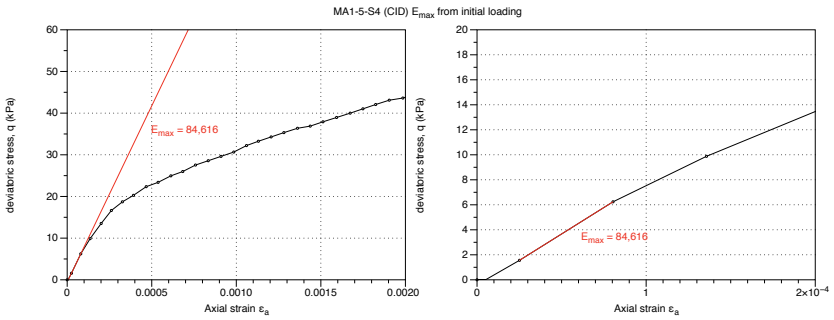

Figure 3.31: Young's Modulus as measured during initial loading. MA1–5–S4 GP Sample CID compression test.

3.1.4 MA1 Cyclic Triaxial Tests

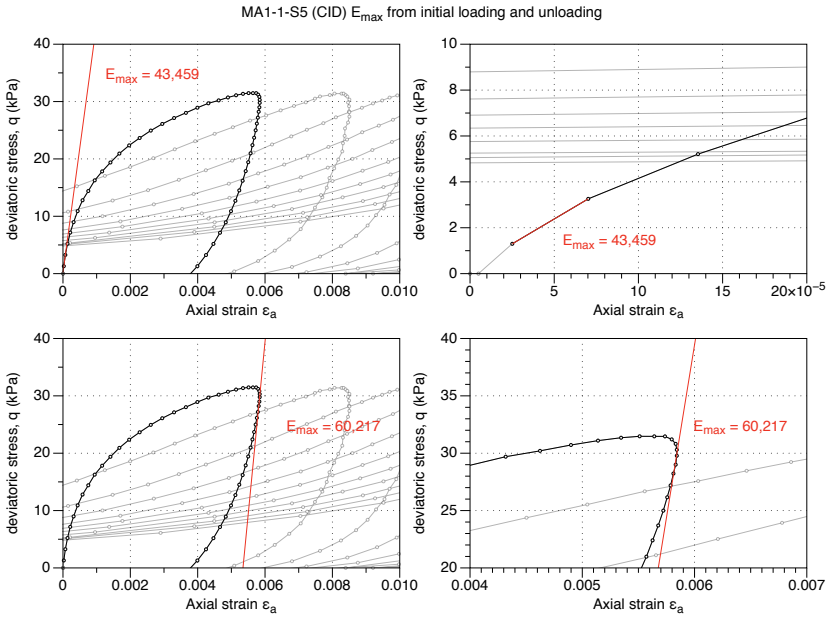

Figure 3.32: Young's Modulus as measured during initial loading and unloading. MA1–1–S5 GP Sample Cyclic Triaxial Test

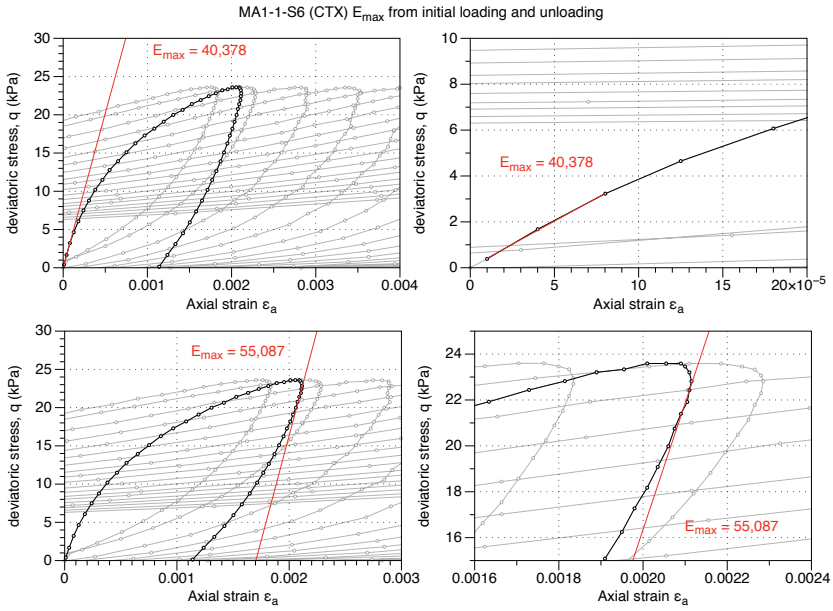

Figure 3.33: Young's Modulus as measured during initial loading and unloading. MA1–1–S6 GP Sample Cyclic Triaxial Test

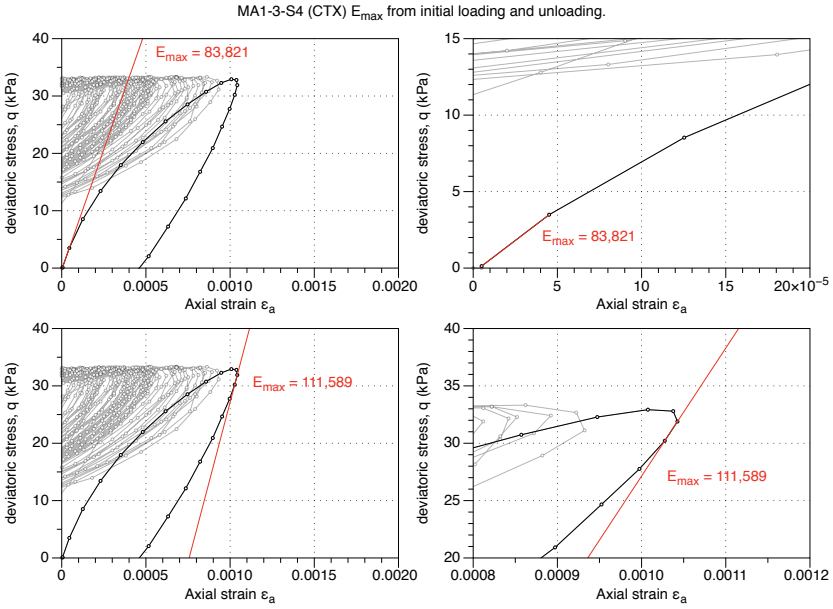

Figure 3.34: Young's Modulus as measured during initial loading and unloading. MA1–3–S4 GP Sample Cyclic Triaxial Test

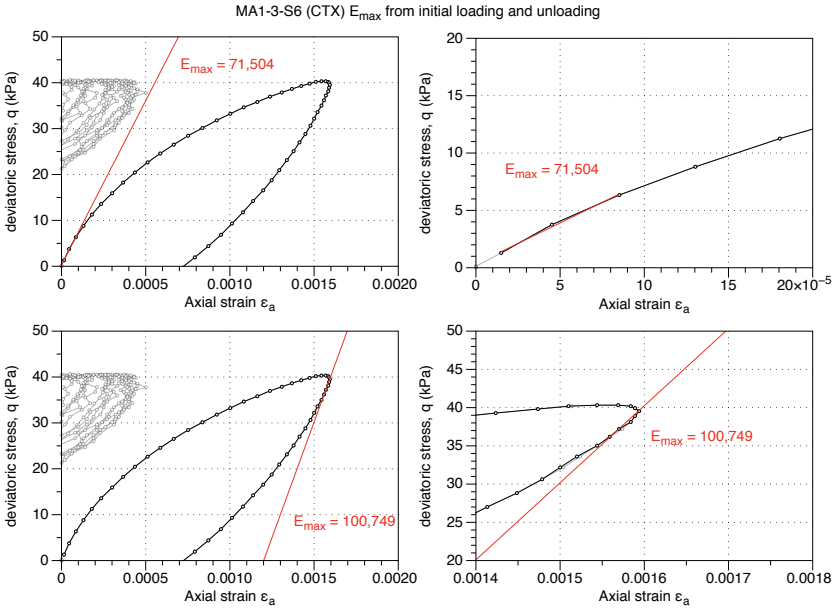

Figure 3.35: Young's Modulus as measured during initial loading and unloading. MA1–3–S6 GP Sample Cyclic Triaxial Test

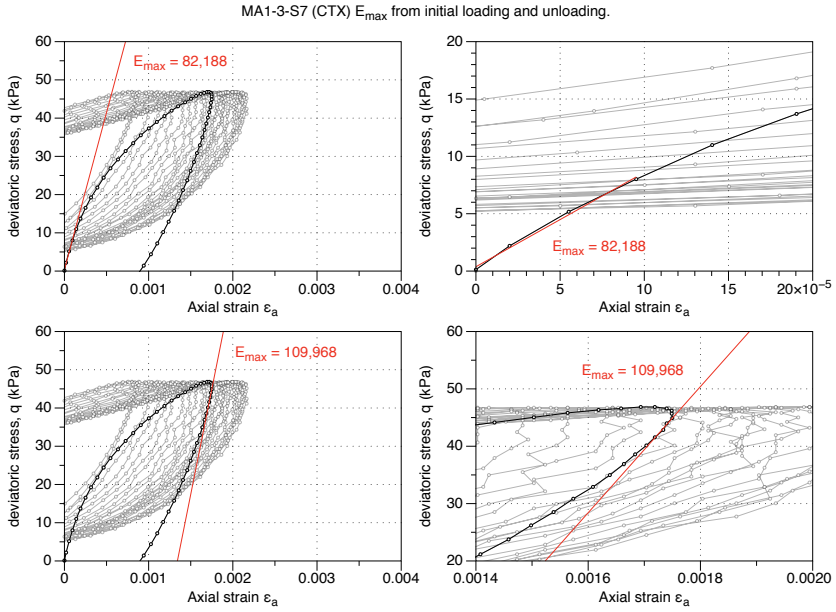

Figure 3.36: Young's Modulus as measured during initial loading and unloading. MA1–3–S7 GP Sample Cyclic Triaxial Test

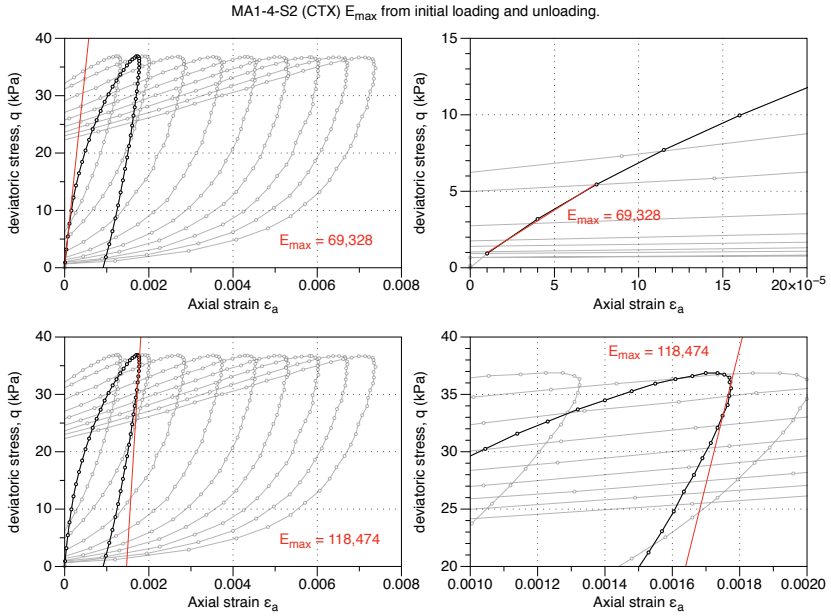

Figure 3.37: Young's Modulus as measured during initial loading and unloading. MA1–4–S2 GP Sample Cyclic Triaxial Test

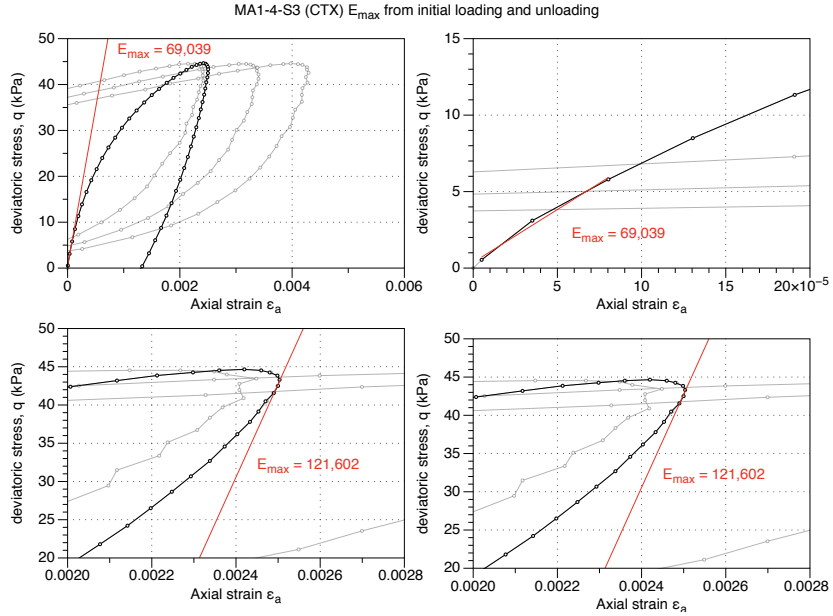

Figure 3.38: Young's Modulus as measured during initial loading and unloading. MA1–4–S3 GP Sample Cyclic Triaxial Test

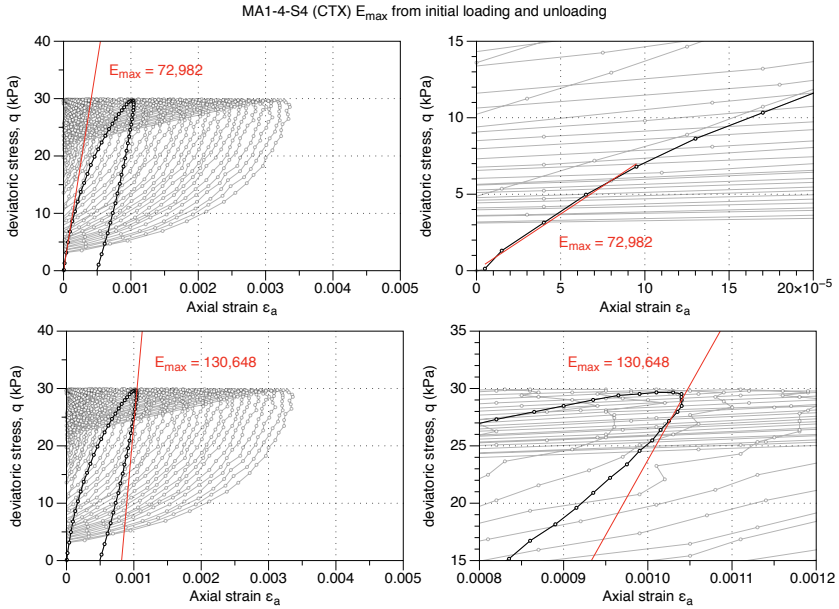

Figure 3.39: Young's Modulus as measured during initial loading and unloading. MA1–4–S4 GP Sample Cyclic Triaxial Test

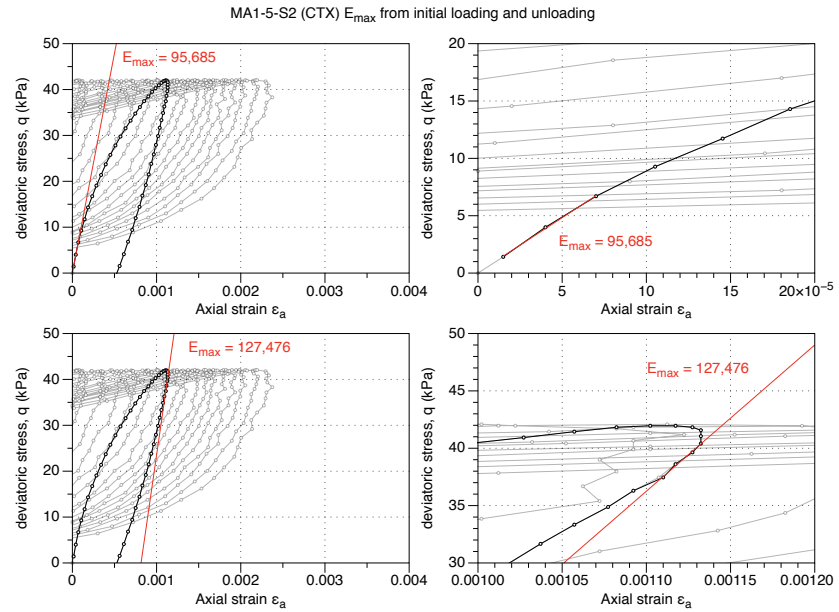

Figure 3.40: Young's Modulus as measured during initial loading and unloading. MA1–5–S2 GP Sample Cyclic Triaxial Test

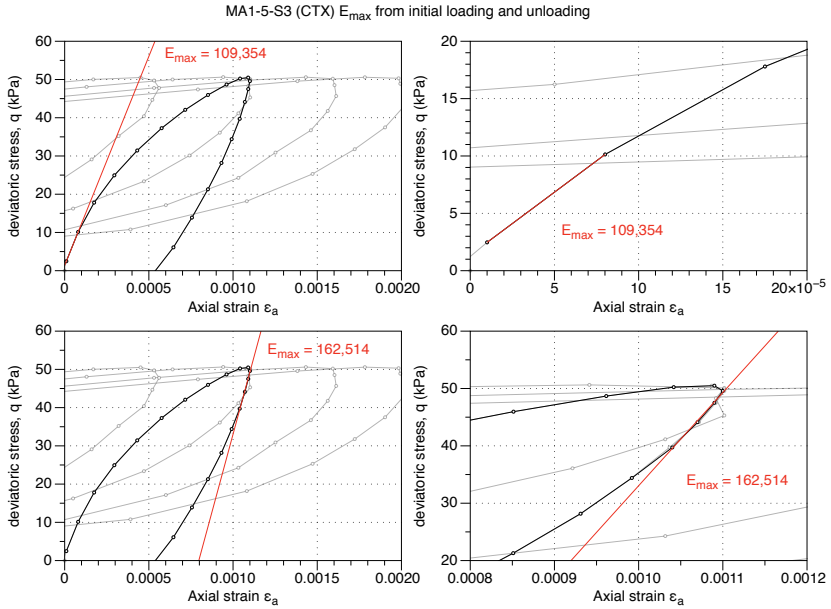

Figure 3.41: Young's Modulus as measured during initial loading and unloading. MA1–5–S3 GP Sample Cyclic Triaxial Test

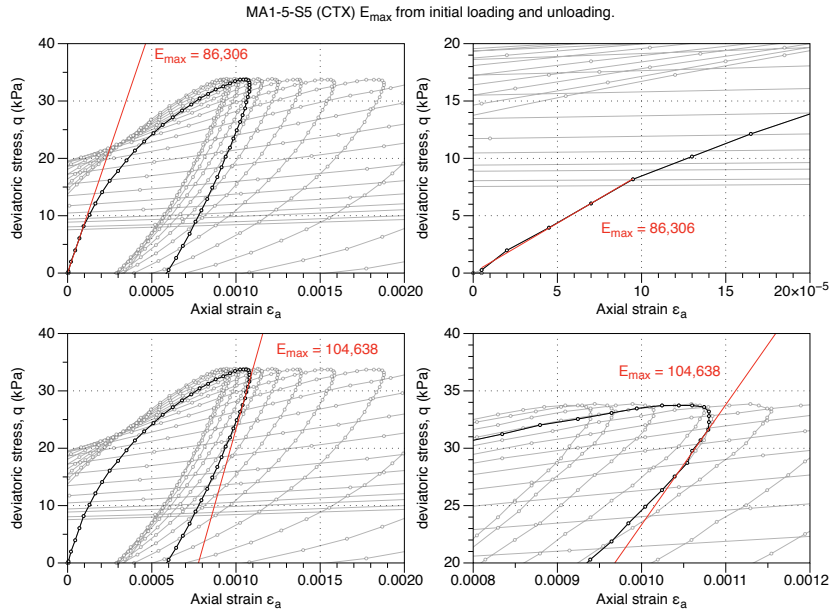

Figure 3.42: Young's Modulus as measured during initial loading and unloading. MA1–5–S5 GP Sample Cyclic Triaxial Test

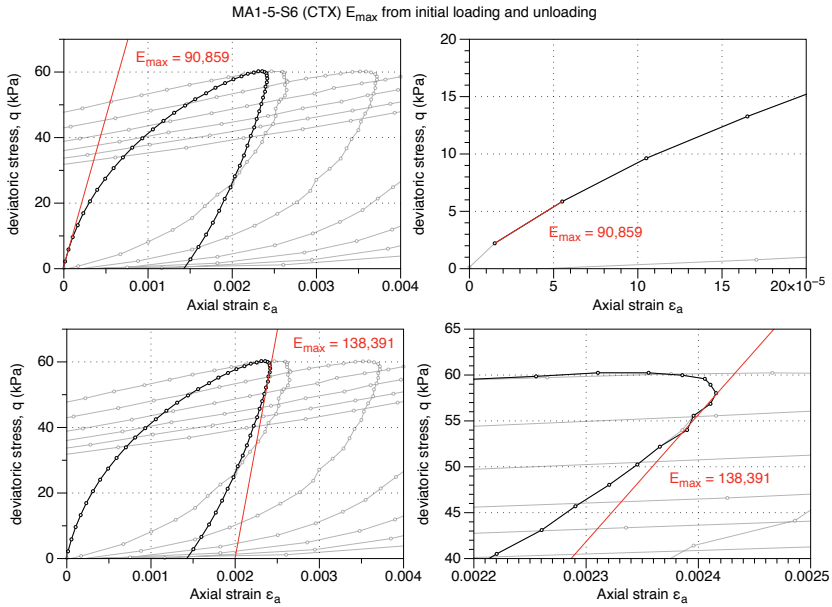

Figure 3.43: Young's Modulus as measured during initial loading and unloading. MA1–5–S6 GP Sample Cyclic Triaxial Test

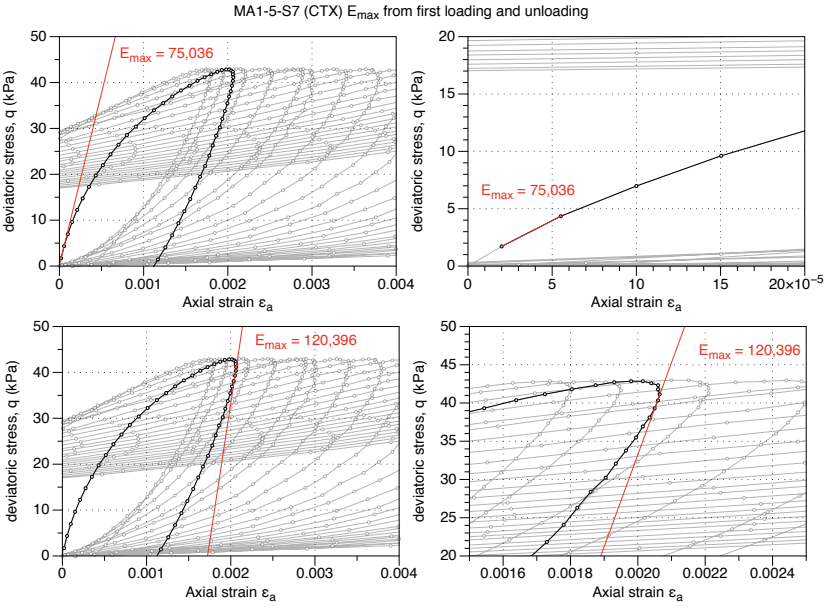

Figure 3.44: Young's Modulus as measured during initial loading and unloading. MA1–5–S7 GP Sample Cyclic Triaxial Test

3.2 Interpretation of Bender Elements - Plots

This section of Appendix C provides plots showing the interpretation of bender element data for GP samples. Reference should be made to tabulated data in the relevant section of the thesis outlining the interpreted shear wave velocities for each sample.

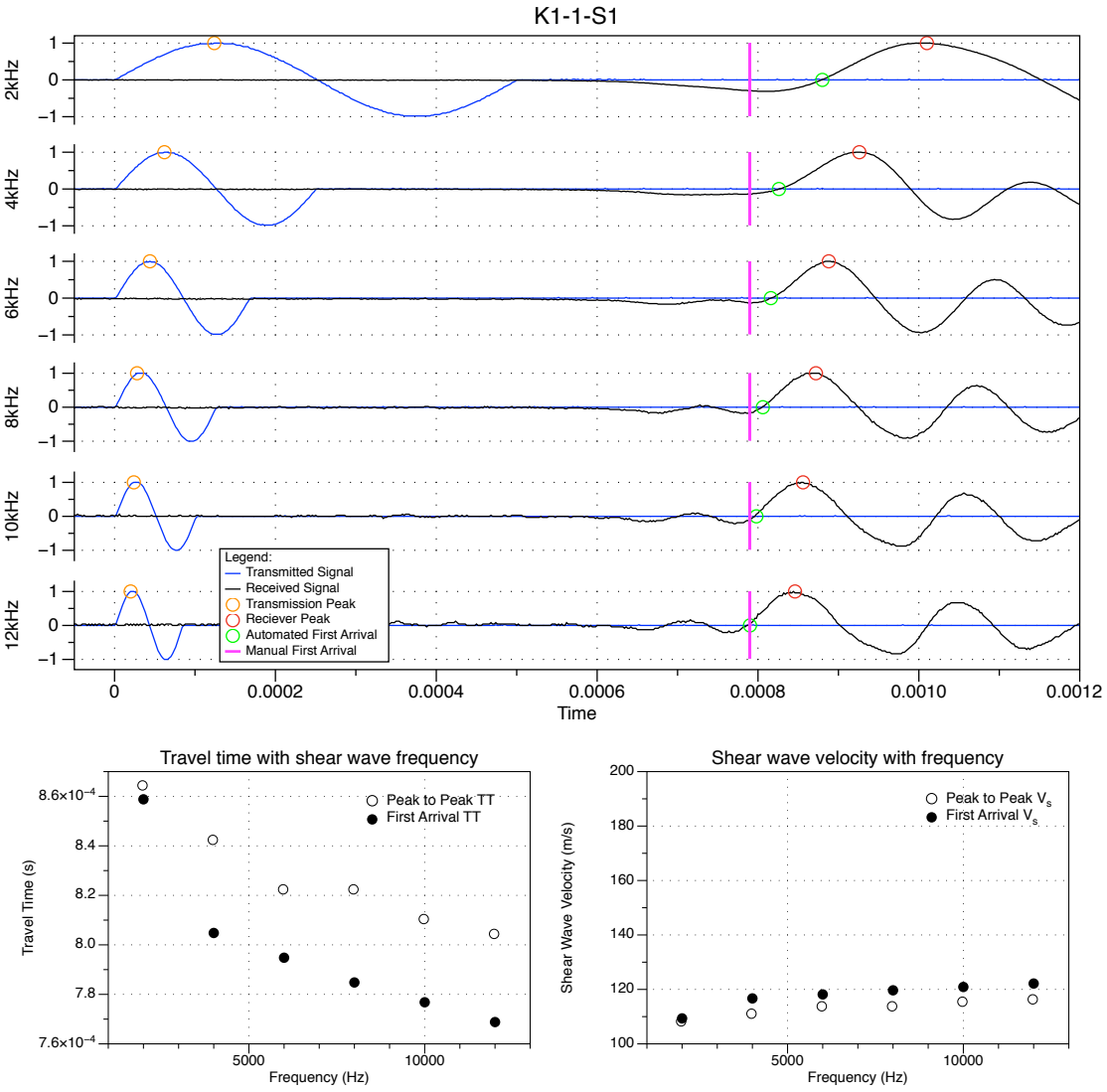

Figure 3.45: Processed bender element test data for sample K1–1–S1

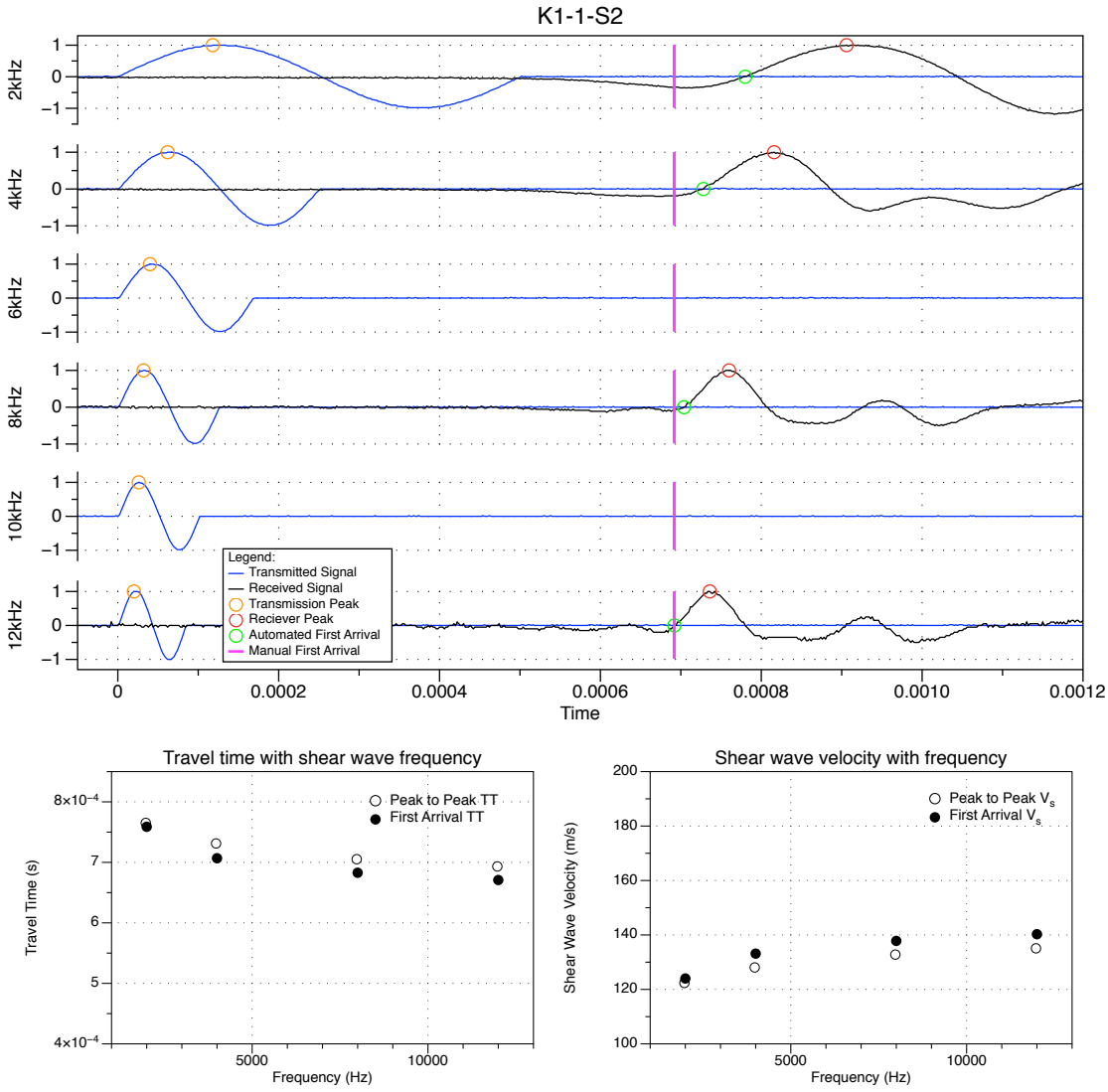

Figure 3.46: Processed bender element test data for sample K1–1–S2

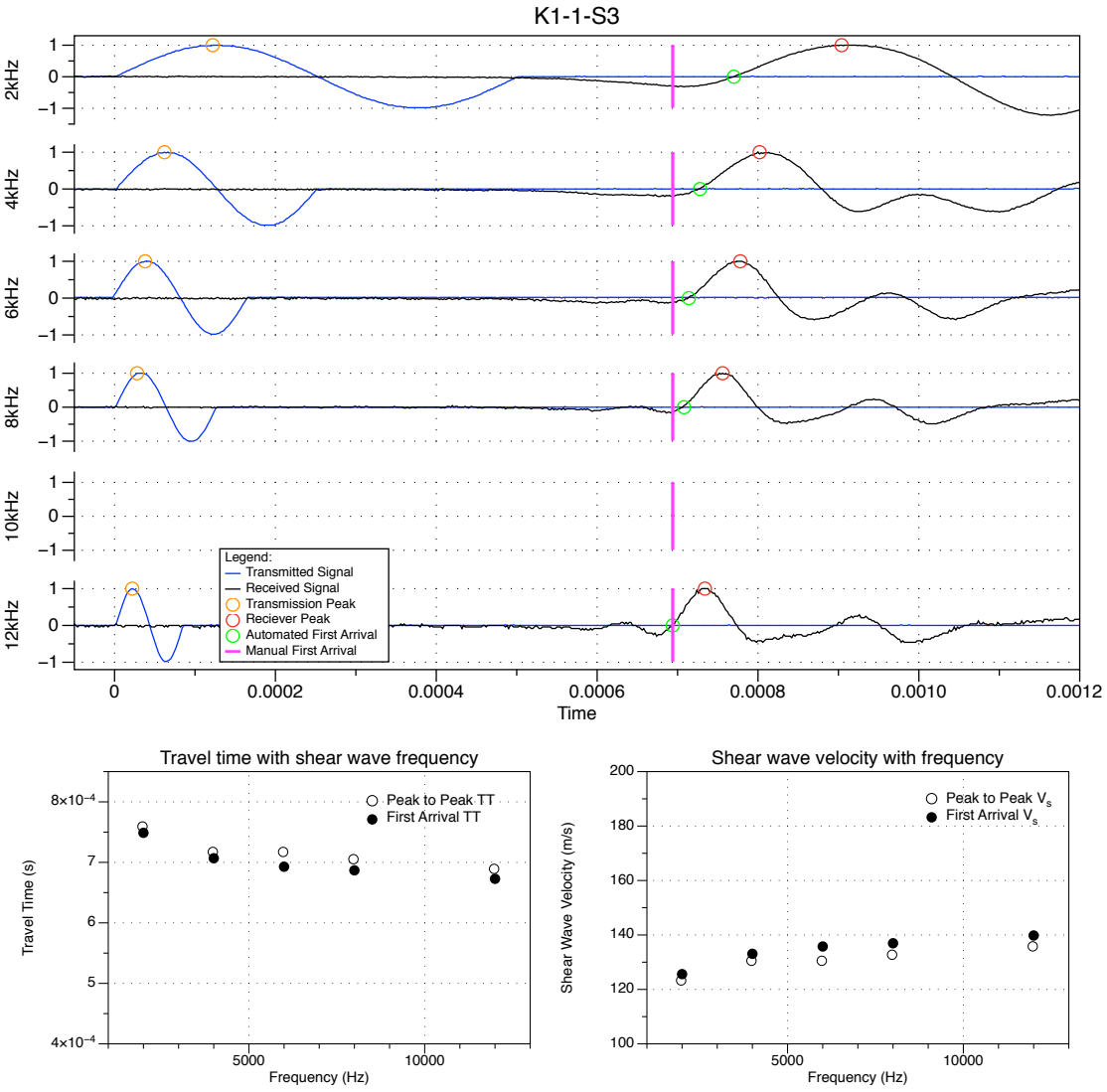

Figure 3.47: Processed bender element test data for sample K1–1–S3

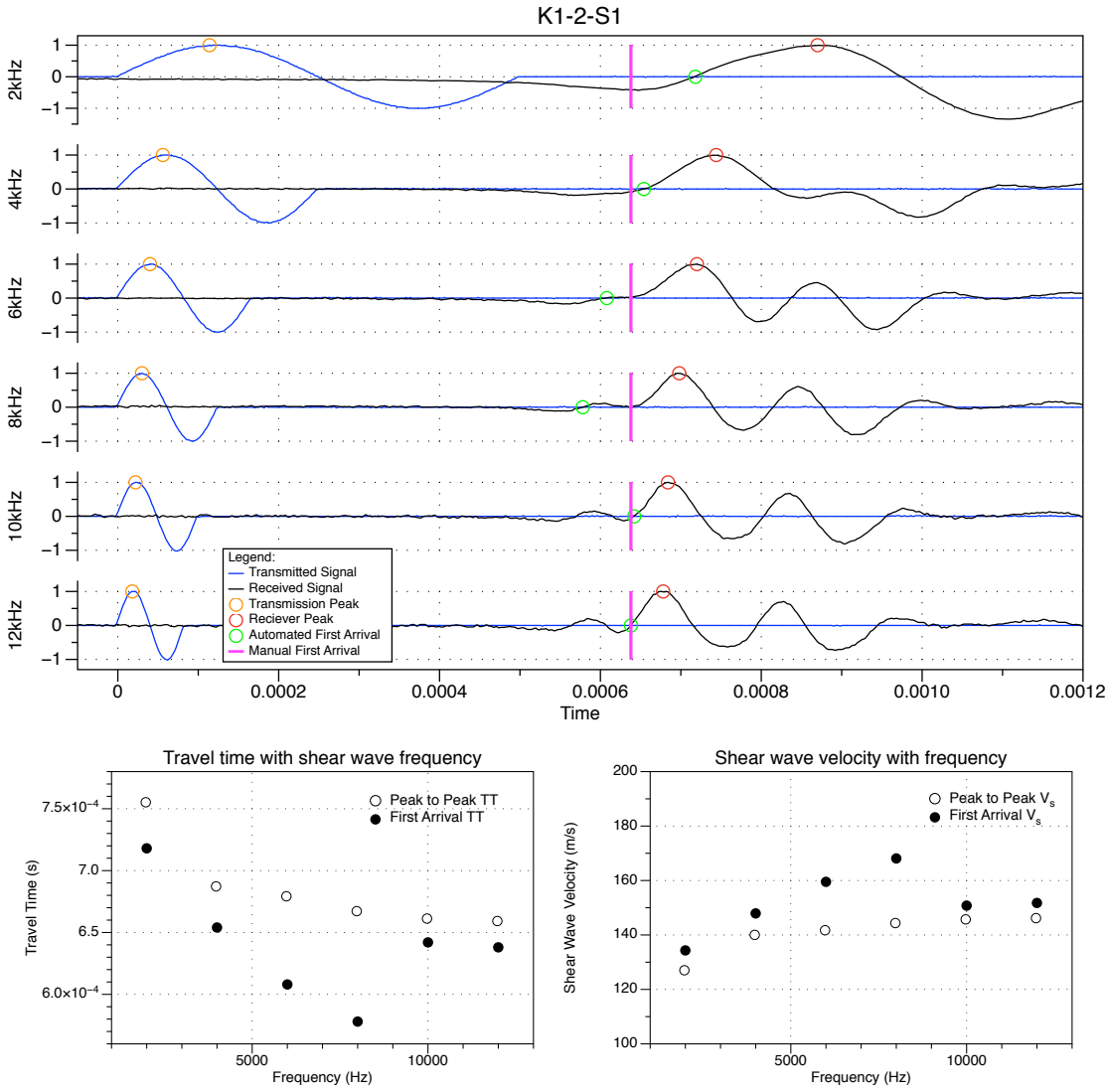

Figure 3.48: Processed bender element test data for sample K1–2–S1

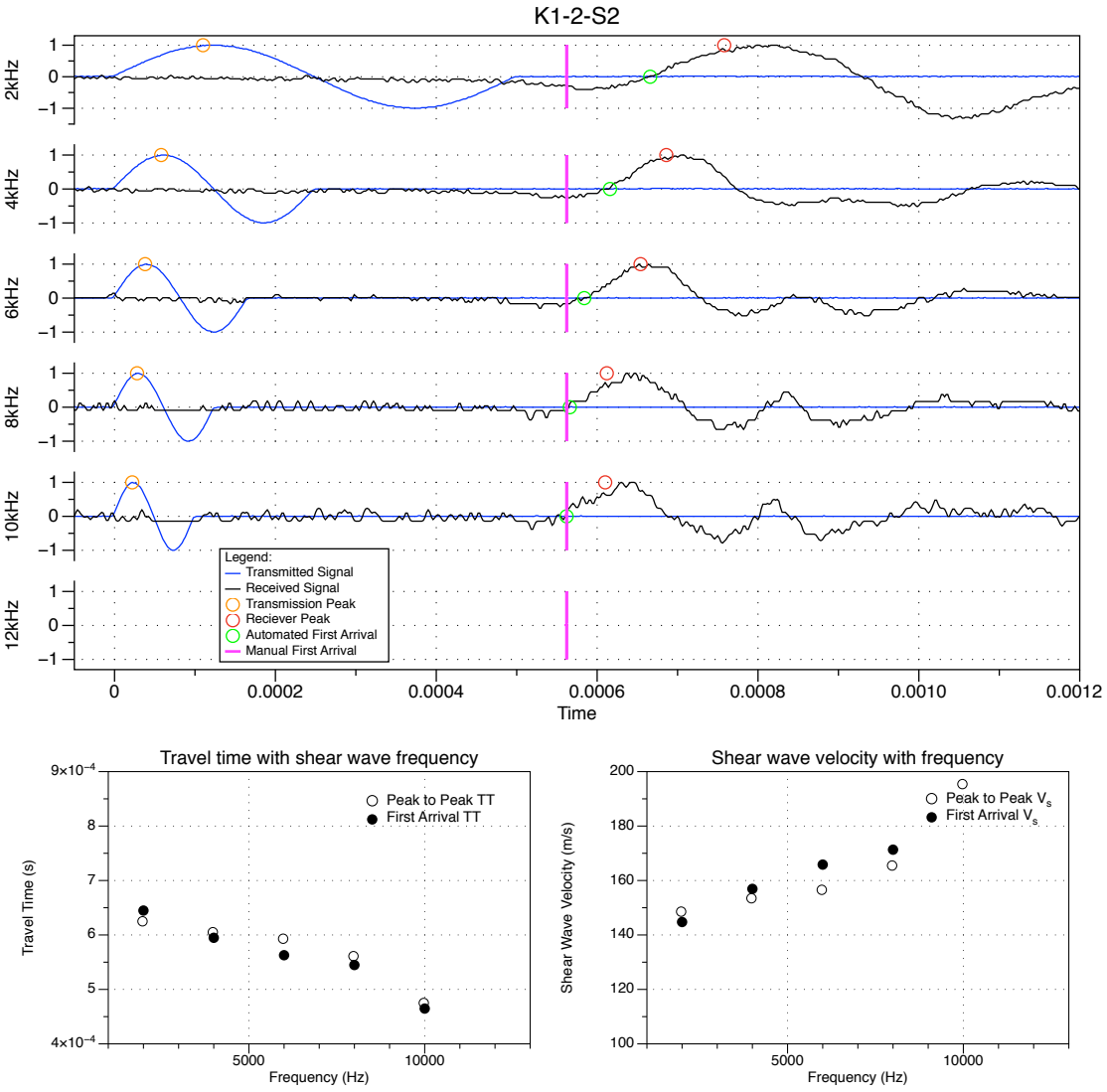

Figure 3.49: Processed bender element test data for sample K1–2–S2

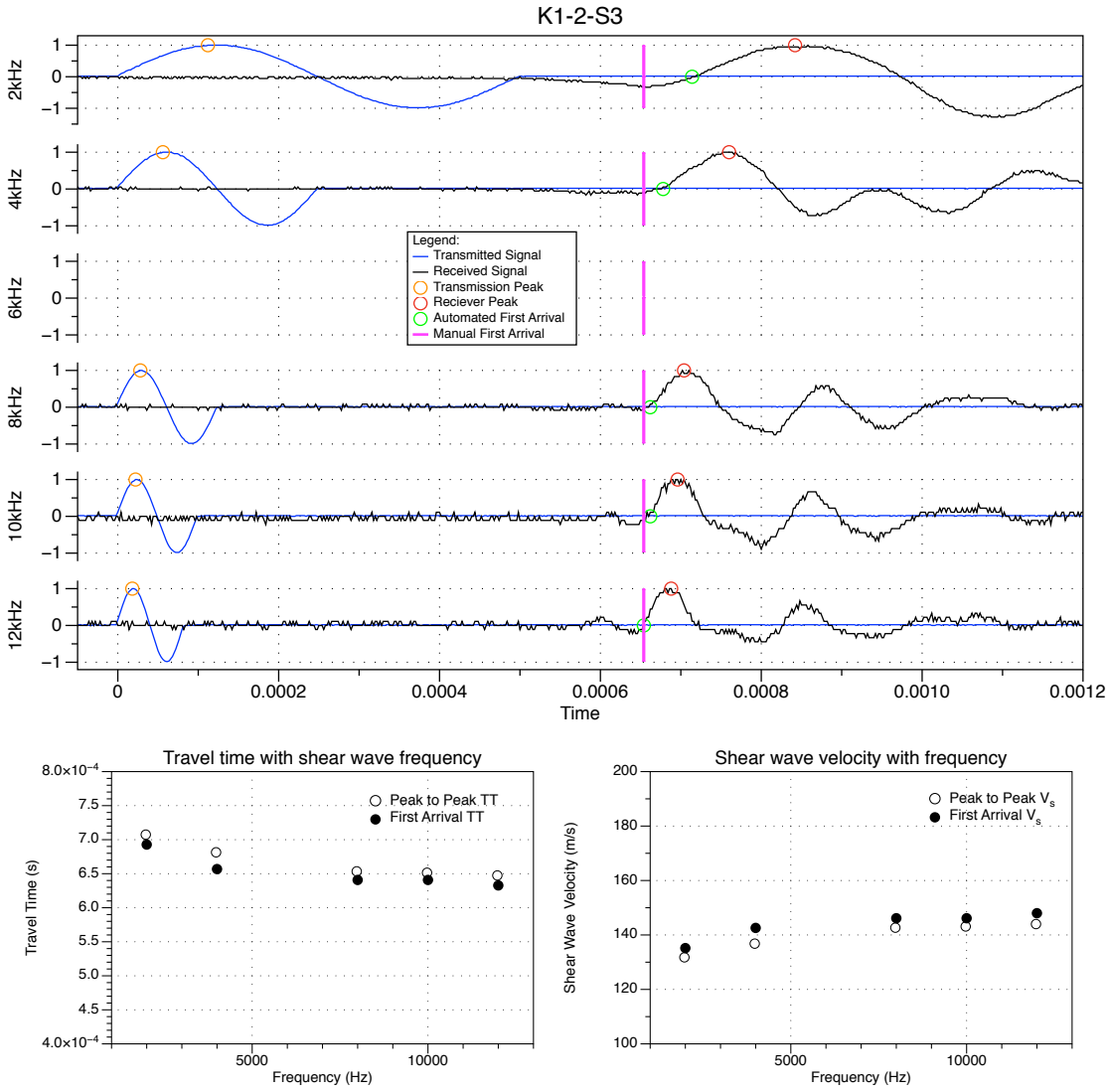

Figure 3.50: Processed bender element test data for sample K1–2–S3

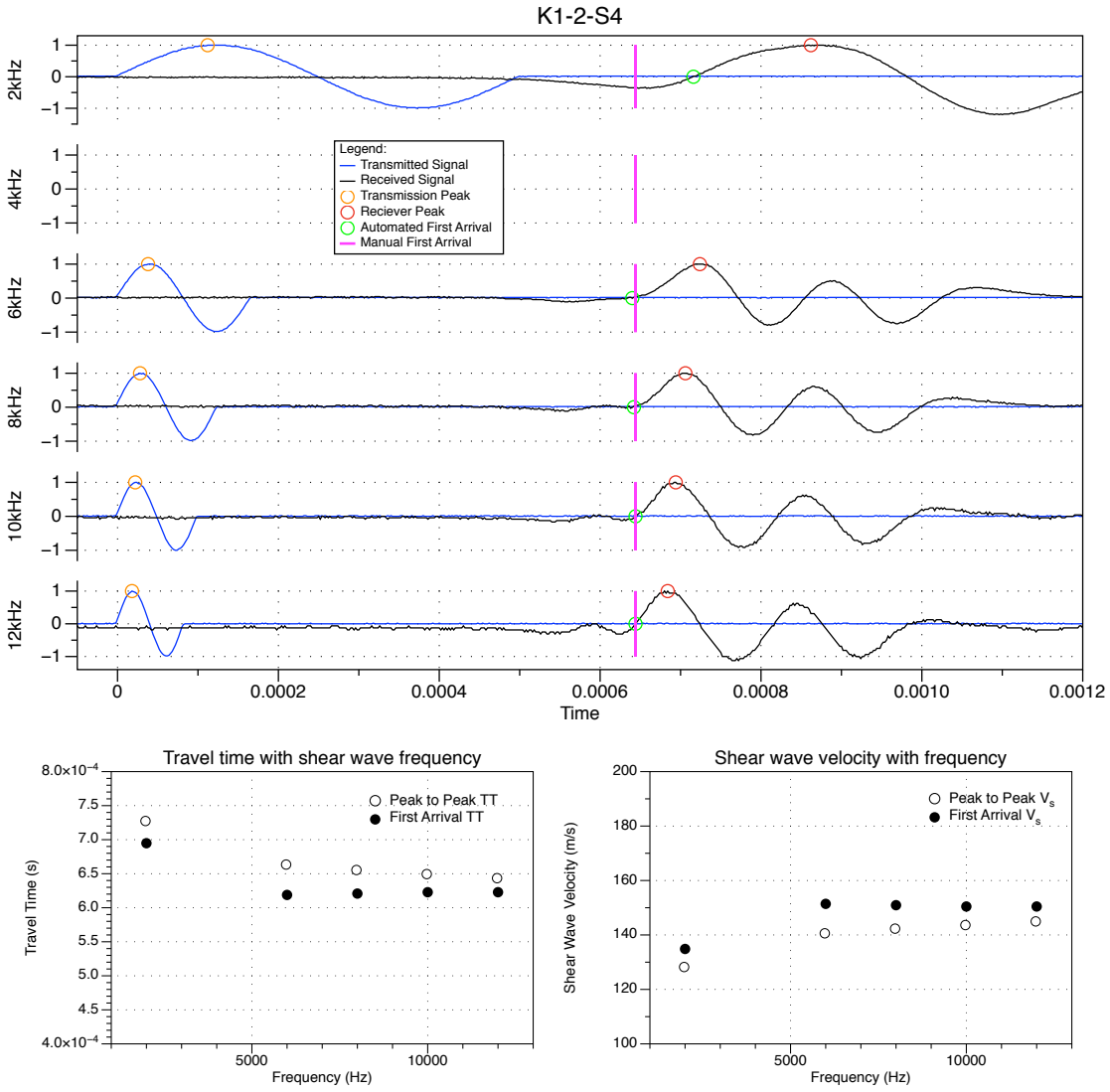

Figure 3.51: Processed bender element test data for sample K1–2–S4

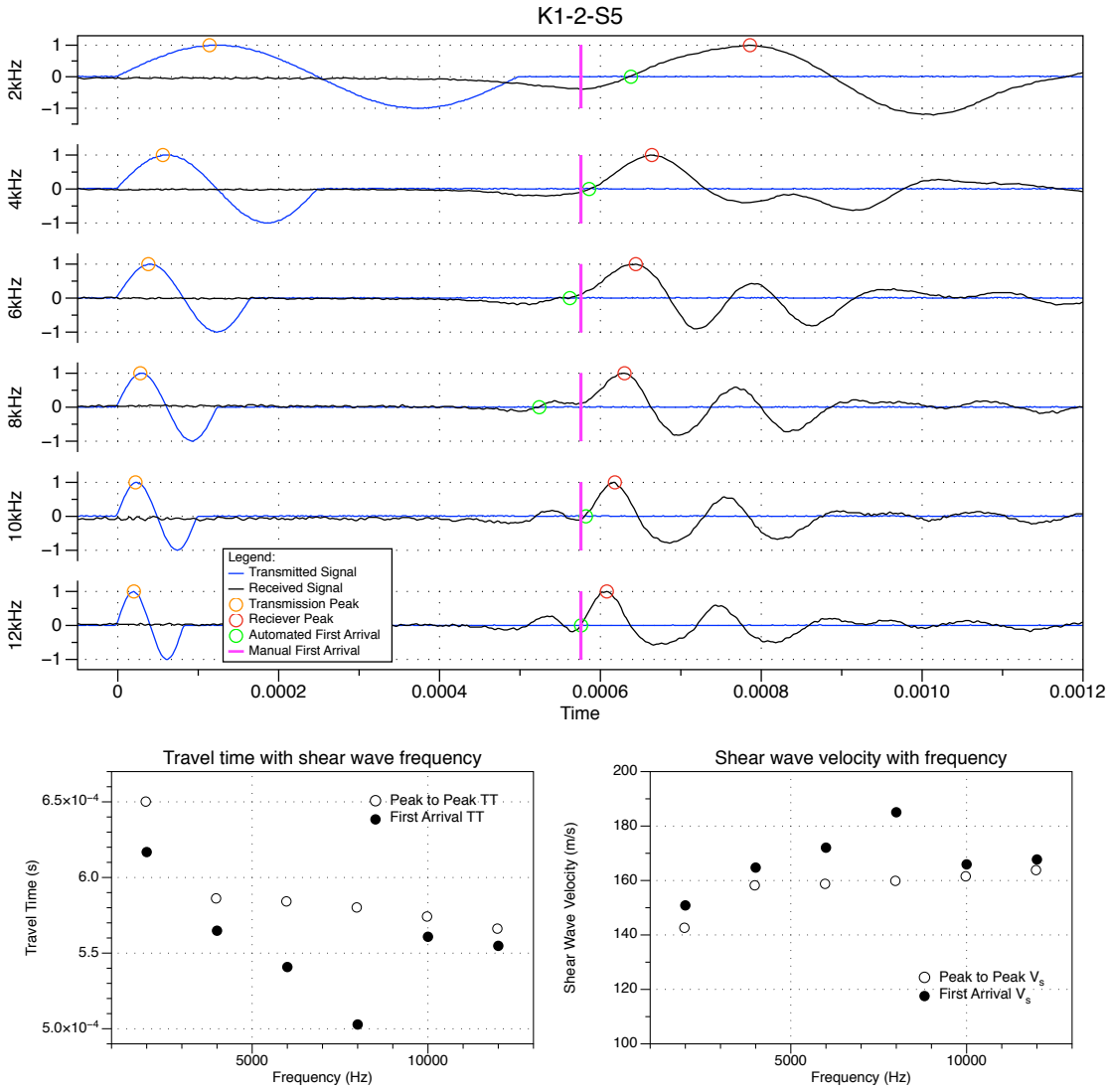

Figure 3.52: Processed bender element test data for sample K1–2–S5

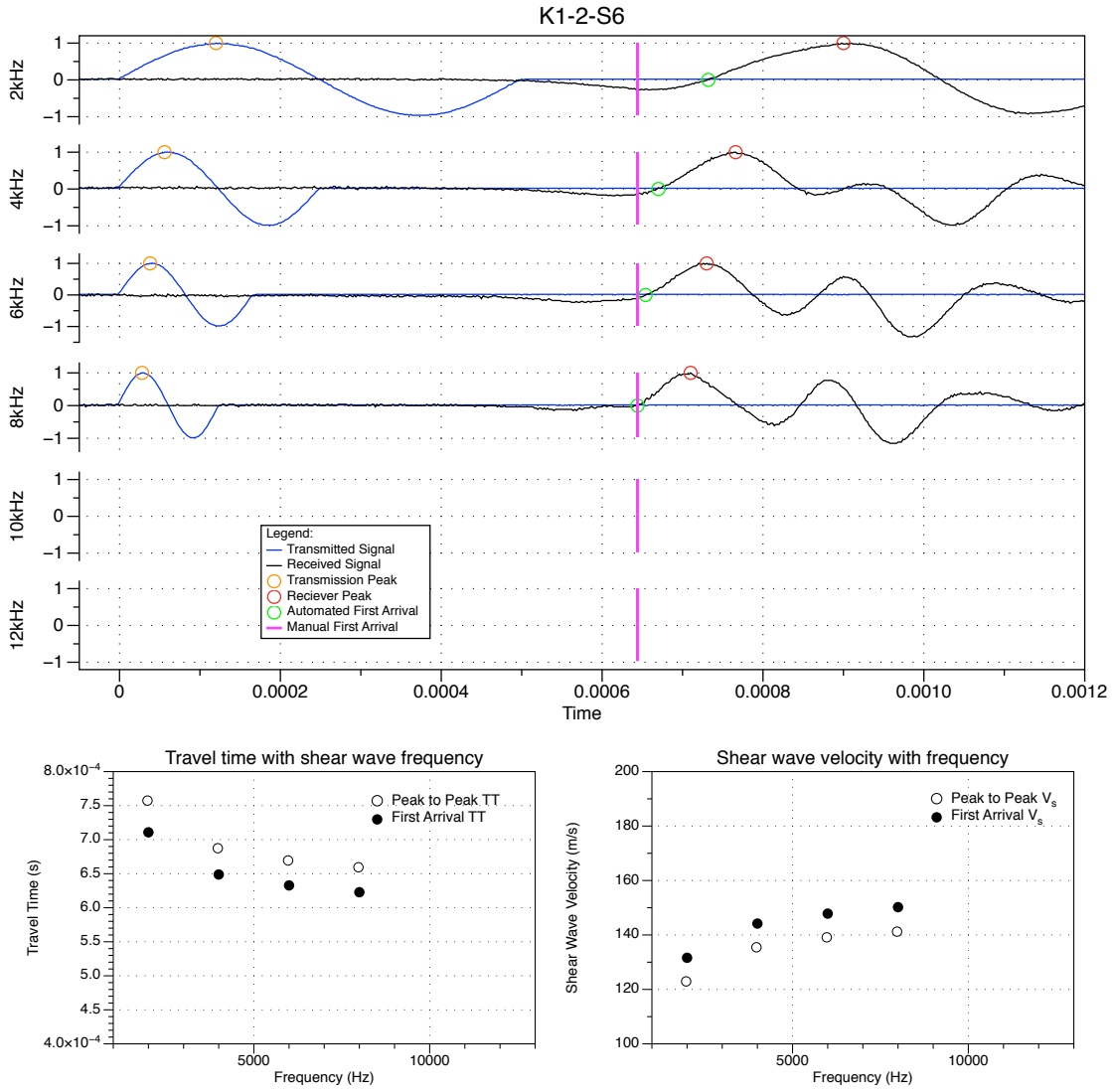

Figure 3.53: Processed bender element test data for sample K1–2-S6

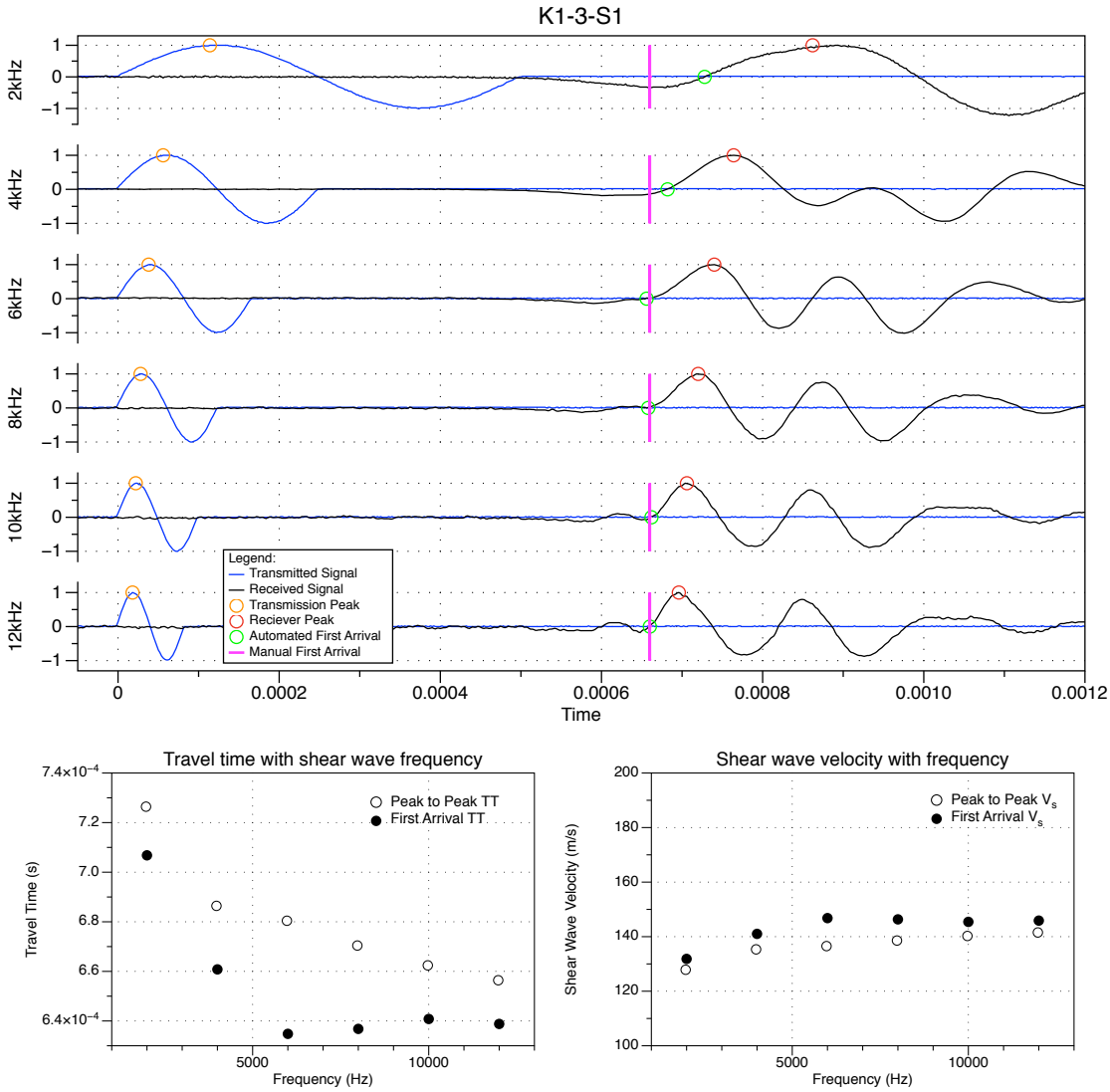

Figure 3.54: Processed bender element test data for sample K1–3-S1

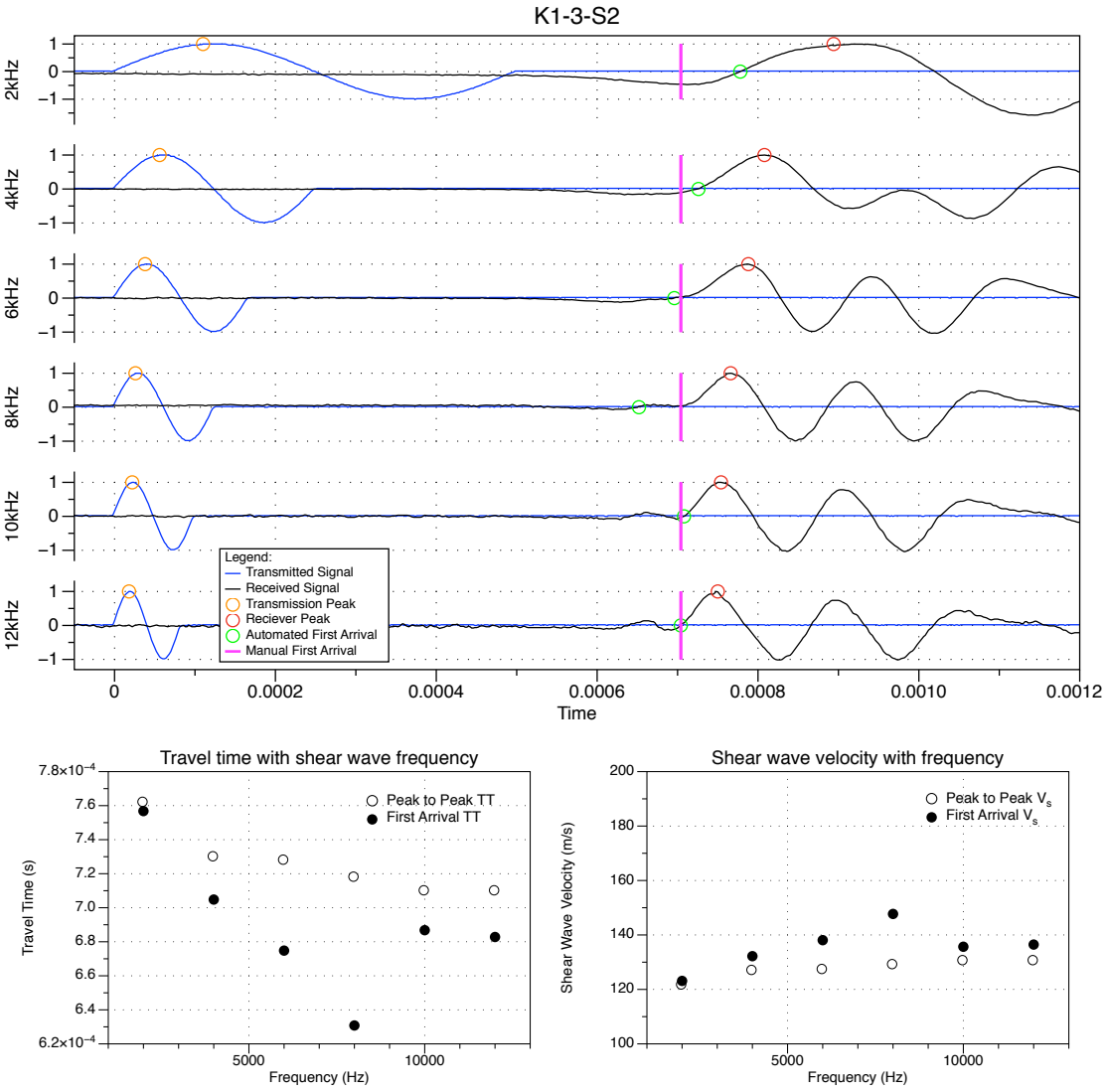

Figure 3.55: Processed bender element test data for sample K1–3–S2

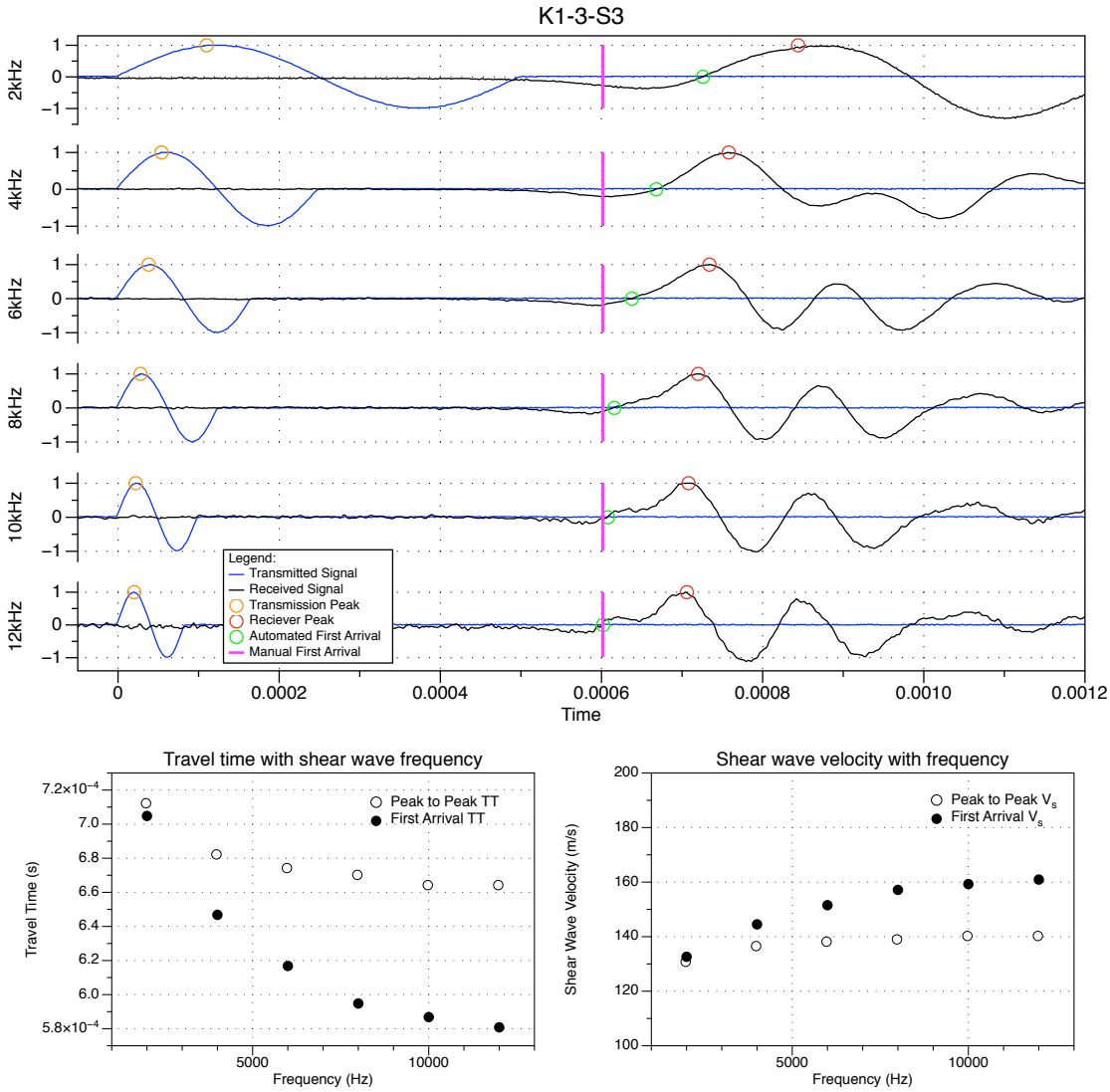

Figure 3.56: Processed bender element test data for sample K1–3–S3

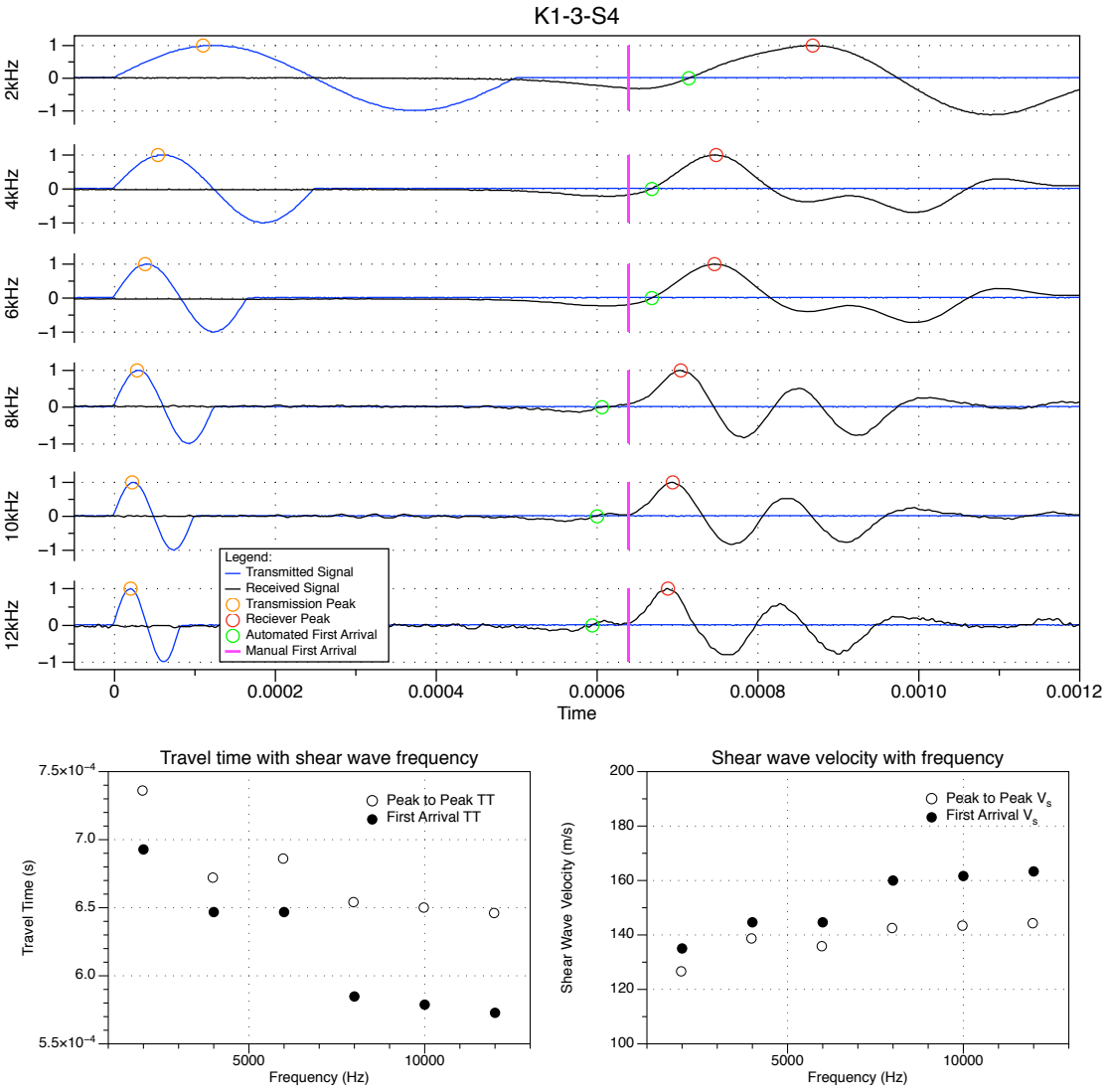

Figure 3.57: Processed bender element test data for sample K1–3–S4

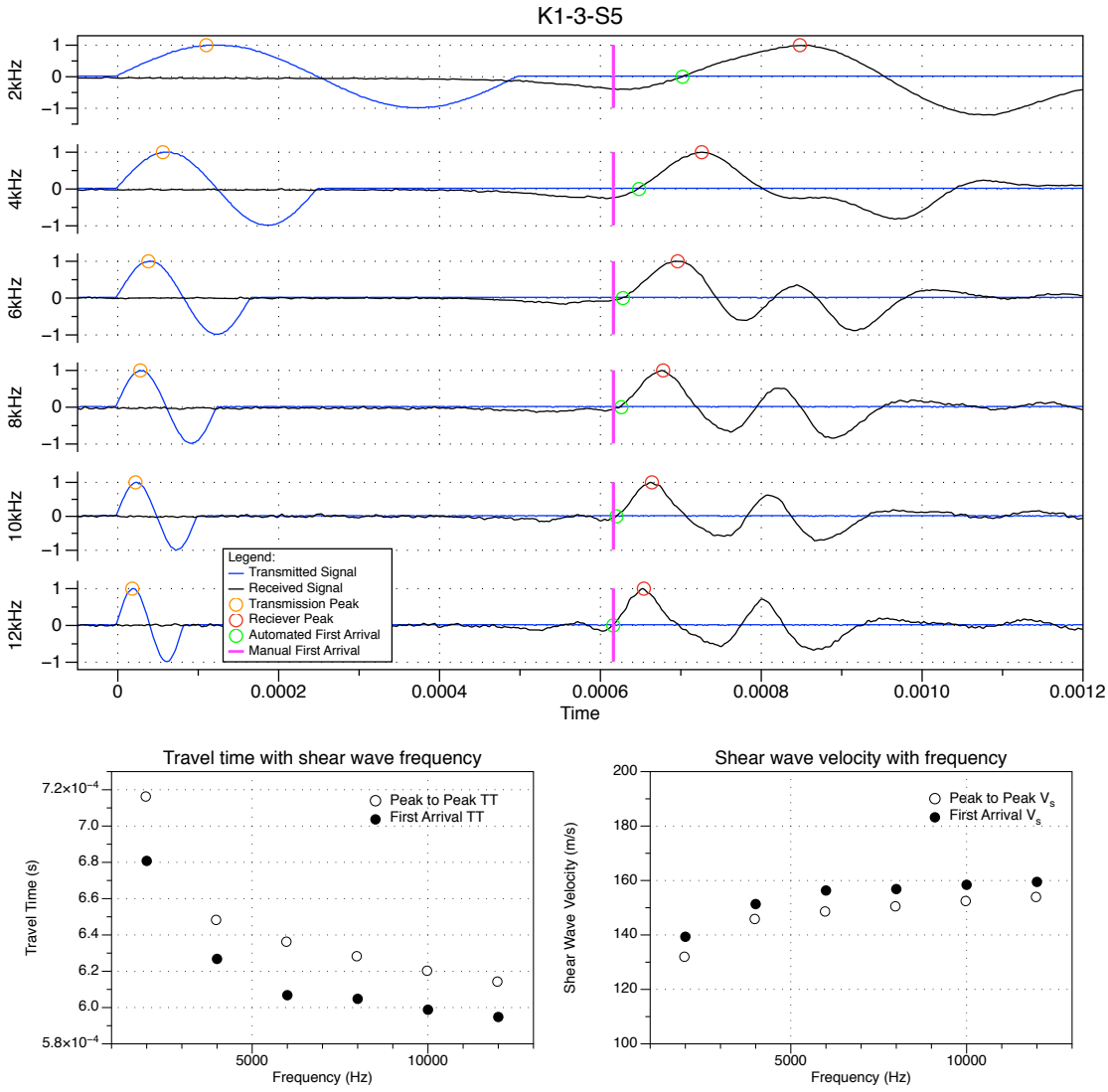

Figure 3.58: Processed bender element test data for sample K1–3–S5

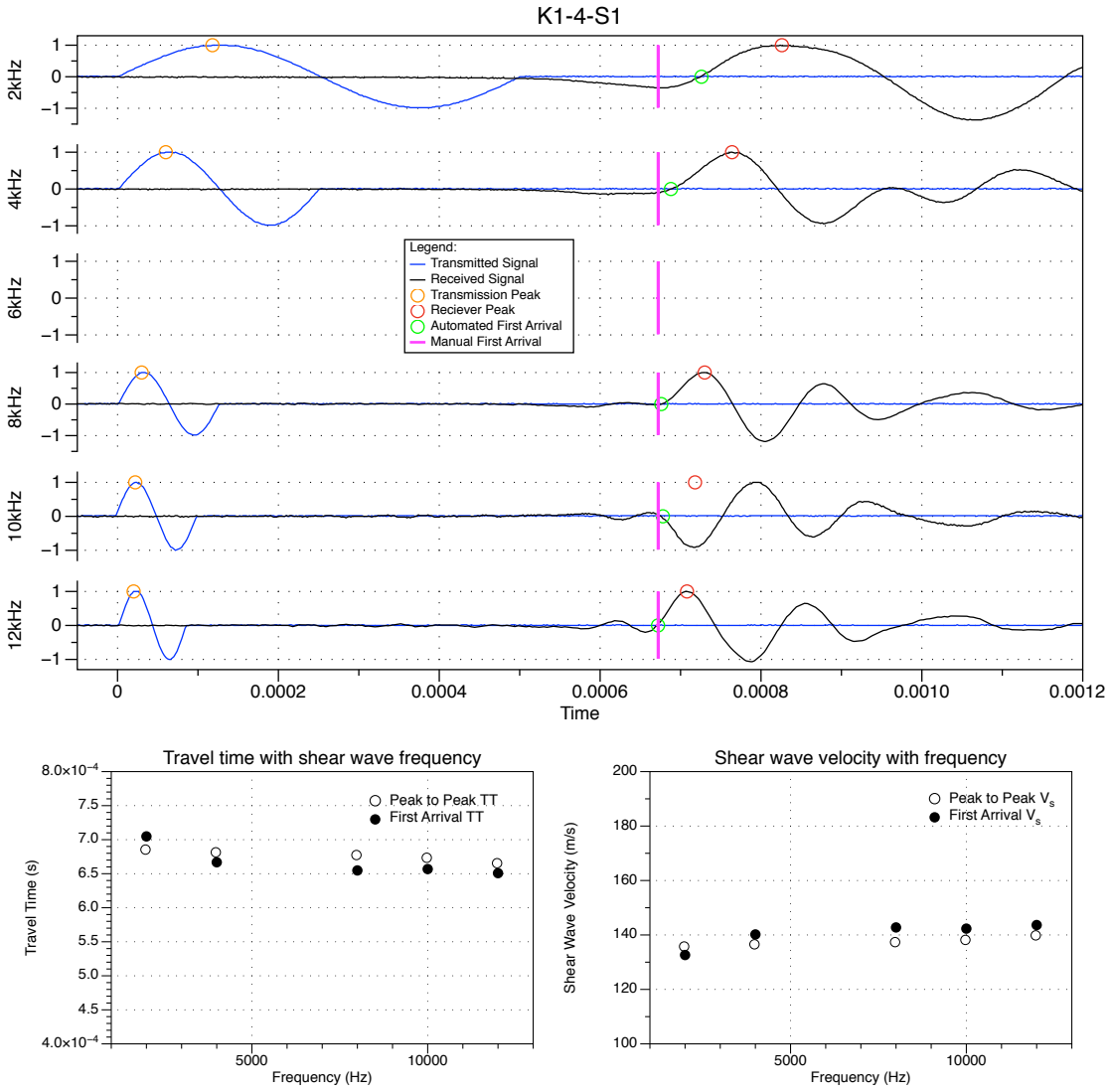

Figure 3.59: Processed bender element test data for sample K1–4–S1

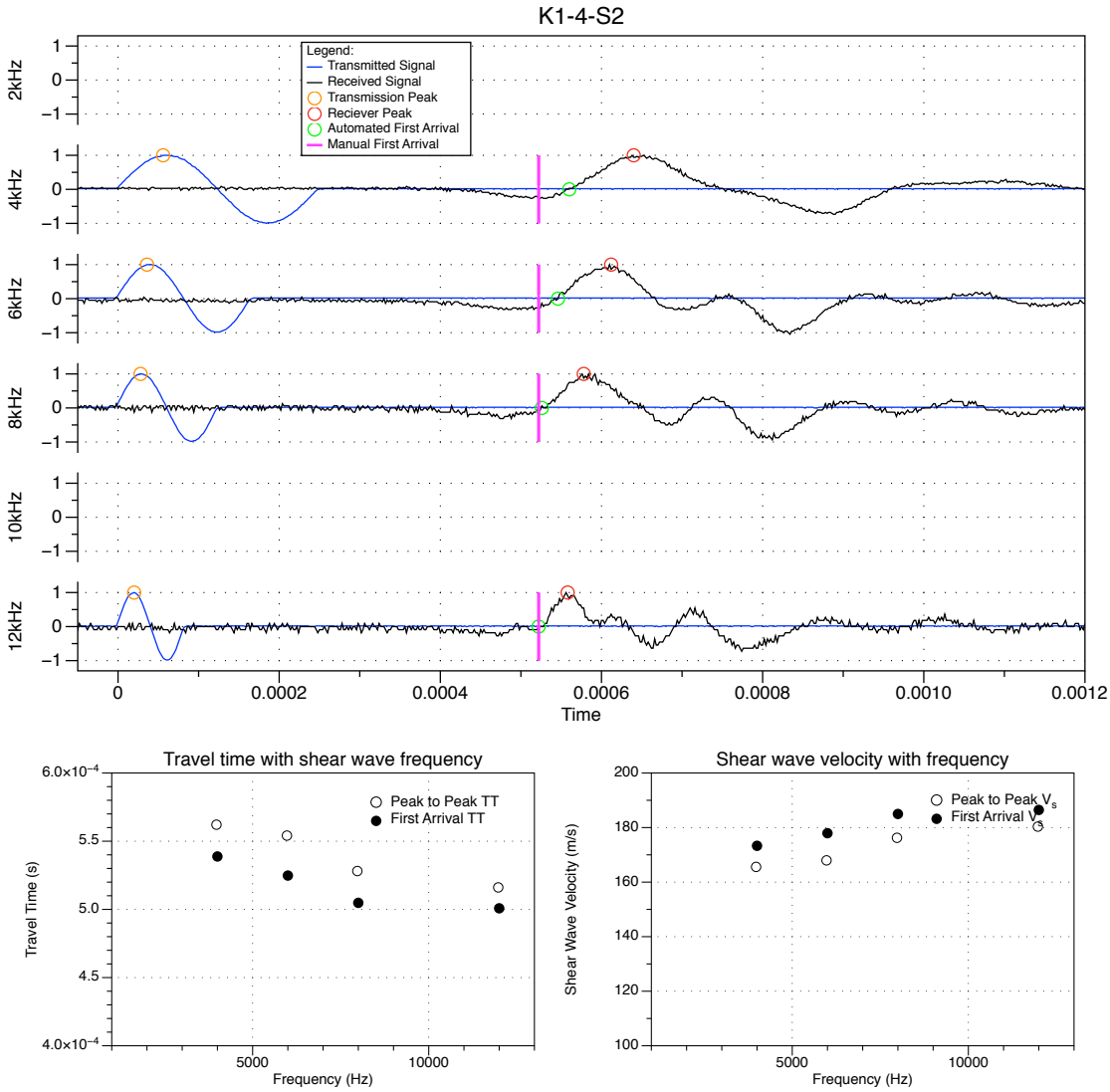

Figure 3.60: Processed bender element test data for sample K1–4–S2

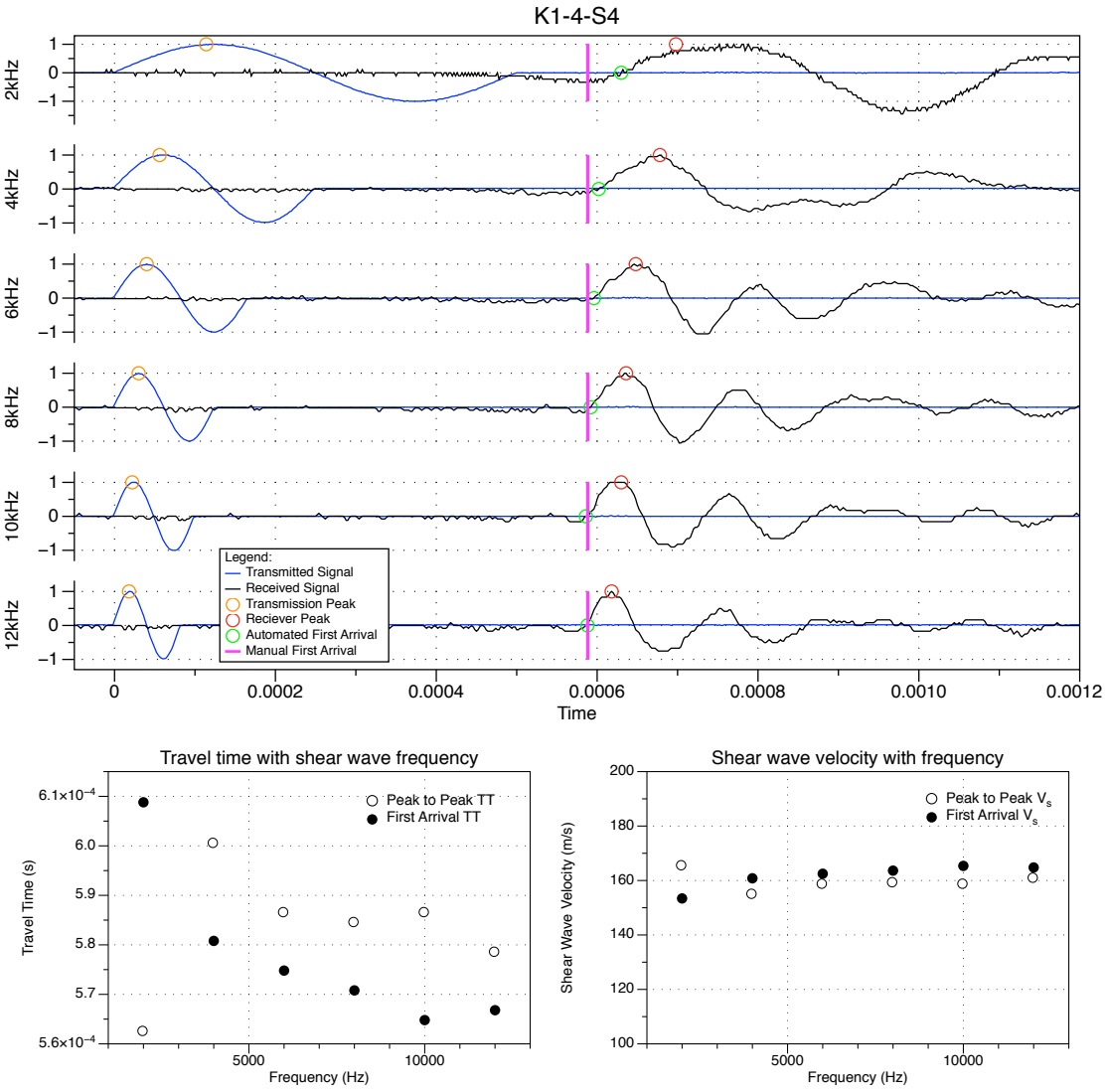

Figure 3.61: Processed bender element test data for sample K1–4–S4

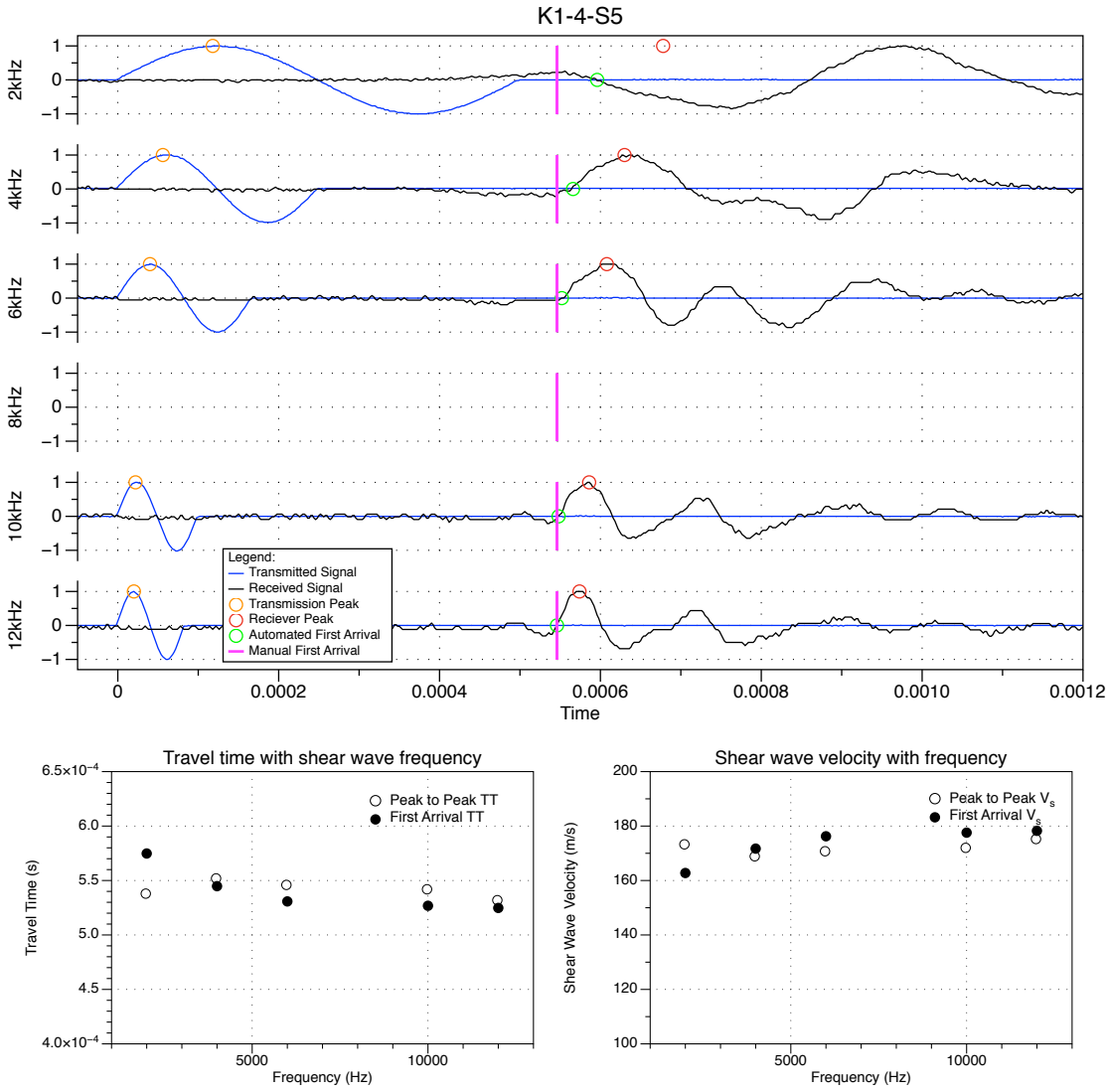

Figure 3.62: Processed bender element test data for sample K1–4–S5

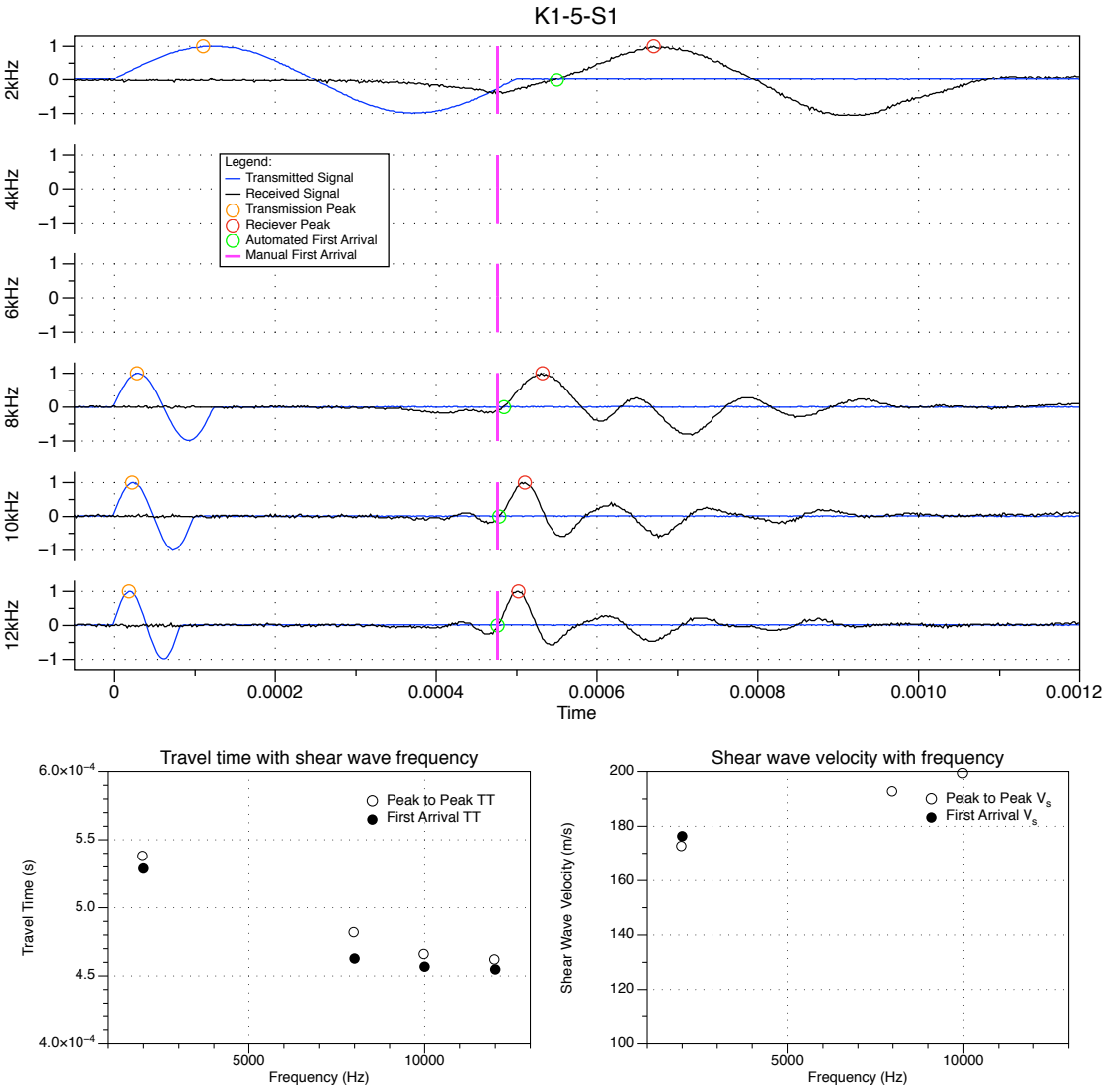

Figure 3.63: Processed bender element test data for sample K1–5–S1

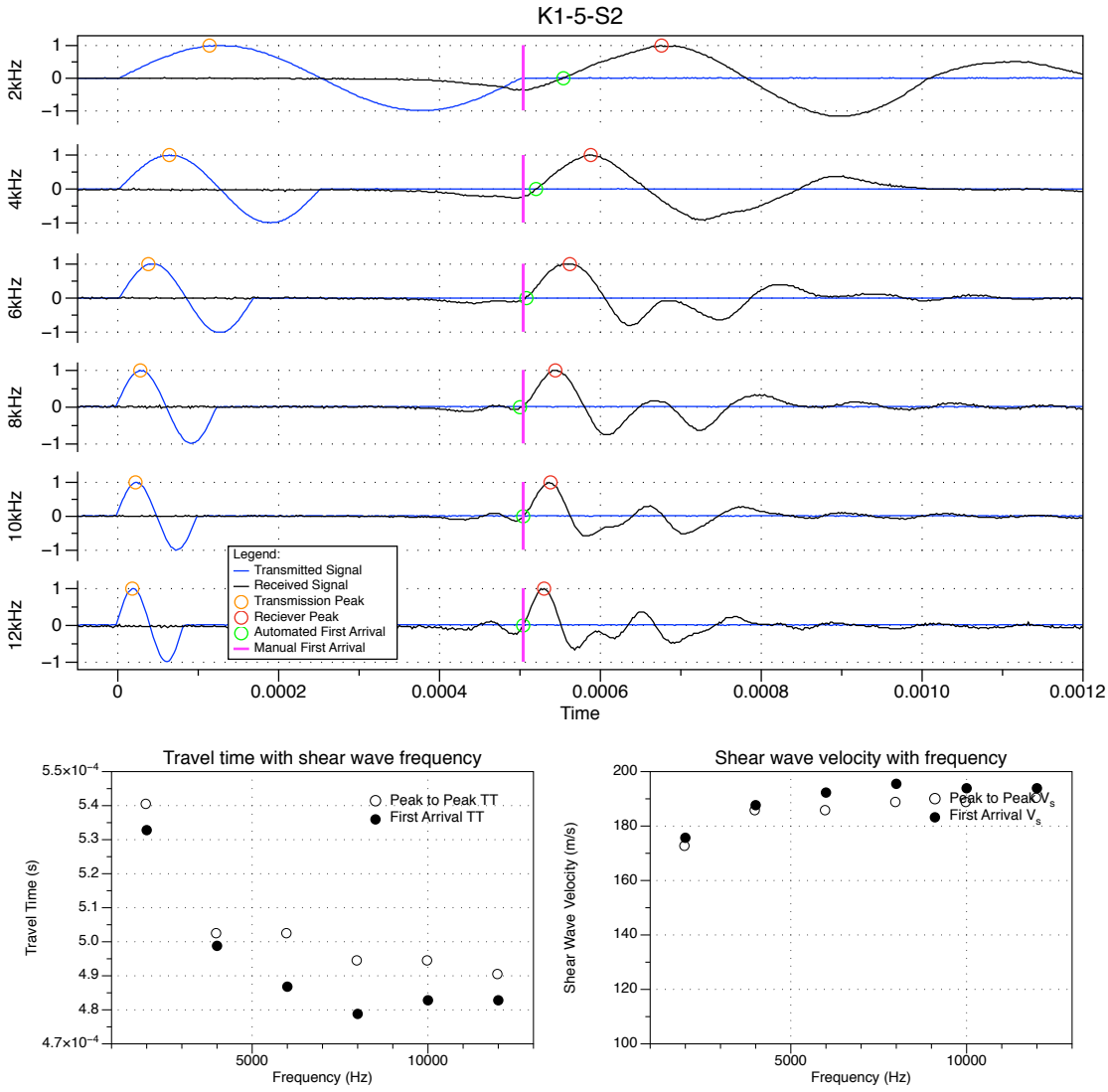

Figure 3.64: Processed bender element test data for sample K1–5–S2

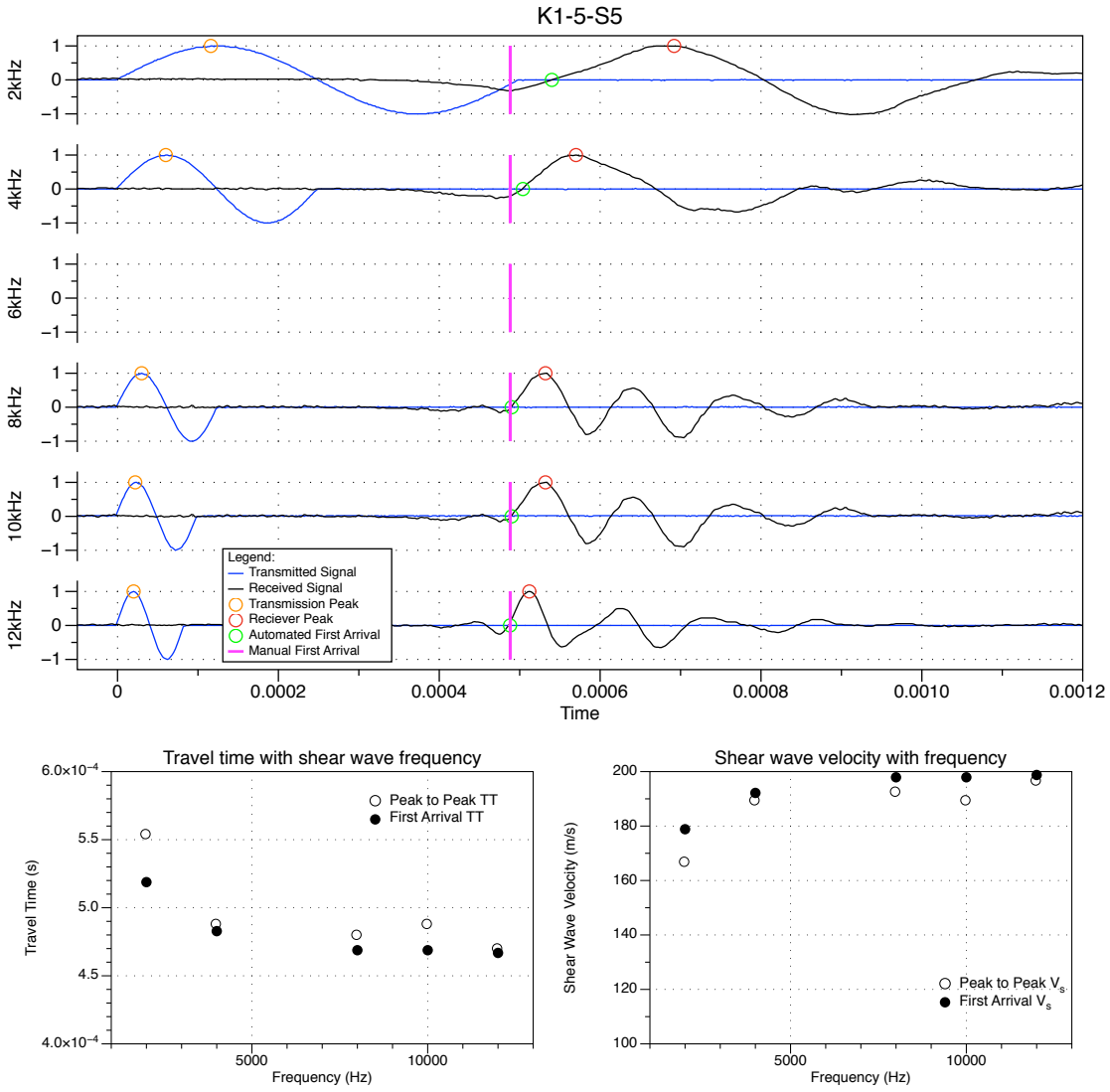

Figure 3.65: Processed bender element test data for sample K1–5–S5

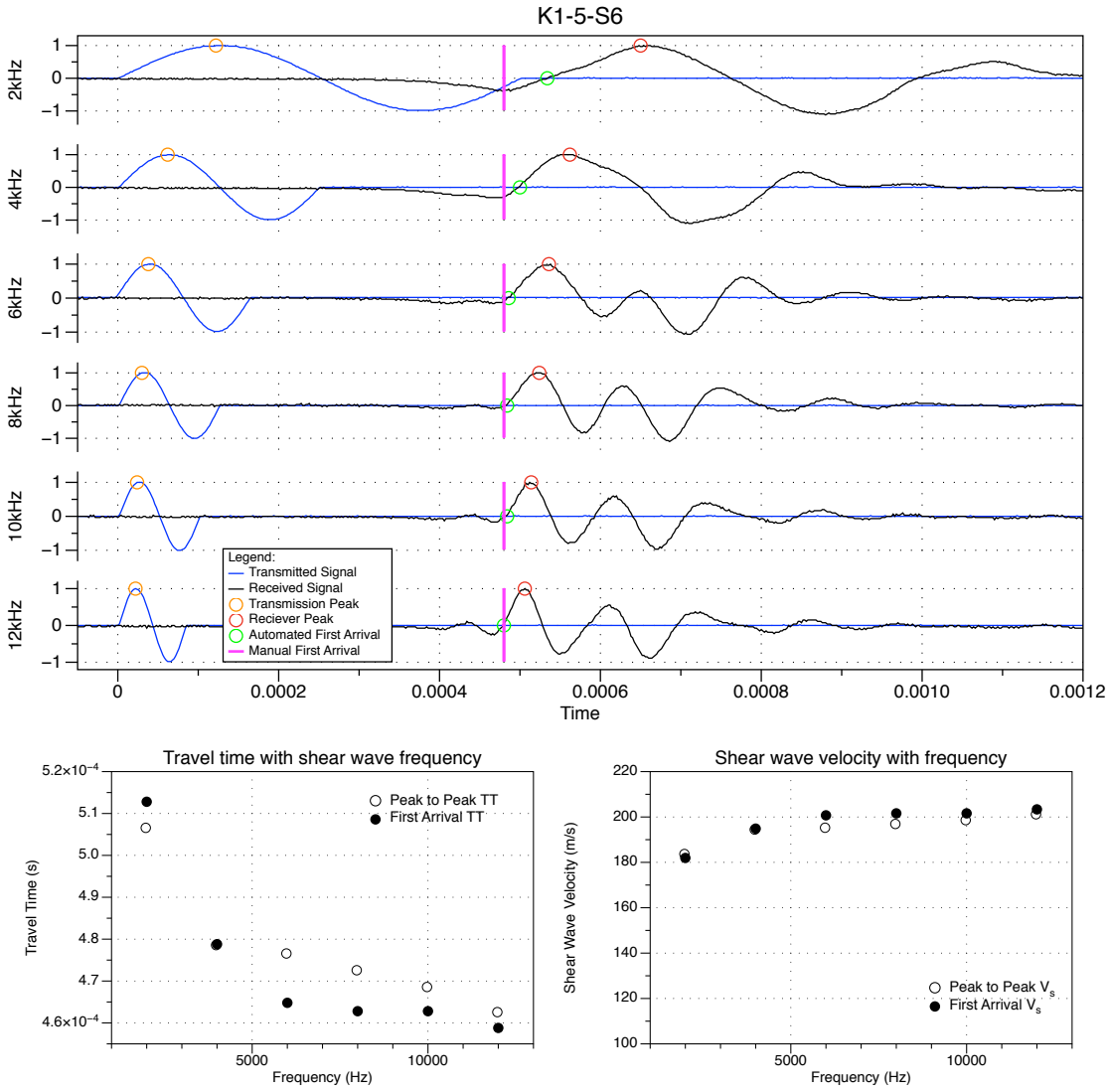

Figure 3.66: Processed bender element test data for sample K1–5–S6

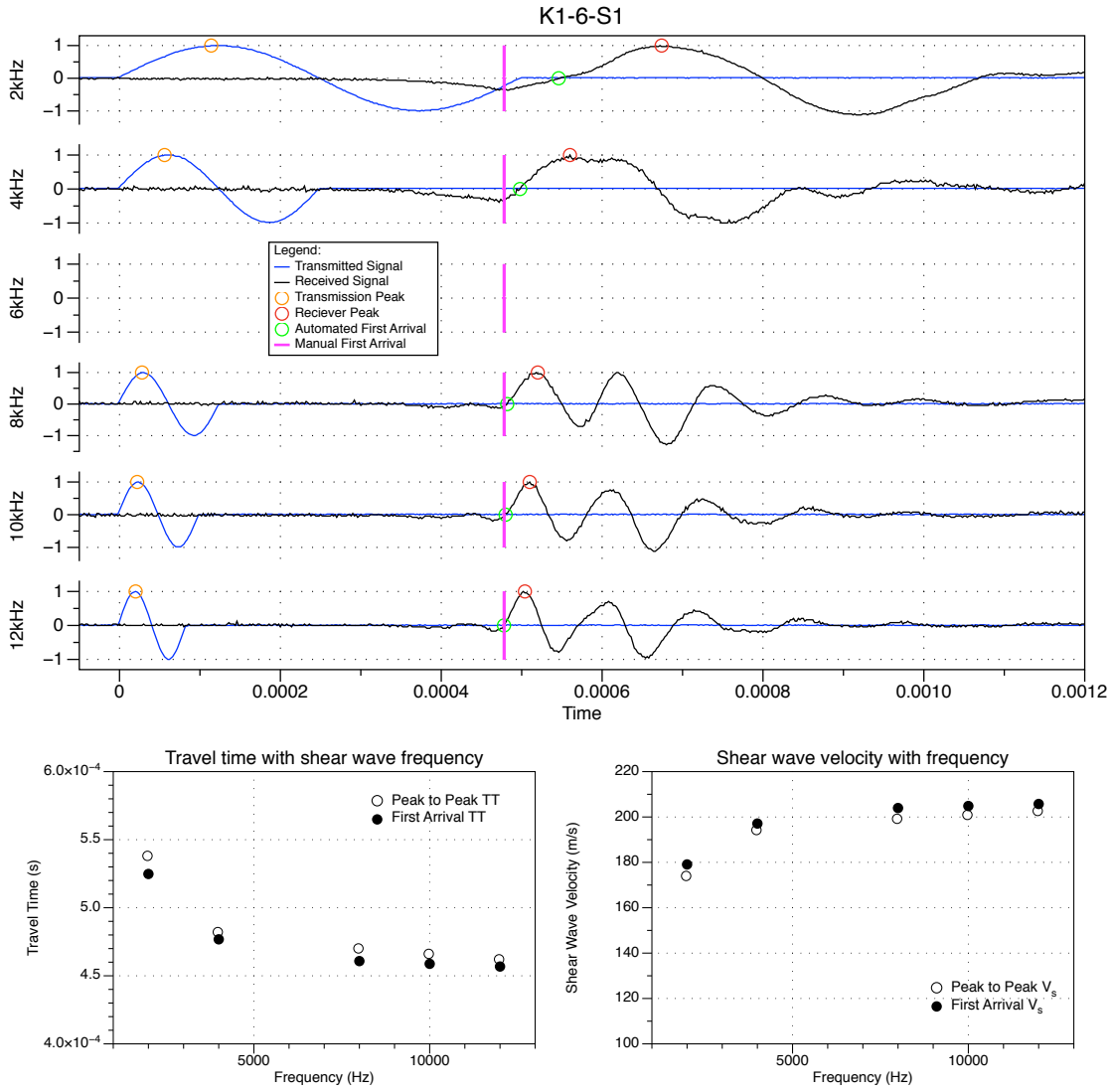

Figure 3.67: Processed bender element test data for sample K1–6–S1

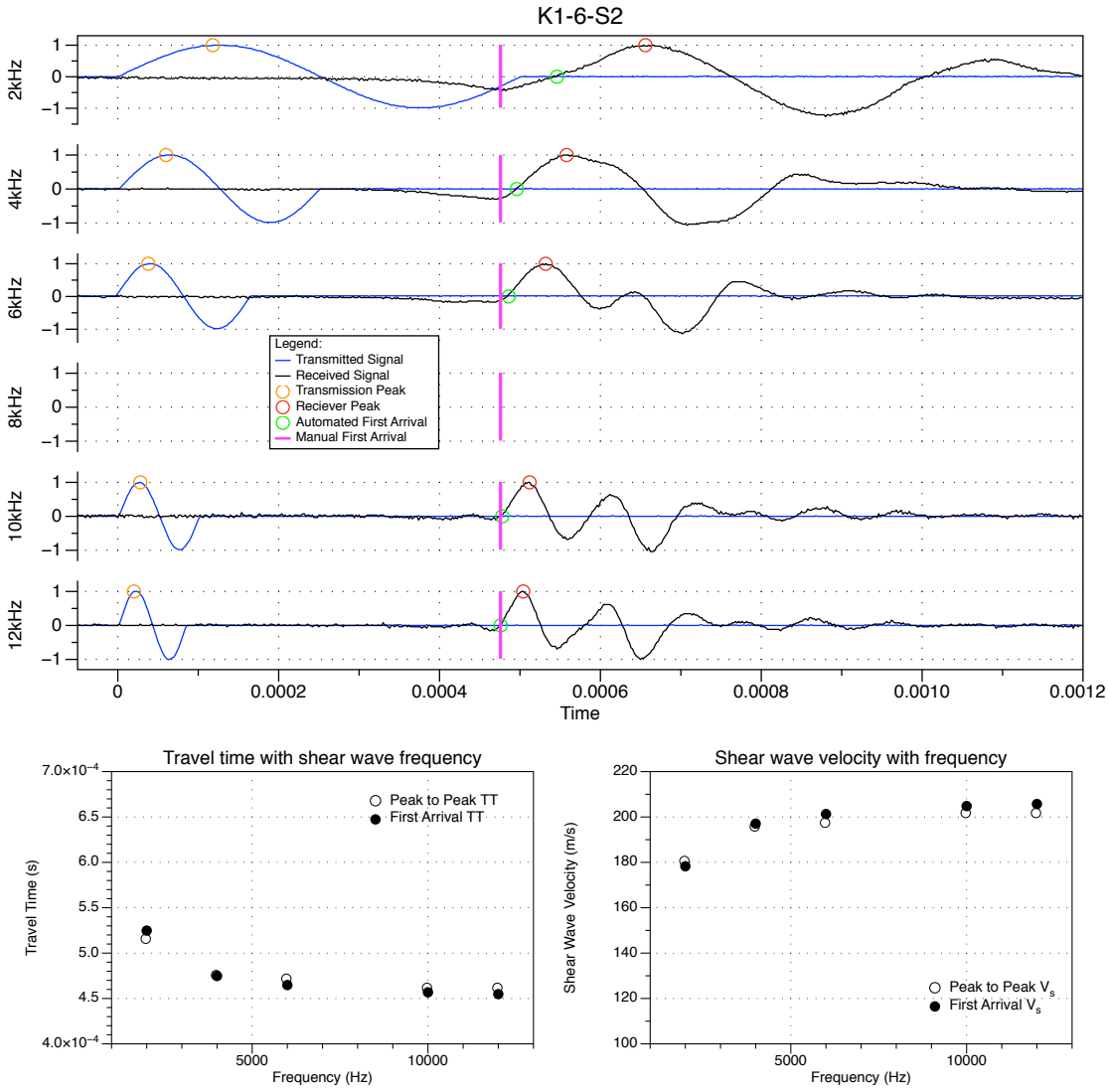

Figure 3.68: Processed bender element test data for sample K1–6–S2

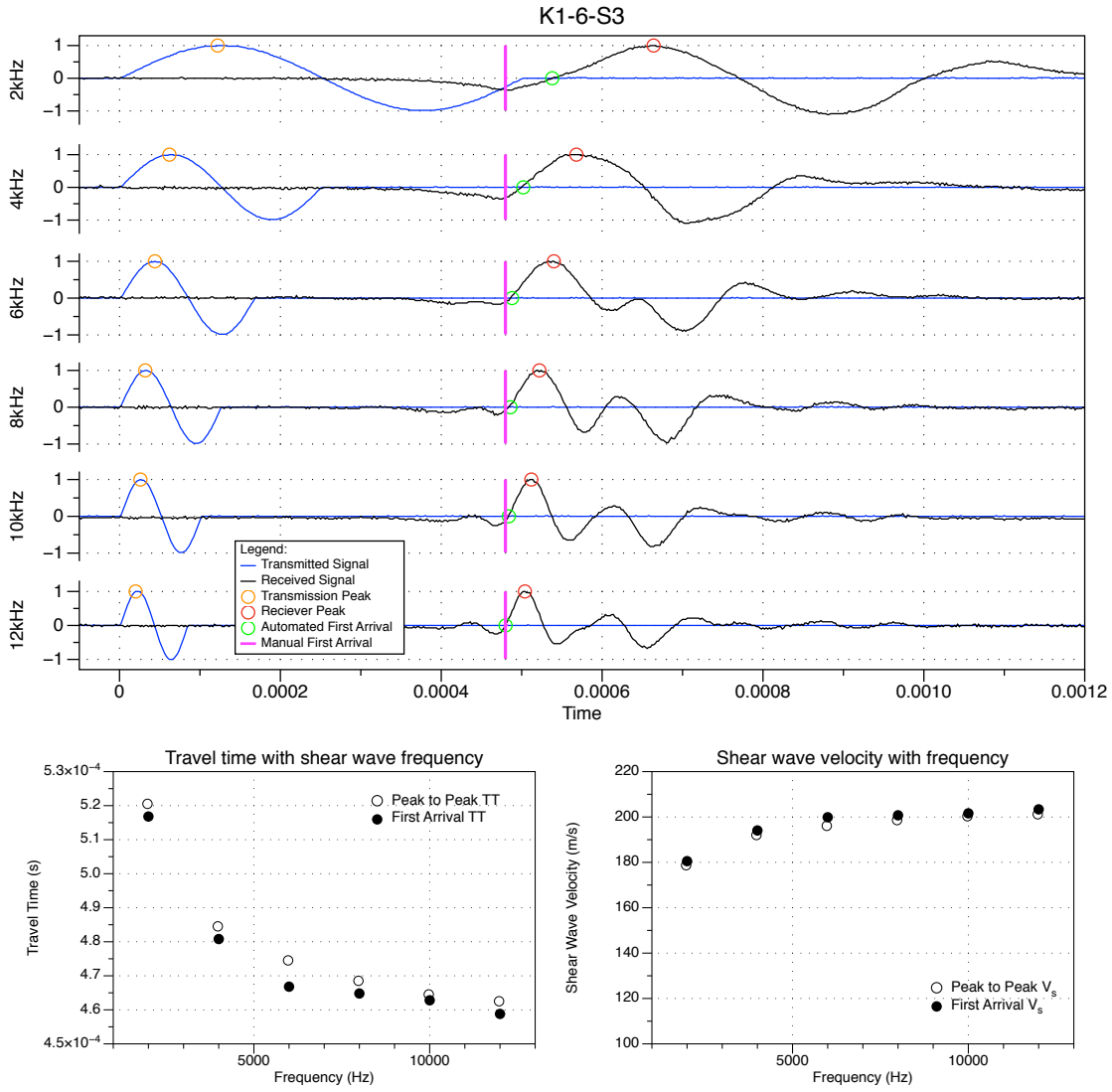

Figure 3.69: Processed bender element test data for sample K1–6–S3

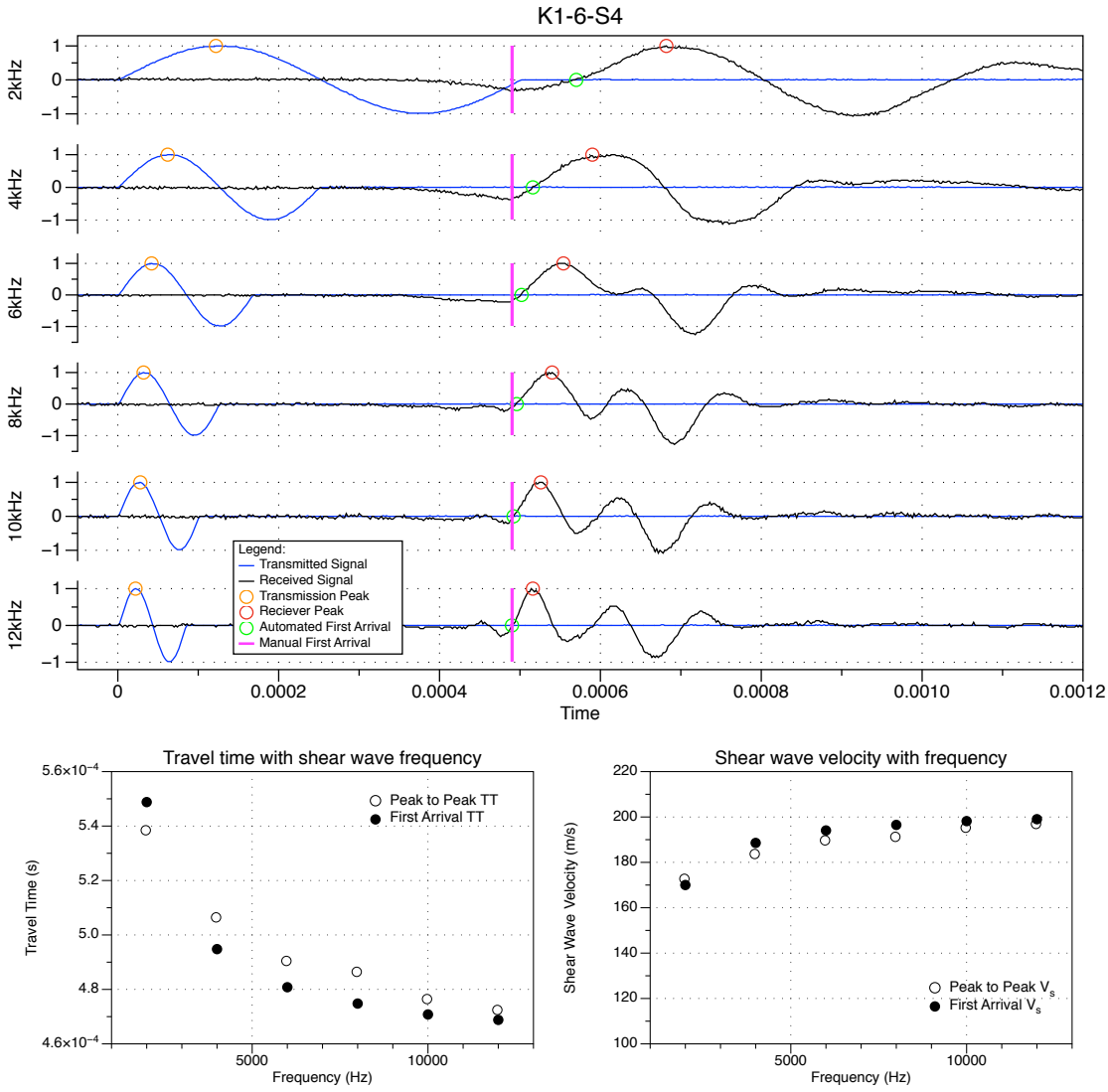

Figure 3.70: Processed bender element test data for sample K1–6–S4

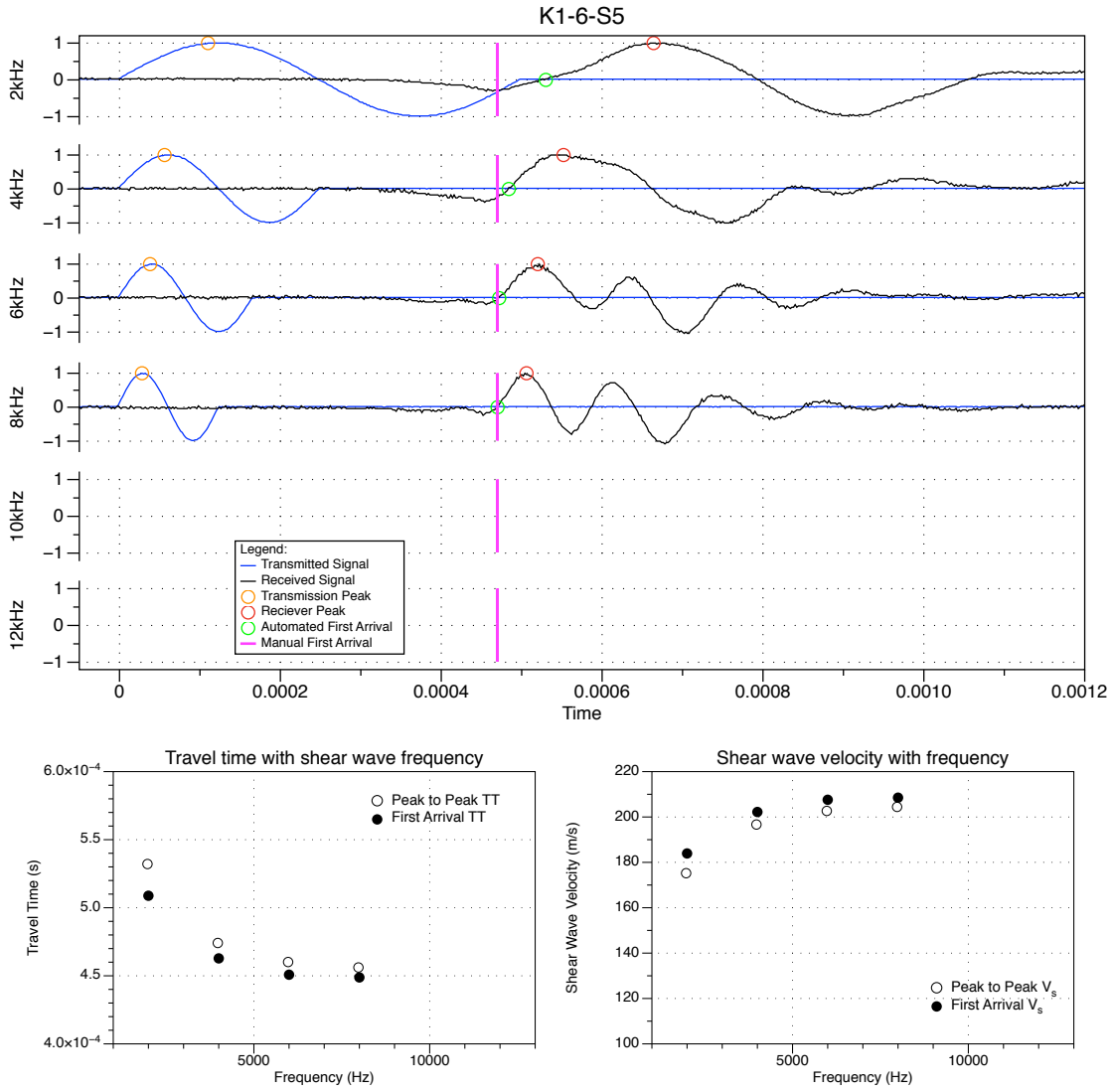

Figure 3.71: Processed bender element test data for sample K1–6–S5

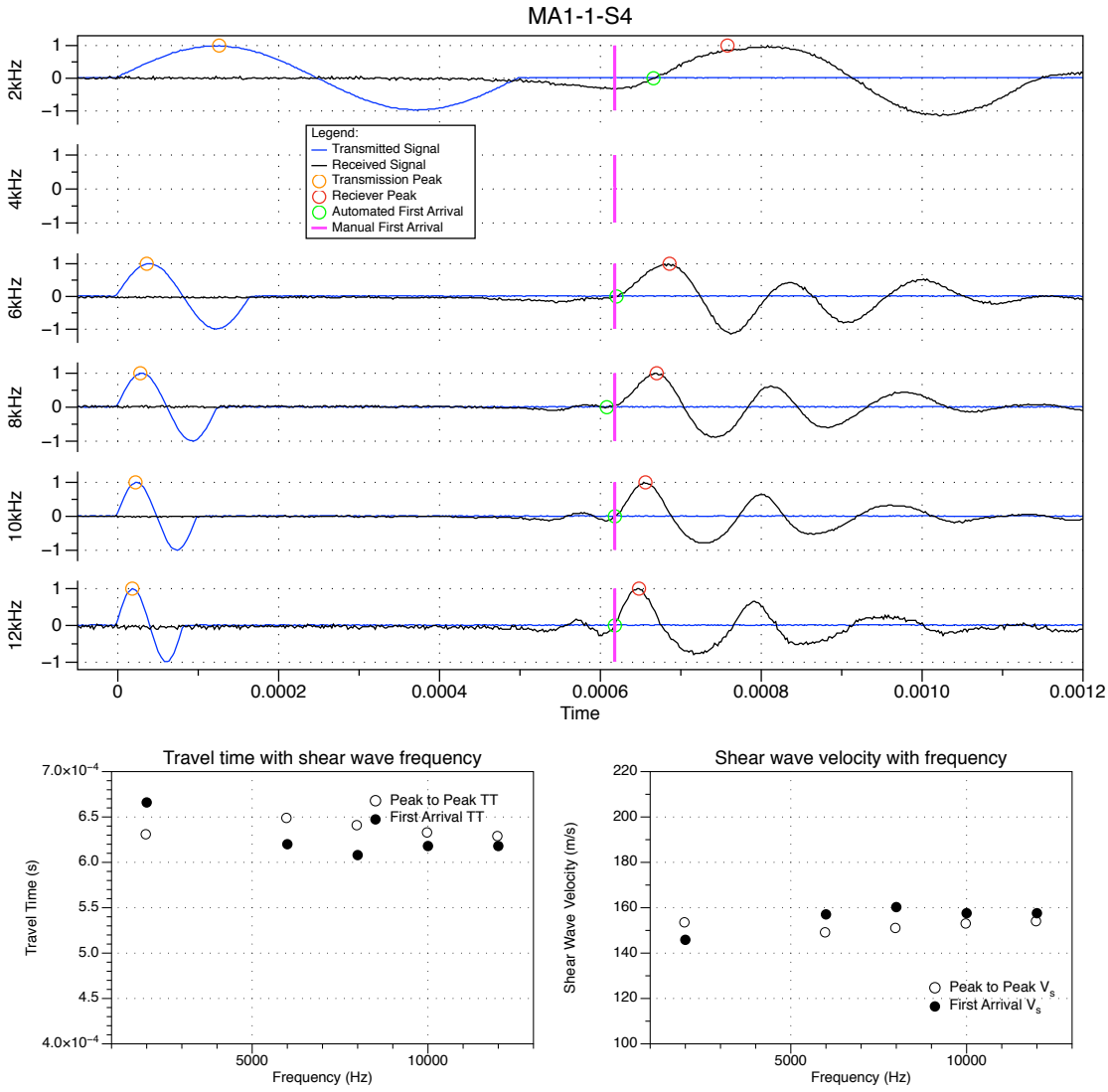

Figure 3.72: Processed bender element test data for sample MA1–1–S4

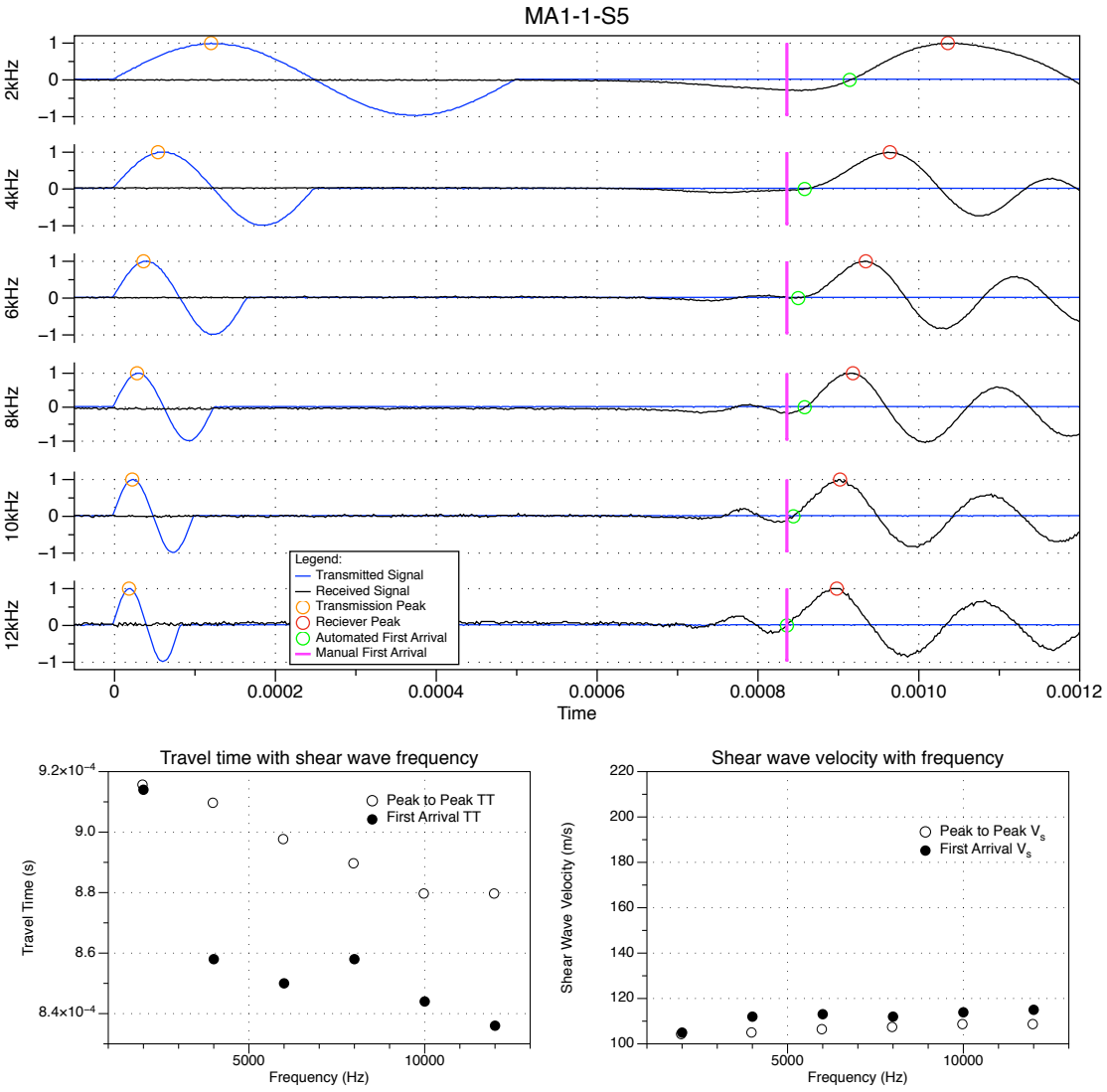

Figure 3.73: Processed bender element test data for sample MA1–1–S5

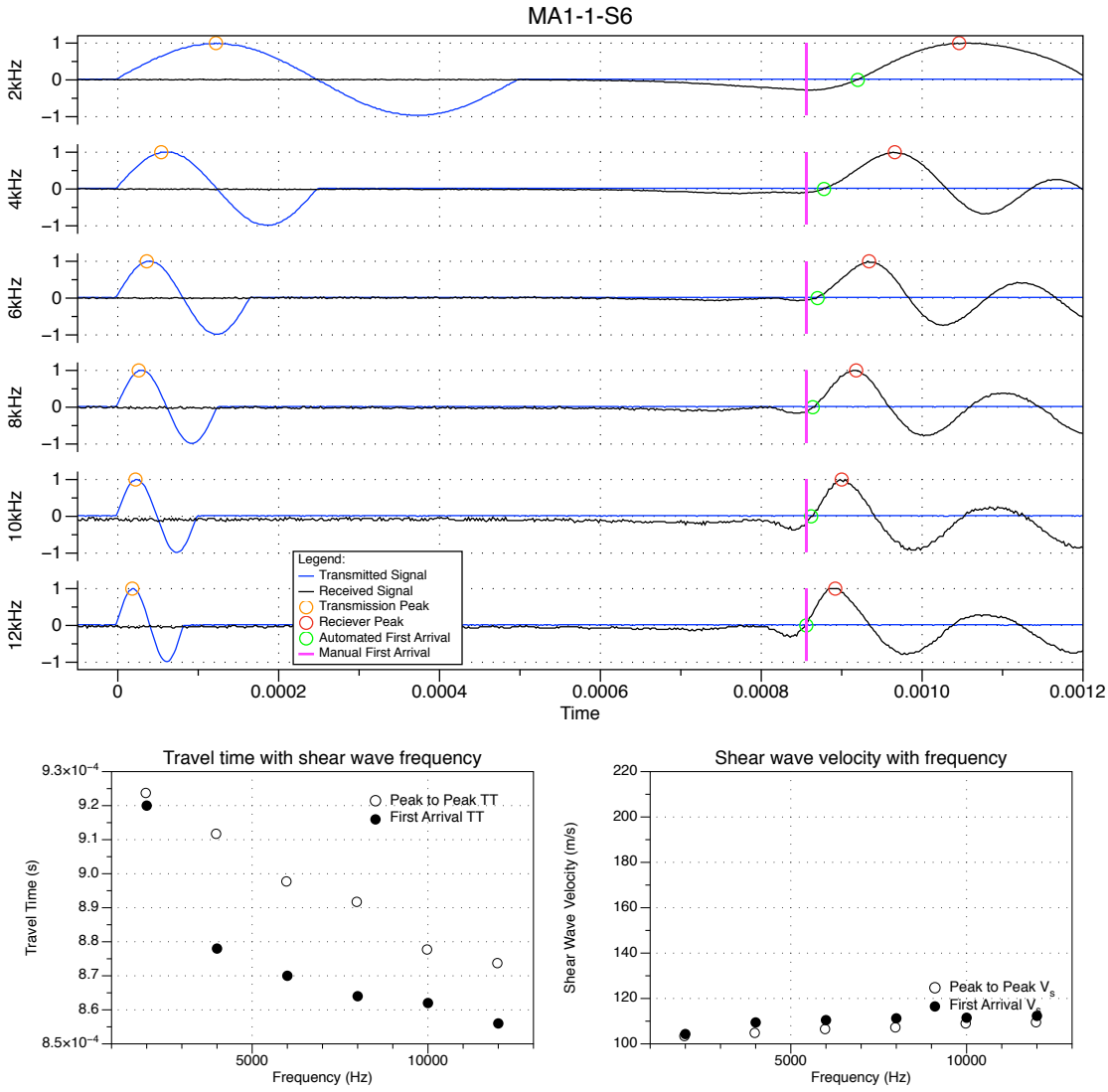

Figure 3.74: Processed bender element test data for sample MA1–1–S6

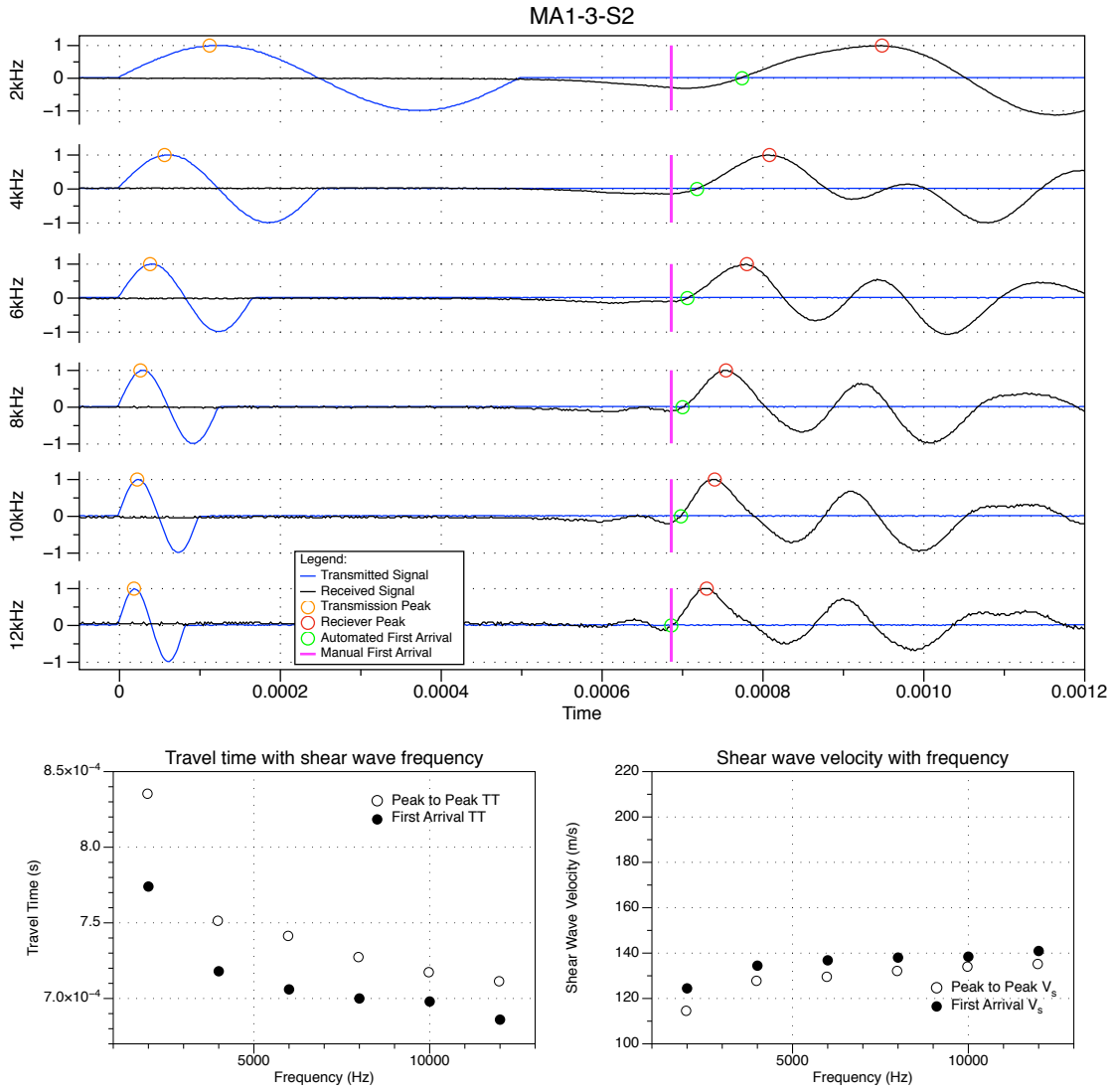

Figure 3.75: Processed bender element test data for sample MA1–3–S2

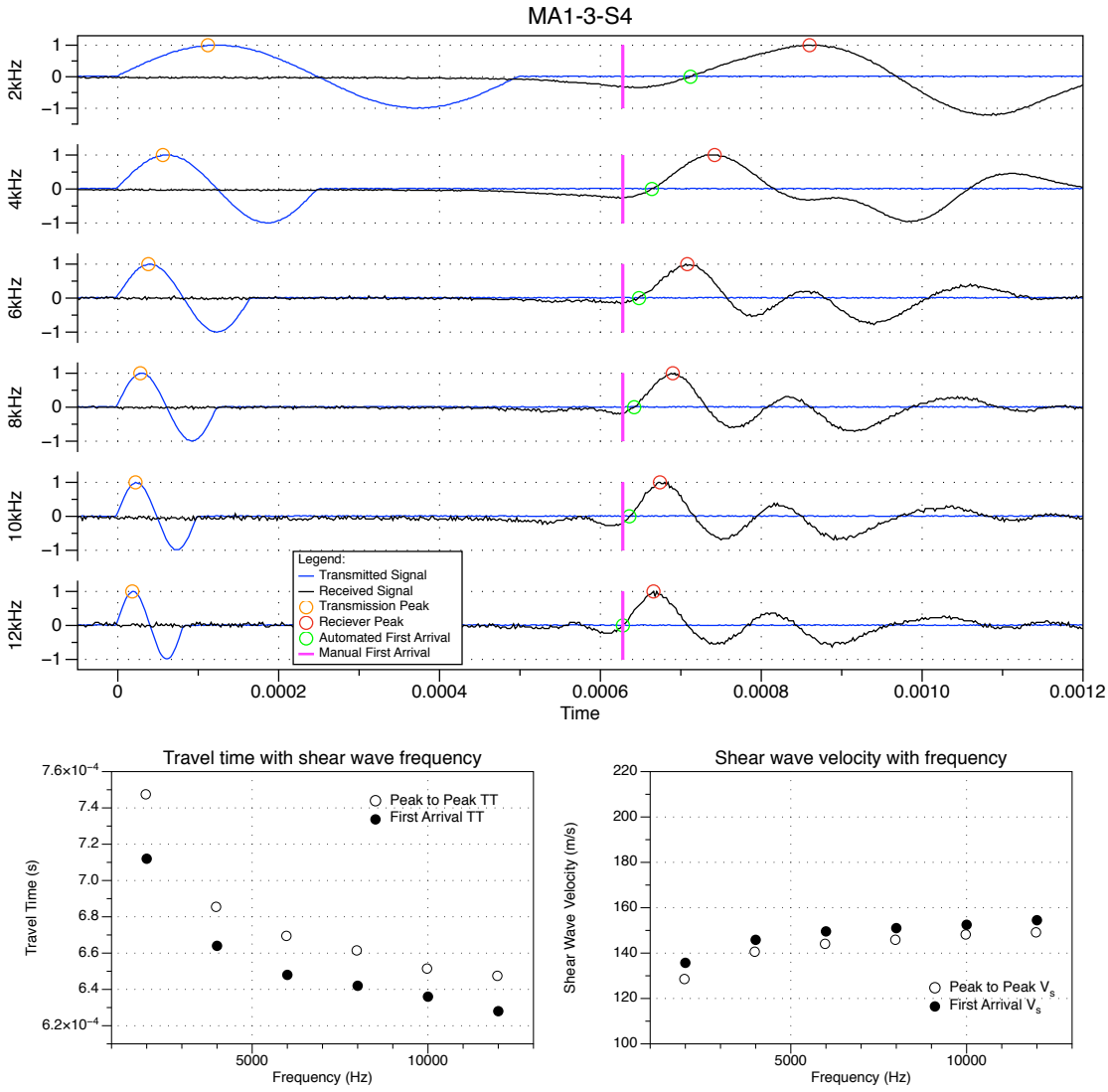

Figure 3.76: Processed bender element test data for sample MA1–3–S4

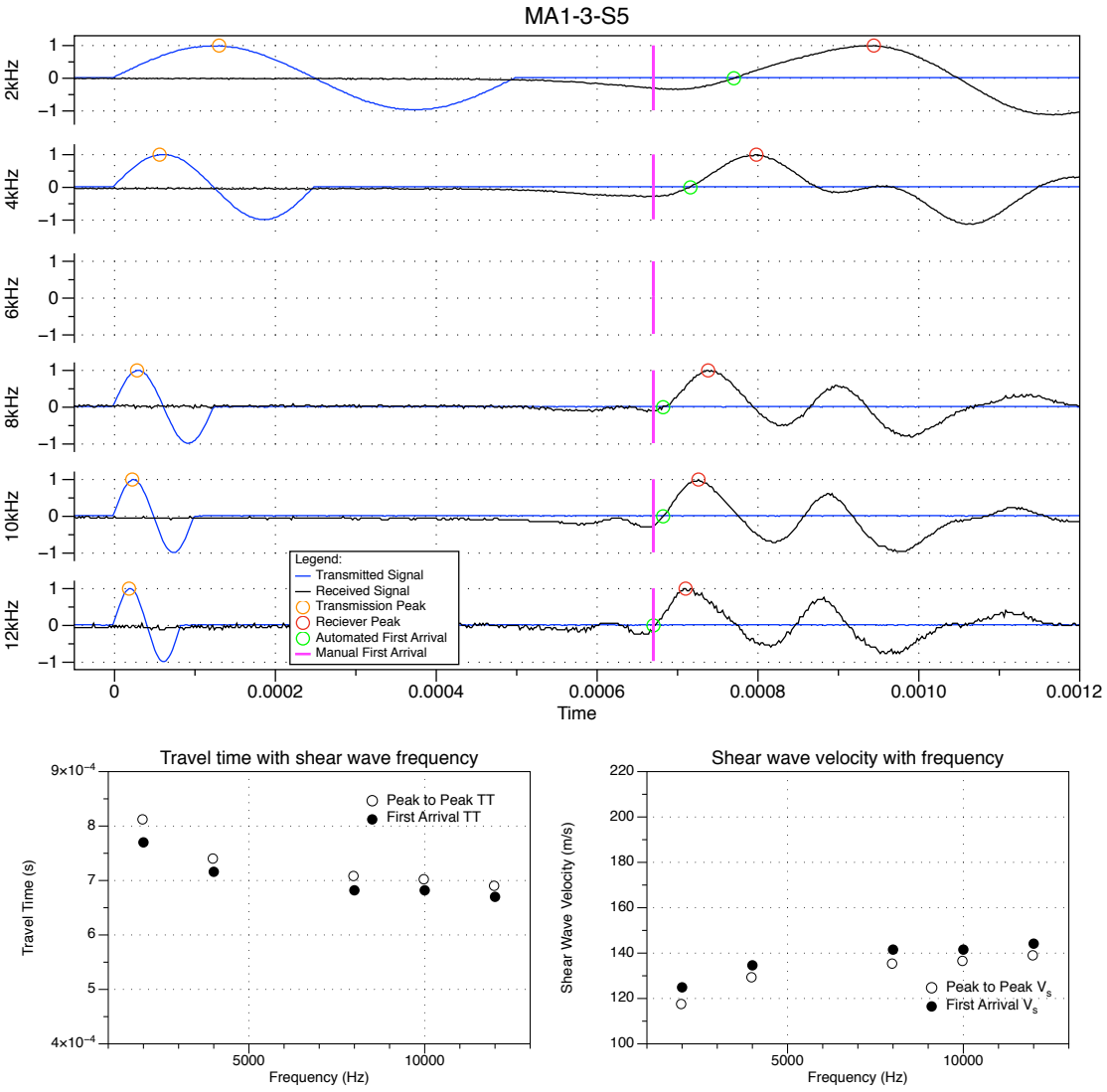

Figure 3.77: Processed bender element test data for sample MA1–3-S5

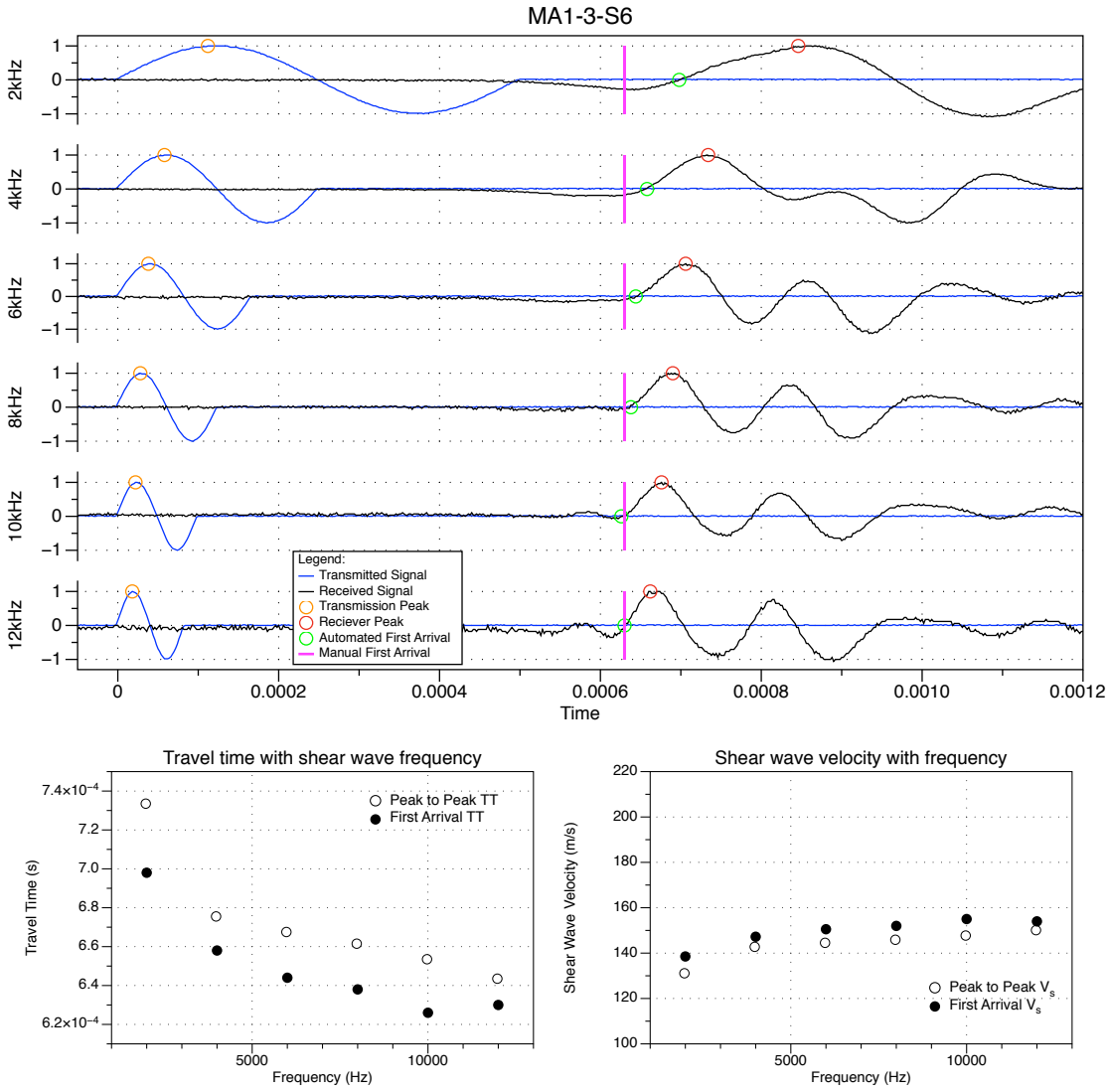

Figure 3.78: Processed bender element test data for sample MA1–3–S6

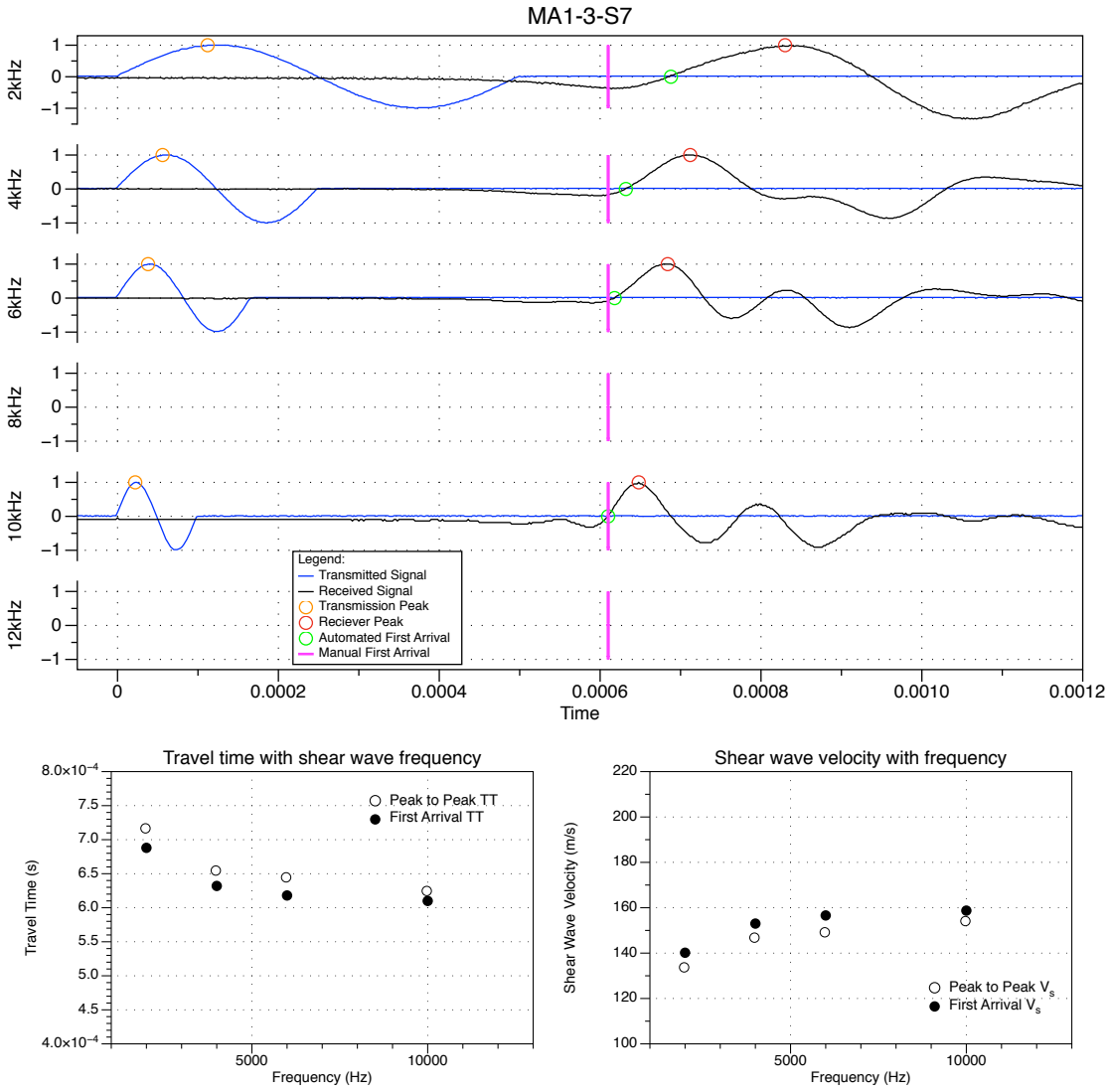

Figure 3.79: Processed bender element test data for sample MA1–3–S7

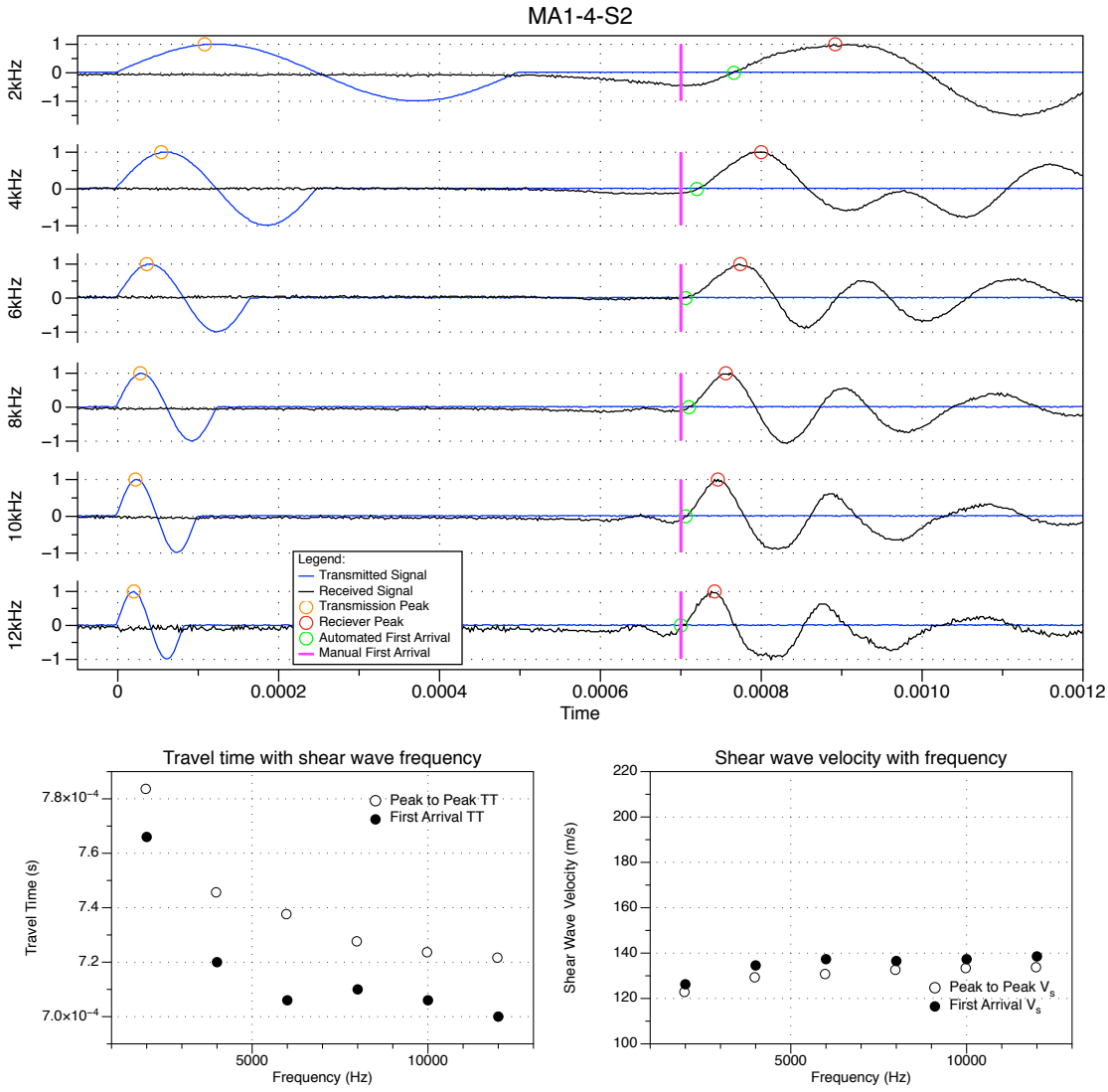

Figure 3.80: Processed bender element test data for sample MA1–4–S2

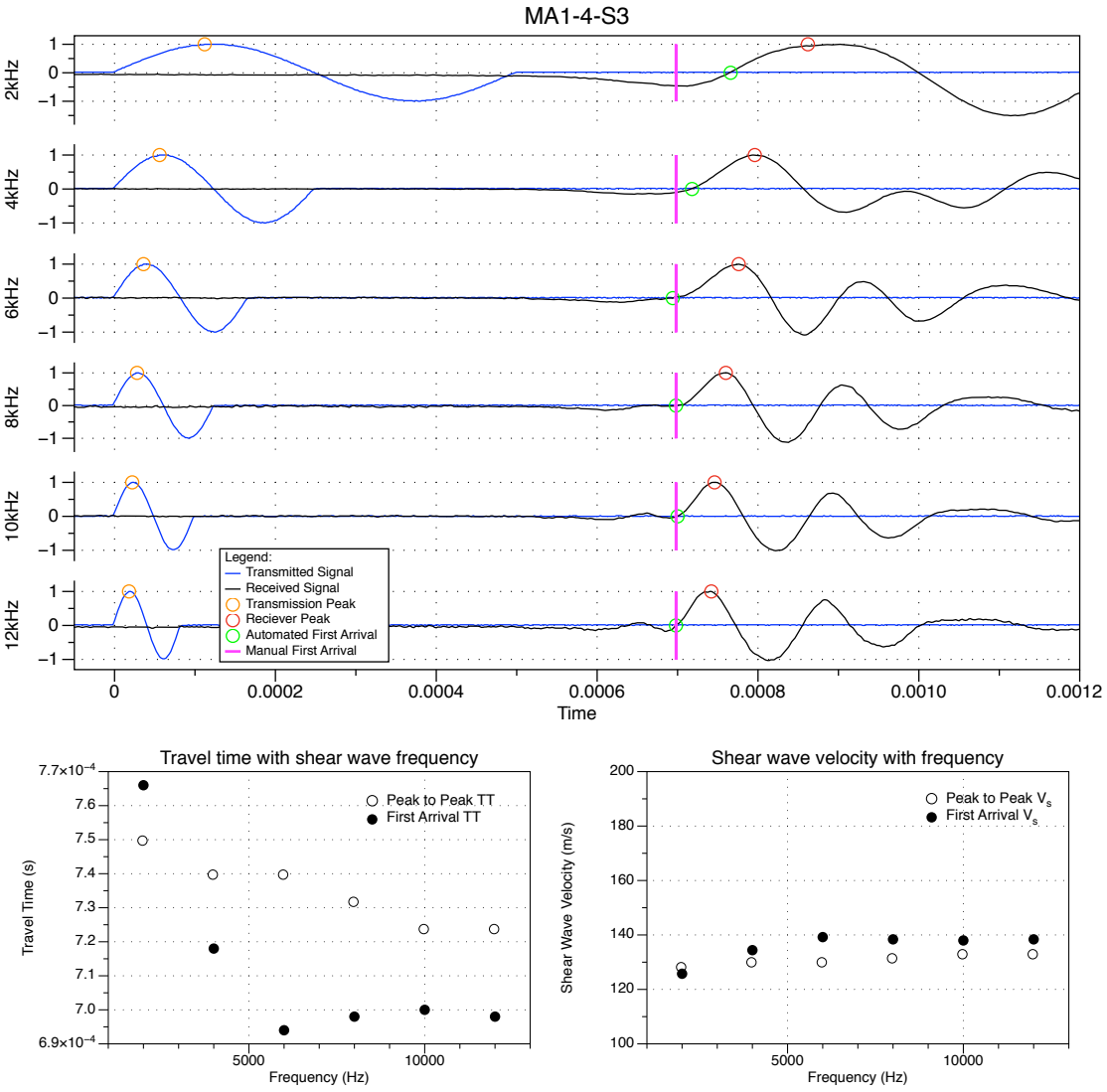

Figure 3.81: Processed bender element test data for sample MA1–4-S3

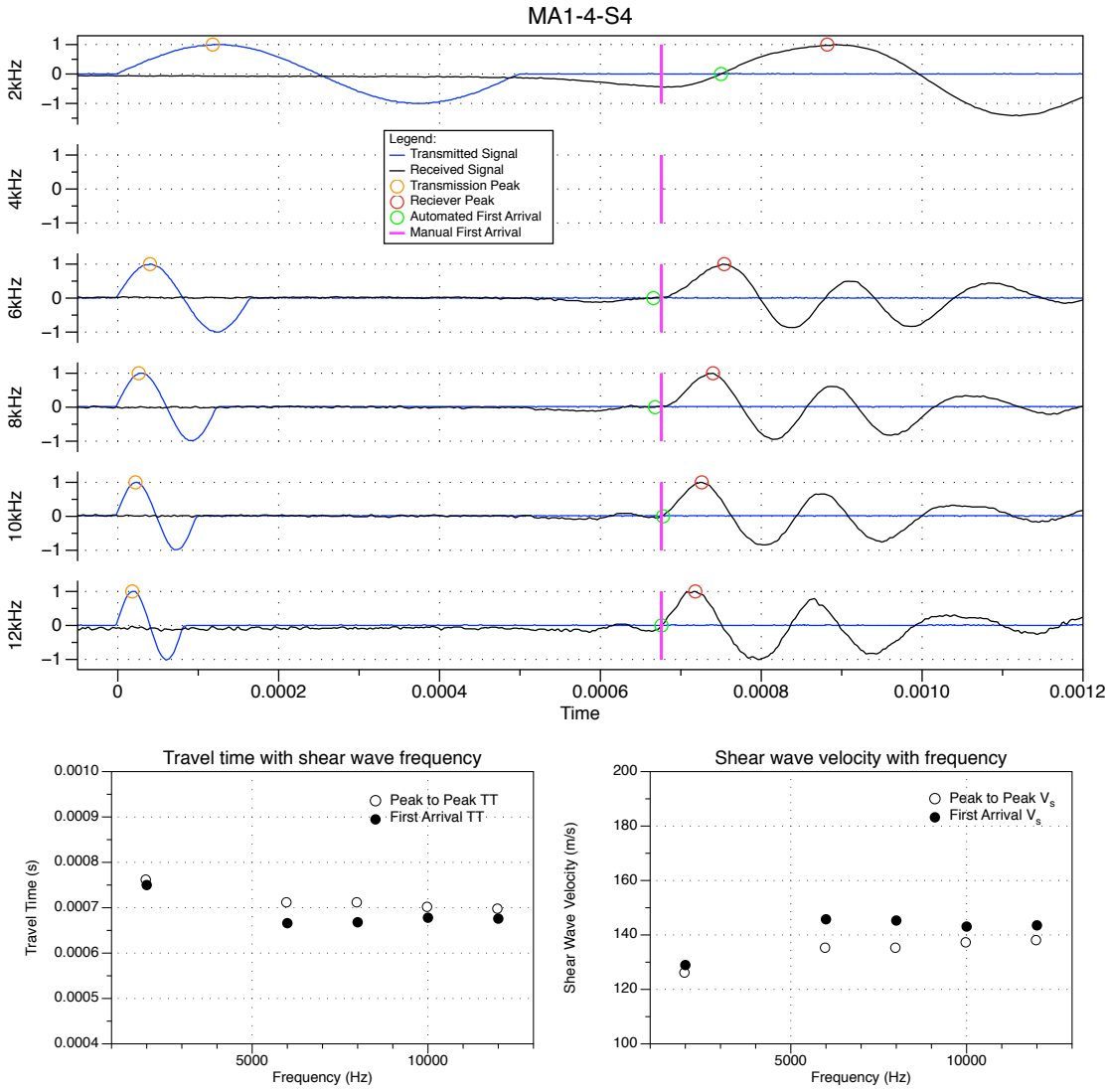

Figure 3.82: Processed bender element test data for sample MA1–4-S4

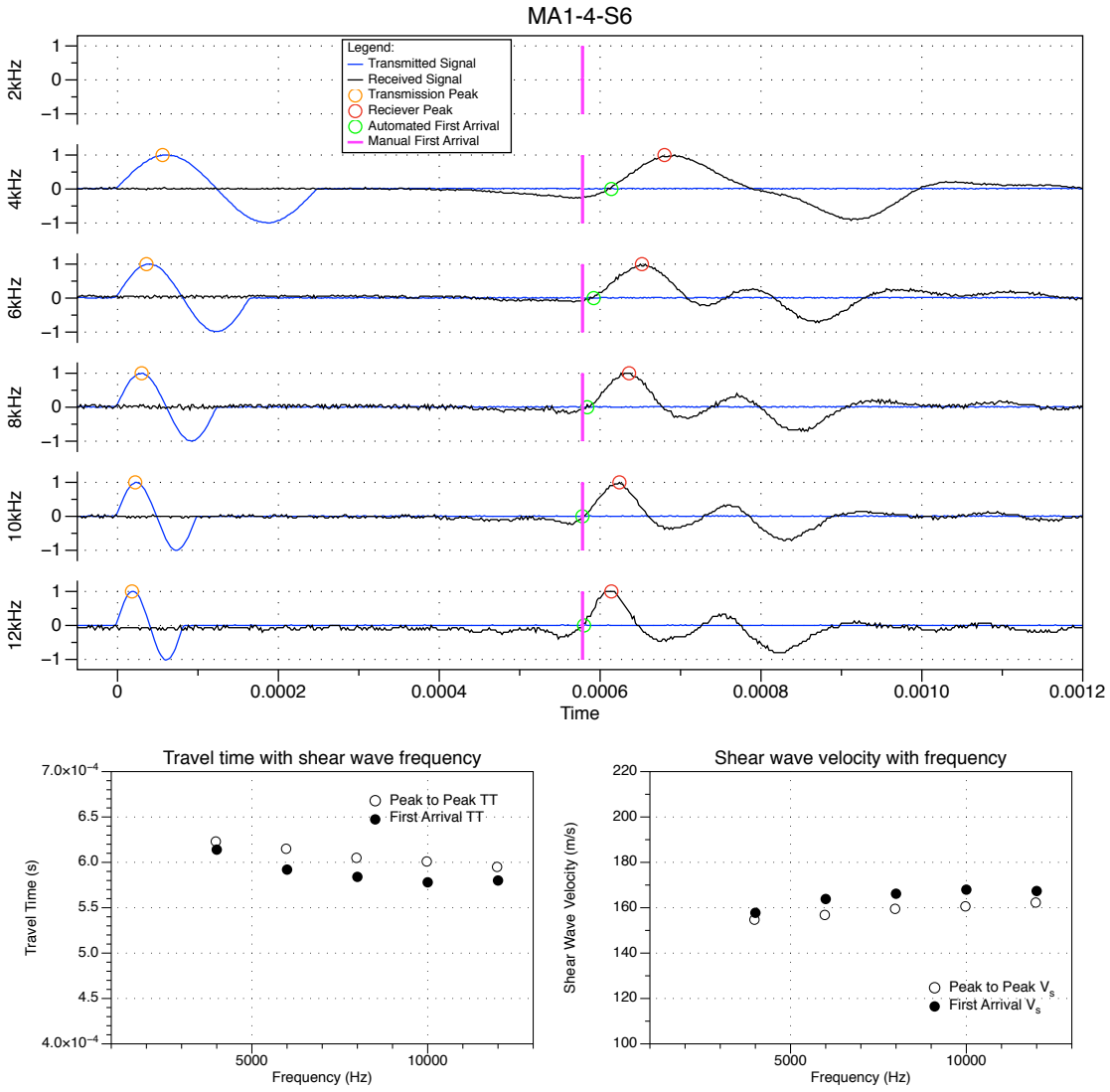

Figure 3.83: Processed bender element test data for sample MA1–4–S6

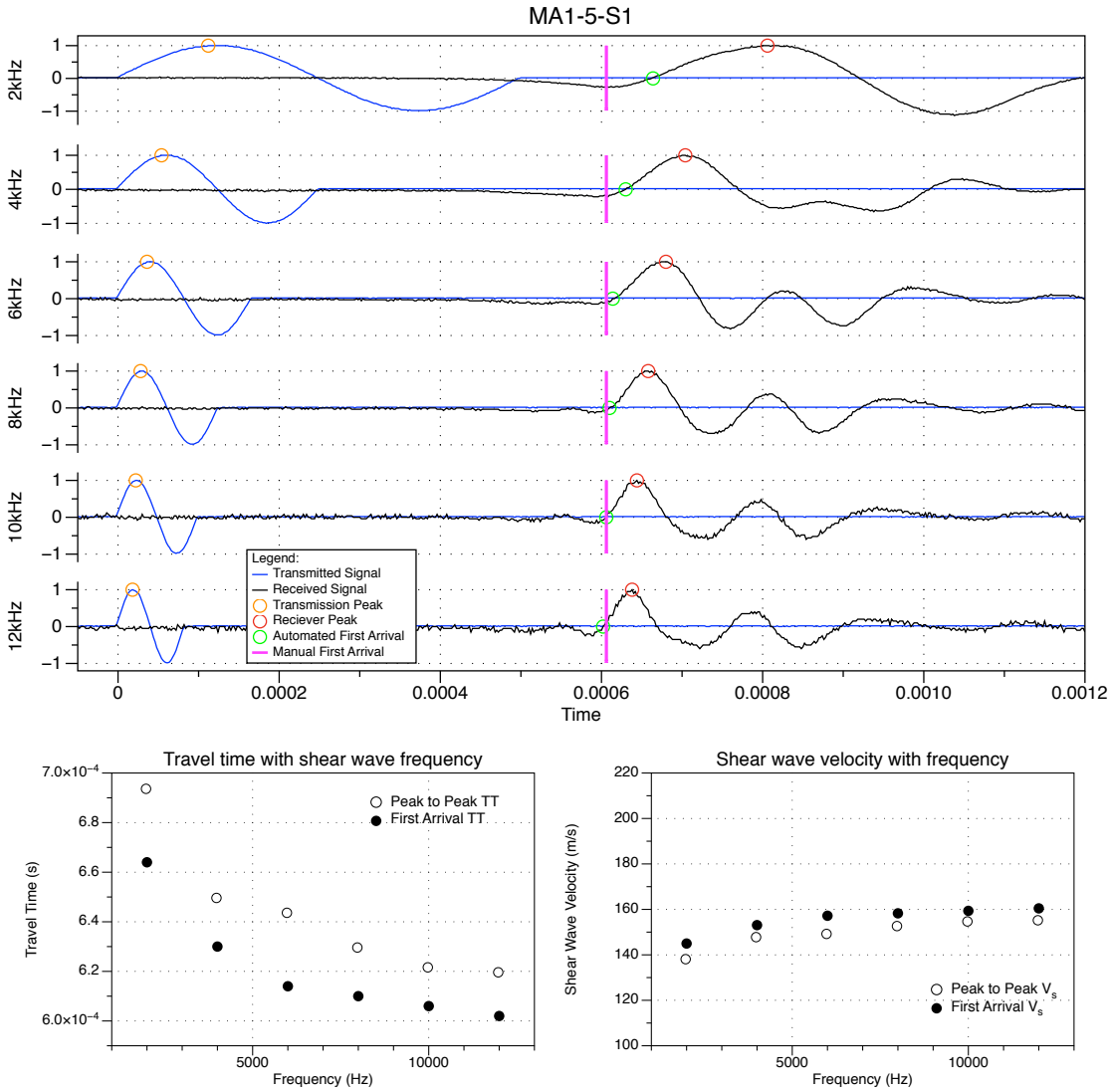

Figure 3.84: Processed bender element test data for sample MA1–5–S1

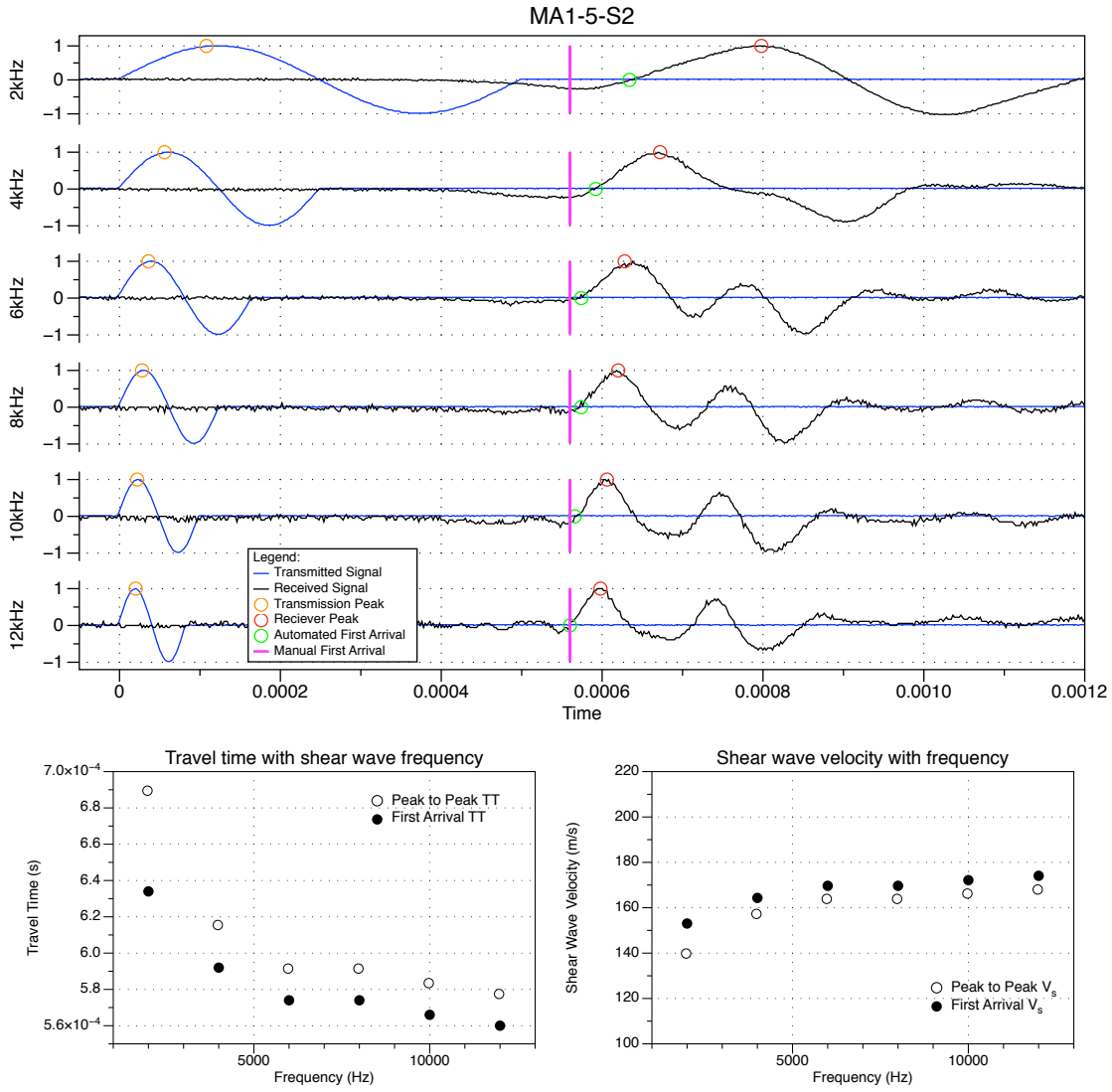

Figure 3.85: Processed bender element test data for sample MA1–5-S2

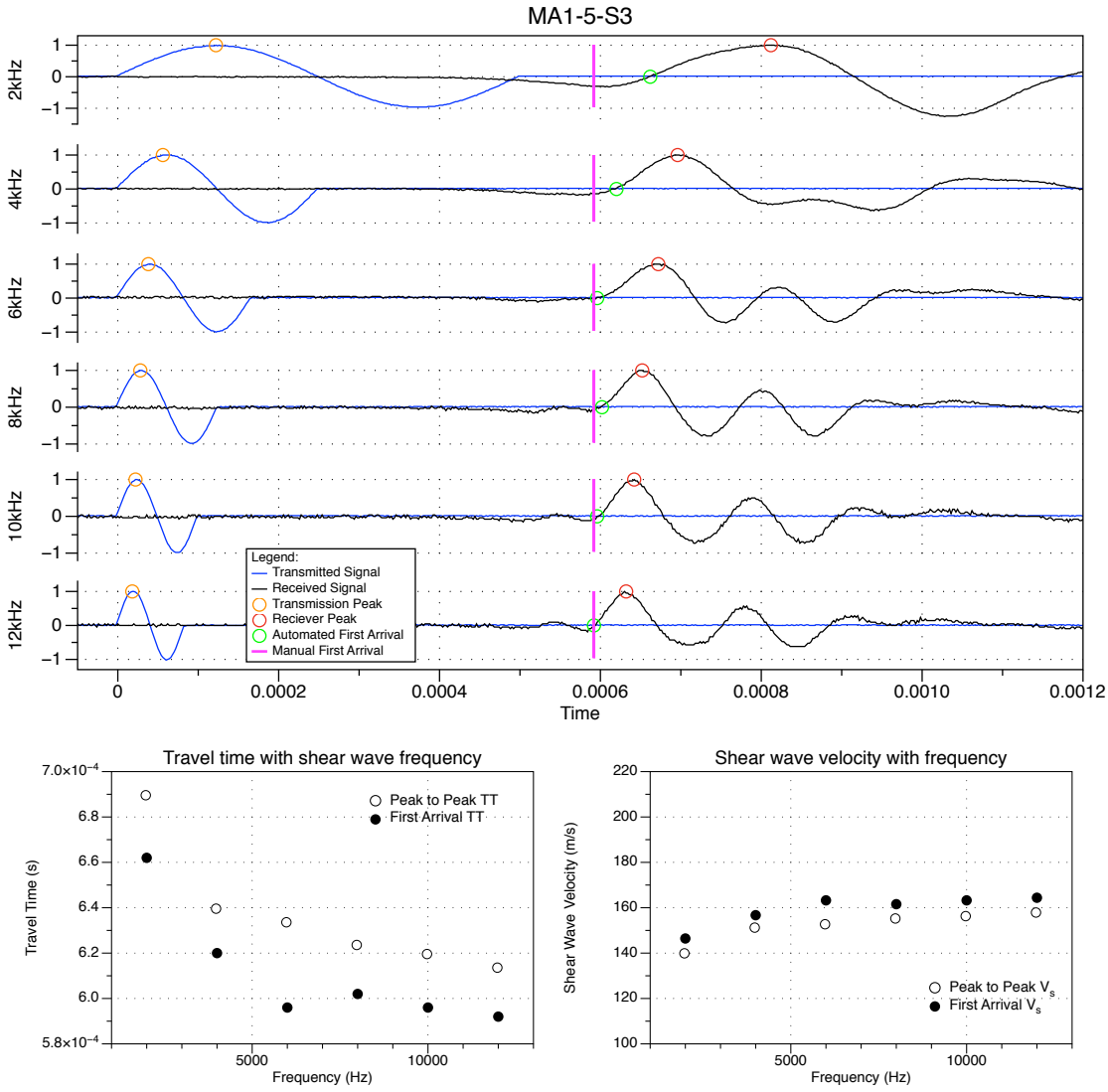

Figure 3.86: Processed bender element test data for sample MA1–5–S3

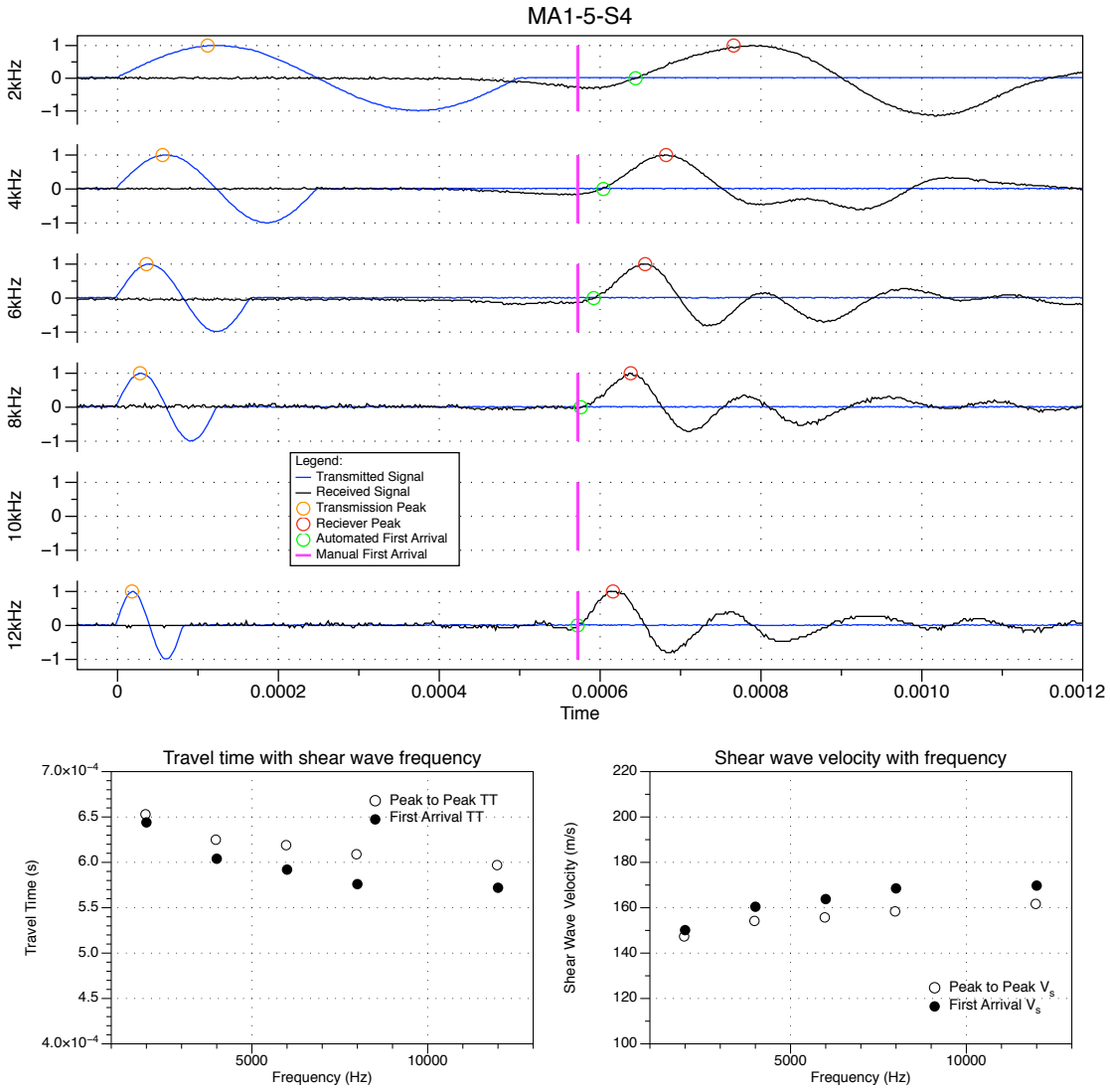

Figure 3.87: Processed bender element test data for sample MA1–5–S4

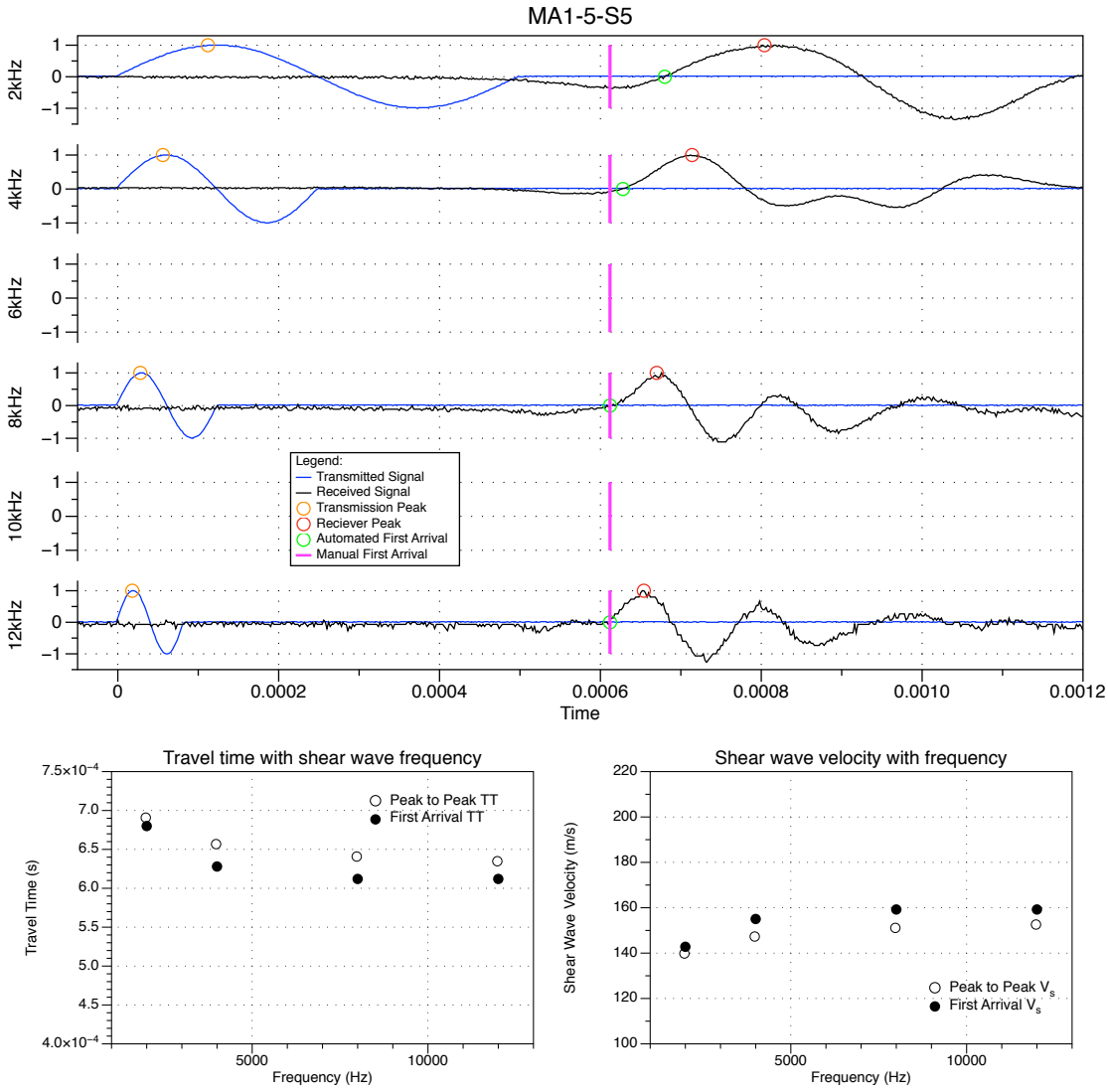

Figure 3.88: Processed bender element test data for sample MA1–5–S5

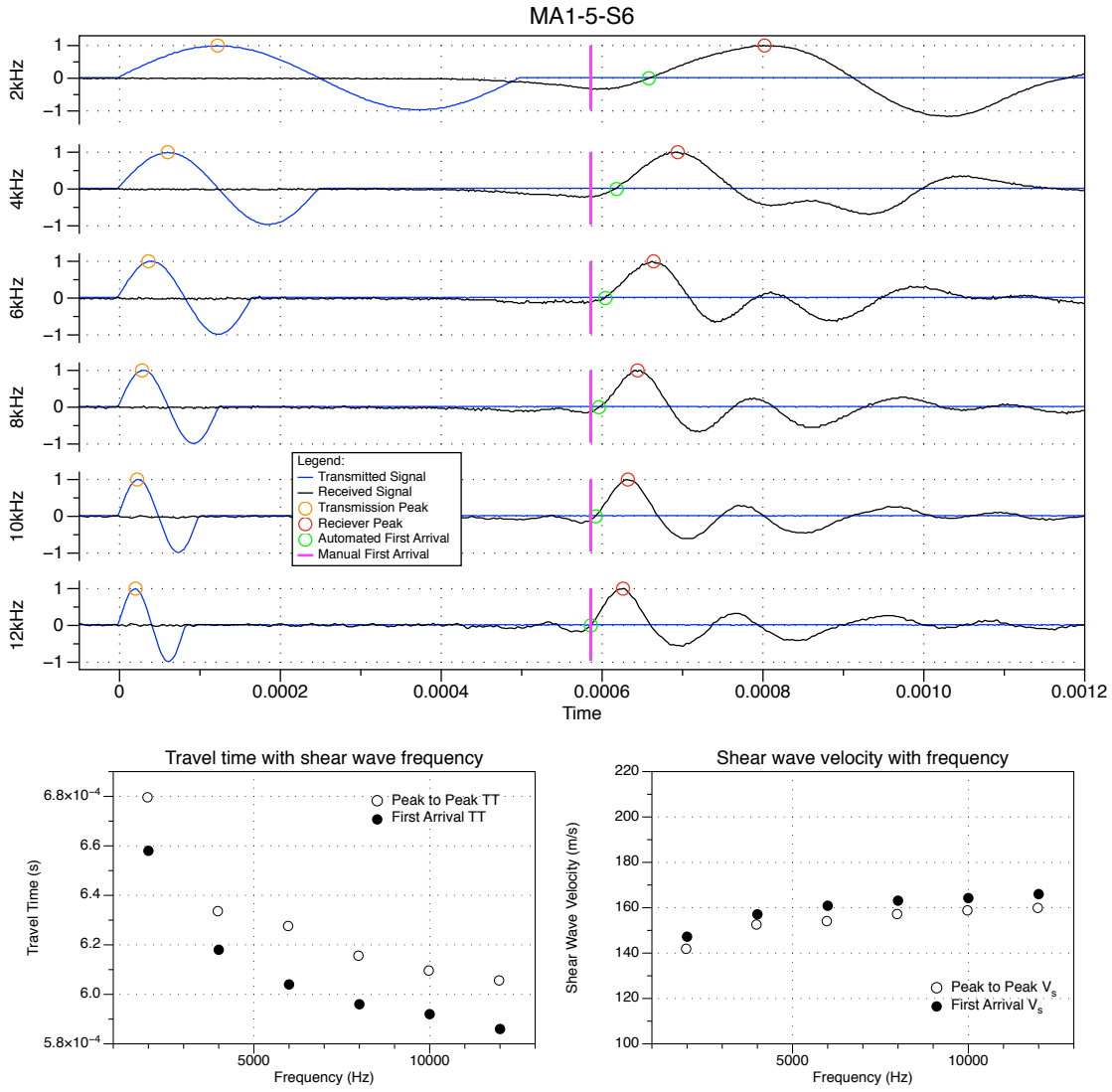

Figure 3.89: Processed bender element test data for sample MA1–5–S6

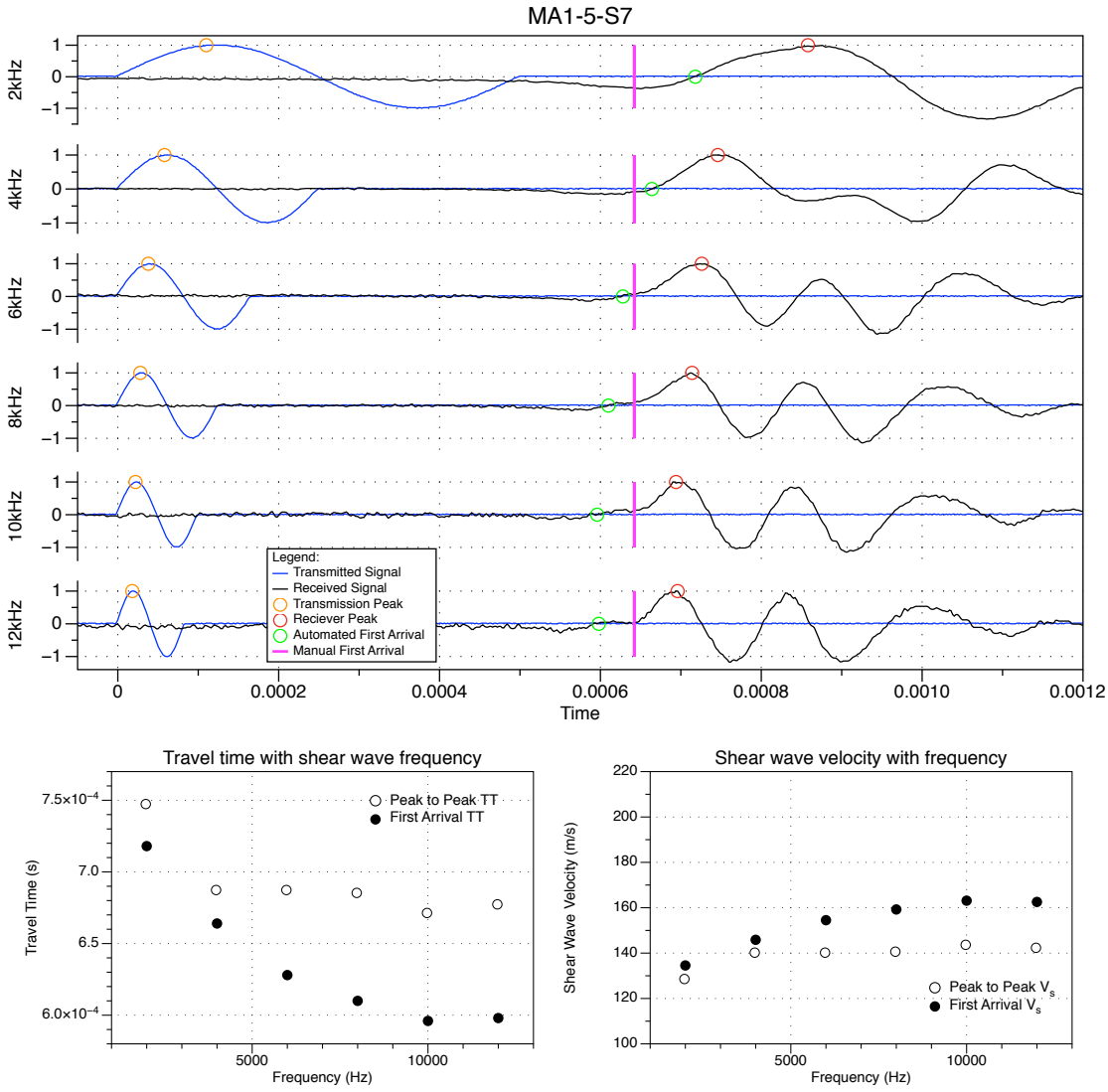

Figure 3.90: Processed bender element test data for sample MA1–5–S7

3.3 Processing of Bender Elements waveforms

This section of Appendix C provides the Visual Basic for Applications code written to process the bender element files and calculate shear wave velocities based on automated picking of peaks and first arrival points. It works fairly well but not fool proof. Plotting in Datagraph followed, including baseline correction, and manual picking of shear wave first arrivals from observed data.

3.3.1 Subroutine taks

The processing subroutine performs the following tasks:

1. Requests the user input the sample height.

2. Calculates the travel time length (tip-to-tip distance between the opposing bender elements).

3. Loops through each channel set of each frequency tested, performing the following operations:

   (a) Calculates the median amplitude in the first 60 rows of data. This is assumed to be a consistent offset of the entire trace from zero, considered to be a form of noise in the signal.

   (b) Reads points in from the channel signal, where each point has the noise determined above removed. The corresponding time is determined.

   (c) Find the row number of possible first arrivals (FA). Candidates are determined for cross over points, either positive or negative trending.

   (d) The central difference approximation of the gradient of the signal is calculated using a 7th order low noise Lanczos differentiator (Holoborodko, 2013), and an array of the gradient of the trace is created.

   (e) For cases where a maxima or minima occurs in the gradient array, a new array of peak points is created, with a corresponding array of times at which those peaks occur. In addition, for each peak point found, the corresponding value of FA candidate (determined in step (c) above,

indicating the immediately preceding cross over point) is entered into a corresponding array.

(f) The peak array is then looped through to find the first peak that is at least half as big as the maximum voltage in the trace in order to meet the criteria. The FA is the cross over that immediately precedes this first peak, and is found in the corresponding array of these candidate values.

(g) For the corresponding peak to peak travel times, and first cross over travel times, shear wave velocities are calculated from the known distance between the bender elements. Both travel times were reduced by the system delay reported to be 21.2 μs in the apparatus manual. The system delay is measured from placing the two bender elements into contact at their tips and measuring the transfer of a wave from one to another. The delay is attributed to the epoxy resin coating on the bender elements (Seiken Inc., 2008).

(h) The results in terms of peak voltages, and the times of first peak and preceding cross over points, and calculated shear wave velocities, are then written to a spreadsheet for the channel being evaluated.

4. An output subroutine then collates all the traces into a single worksheet along with the relevant key points for plotting peaks, crossovers and travel time and V_s against frequency, and saving it as a CSV output file for plotting in an external program.

3.3.2 Plotting and baseline correction:

The traces were plotted with peak points and cross-over points highlighted, as well as the travel time and V_s against frequency plots. It was noted that some of the traces exhibited drift away from the zero-line, possibly due to noise. This would cause the FA pick made by the VBA algorithm to be poor; if the trace had drifted above the zero-line a long way before the arrival of the shear wave, the first crossover would be picked far too early. Therefore a two-step data processing was

carried out whereby the data was processed once with the above VBA routine, then plotted in Datagraph (Adalsteinsson, 2013), and therein baseline corrected.

The baseline correction consisted of calculating the integral of the trace (trapezoidal method), fitting a quadratic polynomial to the integral, which represents the trend of the drift requiring correction, and then adjusting the integral by this quadratic function. This corrected integral is then differentiated to obtain the corrected trace. Figure 3.91 presents a typical plot showing the baseline correction of the receiver signals. It appears that the process of integrating and differentiating the signal has also filtered the signal of noise, however the impact on the automated calculation of V_s was typically less than 1 %. These corrected signals were copied again to the Excel workbook, replacing the raw records, and rerunning the processing algorithm in VBA to obtain revised peak and FA data times. This final output CSV file from Excel was then plotted again in Datagraph, and the results presented in this thesis.

3.3.3 VBA code

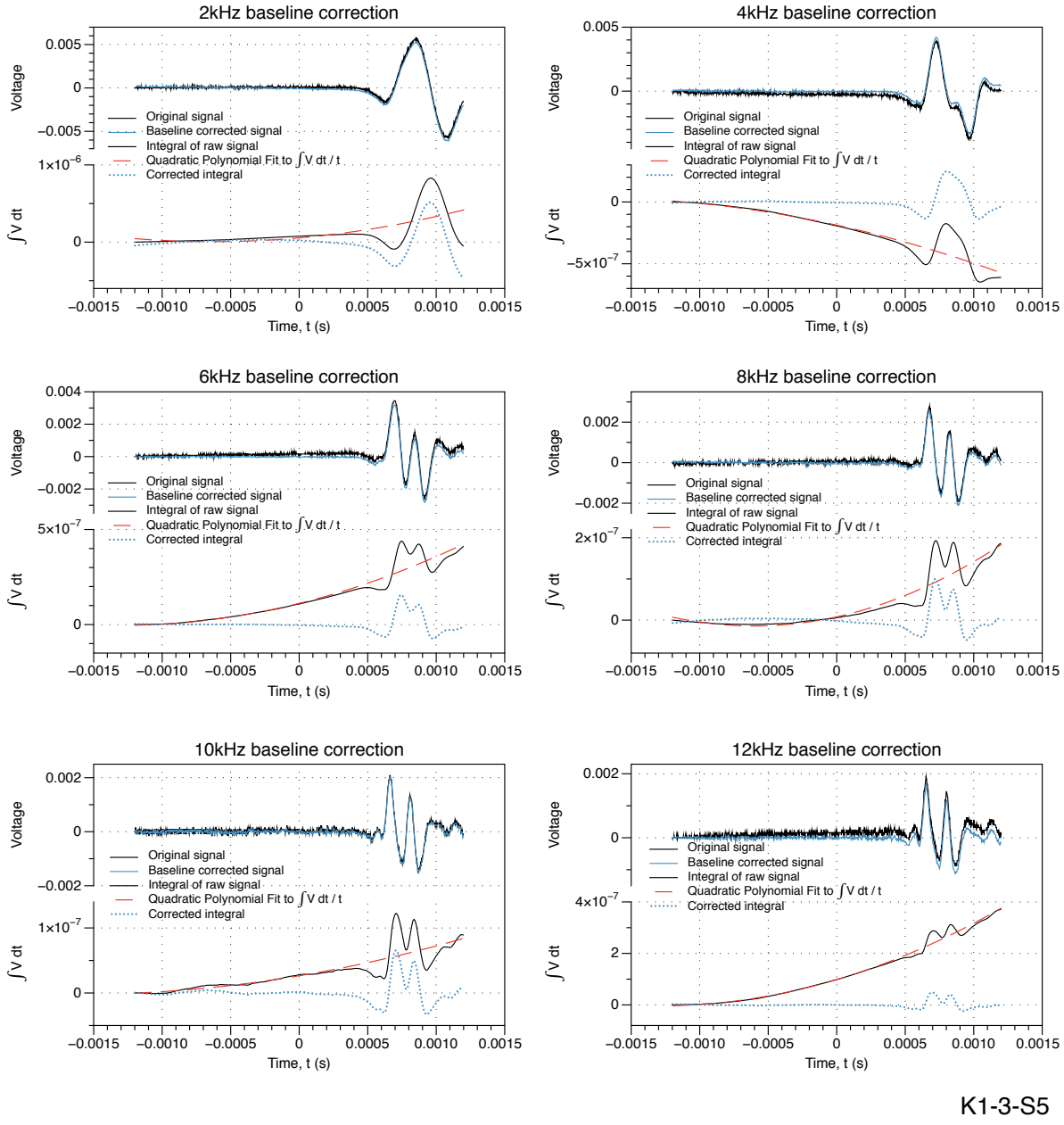

Figure 3.91: Example plot of the baseline correction performed on receiver bender element traces. GP Sample: K1–3–S5.

```
Option Explicit
Option Base 1

Sub Run_BE()
Dim stName As String
'Dim sNameNumber As Single
'Dim stWBName As String

stName = ActiveWorkbook.Name
'sNameNumber = Len(stName)
'stWBName = Left(stName, sNameNumber - 4)

Call ImportBE
Call Process_BE
'need to reactivate original workbook before running output_BE
Application.Workbooks(stName).Activate
Call Output_BE
End Sub

Sub ImportBE()
'Merrick Taylor 27 Jan 2012
'This Macro works brilliantly (err not quite 16-Feb 2013, checking with derivative
'for finding peak)
'Pulls BE data sheets from the specified file path into a single worksheet
'Make sure file path is correct, and make sure the frequencies tested match those being
'looped through

'declaring variables
Dim i As Integer
Dim j As Integer
Dim stFile As String
Dim stName As String
Dim stPath As String
Dim stExtension As String
Dim stCentre As String
Dim stTest As String
Dim stPath2 As String
Dim stPreText As String
Dim stPostText As String
Dim stPath3 As String

'Assigning file path and extension
stPath2 = ActiveWorkbook.Path
stPreText = "TEXT;"
'stPostText = ":" ': for mac \ for pc
stExtension = ".xls"
stCentre = "000Hz_CH"
stPath3 = stPreText & stPath2 & Application.PathSeparator 'stPostText

i = 1
j = 1

For j = 1 To 2          'j are the channels
    For i = 1 To 12     'i is a nested loop, for each frequency of testing

         If i = 1 Or i = 3 Or i = 5 Or i = 7 Or i = 9 Or i = 11 Then
         'remove frequencies not tested between 1-12kHz
         GoTo Out
         Else
            Sheets.Add
                 'adds a new sheet
```

```
            ActiveSheet.Name = i & stCentre & j
             'names sheet based on the frequency and channel no.
            stFile = stPath3 & i & stCentre & j & stExtension
                'path and name of file as a function of frequency and channel no.
            stName = i & stCentre & j

            'this was from a macro recording to import text from an excel worksheet:
            With ActiveSheet.QueryTables.Add(Connection:=stFile, Destination:=Range("A1"))
            .Name = stName
            .FieldNames = True
            .RowNumbers = False
            .FillAdjacentFormulas = False
            .RefreshOnFileOpen = False
            .BackgroundQuery = True
            .RefreshStyle = xlInsertDeleteCells
            .SavePassword = False
            .SaveData = True
            .AdjustColumnWidth = True
            .TextFilePromptOnRefresh = False
            .TextFilePlatform = xlMacintosh
            .TextFileStartRow = 1
            .TextFileParseType = xlDelimited
            .TextFileTextQualifier = xlTextQualifierDoubleQuote
            .TextFileConsecutiveDelimiter = False
            .TextFileTabDelimiter = True
            .TextFileSemicolonDelimiter = False
            .TextFileCommaDelimiter = False
            .TextFileSpaceDelimiter = False
            .TextFileColumnDataTypes = Array(1)
            .Refresh BackgroundQuery:=False
            '.UseListObject = False
            End With

Out:
          End If


        Next i
Next j

Sheets.Add
ActiveSheet.Name = "Path"
With Worksheets("Path")
.Range("A1") = stPath2
.Range("A2") = stPath3
End With

End Sub

Sub Process_BE()

'I'm going to try and replicate the formulae in the original spreadsheet as a macro,
'and output single results in a separate "calcs" sheet
'First step is to find the first peak voltage whether positive or negative in the CH2
'sheets

'looping counters
Dim iRow As Integer
Dim iCol As Integer
Dim i As Integer             'sheet number
Dim j As Integer             'channel number
```

```
Dim k As Integer
Dim m As Integer
Dim n As Integer
Dim ipeak As Integer    'number of peak points in received signal

'Voltages
Dim sV_c As Single           'current value of Voltage in the loop
Dim sV_ca As Single             'current value of Voltage, Absolute value for CH2
Dim sV_p As Single           'previous value of Voltage in the loop
Dim sV_p2 As Single         'previous value of Voltage to V_p in the loop
Dim sV_p3 As Single         'prev value Voltage to V_p2 in the loop
Dim sV_n As Single           'next value of Voltage in the loop
Dim sV_n2 As Single         'next value of Voltage beyond V_n in the loop
Dim sV_n3 As Single         'next value of Voltage beyong V_n2 in the loop
Dim sV_nx As Single         'Average of next 10 values of Voltage beyong sV_n in the
'loop (to try and capture noise in signal)
Dim sVmax_p As Single     'previously calculated maximum in loop
Dim sVmax_c As Single     'currently calculated maximum in loop
Dim sVmax_c2 As Single
Dim MyArray(60) As Single   'Array of values for median calculation'
Dim sVnoise As Single         'median noise voltage over first 60 values
Dim List(60) As Single          'array of values for median calculation
Dim VPeak() As Single          'Dynamic array of values for finding peaks in the received
' signal. NB: not yet dimensioned
Dim TPeak() As Single
Dim sTminPeak() As Single
Dim iRowPeak() As Single

'Central difference Approximation of the differntiation. Use
Dim sCDiff As Single     'current value of the CD approx.
Dim CDiff(1200) As Single      'array of values for finding peaks int he received signal.

'Time values
Dim sT_c As Single                 'corresponding time value for current value of voltage
                                   ' in loop
Dim sT_p As Single                 'previous time value to current
Dim sTmin_c As Single            'current minimum value of time
Dim sTmin_p As Single            'previous calculated minimum value of time
Dim sT_Vmax_c As Single        'corresponding time value for sVmax_c
Dim sT_Vmax_p As Single        'previous calc maximum voltage time
Dim sT_FA As Single                'first arrival value
Dim sT_Vmax_CH1 As Single    'CH1 output peak time
Dim sT_Vmax_CH2 As Single    'CH2 output peak time
Dim sT_Vmax_c2 As Single
Dim sT_FA2 As Single
Dim sTdelay As Single              'resin delay 21.2 microseconds according to
'                                     manufacturer, Arefi (2013)

'Row labels in sheet
Dim iRow_T_Vmax As Integer     'corresponding row number in sheet to peak voltage
Dim iRow_F_c As Single         'corresponding row number in sheet to first arrival
'(current in loop)
Dim iRow_FA As Integer         'row at first arrival
Dim iRow_F_p As Integer       'corresponding row number in sheet to first arrival
'(previous in loop)
Dim iRow_FA2 As Integer

'Labels
Dim stFreq As String                   'frequency of test as string
Dim stSheet As String                  'text in the rest of the sheet name
Dim stExt As String                     'file extension
```

```
184 Dim stPath As String                    'file path
185
186 'Dimensions
187 Dim BenderL As Single         'length of bender elements
188 Dim SampleL As Single        'length of sample
189 Dim TTL As Single              'Tip to Tip length
190
191 'Calculated Vs values
192 Dim Vs_pp As Single             'peak to peak Vs
193 Dim Vs_fa As Single             'first arrival Vs
194
195 'Get length of sample from user
196 SampleL = InputBox("Length of Sample (mm)")
197 If SampleL < 0 Then                          'has endif 1
198 MsgBox "Error, sample must be greater than zero. Please try again"
199 ElseIf SampleL < 10 Then
200 MsgBox "Error, sample must be greater than 10mm. Please try again"
201 Else:
202 BenderL = 3
203 TTL = SampleL - 2 * BenderL
204 End If                                              'has if 1
205
206 'file extension and path of output file
207 stExt = ".csv"
208 stPath = ActiveWorkbook.Path & Application.PathSeparator  '":" ': for mac, \ for pc
209
210 'Print the outputs in a sheet:
211 Sheets.Add
212 ActiveSheet.Name = "Arrival Times"
213
214 With Worksheets("Arrival Times")
215 .Range("A1") = "Bender Element Test Results"
216 .Range("A2") = "Evaluated by Merrick Taylor"
217 .Range("A4") = "Test Frequency"
218 .Range("B4") = "CH1 t_peak"
219 .Range("C4") = "CH2 t_peak"
220 .Range("D4") = "T peak to peak"
221 .Range("E4") = "T FA Row No."
222 .Range("F4") = "T_first arrival"
223 .Range("G4") = "Vpeak CH1"
224 .Range("H4") = "Vpeak CH2"
225 .Range("I4") = "CH1 noise"
226 .Range("J4") = "Vs peak to peak"
227 .Range("K4") = "Vs first arrival"
228 End With
229
230 With Worksheets("Arrival Times").Range("A1").Font
231     .Bold = True
232     .Size = 14
233     .Name = "Times New Roman"
234 End With
235
236 'initial values
237 i = 1
238 j = 1
239 k = 0
240 m = 1
241 n = 1
242 stSheet = "000Hz_CH"
243 sTdelay = 21.2 / 1000000   '21.2ms is the delay in the system between sending and
244 'receiving BEs
```

```
245
246 'Identifying First Peak voltage and corresponding time in both CH1 and 2 sheets,
247 'note that since CH1 is done first, the value for T_first arrival in the table will
248 'only be populated with the CH2 value.
249
250 For j = 1 To 2 'looping channels                '*** For level 1
251
252     For i = 1 To 12 'nested looping of frequencies      ***For Level 2
253
254 'reseting these values for each 2nd degree nested loop
255     sVmax_p = 0
256     sTmin_p = 0
257     sTmin_c = 0
258     stFreq = i & "000"
259     sT_Vmax_p = 0
260     sV_p = 0
261     sV_p2 = 0
262     sVmax_c = 0
263     sVnoise = 0
264     iRow_F_c = 1
265     iRow_FA = 1
266     iRow_F_p = 1
267     ipeak = 1
268
269         If i = 1 Or i = 3 Or i = 5 Or i = 7 Or i = 9 Or i = 11 Then
270         ' remove frequencies not tested between 1-12kHz  'has endIf 2
271         k = i
272         GoTo Out
273
274         Else
275             With Worksheets(i & stSheet & j)   '*With L1
276
277                     'Calculates median noise over first 60 data points in CH2 only
278                     '(it is working now)
279                     If j = 2 Then               'has endif 3
280                         'populate the array with values
281                         For iRow = 1 To 60
282
283                         MyArray(iRow) = .Range("B10").Cells(iRow + 1, 1).Value
284                         Next iRow
285
286                         'Sort Array in Ascending Order
287                         Call BubbleSort(MyArray, List)
288
289                         'set noise level to the middle value of the sorted array
290                          sVnoise = List(30)
291
292                         End If              'has if 3
293
294                     'this loops through each row to find max voltage in CH1 and CH2
295
296                     For iRow = 0 To 1199            '''''''*For Loop L3
297
298                     'setting up values to loop through
299                     sV_c = .Range("B12").Cells(iRow + 1, 1).Value - sVnoise
300                     'ignores first point
301                     sV_p = .Range("B11").Cells(iRow + 1, 1).Value - sVnoise
302                     sV_p2 = .Range("B10").Cells(iRow + 1, 1).Value - sVnoise
303                     sV_p3 = .Range("B9").Cells(iRow + 1, 1).Value - sVnoise
304                     sV_n = .Range("B13").Cells(iRow + 1, 1).Value - sVnoise
305                     sV_n2 = .Range("B14").Cells(iRow + 1, 1).Value - sVnoise
```

```
306                     sV_n3 = .Range("B15").Cells(iRow + 1, 1).Value - sVnoise
307                     sT_c = .Range("C12").Cells(iRow + 1, 1).Value
308                     sT_p = .Range("C11").Cells(iRow + 1, 1).Value
309
310
311                         'identify time and row number for possible first arrivals
312                         '(this is now working)
313
314                         If sV_c >= 0 And sV_p < 0 Then      'has endif 4
315                         sTmin_c = sT_c
316                         iRow_F_c = iRow
317                         ElseIf sV_c <= 0 And sV_p > 0 Then
318                         sTmin_c = sT_c
319                         iRow_F_c = iRow
320                         Else
321                         sTmin_c = sTmin_p
322                         iRow_F_c = iRow_F_p
323                         End If                                              'has if 4
324
325 'central difference approximation to calculate the gradient of the signal, using a
326 'low-noise Lanczos differentiator
327 'see http://www.holoborodko.com/pavel/numerical-methods/numerical-derivative
328 '/smooth-low-noise-differentiators/#noiserobust_2
329 'N = 5 order, (2(f_1-f_{-1}) + f_2 -f_{-2})/8h, where h is the step (1 used).
330 'N = 7 order, (5(f_1-f_{-1})+4(f_2 - f_{-2}) + f_3-f_{-3})/32h, where h is the step
331 '(1 used)
332
333                         'sCDiff = (2 * (sV_n - sV_p) + sV_n2 - sV_p2) / 8
334                 sCDiff = (5 * (sV_n - sV_p) + 4 * (sV_n2 - sV_p2) + sV_n3 - sV_p3) / 32
335                         'populates the array with values
336
337                         If iRow <= 2 Then            'has endif 5
338                         CDiff(iRow + 1) = 0
339                         Else
340                         CDiff(iRow + 1) = sCDiff
341                         End If                      'has if 5
342
343                         If j = 2 And iRow >= 3 Then                         'has endif 5
344 If CDiff(iRow + 1)>0 And CDiff(iRow) <= 0 Or CDiff(iRow + 1) <= 0 And CDiff(iRow) > 0 Then 'has en
345                                 ReDim Preserve VPeak(ipeak) As Single
346                                 ReDim Preserve TPeak(ipeak) As Single
347                                 ReDim Preserve sTminPeak(ipeak) As Single
348                                 ReDim Preserve iRowPeak(ipeak) As Single
349                                 VPeak(ipeak) = Abs(sV_c)
350                                 TPeak(ipeak) = sT_c
351                                 sTminPeak(ipeak) = sTmin_c
352                                 iRowPeak(ipeak) = iRow_F_c
353
354                                 ipeak = ipeak + 1
355                             End If          'has if 6
356                          End If 'has if 5
357
358                         'findin Tg peak Voltage and corresponding time and row numbers
359                         If j = 2 Then
360                         sV_ca = Abs(sV_c)
361                         Else
362                         sV_ca = sV_c
363                         End If
364
365                         If sV_ca > sVmax_p Then         'has endif 6
366                         sVmax_c = sV_ca
```

```
                        sT_Vmax_c = sT_c
                        iRow_T_Vmax = iRow
                        sT_FA = sTmin_c
                        iRow_FA = iRow_F_c
                        Else
                        sVmax_c = sVmax_p
                        sT_Vmax_c = sT_Vmax_p
                        End If                                          'has if 6


                        'change previous values for next loop
                        sT_Vmax_p = sT_Vmax_c
                        sVmax_p = sVmax_c
                        sTmin_p = sTmin_c
                        iRow_F_p = iRow_F_c

                    Next iRow ' For loop L3

                End With 'with L1 ends

'Checking first peak arrival is the maximum peak:

 'reset iRow, and loop through Peak array to find first peak that is at least half as big
 ' as the maximum Voltage to meet criteria
        If j = 2 Then                   'has endif 7
            iRow = 1

            Do                      'Do loop 1
                    sVmax_c2 = VPeak(iRow)
                    sT_Vmax_c2 = TPeak(iRow)
                    sT_FA2 = sTminPeak(iRow)
                    iRow_FA2 = iRowPeak(iRow)
                    iRow = iRow + 1
            Loop Until sVmax_c2 >= 0.5 * sVmax_c  'end do loop

            sVmax_c = sVmax_c2
            sT_Vmax_c = sT_Vmax_c2
            sT_FA = sT_FA2
            iRow_FA = iRow_FA2

        End If                              'has if 7

'Determining which row to paste into

               If i = 1 Then           'has endif 8
                    m = 1
                    ElseIf i = 2 Then
                        m = 2
                        Else
                            m = i - (k - i / 2)
                            End If          'has if 8


                    'Printing the results to the Calc sheet:
                    With Worksheets("Arrival Times")                    'End with L1
                    .Range("A5").Cells(m + 1, 1) = stFreq
                    .Range("B5").Cells(m + 1, j) = sT_Vmax_c
                    .Range("G5").Cells(m + 1, j) = sVmax_c
                    .Range("I5").Cells(m + 1, 1) = sVnoise
                    End With   'With L1

```

```
                If j = 2 Then           'has endif 9

                With Worksheets("Arrival Times")
                .Range("E5").Cells(m + 1, 1) = iRow_FA
                .Range("F5").Cells(m + 1, 1) = sT_FA - sTdelay
                End With

                'Print data for debugging
                'With Worksheets("Arrival Times")
                '.Range("A21").Offset(1, n) = i & "V Peak"
                '.Range("B21").Offset(1, n) = "T Peak"
                '.Range("C21").Offset(1, n) = "CDiff"
                '.Range("A22:A1221").Offset(1, n) = WorksheetFunction.Transpose(VPeak)
                '.Range("B22:B1221").Offset(1, n) = WorksheetFunction.Transpose(TPeak)
                '.Range("C22:C1221").Offset(1, n) = WorksheetFunction.Transpose(CDiff)
                'End With
                'n = n + 3
                End If                      'has if 9

Out:
        End If      'has if 2

    Next i      'for level 2
Next j          'for level 1


'Calculate peak to peak travel time & Vs values
For iRow = 1 To m
With Worksheets("Arrival Times")
sT_Vmax_CH1 = .Range("B5").Cells(iRow + 1, 1).Value
sT_Vmax_CH2 = .Range("C5").Cells(iRow + 1, 1).Value
.Range("D5").Cells(iRow + 1, 1) = sT_Vmax_CH2 - sT_Vmax_CH1 - sTdelay
If sT_Vmax_CH2 - sT_Vmax_CH1 = 0 Or .Range("F5").Cells(iRow + 1, 1).Value = 0 Then
GoTo Out2
Else
Vs_pp = (TTL / 1000) / .Range("D5").Cells(iRow + 1, 1).Value
Vs_fa = (TTL / 1000) / .Range("F5").Cells(iRow + 1, 1).Value
.Range("J5").Cells(iRow + 1, 1) = Vs_pp
.Range("K5").Cells(iRow + 1, 1) = Vs_fa
End If
End With
Out2:
Next iRow
Sheets("Arrival Times").Select
Sheets("Arrival Times").Copy
ActiveWorkbook.SaveAs Filename:= _
stPath & "Arrival Times" & stExt, FileFormat:= _
xlCSV, CreateBackup:=False

End Sub

Public Sub BubbleSort(MyArray() As Single, List() As Single)
'This private sub sorts an array

    Dim First           As Integer
    Dim Last            As Integer
    Dim i               As Integer
    Dim j               As Integer
    Dim Temp            As Single

    First = LBound(MyArray)
```

```
    Last = UBound(MyArray)
    For i = First To Last - 1
        For j = i + 1 To Last
            If MyArray(i) > MyArray(j) Then
                Temp = MyArray(j)
                MyArray(j) = MyArray(i)
                MyArray(i) = Temp
            End If
        Next j
    Next i

    For i = 1 To UBound(MyArray)
        List(i) = MyArray(i)
    Next
    End Sub

Sub Output_BE()
'This sub will create a new sheet and copy data from each of the individual frequency
'channels into a single sheet for output to a CSV and plotting in R or other program

'Defining integers
Dim iRow As Integer           'loop counter
Dim j As Integer               'channel number
Dim i As Integer               'frequency number
Dim m As Integer               'output column offset
Dim n As Integer               'input column offset
Dim k As Integer

'Strings baby
Dim stSheet As String      'string to name the sheets
Dim stPath As String        'file path
Dim stName As String      'file name
Dim stExt As String          'extension of output file

'Arrays
Dim VoltArray(1200) As Single           'voltage array of values
Dim TimeArray(1200) As Single          'time array of values
Dim NegVolt(1200) As Single             'negative of voltage array
Dim MyArray(60) As Single                'noise array
Dim List(60) As Single                       'sorted noise array
Dim FreqArray(6) As Single                'Frequencies tested'
Dim TPk2PkArray(6) As Single            'Peak to peak travel time
Dim TFAArray(6) As Single                 'First arrival travel time
Dim VsPk2Pk(6) As Single                  'Vs peak to peak'
Dim VsFA(6) As Single                        'Vs first arrival

'Values
Dim sVnoise As Single           'median noise
Dim sCh1T_Pk As Single        'Time of CH1 peak
Dim sCh2T_Pk As Single        'Time of CH2 peak
Dim sCh2_FA As Single          'Time of CH2 first arrival
Dim sCH2_V_Pk As Single      'Voltage of CH2 peak

'read in Arrival Time arrays
With Worksheets("Arrival Times")
For iRow = 1 To 6 'looping baby
FreqArray(iRow) = .Range("A7").Cells(iRow, 1).Value
TPk2PkArray(iRow) = .Range("D7").Cells(iRow, 1).Value
TFAArray(iRow) = .Range("F7").Cells(iRow, 1).Value
VsPk2Pk(iRow) = .Range("J7").Cells(iRow, 1).Value
VsFA(iRow) = .Range("K7").Cells(iRow, 1).Value
```

```
Next iRow
End With

'Print the outputs in a sheet:
Sheets.Add
ActiveSheet.Name = "Output"

'defining some strings
stPath = ActiveWorkbook.Path & Application.PathSeparator '   ":" ': for mac, \ for PC
stName = ActiveWorkbook.Name
stExt = ".csv"
stSheet = "000Hz_CH"

'initial Values
k = 0
m = 0
n = 0


'Creating Voltage, Time and Neg Volt arrays

For i = 1 To 12 'looping frequencies

    For j = 1 To 2 'nested looping of channels

        If i = 1 Or i = 3 Or i = 5 Or i = 7 Or i = 9 Or i = 11 Then
        ' remove frequencies not tested between 1-12kHz
        k = i
        GoTo Out

        Else
            With Worksheets(i & stSheet & j)

                    'Calculates median noise over first 60 data points in CH2 only
                    '(it is working now)
                    If j = 2 Then
                        'populate the array with values
                        For iRow = 1 To 60
                        MyArray(iRow) = .Range("B10").Cells(iRow, 1).Value
                        Next iRow
                        'Sort Array in Ascending Order
                        Call BubbleSort(MyArray, List)
                        'set noise level to the middle value of the sorted array
                         sVnoise = List(30)
                    Else
                    sVnoise = 0
                    End If

                    For iRow = 1 To 1200

                    VoltArray(iRow) = .Range("B10").Cells(iRow, 1).Value - sVnoise
                    TimeArray(iRow) = .Range("C10").Cells(iRow, 1).Value
                    NegVolt(iRow) = VoltArray(iRow) * (-1)
                    Next iRow
            End With

  '----------------------------------------

            'Need to select output sheet.
            With Worksheets("Output")                                   'With L1
        'Sheet names, & Voltage labels
```

```
611             Range("A1").Cells(1, 1 + m) = i & stSheet & j & "Voltage, V"
612           'Time Labels
613             Range("B1").Cells(1, 1 + m) = i & stSheet & j & "Time, s"
614
615   '--------------------------------------
616
617                 'this selects row to read from
618                ' If i = 1 Then           'has endif 8
619                 '    n = 1
620                    ' ElseIf i = 2 Then
621                       '   n = 2
622                         ' Else
623                             n = i - (k - i / 2)
624                             'End If          'has if 8
625
626
627                       'Reading the results from the Arrival Times sheet:
628                       If j = 2 Then
629                       With Worksheets("Arrival Times")                        'With L2
630                       sCh1T_Pk = .Range("B5").Cells(n + 1, 1)
631                       sCh2T_Pk = .Range("C5").Cells(n + 1, 1)
632                       sCh2_FA = .Range("F5").Cells(n + 1, 1)
633                       sCH2_V_Pk = .Range("H5").Cells(n + 1, 1)
634
635                       End With   'With L2
636                       End If
637
638                   'If j = 2 Then           'has endif 9
639
640
641             With Worksheets("Output")
642             'Data output
643             Range("A2:A1201").Offset(0, m) = WorksheetFunction.Transpose(VoltArray)
644             Range("B2:B1201").Offset(0, m) = WorksheetFunction.Transpose(TimeArray)
645             If j = 2 Then
646             Range("C2:C1201").Offset(0, m) = WorksheetFunction.Transpose(NegVolt)
647             Range("C1").Cells(1, m + 1) = "Neg. Volt"
648             Range("D1").Cells(1, m + 1) = "CH1 T_Pk"
649             Range("E1").Cells(1, m + 1) = "CH2 T_Pk"
650             Range("F1").Cells(1, m + 1) = "CH2 T_FA"
651             Range("G1").Cells(1, m + 1) = "CH2 V_Pk"
652             Range("H1").Cells(1, m + 1) = "LinReg"
653             Range("D2").Offset(0, m) = sCh1T_Pk
654             Range("E2").Offset(0, m) = sCh2T_Pk
655             Range("F2").Offset(0, m) = sCh2_FA
656             Range("G2").Offset(0, m) = sCH2_V_Pk
657
658
659             m = m + 8
660
661             Else
662             m = m + 2
663             End If
664             End With
665             'if the above doesnt work try this: (try it anyway)
666             'Range("A3:A1202").Offset(1, m).Value = VoltageArray
667             End With
668
669
670   Out:
671       End If
```

```
672
673     Next j
674
675 Next i
676
677 With Worksheets("Output")
678 'At end of sheet we must paste in the Arrival Time arrays:
679 'Data output, need to use final m from above to know where to paste!
680 Range("A1").Cells(1, m + 1) = "Frequency"
681 Range("B1").Cells(1, m + 1) = "Peak to Peak TT"
682 Range("C1").Cells(1, m + 1) = "Peak to Peak Vs"
683 Range("D1").Cells(1, m + 1) = "First Arrival TT"
684 Range("E1").Cells(1, m + 1) = "First Arrival Vs"
685 Range("A2:A7").Offset(0, m) = WorksheetFunction.Transpose(FreqArray)
686 Range("B2:B7").Offset(0, m) = WorksheetFunction.Transpose(TPk2PkArray)
687 Range("C2:C7").Offset(0, m) = WorksheetFunction.Transpose(VsPk2Pk)
688 Range("D2:D7").Offset(0, m) = WorksheetFunction.Transpose(TFAArray)
689 Range("E2:E7").Offset(0, m) = WorksheetFunction.Transpose(VsFA)
690 End With
691
692 'below is from ozgrid.com for outputting as a CSV file. Manipulate to save as a
693 'desired sheet, file name and path
694 Sheets("Output").Select
695 Sheets("Output").Copy
696 ActiveWorkbook.SaveAs Filename:= _
697 stPath & "Output" & stExt, FileFormat:= _
698 xlCSV, CreateBackup:=False
699
700 End Sub
701
702 'have fun
703
704
705
706
707
708
709
710
```

3.4 Void Ratio Measurement -details

This Appendix presents:

- Maximum and Minimum void ratio test.
- Discussion on efficacy of void ratio measurement procedures.

3.4.1 Maximum and Minimum Void Ratio Test

This test is in accordance with the Japanese Standard JIS A 1224:2000 Test Method for Minimum and Maximum Densities of Sands (refer Figure 3.92). Japanese Geotechnical Society [In Japanese]. Translation to English by Dr. Yasuyo Hosono.

At least 95 % of the material must be sand (75 μm < D < 2 mm).

3.4.1.1 Minimum dry density

The funnel is placed inside the mould (Figure 3.93 1 & 2 respectively) and filled with soil. The funnel is carefully lifted-up at a constant speed so as to exit the top of the mould in 20 to 30 seconds. The funnel must be always in contact with the soil beneath it when lifting it up. The superficial soil above the mould top is removed by the knife (straight edge).

3.4.1.2 Maximum dry density

The soil is divided in ten equal portions. Each portion is placed in the mould, and the mould is hit 100 times with a wooden hammer (3 cm in diameter).

The mould should sit on a table, as well as the hammer. The swing of the hammer is about 5 cm. The mould is hit about 5 times per second, and after each series of hits, the mould is rotated 45-90°.

For the 10th layer, the extension mould is added (Figure 3.93 1b). At the end, the extension mould is removed, the sand surface is flattened by the knife, and the weight is measured.

To eliminate the human factor as much a possible, recently automatic devices were standardised. However, both procedures with and without devices can be used.

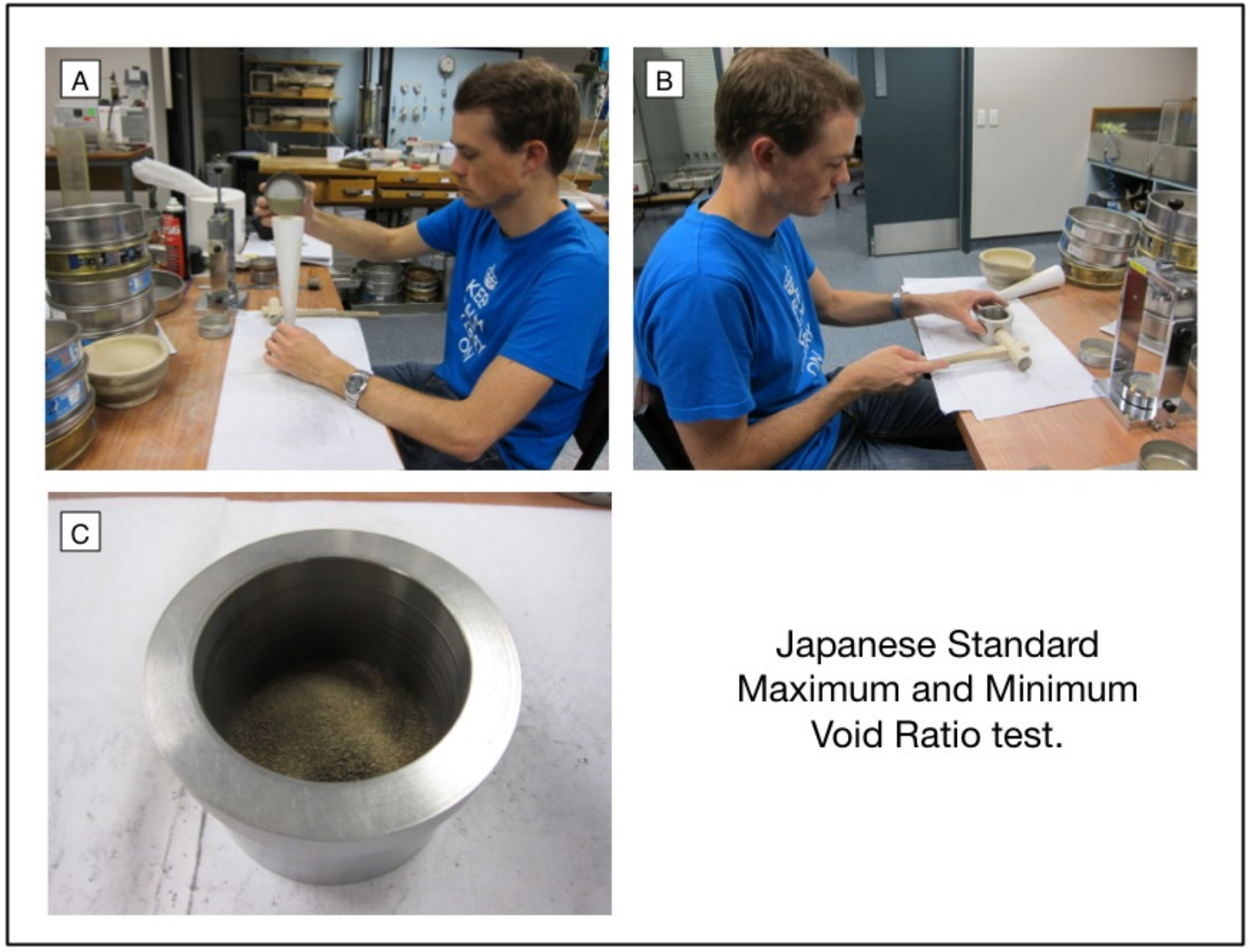

Figure 3.92: Japanese Standard test for maximum and minimum void ratio. A: Pouring sand into mould using paper funnel for maximum void ratio test. B: Tapping mould using a wooden hammer for minimum void ratio test. C: Steel mould for performing the tests.

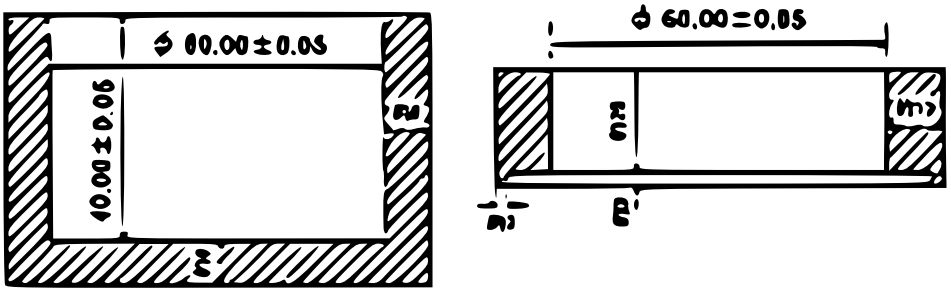

(a) モールド　　(b) カラー

図－1　モールドとカラーの例（単位：mm）

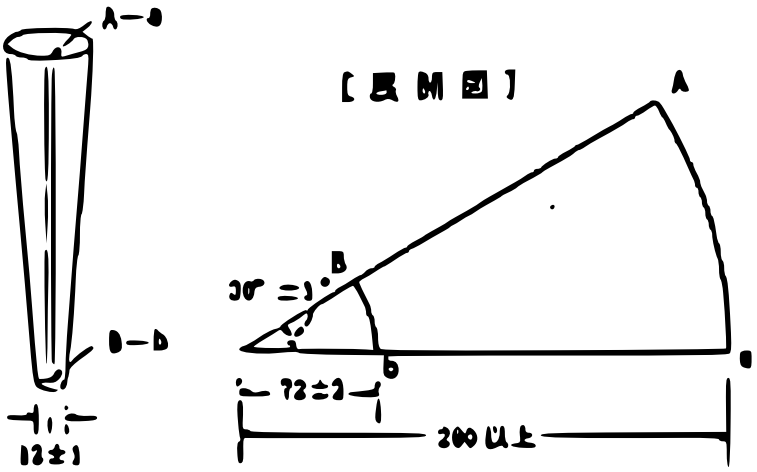

図－2　漏斗の例（単位：mm）

Figure 3.93: Apparatus required to conduct e_{max} and e_{min} test.

3.4.2 Discussion on efficacy of void ratio measurement procedures

Following this approach, both Verdugo (1992) and Rees (2010) were able to achieve highly accurate void ratio measurements post test and during the test itself by applying volume changes recorded during the test phases from the end of the test working backwards to the post saturation phase prior to consolidation. Rees (2010), using the GDS triaxial apparatus was able to disassemble the entire sample with platens, porous stones, filter paper, and membrane and weigh this unit together. From known dry weights of the membrane, platens, porous stones, and filter paper the wet mass of the specimen at the end of the test could be accurately obtained. Unfortunately this technique could not be replicated as accurately with the Seiken apparatus, due to differences in the connections between the platens and the apparatus, and the drainage tubes between apparatus and platens. Thus it remains possible for migration of water between the platens/drainage tubes and the specimen during deconstruction of the apparatus and extraction of the sample for weighing. As noted by Verdugo and Ishihara (1996), the sample is under vacuum when the top cap is removed, allowing air to enter the specimen, and equalise the pressure with the atmosphere, these pressure changes however, may cause migration of fluid as well (cannot be ruled out). This presents a potential source of error in the void ratio measurements, along with errors in reading the burette volume, and weight measurements of sample before and after oven drying. The burette readings were conducted using the digital pressure gauge which allowed recording to datafile the changes in volume during these post-test steps.

Variation in void ratio measurements: Figure 3.94 presents a direct comparison between the two methods to measure the void ratio post-consolidation. Typically the same or higher void ratios are measured using the backward method. Further comparisons between the reconstituted *representative* specimens are presented in Figure 3.95. The trend noticed for GP samples generally holds for the reconstituted specimens, except for higher void ratio specimens, where the forward estimate predicts higher void ratios ($e > 0.9$) than the backward method, perhaps indicative of changes in volume of the specimen on wetting during the saturation phase, not captured by the forward estimate method. This was more noticeably

in samples K1–4-S4 (FC 17 %), and K1–2-S4 (FC 40 %). The observed variations are significant as uncertainty in void ratio measurement affects the estimate of the critical state line on the state diagram ($e : p'$ space), which shall be discussed further later in this chapter where CS lines for these *typical* soils are presented.

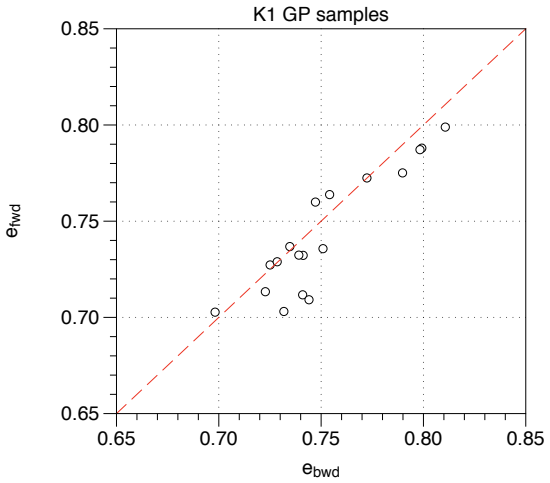

Figure 3.94: Comparison of void ratio measurements for K1 GP samples. Backward and forward measurement methods.

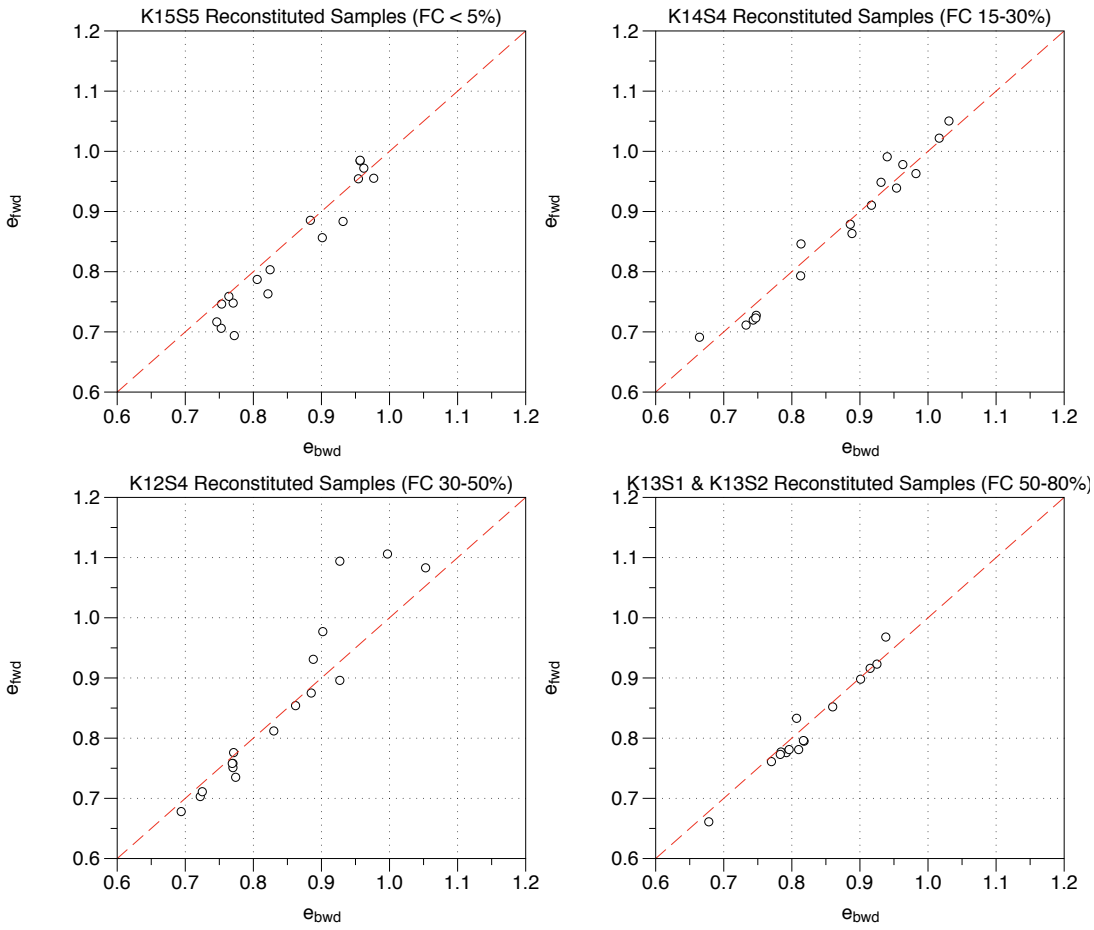

Figure 3.95: Comparison of void ratio measurements for reconstituted samples. Backward and forward measurement methods.

3.5 Index Data comparisons

This section of the appendix presents:

- Maximum and Minimum void ratios compared to published datasets;
- Evaluating Compressibility factor C_D from K1 site data.

3.5.1 Maximum and minimum void ratios compared to published datasets

Values of e_{max} and e_{min}: Cubrinovski and Ishihara (2002) and Cho et al. (2006) collated data on the void ratio characteristics from a variety of sands published in the literature. A selection of commonly tested *benchmark* sands, tabulated in Table 3.1, have been plotted against the data in this study, and presented in Figure 3.96. The marine clean sand at K1 (*Ch. Fm.*) is similar to the sub-angular to sub-rounded Toyoura and Ticino sands. Sands with rounder grains typically have lower e_{max} and e_{min} values. Monterey Sand with 16 % angular fines added to this subrounded sand, exhibits lower values than at 0 % fines, while Chiba sand with 18 % fines exhibited an increase in void ratio limits of similar order to that observed for the fluvial silty sand at K1 (*Sp. Fm.*). These stark differences in response to added fines suggests that the Monterey#16 soil may be gap-graded, allowing the fines to fill the voids in the matrix between the larger sand particles, resulting in higher densities than clean materials. The high uniformity of the natural specimens from K1 and the increasing e_{max} suggests the fines remain integral to the structure of the sand, and allow for lower densities to be achieved.

Further comparisons with benchmark sands from the literature are included to compare the site-specific correlations presented in the above plots with general published correlations. Note that different researchers adopted different test methods to determine the void ratio limits of some of the benchmark sands considered here, which may also contribute to the observed differences. Observed differences are summarised below:

- Particle shape effect on maximum and minimum void ratio: The e_{max} and e_{min} values projected for no fines content of both *Sp. Fm.* and *Ch. Fm.* soils, along with estimates of soil particle Roundness, are compared in Figure 3.97

Table 3.1: Selected Benchmark Sands

Soil Name	e_{max}	e_{min}	Grain shape	FC [%]	D_{50} [mm]	Ref.
Cambria	0.767	0.538	R	0	1.5	1
Toyoura	0.988	0.616	SR-SA	0	0.17	2
Ottawa	0.78	0.48	R-SR	0	0.39	3
Fraser River	0.94	0.62	A-SR	0	0.26	4
Ham River	0.87	0.526	SA	0	-	5
Nevada	0.85	0.57	SR-R	0	0.15	6
Ticino	0.99	0.574	SA-SR	0	0.58	6
Chiba#3	1.271	0.839	-	3	0.17	7
Chiba#18	1.307	0.685	-	18	0.15	7
Monterey#0	0.86	0.53	R-SR	0	0.38	8
Monterey#16	0.71	0.49	SR-SA	16	1.3	9
Sydney	0.855	0.565	-	0	0.3	10

References: 1. Lade et al. (1998), 2. Zlatovic (1994), 3. Salgado et al. (1998)
4. Wijewickreme et al. (2005), 5. Georgiannou (2006), 6. Cho et al. (2006)
7. Ishihara (1993), 8. Riemer et al. (1990), 9. Riemer and Seed (1997)
10. Chu and Lo (1993)

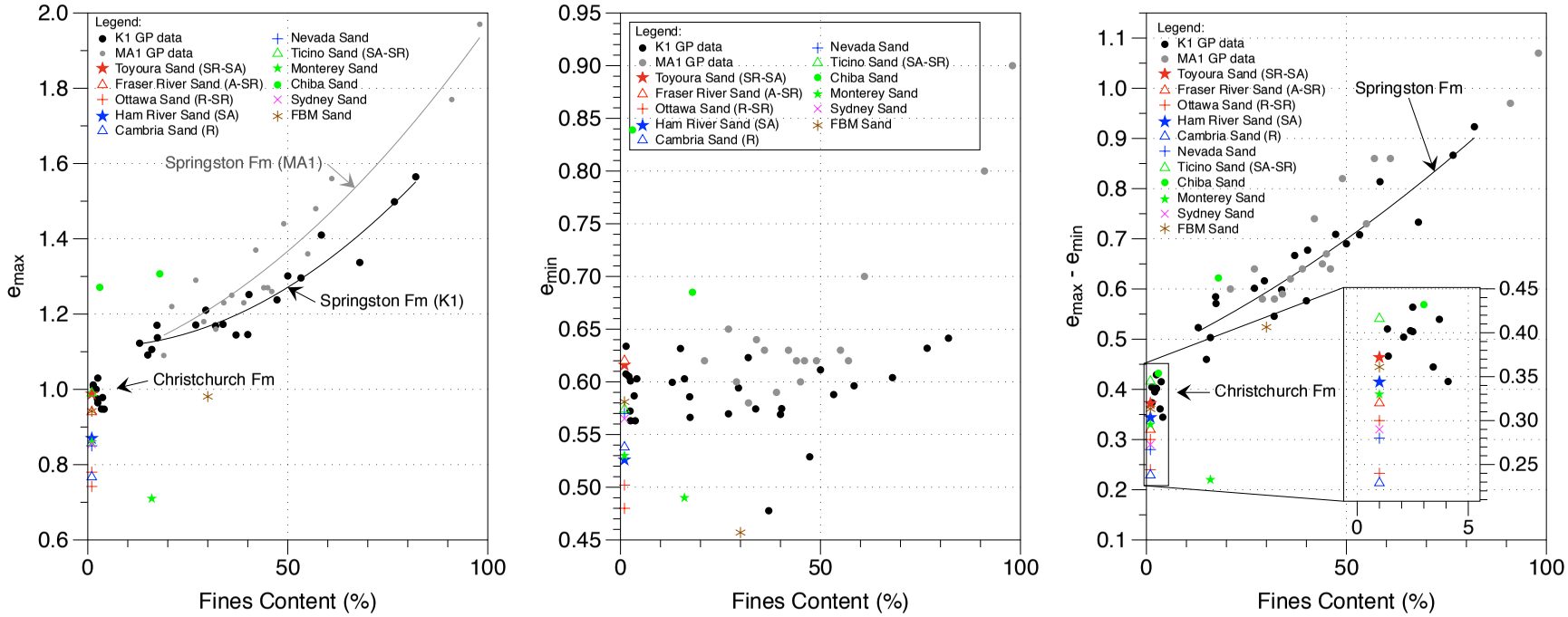

Figure 3.96: Comparison K1 and MA1 GP index data with selected benchmark sands. Left: e_{max} plotted against FC. Centre: e_{min} plotted against FC. Right: Void ratio range, $e_{max} - e_{min}$ against FC.

to the curves suggested by Youd (1973) and Shimobe and Moroto (1995) and the data presented by Santamarina and Cho (2004). The Christchurch data fits well with the general trends observed.

- Relationship between e_{max} and e_{min}: Cubrinovski and Ishihara (2002) presented relationships between the void ratio limits based on a large dataset, which show a correlation between the two indices, and the trend for higher values with higher fines contents. Figure 3.98 reproduces this plot with the data from this study overlaid in colour. Generally the same trends are observed, however Christchurch soils with high fines contents (up to 98%) are observed to extend to lower minimum void ratios than the published data.

- Relationship between void ratio range, $e_{max} - e_{min}$, and fines content, FC: Cubrinovski and Ishihara (2002) presented a relationship between these values. Figure 3.99 presents the data from this study overlaid in colour. The K1 and MA1 data falls within the middle to lower bound of the range of published test data.

- Relationship between void ratio range, $e_{max} - e_{min}$, and median grain size, D_{50}: Cubrinovski and Ishihara (2002) presented a relationship between these values. Figure 3.100 presents the data from this study overlaid in colour. The K1 and MA1 data falls on the lower-bound of the range of the dataset. This is considered to be due to the uniform nature of the PSD gradation curves (soils with higher D_{50} and significant fines indicate well graded sands). Also the fines are essentially non-plastic and lacking in clay-sized particles, likely also influencing the lower-position of the relationship. A revised curve for the Christchurch dataset is provided with the same functional form as: $e_{max} - e_{min} = 0.3 + 0.028/D_{50}$.

- Relationship between void ratio range, $e_{max} - e_{min}$, and the compressibility factor, C_D, where: $C_D = (N_1)_{78}/D_R^2$, providing correlation between penetration resistance and relative density: Cubrinovski and Ishihara (1999) presented a relationship between C_D and $e_{max} - e_{min}$ with *in situ* densities obtained from high quality undisturbed samples, showing that the correlation

between the two parameters was affected by void ratio range $e_{max} - e_{min}$, itself a function of soil gradation and granular characteristics (refer Figure 3.101A). Figure 3.101B presents the data from this study plotted with the dataset presented by Cubrinovski and Ishihara (1999) showing generally good agreement (i.e. within the upper and lower-bounds), but some samples falling below the range of the published dataset.

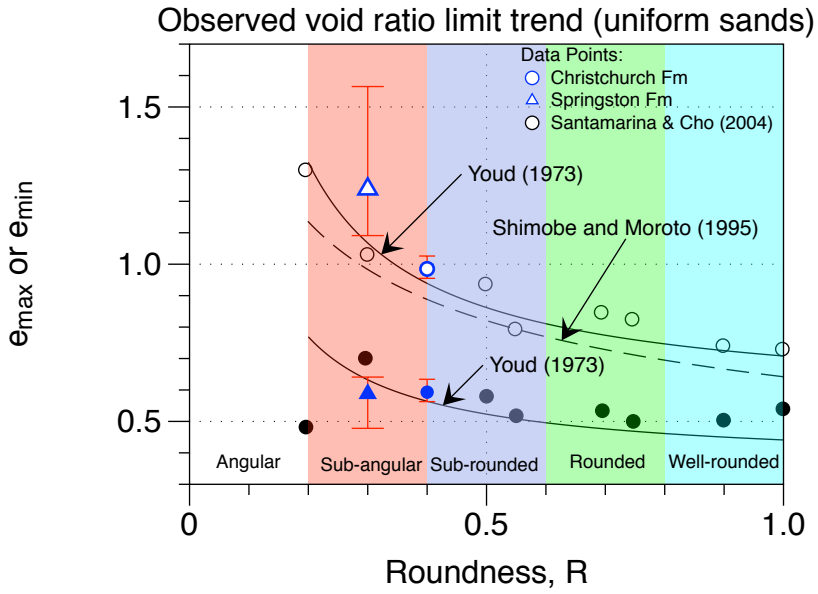

Figure 3.97: Christchurch and Springston Formation index and particle roundness relationship compared to published trends (Shimobe and Moroto, 1995; Youd, 1973).

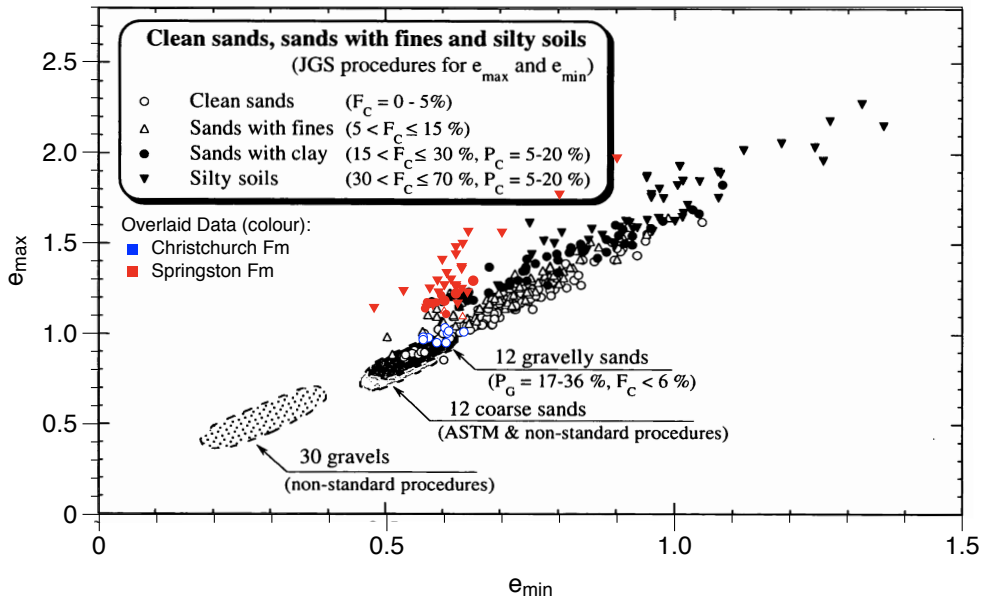

Figure 3.98: Comparison K1 and MA1 GP index data with published correlation between e_{max} and e_{min} after Cubrinovski and Ishihara (2002).

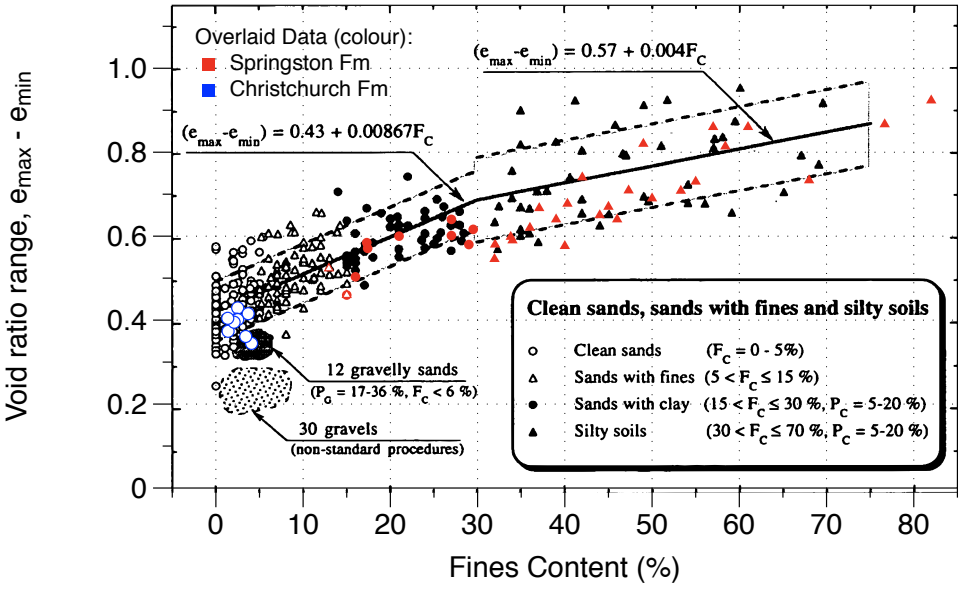

Figure 3.99: Comparison K1 and MA1 GP index data with published correlation between void ratio range, $e_{max} - e_{min}$, and fines content, FC after Cubrinovski and Ishihara (2002).

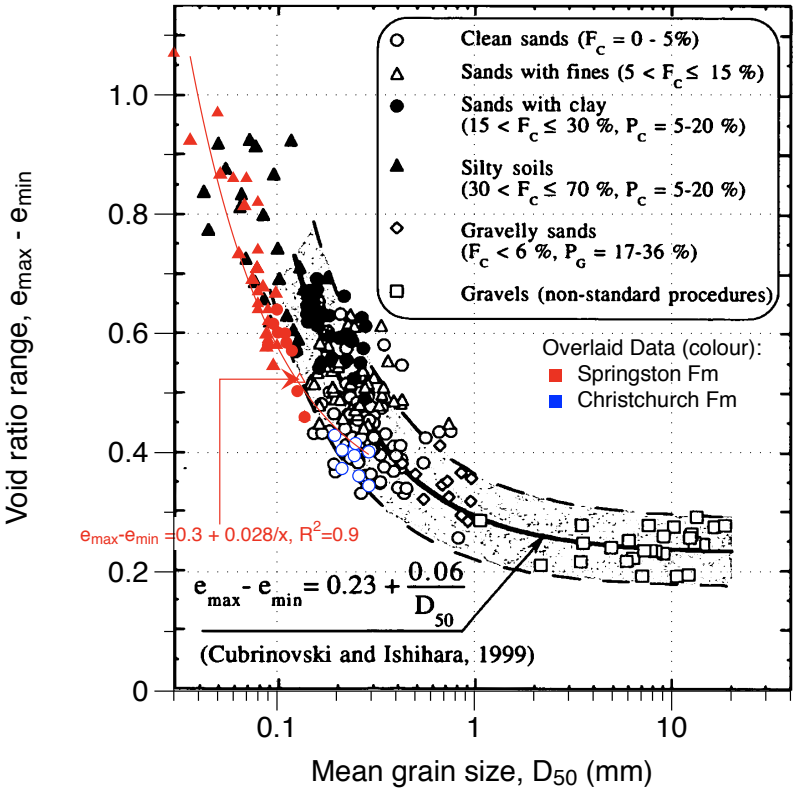

Figure 3.100: Comparison K1 and MA1 GP index data with published correlation between void ratio range, $e_{max} - e_{min}$, and D_{50} after Cubrinovski and Ishihara (2002).

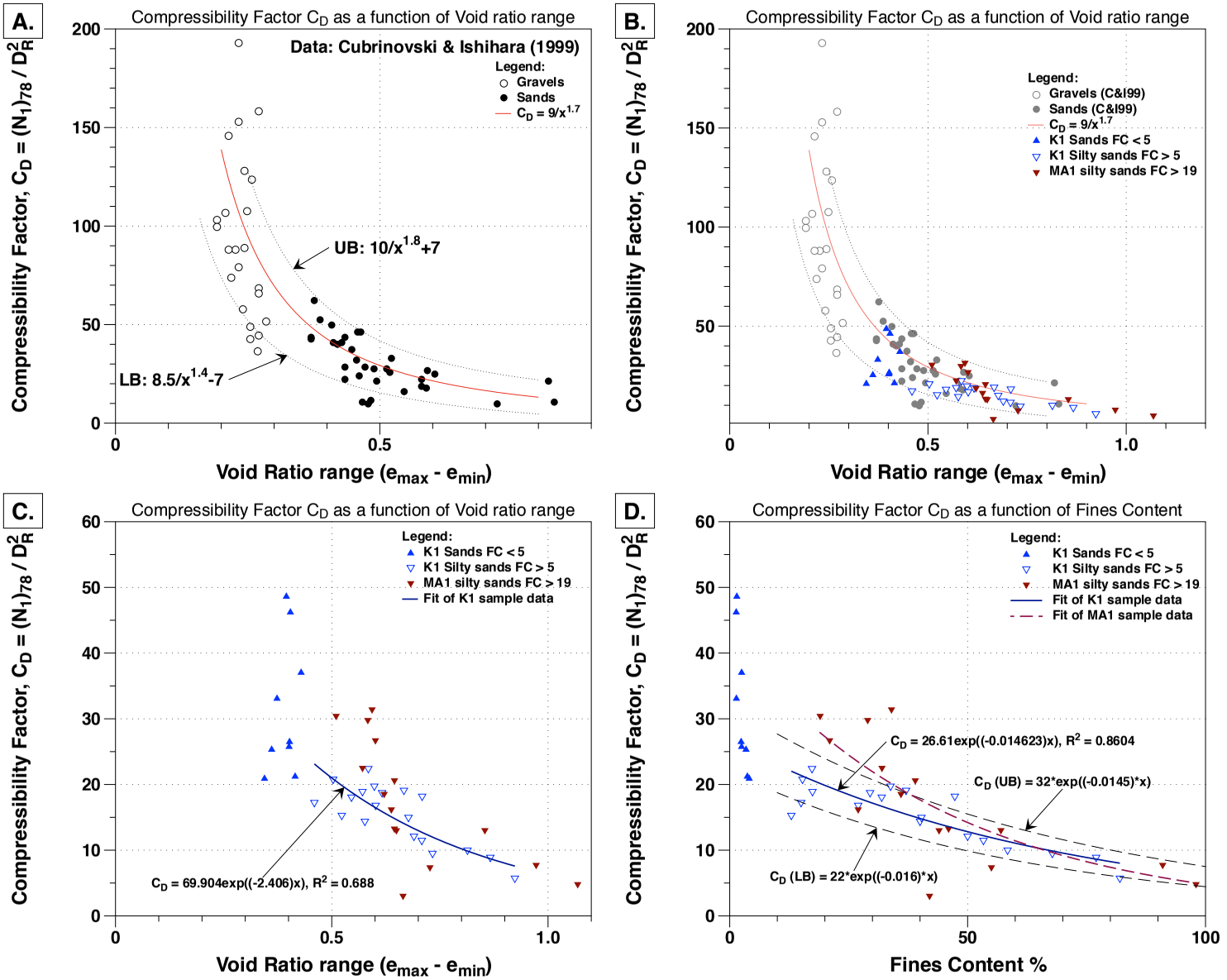

Figure 3.101: Plots of Compressibility factor C_D as a function of void ratio range, $e_{max} - e_{min}$, and fines content. A. Dataset and suggested relationship presented by Cubrinovski and Ishihara (1999). B. Overlaid K1 and MA1 GP sample data from specimen D_R and SPT $(N_1)_{78}$ (correlated from adjacent CPT using published SPT-CPT correlation). C: K1 and MA1 data only, with curve fitting of K1 silty sands. D: C_D correlated with FC.

3.5.1.1 Evaluating Compressibility factor C_D from K1 site data

To estimate C_D from K1 site data, an estimate of equivalent SPT $(N_1)_{78}$ values as used by Cubrinovski and Ishihara (1999) are required. A published correlation between CPT q_c and SPT $(N_1)_{60}$ after Jefferies and Davies (1993) was adopted (Robertson and Cabal, 2012, p. 34), using the CPT profile data immediately adjacent to the sample hole. This correlation is a function of soil behaviour type index, I_c, when rearranged may be expressed as:

$$(N_1)_{78} = \frac{(N_1)_{60}}{C_E} = \left(\frac{q_{c1N}}{C_E \cdot 8.5 \left(1 - \frac{I_c}{4.6}\right)} \right) \tag{3.1}$$

where C_E is the energy ratio between North American standard SPT $(N_1)_{60}$ used in the CPT- SPT correlation, and the Japanese standard $(N_1)_{78}$ used in the correlation between C_D and void ratio range. It is equal to the ratio 78/60.

The observed differences in the GP sample $C_D : (e_{max} - e_{min})$ data and the dataset presented by Cubrinovski and Ishihara (1999) may be on account of both the characteristics of these soils, but may also be due to compression occurring on account of sampling disturbance. The published dataset contains few specimens with void ratio range above 0.6, and a significant number of such specimens are included in this study. A site-specific correlation based on the higher quality K1 *Sp. Fm.* silty sands is presented in Figure 3.101C, and is expressed as:

$$C_D = 69.9 \exp(-2.406(e_{max} - e_{min})) \tag{3.2}$$

with a coefficient of determination, R^2, of 0.69, noting that the scatter is significantly less for these soils than for either the *Ch. Fm.* marine sands, or the MA1 soils, again possibly on account of sampling disturbance, or variations in the soil parameters.

Figure 3.101D presents the $C_D : FC$ relationship for the GP sample data, from both K1 and MA1 soils. A line of best fit has been constructed through the K1 *Sp. Fm.* data, and upper and lower-bound lines constructed manually to encompass the majority of the data scatter. It may be readily observed from Figure 3.101D that the measured index properties of the *Ch. Fm.* sands with FC < 5 % do not occur along the same trends observed in the *Sp. Fm.* soils as a

function of fines content, and that I_c values in these materials likewise do not show a trend consistent with the *Sp. Fm.* soils, thus grouping both data-sets together to establish a site-specific correlation would result in significantly more scatter and a less reliable correlation. Because of this the correlation presented has been limited to soils with FC > 10 %, typical of materials obtained from the upper 9 m at K1. It has the following form:

$$C_D = 26.6 \exp\left(-\frac{FC}{68.39}\right) \tag{3.3}$$

A site specific correlation between C_D and FC directly for these materials seems more appropriate, results in a much higher coefficient of determination, R^2 of 0.86, and consequently tighter upper and lower bounds. This relationship is used in this study to relate reconstituted K1 specimens prepared at a particular density to field penetration resistance.

This relationship has been further scrutinised by considering the quality of the specimens and the likelihood they were disturbed by sampling. The specimen quality index (SQI) evaluated for the GP specimens was used for this purpose, to remove specimens with obvious signs of disturbance or resulting in poor overall SQI. Figure 3.102 presents plots of C_D as a function of void ratio range and fines content, with some revision of the resulting relationships:

$$C_D = \frac{7}{(e_{max} - e_{min})^{1.657}} \tag{3.4}$$

with an R^2 of 0.62.

$$C_D = 30.75 \exp\left(-\frac{FC}{54.38}\right) \tag{3.5}$$

with an R^2 of 0.95.

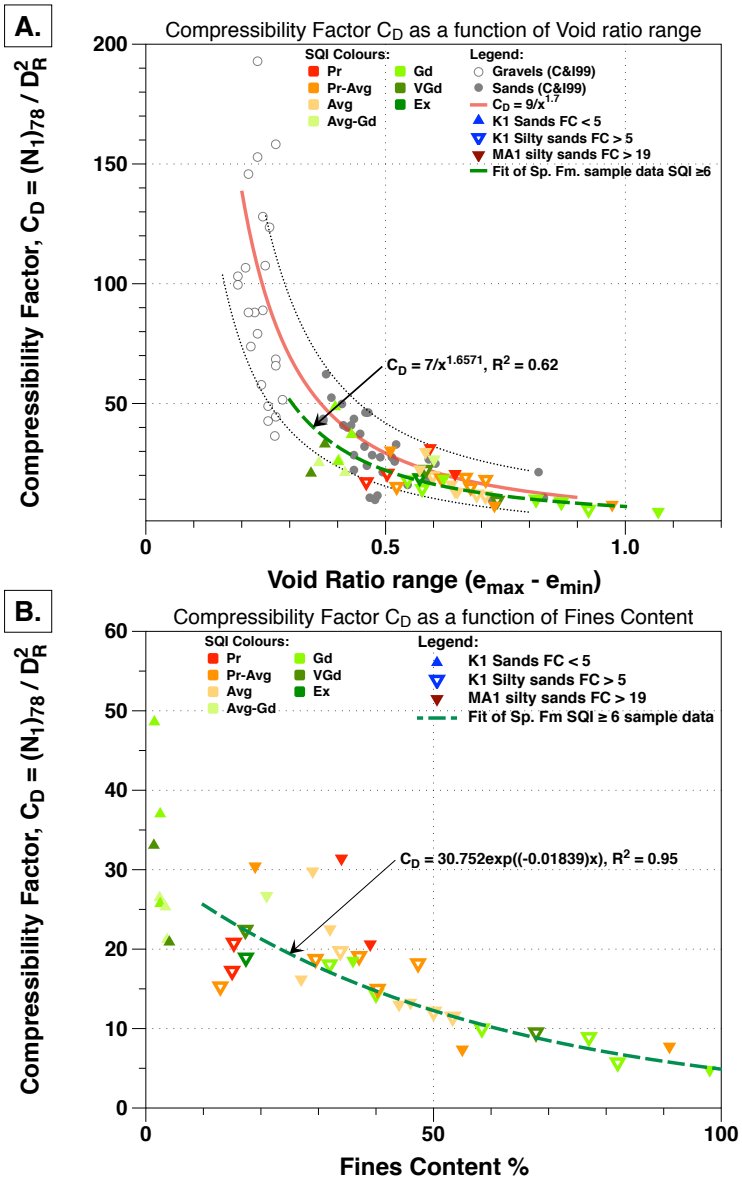

Figure 3.102: Revised empirical C_D relationships for K1 GP specimens, where only samples with Specimen Quality Index values ≥ 6 were used to derive the correlations with void ratio range (A.) and fines content (B.).

3.6 Membrane Effects - Details.

This Appendix presents:

- Discussion on efficacy of void ratio measurement procedures.
- Membrane Penetration -literature review.
- Measurement of Membrane stiffness.

3.6.1 Membrane Penetration

Verdugo (1992) presents a thorough review of the issue of membrane penetration as it affects the measurement of soil response to changes in load condition. The membrane penetration effect is essentially a change in volume that may be measured that is not purely that of the soil skeleton, but also the deflection of the membrane between the points of contact between the membrane and the soil grains (Figure 3.103 andFigure 3.104). During undrained tests this effect also influences the measurement of excess pore water pressure.

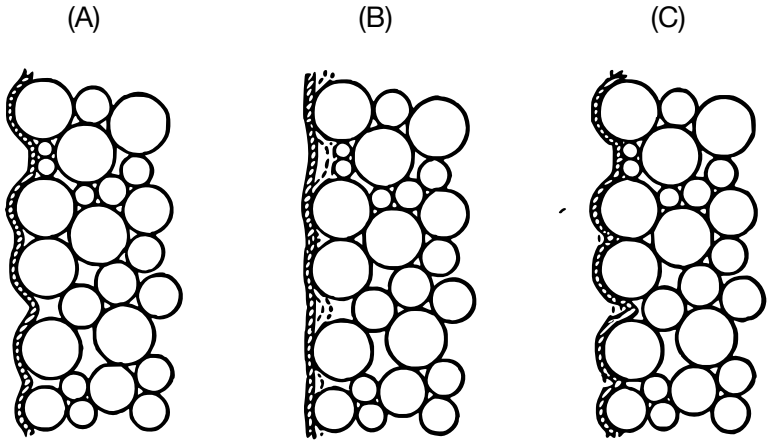

Figure 3.103: Deformed shape of membrane: (A) At end of consolidation; (B) During undrained test with increasing pore water pressure; (C) During drained test with increasing cell pressure. Figure from Kramer et al. (1990).

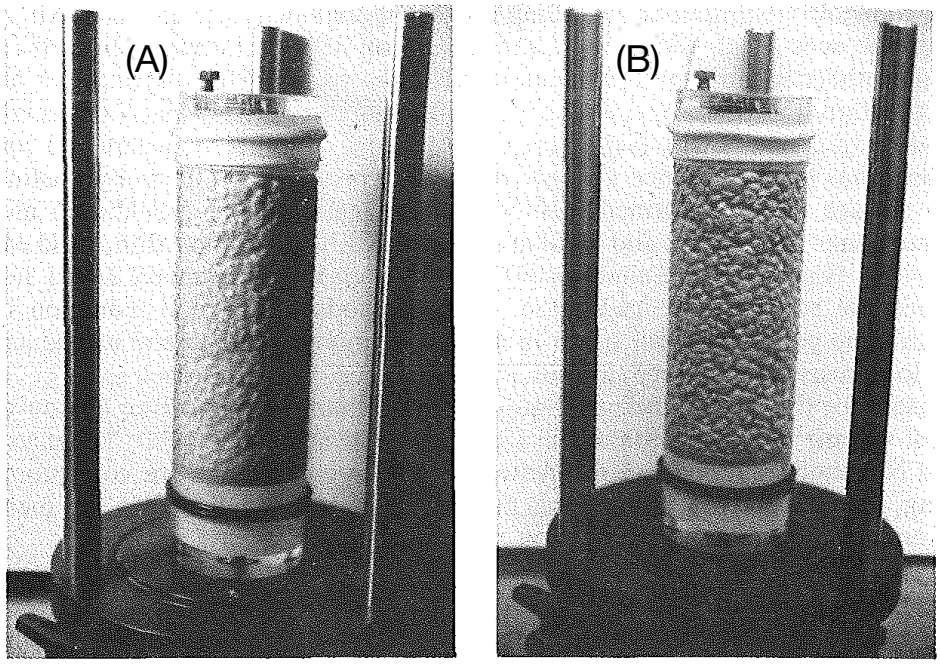

Figure 3.104: Membrane penetration in triaxial sample of coarse sand: (A) Low confining pressure; and (B) High confining pressure. Photos from Kramer et al. (1990).

In the evaluation of the effect, Verdugo (1992) drew on the the work of Baldi and Nova (1984) who developed a simplified analysis of membrane penetration, which has been validated by experimental results reported in the literature (e.g. Sladen et al. (1985) refer Figure 3.105). A semi-empirical equation to consider the volumetric strain caused by membrane penetration is as follows:

$$\Delta V_m = \frac{d_g V_0}{2D}\left[\frac{d_g}{E_m t_m}\right]^{1/3}\left[\sigma_r'^{1/3} - \sigma_{r0}'^{1/3}\right] \tag{3.6}$$

where: V_m is the volumetric strain caused by membrane penetration; D is the diameter of the sample; V_0 is the initial volume of the sample; d_g is the grain size; σ_r' is the effective confining pressure; E_m the Young's modulus of the membrane; and t_m the membrane thickness.

The results indicate that the membrane penetration effect is negligible for fine grained sands, but becomes increasingly significant with large grain sized materials, where d_g in the above equation s assumed to be D_{50} the median grain size. This effect may be readily observed in Figure 3.105.

In evaluating the membrane penetration effect for his tests, conducted using a conventional triaxial cell and using Toyoura sand, Verdugo (1992) took the following values for the parameters in the semi-empirical equation 3.6:

- $d_g = 0.16$ mm
- $t_m = 0.3$ mm
- $E_m = 1491$ kPa
- $V_0 = 196{,}000$ mm^3
- $D = 50$ mm
- $\sigma_{r0}' = 20$ kPa

With these values the volume changes was calculated to be a function of the confining stress applied during testing. When the maximum possible range of ≈ 600 kPa confining stress change was considered, the potential volume change

caused by membrane penetration was estimated as 120 mm^3, which equates to a change in void ratio of a typical soil specimen of $\Delta e = 0.001$. This value is considered to be very small, and not worth correcting for.

Rees (2010) applied the same logic that the as the sand he was testing was very fine (maximum D_{50} of 0.21 mm), the error associated with membrane penetration was considered negligible, citing Sladen and Handford (1987).

For the soils tested in this project the majority of samples tested were fine grained silty sands of the Springston Formation, with D_{50} values less than 0.15 mm. The Christchurch Formation sands had little to no fines, and consequently larger D_{50} values, the largest being the deepest samples obtained from K1 borehole, K1-6-S4 and K1-6-S5, which had a D_{50} of 0.29 mm. Using Equation 3.6 the following change in volume (mm^3), was obtained as a function of change in confining stress:

$$\Delta V_m = 528.5\sigma_r'^{1/3} - 143.5 \tag{3.7}$$

By the same logic outlined by Verdugo (1992), for a confining stress change of 600 kPa, and assuming a typical soil mass of specimen of 280 g, the change in void ratio, Δe due to membrane penetration effect would be of the order of 0.003. This is considered to be negligible for the purposes of assessing sample relative density and position of the steady state line.

3.6.2 Measurement of membrane stiffness.

The stiffness of the latex rubber membrane has an impact on not just the membrane penetration as discussed previously, but also the estimate of the end point of a trivial test, particularly when the specimen is very loose and contractive behaviour is observed.

Baxter (2000, pp. 303-317) presents a thorough review of membrane strength corrections referring to early work by Henkel and Gilbert (1952) identifying the issue and proposing corrections to account for the effect of membrane strength during undrained shear, based on compression shell theory and hoop stress theory. The former would apply when the confining stress caused the membrane to maintain contact with the soil sample, while the latter would apply if the membrane "buckled", or separate from the sample. They also proposed a method to esti-

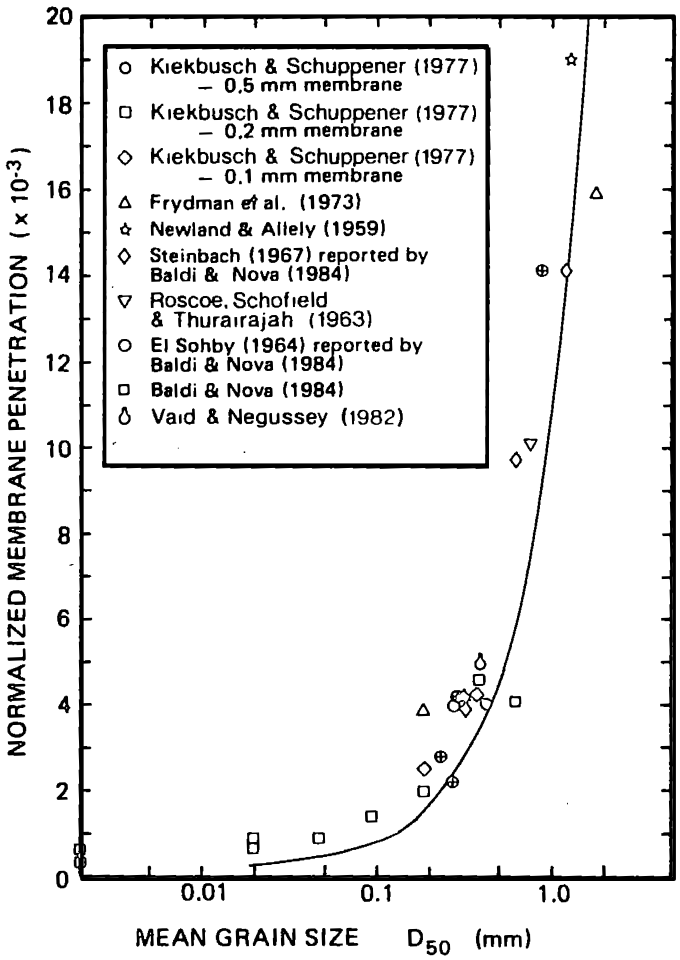

Figure 3.105: Evaluation of membrane penetration. Reproduced from Verdugo (1992) after Sladen et al. (1985).

mate the extension modulus of the membrane, using a load-extension test. The modulus, M, in units of load per cm per strain, is related to Young's Modulus, E, by; $E = M/t$, where t is the thickness of the membrane. Later Duncan and Seed (1967) applied a new compression shell theory based correction for stresses and strains that occur during consolidation. La Rochelle et al. (1988) used the shell theory correction of Henkel and Gilbert (1952), while developing a new hoop-stress correction to fit with experimental results performed on rubber dummy samples. They provide two corrections, one for bulging type failure observed on soft samples, and a correction for shear plane development in dense samples with a correction for the loading of the membrane for this condition. La Rochelle et al. (1988) note that if buckling occurs the membrane cannot support an axial load (as assumed for the earlier noted corrections), and its circumferential stretching contributes to increasing the lateral stress on the specimen, and this is not a negligible stress at large strains, especially on soft samples. The correction for bulging of the sample in this latter case is considered here, with the correction being applied to the σ_3 stress:

$$\sigma_{3m} = p_{om} + 0.75\frac{M\sqrt{\varepsilon_a}}{d_0} \tag{3.8}$$

where:

- p_{om} is the initial confining pressure.
- M is the modulus of the membrane
- d_0 is the diameter of the specimen at the end of consolidation.

They note that p_{om} should not be taken into account if the weight of the piston on the specimen has been balanced, cancelling the effect of initial contact pressure of the membrane. The modulus recommended by La Rochelle et al. (1988) for use with the above relation is for a 15 % strain condition.

The ASTM standards for triaxial testing (D7181-11, D4767-11) provide a recommended correction due to the axial contribution of the membrane during shear-

ing.

$$\Delta(\sigma_1 - \sigma_3)_m = (4E_m t_m \varepsilon_a)/D_c \tag{3.9}$$

where:

- $\Delta(\sigma_1 - \sigma_3)_m$ = membrane correction to be subtracted from the measured principal stress difference (deviator stress), kPa.
- $D_c = \sqrt{4A_c/\pi}$ = diameter of specimen after consolidation, mm.
- E_m = Young's modulus for the membrane material, kPa.
- t_m = thickness of the membrane, mm.
- ε_a = axial strain (decimal form).

The ASTM standard notes the procedure by which the Young's modulus of the membrane may be determined by hanging a 15 mm circumferential strip of membrane using a thin rod, placing another rod through the bottom of the hanging membrane, and measuring the force per unit strain obtained by stretching the membrane. The modulus value may be computed using the following equation:

$$E_m = (F/A_m)/(\Delta L/L) \tag{3.10}$$

where:

- E_m = Young's modulus of the membrane material, kPa.
- F = force applied to stretch the membrane, N
- L = unstretched length of membrane, mm.
- ΔL = change in length of the membrane due to the force, F, mm.
- A_m = area of membrane = $2t_m \cdot W_s$, where:

- W_s is the width of the circumferential strip of membrane, 15 mm.

They note a typical value of E_m for latex membranes is 1400 kPa.

The corrected deviator stress is simply: $q_c = P/A - (\sigma_1 - \sigma_3)_m$.

This procedure was approximately followed in order to measure the Young's Modulus of the GDS supplied latex membrane used in these tests. The membrane has a nominal thickness of 0.25 mm. Instead of looping the membrane around glass tamping rods, a single strip of 10 mm wide membrane was attached to two steel washers with superglue. Hanging from a washer at one end of the membrane, was a small plastic plate connected via cotton thread to three evenly spaced locations on the plates circumference. The plate allowed weight to be placed to apply load to the membrane. To measure the total force applied including the weight of metal washer and plastic plate, the upper washer was connected to digital scales by cotton thread. The set up is shown diagrammatically in Figure 3.106. The measurement of deflection of the membrane was made via use of vernier callipers, with the corresponding weight of the scales for each deflection measurement logged. It is assumed that the stiffness of the cotton thread is much greater than that of the membrane.

The resulting load deflection plot and calculated modulus values as a function of strain are shown in Figure 3.107. Large and small strain values for use in calculations are shown for reference.

Baxter (2000, p. 305) considers the ASTM correction to be based on compression shell theory, modified to correct for changing area of the membrane but notes that no derivations are given. He then goes on to present a new correction (referred to as at the *Baxter and Filz correction*), based on compression shell theory, modified from earlier corrections to account for:

- Stress and strain of the membrane during consolidation
- Correct both the sample area and the membrane area for right cylinder deformation
- Incorporate the initial diameter of the membrane

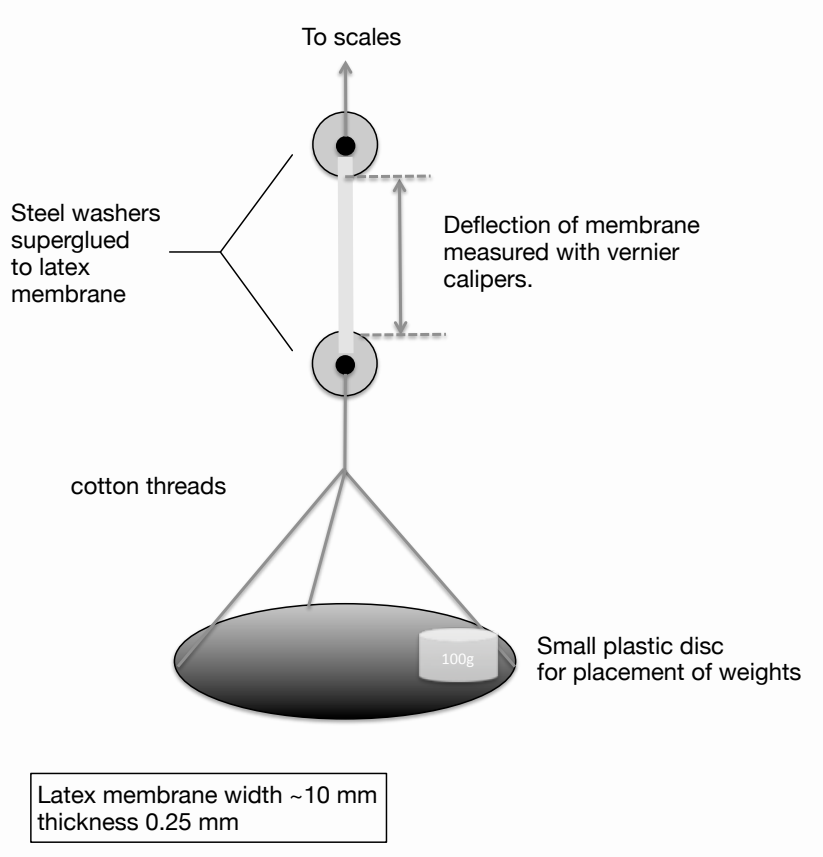

Figure 3.106: Diagram depicting the test configuration to measure the elastic modulus of the latex membrane.

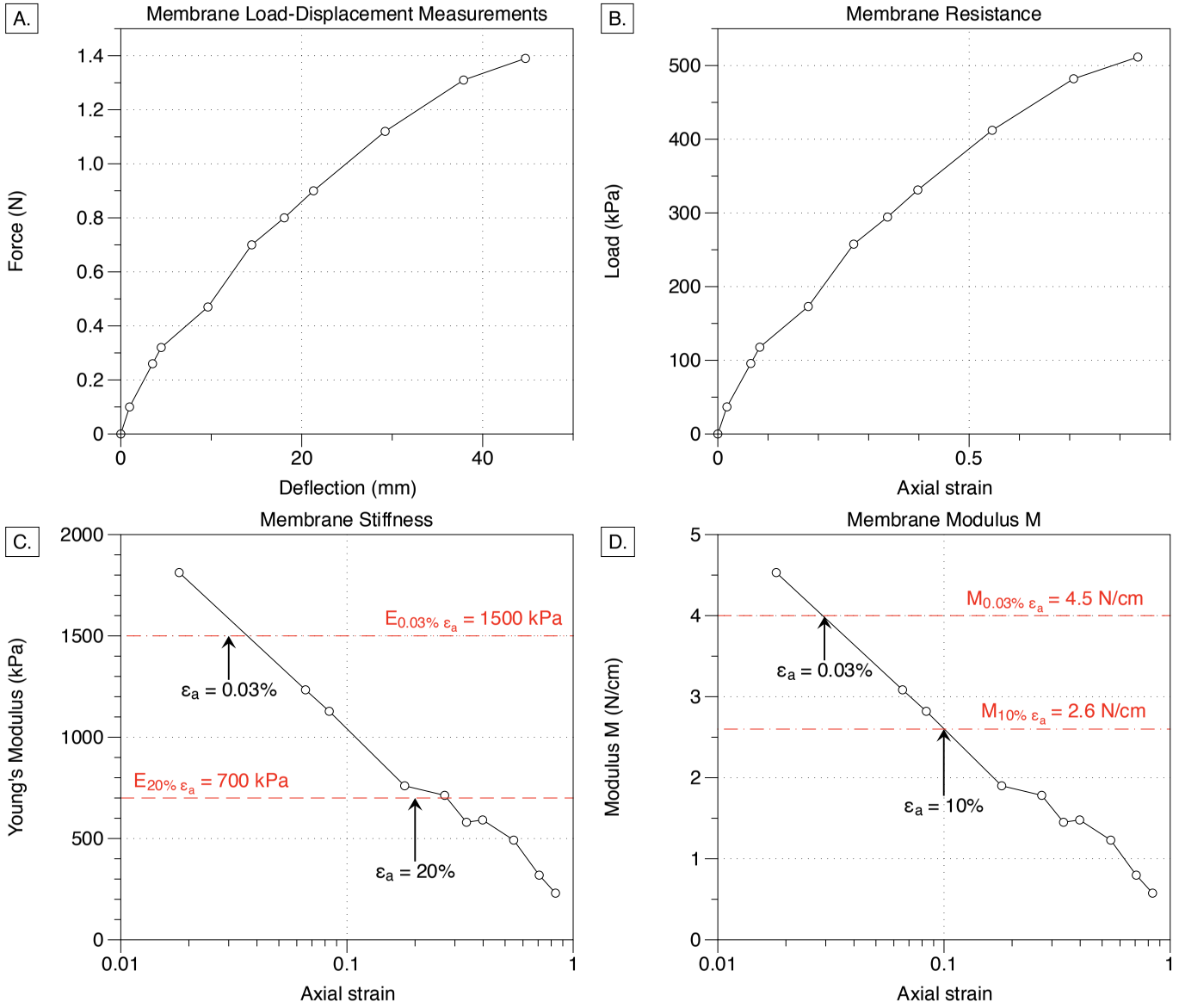

Figure 3.107: Measurement of membrane modulus in extension. A) Force- displacement curve, with (B) corresponding Load- deformation curve (C), Tangent Young's Modulus degradation with strain, and (D) corresponding Membrane Modulus degradation with strain.

- The initial tangent modulus was used instead of an average secant modulus.

They did not apply hoop stress theory considering the effect of "buckling" of the membrane as identified by Henkel and Gilbert (1952) to be a local effect only, and the membrane continued to be held in place above and below the observed wrinkles in the membrane. From elastic theory they considered corrections to both σ_1 and σ_3 principal stresses during consolidation:

$$\Delta\sigma_{1,con} = 4\sigma_a t/D \tag{3.11}$$

$$\Delta\sigma_{3,con} = \sigma_t t/r \tag{3.12}$$

where:

- t = thickness of membrane after consolidation
- D = diameter of sample after consolidation
- r = radius of sample after consolidation
- σ_a = axial stress in membrane after consolidation
- σ_t = tangential stress in membrane after consolidation.

During shearing, the following correction was derived for the major principal stress in the specimen:

$$\Delta\sigma_{1,shear} = \frac{4\varepsilon_a t_0 E}{D_0(1-\varepsilon_{vol})} \tag{3.13}$$

where:

- ε_a = axial strain measured from the beginning of shear
- ε_{vol} = volumetric strain measured from the beginning of shear
- t_0 = thickness of the membrane at the beginning of shear

- D_0 = diameter of the sample at the beginning of shear.

In summary, there are different corrections to account for the forces generated in the membrane during consolidation and/or shear testing. These apply elastic theory to estimate the stresses generated and applied to the soil sample, so that they may be removed from the recorded data from a test. The corrections consider axial forces induced in the membrane during consolidation, and during shearing. The ASTM standard ignores stresses developed during consolidation, while Baxter (2000) considers this effect in addition to the shearing phase. La Rochelle et al. (1988) consider the buckling of the membrane and transfer of radial stress to the sample upon release of the axial stress, while others, e.g. Baxter (2000) and ASTM standard do not consider this case. La Rochelle et al. (1988) notes that careful observation of the test should be made to note whether buckling of the membrane occurs.

While during some tests performed during this research programme did note buckling of the membrane, this was not specifically and consistently looked for or noted for testing. In considering the application of membrane corrections to the test data collated for this research project, it has been observed that these corrections have little effect for drained tests, or undrained dense and dilative specimens, but have a significant effect for contractive specimens. In determining which correction to apply, each test has been considered separately, with the default application of the ASTM correction. The stress-ratio ($\eta = q/p'$ vs. strain (ε_a, and vs. plastic dilation, D_p plots were considered along with the effective stress-path in *q, p'* space, in order to check whether the large strain behaviour was as expected, or if a variation to the La Rochelle et al. (1988) or *Baxter and Filz* corrections produced more appropriate corrections. A further aspect of uncertainty is the appropriate modulus to use for the corrections, given the method to measure is extension and some of the corrections assume compression of the modulus (e.g. Baxter and Filz, ASTM), which imply a smaller strain modulus should be used than measured at larger strains. The approach used relies on interpretation/ judgement basis. An example plot showing a contractive undrained test with these different corrections applied is shown in Figure 3.108.

In this example, both the *ASTM* and *Baxter and Filz* corrections that account

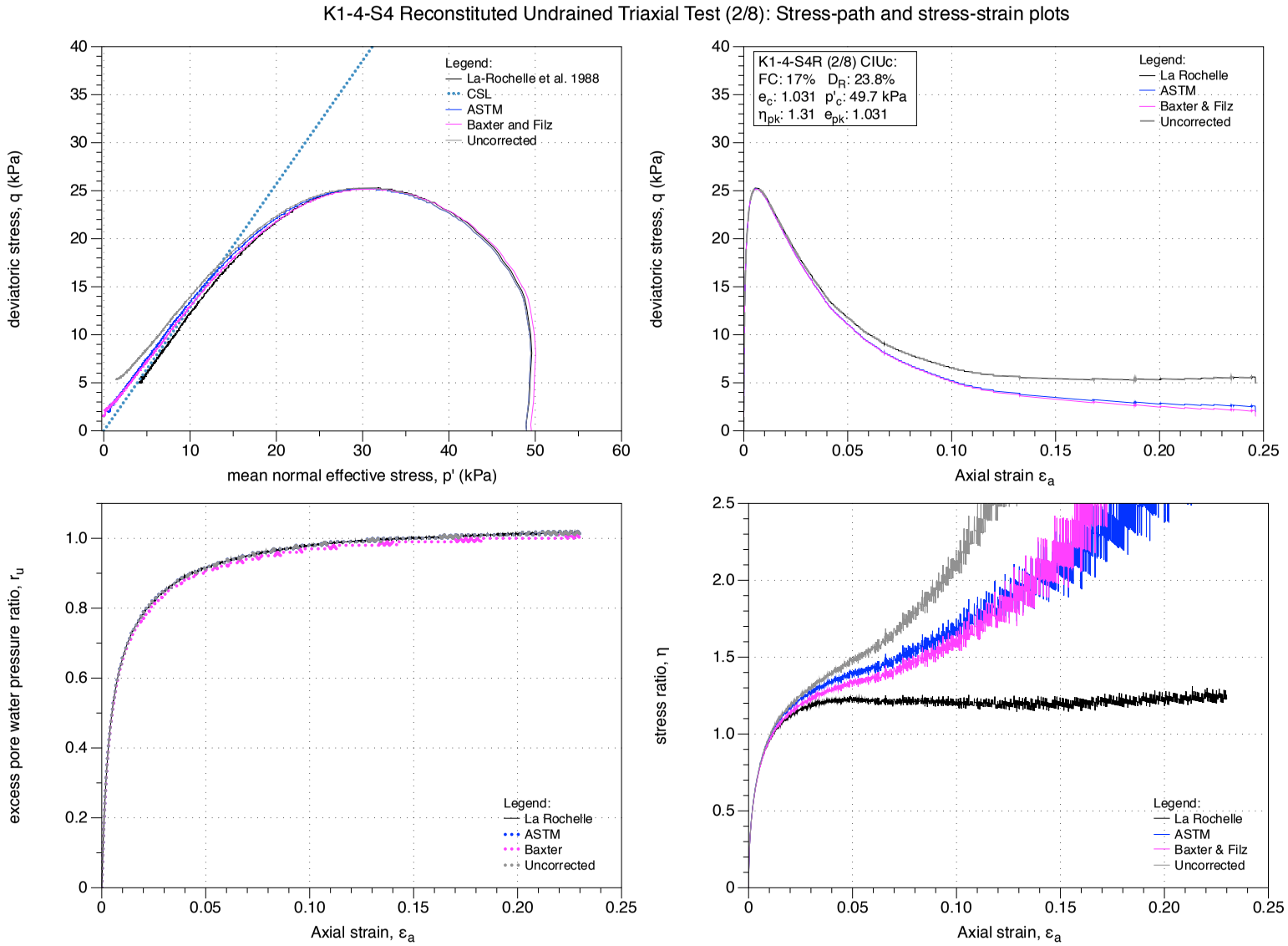

Figure 3.108: Undrained Monotonic triaxial test on loose sand showing effect of membrane corrections on stress path, stress-strain, and stress ratio plots. K1-4-S4 reconstituted test CIU 2 of 8.

for axial load on the membrane over-corrected the effect on deviatoric stress at large strains, while the La Rochelle et al. (1988) correction for buckling of the membrane adequately corrects the mean stress for the effects of membrane stress without adjusting the deviatoric stress. The resulting stress-path and stress-ratios are shown to be more reasonable out to large strains. In other cases, the ASTM correction was found to be more appropriate than the La Rochelle et al. (1988) correction, and thus each test was evaluated on a case-by-case basis, including the appropriate modulus values to apply to correct the stress ratio in particular. Such corrections were only applied to monotonic tests and not cyclic triaxial tests.

Chapter IV

Triaxial Testing Results

Appendix D includes additional content relating to the the processing and plotting of monotonic and cyclic triaxial tests. Contents as below:

1. Triaxial Tests on reconstituted Fitzgerald Bridge Mixture (FBM) Sand.

2. Triaxial Tests on undisturbed Gel-push Samples - Site K1.

3. Triaxial Tests on undisturbed Gel-push Samples - Site MA1.

4. Triaxial Tests on reconstituted K1 *representative* sands.

5. Undrained stress-dilatancy plot.

4.1 Triaxial testing on Fitzgerald Bridge Mixture (FBM) sands.

This section of Appendix D presents individual triaxial test results performed on moist tamped reconstituted specimens of Fitzgerald Bridge Mixture sands.

4.1.1 FBM Monotonic Triaxial Tests

Plots include the effective stress path, stress strain plot, state stress path, and volumetric strain-axial strain (drained test) or excess pore pressure ratio-axial strain (undrained test) plots. Additional plots for each monotonic test include stress-dilatancy plots, stiffness degradation curves, normalised shear work, and normalised shear work gradient plots with strain.

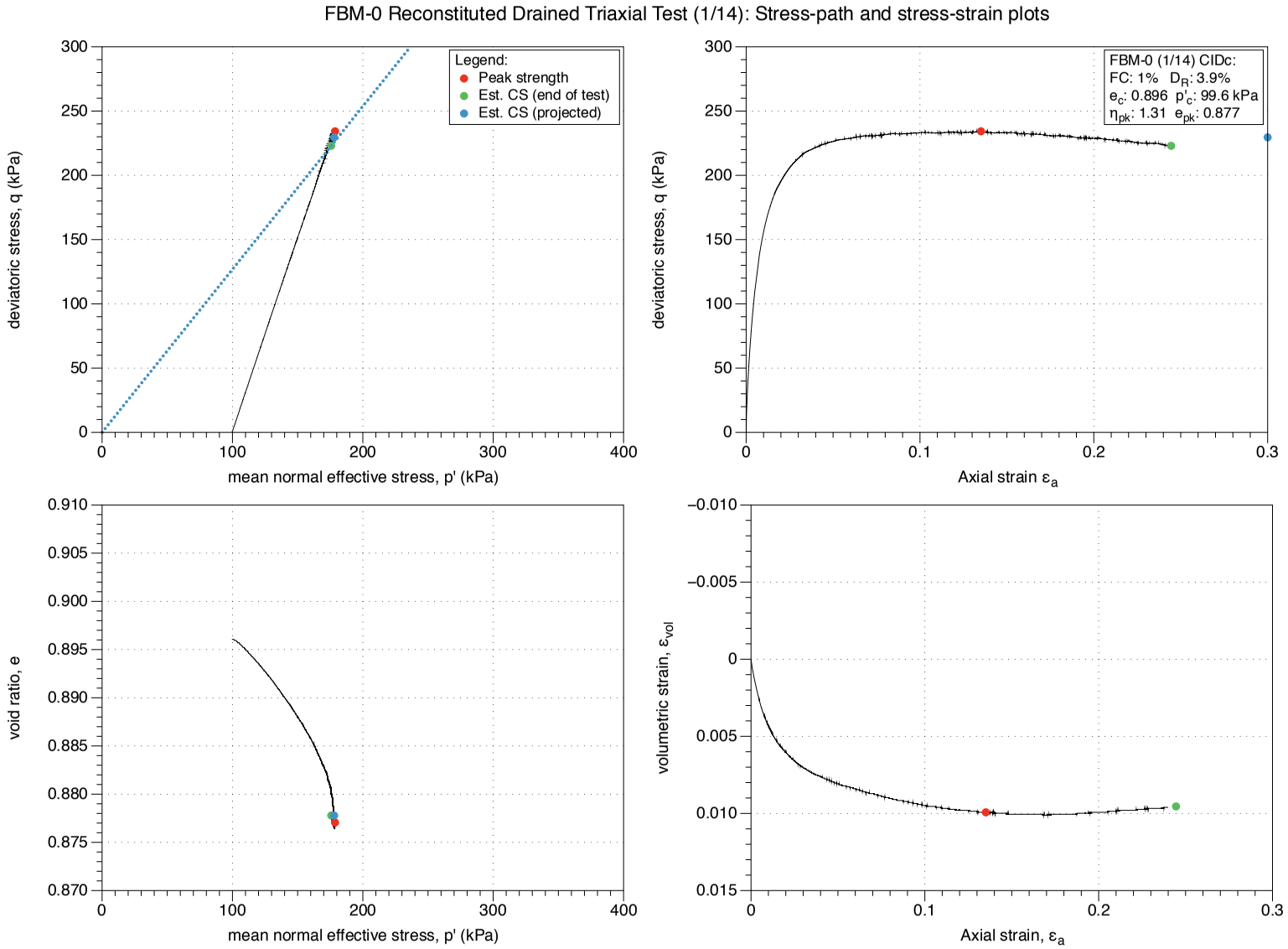

Figure 4.1: FBM with 0 % fines, moist tamped reconstituted sample, triaxial test 1/14. Stress-path and stress-strain plots.

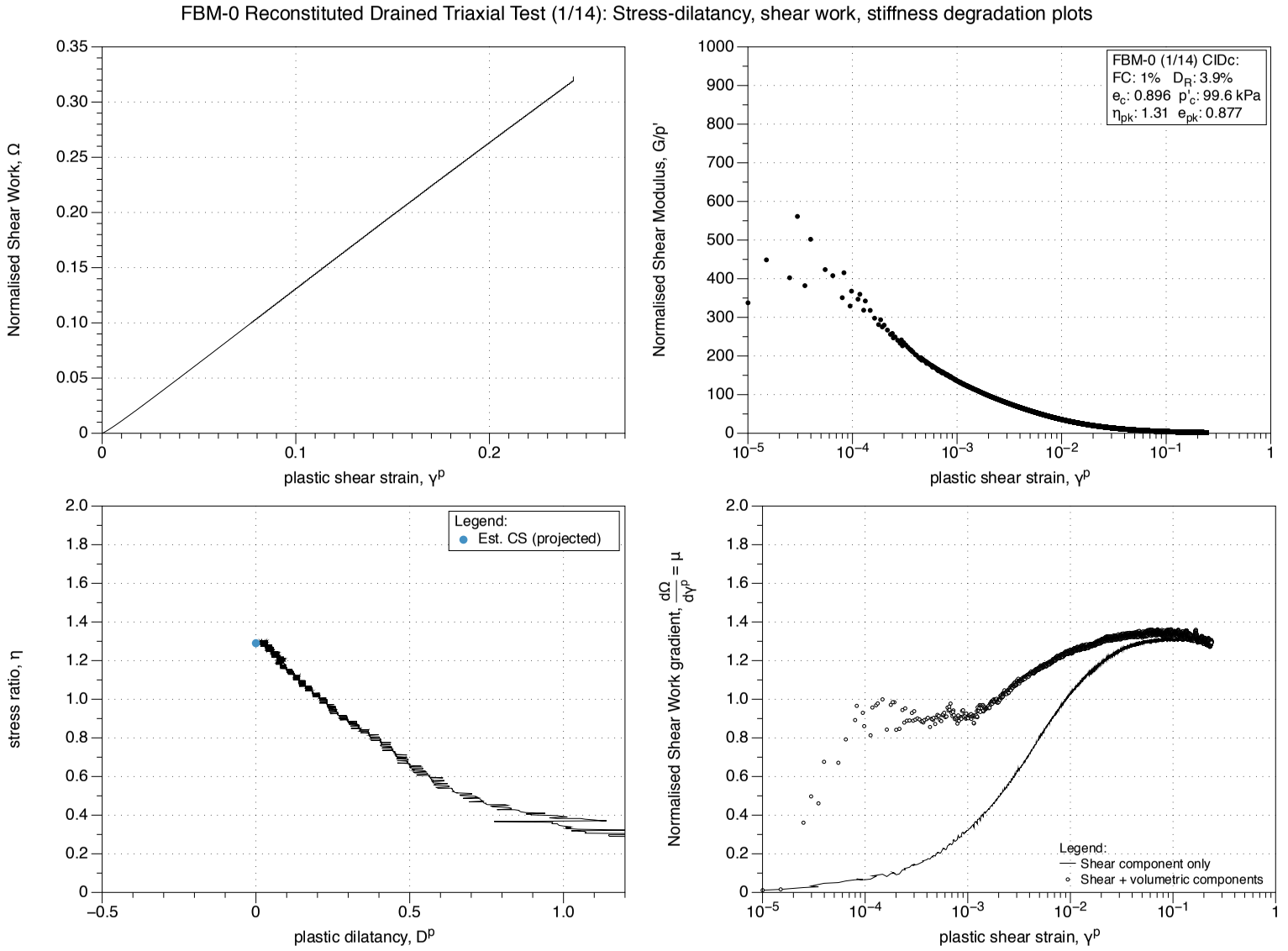

Figure 4.2: FBM with 0 % fines, moist tamped reconstituted sample, triaxial test 1/14. Stress-dilatancy, shear work, stiffness degradation plots.

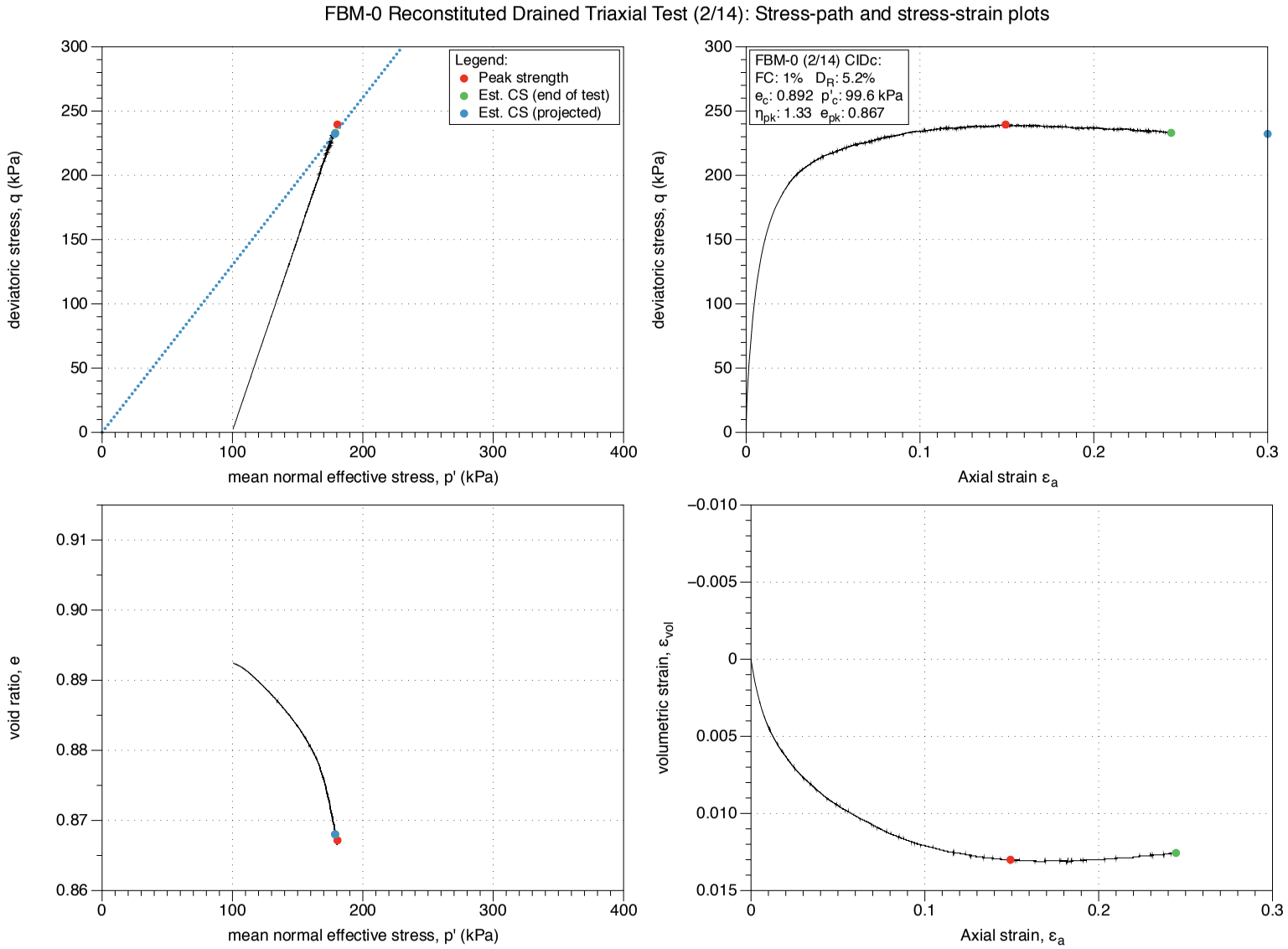

Figure 4.3: FBM with 0 % fines, moist tamped reconstituted sample, triaxial test 2/14. Stress-path and stress-strain plots.

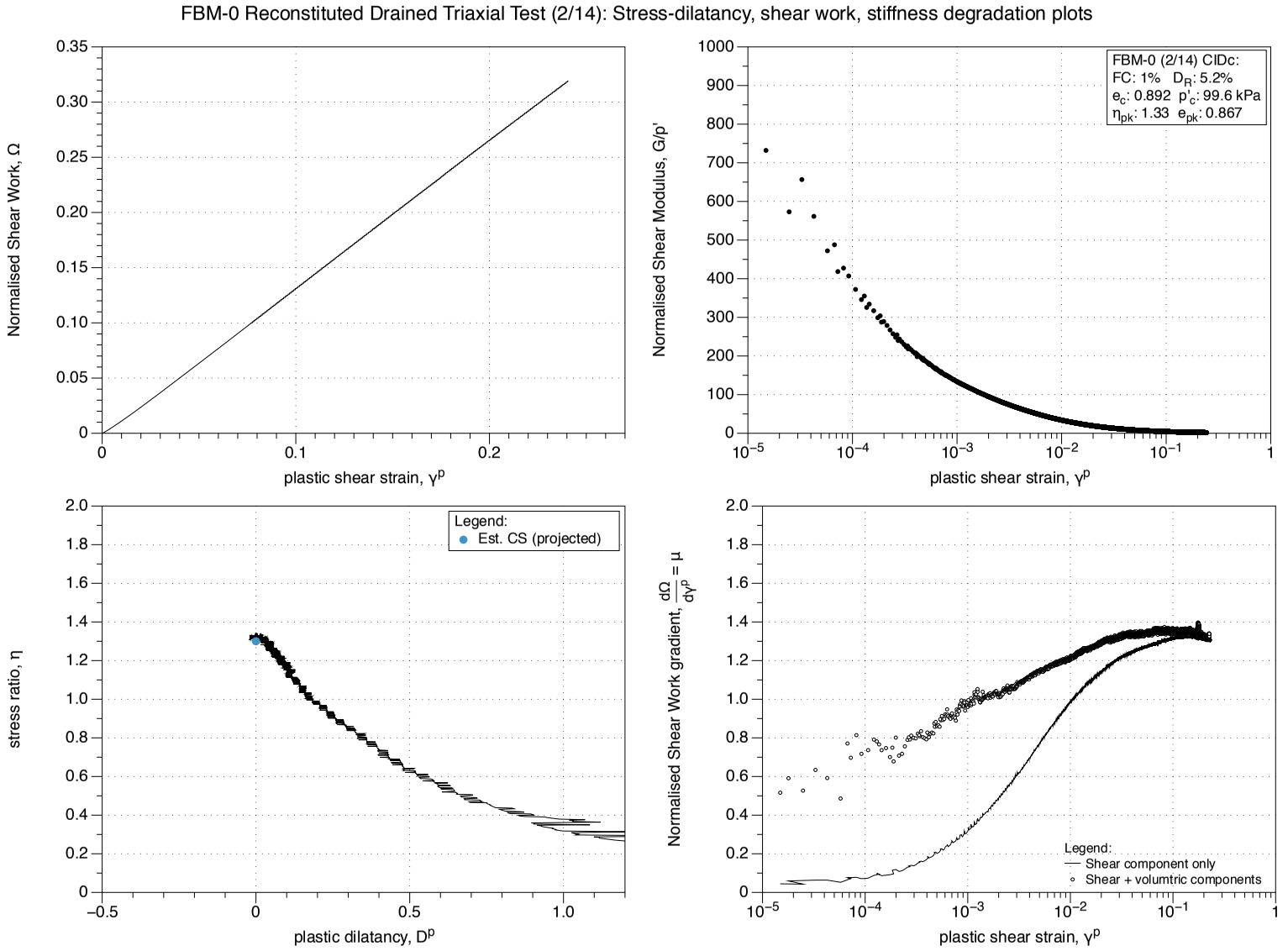

Figure 4.4: FBM with 0 % fines, moist tamped reconstituted sample, triaxial test 2/14. Stress-dilatancy, shear work, stiffness degradation plots.

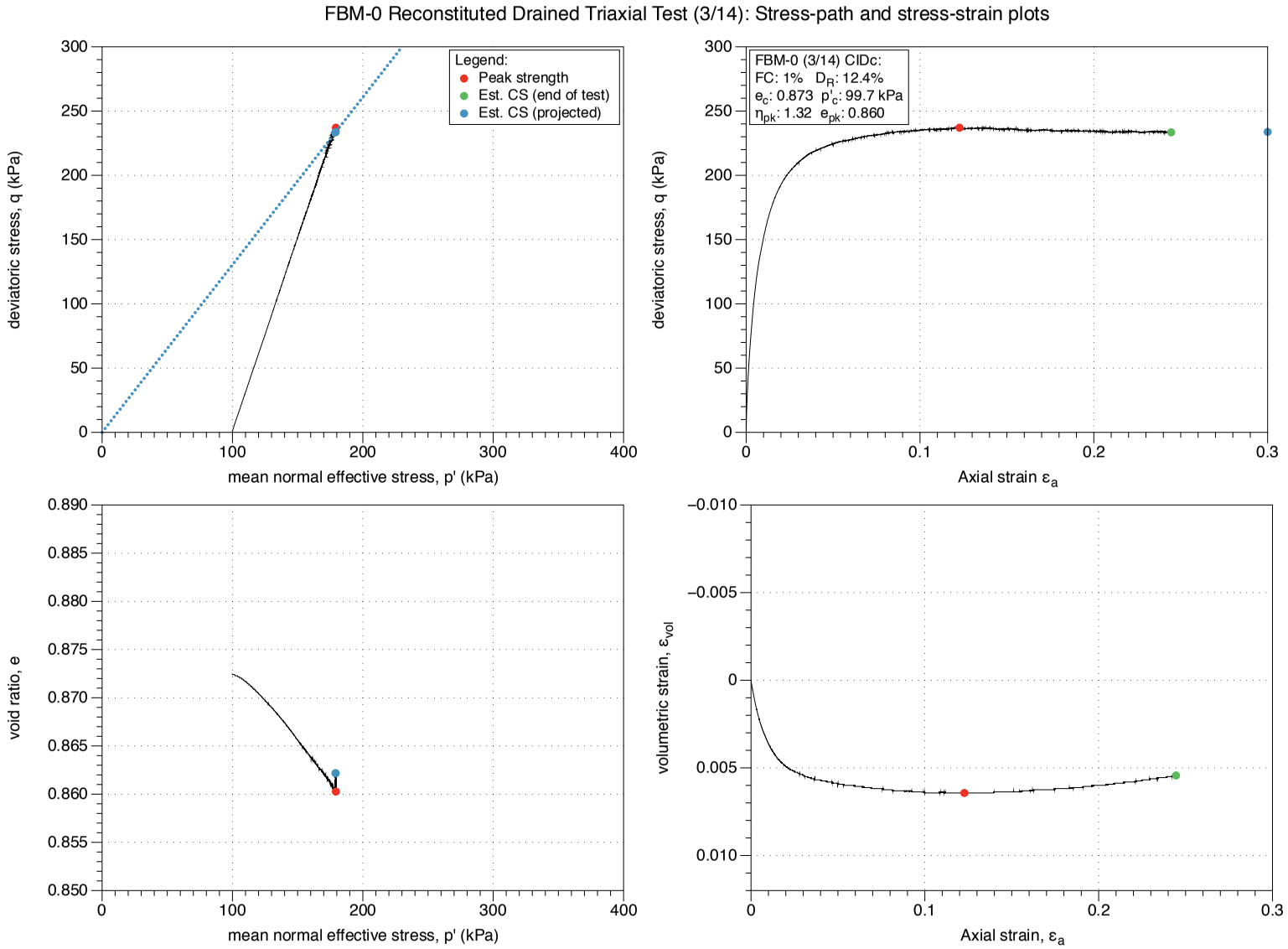

Figure 4.5: FBM with 0 % fines, moist tamped reconstituted sample, triaxial test 3/14. Stress-path and stress-strain plots.

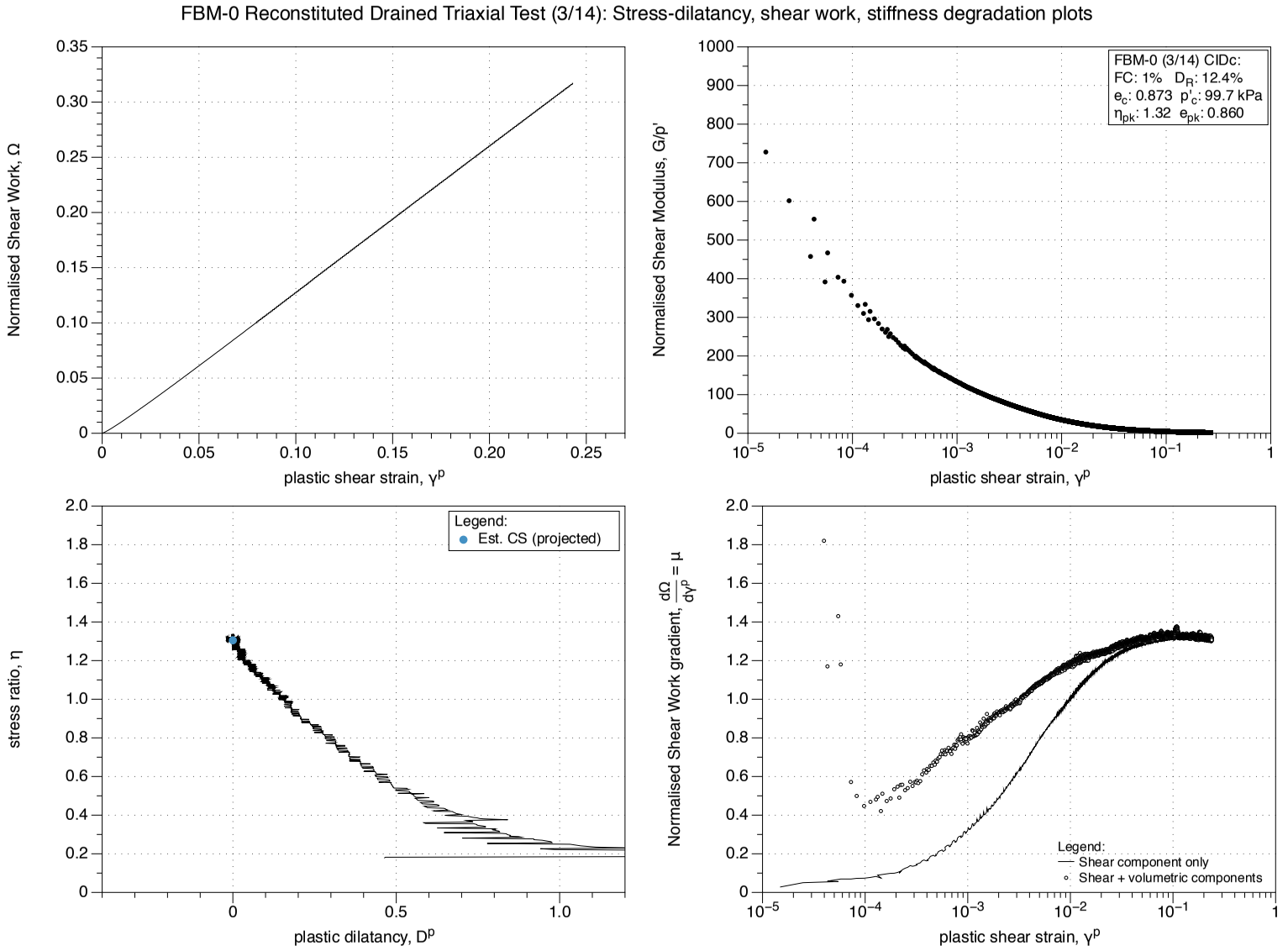

Figure 4.6: FBM with 0 % fines, moist tamped reconstituted sample, triaxial test 3/14. Stress-dilatancy, shear work, stiffness degradation plots.

Test 5 is not plotted.

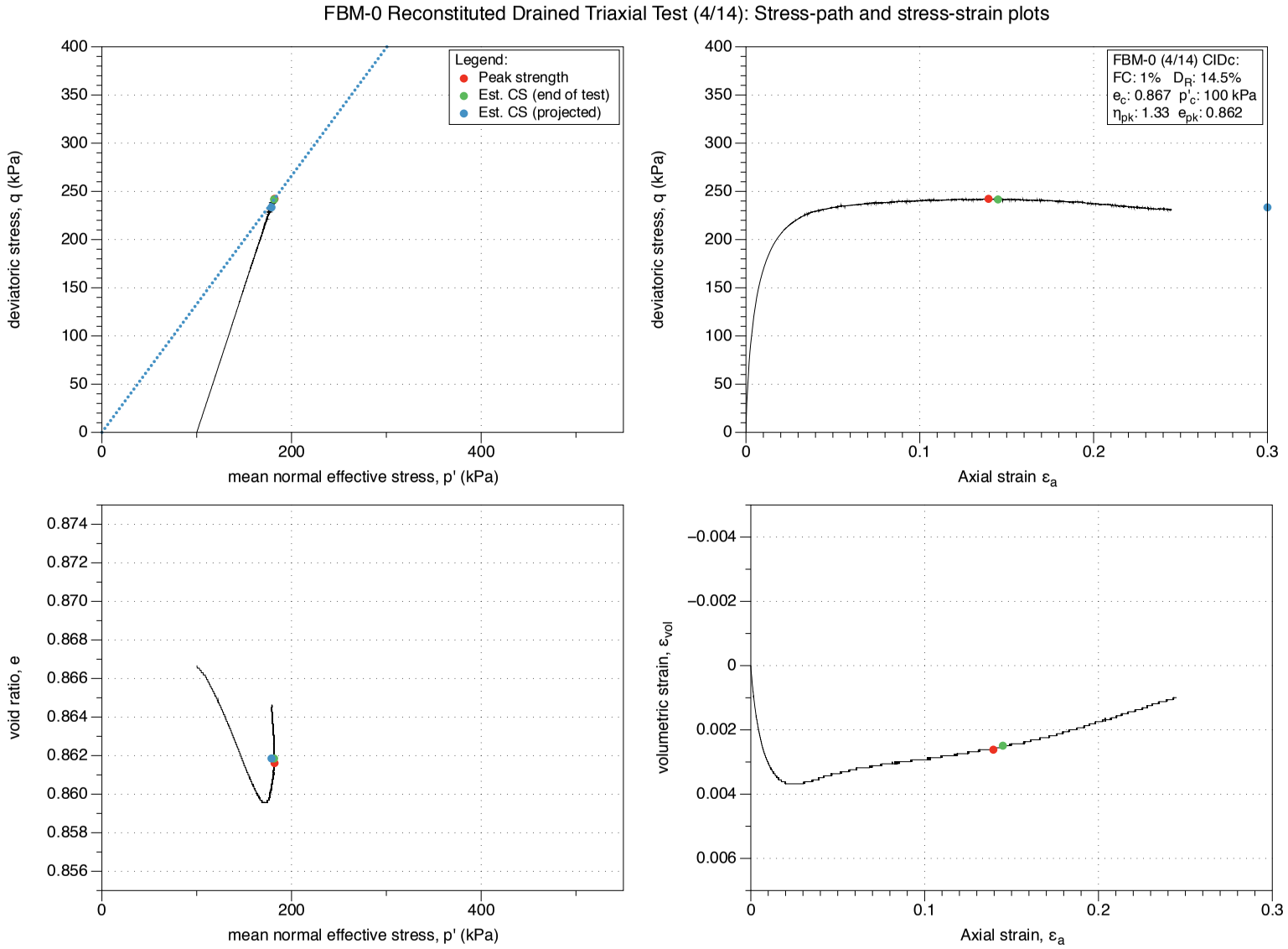

Figure 4.7: FBM with 0 % fines, moist tamped reconstituted sample, triaxial test 4/14. Stress-path and stress-strain plots.

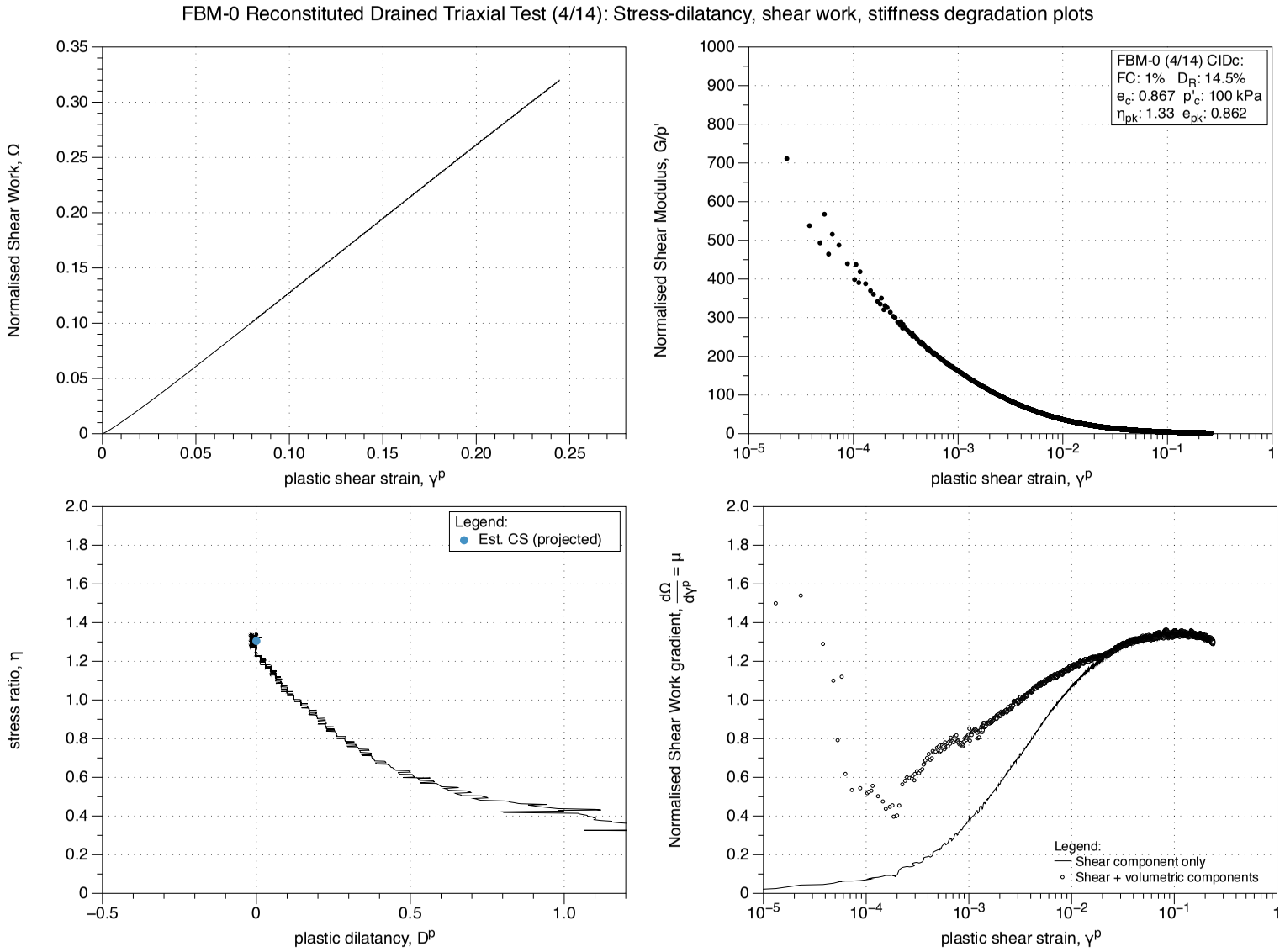

Figure 4.8: FBM with 0 % fines, moist tamped reconstituted sample, triaxial test 4/14. Stress-dilatancy, shear work, stiffness degradation plots.

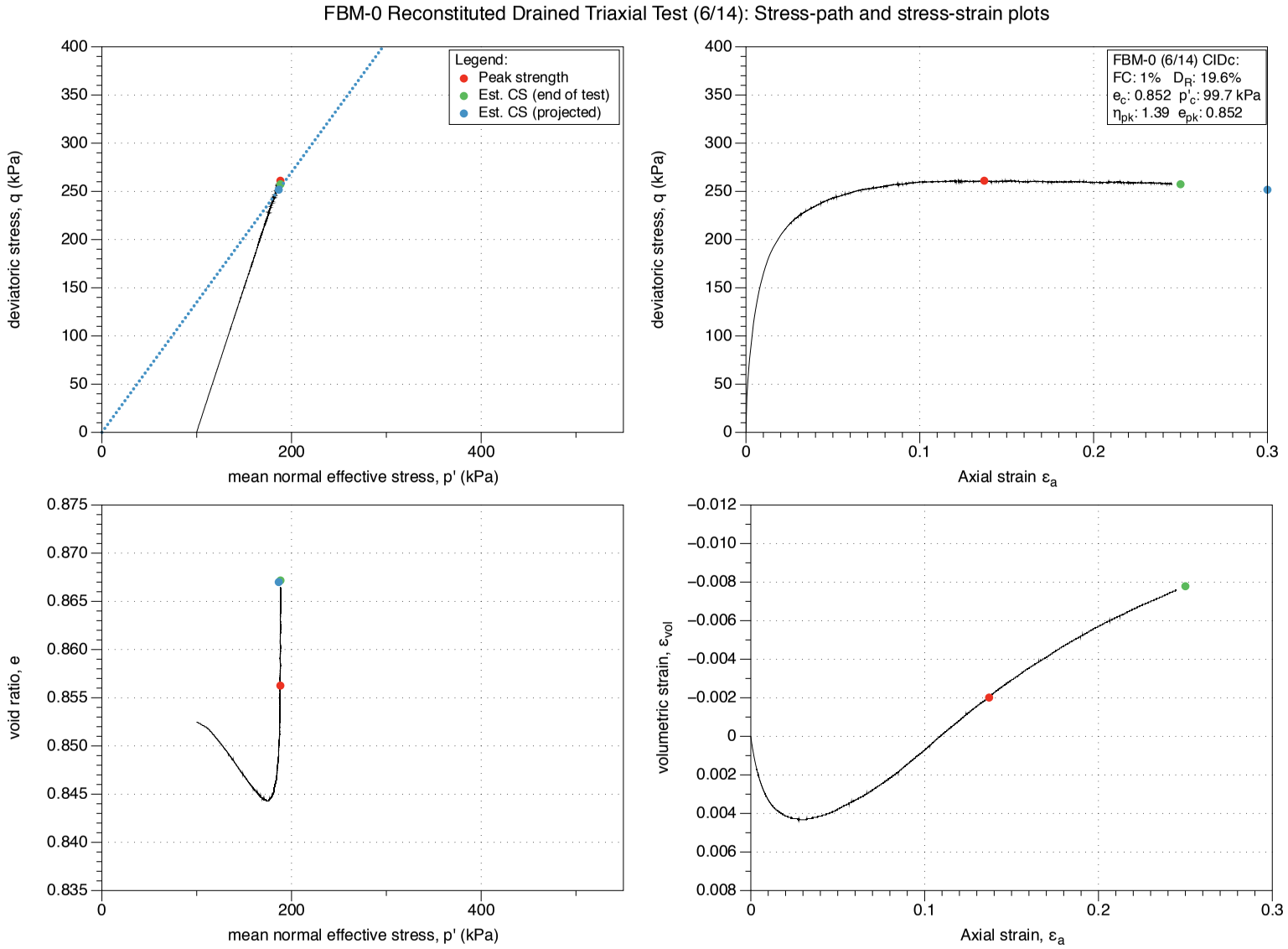

Figure 4.9: FBM with 0 % fines, moist tamped reconstituted sample, triaxial test 6/14. Stress-path and stress-strain plots.

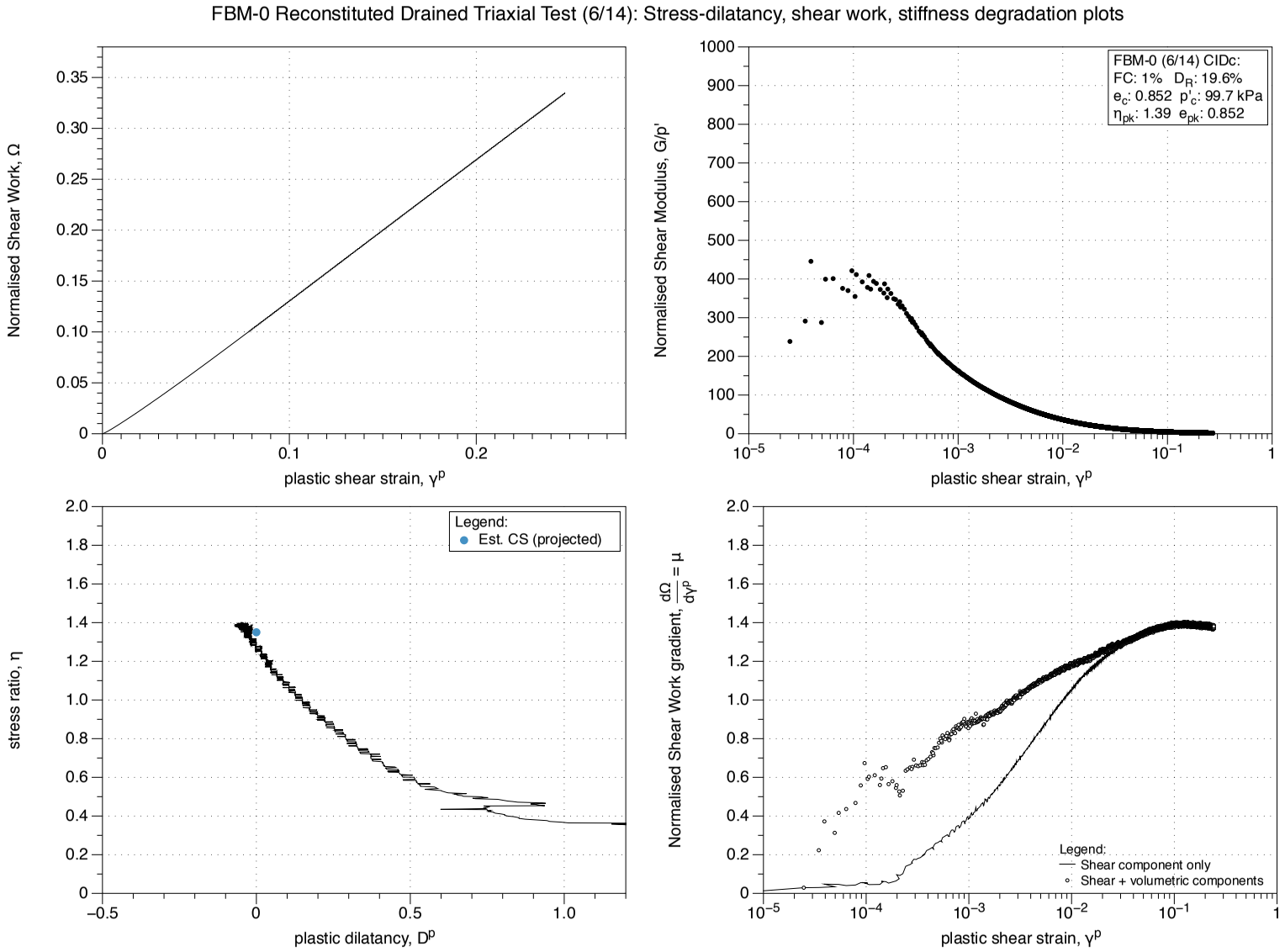

Figure 4.10: FBM with 0 % fines, moist tamped reconstituted sample, triaxial test 6/14. Stress-dilatancy, shear work, stiffness degradation plots.

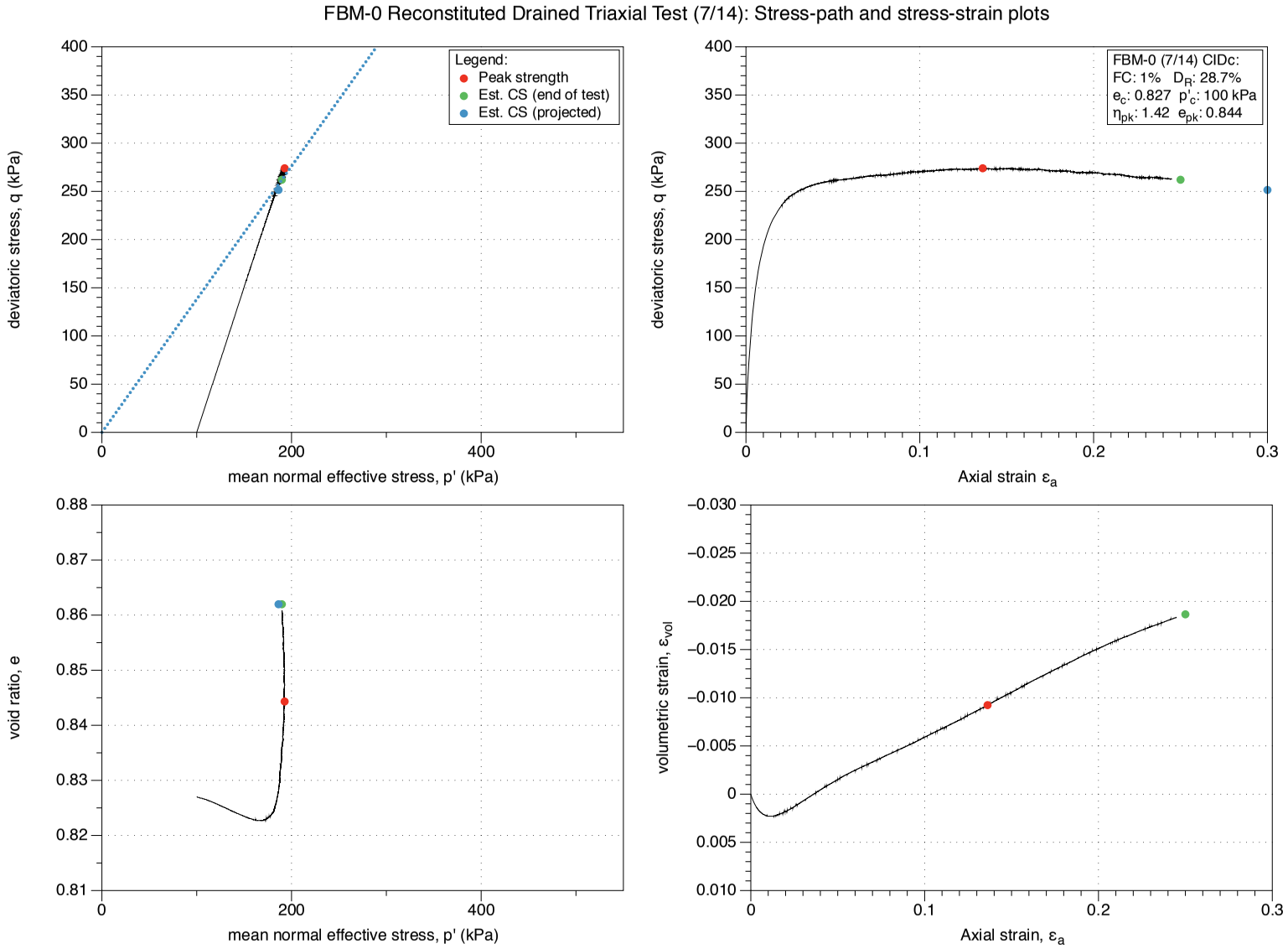

Figure 4.11: FBM with 0 % fines, moist tamped reconstituted sample, triaxial test 7/14. Stress-path and stress-strain plots.

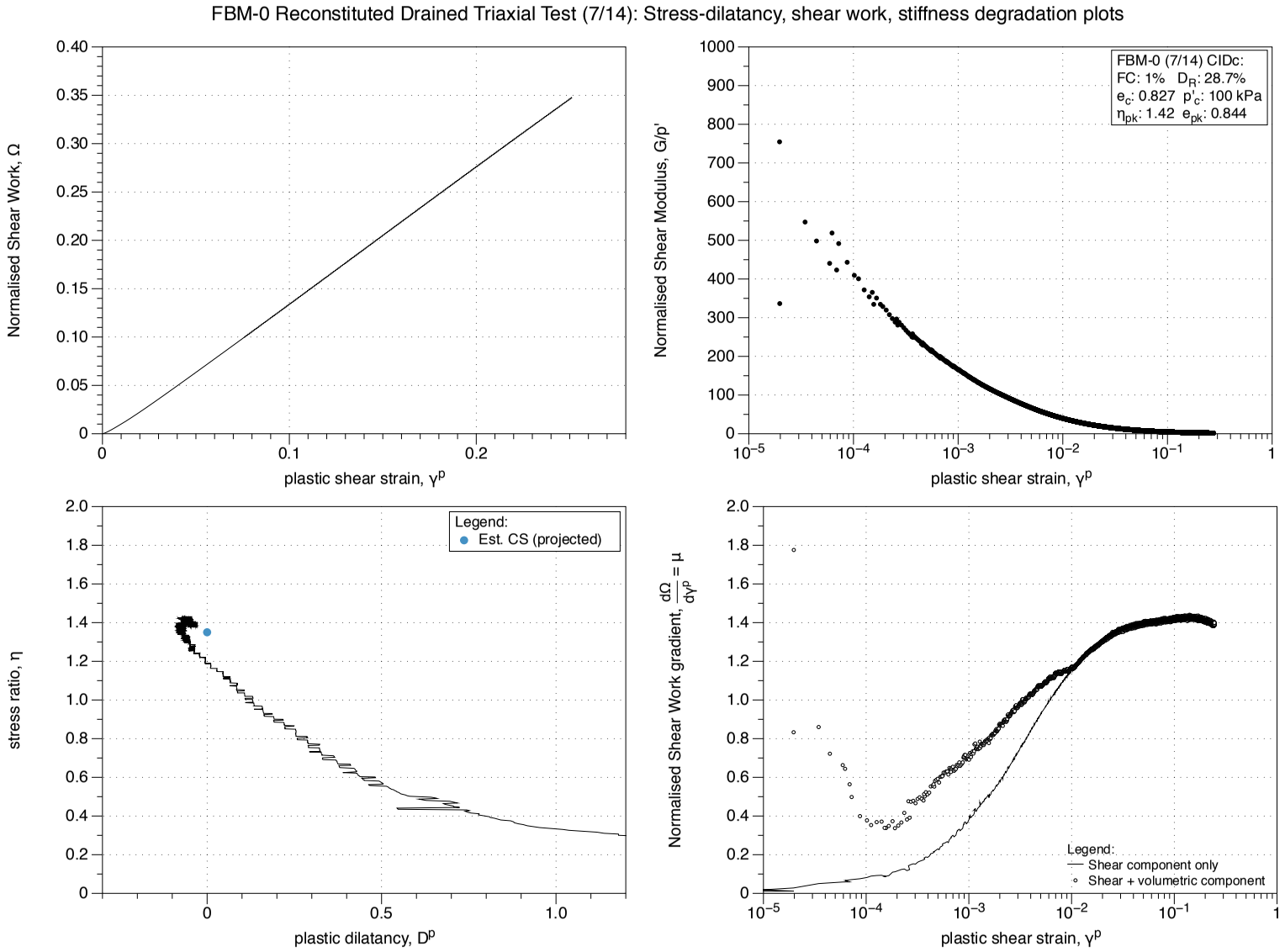

Figure 4.12: FBM with 0 % fines, moist tamped reconstituted sample, triaxial test 7/14. Stress-dilatancy, shear work, stiffness degradation plots.

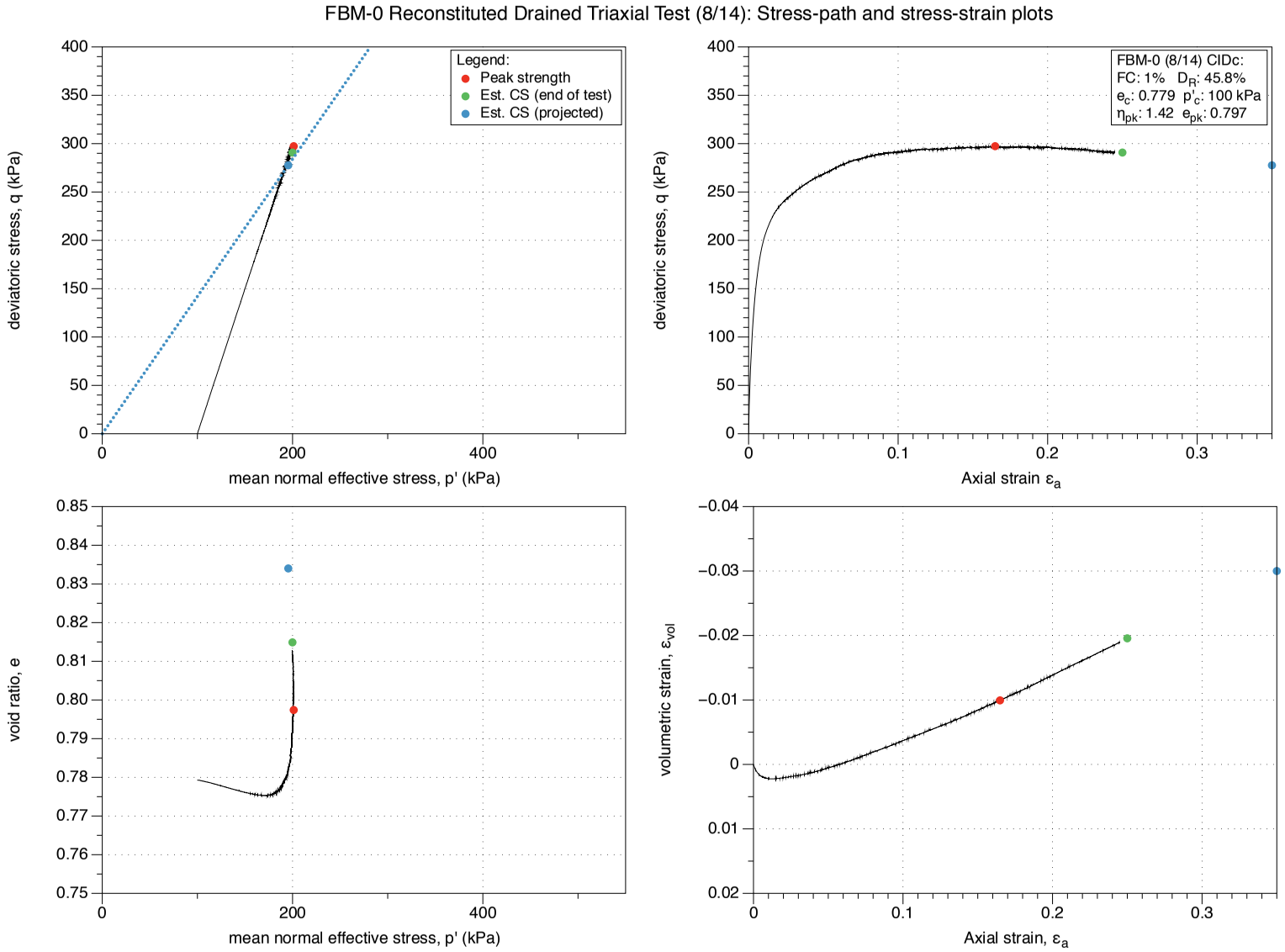

Figure 4.13: FBM with 0 % fines, moist tamped reconstituted sample, triaxial test 8/14. Stress-path and stress-strain plots.

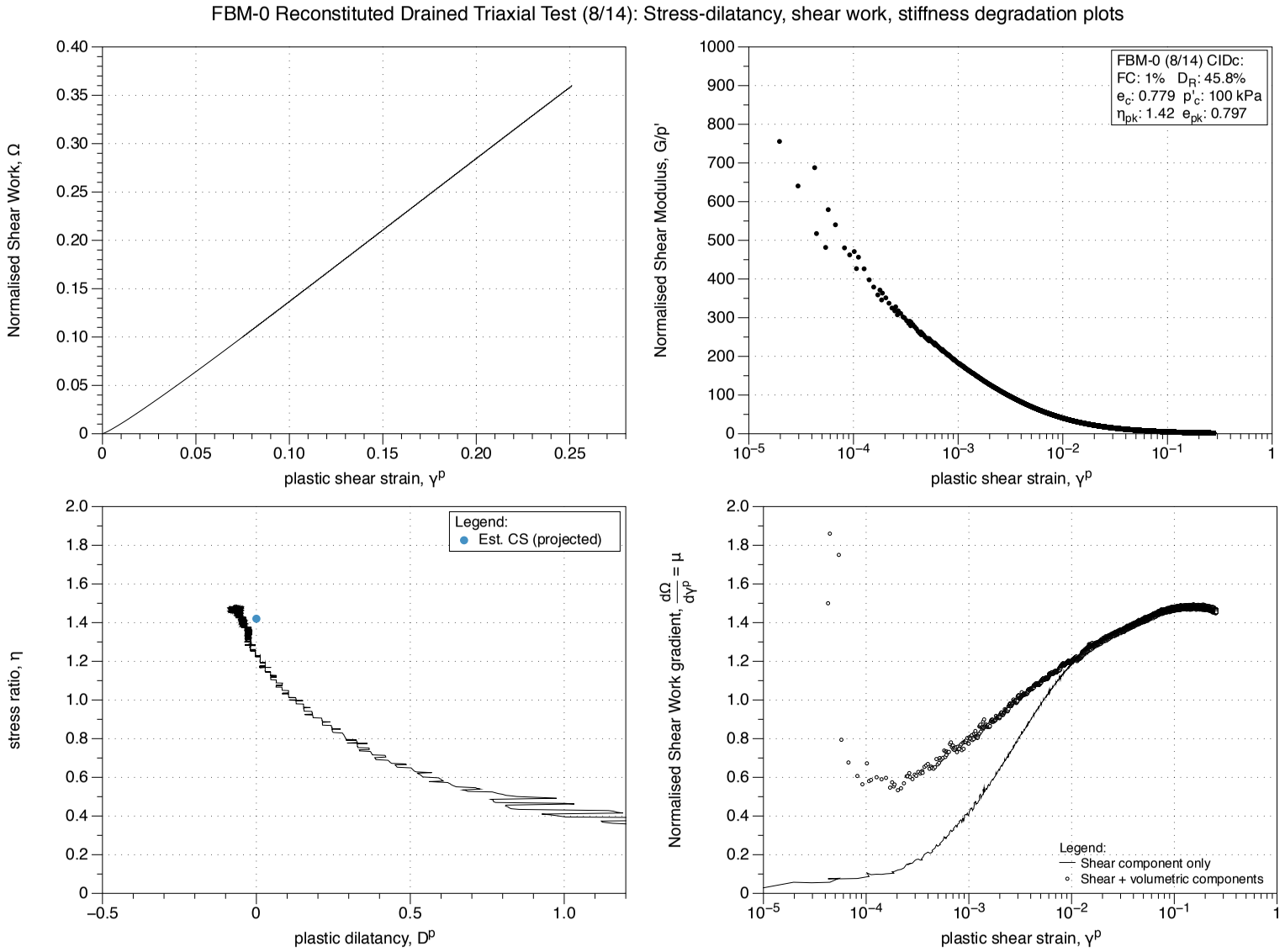

Figure 4.14: FBM with 0 % fines, moist tamped reconstituted sample, triaxial test 8/14. Stress-dilatancy, shear work, stiffness degradation plots.

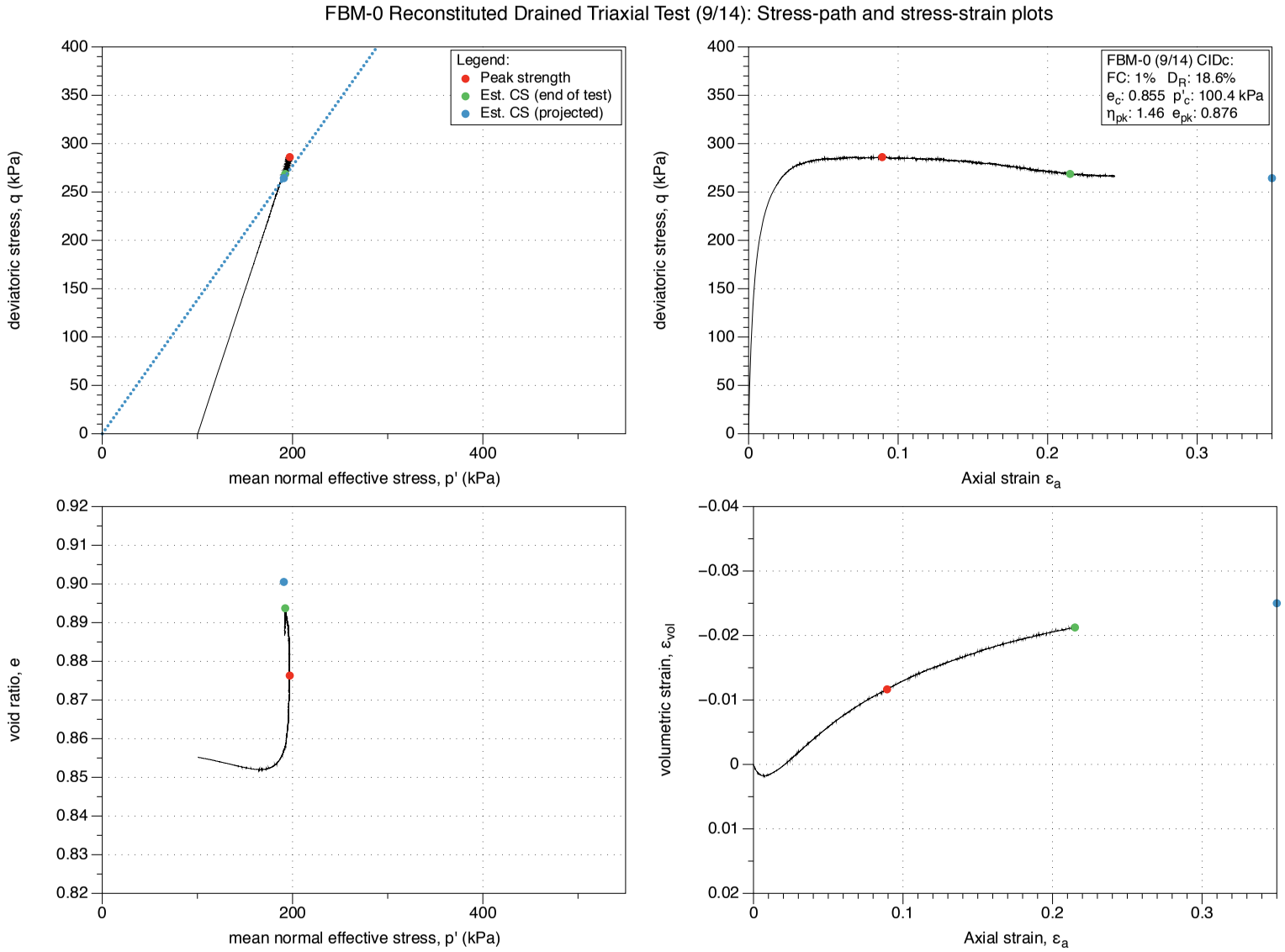

Figure 4.15: FBM with 0 % fines, moist tamped reconstituted sample, triaxial test 9/14. Stress-path and stress-strain plots.

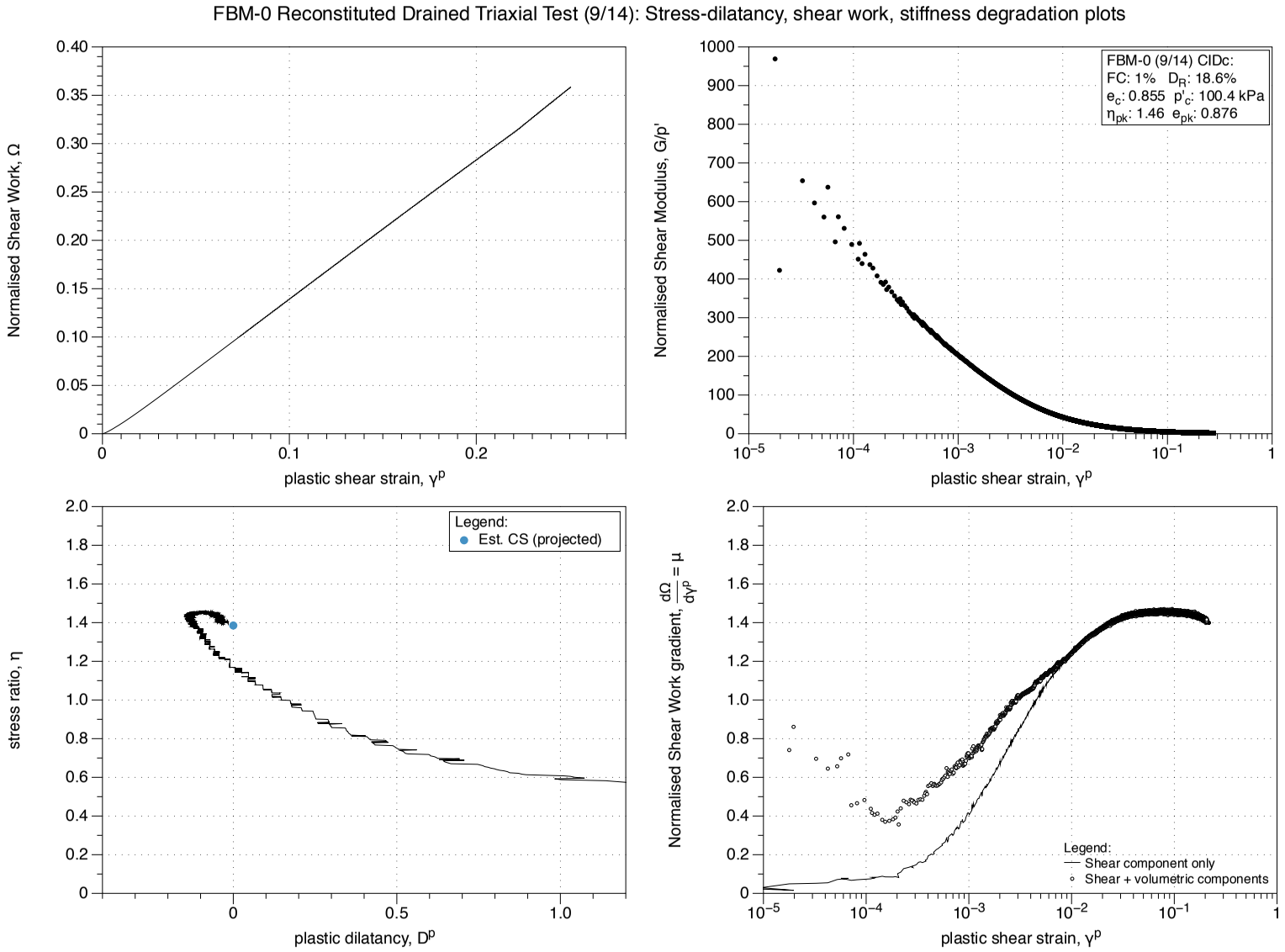

Figure 4.16: FBM with 0 % fines, moist tamped reconstituted sample, triaxial test 9/14. Stress-dilatancy, shear work, stiffness degradation plots.

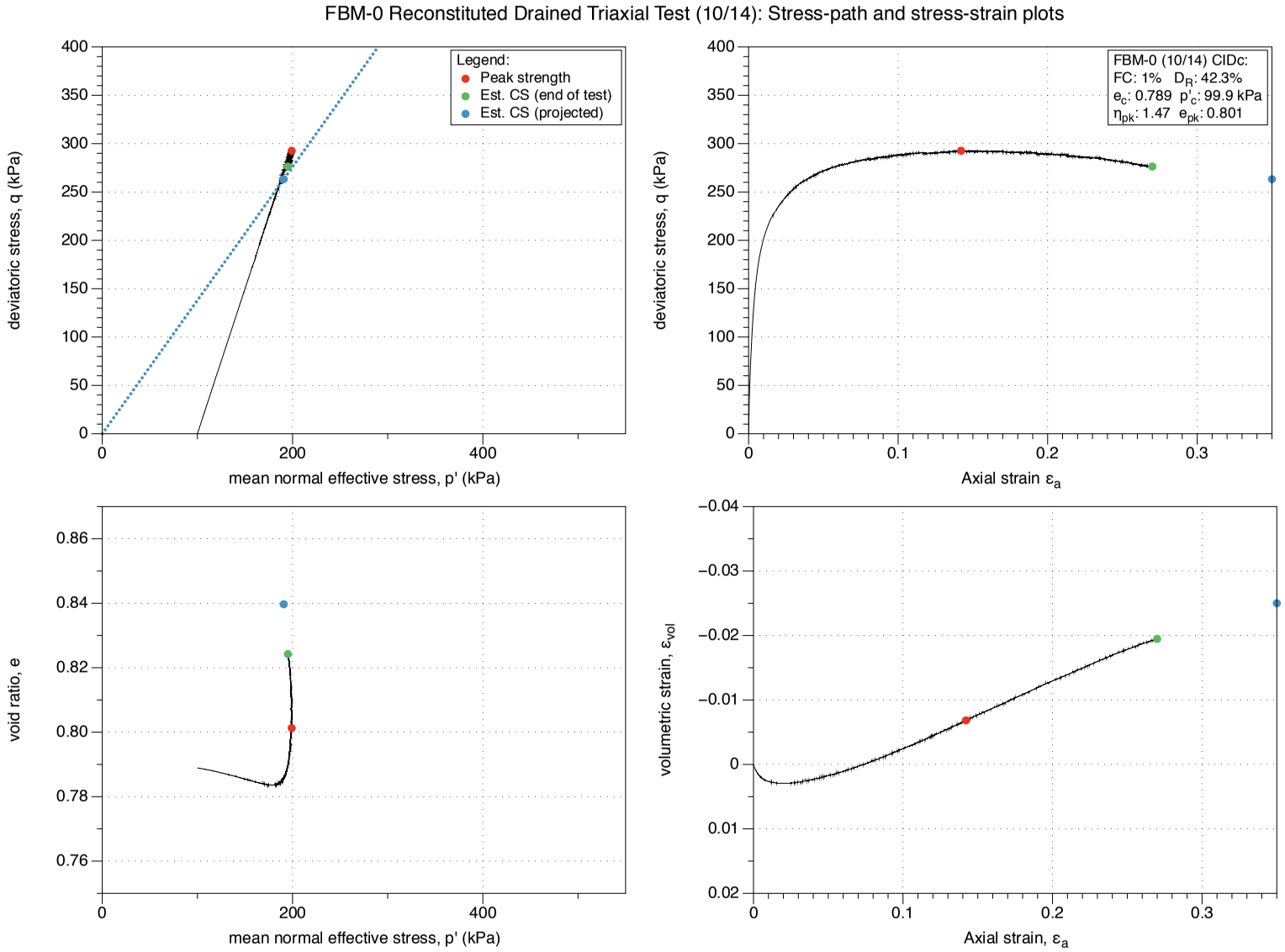

Figure 4.17: FBM with 0 % fines, moist tamped reconstituted sample, triaxial test 10/14. Stress-path and stress-strain plots.

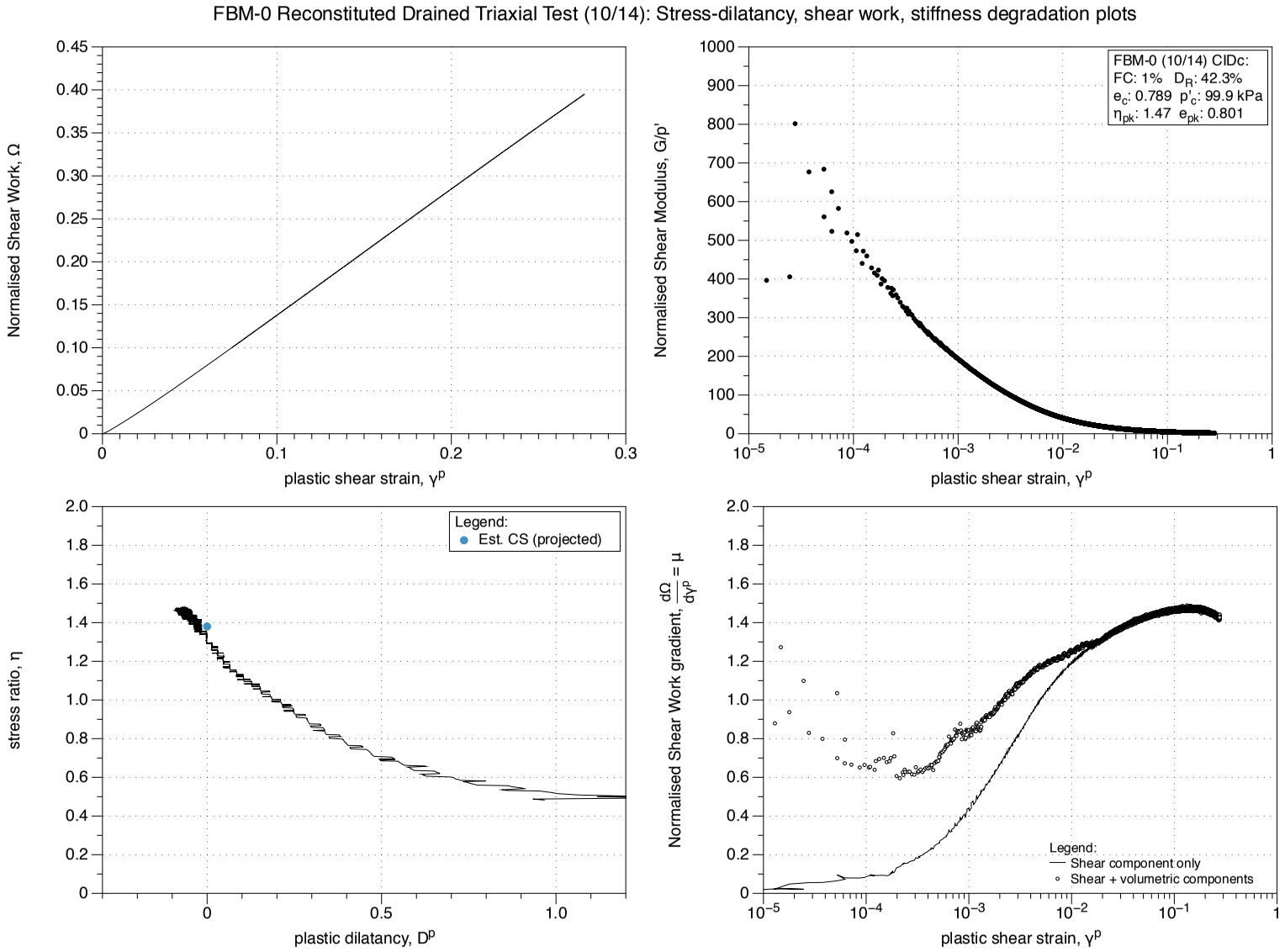

Figure 4.18: FBM with 0 % fines, moist tamped reconstituted sample, triaxial test 10/14. Stress-dilatancy, shear work, stiffness degradation plots.

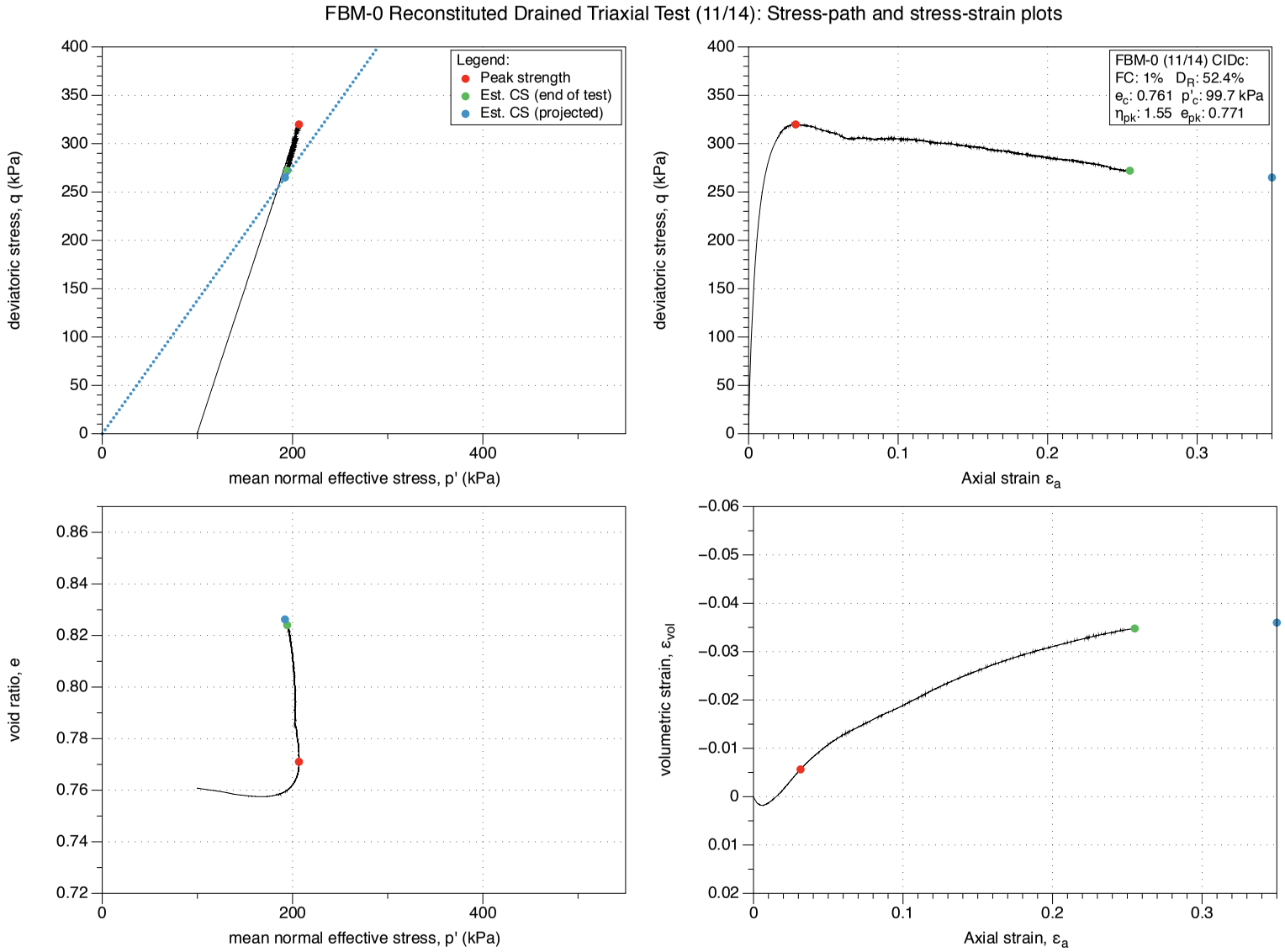

Figure 4.19: FBM with 0 % fines, moist tamped reconstituted sample, triaxial test 11/14. Stress-path and stress-strain plots.

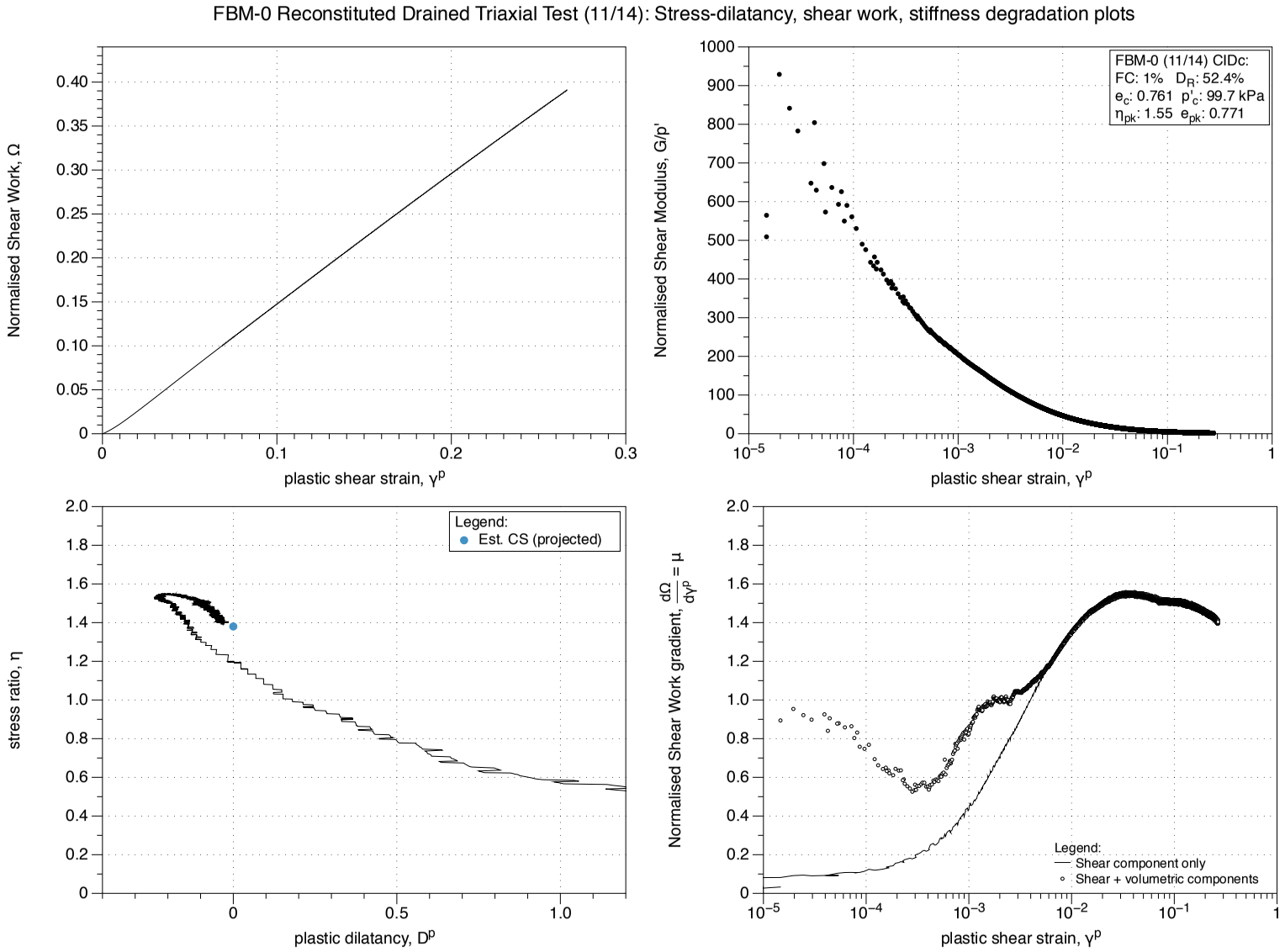

Figure 4.20: FBM with 0 % fines, moist tamped reconstituted sample, triaxial test 11/14. Stress-dilatancy, shear work, stiffness degradation plots.

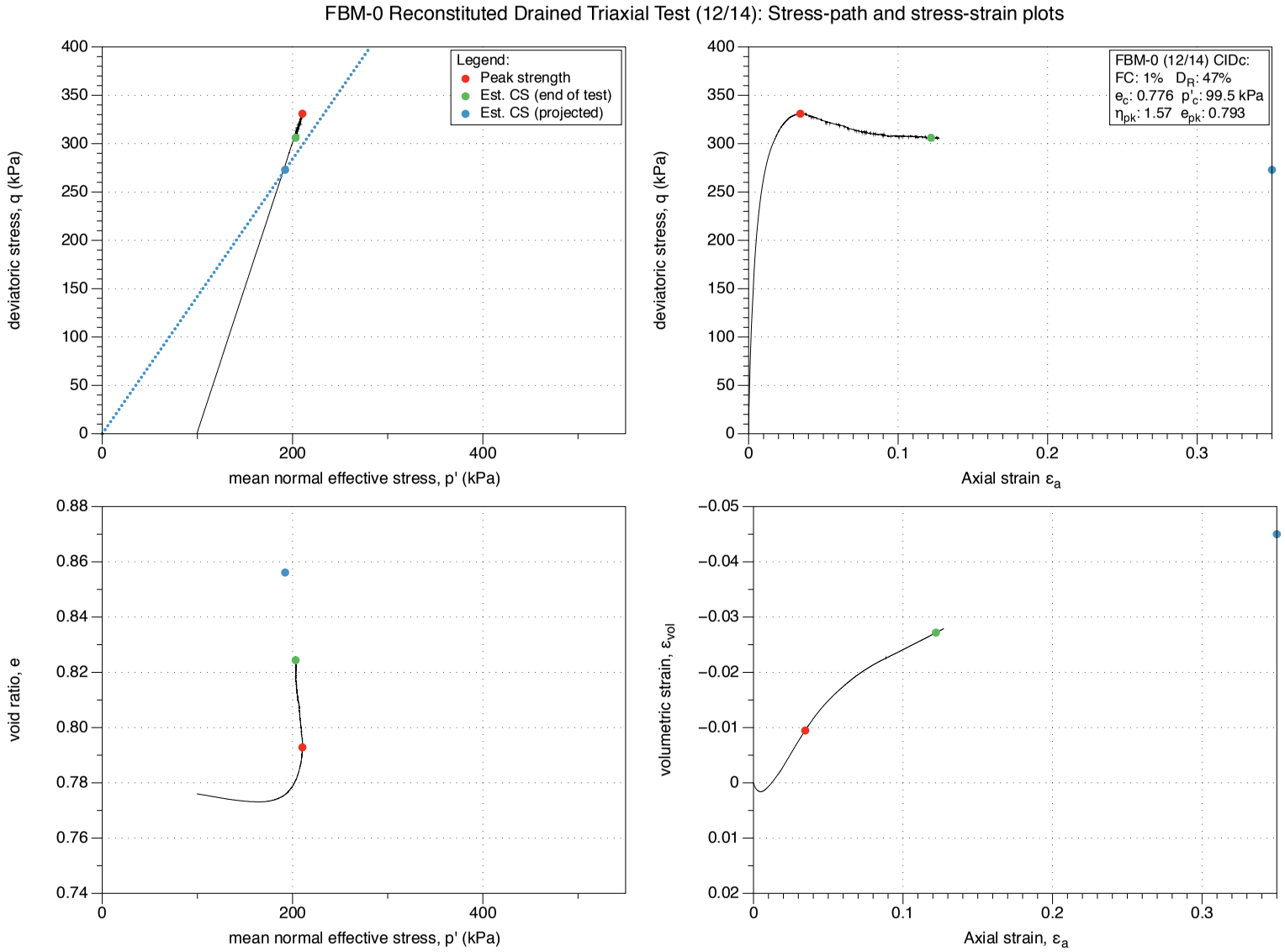

Figure 4.21: FBM with 0 % fines, moist tamped reconstituted sample, triaxial test 12/14. Stress-path and stress-strain plots.

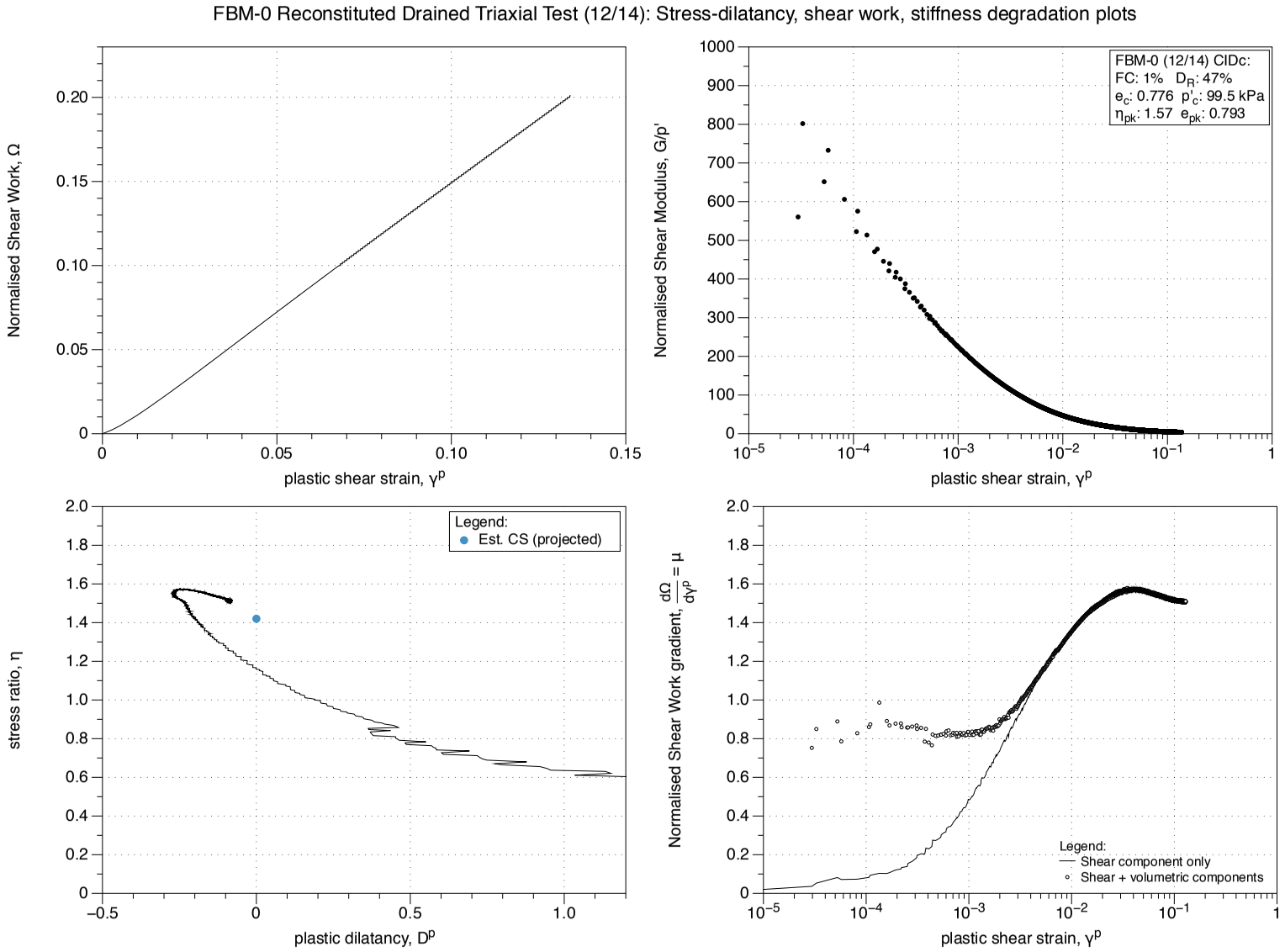

Figure 4.22: FBM with 0 % fines, moist tamped reconstituted sample, triaxial test 12/14. Stress-dilatancy, shear work, stiffness degradation plots.

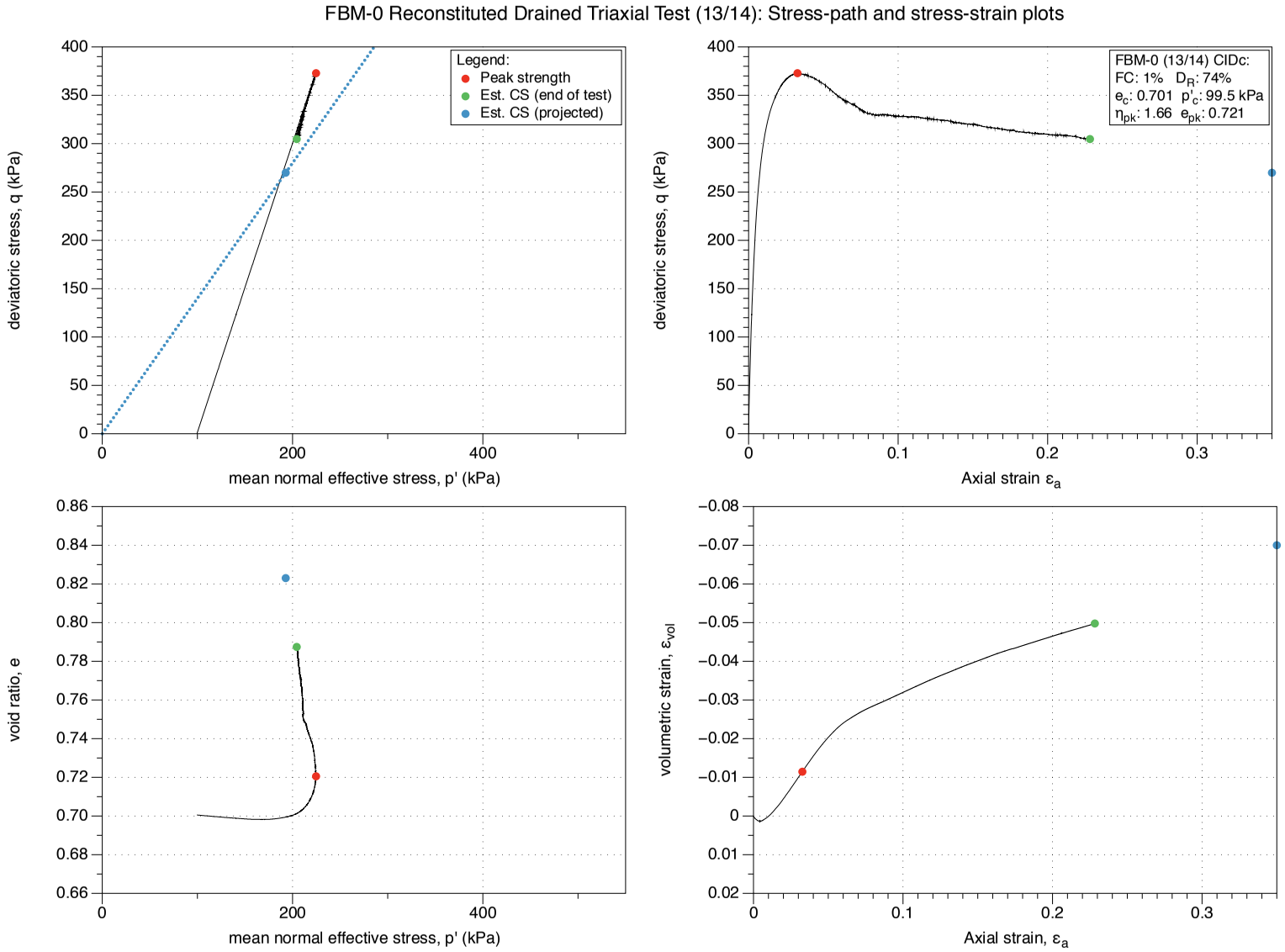

Figure 4.23: FBM with 0 % fines, moist tamped reconstituted sample, triaxial test 13/14. Stress-path and stress-strain plots.

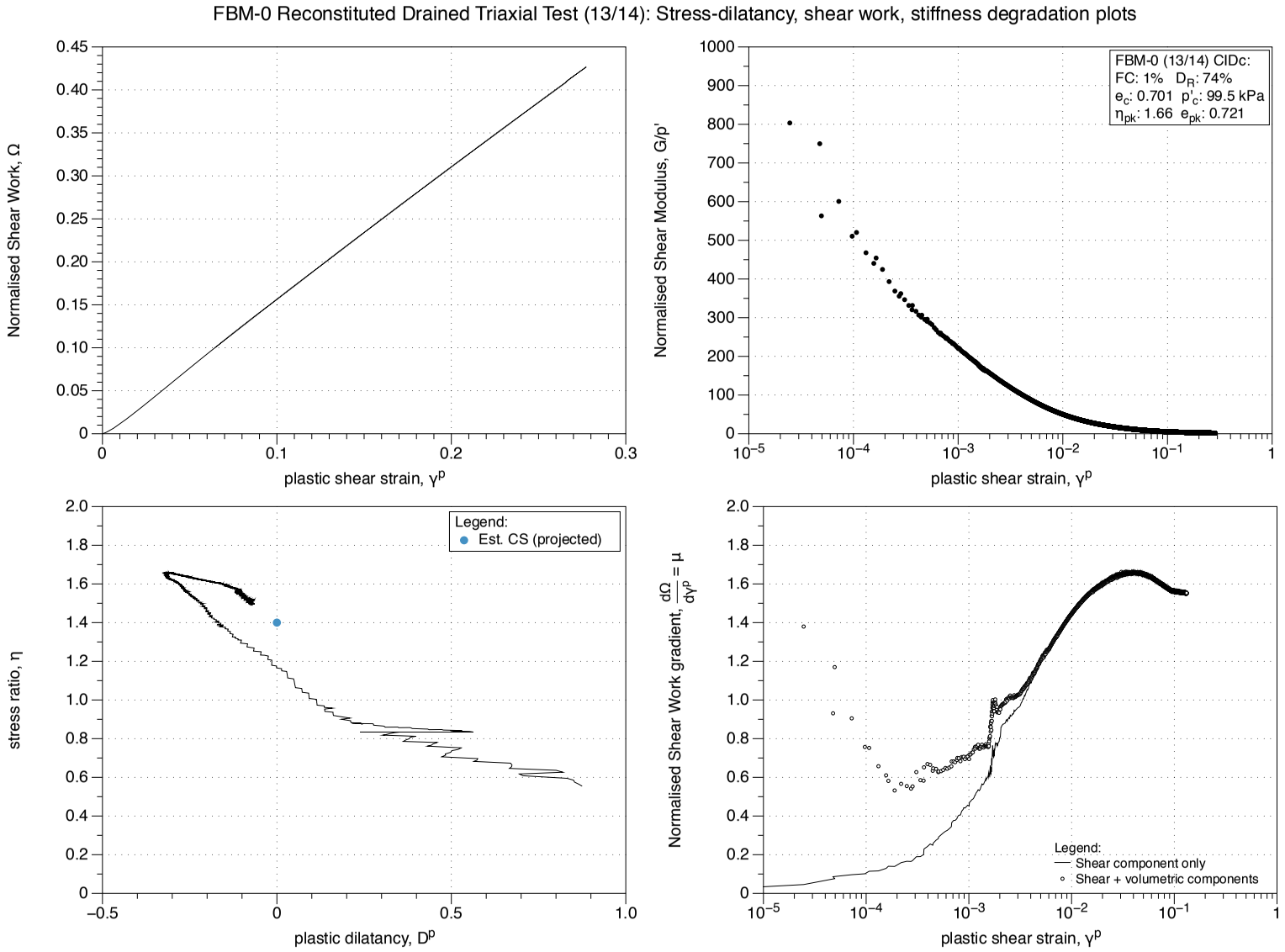

Figure 4.24: FBM with 0 % fines, moist tamped reconstituted sample, triaxial test 13/14. Stress-dilatancy, shear work, stiffness degradation plots.

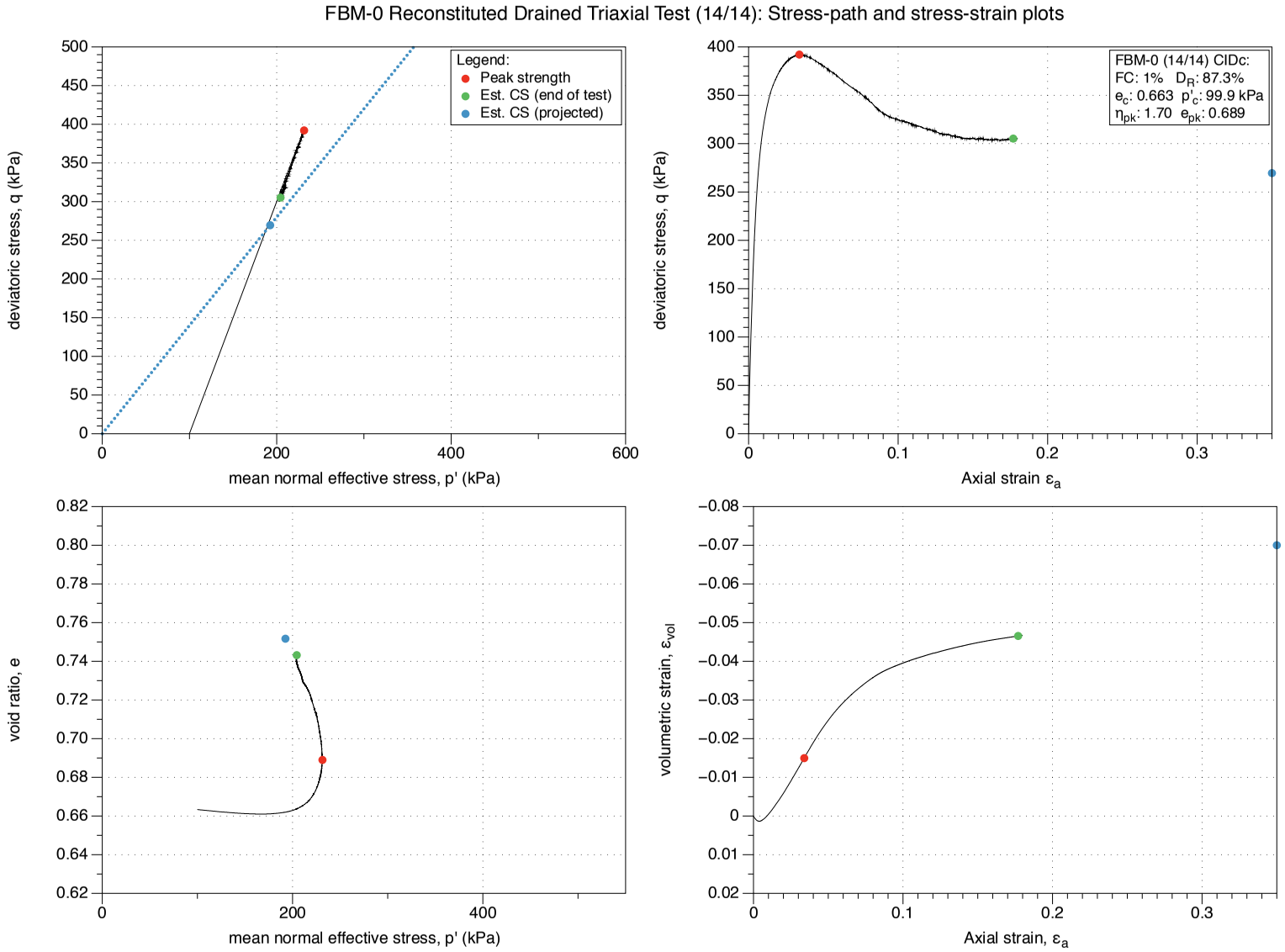

Figure 4.25: FBM with 0 % fines, moist tamped reconstituted sample, triaxial test 14/14. Stress-path and stress-strain plots.

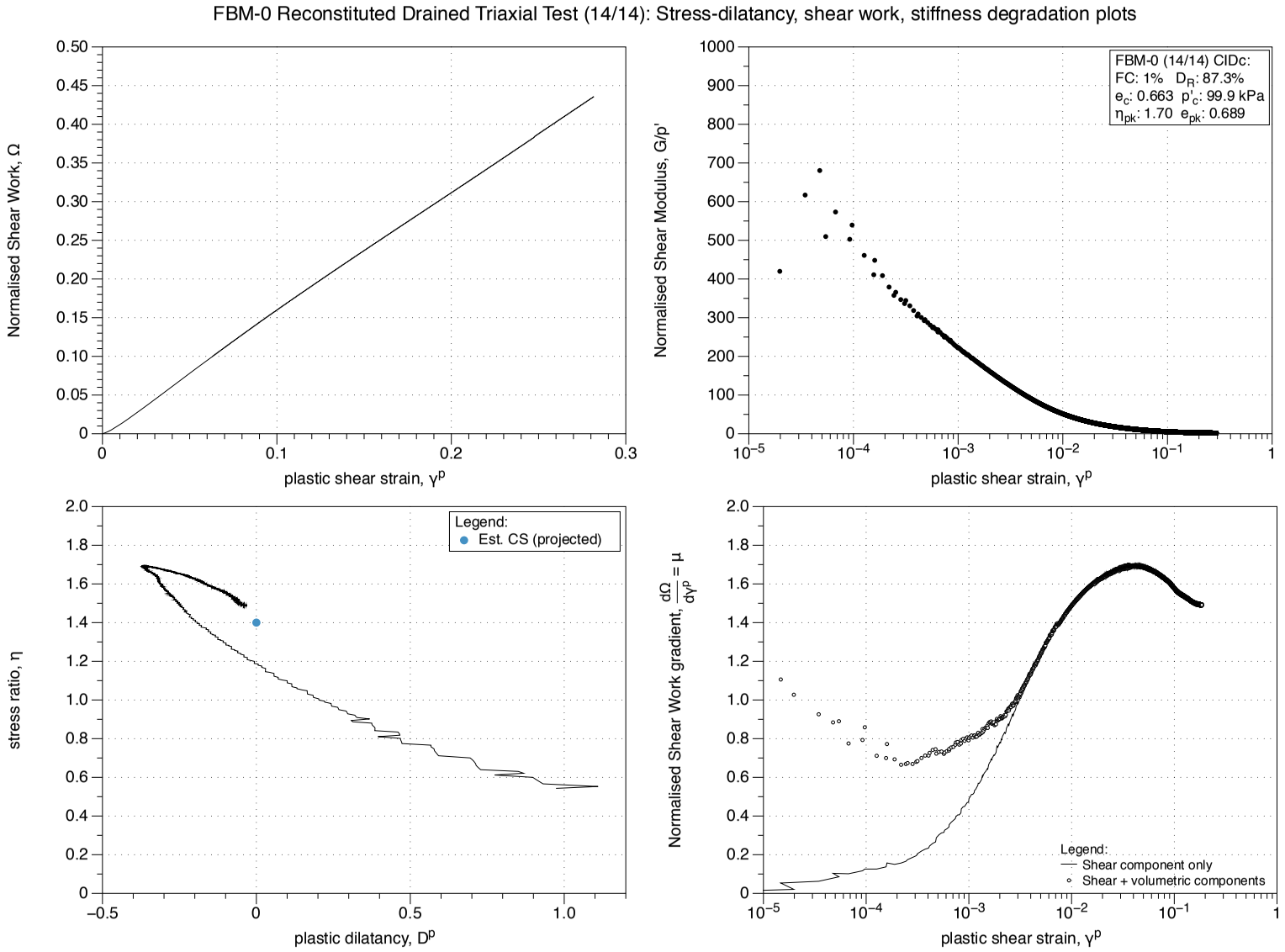

Figure 4.26: FBM with 0 % fines, moist tamped reconstituted sample, triaxial test 14/14. Stress-dilatancy, shear work, stiffness degradation plots.

4.1.2 FBM Cyclic Triaxial Tests

Plots include the effective stress path, stress strain plot, and change in excess pore pressure ratio with number of cycles, and axial strain with number of cycles. Additional plots for each cyclic test depict the development of double amplitude strain, excess pore pressure ratio (maximum and residual), with number of cycles and the square-root of normalised shear work.

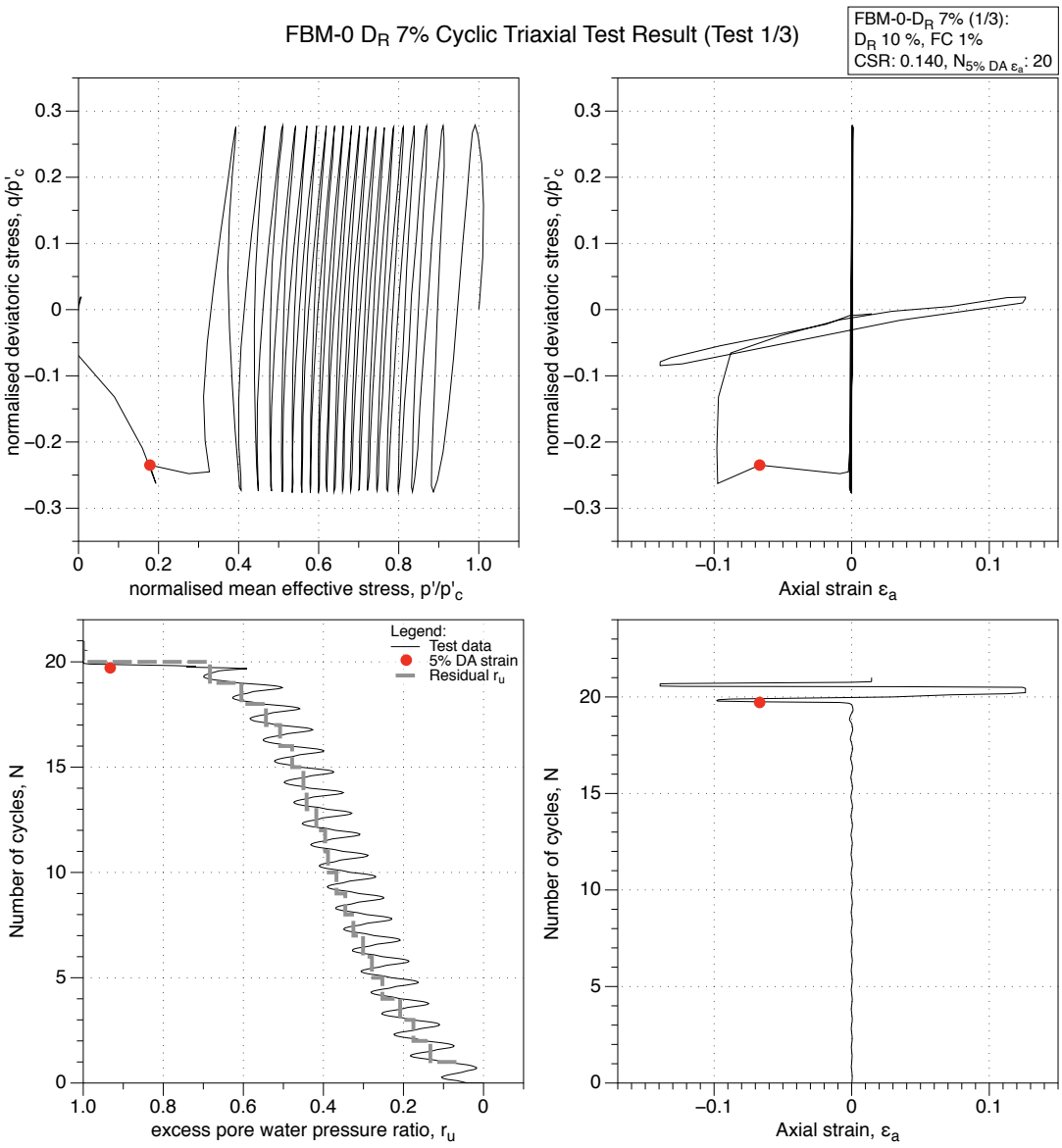

Figure 4.27: FBM with 0 % fines, moist tamped reconstituted sample, Target D_R 7 %, cyclic triaxial test result (test 1/3).

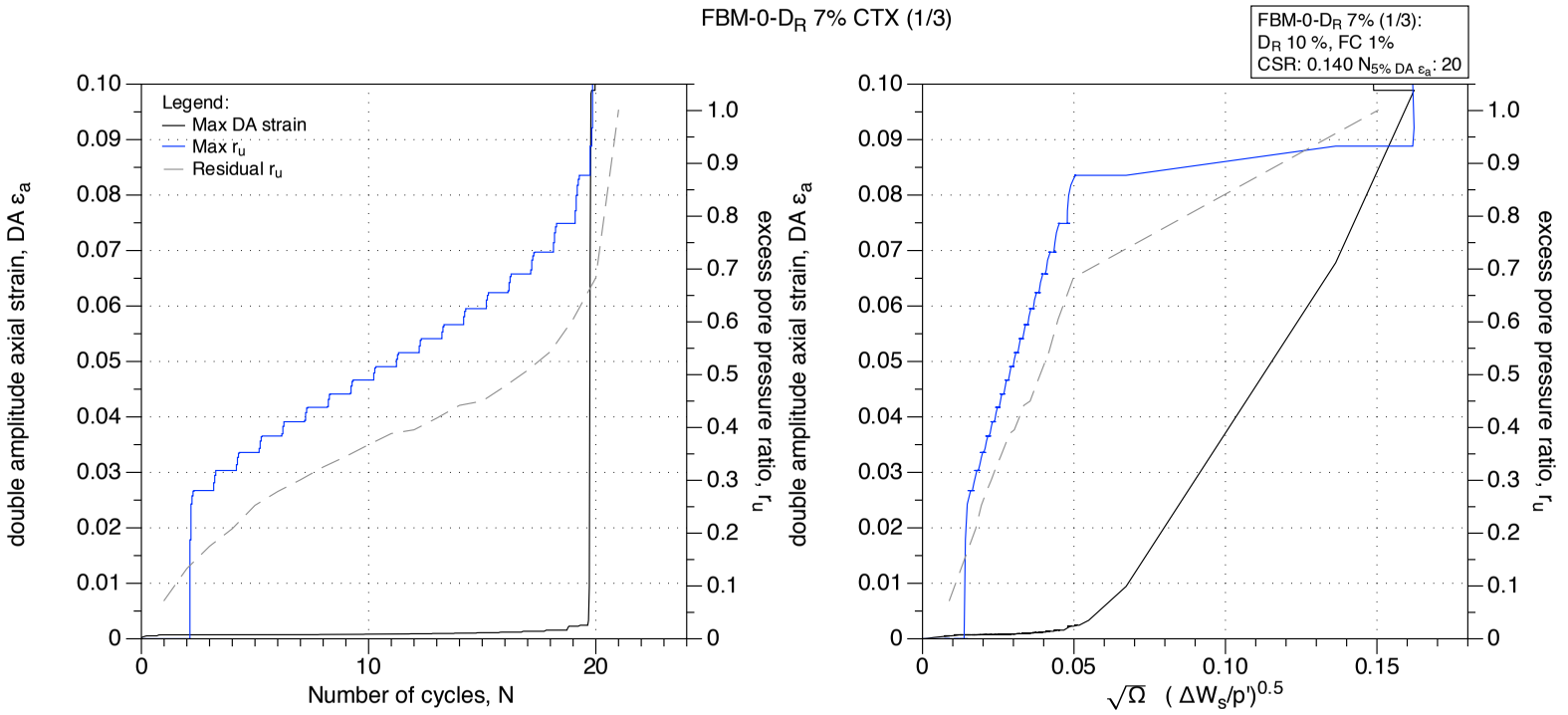

Figure 4.28: FBM-0, D_R 7 %, CTX result (test 1/3). Development of strain and excess pore water pressure with number of cycles and normalised shear work.

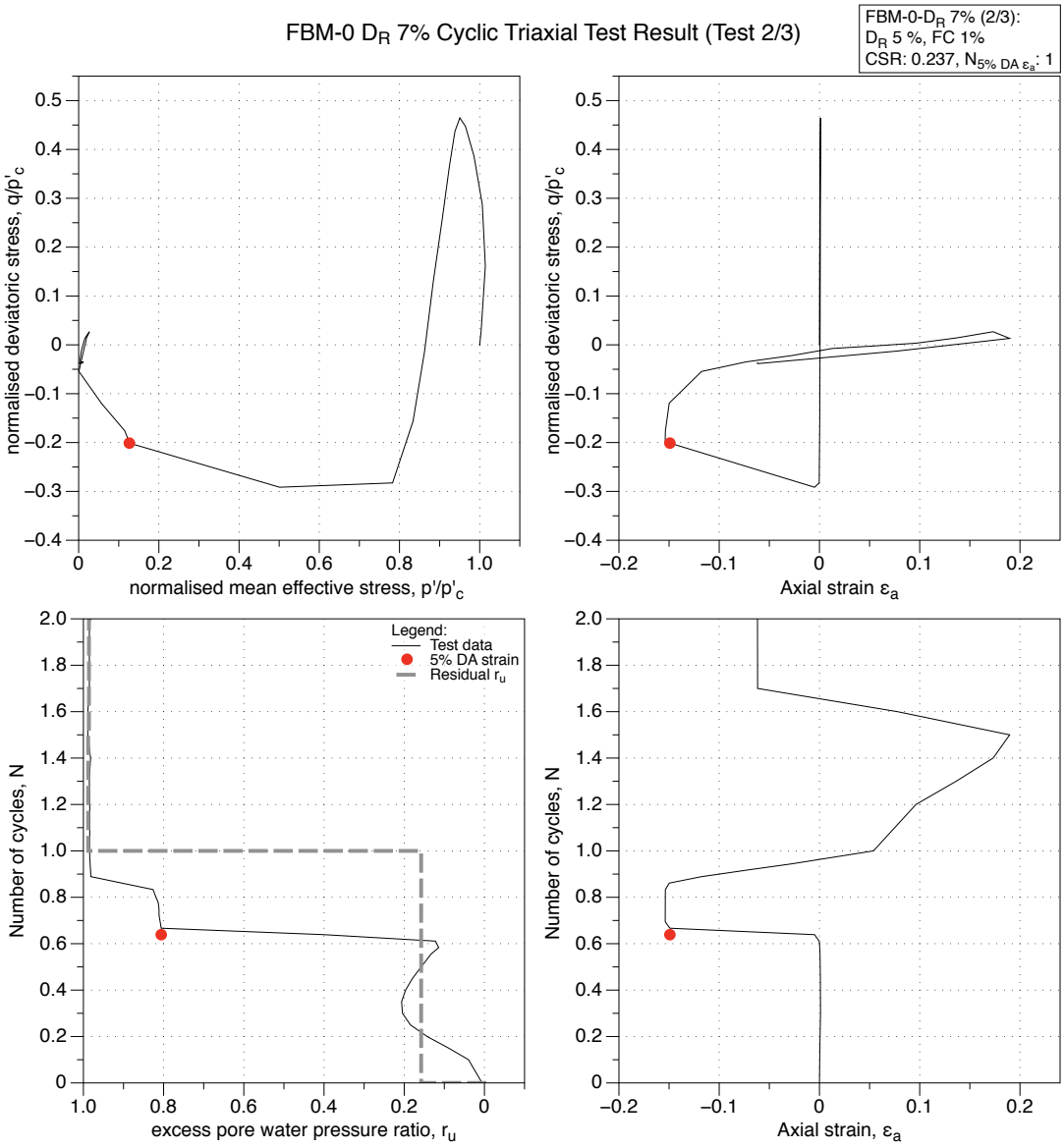

Figure 4.29: FBM with 0 % fines, moist tamped reconstituted sample, Target D_R 7 %, cyclic triaxial test result (test 2/3).

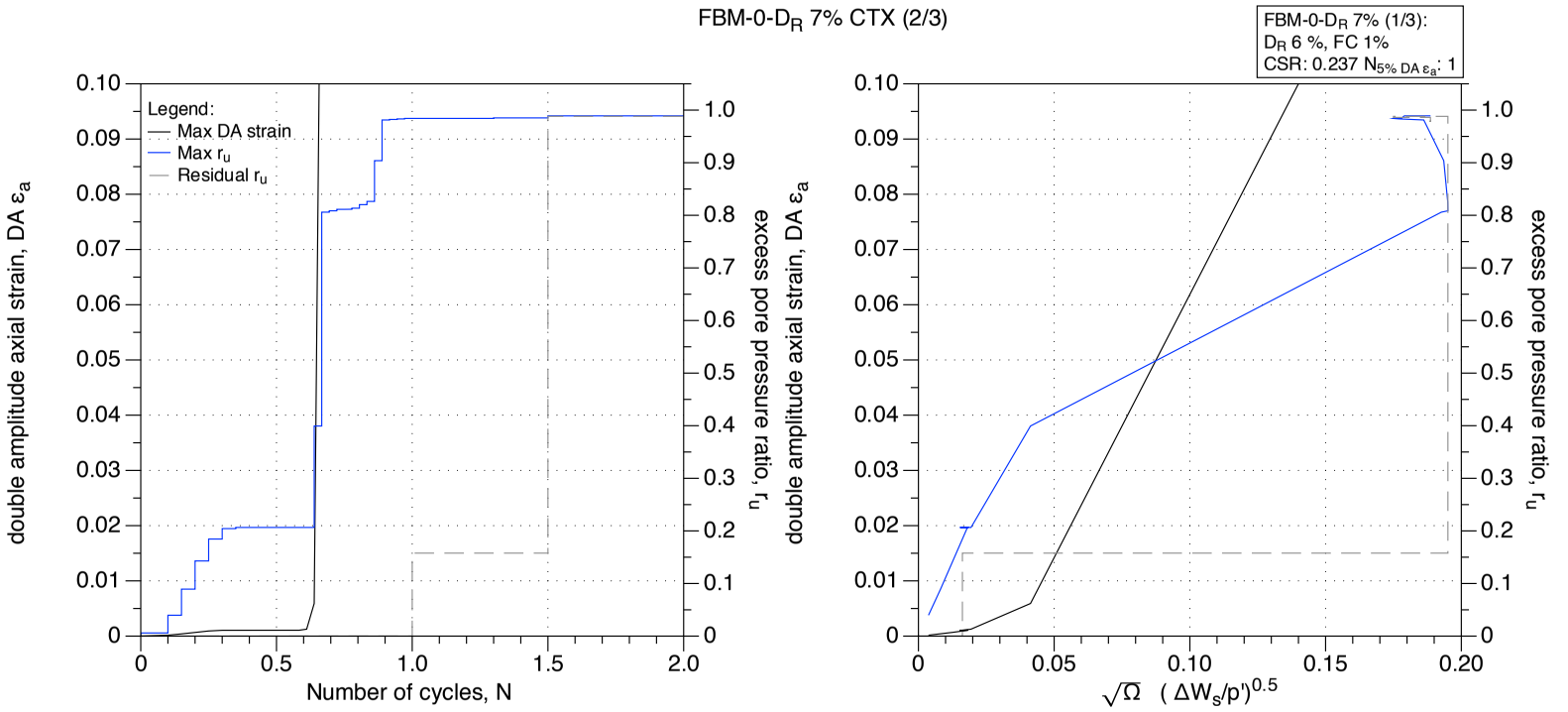

Figure 4.30: FBM-0, D_R 7 %, CTX result (test 2/3). Development of strain and excess pore water pressure with number of cycles and normalised shear work.

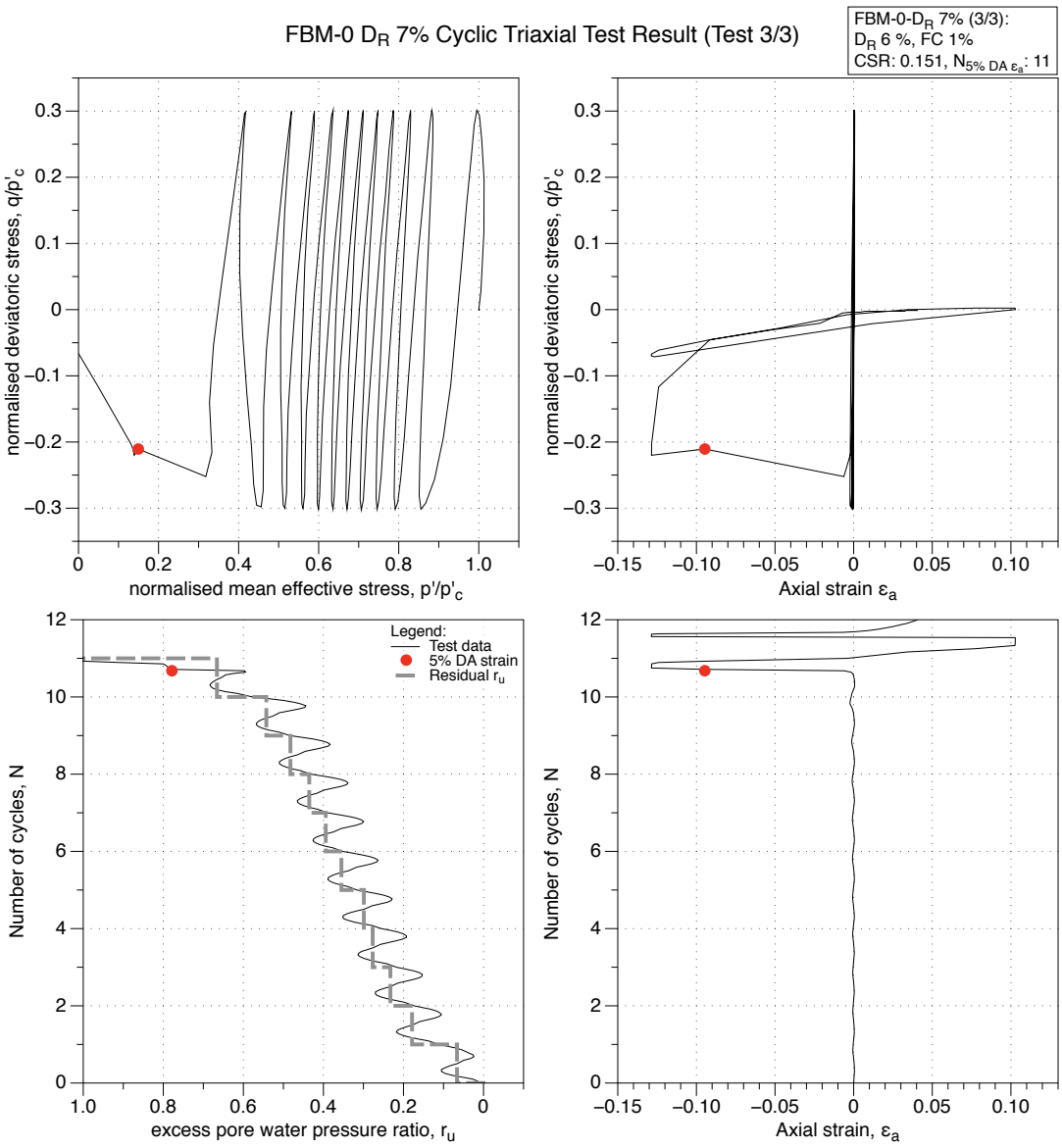

Figure 4.31: FBM with 0 % fines, moist tamped reconstituted sample, Target D_R 7 %, cyclic triaxial test result (test 3/3).

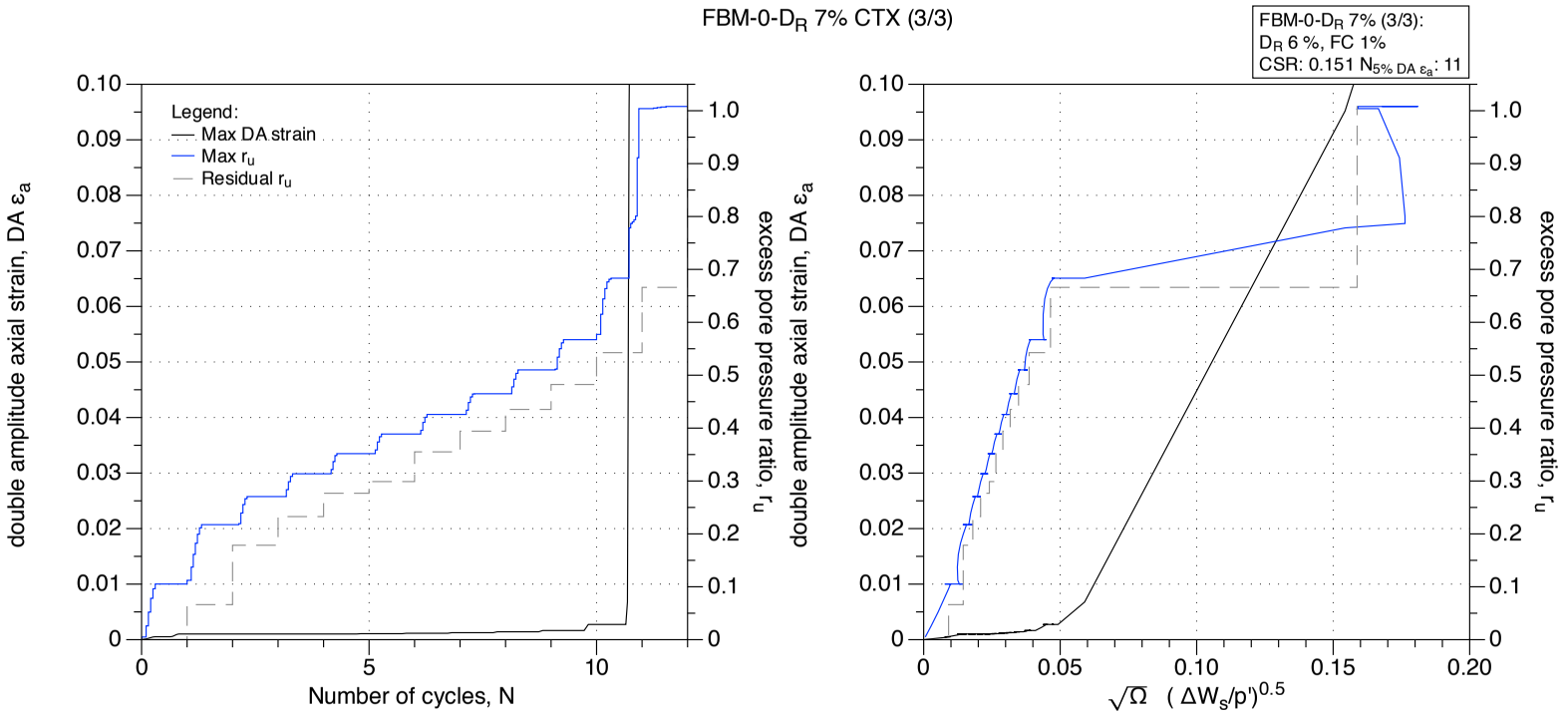

Figure 4.32: FBM-0, D_R 7 %, CTX result (test 3/3). Development of strain and excess pore water pressure with number of cycles and normalised shear work.

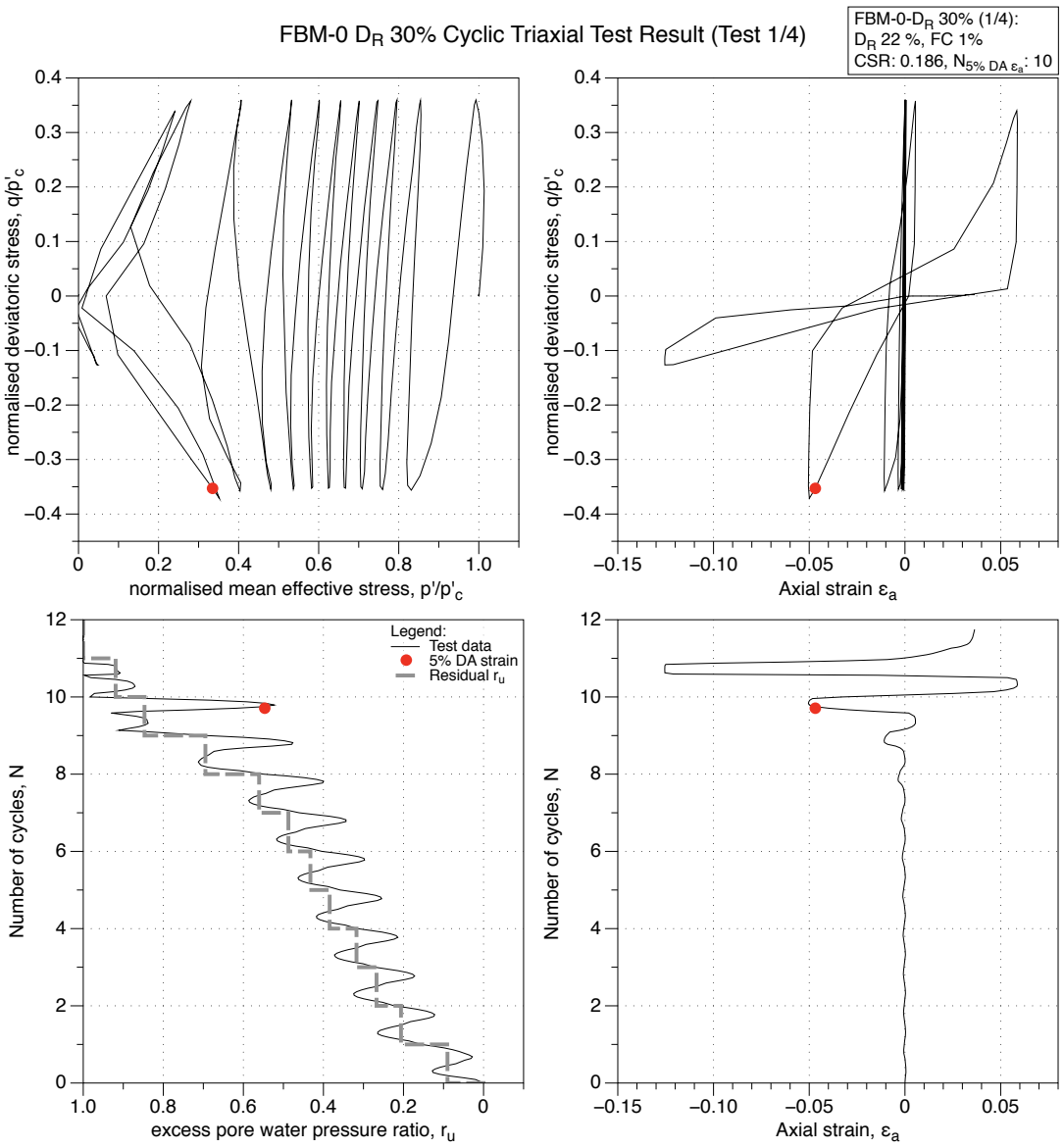

Figure 4.33: FBM with 0 % fines, moist tamped reconstituted sample, Target D_R 30 %, cyclic triaxial test result (test 1/4).

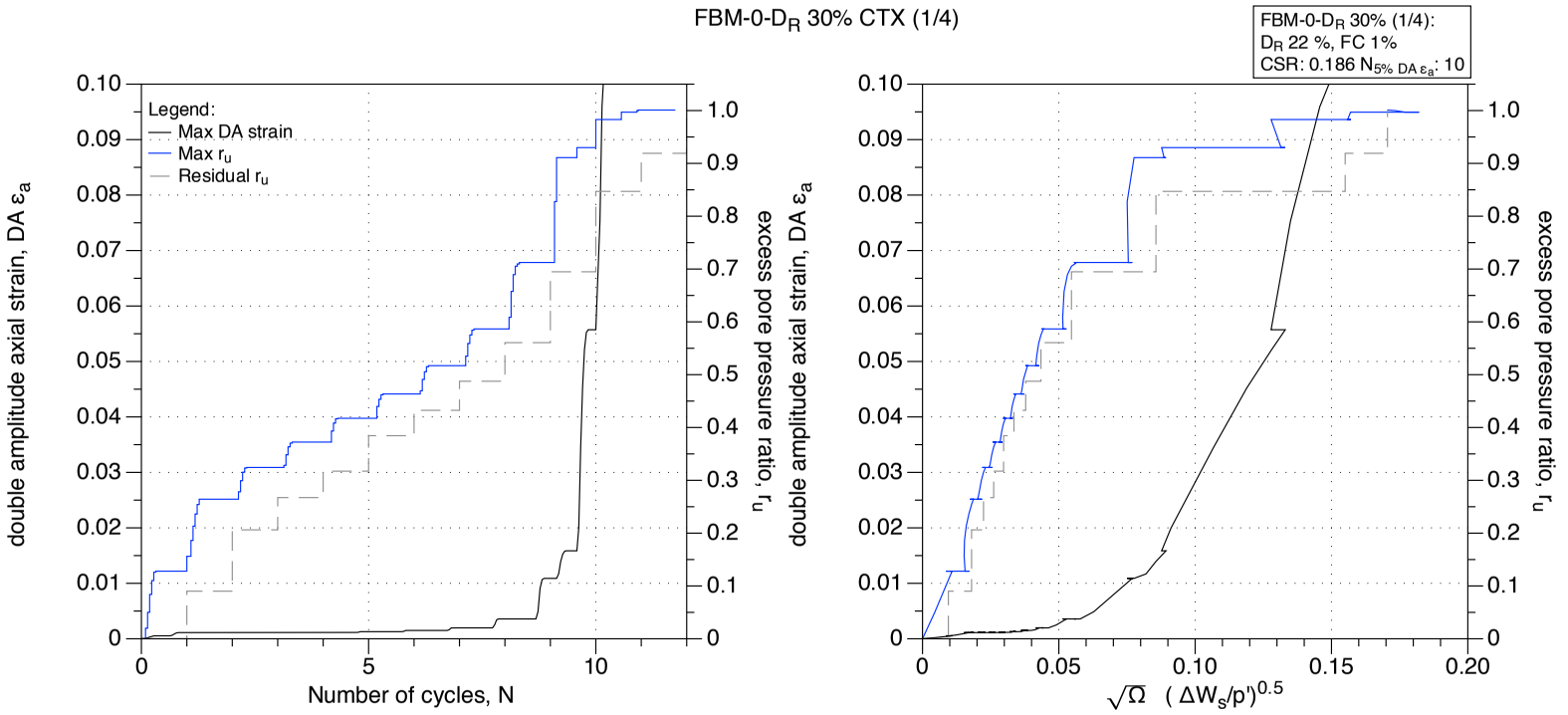

Figure 4.34: FBM-0, D_R 30 %, CTX result (test 1/4). Development of strain and excess pore water pressure with number of cycles and normalised shear work.

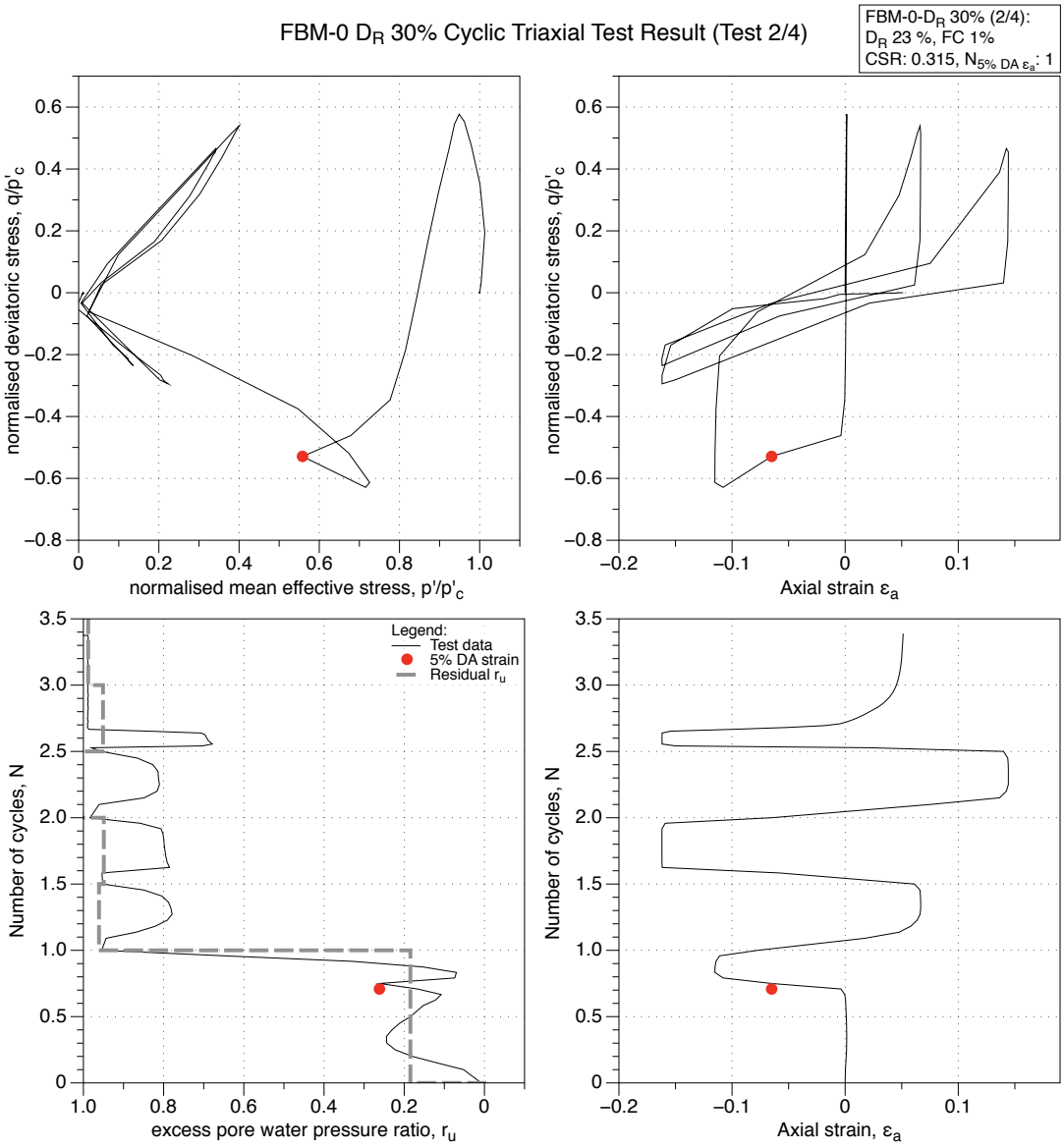

Figure 4.35: FBM with 0 % fines, moist tamped reconstituted sample, Target D_R 30 %, cyclic triaxial test result (test 2/4).

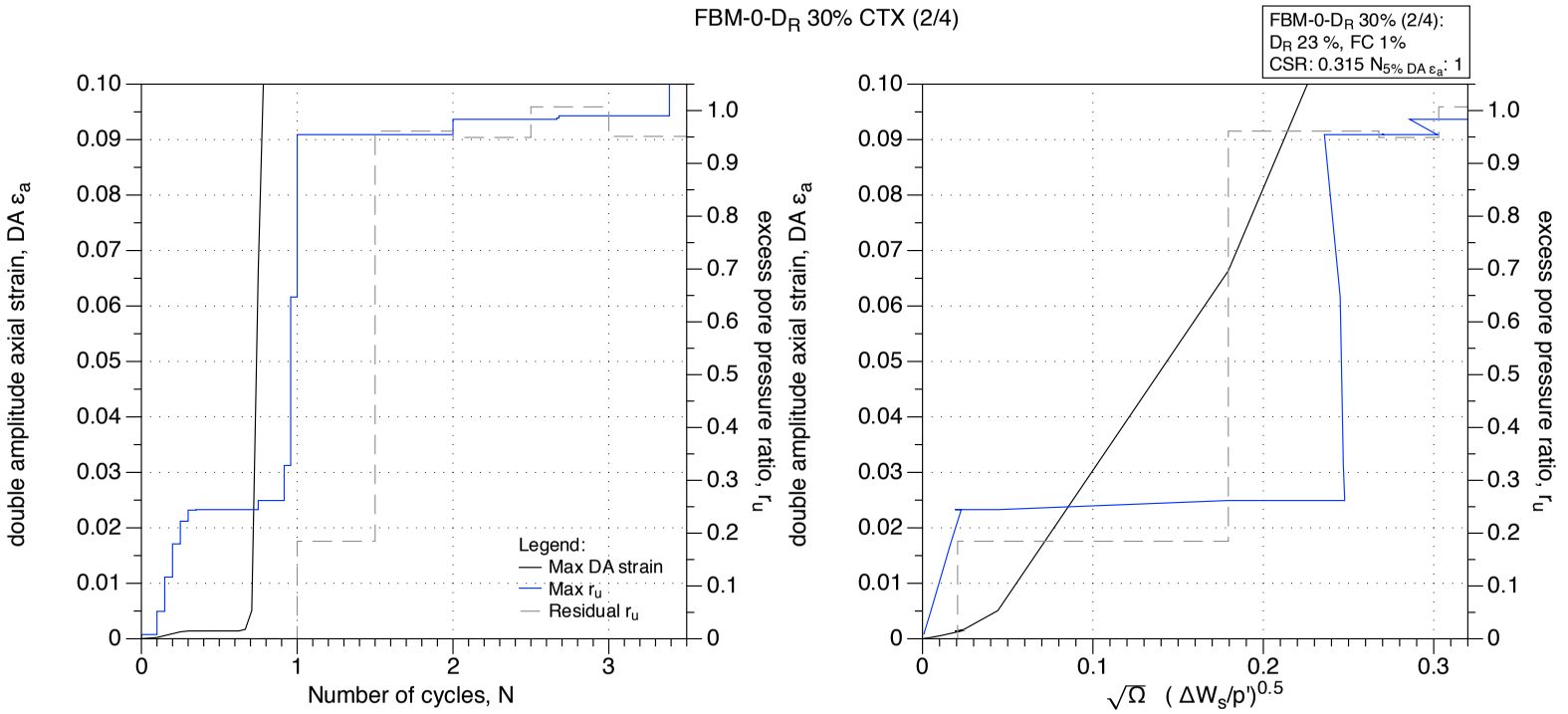

Figure 4.36: FBM-0, D_R 30 %, CTX result (test 2/4). Development of strain and excess pore water pressure with number of cycles and normalised shear work.

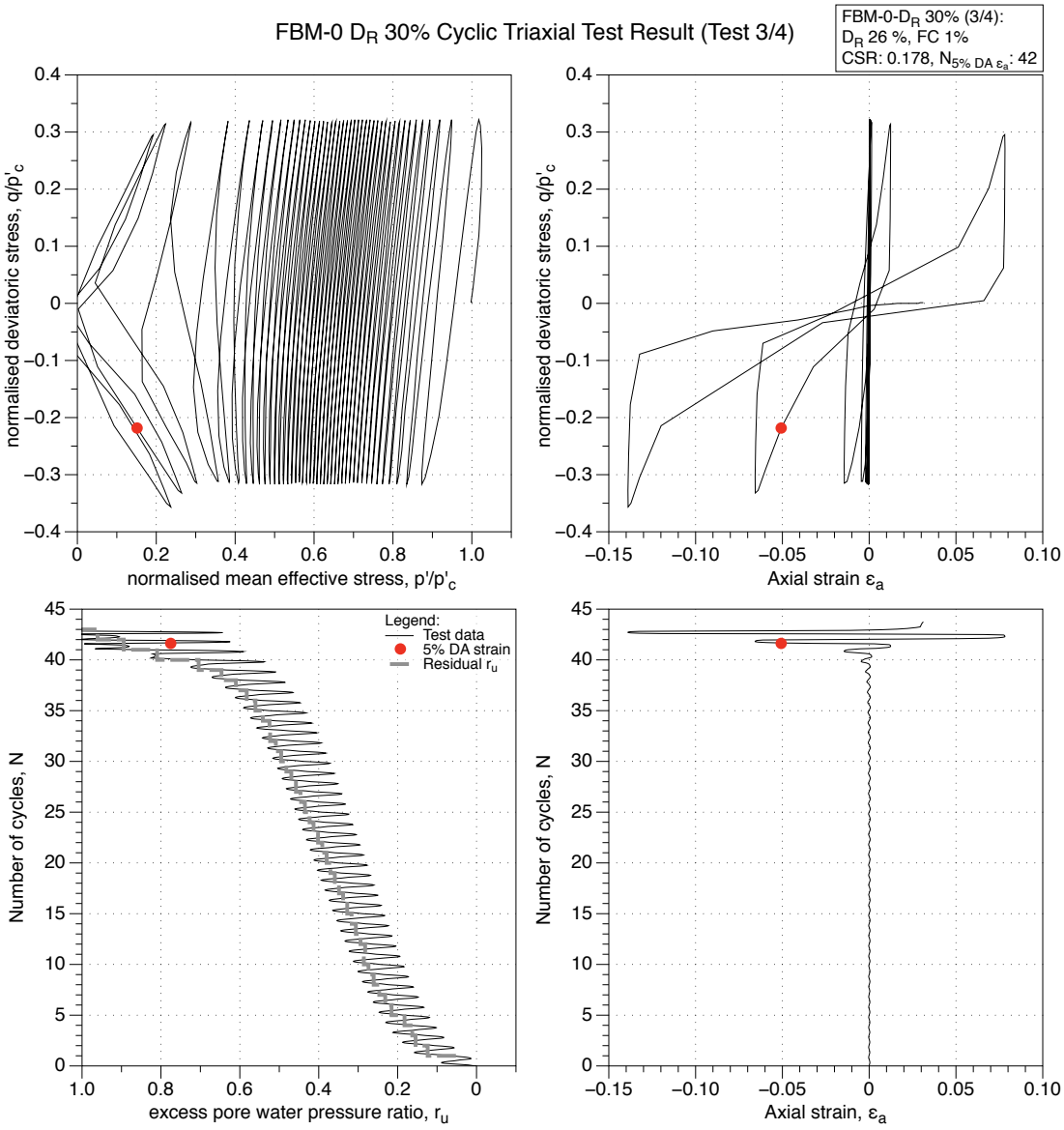

Figure 4.37: FBM with 0 % fines, moist tamped reconstituted sample, Target D_R 30 %, cyclic triaxial test result (test 3/4).

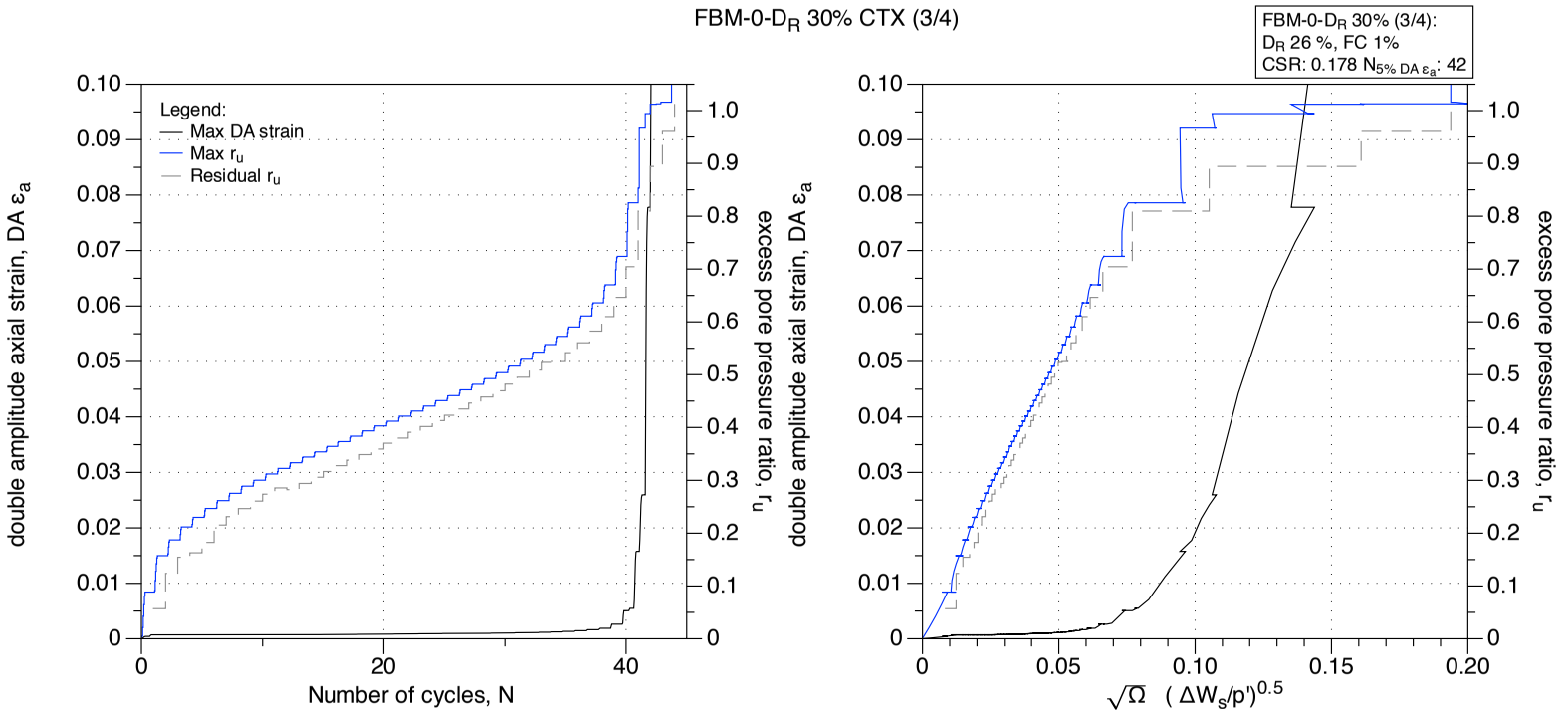

Figure 4.38: FBM-0, D_R 30 %, CTX result (test 3/4). Development of strain and excess pore water pressure with number of cycles and normalised shear work.

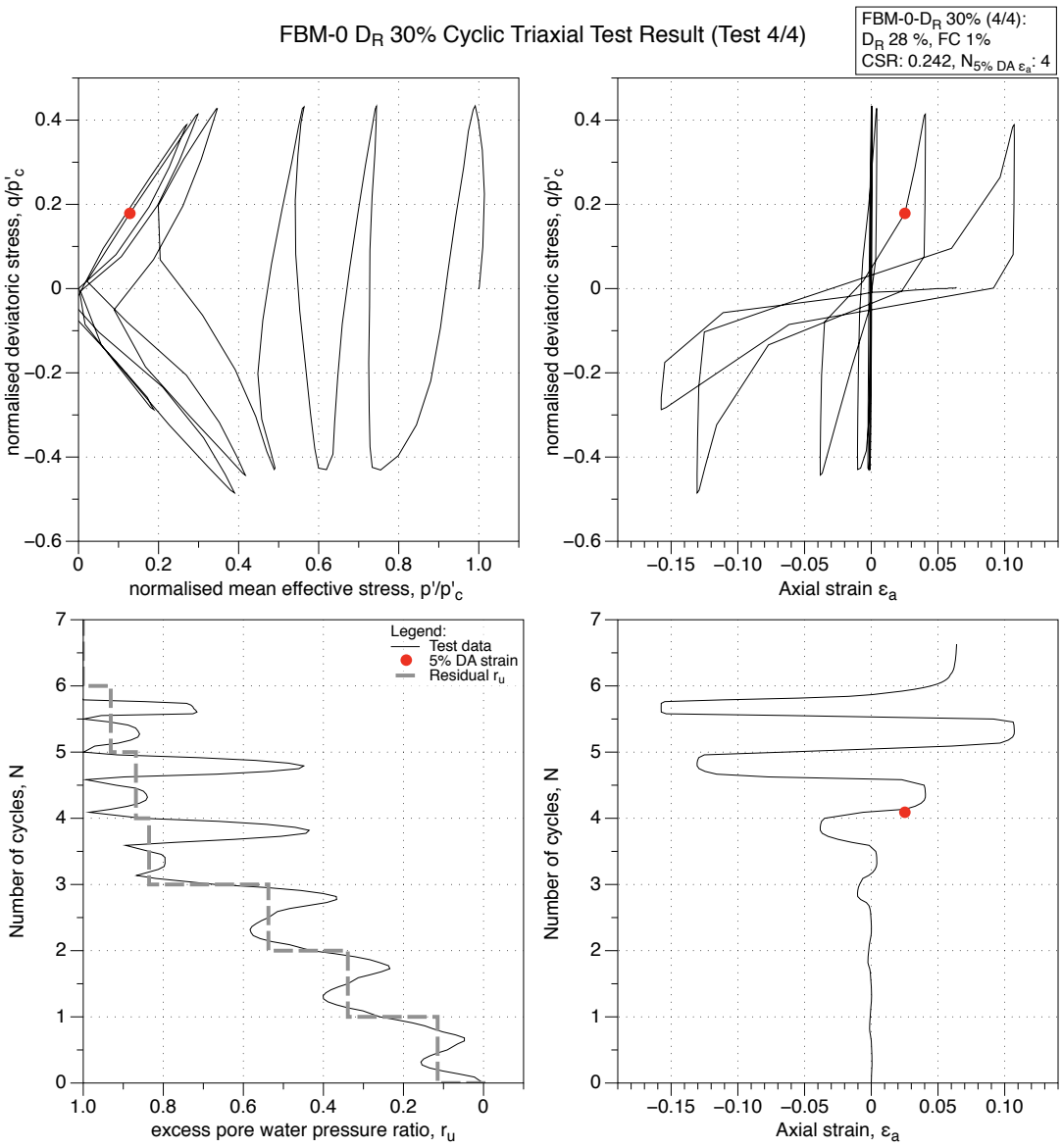

Figure 4.39: FBM with 0 % fines, moist tamped reconstituted sample, Target D_R 30 %, cyclic triaxial test result (test 4/4).

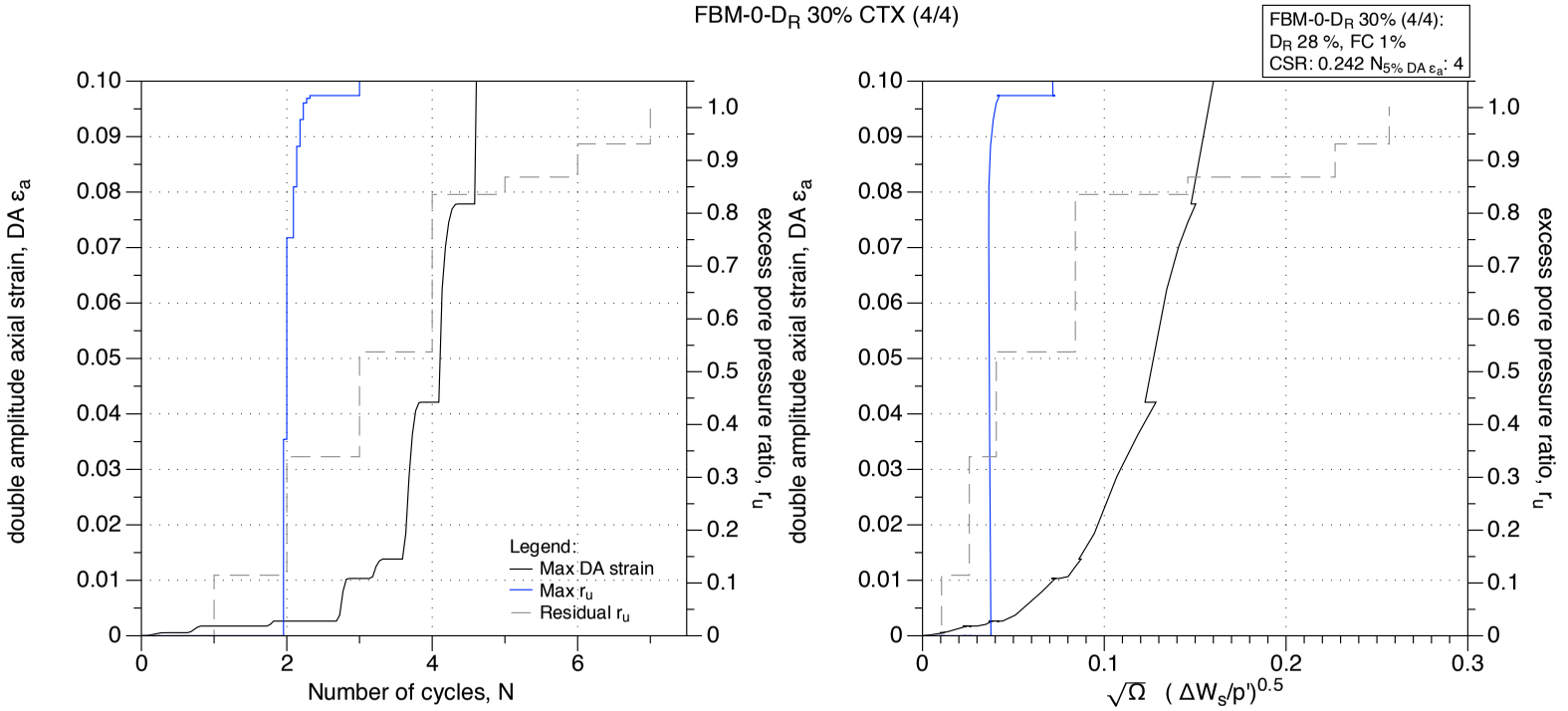

Figure 4.40: FBM-0, D_R 30 %, CTX result (test 4/4). Development of strain and excess pore water pressure with number of cycles and normalised shear work.

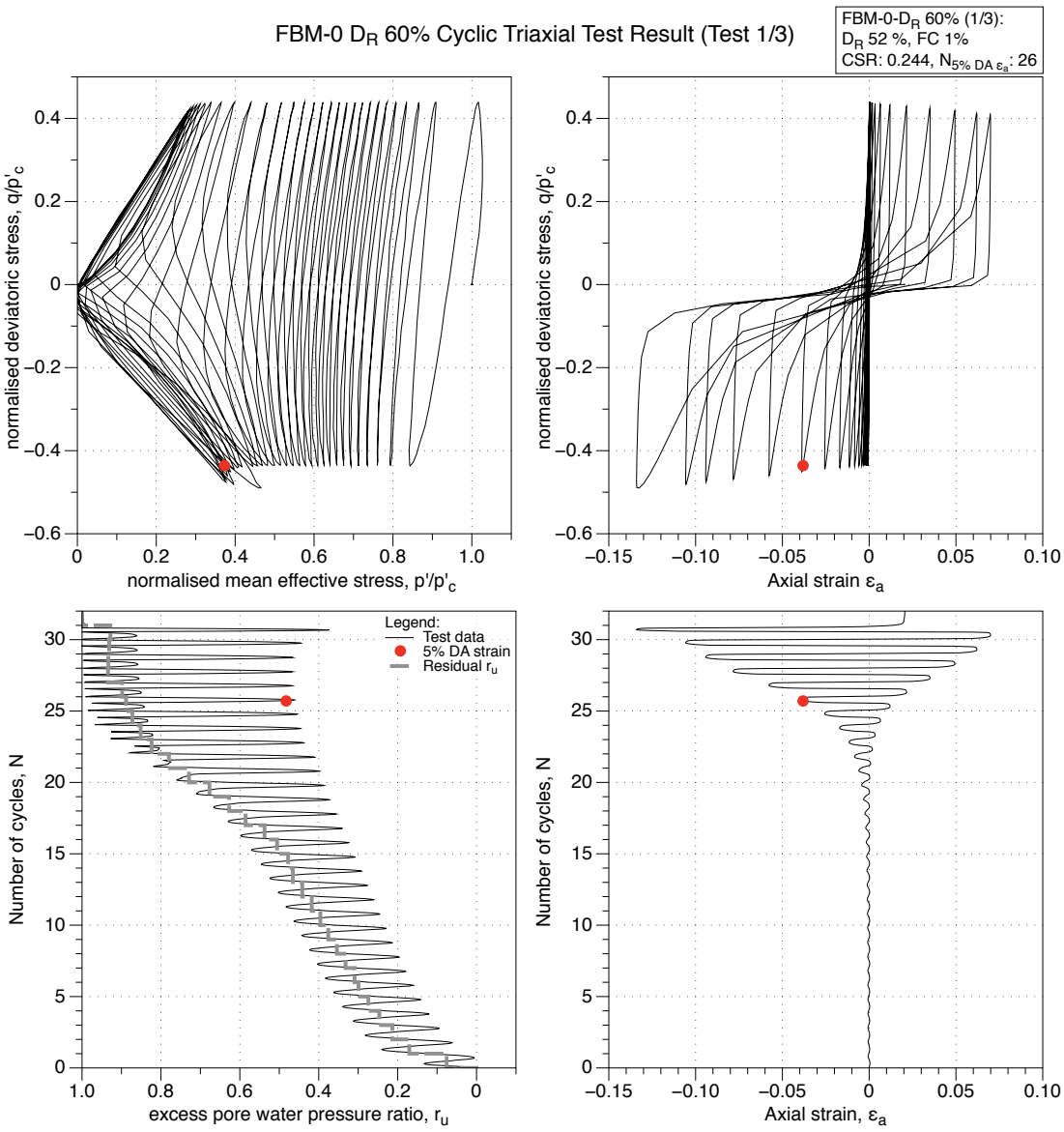

Figure 4.41: FBM with 0 % fines, moist tamped reconstituted sample, Target D_R 60 %, cyclic triaxial test result (test 1/3).

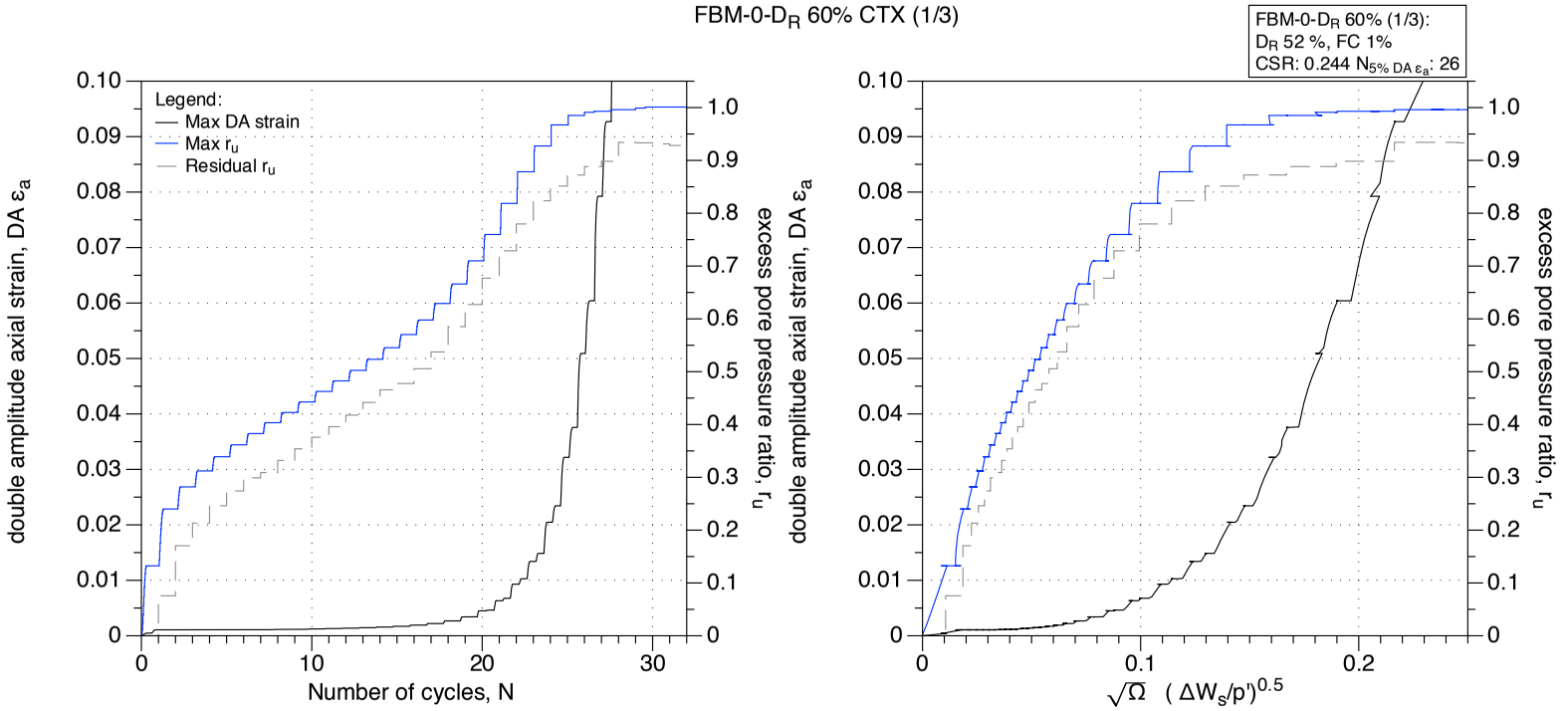

Figure 4.42: FBM-0, D_R 60 %, CTX result (test 1/3). Development of strain and excess pore water pressure with number of cycles and normalised shear work.

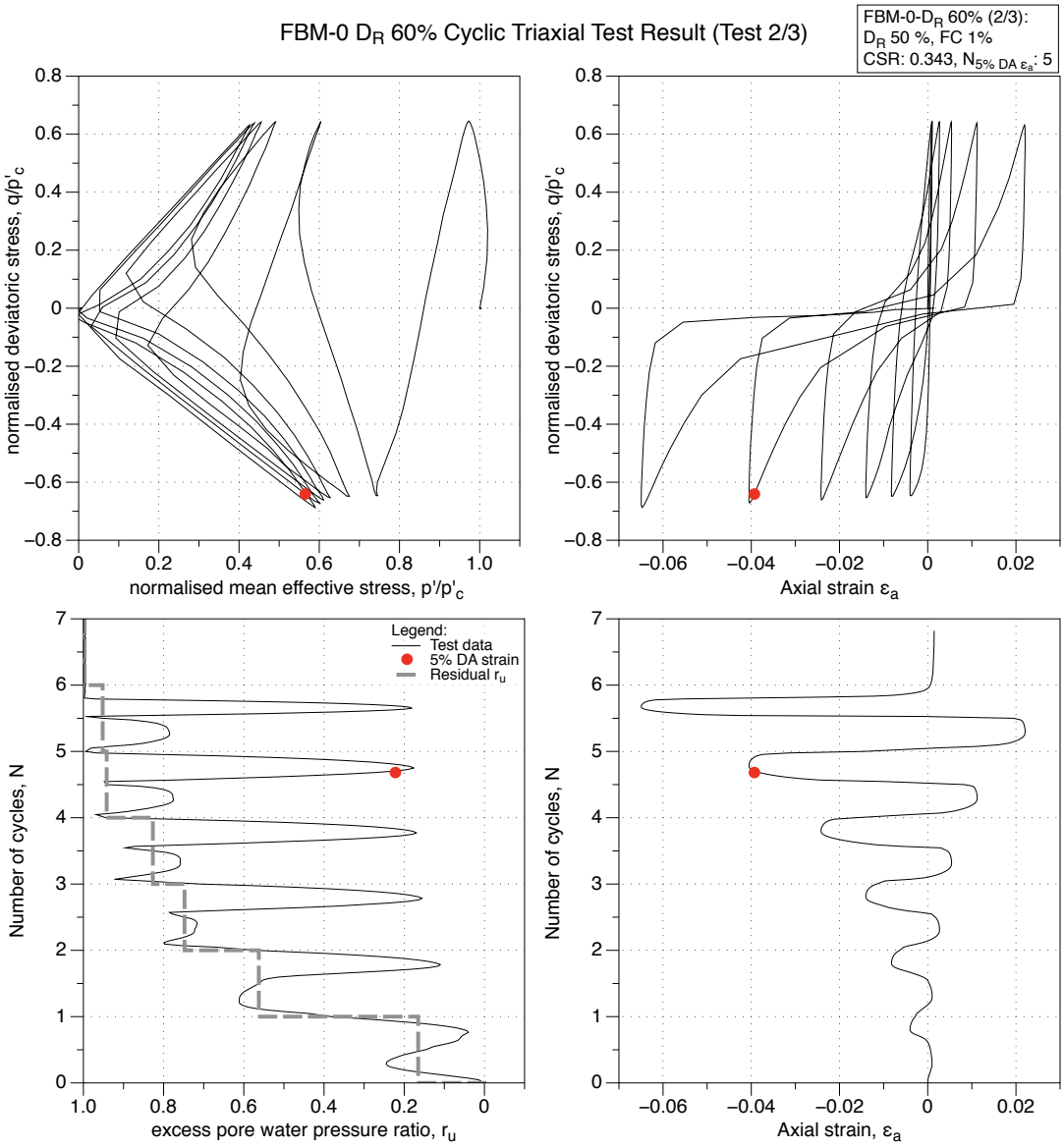

Figure 4.43: FBM with 0 % fines, moist tamped reconstituted sample, Target D_R 60 %, cyclic triaxial test result (test 2/3).

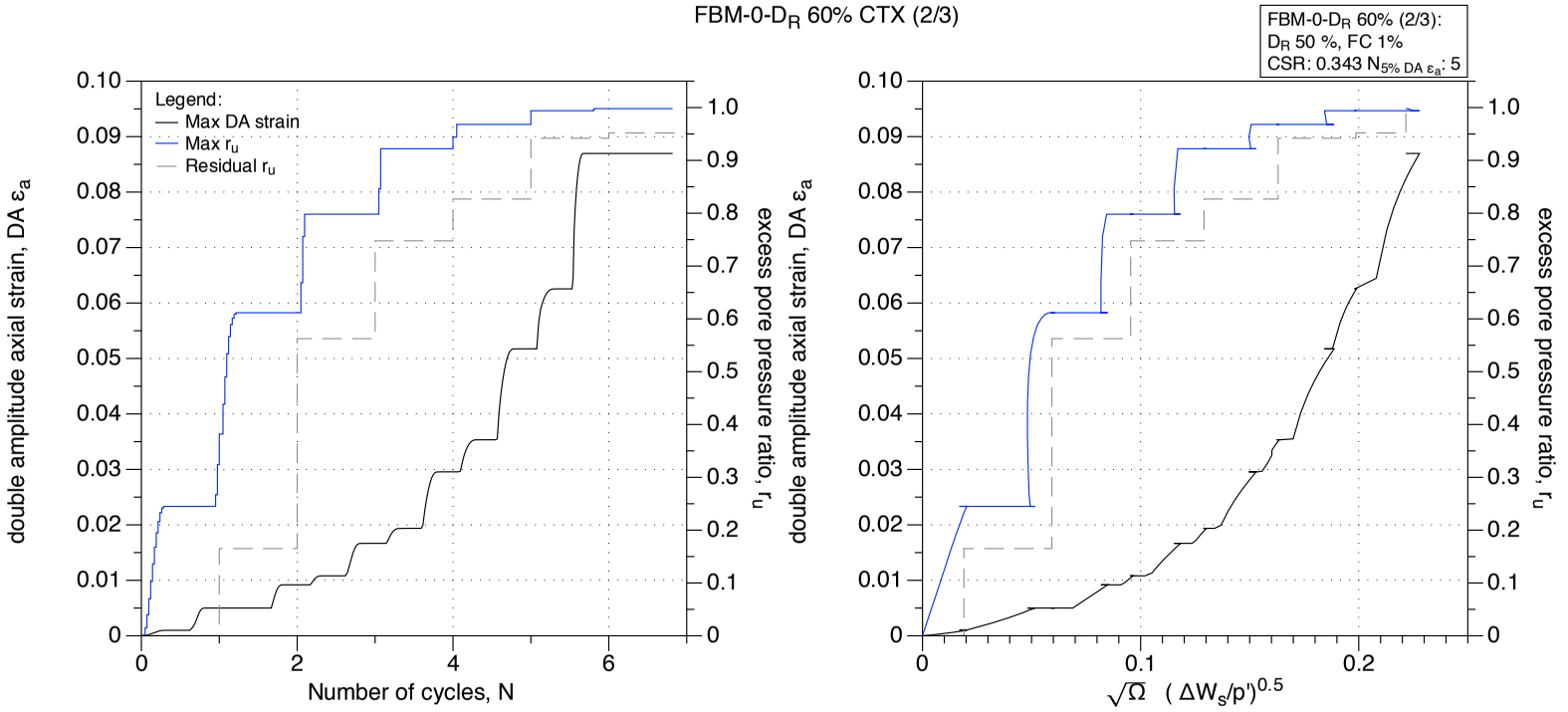

Figure 4.44: FBM-0, D_R 60 %, CTX result (test 2/3). Development of strain and excess pore water pressure with number of cycles and normalised shear work.

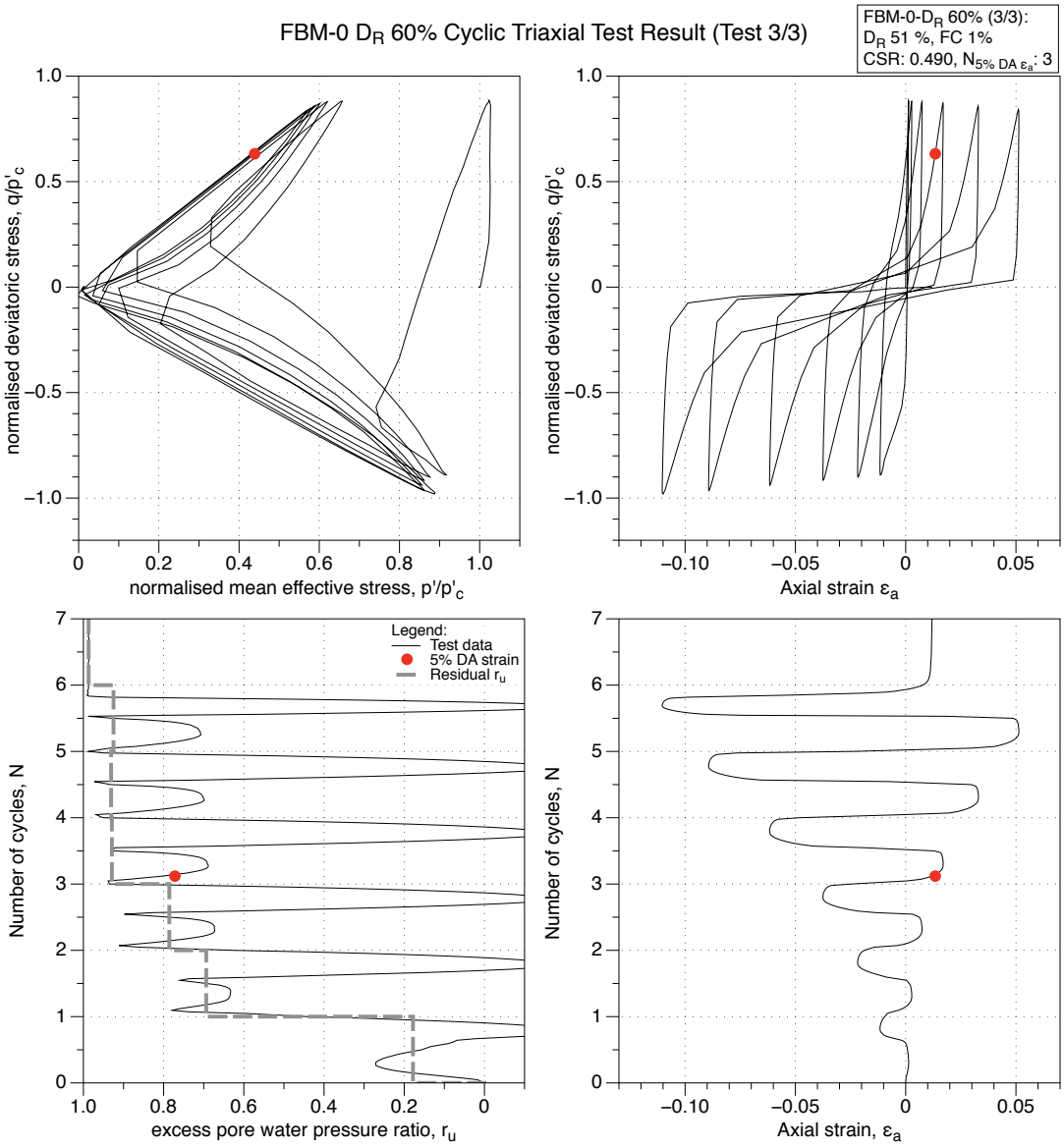

Figure 4.45: FBM with 0 % fines, moist tamped reconstituted sample, Target D_R 60 %, cyclic triaxial test result (test 3/3).

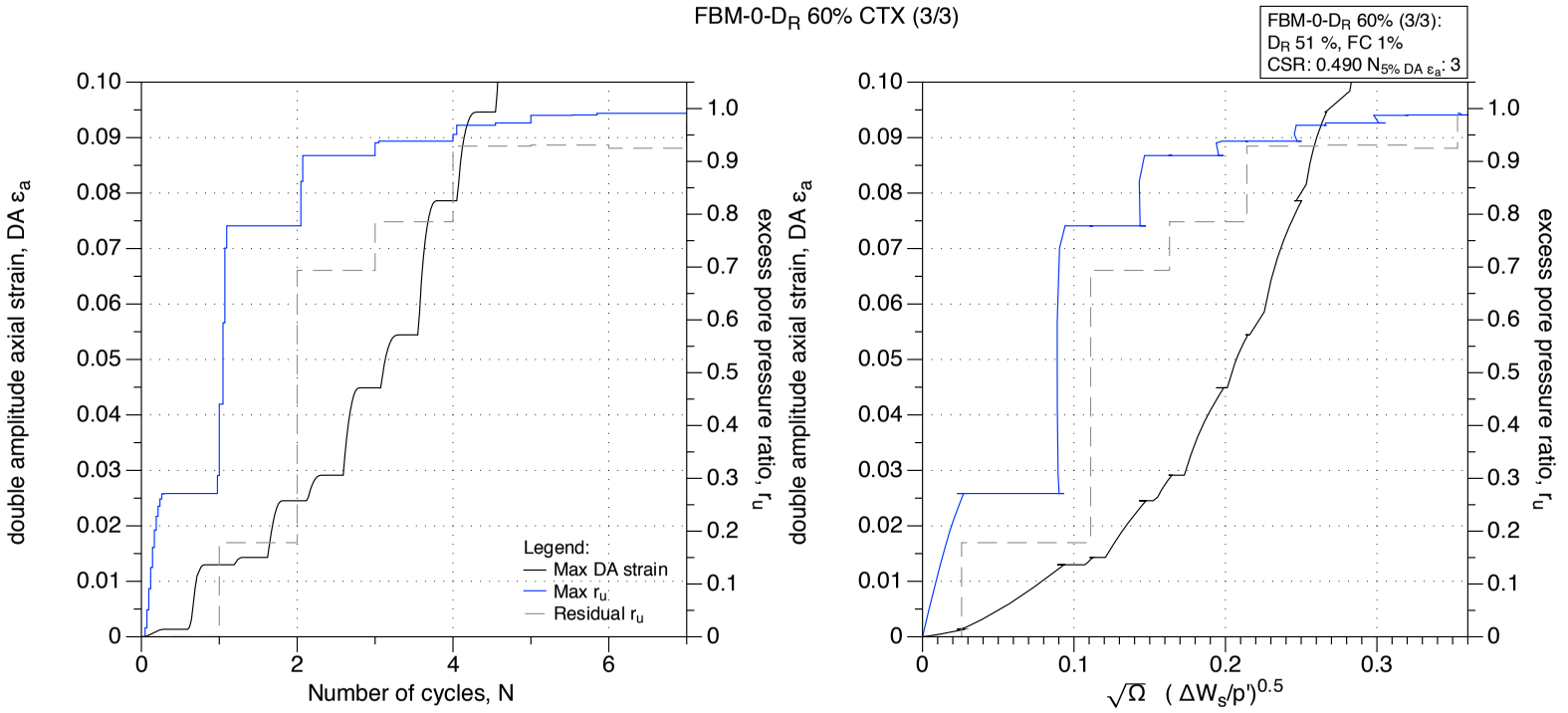

Figure 4.46: FBM-0, D_R 60 %, CTX result (test 3/3). Development of strain and excess pore water pressure with number of cycles and normalised shear work.

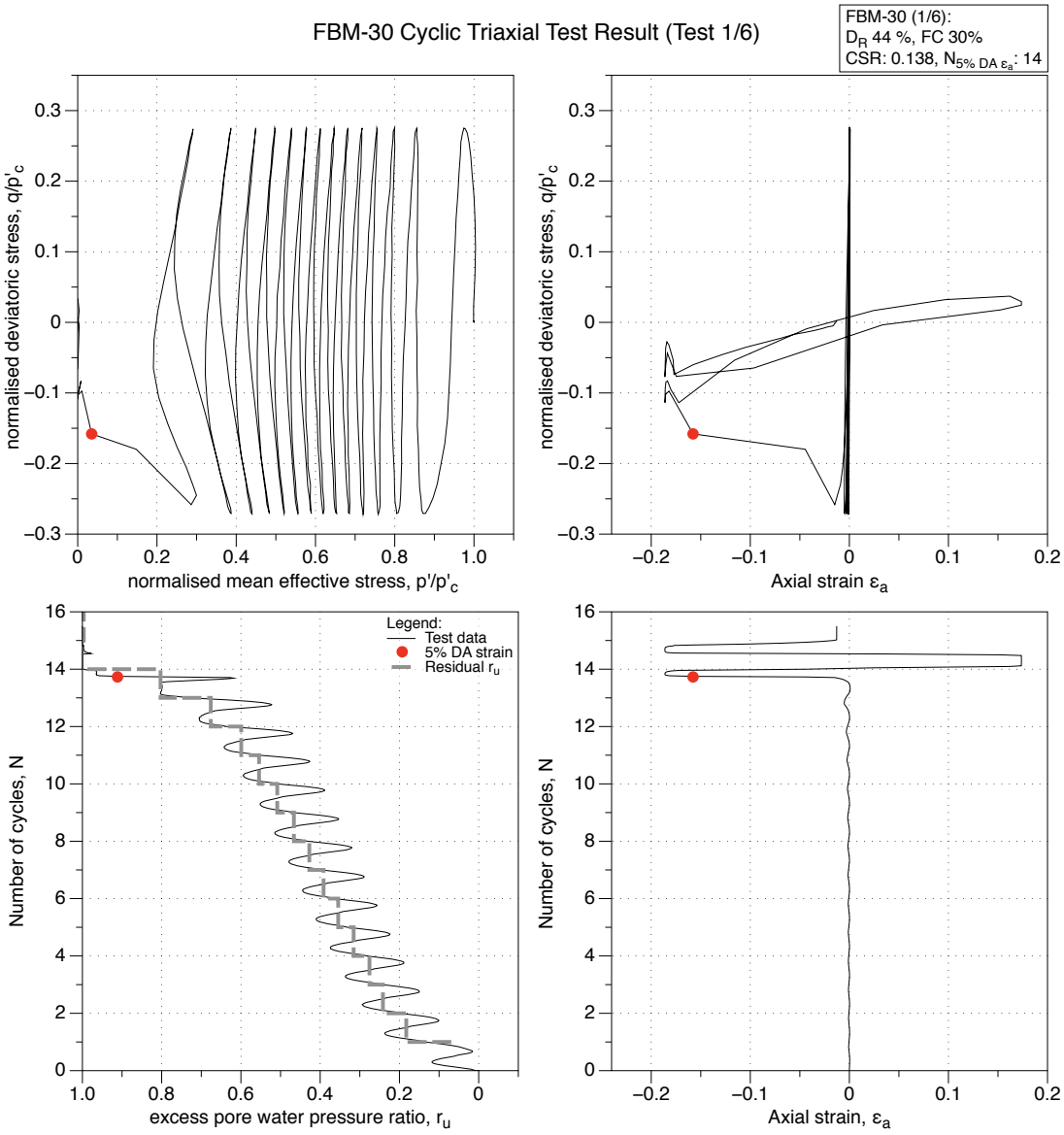

Figure 4.47: FBM with 30 % fines, moist tamped reconstituted sample, cyclic triaxial test result (test 1/6).

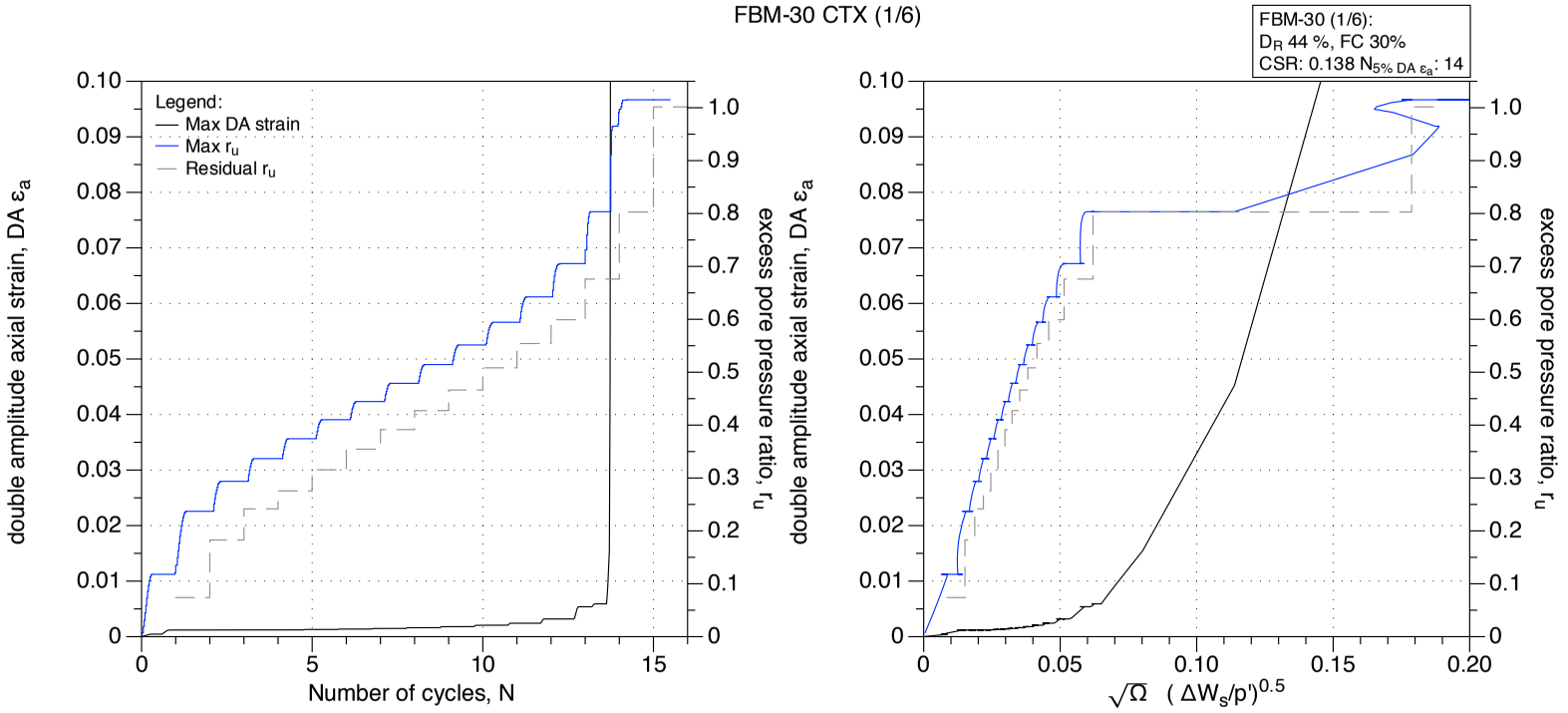

Figure 4.48: FBM-30, CTX result (test 1/6). Development of strain and excess pore water pressure with number of cycles and normalised shear work.

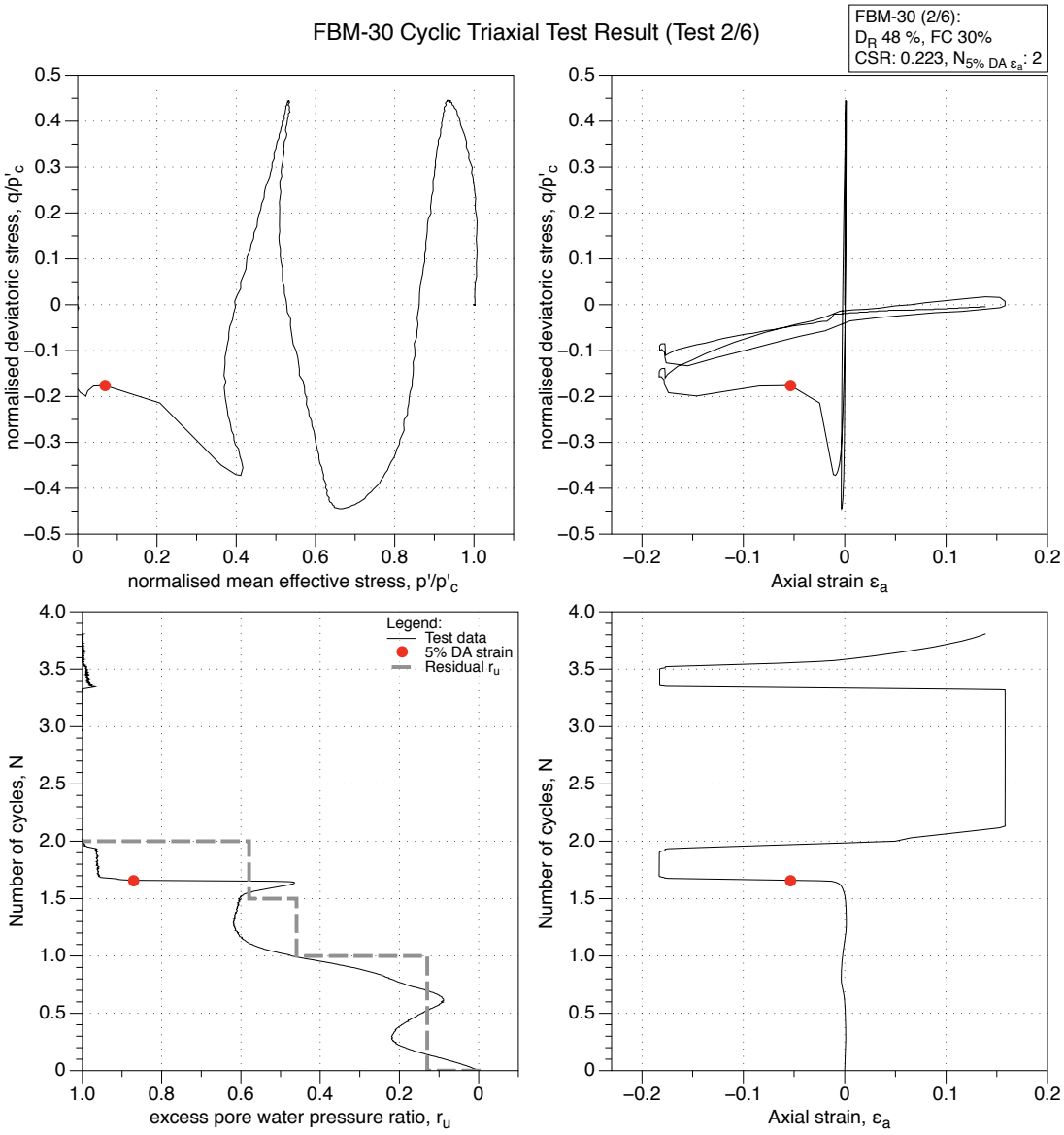

Figure 4.49: FBM with 30 % fines, moist tamped reconstituted sample, cyclic triaxial test result (test 2/6).

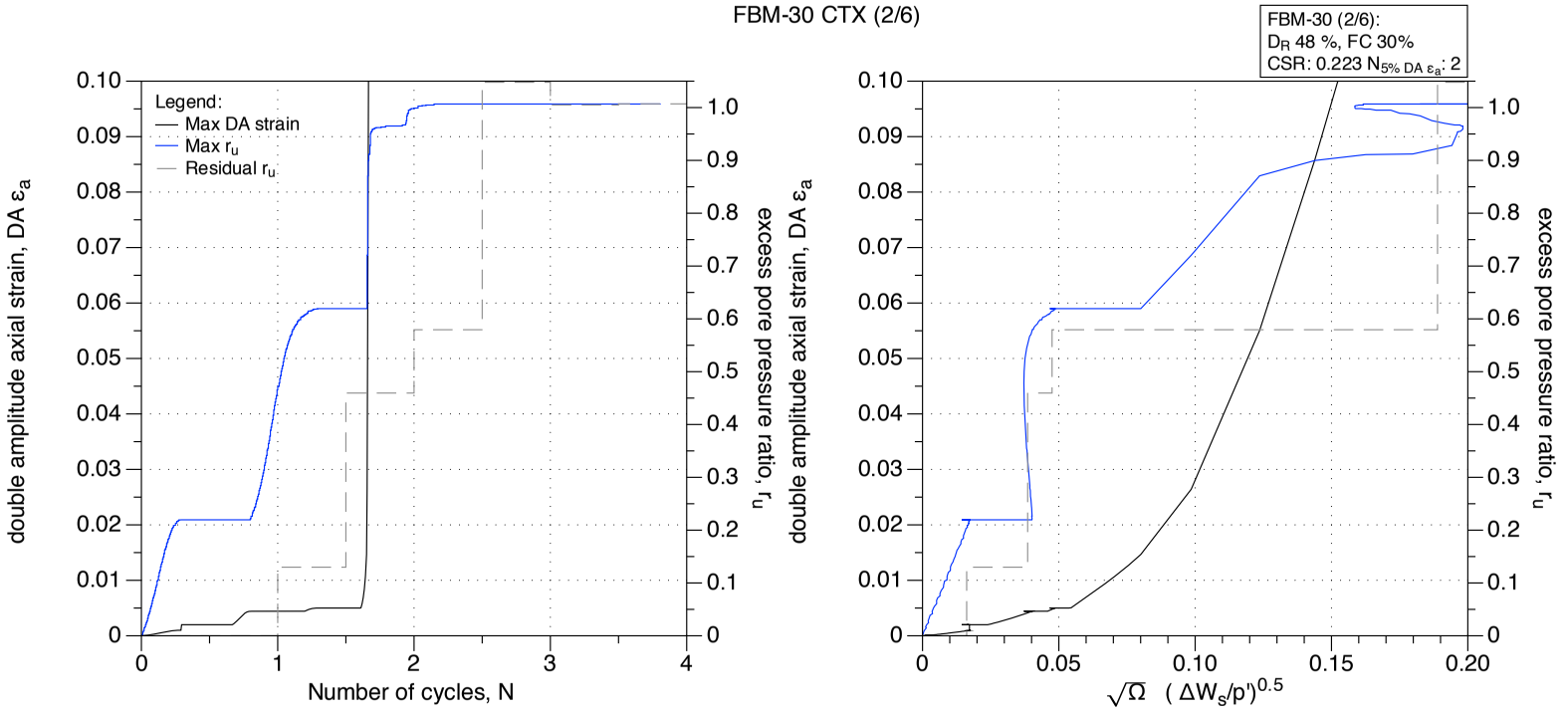

Figure 4.50: FBM-30, CTX result (test 2/6). Development of strain and excess pore water pressure with number of cycles and normalised shear work.

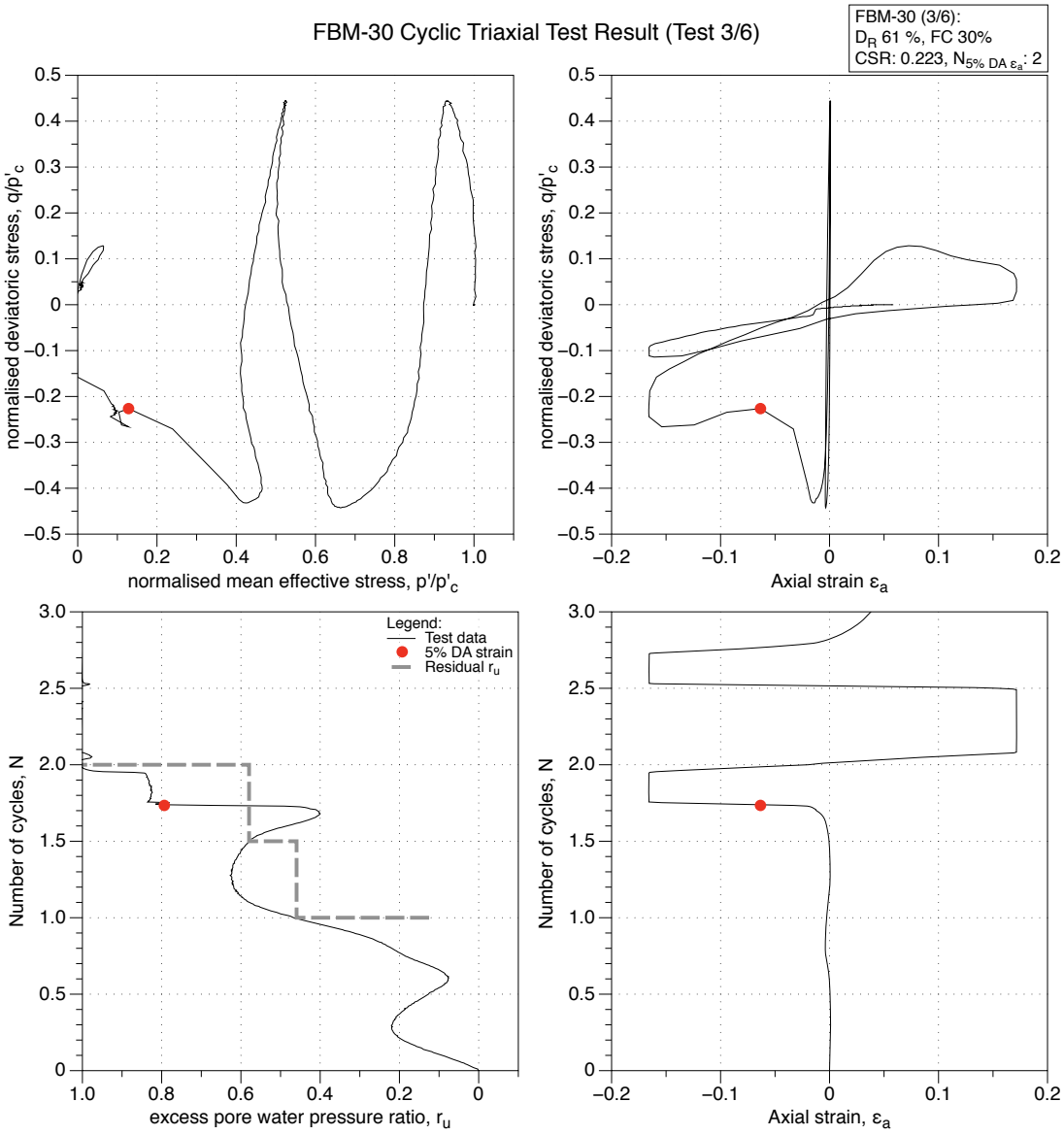

Figure 4.51: FBM with 30 % fines, moist tamped reconstituted sample, cyclic triaxial test result (test 3/6).

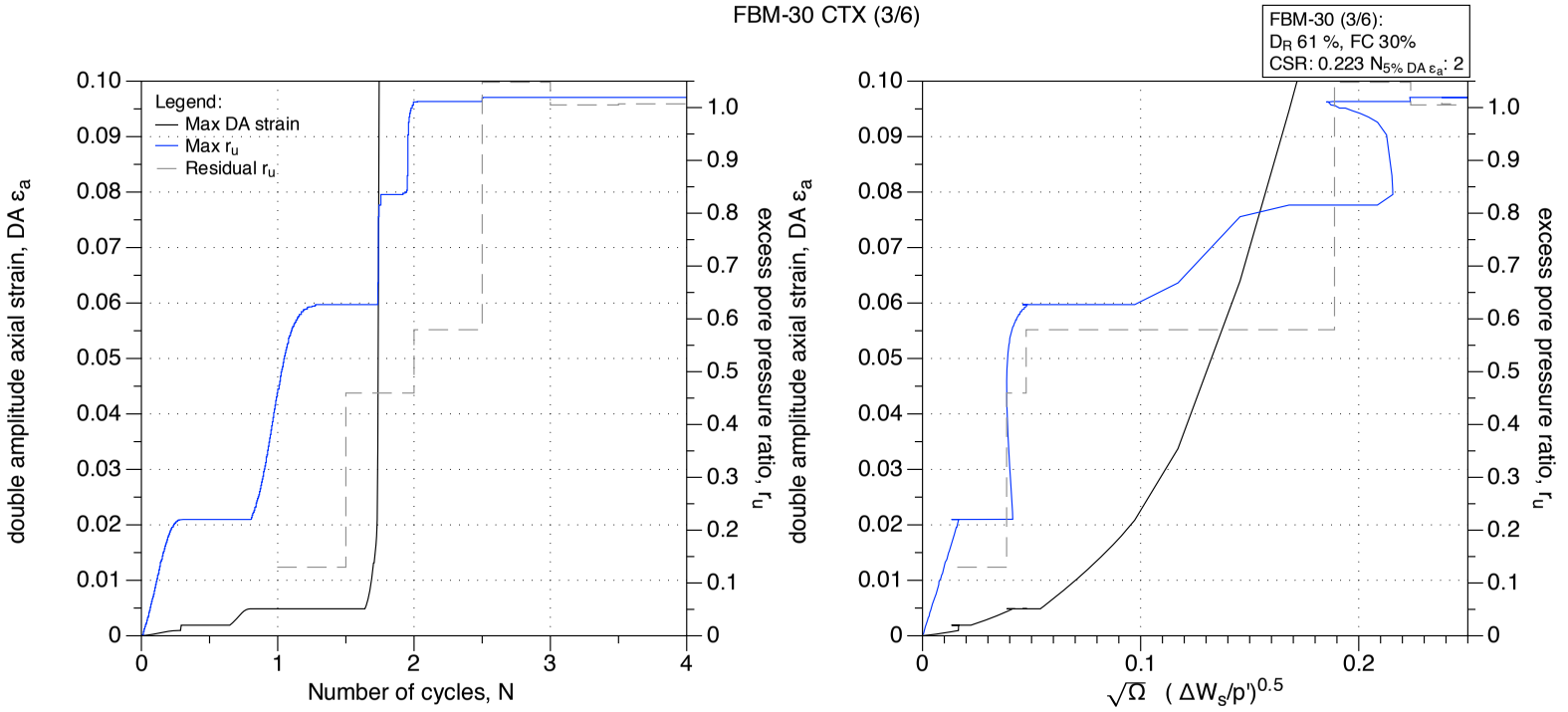

Figure 4.52: FBM-30, CTX result (test 3/6). Development of strain and excess pore water pressure with number of cycles and normalised shear work.

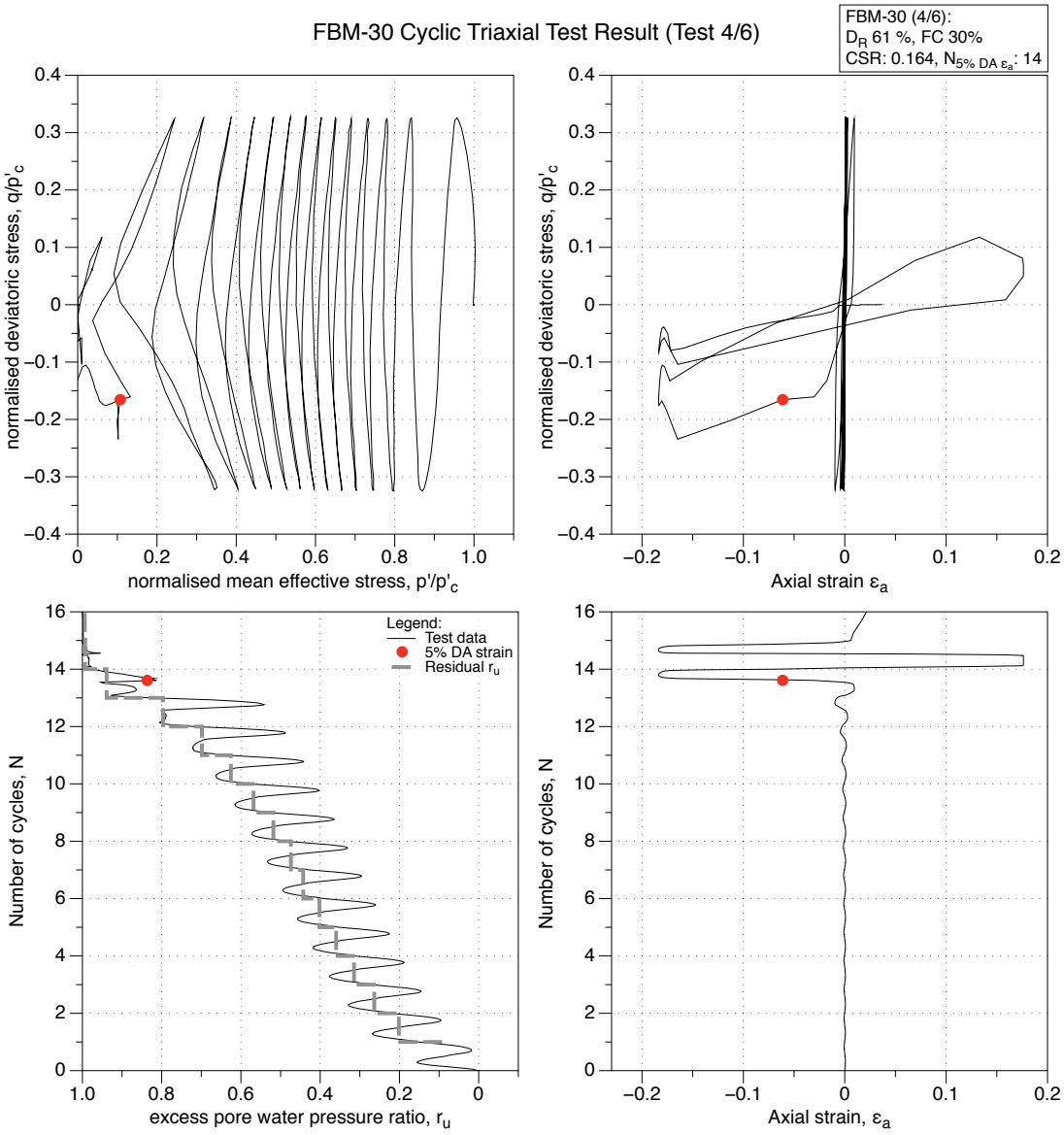

Figure 4.53: FBM with 30 % fines, moist tamped reconstituted sample, cyclic triaxial test result (test 4/6).

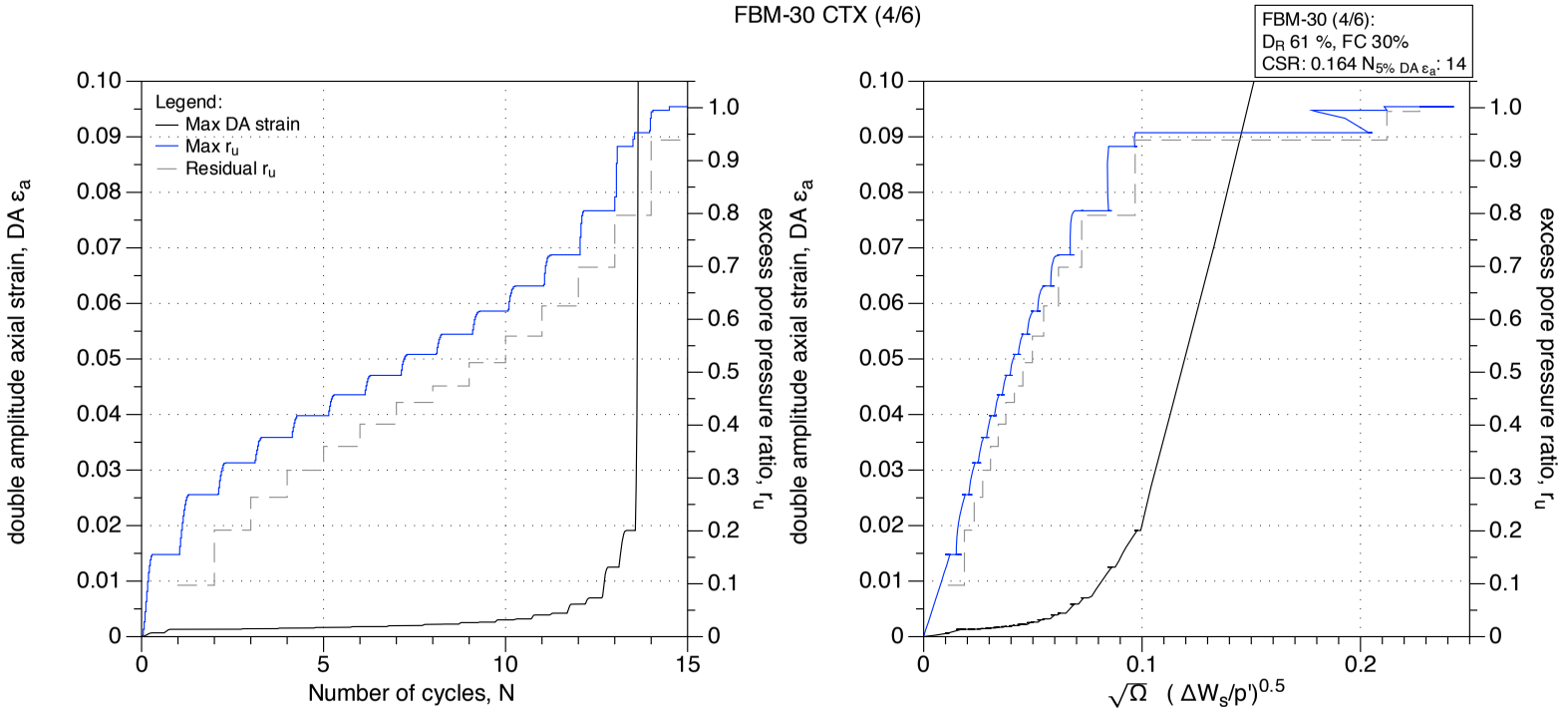

Figure 4.54: FBM-30, CTX result (test 4/6). Development of strain and excess pore water pressure with number of cycles and normalised shear work.

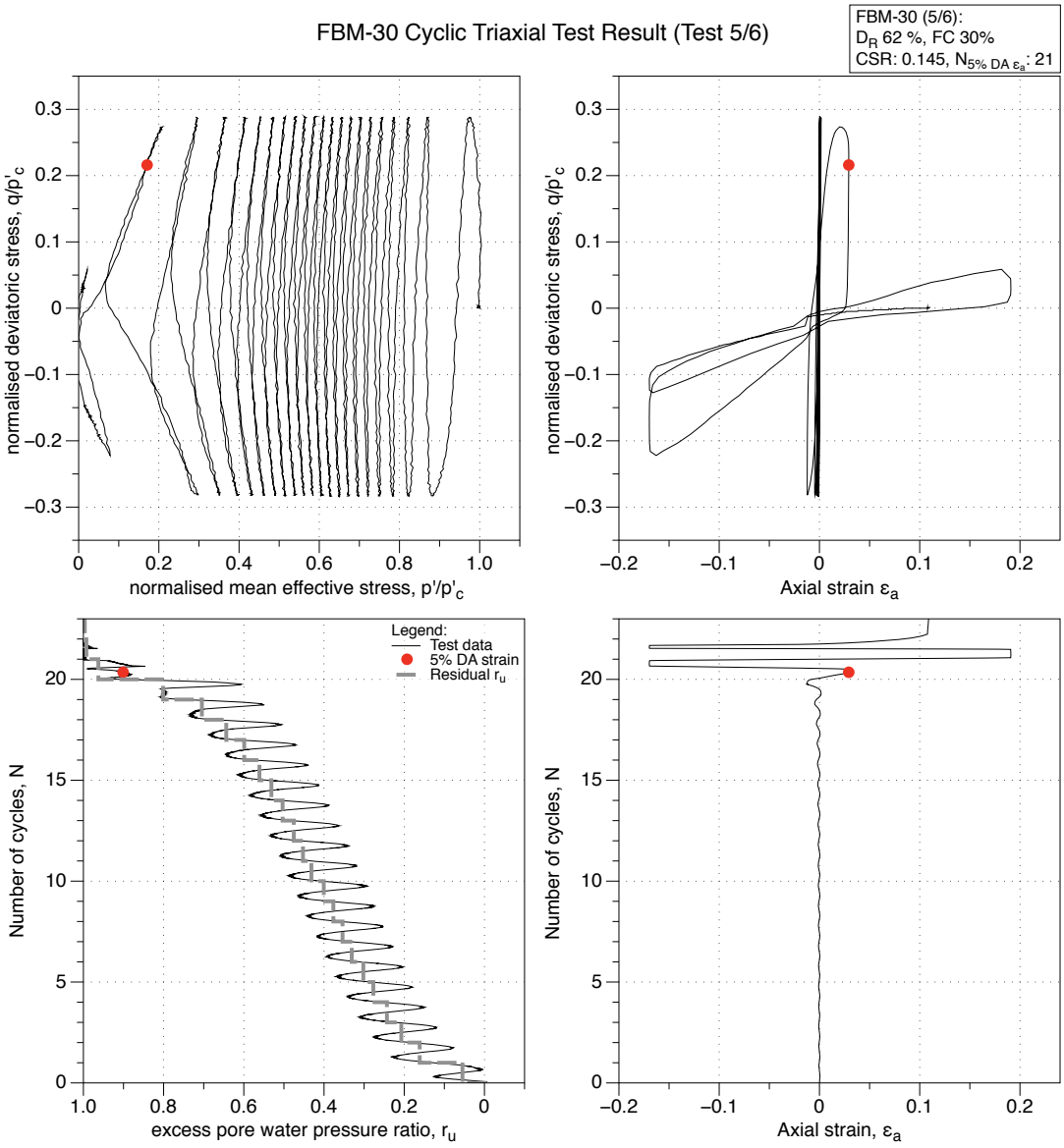

Figure 4.55: FBM with 30 % fines, moist tamped reconstituted sample, cyclic triaxial test result (test 5/6).

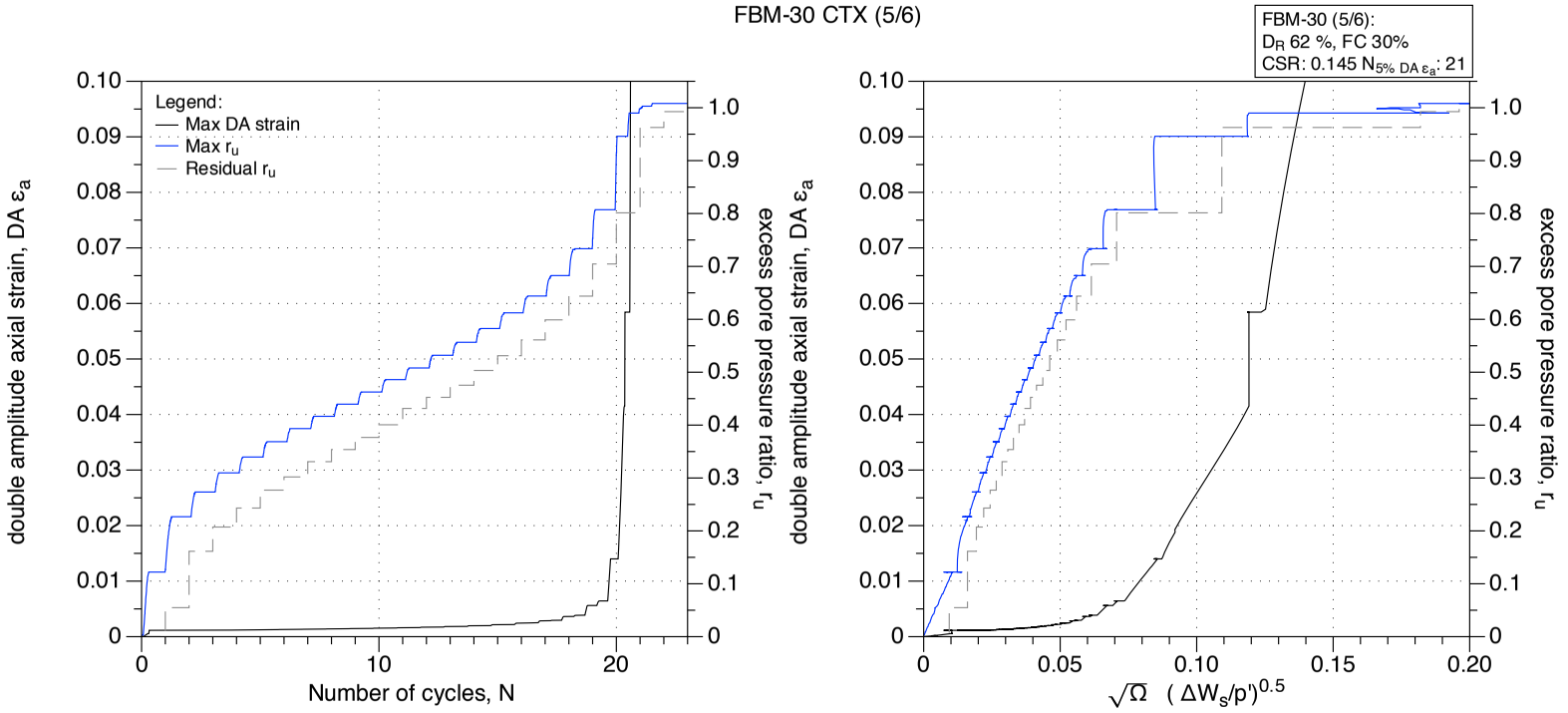

Figure 4.56: FBM-30, CTX result (test 5/6). Development of strain and excess pore water pressure with number of cycles and normalised shear work.

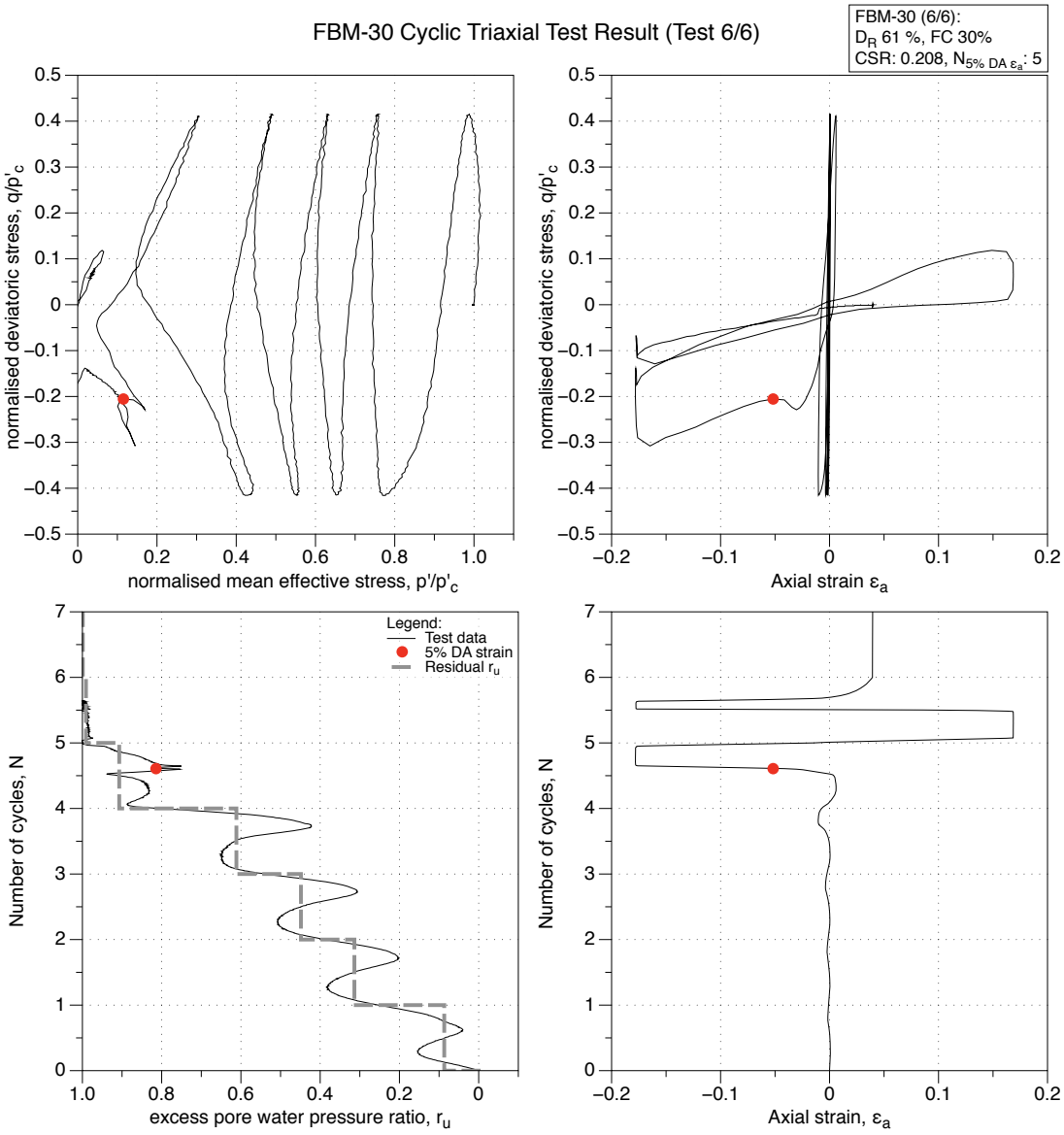

Figure 4.57: FBM with 30 % fines, moist tamped reconstituted sample, cyclic triaxial test result (test 6/6).

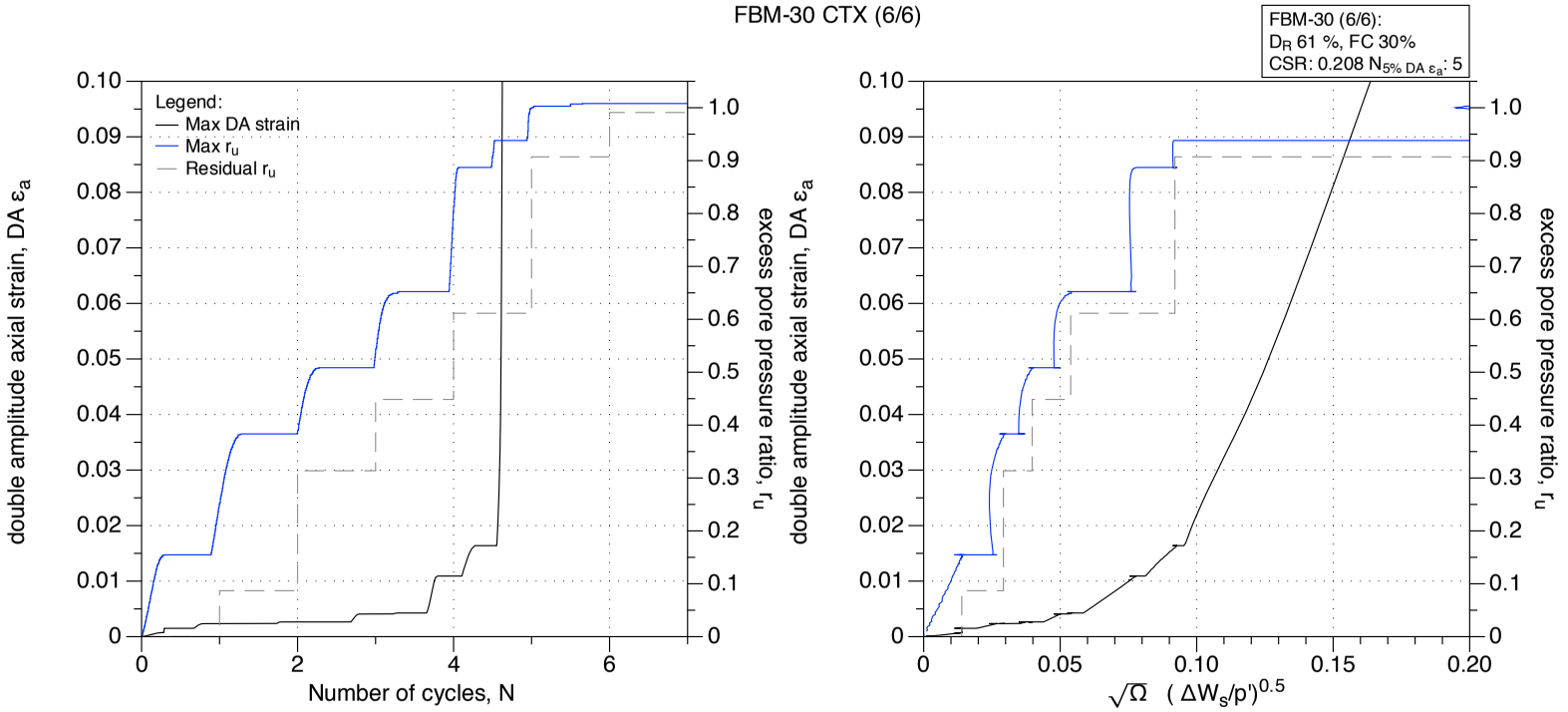

Figure 4.58: FBM-30, CTX result (test 6/6). Development of strain and excess pore water pressure with number of cycles and normalised shear work.

4.2 Triaxial testing on Gel-push samples from borehole K1.

This section of Appendix D presents individual triaxial test results performed on Gel-push specimens obtained from Borehole K1.

4.2.1 K1 GP Monotonic Triaxial Tests

Plots include the effective stress path, stress strain plot, state stress path, and volumetric strain-axial strain (drained test) or excess pore pressure ratio-axial strain (undrained test) plots. Additional plots for each monotonic test include stress-dilatancy plots, stiffness degradation curves, normalised shear work, and normalised shear work gradient plots with strain.

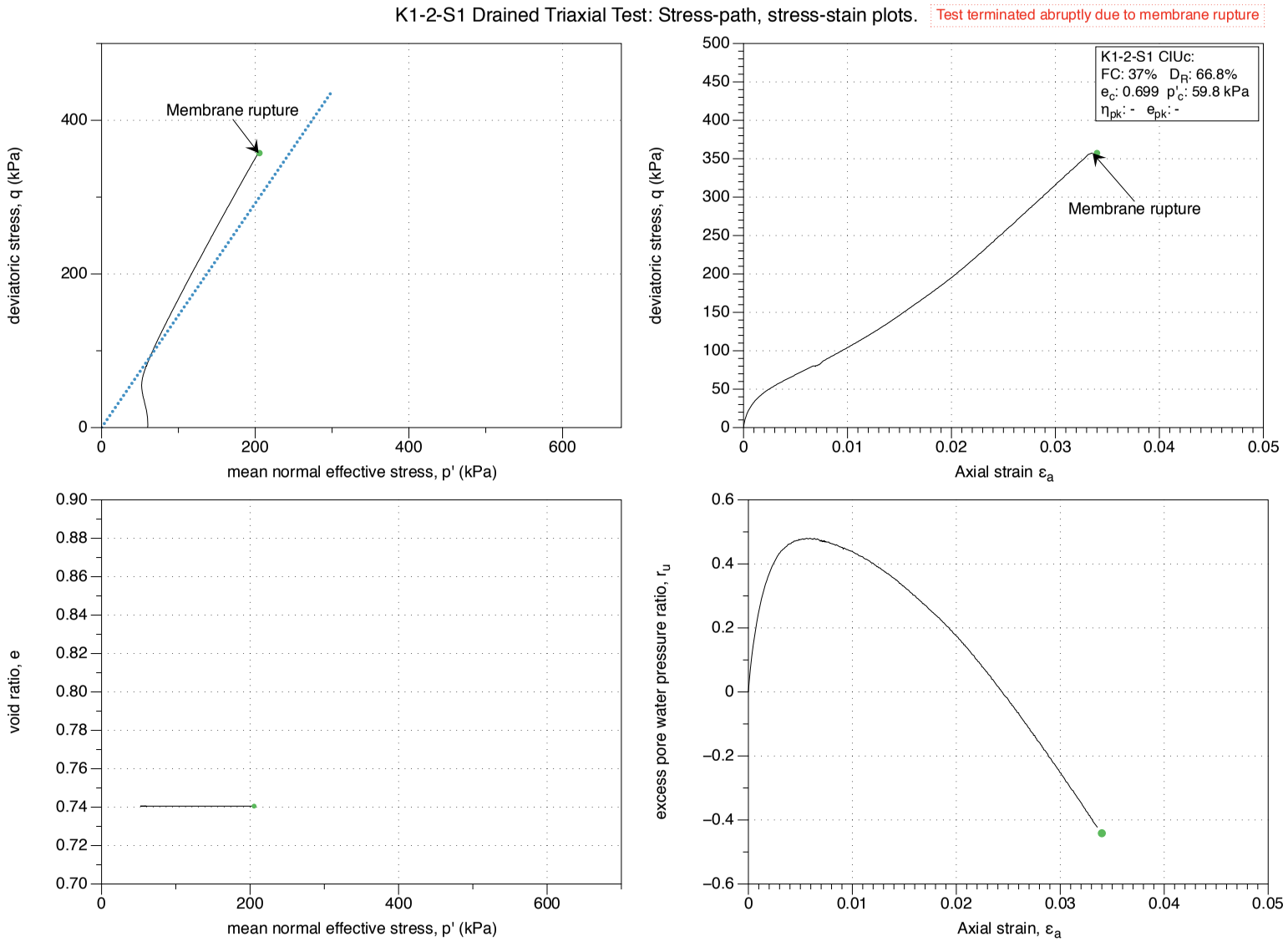

Figure 4.59: K1-2-S1 GP sample, undrained monotonic triaxial test (CIU_C). Stress-path and stress-strain plots.

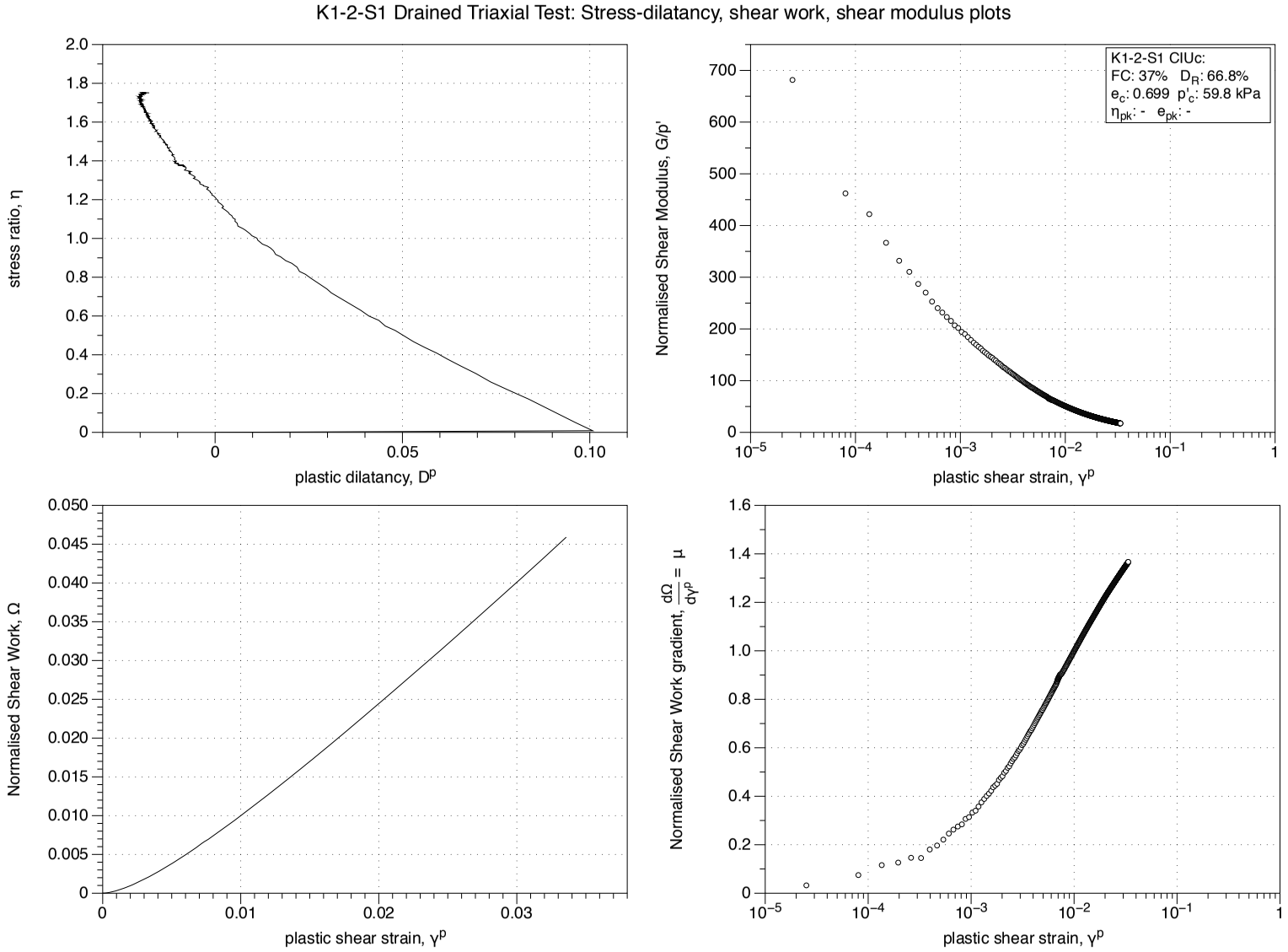

Figure 4.60: K1-2-S1 GP sample, undrained monotonic triaxial test (CIU_C). Stress-path and stress-strain plots. Stress-dilatancy, shear work, stiffness degradation plots.

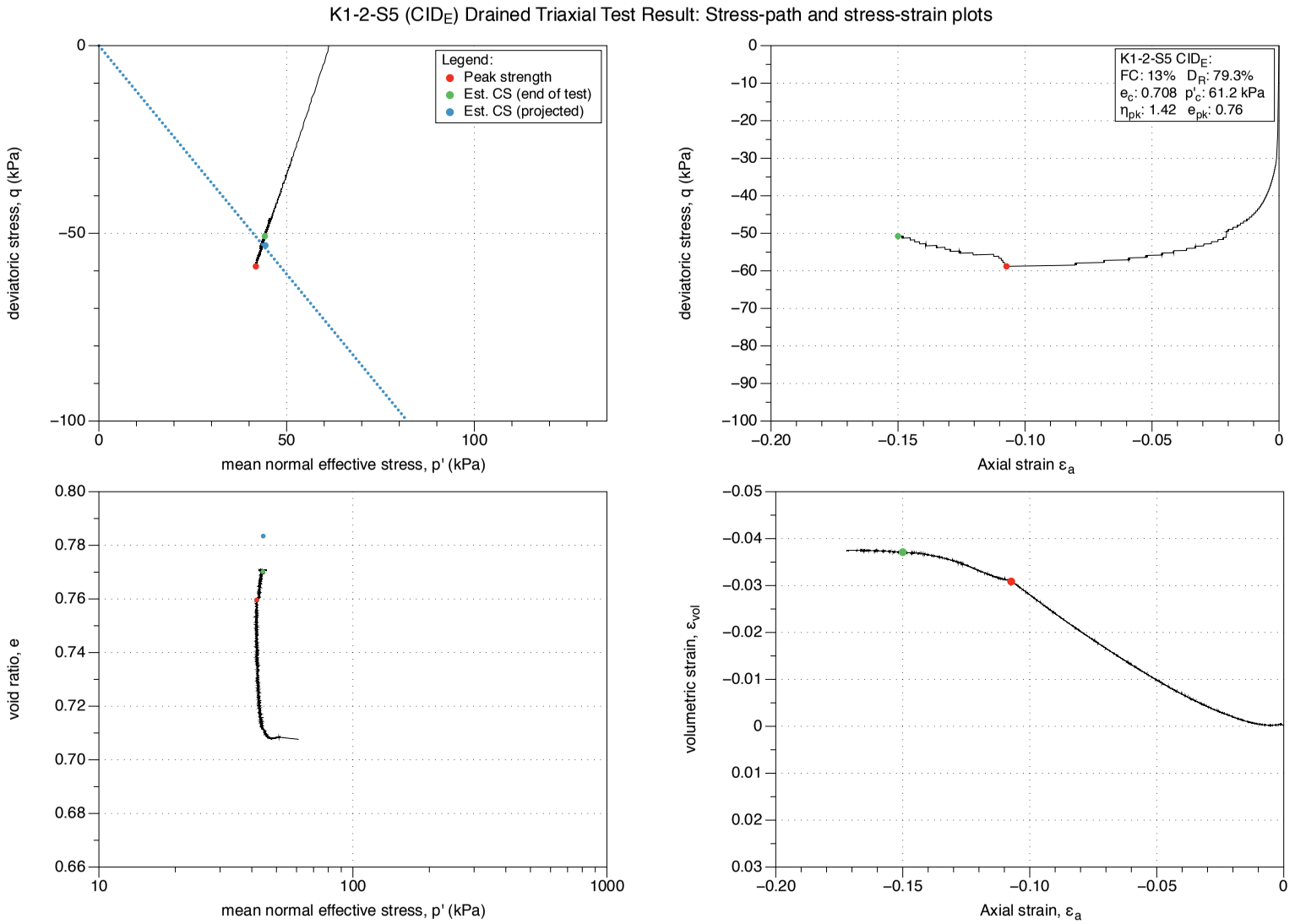

Figure 4.61: K1-2-S5 GP sample, drained monotonic triaxial test (CID_E). Stress-path and stress-strain plots.

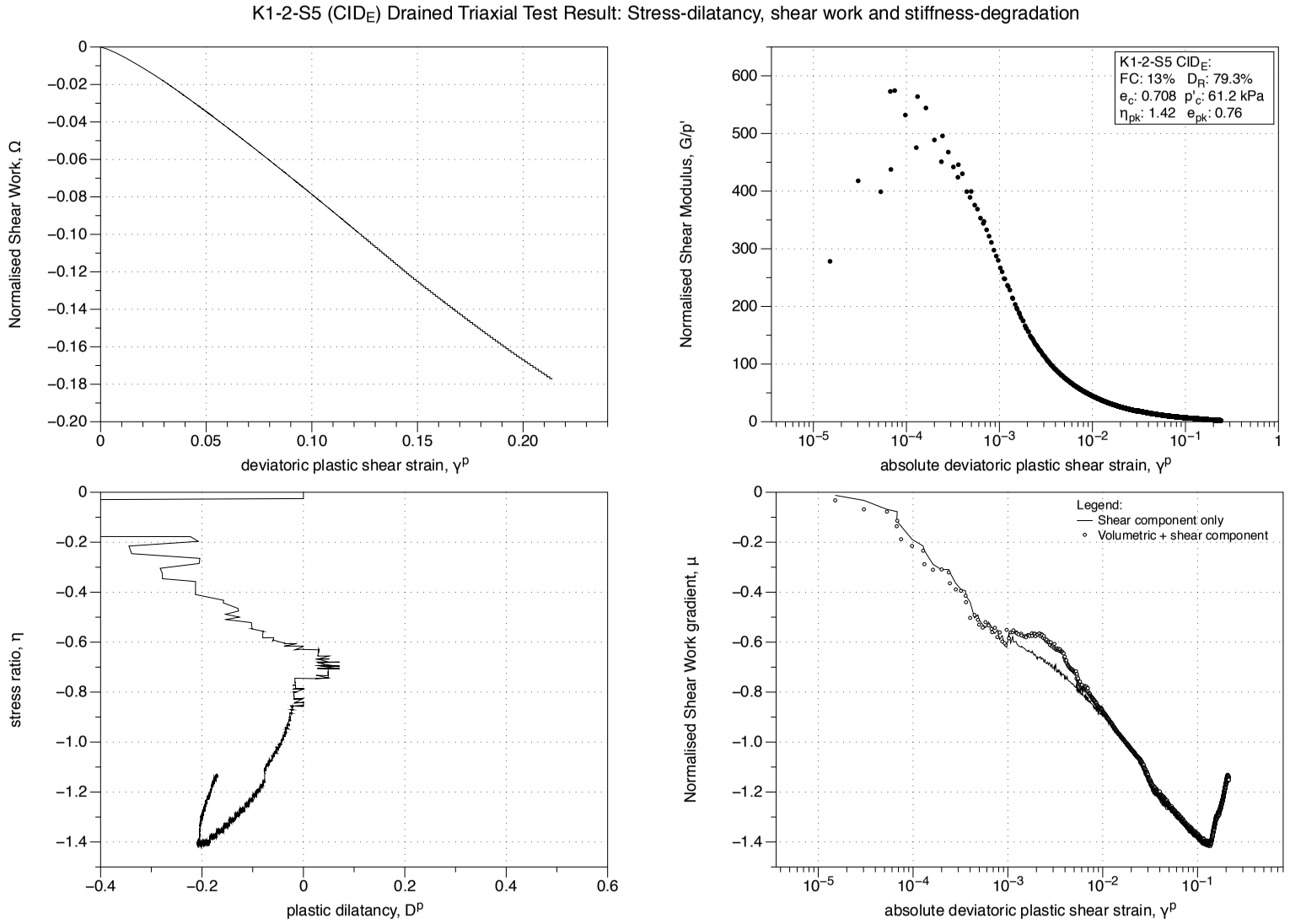

Figure 4.62: K1-2-S5 GP sample, drained monotonic triaxial test (CID_E). Stress-path and stress-strain plots. Stress-dilatancy, shear work, stiffness degradation plots.

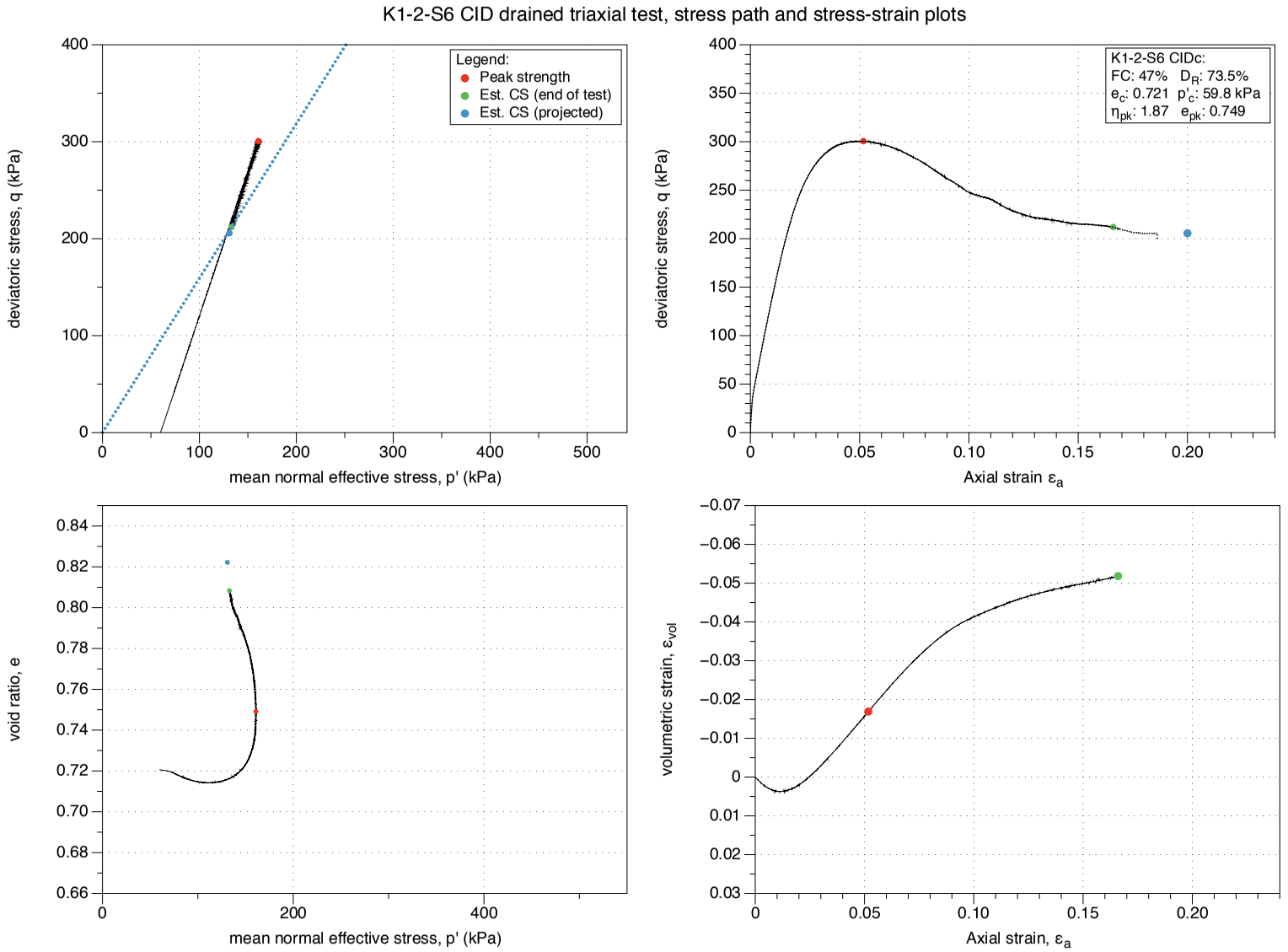

Figure 4.63: K1-2-S6 GP sample, drained monotonic triaxial test (CID_C). Stress-path and stress-strain plots.

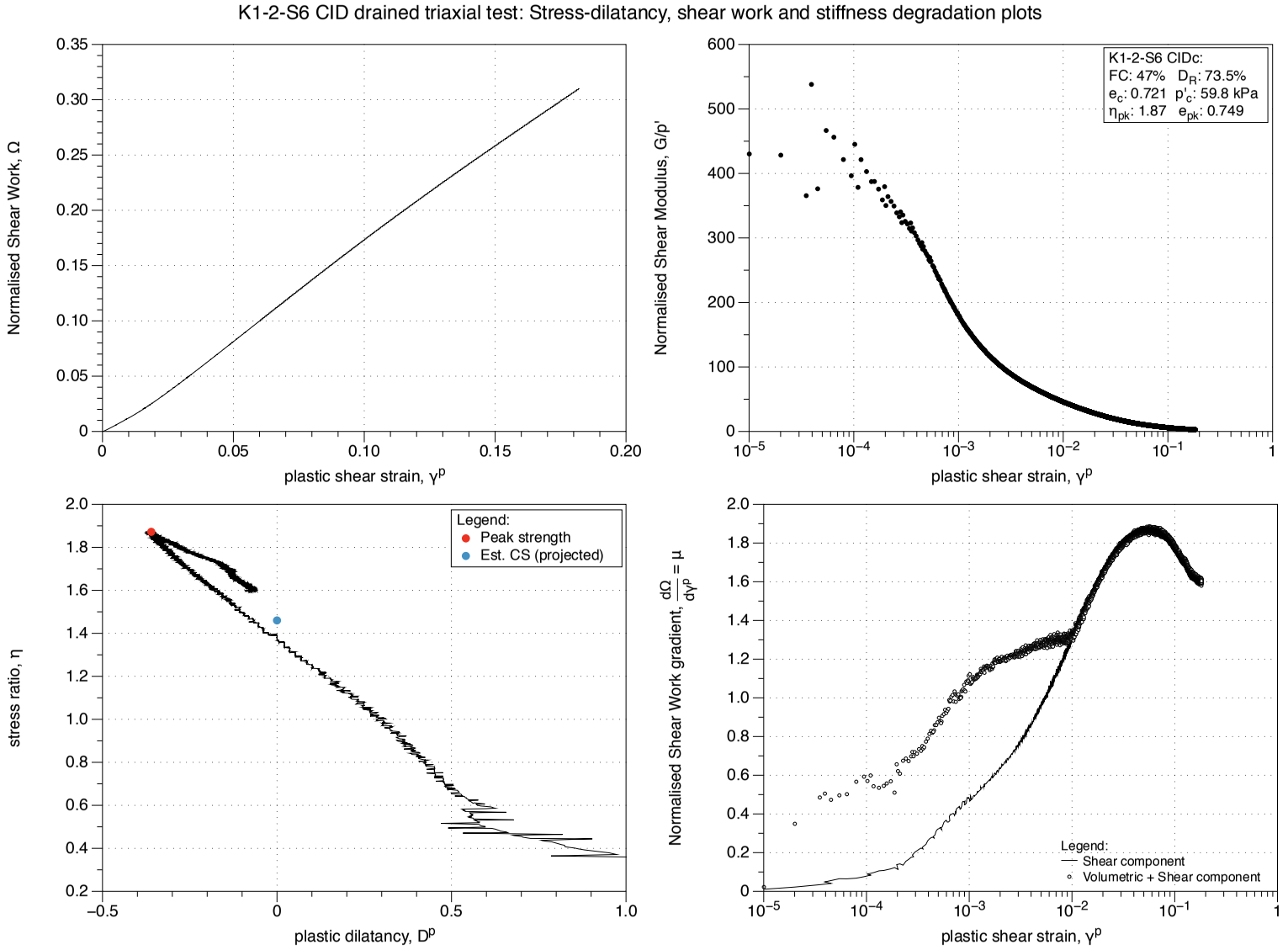

Figure 4.64: K1-2-S6 GP sample, drained monotonic triaxial test (CID_C). Stress-path and stress-strain plots. Stress-dilatancy, shear work, stiffness degradation plots.

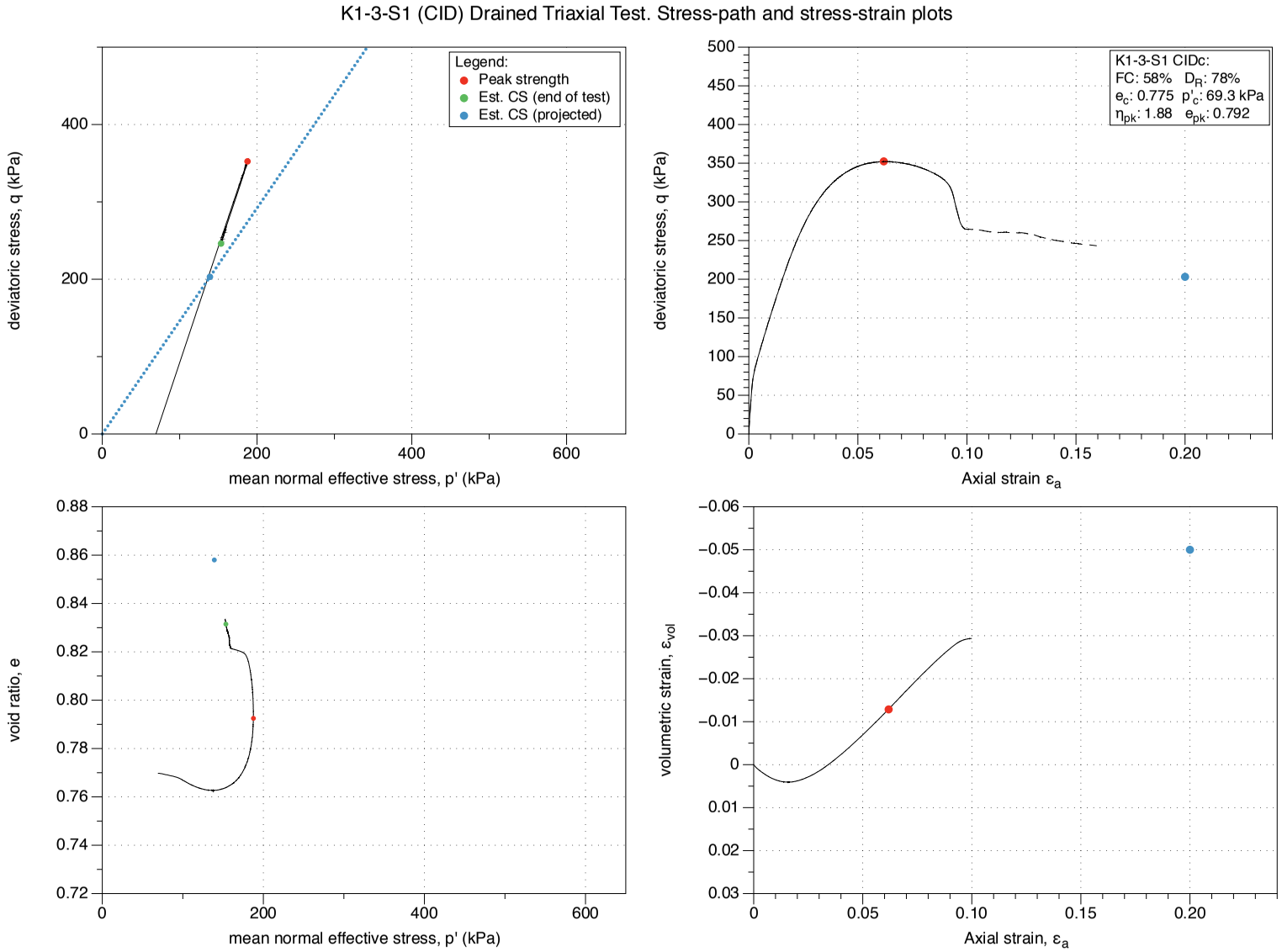

Figure 4.65: K1-3-S1 GP sample, drained monotonic triaxial test (CID_C). Stress-path and stress-strain plots.

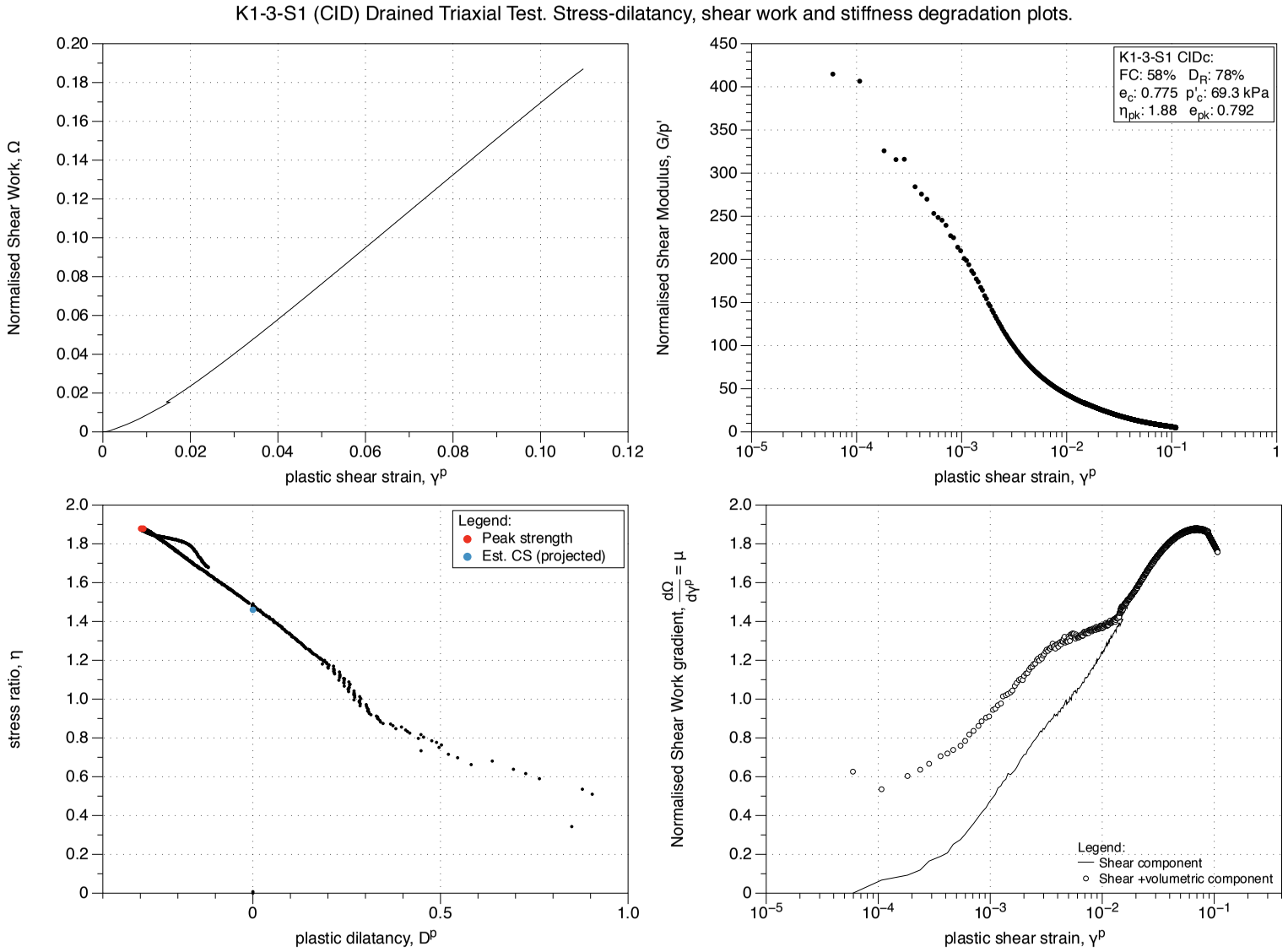

Figure 4.66: K1-3-S1 GP sample, drained monotonic triaxial test (CID_C). Stress-path and stress-strain plots. Stress-dilatancy, shear work, stiffness degradation plots.

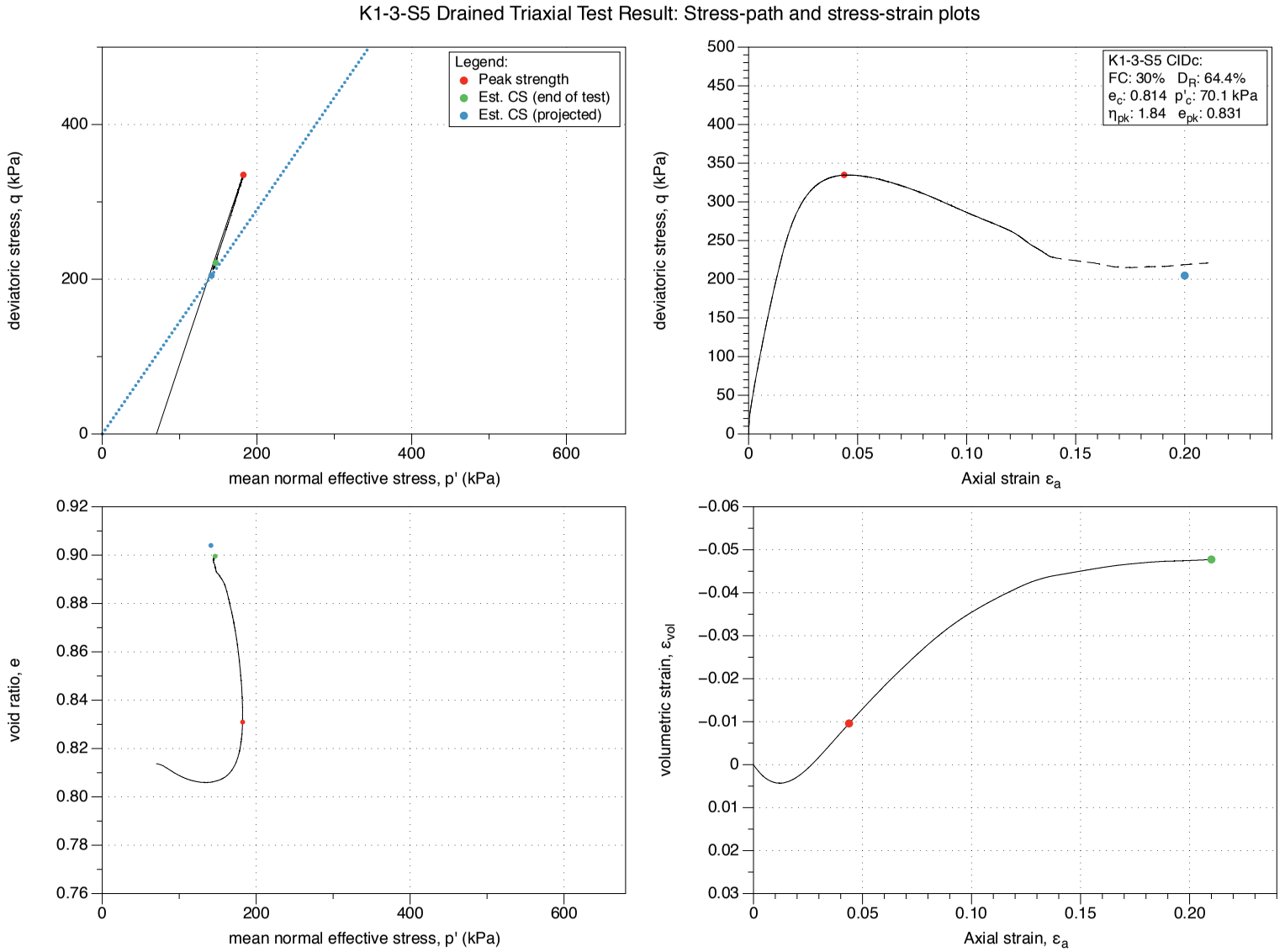

Figure 4.67: K1-3-S5 GP sample, drained monotonic triaxial test (CID_C). Stress-path and stress-strain plots.

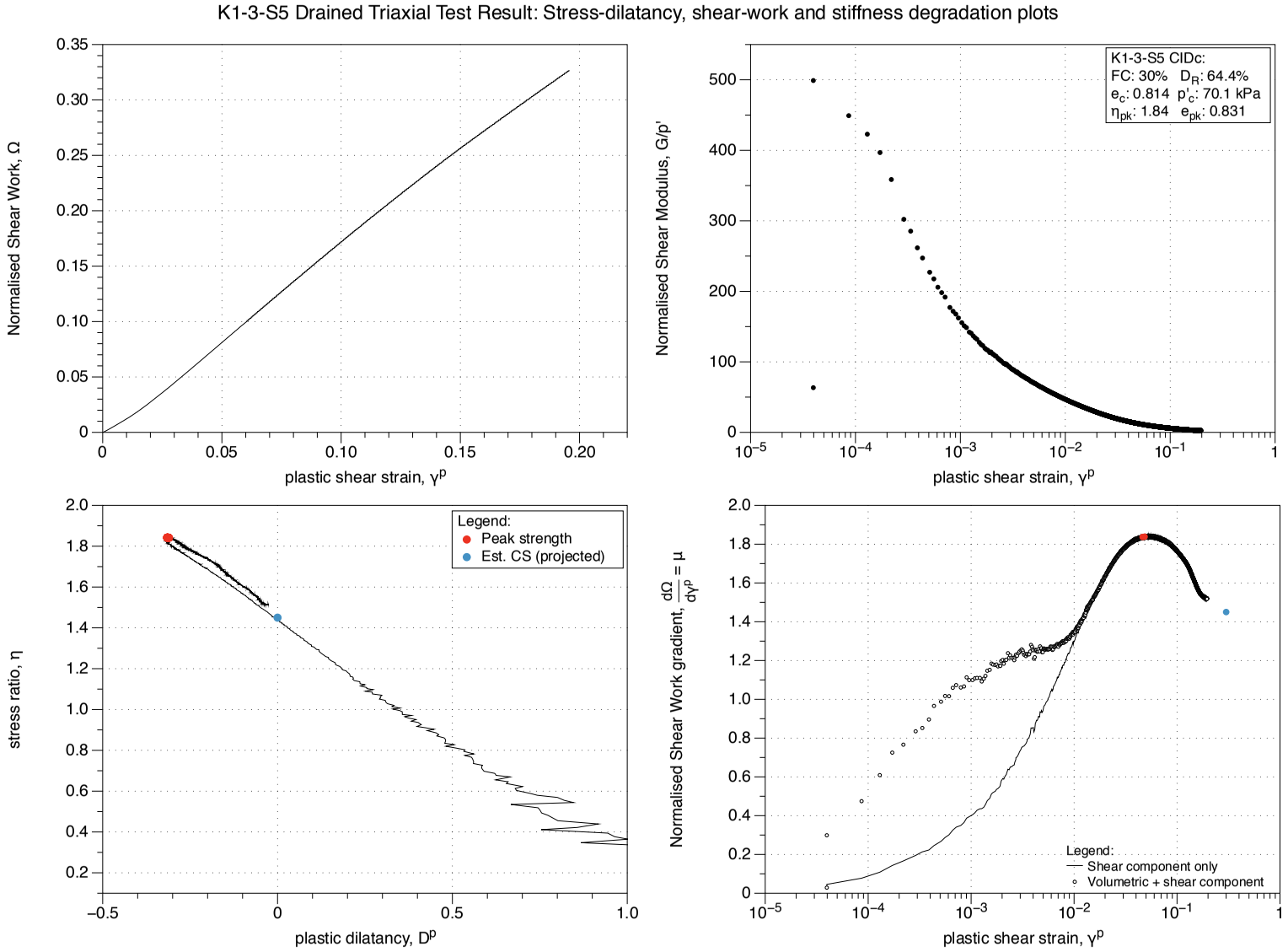

Figure 4.68: K1-3-S5 GP sample, drained monotonic triaxial test (CID_C). Stress-path and stress-strain plots. Stress-dilatancy, shear work, stiffness degradation plots.

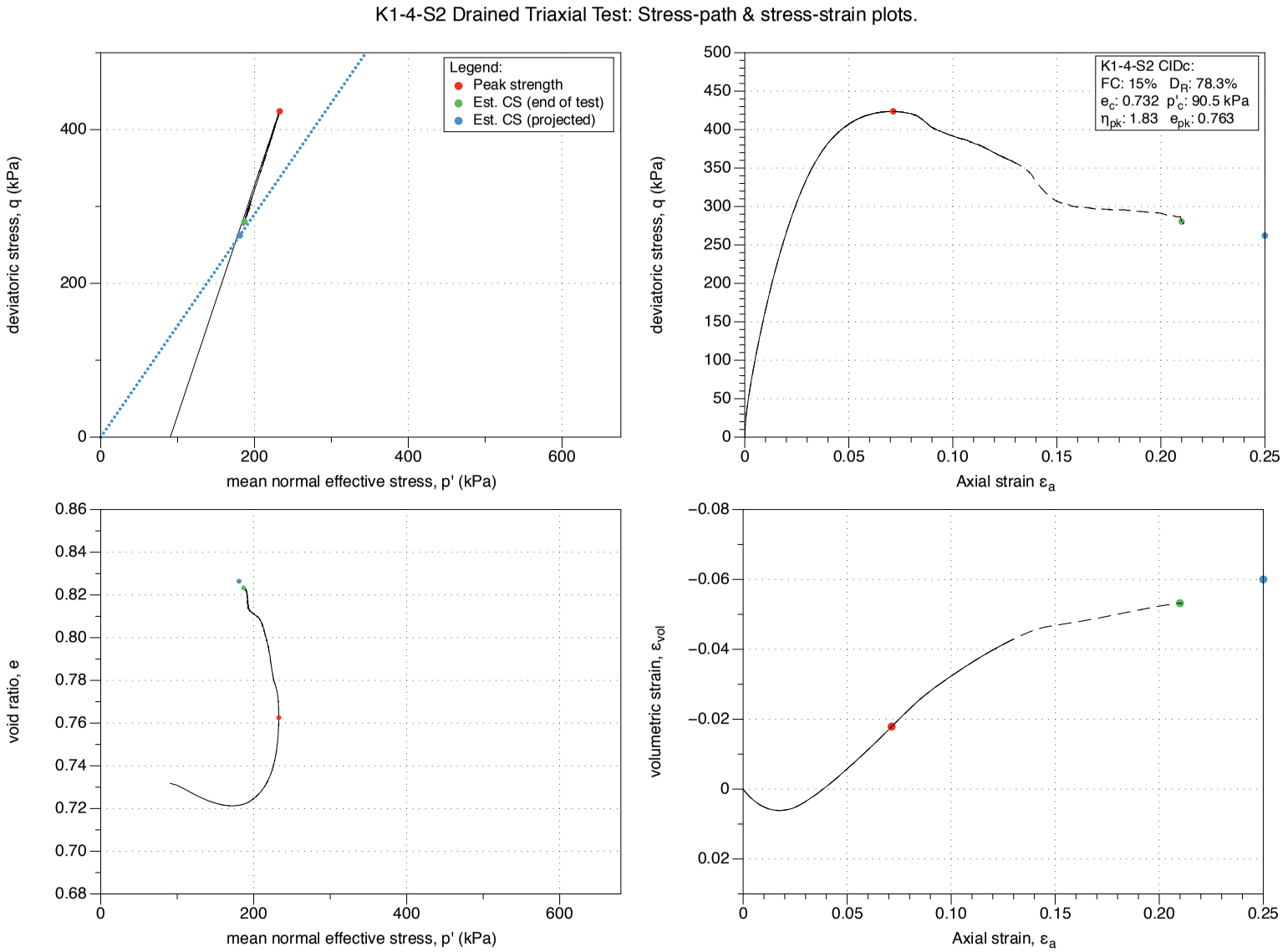

Figure 4.69: K1-4-S2 GP sample, drained monotonic triaxial test (CID_C). Stress-path and stress-strain plots.

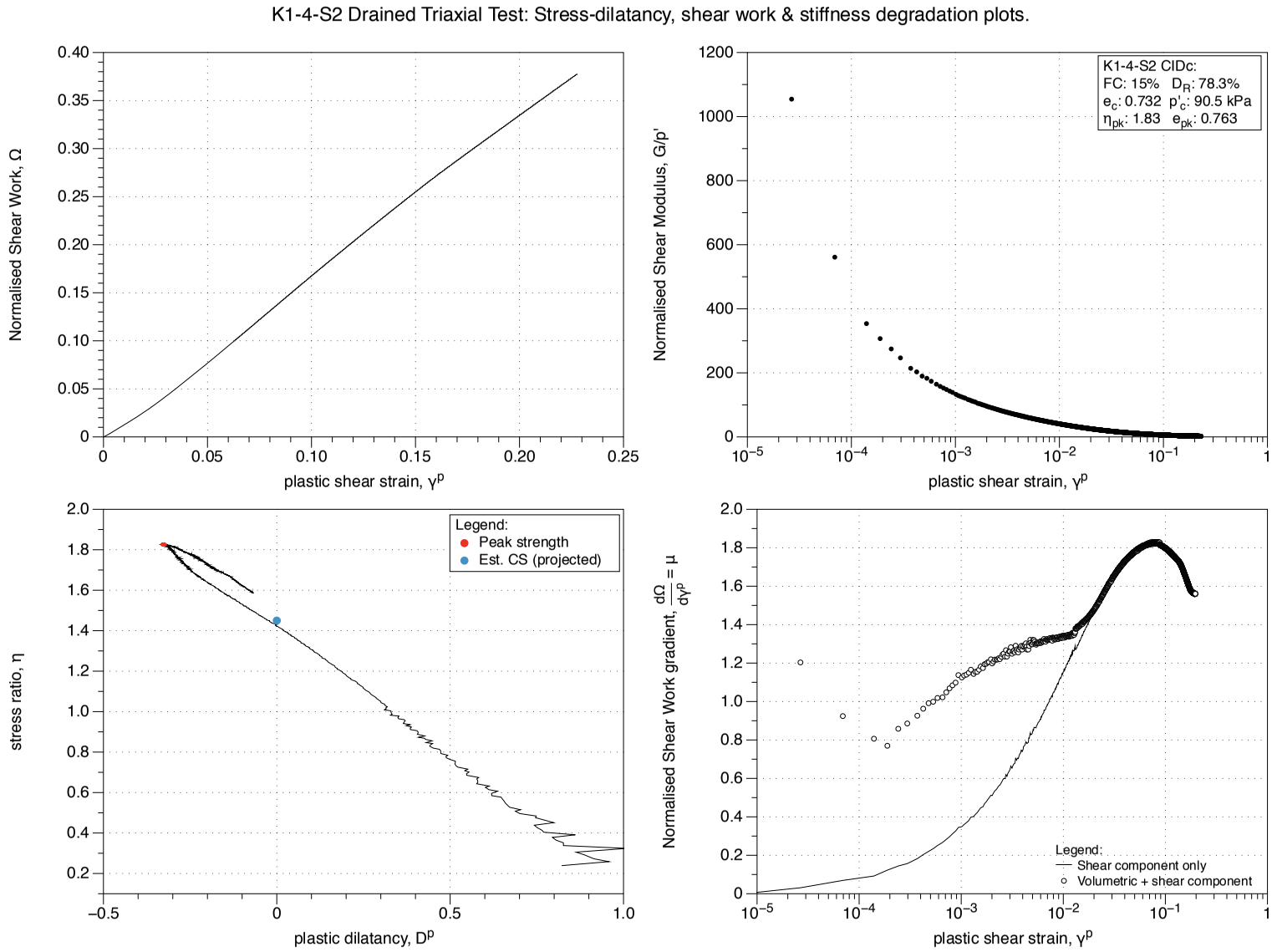

Figure 4.70: K1-4-S2 GP sample, drained monotonic triaxial test (CID_C). Stress-path and stress-strain plots. Stress-dilatancy, shear work, stiffness degradation plots.

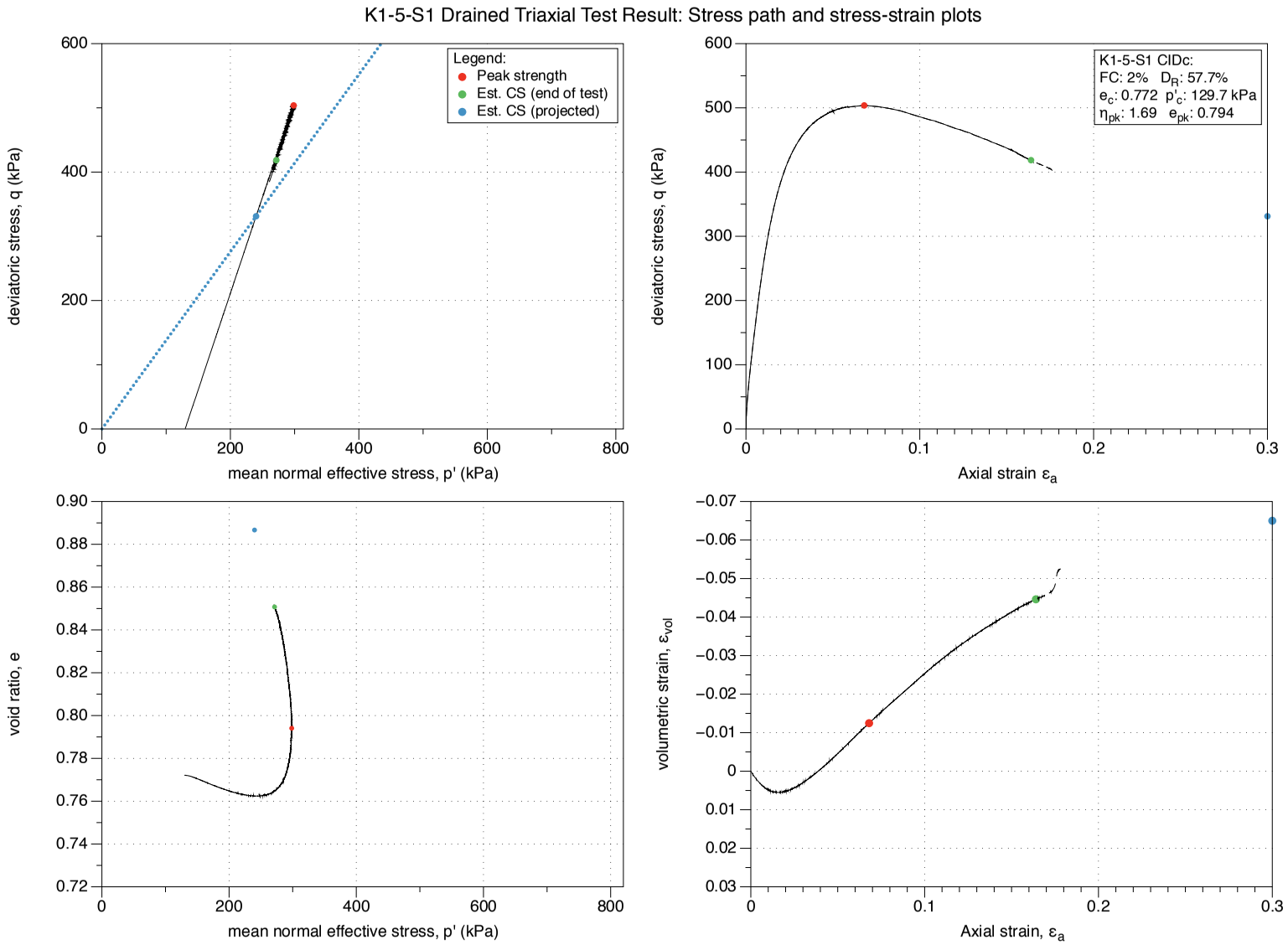

Figure 4.71: K1-5-S1 GP sample, drained monotonic triaxial test (CID_C). Stress-path and stress-strain plots.

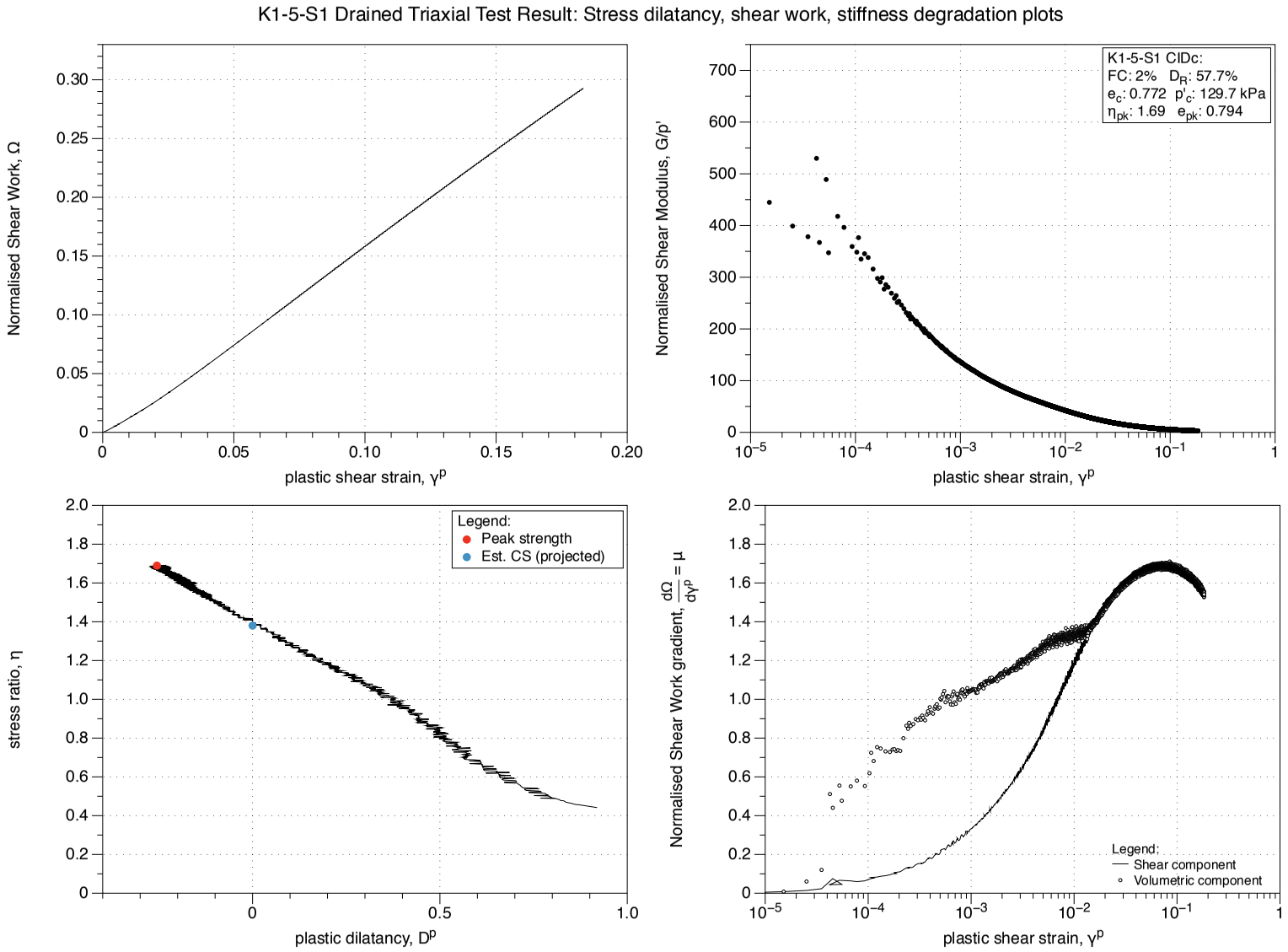

Figure 4.72: K1-5-S1 GP sample, drained monotonic triaxial test (CID_C). Stress-path and stress-strain plots. Stress-dilatancy, shear work, stiffness degradation plots.

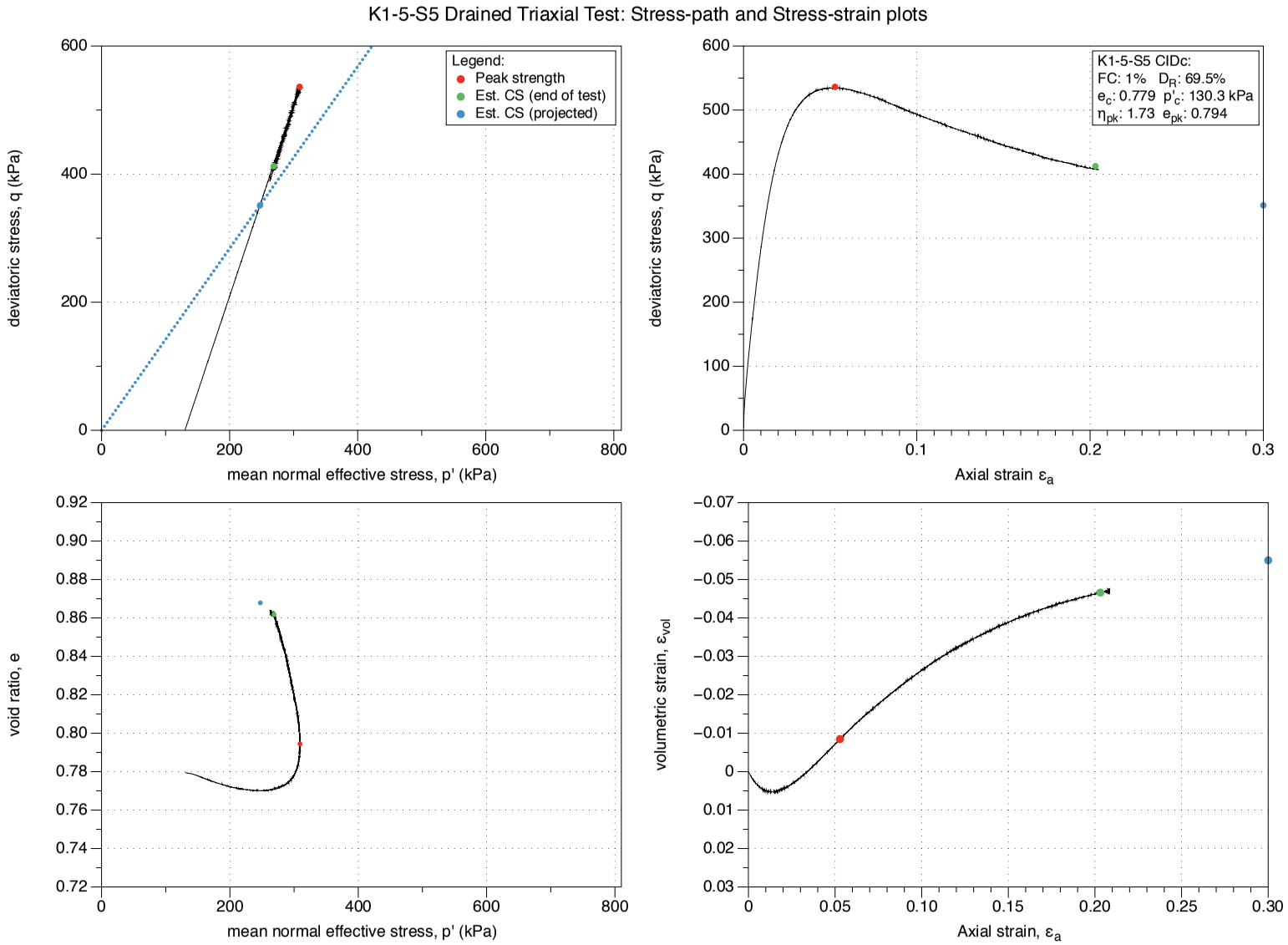

Figure 4.73: K1-5-S5 GP sample, drained monotonic triaxial test (CID_C). Stress-path and stress-strain plots.

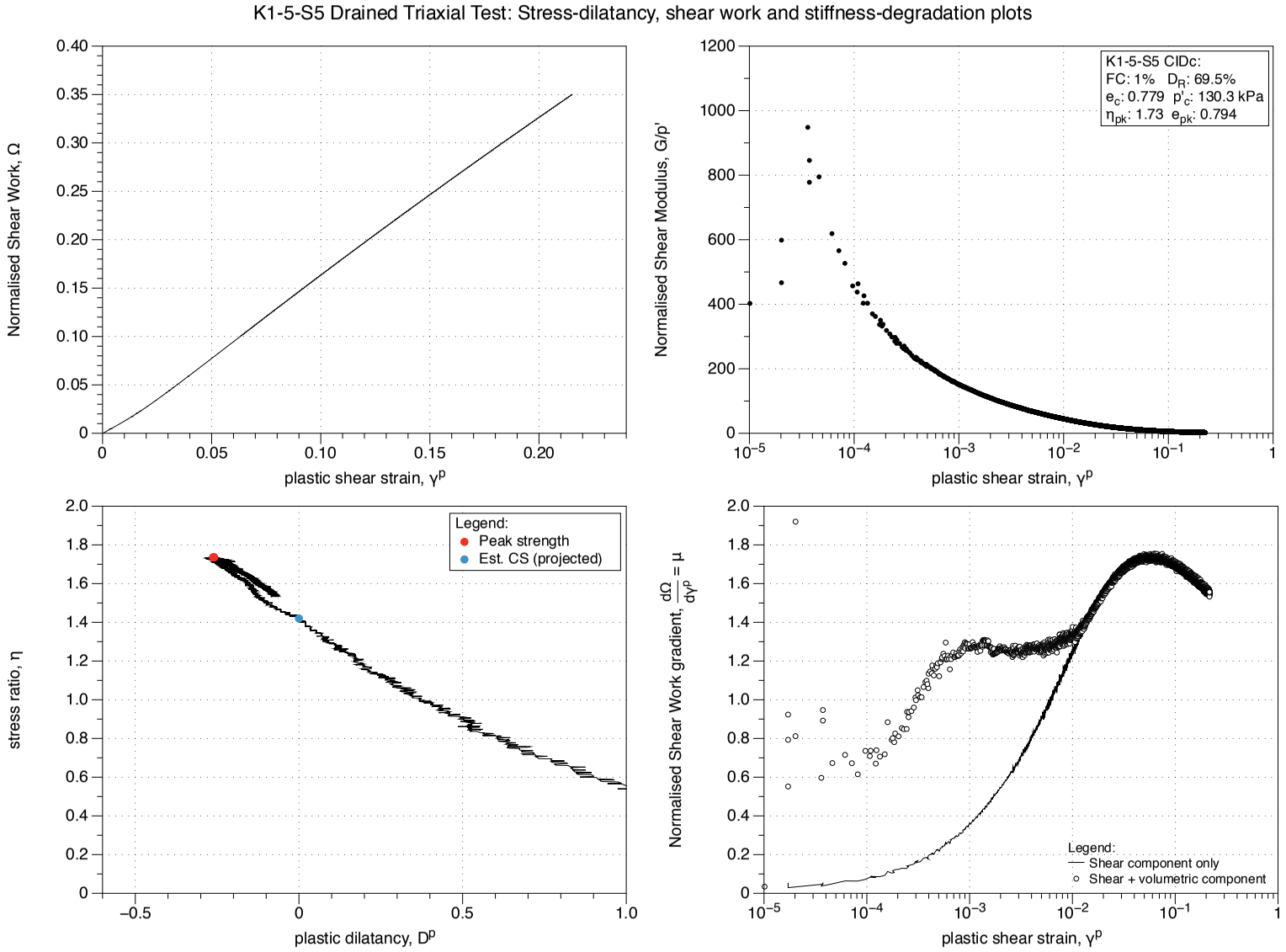

Figure 4.74: K1-5-S5 GP sample, drained monotonic triaxial test (CID_C). Stress-path and stress-strain plots. Stress-dilatancy, shear work, stiffness degradation plots.

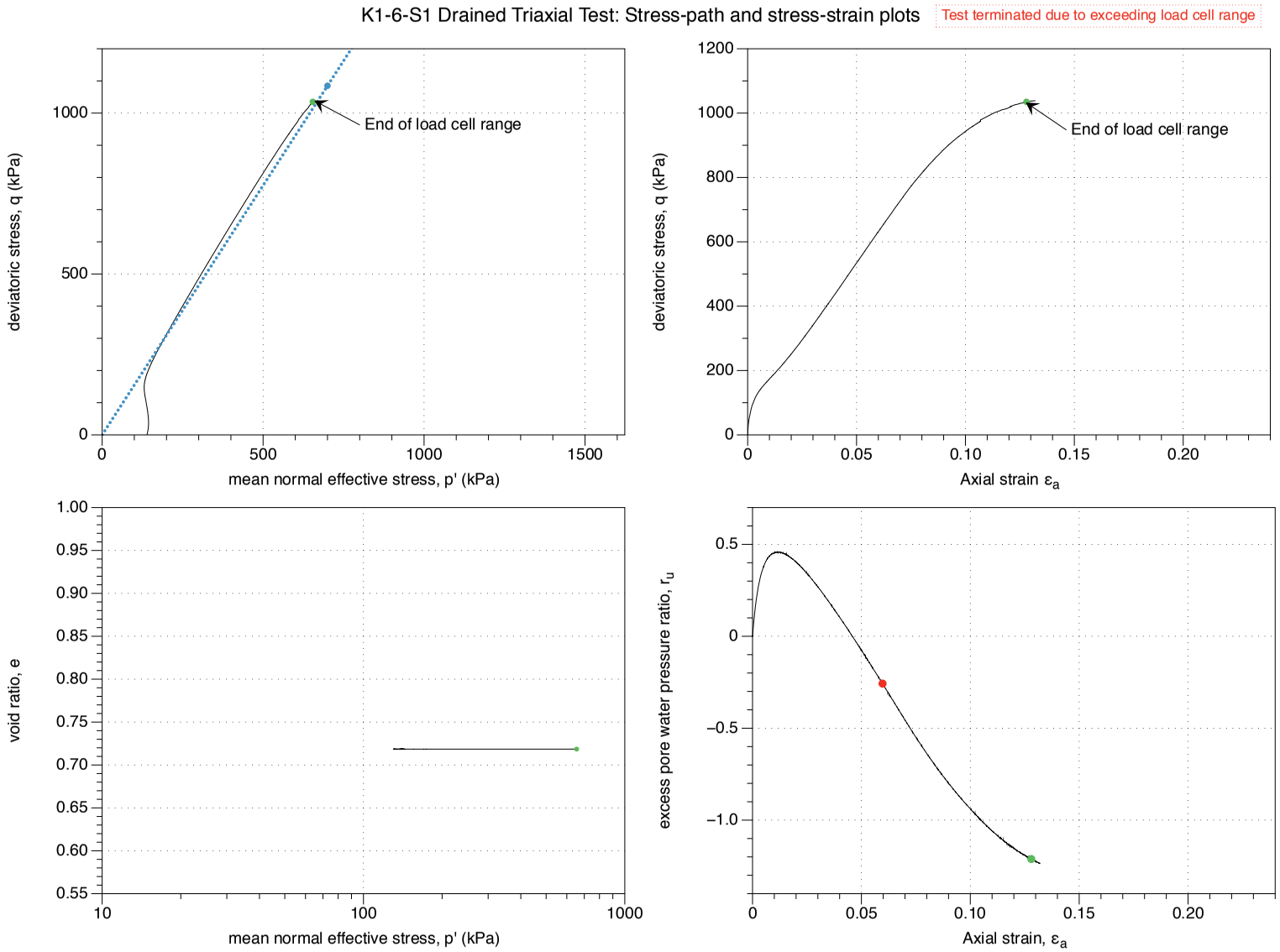

Figure 4.75: K1-6-S1 GP sample, undrained monotonic triaxial test (CIU_C). Stress-path and stress-strain plots.

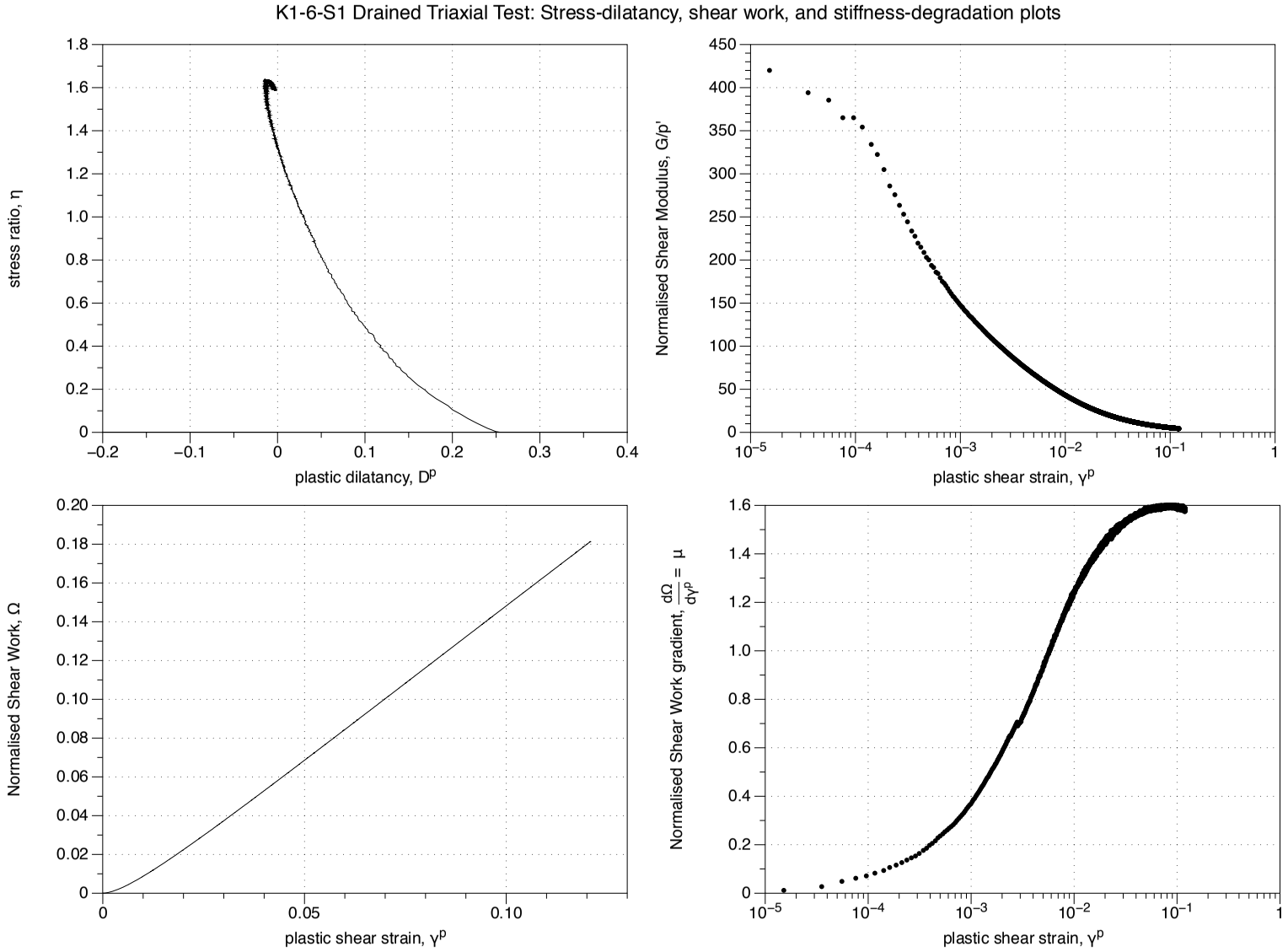

Figure 4.76: K1-6-S1 GP sample, undrained monotonic triaxial test (CIU_C). Stress-path and stress-strain plots. Stress-dilatancy, shear work, stiffness degradation plots.

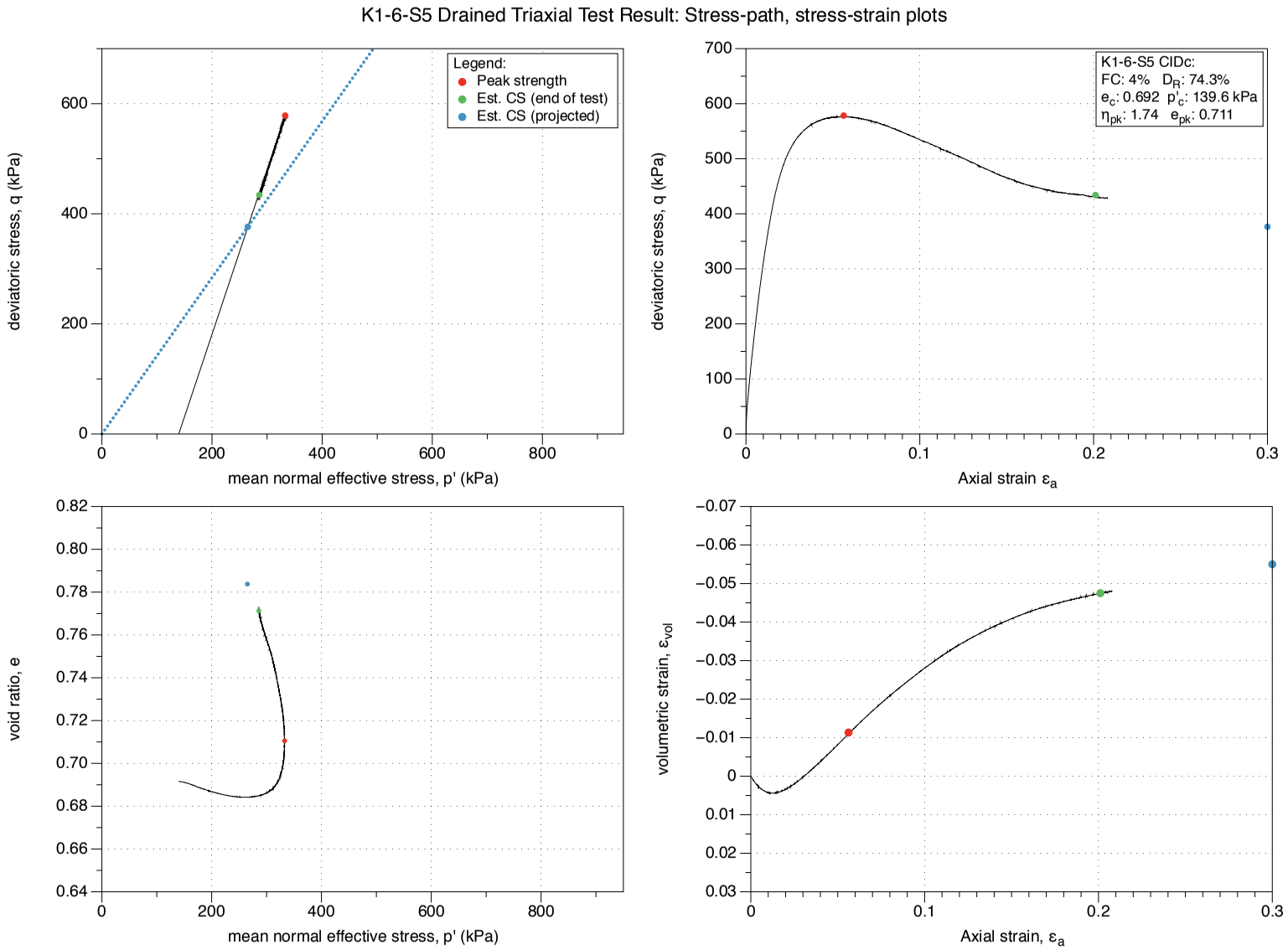

Figure 4.77: K1-6-S5 GP sample, drained monotonic triaxial test (CID_C). Stress-path and stress-strain plots.

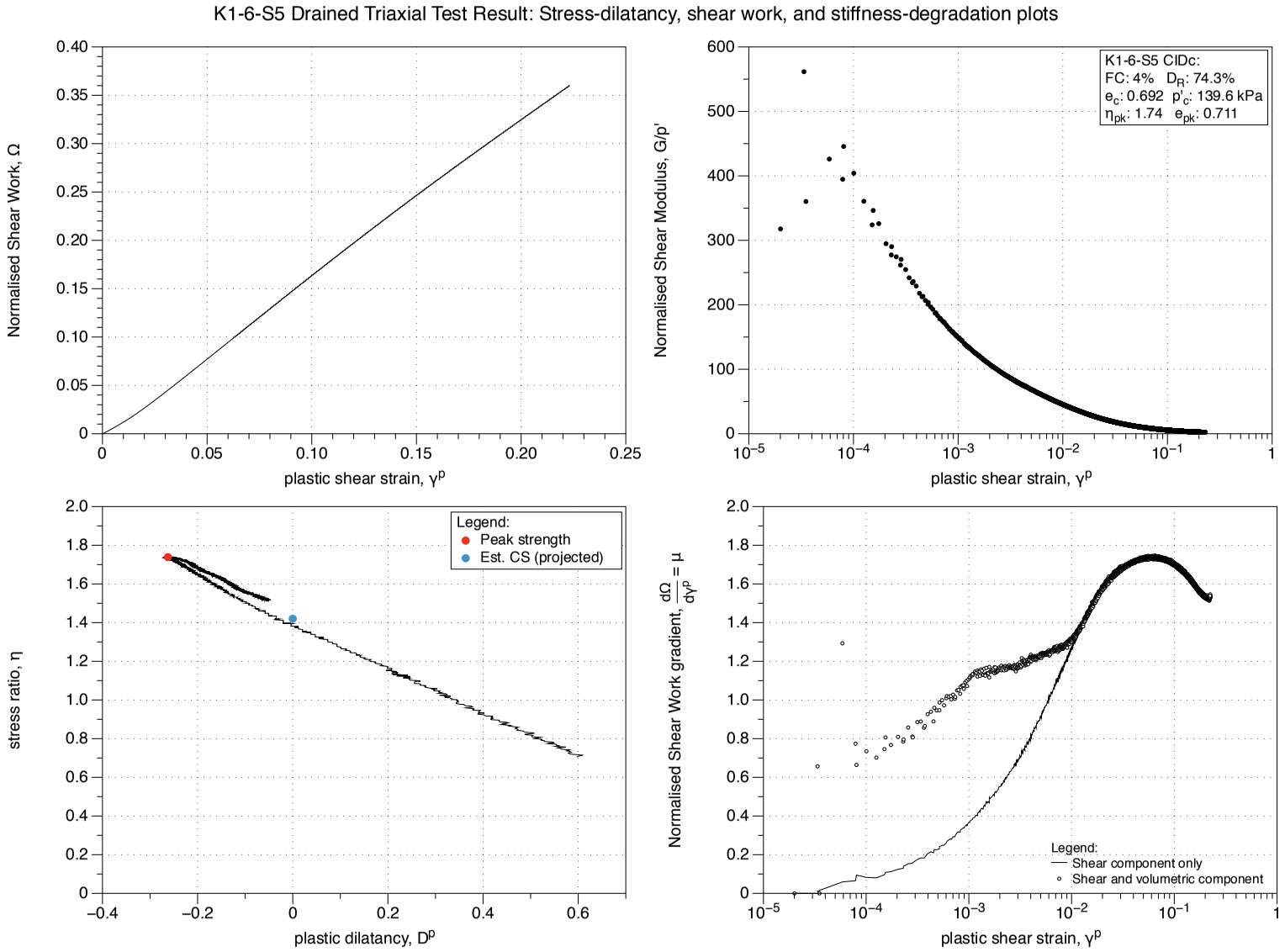

Figure 4.78: K1-6-S5 GP sample, drained monotonic triaxial test (CID_C). Stress-path and stress-strain plots. Stress-dilatancy, shear work, stiffness degradation plots.

4.2.2 K1 GP Cyclic Triaxial Tests

Plots include the normalised effective stress path, stress strain plot, and change in excess pore pressure ratio (incremental and residual) with number of cycles, and axial strain with number of cycles. Additional plots for each cyclic test depict the development of maximum double amplitude strain, excess pore pressure ratio (maximum and residual), with number of cycles and the square-root of normalised shear work.

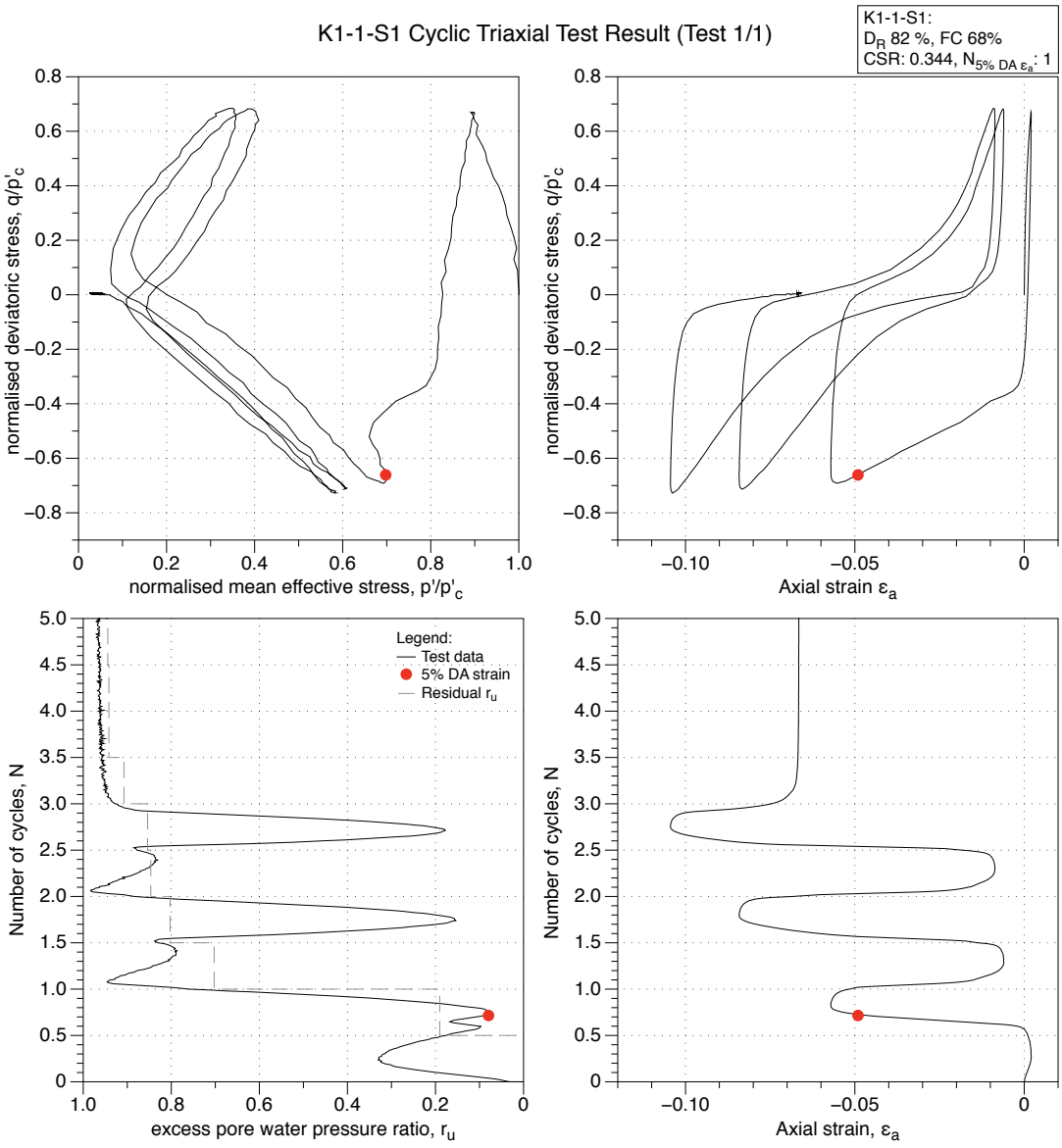

Figure 4.79: K1-1-S1 GP sample, undrained cyclic triaxial test (CTX). Effective stress-path, stress-strain, excess pore water pressure ratio and strain development plots.

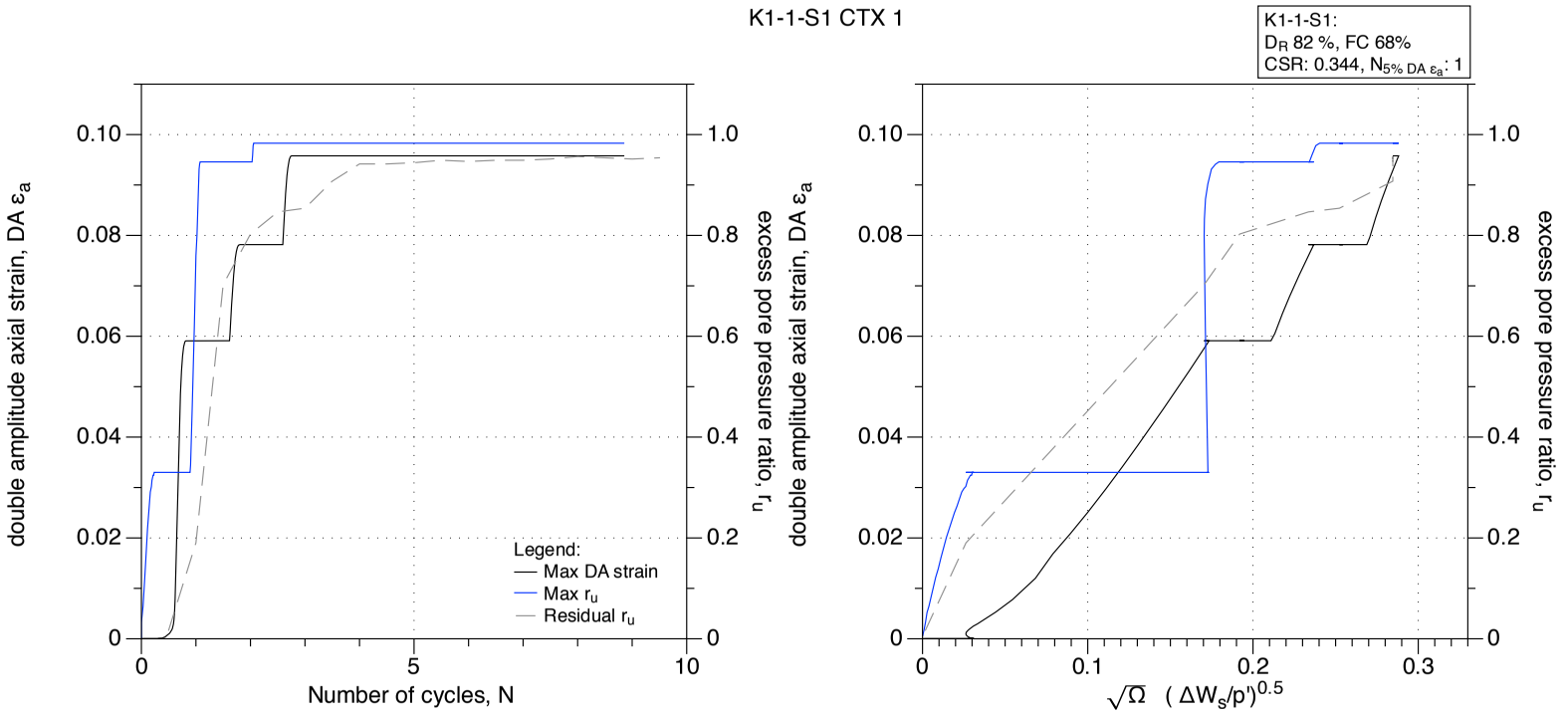

Figure 4.80: K1-1-S1 GP sample, undrained cyclic triaxial test (CTX). Development of strain and excess pore water pressure with number of cycles and normalised shear work.

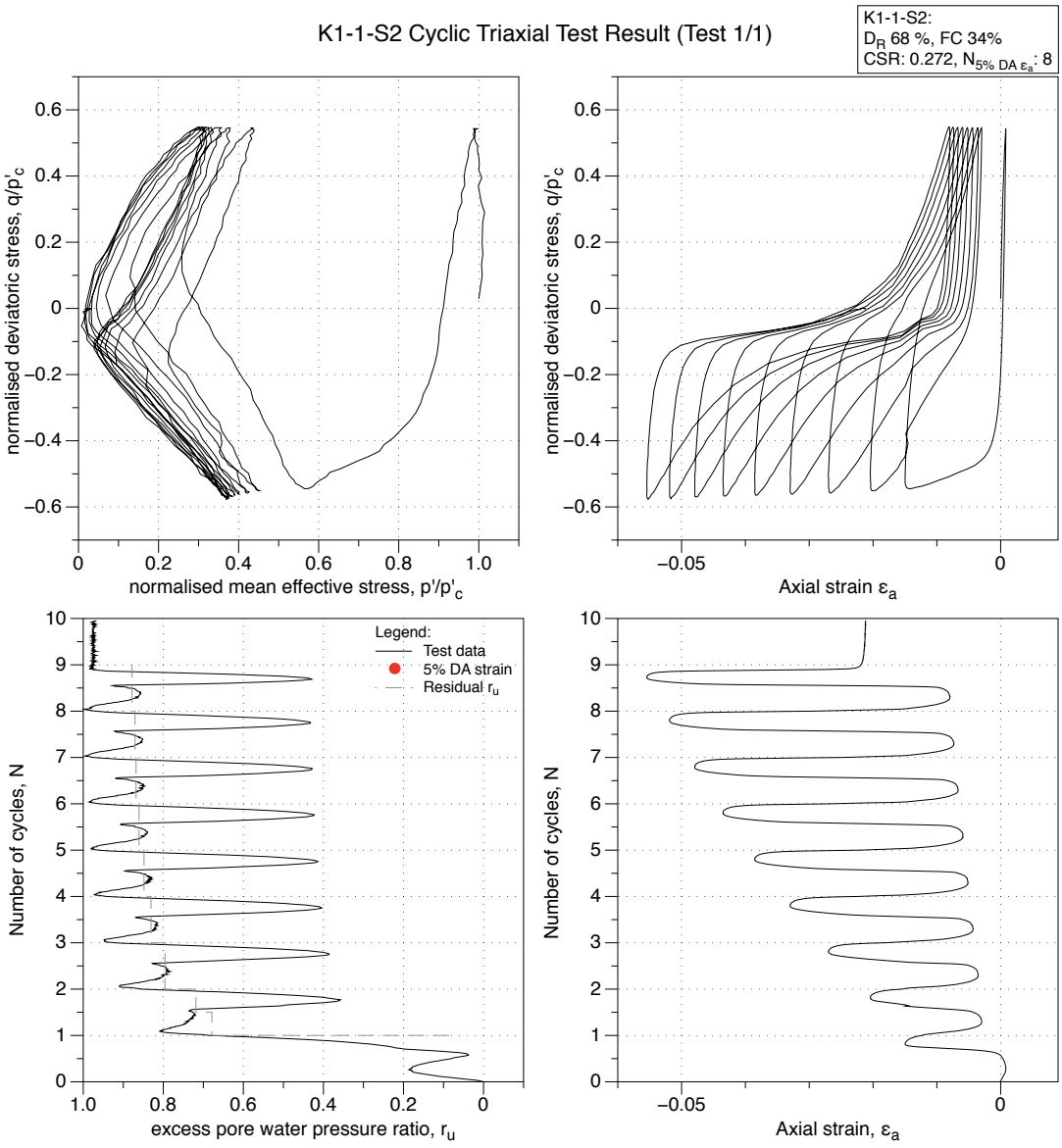

Figure 4.81: K1-1-S2 GP sample, undrained cyclic triaxial test (CTX). Effective stress-path, stress-strain, excess pore water pressure ratio and strain development plots.

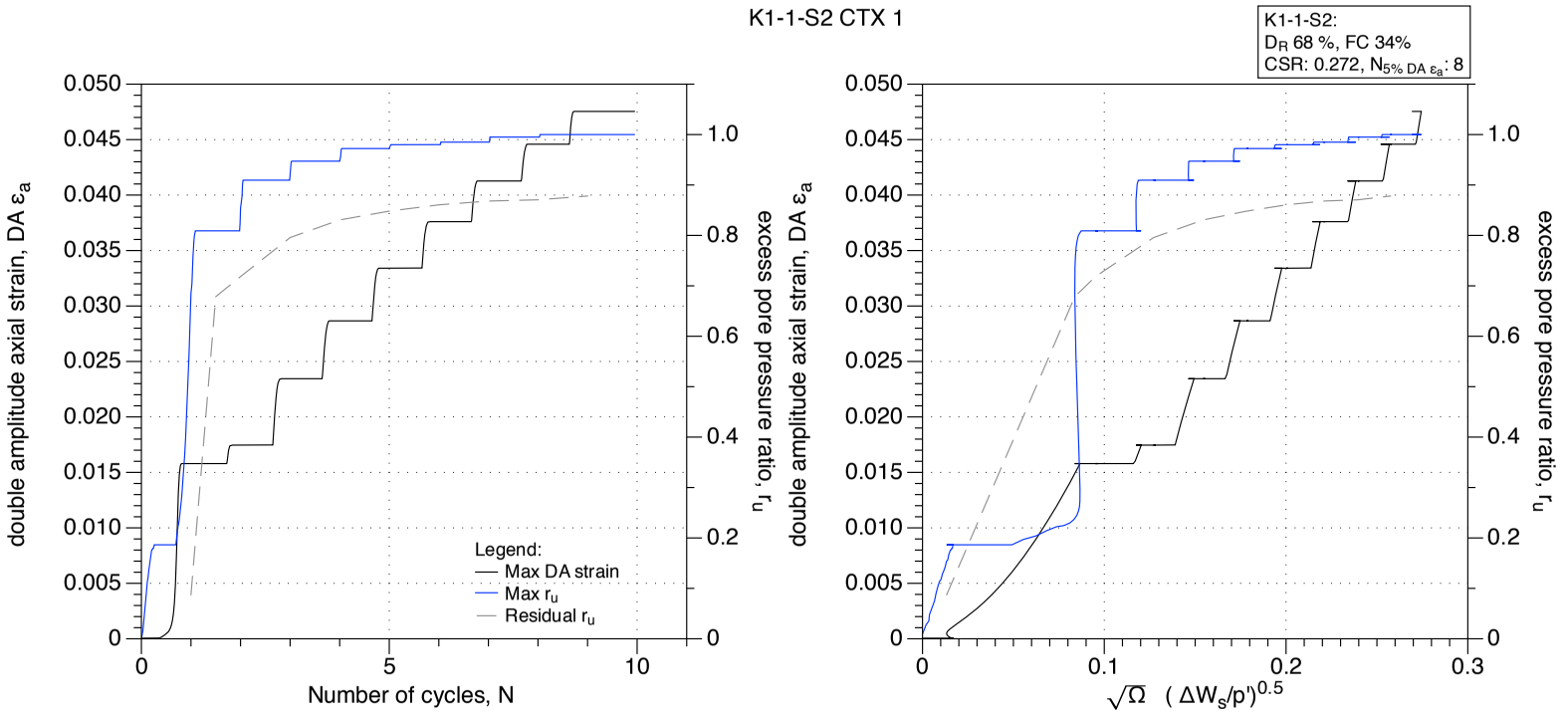

Figure 4.82: K1-1-S2 GP sample, undrained cyclic triaxial test (CTX). Development of strain and excess pore water pressure with number of cycles and normalised shear work.

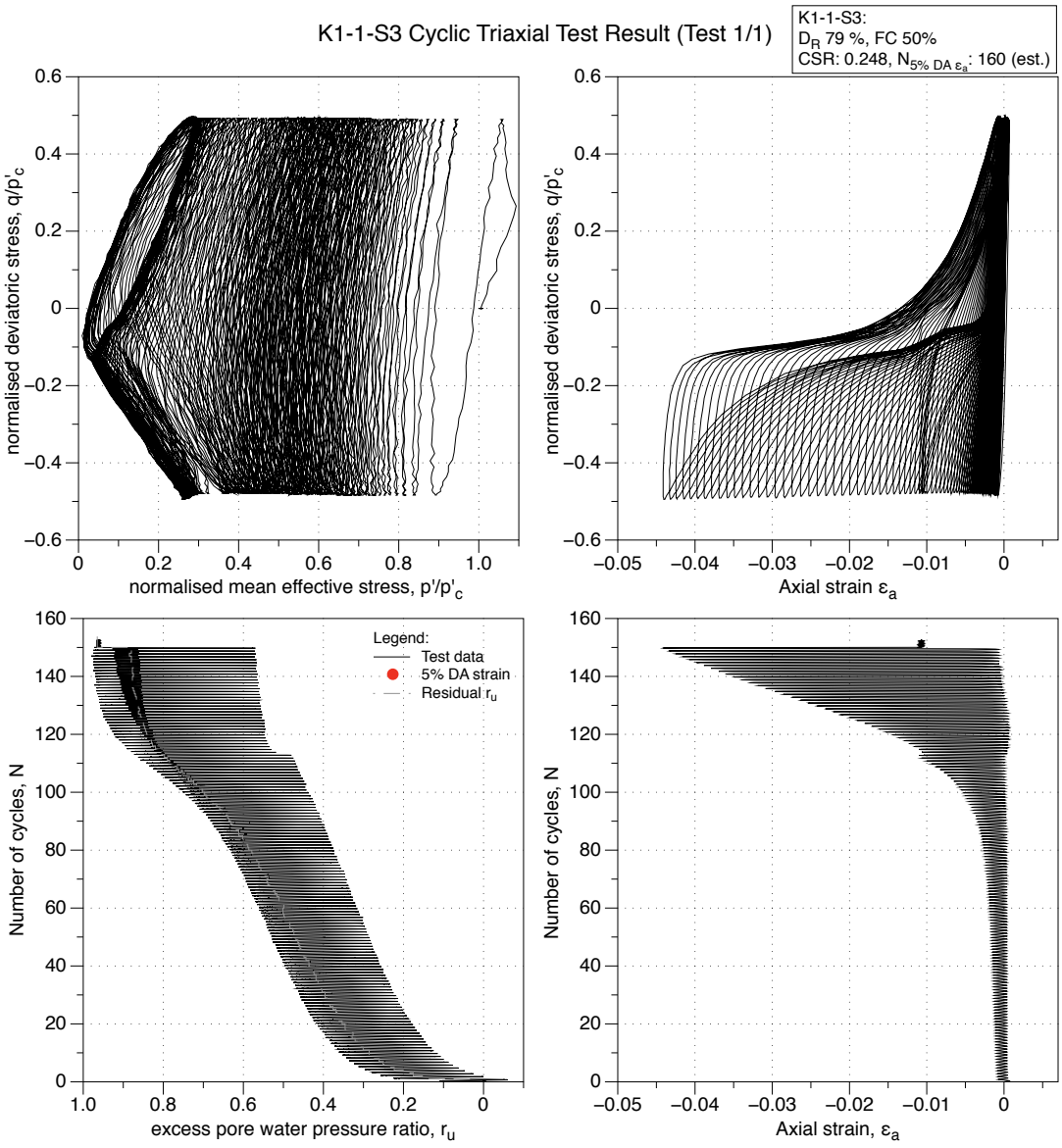

Figure 4.83: K1-1-S3 GP sample, undrained cyclic triaxial test (CTX). Effective stress-path, stress-strain, excess pore water pressure ratio and strain development plots.

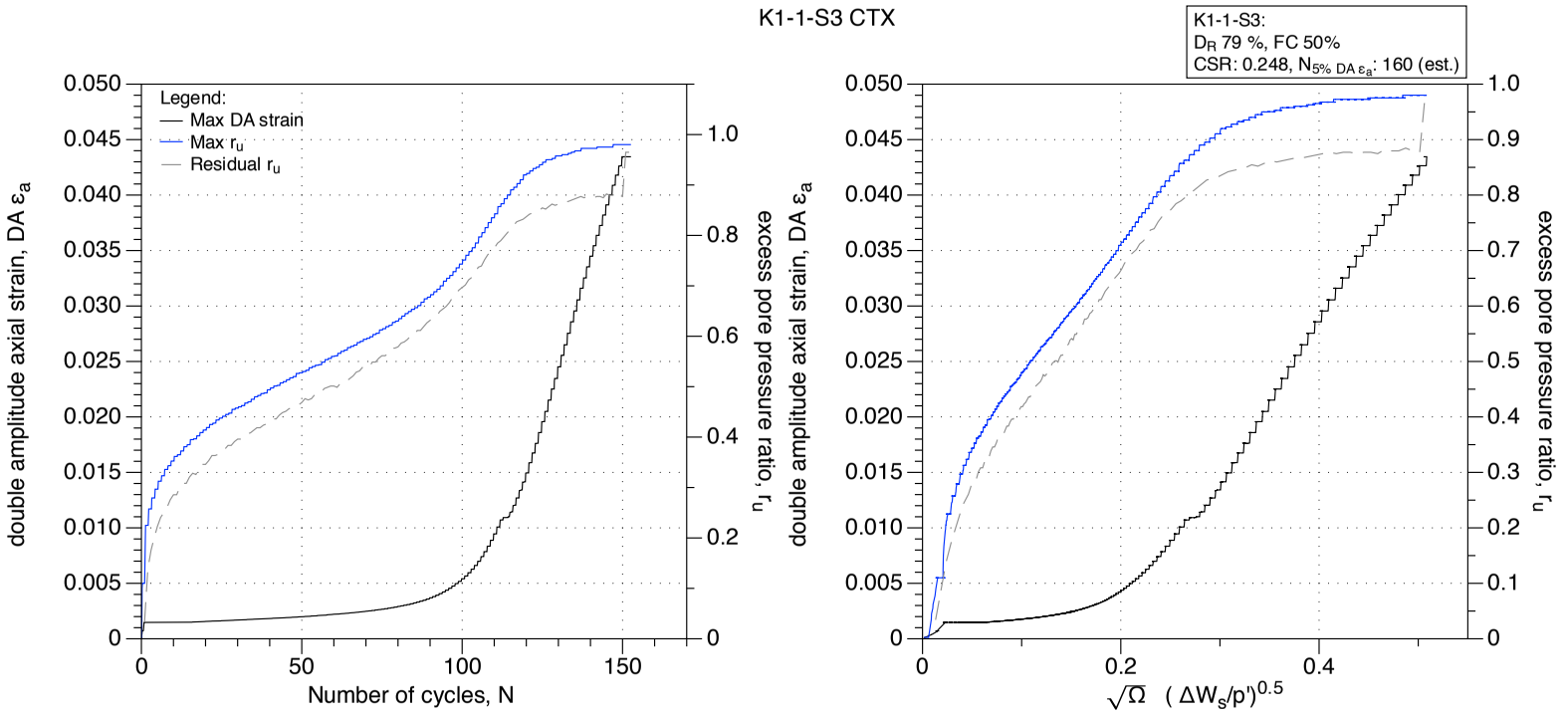

Figure 4.84: K1-1-S3 GP sample, undrained cyclic triaxial test (CTX). Development of strain and excess pore water pressure with number of cycles and normalised shear work.

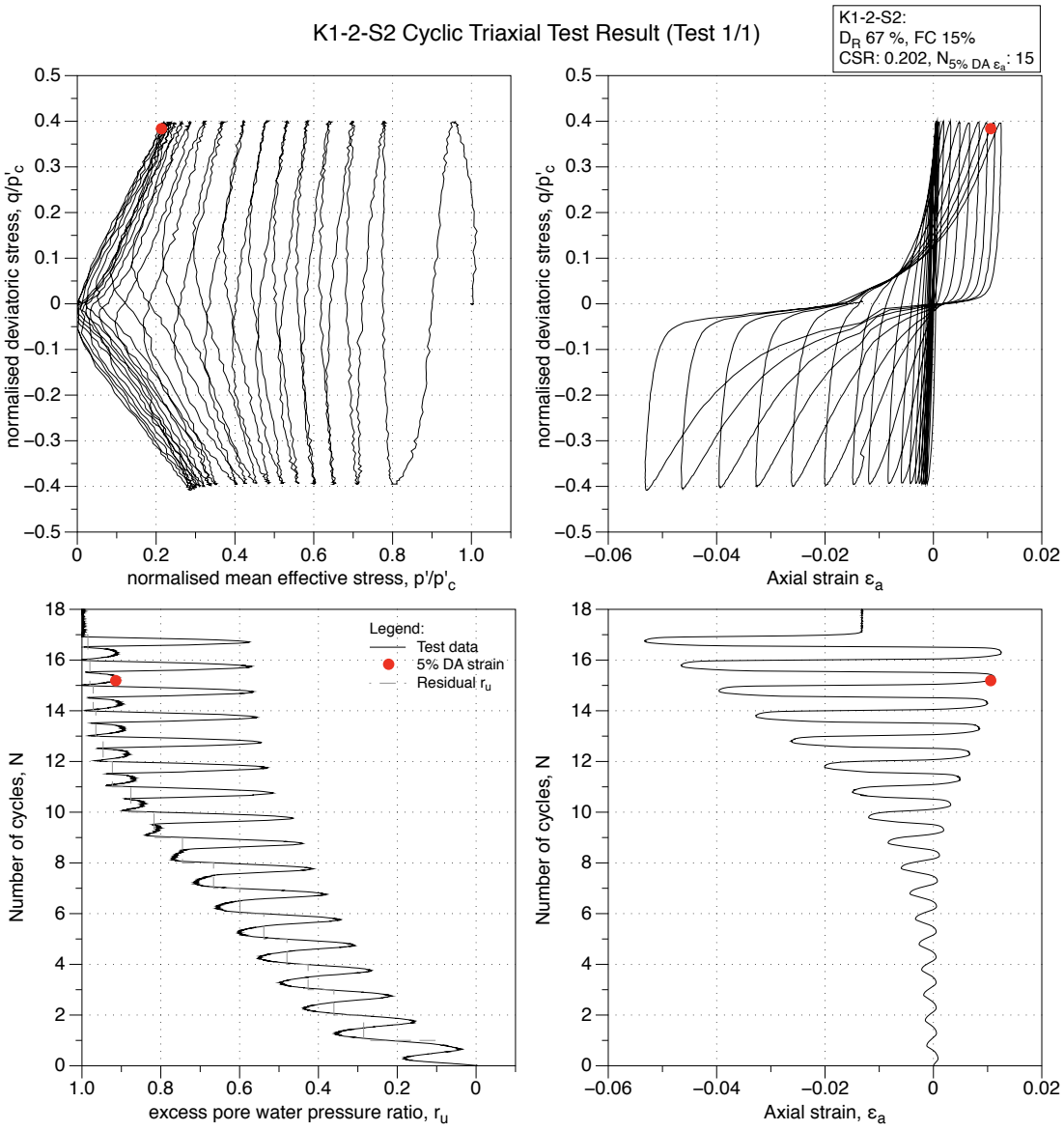

Figure 4.85: K1-2-S2 GP sample, undrained cyclic triaxial test (CTX). Effective stress-path, stress-strain, excess pore water pressure ratio and strain development plots.

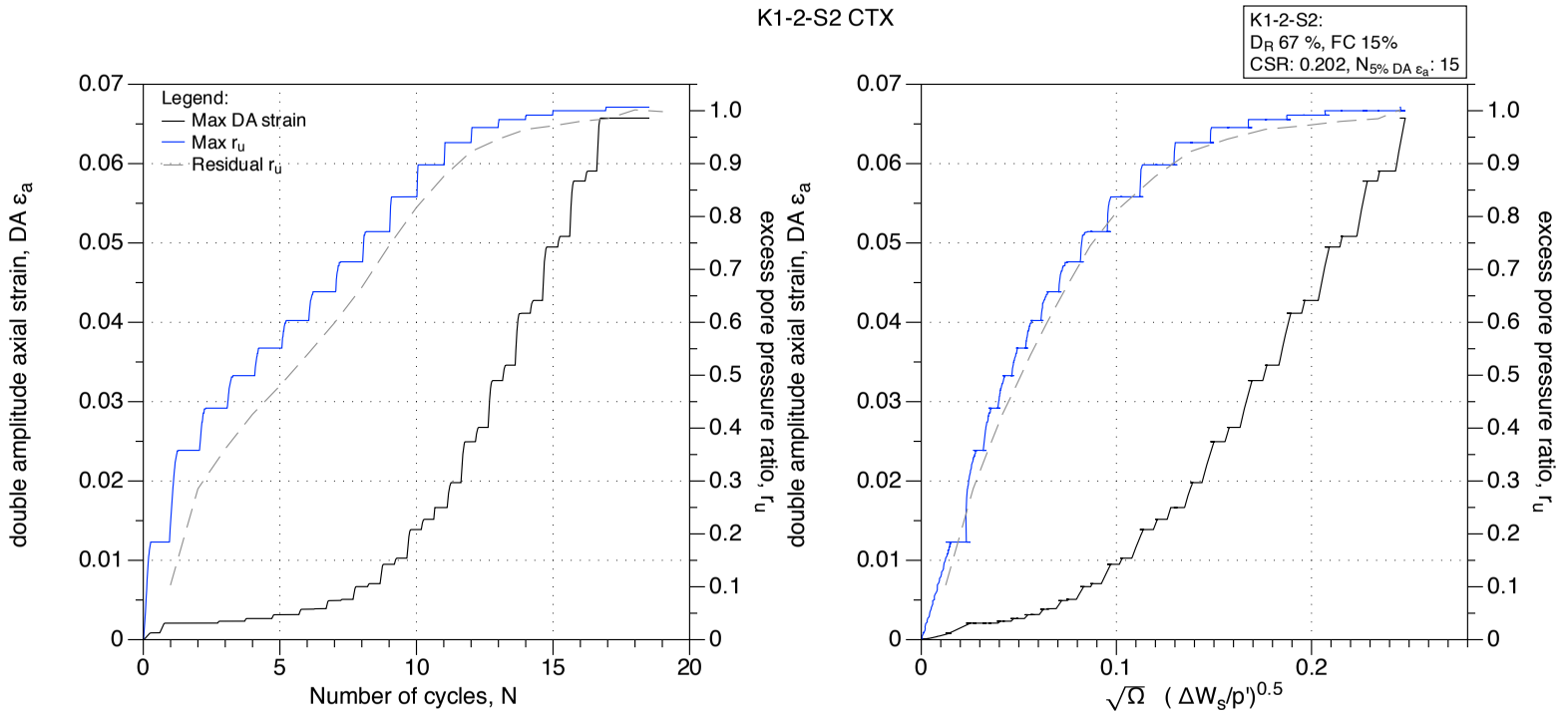

Figure 4.86: K1-2-S2 GP sample, undrained cyclic triaxial test (CTX). Development of strain and excess pore water pressure with number of cycles and normalised shear work.

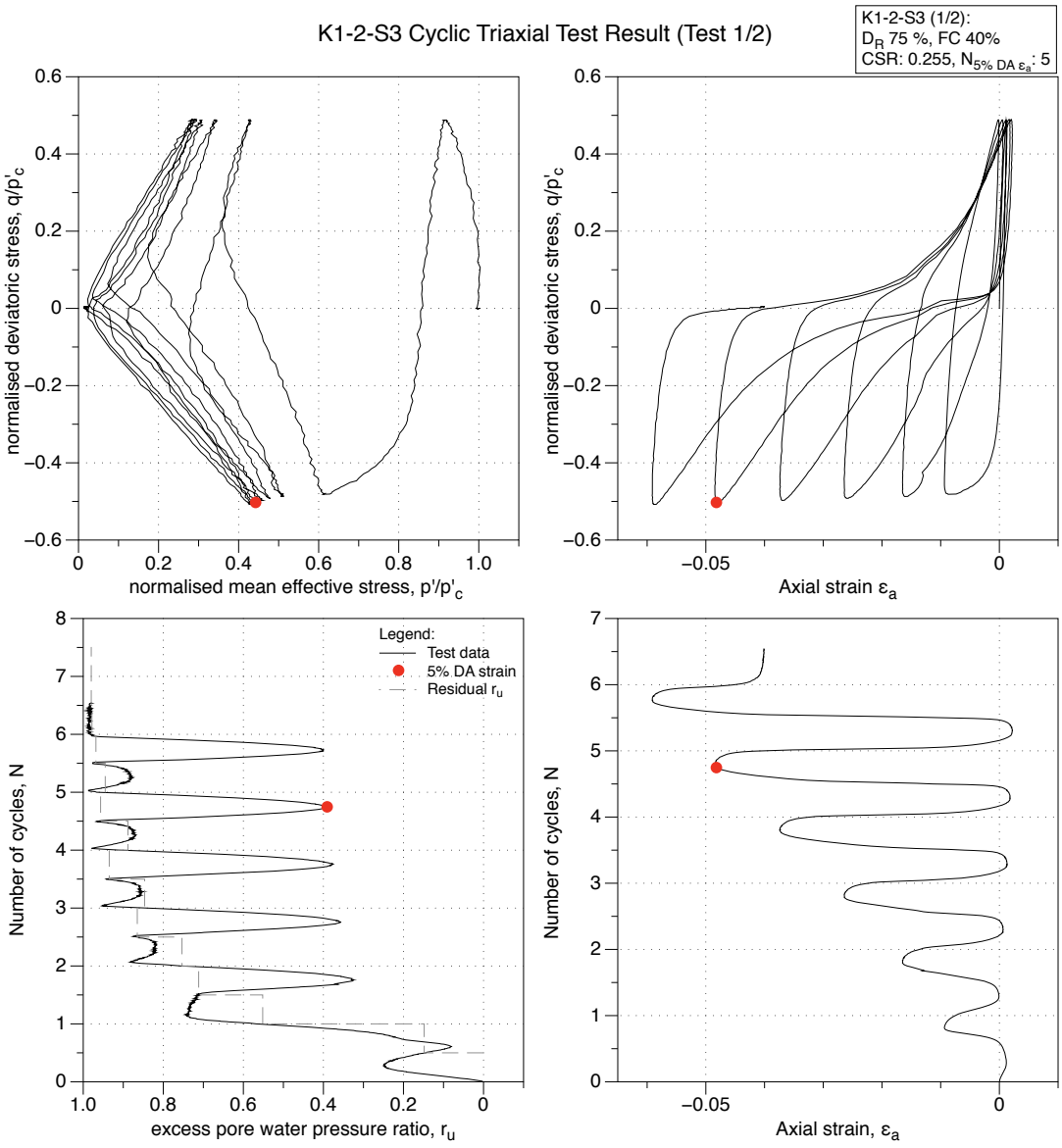

Figure 4.87: K1-2-S3 GP sample, undrained cyclic triaxial test (CTX). Effective stress-path, stress-strain, excess pore water pressure ratio and strain development plots.

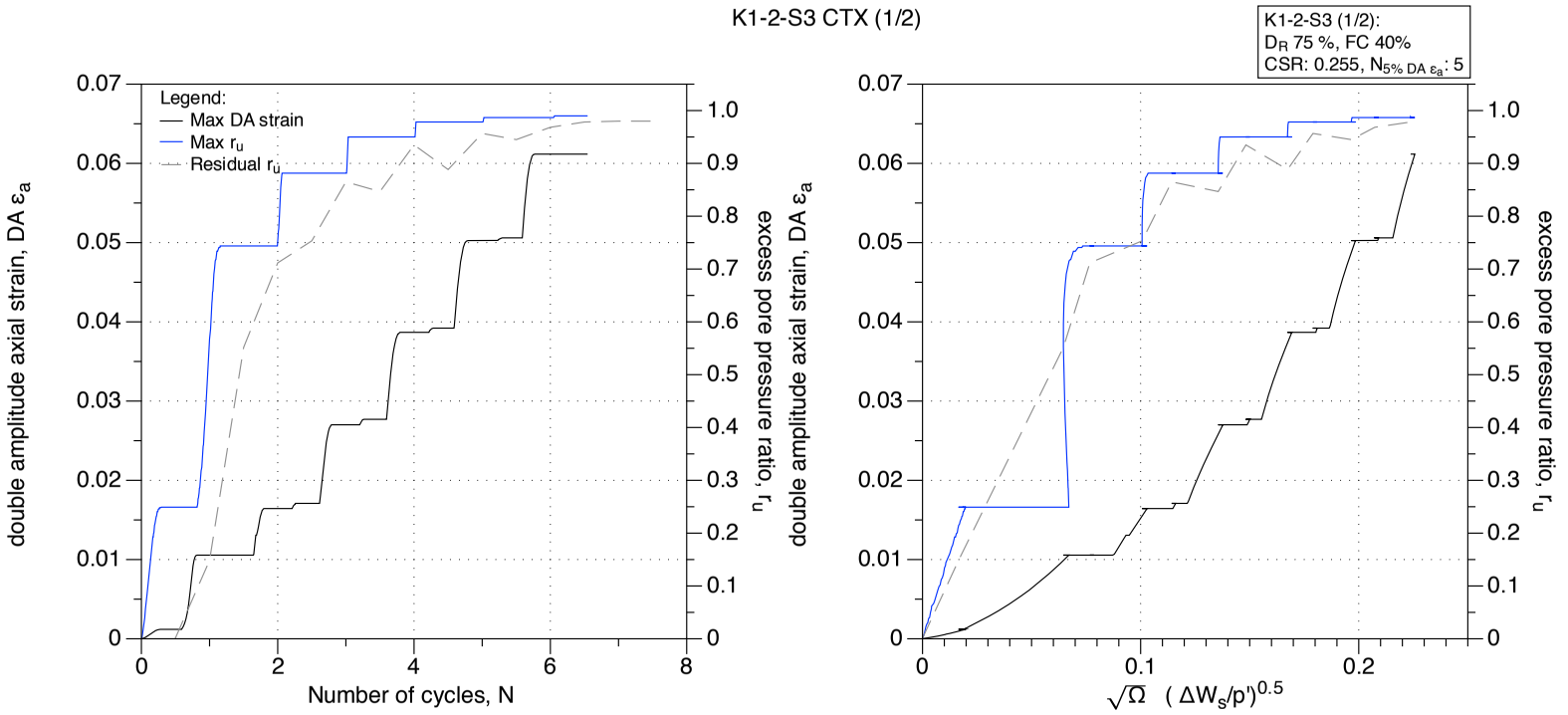

Figure 4.88: K1-2-S3 GP sample, undrained cyclic triaxial test (CTX). Development of strain and excess pore water pressure with number of cycles and normalised shear work.

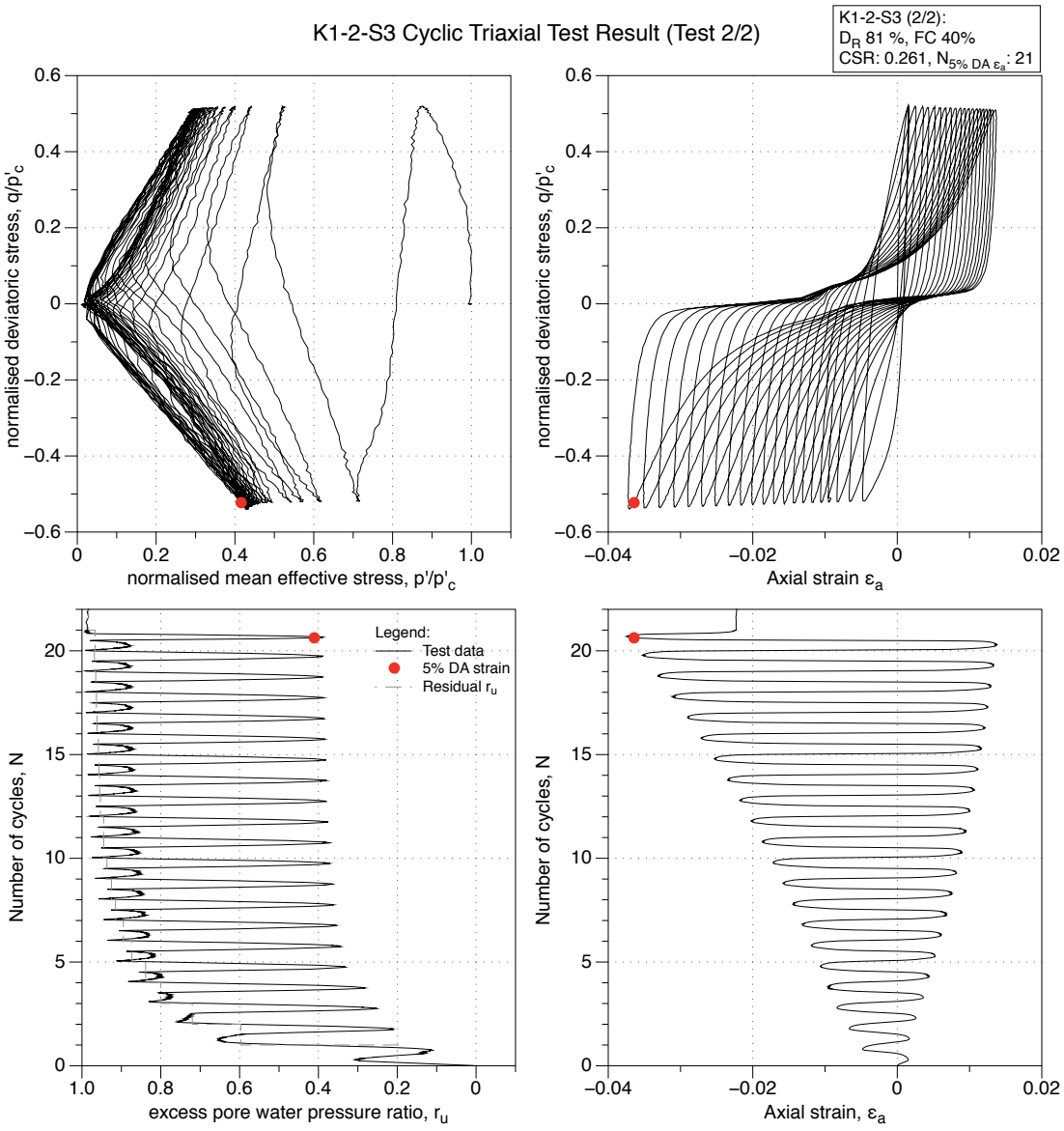

Figure 4.89: K1-2-S3 GP sample, reliquefaction undrained cyclic triaxial test (CTX). Effective stress-path, stress-strain, excess pore water pressure ratio and strain development plots.

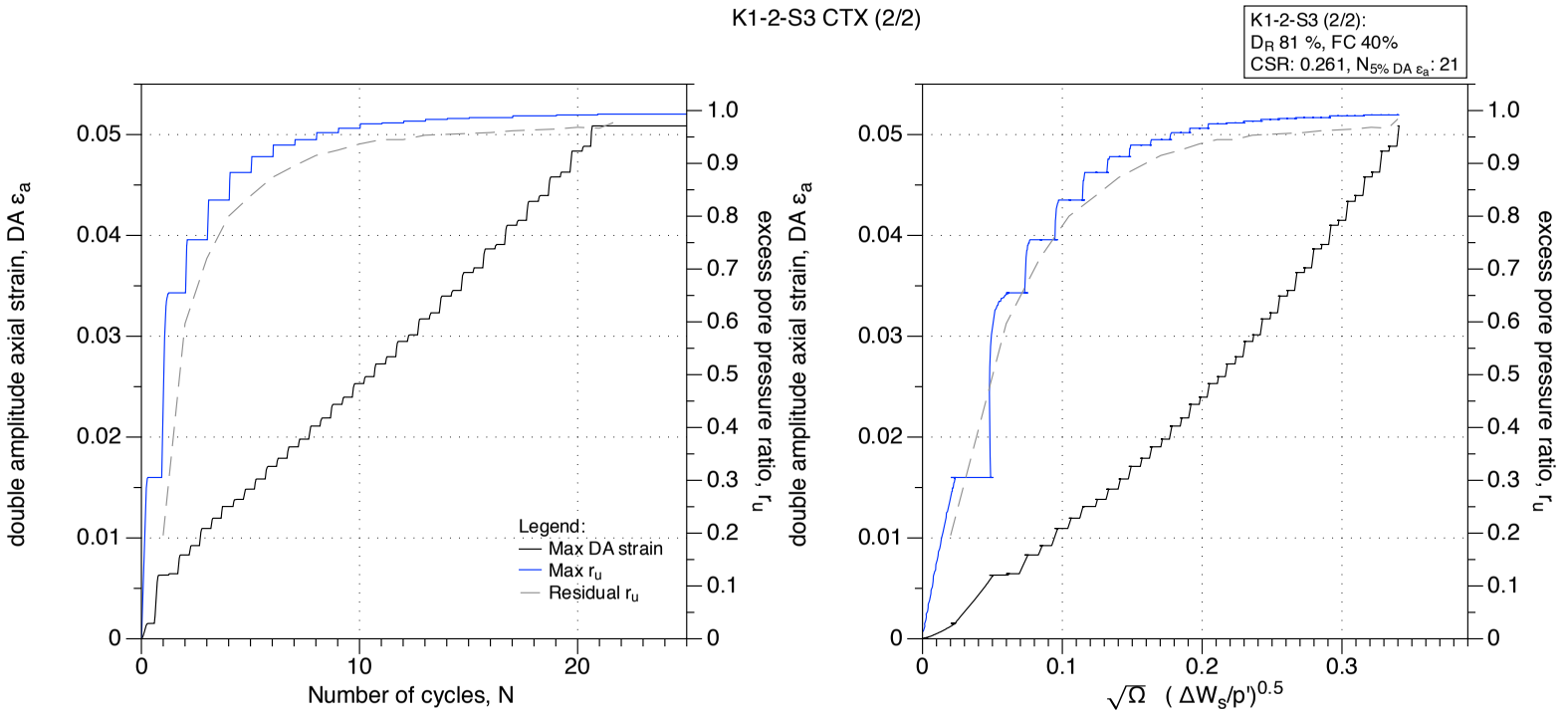

Figure 4.90: K1-2-S3 GP sample, reliquefaction undrained cyclic triaxial test (CTX). Development of strain and excess pore water pressure with number of cycles and normalised shear work.

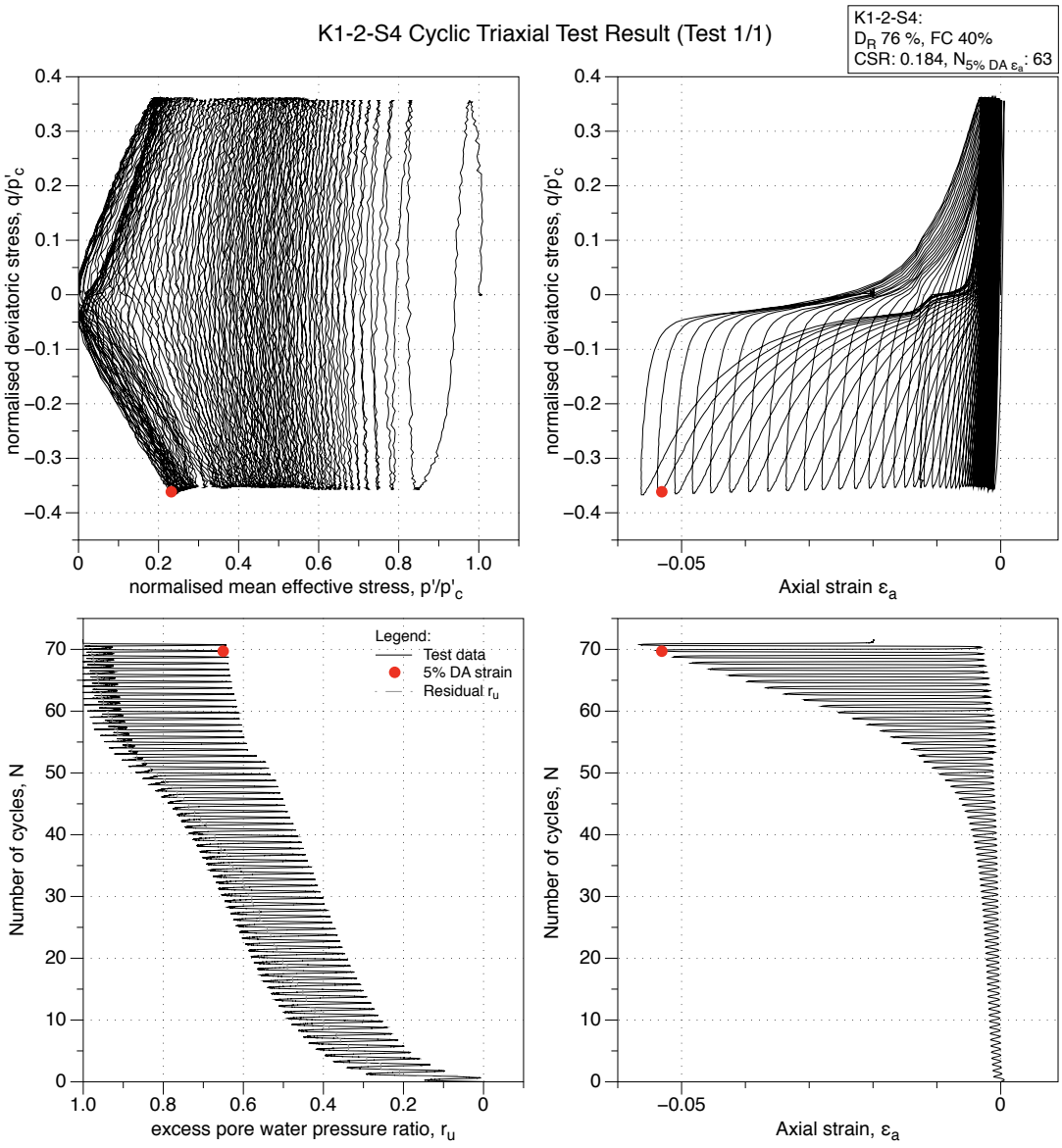

Figure 4.91: K1-2-S4 GP sample, undrained cyclic triaxial test (CTX). Effective stress-path, stress-strain, excess pore water pressure ratio and strain development plots.

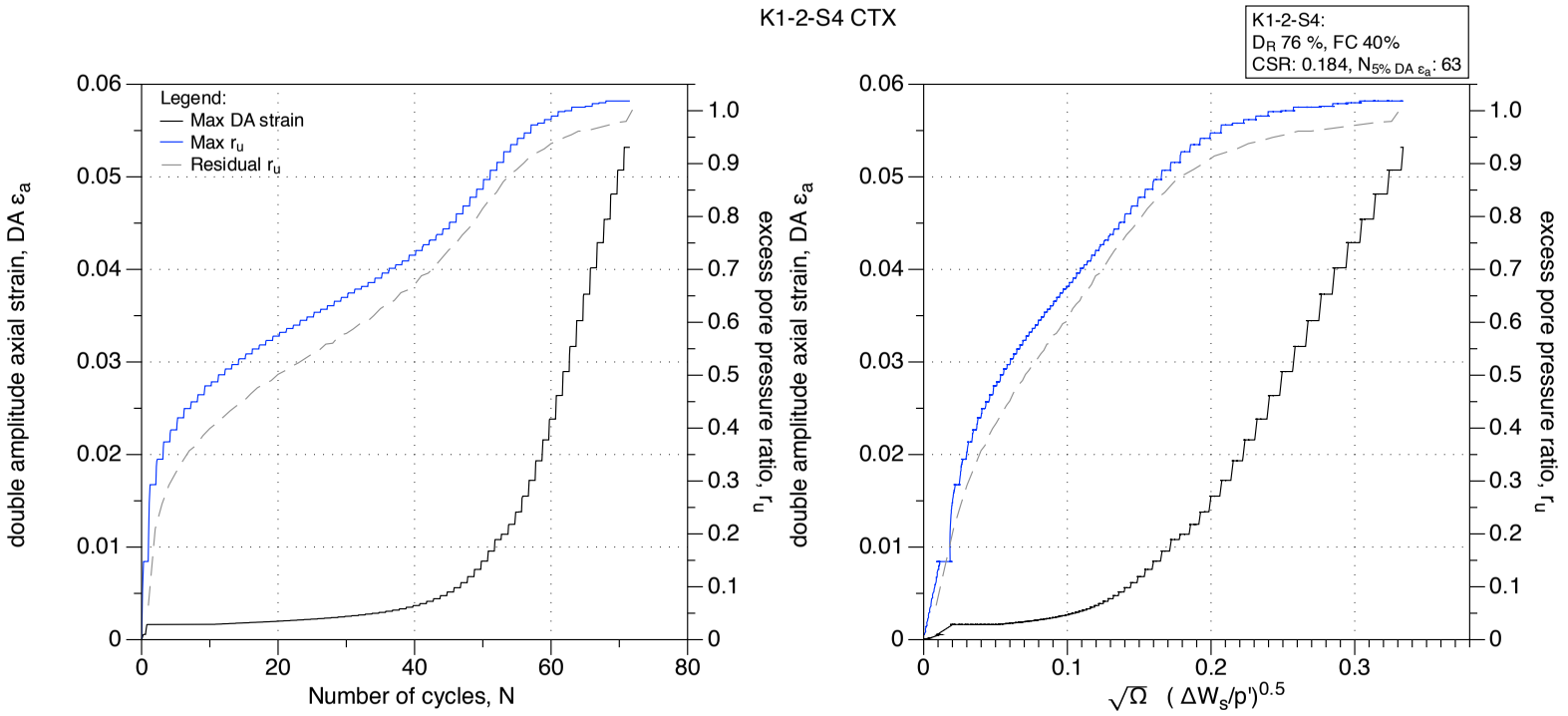

Figure 4.92: K1-2-S4 GP sample, undrained cyclic triaxial test (CTX). Development of strain and excess pore water pressure with number of cycles and normalised shear work.

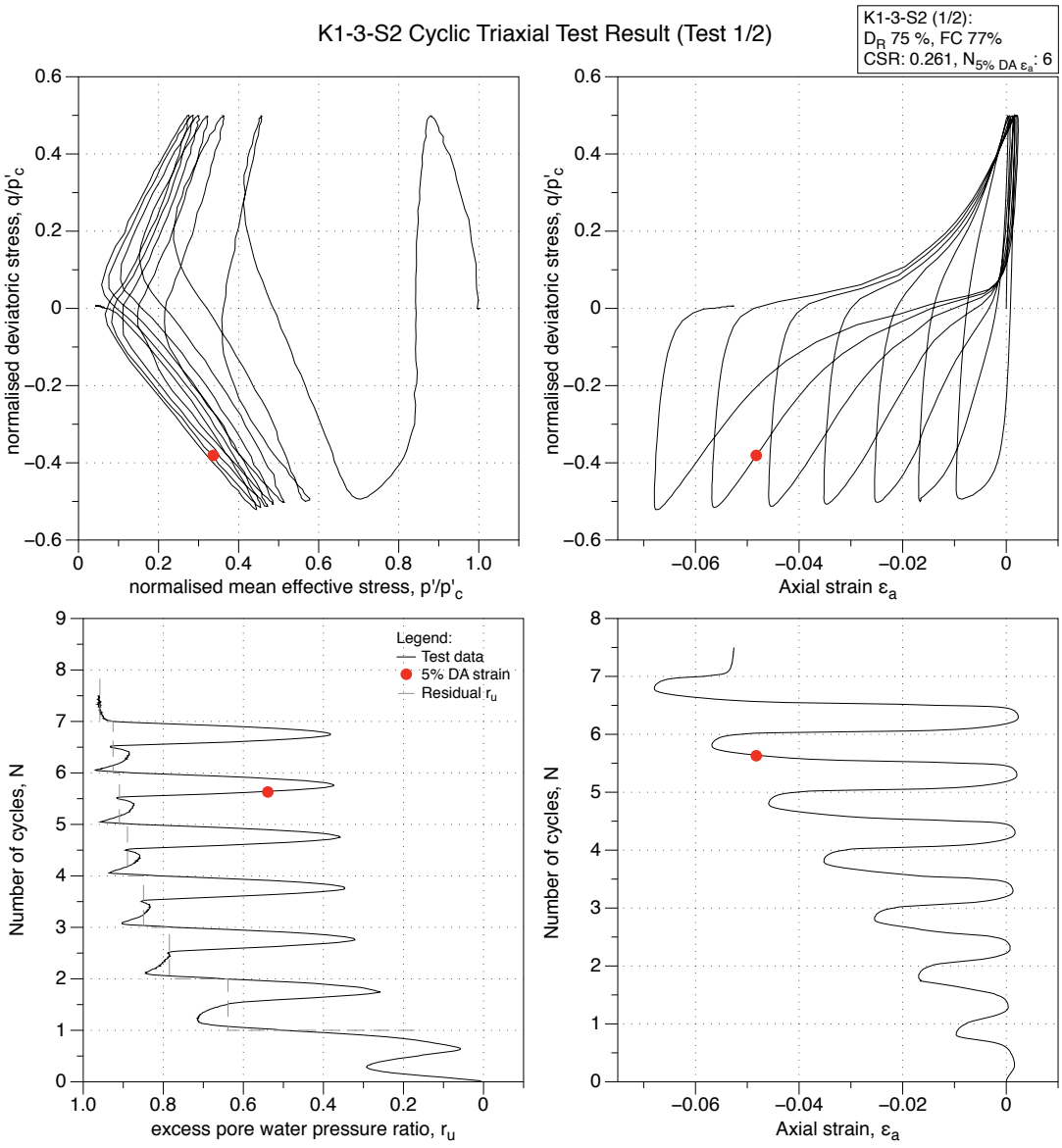

Figure 4.93: K1-3-S2 GP sample, undrained cyclic triaxial test (CTX). Effective stress-path, stress-strain, excess pore water pressure ratio and strain development plots.

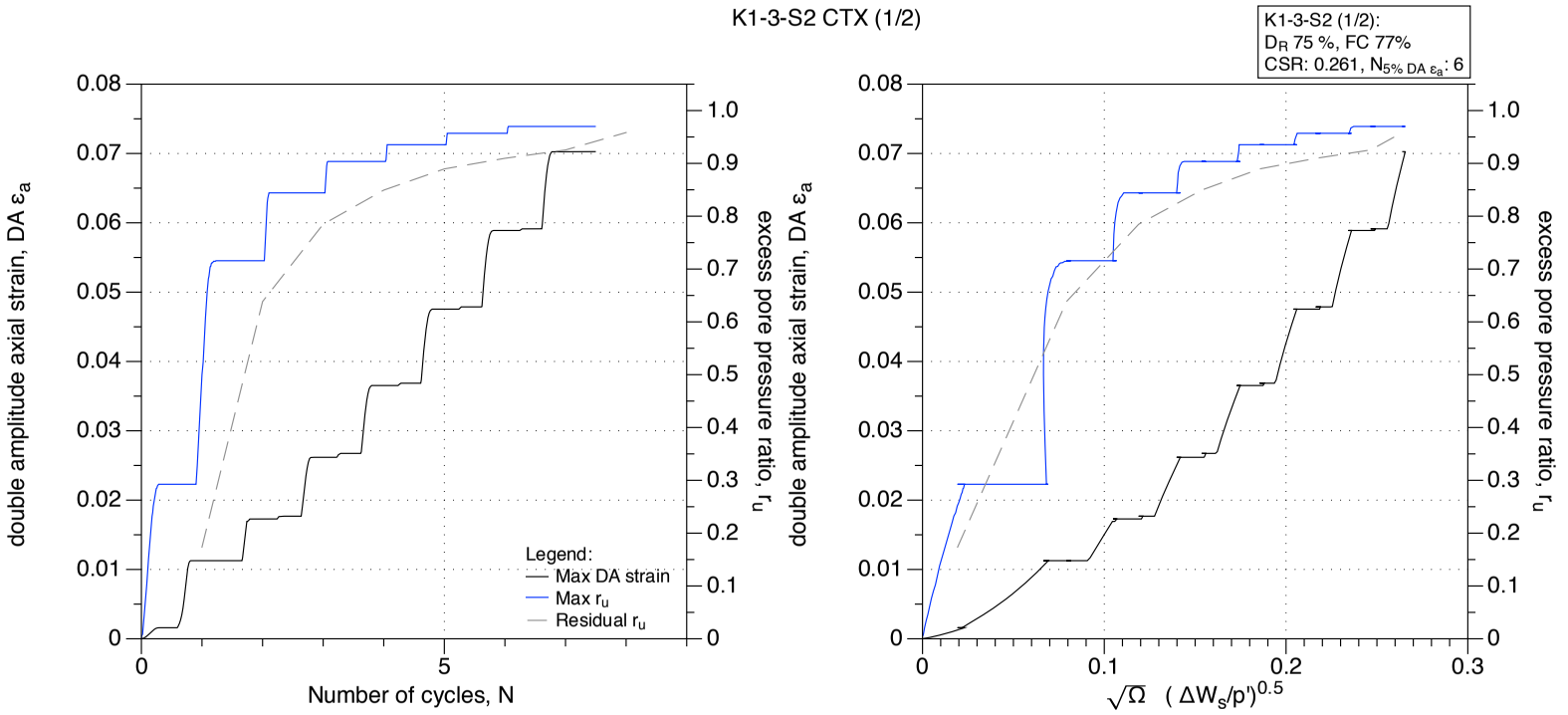

Figure 4.94: K1-3-S2 GP sample, undrained cyclic triaxial test (CTX). Development of strain and excess pore water pressure with number of cycles and normalised shear work.

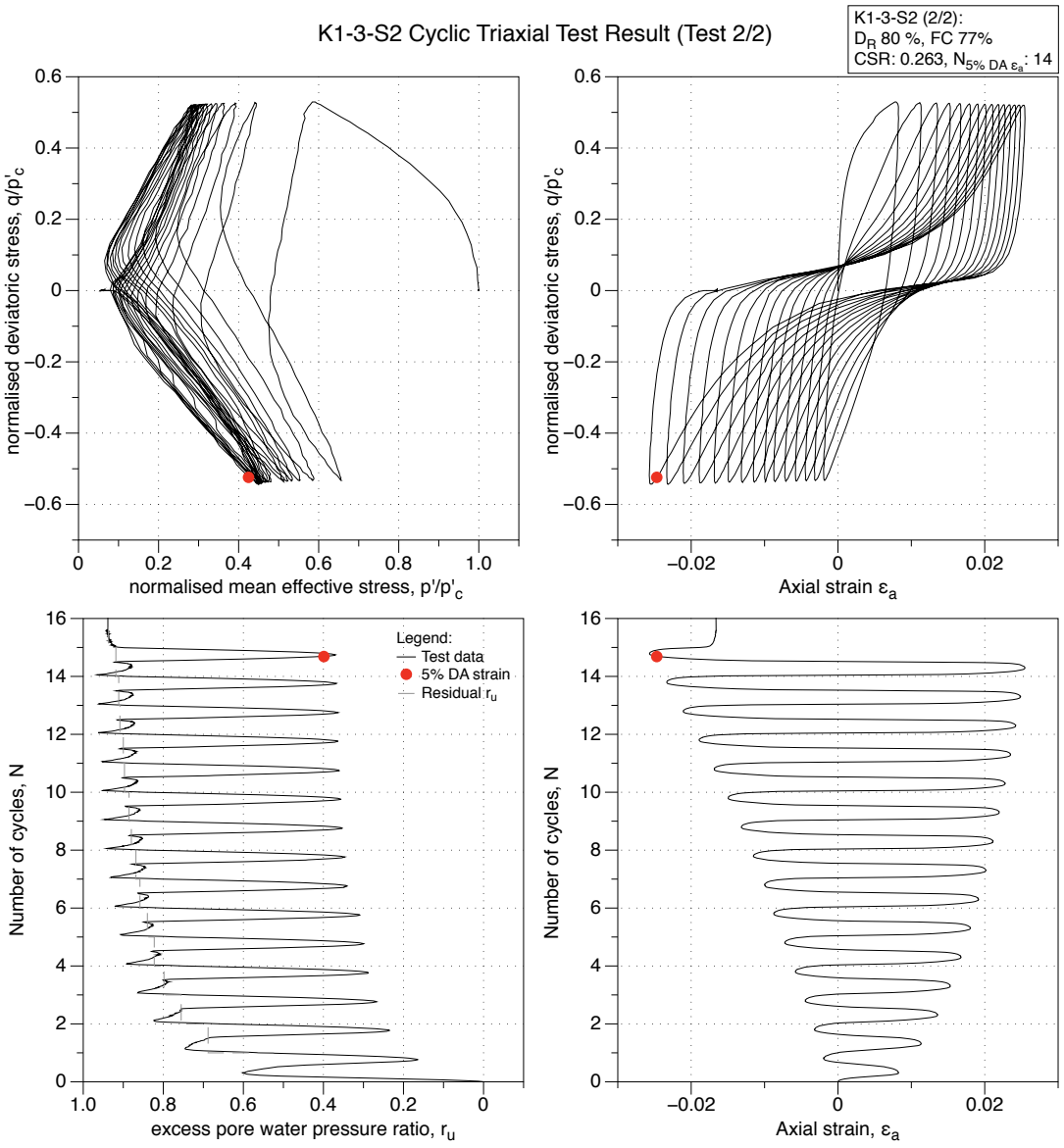

Figure 4.95: K1-3-S2 GP sample, reliquefaction undrained cyclic triaxial test (CTX). Effective stress-path, stress-strain, excess pore water pressure ratio and strain development plots.

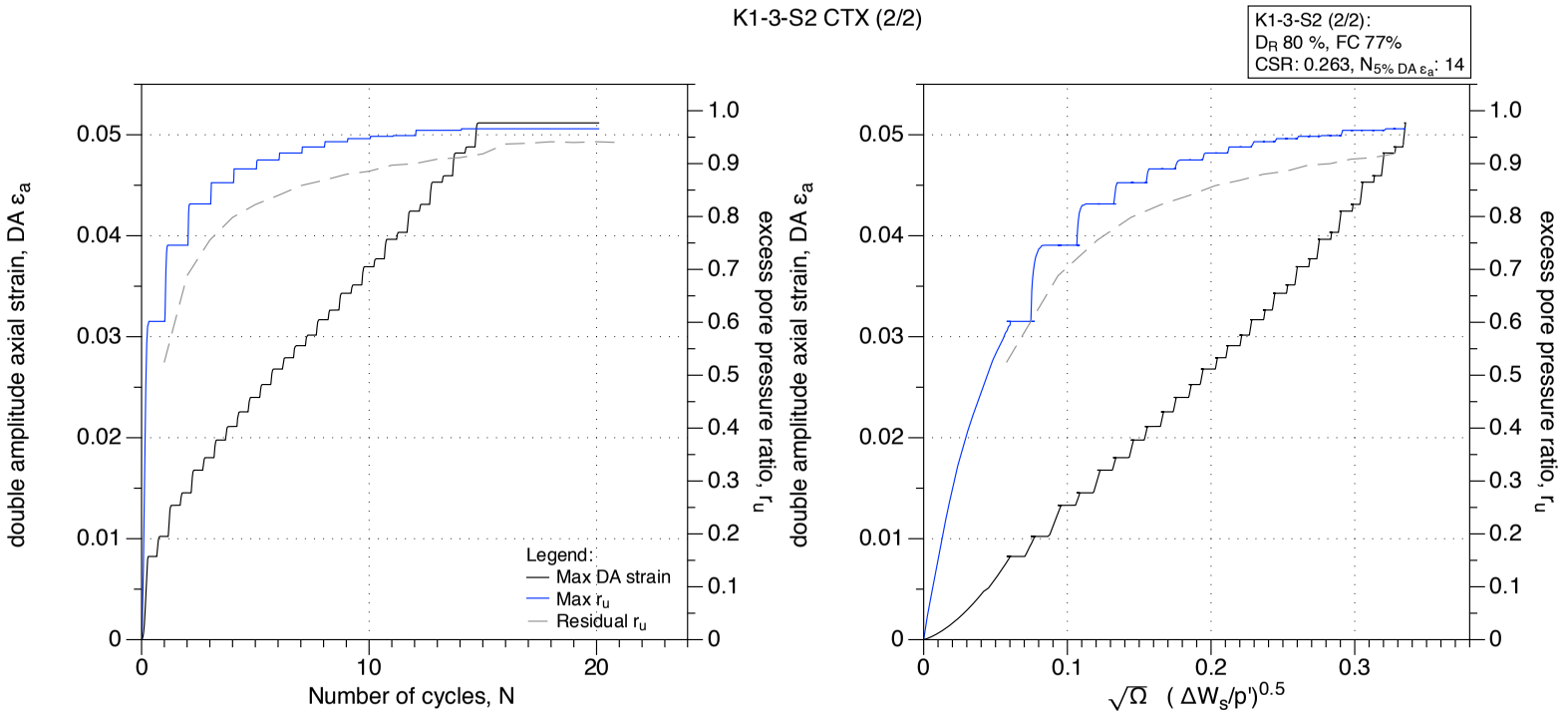

Figure 4.96: K1-3-S2 GP sample, reliquefaction undrained cyclic triaxial test (CTX). Development of strain and excess pore water pressure with number of cycles and normalised shear work.

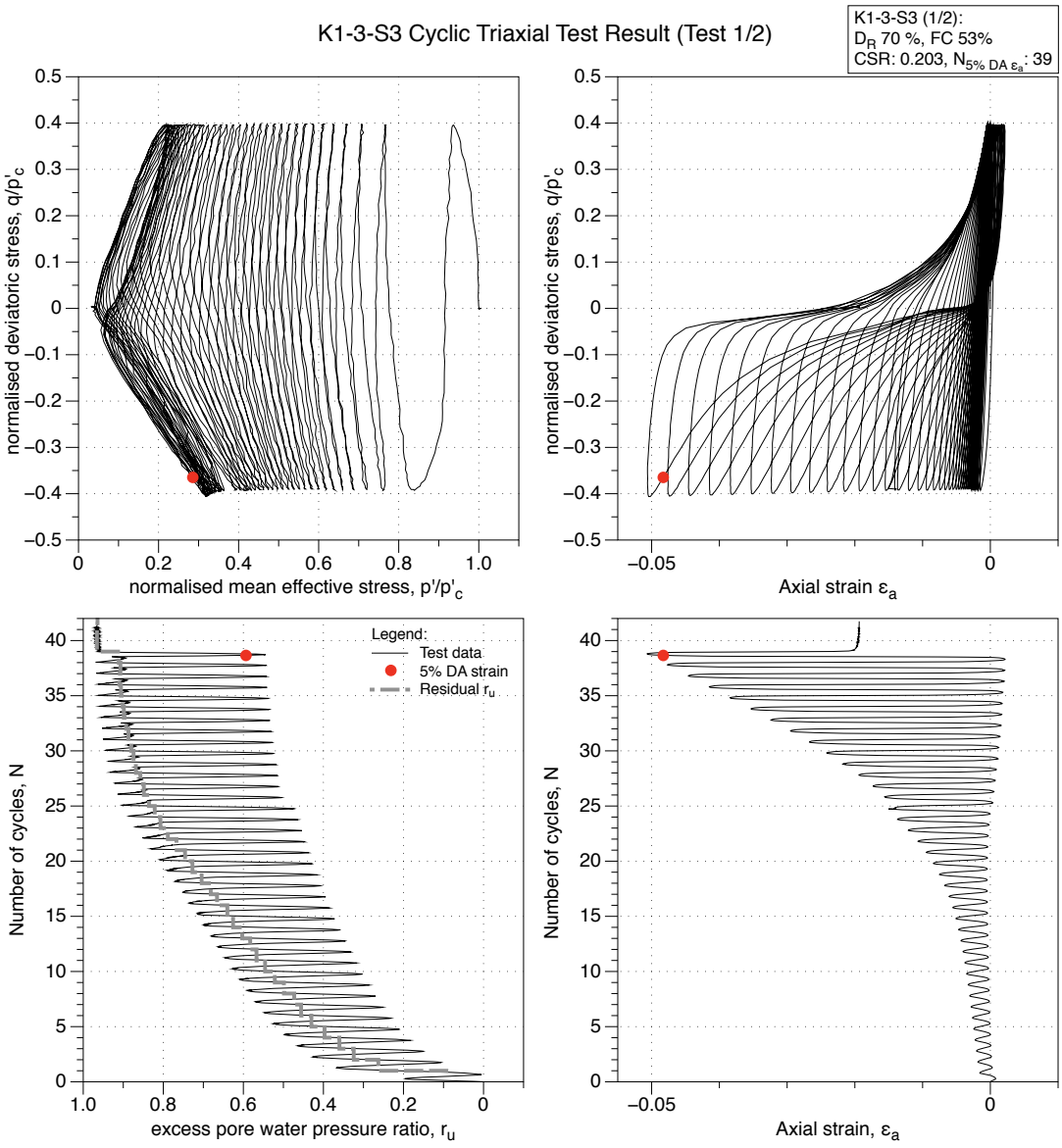

Figure 4.97: K1-3-S3 GP sample, undrained cyclic triaxial test (CTX). Effective stress-path, stress-strain, excess pore water pressure ratio and strain development plots.

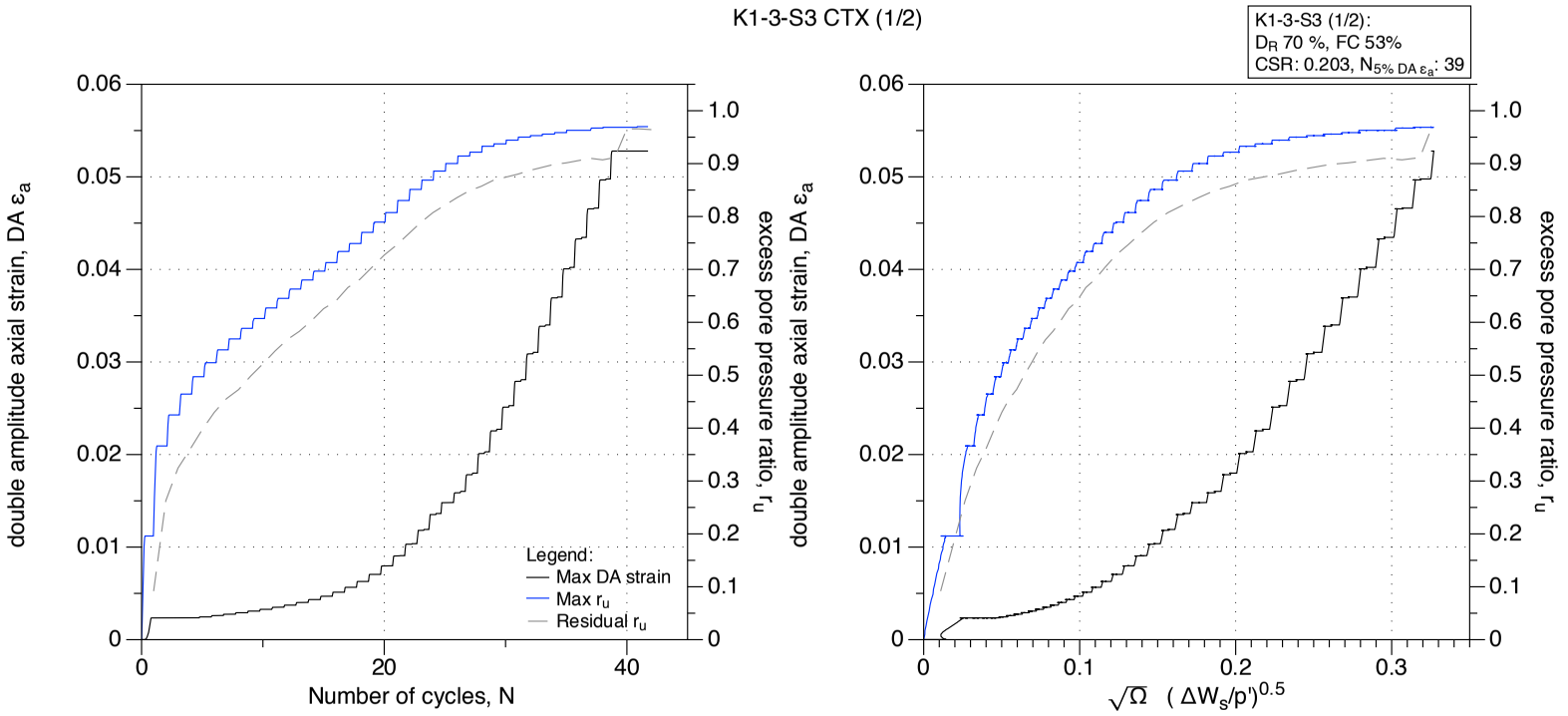

Figure 4.98: K1-3-S3 GP sample, undrained cyclic triaxial test (CTX). Development of strain and excess pore water pressure with number of cycles and normalised shear work.

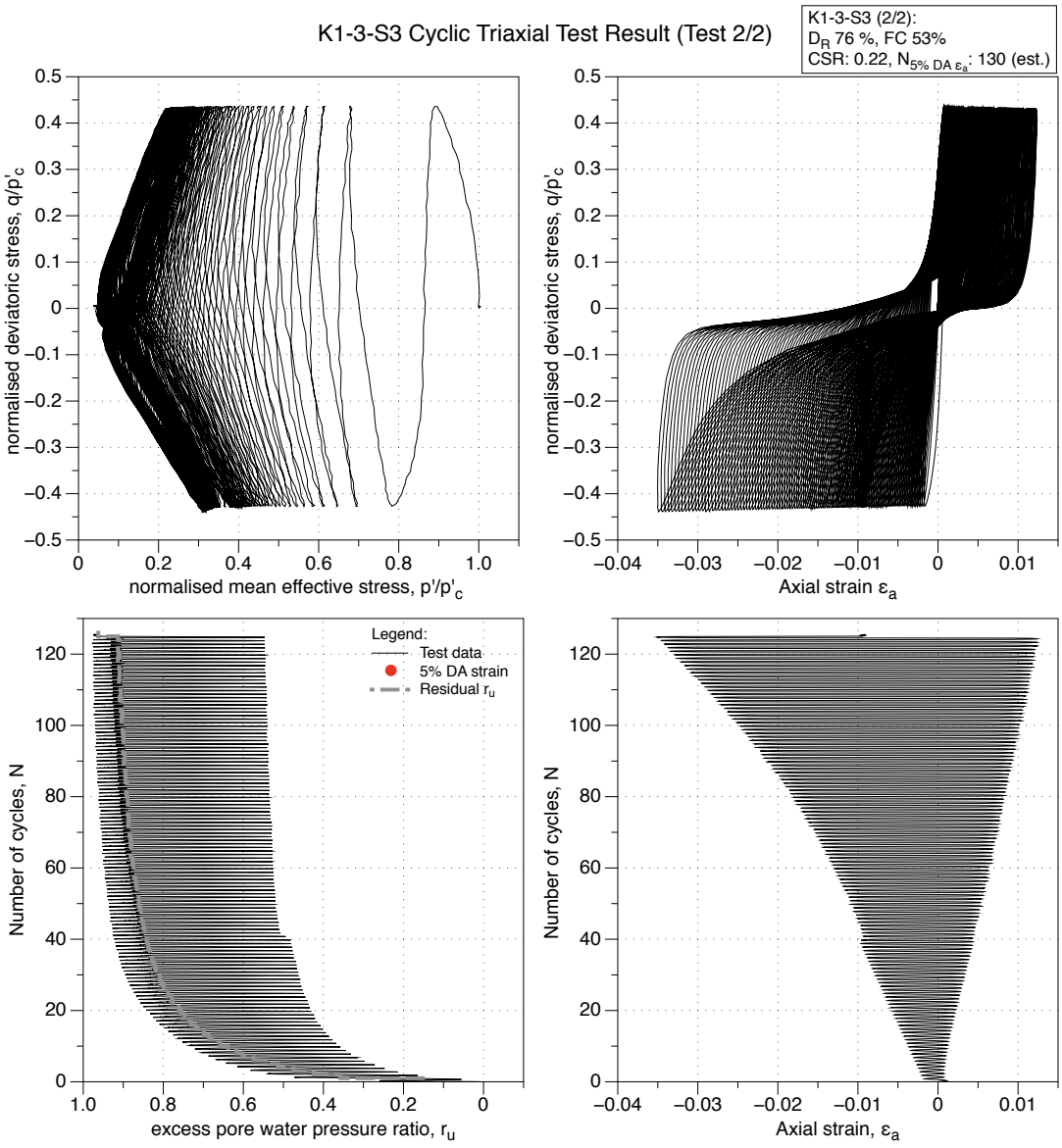

Figure 4.99: K1-3-S3 GP sample, reliquefaction undrained cyclic triaxial test (CTX). Effective stress-path, stress-strain, excess pore water pressure ratio and strain development plots.

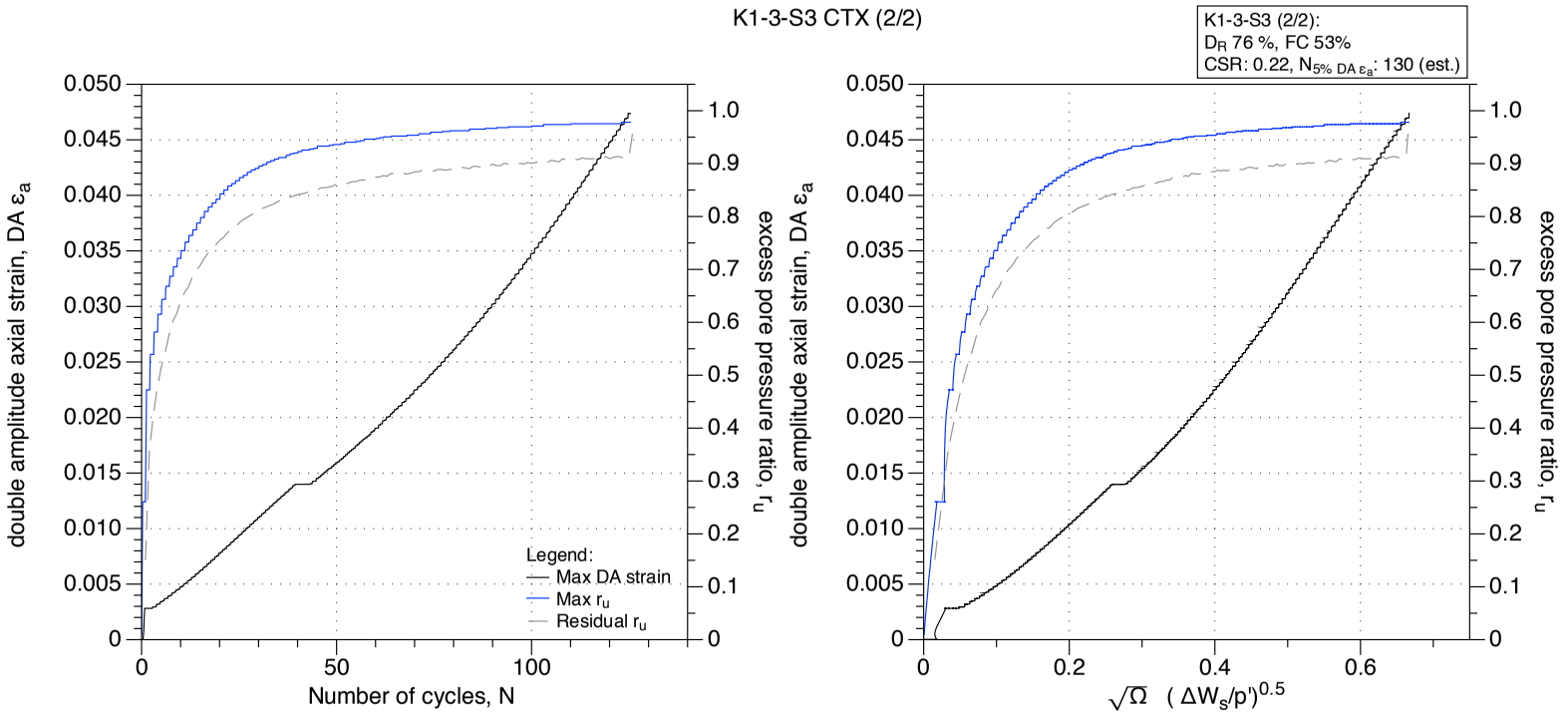

Figure 4.100: K1-3-S3 GP sample, reliquefaction undrained cyclic triaxial test (CTX). Development of strain and excess pore water pressure with number of cycles and normalised shear work.

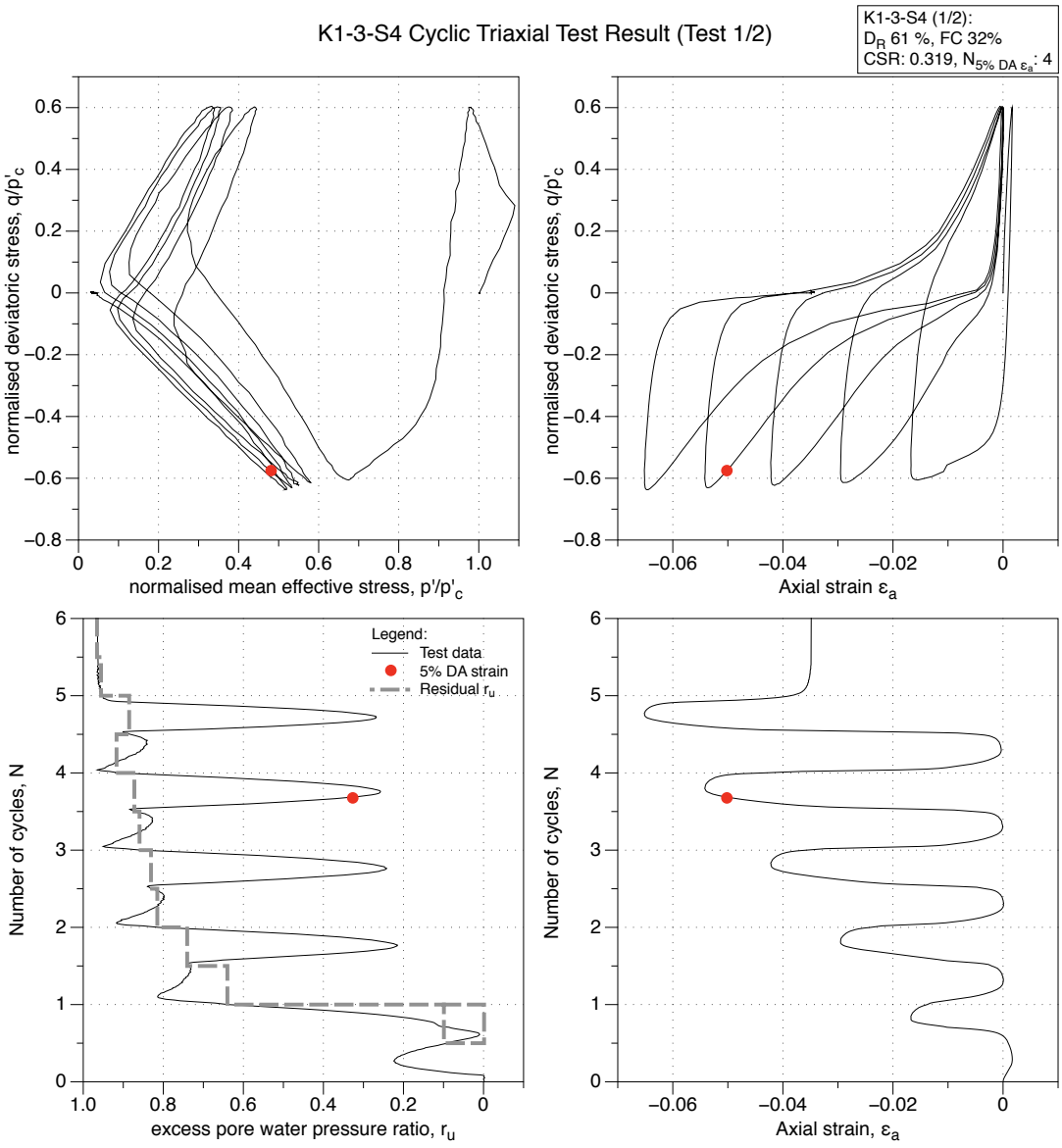

Figure 4.101: K1-3-S4 GP sample, undrained cyclic triaxial test (CTX). Effective stress-path, stress-strain, excess pore water pressure ratio and strain development plots.

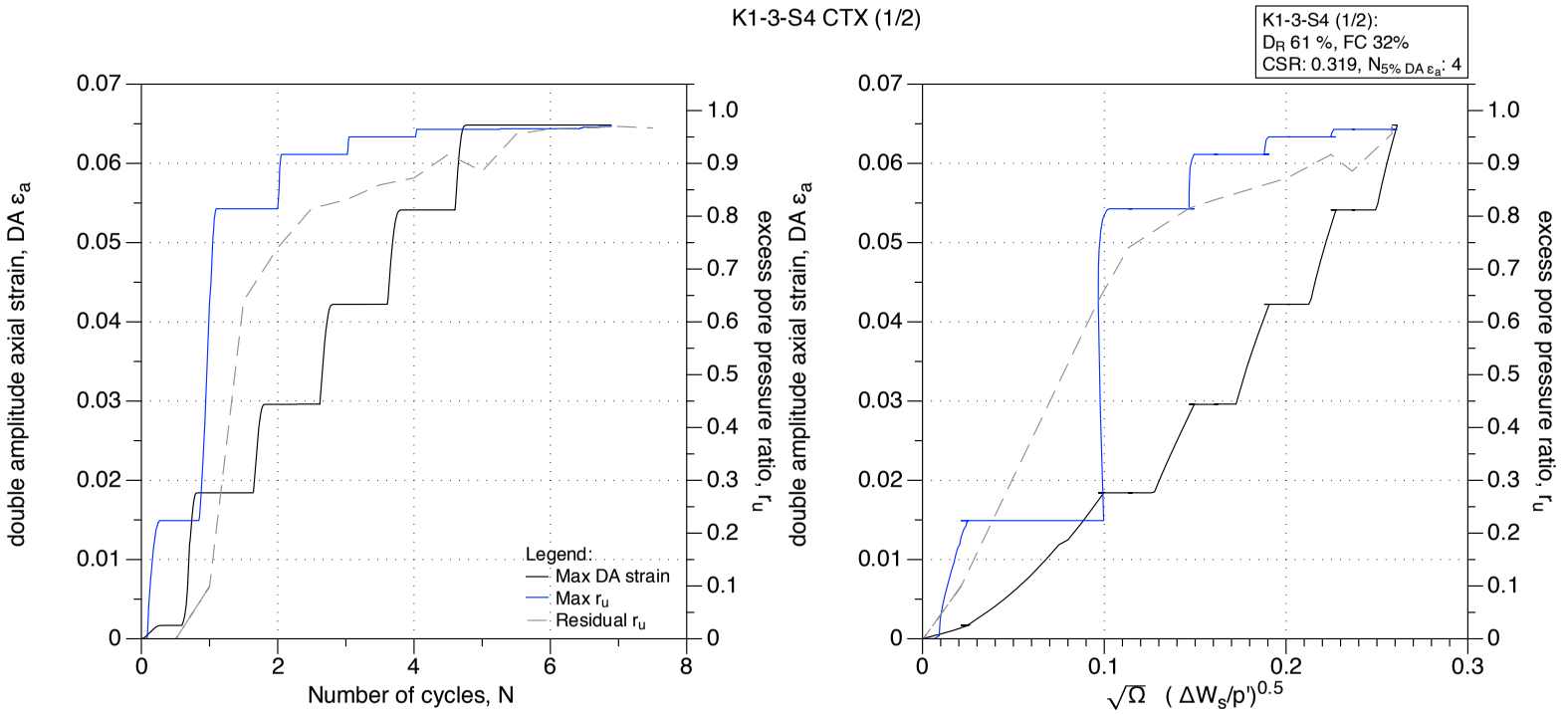

Figure 4.102: K1-3-S4 GP sample, undrained cyclic triaxial test (CTX). Development of strain and excess pore water pressure with number of cycles and normalised shear work.

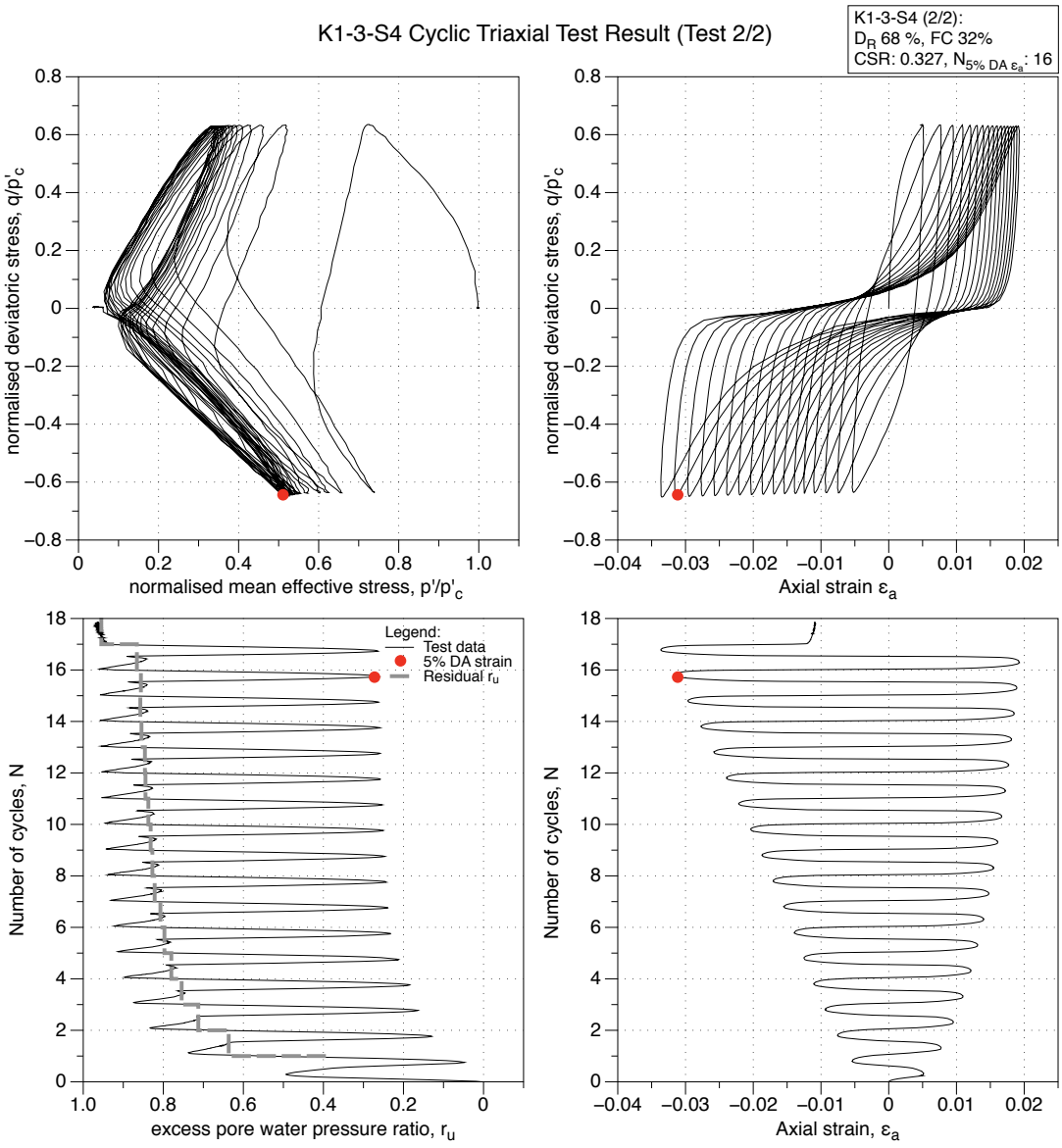

Figure 4.103: K1-3-S4 GP sample, reliquefaction undrained cyclic triaxial test (CTX). Effective stress-path, stress-strain, excess pore water pressure ratio and strain development plots.

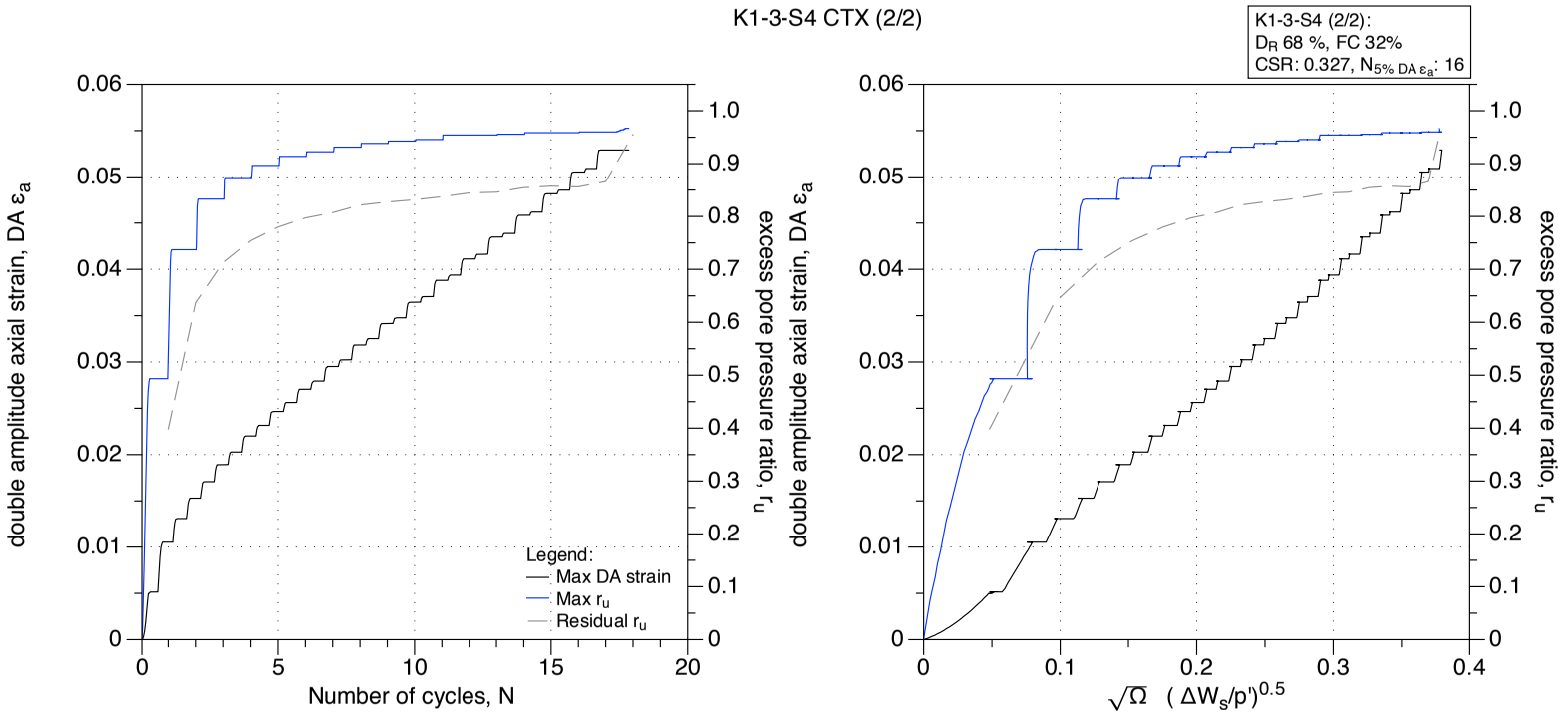

Figure 4.104: K1-3-S4 GP sample, reliquefaction undrained cyclic triaxial test (CTX). Development of strain and excess pore water pressure with number of cycles and normalised shear work.

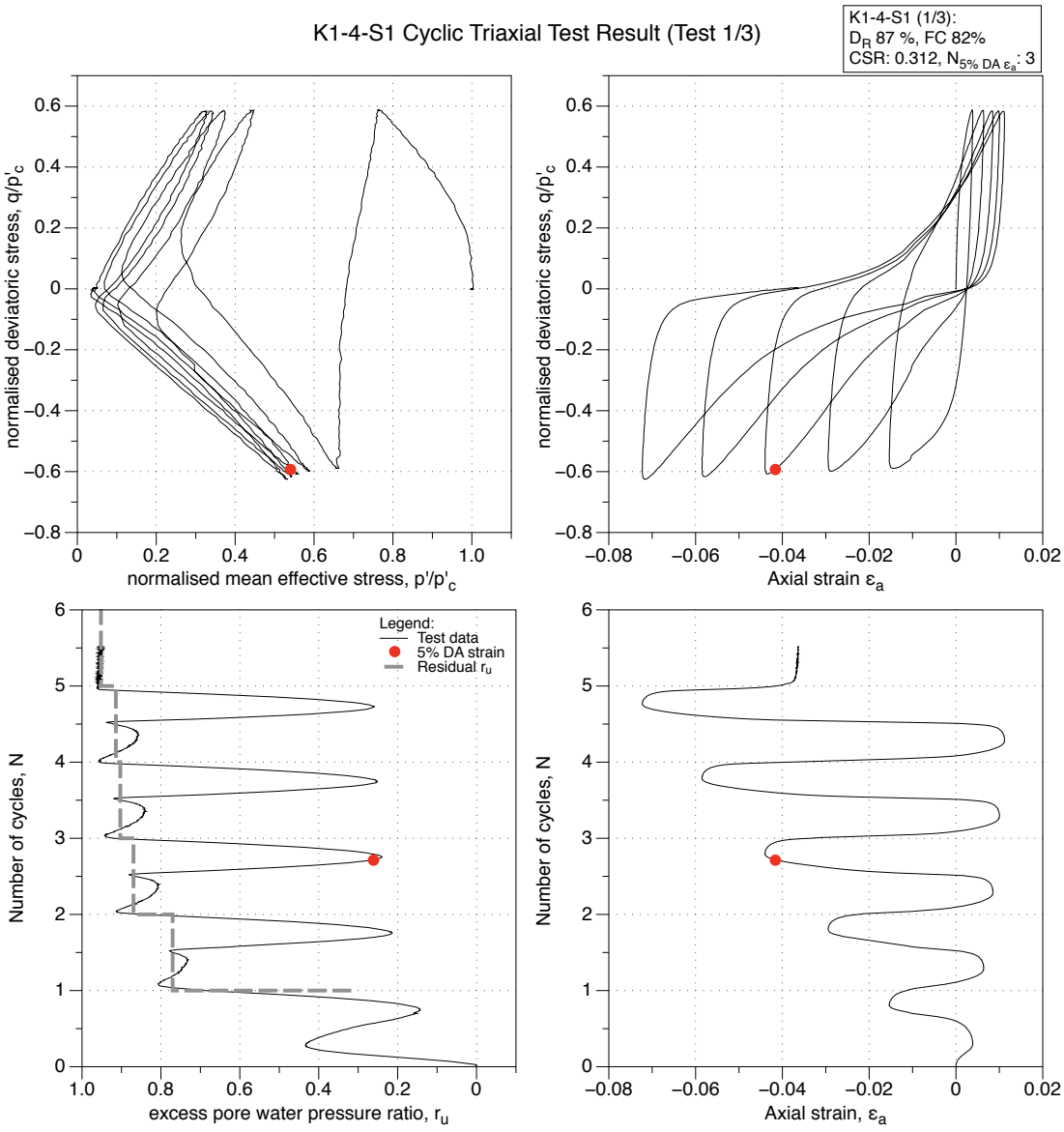

Figure 4.105: K1-4-S1 GP sample, undrained cyclic triaxial test (CTX). Effective stress-path, stress-strain, excess pore water pressure ratio and strain development plots.

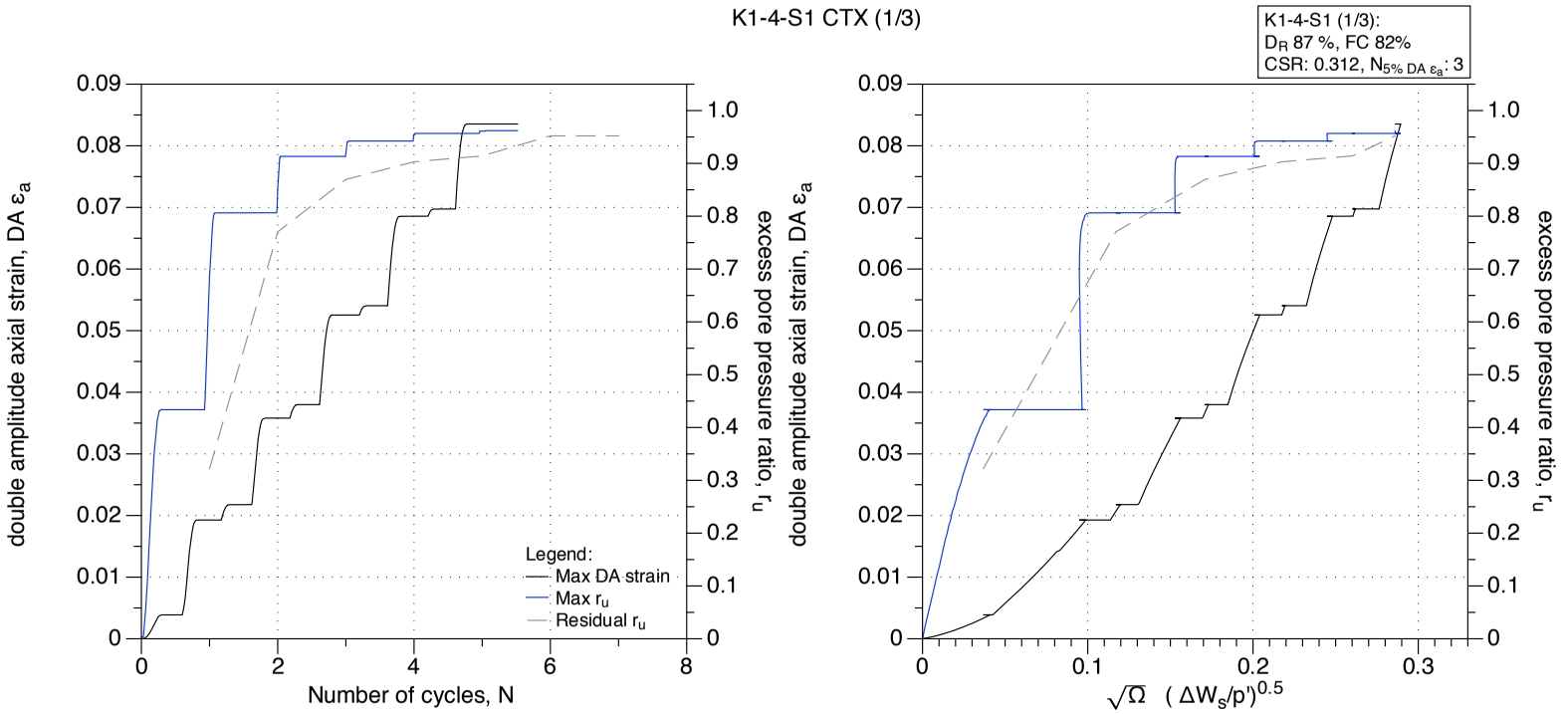

Figure 4.106: K1-4-S1 GP sample, undrained cyclic triaxial test (CTX). Development of strain and excess pore water pressure with number of cycles and normalised shear work.

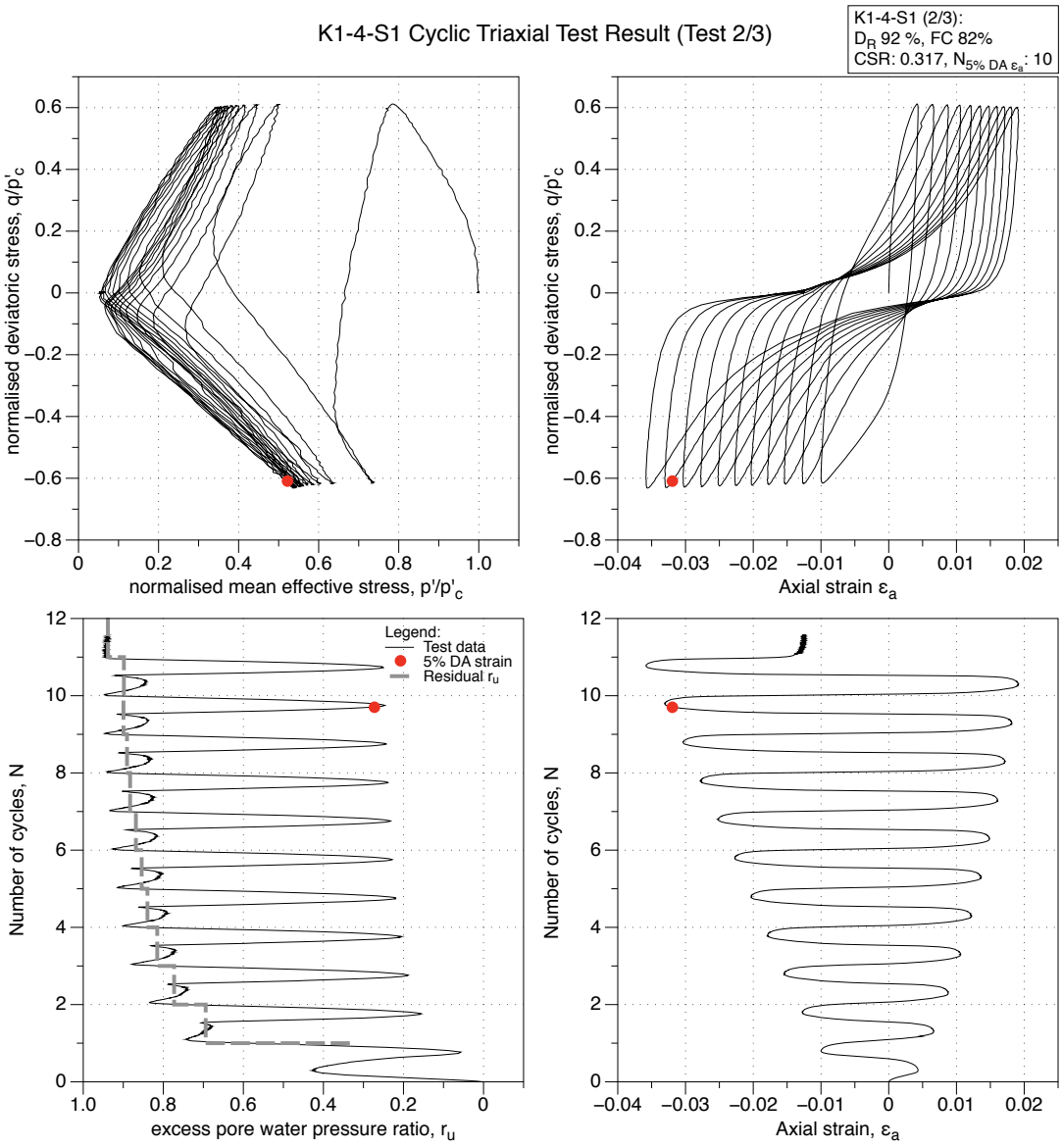

Figure 4.107: K1-4-S1 GP sample, reliquefaction undrained cyclic triaxial test (CTX). Effective stress-path, stress-strain, excess pore water pressure ratio and strain development plots.

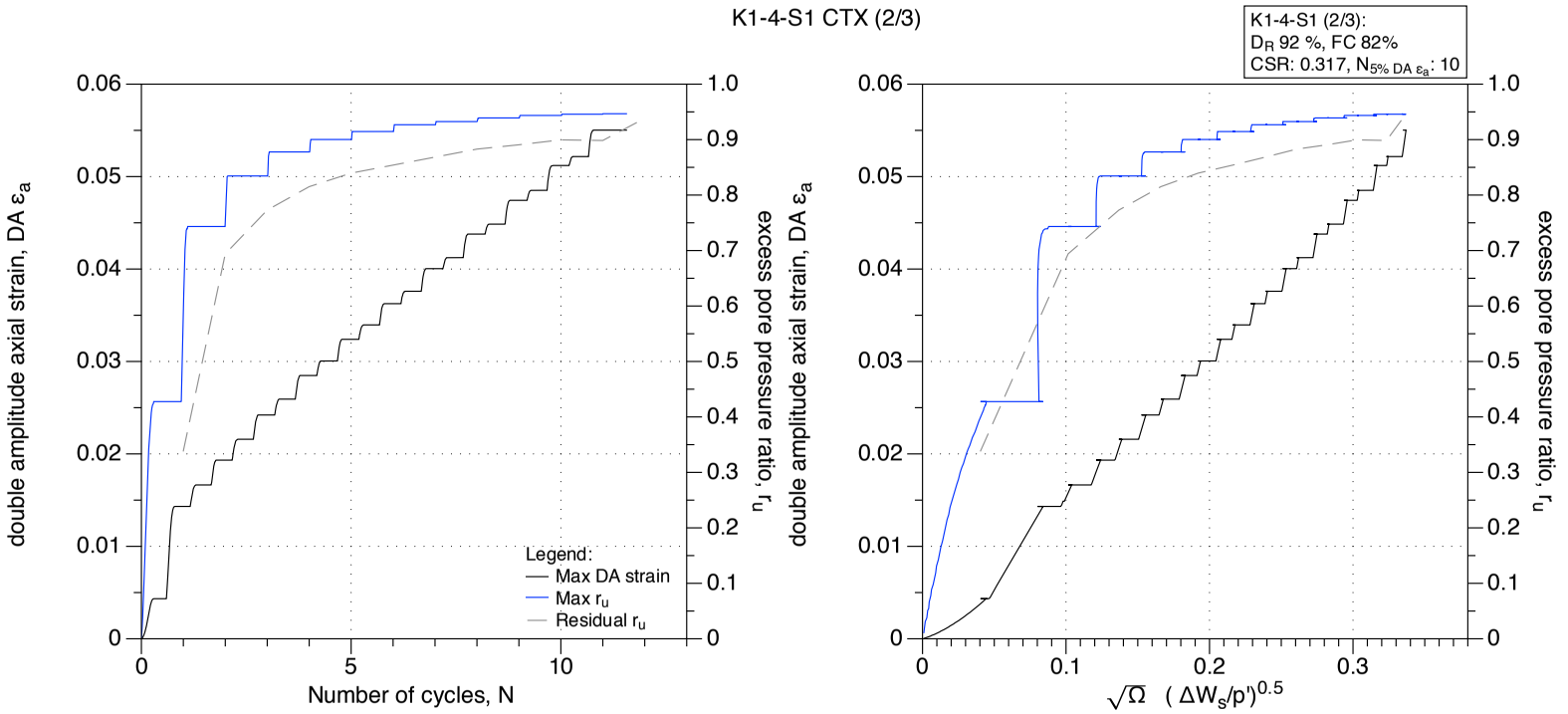

Figure 4.108: K1-4-S1 GP sample, reliquefaction undrained cyclic triaxial test (CTX). Development of strain and excess pore water pressure with number of cycles and normalised shear work.

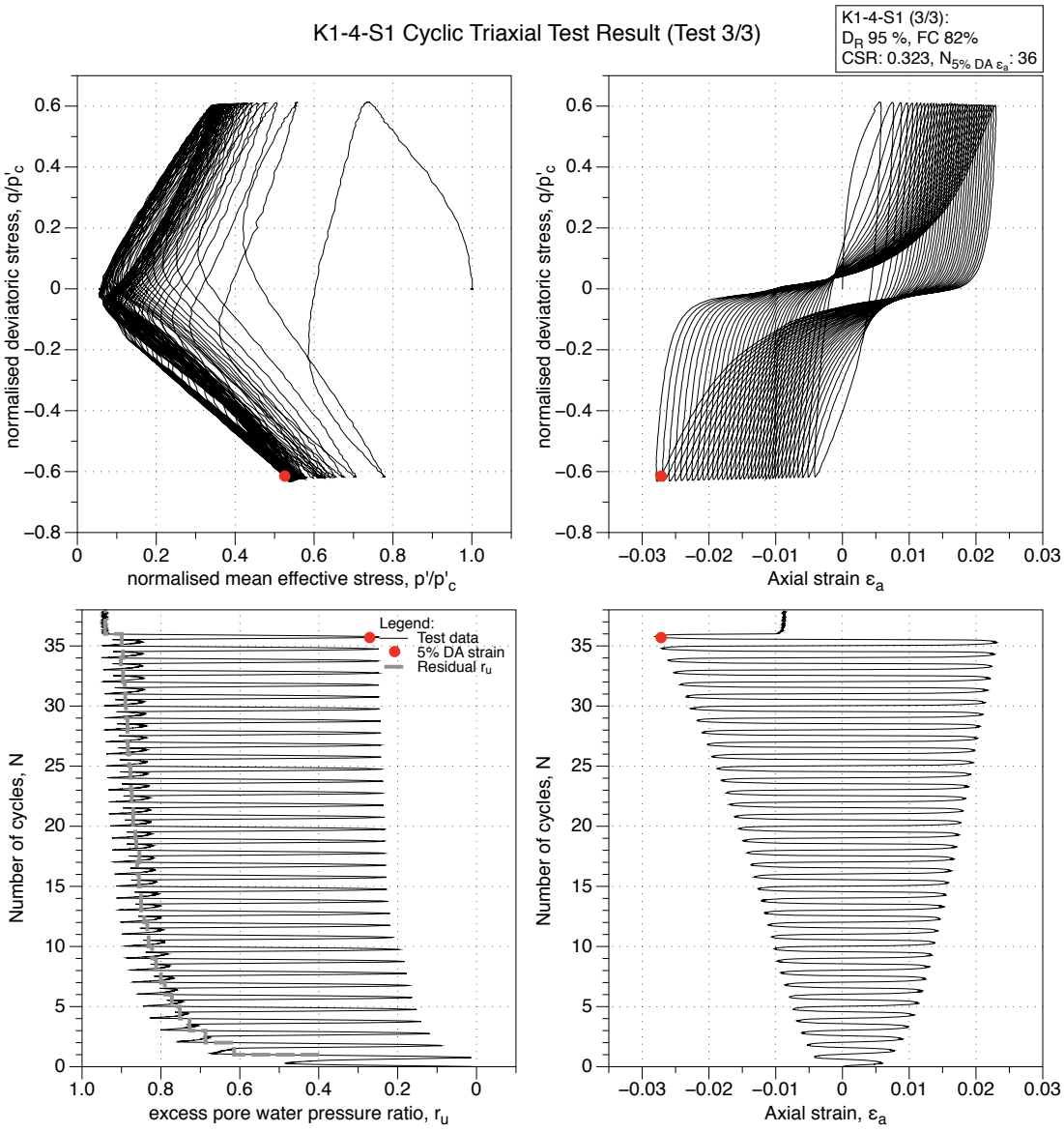

Figure 4.109: K1-4-S1 GP sample, second reliquefaction undrained cyclic triaxial test (CTX). Effective stress-path, stress-strain, excess pore water pressure ratio and strain development plots.

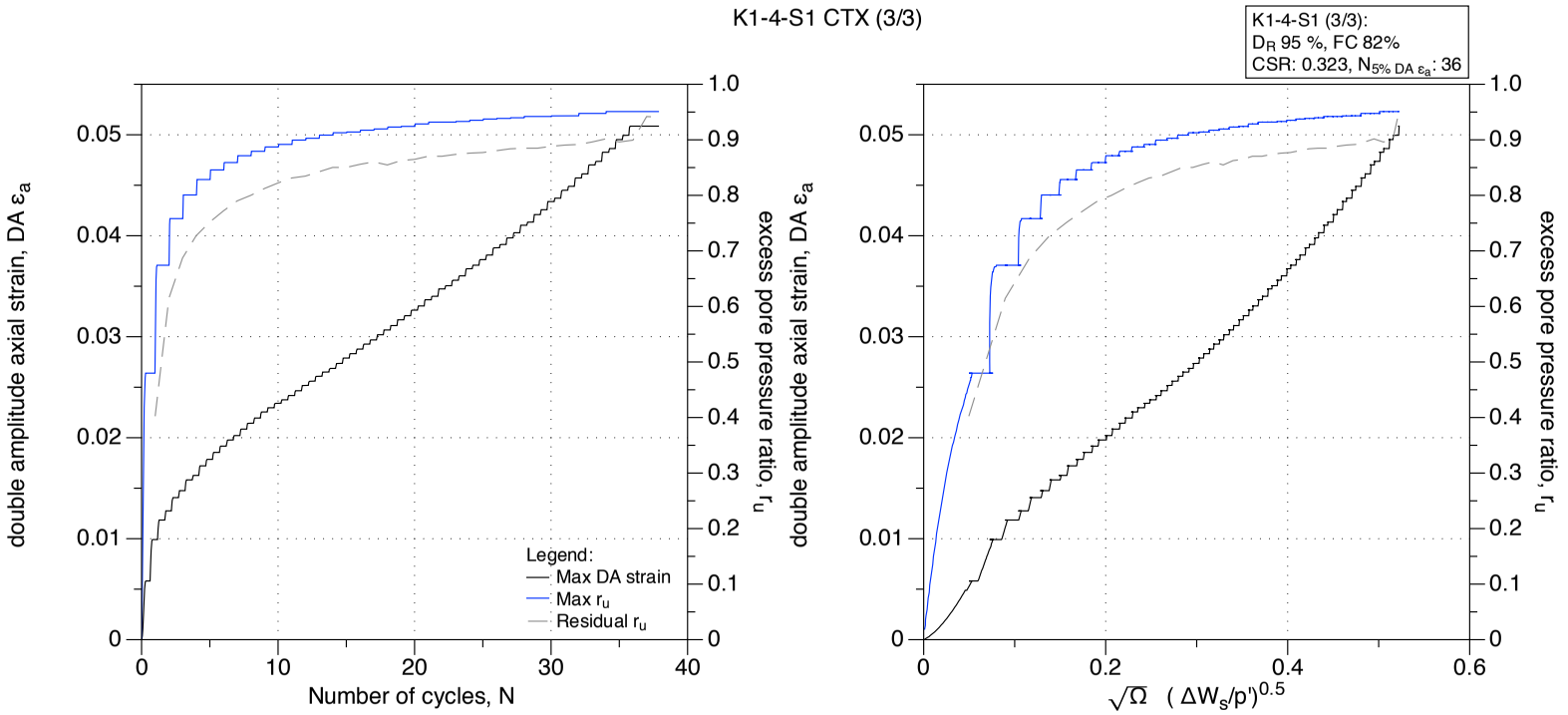

Figure 4.110: K1-4-S1 GP sample, second reliquefaction undrained cyclic triaxial test (CTX). Development of strain and excess pore water pressure with number of cycles and normalised shear work.

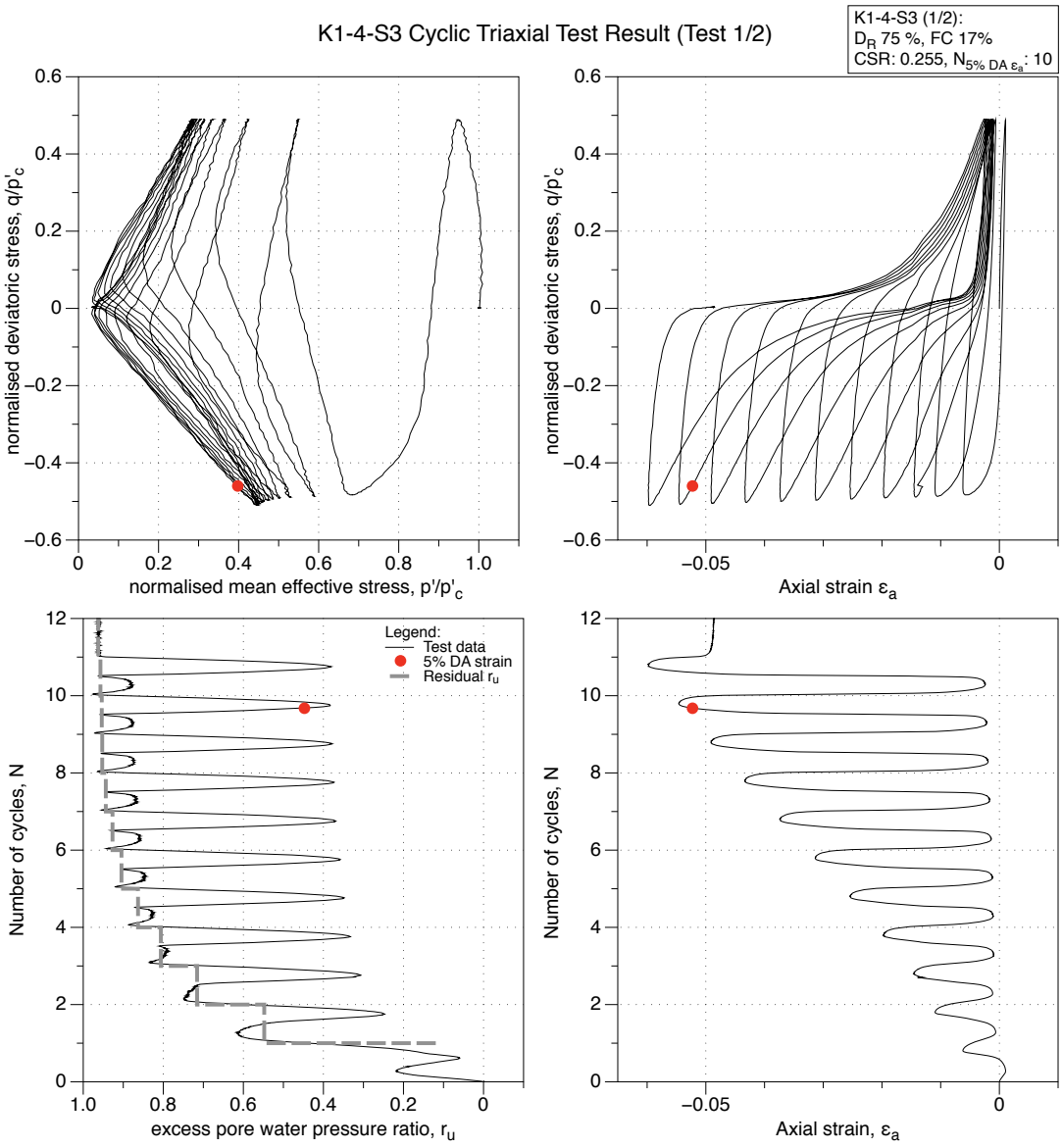

Figure 4.111: K1-4-S3 GP sample, undrained cyclic triaxial test (CTX). Effective stress-path, stress-strain, excess pore water pressure ratio and strain development plots.

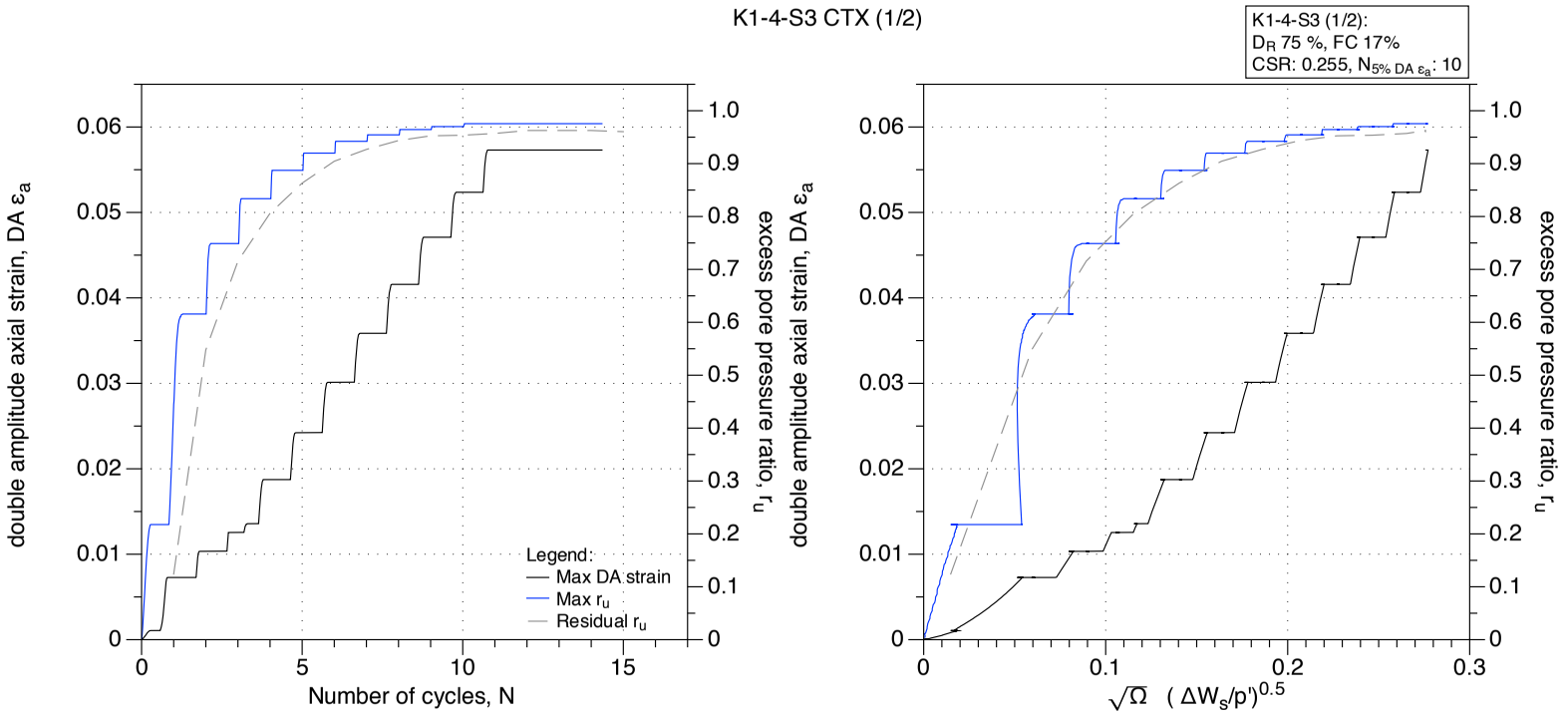

Figure 4.112: K1-4-S3 GP sample, undrained cyclic triaxial test (CTX). Development of strain and excess pore water pressure with number of cycles and normalised shear work.

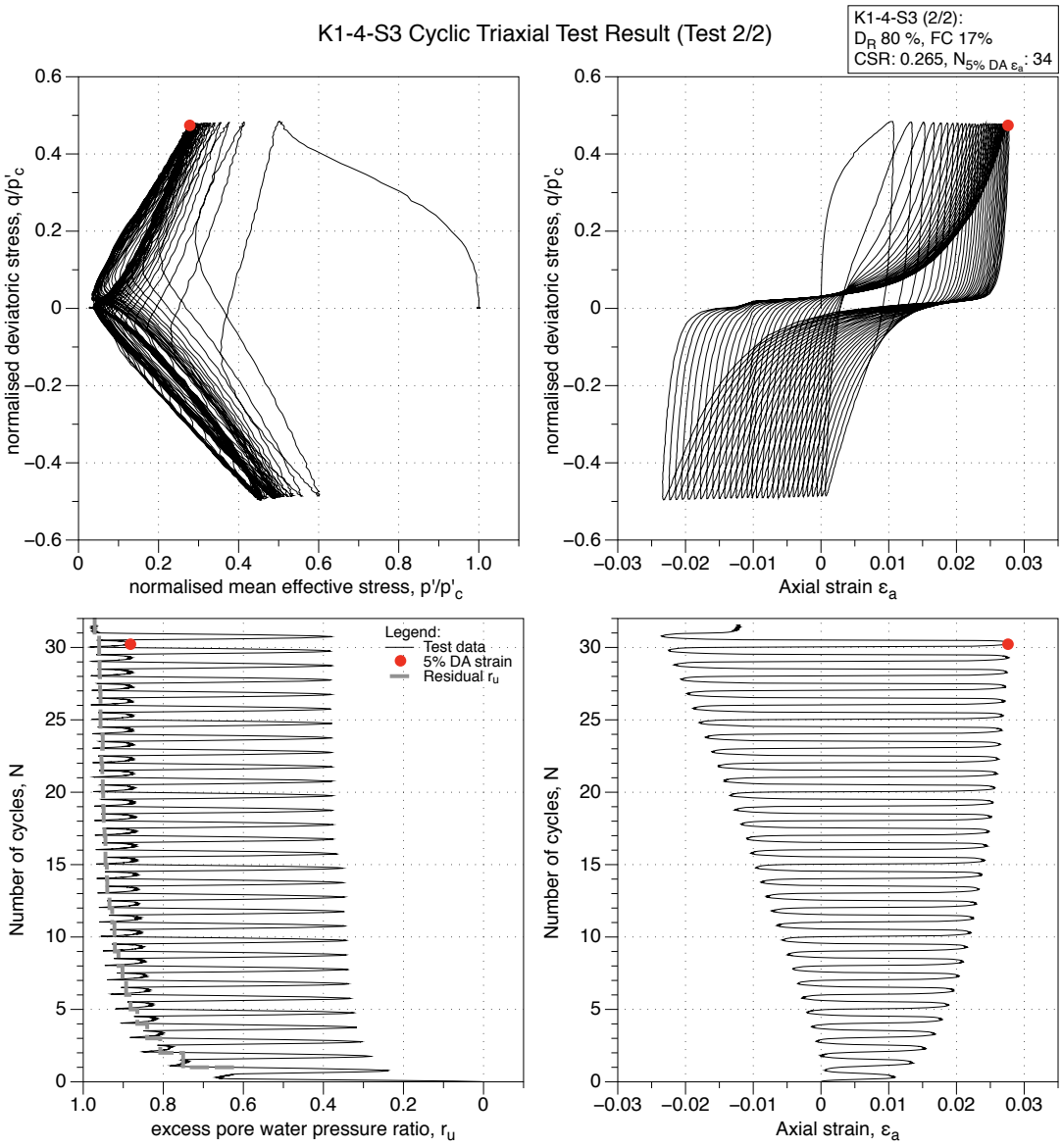

Figure 4.113: K1-4-S3 GP sample, reliquefaction undrained cyclic triaxial test (CTX). Effective stress-path, stress-strain, excess pore water pressure ratio and strain development plots.

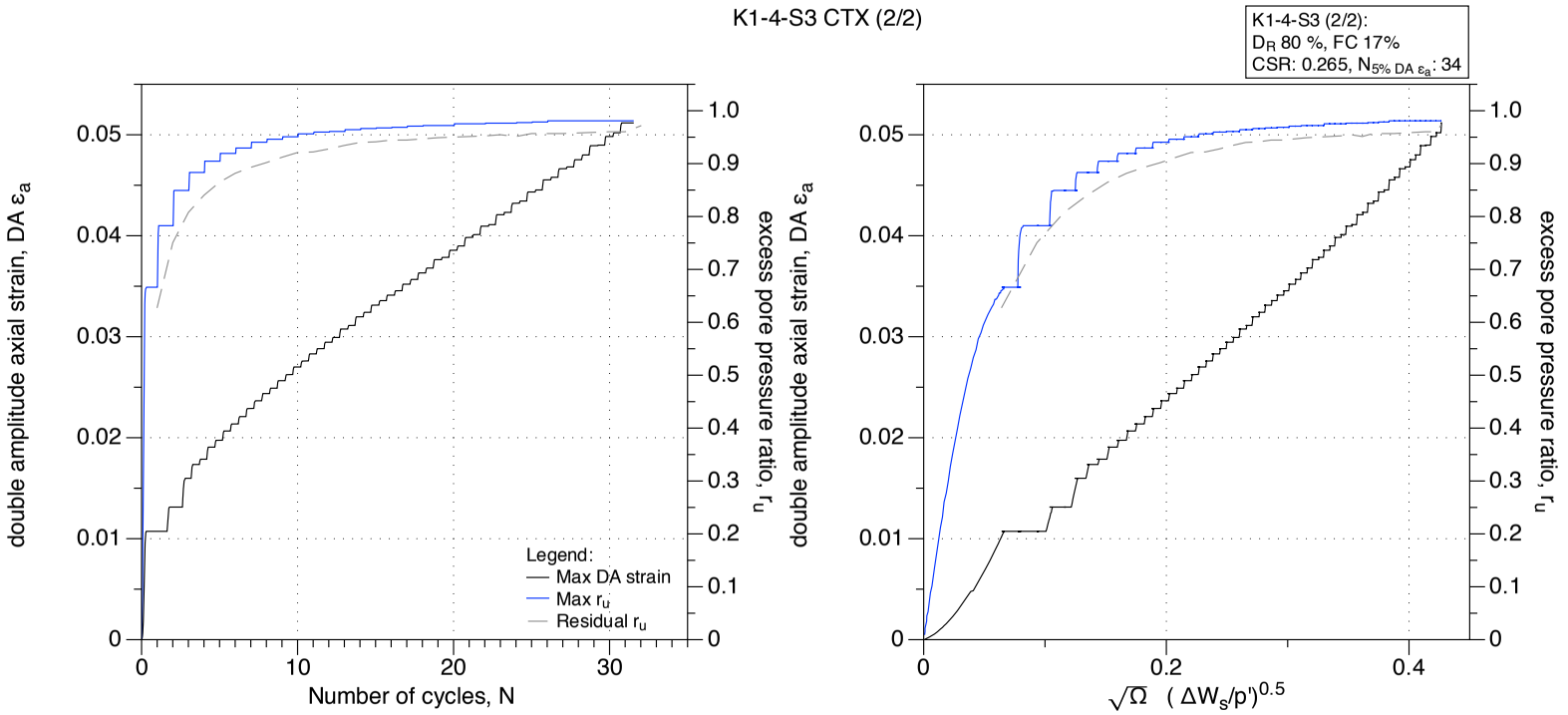

Figure 4.114: K1-4-S3 GP sample, reliquefaction undrained cyclic triaxial test (CTX). Development of strain and excess pore water pressure with number of cycles and normalised shear work.

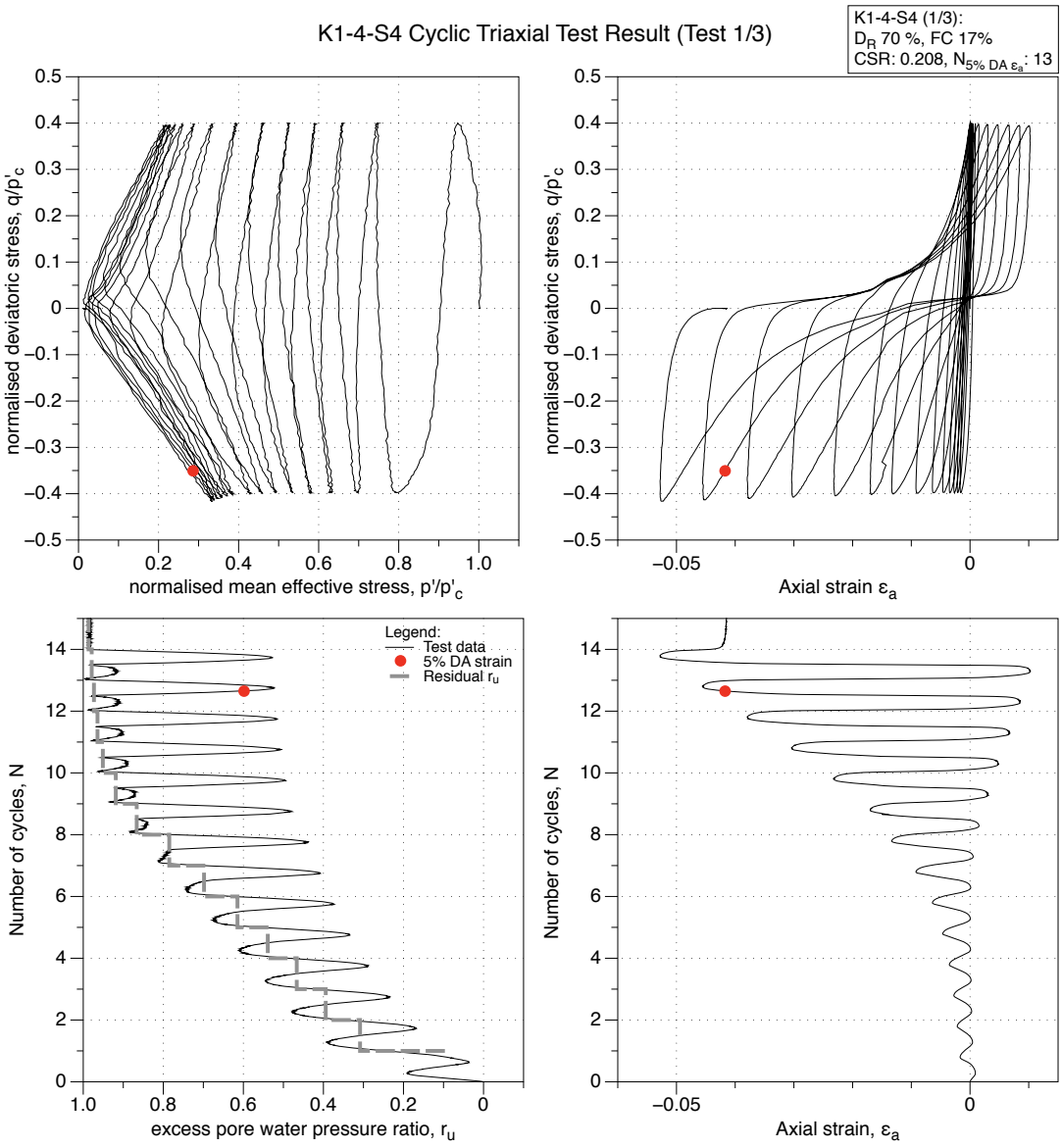

Figure 4.115: K1-4-S4 GP sample, undrained cyclic triaxial test (CTX). Effective stress-path, stress-strain, excess pore water pressure ratio and strain development plots.

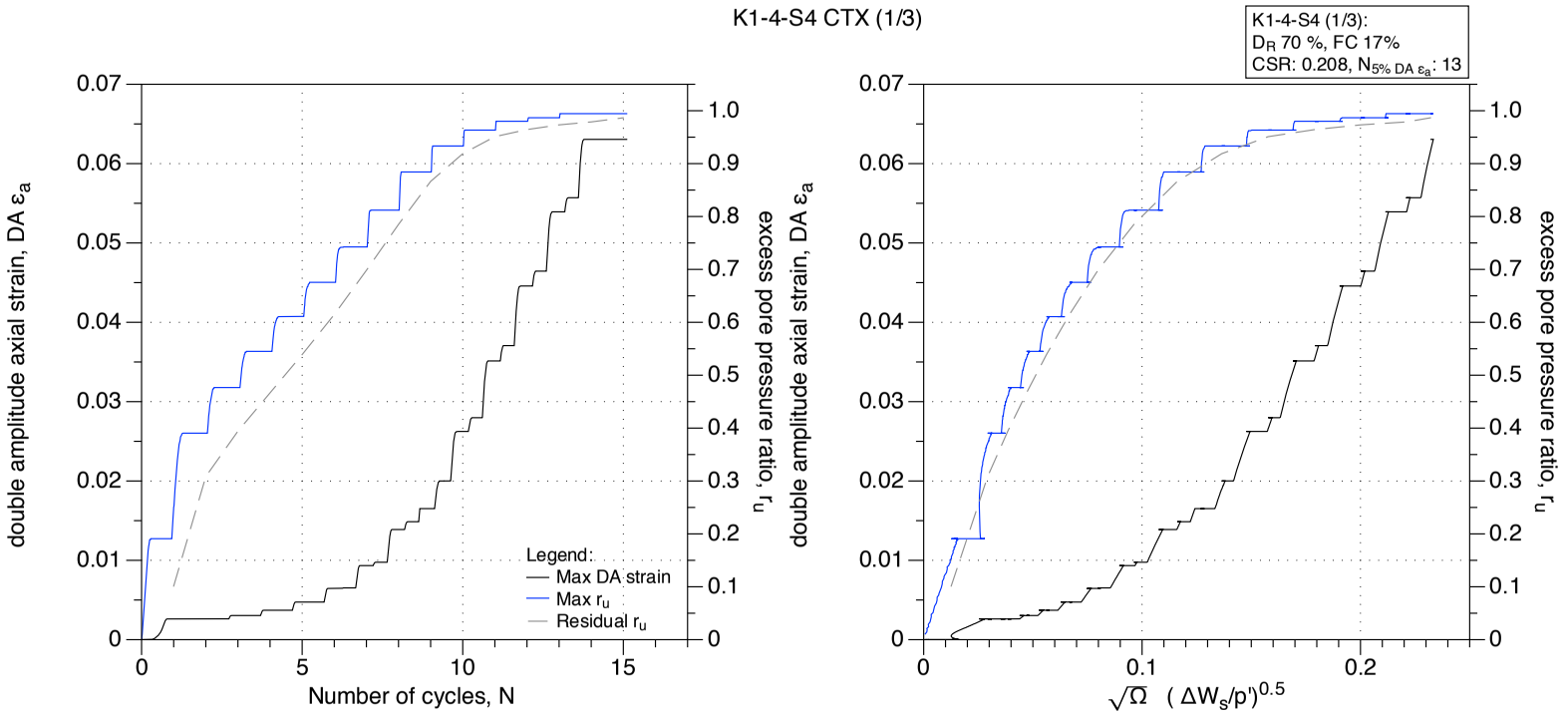

Figure 4.116: K1-4-S4 GP sample, undrained cyclic triaxial test (CTX). Development of strain and excess pore water pressure with number of cycles and normalised shear work.

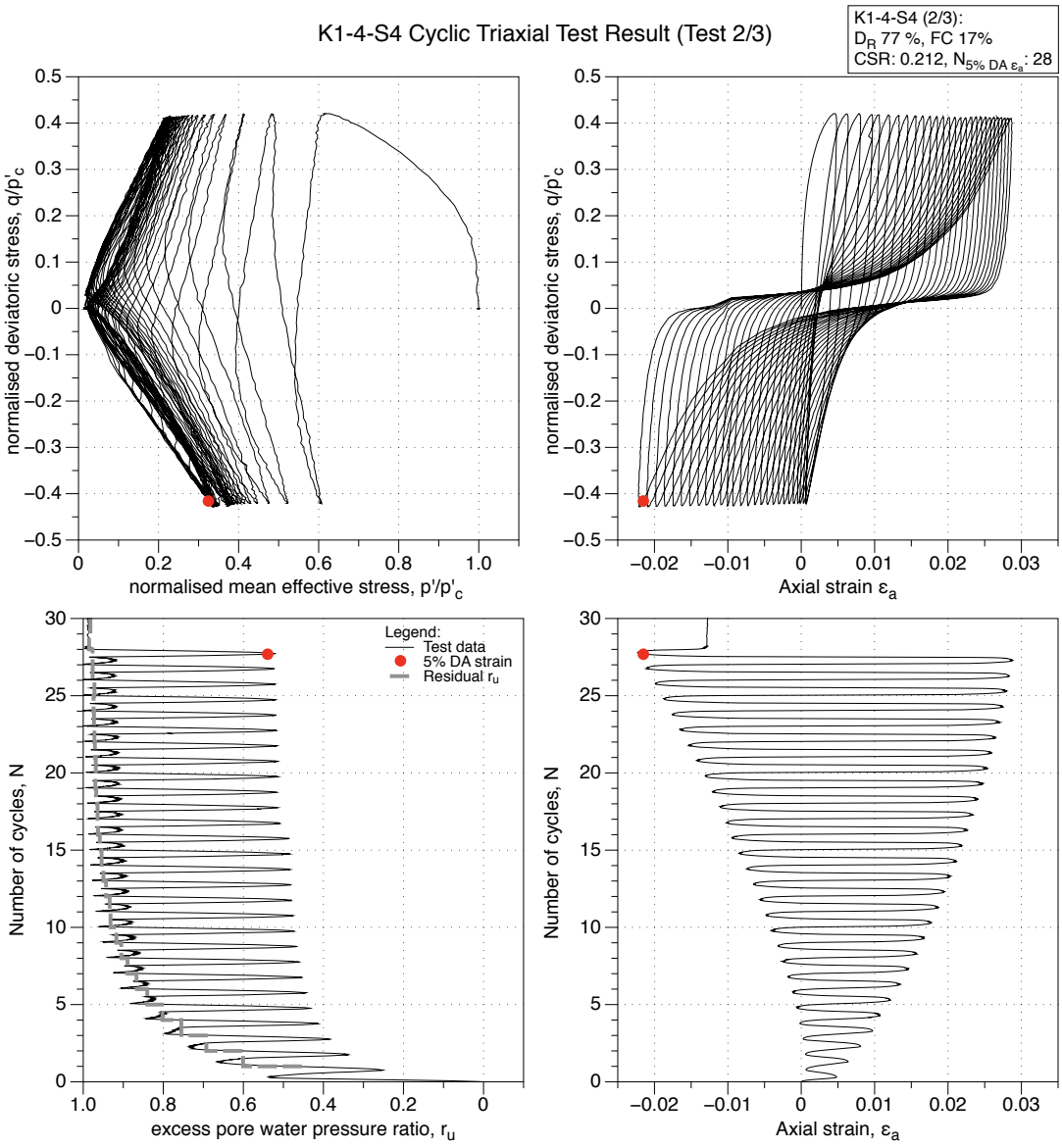

Figure 4.117: K1-4-S4 GP sample, reliquefaction undrained cyclic triaxial test (CTX). Effective stress-path, stress-strain, excess pore water pressure ratio and strain development plots.

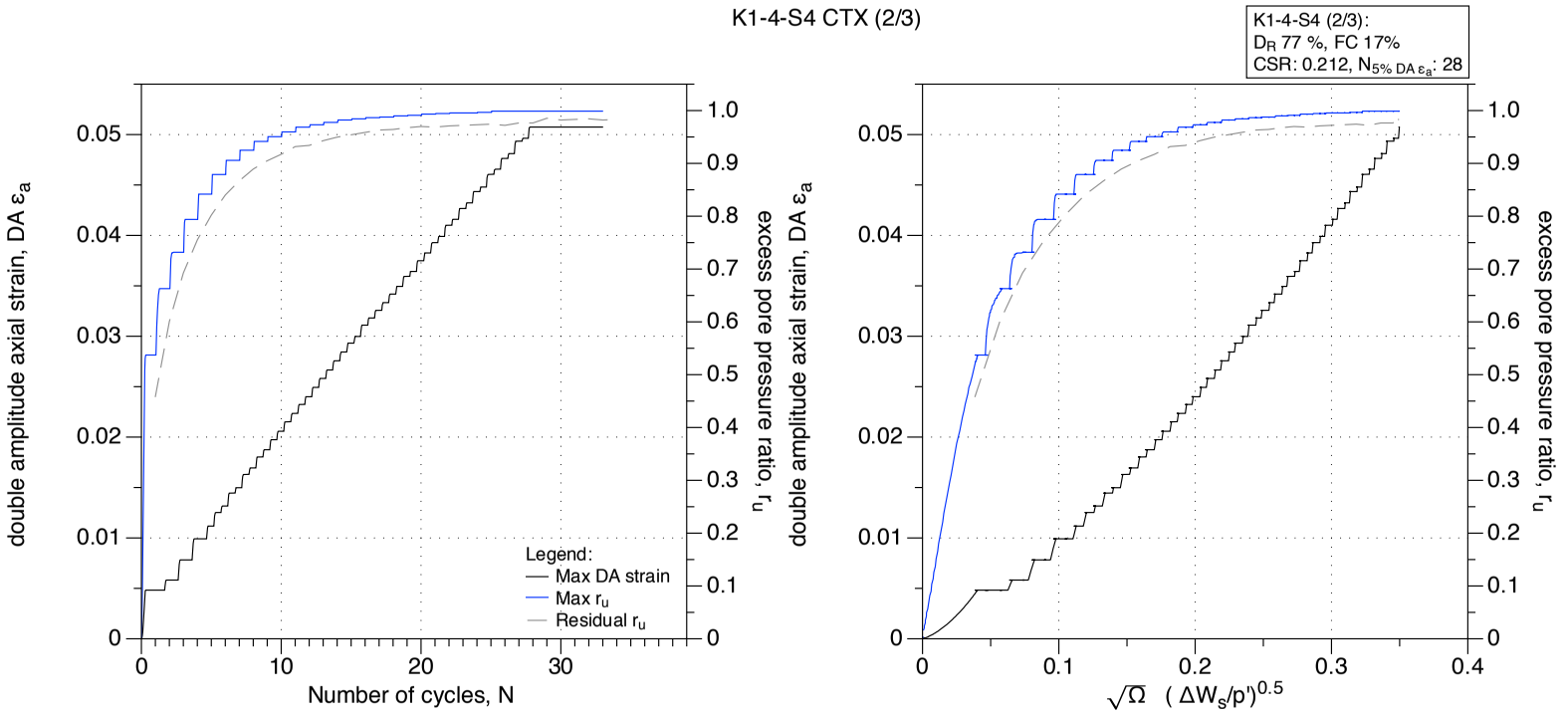

Figure 4.118: K1-4-S4 GP sample, reliquefaction undrained cyclic triaxial test (CTX). Development of strain and excess pore water pressure with number of cycles and normalised shear work.

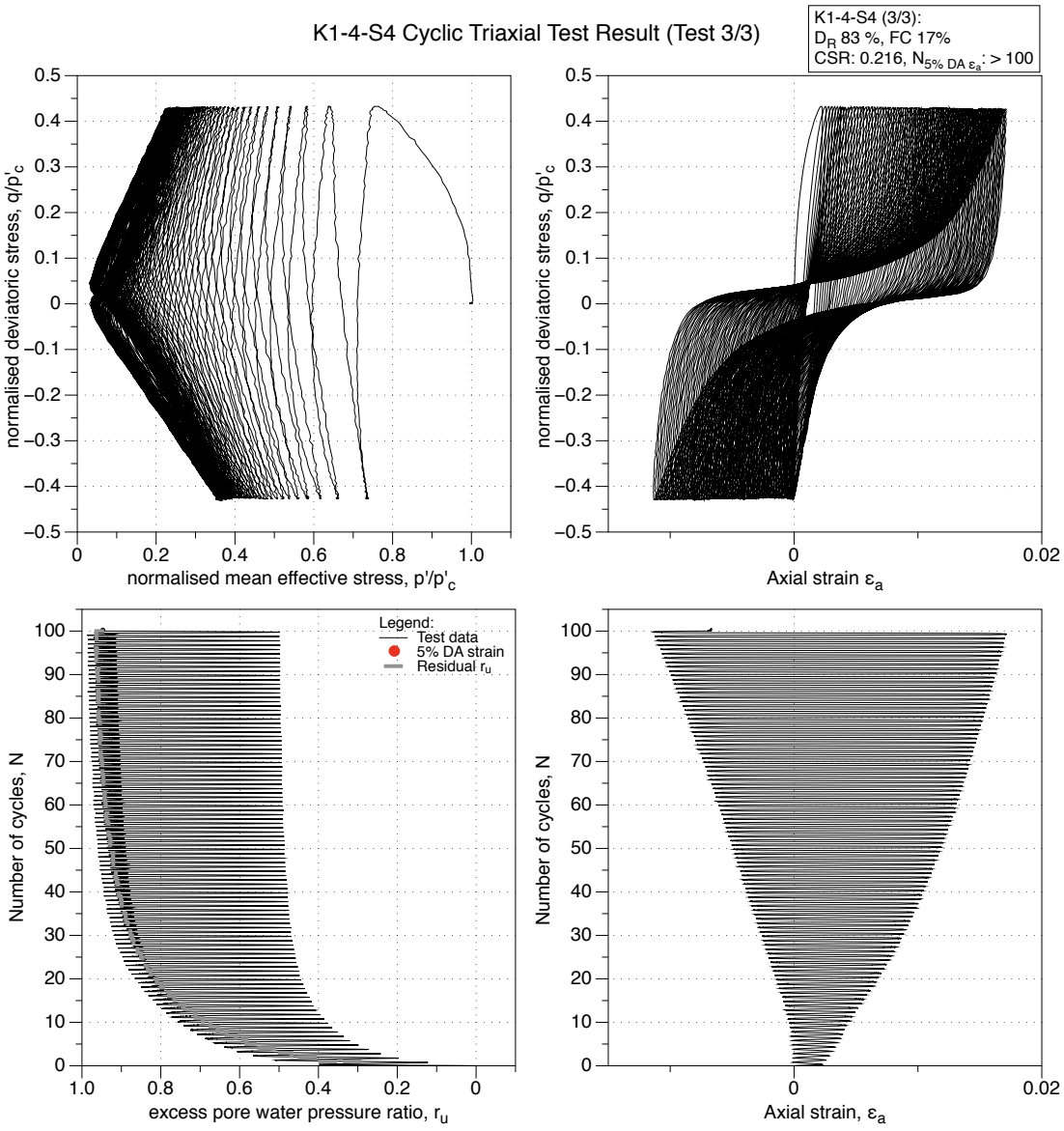

Figure 4.119: K1-4-S4 GP sample, second reliquefaction undrained cyclic triaxial test (CTX). Effective stress-path, stress-strain, excess pore water pressure ratio and strain development plots.

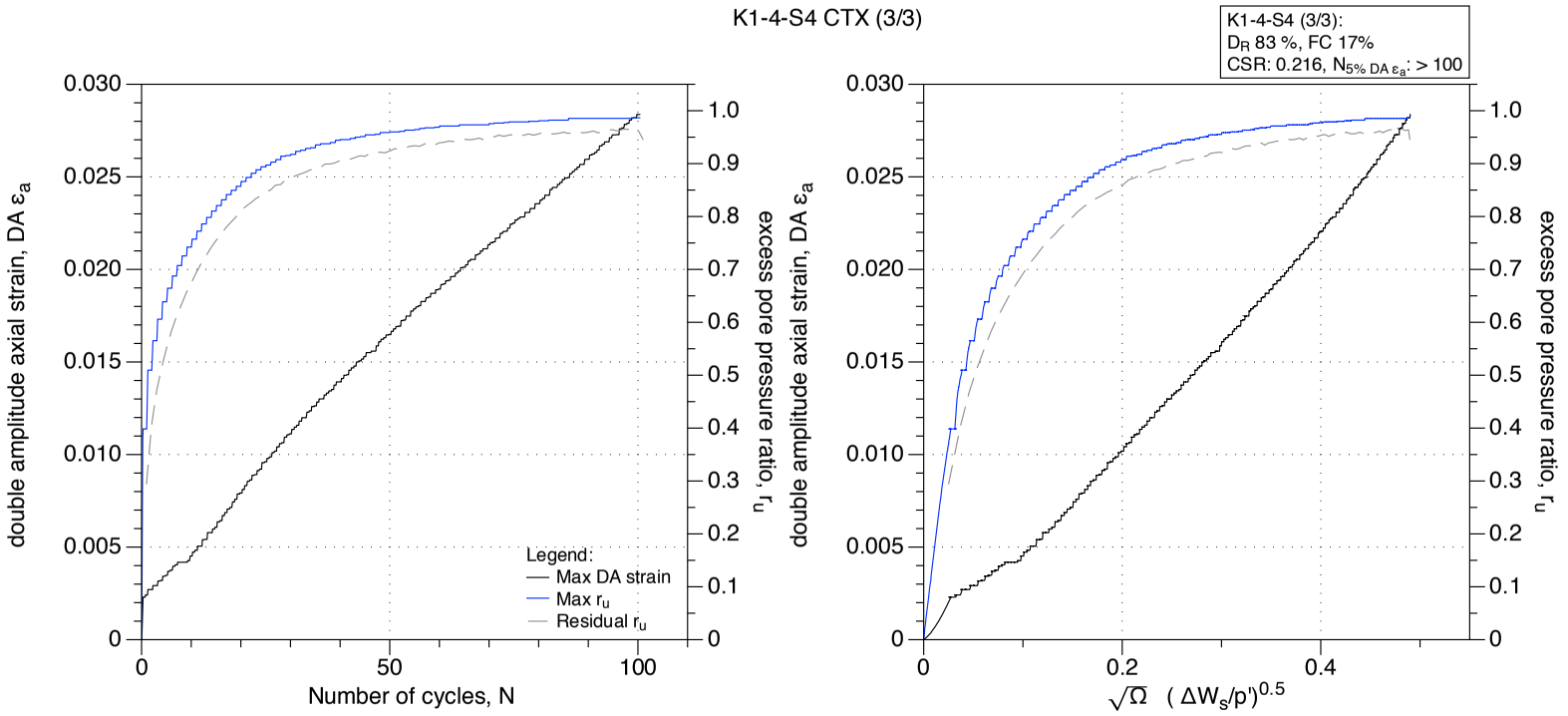

Figure 4.120: K1-4-S4 GP sample, second reliquefaction undrained cyclic triaxial test (CTX). Development of strain and excess pore water pressure with number of cycles and normalised shear work.

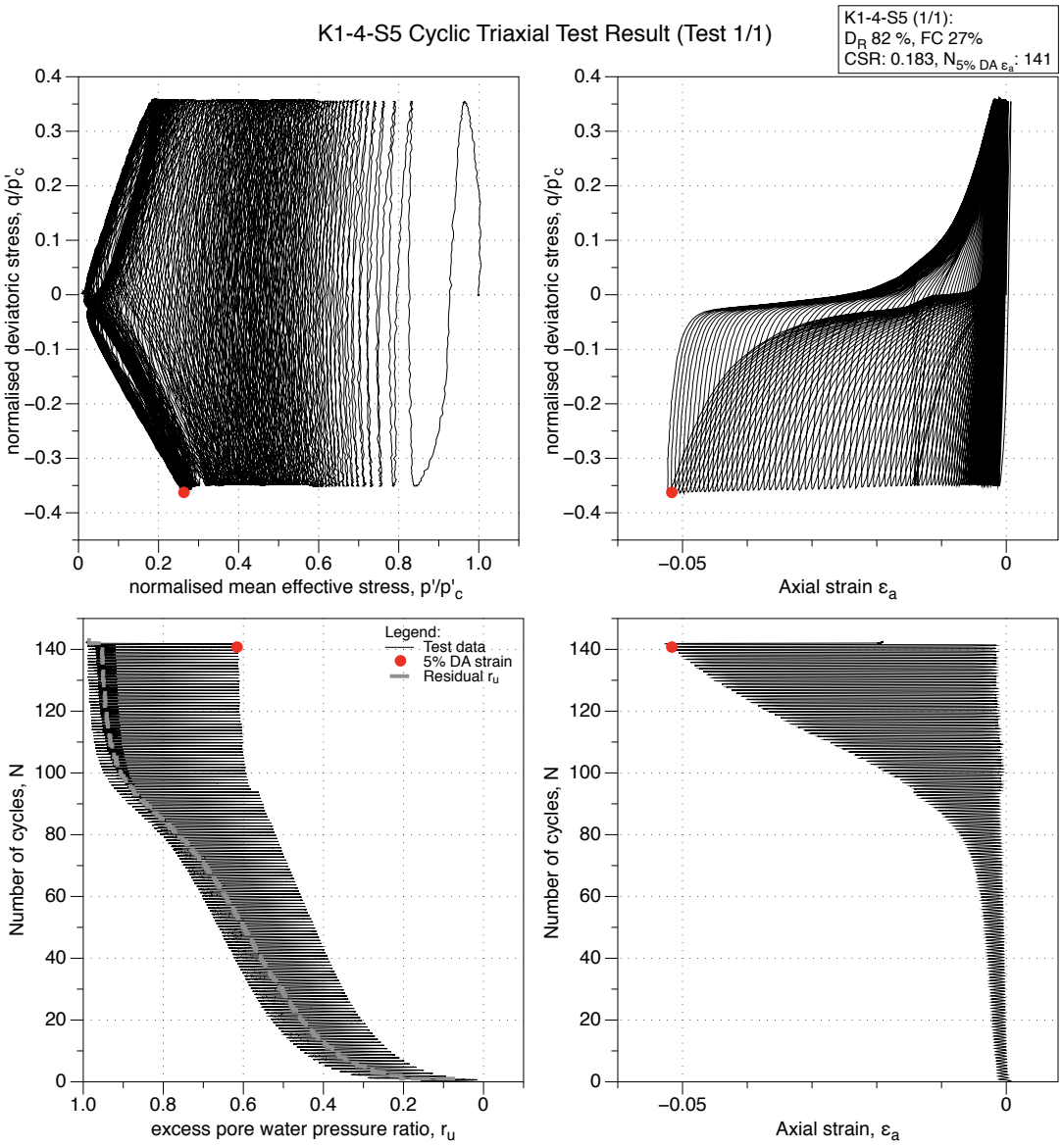

Figure 4.121: K1-4-S5 GP sample, undrained cyclic triaxial test (CTX). Effective stress-path, stress-strain, excess pore water pressure ratio and strain development plots.

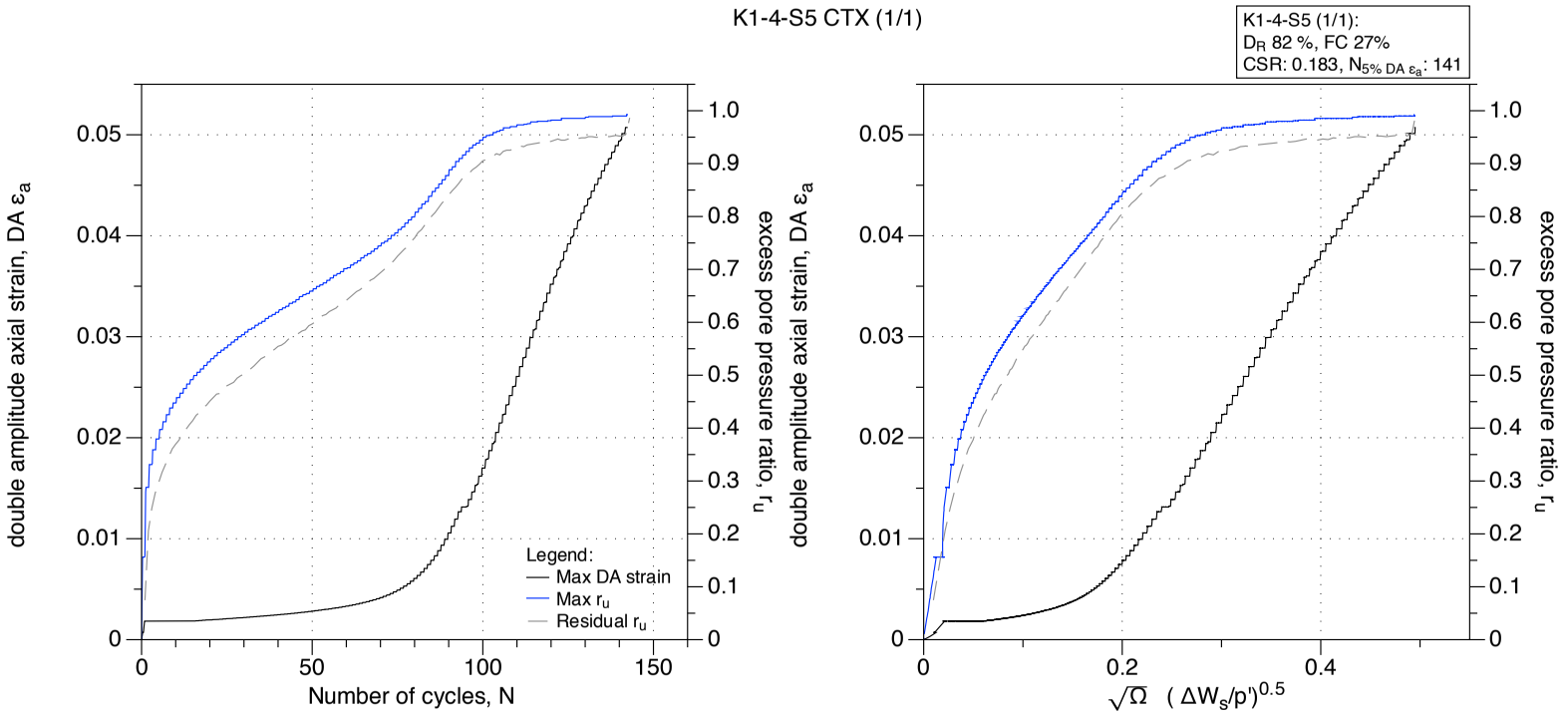

Figure 4.122: K1-4-S5 GP sample, undrained cyclic triaxial test (CTX). Development of strain and excess pore water pressure with number of cycles and normalised shear work.

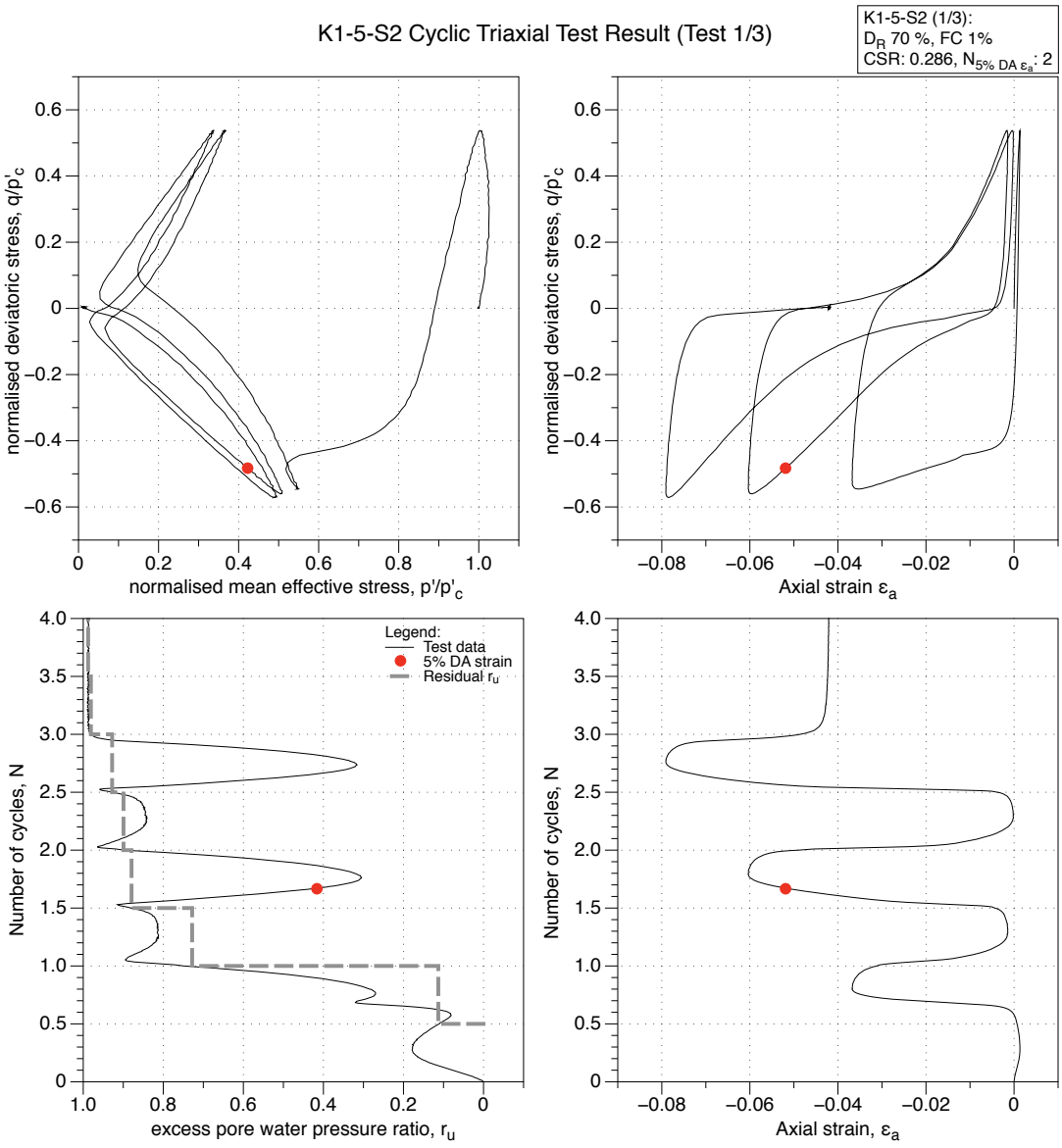

Figure 4.123: K1-5-S2 GP sample, undrained cyclic triaxial test (CTX). Effective stress-path, stress-strain, excess pore water pressure ratio and strain development plots.

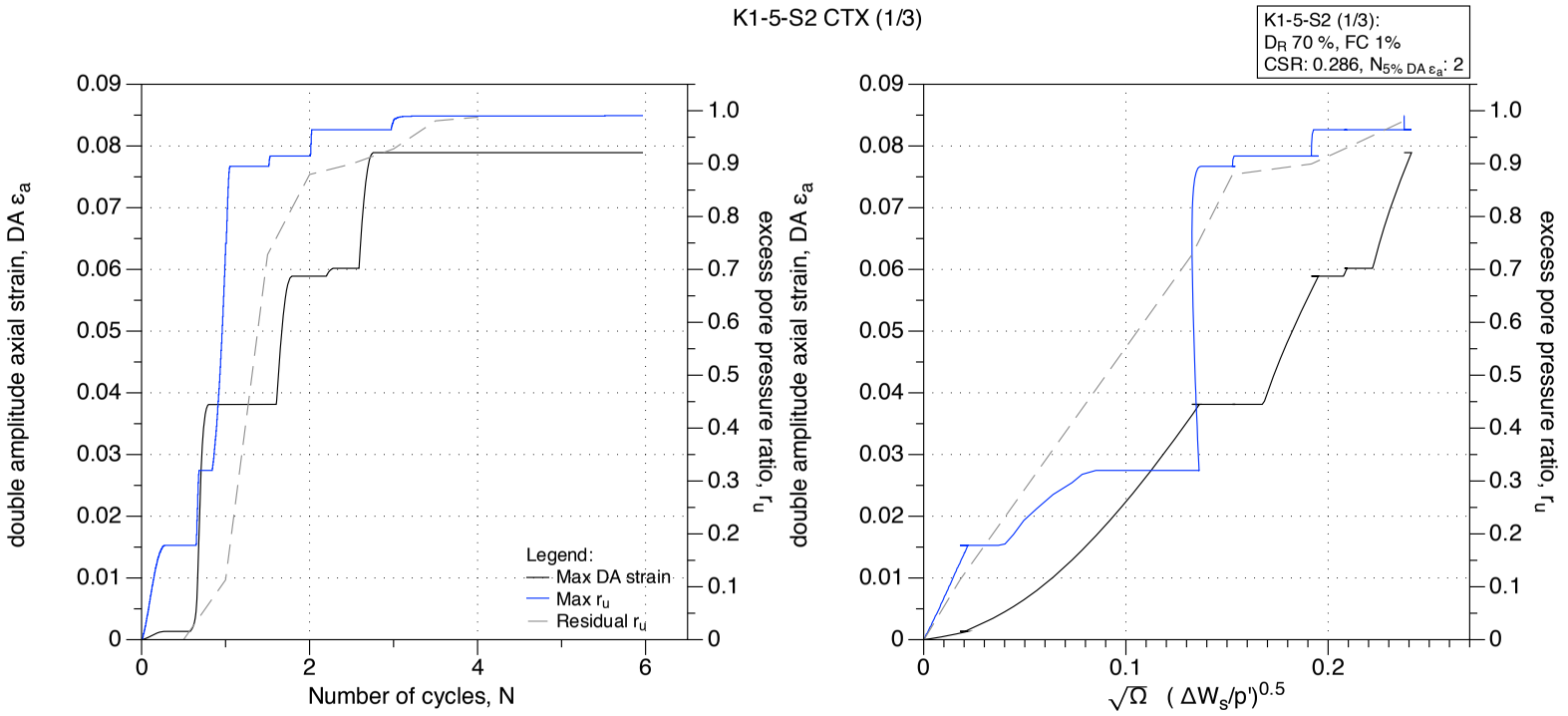

Figure 4.124: K1-5-S2 GP sample, undrained cyclic triaxial test (CTX). Development of strain and excess pore water pressure with number of cycles and normalised shear work.

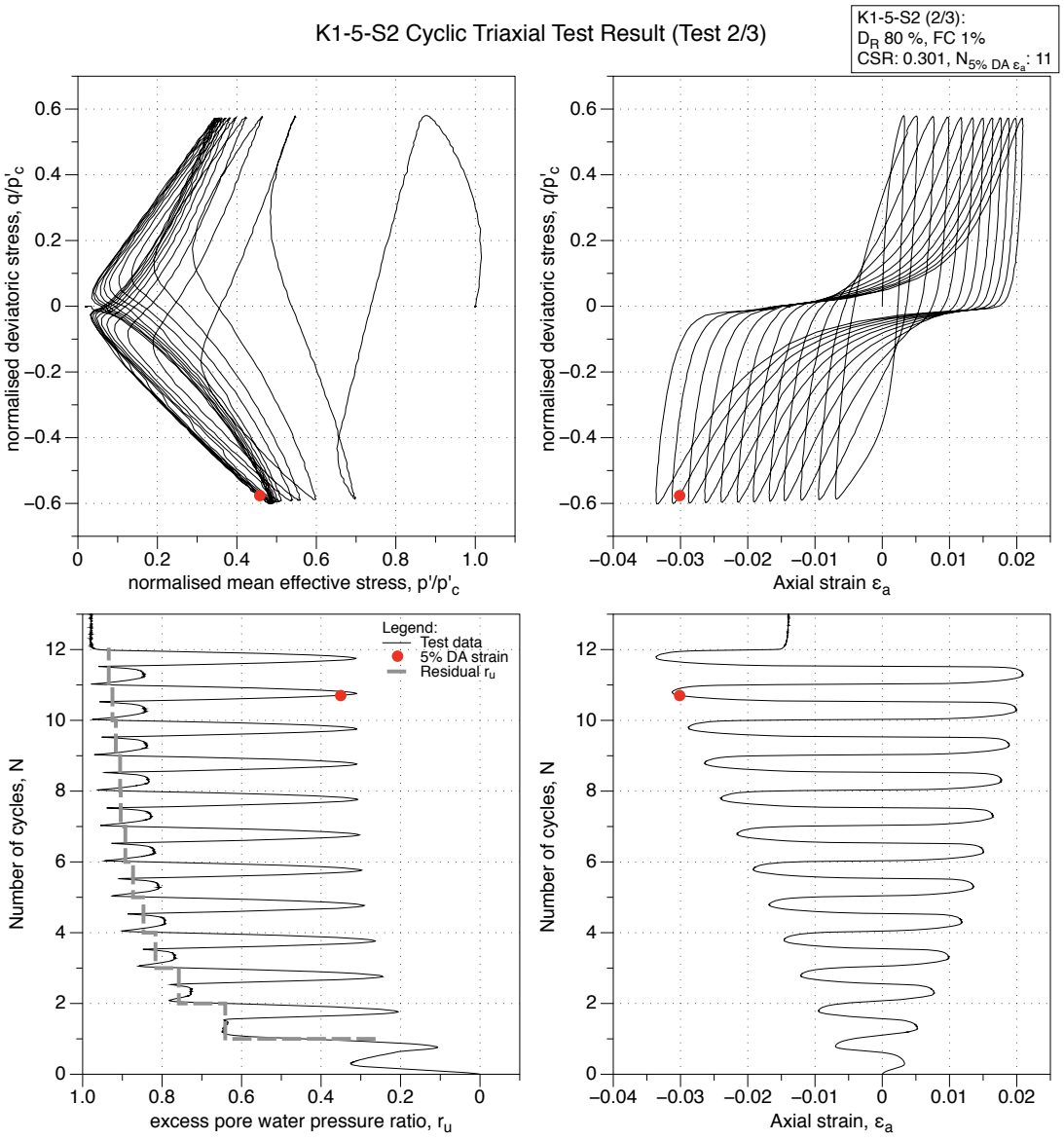

Figure 4.125: K1-5-S2 GP sample, reliquefaction undrained cyclic triaxial test (CTX). Effective stress-path, stress-strain, excess pore water pressure ratio and strain development plots.

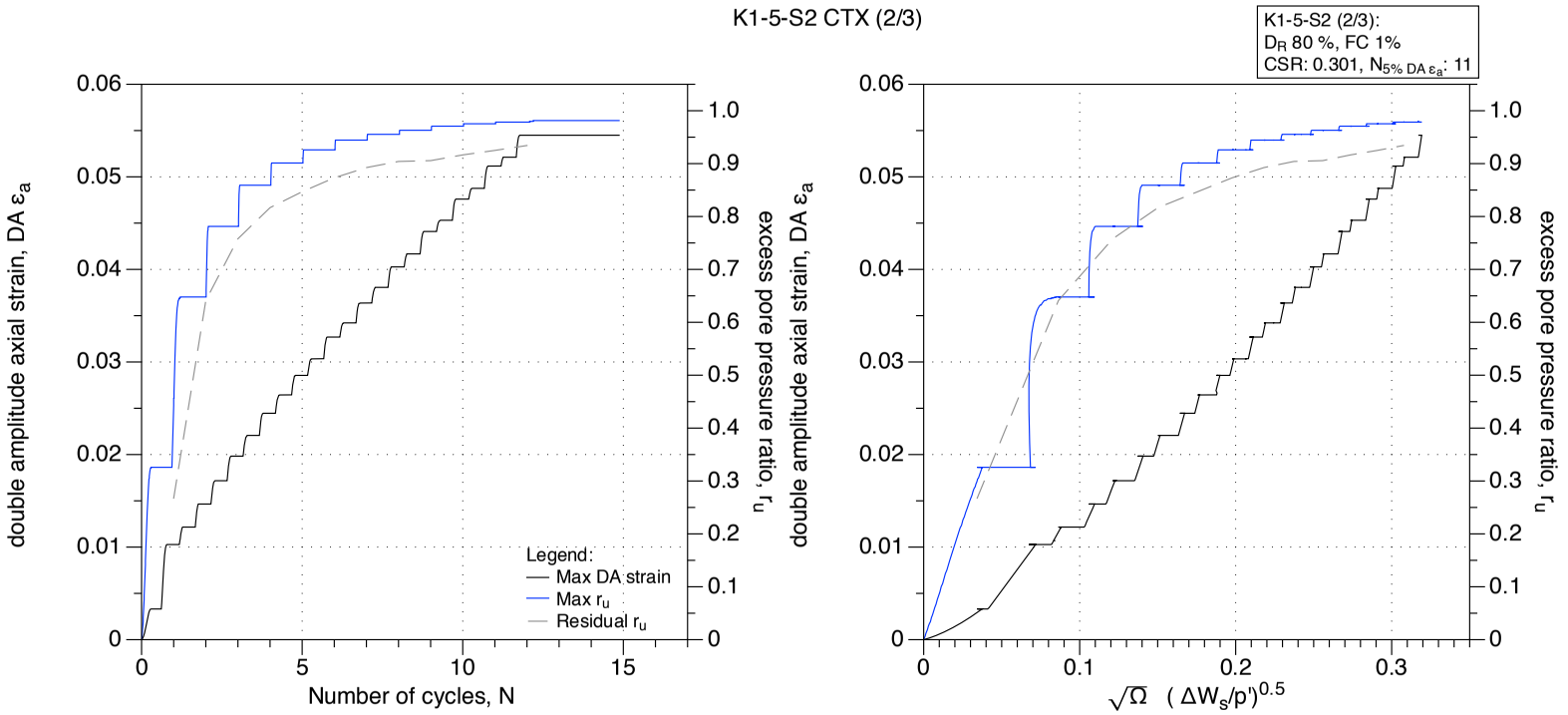

Figure 4.126: K1-5-S2 GP sample, reliquefaction undrained cyclic triaxial test (CTX). Development of strain and excess pore water pressure with number of cycles and normalised shear work.

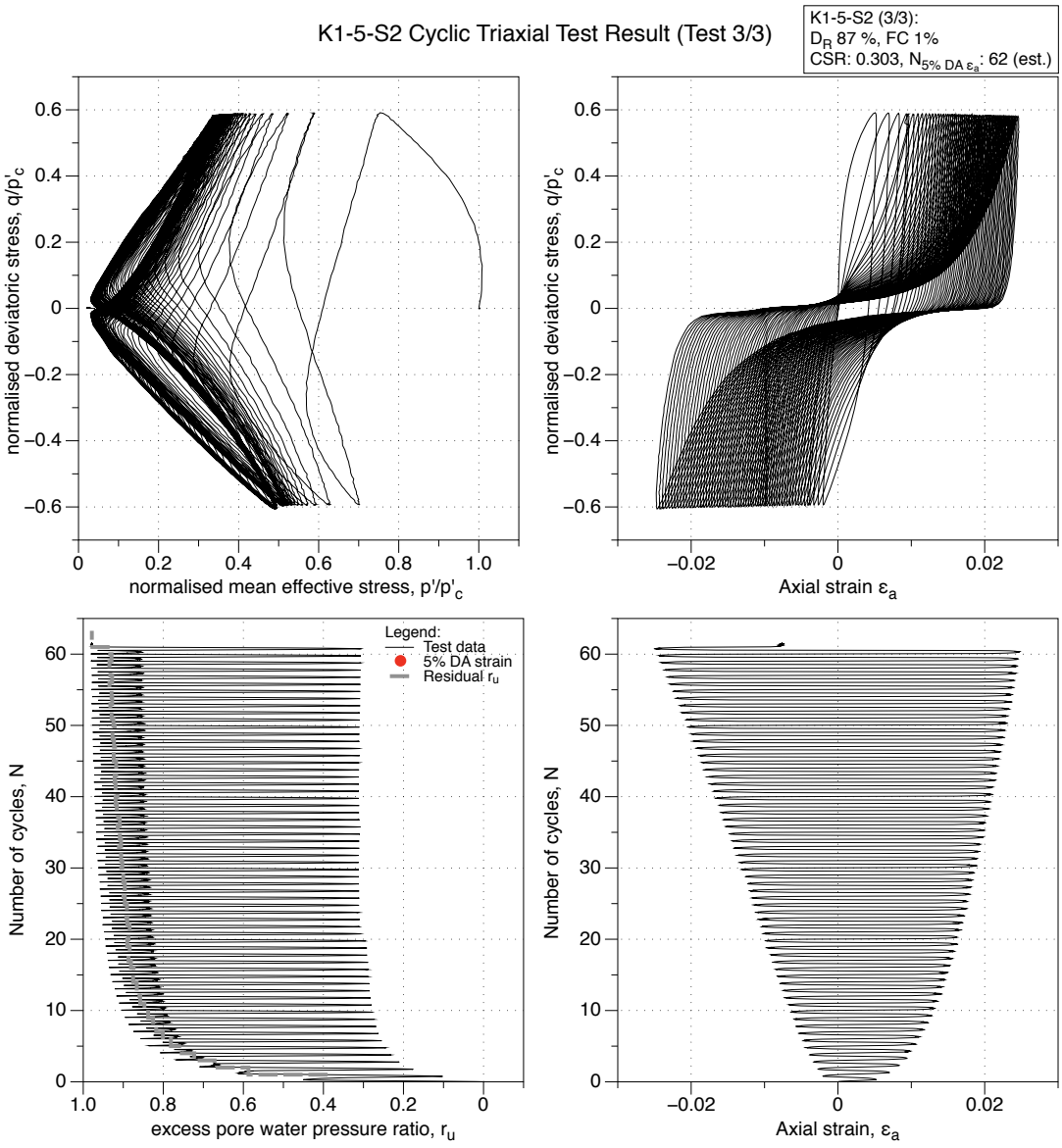

Figure 4.127: K1-5-S2 GP sample, second reliquefaction undrained cyclic triaxial test (CTX). Effective stress-path, stress-strain, excess pore water pressure ratio and strain development plots.

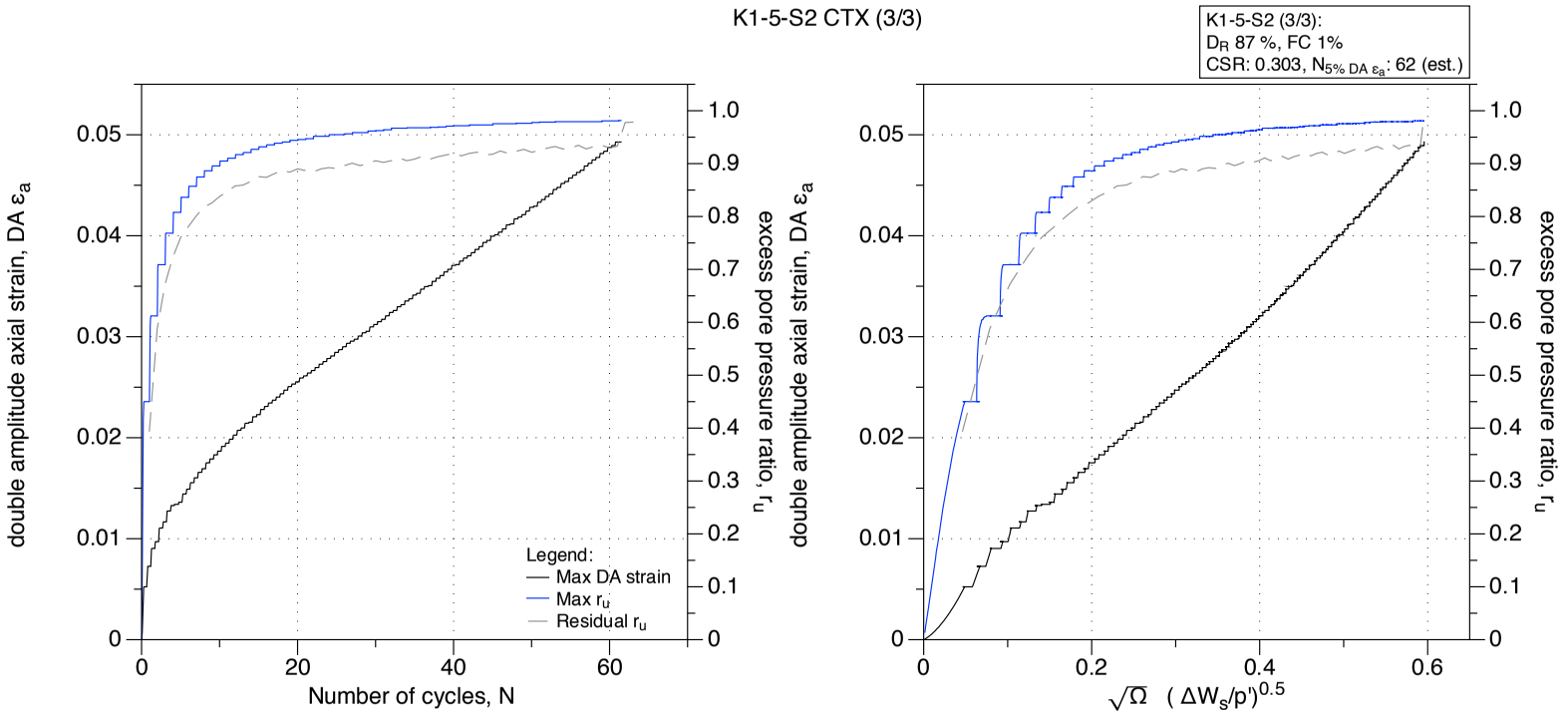

Figure 4.128: K1-5-S2 GP sample, second reliquefaction undrained cyclic triaxial test (CTX). Development of strain and excess pore water pressure with number of cycles and normalised shear work.

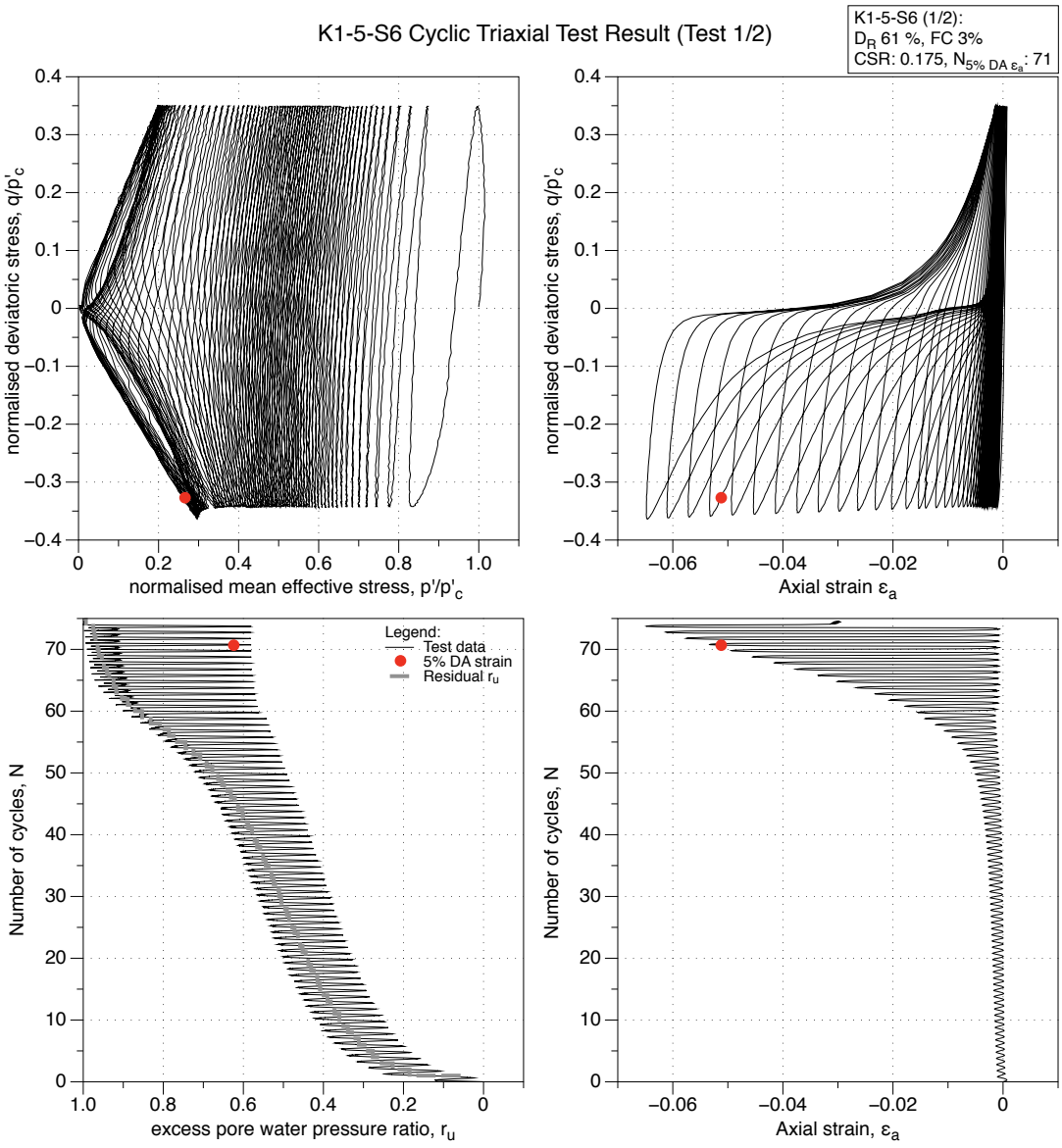

Figure 4.129: K1-5-S6 GP sample, undrained cyclic triaxial test (CTX). Effective stress-path, stress-strain, excess pore water pressure ratio and strain development plots.

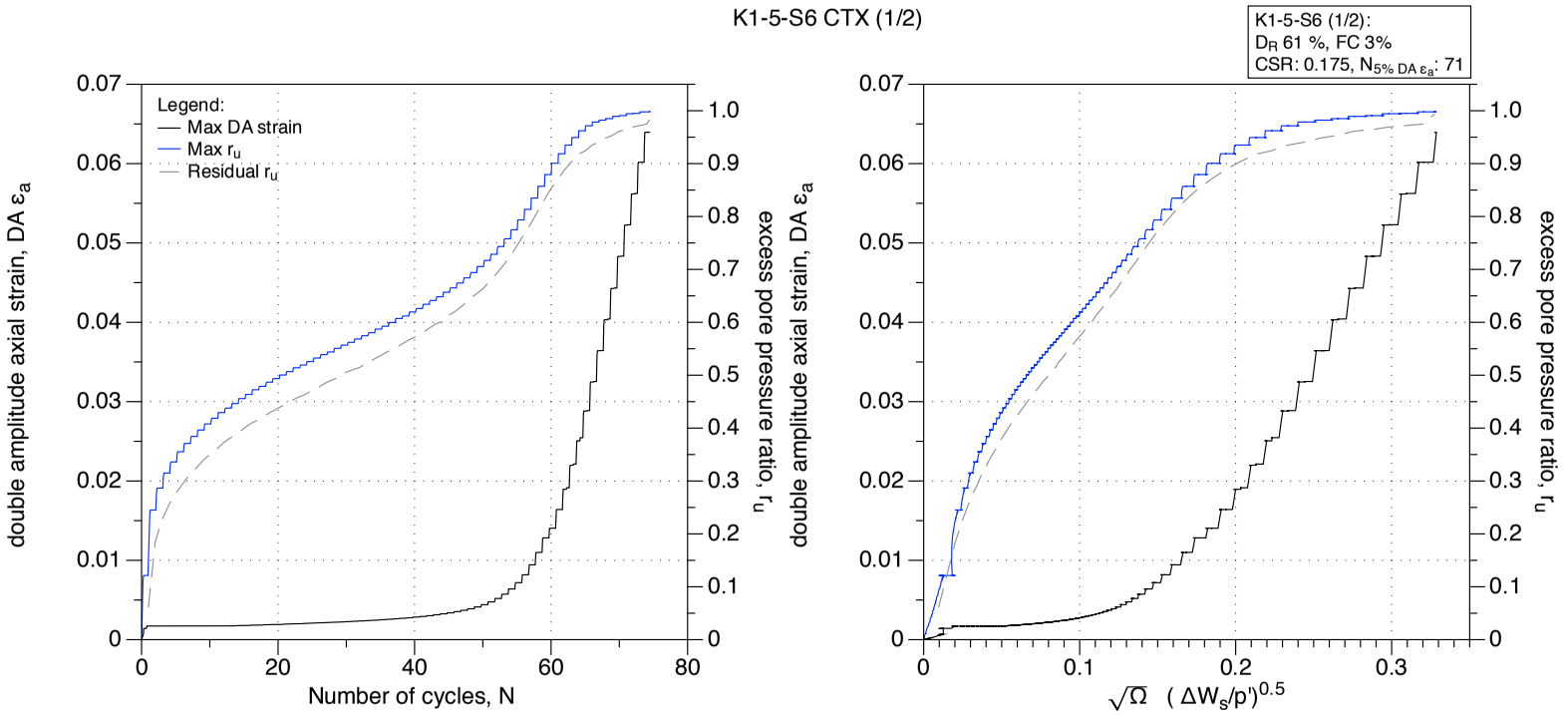

Figure 4.130: K1-5-S6 GP sample, undrained cyclic triaxial test (CTX). Development of strain and excess pore water pressure with number of cycles and normalised shear work.

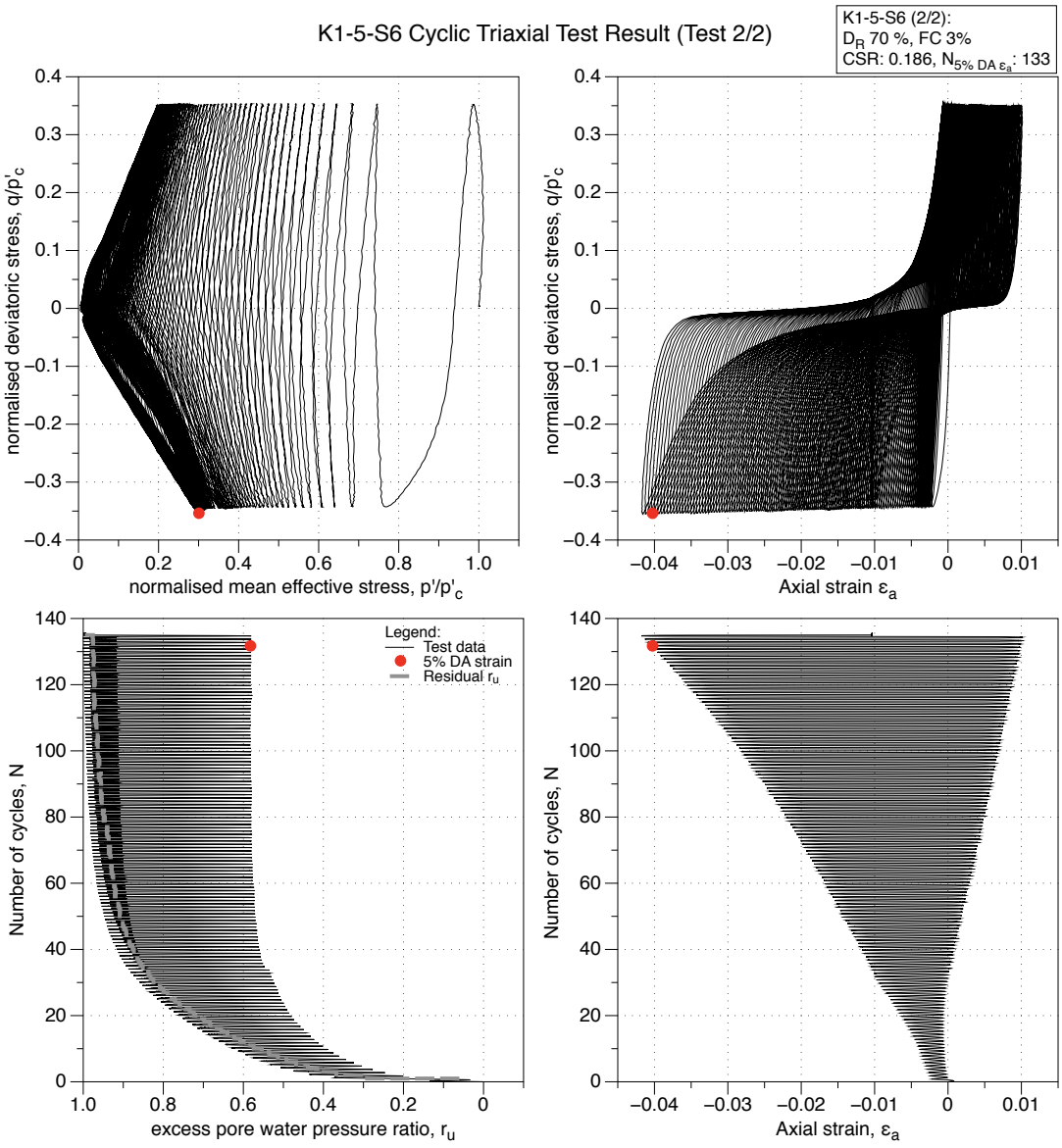

Figure 4.131: K1-5-S6 GP sample, reliquefaction undrained cyclic triaxial test (CTX). Effective stress-path, stress-strain, excess pore water pressure ratio and strain development plots.

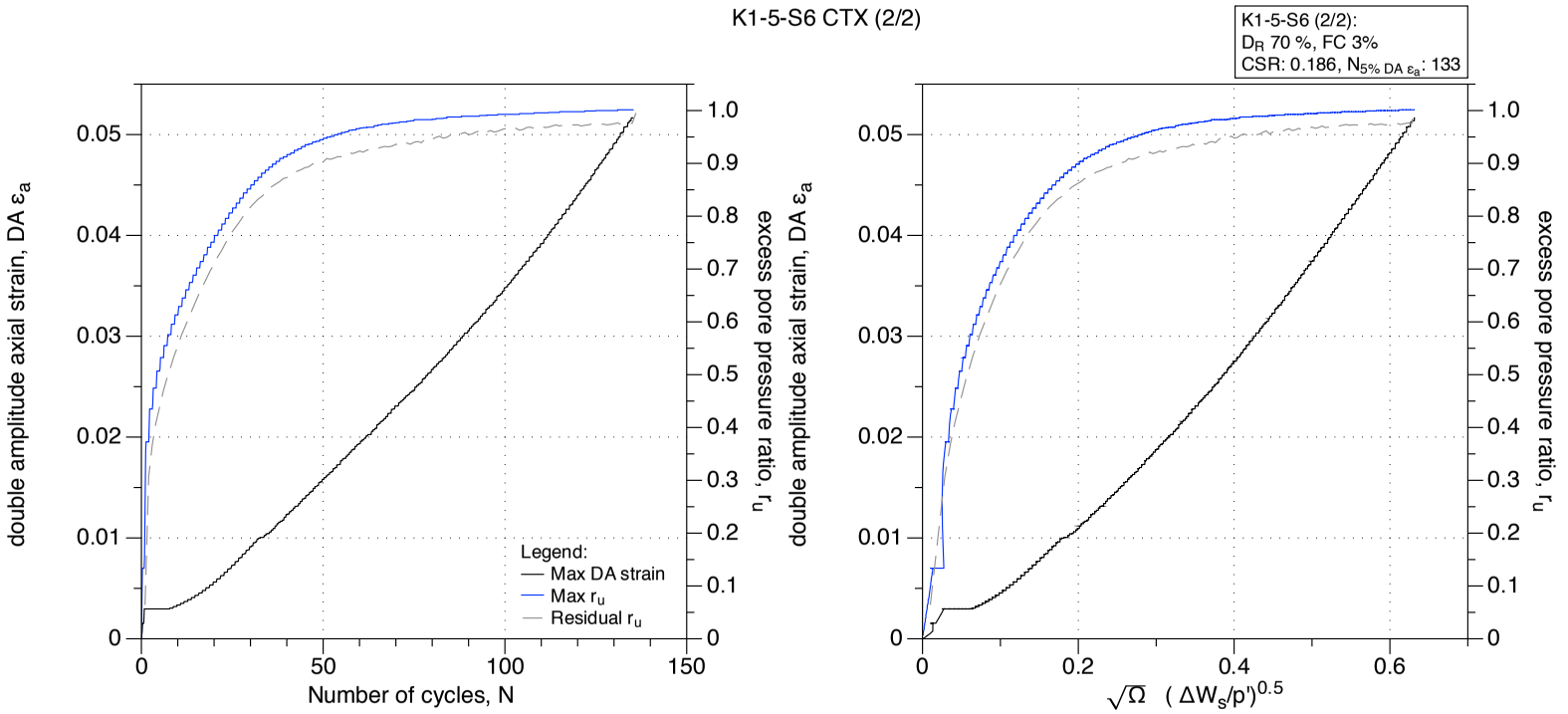

Figure 4.132: K1-5-S6 GP sample, reliquefaction undrained cyclic triaxial test (CTX). Development of strain and excess pore water pressure with number of cycles and normalised shear work.

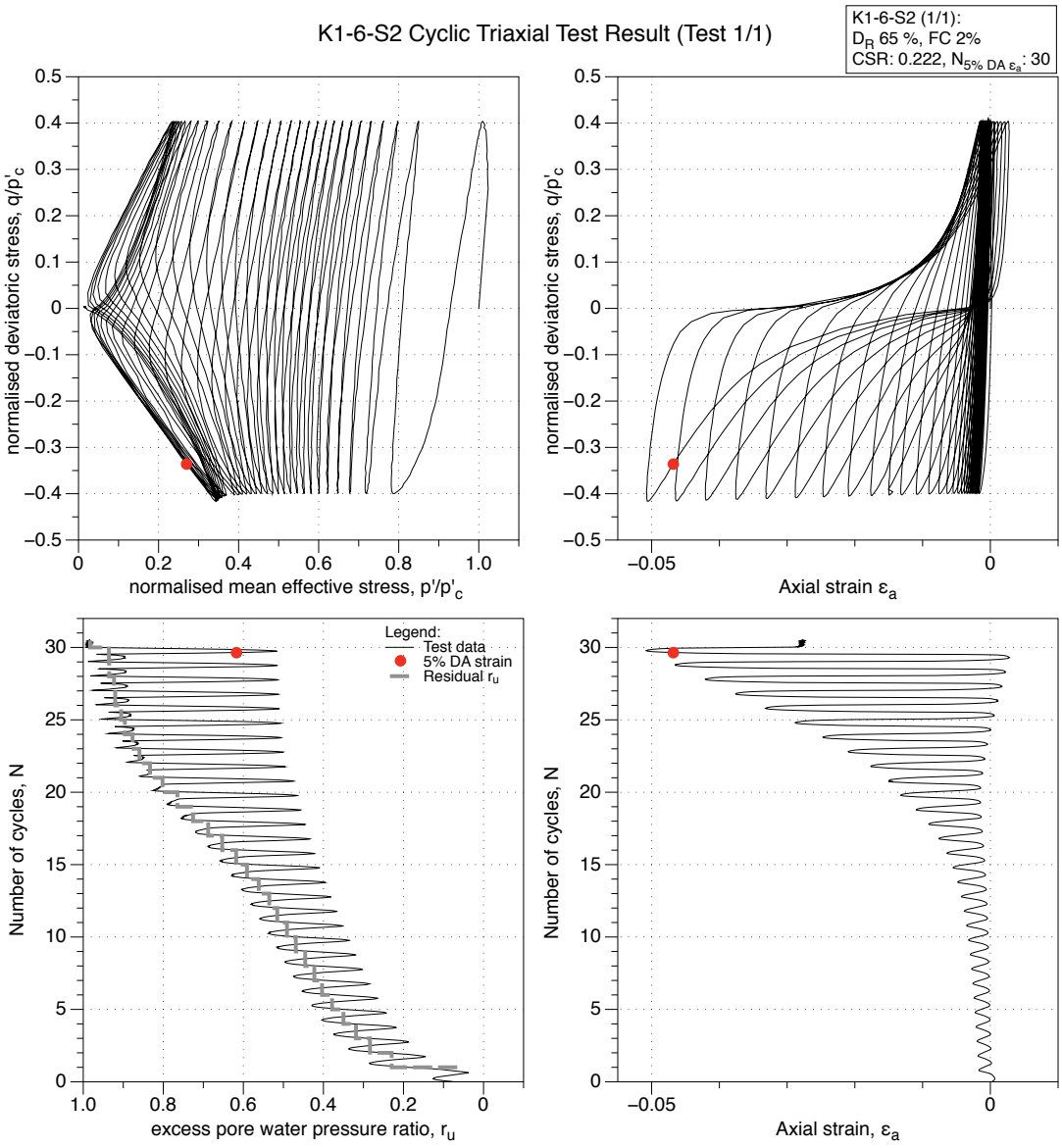

Figure 4.133: K1-6-S2 GP sample, undrained cyclic triaxial test (CTX). Effective stress-path, stress-strain, excess pore water pressure ratio and strain development plots.

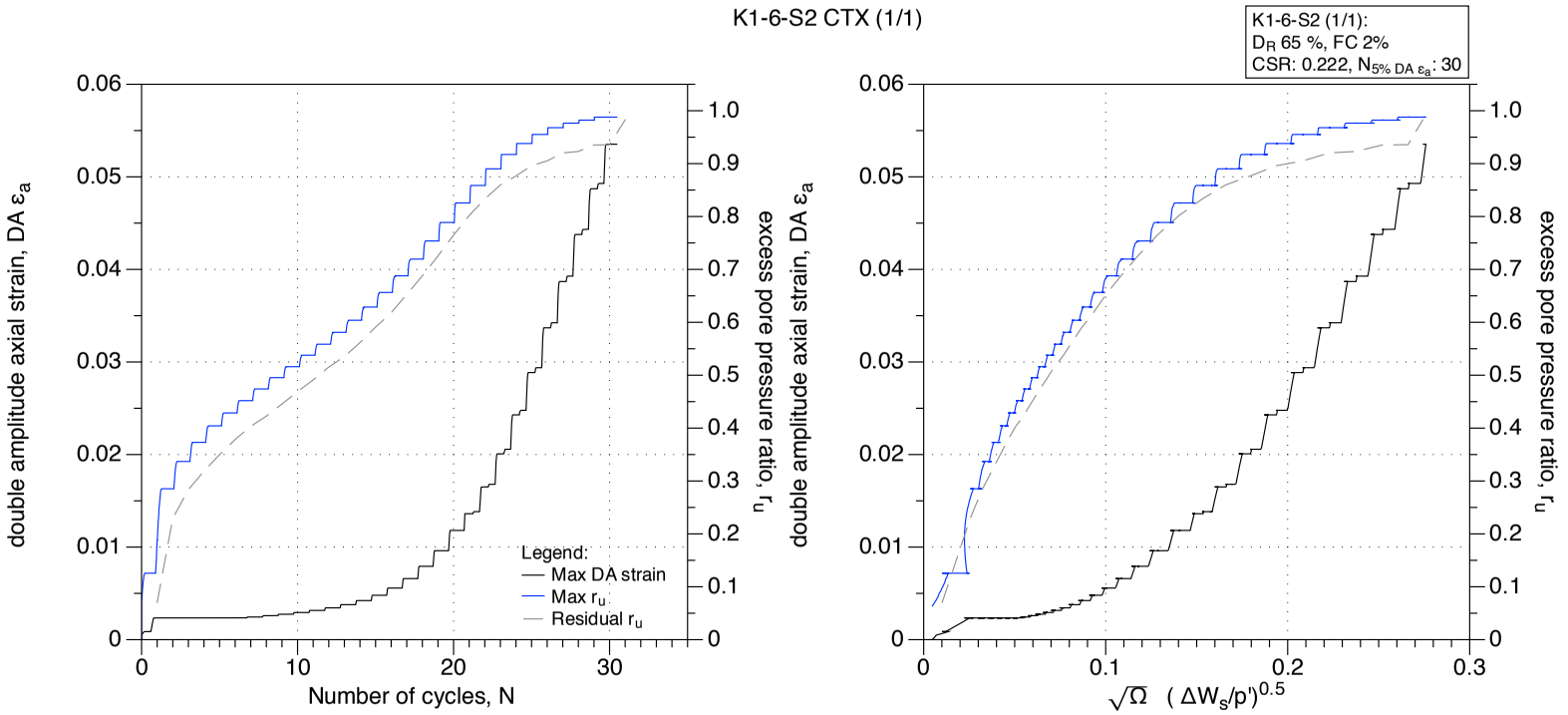

Figure 4.134: K1-6-S2 GP sample, undrained cyclic triaxial test (CTX). Development of strain and excess pore water pressure with number of cycles and normalised shear work.

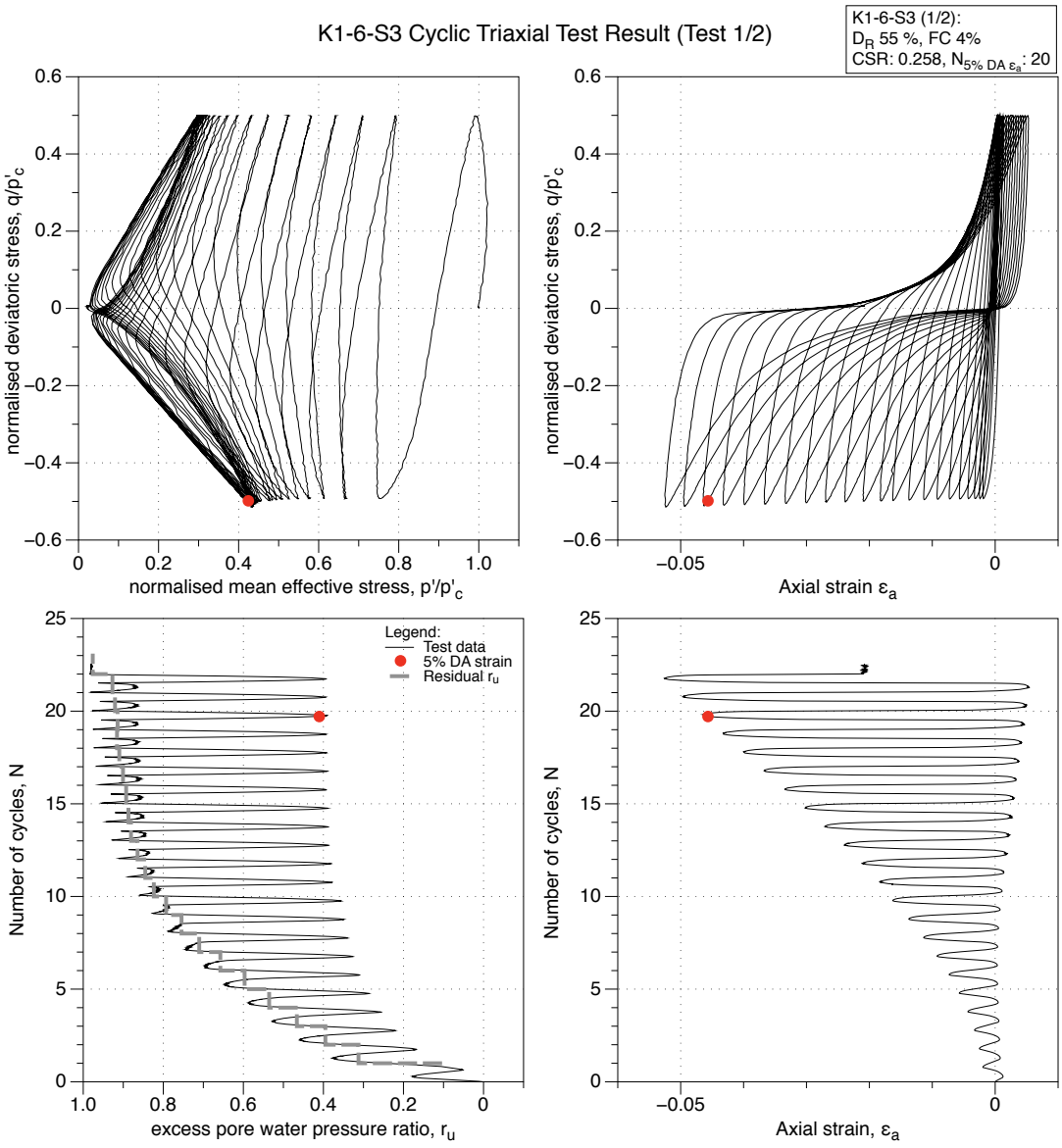

Figure 4.135: K1-6-S3 GP sample, undrained cyclic triaxial test (CTX). Effective stress-path, stress-strain, excess pore water pressure ratio and strain development plots.

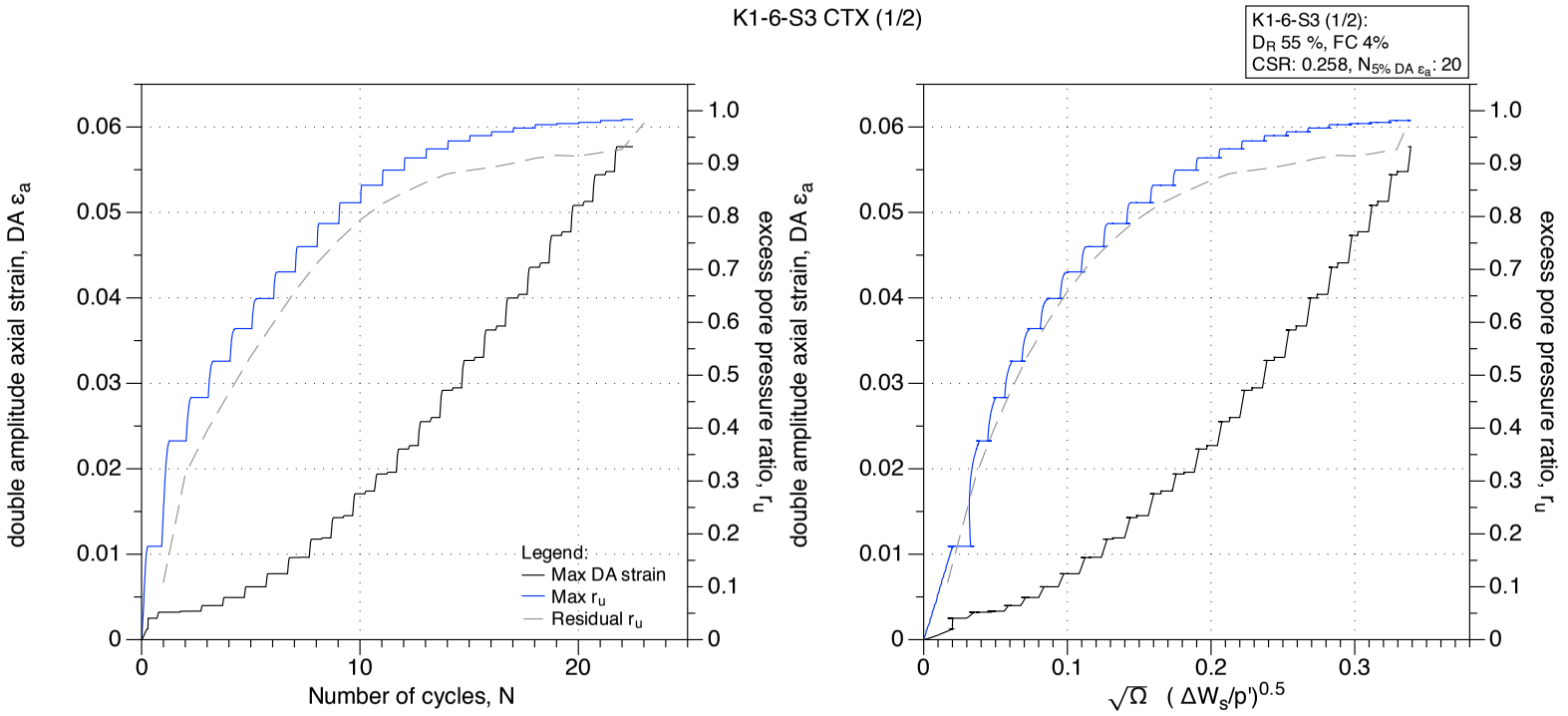

Figure 4.136: K1-6-S3 GP sample, undrained cyclic triaxial test (CTX). Development of strain and excess pore water pressure with number of cycles and normalised shear work.

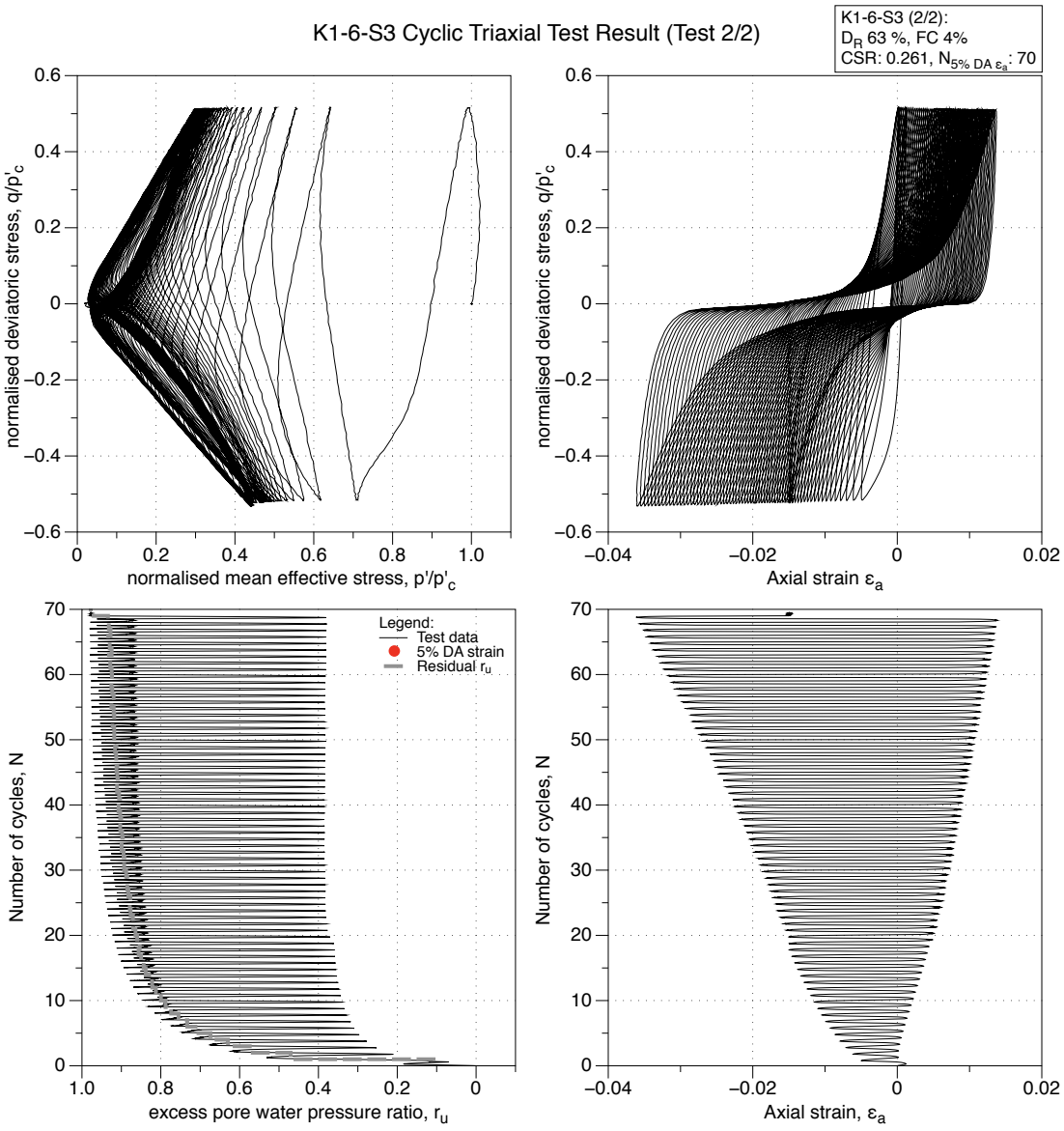

Figure 4.137: K1-6-S3 GP sample, reliquefaction undrained cyclic triaxial test (CTX). Effective stress-path, stress-strain, excess pore water pressure ratio and strain development plots.

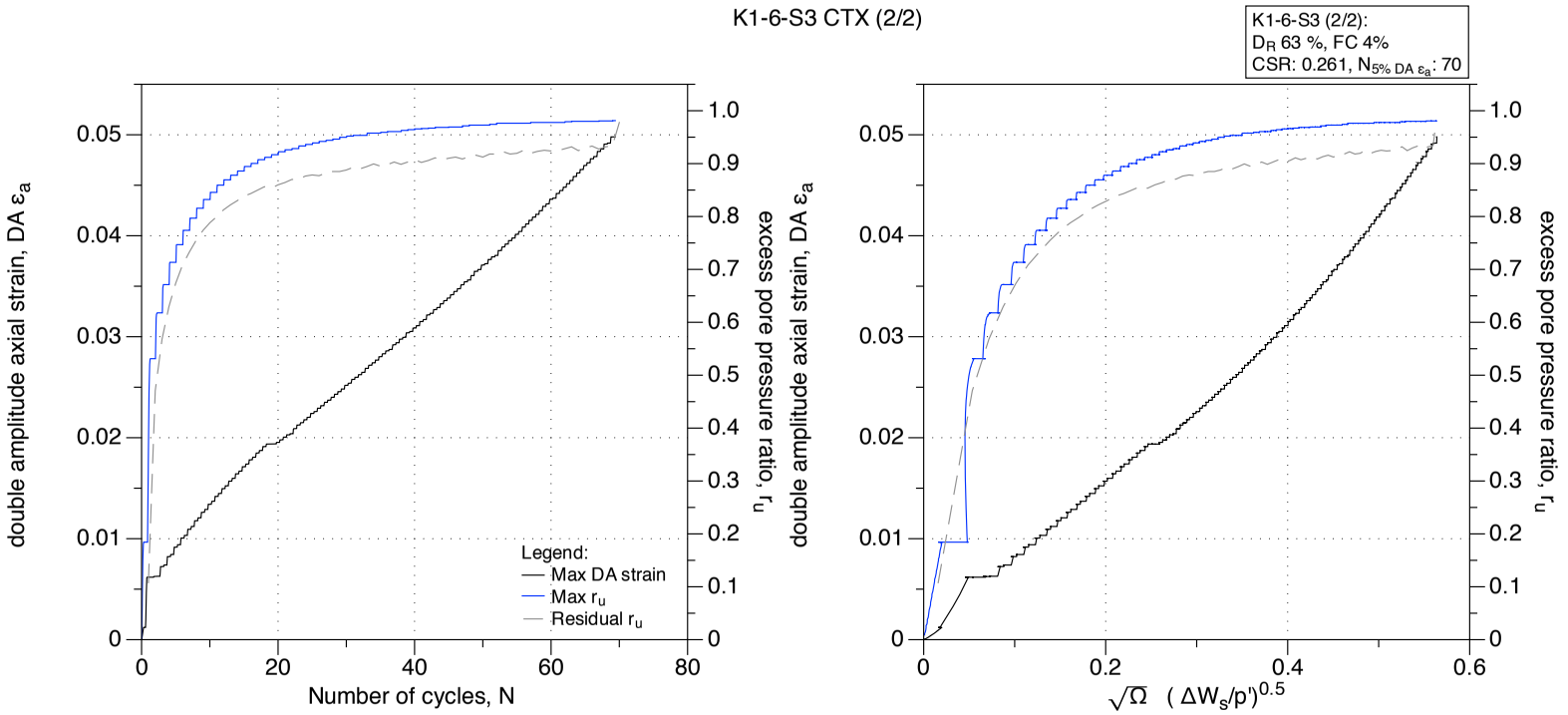

Figure 4.138: K1-6-S3 GP sample, reliquefaction undrained cyclic triaxial test (CTX). Development of strain and excess pore water pressure with number of cycles and normalised shear work.

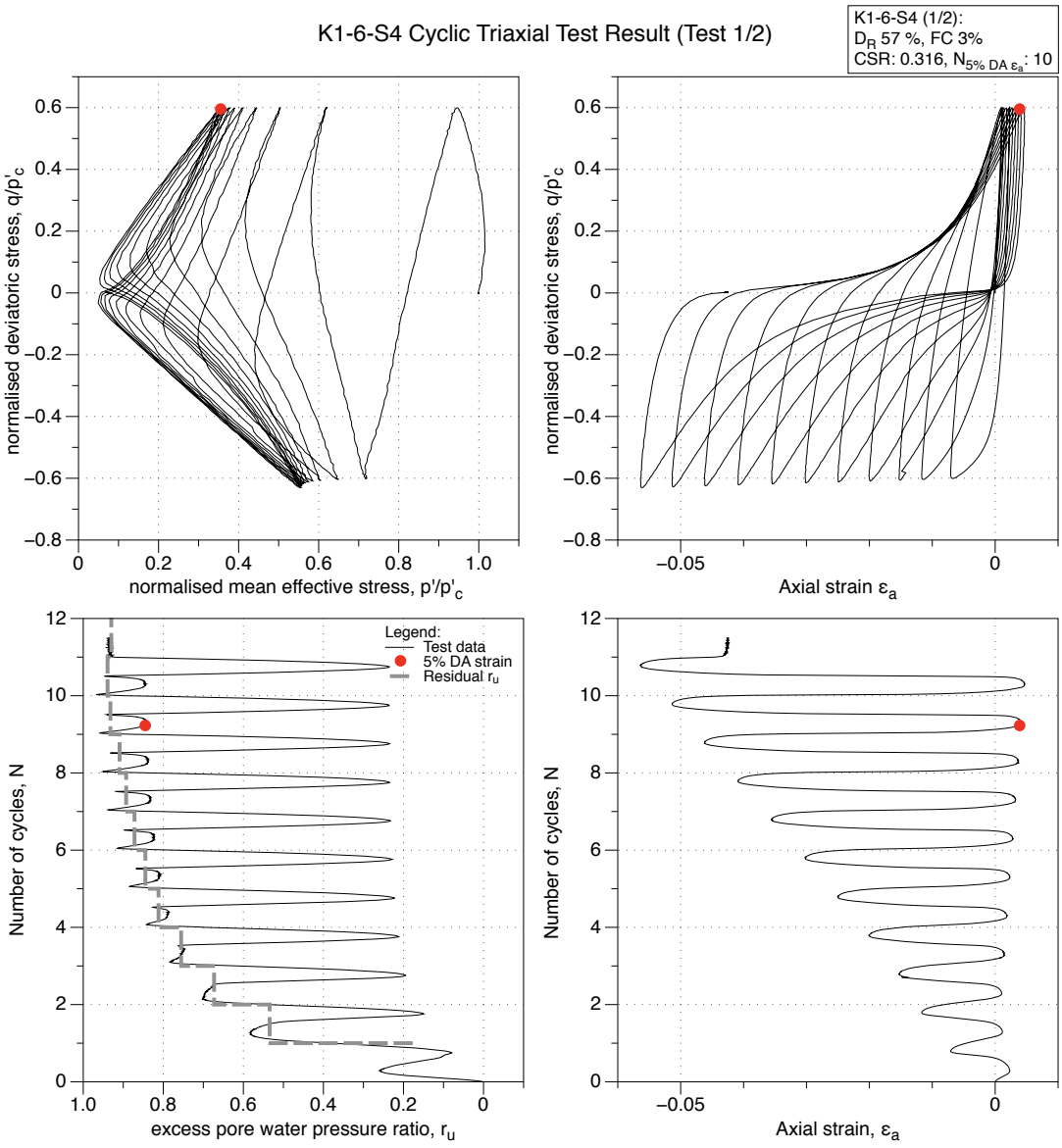

Figure 4.139: K1-6-S4 GP sample, undrained cyclic triaxial test (CTX). Effective stress-path, stress-strain, excess pore water pressure ratio and strain development plots.

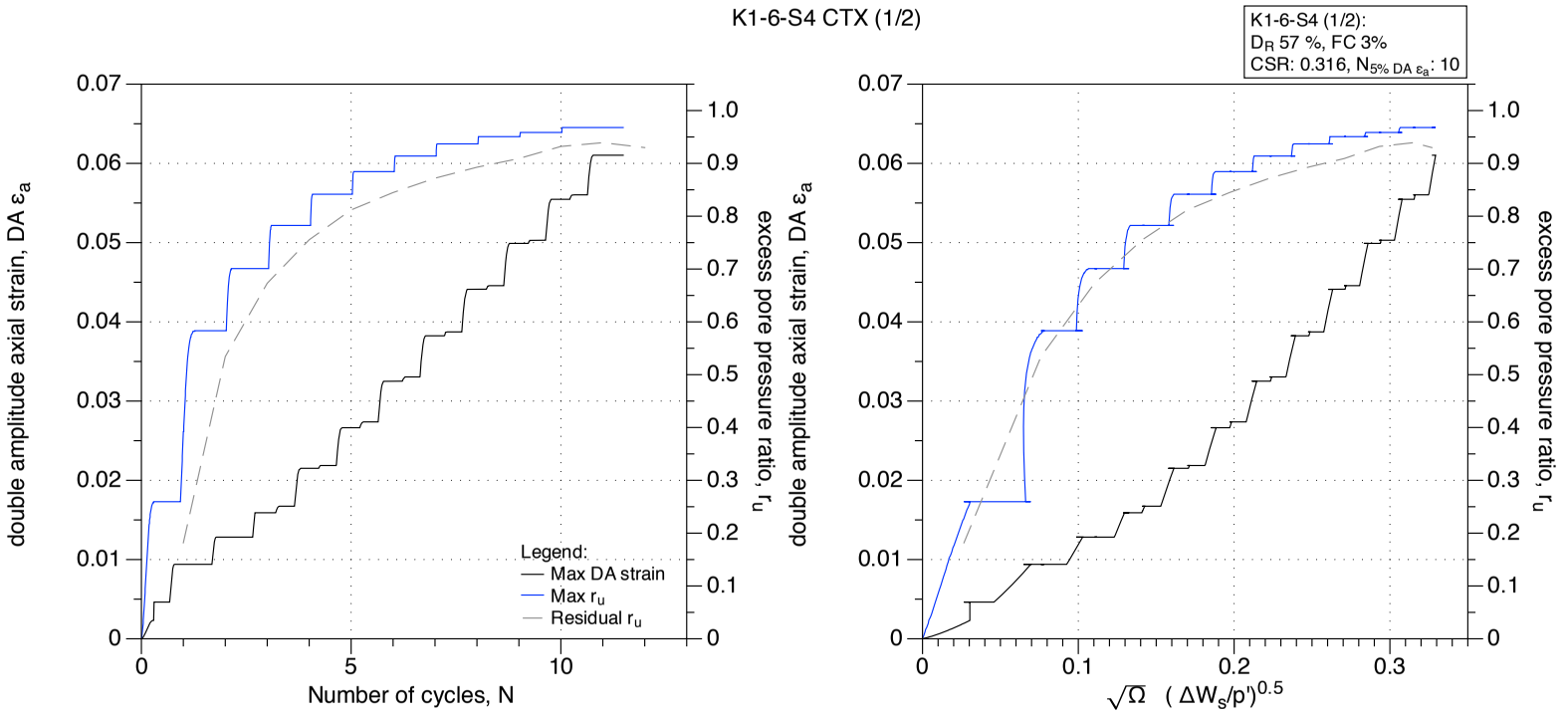

Figure 4.140: K1-6-S4 GP sample, undrained cyclic triaxial test (CTX). Development of strain and excess pore water pressure with number of cycles and normalised shear work.

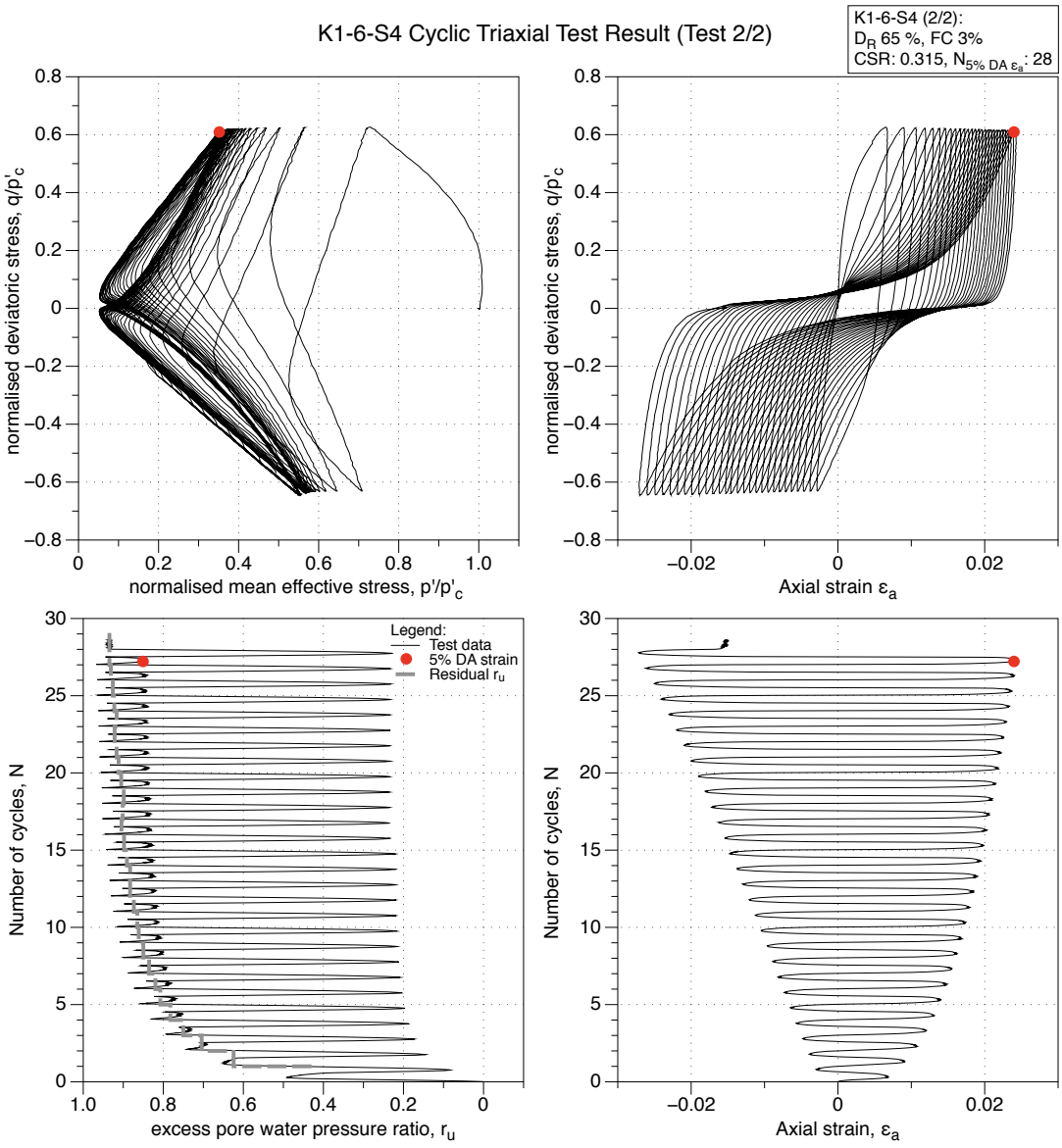

Figure 4.141: K1-6-S4 GP sample, reliquefaction undrained cyclic triaxial test (CTX). Effective stress-path, stress-strain, excess pore water pressure ratio and strain development plots.

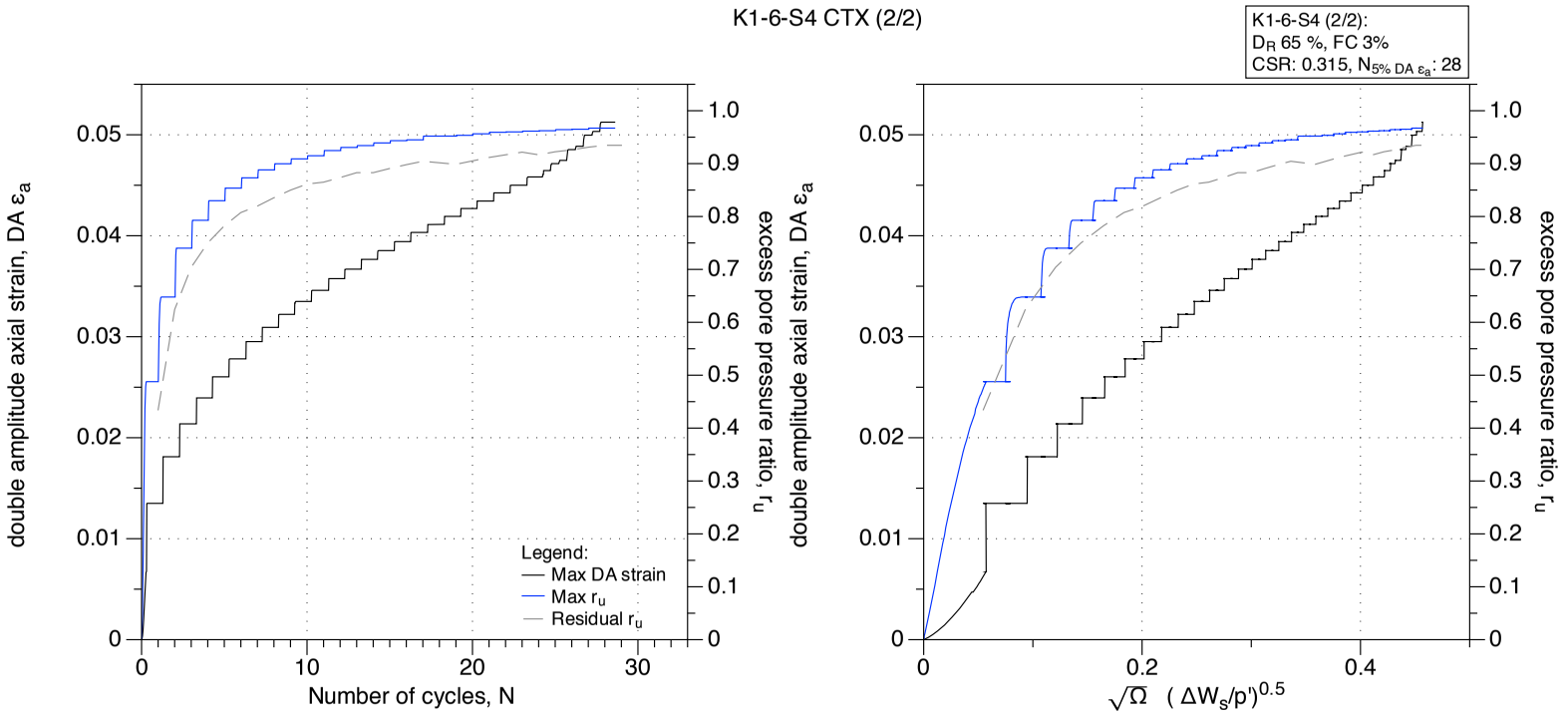

Figure 4.142: K1-6-S4 GP sample, reliquefaction undrained cyclic triaxial test (CTX). Development of strain and excess pore water pressure with number of cycles and normalised shear work.

4.3 Triaxial testing on Gel-push samples from borehole MA1.

This section of Appendix D presents individual triaxial test results performed on Gel-push specimens obtained from Borehole MA1.

4.3.1 MA1 GP Monotonic Triaxial Tests

Plots include the effective stress path, stress strain plot, state stress path, and volumetric strain-axial strain (drained test) or excess pore pressure ratio-axial strain (undrained test) plots. Additional plots for each monotonic test include stress-dilatancy plots, stiffness degradation curves, normalised shear work, and normalised shear work gradient plots with strain.

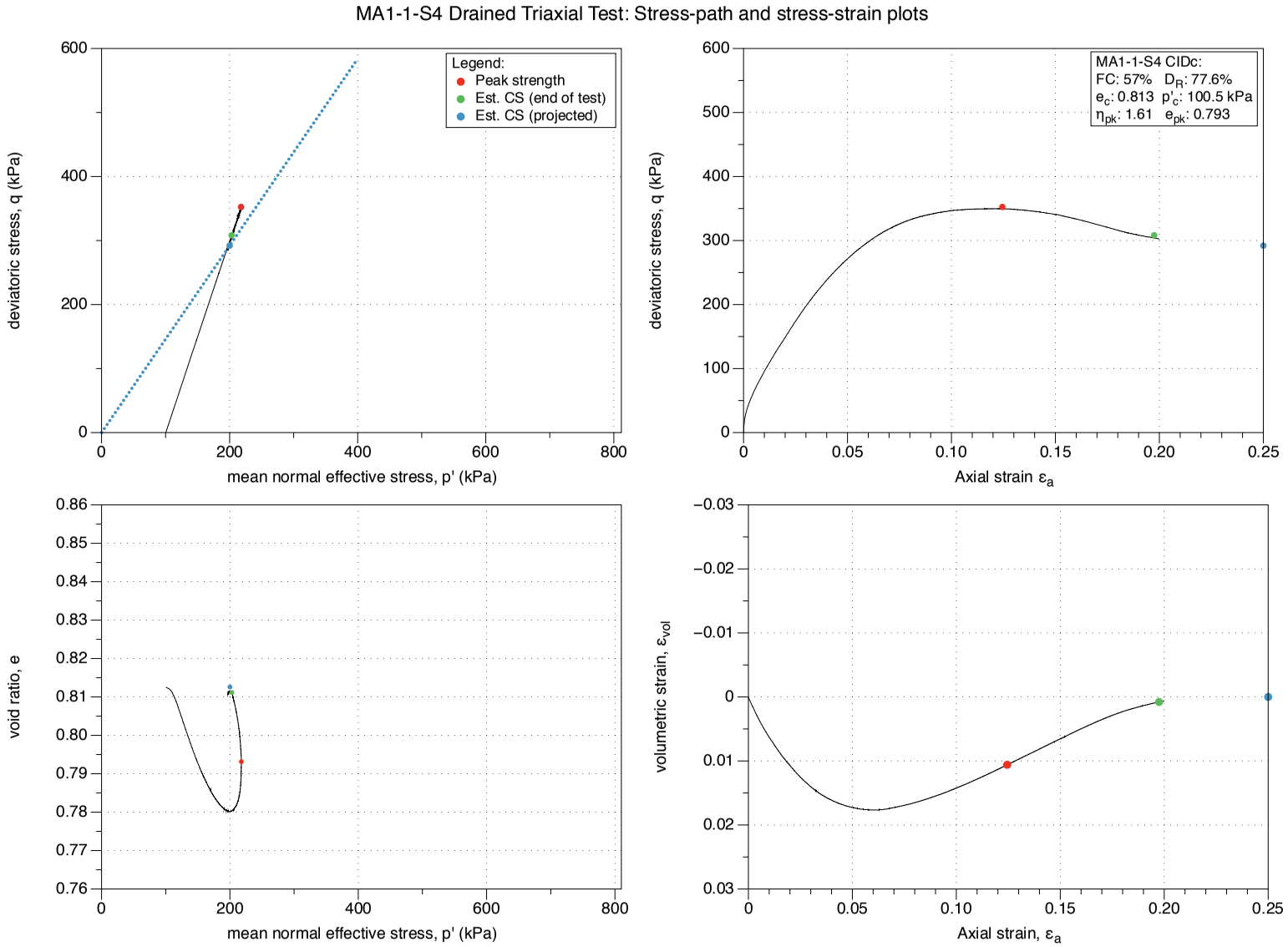

Figure 4.143: MA1-1-S4 GP sample, drained monotonic triaxial test (CID_C). Stress-path and stress-strain plots.

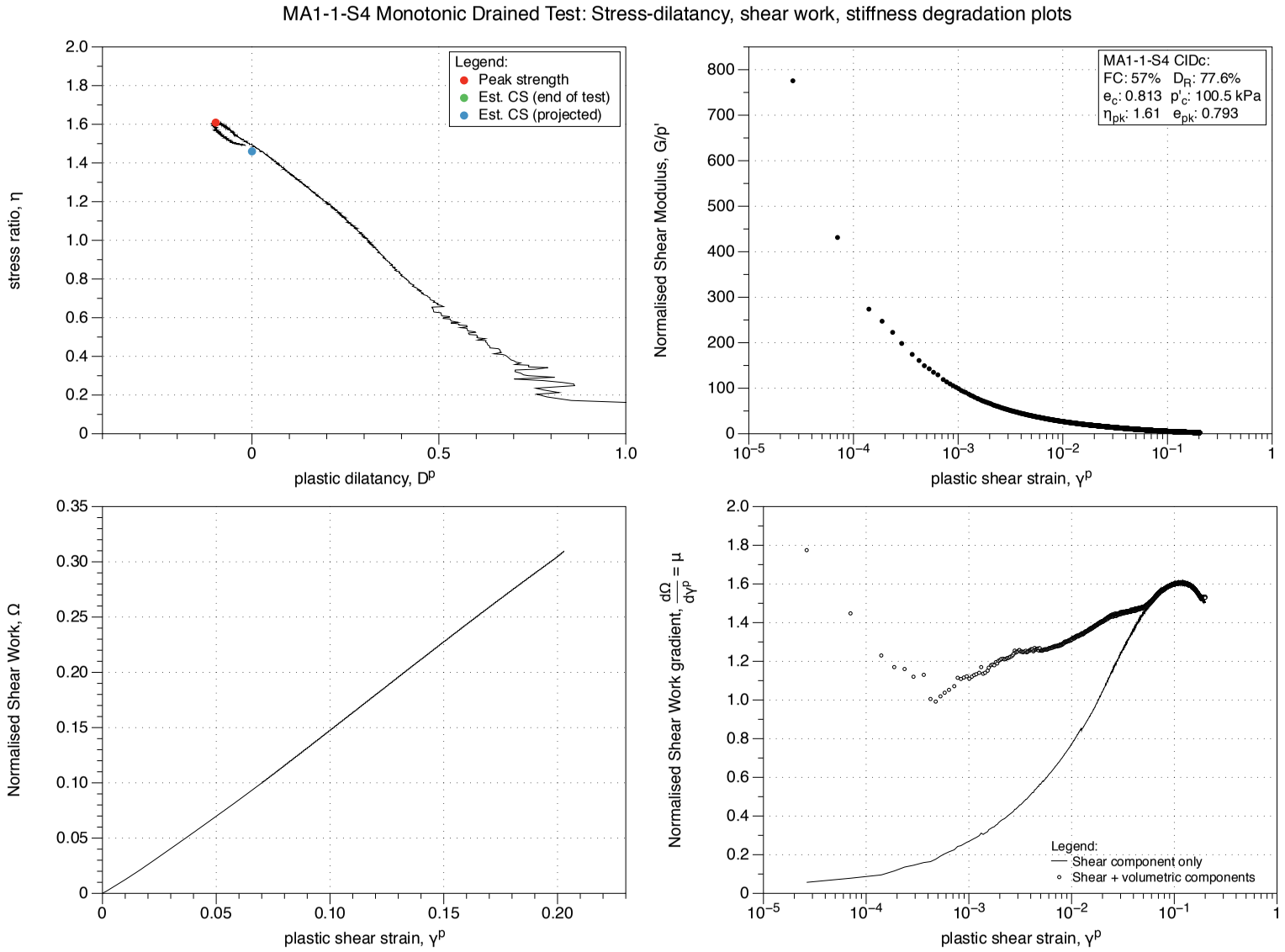

Figure 4.144: MA1-1-S4 GP sample, drained monotonic triaxial test (CID_C). Stress-path and stress-strain plots. Stress-dilatancy, shear work, stiffness degradation plots.

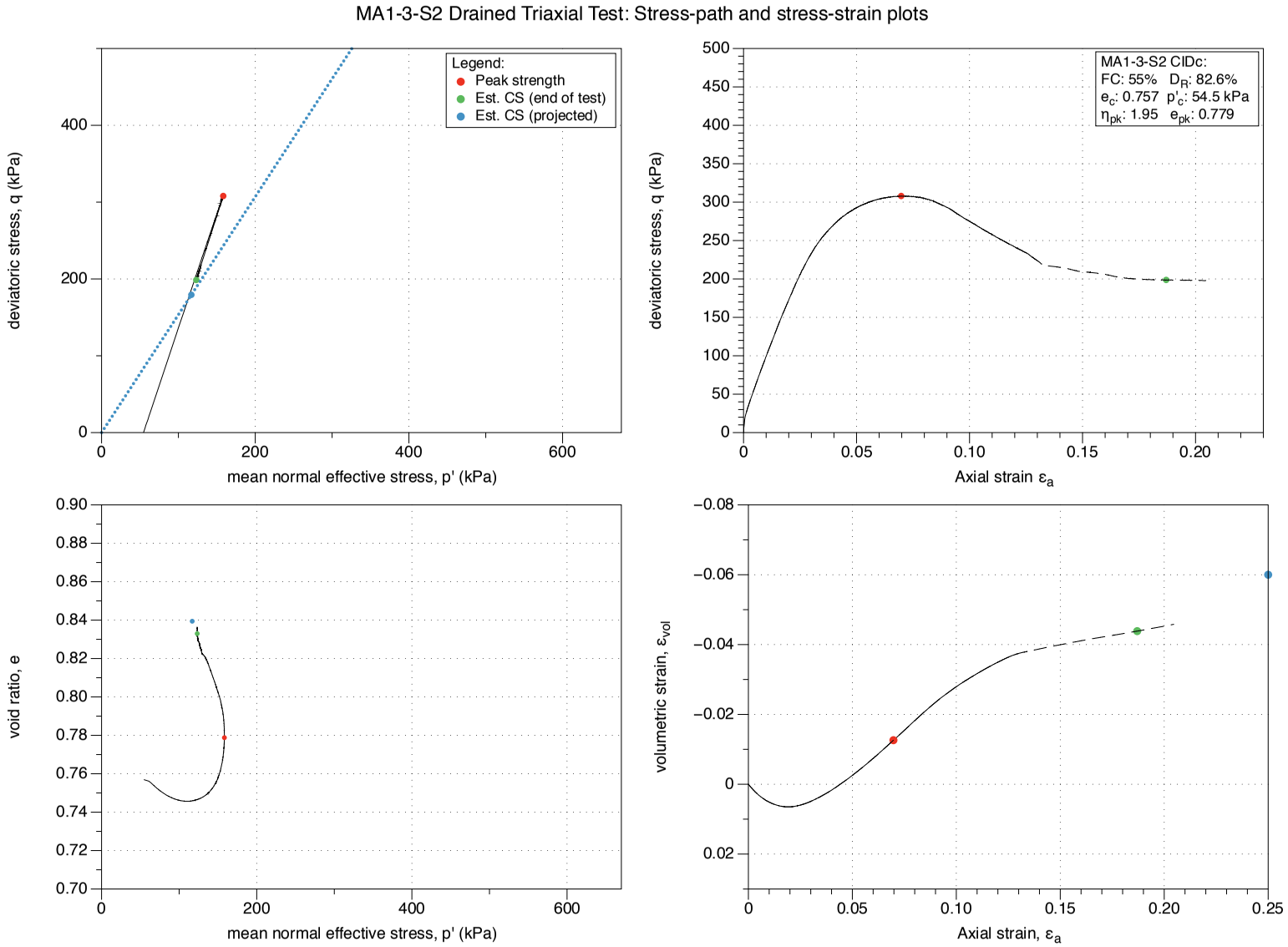

Figure 4.145: MA1-3-S2 GP sample, drained monotonic triaxial test (CID_C). Stress-path and stress-strain plots.

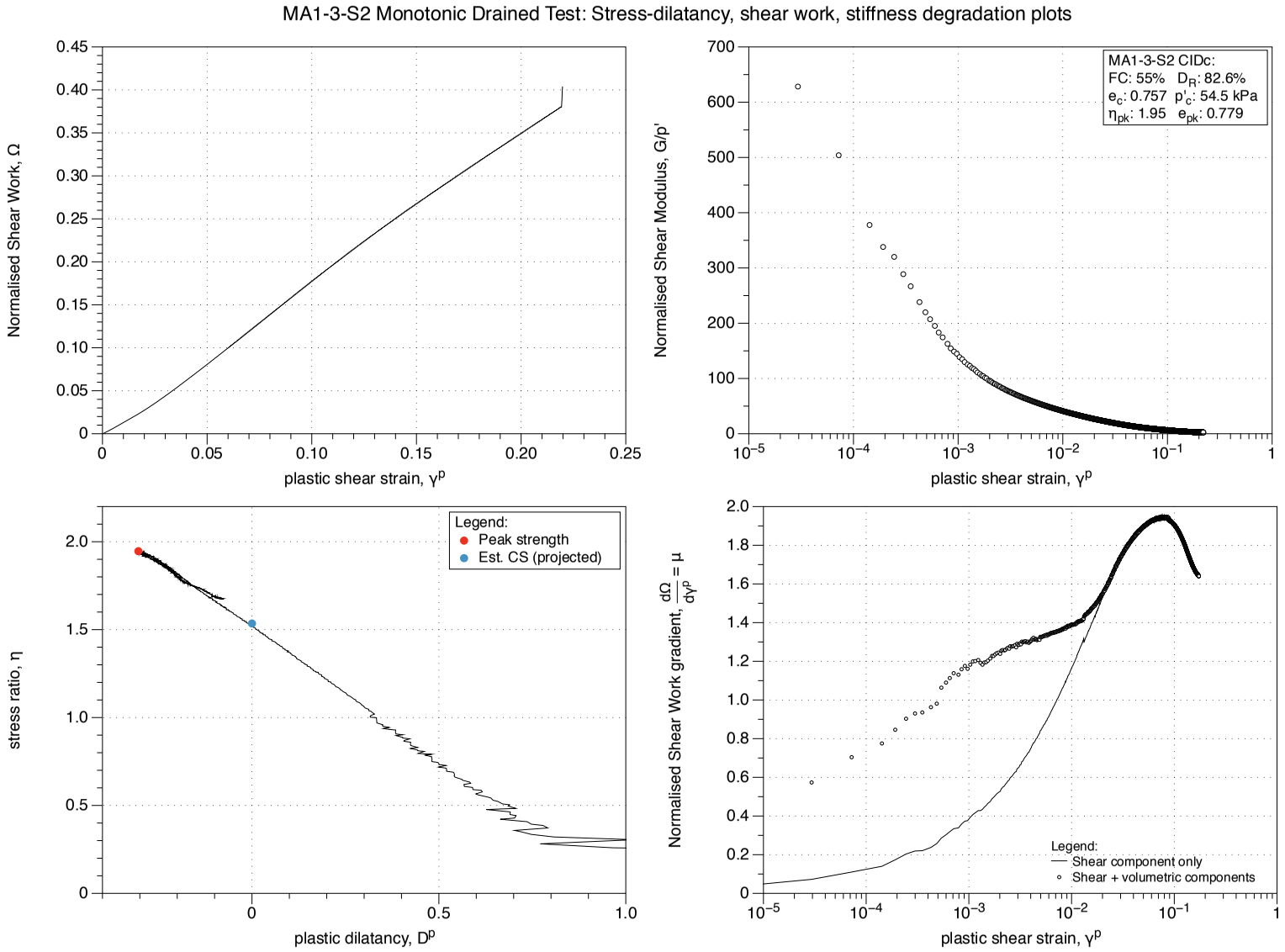

Figure 4.146: MA1-3-S2 GP sample, drained monotonic triaxial test (CID_C). Stress-path and stress-strain plots. Stress-dilatancy, shear work, stiffness degradation plots.

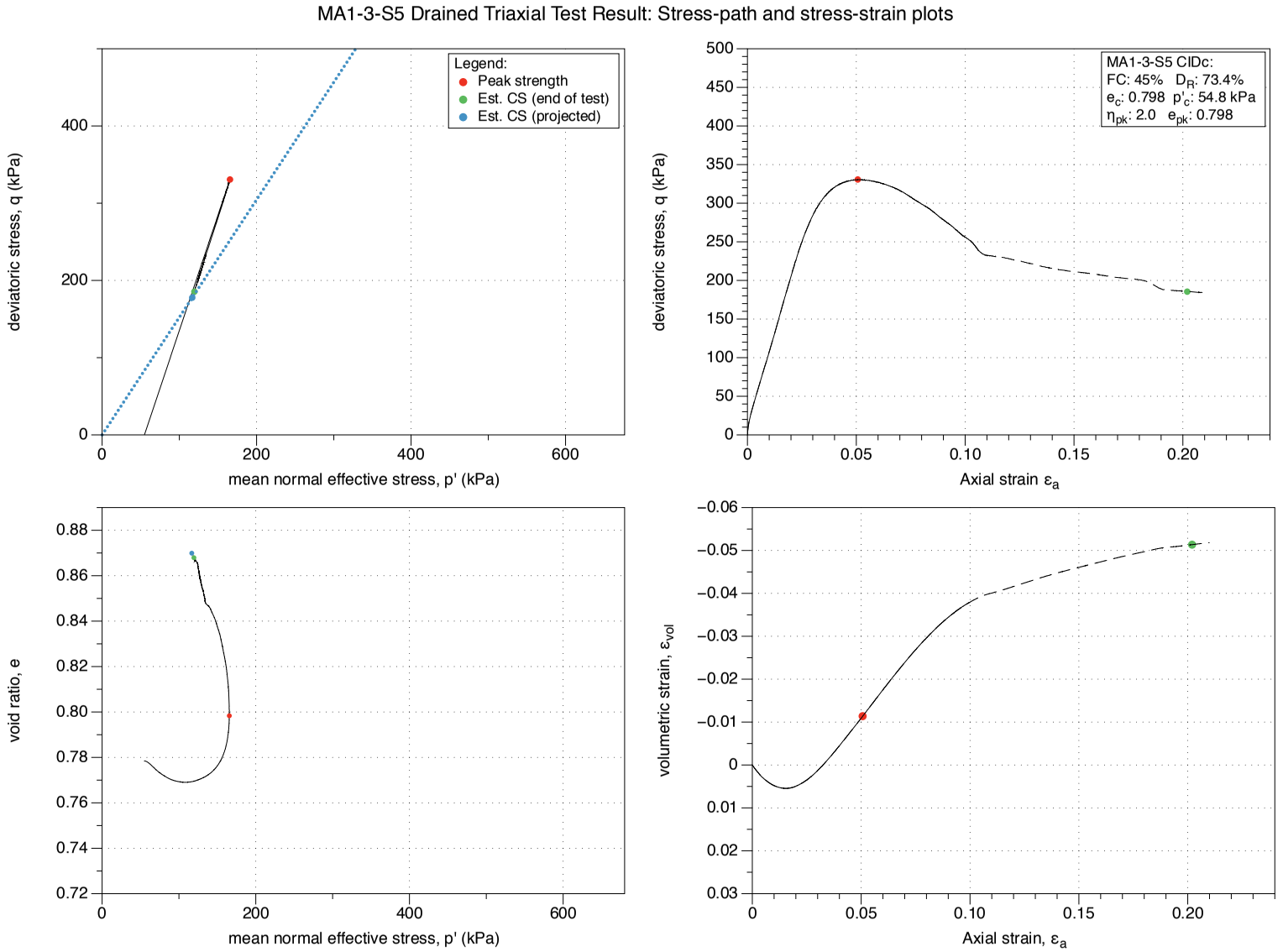

Figure 4.147: MA1-3-S5 GP sample, drained monotonic triaxial test (CID_C). Stress-path and stress-strain plots.

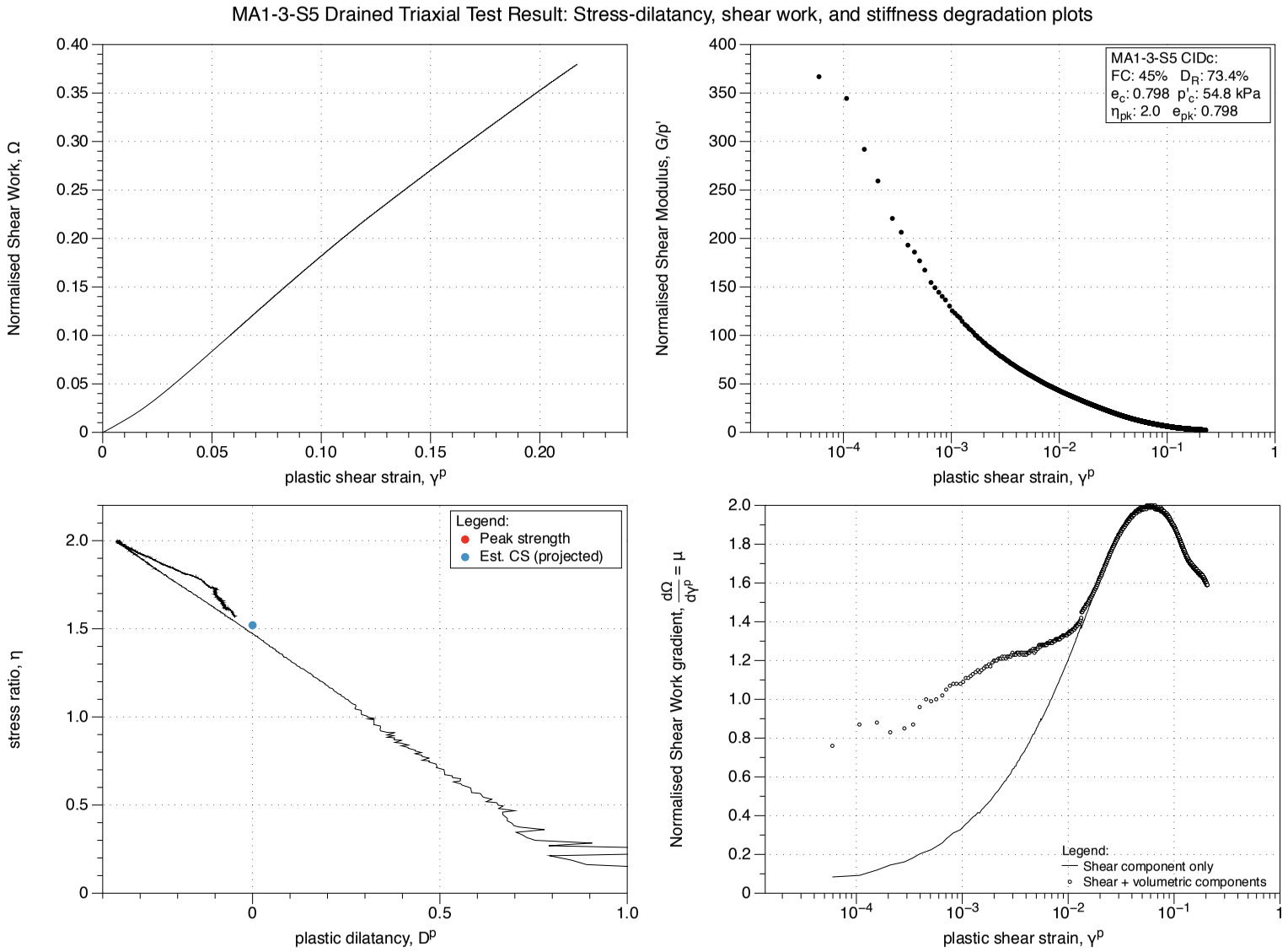

Figure 4.148: MA1-3-S5 GP sample, drained monotonic triaxial test (CID_C). Stress-path and stress-strain plots. Stress-dilatancy, shear work, stiffness degradation plots.

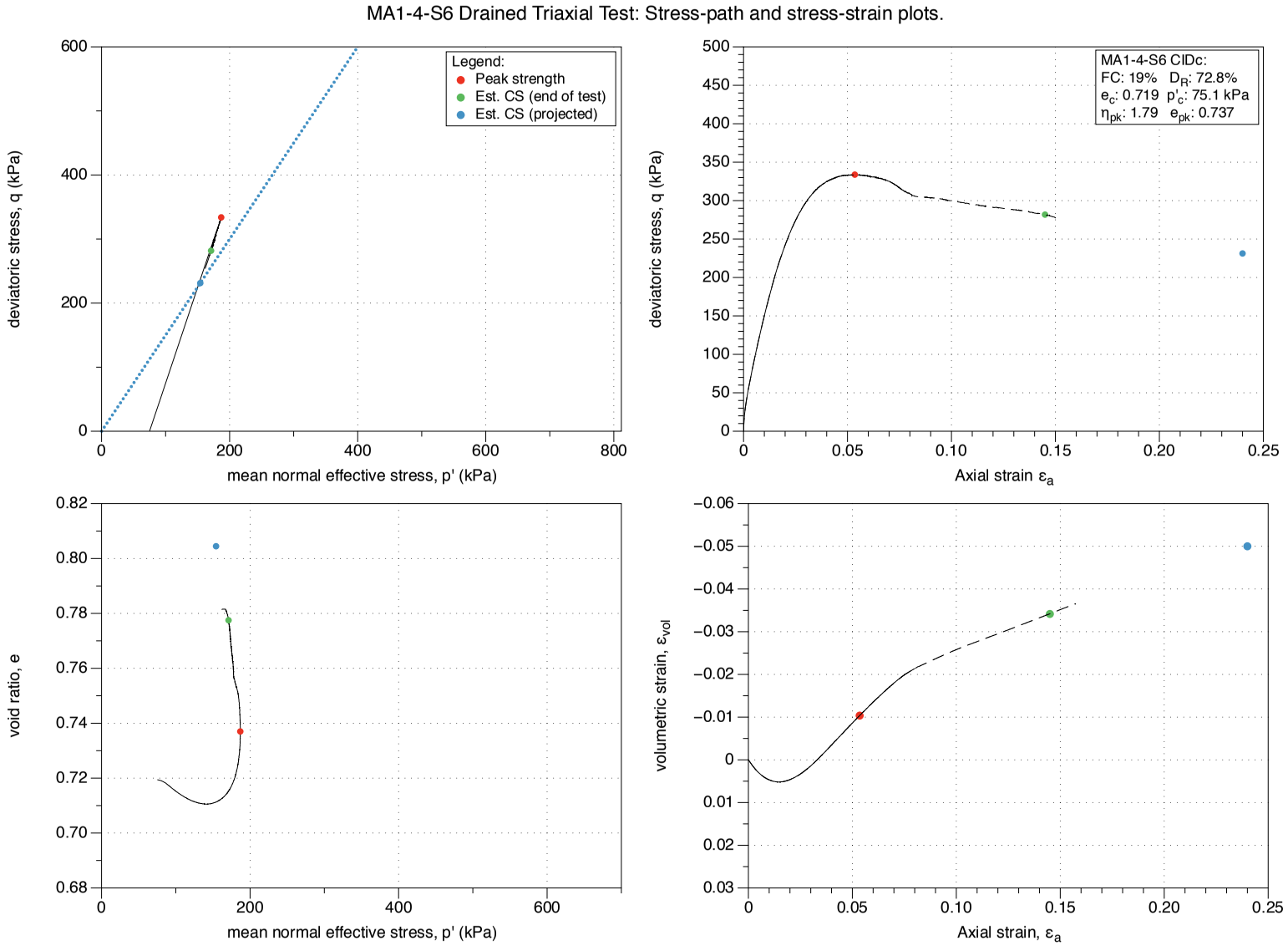

Figure 4.149: MA1-4-S6 GP sample, drained monotonic triaxial test (CID_C). Stress-path and stress-strain plots.

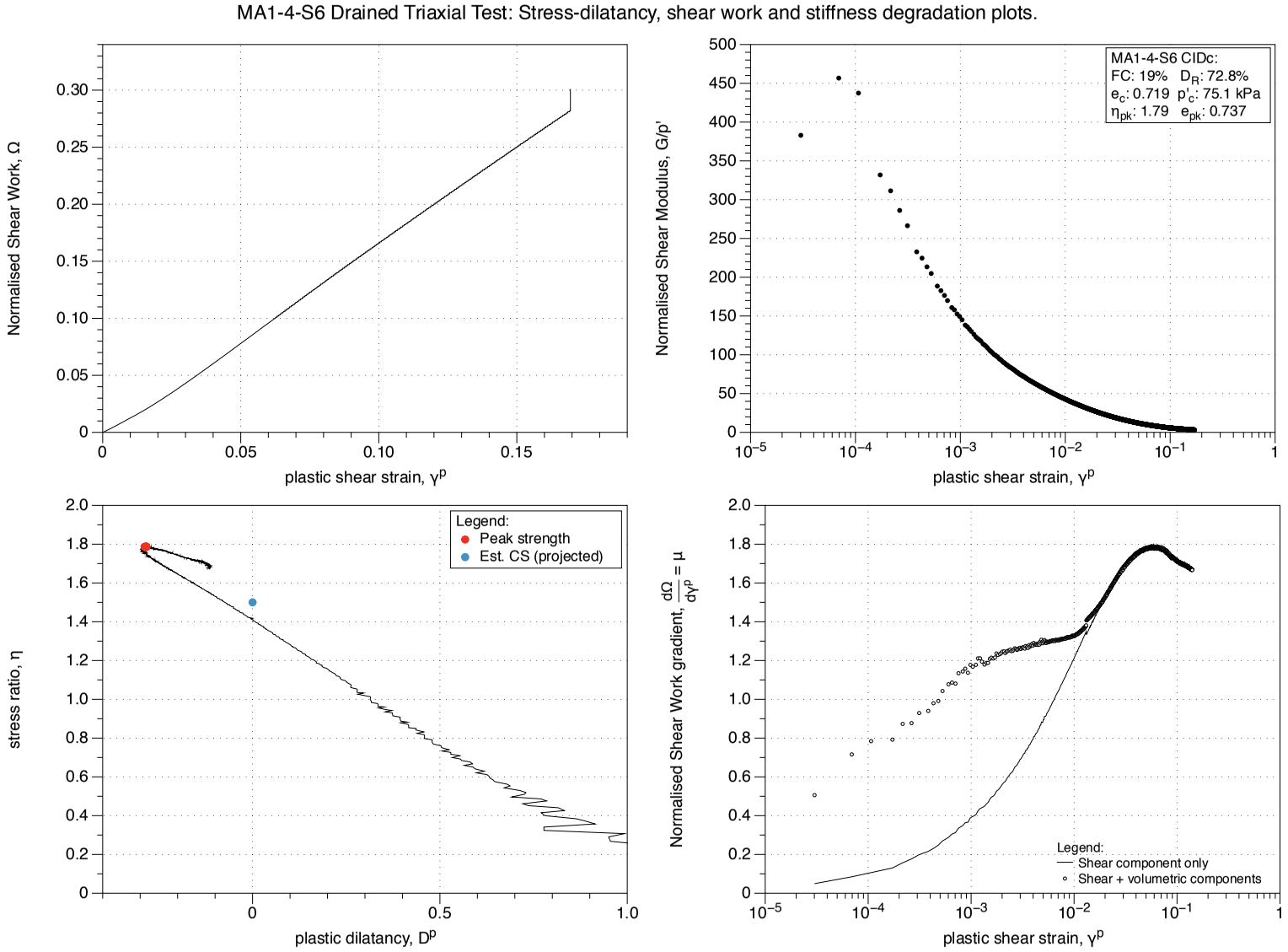

Figure 4.150: MA1-4-S6 GP sample, drained monotonic triaxial test (CID_C). Stress-path and stress-strain plots. Stress-dilatancy, shear work, stiffness degradation plots.

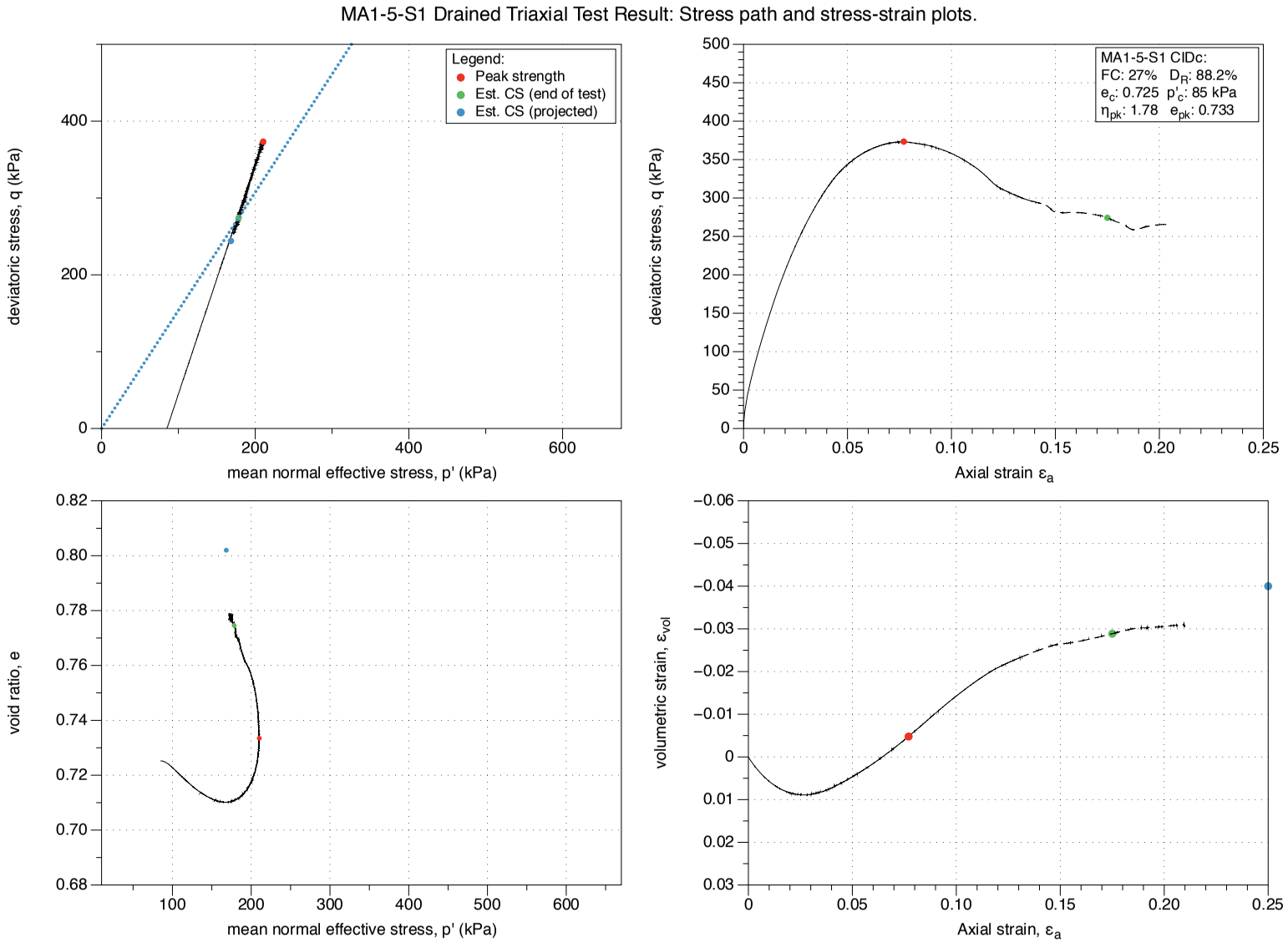

Figure 4.151: MA1-5-S1 GP sample, drained monotonic triaxial test (CID_C). Stress-path and stress-strain plots.

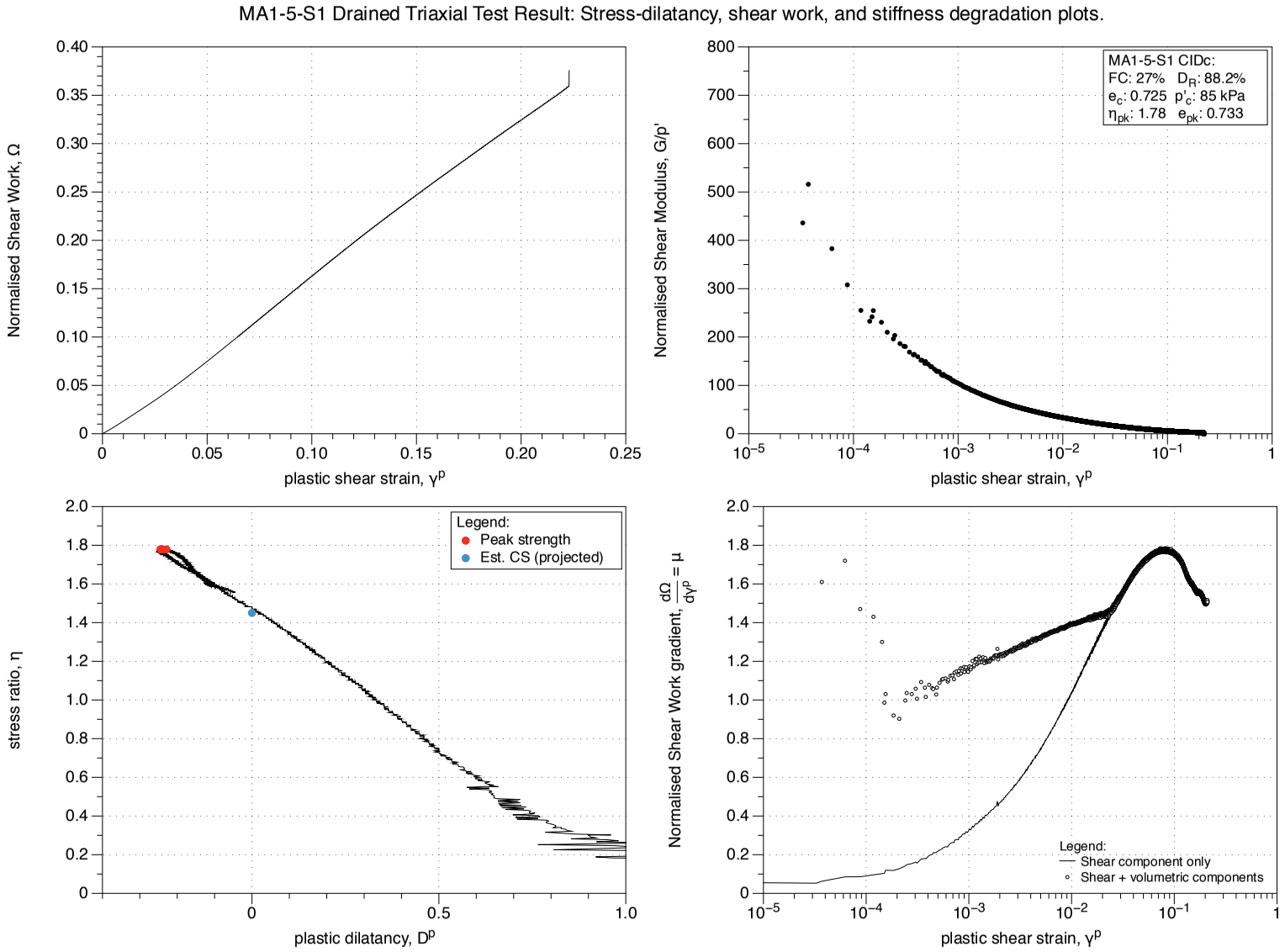

Figure 4.152: MA1-5-S1 GP sample, drained monotonic triaxial test (CID_C). Stress-path and stress-strain plots. Stress-dilatancy, shear work, stiffness degradation plots.

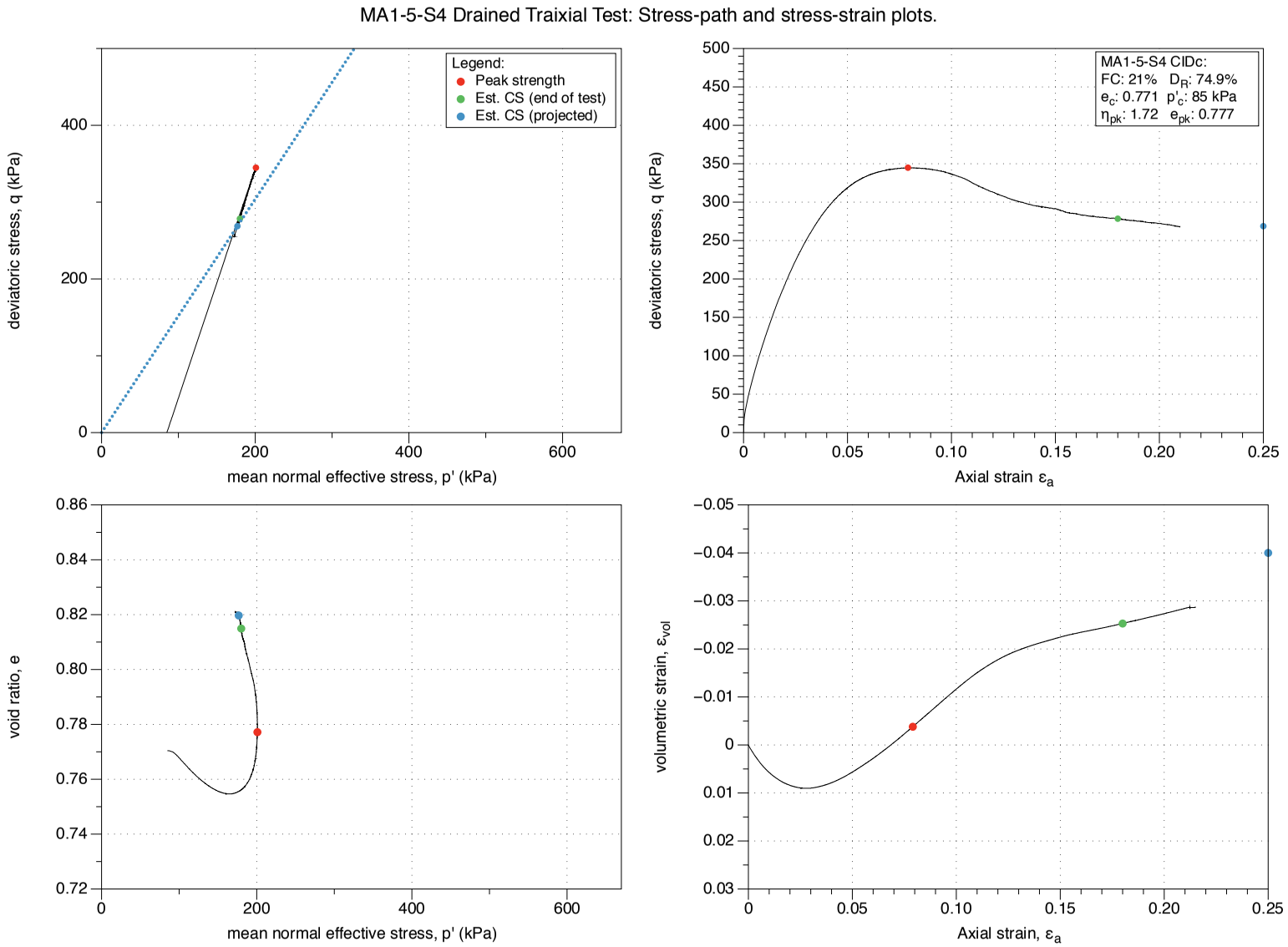

Figure 4.153: MA1-5-S4 GP sample, drained monotonic triaxial test (CID_C). Stress-path and stress-strain plots.

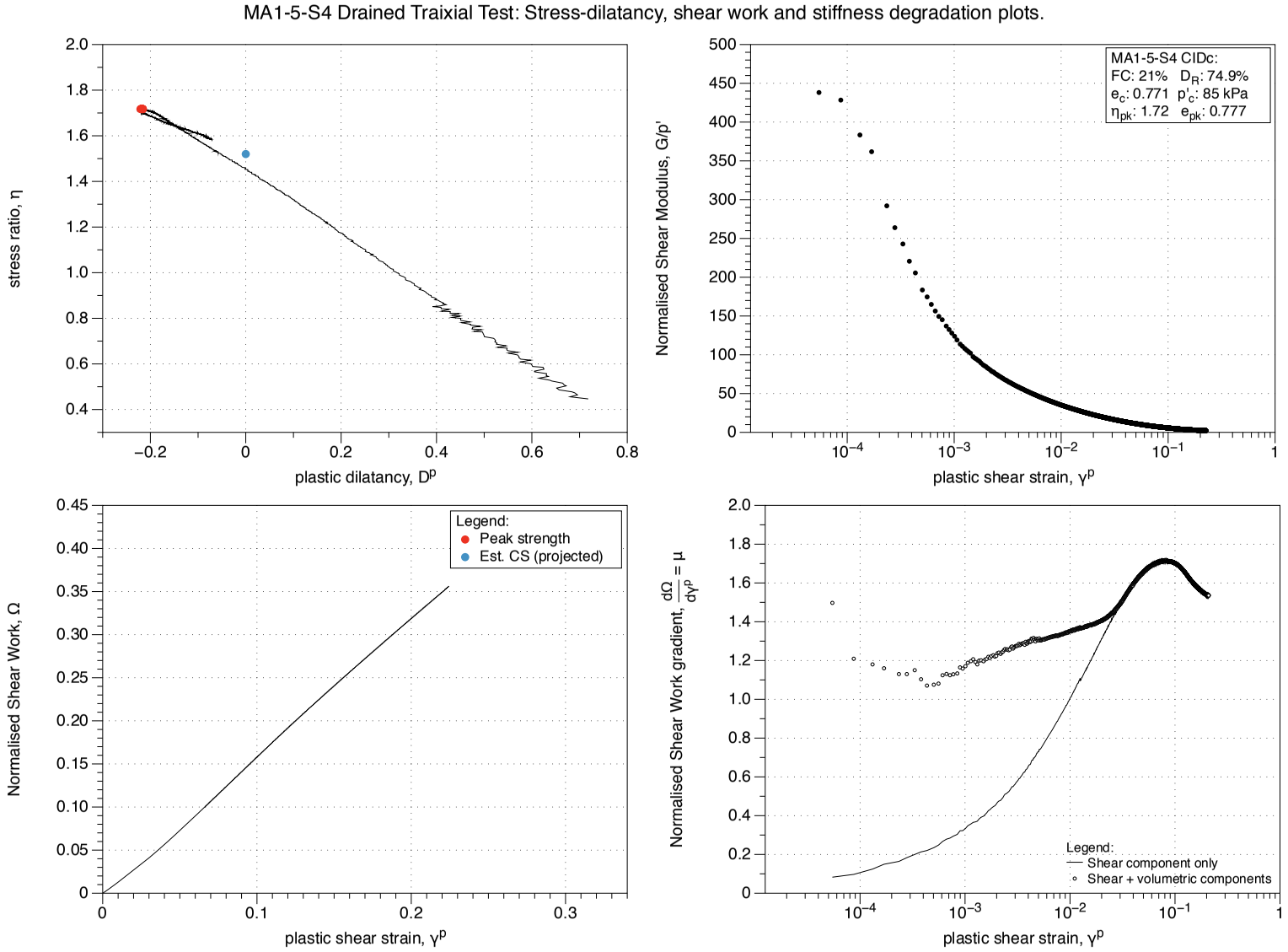

Figure 4.154: MA1-5-S4 GP sample, drained monotonic triaxial test (CID_C). Stress-path and stress-strain plots. Stress-dilatancy, shear work, stiffness degradation plots.

4.3.2 MA1 GP Cyclic Triaxial Tests

Plots include the normalised effective stress path, stress strain plot, and change in excess pore pressure ratio (incremental and residual) with number of cycles, and axial strain with number of cycles. Additional plots for each cyclic test depict the development of maximum double amplitude strain, excess pore pressure ratio (maximum and residual), with number of cycles and the square-root of normalised shear work.

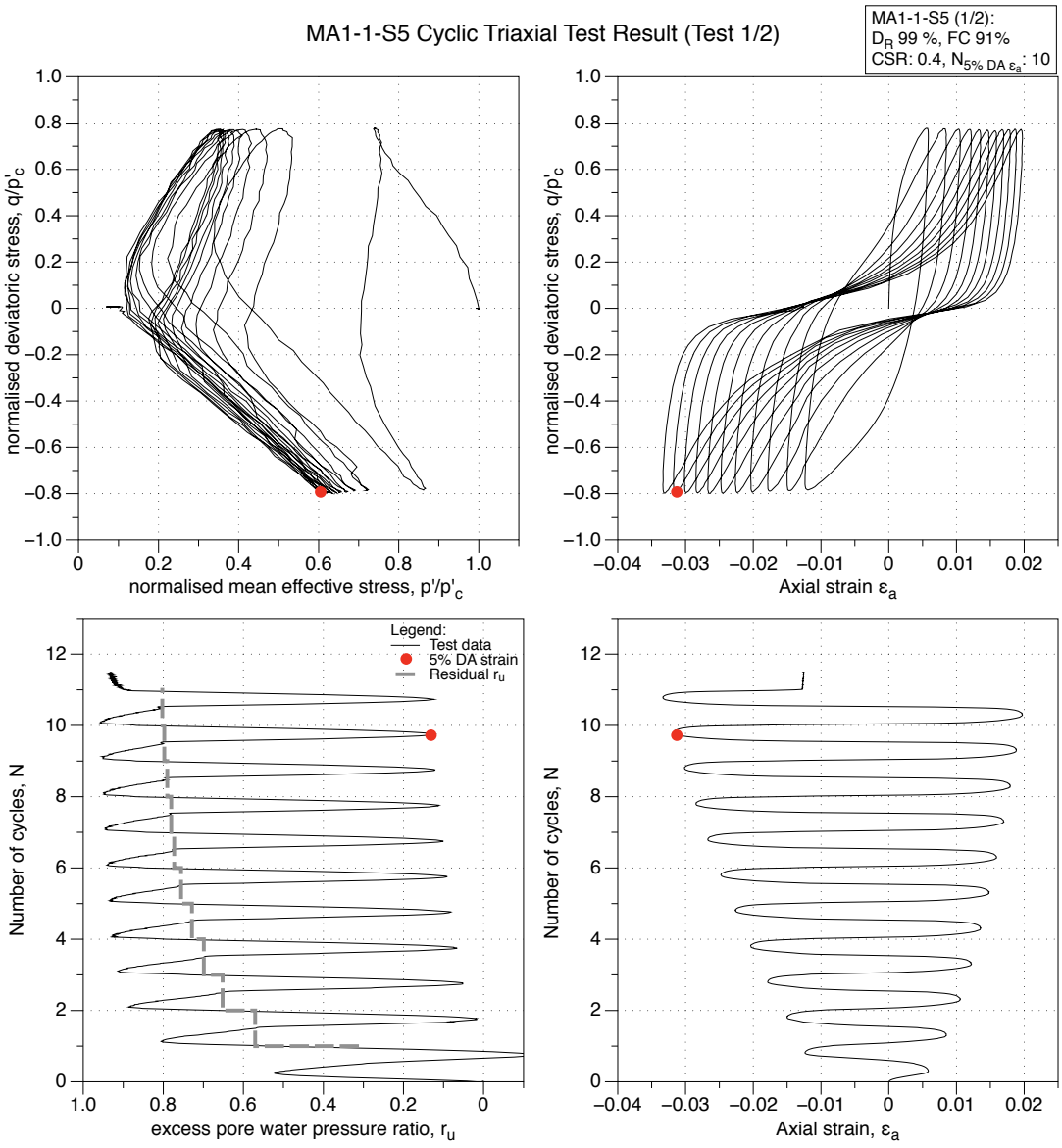

Figure 4.155: MA1-1-S5 GP sample, undrained cyclic triaxial test (CTX). Effective stress-path, stress-strain, excess pore water pressure ratio and strain development plots.

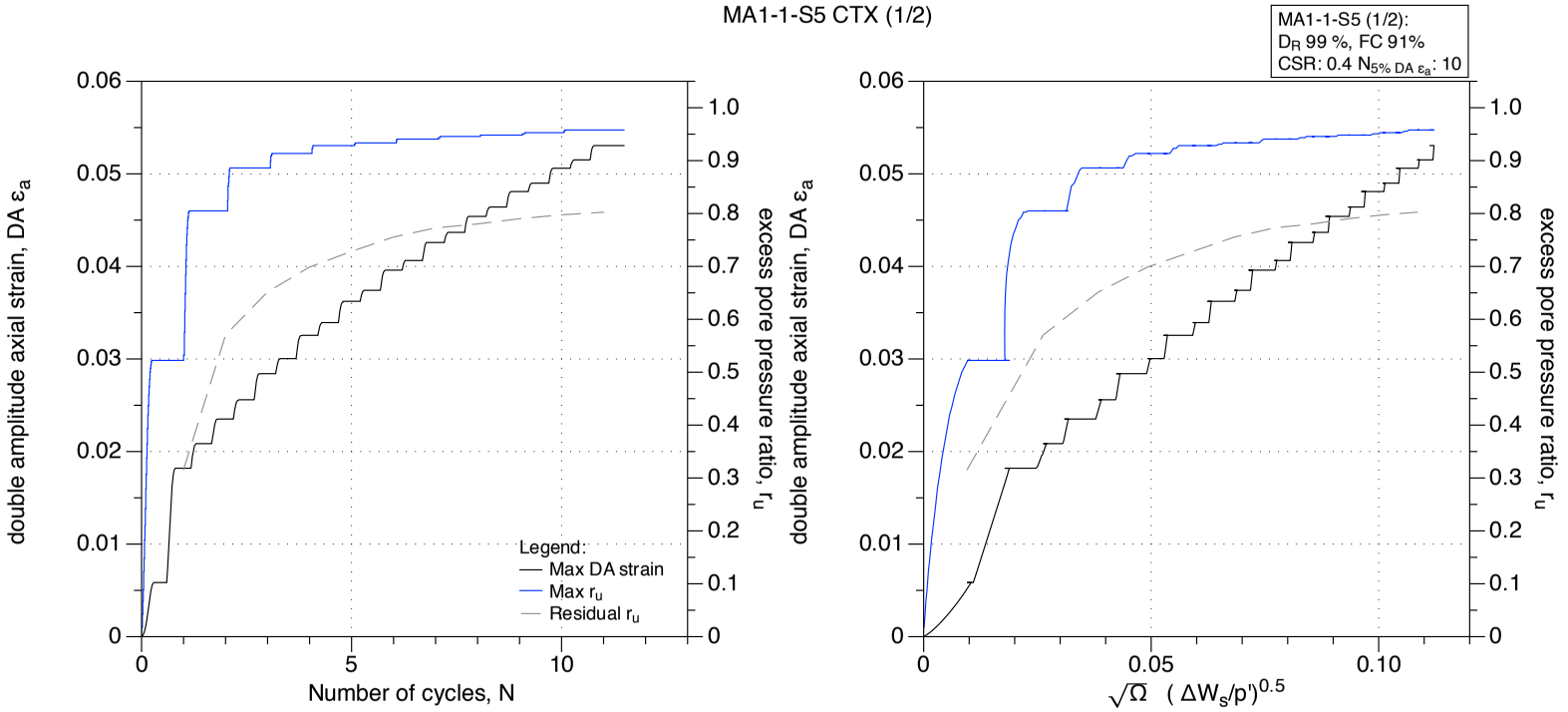

Figure 4.156: MA1-1-S5 GP sample, undrained cyclic triaxial test (CTX). Development of strain and excess pore water pressure with number of cycles and normalised shear work.

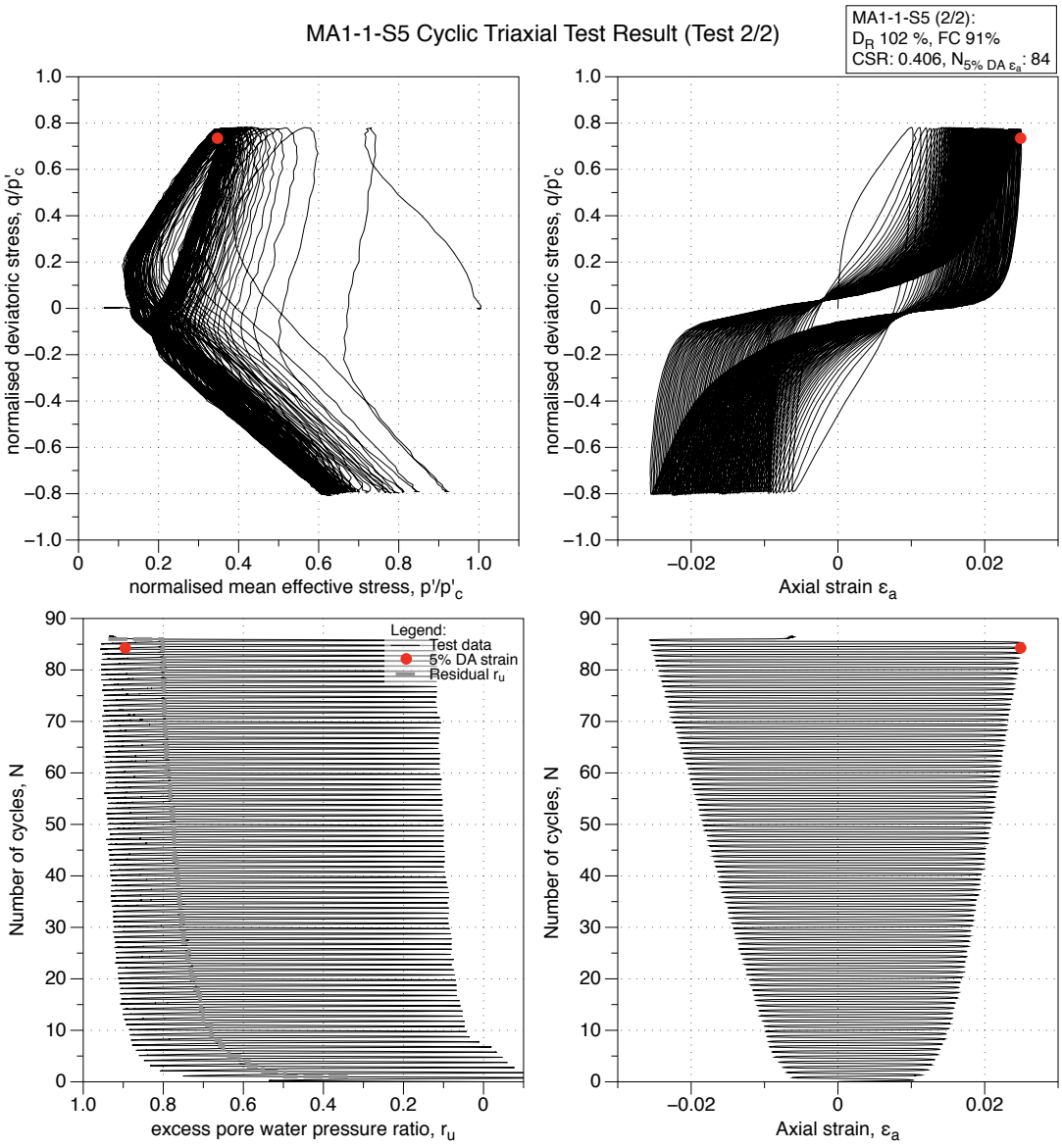

Figure 4.157: MA1-1-S5 GP sample, reliquefaction undrained cyclic triaxial test (CTX). Effective stress-path, stress-strain, excess pore water pressure ratio and strain development plots.

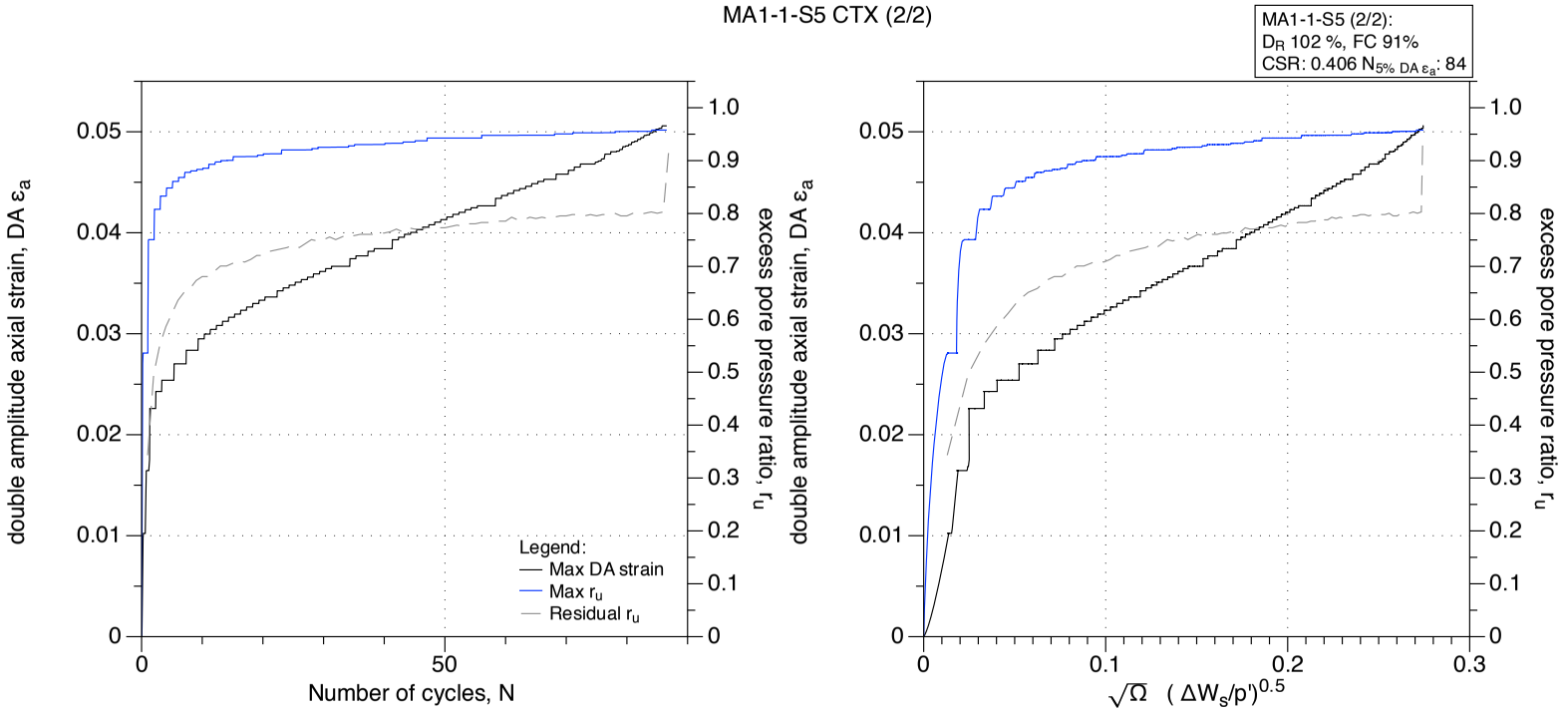

Figure 4.158: MA1-1-S5 GP sample, reliquefaction undrained cyclic triaxial test (CTX). Development of strain and excess pore water pressure with number of cycles and normalised shear work.

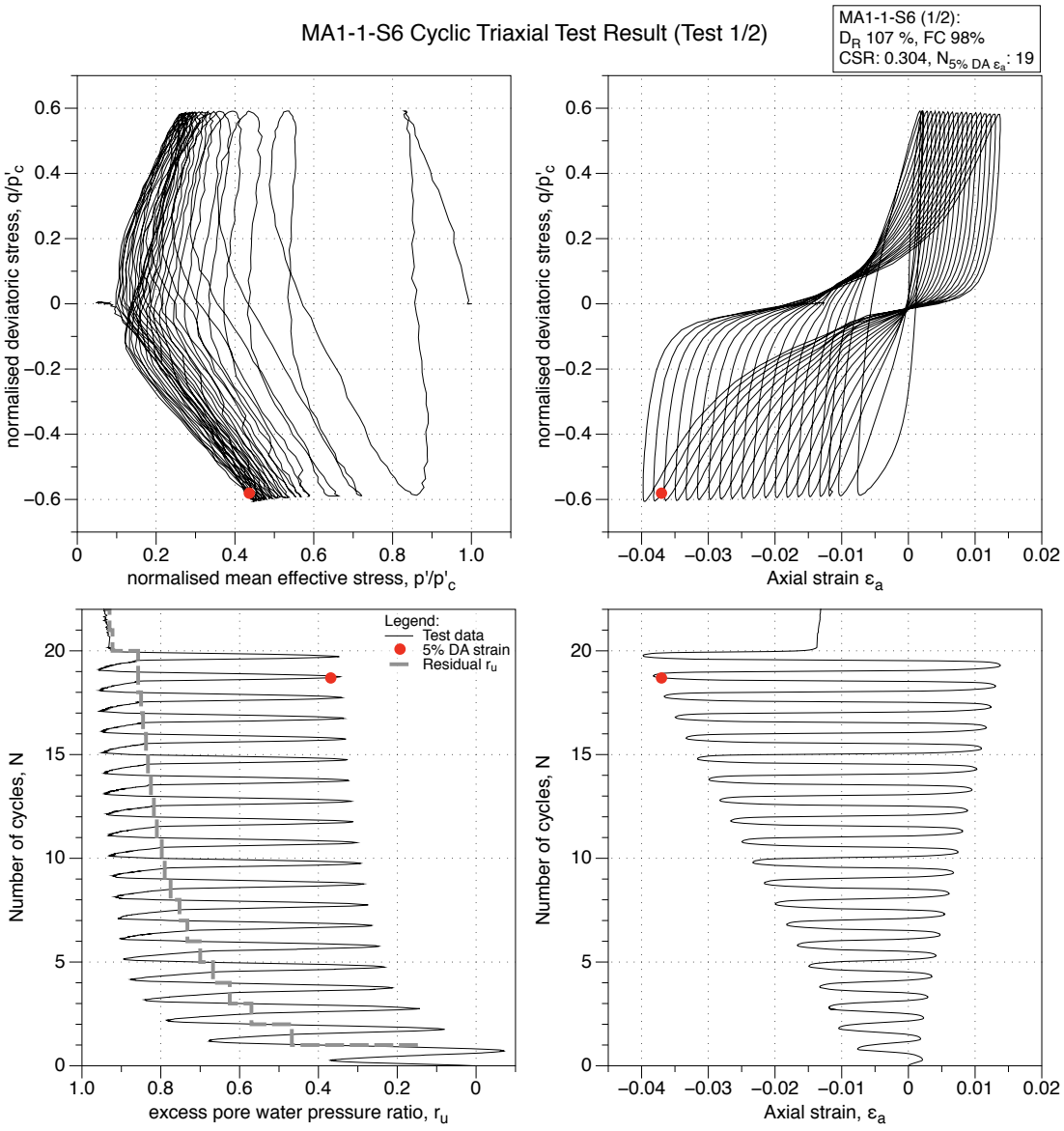

Figure 4.159: MA1-1-S6 GP sample, undrained cyclic triaxial test (CTX). Effective stress-path, stress-strain, excess pore water pressure ratio and strain development plots.

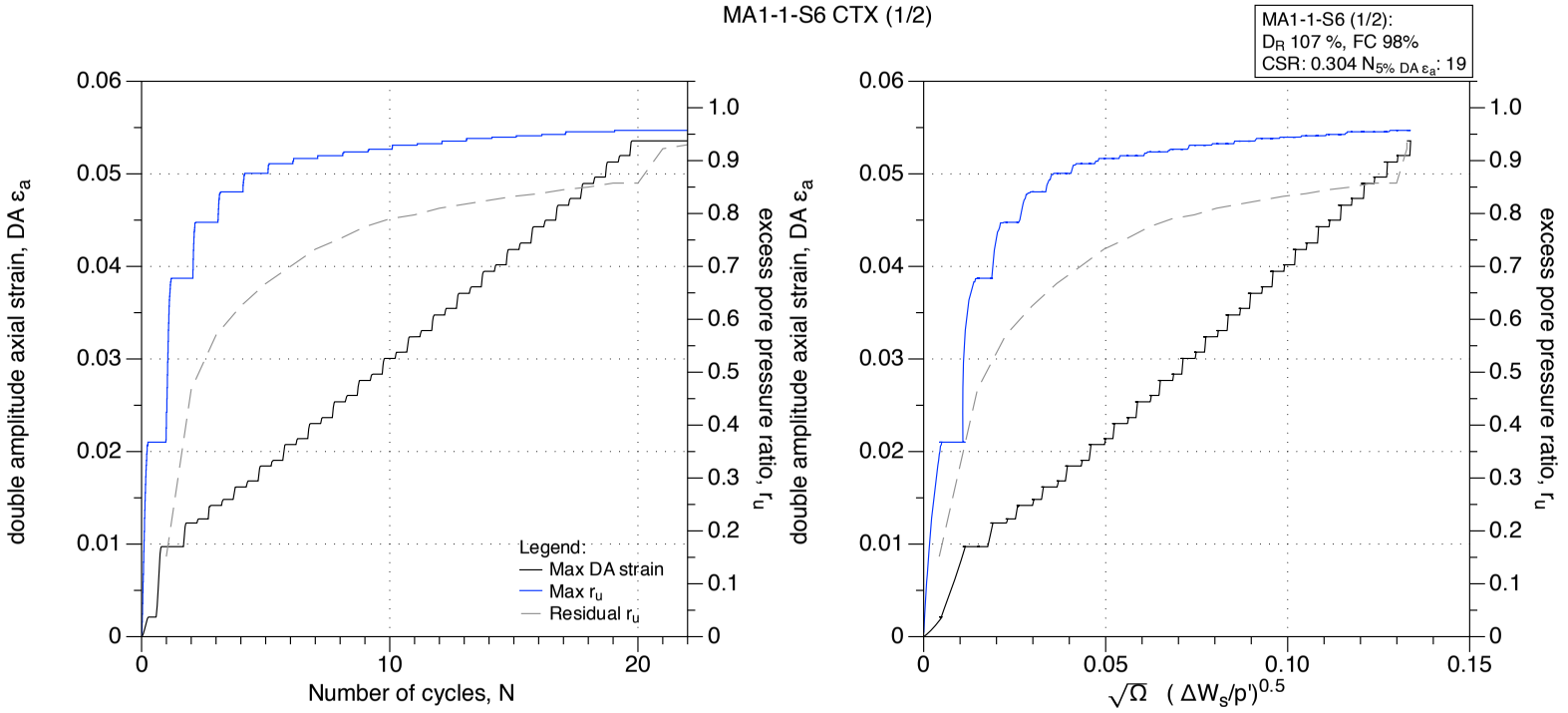

Figure 4.160: MA1-1-S6 GP sample, undrained cyclic triaxial test (CTX). Development of strain and excess pore water pressure with number of cycles and normalised shear work.

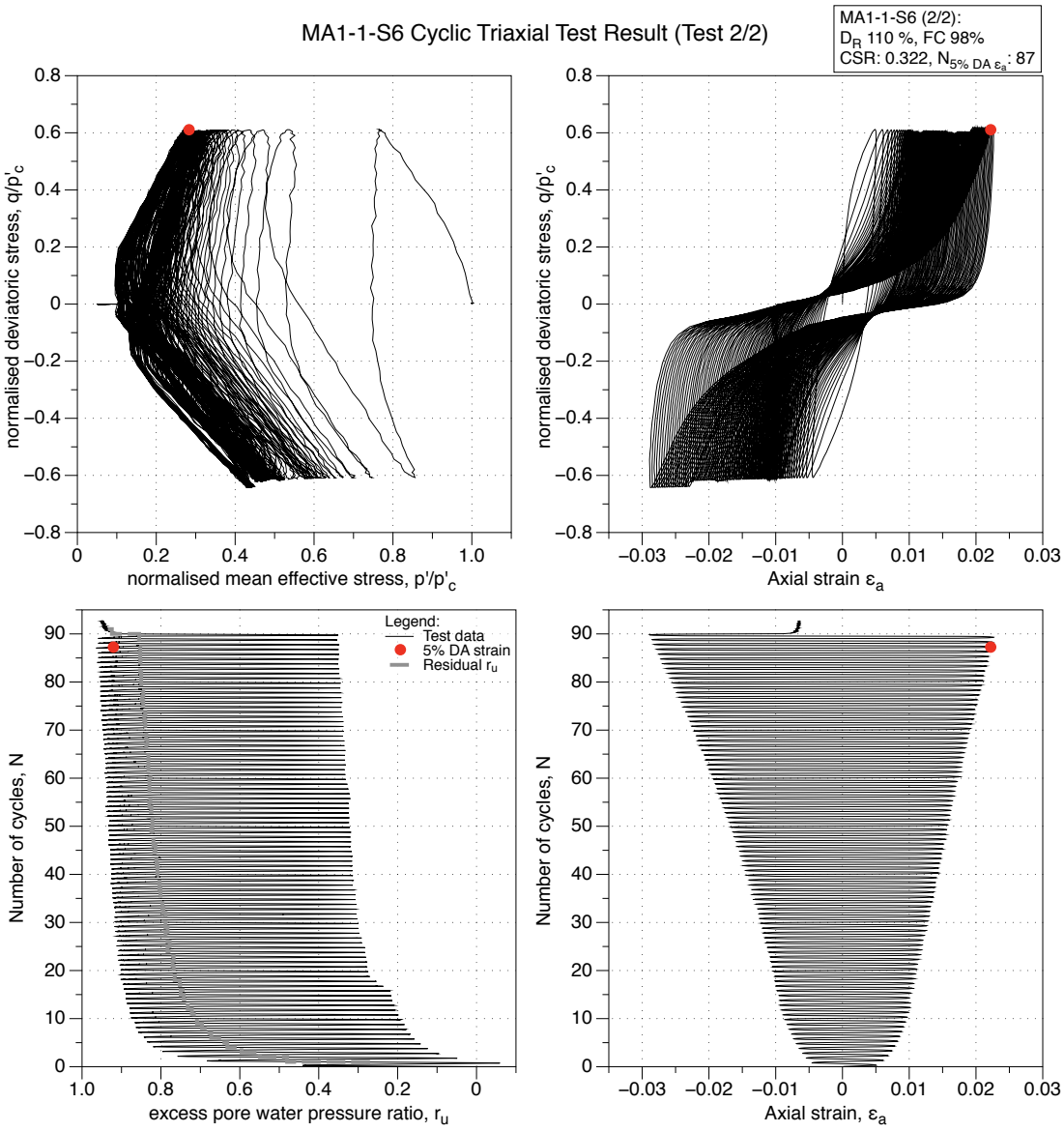

Figure 4.161: MA1-1-S6 GP sample, reliquefaction undrained cyclic triaxial test (CTX). Effective stress-path, stress-strain, excess pore water pressure ratio and strain development plots.

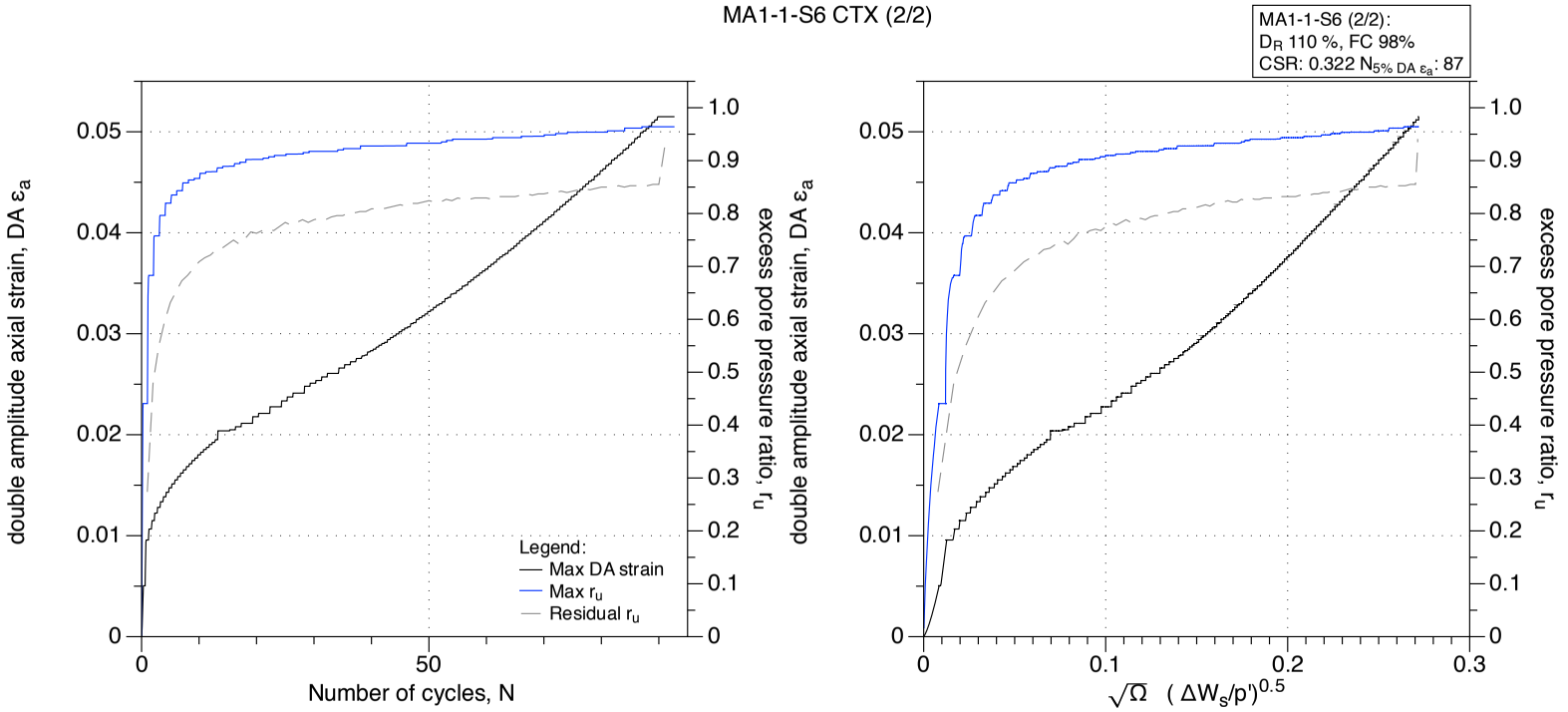

Figure 4.162: MA1-1-S6 GP sample, reliquefaction undrained cyclic triaxial test (CTX). Development of strain and excess pore water pressure with number of cycles and normalised shear work.

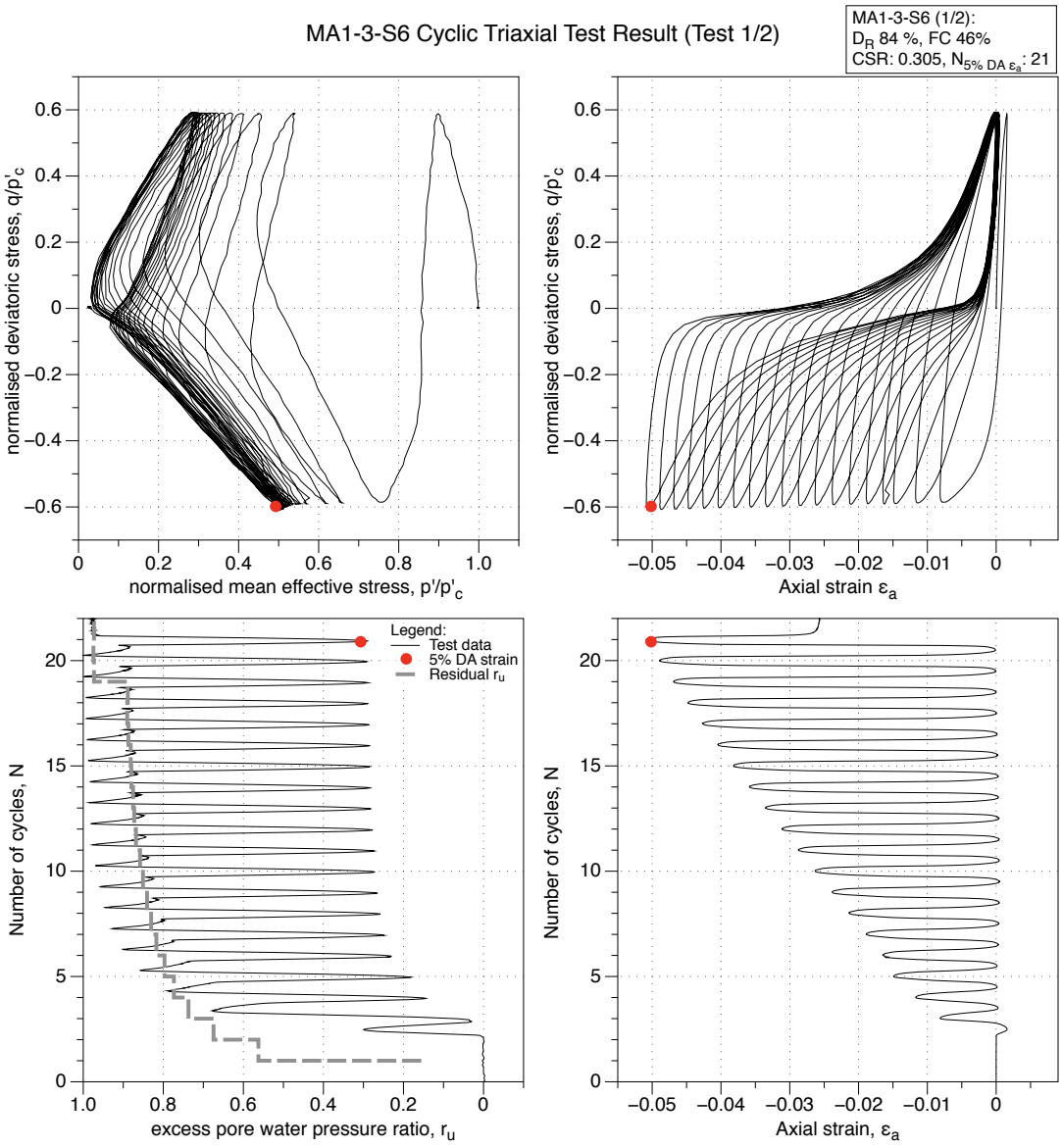

Figure 4.163: MA1-3-S6 GP sample, undrained cyclic triaxial test (CTX). Effective stress-path, stress-strain, excess pore water pressure ratio and strain development plots.

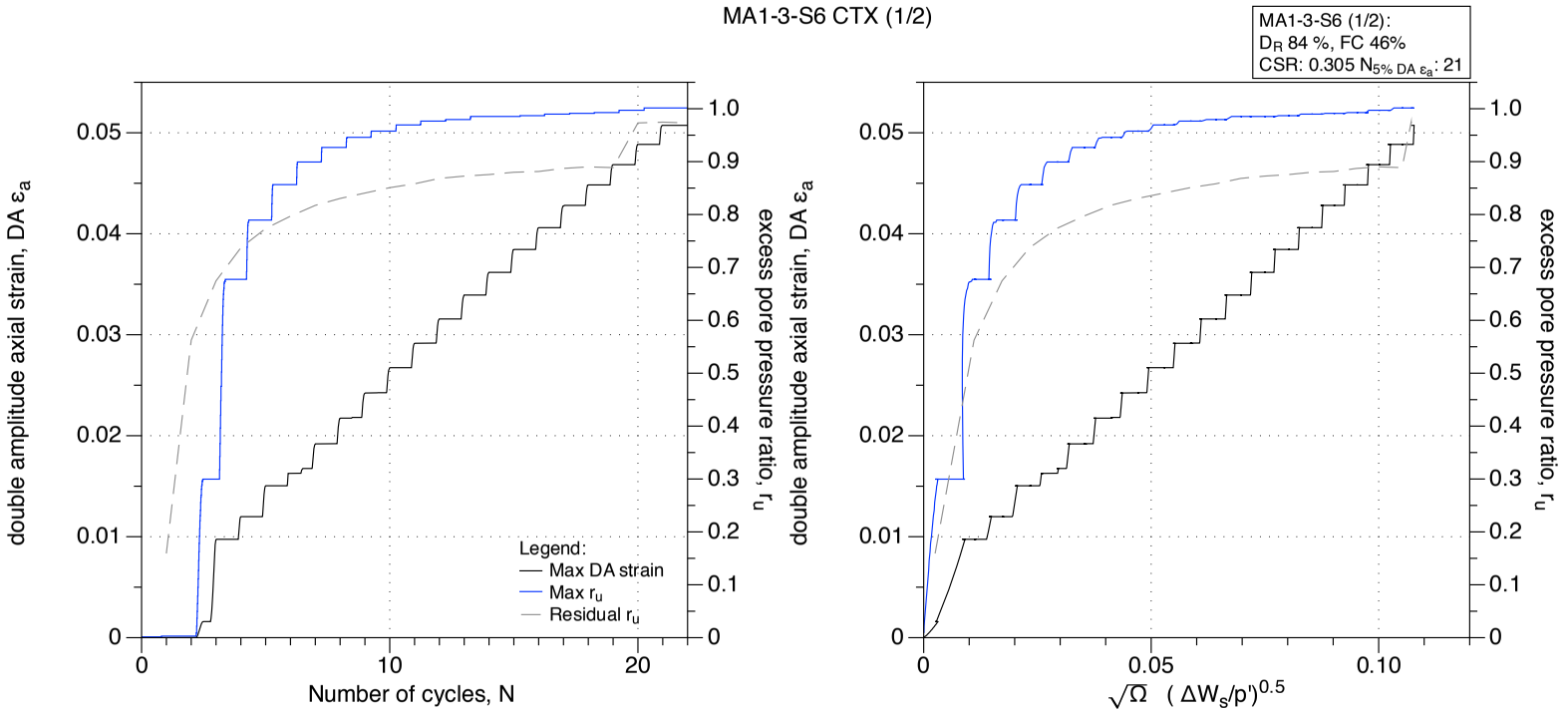

Figure 4.164: MA1-3-S6 GP sample, undrained cyclic triaxial test (CTX). Development of strain and excess pore water pressure with number of cycles and normalised shear work.

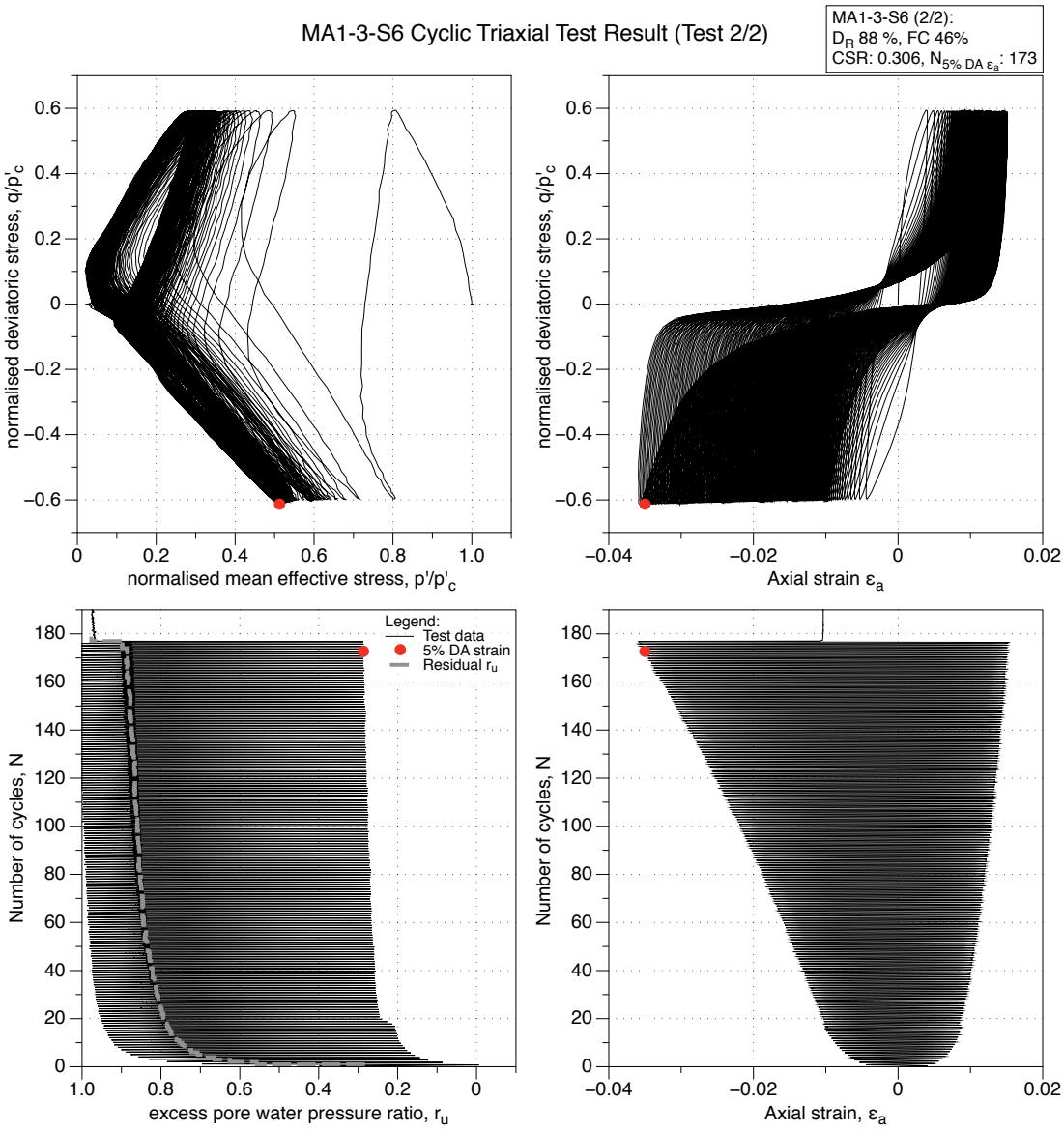

Figure 4.165: MA1-3-S6 GP sample, reliquefaction undrained cyclic triaxial test (CTX). Effective stress-path, stress-strain, excess pore water pressure ratio and strain development plots.

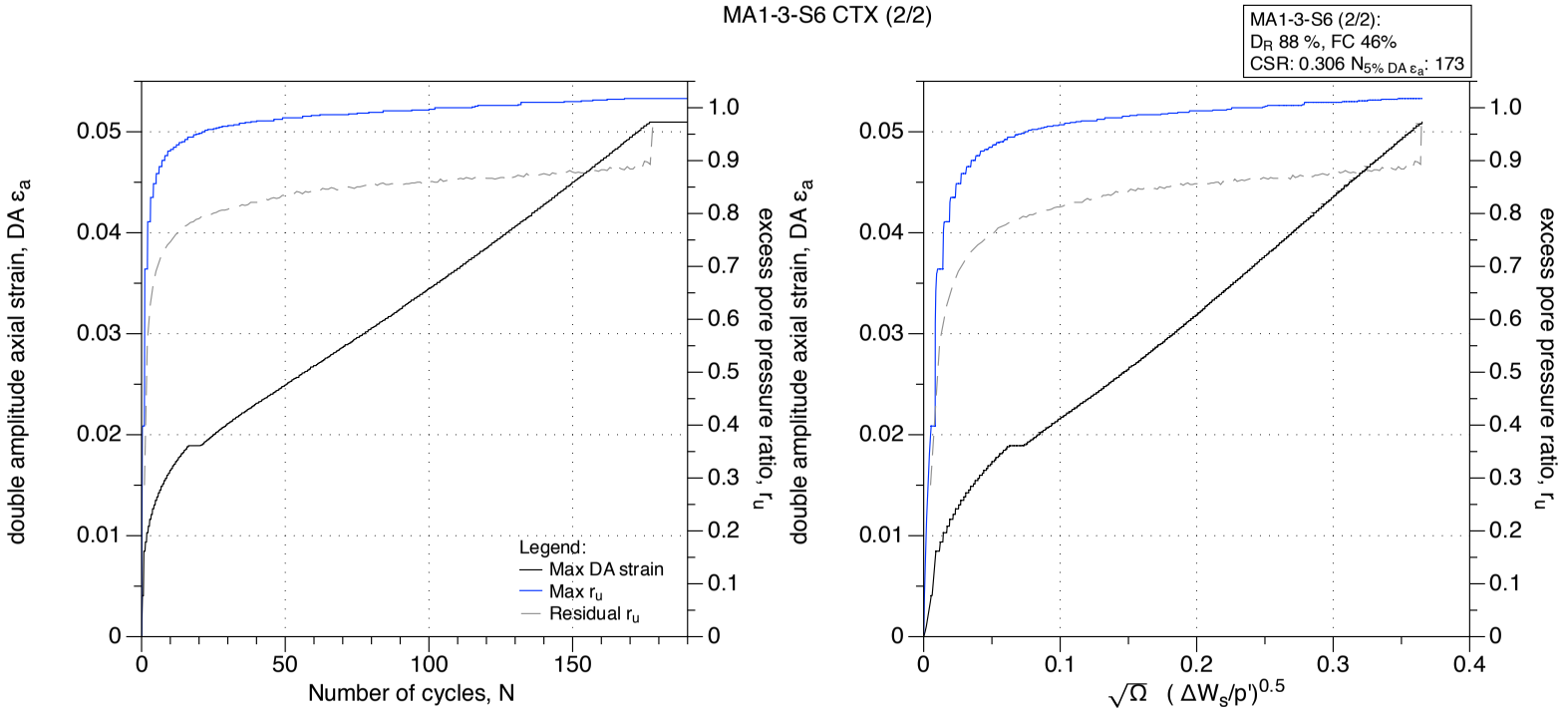

Figure 4.166: MA1-3-S6 GP sample, reliquefaction undrained cyclic triaxial test (CTX). Development of strain and excess pore water pressure with number of cycles and normalised shear work.

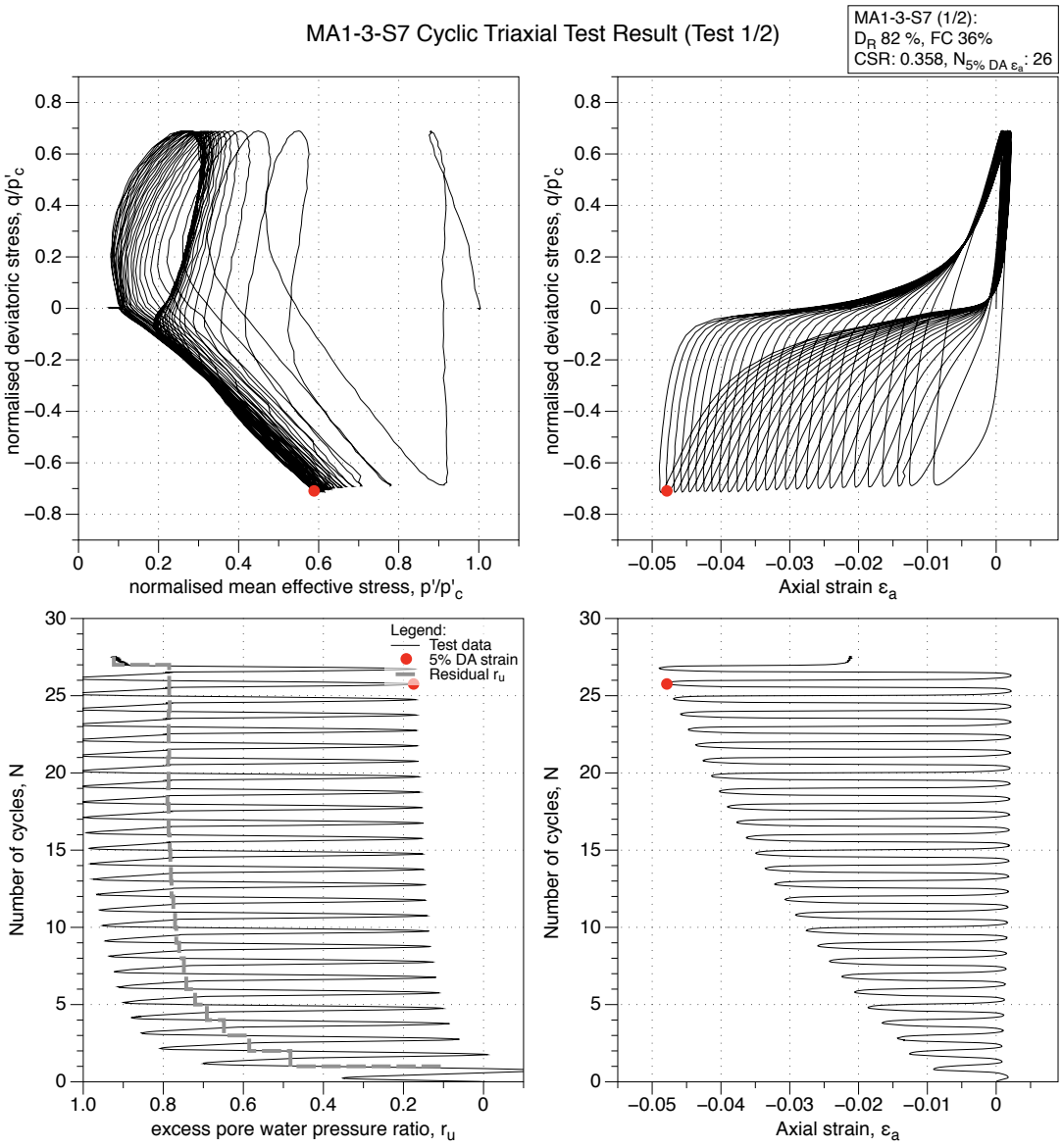

Figure 4.167: MA1-3-S7 GP sample, undrained cyclic triaxial test (CTX). Effective stress-path, stress-strain, excess pore water pressure ratio and strain development plots.

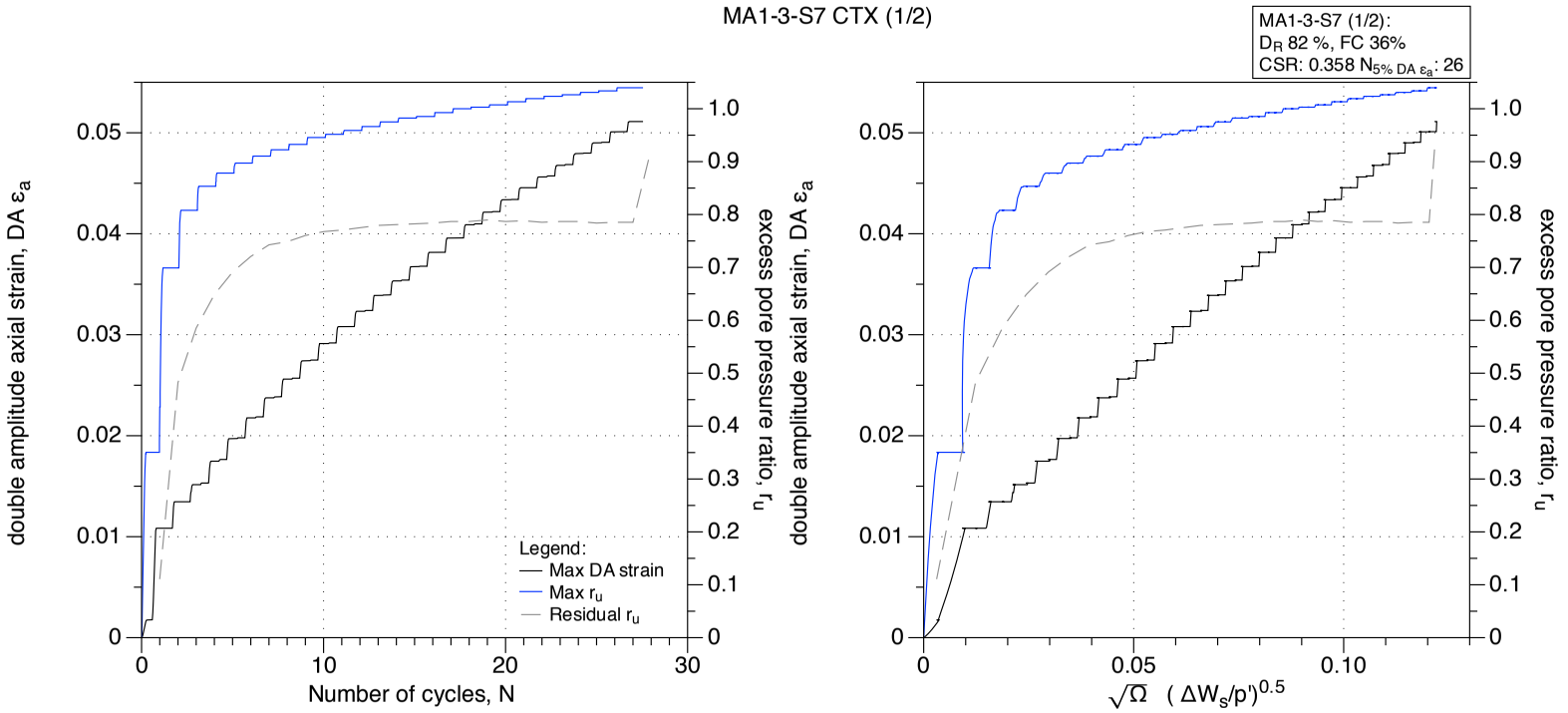

Figure 4.168: MA1-3-S7 GP sample, undrained cyclic triaxial test (CTX). Development of strain and excess pore water pressure with number of cycles and normalised shear work.

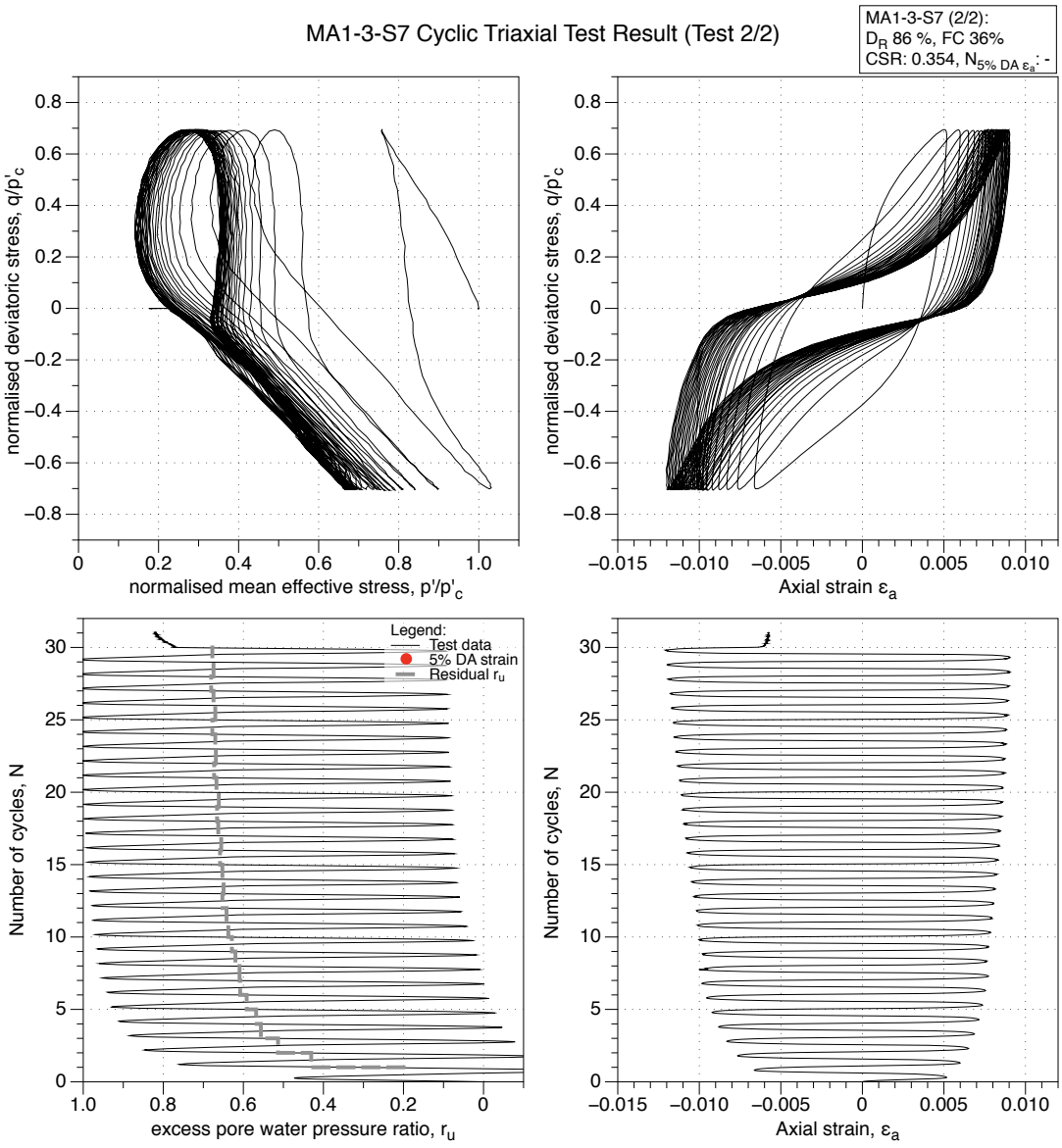

Figure 4.169: MA1-3-S7 GP sample, reliquefaction undrained cyclic triaxial test (CTX). Effective stress-path, stress-strain, excess pore water pressure ratio and strain development plots.

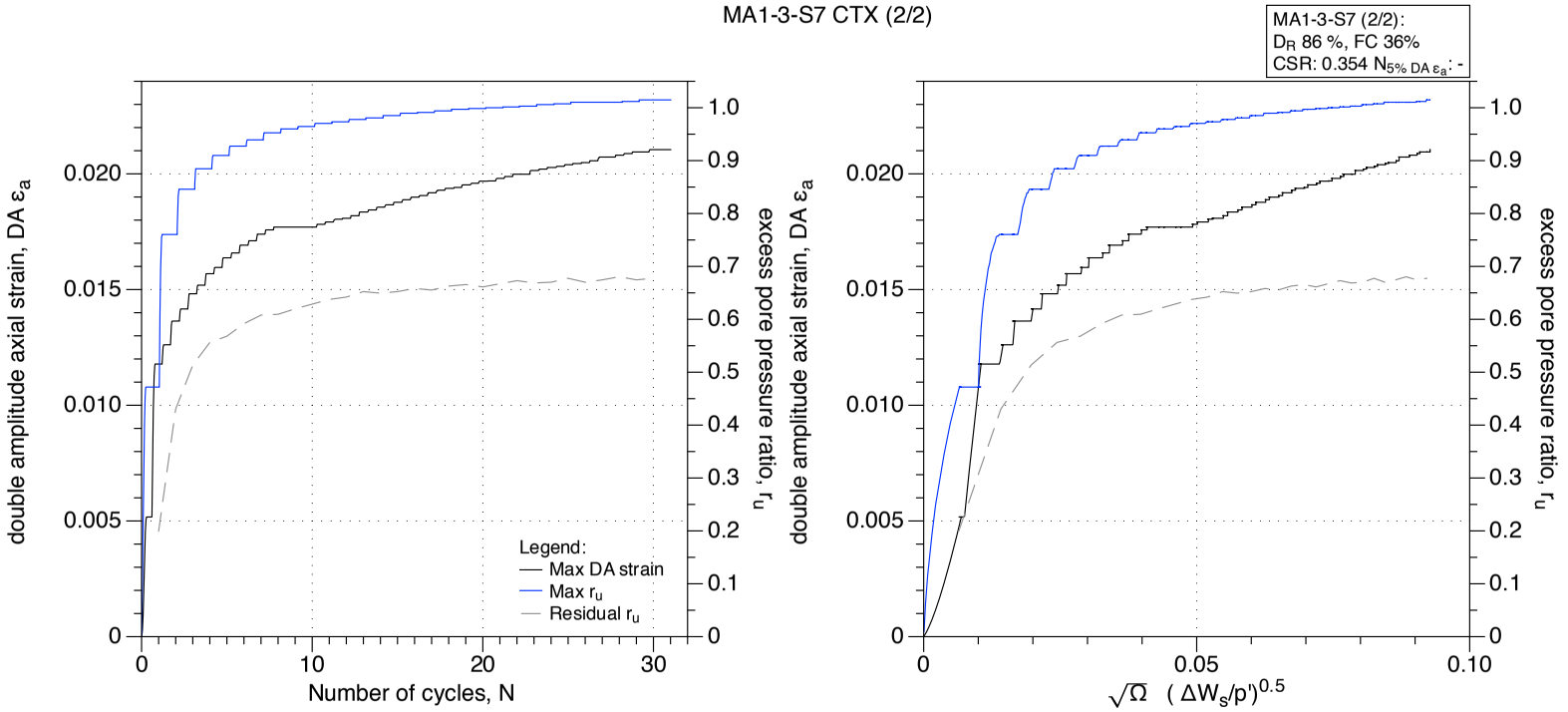

Figure 4.170: MA1-3-S7 GP sample, reliquefaction undrained cyclic triaxial test (CTX). Development of strain and excess pore water pressure with number of cycles and normalised shear work.

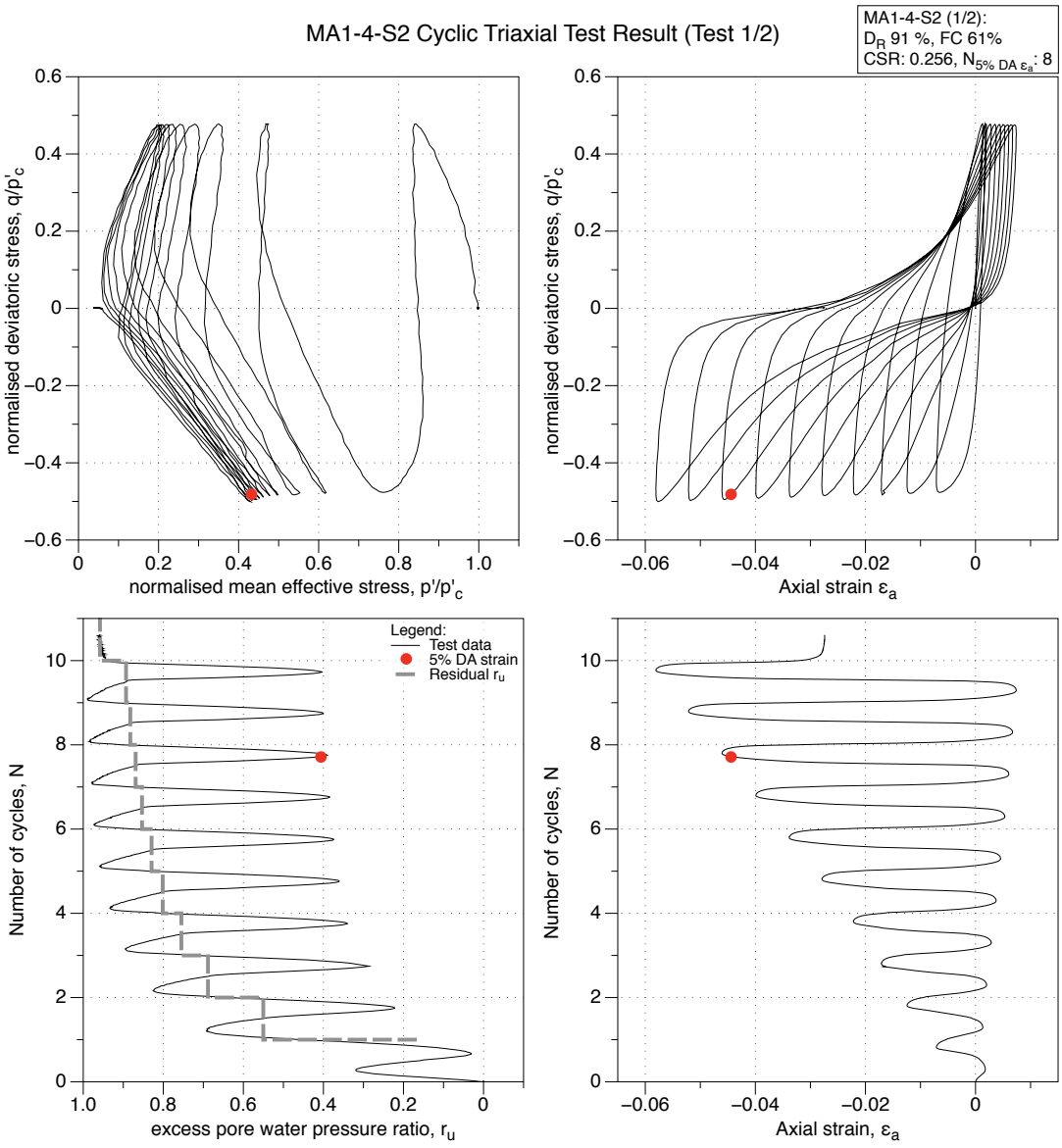

Figure 4.171: MA1-4-S2 GP sample, undrained cyclic triaxial test (CTX). Effective stress-path, stress-strain, excess pore water pressure ratio and strain development plots.

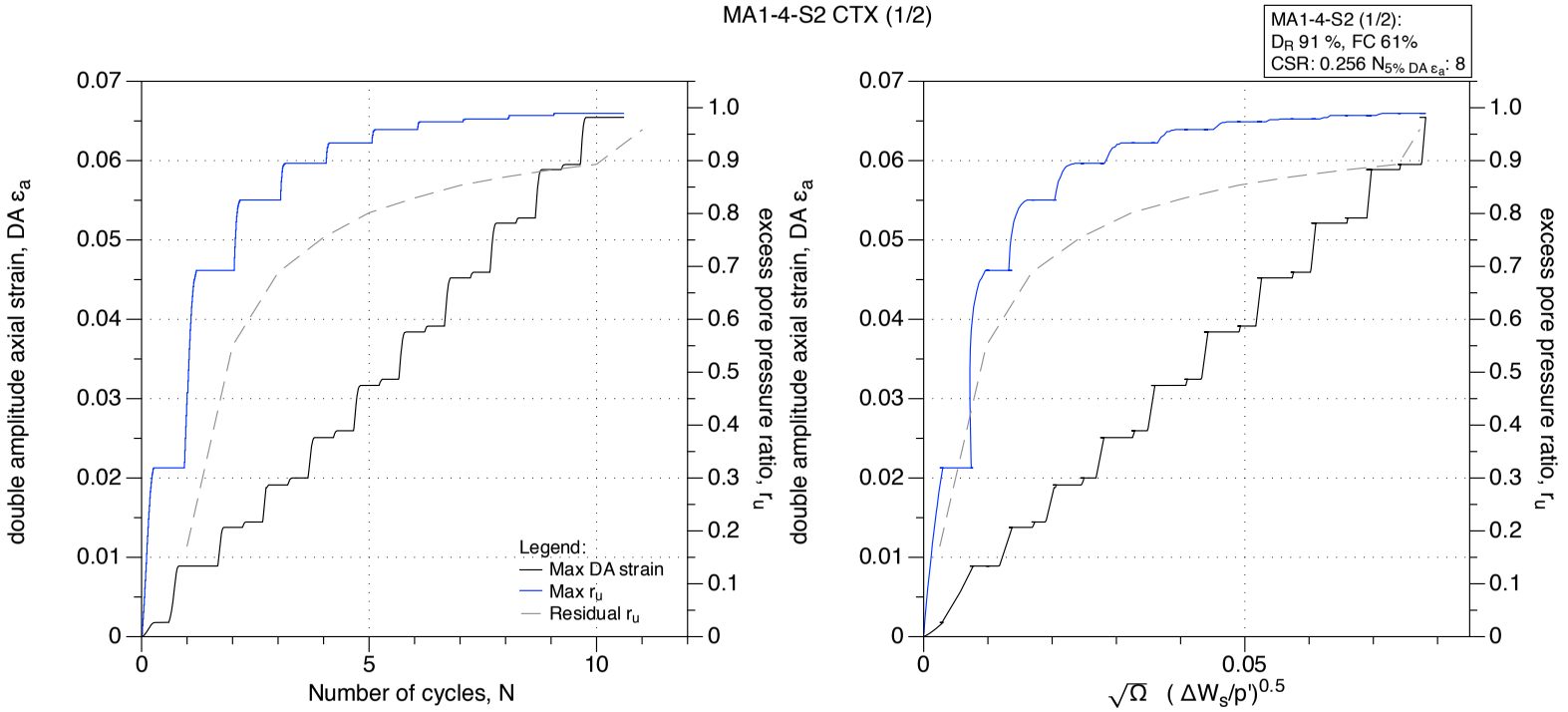

Figure 4.172: MA1-4-S2 GP sample, undrained cyclic triaxial test (CTX). Development of strain and excess pore water pressure with number of cycles and normalised shear work.

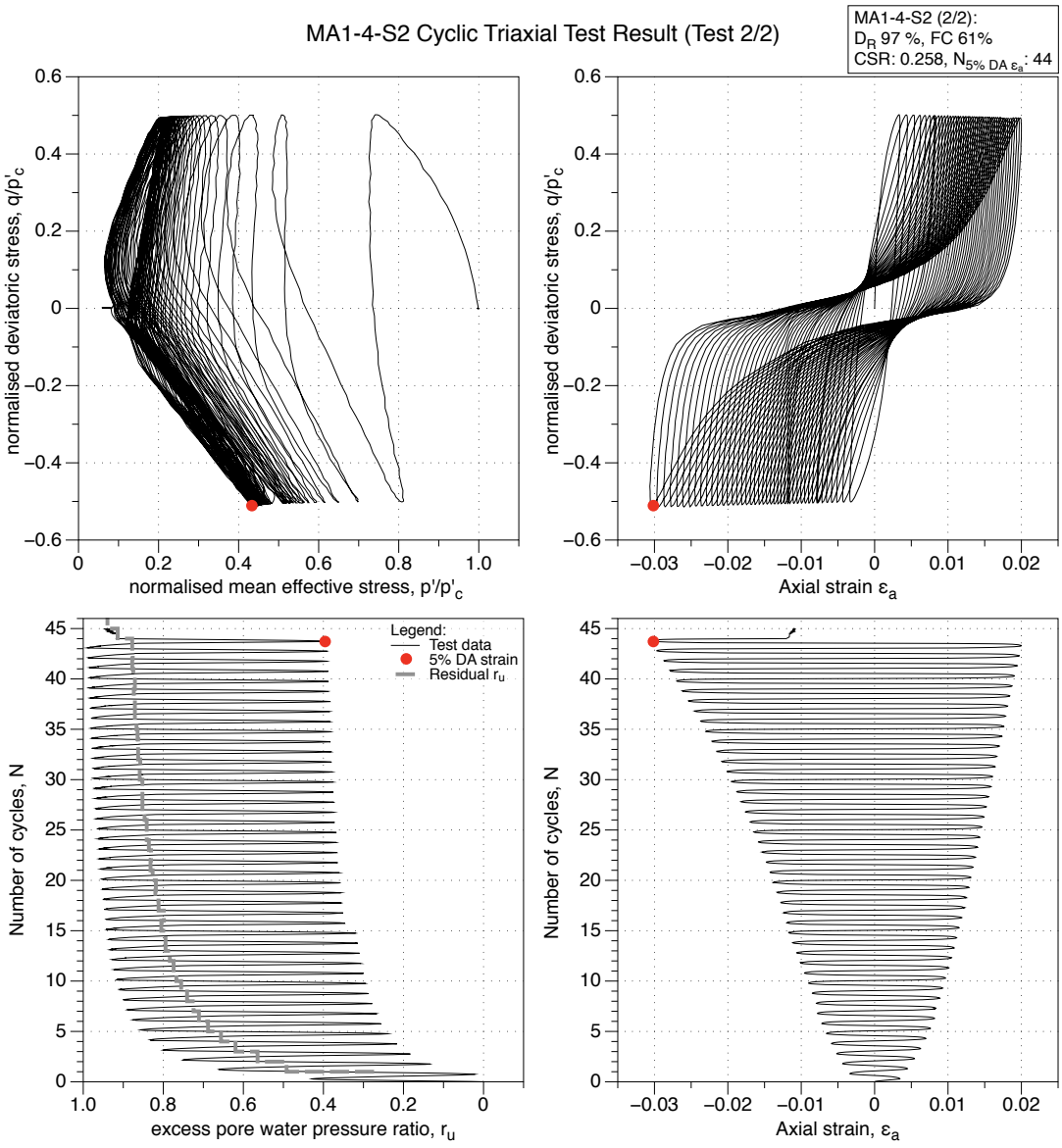

Figure 4.173: MA1-4-S2 GP sample, reliquefaction undrained cyclic triaxial test (CTX). Effective stress-path, stress-strain, excess pore water pressure ratio and strain development plots.

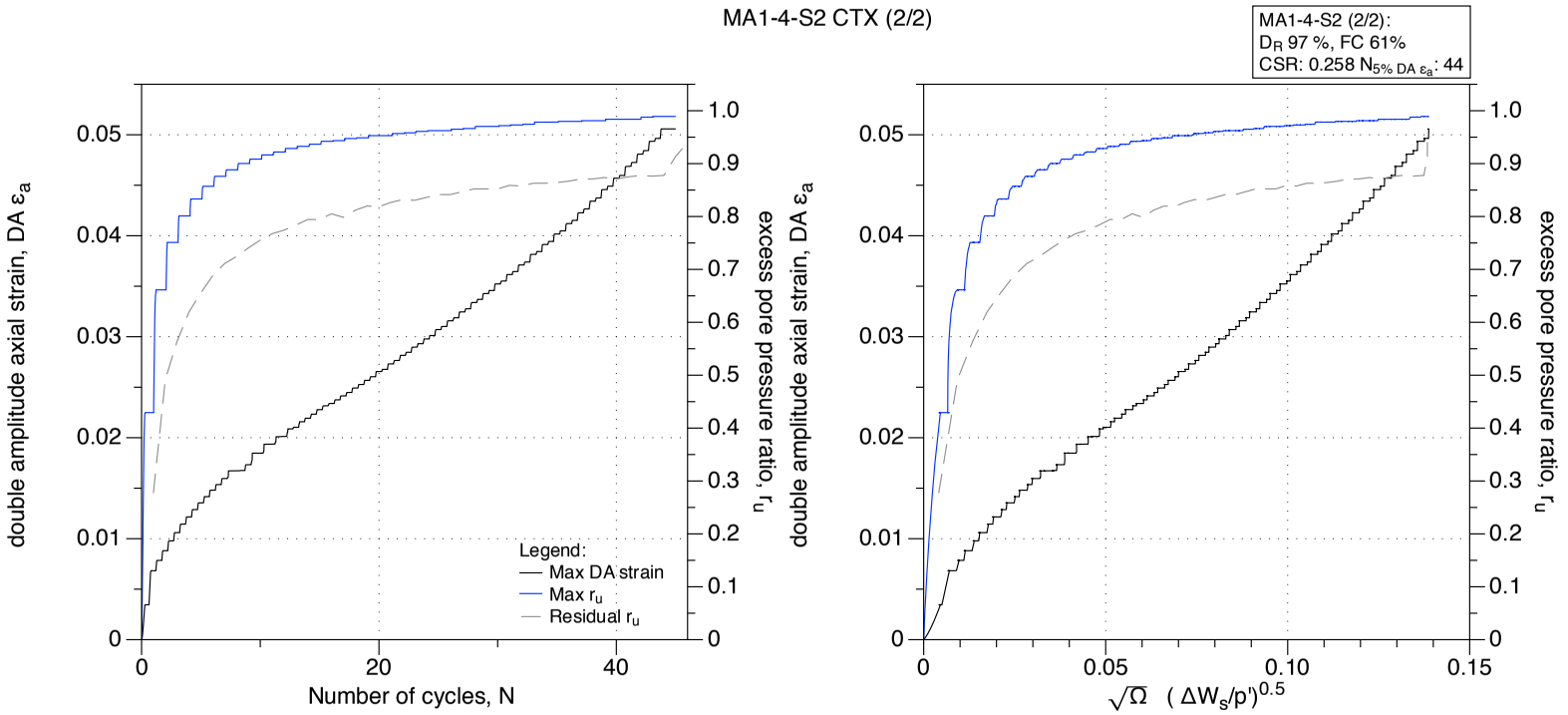

Figure 4.174: MA1-4-S2 GP sample, reliquefaction undrained cyclic triaxial test (CTX). Development of strain and excess pore water pressure with number of cycles and normalised shear work.

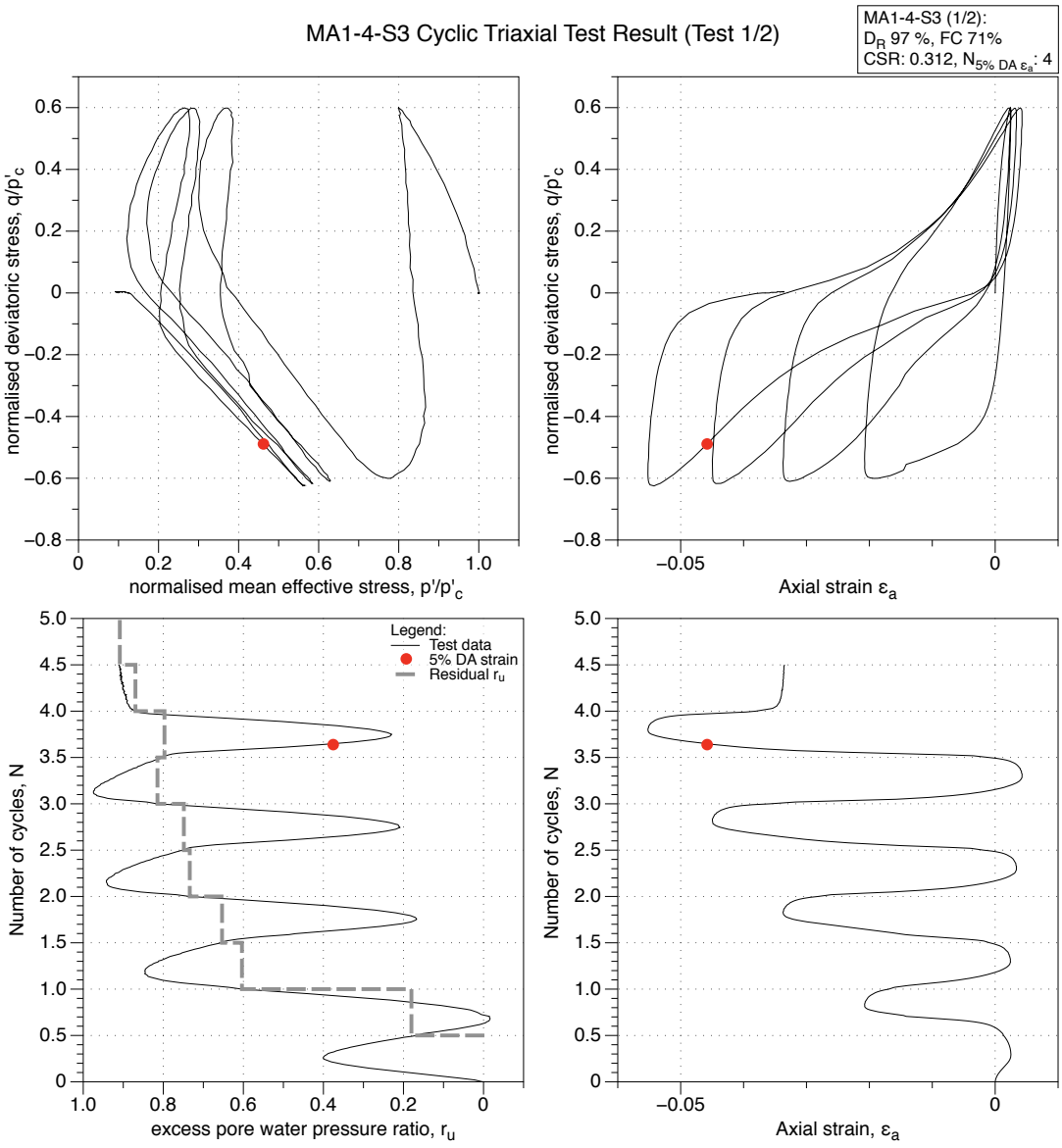

Figure 4.175: MA1-4-S3 GP sample, undrained cyclic triaxial test (CTX). Effective stress-path, stress-strain, excess pore water pressure ratio and strain development plots.

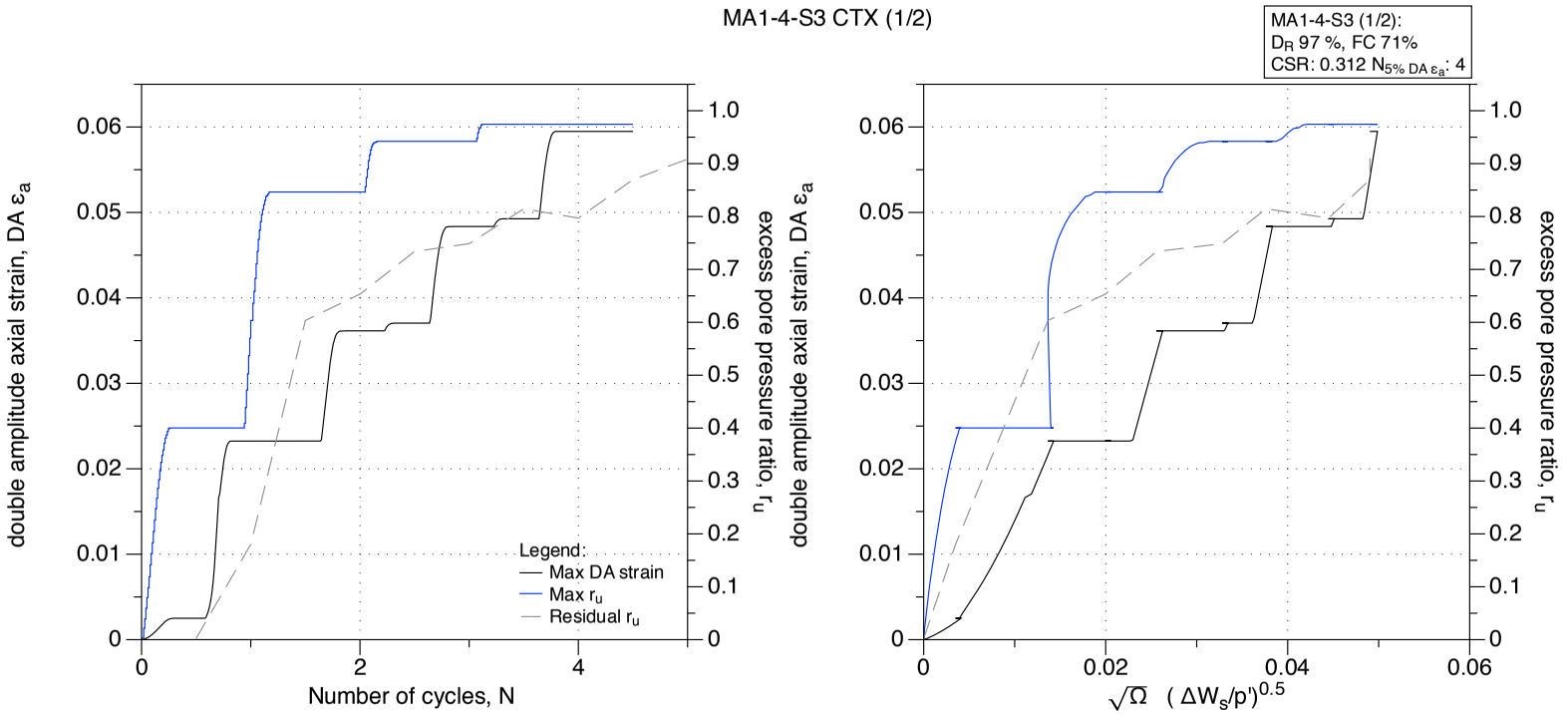

Figure 4.176: MA1-4-S3 GP sample, undrained cyclic triaxial test (CTX). Development of strain and excess pore water pressure with number of cycles and normalised shear work.

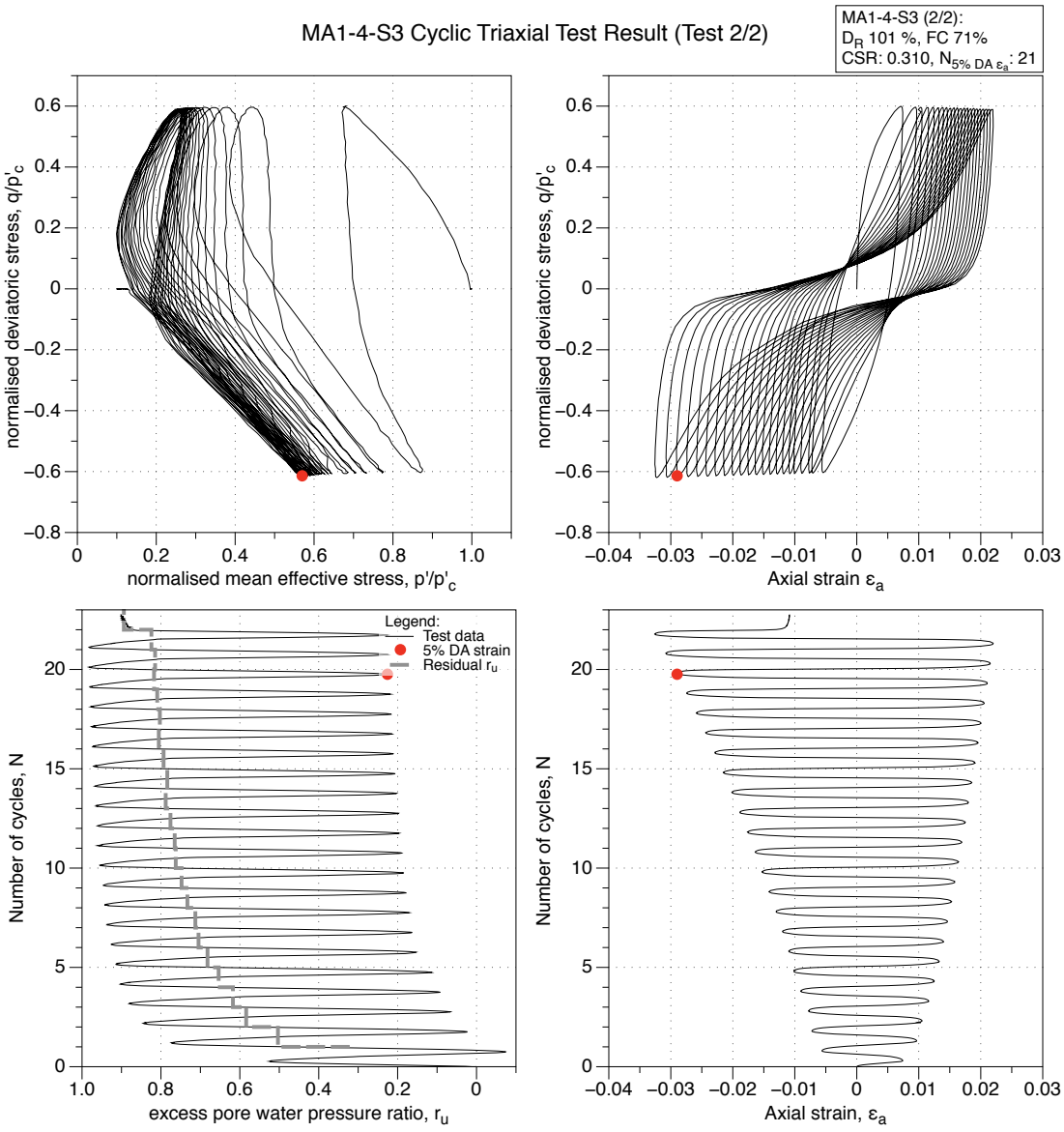

Figure 4.177: MA1-4-S3 GP sample, reliquefaction undrained cyclic triaxial test (CTX). Effective stress-path, stress-strain, excess pore water pressure ratio and strain development plots.

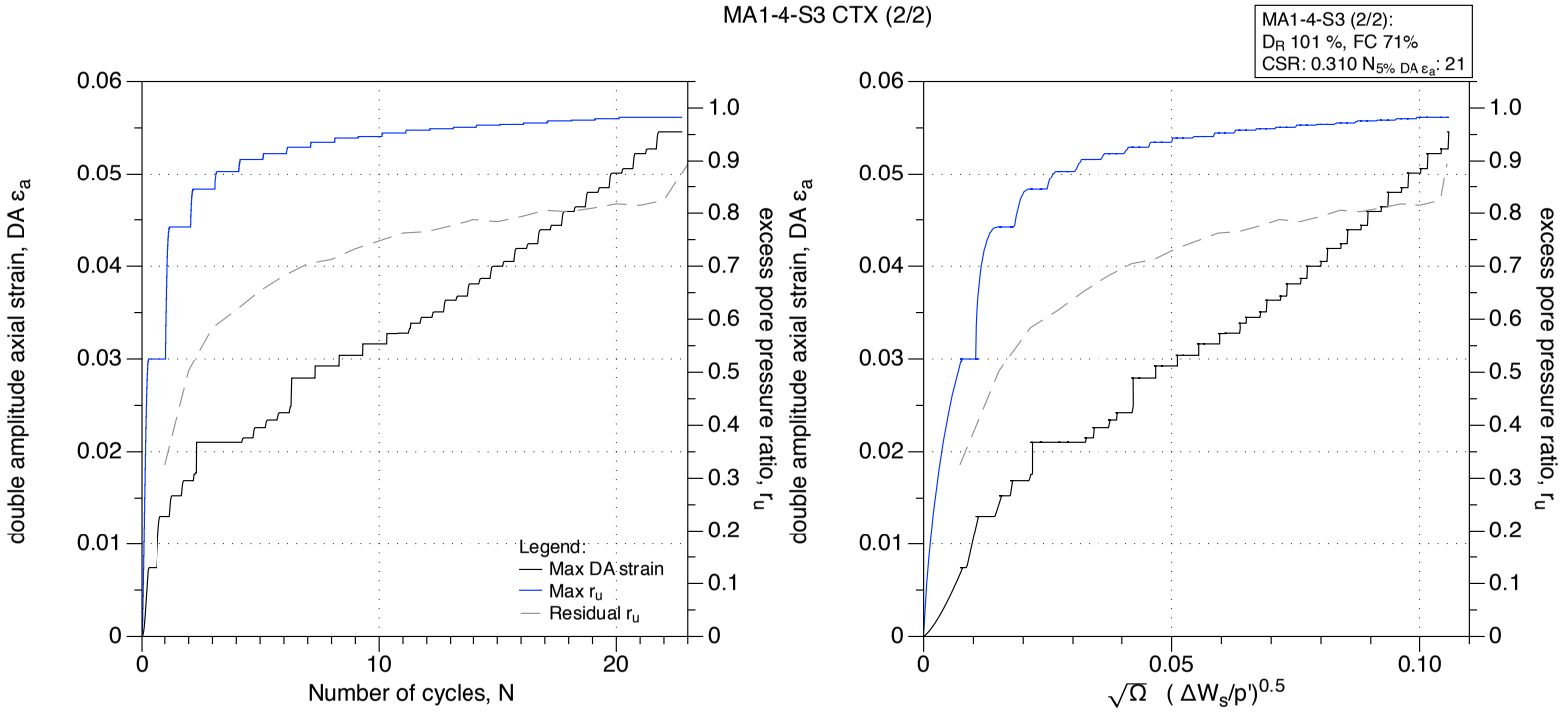

Figure 4.178: MA1-4-S3 GP sample, reliquefaction undrained cyclic triaxial test (CTX). Development of strain and excess pore water pressure with number of cycles and normalised shear work.

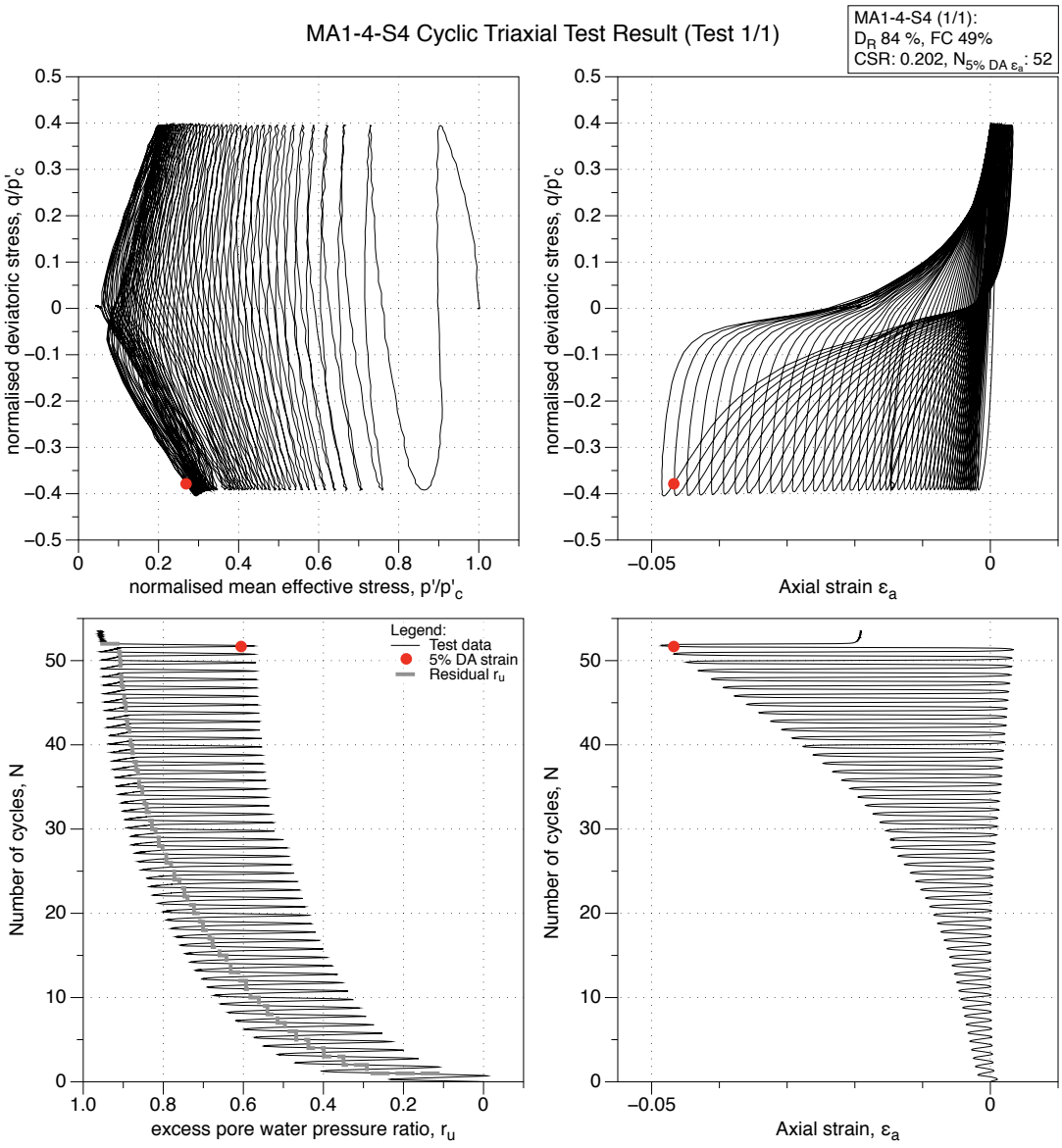

Figure 4.179: MA1-4-S4 GP sample, undrained cyclic triaxial test (CTX). Effective stress-path, stress-strain, excess pore water pressure ratio and strain development plots.

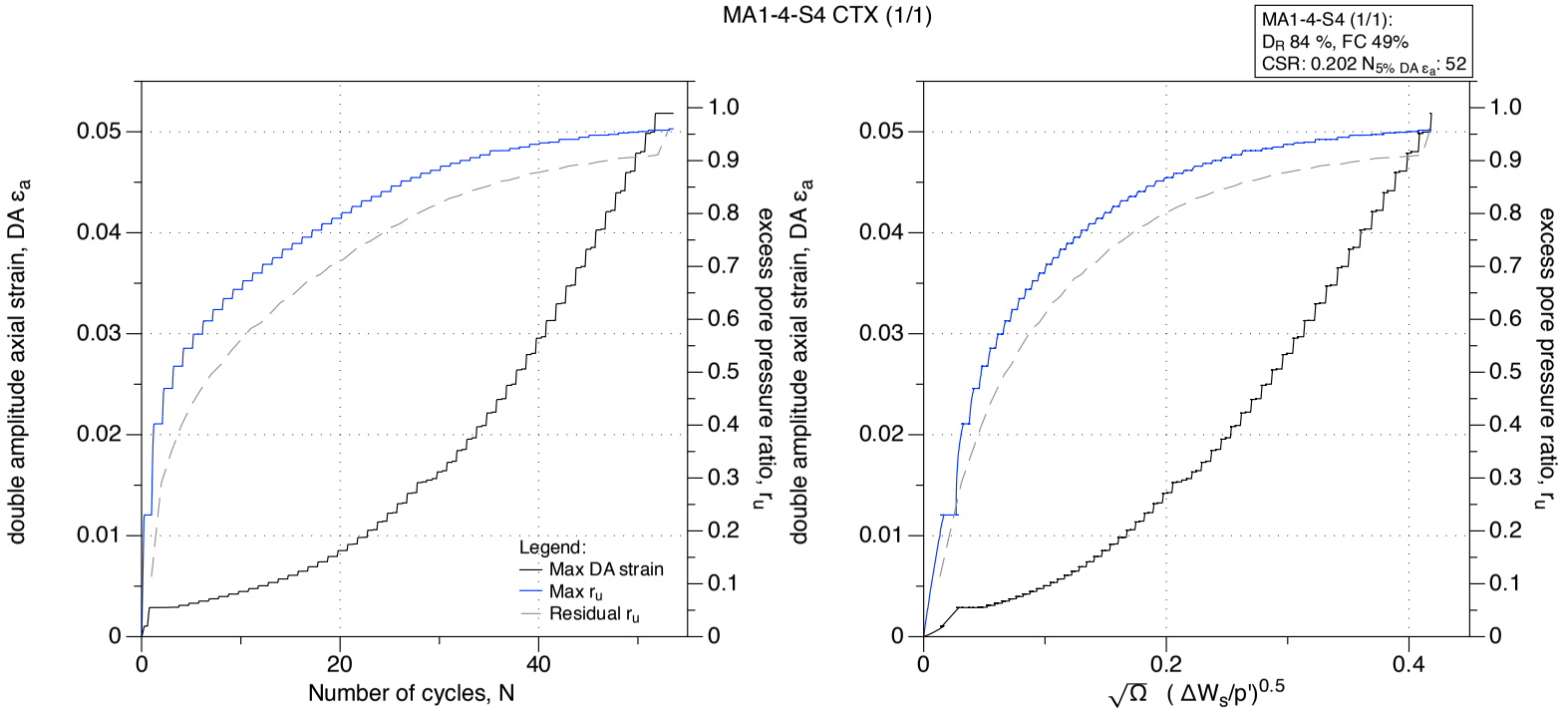

Figure 4.180: MA1-4-S4 GP sample, undrained cyclic triaxial test (CTX). Development of strain and excess pore water pressure with number of cycles and normalised shear work.

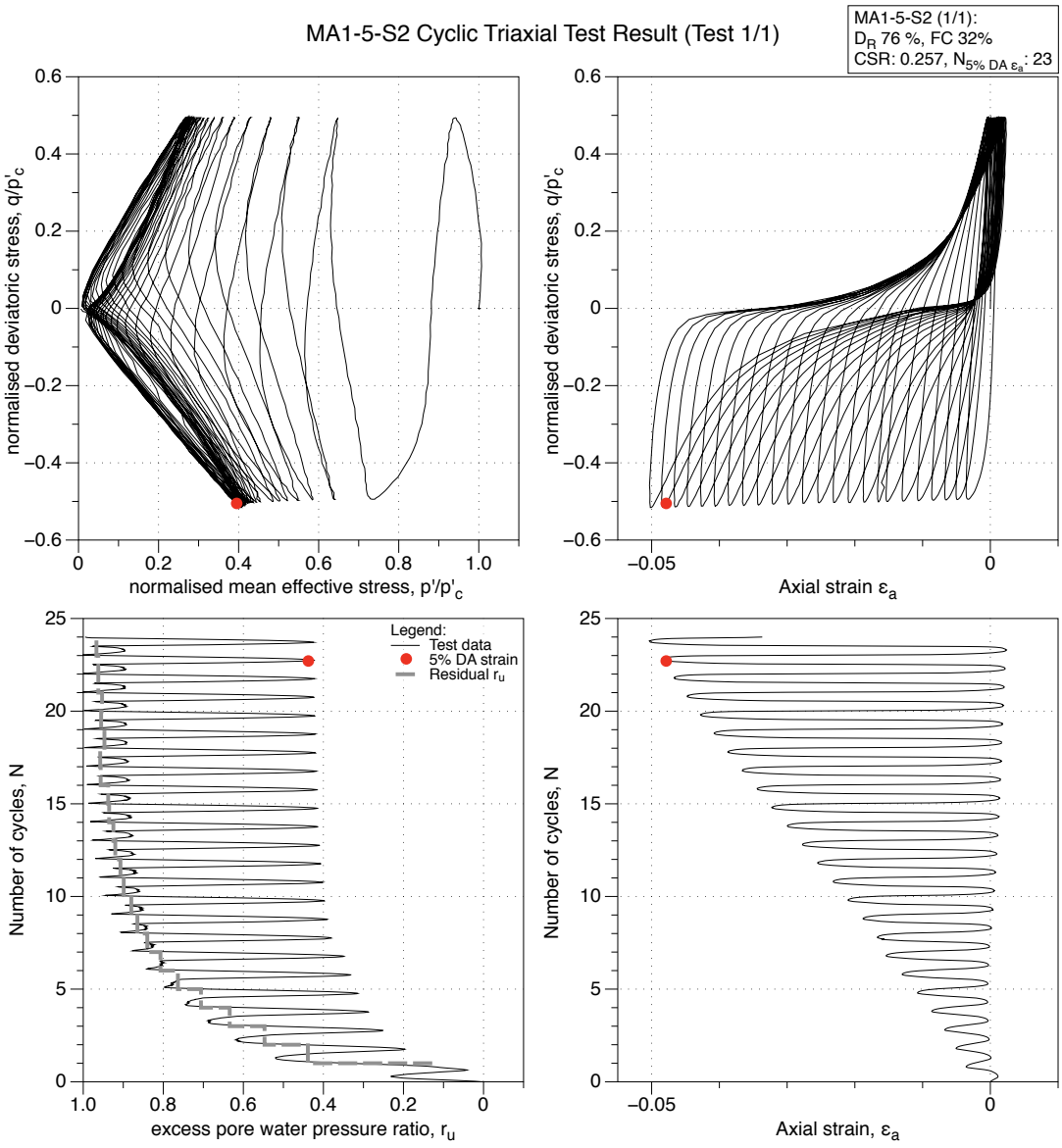

Figure 4.181: MA1-5-S2 GP sample, undrained cyclic triaxial test (CTX). Effective stress-path, stress-strain, excess pore water pressure ratio and strain development plots.

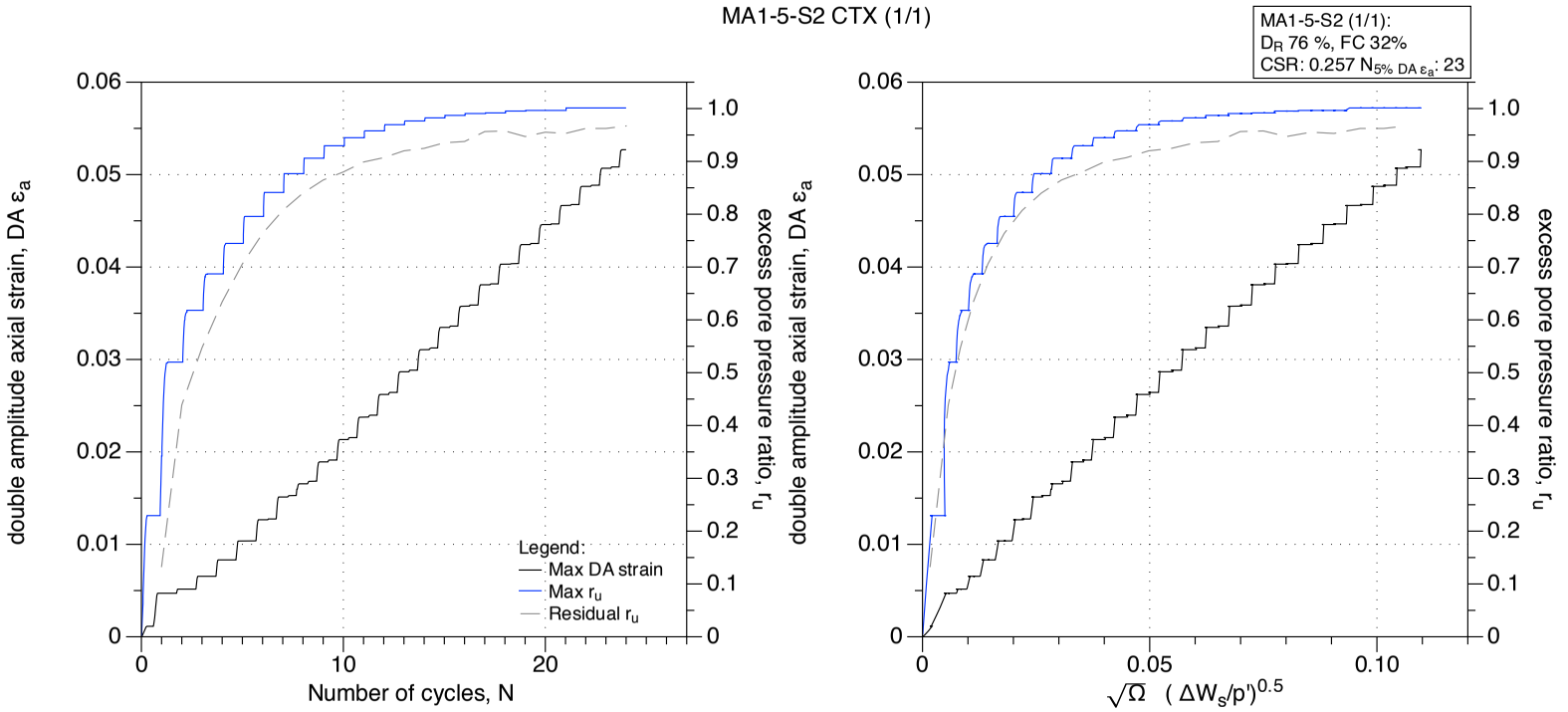

Figure 4.182: MA1-5-S2 GP sample, undrained cyclic triaxial test (CTX). Development of strain and excess pore water pressure with number of cycles and normalised shear work.

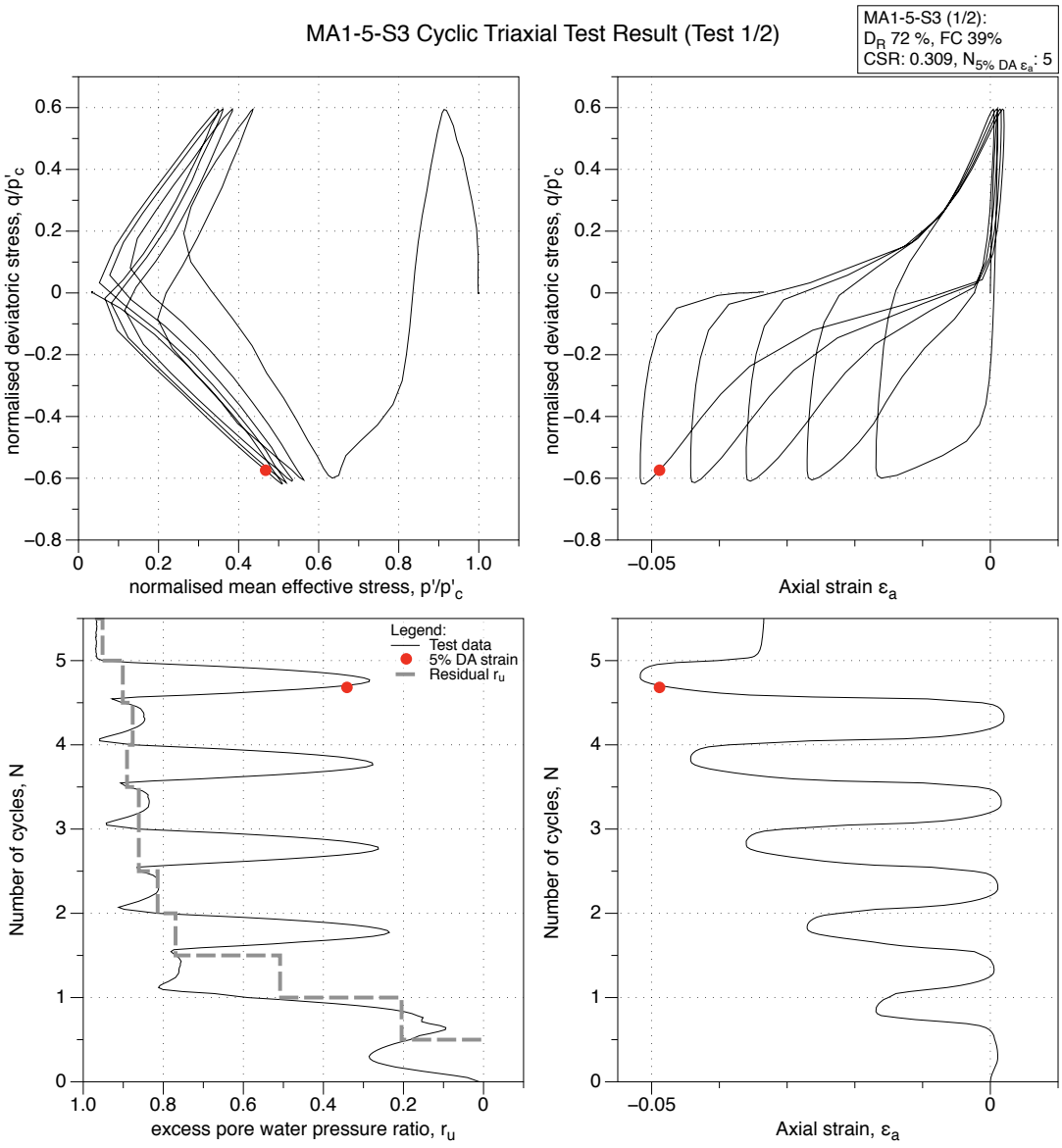

Figure 4.183: MA1-5-S3 GP sample, undrained cyclic triaxial test (CTX). Effective stress-path, stress-strain, excess pore water pressure ratio and strain development plots.

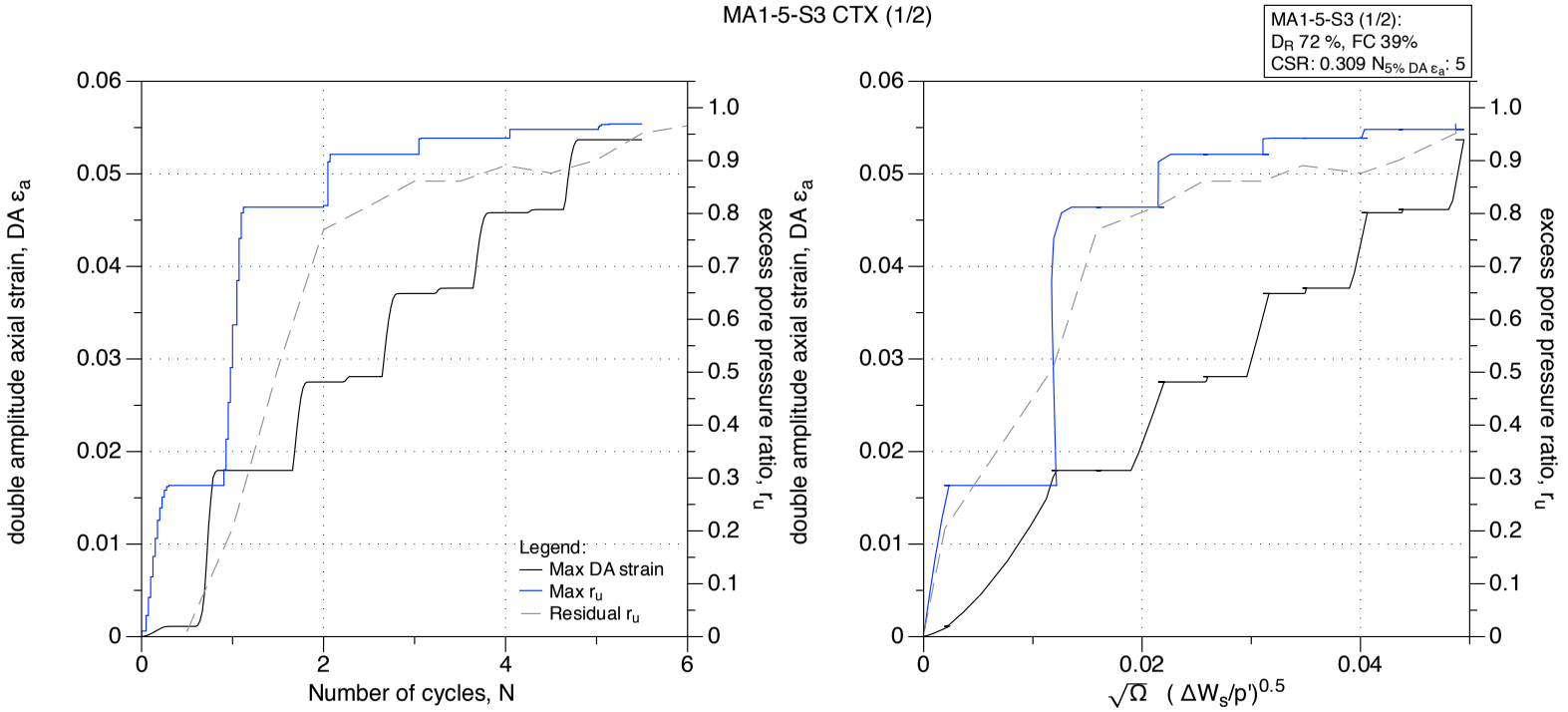

Figure 4.184: MA1-5-S3 GP sample, undrained cyclic triaxial test (CTX). Development of strain and excess pore water pressure with number of cycles and normalised shear work.

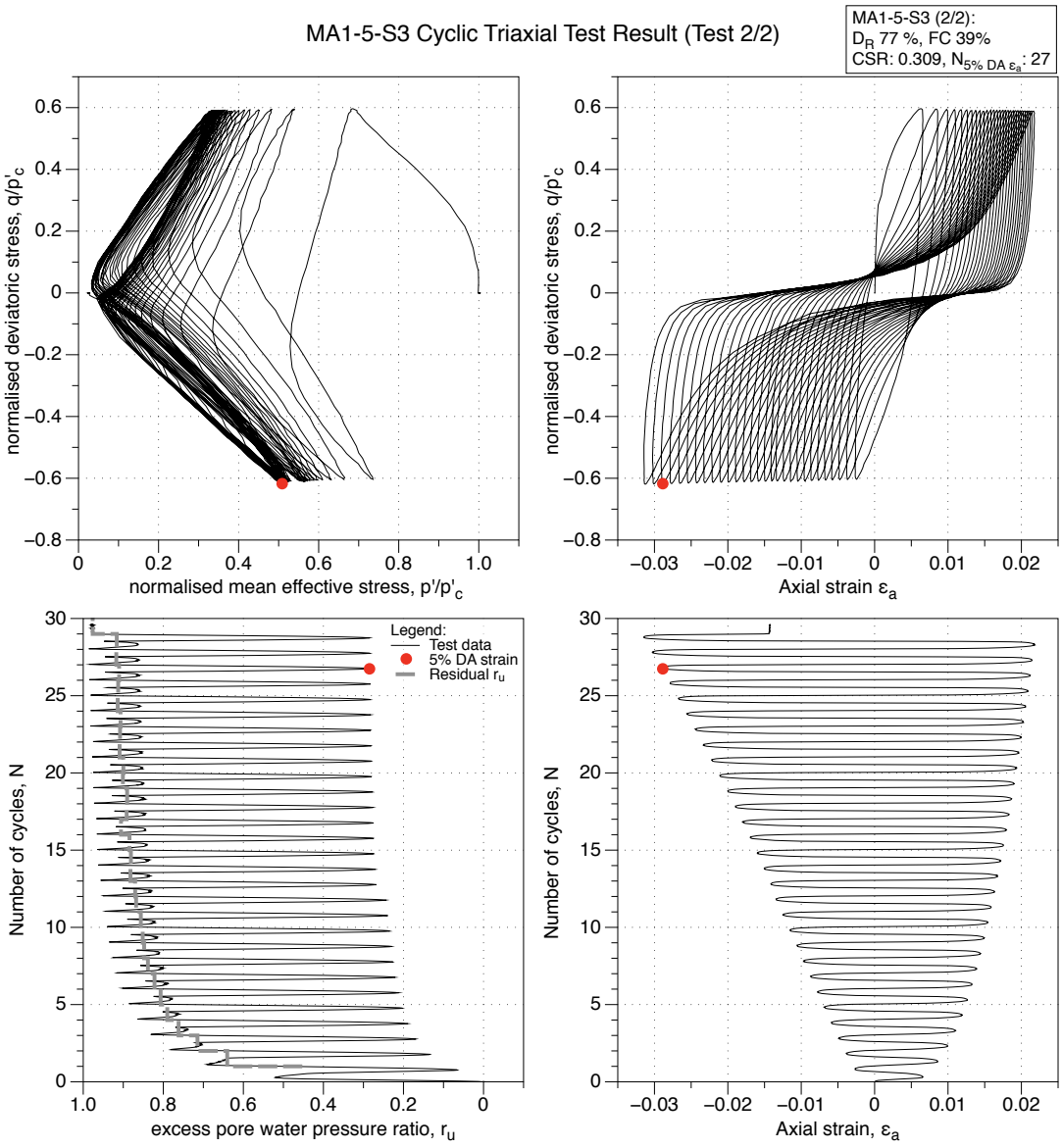

Figure 4.185: MA1-5-S3 GP sample, reliquefaction undrained cyclic triaxial test (CTX). Effective stress-path, stress-strain, excess pore water pressure ratio and strain development plots.

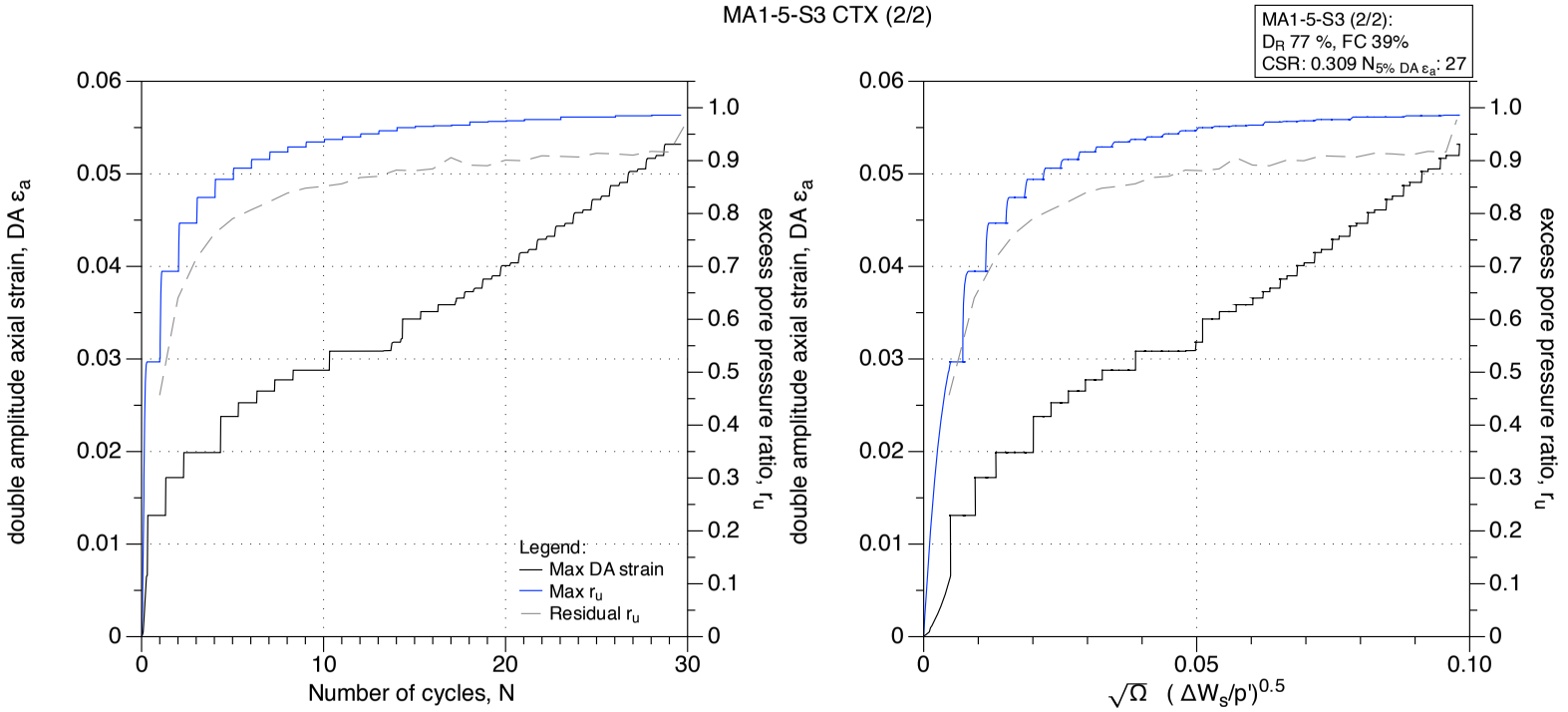

Figure 4.186: MA1-5-S3 GP sample, reliquefaction undrained cyclic triaxial test (CTX). Development of strain and excess pore water pressure with number of cycles and normalised shear work.

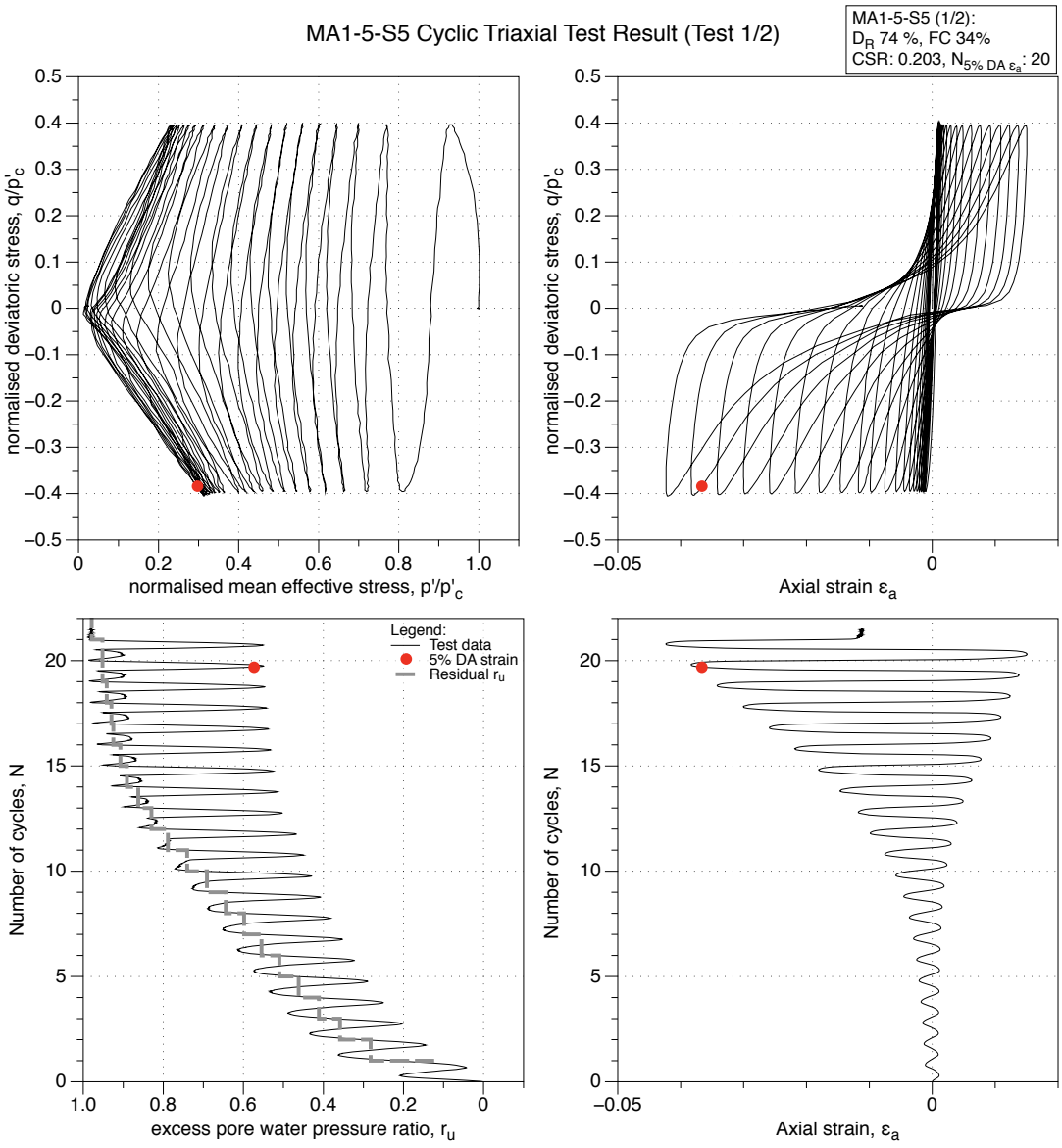

Figure 4.187: MA1-5-S5 GP sample, undrained cyclic triaxial test (CTX). Effective stress-path, stress-strain, excess pore water pressure ratio and strain development plots.

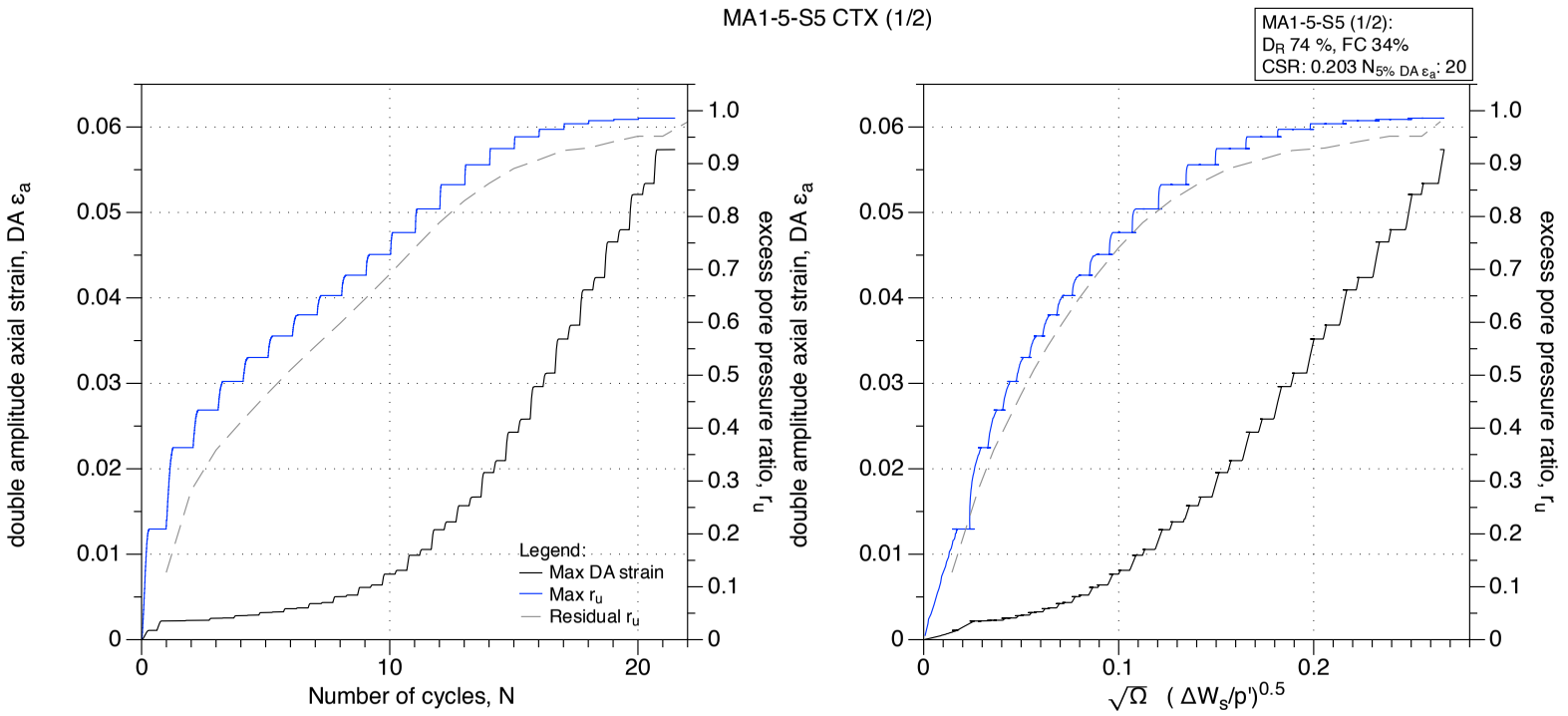

Figure 4.188: MA1-5-S5 GP sample, undrained cyclic triaxial test (CTX). Development of strain and excess pore water pressure with number of cycles and normalised shear work.

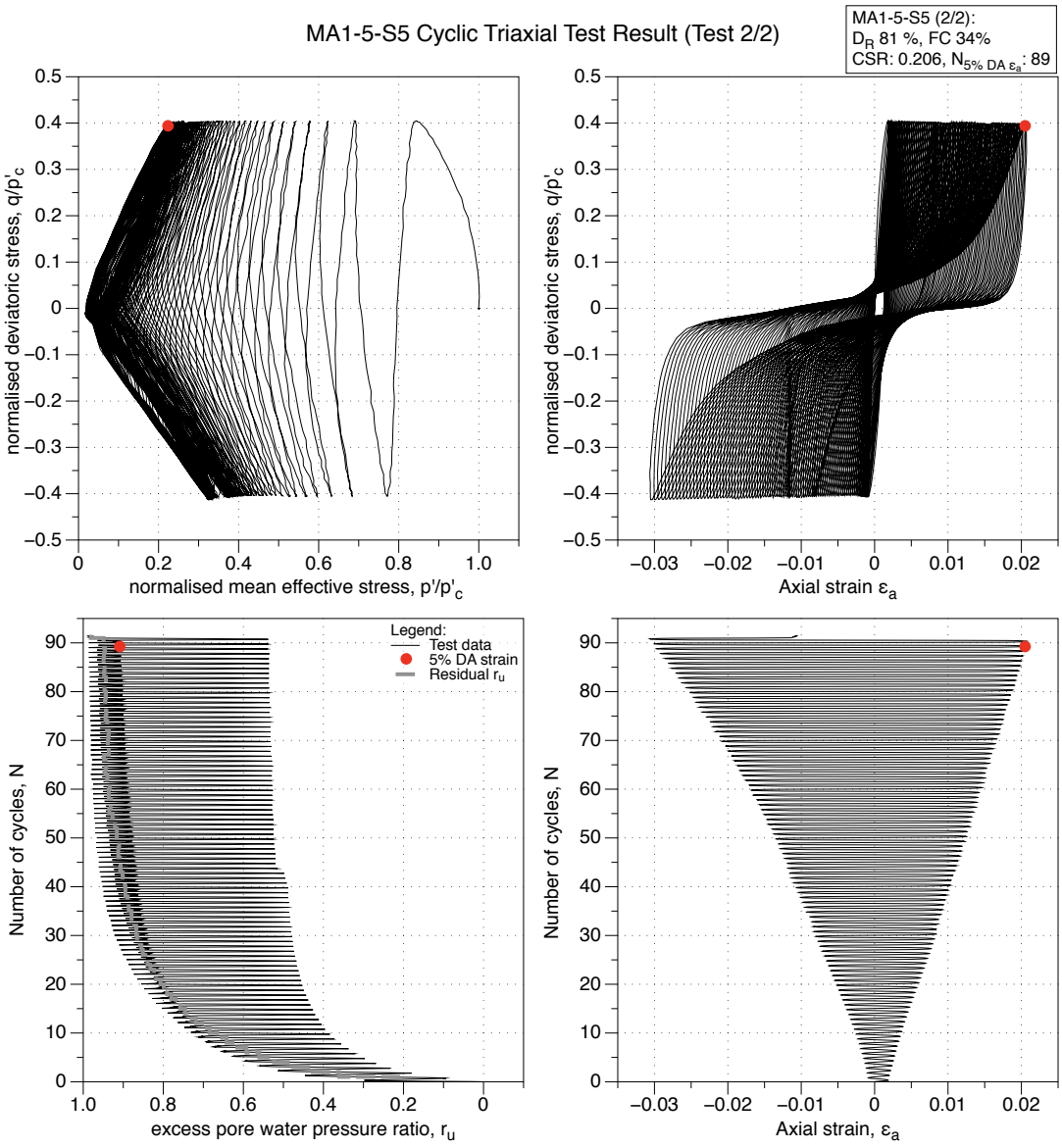

Figure 4.189: MA1-5-S5 GP sample, reliquefaction undrained cyclic triaxial test (CTX). Effective stress-path, stress-strain, excess pore water pressure ratio and strain development plots.

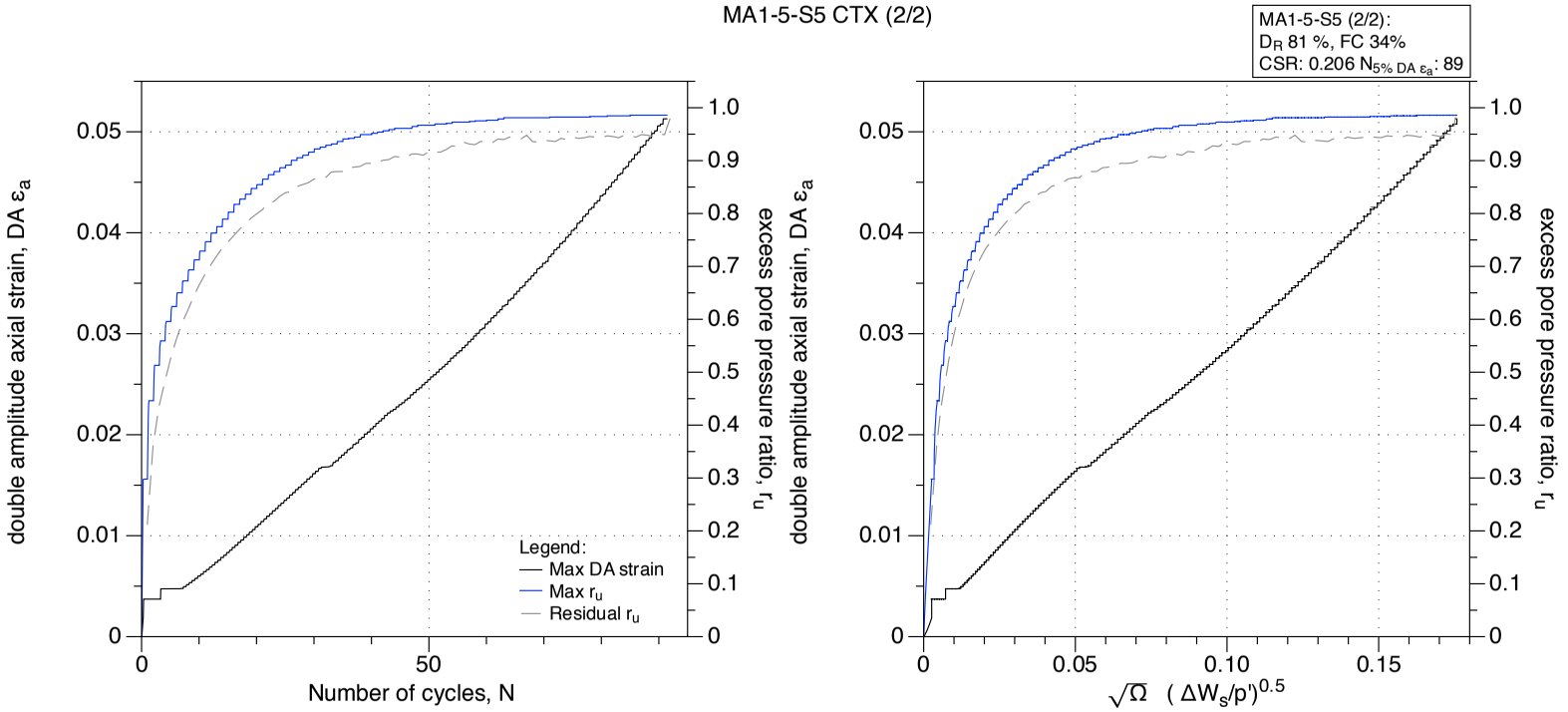

Figure 4.190: MA1-5-S5 GP sample, reliquefaction undrained cyclic triaxial test (CTX). Development of strain and excess pore water pressure with number of cycles and normalised shear work.

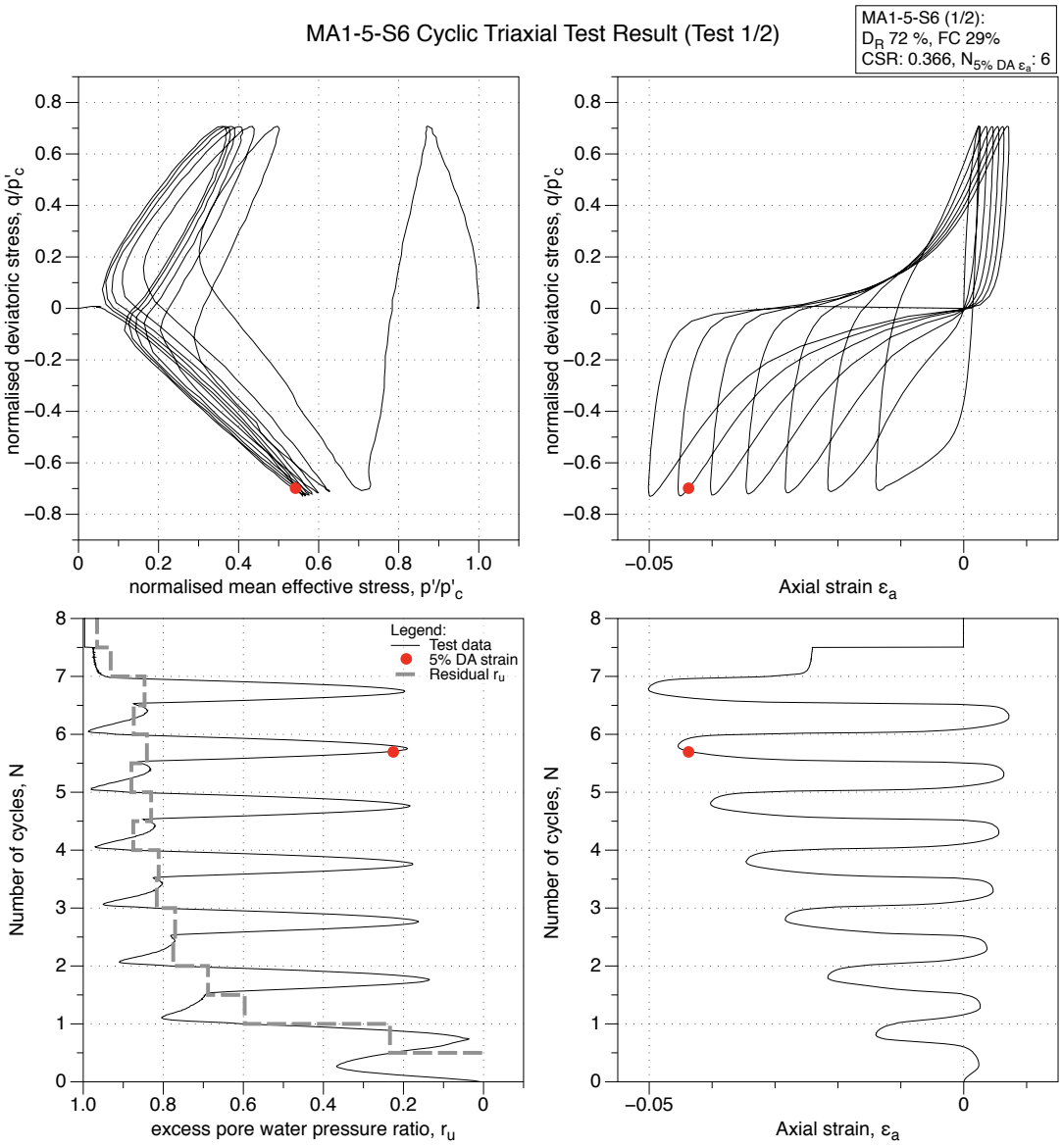

Figure 4.191: MA1-5-S6 GP sample, undrained cyclic triaxial test (CTX). Effective stress-path, stress-strain, excess pore water pressure ratio and strain development plots.

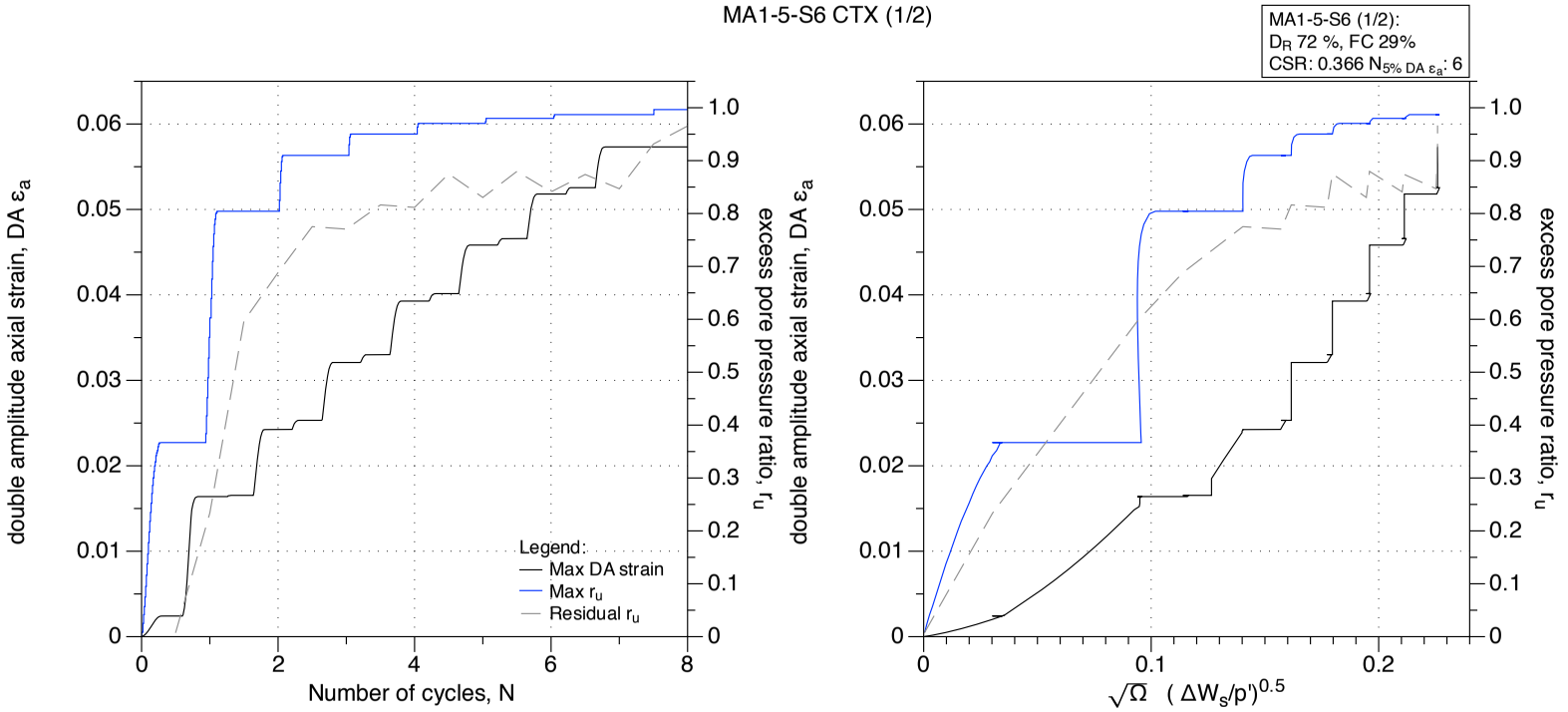

Figure 4.192: MA1-5-S6 GP sample, undrained cyclic triaxial test (CTX). Development of strain and excess pore water pressure with number of cycles and normalised shear work.

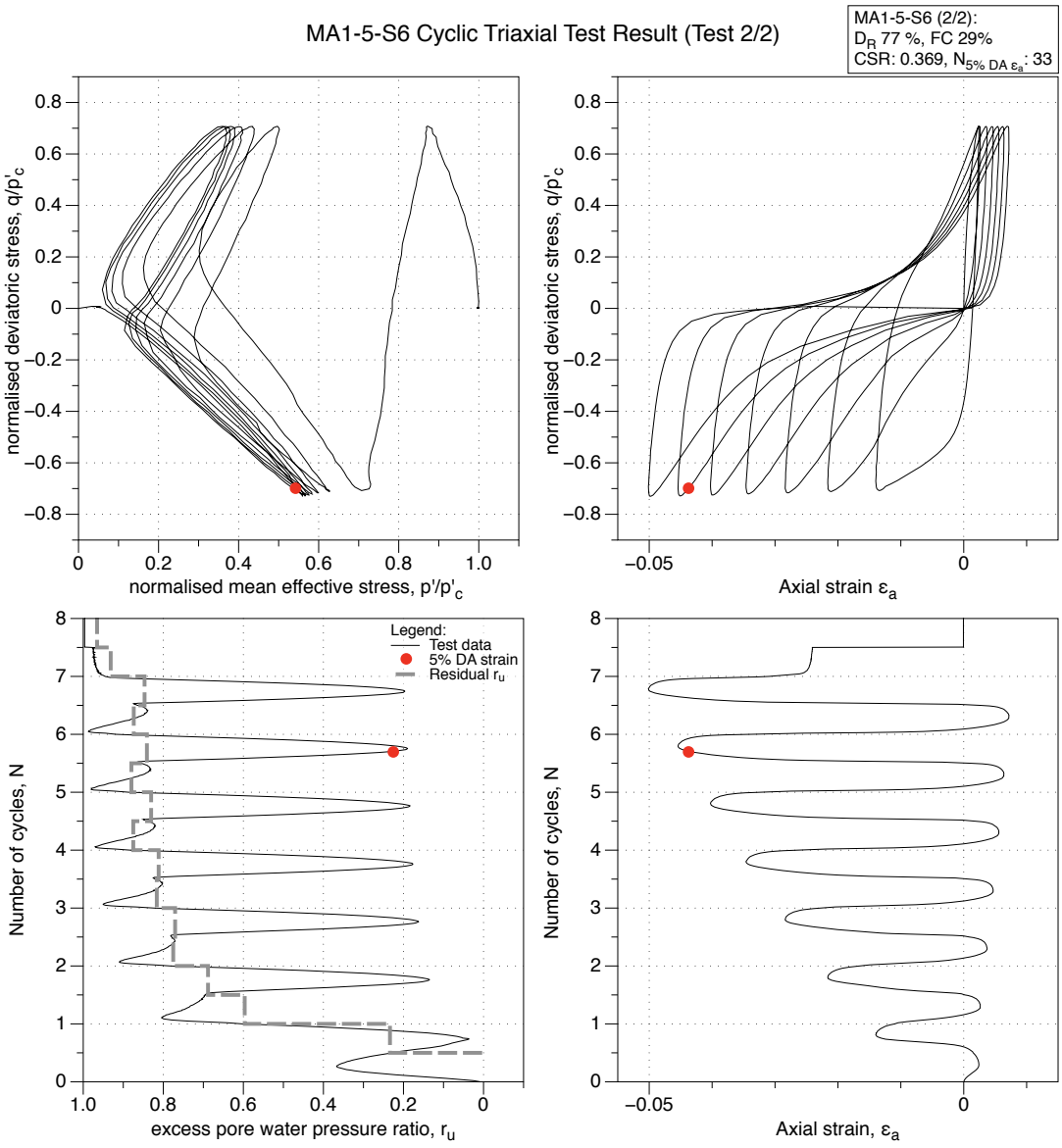

Figure 4.193: MA1-5-S6 GP sample, reliquefaction undrained cyclic triaxial test (CTX). Effective stress-path, stress-strain, excess pore water pressure ratio and strain development plots.

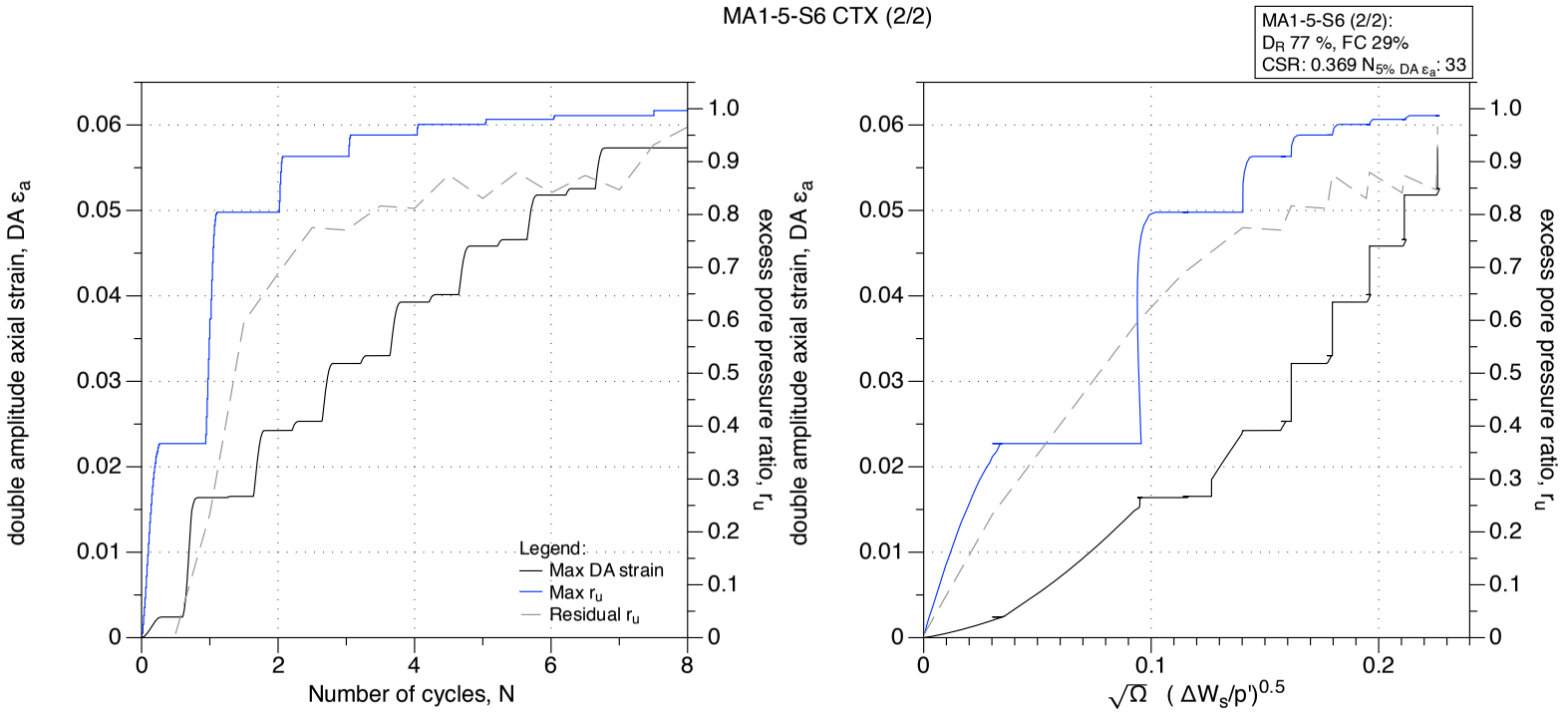

Figure 4.194: MA1-5-S6 GP sample, reliquefaction undrained cyclic triaxial test (CTX). Development of strain and excess pore water pressure with number of cycles and normalised shear work.

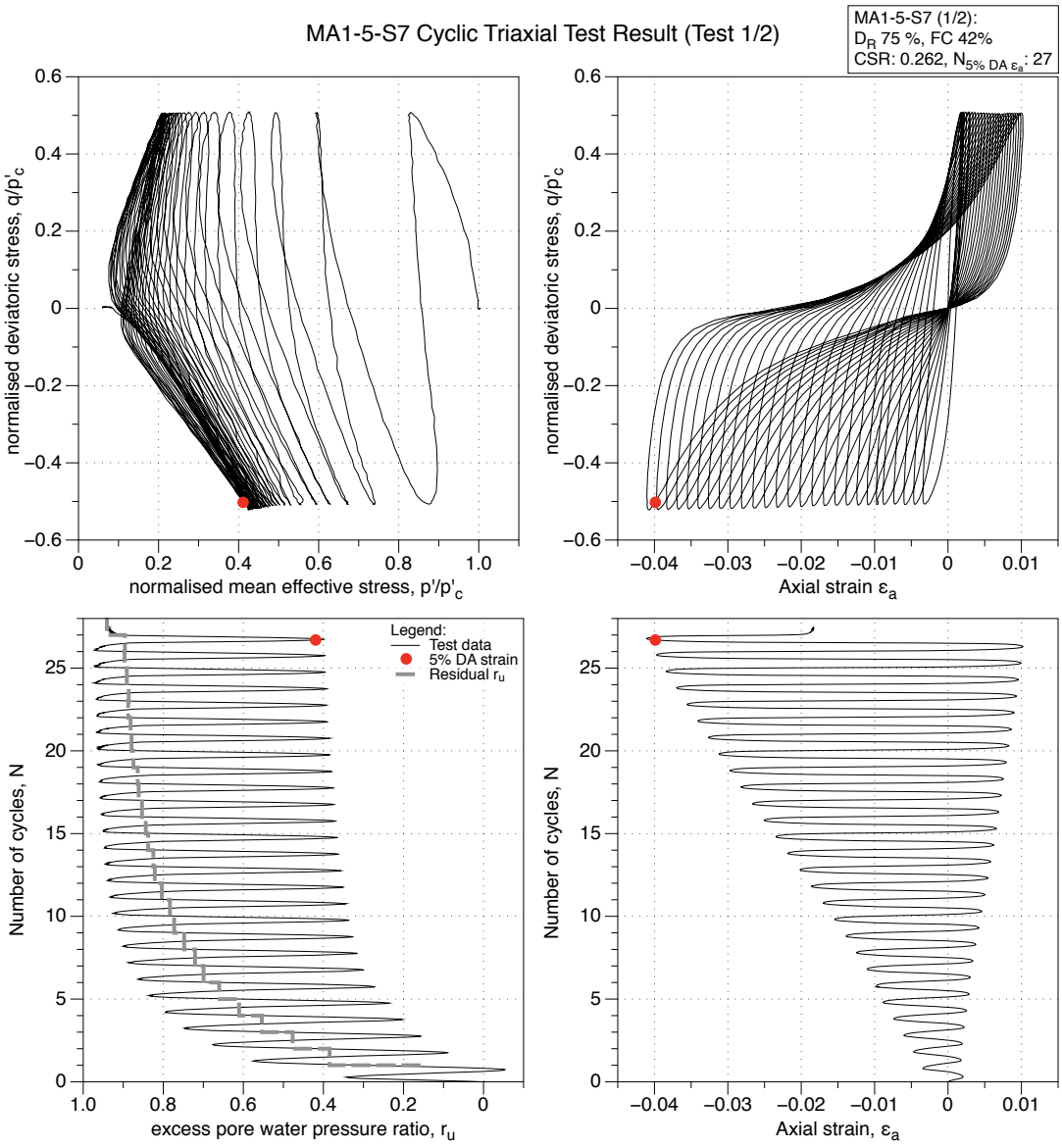

Figure 4.195: MA1-5-S7 GP sample, undrained cyclic triaxial test (CTX). Effective stress-path, stress-strain, excess pore water pressure ratio and strain development plots.

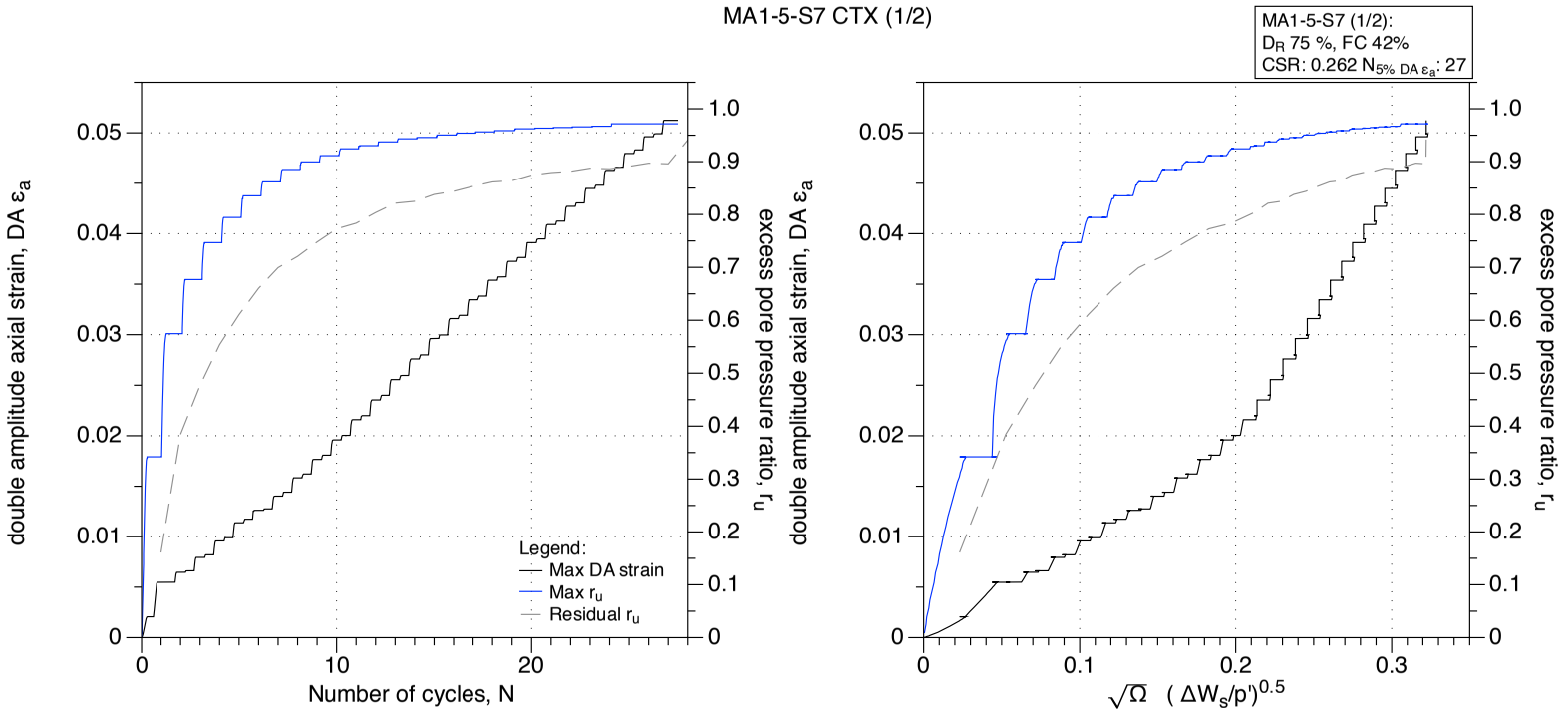

Figure 4.196: MA1-5-S7 GP sample, undrained cyclic triaxial test (CTX). Development of strain and excess pore water pressure with number of cycles and normalised shear work.

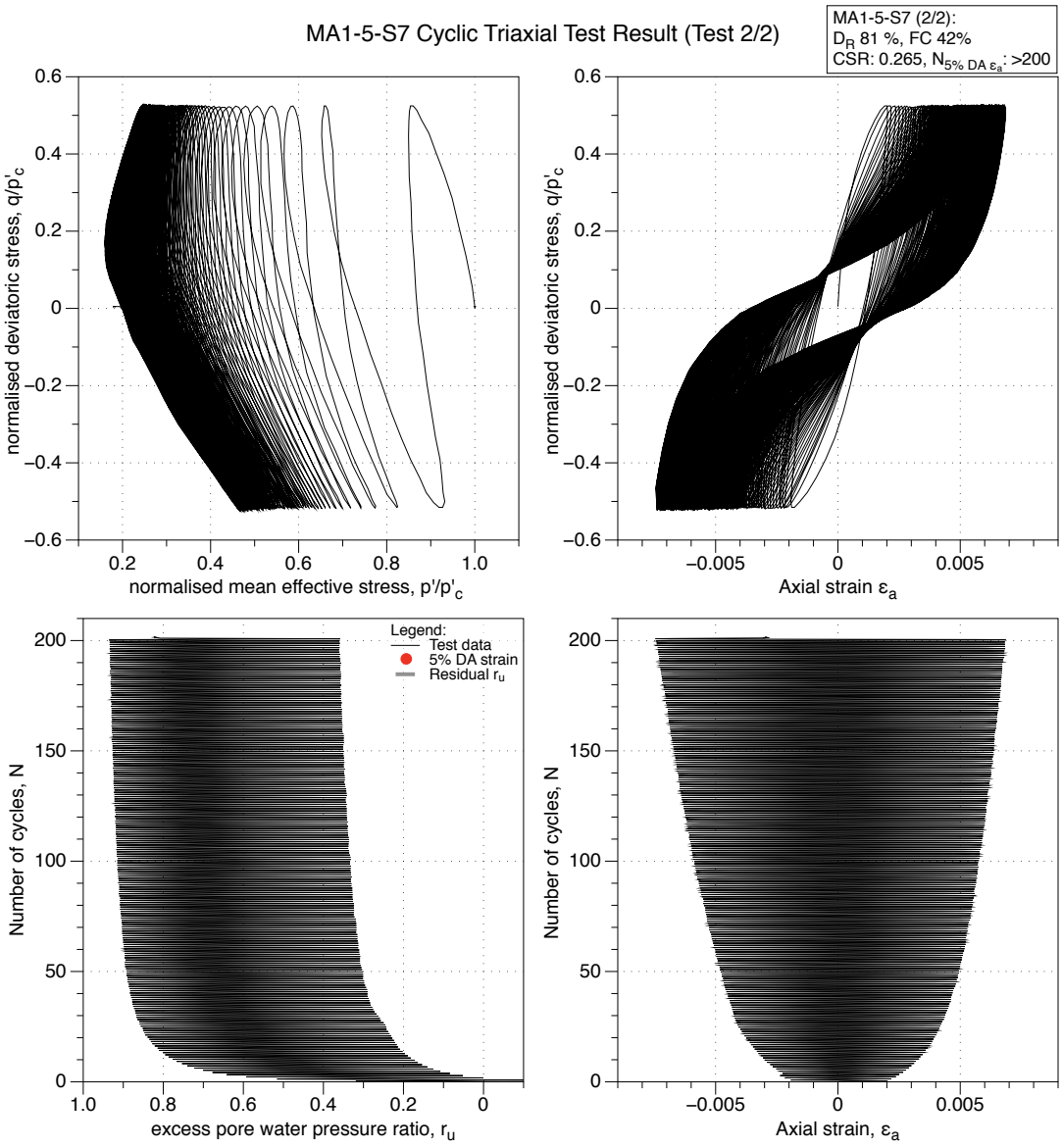

Figure 4.197: MA1-5-S7 GP sample, reliquefaction undrained cyclic triaxial test (CTX). Effective stress-path, stress-strain, excess pore water pressure ratio and strain development plots.

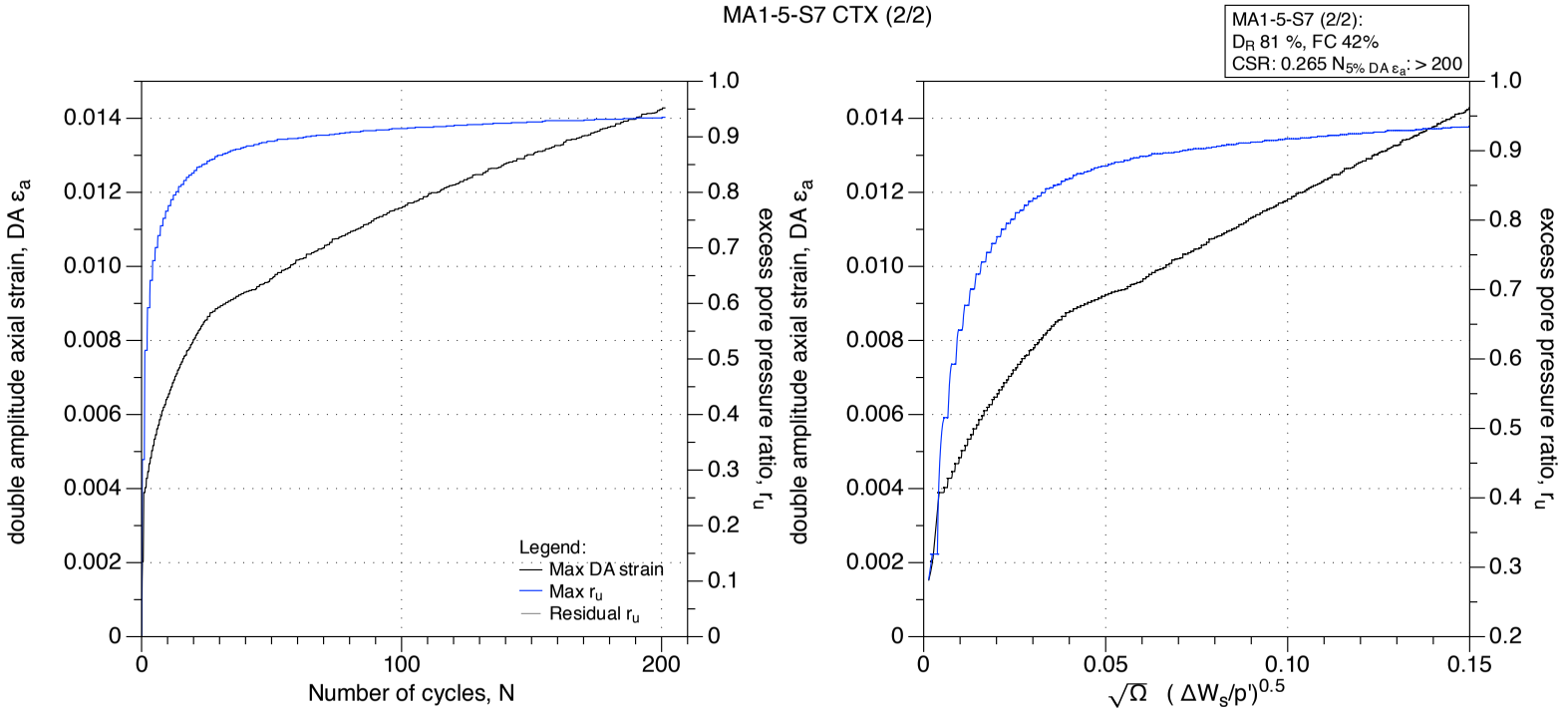

Figure 4.198: MA1-5-S7 GP sample, reliquefaction undrained cyclic triaxial test (CTX). Development of strain and excess pore water pressure with number of cycles and normalised shear work.

4.4 Triaxial testing on Reconstituted Tests of samples of 'typical' soils from borehole K1.

This section of Appendix D presents individual triaxial test results performed on moist-tamped (MT) reconstituted specimens of typical soils obtained from Borehole K1.

4.4.1 K1 MT Monotonic Triaxial Tests

Plots include the effective stress path, stress strain plot, state stress path, and volumetric strain-axial strain (drained test) or excess pore pressure ratio-axial strain (undrained test) plots. Additional plots for each monotonic test include stress-dilatancy plots, stiffness degradation curves, normalised shear work, and normalised shear work gradient plots with strain.

4.4.1.1 CID Tests on samples (FC 30 - 50 %)

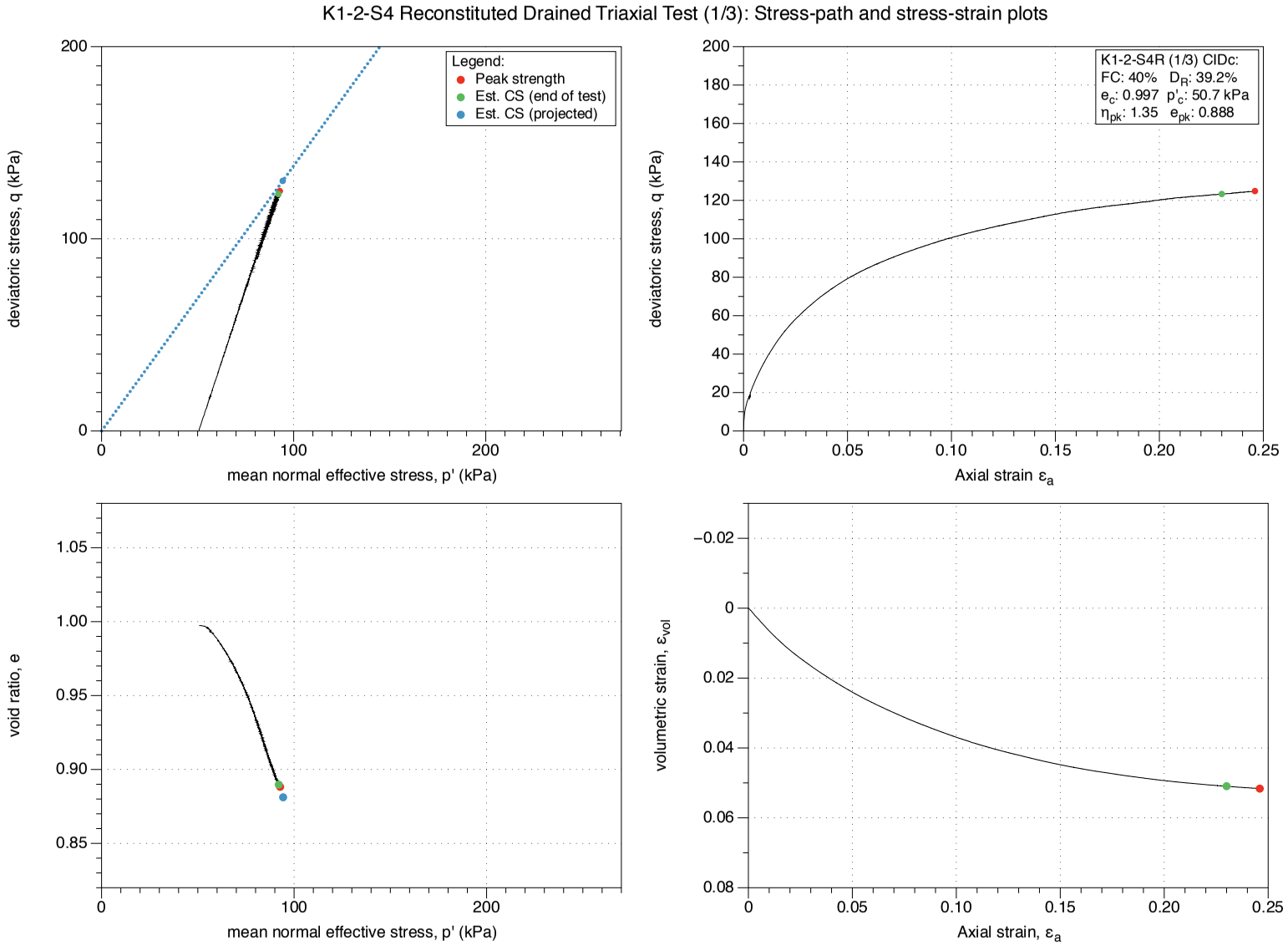

Figure 4.199: K1-2-S4 MT reconstituted sample (FC 40%), drained monotonic triaxial test (CID_C), test 1/3. Stress-path and stress-strain plots.

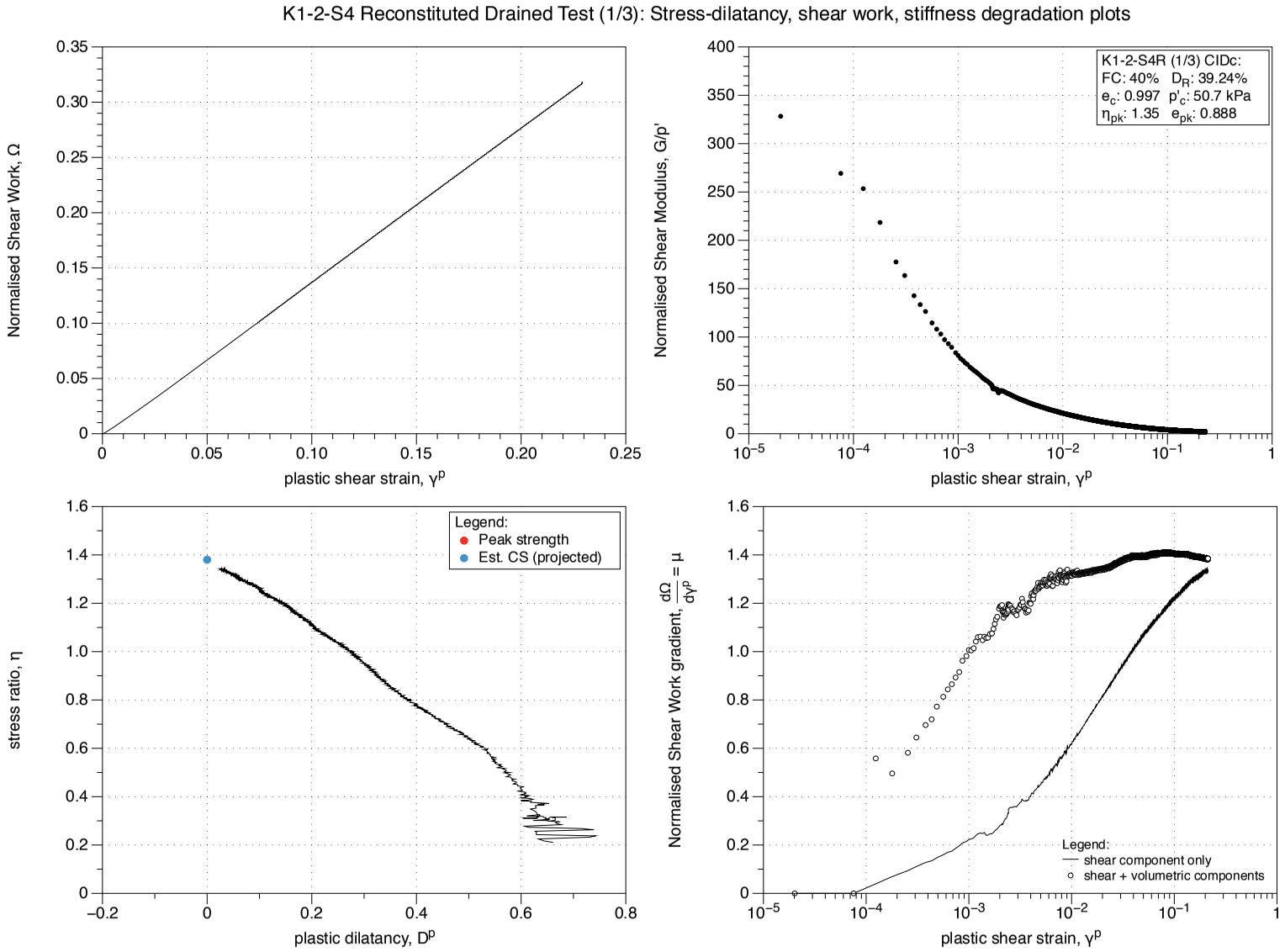

Figure 4.200: K1-2-S4 MT reconstituted sample (FC 40%), drained monotonic triaxial test (CID_C), test 1/3. Stress-dilatancy, shear work, stiffness degradation plots.

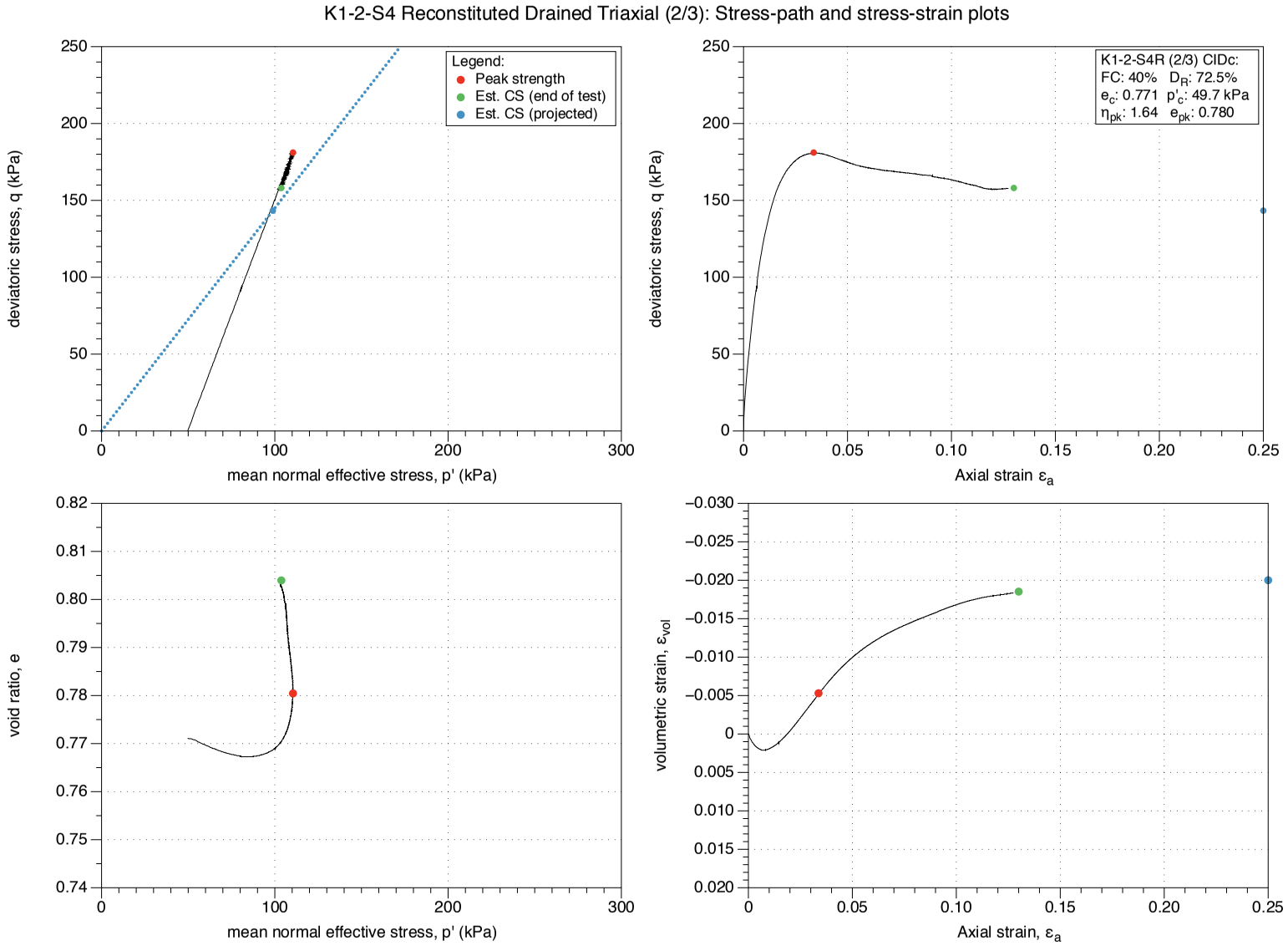

Figure 4.201: K1-2-S4 MT reconstituted sample (FC 40%), drained monotonic triaxial test (CID_C), test 2/3. Stress-path and stress-strain plots.

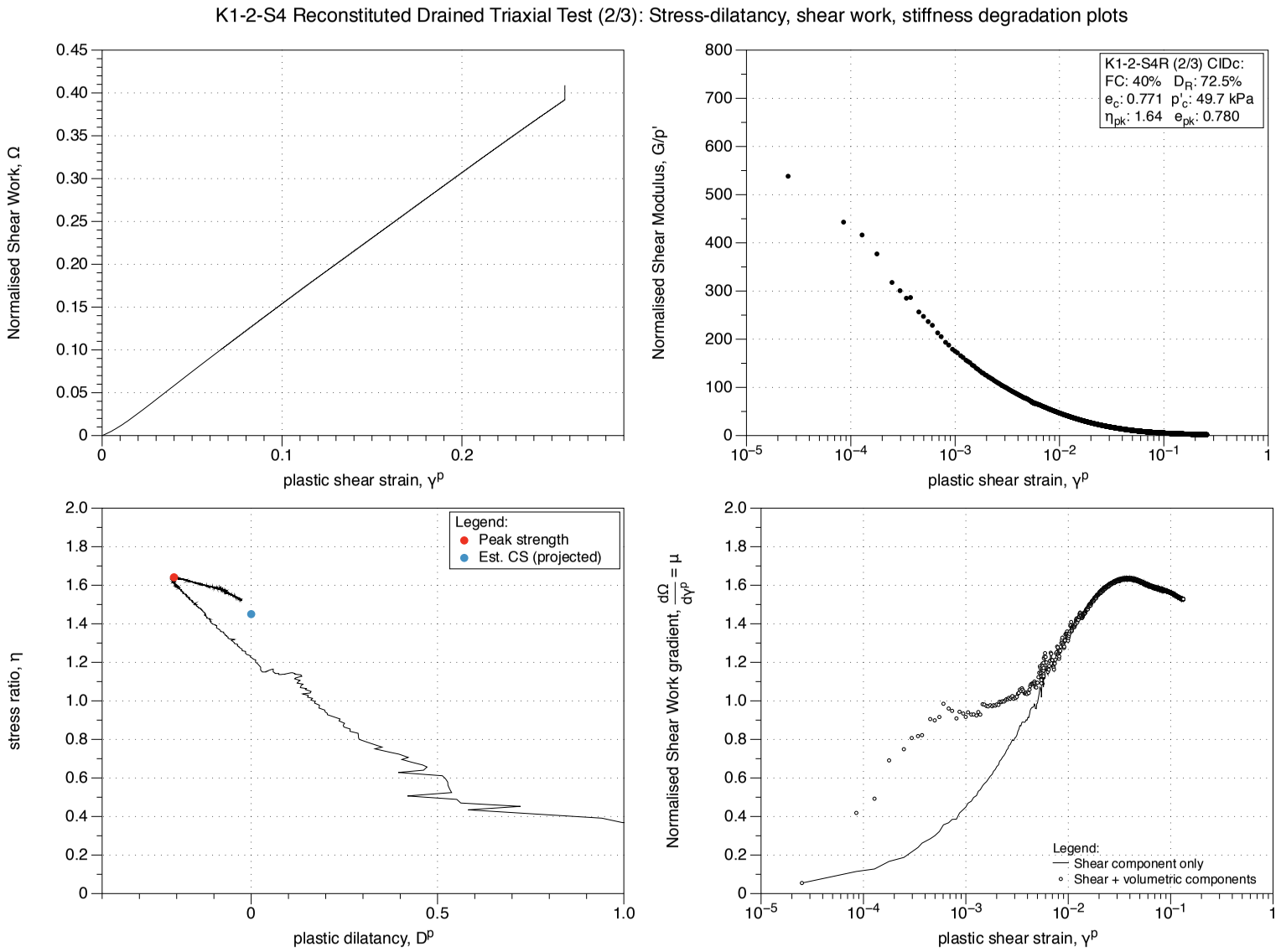

Figure 4.202: K1-2-S4 MT reconstituted sample (FC 40%), drained monotonic triaxial test (CID_C), test 2/3. Stress-dilatancy, shear work, stiffness degradation plots.

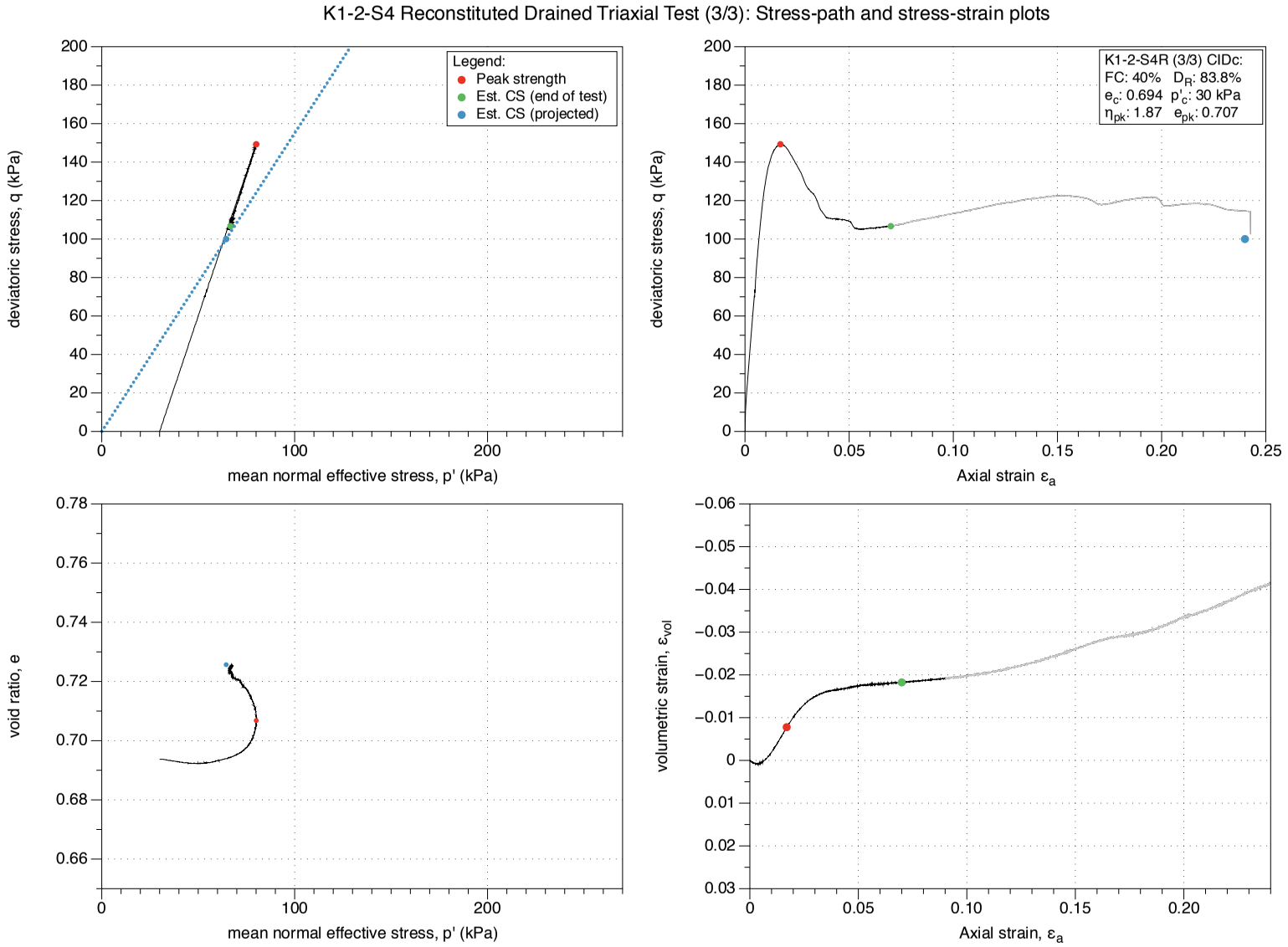

Figure 4.203: K1-2-S4 MT reconstituted sample (FC 40%), drained monotonic triaxial test (CID_C), test 3/3. Stress-path and stress-strain plots.

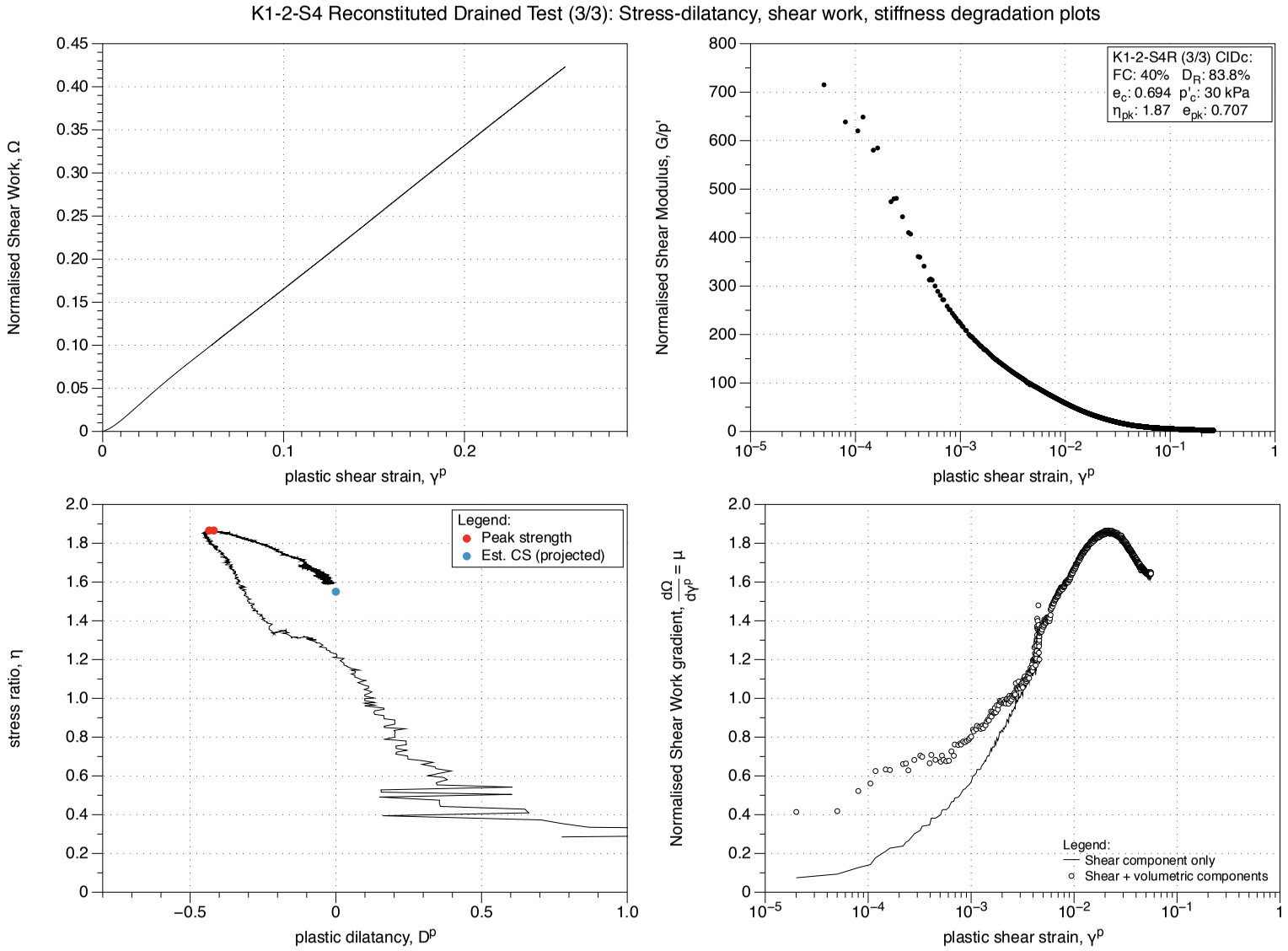

Figure 4.204: K1-2-S4 MT reconstituted sample (FC 40%), drained monotonic triaxial test (CID_C), test 3/3. Stress-dilatancy, shear work, stiffness degradation plots.

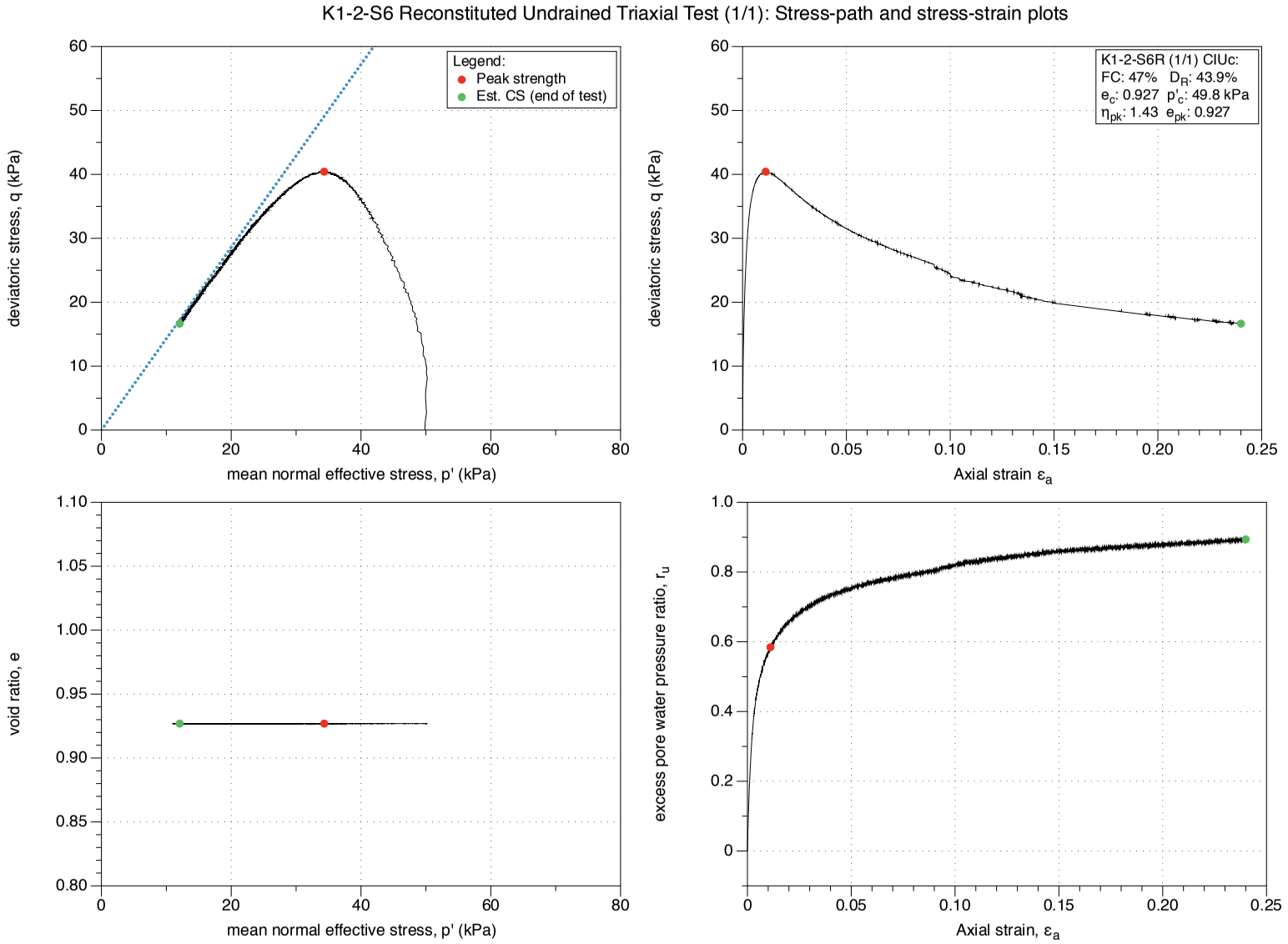

Figure 4.205: K1-2-S6 MT reconstituted sample (FC 47%), drained monotonic triaxial test (CIU_C), test 1/1. Stress-path and stress-strain plots.

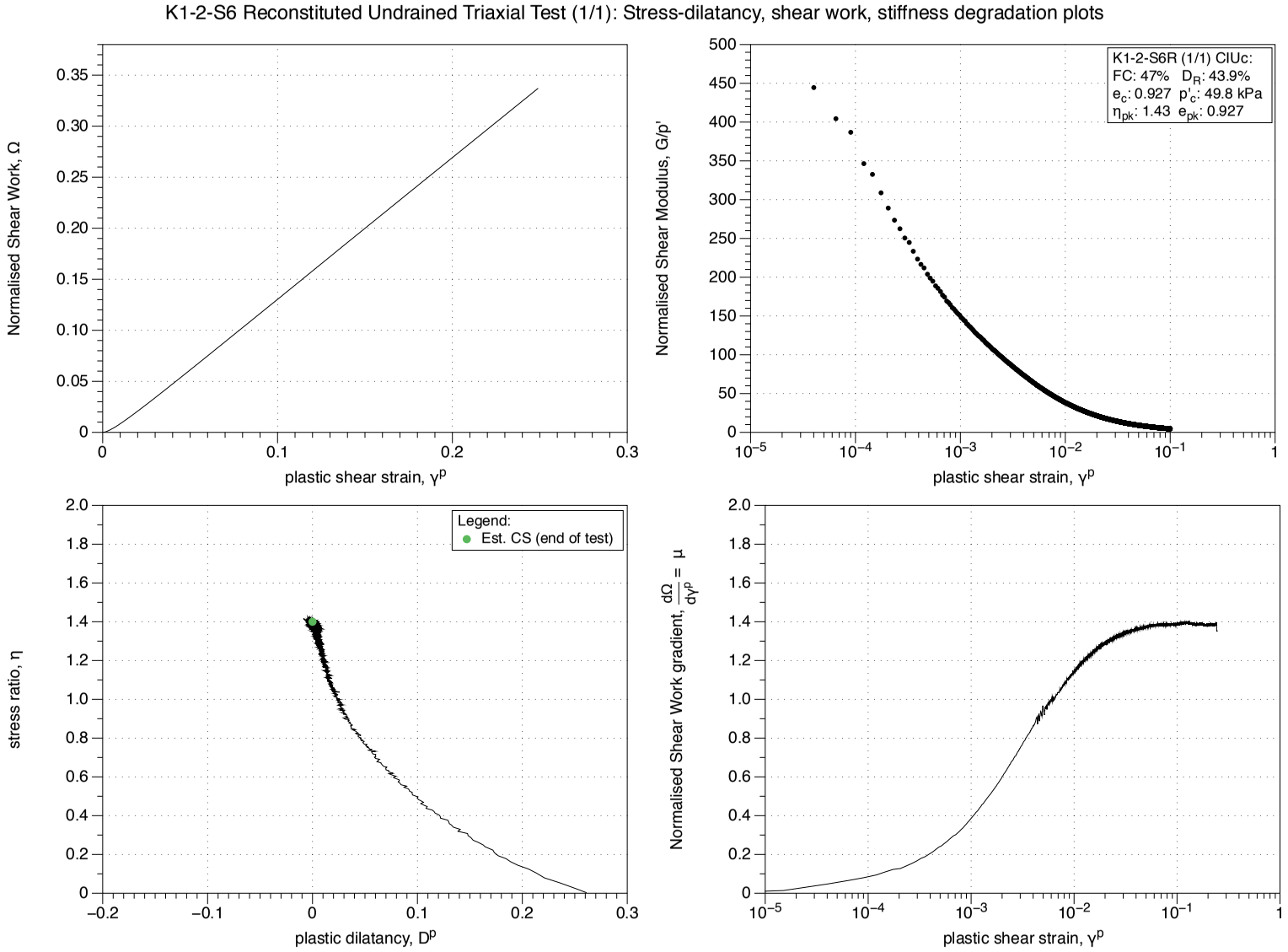

Figure 4.206: K1-2-S6 MT reconstituted sample (FC 47%), drained monotonic triaxial test (CIU_C), test 1/1. Stress-dilatancy, shear work, stiffness degradation plots.

4.4.1.2 CIU Tests on sample K1-2-S4 (FC 40 %)

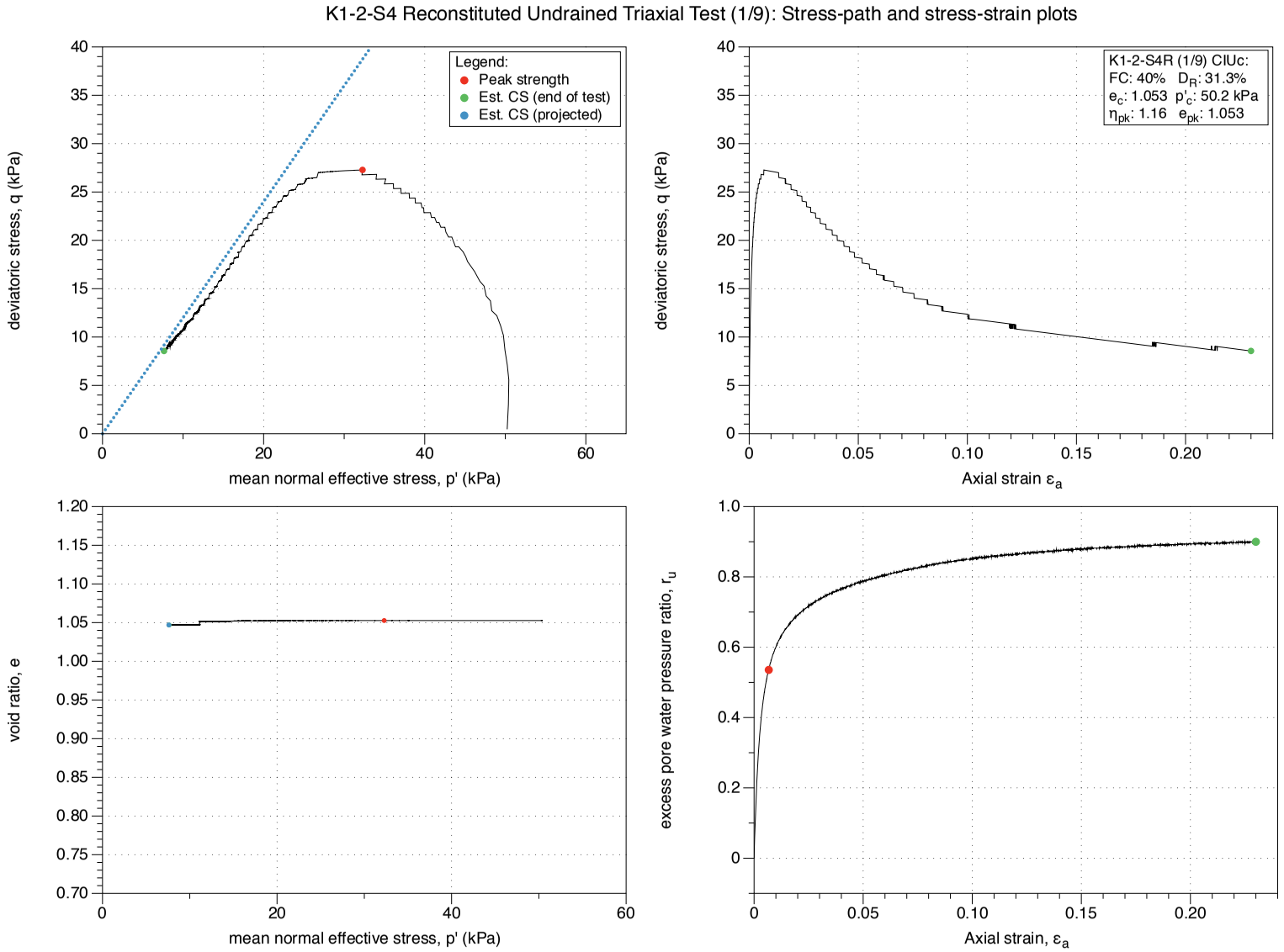

Figure 4.207: K1-2-S4 MT reconstituted sample (FC 40%), undrained monotonic triaxial test (CIU_C), test 1/9. Stress-path and stress-strain plots.

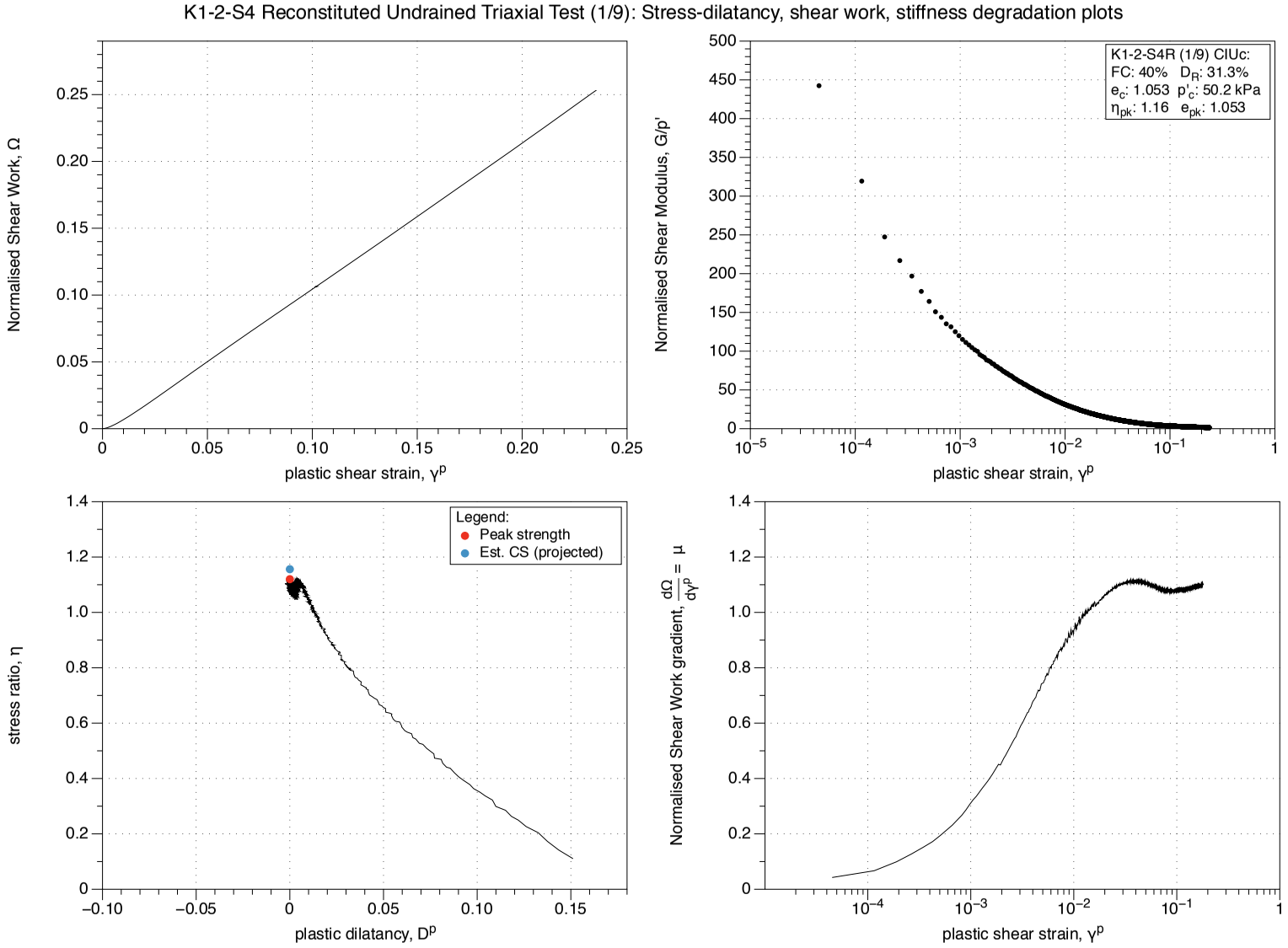

Figure 4.208: K1-2-S4 MT reconstituted sample (FC 40%), undrained monotonic triaxial test (CIU_C), test 1/9. Stress-dilatancy, shear work, stiffness degradation plots.

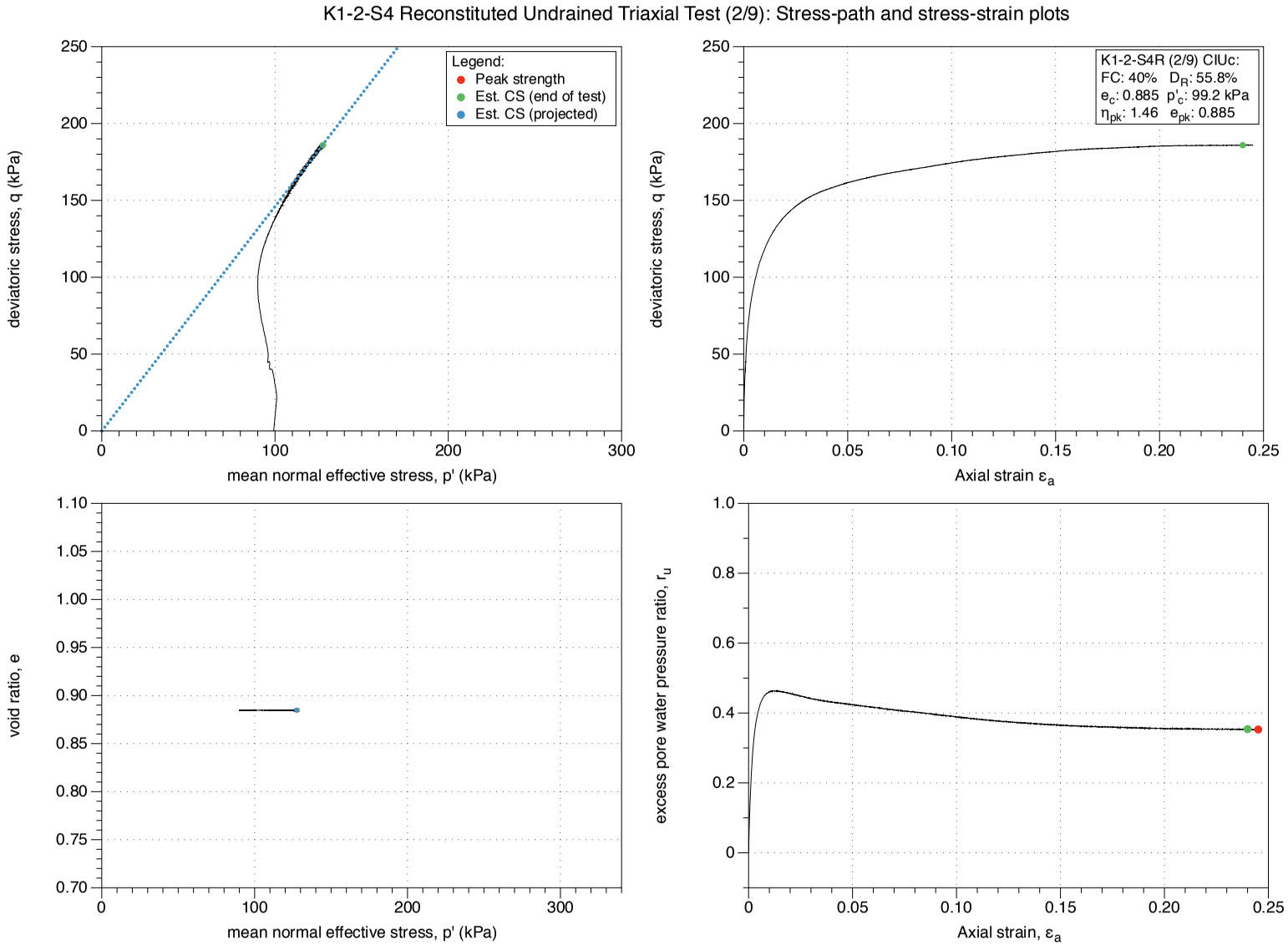

Figure 4.209: K1-2-S4 MT reconstituted sample (FC 40%), undrained monotonic triaxial test (CIU_C), test 2/9. Stress-path and stress-strain plots.

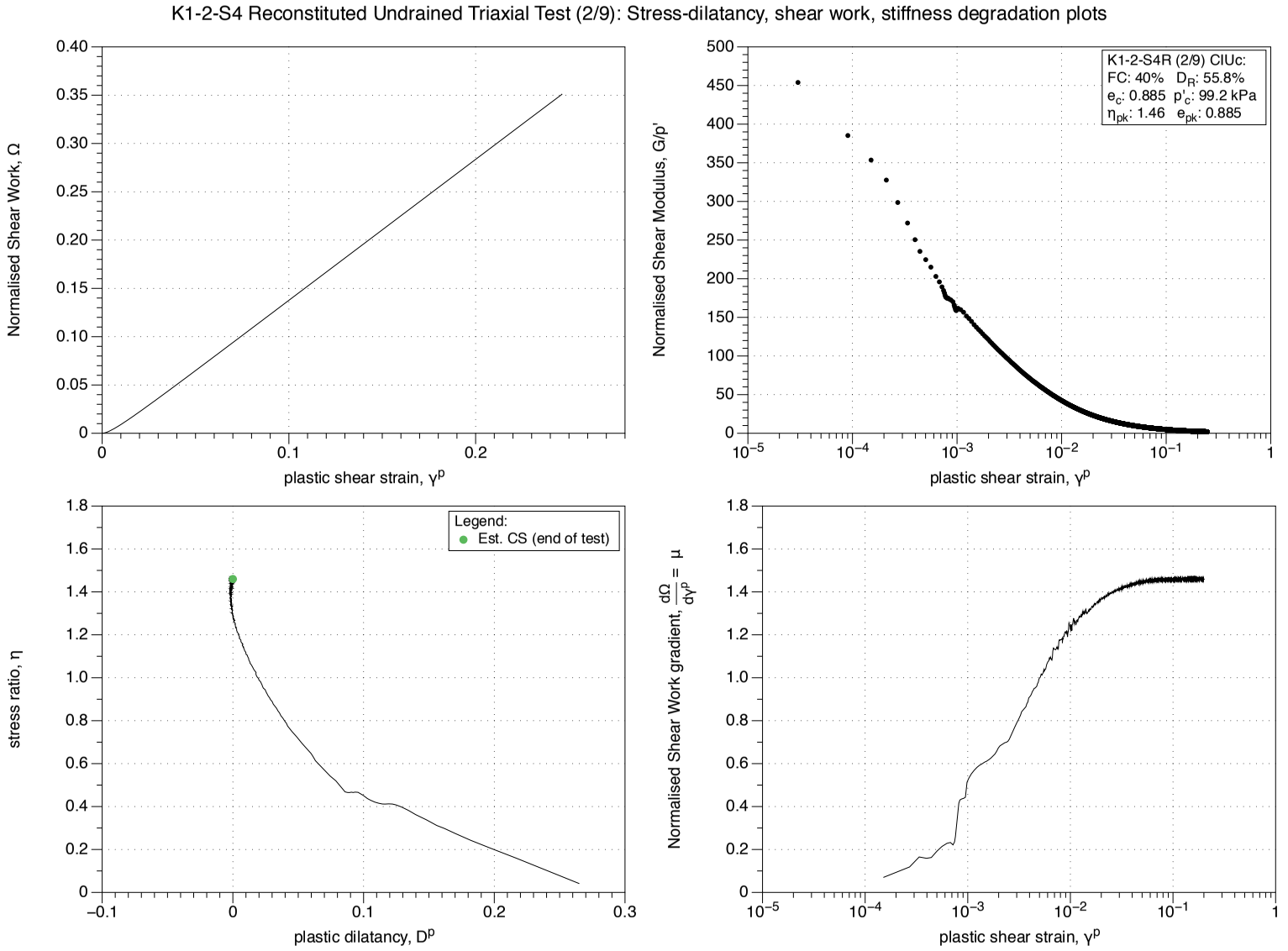

Figure 4.210: K1-2-S4 MT reconstituted sample (FC 40%), undrained monotonic triaxial test (CIU_C), test 2/9. Stress-dilatancy, shear work, stiffness degradation plots.

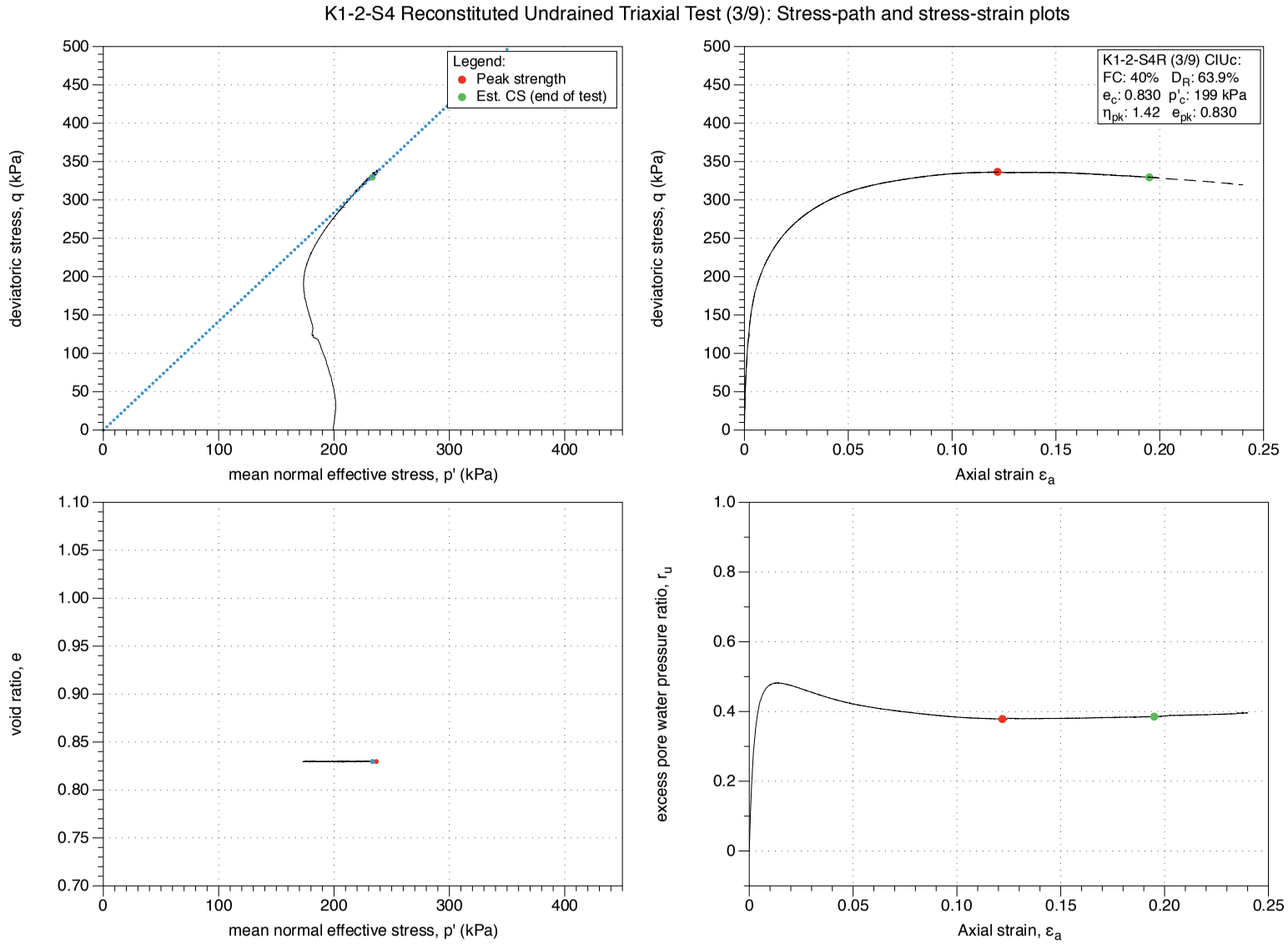

Figure 4.211: K1-2-S4 MT reconstituted sample, undrained monotonic triaxial test (CIU_C), test 3/9. Stress-path and stress-strain plots.

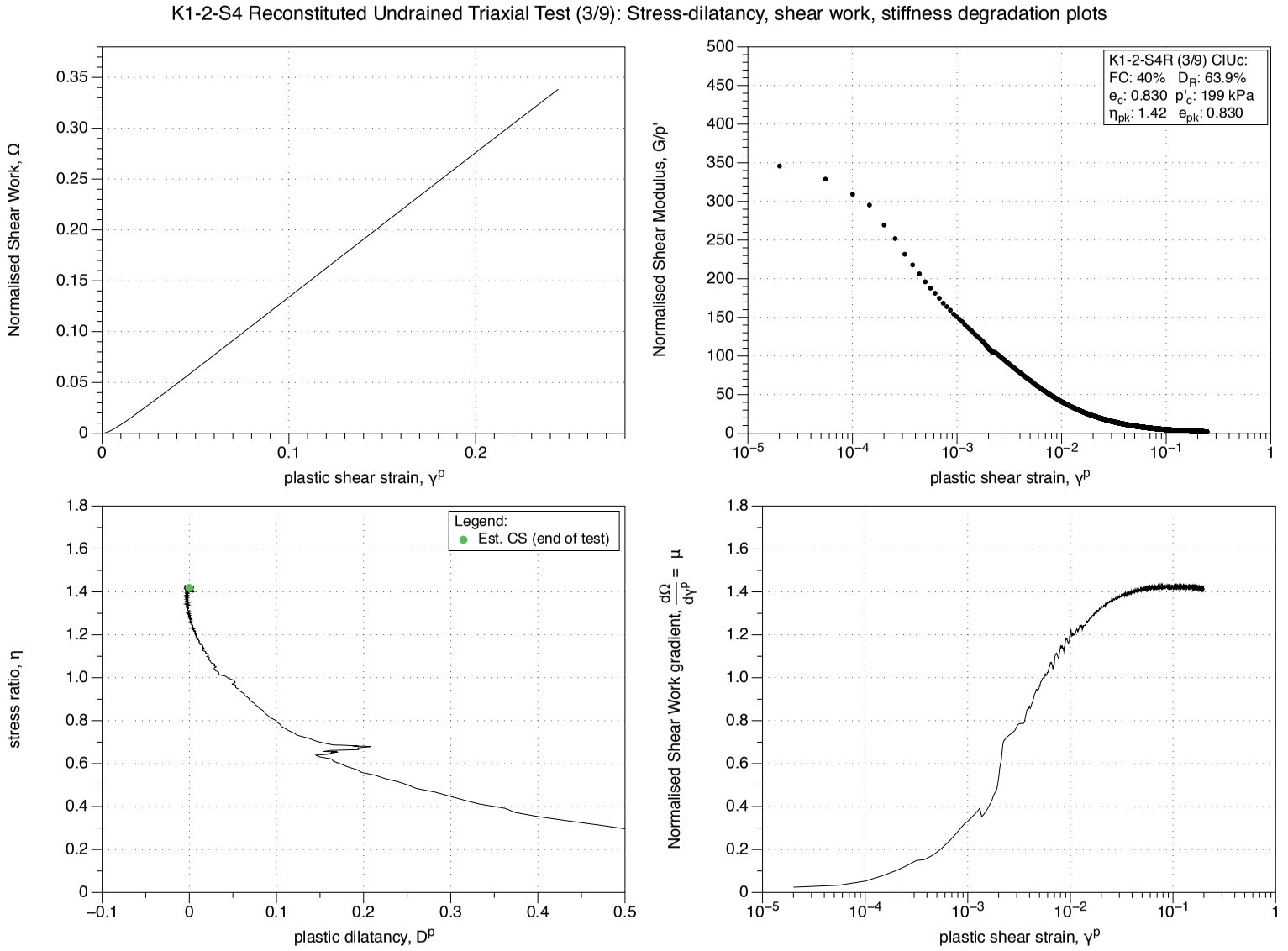

Figure 4.212: K1-2-S4 MT reconstituted sample (FC 40%), undrained monotonic triaxial test (CIU_C), test 3/9. Stress-dilatancy, shear work, stiffness degradation plots.

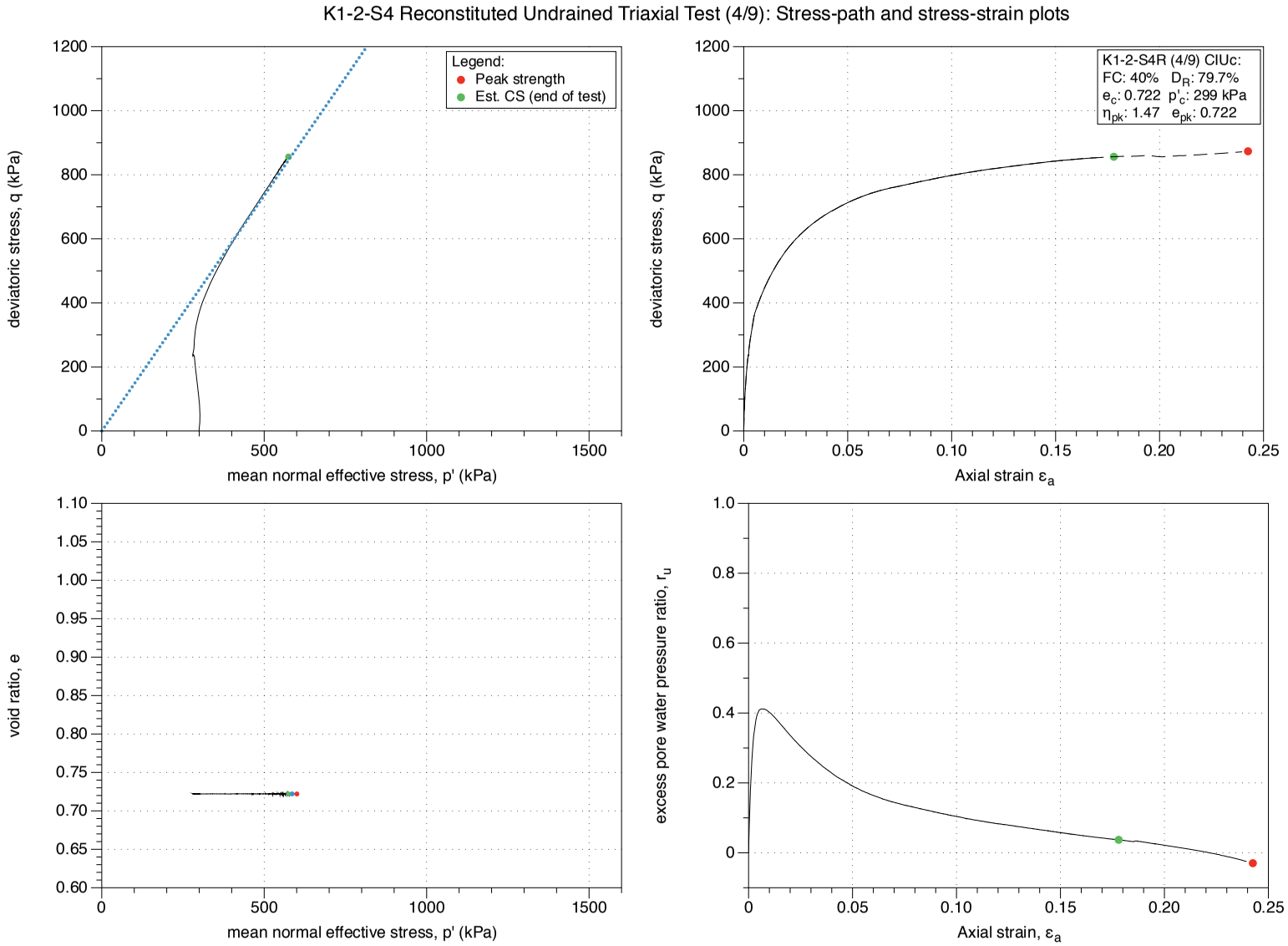

Figure 4.213: K1-2-S4 MT reconstituted sample (FC 40%), undrained monotonic triaxial test (CIU_C), test 4/9. Stress-path and stress-strain plots.

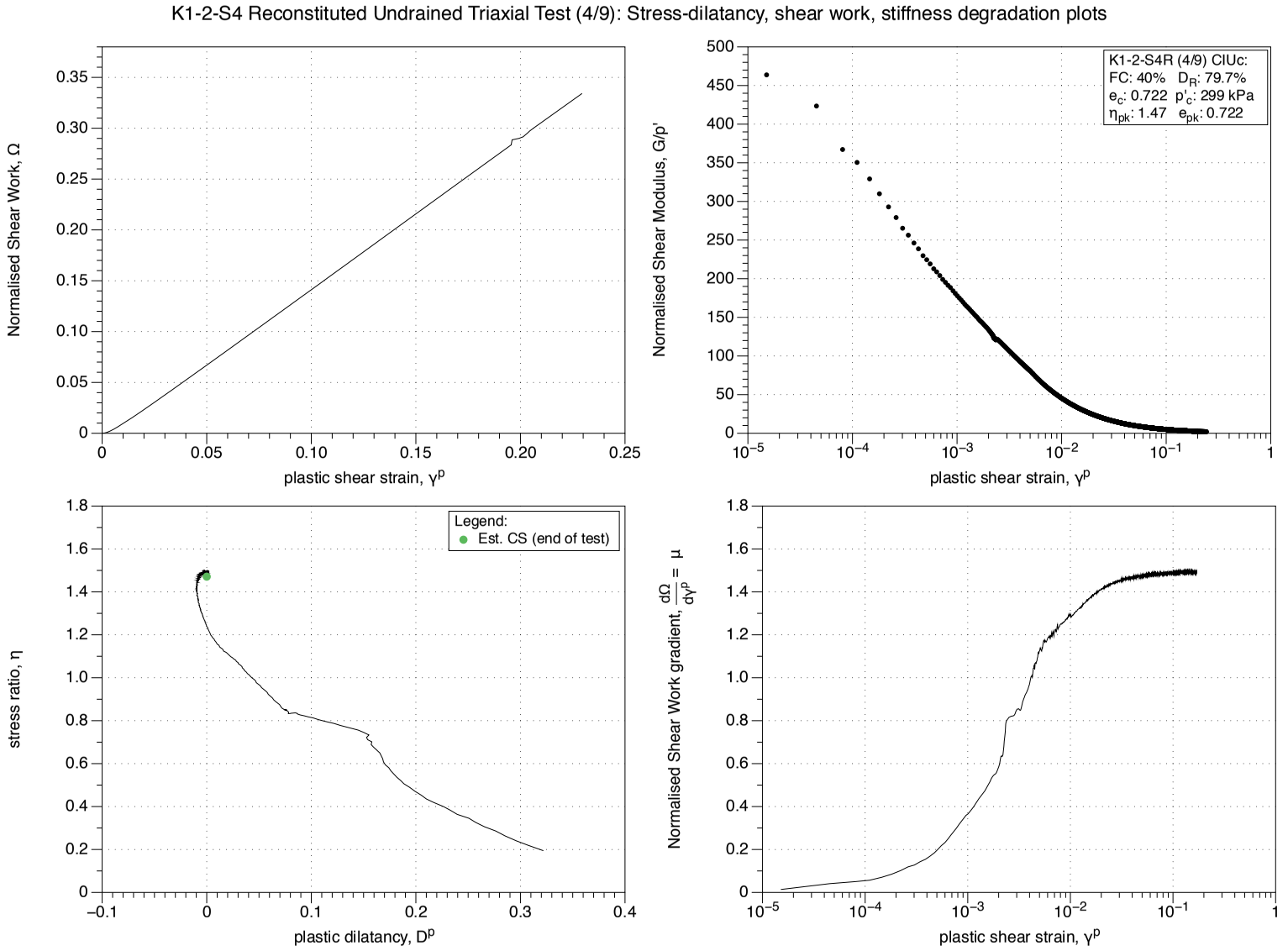

Figure 4.214: K1-2-S4 MT reconstituted sample (FC 40%), undrained monotonic triaxial test (CIU_C), test 4/9. Stress-dilatancy, shear work, stiffness degradation plots.

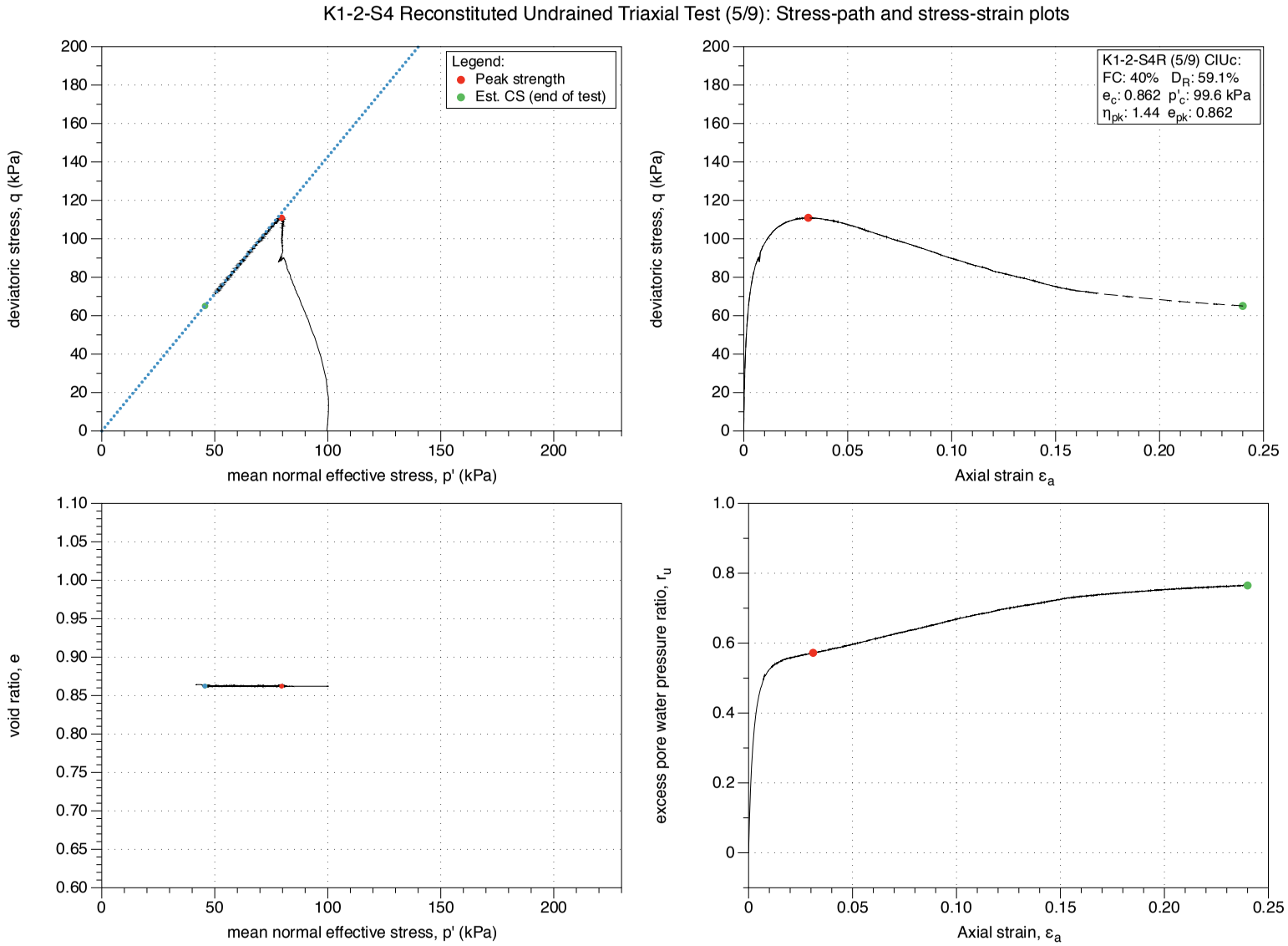

Figure 4.215: K1-2-S4 MT reconstituted sample (FC 40%), undrained monotonic triaxial test (CIU_C), test 5/9. Stress-path and stress-strain plots.

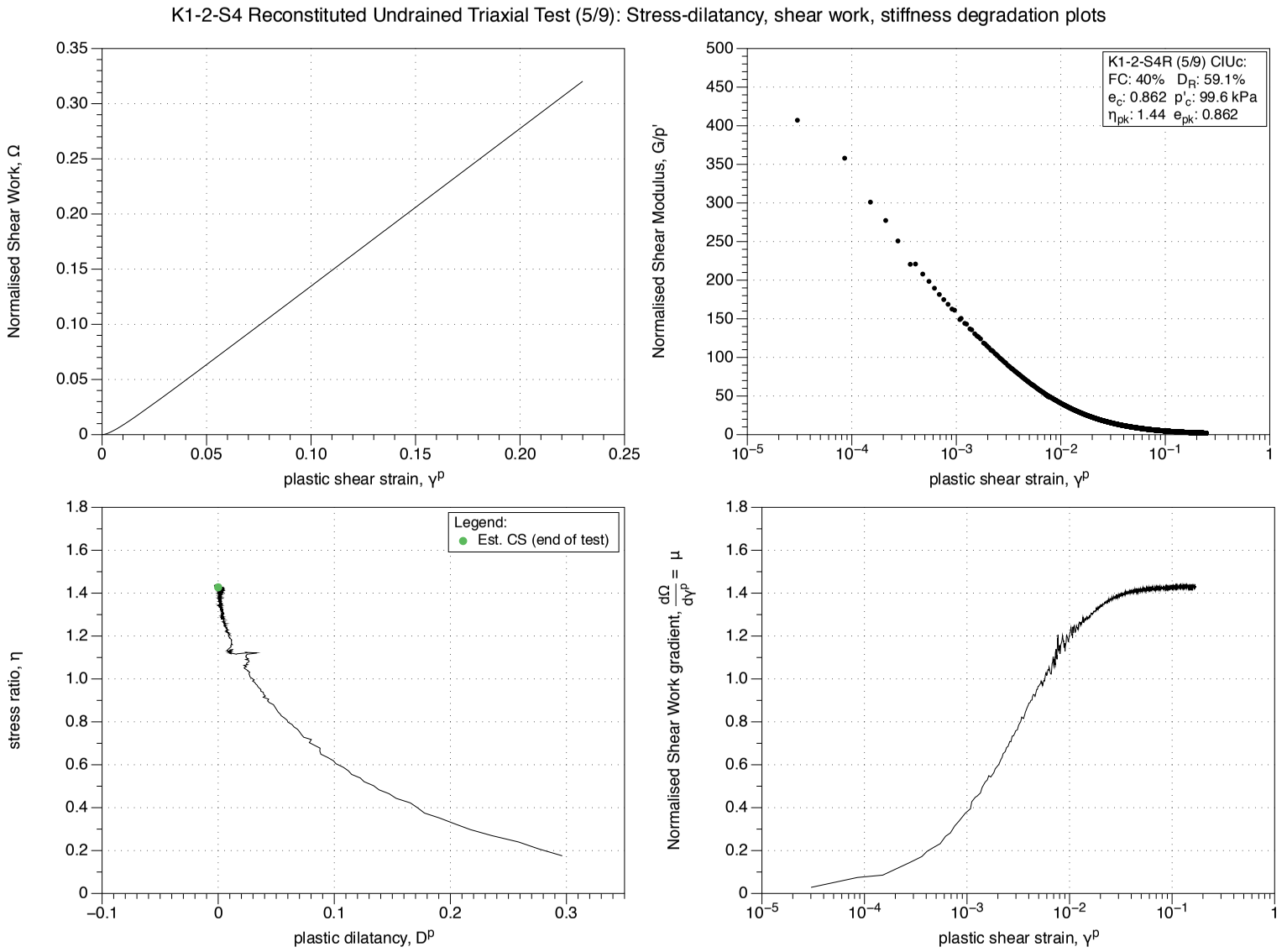

Figure 4.216: K1-2-S4 MT reconstituted sample (FC 40%), undrained monotonic triaxial test (CIU_C), test 5/9. Stress-dilatancy, shear work, stiffness degradation plots.

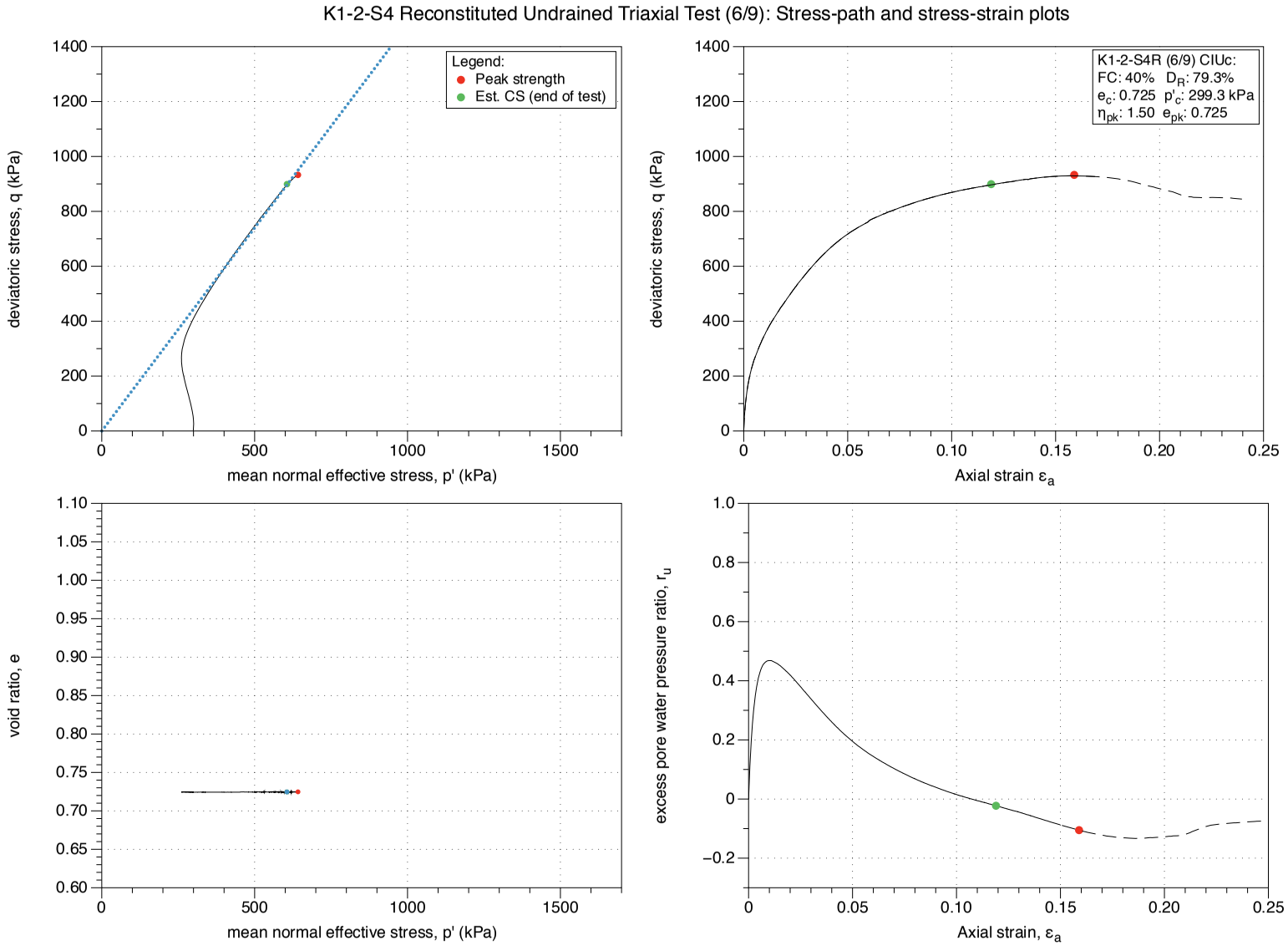

Figure 4.217: K1-2-S4 MT reconstituted sample (FC 40%), drained monotonic triaxial test (CIU_C), test 6/9. Stress-path and stress-strain plots.

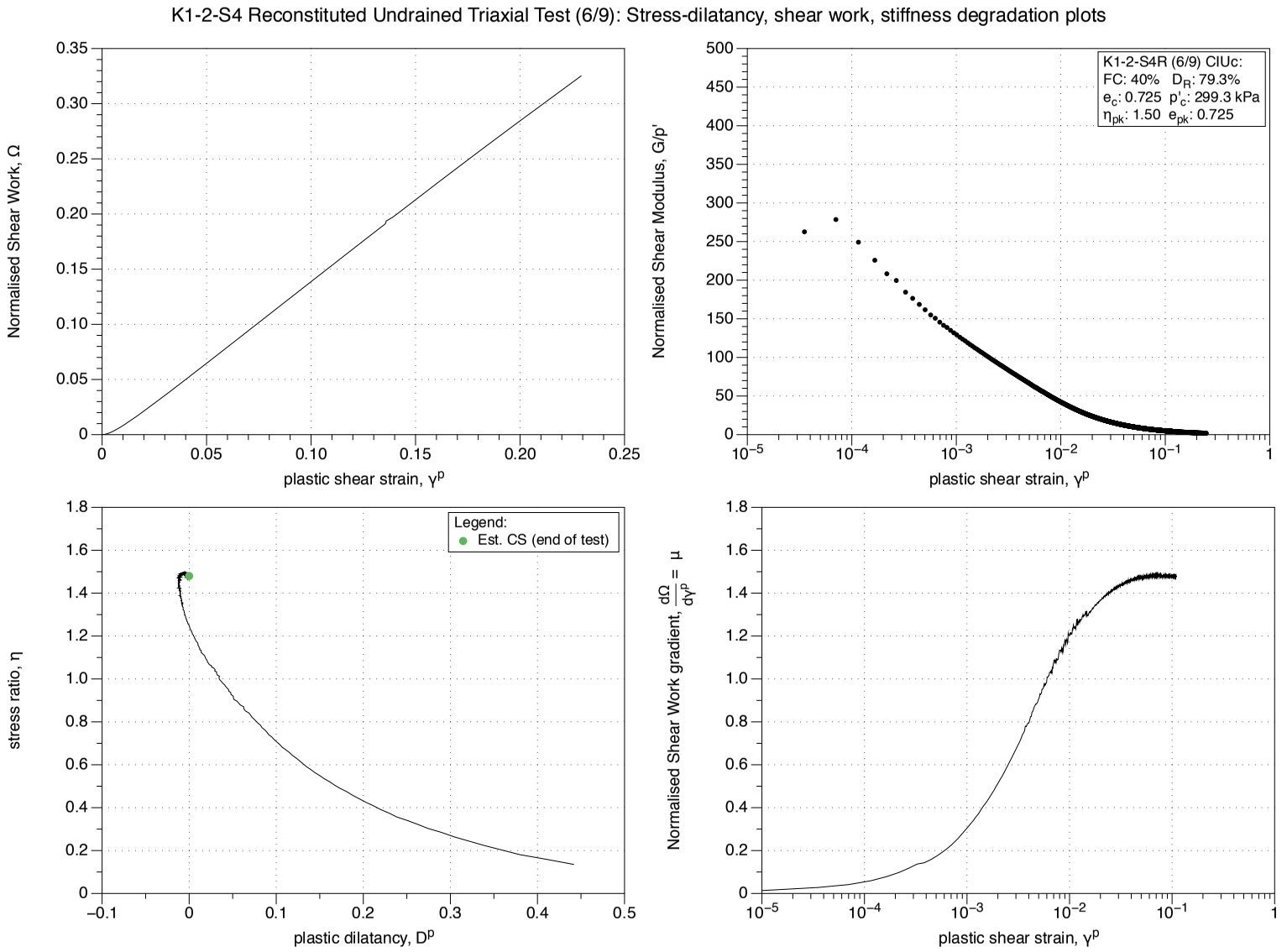

Figure 4.218: K1-2-S4 MT reconstituted sample (FC 40%), undrained monotonic triaxial test (CIU_C), test 6/9. Stress-dilatancy, shear work, stiffness degradation plots.

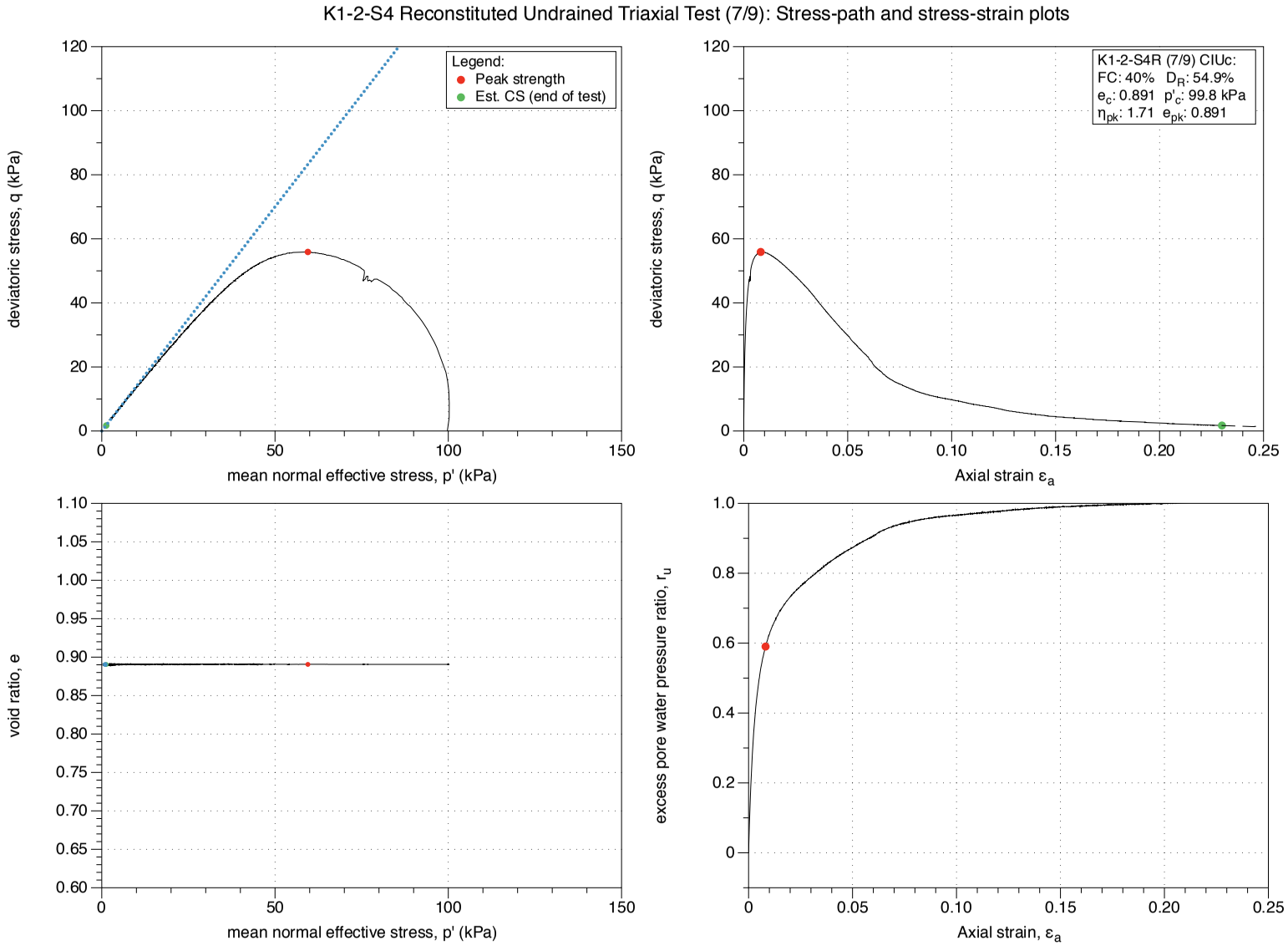

Figure 4.219: K1-2-S4 MT reconstituted sample (FC 40%), undrained monotonic triaxial test (CIU_C), test 7/9. Stress-path and stress-strain plots.

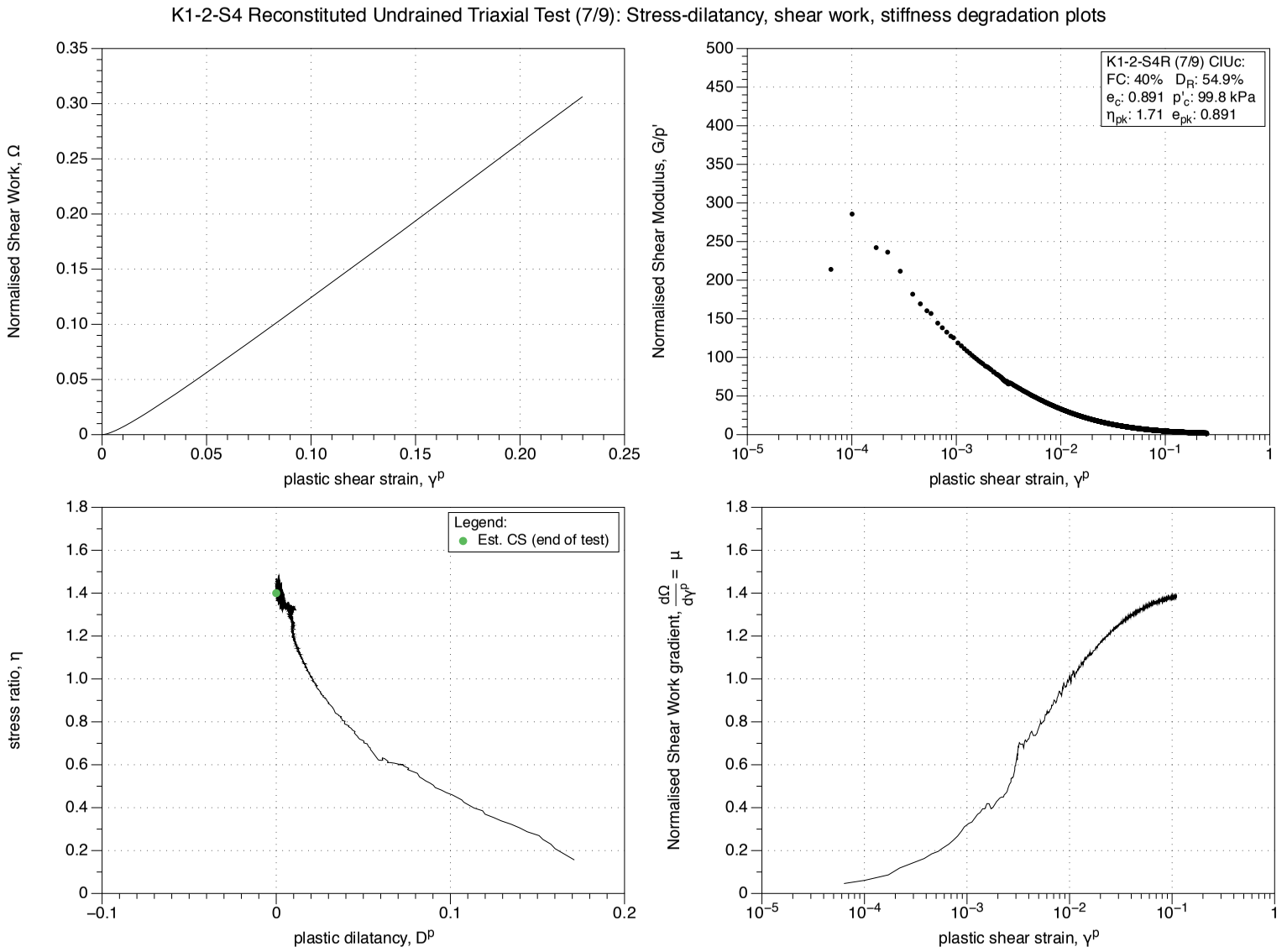

Figure 4.220: K1-2-S4 MT reconstituted sample (FC 40%), undrained monotonic triaxial test (CIU_C), test 7/9. Stress-dilatancy, shear work, stiffness degradation plots.

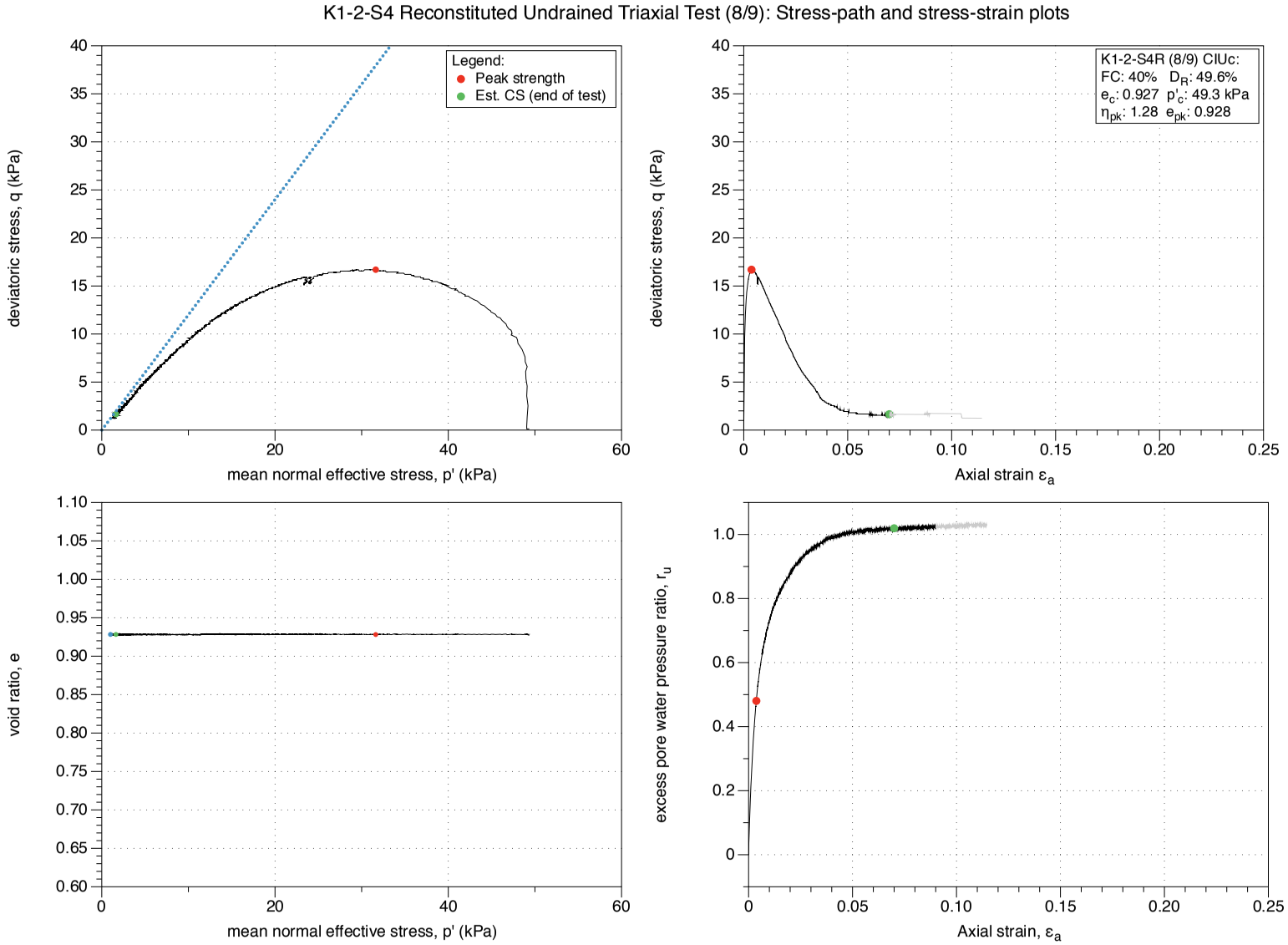

Figure 4.221: K1-2-S4 MT reconstituted sample (FC 40%), undrained monotonic triaxial test (CIU_C), test 8/9. Stress-path and stress-strain plots.

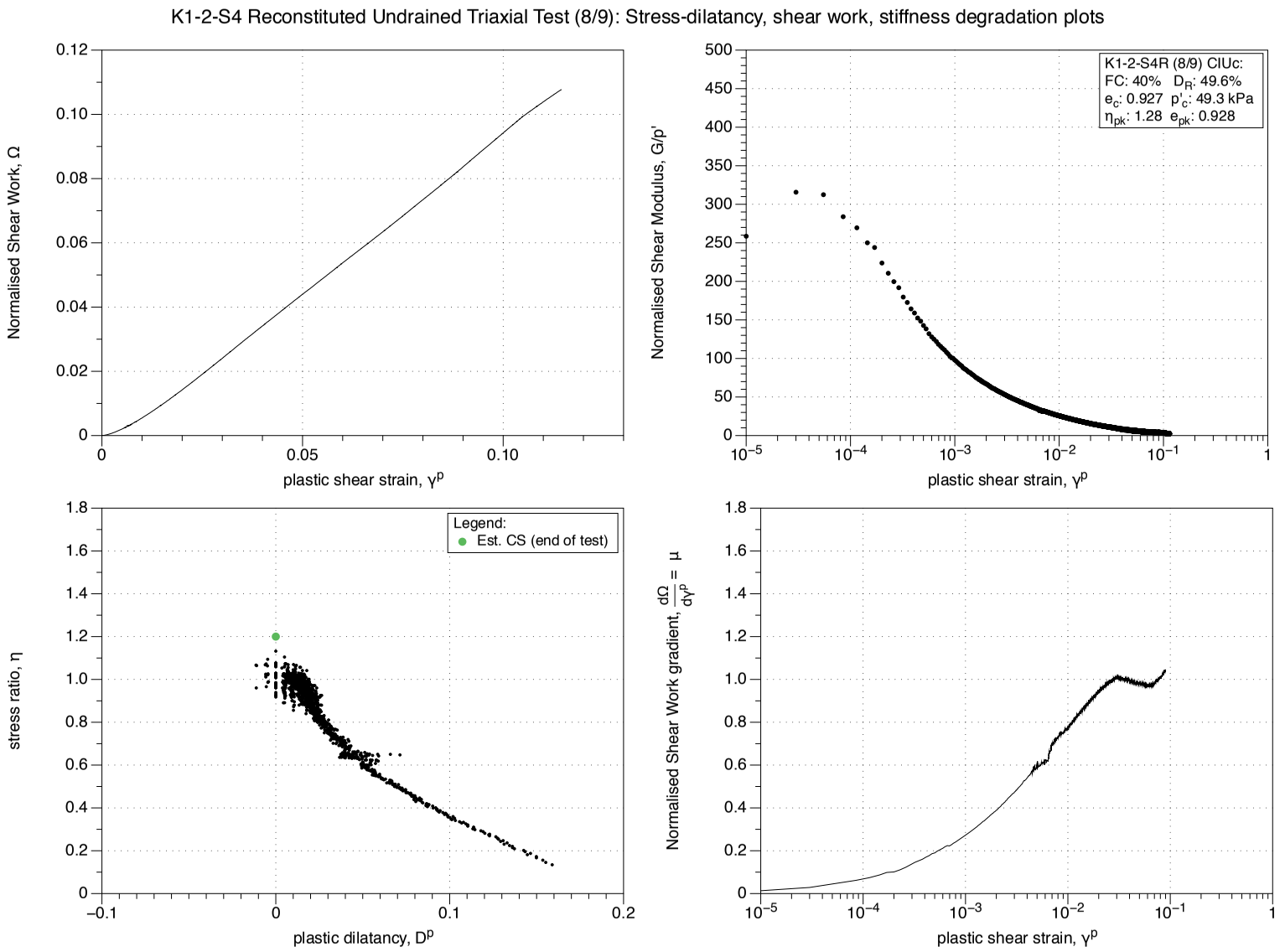

Figure 4.222: K1-2-S4 MT reconstituted sample (FC 40%), undrained monotonic triaxial test (CIU_C), test 8/9. Stress-dilatancy, shear work, stiffness degradation plots.

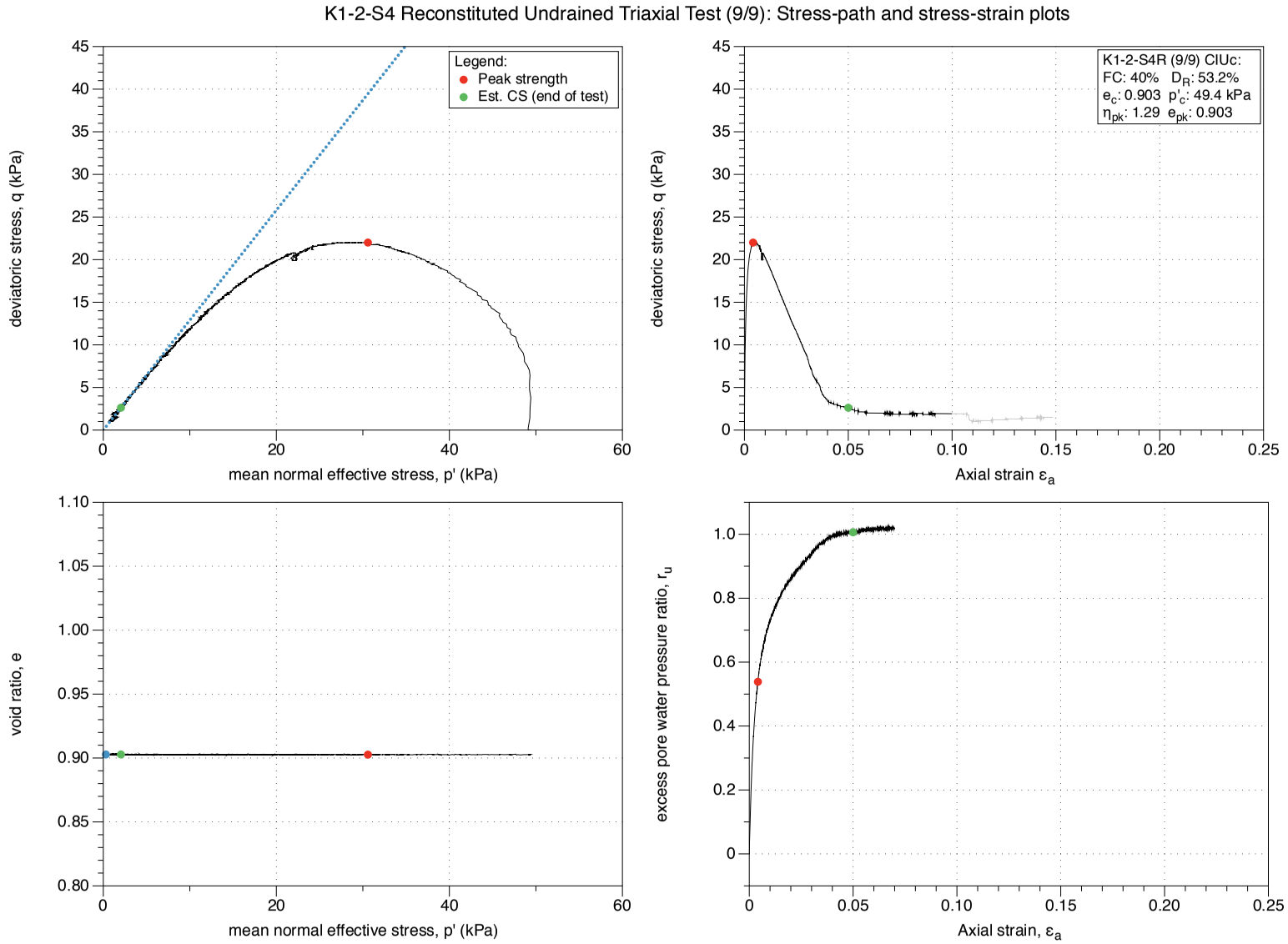

Figure 4.223: K1-2-S4 MT reconstituted sample (FC 40%), undrained monotonic triaxial test (CIU_C), test 9/9. Stress-path and stress-strain plots.

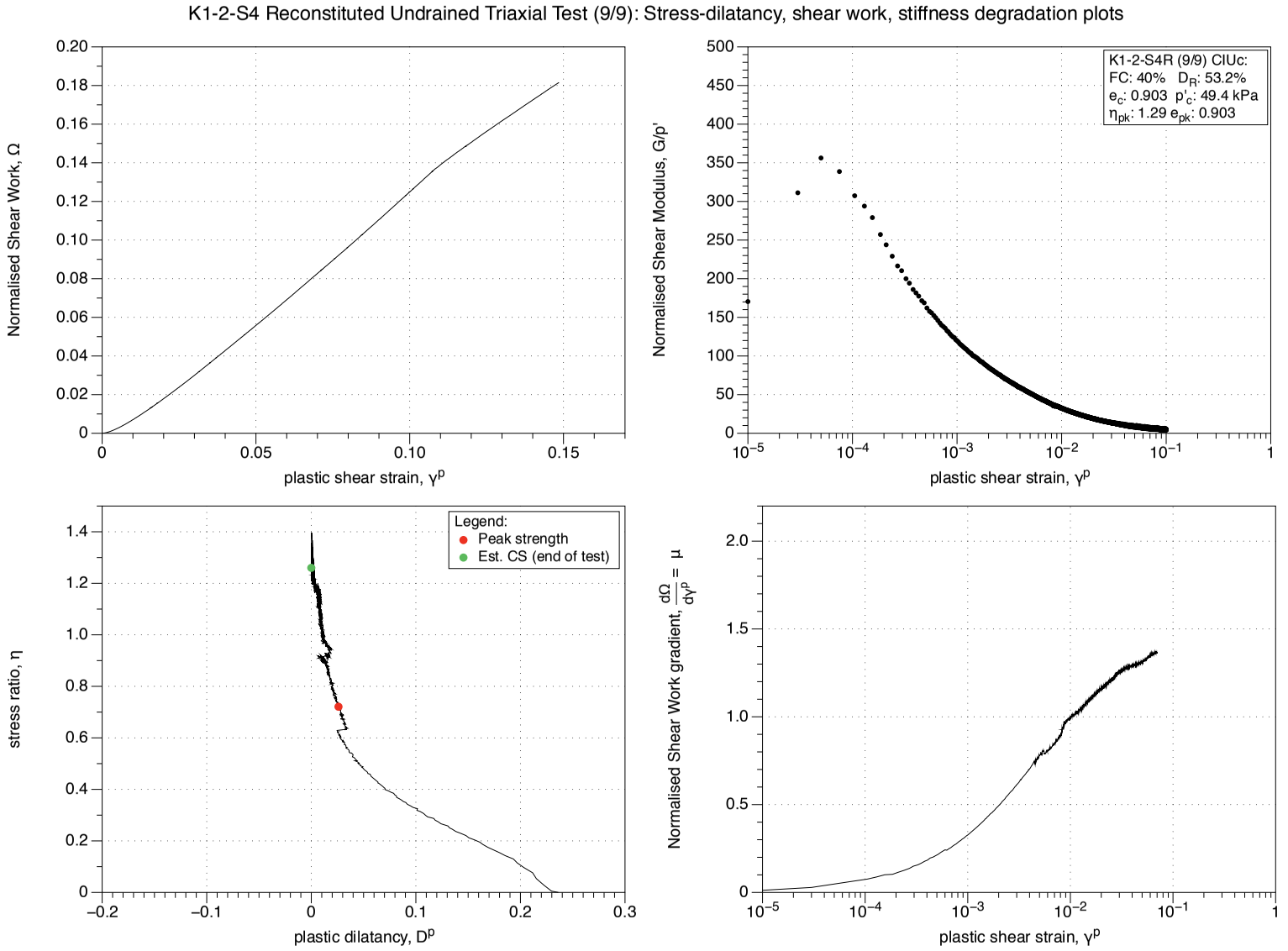

Figure 4.224: K1-2-S4 MT reconstituted sample (FC 40%), undrained monotonic triaxial test (CIU_C), test 9/9. Stress-dilatancy, shear work, stiffness degradation plots.

4.4.1.3 CID Tests on samples (FC 50 - 80 %)

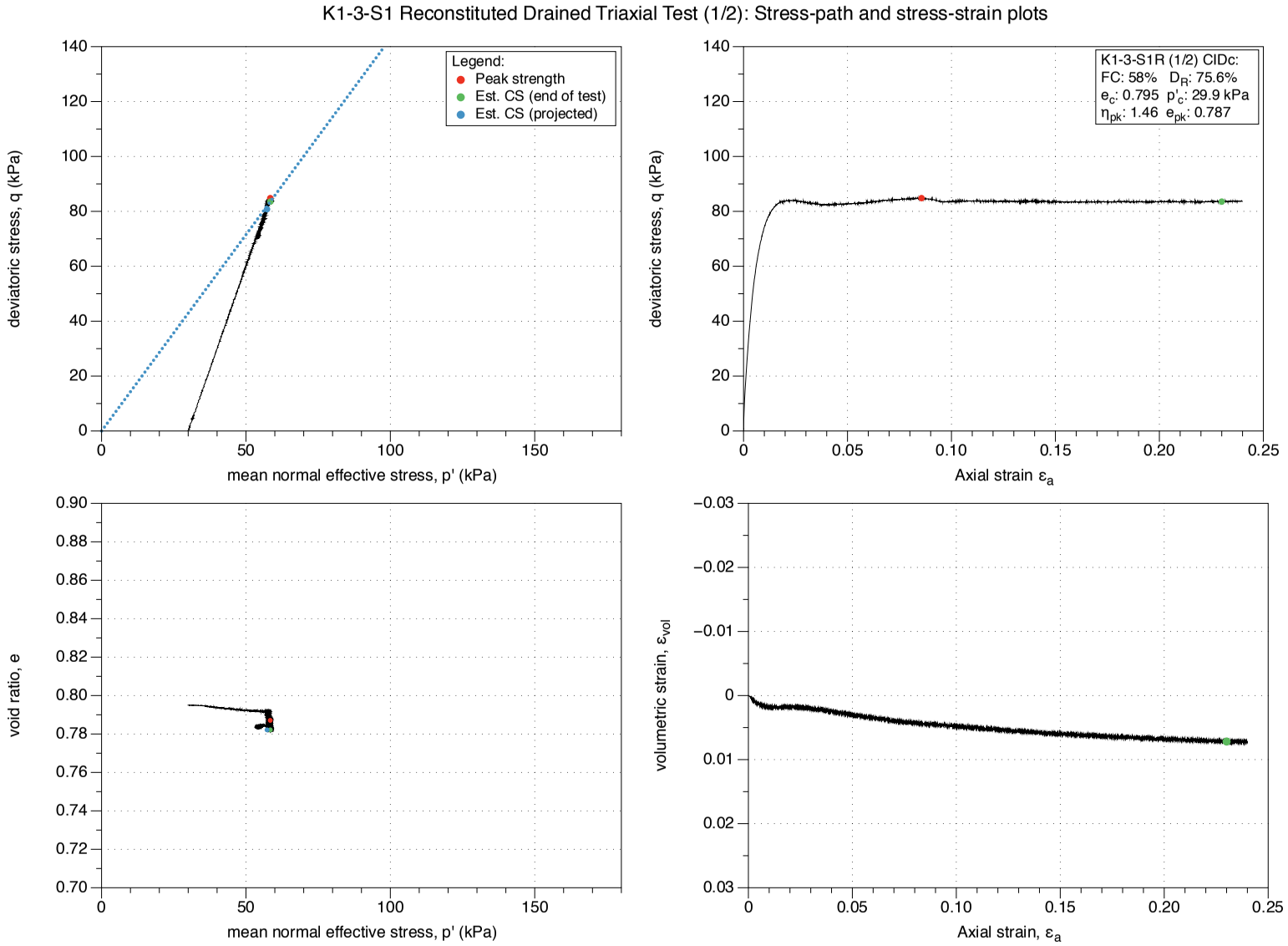

Figure 4.225: K1-3-S1 MT reconstituted sample (FC 58%), drained monotonic triaxial test (CID_C), test 1/2. Stress-path and stress-strain plots.

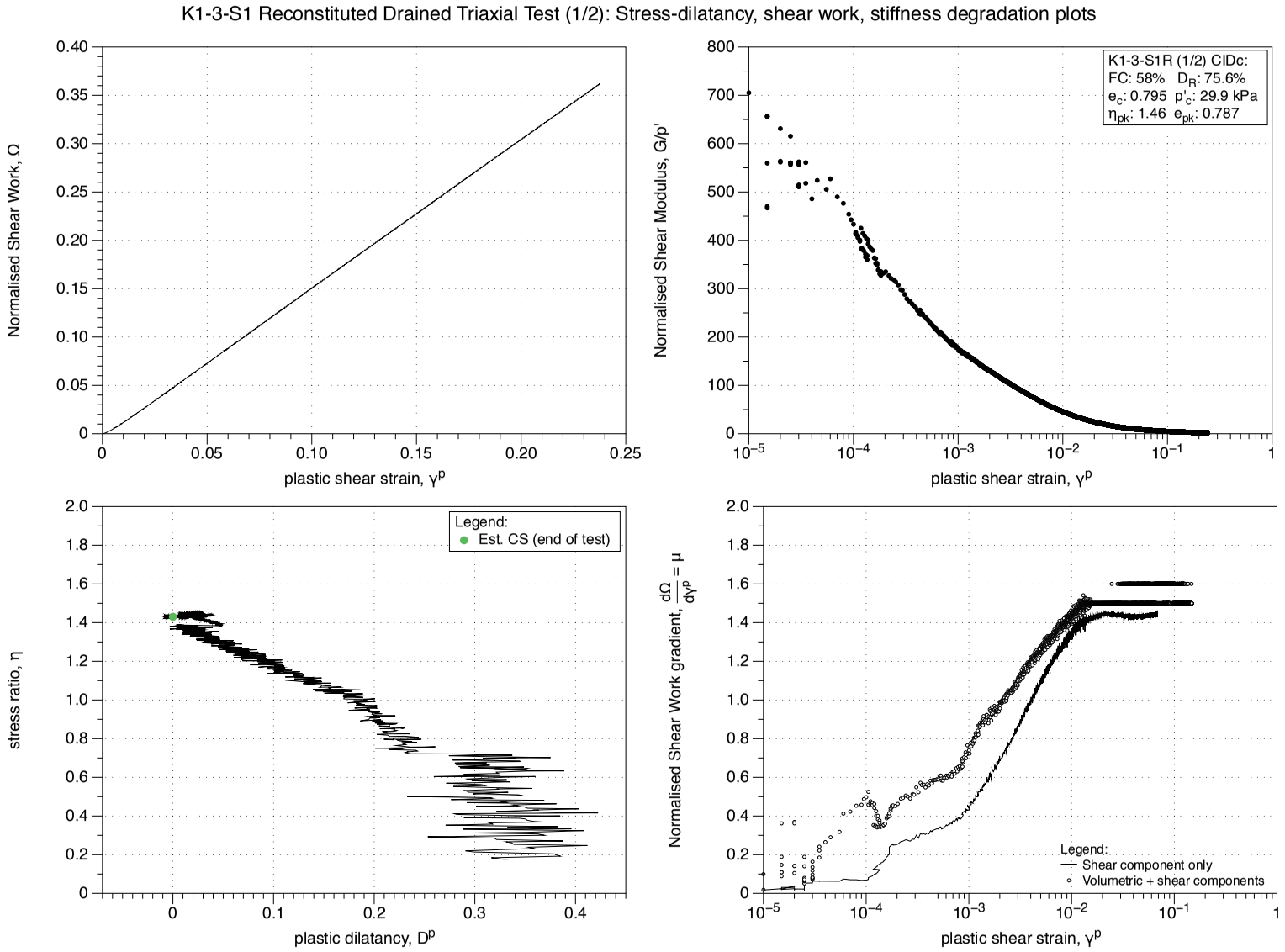

Figure 4.226: K1-3-S1 MT reconstituted sample (FC 58%), drained monotonic triaxial test (CID_C), test 1/2. Stress-dilatancy, shear work, stiffness degradation plots.

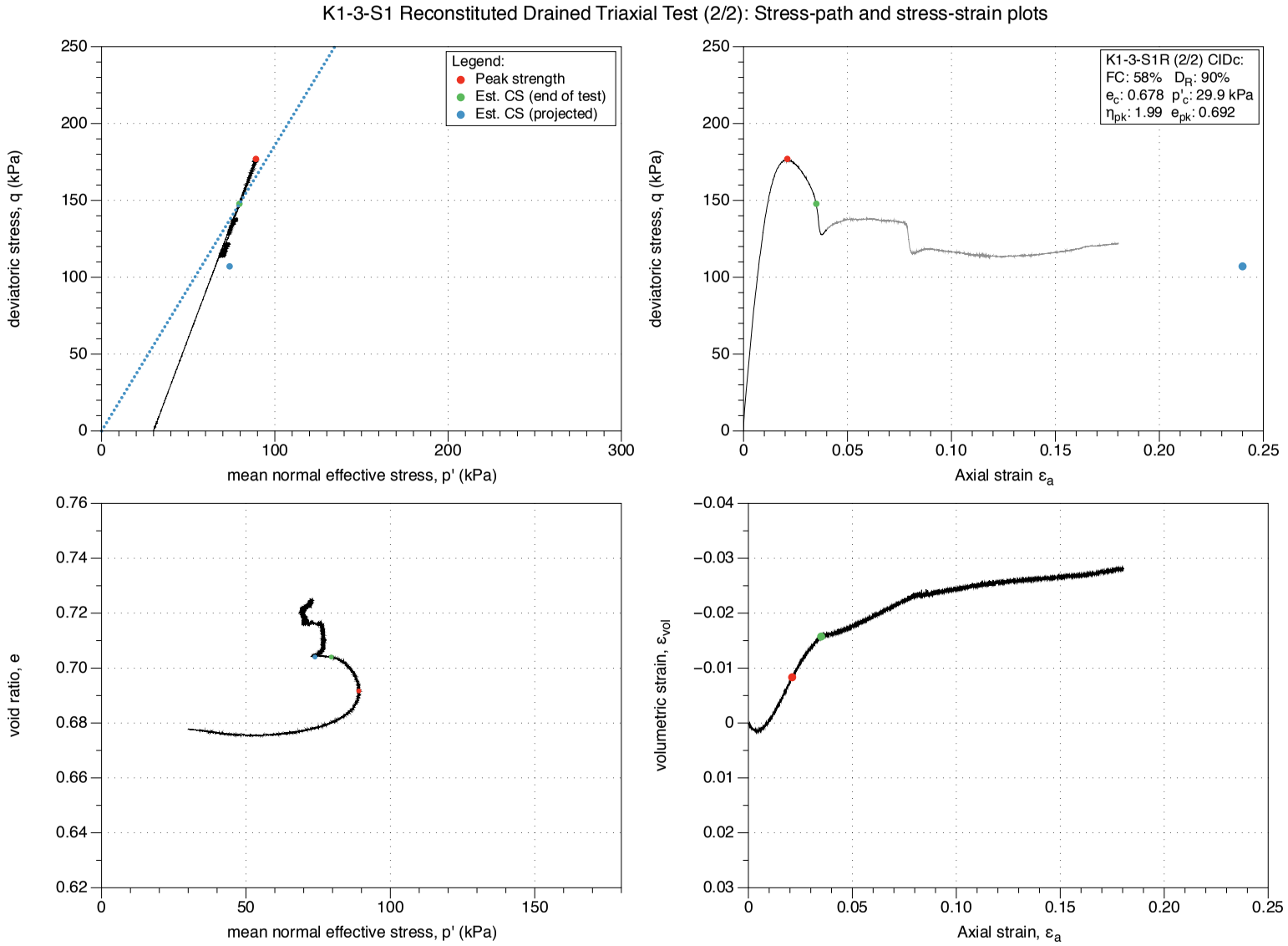

Figure 4.227: K1-3-S1 MT reconstituted sample (FC 58%), drained monotonic triaxial test (CID_C), test 2/2. Stress-path and stress-strain plots.

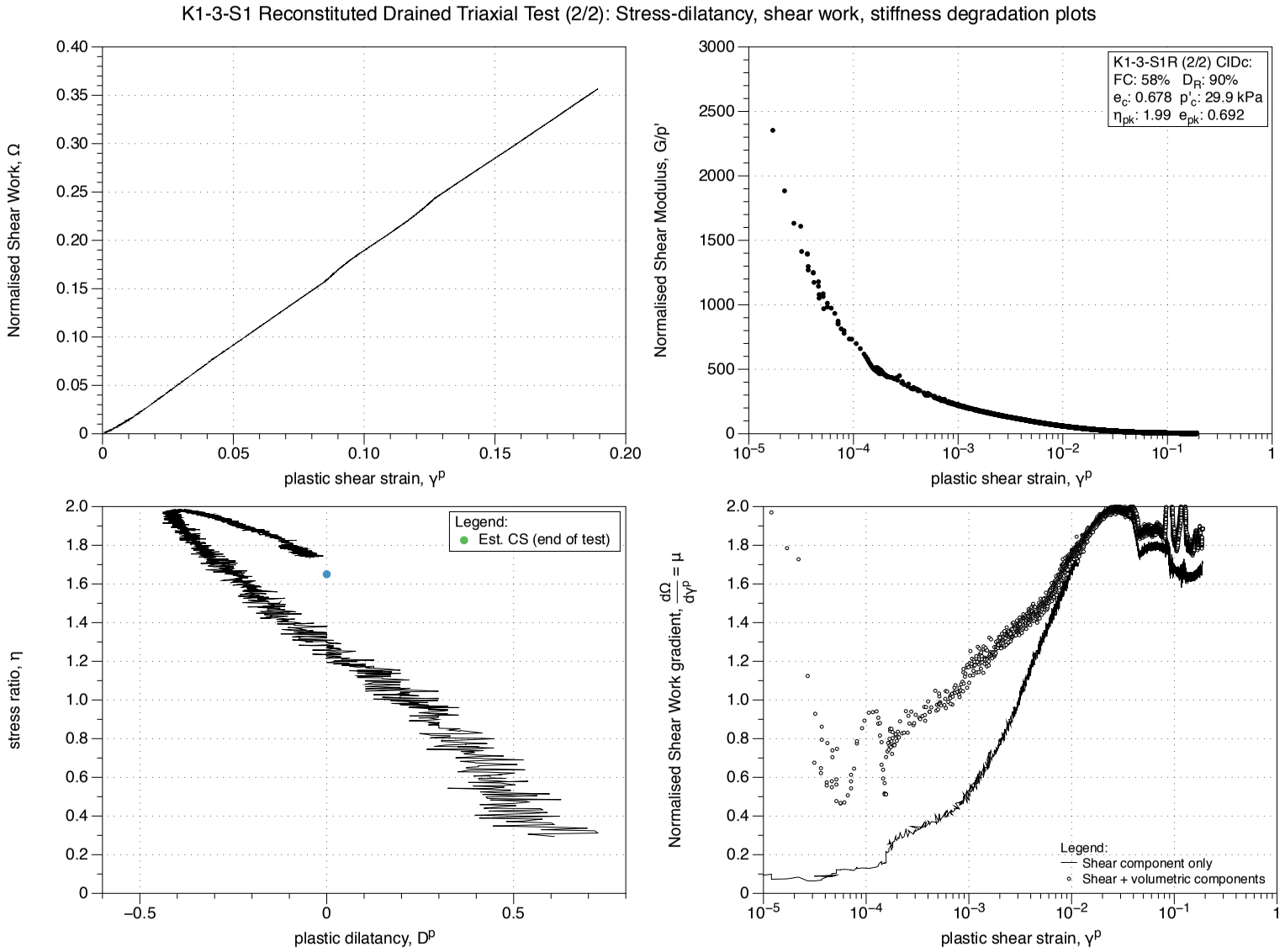

Figure 4.228: K1-3-S1 MT reconstituted sample (FC 58%), drained monotonic triaxial test (CID_C), test 2/2. Stress-dilatancy, shear work, stiffness degradation plots.

4.4.1.4 CIU Tests on samples (FC 50 - 80 %)

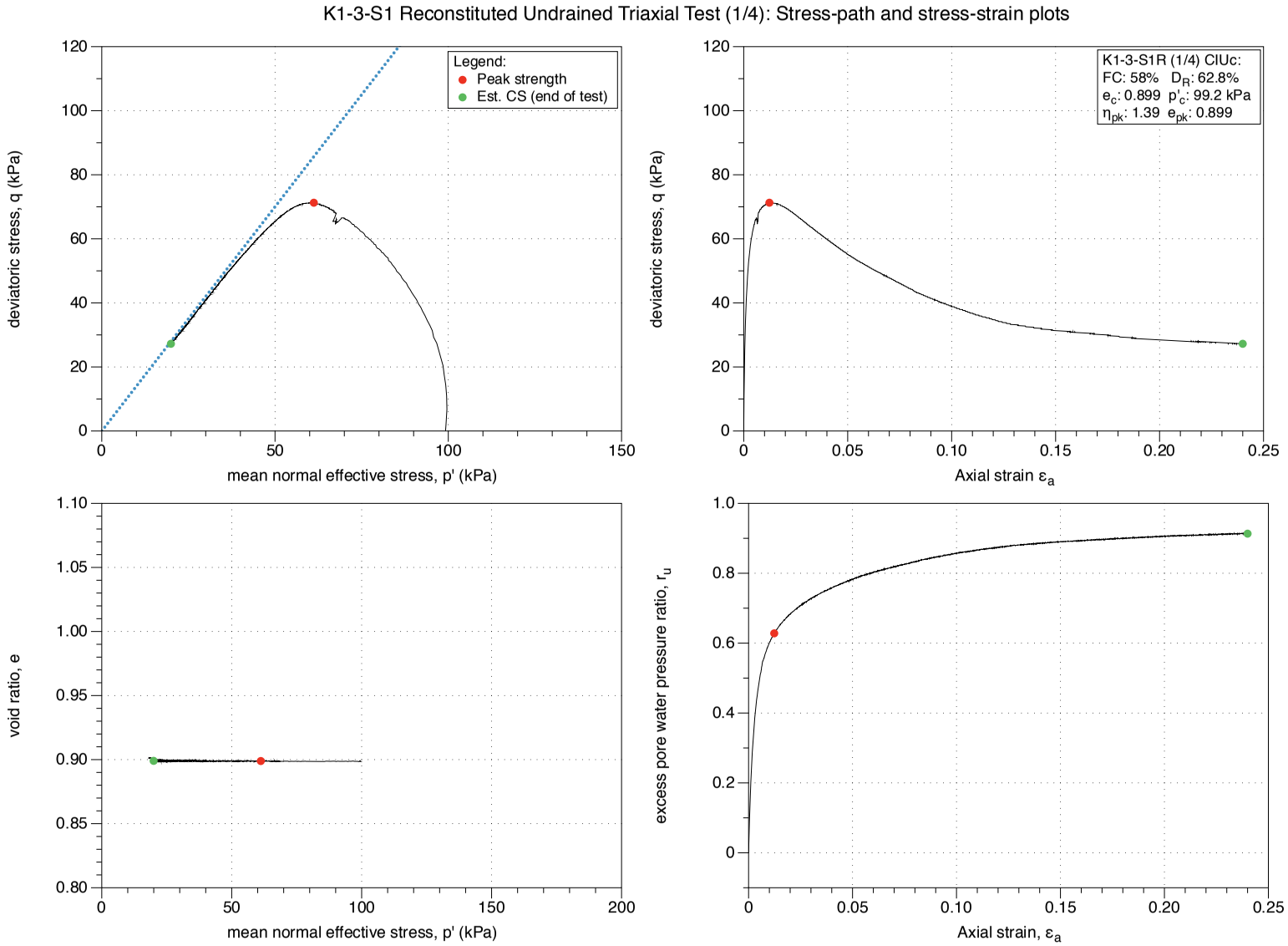

Figure 4.229: K1-3-S1 MT reconstituted sample (FC 58%), undrained monotonic triaxial test (CIU_C), test 1/4. Stress-path and stress-strain plots.

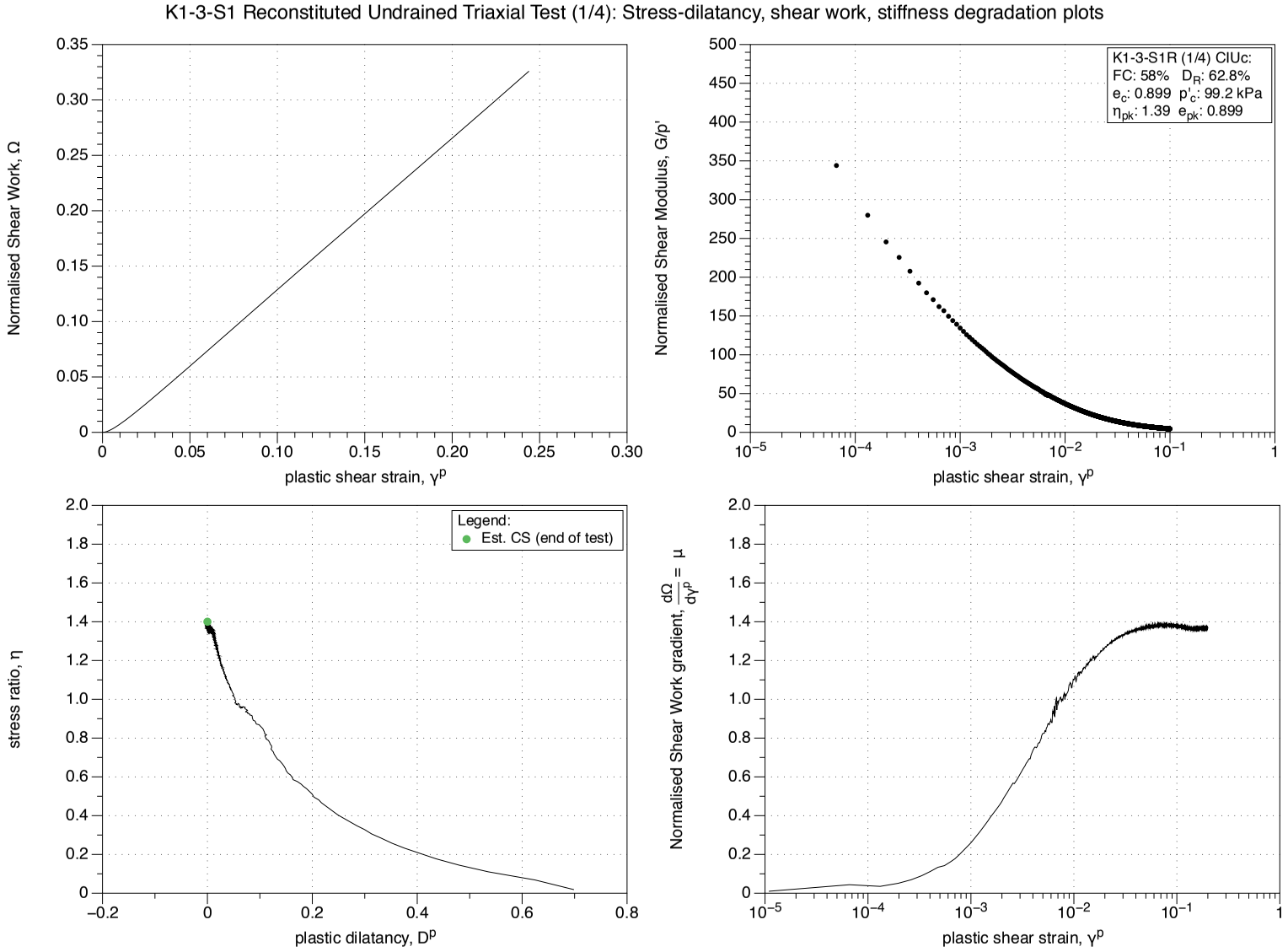

Figure 4.230: K1-3-S1 MT reconstituted sample (FC 58%), undrained monotonic triaxial test (CIU_C), test 1/4. Stress-dilatancy, shear work, stiffness degradation plots.

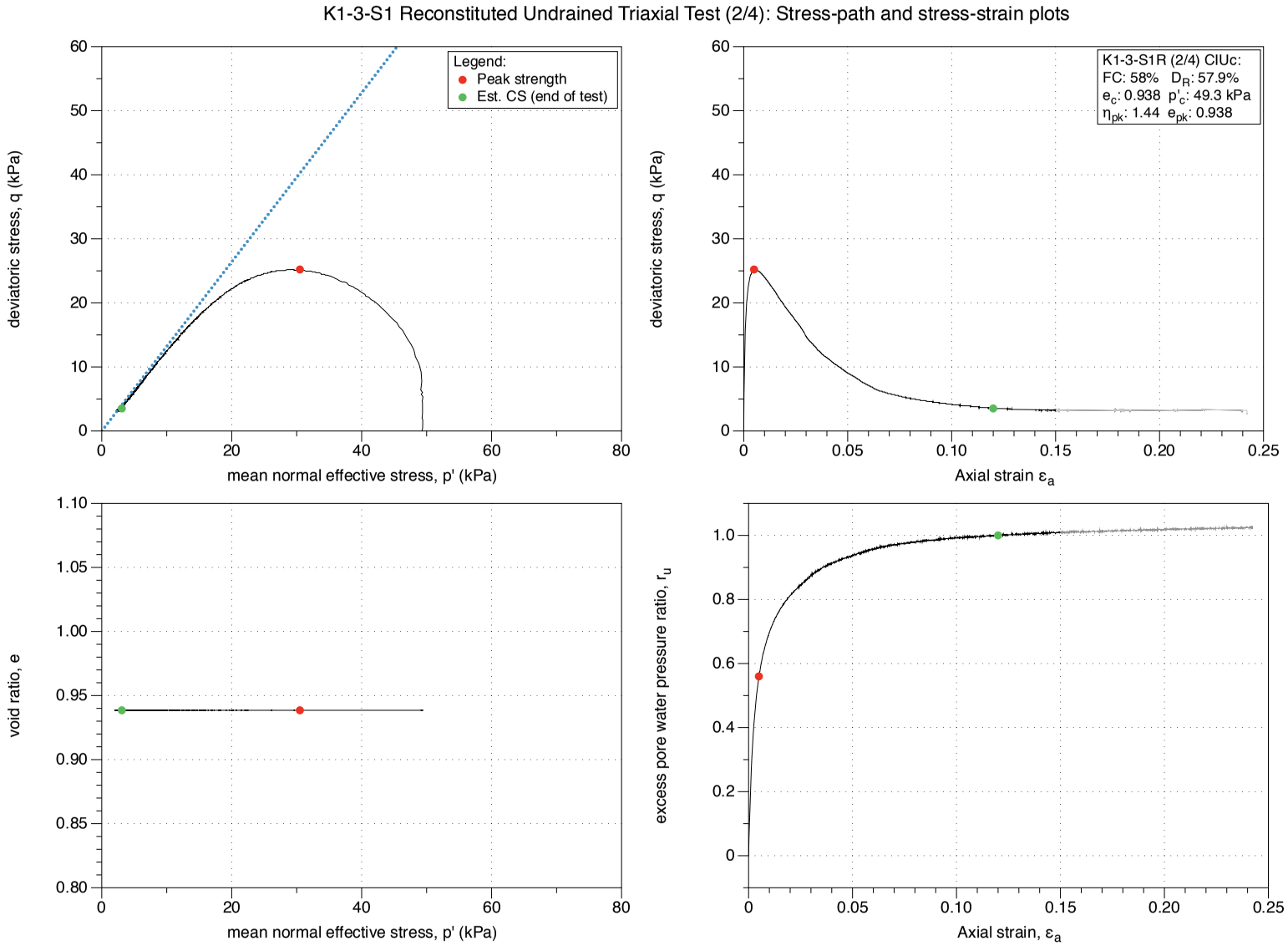

Figure 4.231: K1-3-S1 MT reconstituted sample (FC 58%), undrained monotonic triaxial test (CIU_C), test 2/4. Stress-path and stress-strain plots.

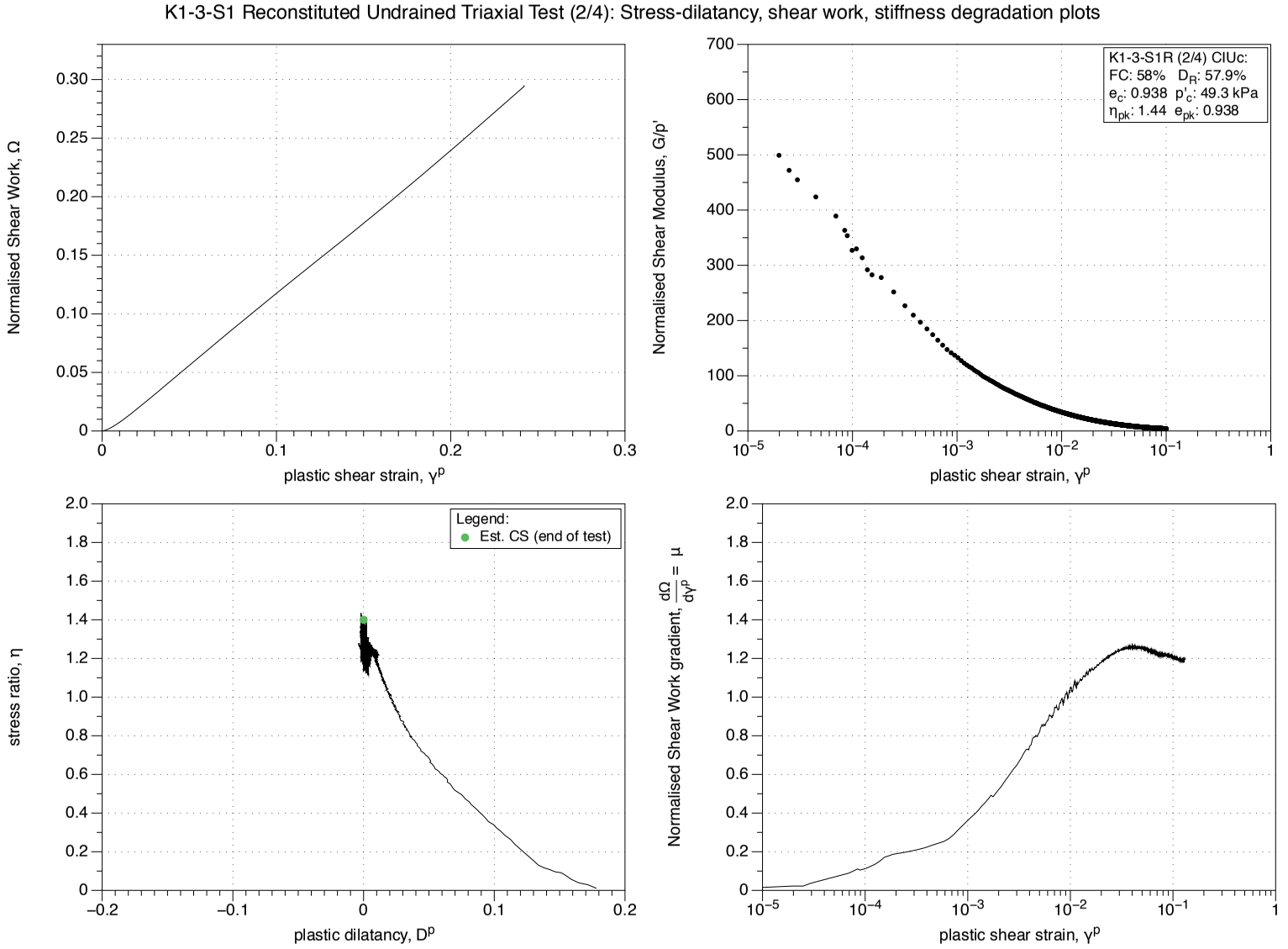

Figure 4.232: K1-3-S1 MT reconstituted sample (FC 58%), undrained monotonic triaxial test (CIU_C), test 2/4. Stress-dilatancy, shear work, stiffness degradation plots.

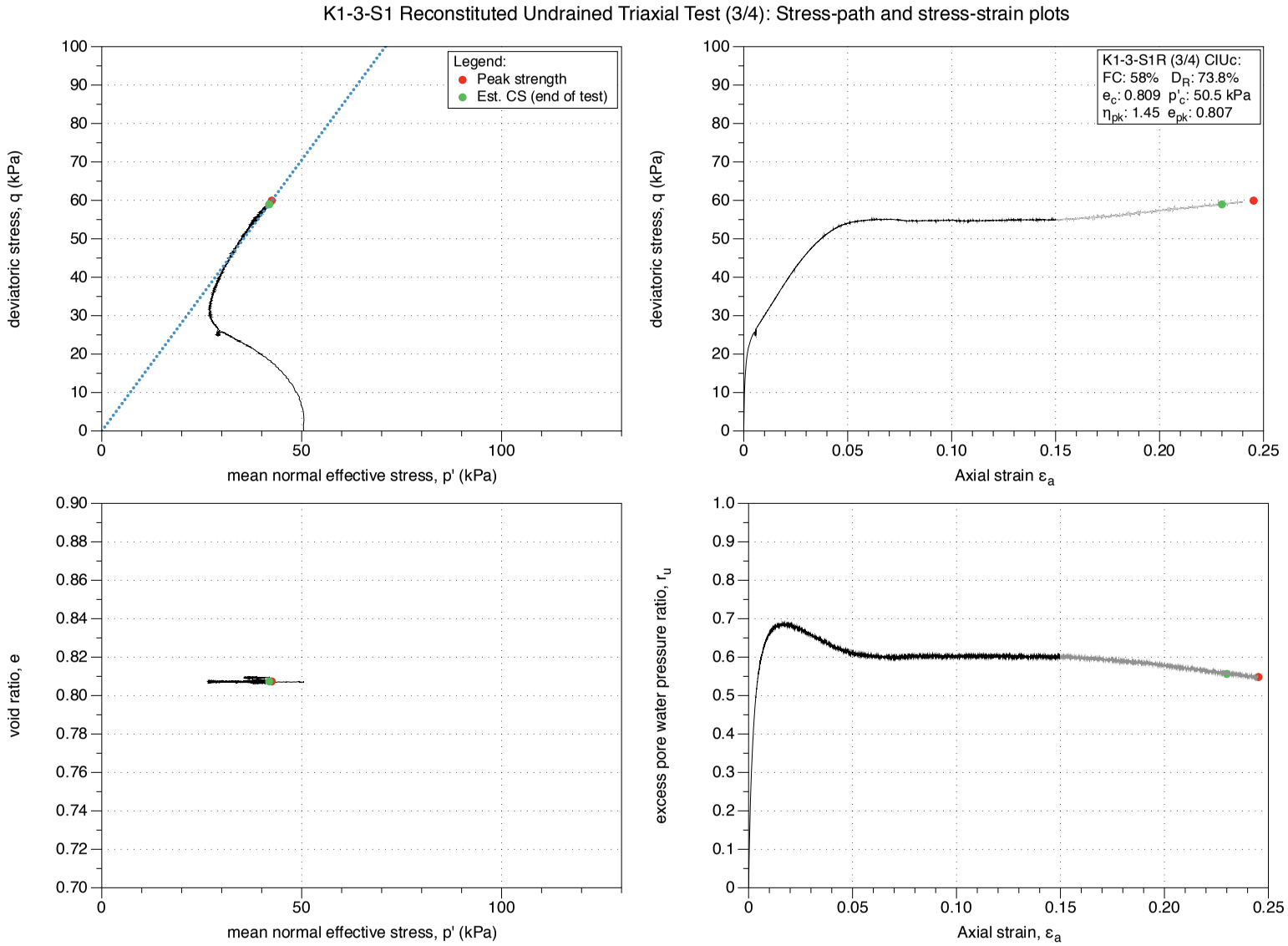

Figure 4.233: K1-3-S1 MT reconstituted sample (FC 58%), undrained monotonic triaxial test (CIU_C), test 3/4. Stress-path and stress-strain plots.

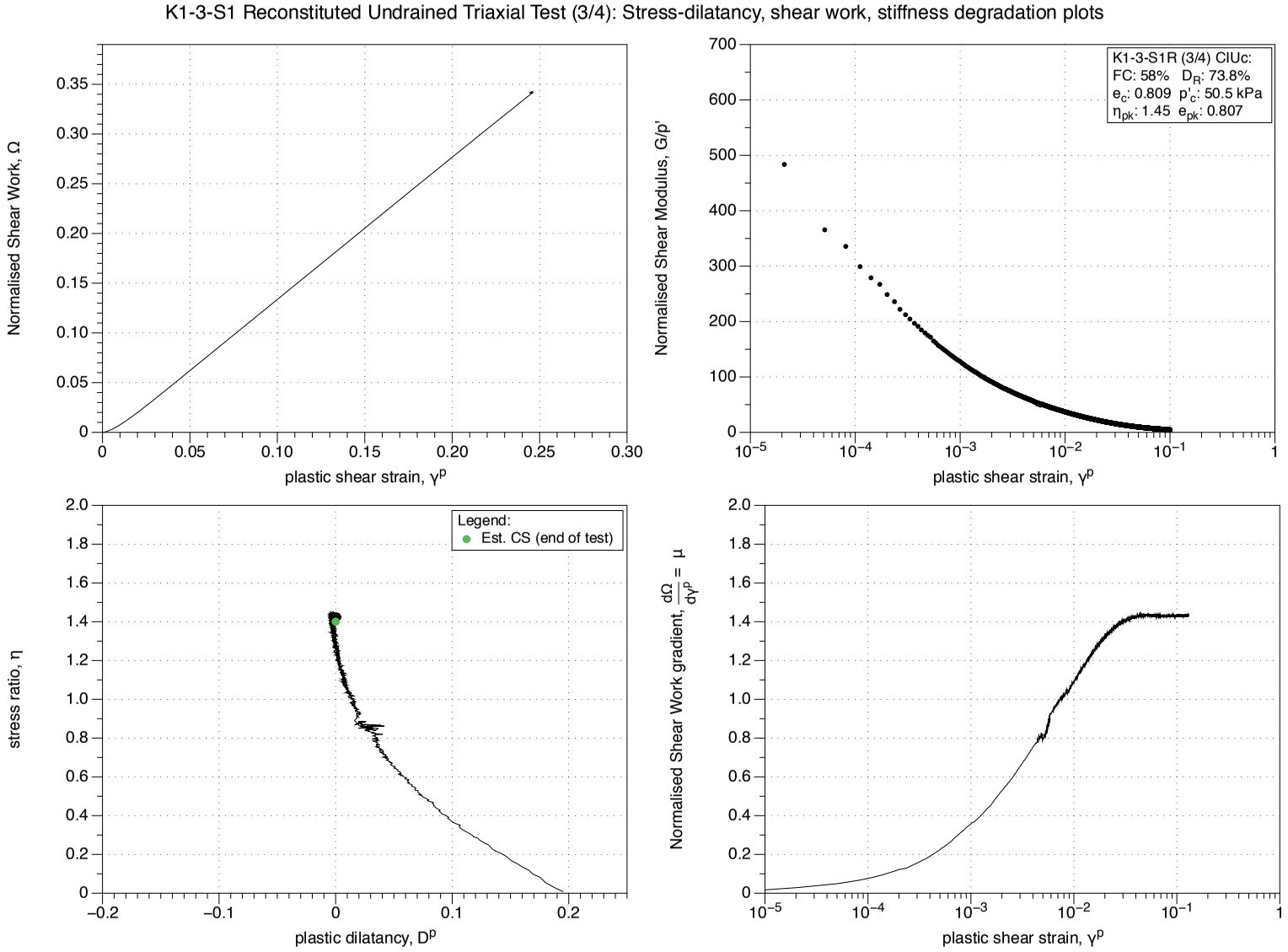

Figure 4.234: K1-3-S1 MT reconstituted sample (FC 58%), undrained monotonic triaxial test (CIU_C), test 3/4. Stress-dilatancy, shear work, stiffness degradation plots.

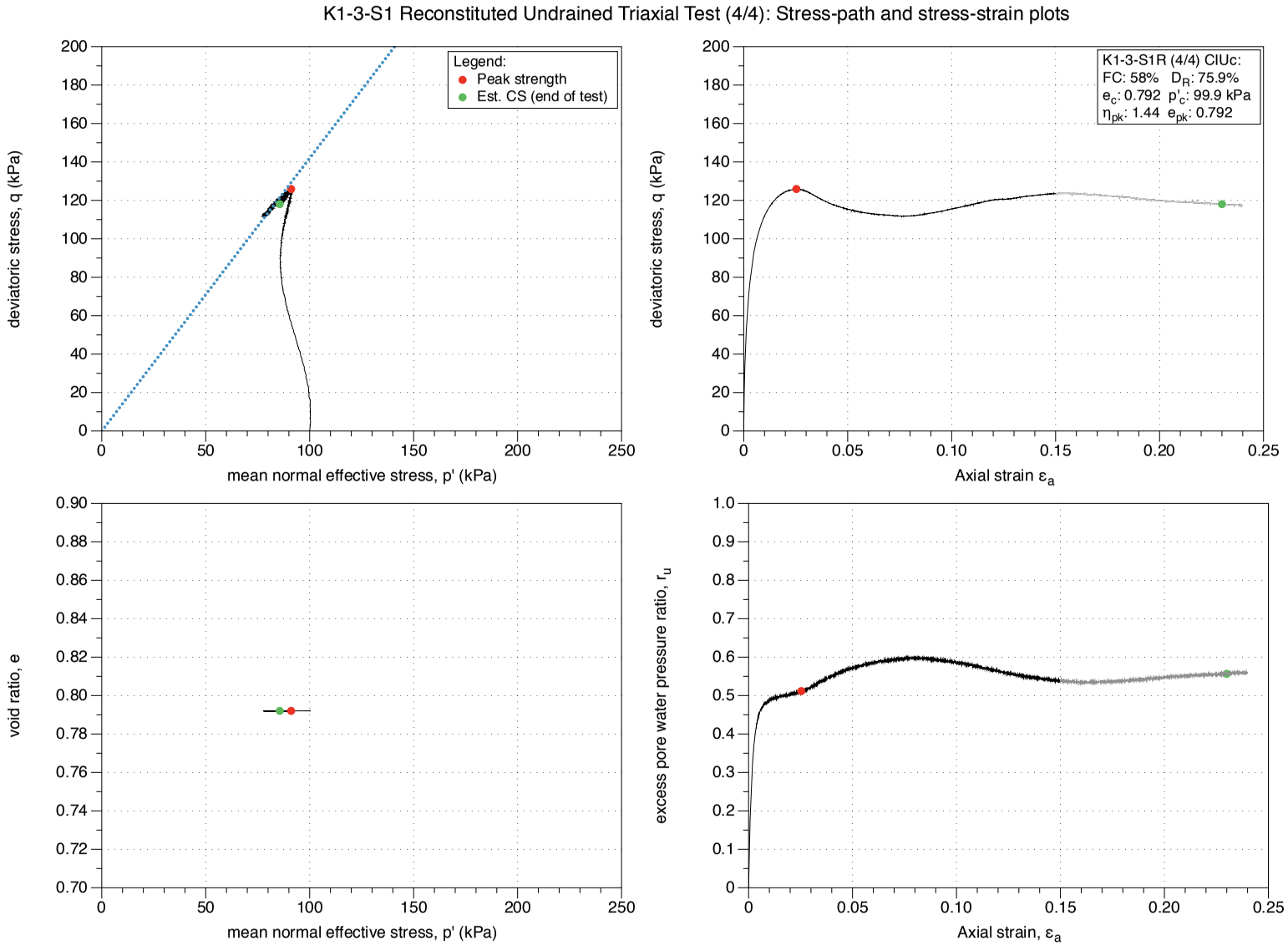

Figure 4.235: K1-3-S1 MT reconstituted sample (FC 58%), undrained monotonic triaxial test (CIU_C), test 4/4. Stress-path and stress-strain plots.

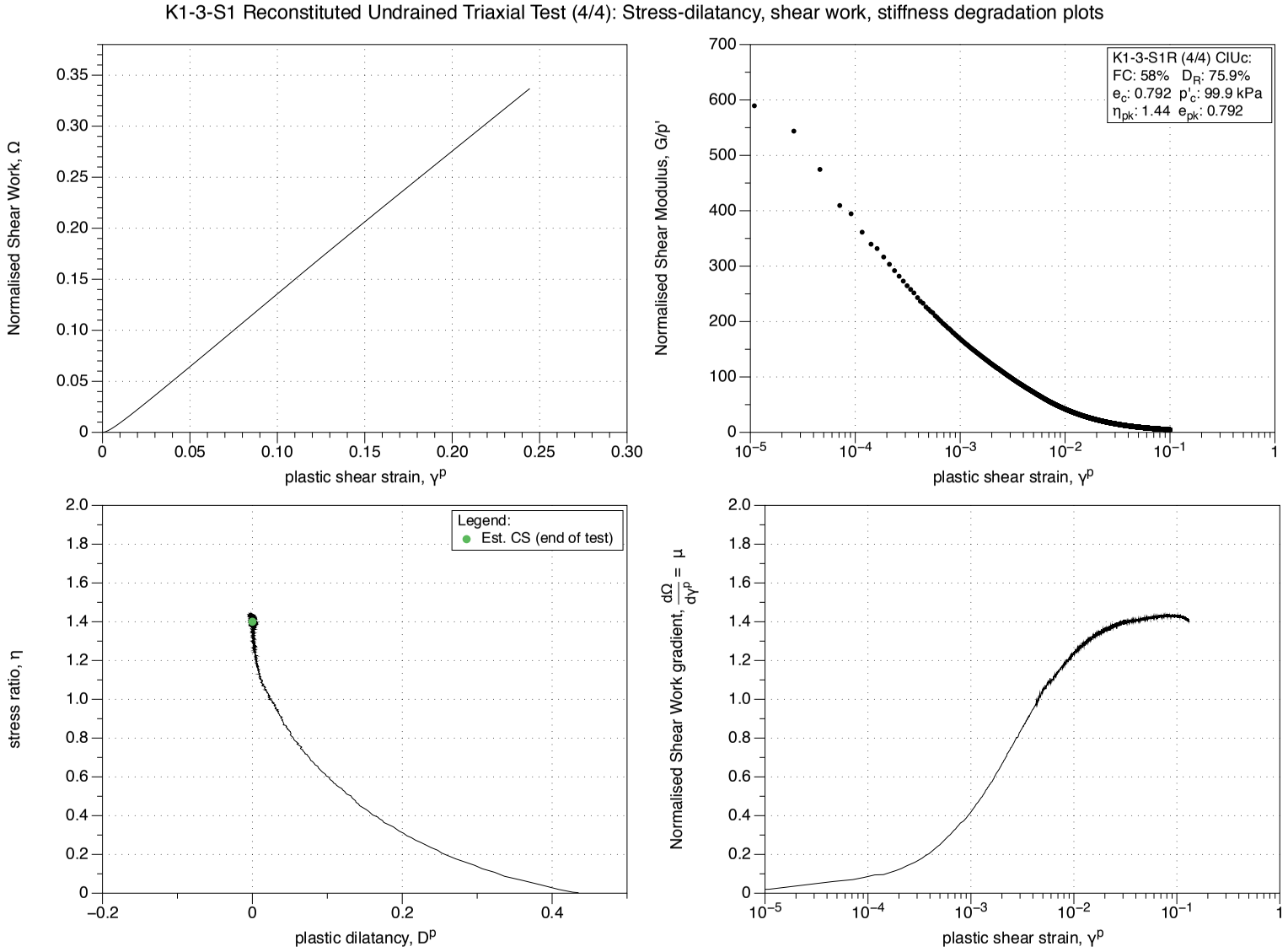

Figure 4.236: K1-3-S1 MT reconstituted sample (FC 58%), undrained monotonic triaxial test (CIU_C), test 4/4. Stress-dilatancy, shear work, stiffness degradation plots.

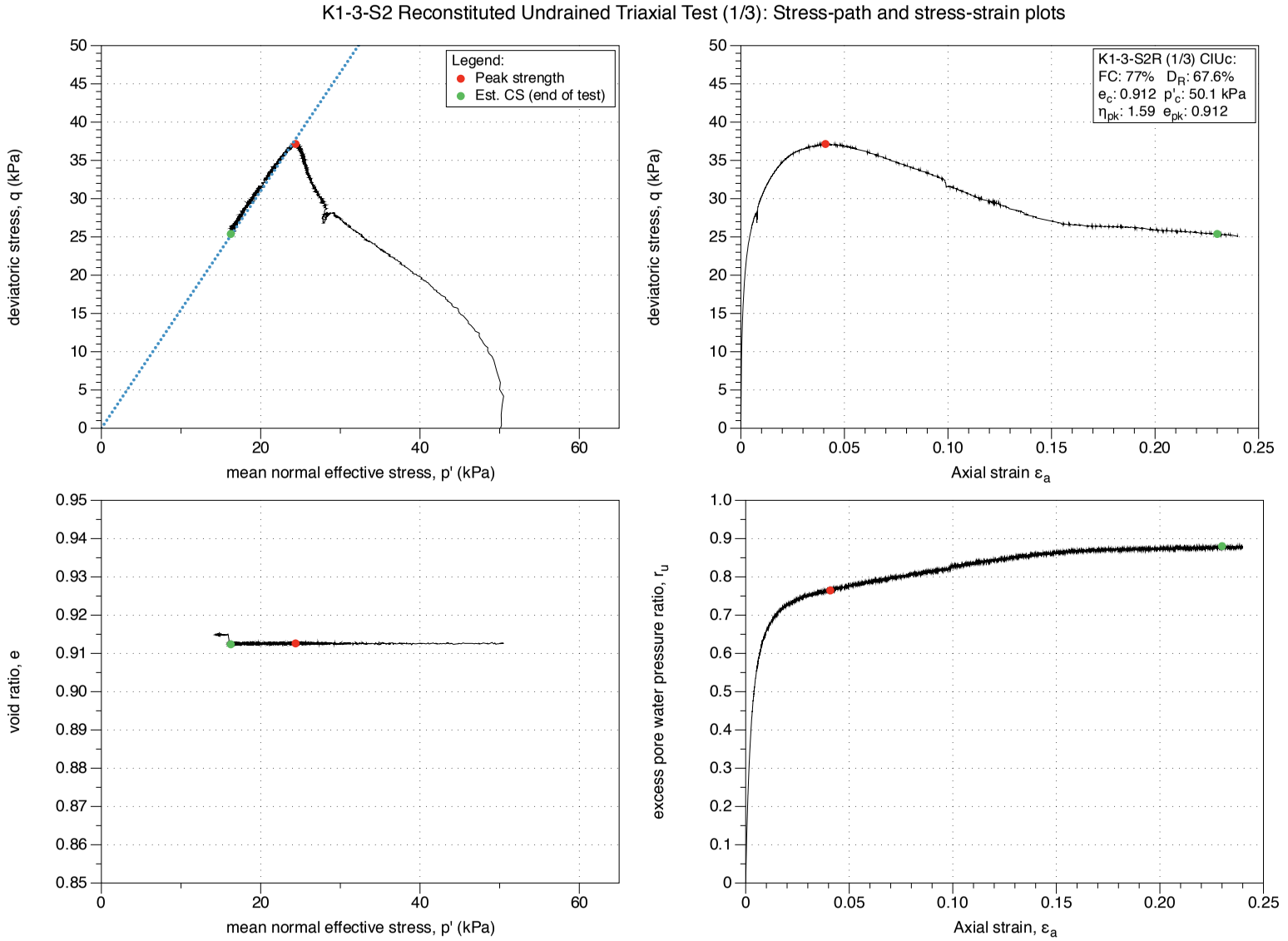

Figure 4.237: K1-3-S2 MT reconstituted sample (FC 77%), undrained monotonic triaxial test (CIU_C), test 1/3. Stress-path and stress-strain plots.

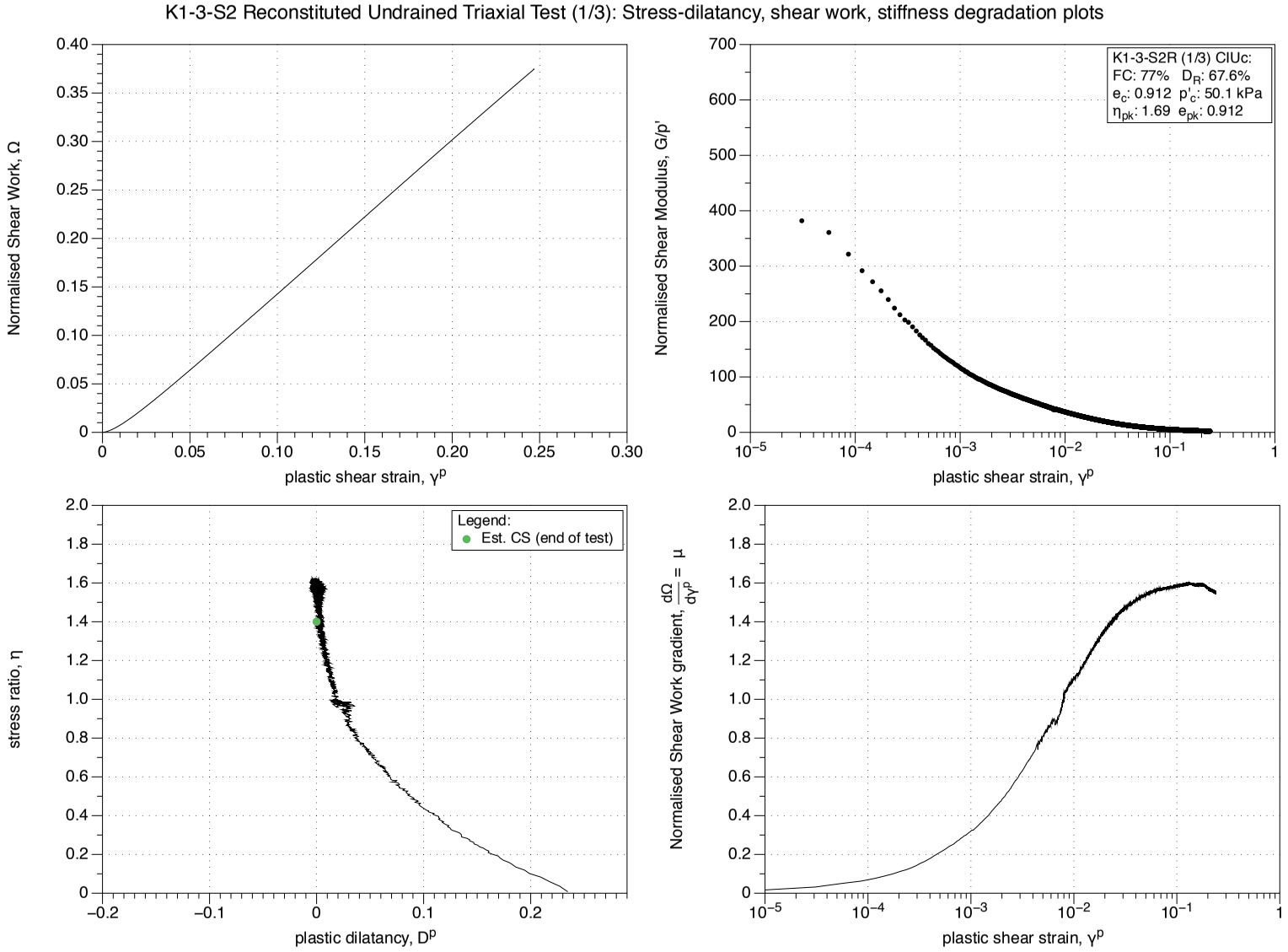

Figure 4.238: K1-3-S2 MT reconstituted sample (FC 77%), undrained monotonic triaxial test (CIU_C), test 1/3. Stress-dilatancy, shear work, stiffness degradation plots.

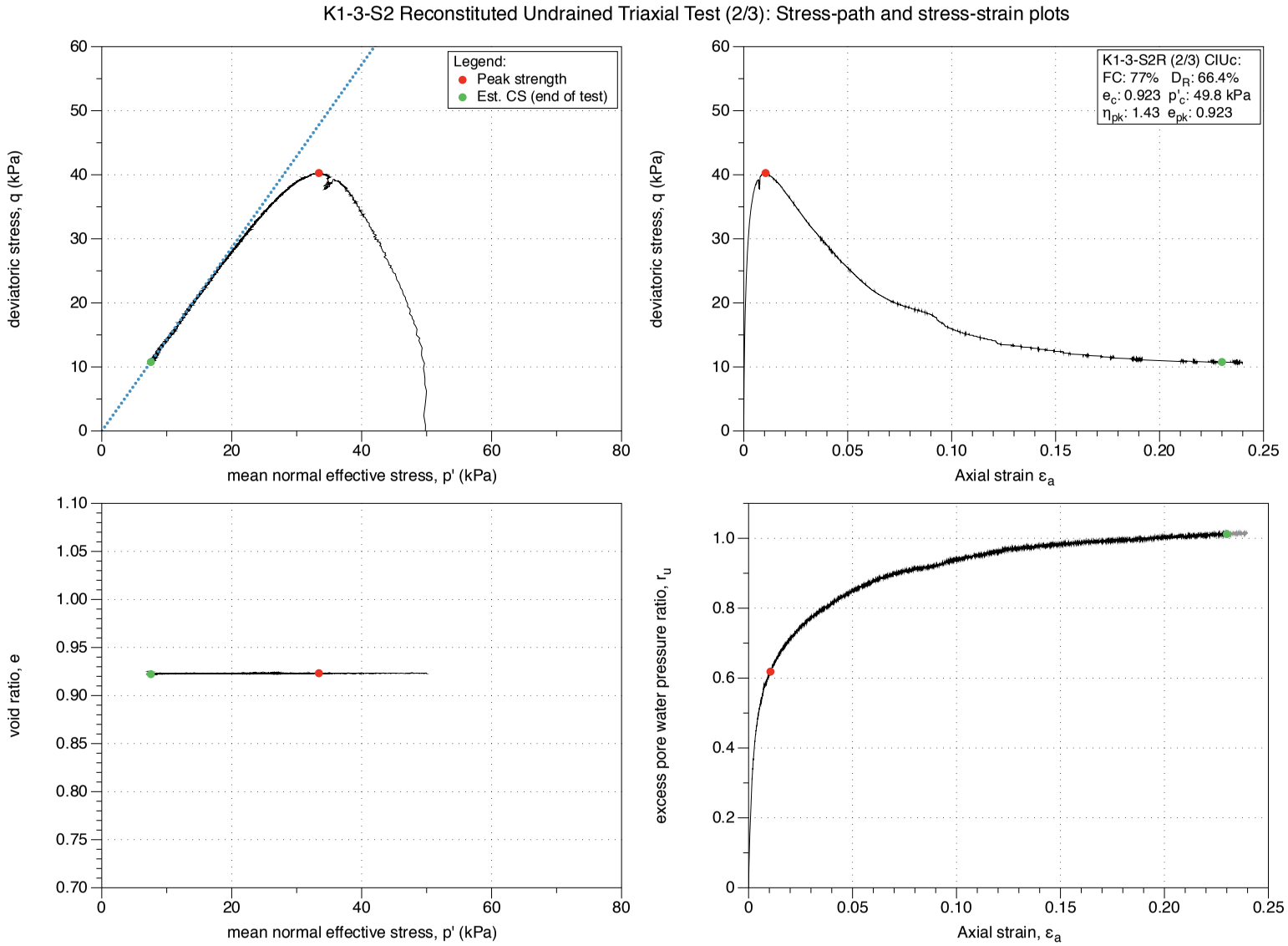

Figure 4.239: K1-3-S2 MT reconstituted sample (FC 77%), undrained monotonic triaxial test (CIU_C), test 2/3. Stress-path and stress-strain plots.

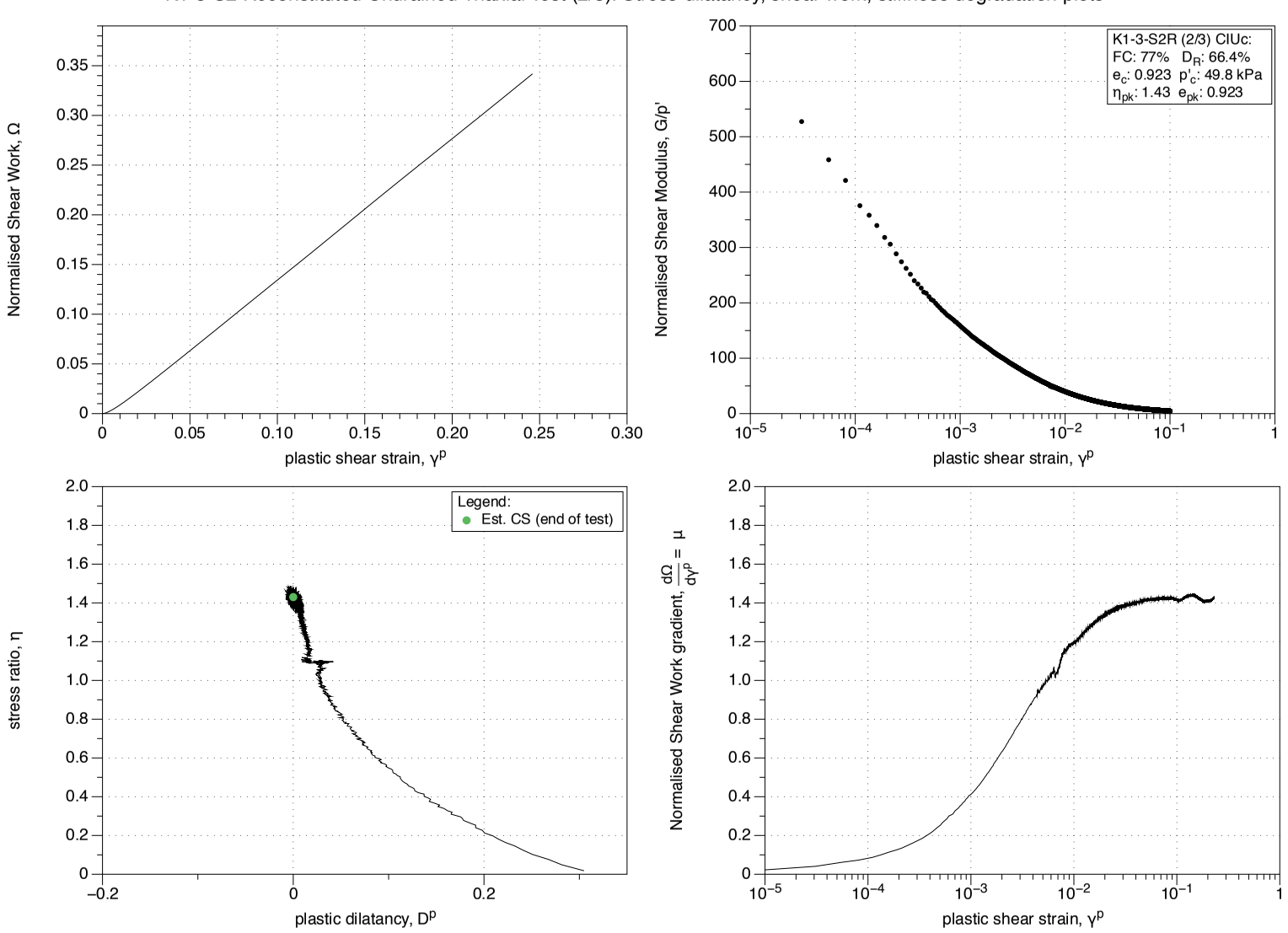

Figure 4.240: K1-3-S2 MT reconstituted sample (FC 77%), undrained monotonic triaxial test (CIU_C), test 2/3. Stress-dilatancy, shear work, stiffness degradation plots.

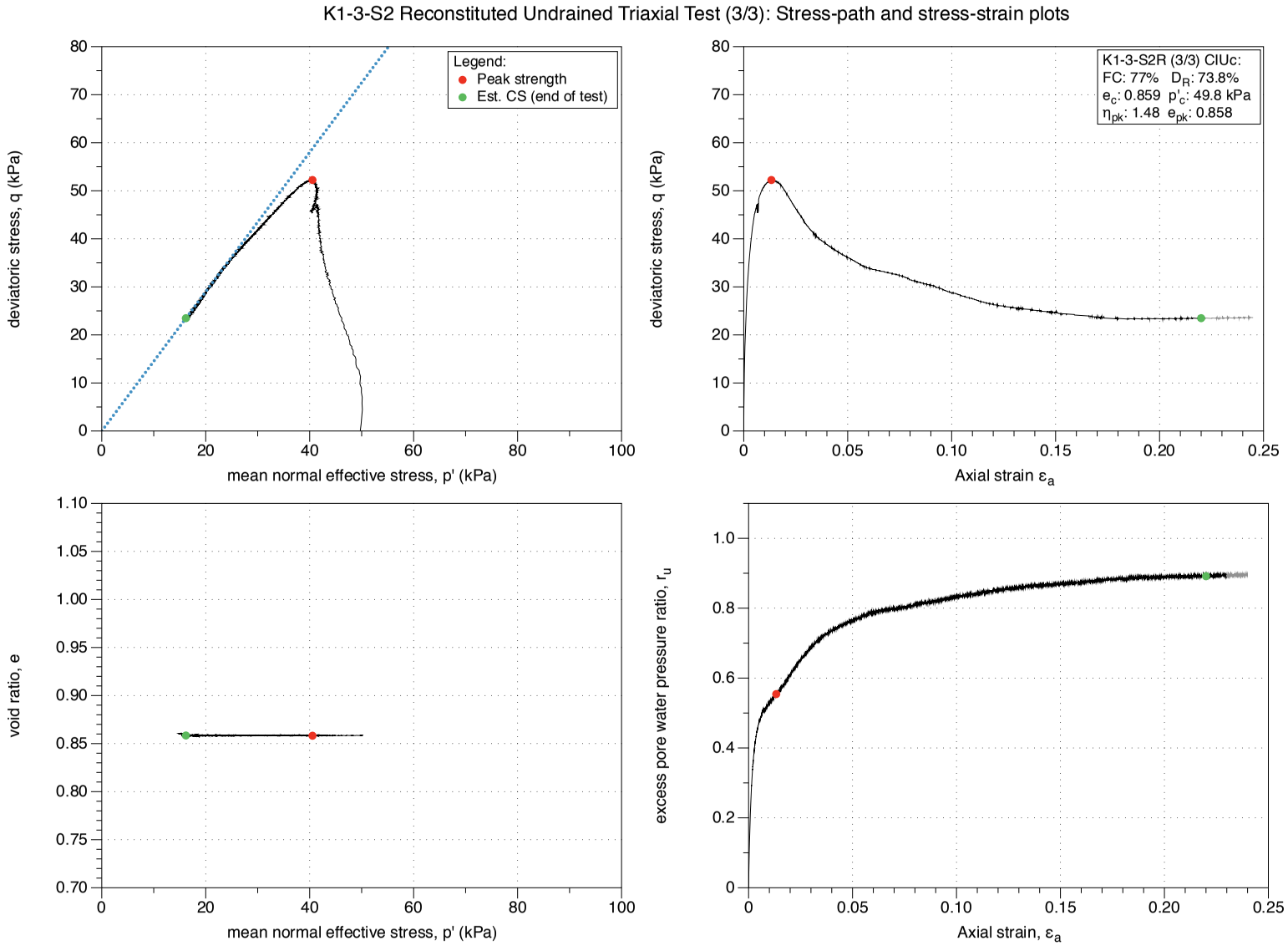

Figure 4.241: K1-3-S2 MT reconstituted sample (FC 77%), undrained monotonic triaxial test (CIU_C), test 3/3. Stress-path and stress-strain plots.

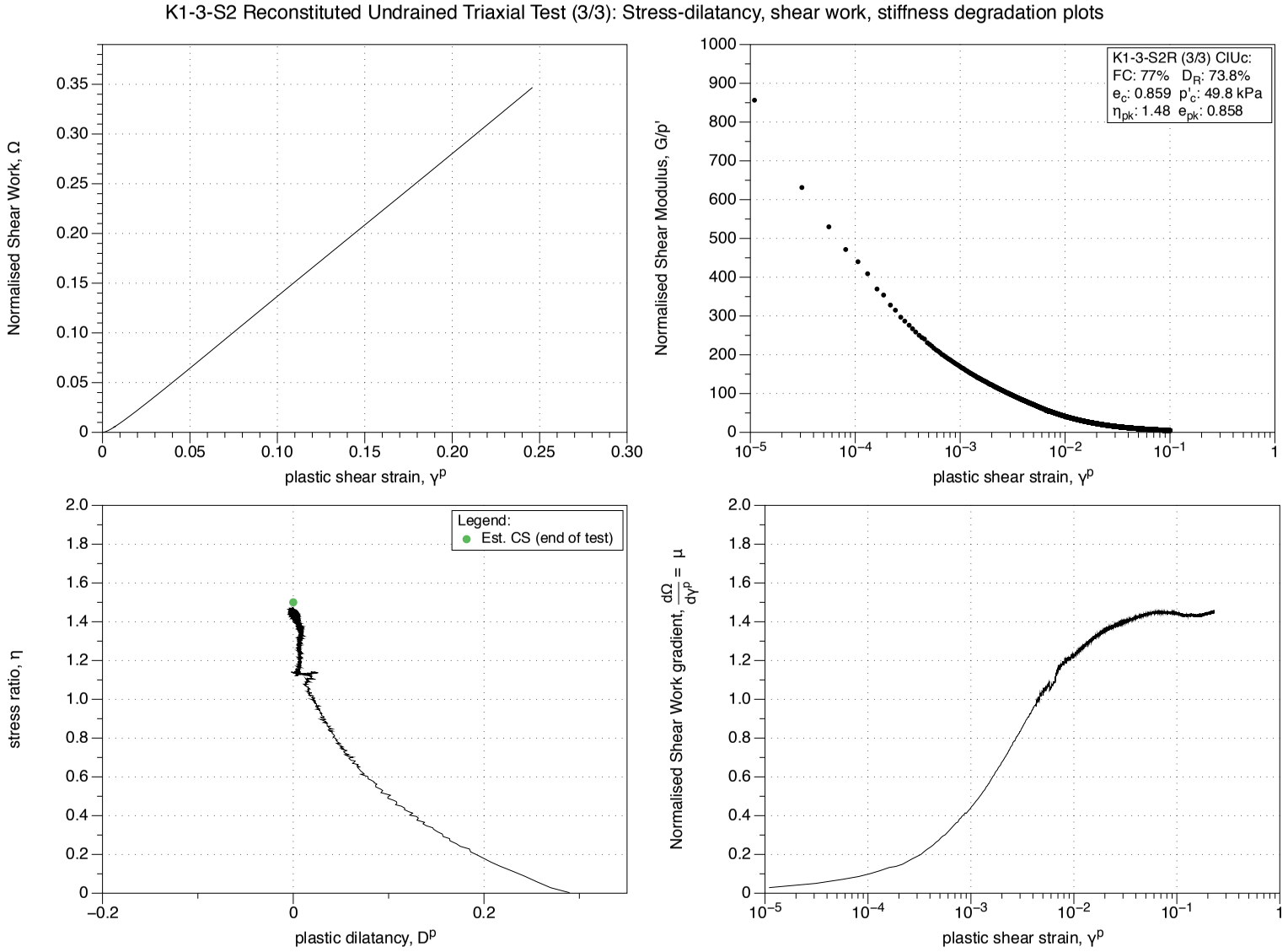

Figure 4.242: K1-3-S2 MT reconstituted sample (FC 77%), undrained monotonic triaxial test (CIU_C), test 3/3. Stress-dilatancy, shear work, stiffness degradation plots.

4.4.1.5 CID Tests on samples (FC 15 - 20 %)

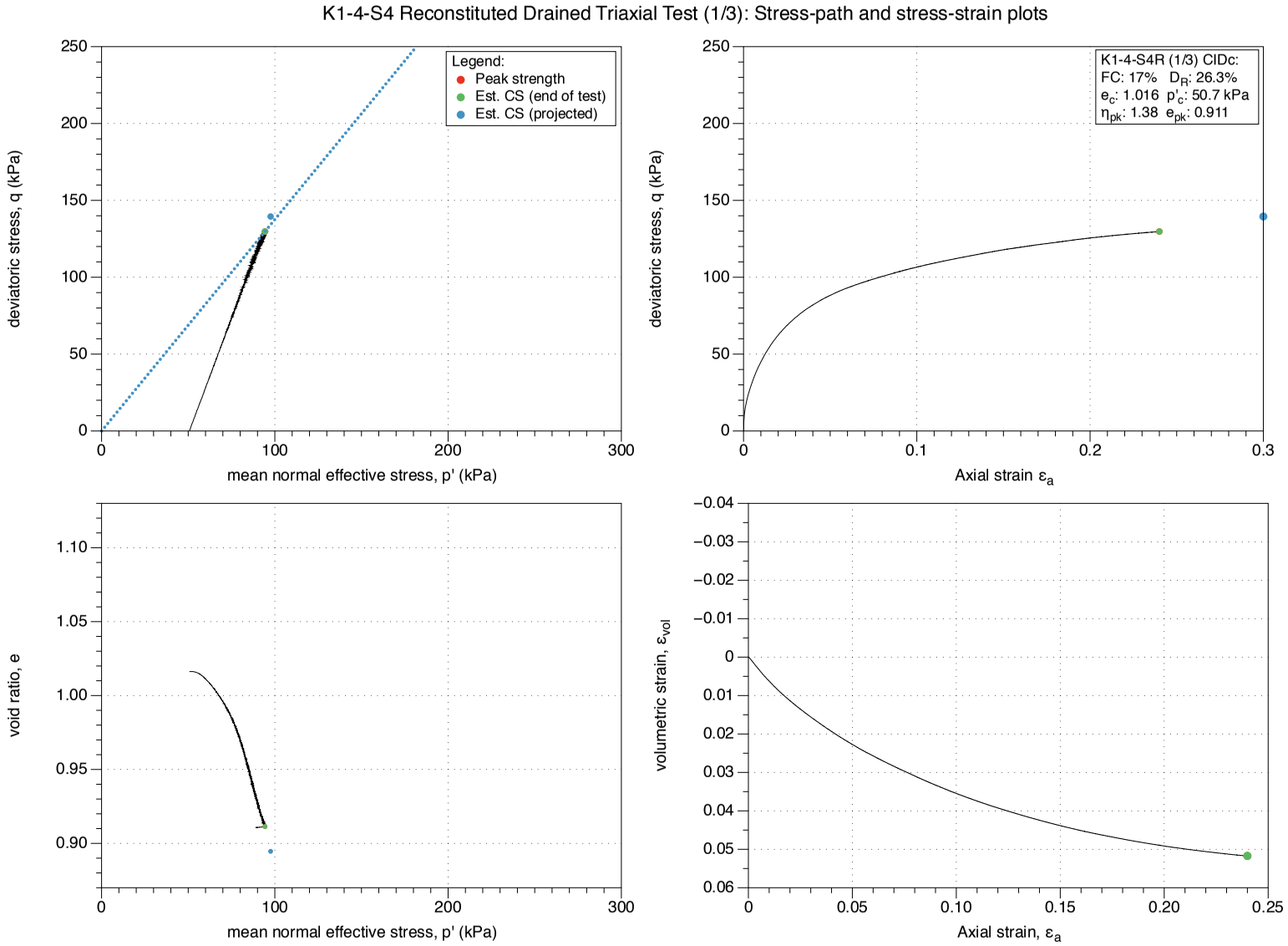

Figure 4.243: K1-4-S4 MT reconstituted sample (FC 15%), drained monotonic triaxial test (CID_C), test 1/3. Stress-path and stress-strain plots.

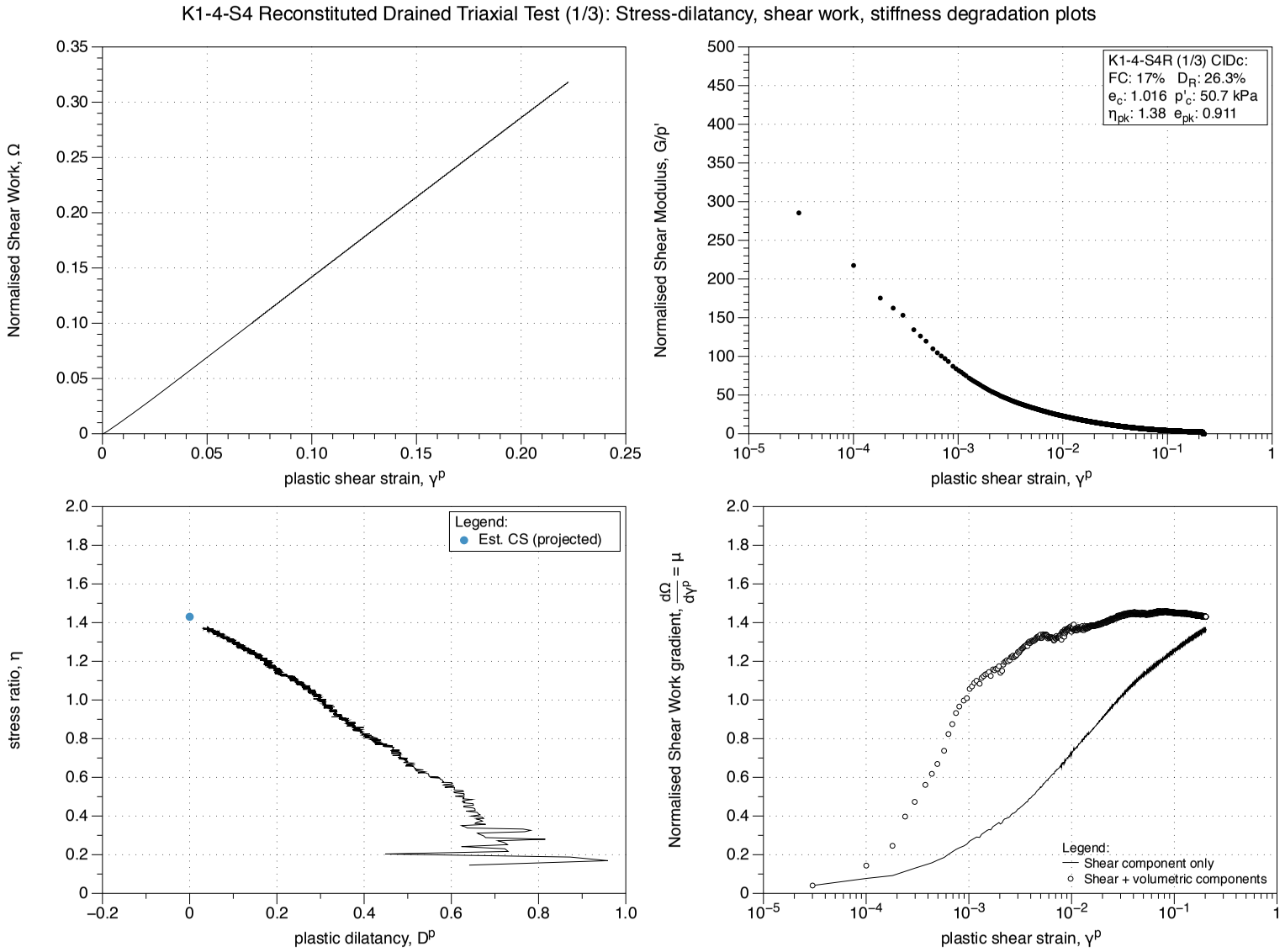

Figure 4.244: K1-4-S4 MT reconstituted sample (FC 15%), drained monotonic triaxial test (CID_C), test 1/3. Stress-dilatancy, shear work, stiffness degradation plots.

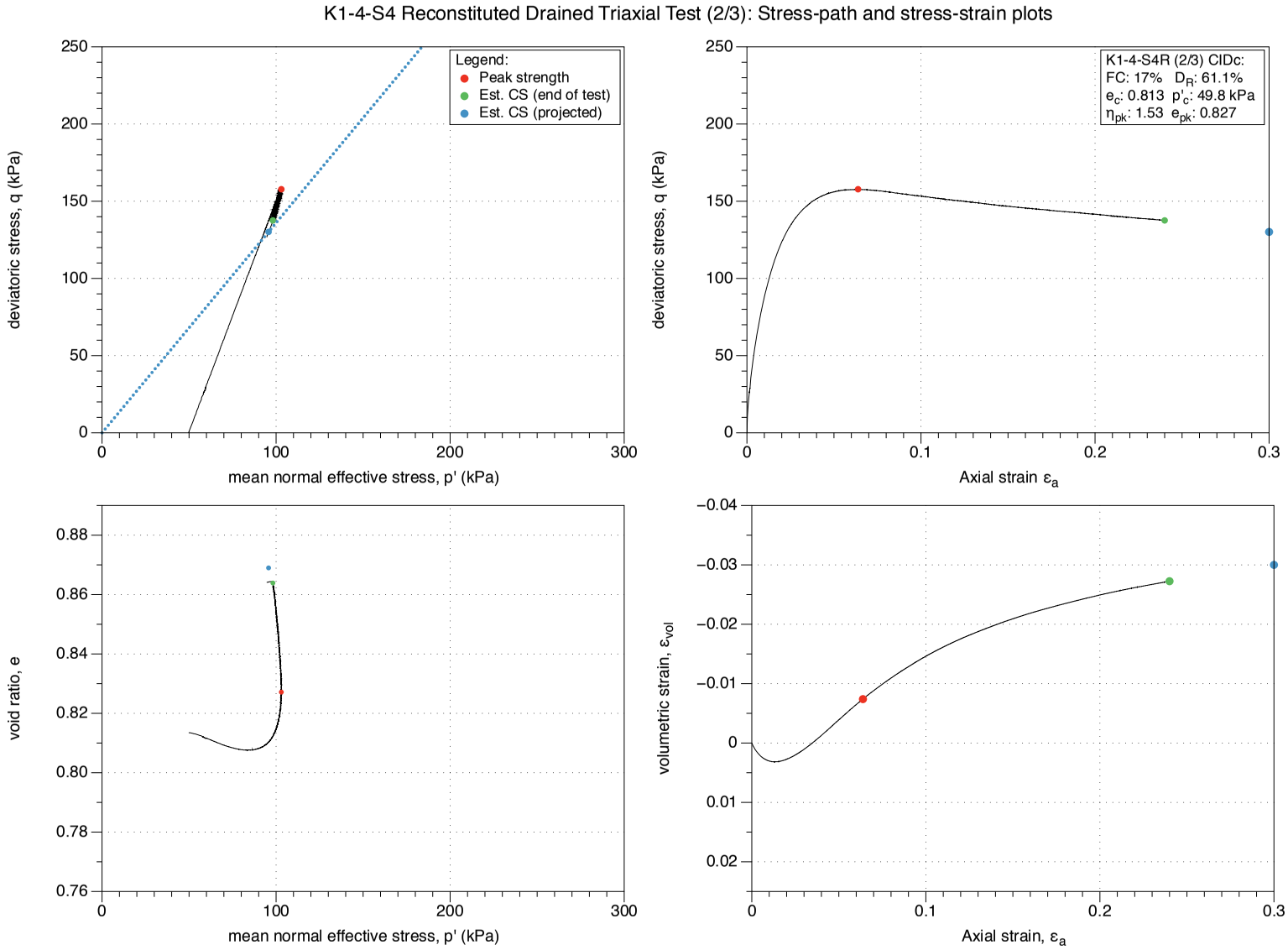

Figure 4.245: K1-4-S4 MT reconstituted sample (FC 15%), drained monotonic triaxial test (CID_C), test 2/3. Stress-path and stress-strain plots.

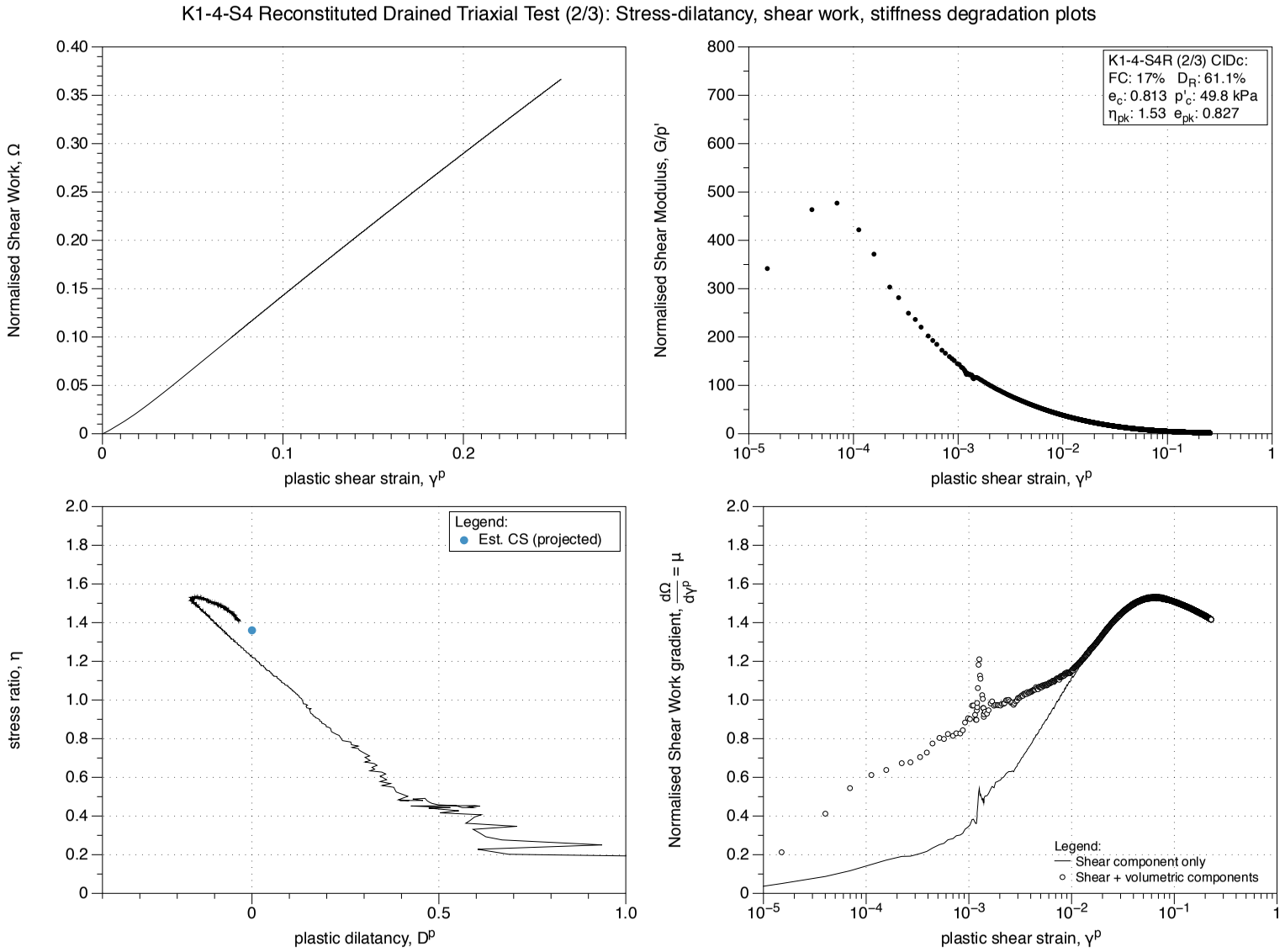

Figure 4.246: K1-4-S4 MT reconstituted sample (FC 15%), drained monotonic triaxial test (CID_C), test 2/3. Stress-dilatancy, shear work, stiffness degradation plots.

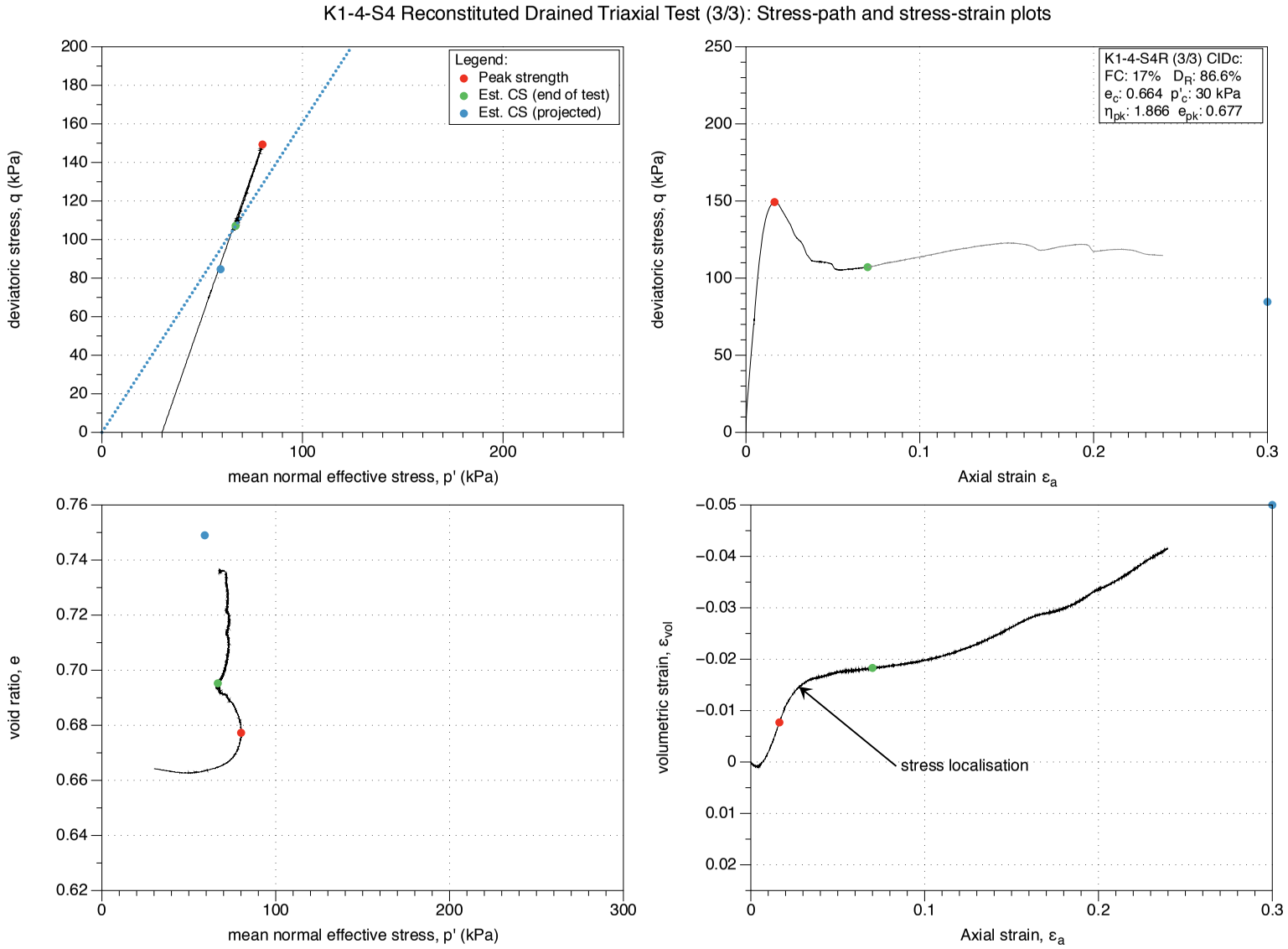

Figure 4.247: K1-4-S4 MT reconstituted sample (FC 15%), drained monotonic triaxial test (CID_C), test 3/3. Stress-path and stress-strain plots.

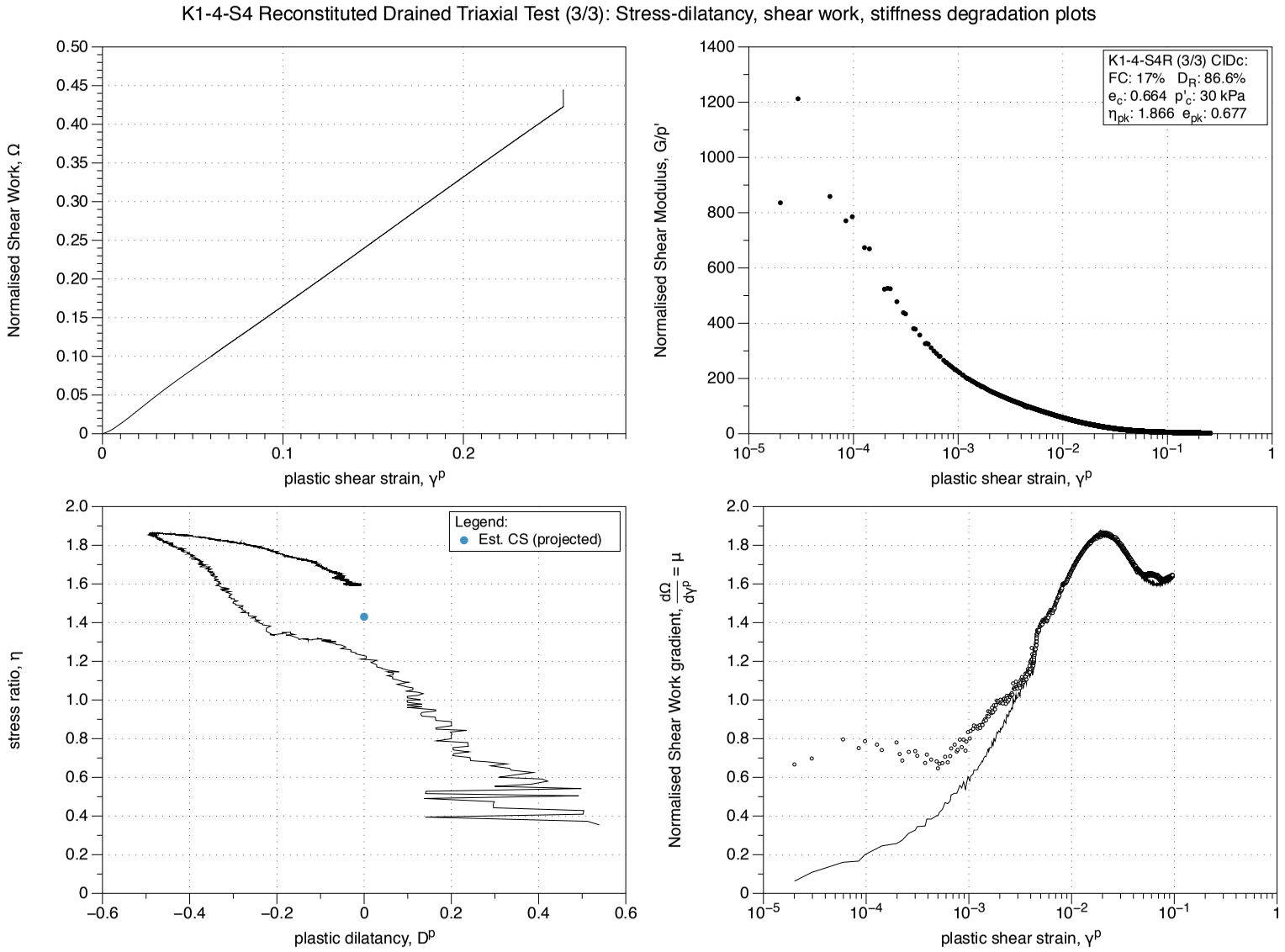

Figure 4.248: K1-4-S4 MT reconstituted sample (FC 15%), drained monotonic triaxial test (CID_C), test 3/3. Stress-dilatancy, shear work, stiffness degradation plots.

4.4.1.6 CIU Tests on samples (FC 15 - 20 %)

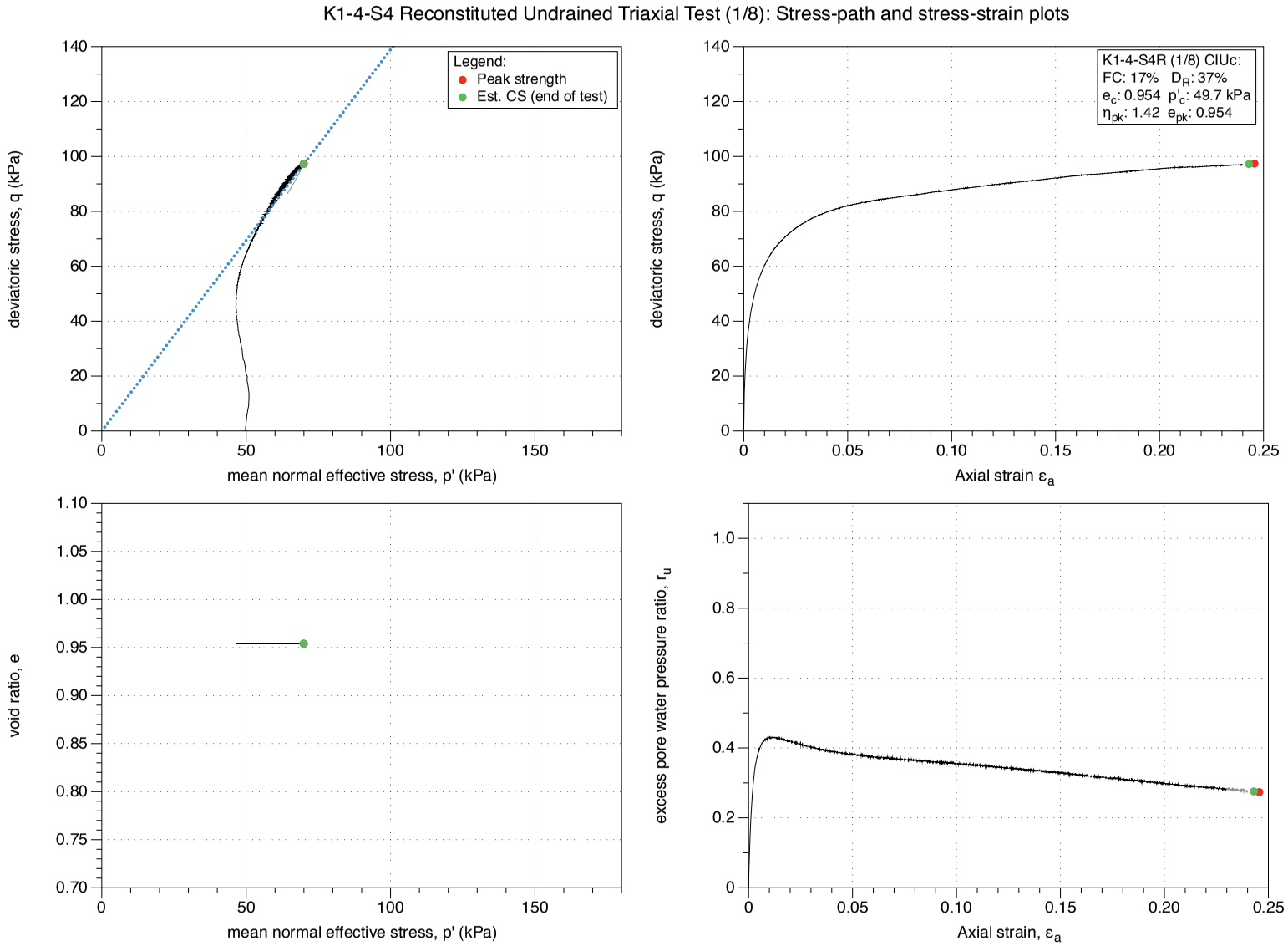

Figure 4.249: K1-4-S4 MT reconstituted sample (FC 17%), undrained monotonic triaxial test (CIU_C), test 1/8. Stress-path and stress-strain plots.

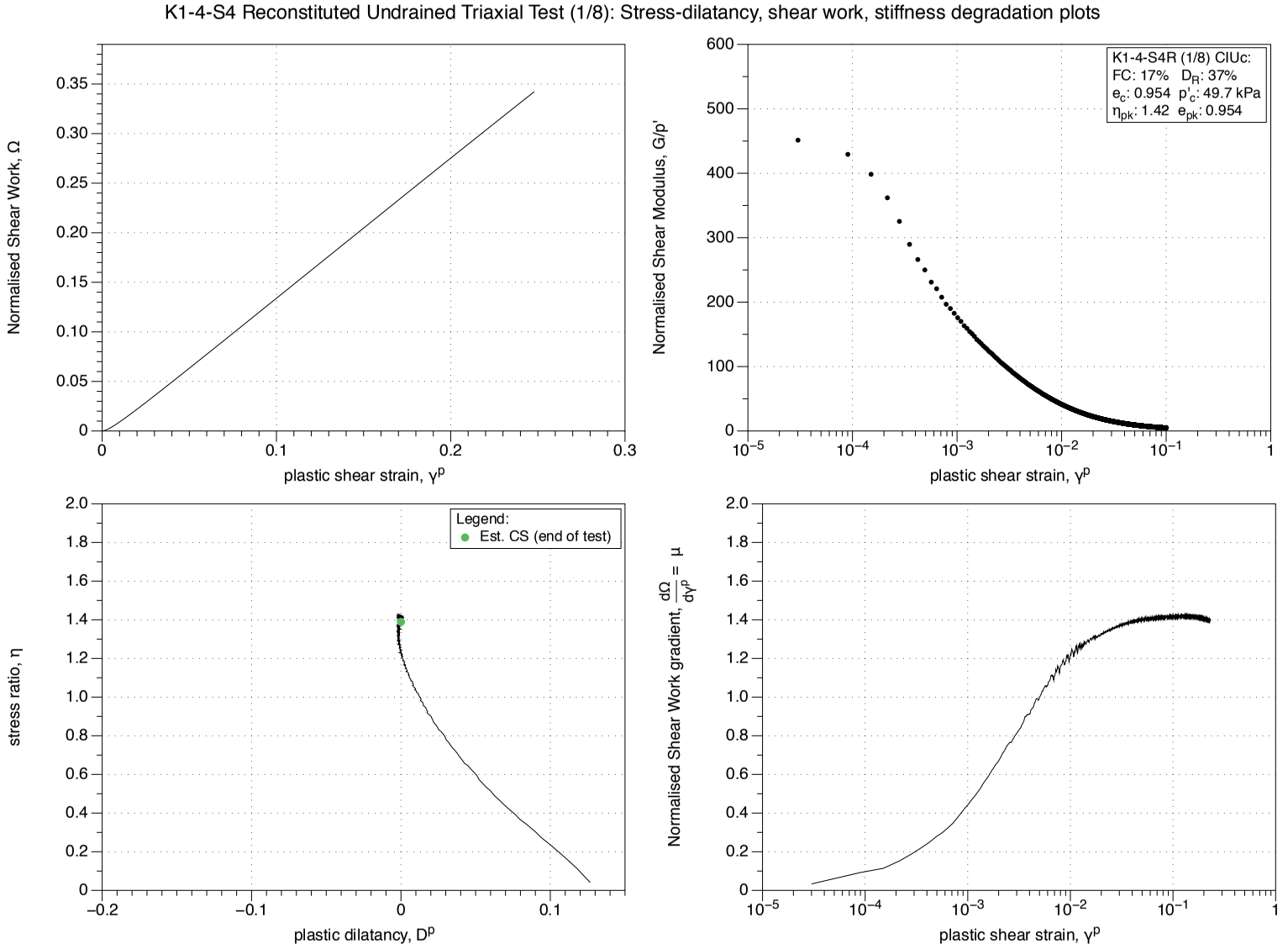

Figure 4.250: K1-4-S4 MT reconstituted sample (FC 17%), undrained monotonic triaxial test (CIU_C), test 1/8. Stress-dilatancy, shear work, stiffness degradation plots.

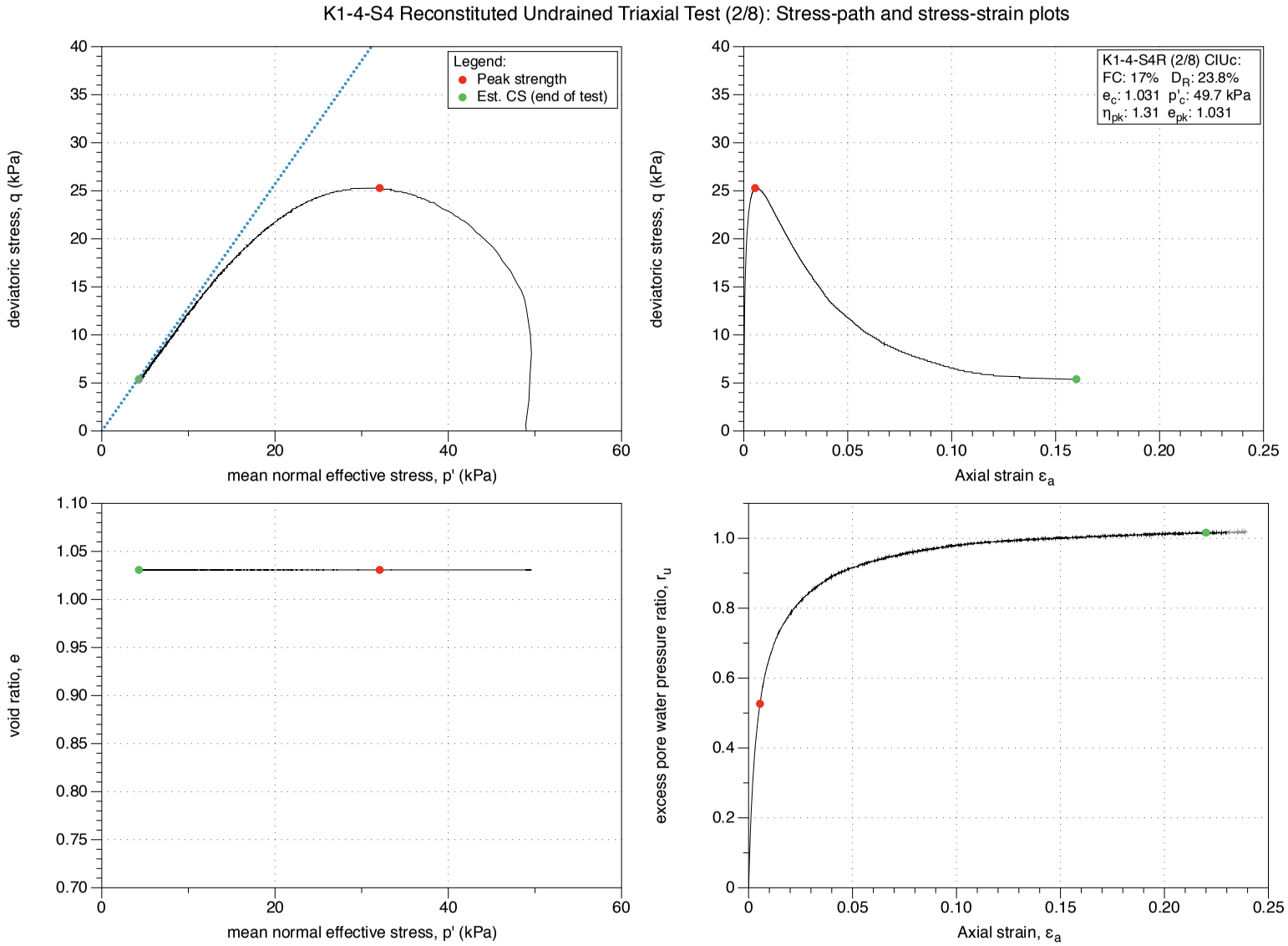

Figure 4.251: K1-4-S4 MT reconstituted sample (FC 17%), undrained monotonic triaxial test (CIU_C), test 2/8. Stress-path and stress-strain plots.

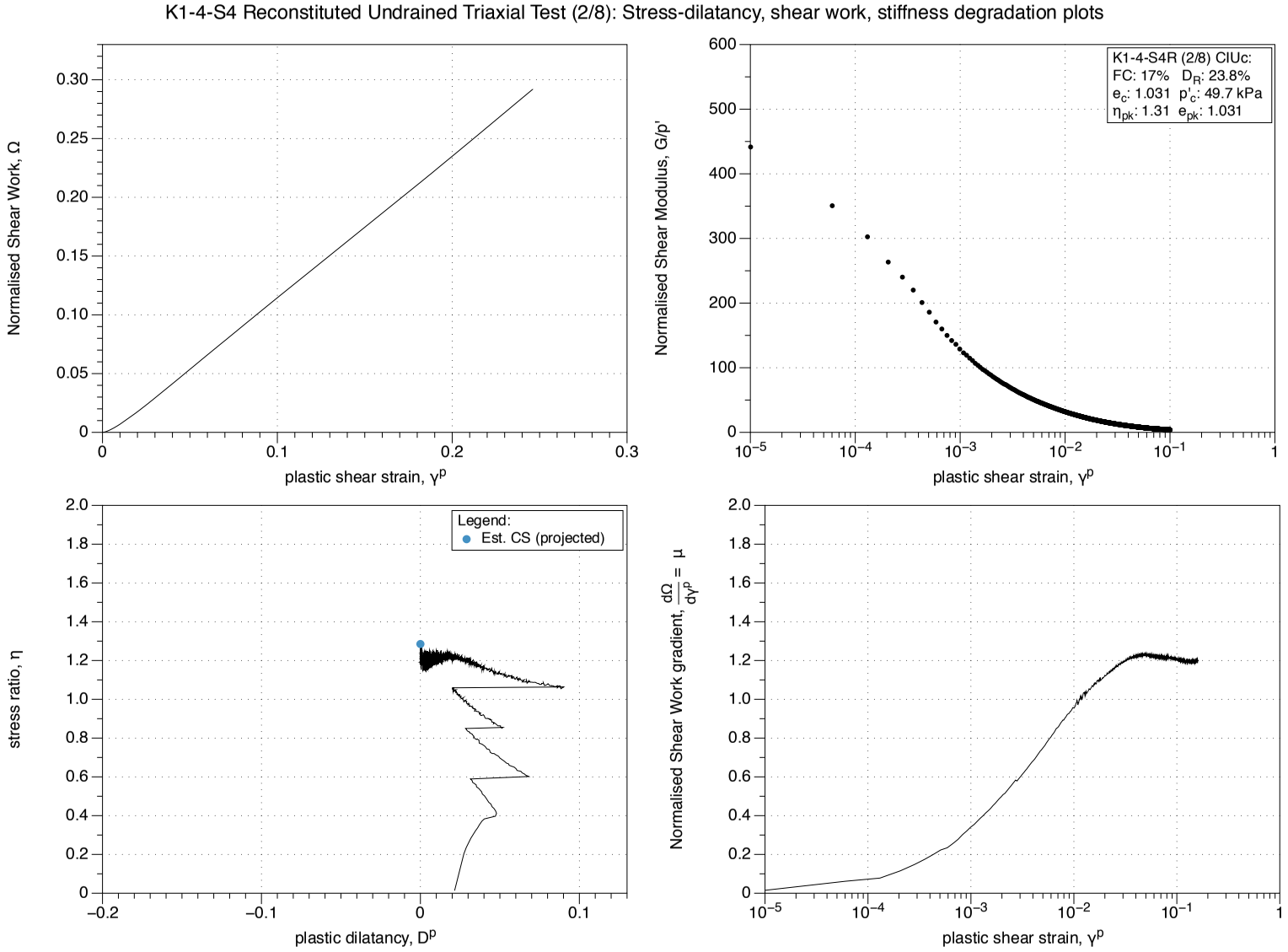

Figure 4.252: K1-4-S4 MT reconstituted sample (FC 17%), undrained monotonic triaxial test (CIU_C), test 2/8. Stress-dilatancy, shear work, stiffness degradation plots.

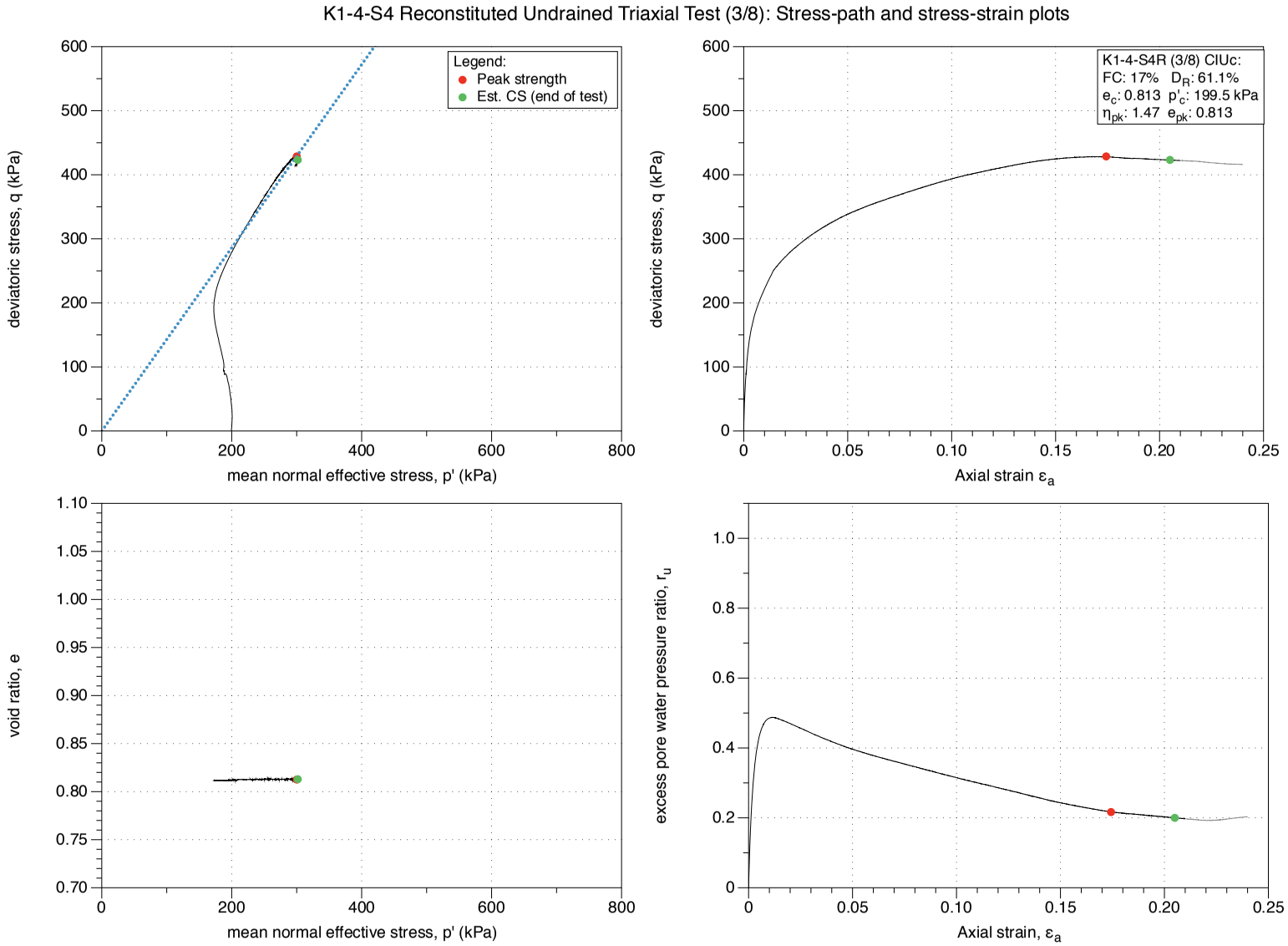

Figure 4.253: K1-4-S4 MT reconstituted sample (FC 17%), undrained monotonic triaxial test (CIU_C), test 3/8. Stress-path and stress-strain plots.

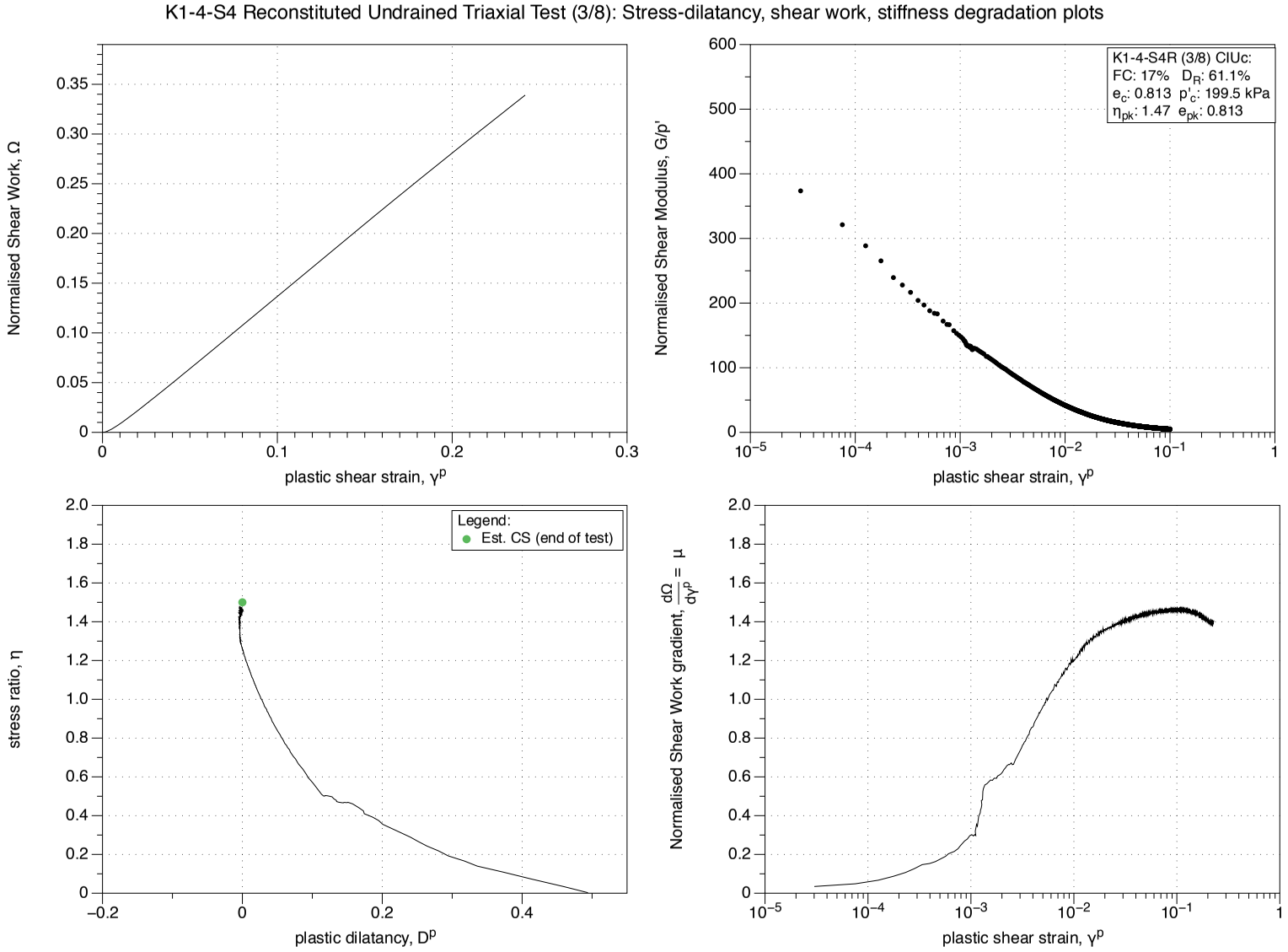

Figure 4.254: K1-4-S4 MT reconstituted sample (FC 17%), undrained monotonic triaxial test (CIU_C), test 3/8. Stress-dilatancy, shear work, stiffness degradation plots.

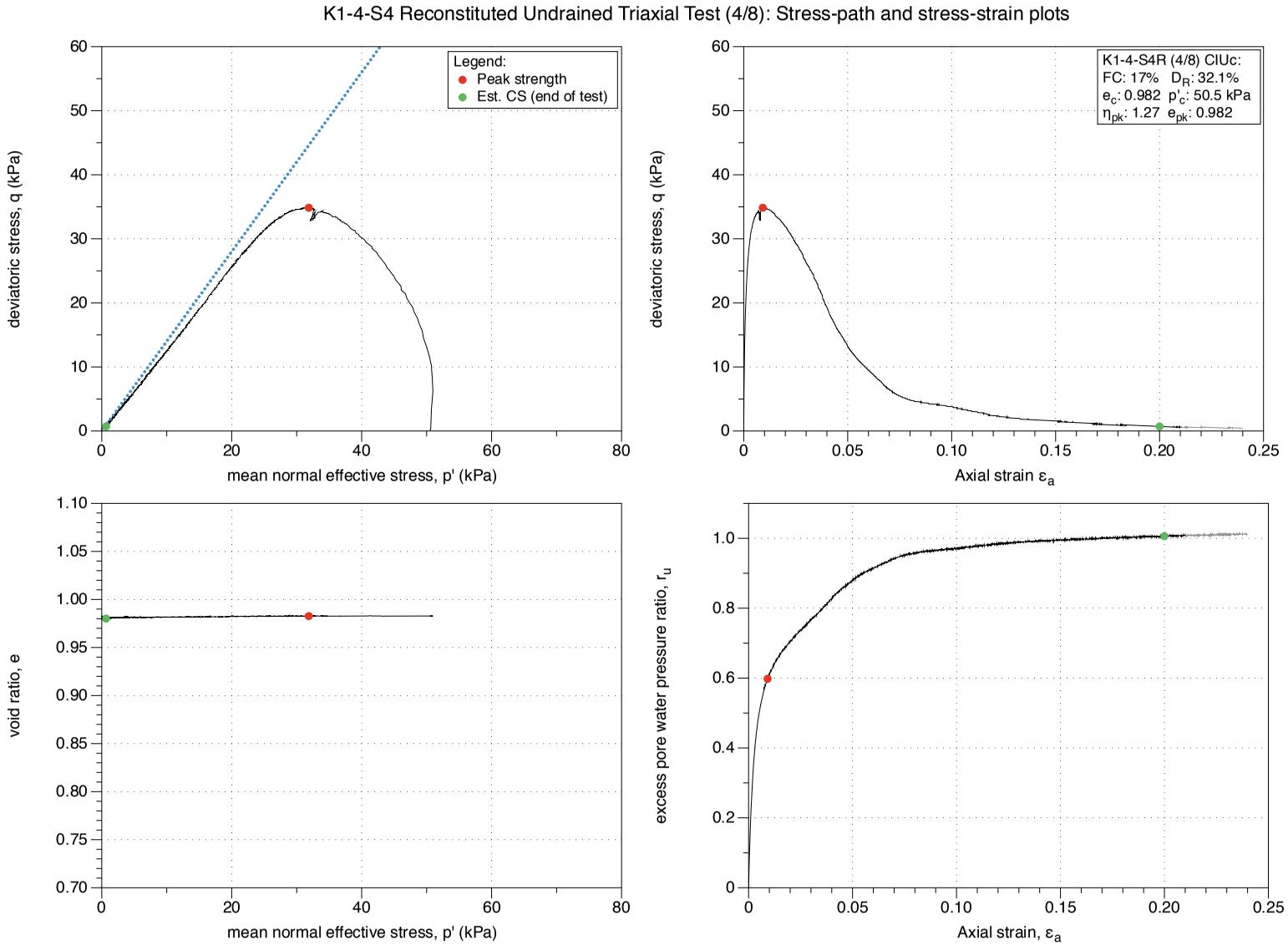

Figure 4.255: K1-4-S4 MT reconstituted sample (FC 17%), undrained monotonic triaxial test (CIU_C), test 4/8. Stress-path and stress-strain plots.

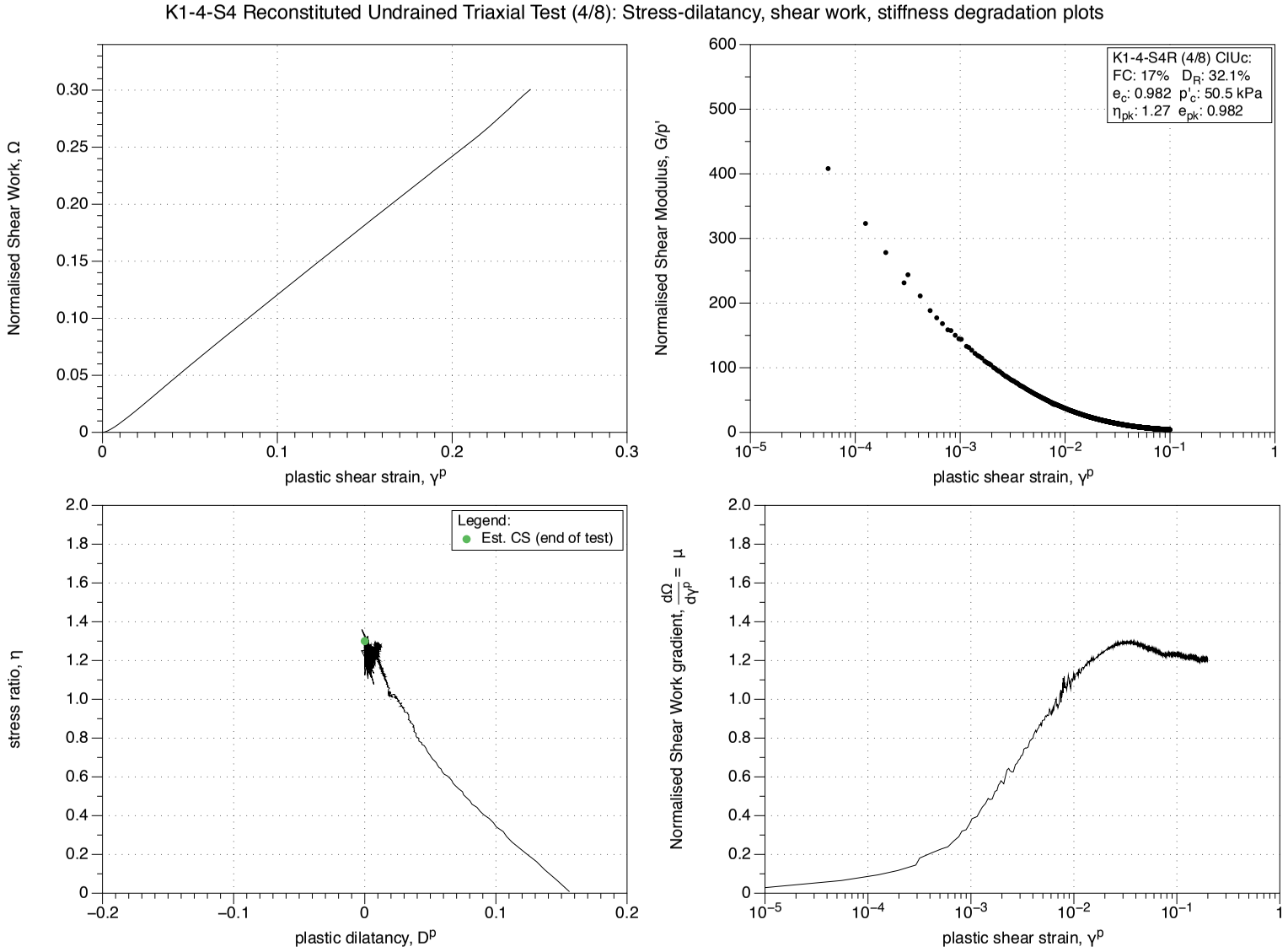

Figure 4.256: K1-4-S4 MT reconstituted sample (FC 17%), undrained monotonic triaxial test (CIU_C), test 4/8. Stress-dilatancy, shear work, stiffness degradation plots.

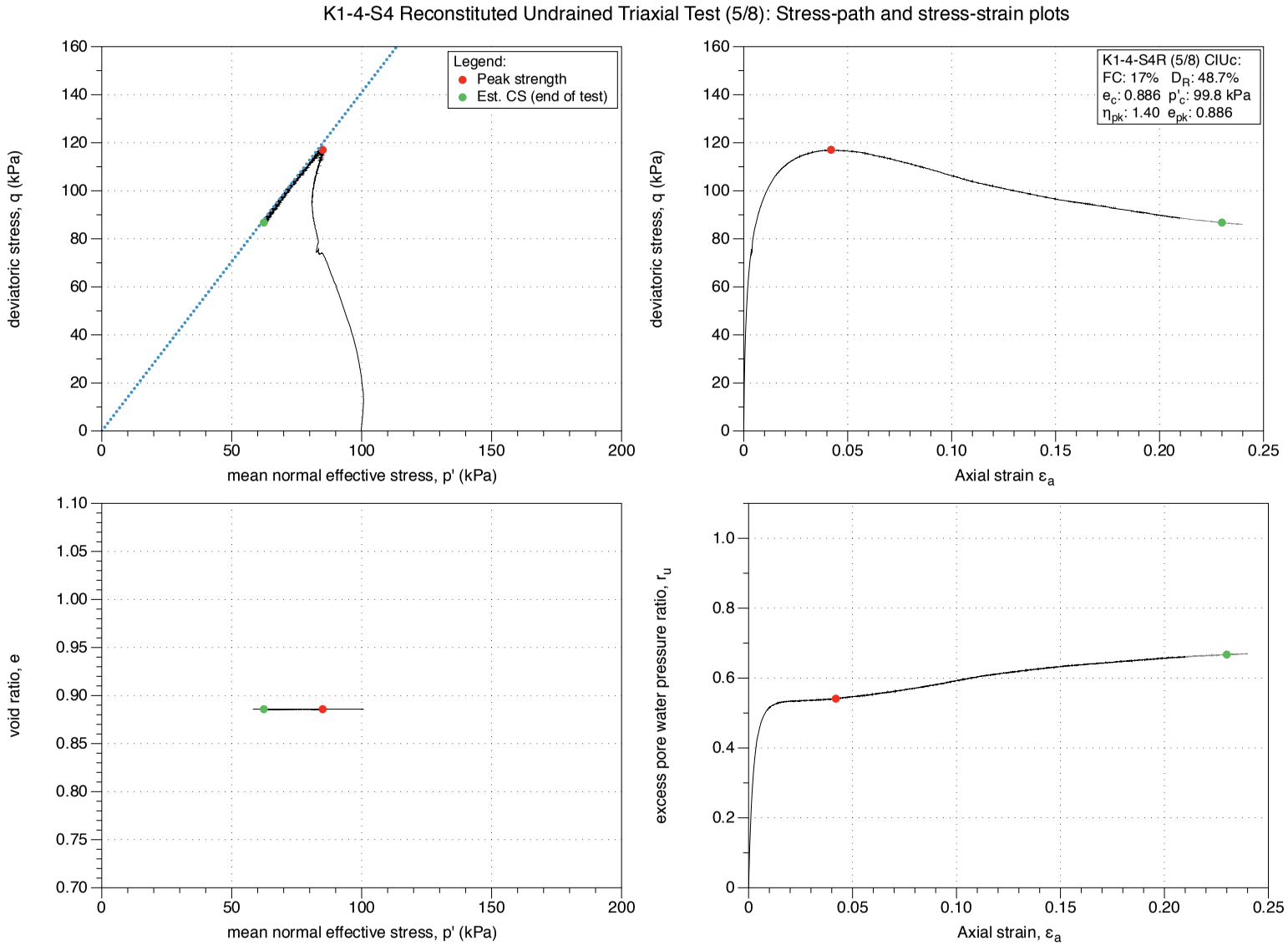

Figure 4.257: K1-4-S4 MT reconstituted sample (FC 17%), undrained monotonic triaxial test (CIU_C), test 5/8. Stress-path and stress-strain plots.

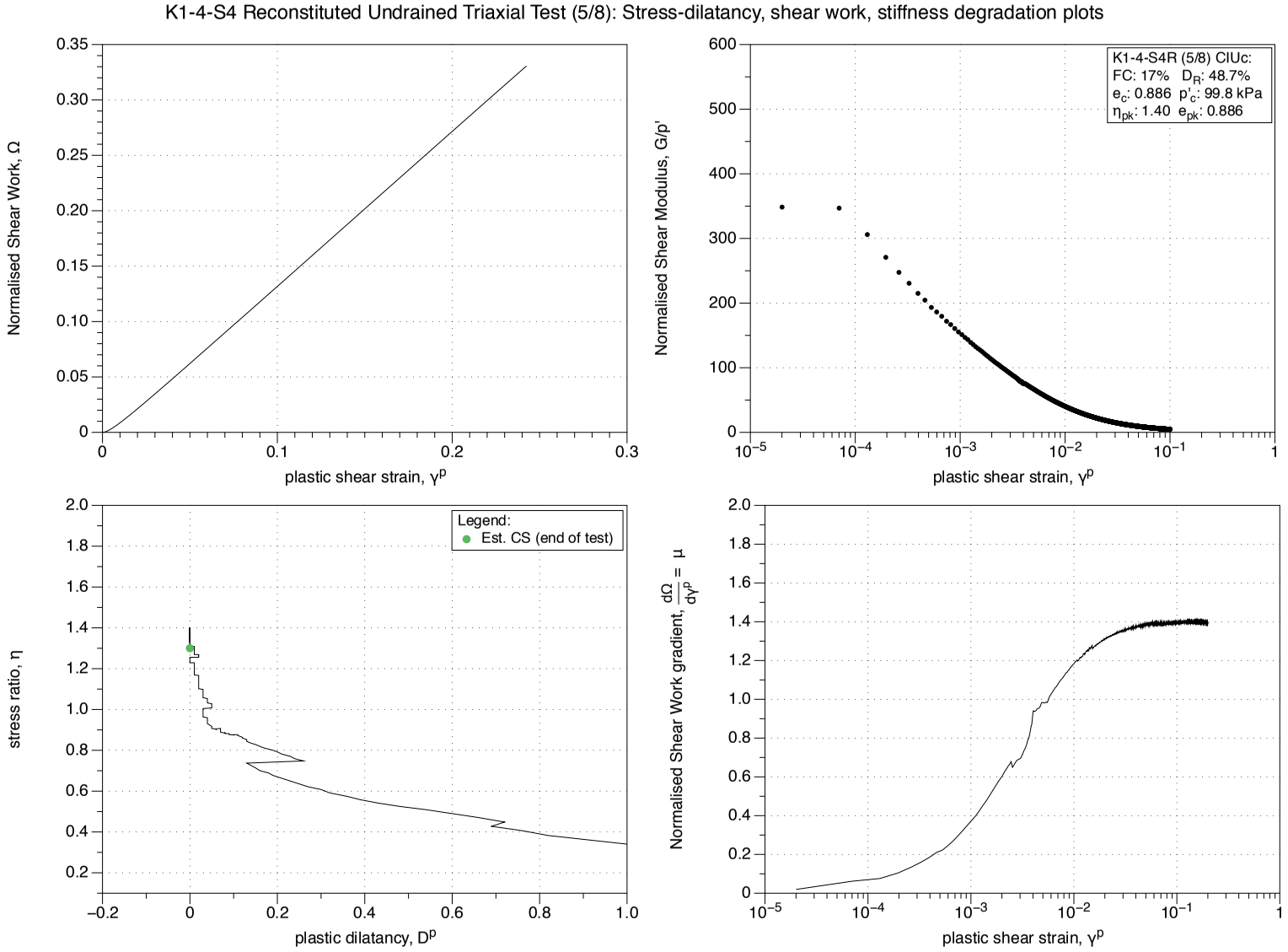

Figure 4.258: K1-4-S4 MT reconstituted sample (FC 17%), undrained monotonic triaxial test (CIU_C), test 5/8. Stress-dilatancy, shear work, stiffness degradation plots.

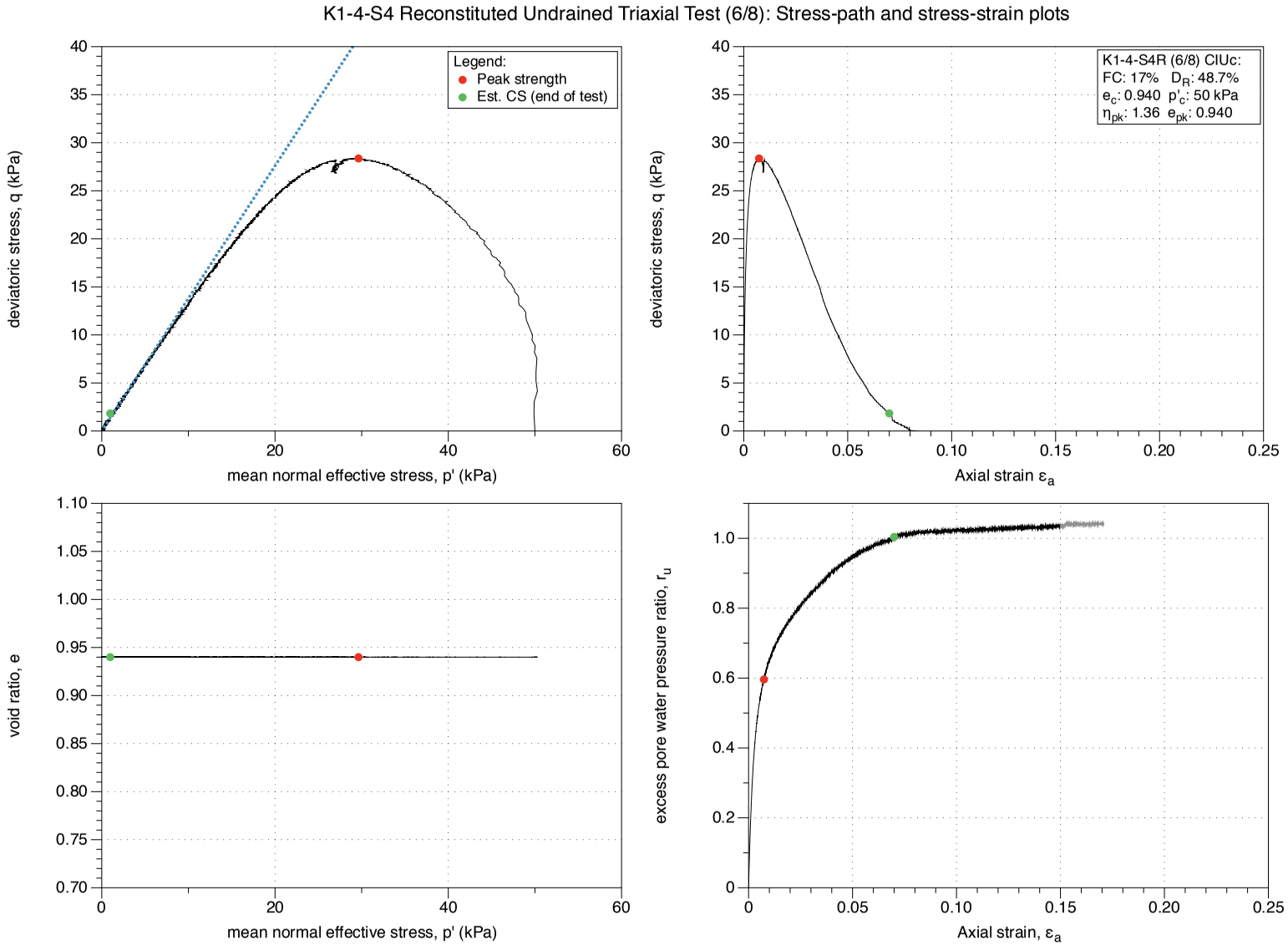

Figure 4.259: K1-4-S4 MT reconstituted sample (FC 17%), undrained monotonic triaxial test (CIU_C), test 6/8. Stress-path and stress-strain plots.

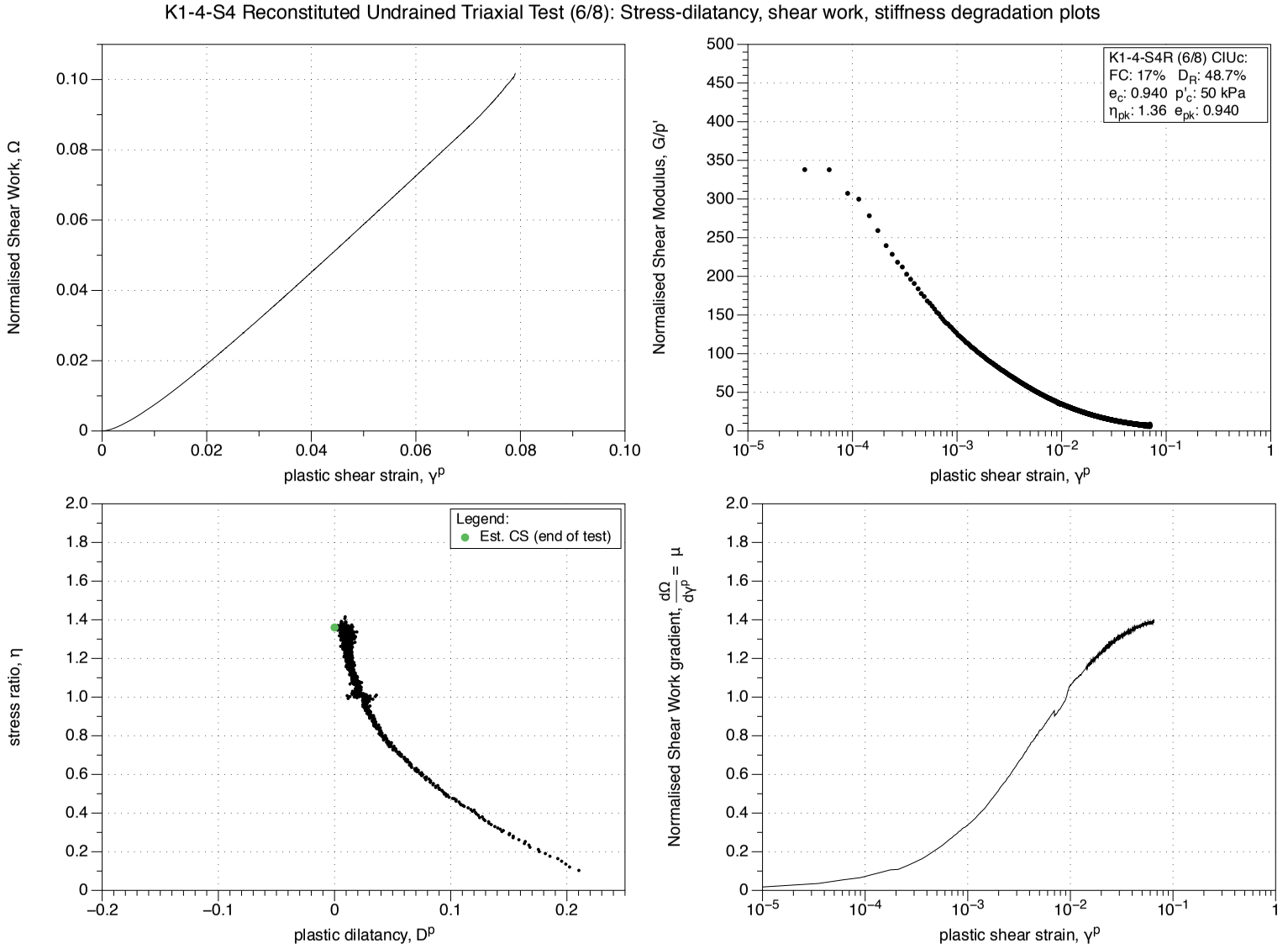

Figure 4.260: K1-4-S4 MT reconstituted sample (FC 17%), undrained monotonic triaxial test (CIU_C), test 6/8. Stress-dilatancy, shear work, stiffness degradation plots.

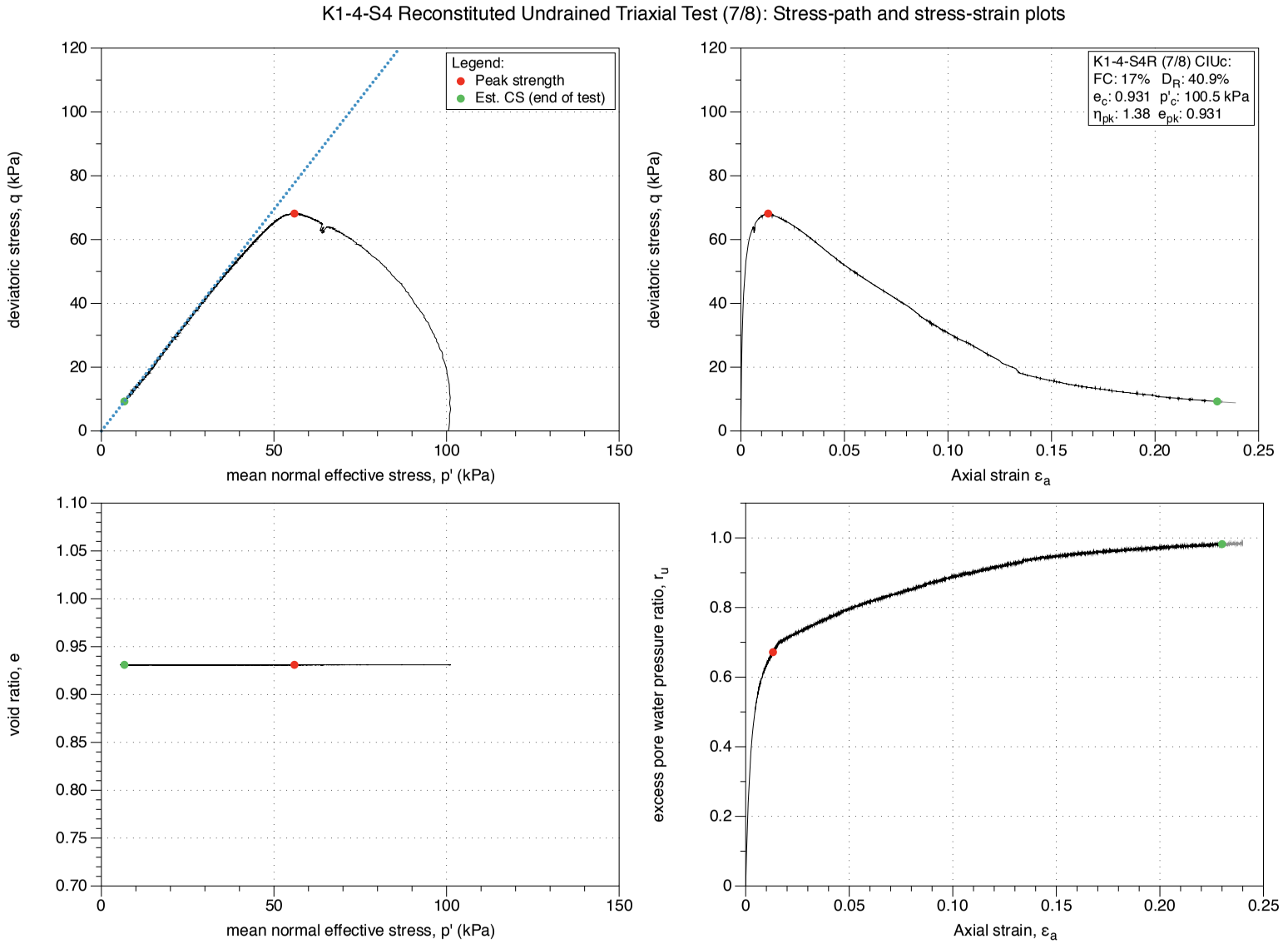

Figure 4.261: K1-4-S4 MT reconstituted sample (FC 17%), undrained monotonic triaxial test (CIU_C), test 7/8. Stress-path and stress-strain plots.

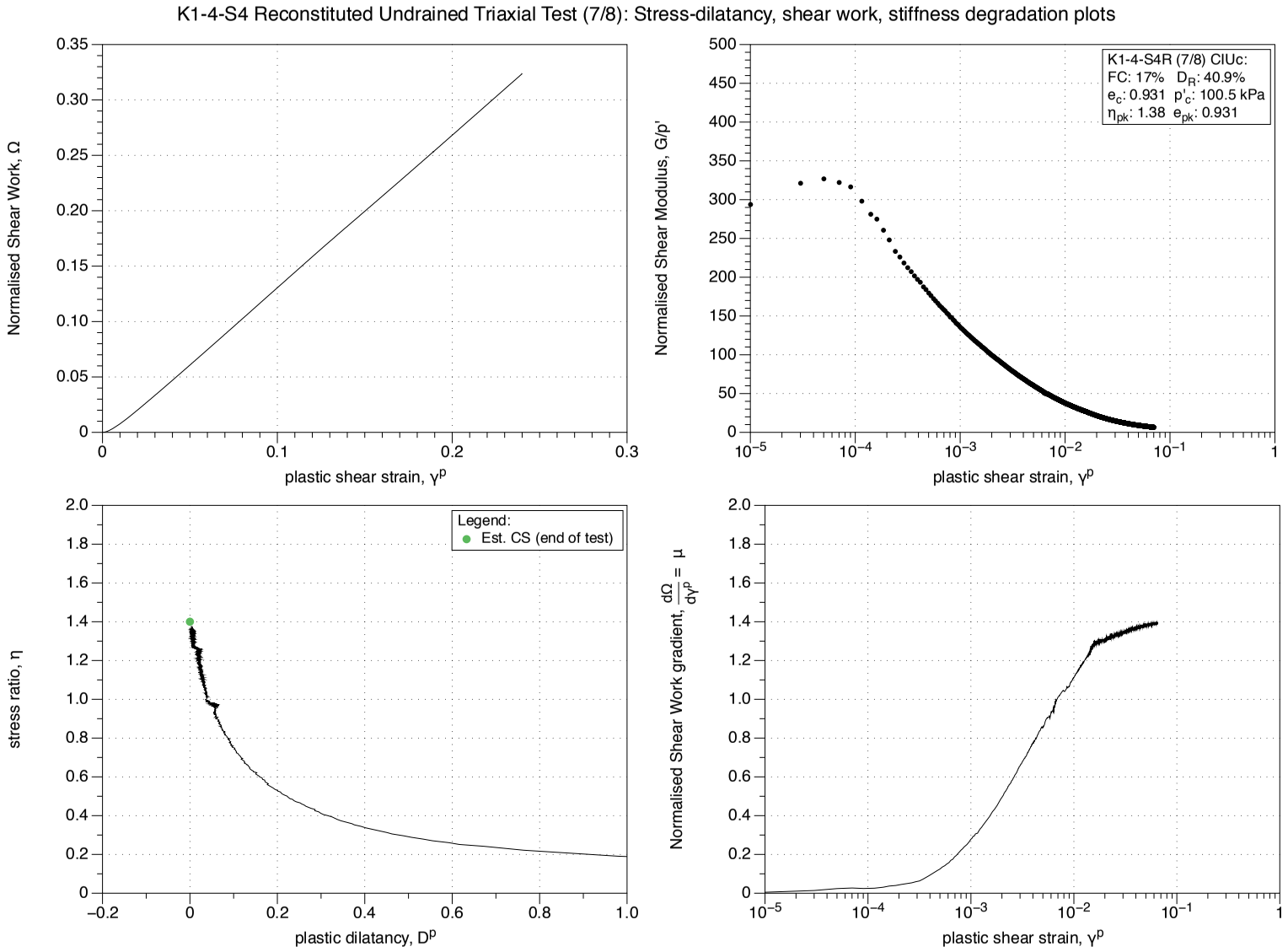

Figure 4.262: K1-4-S4 MT reconstituted sample (FC 17%), undrained monotonic triaxial test (CIU_C), test 7/8. Stress-dilatancy, shear work, stiffness degradation plots.

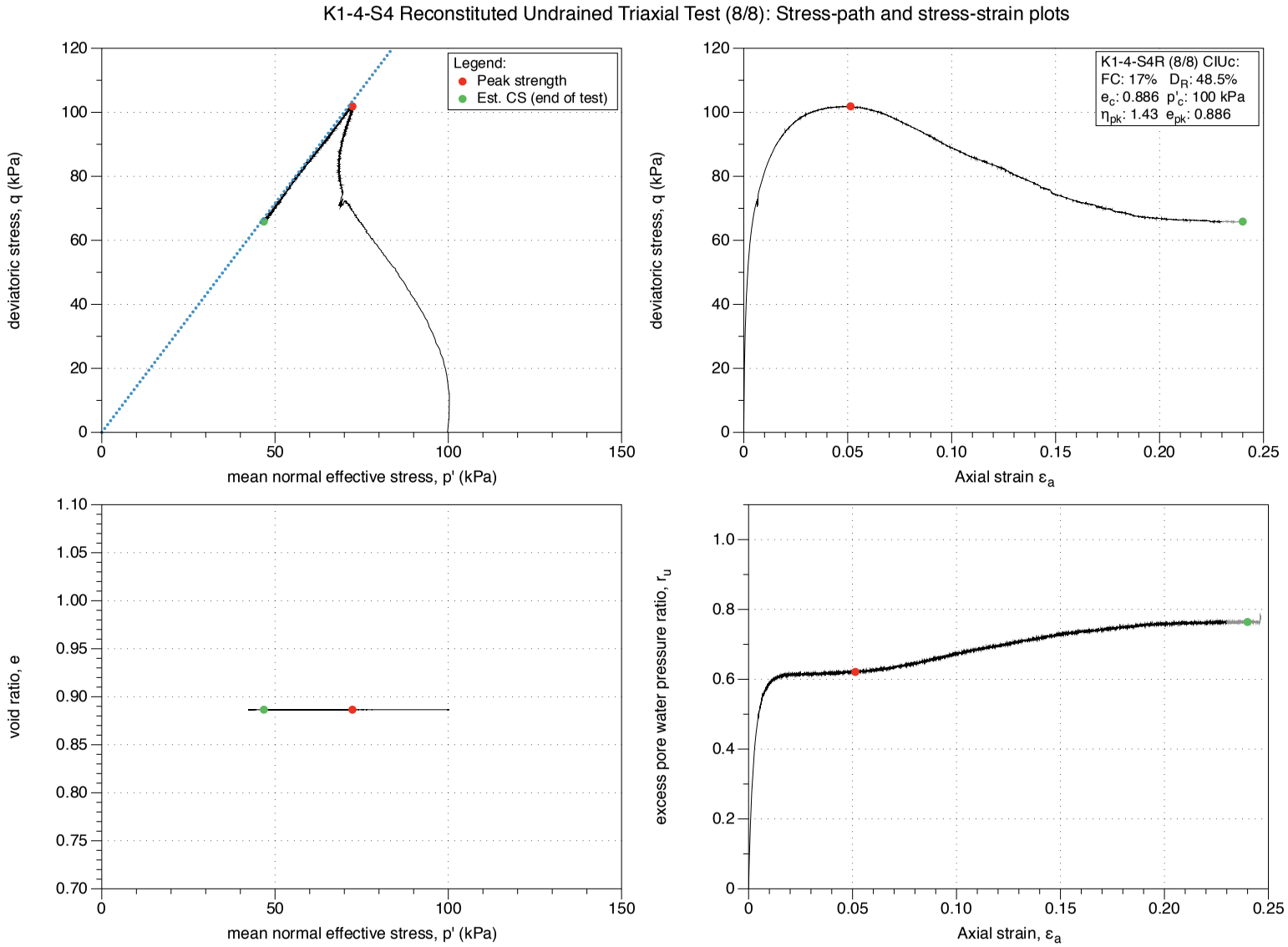

Figure 4.263: K1-4-S4 MT reconstituted sample (FC 17%), undrained monotonic triaxial test (CIU_C), test 8/8. Stress-path and stress-strain plots.

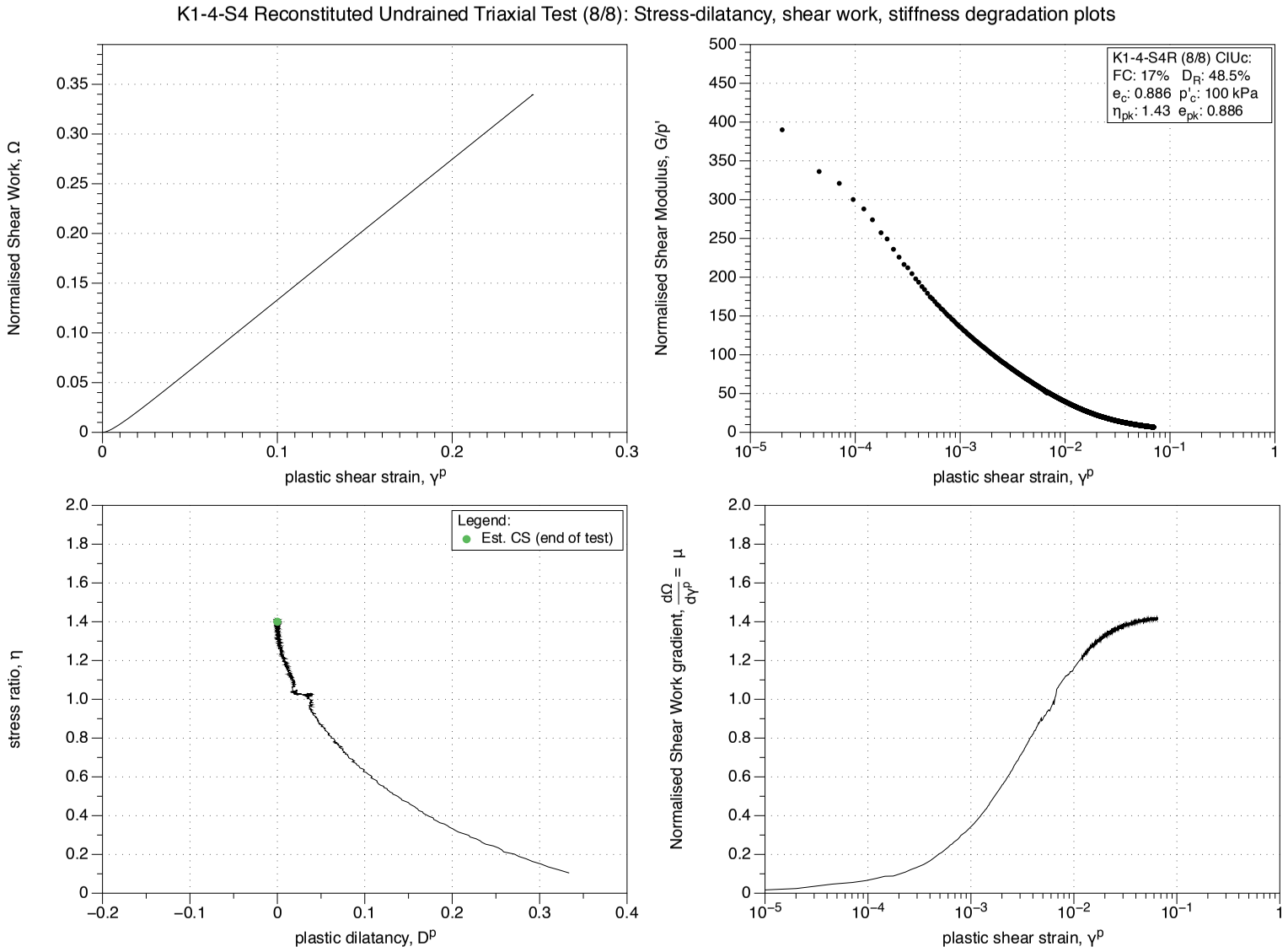

Figure 4.264: K1-4-S4 MT reconstituted sample (FC 17%), undrained monotonic triaxial test (CIU_C), test 8/8. Stress-dilatancy, shear work, stiffness degradation plots.

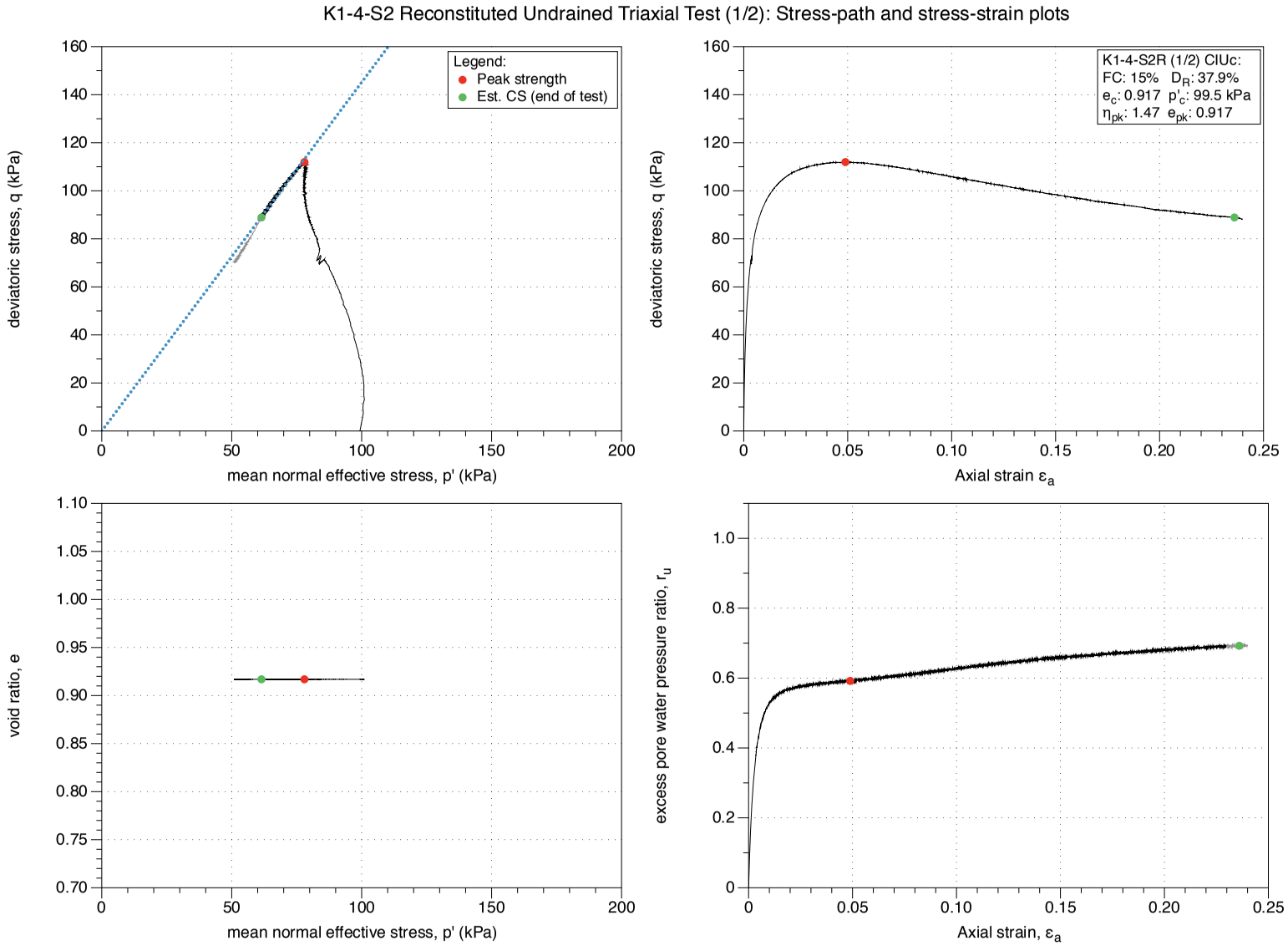

Figure 4.265: K1-4-S2 MT reconstituted sample (FC 15%), undrained monotonic triaxial test (CIU_C), test 1/3. Stress-path and stress-strain plots.

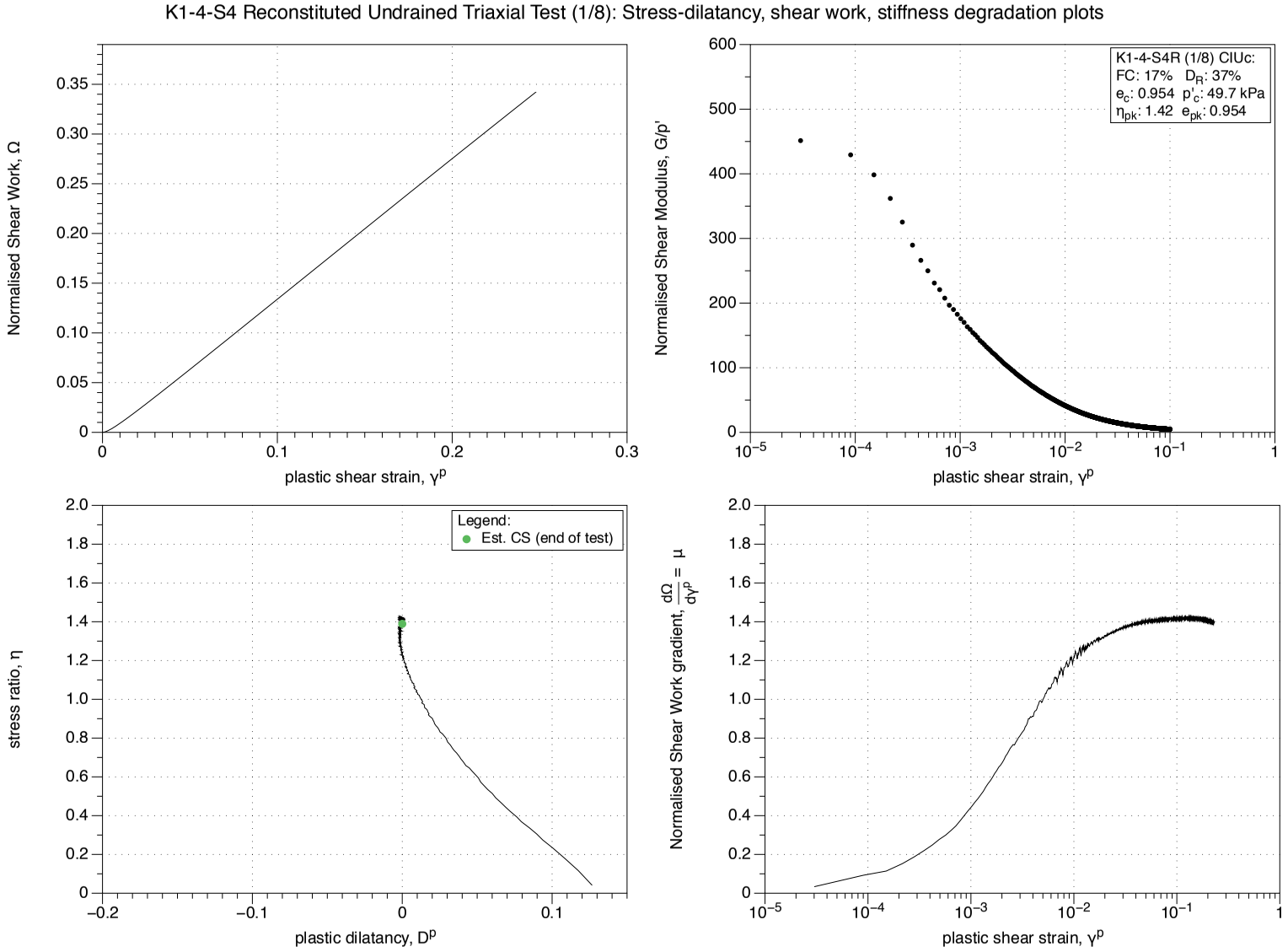

Figure 4.266: K1-4-S2 MT reconstituted sample (FC 15%), undrained monotonic triaxial test (CIU_C), test 1/3. Stress-dilatancy, shear work, stiffness degradation plots.

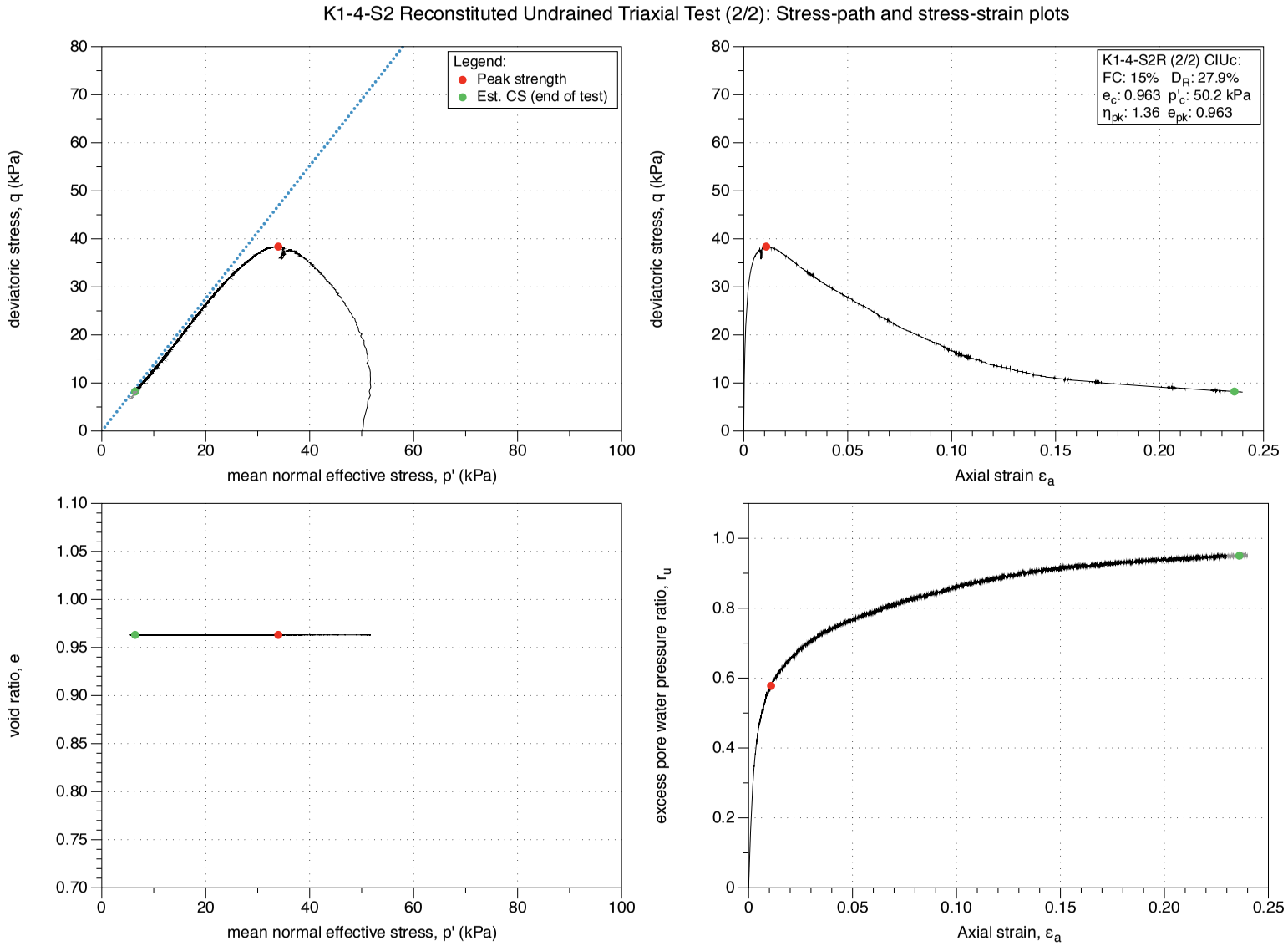

Figure 4.267: K1-4-S2 MT reconstituted sample (FC 15%), undrained monotonic triaxial test (CIU_C), test 2/3. Stress-path and stress-strain plots.

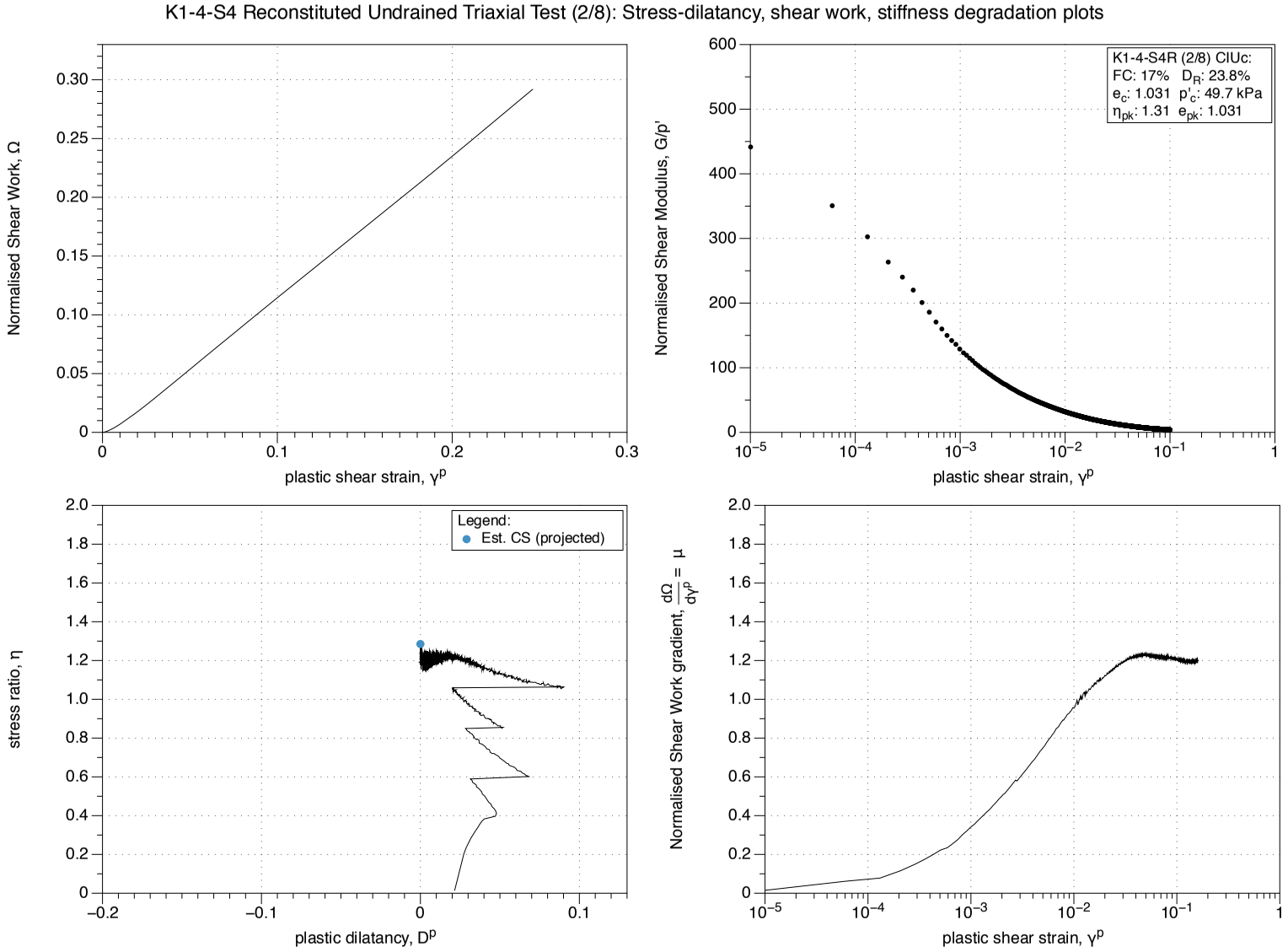

Figure 4.268: K1-4-S2 MT reconstituted sample (FC 15%), undrained monotonic triaxial test (CIU_C), test 2/3. Stress-dilatancy, shear work, stiffness degradation plots.

4.4.1.7 CID Tests on samples (FC 0 - 5 %)

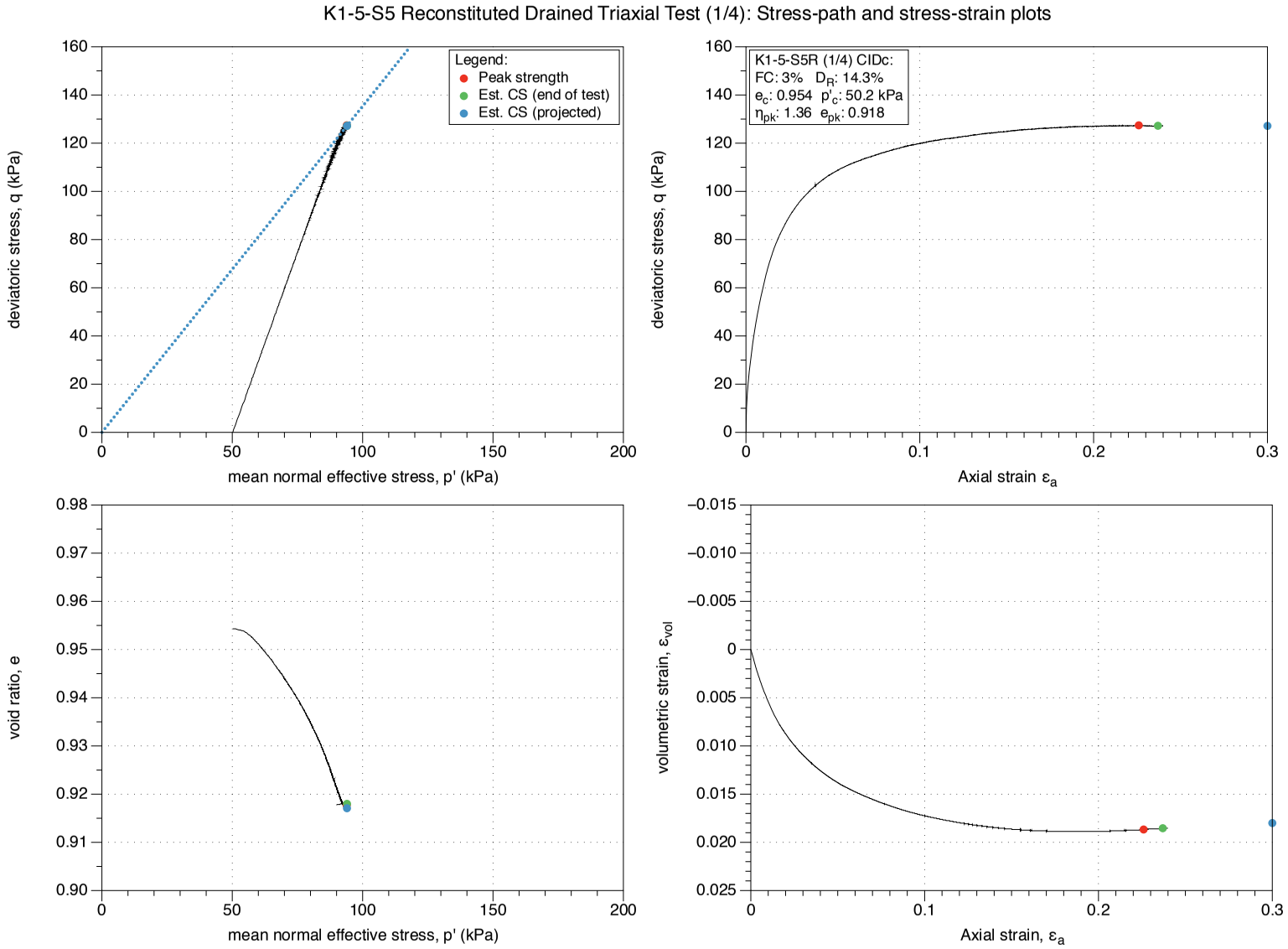

Figure 4.269: K1-5-S5 MT reconstituted sample (FC 1%), drained monotonic triaxial test (CID_C), test 1/4. Stress-path and stress-strain plots.

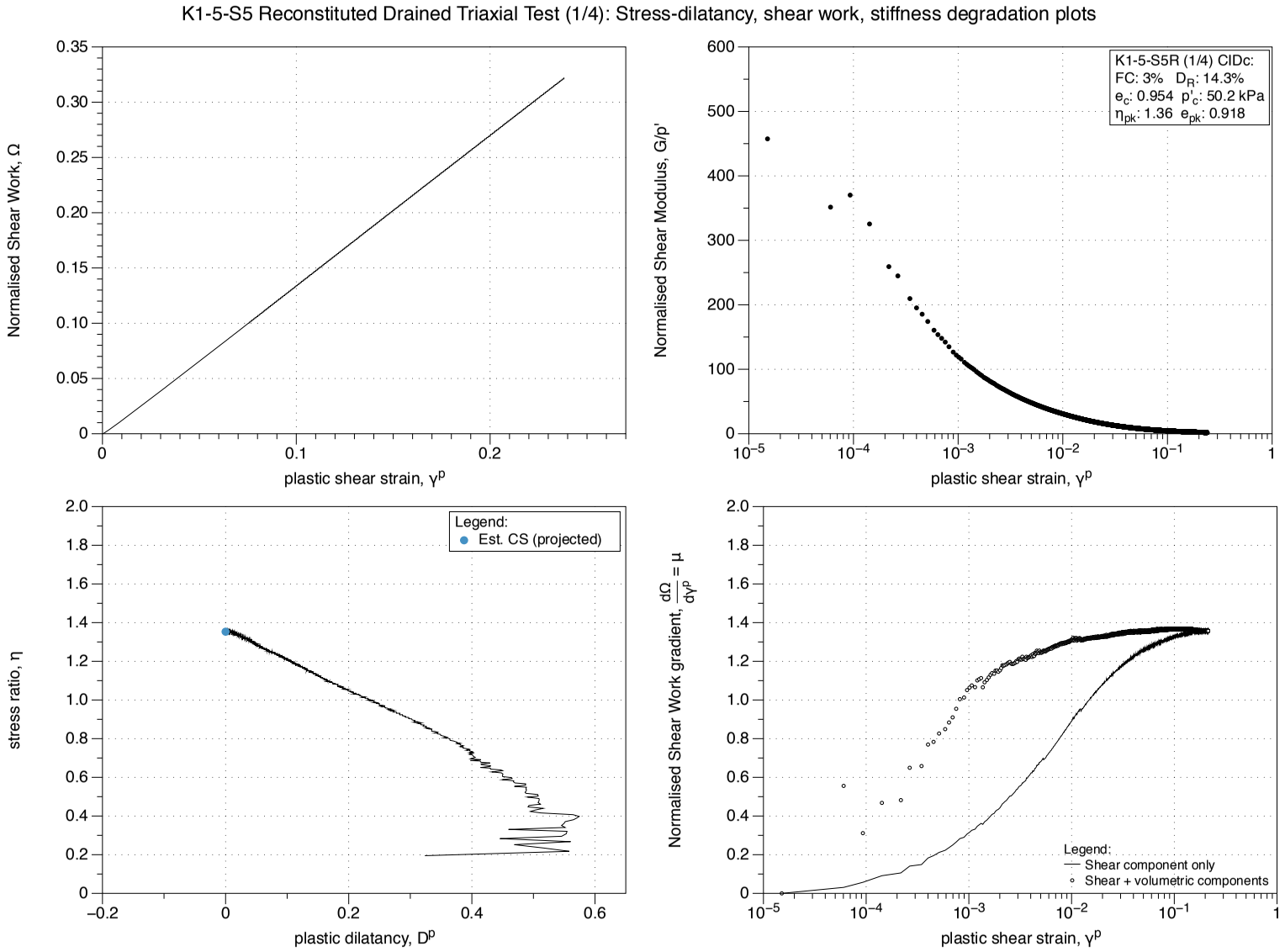

Figure 4.270: K1-5-S5 MT reconstituted sample (FC 1%), drained monotonic triaxial test (CID_C), test 1/4. Stress-dilatancy, shear work, stiffness degradation plots.

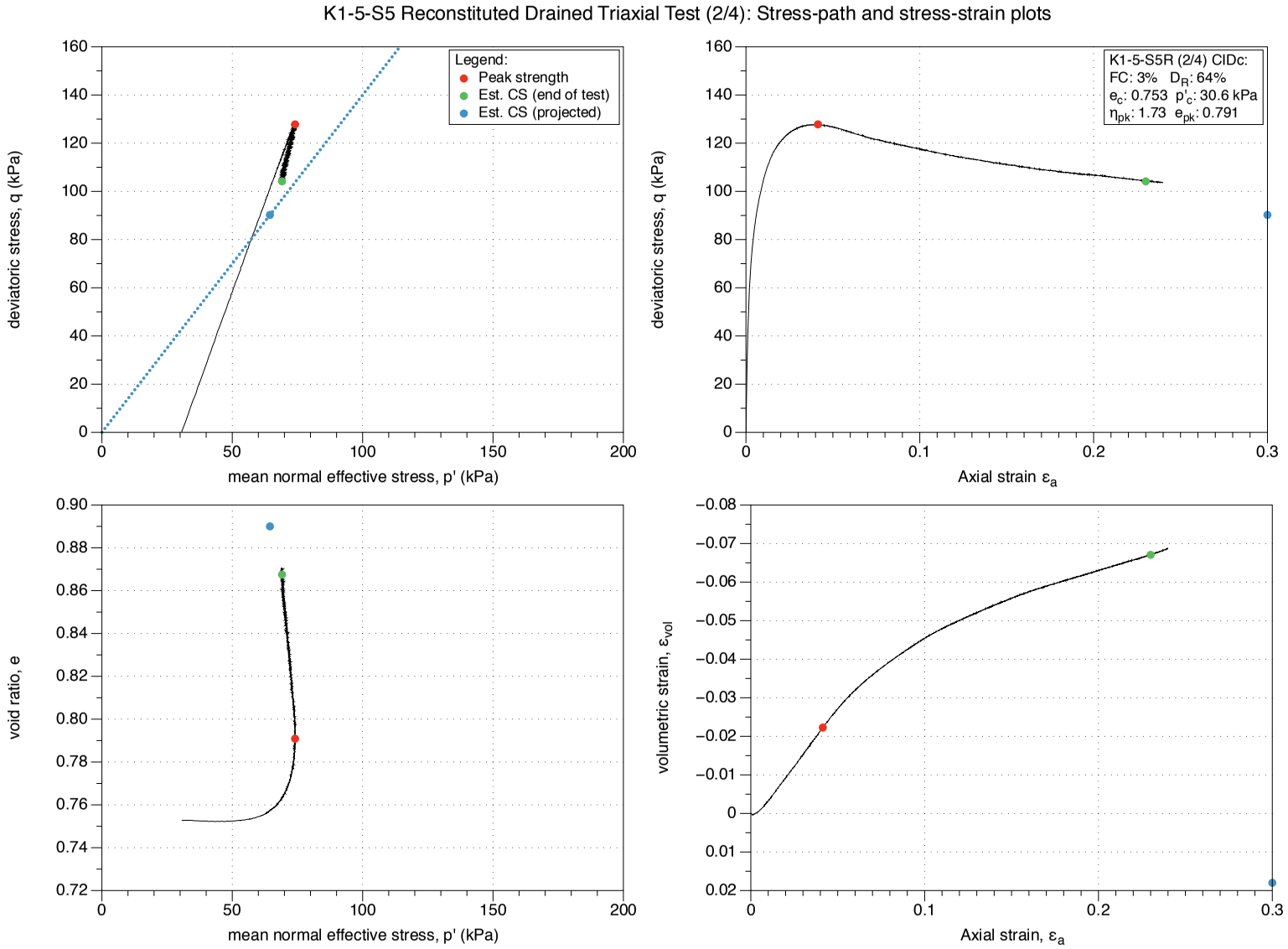

Figure 4.271: K1-5-S5 MT reconstituted sample (FC 1%), drained monotonic triaxial test (CID_C), test 2/4. Stress-path and stress-strain plots.

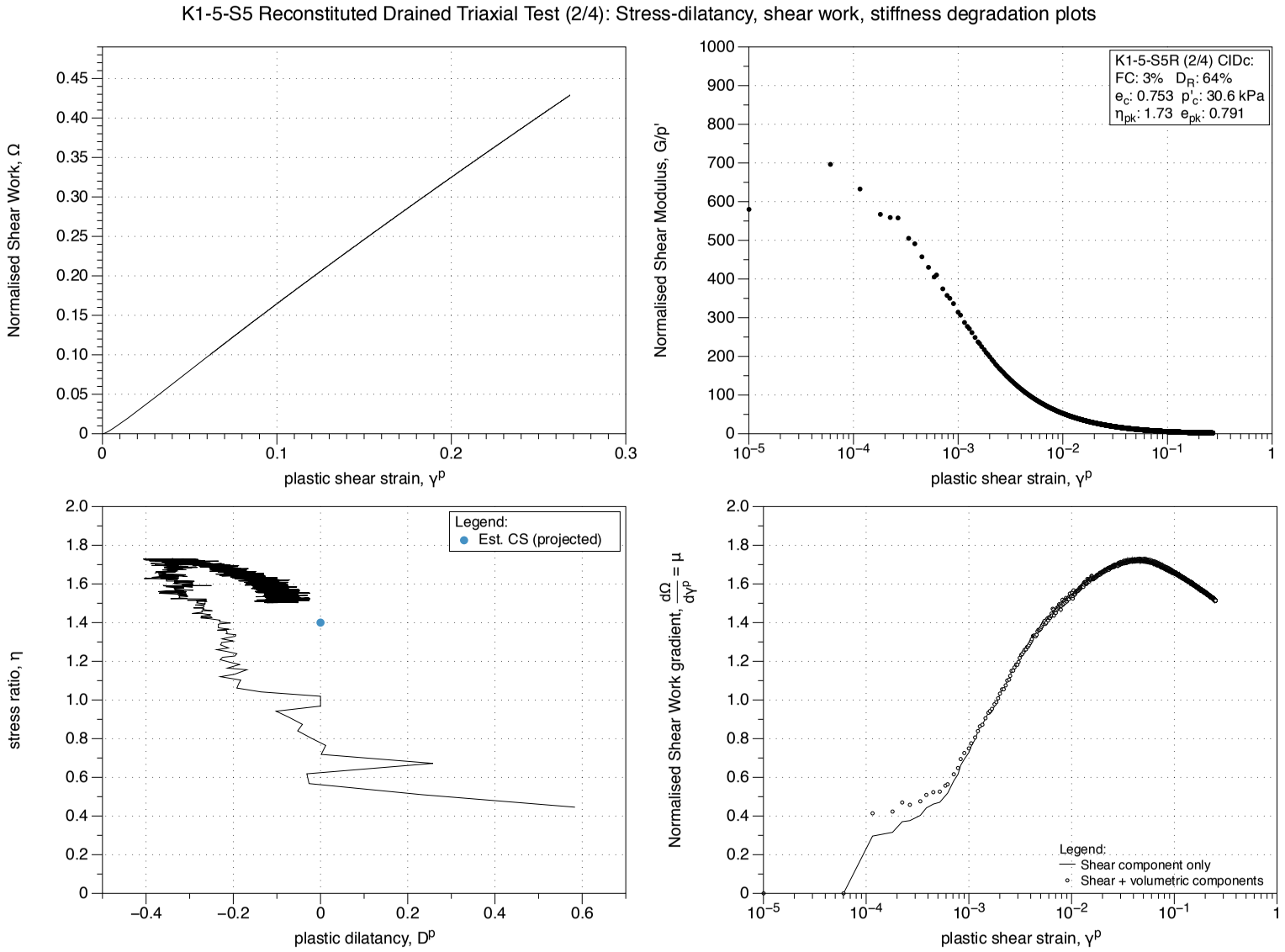

Figure 4.272: K1-5-S5 MT reconstituted sample (FC 1%), drained monotonic triaxial test (CID_C), test 2/4. Stress-dilatancy, shear work, stiffness degradation plots.

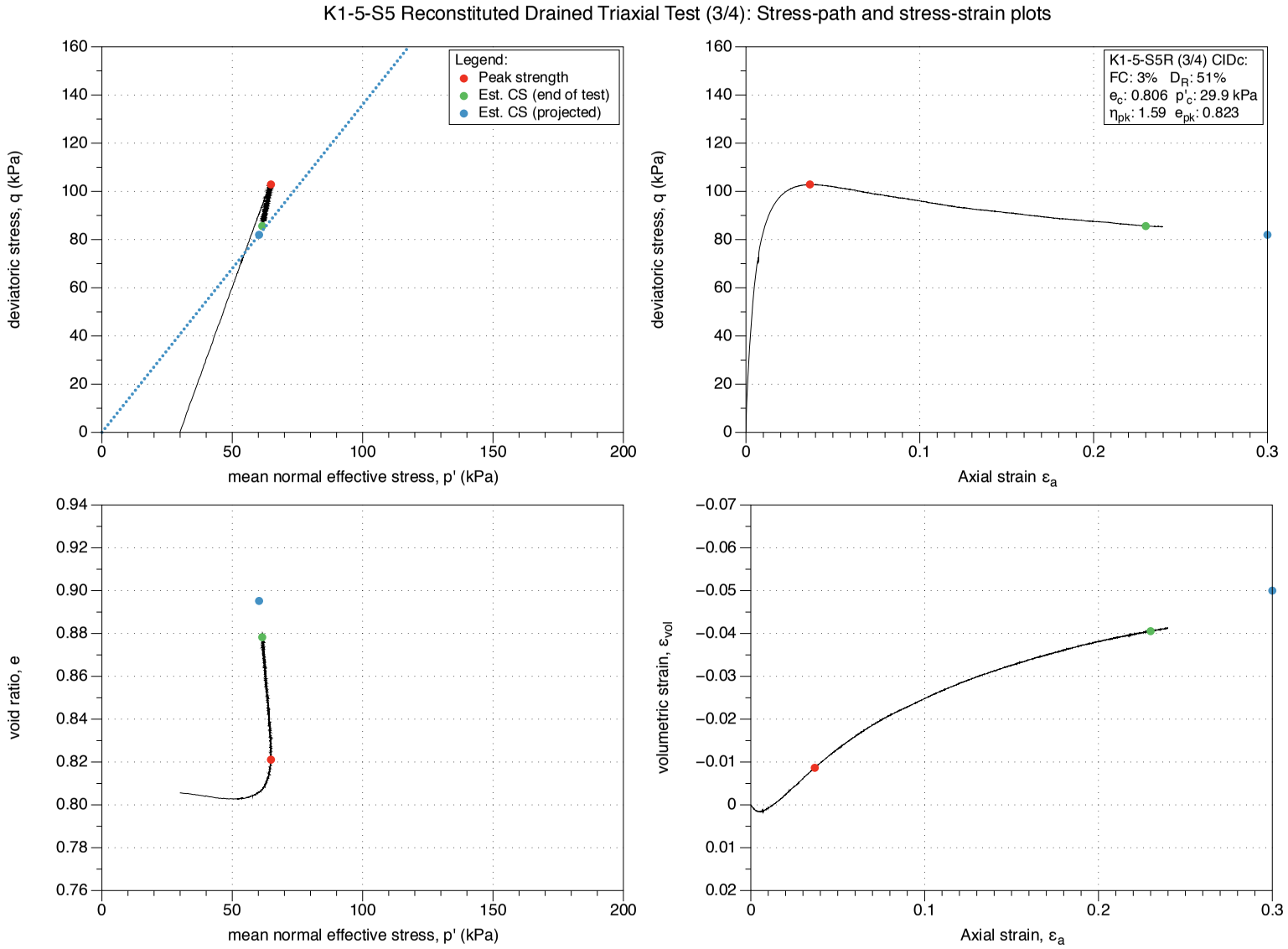

Figure 4.273: K1-5-S5 MT reconstituted sample (FC 1%), drained monotonic triaxial test (CID_C), test 3/4. Stress-path and stress-strain plots.

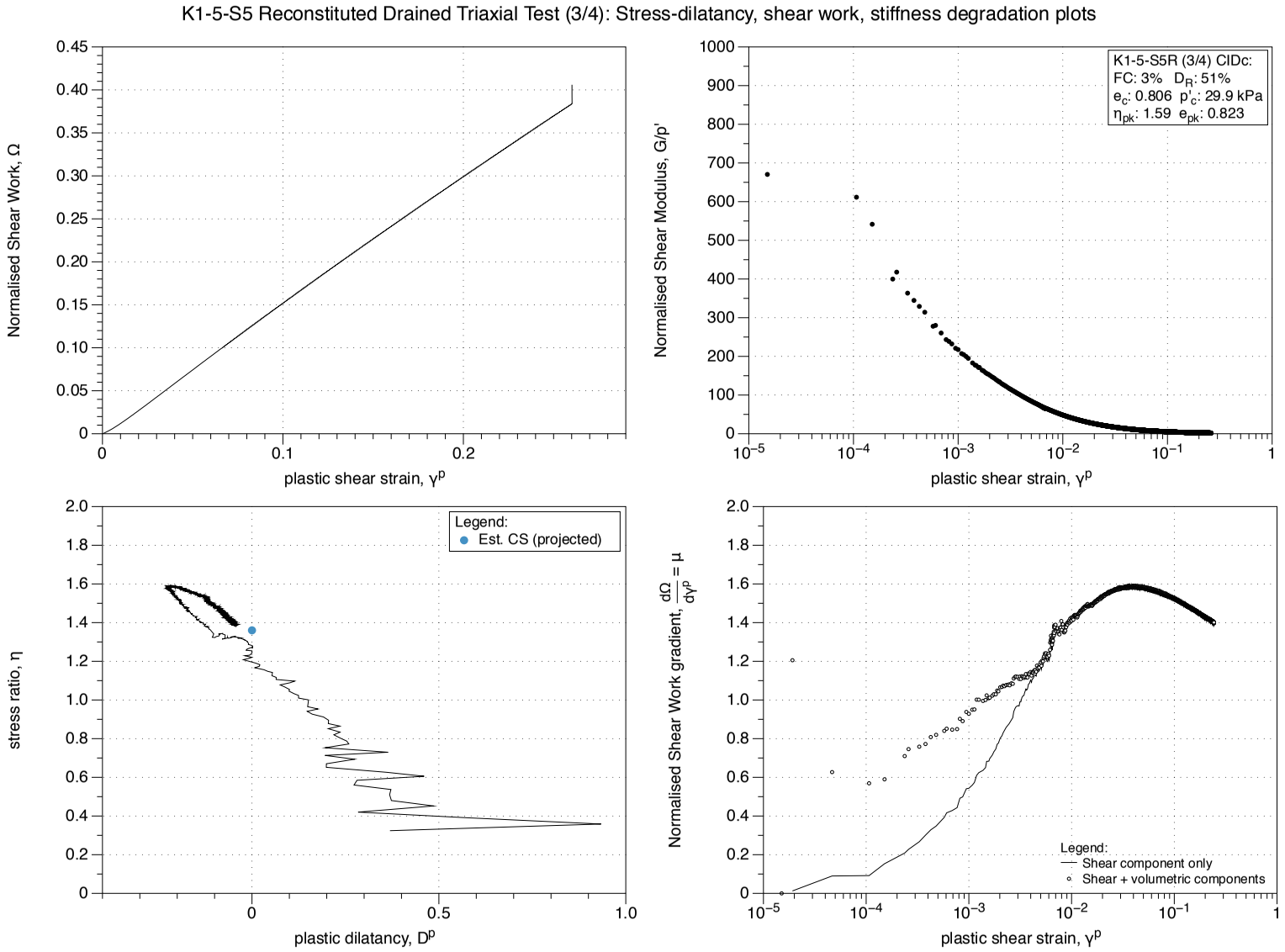

Figure 4.274: K1-5-S5 MT reconstituted sample (FC 1%), drained monotonic triaxial test (CID_C), test 3/4. Stress-dilatancy, shear work, stiffness degradation plots.

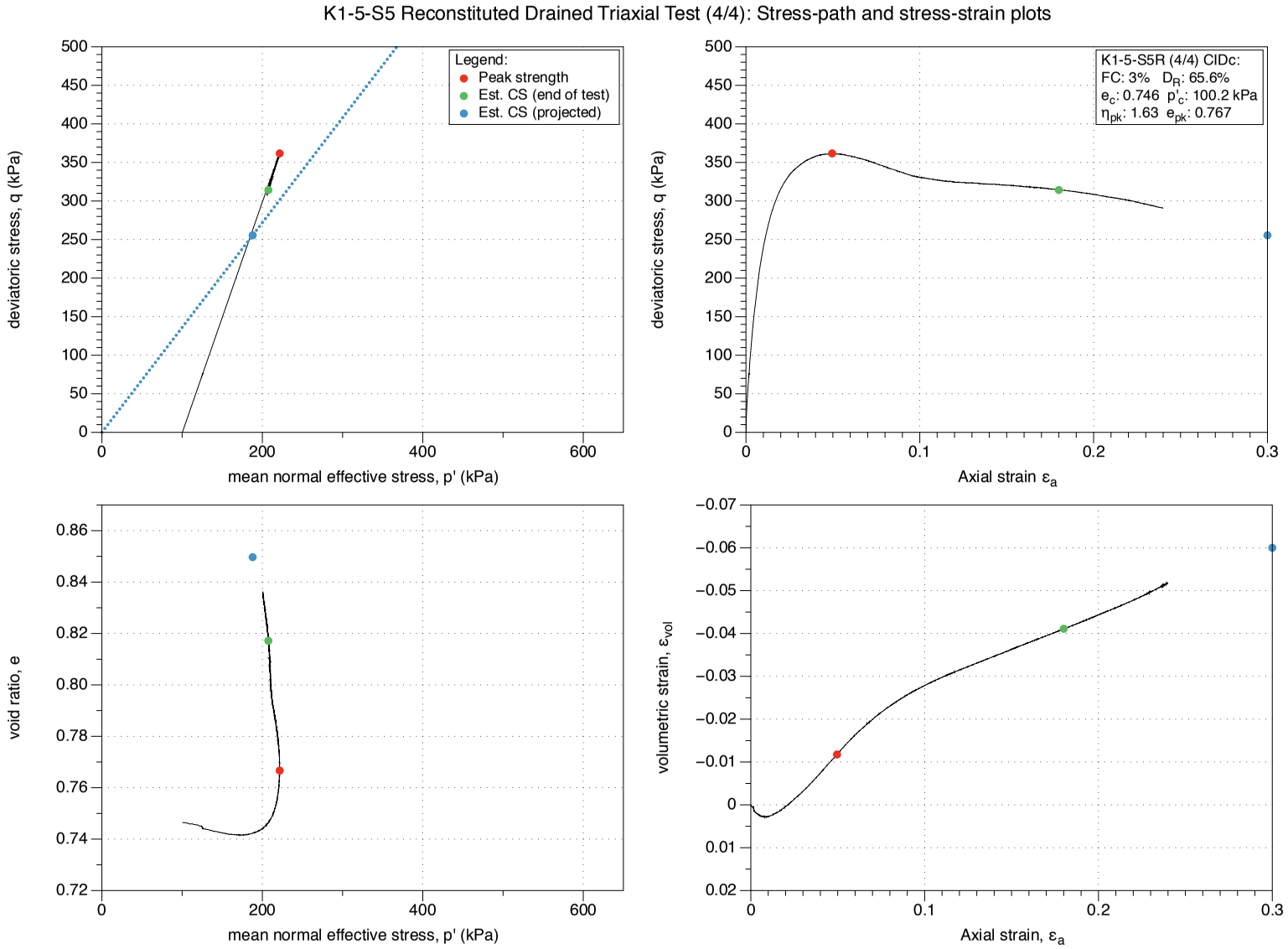

Figure 4.275: K1-5-S5 MT reconstituted sample (FC 1%), drained monotonic triaxial test (CID_C), test 4/4. Stress-path and stress-strain plots.

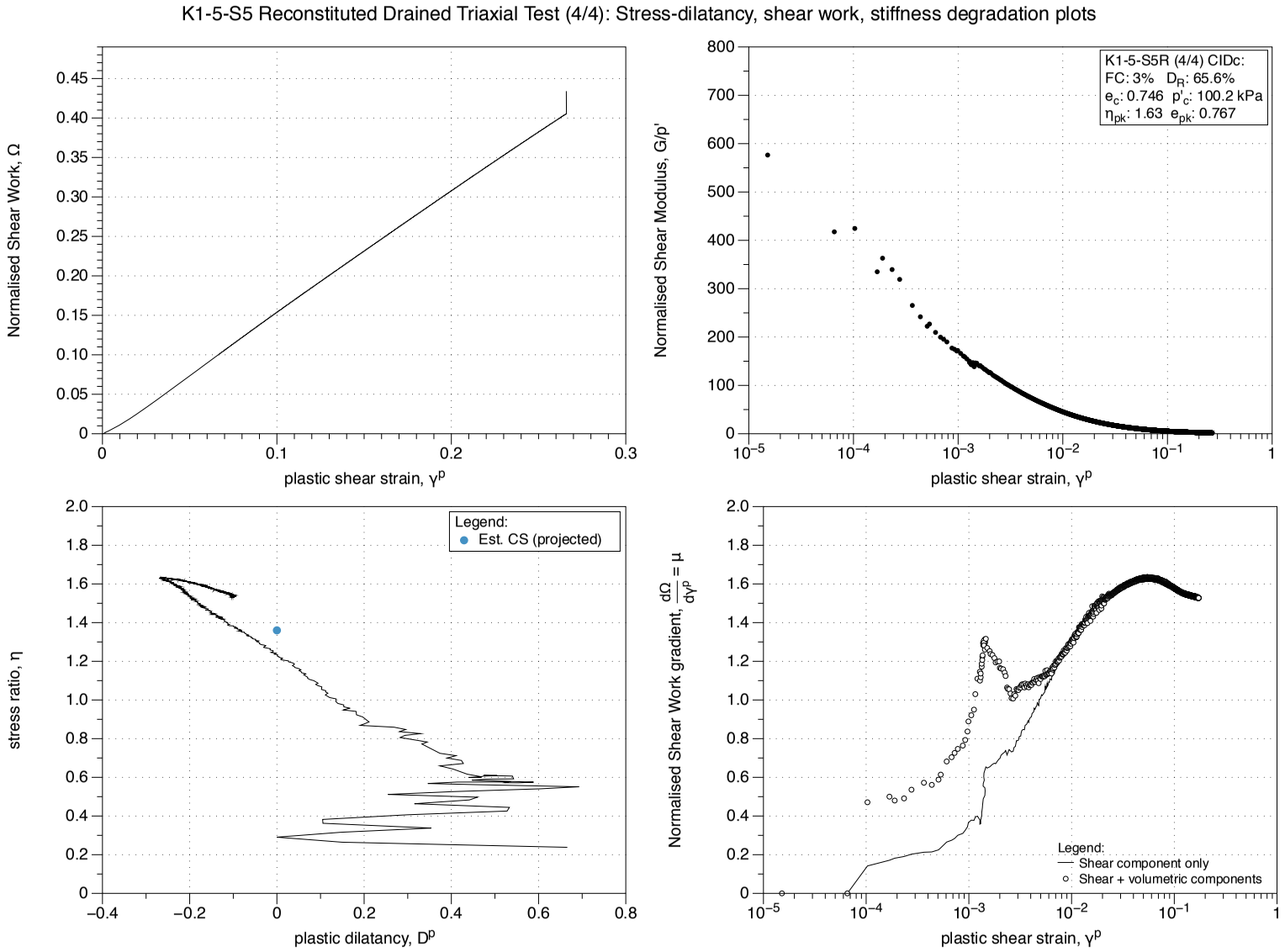

Figure 4.276: K1-5-S5 MT reconstituted sample (FC 1%), drained monotonic triaxial test (CID_C), test 4/4. Stress-dilatancy, shear work, stiffness degradation plots.

4.4.1.8 CIU Tests on samples (FC 0 - 5 %)

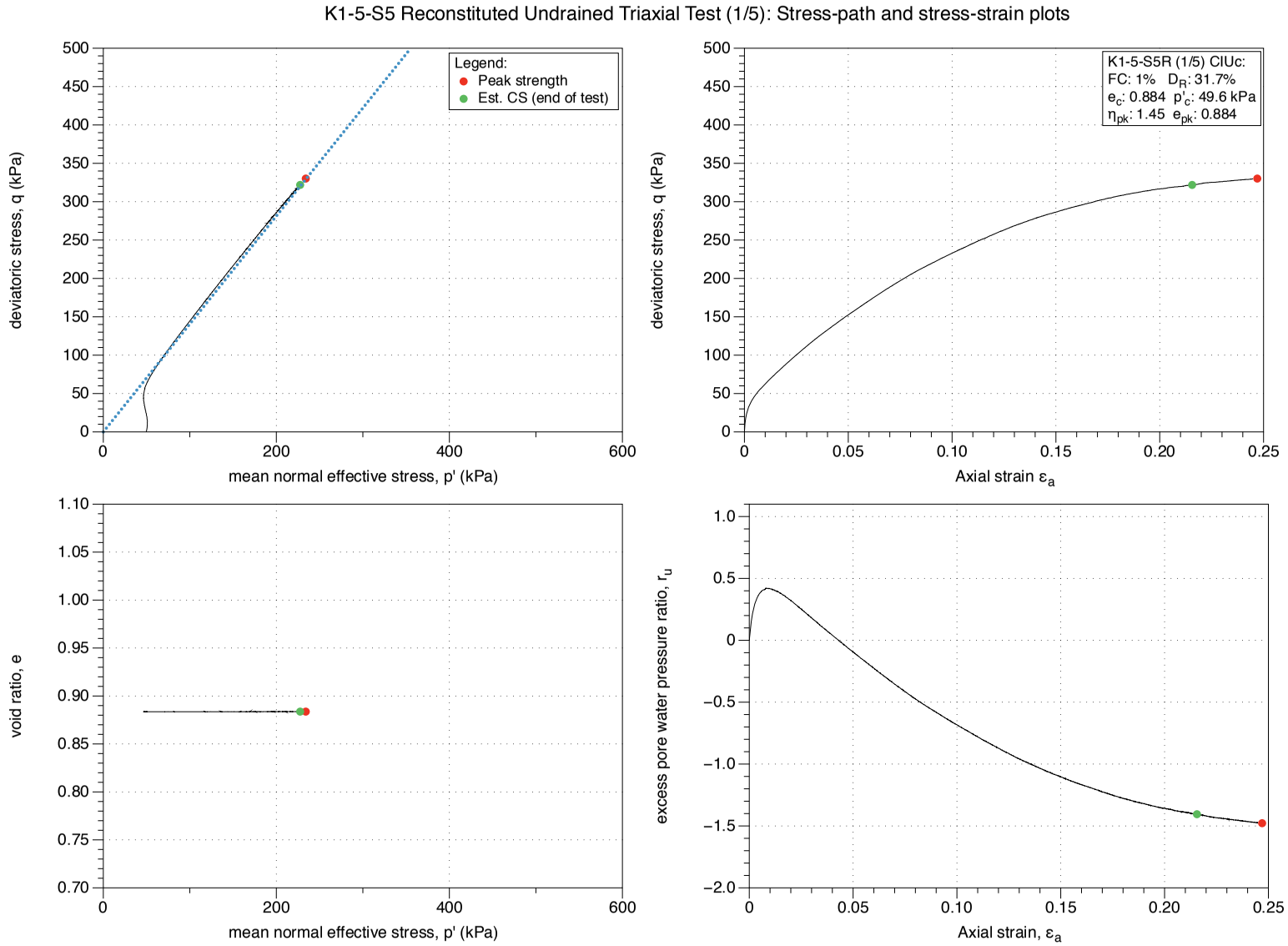

Figure 4.277: K1-5-S5 MT reconstituted sample (FC 1%), undrained monotonic triaxial test (CIU_C), test 1/5. Stress-path and stress-strain plots.

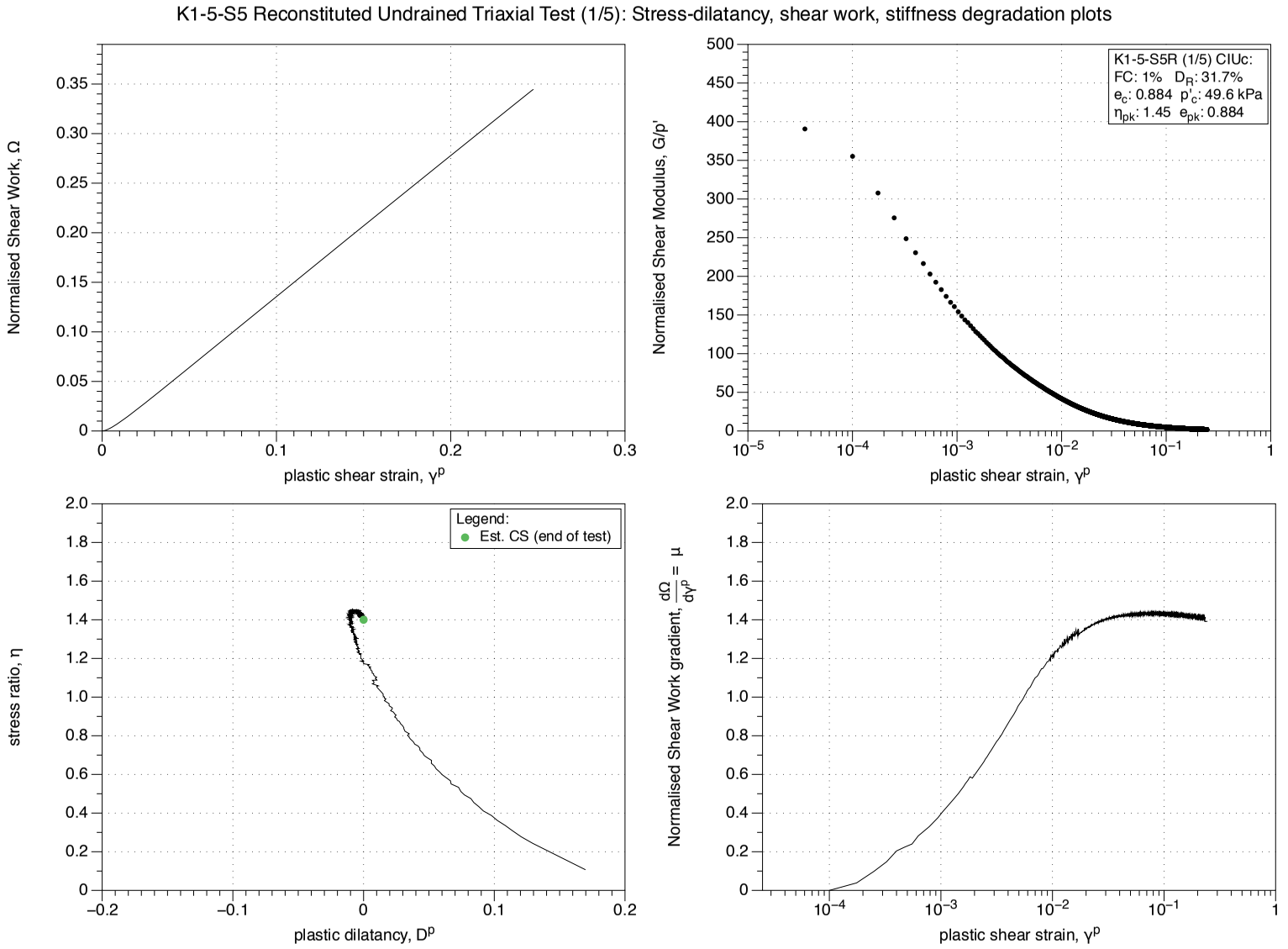

Figure 4.278: K1-5-S5 MT reconstituted sample (FC 1%), undrained monotonic triaxial test (CIU_C), test 1/5. Stress-dilatancy, shear work, stiffness degradation plots.

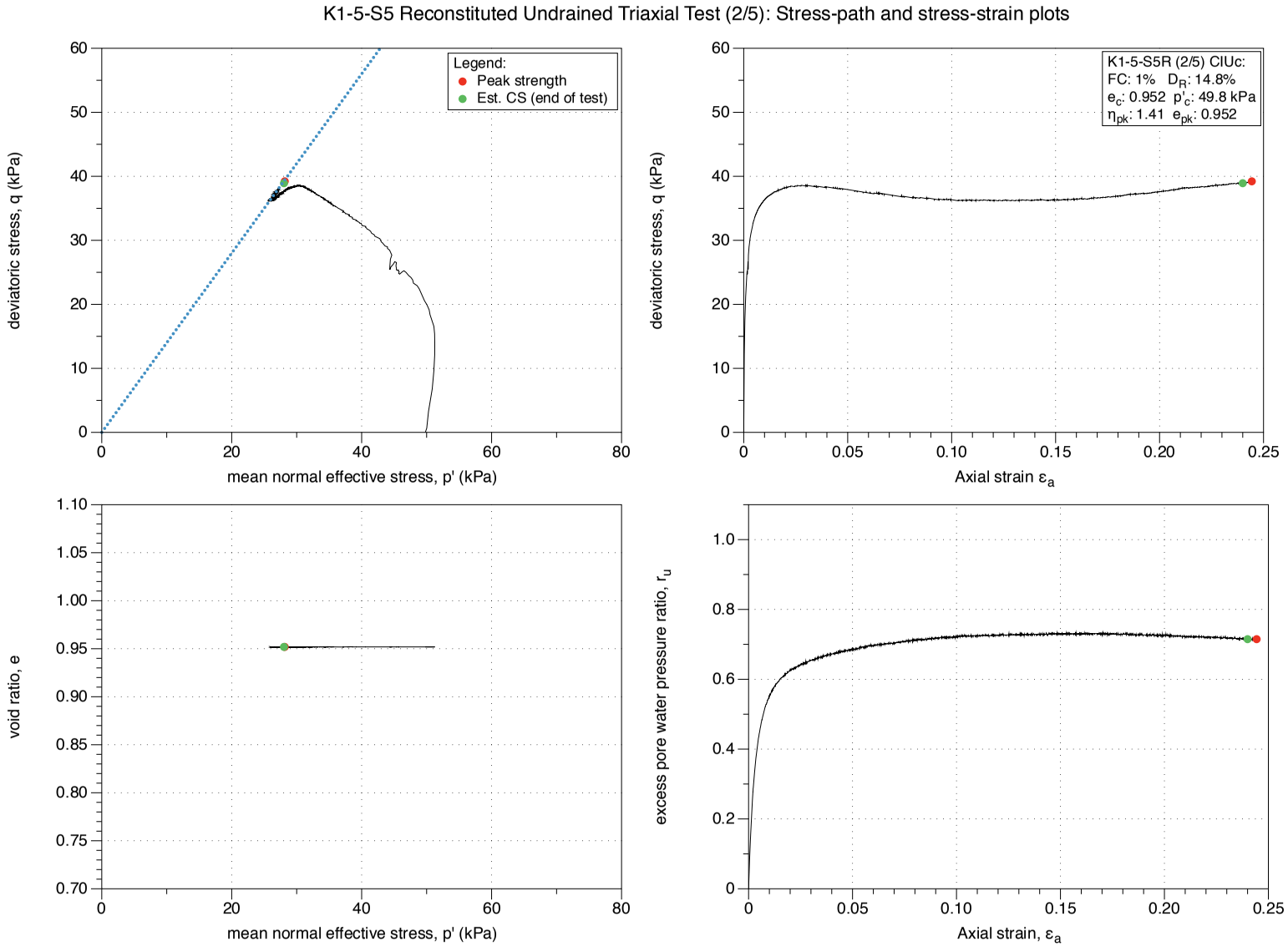

Figure 4.279: K1-5-S5 MT reconstituted sample (FC 1%), undrained monotonic triaxial test (CIU_C), test 2/5. Stress-path and stress-strain plots.

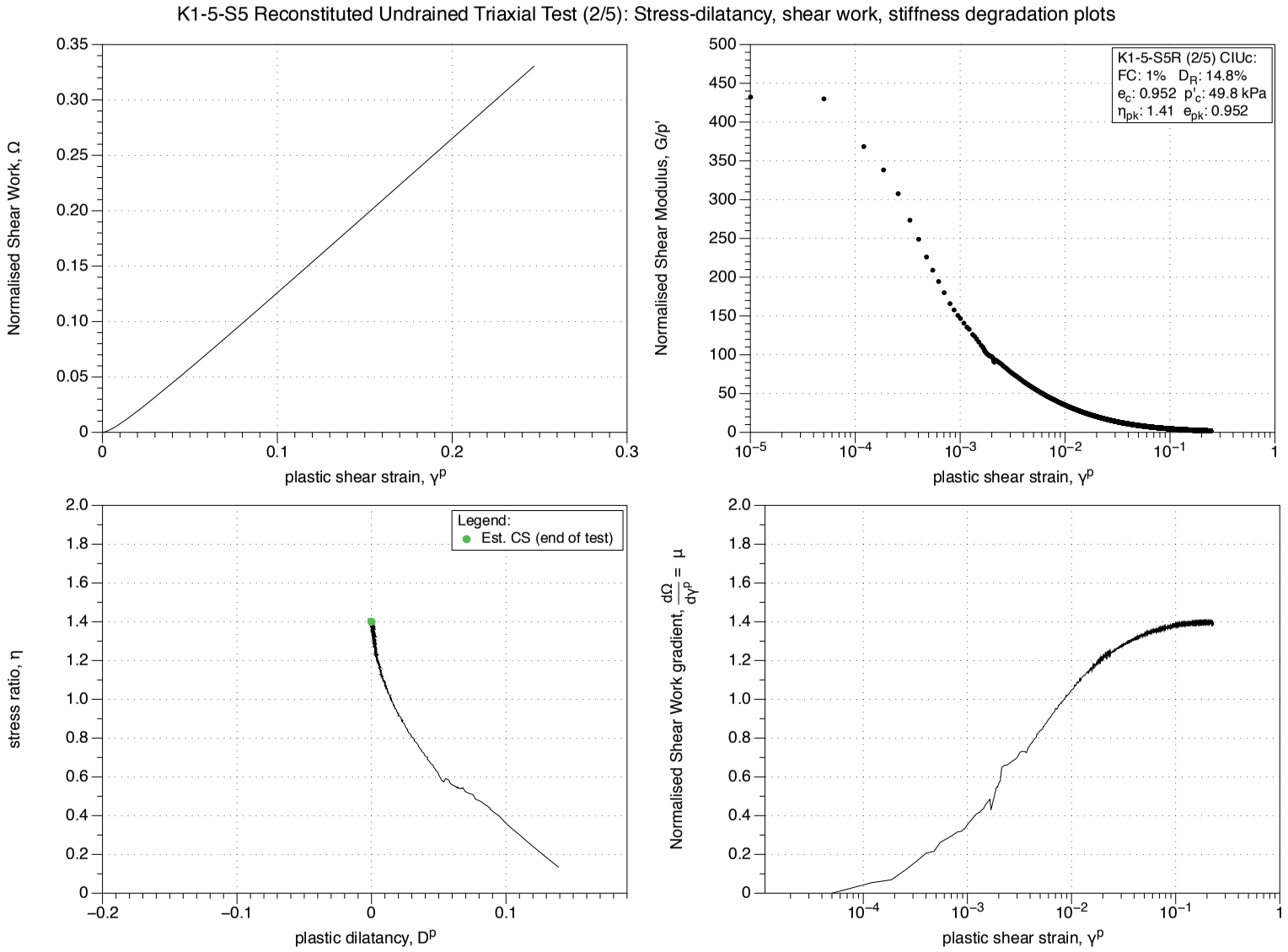

Figure 4.280: K1-5-S5 MT reconstituted sample (FC 1%), undrained monotonic triaxial test (CIU_C), test 2/5. Stress-dilatancy, shear work, stiffness degradation plots.

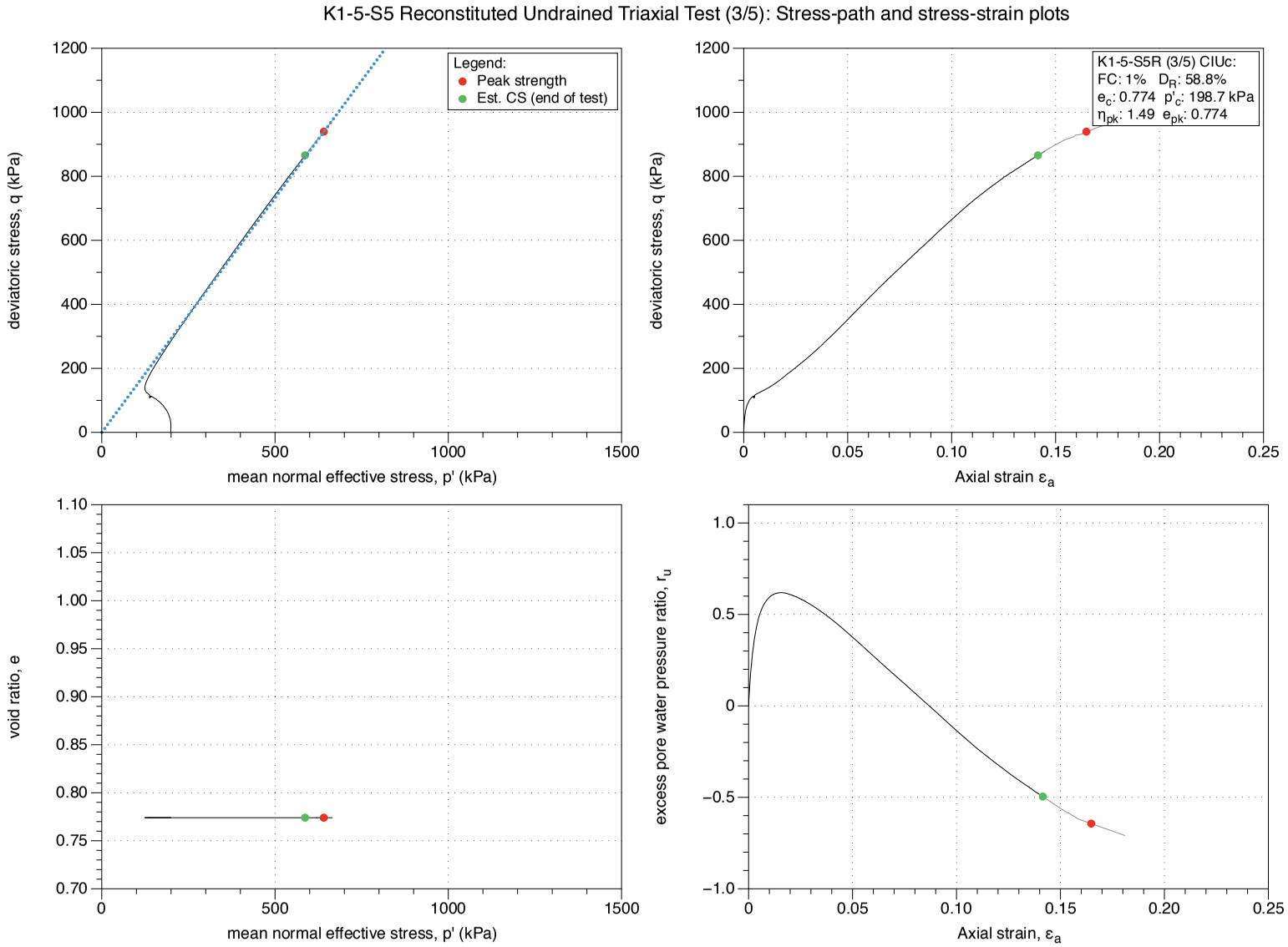

Figure 4.281: K1-5-S5 MT reconstituted sample (FC 1%), undrained monotonic triaxial test (CIU_C), test 3/5. Stress-path and stress-strain plots.

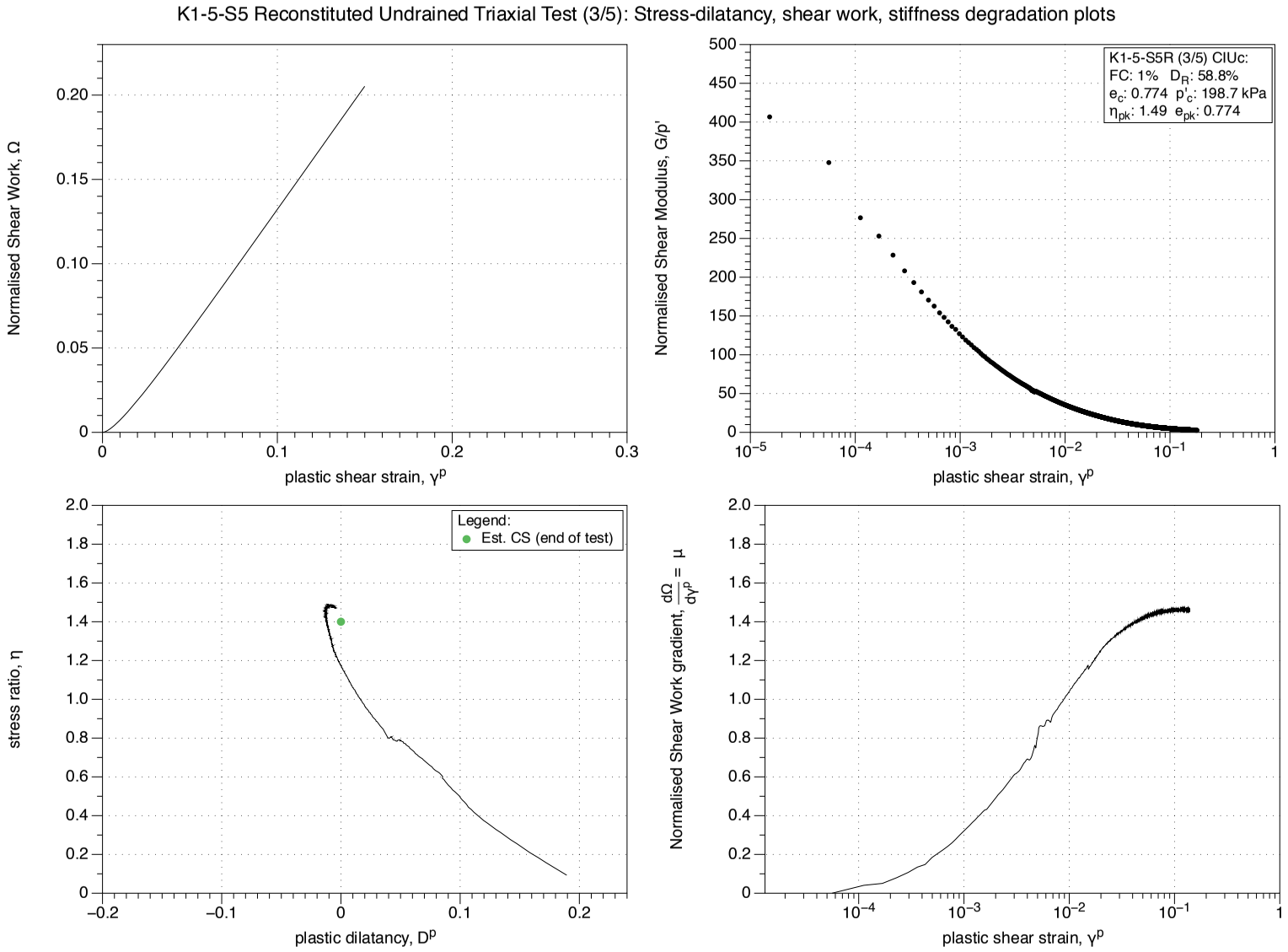

Figure 4.282: K1-5-S5 MT reconstituted sample (FC 1%), undrained monotonic triaxial test (CIU_C), test 3/5. Stress-dilatancy, shear work, stiffness degradation plots.

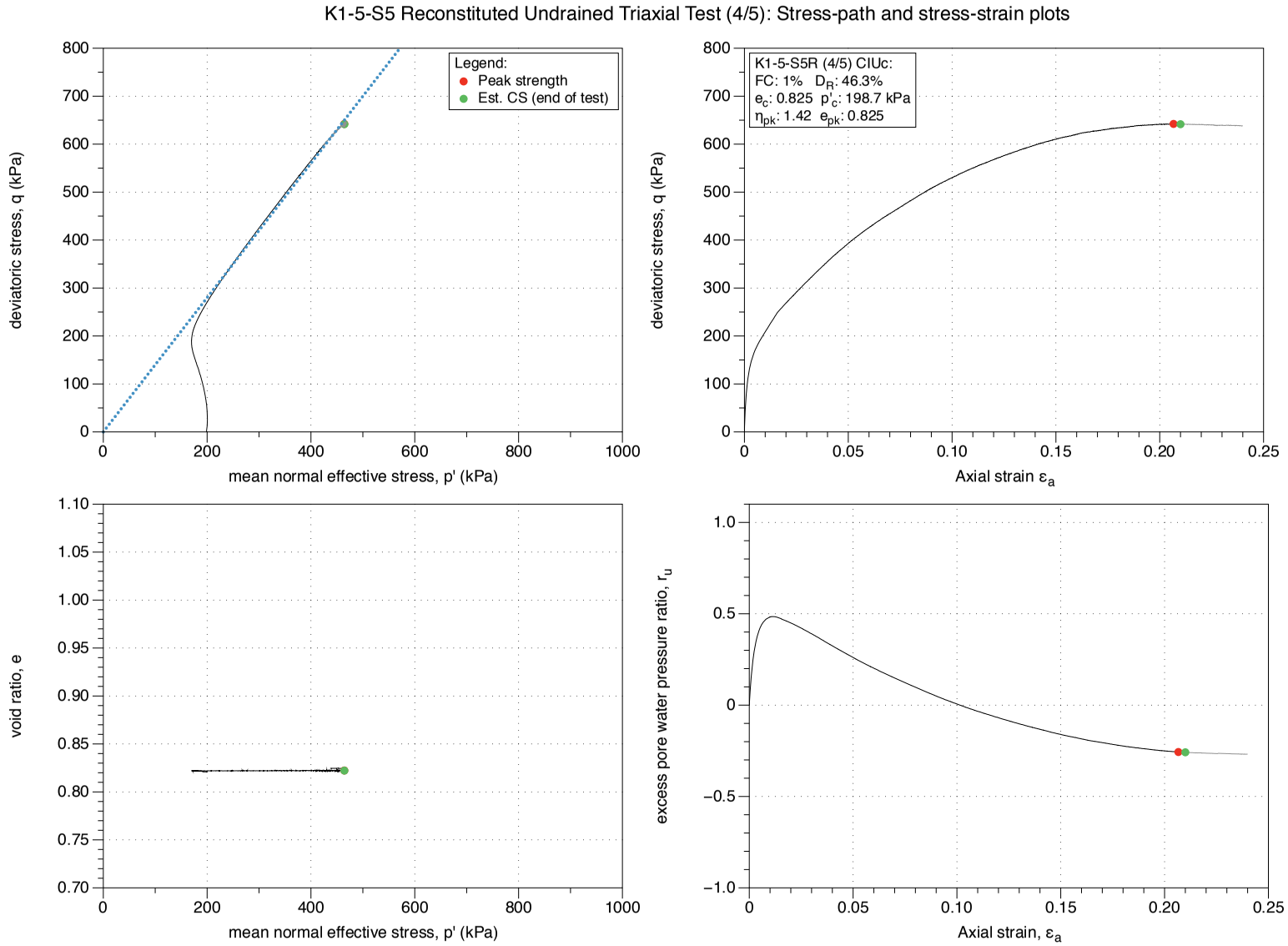

Figure 4.283: K1-5-S5 MT reconstituted sample (FC 1%), undrained monotonic triaxial test (CIU_C), test 4/5. Stress-path and stress-strain plots.

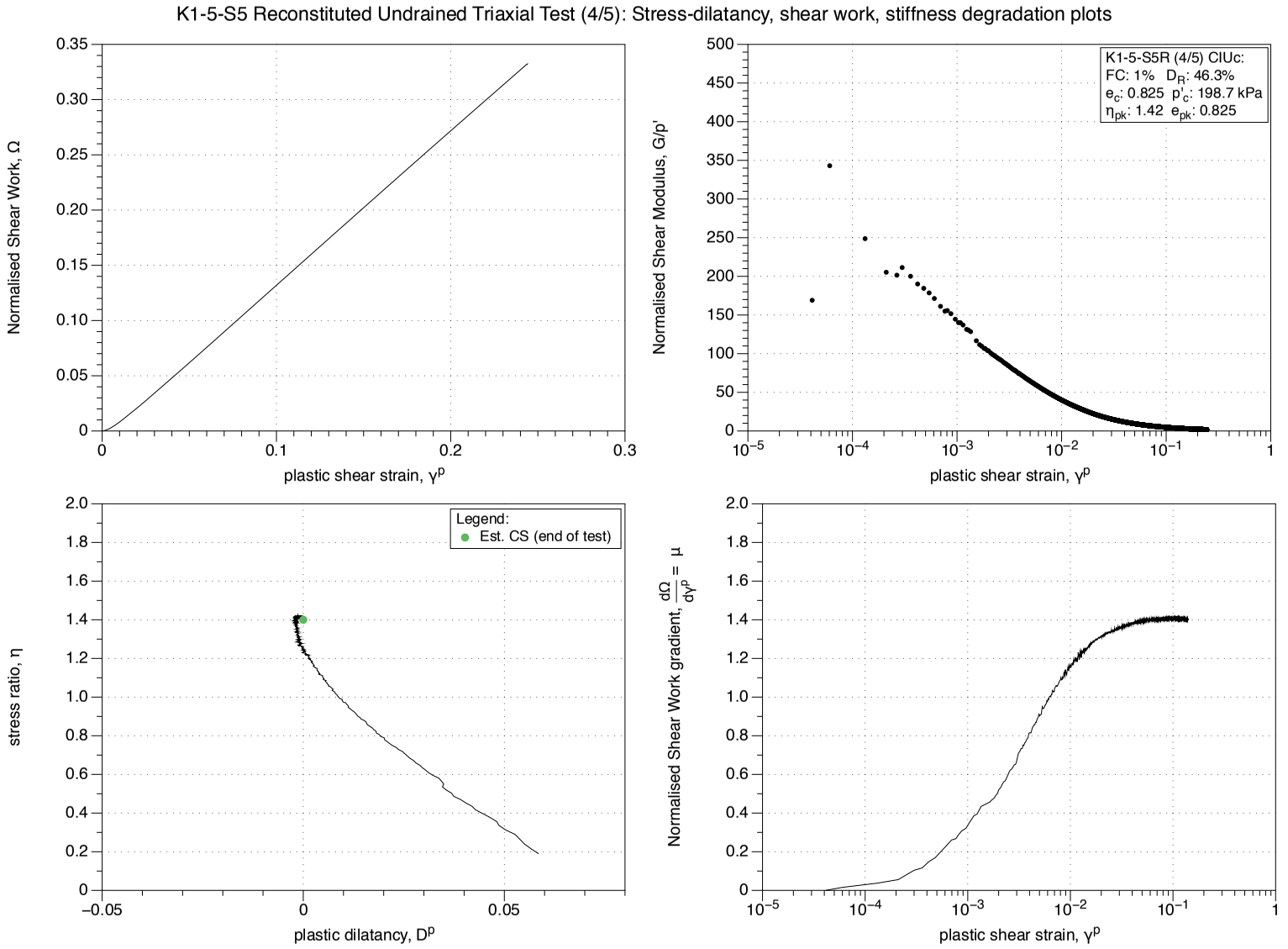

Figure 4.284: K1-5-S5 MT reconstituted sample (FC 1%), undrained monotonic triaxial test (CIU_C), test 4/5. Stress-dilatancy, shear work, stiffness degradation plots.

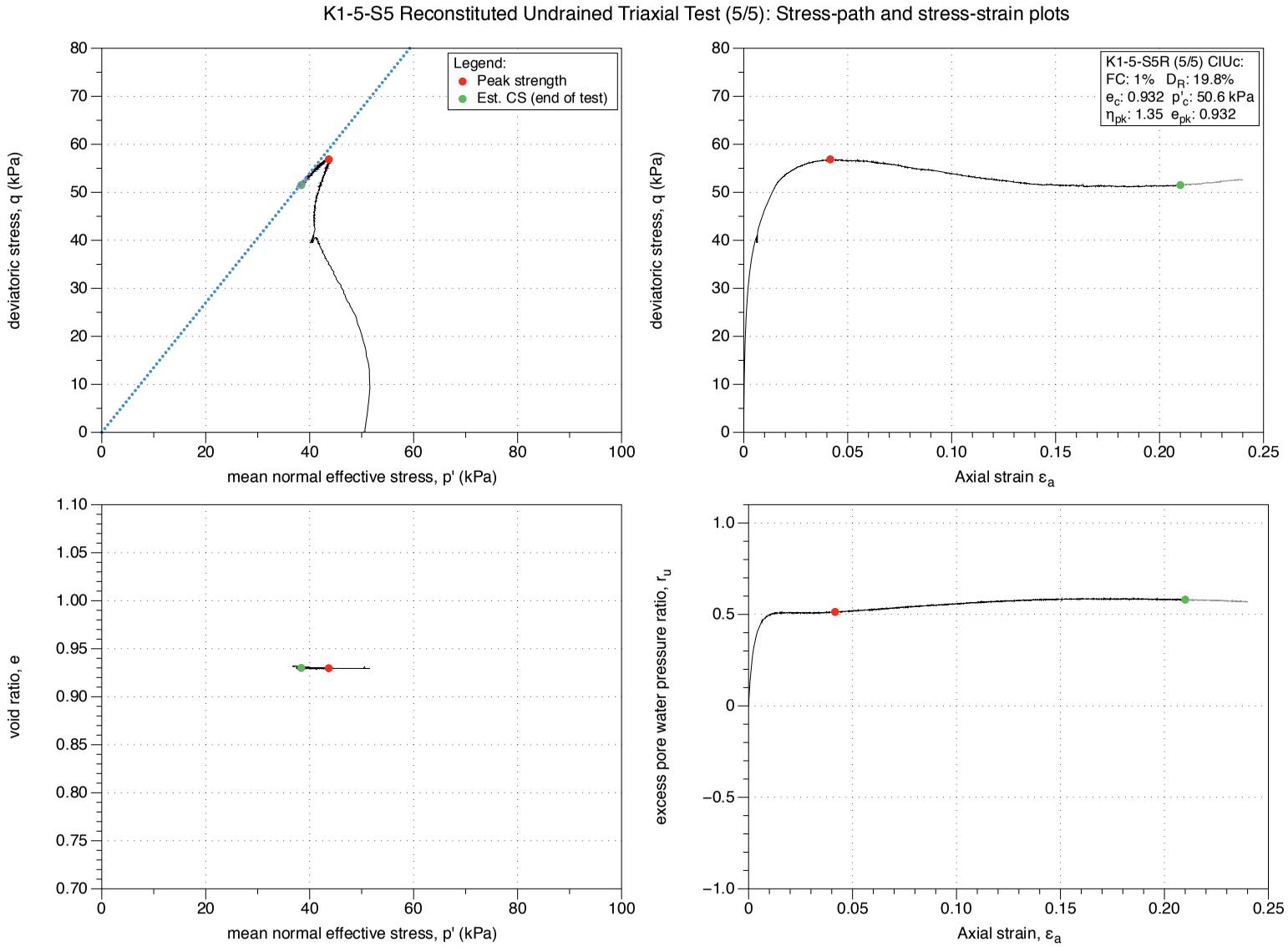

Figure 4.285: K1-5-S5 MT reconstituted sample (FC 1%), undrained monotonic triaxial test (CIU_C), test 5/5. Stress-path and stress-strain plots.

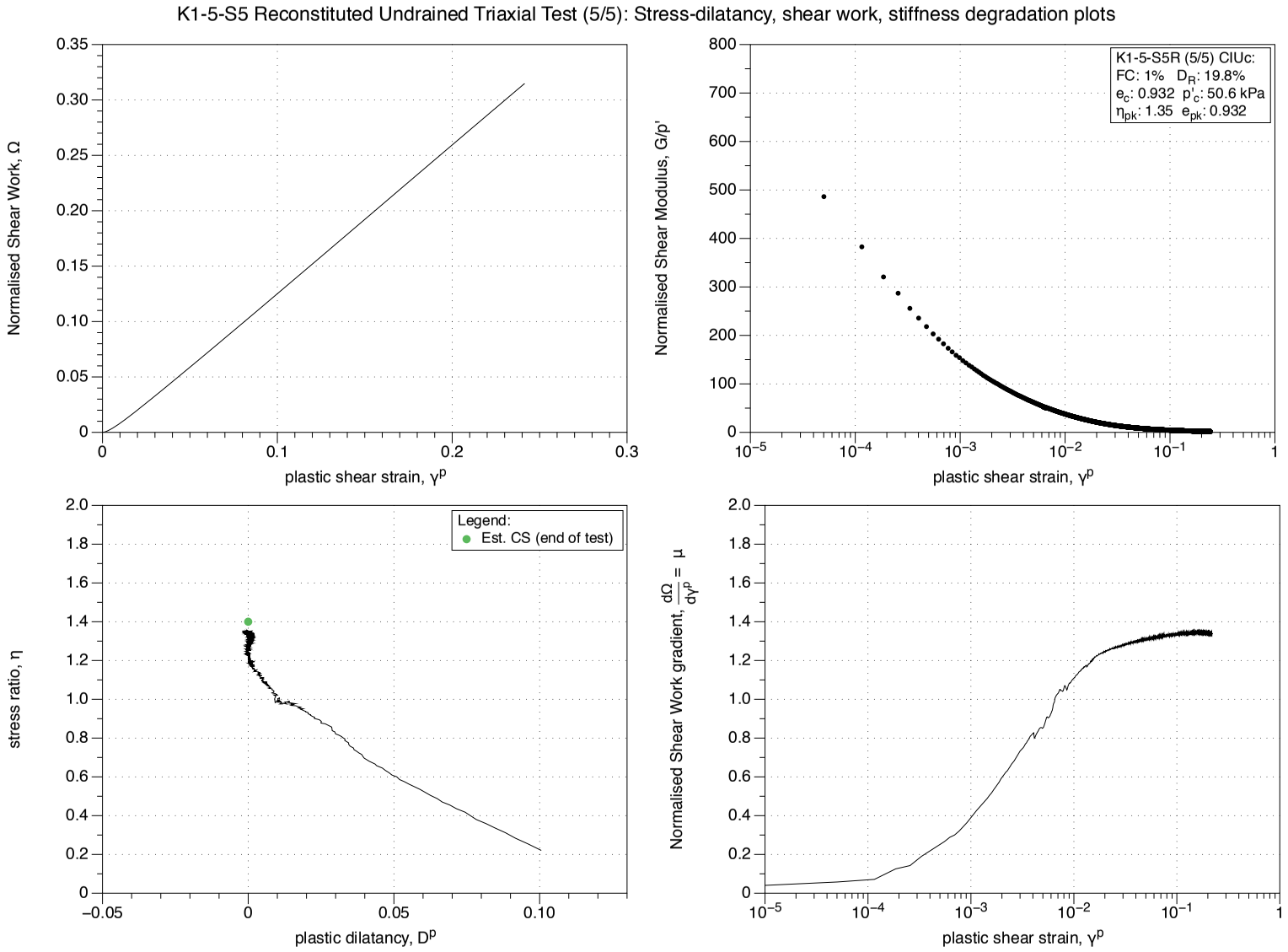

Figure 4.286: K1-5-S5 MT reconstituted sample (FC 1%), undrained monotonic triaxial test (CIU_C), test 5/5. Stress-dilatancy, shear work, stiffness degradation plots.

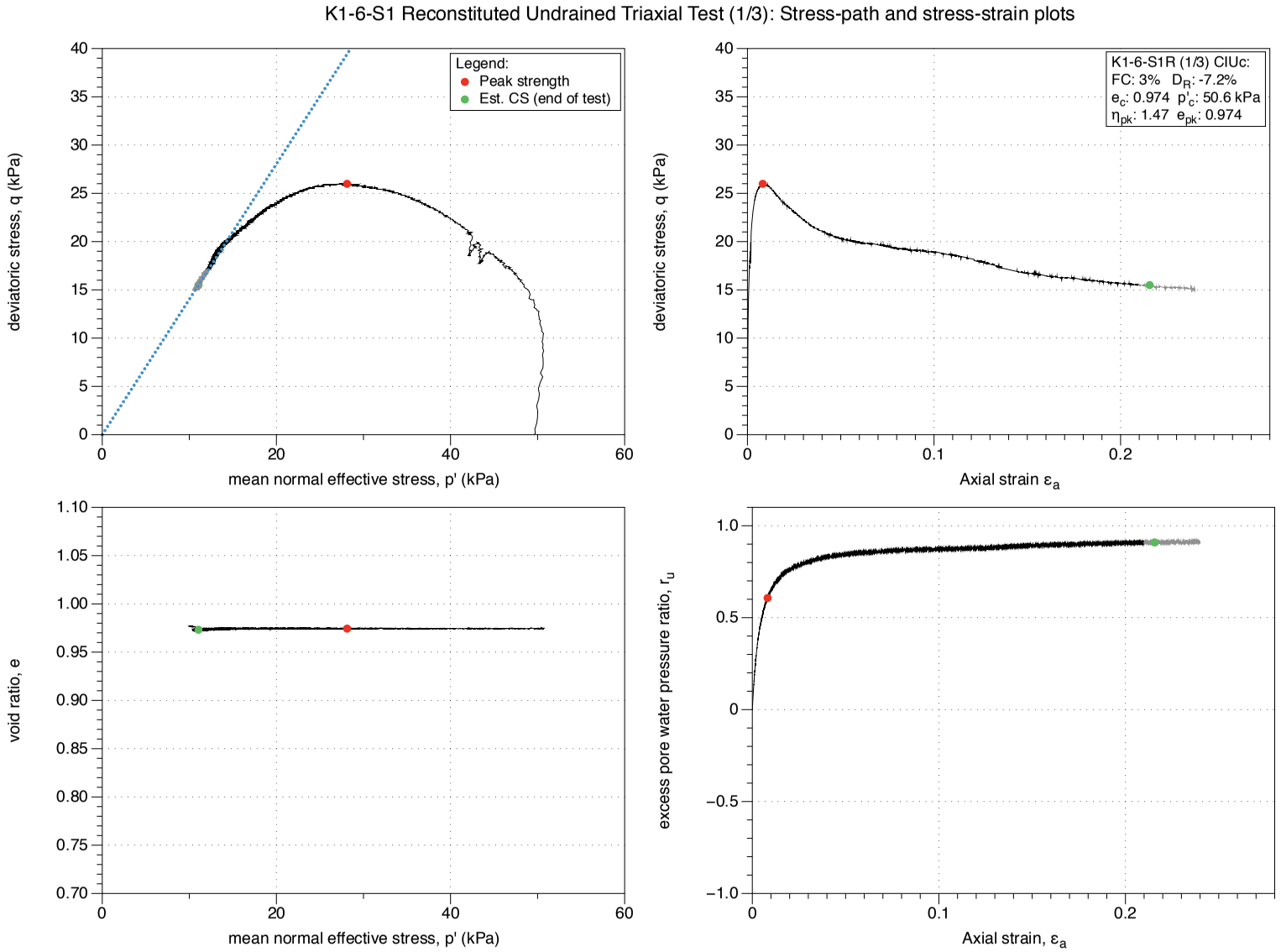

Figure 4.287: K1-6-S1 MT reconstituted sample (FC 3%), undrained monotonic triaxial test (CIU_C), test 1/3. Stress-path and stress-strain plots.

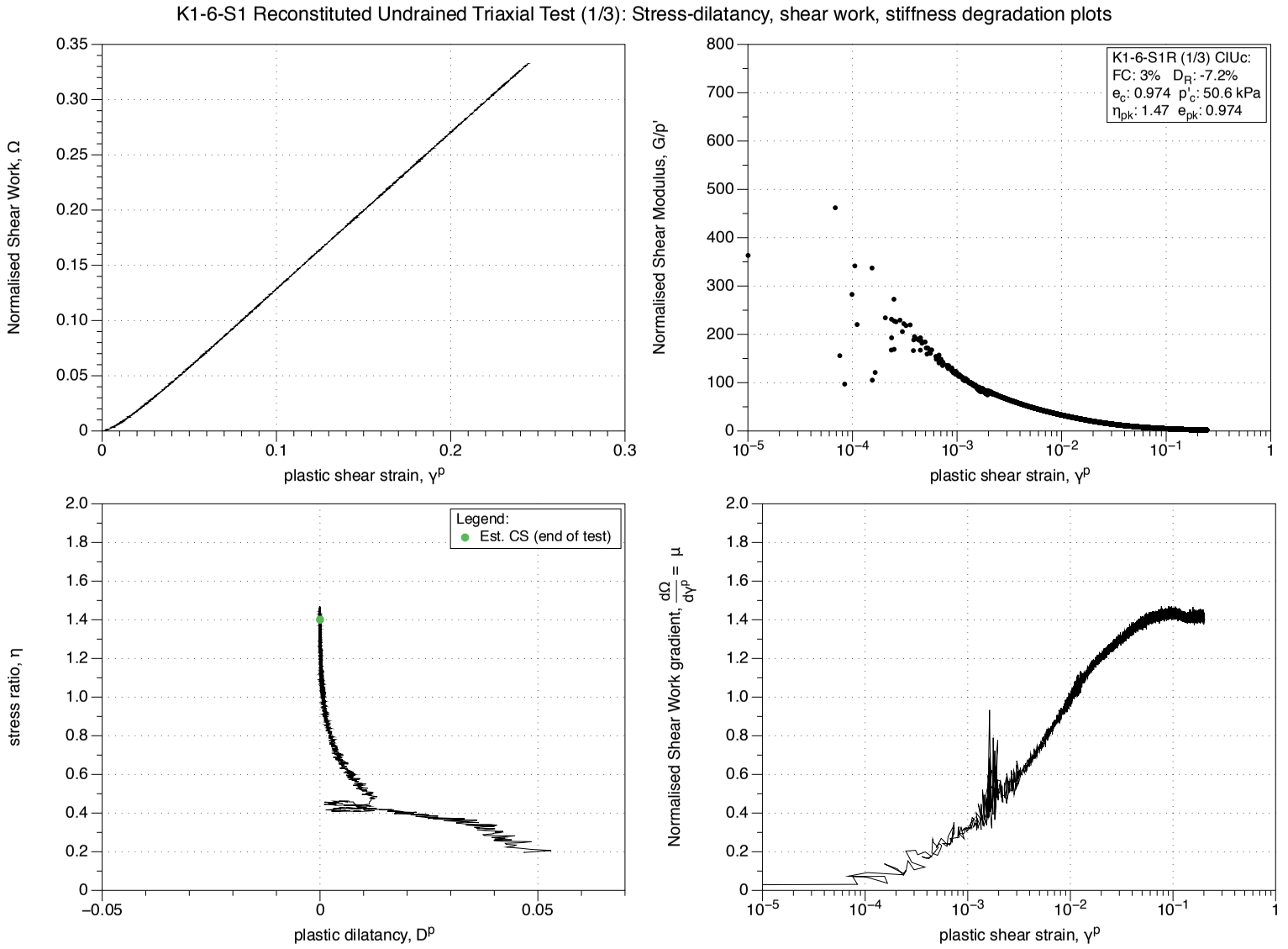

Figure 4.288: K1-6-S1 MT reconstituted sample (FC 3%), undrained monotonic triaxial test (CIU_C), test 1/3. Stress-dilatancy, shear work, stiffness degradation plots.

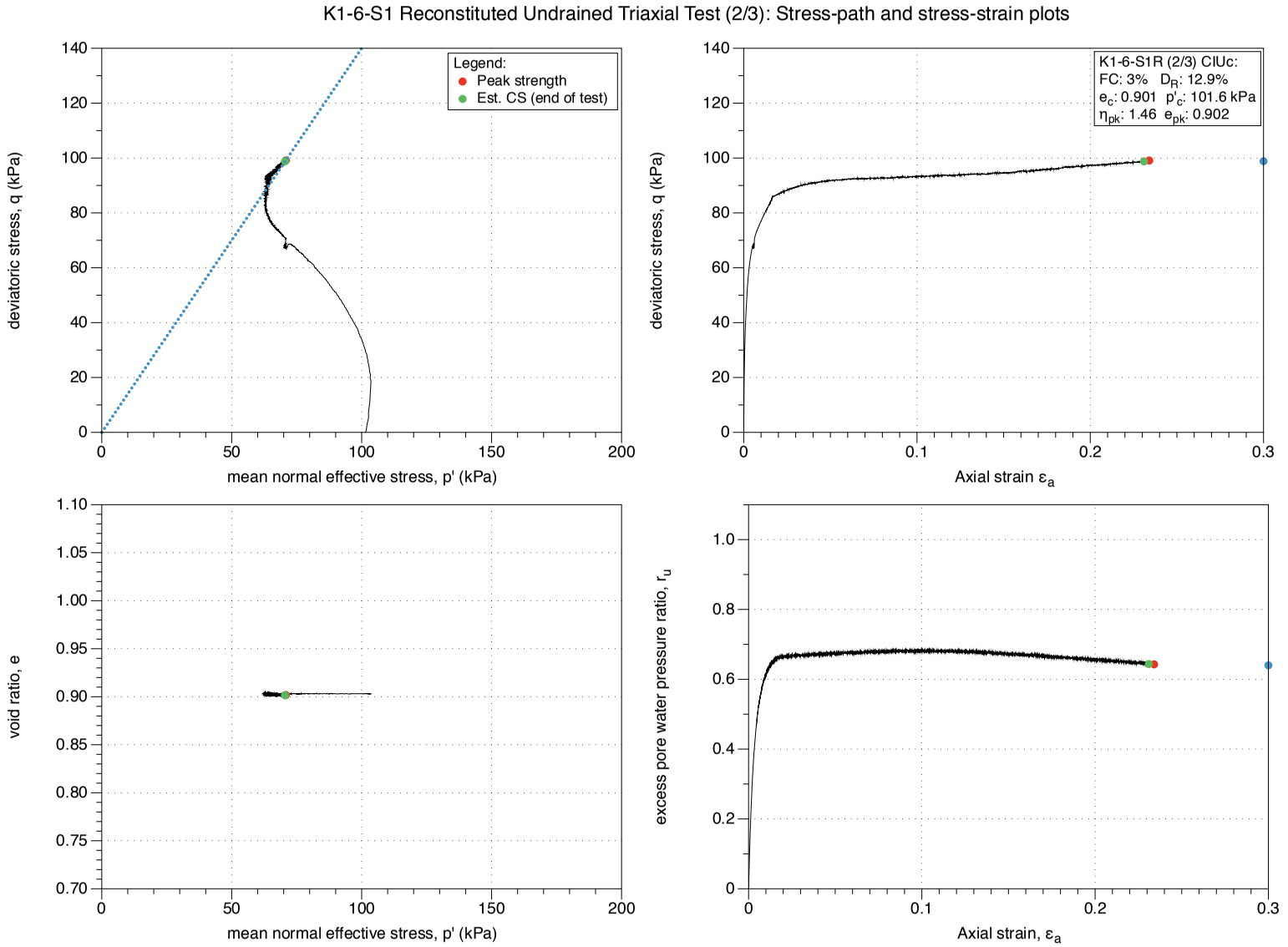

Figure 4.289: K1-6-S1 MT reconstituted sample (FC 3%), undrained monotonic triaxial test (CIU_C), test 2/3. Stress-path and stress-strain plots.

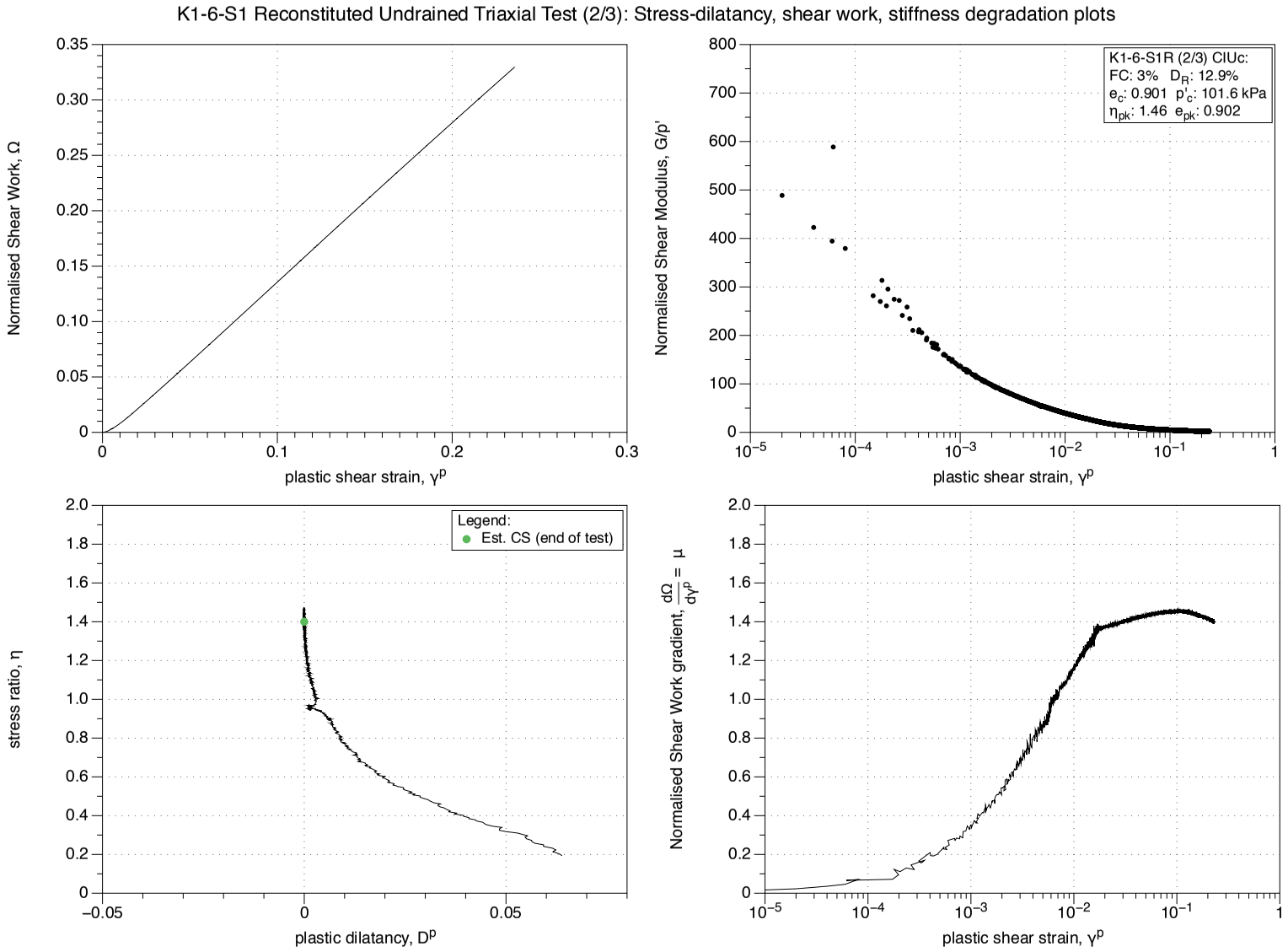

Figure 4.290: K1-6-S1 MT reconstituted sample (FC 3%), undrained monotonic triaxial test (CIU_C), test 2/3. Stress-dilatancy, shear work, stiffness degradation plots.

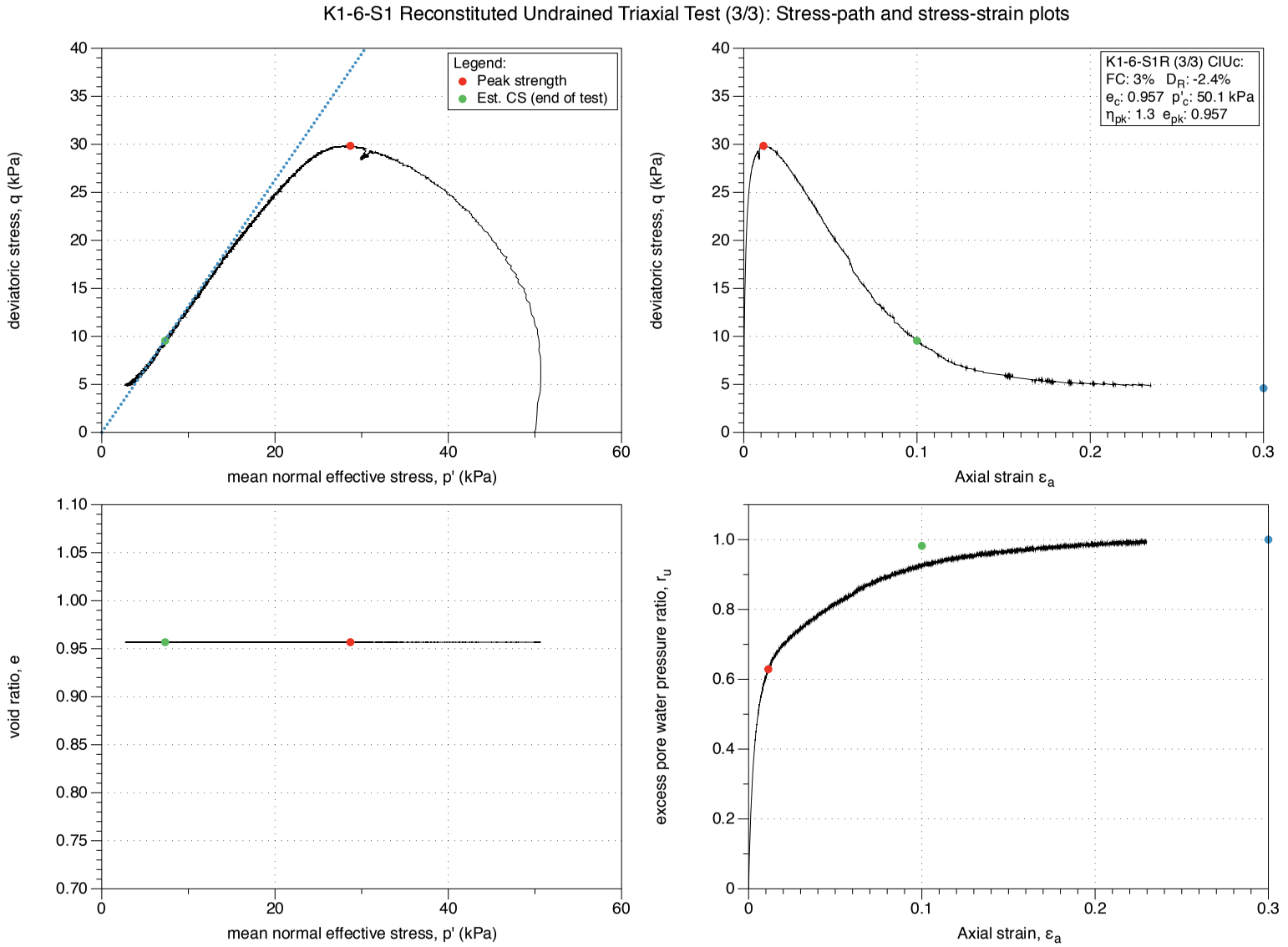

Figure 4.291: K1-6-S1 MT reconstituted sample (FC 3%), undrained monotonic triaxial test (CIU_C), test 3/3. Stress-path and stress-strain plots.

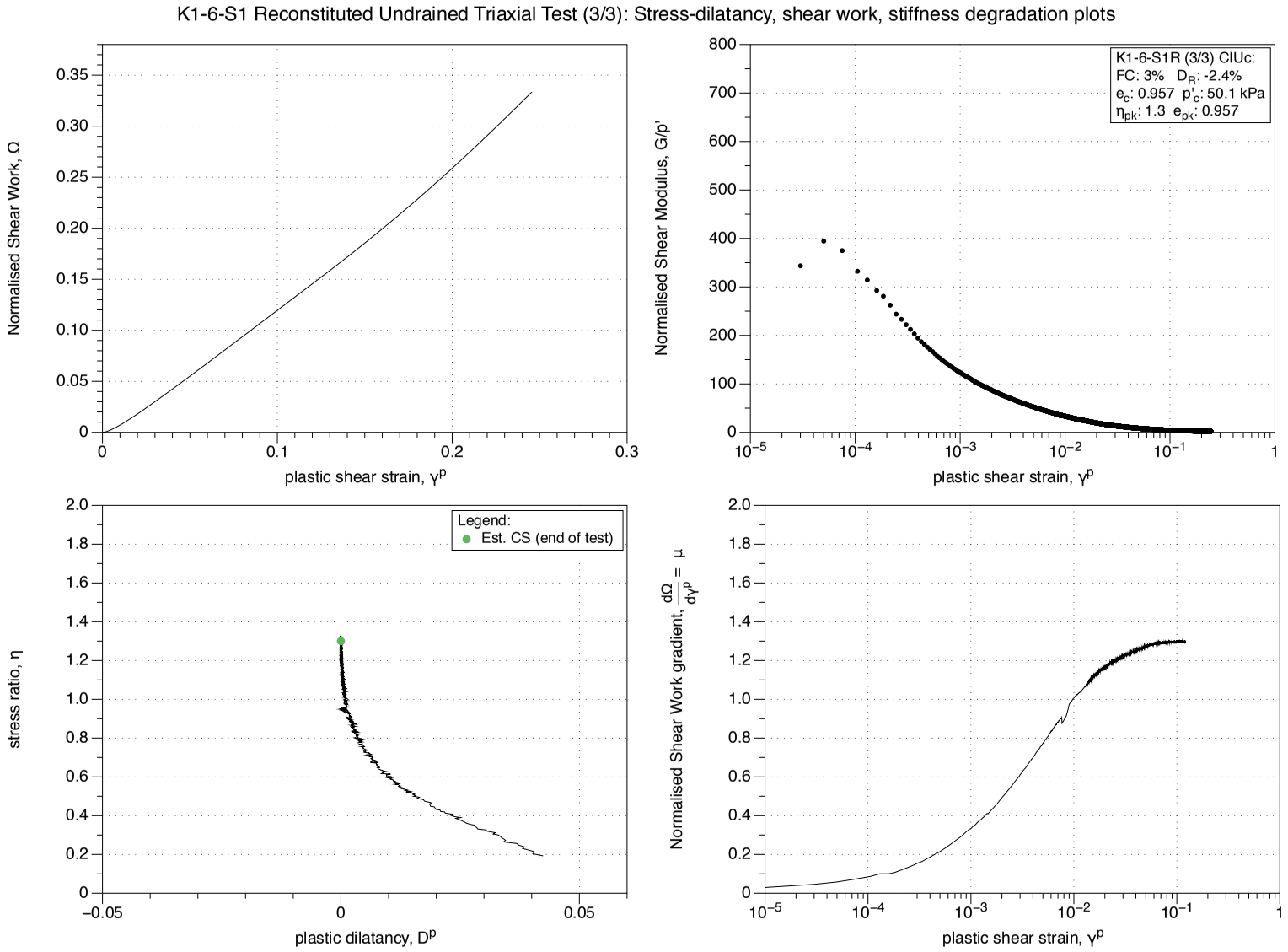

Figure 4.292: K1-6-S1 MT reconstituted sample (FC 3%), undrained monotonic triaxial test (CIU_C), test 3/3. Stress-dilatancy, shear work, stiffness degradation plots.

4.4.2 K1 MT Cyclic Triaxial Tests

Plots include the normalised effective stress path, stress strain plot, and change in excess pore pressure ratio (incremental and residual) with number of cycles, and axial strain with number of cycles. Additional plots for each cyclic test depict the development of maximum double amplitude strain, excess pore pressure ratio (maximum and residual), with number of cycles and the square-root of normalised shear work.

4.4.2.1 CTX Tests on samples (FC 30 - 50 %)

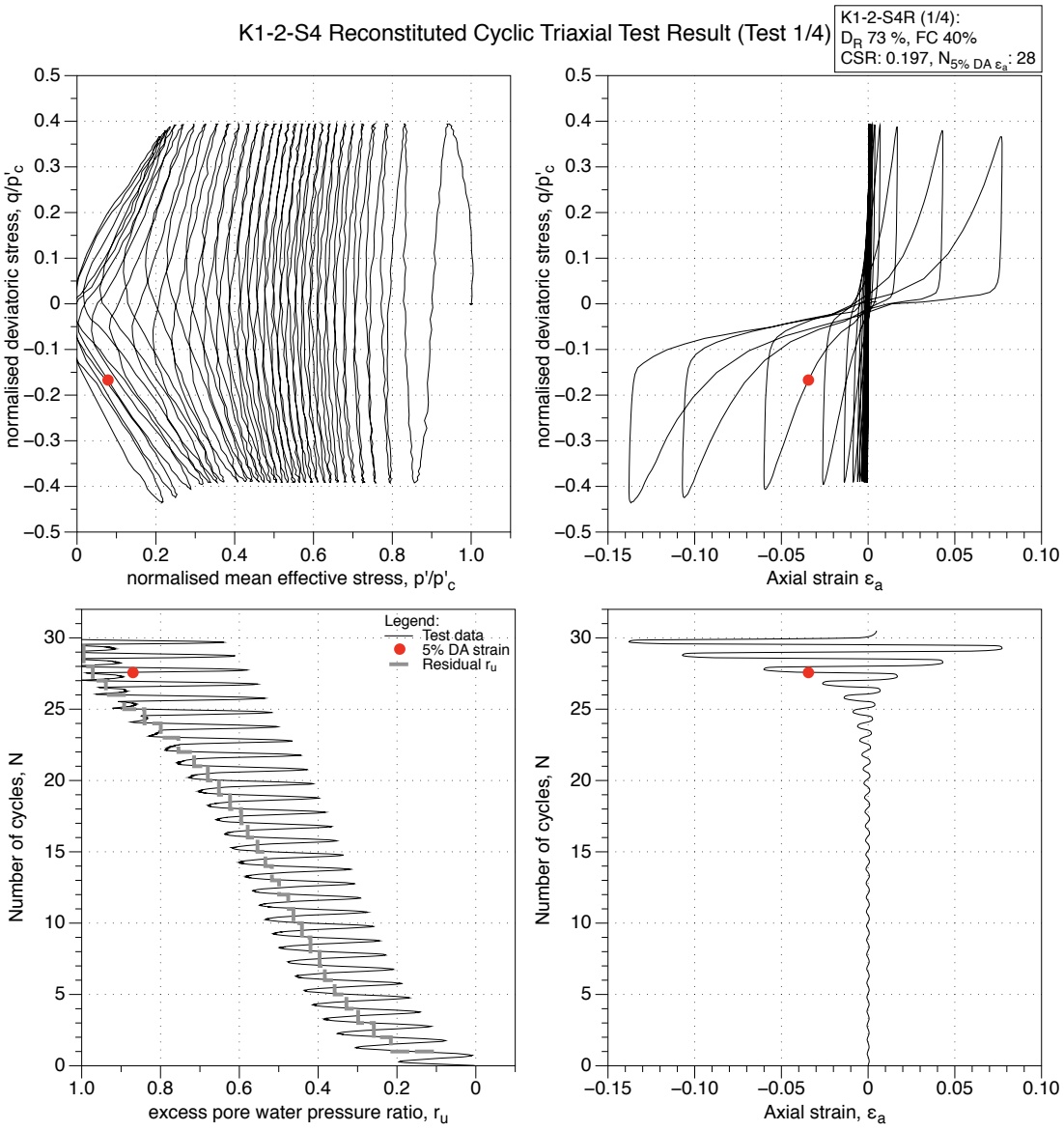

Figure 4.293: K1-2-S4 MT reconstituted sample (FC 40%), undrained cyclic triaxial test (CTX), test (1/4). Effective stress-path, stress-strain, excess pore water pressure ratio and strain development plots.

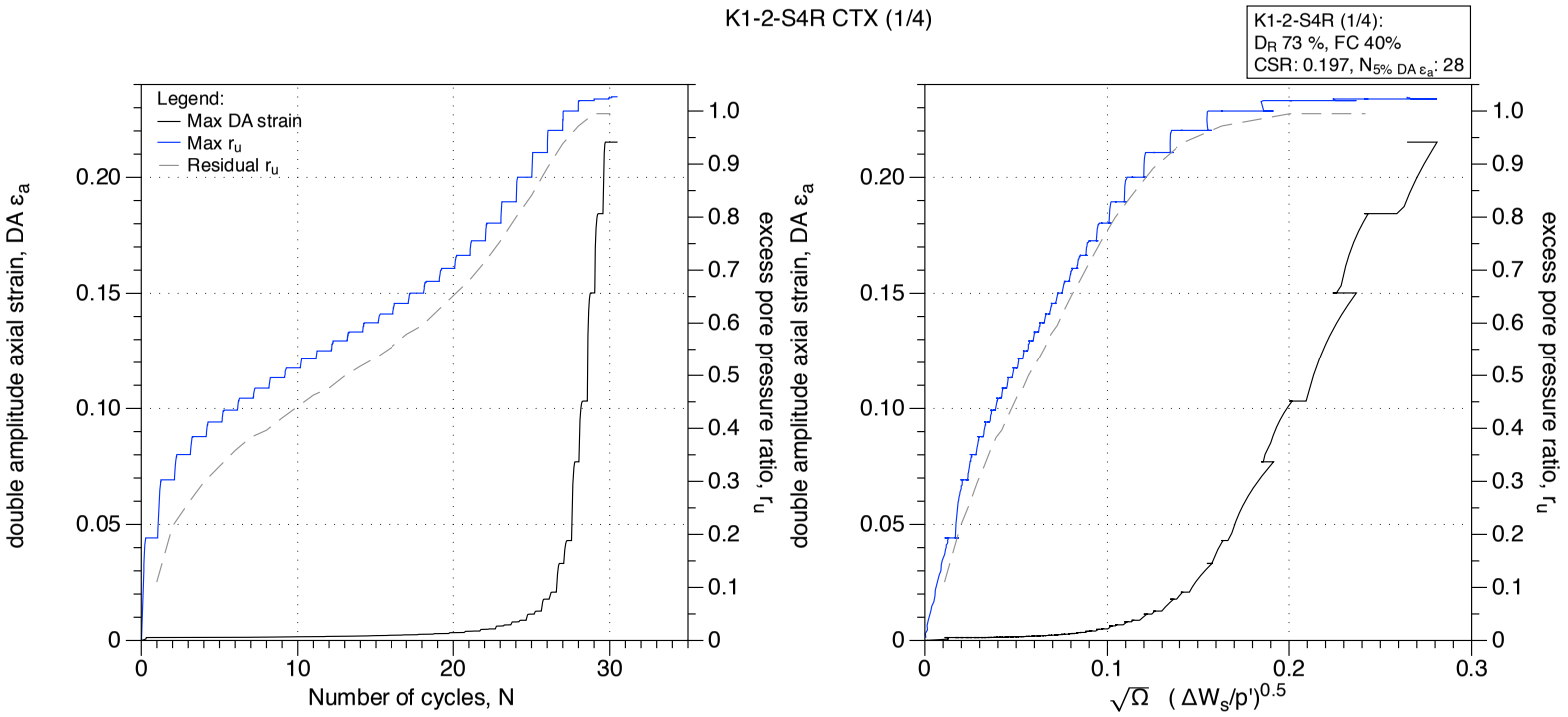

Figure 4.294: K1-2-S4 MT reconstituted sample (FC 40%), undrained cyclic triaxial test (CTX), test (1/4). Development of strain and excess pore water pressure with number of cycles and normalised shear work.

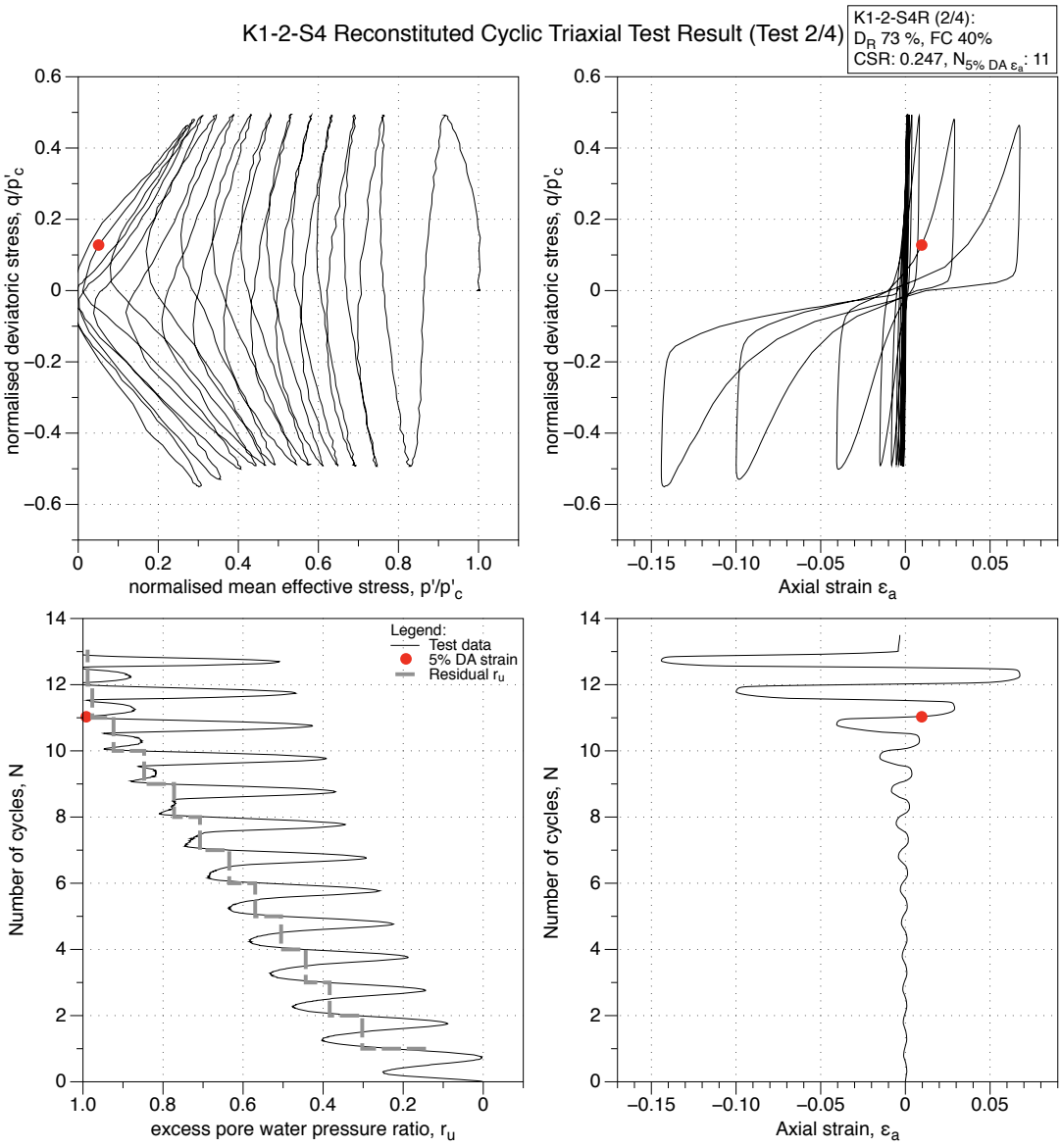

Figure 4.295: K1-2-S4 MT reconstituted sample (FC 40%), undrained cyclic triaxial test (CTX), test (2/4). Effective stress-path, stress-strain, excess pore water pressure ratio and strain development plots.

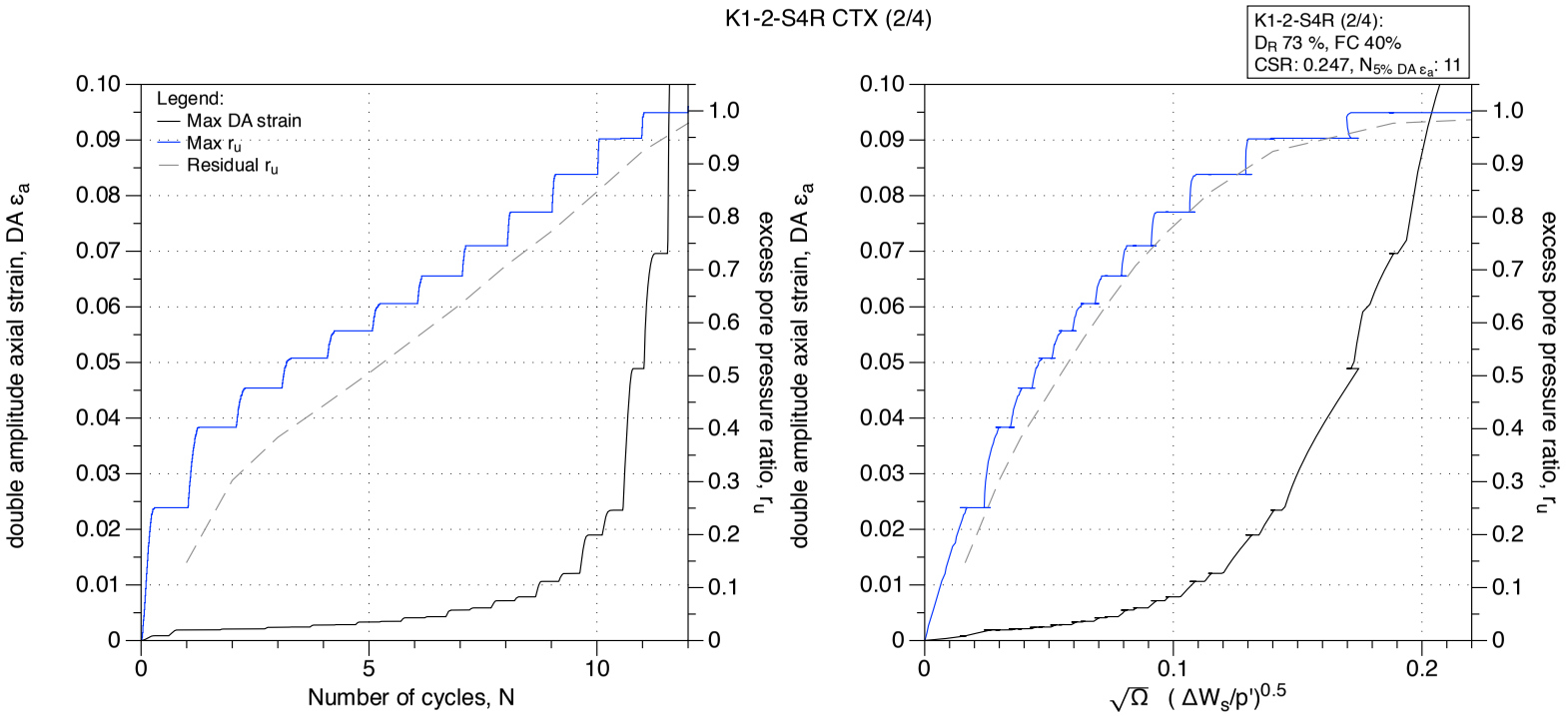

Figure 4.296: K1-2-S4 MT reconstituted sample (FC 40%), undrained cyclic triaxial test (CTX), test (2/4). Development of strain and excess pore water pressure with number of cycles and normalised shear work.

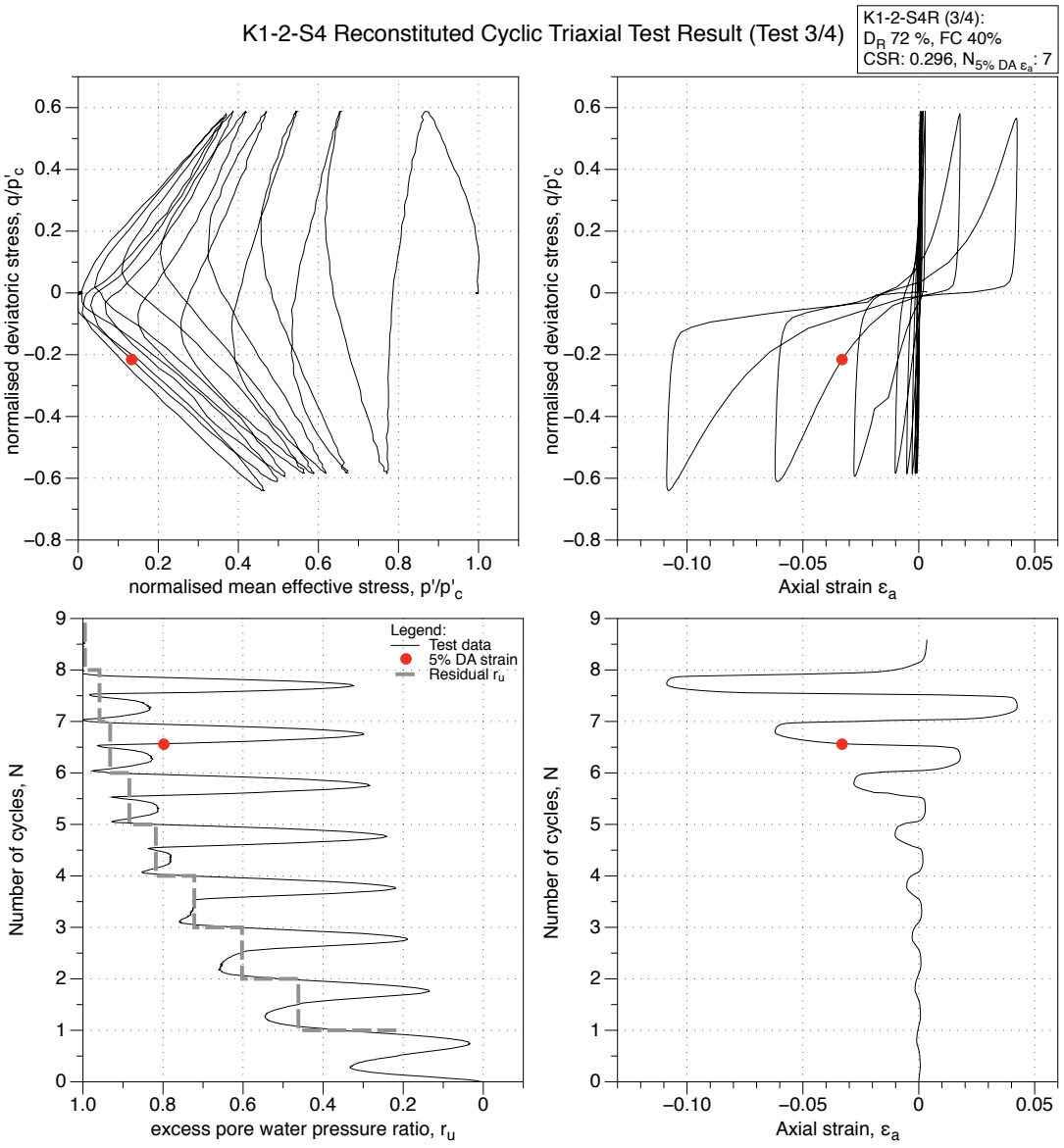

Figure 4.297: K1-2-S4 MT reconstituted sample (FC 40%), undrained cyclic triaxial test (CTX), test (3/4). Effective stress-path, stress-strain, excess pore water pressure ratio and strain development plots.

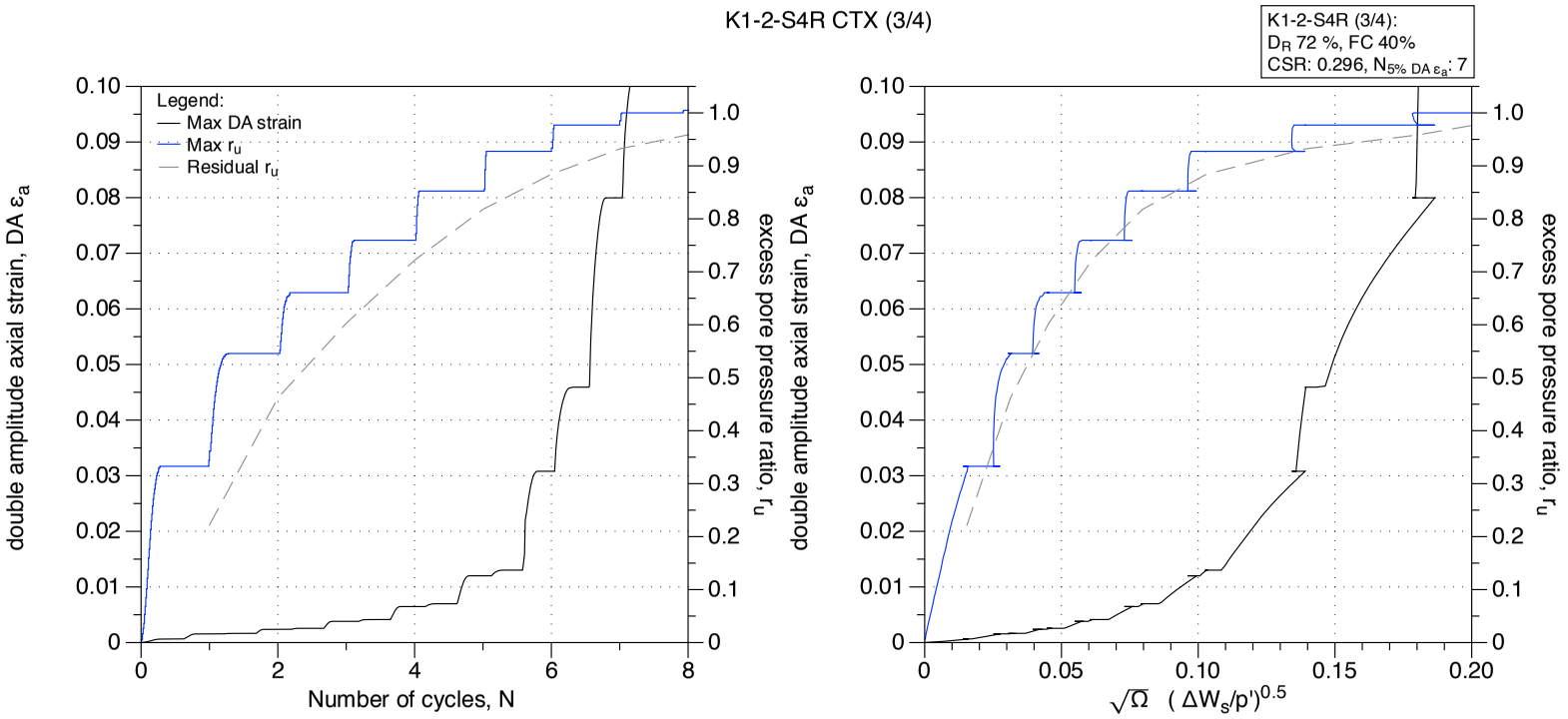

Figure 4.298: K1-2-S4 MT reconstituted sample (FC 40%), undrained cyclic triaxial test (CTX), test (3/4). Development of strain and excess pore water pressure with number of cycles and normalised shear work.

4.4.2.2 CTX Tests on samples (FC 50 - 80 %)

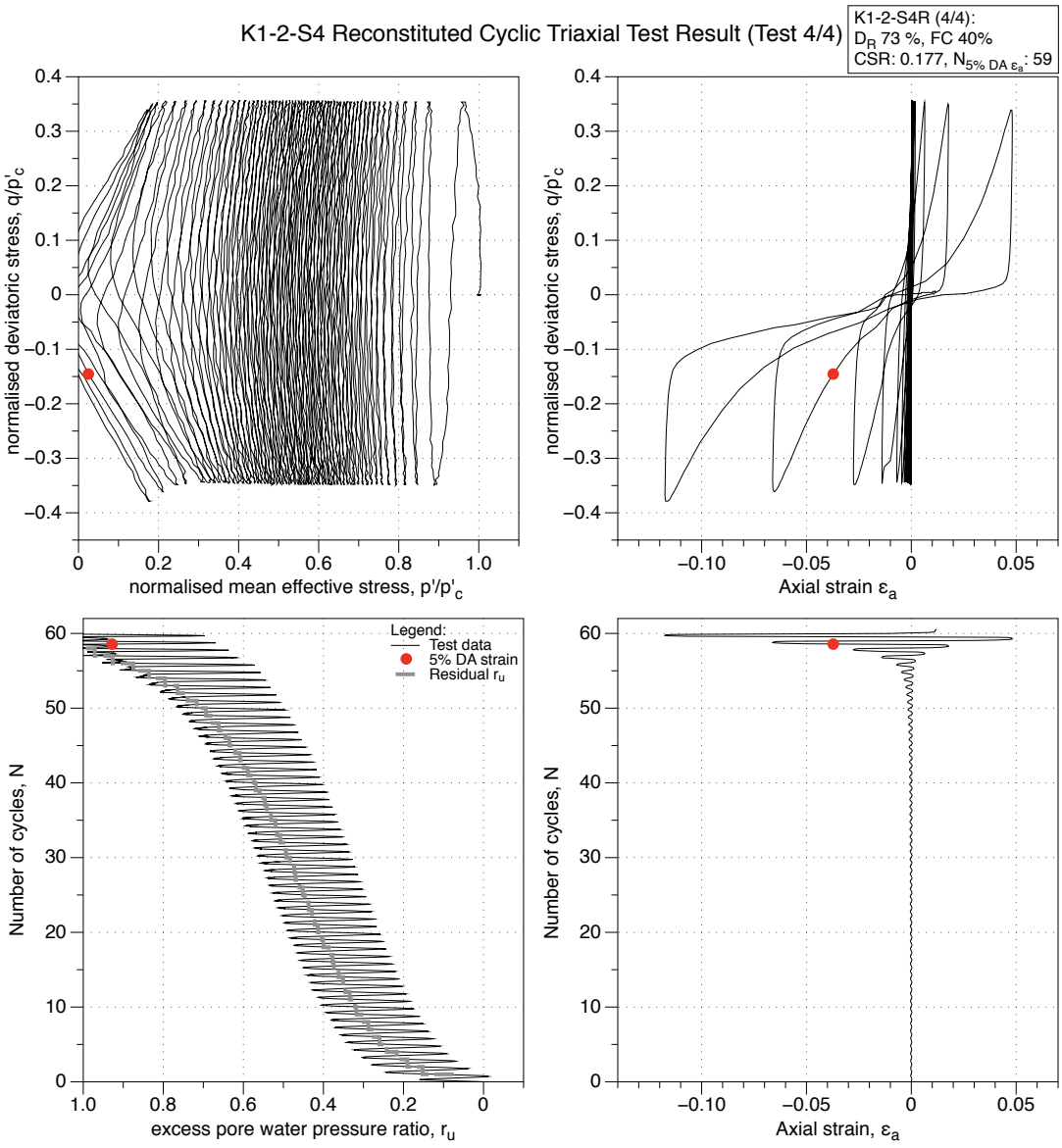

Figure 4.299: K1-2-S4 MT reconstituted sample (FC 40%), undrained cyclic triaxial test (CTX), test (4/4). Effective stress-path, stress-strain, excess pore water pressure ratio and strain development plots.

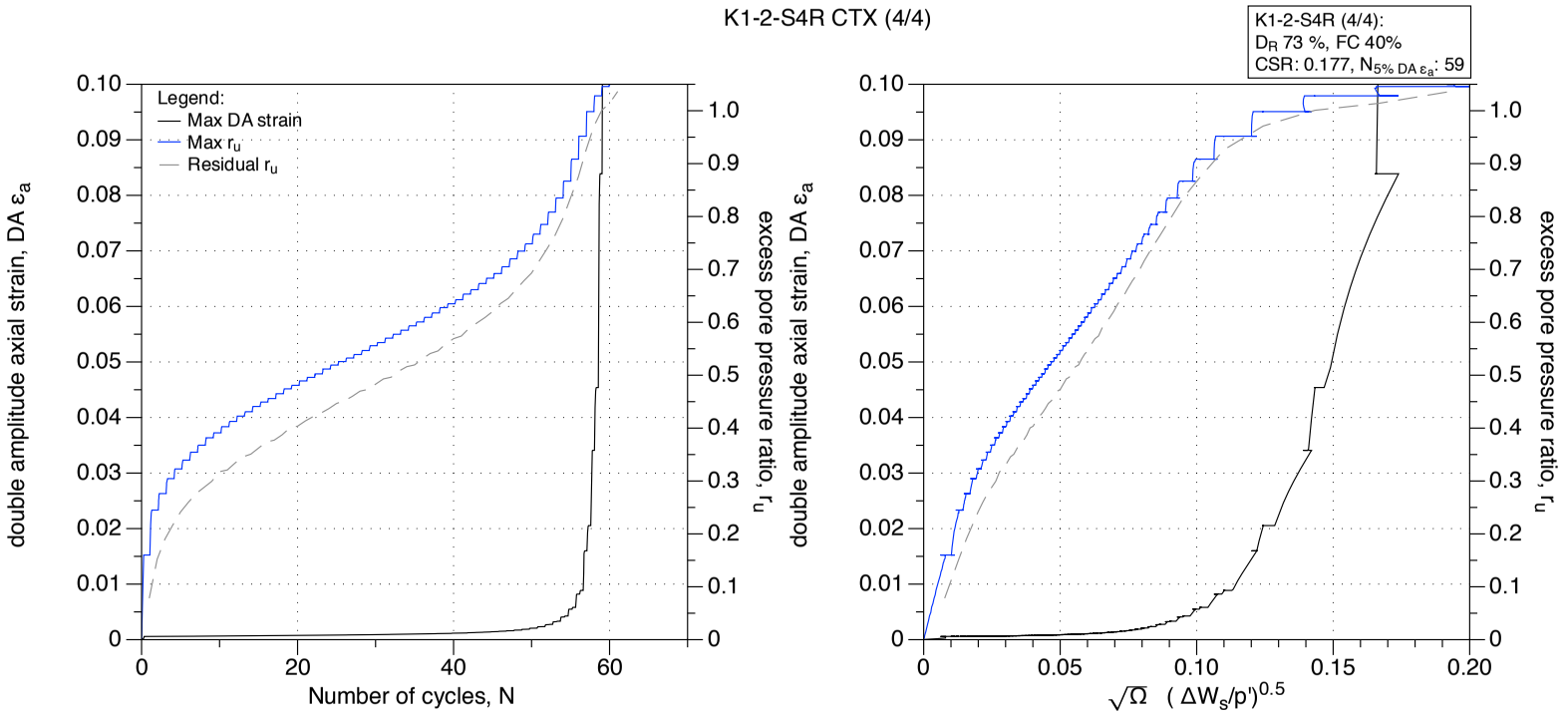

Figure 4.300: K1-2-S4 MT reconstituted sample (FC 40%), undrained cyclic triaxial test (CTX), test (4/4). Development of strain and excess pore water pressure with number of cycles and normalised shear work.

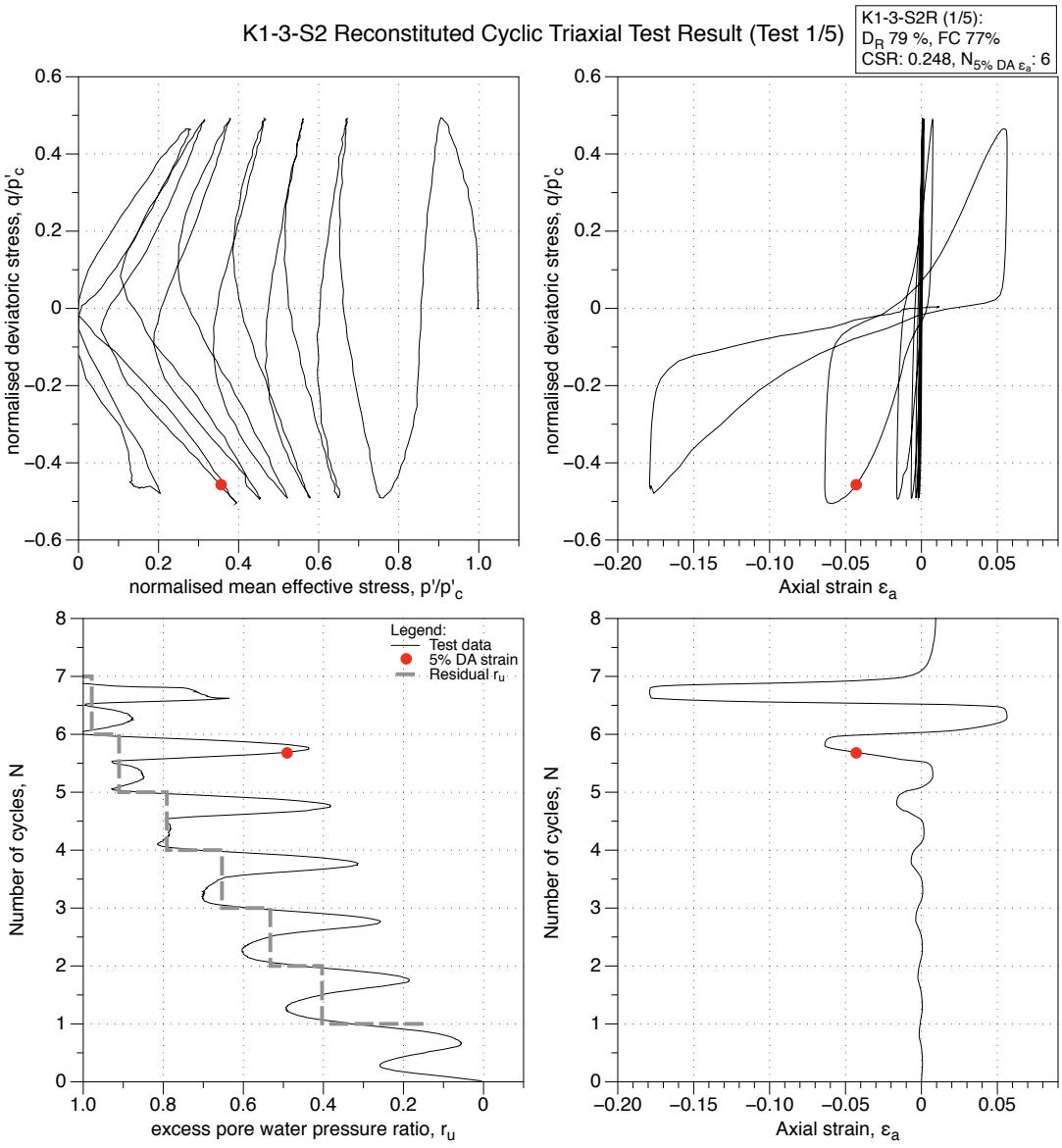

Figure 4.301: K1-3-S2 MT reconstituted sample (FC 77%), undrained cyclic triaxial test (CTX), test (1/5). Effective stress-path, stress-strain, excess pore water pressure ratio and strain development plots.

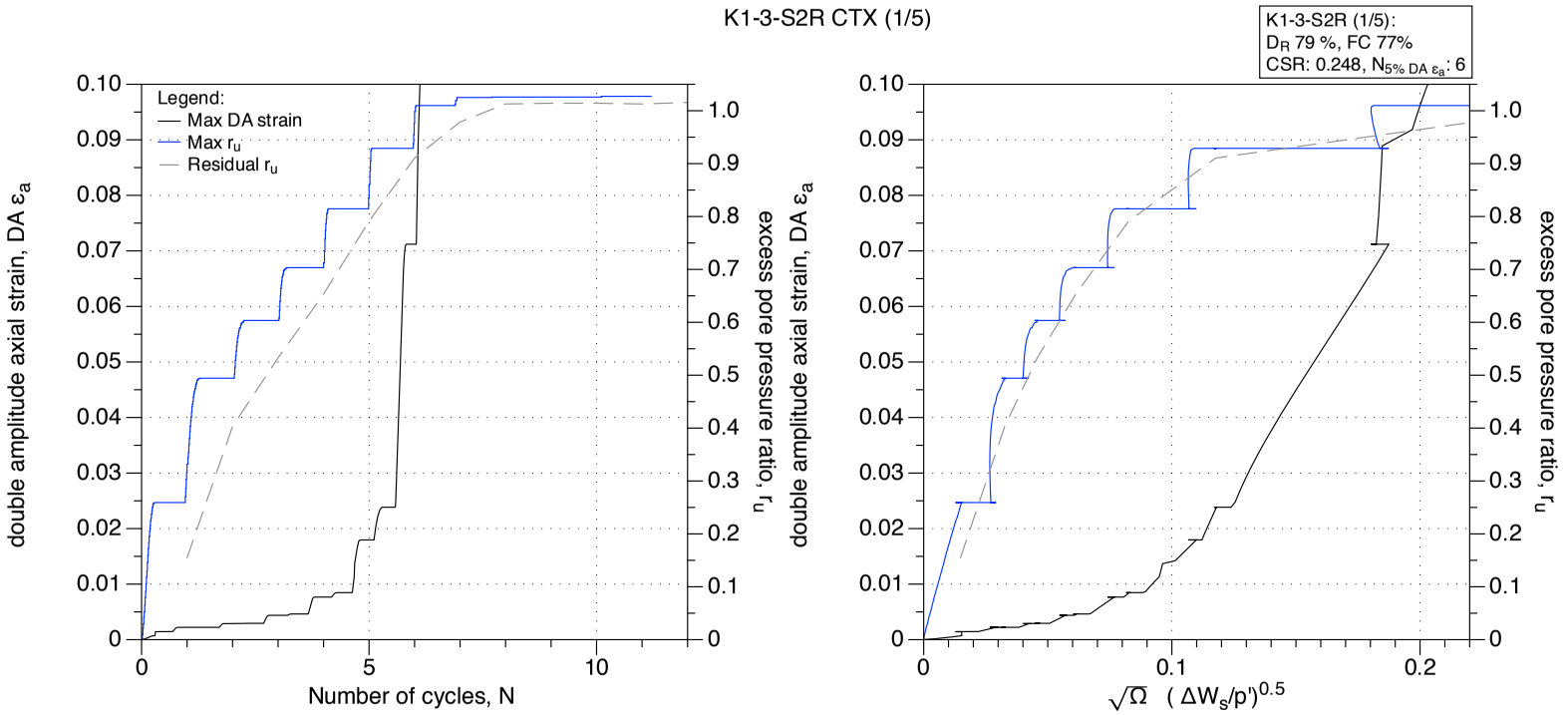

Figure 4.302: K1-3-S2 MT reconstituted sample (FC 77%), undrained cyclic triaxial test (CTX), test (1/5). Development of strain and excess pore water pressure with number of cycles and normalised shear work.

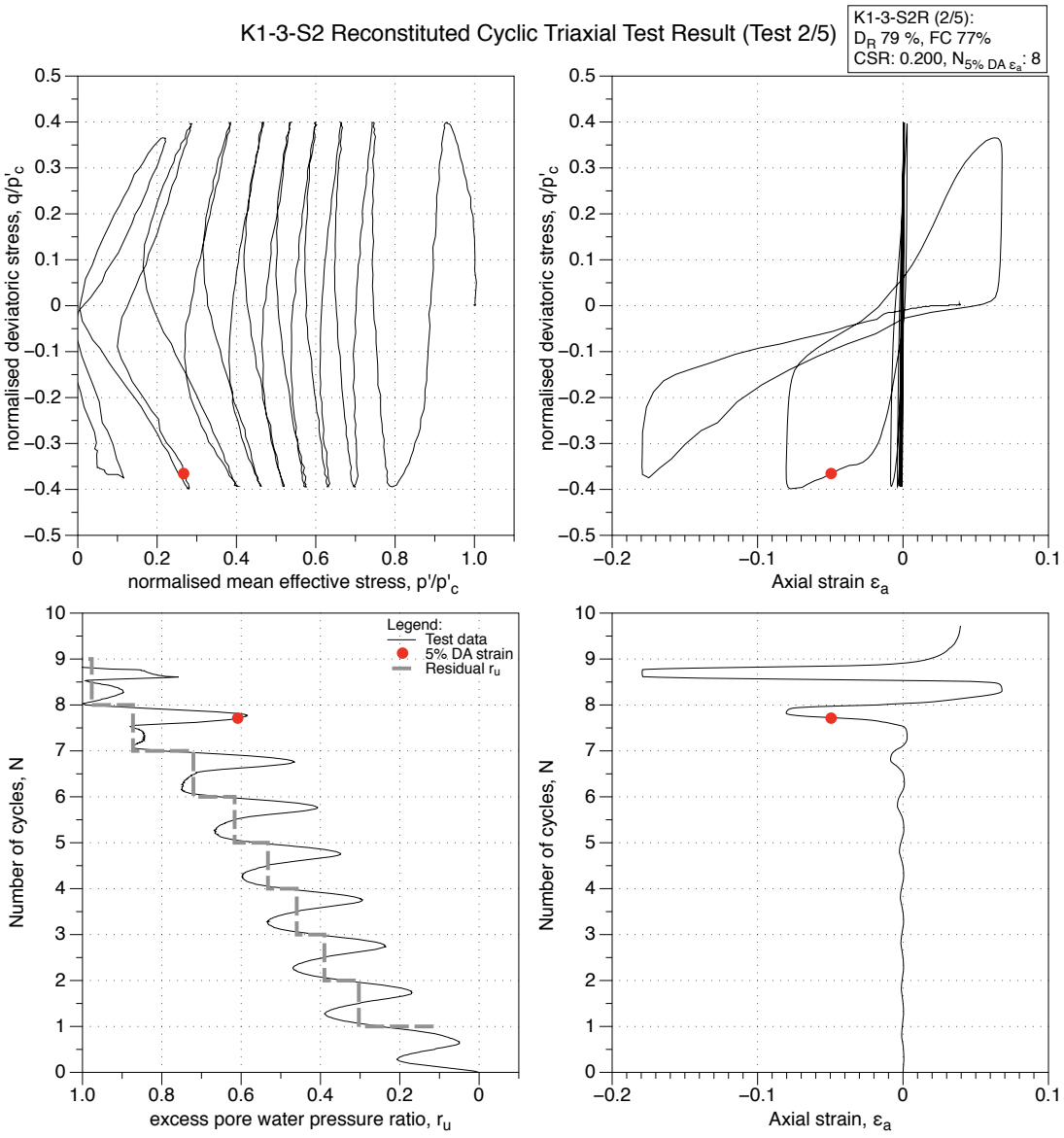

Figure 4.303: K1-3-S2 MT reconstituted sample (FC 77%), undrained cyclic triaxial test (CTX), test (2/5). Effective stress-path, stress-strain, excess pore water pressure ratio and strain development plots.

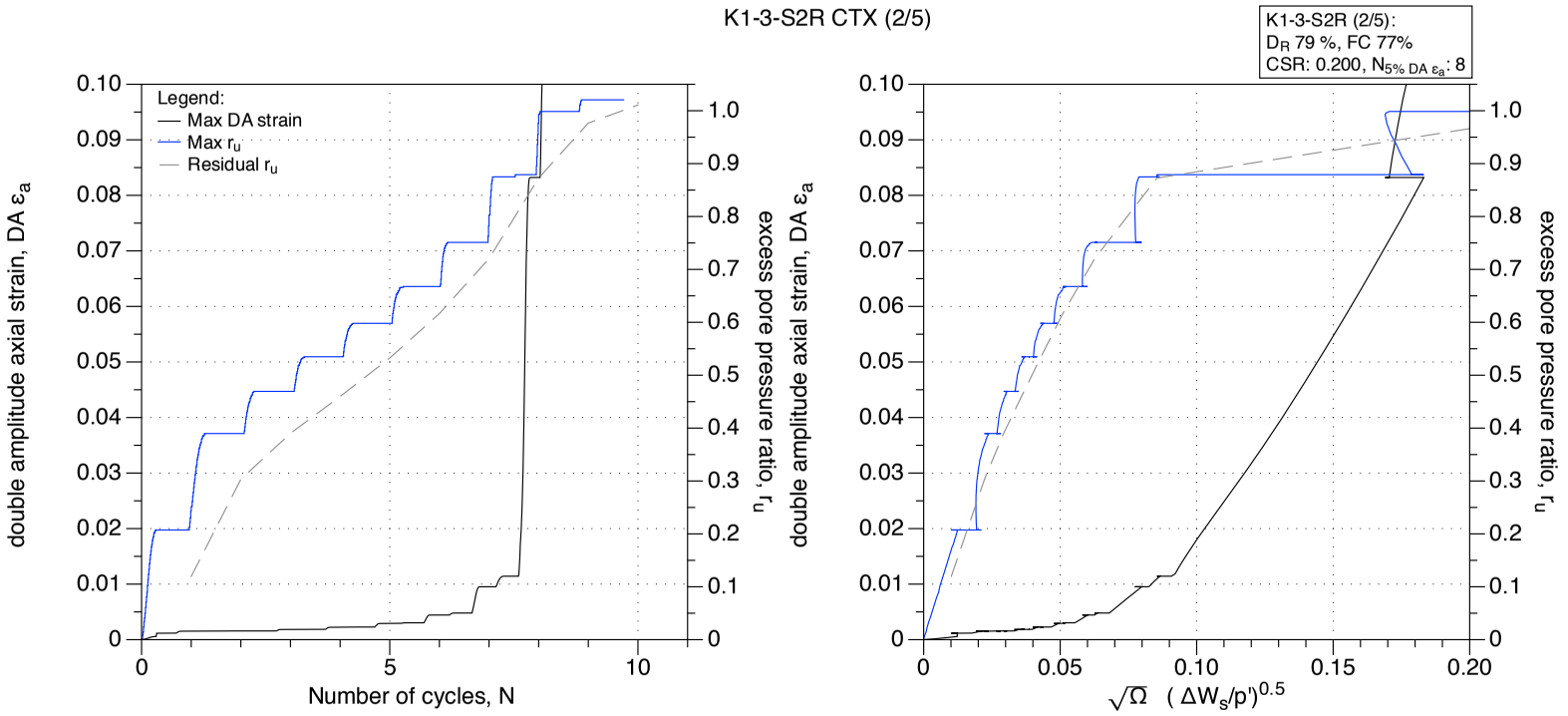

Figure 4.304: K1-3-S2 MT reconstituted sample (FC 77%), undrained cyclic triaxial test (CTX), test (2/5). Development of strain and excess pore water pressure with number of cycles and normalised shear work.

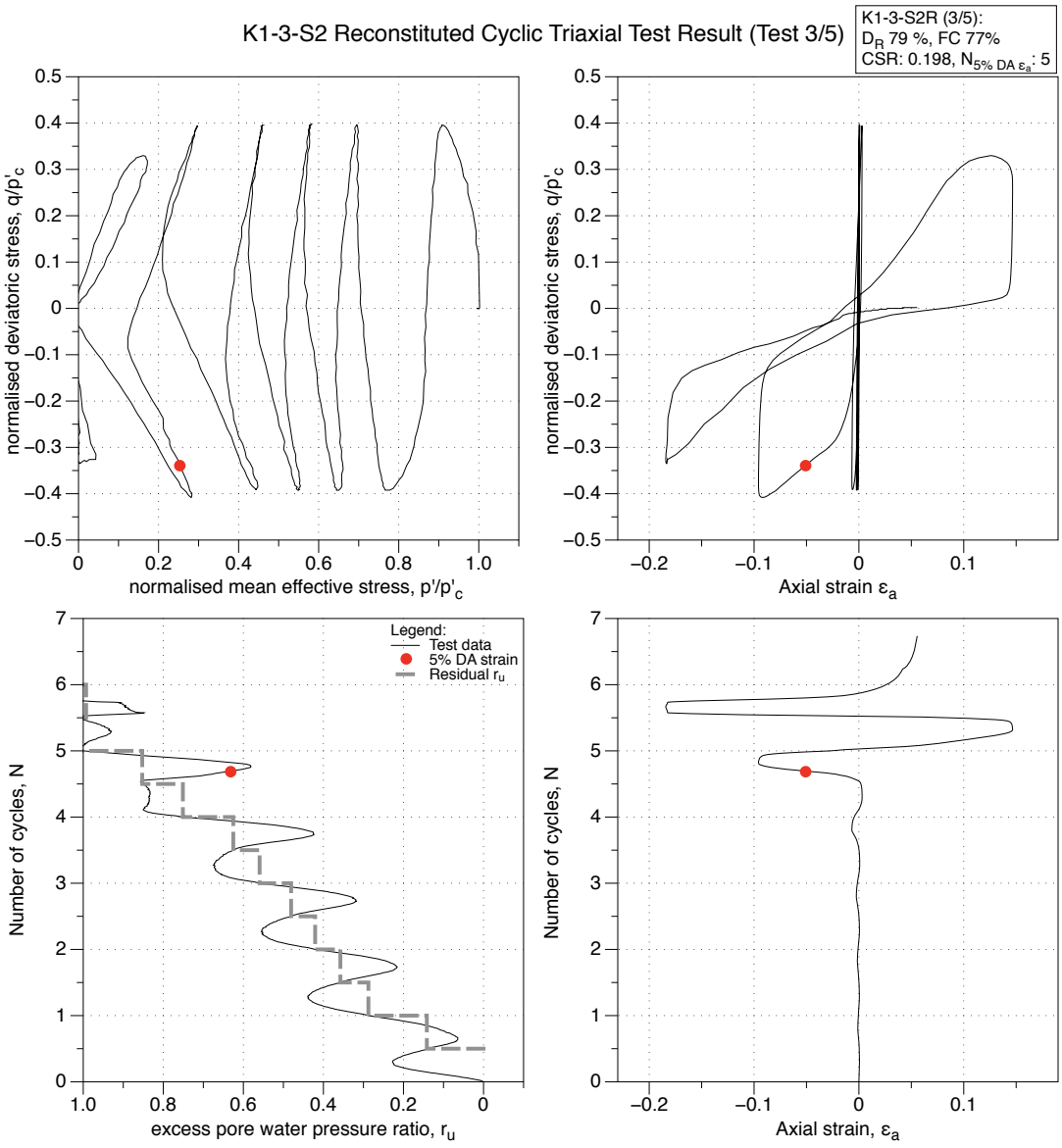

Figure 4.305: K1-3-S2 MT reconstituted sample (FC 77%), undrained cyclic triaxial test (CTX), test (3/5). Effective stress-path, stress-strain, excess pore water pressure ratio and strain development plots.

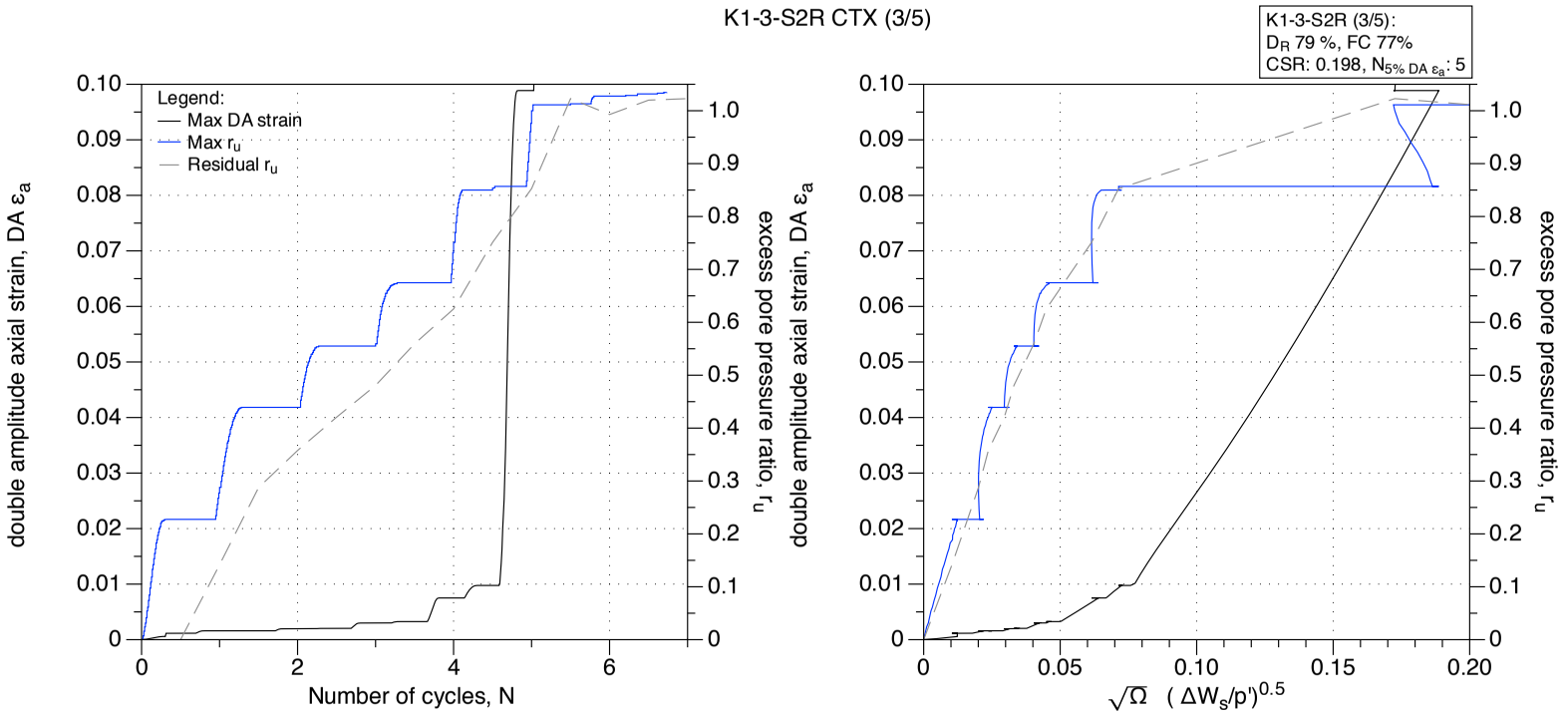

Figure 4.306: K1-3-S2 MT reconstituted sample (FC 77%), undrained cyclic triaxial test (CTX), test (3/5). Development of strain and excess pore water pressure with number of cycles and normalised shear work.

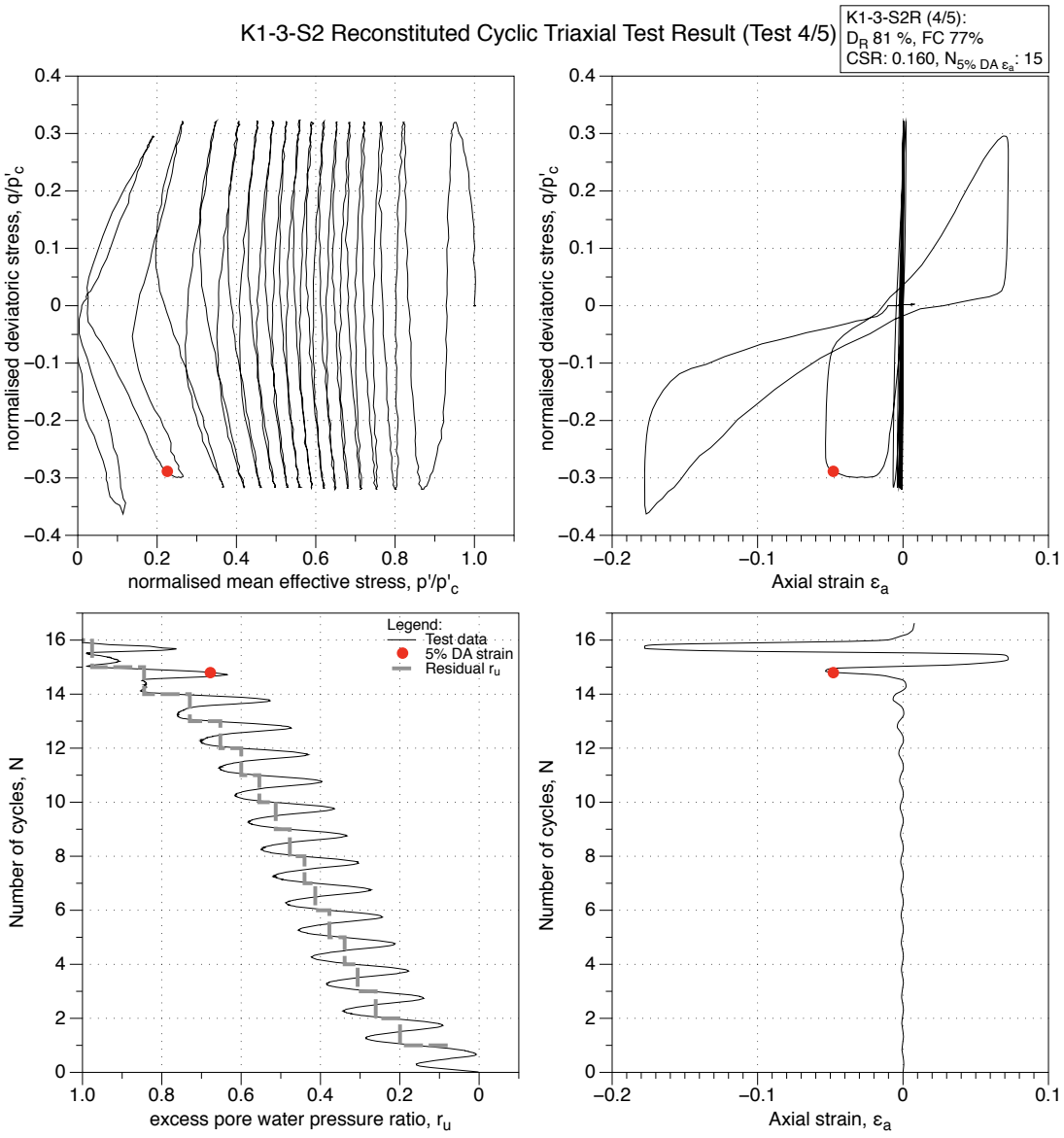

Figure 4.307: K1-3-S2 MT reconstituted sample (FC 77%), undrained cyclic triaxial test (CTX), test (4/5). Effective stress-path, stress-strain, excess pore water pressure ratio and strain development plots.

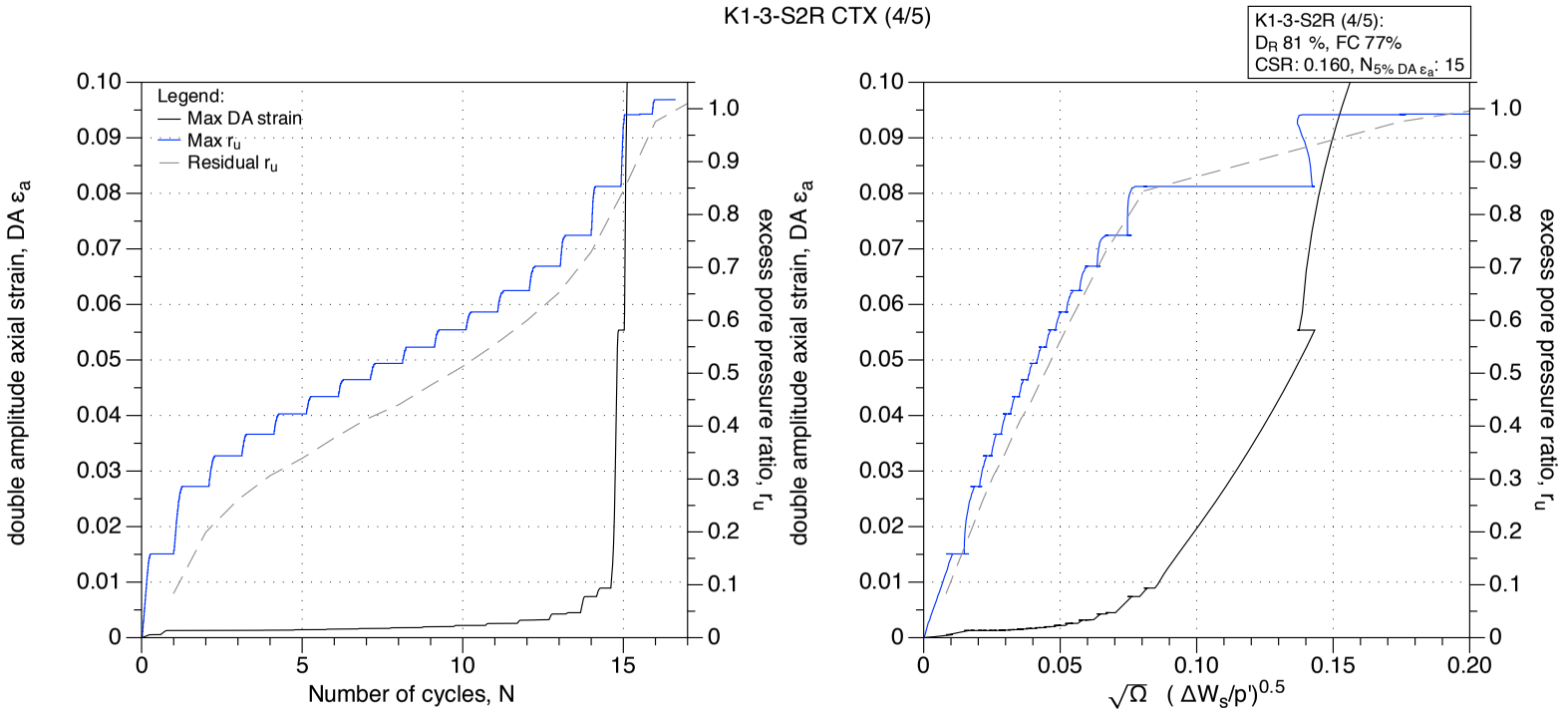

Figure 4.308: K1-3-S2 MT reconstituted sample (FC 77%), undrained cyclic triaxial test (CTX), test (4/5). Development of strain and excess pore water pressure with number of cycles and normalised shear work.

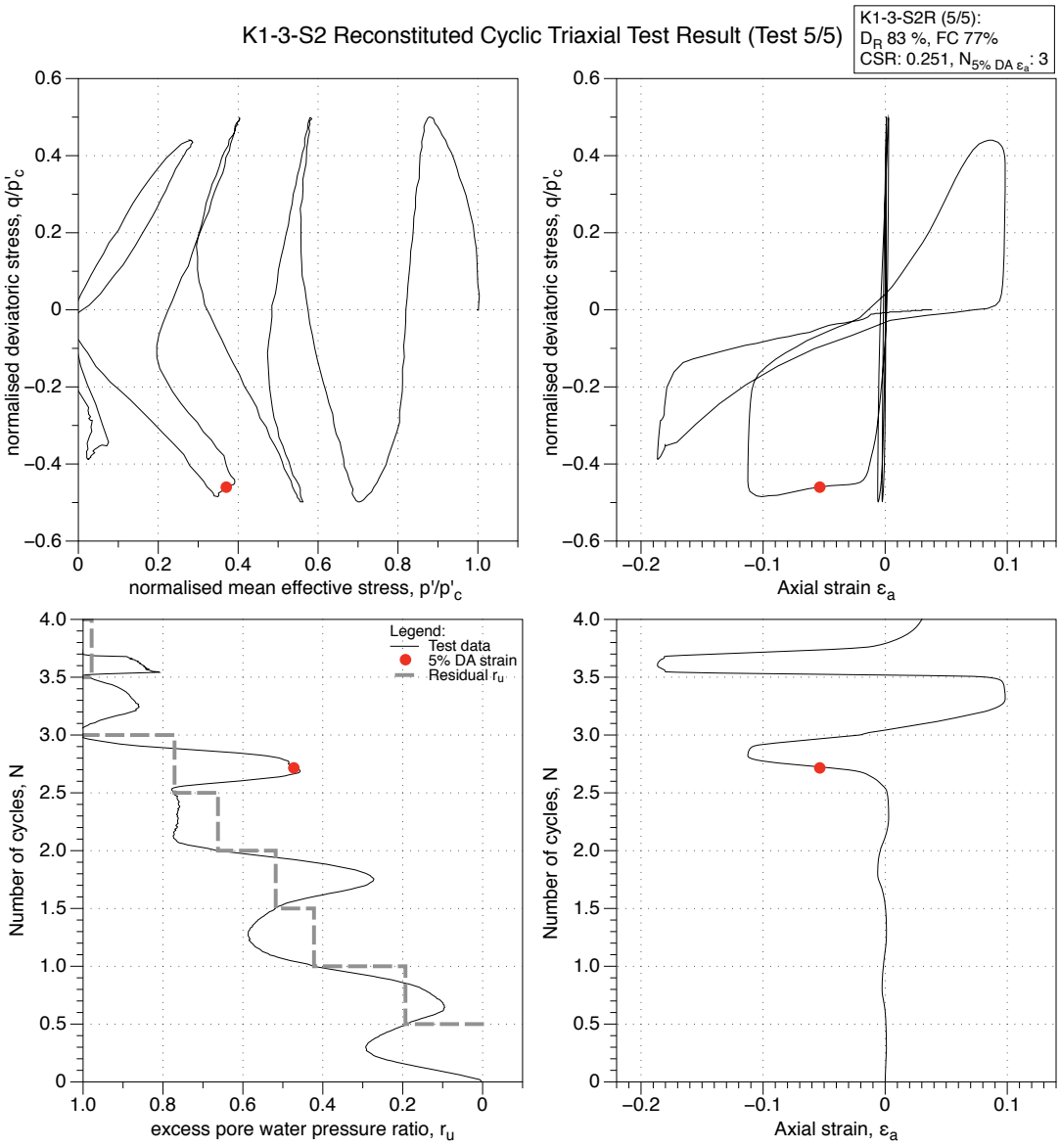

Figure 4.309: K1-3-S2 MT reconstituted sample (FC 77%), undrained cyclic triaxial test (CTX), test (5/5). Effective stress-path, stress-strain, excess pore water pressure ratio and strain development plots.

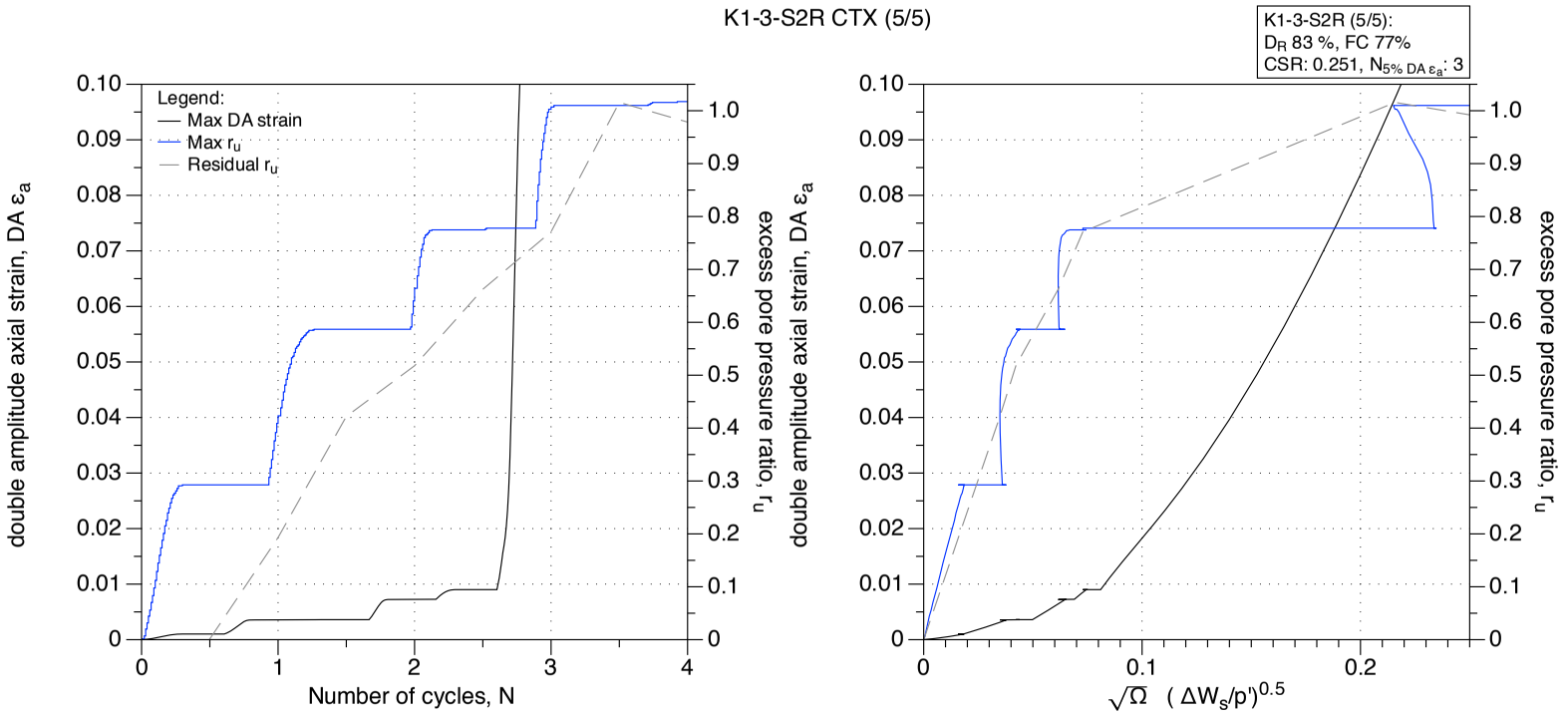

Figure 4.310: K1-3-S2 MT reconstituted sample (FC 77%), undrained cyclic triaxial test (CTX), test (5/5). Development of strain and excess pore water pressure with number of cycles and normalised shear work.

4.4.2.3 CTX Tests on samples (FC 15 - 20 %)

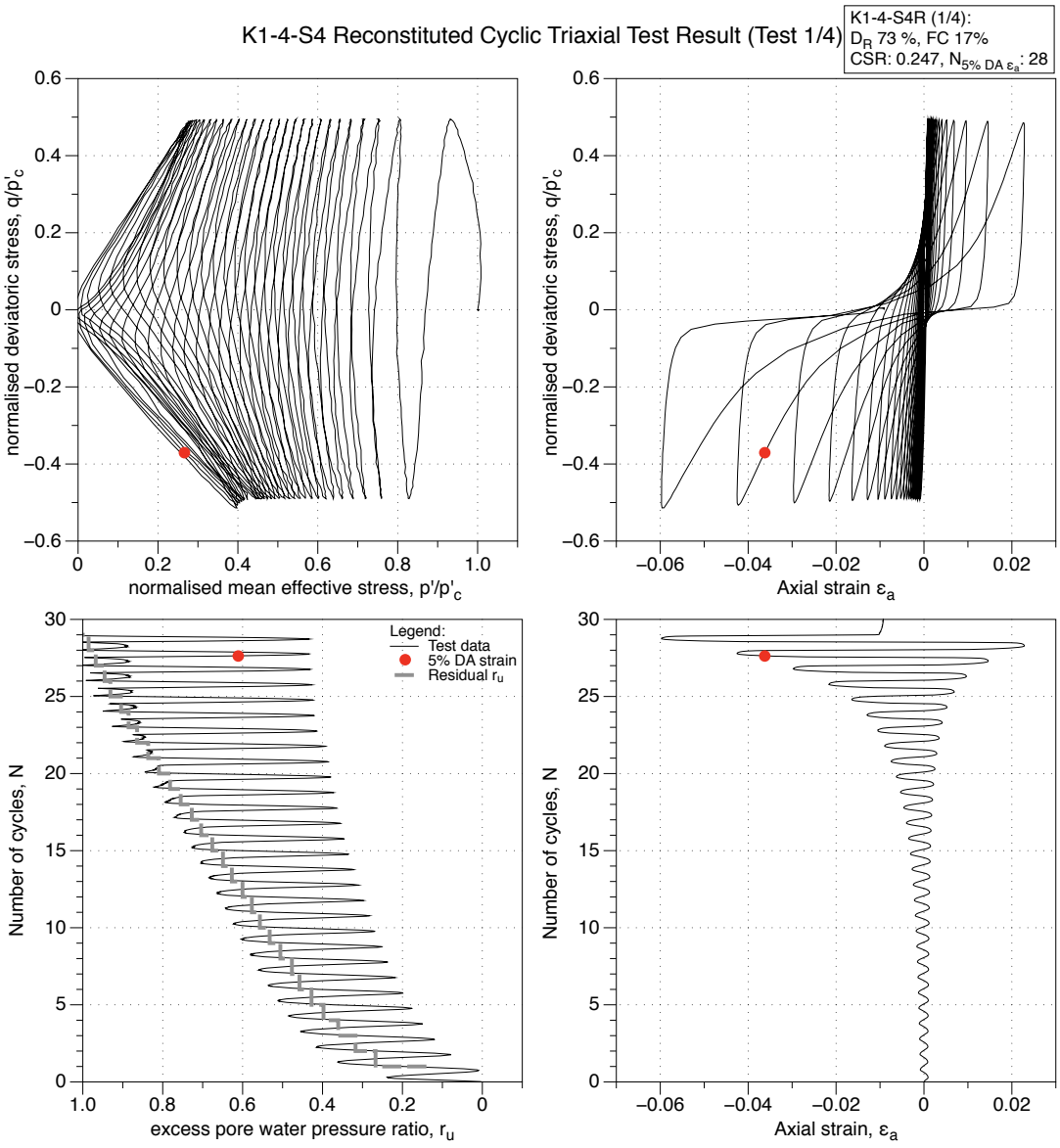

Figure 4.311: K1-4-S4 MT reconstituted sample (FC 17%), undrained cyclic triaxial test (CTX), test (1/4). Effective stress-path, stress-strain, excess pore water pressure ratio and strain development plots.

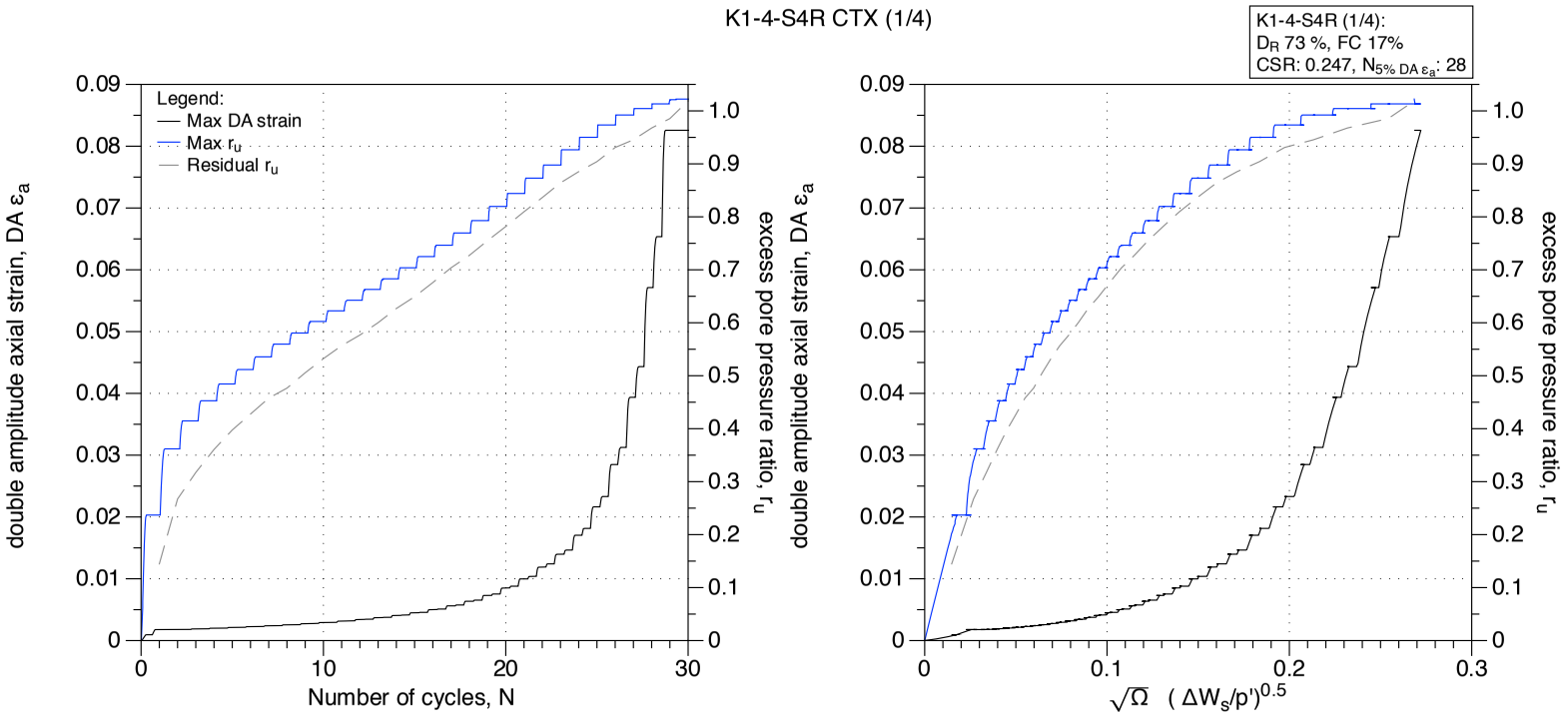

Figure 4.312: K1-4-S4 MT reconstituted sample (FC 17%), undrained cyclic triaxial test (CTX), test (1/4). Development of strain and excess pore water pressure with number of cycles and normalised shear work.

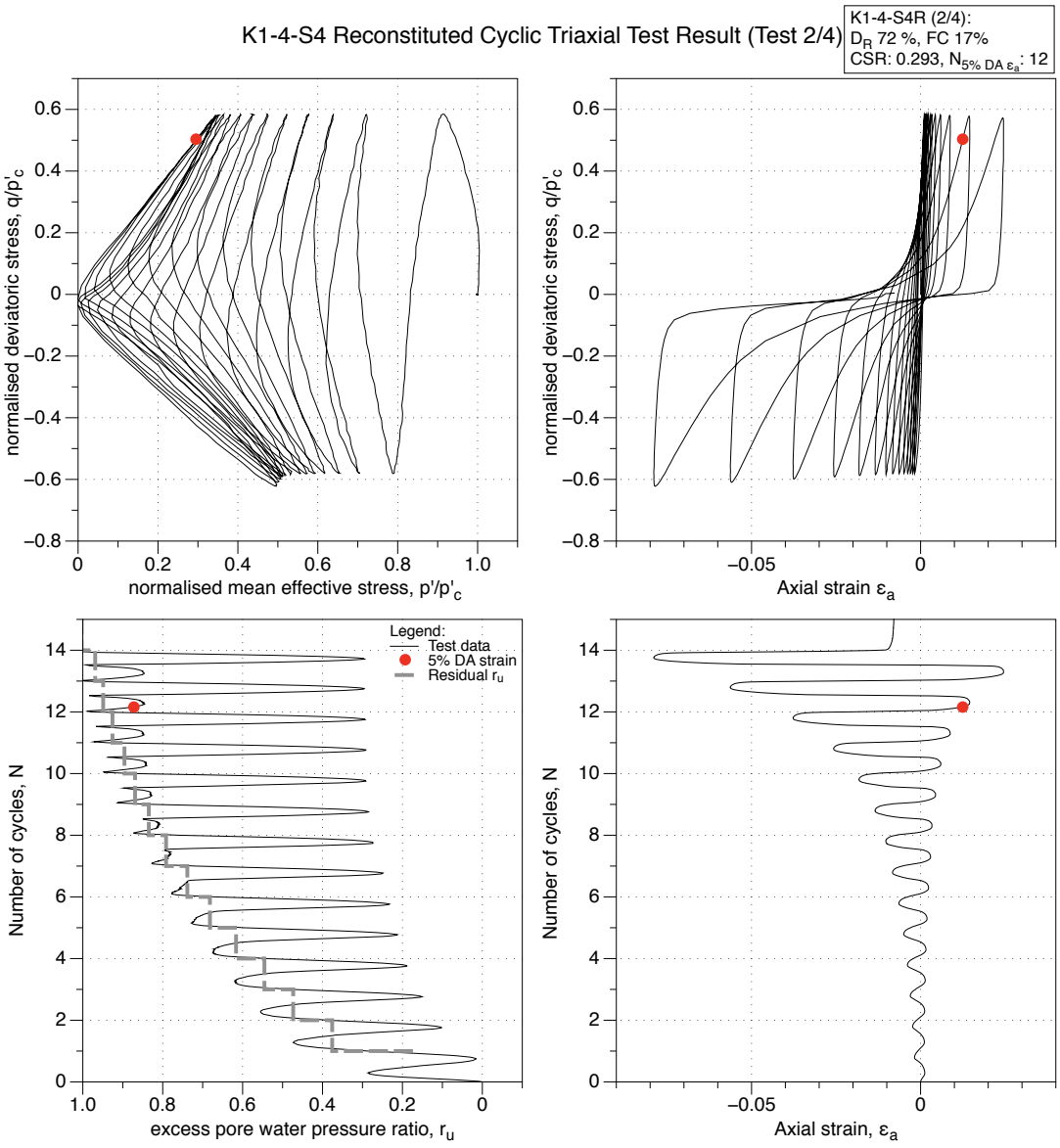

Figure 4.313: K1-4-S4 MT reconstituted sample (FC 17%), undrained cyclic triaxial test (CTX), test (2/4). Effective stress-path, stress-strain, excess pore water pressure ratio and strain development plots.

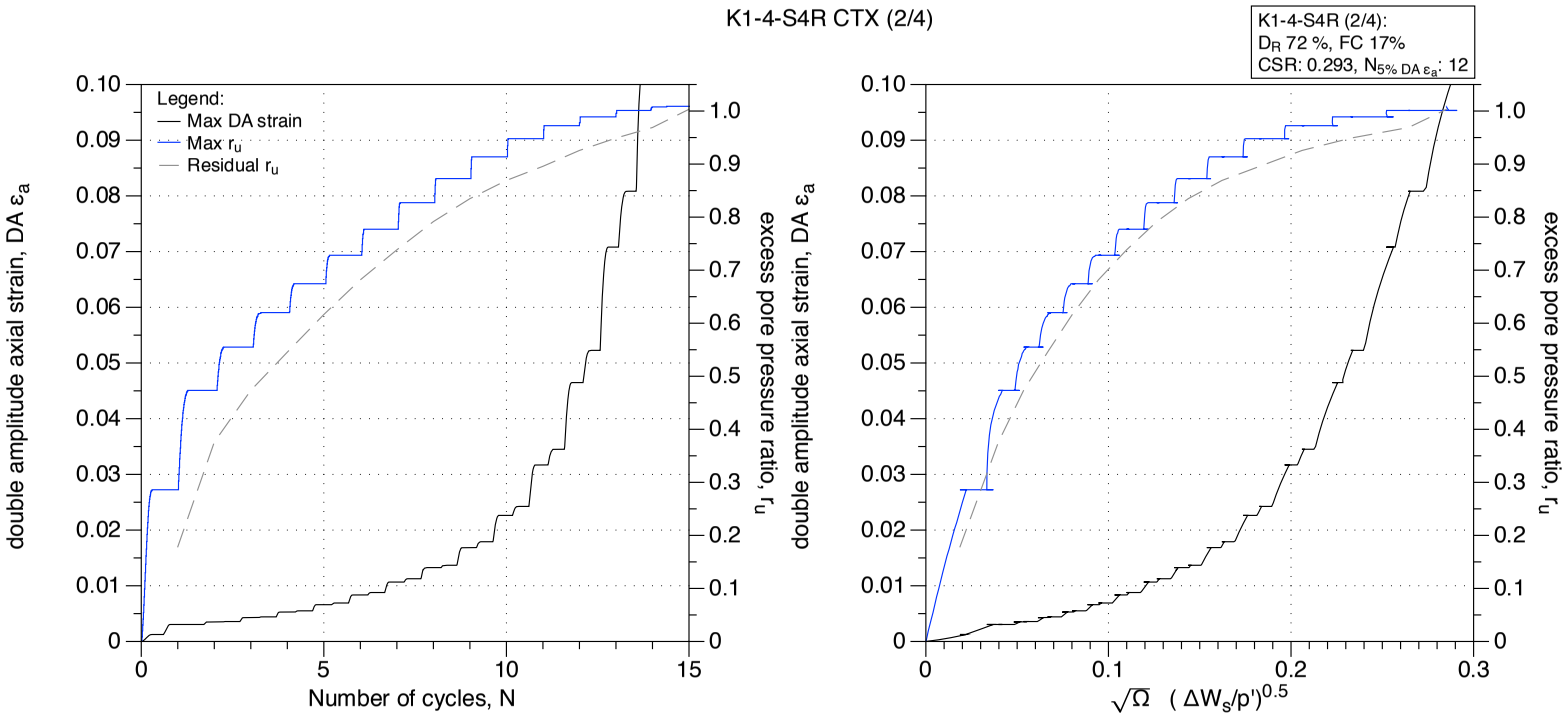

Figure 4.314: K1-4-S4 MT reconstituted sample (FC 17%), undrained cyclic triaxial test (CTX), test (2/4). Development of strain and excess pore water pressure with number of cycles and normalised shear work.

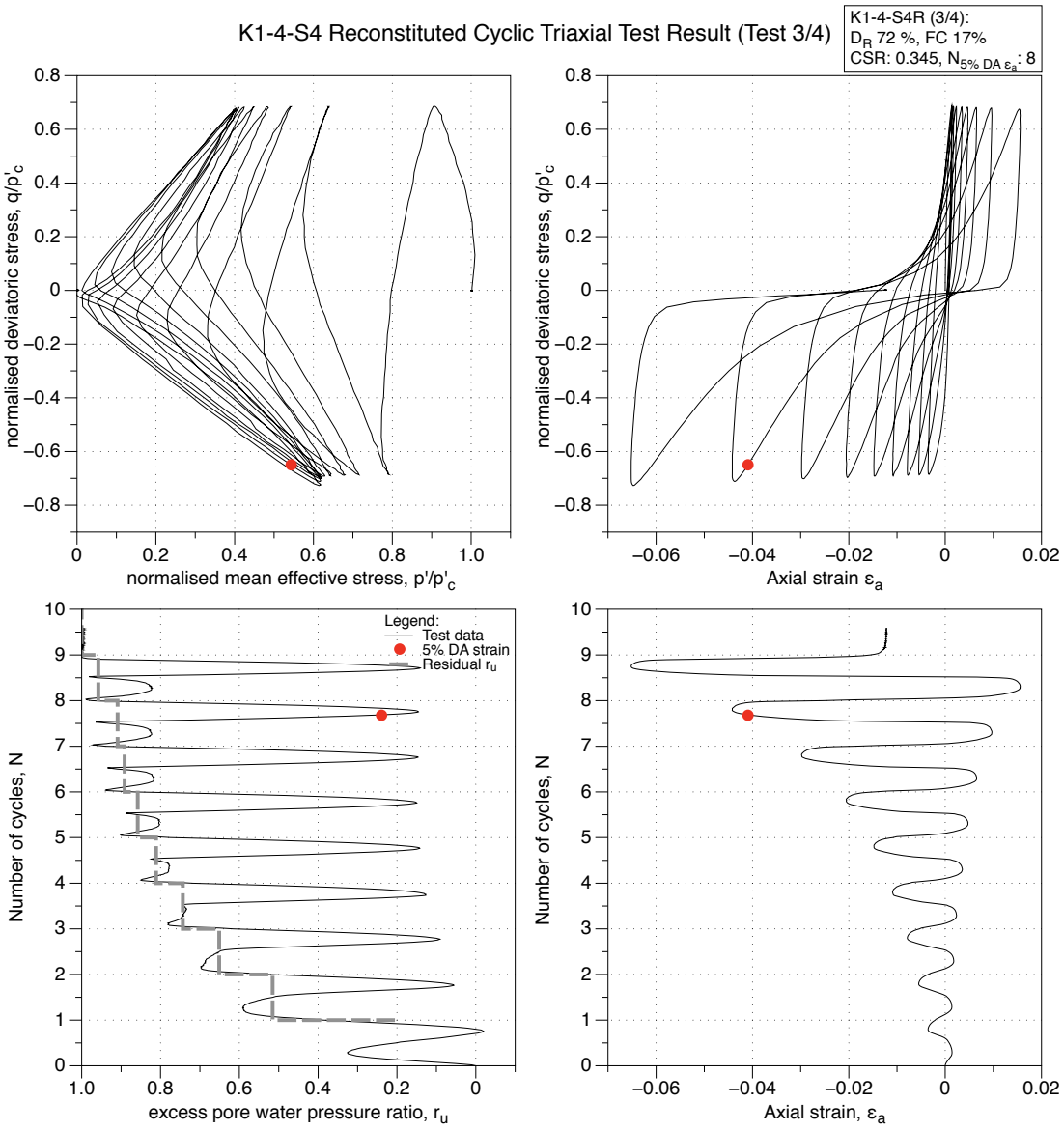

Figure 4.315: K1-4-S4 MT reconstituted sample (FC 17%), undrained cyclic triaxial test (CTX), test (3/4). Effective stress-path, stress-strain, excess pore water pressure ratio and strain development plots.

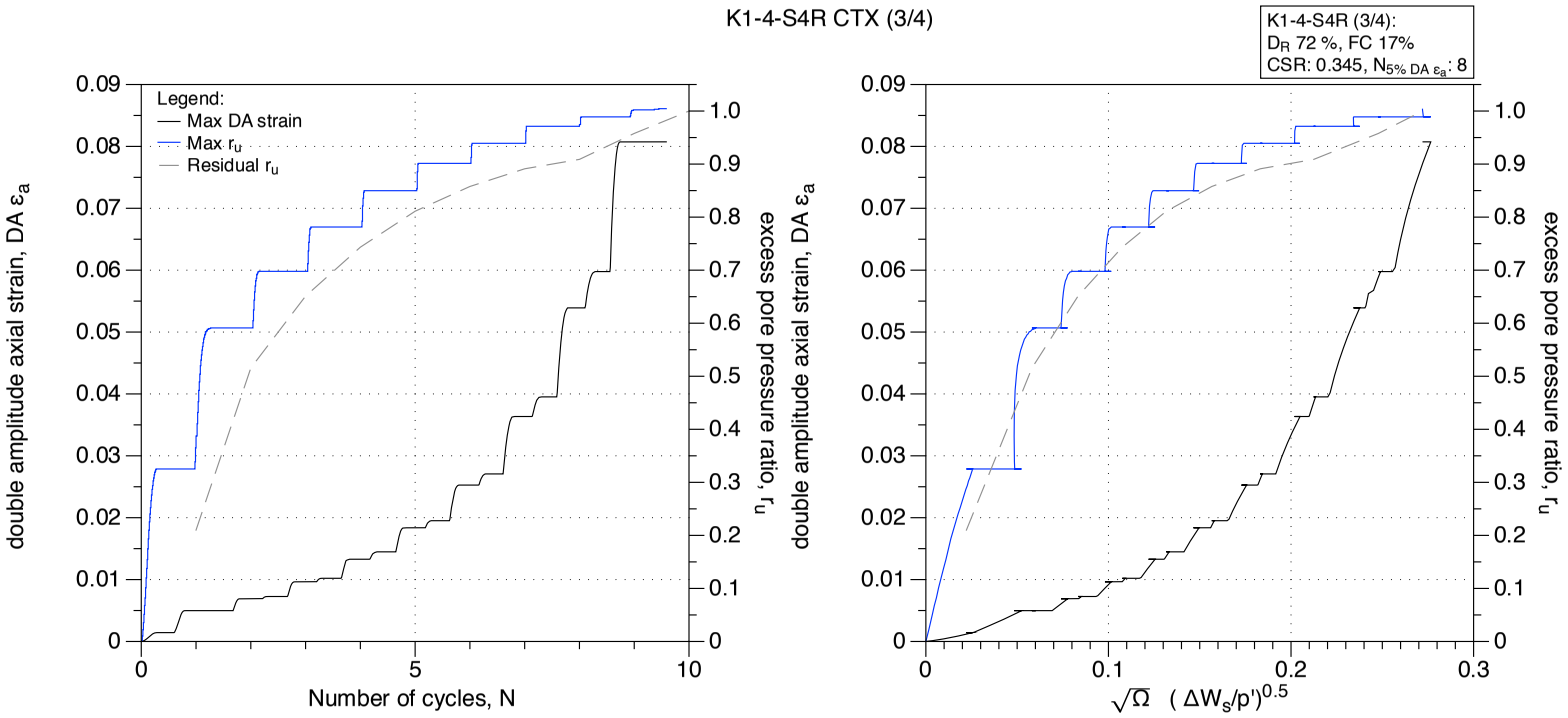

Figure 4.316: K1-4-S4 MT reconstituted sample (FC 17%), undrained cyclic triaxial test (CTX), test (3/4). Development of strain and excess pore water pressure with number of cycles and normalised shear work.

4.4.2.4 CTX Tests on samples (FC 0 - 5 %)

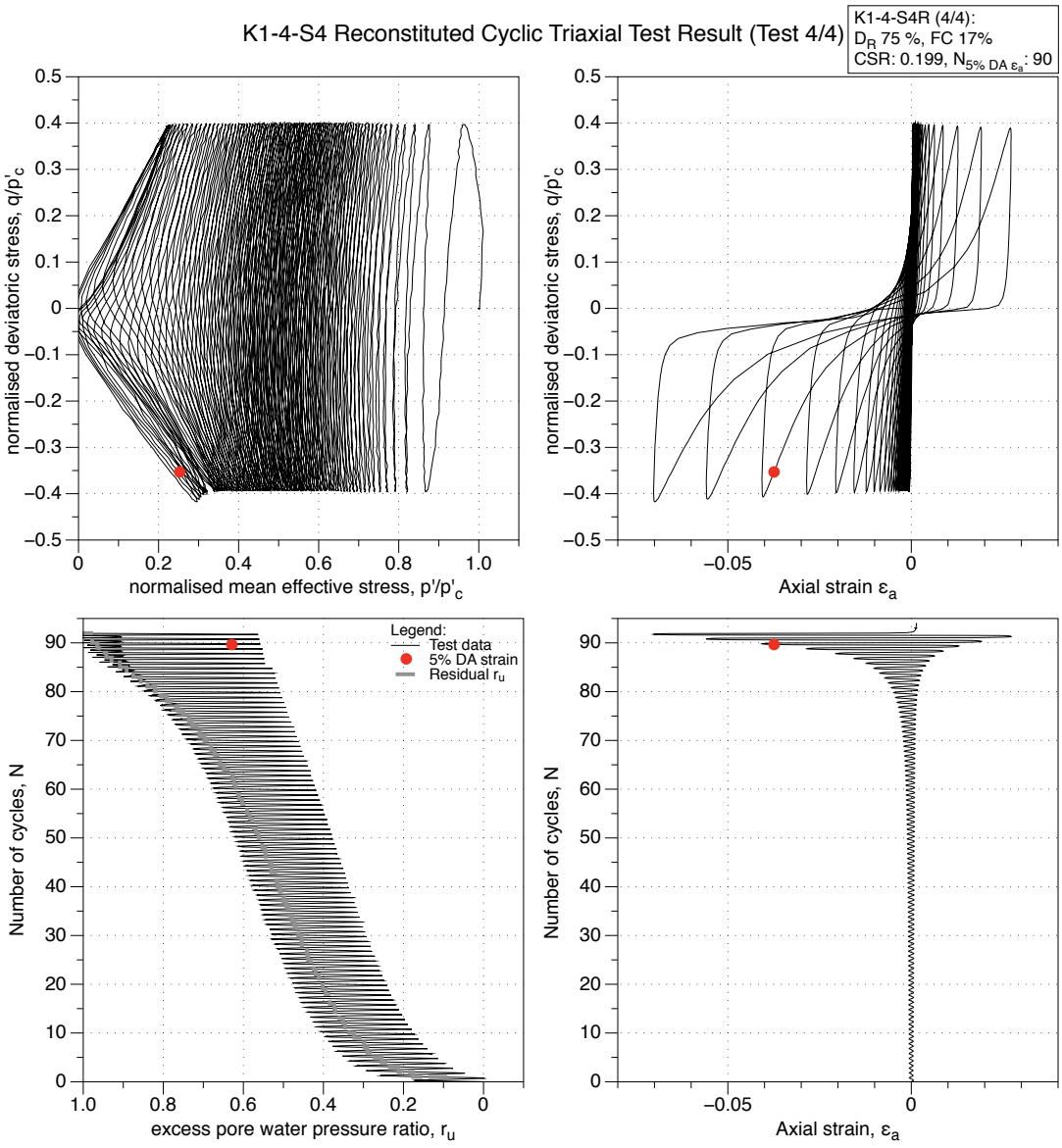

Figure 4.317: K1-4-S4 MT reconstituted sample (FC 17%), undrained cyclic triaxial test (CTX), test (4/4). Effective stress-path, stress-strain, excess pore water pressure ratio and strain development plots.

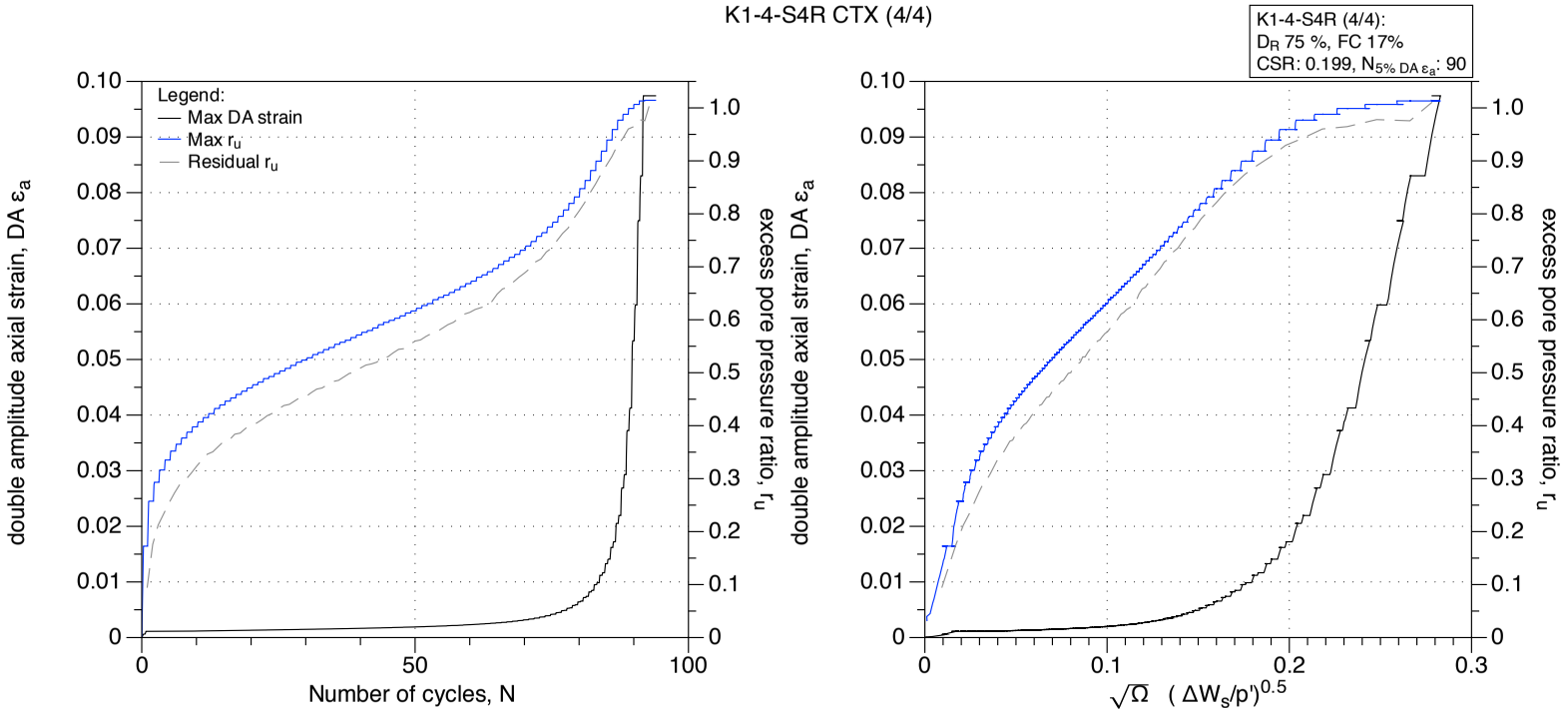

Figure 4.318: K1-4-S4 MT reconstituted sample (FC 17%), undrained cyclic triaxial test (CTX), test (4/4). Development of strain and excess pore water pressure with number of cycles and normalised shear work.

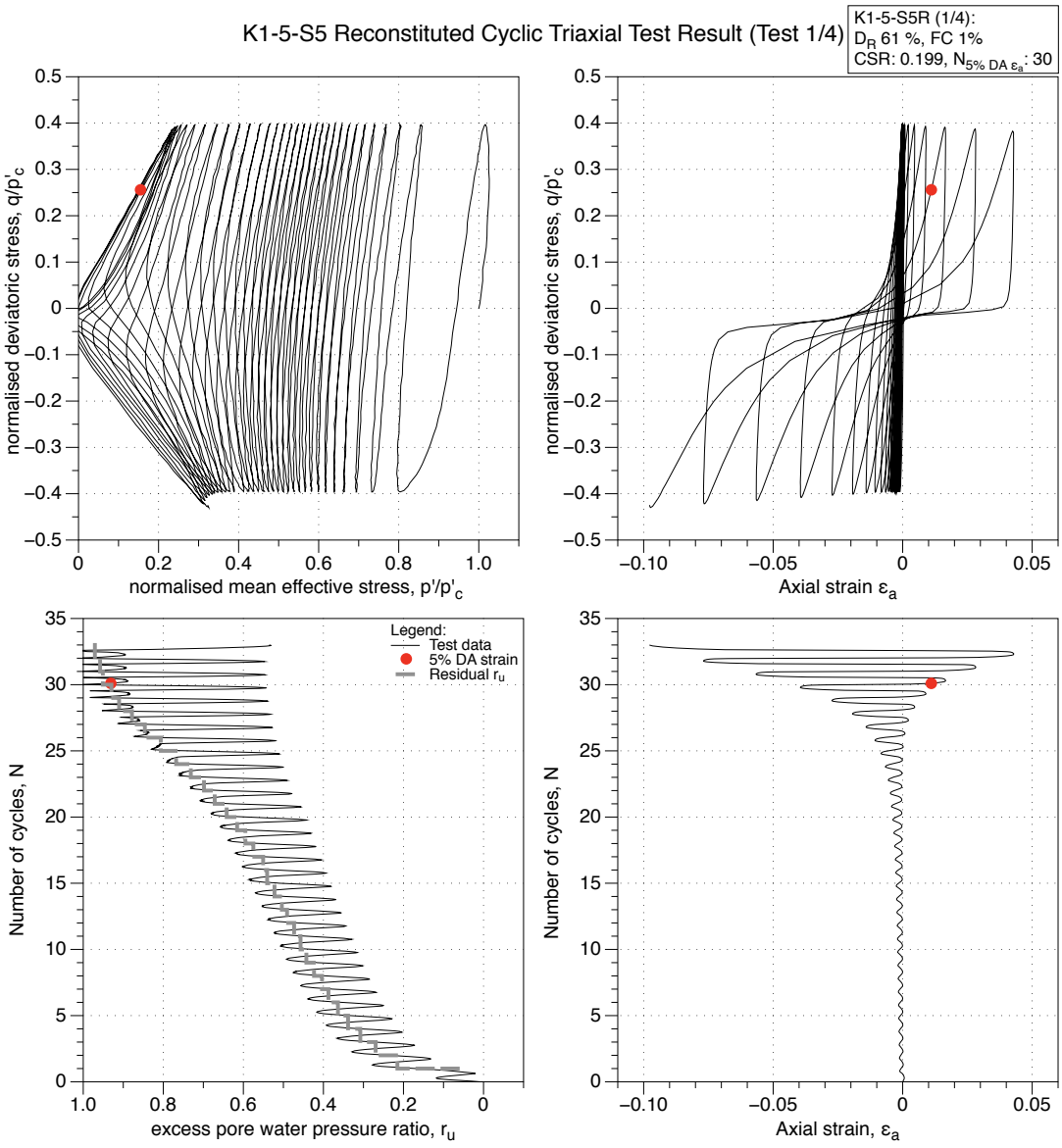

Figure 4.319: K1-5-S5 MT reconstituted sample (FC 1%), undrained cyclic triaxial test (CTX), test (1/4). Effective stress-path, stress-strain, excess pore water pressure ratio and strain development plots.

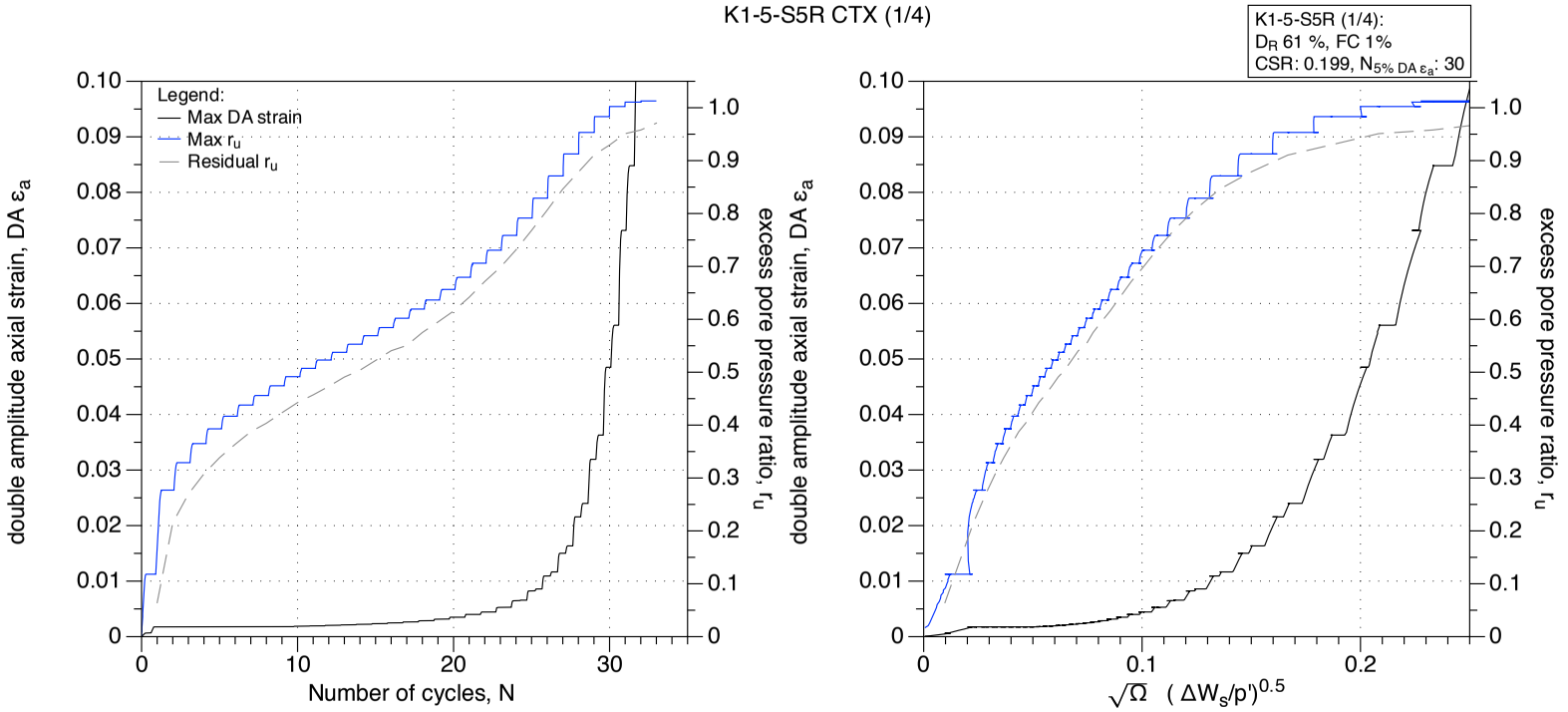

Figure 4.320: K1-5-S5 MT reconstituted sample (FC 1%), undrained cyclic triaxial test (CTX), test (1/4). Development of strain and excess pore water pressure with number of cycles and normalised shear work.

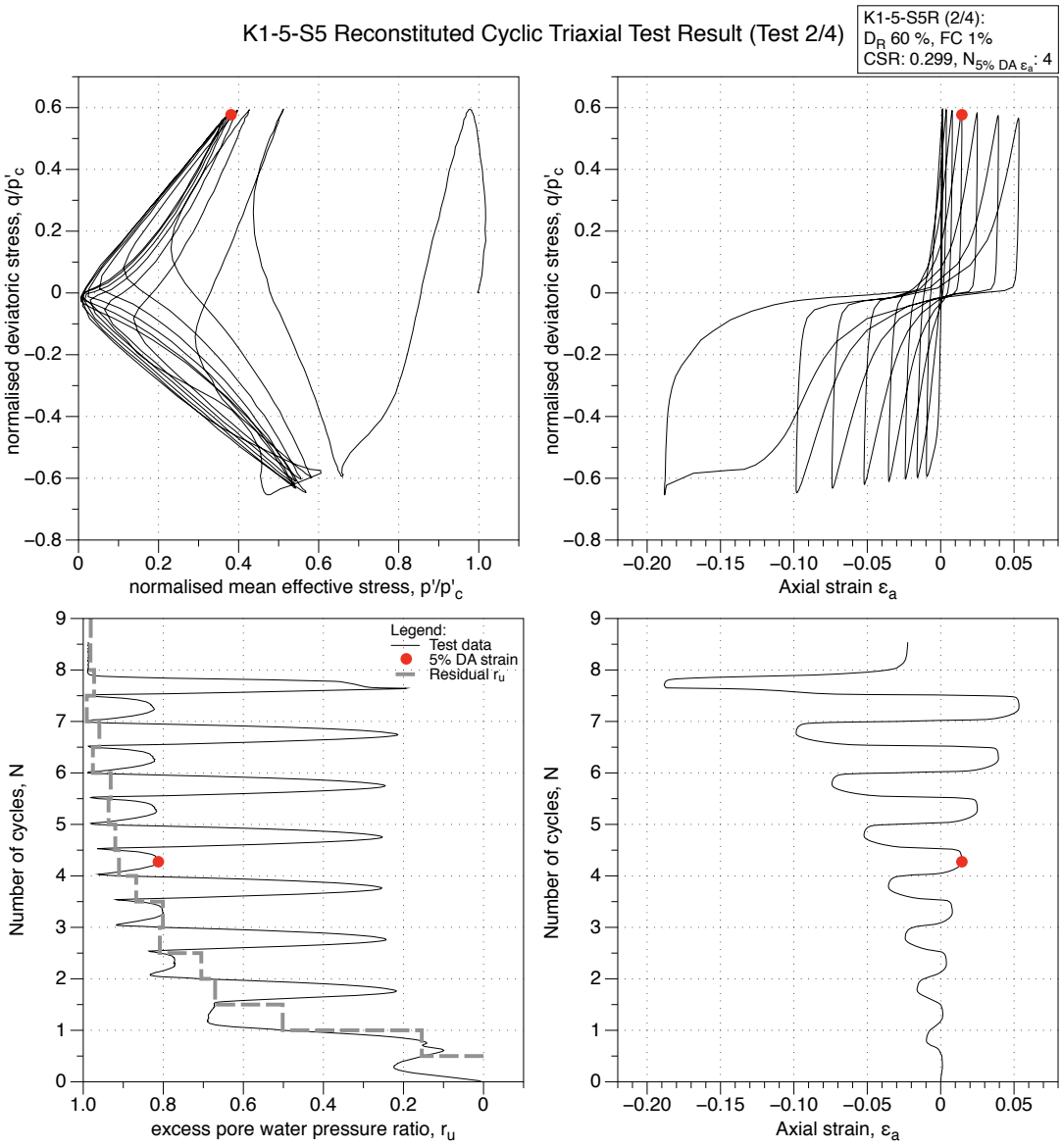

Figure 4.321: K1-5-S5 MT reconstituted sample (FC 1%), undrained cyclic triaxial test (CTX), test (2/4). Effective stress-path, stress-strain, excess pore water pressure ratio and strain development plots.

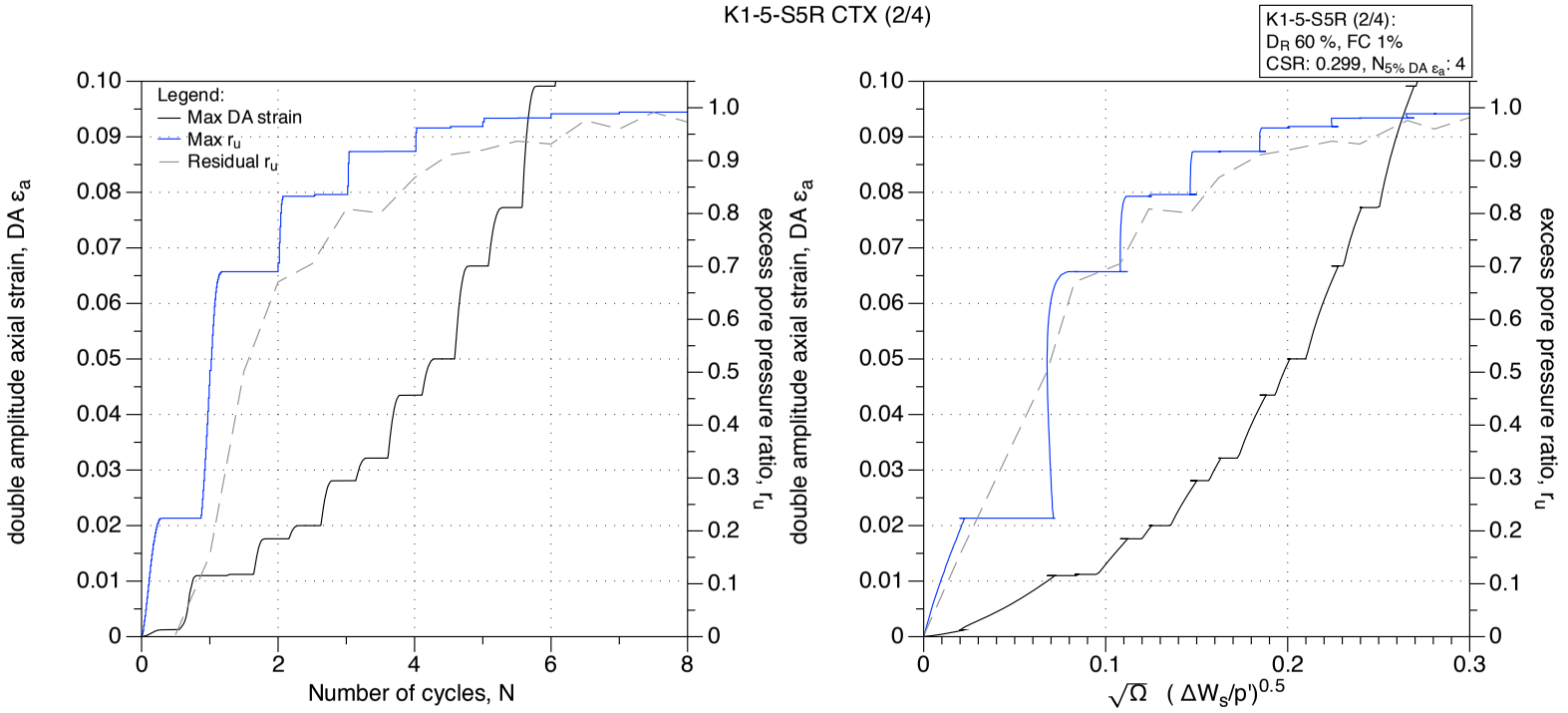

Figure 4.322: K1-5-S5 MT reconstituted sample (FC 1%), undrained cyclic triaxial test (CTX), test (2/4). Development of strain and excess pore water pressure with number of cycles and normalised shear work.

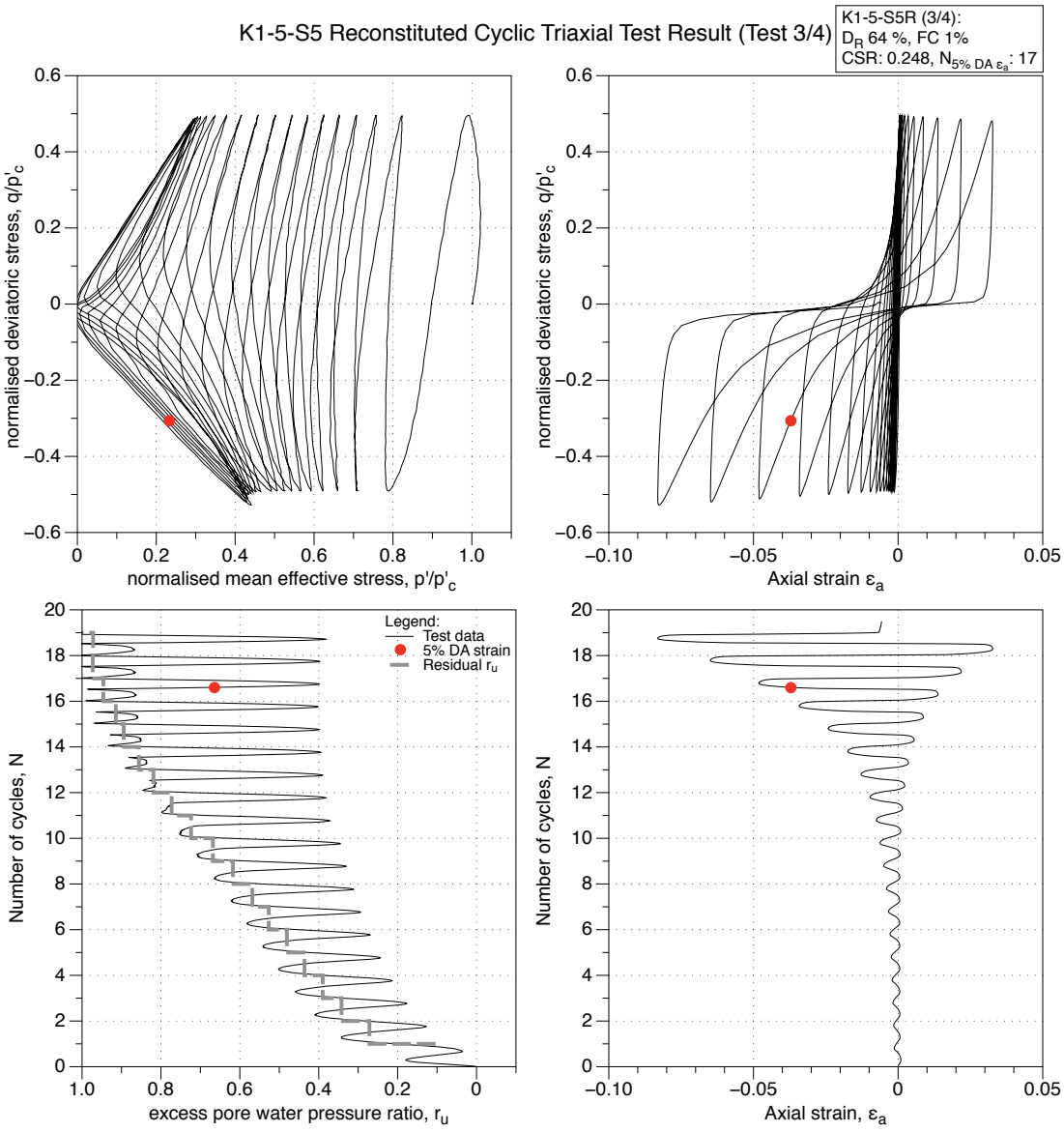

Figure 4.323: K1-5-S5 MT reconstituted sample (FC 1%), undrained cyclic triaxial test (CTX), test (3/4). Effective stress-path, stress-strain, excess pore water pressure ratio and strain development plots.

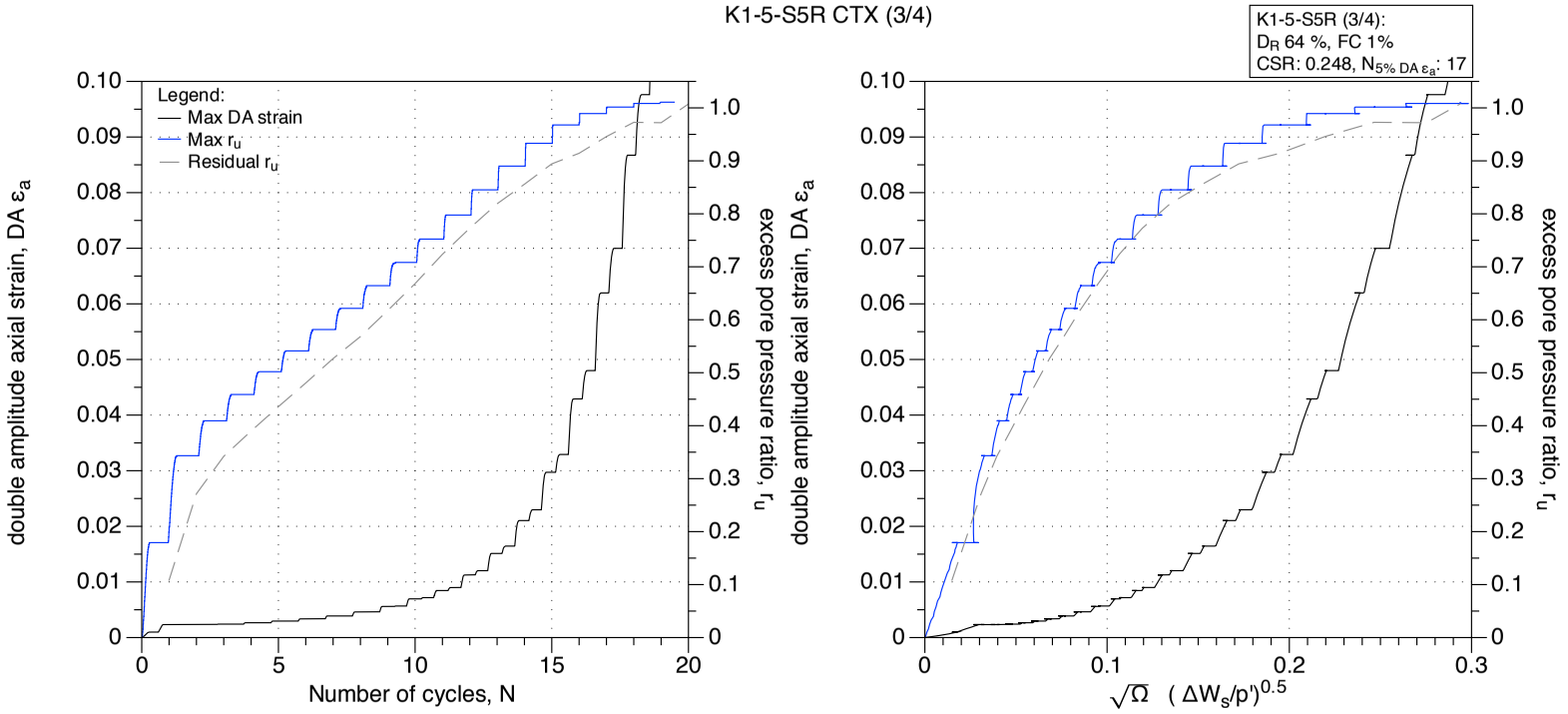

Figure 4.324: K1-5-S5 MT reconstituted sample (FC 1%), undrained cyclic triaxial test (CTX), test (3/4). Development of strain and excess pore water pressure with number of cycles and normalised shear work.

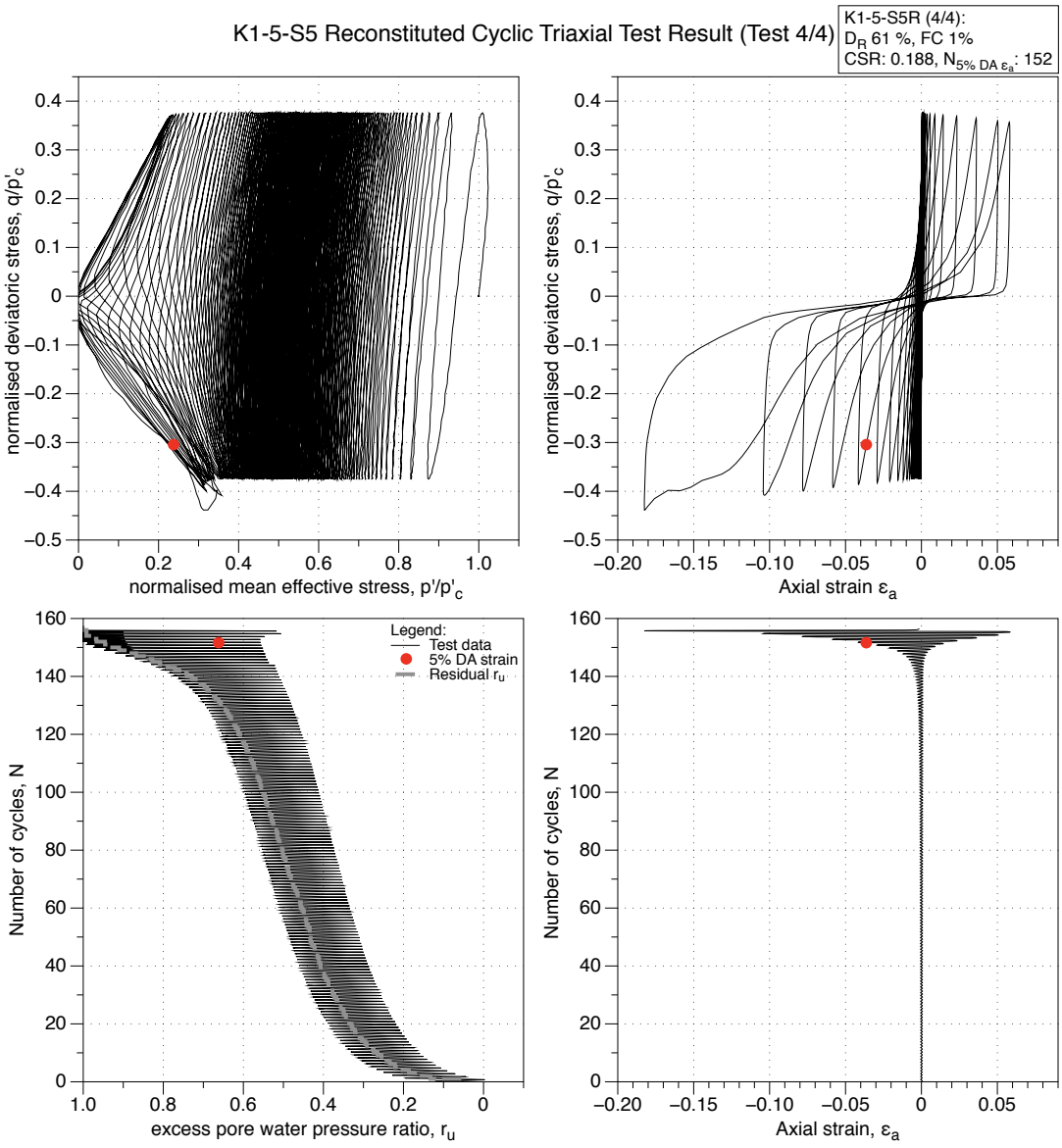

Figure 4.325: K1-5-S5 MT reconstituted sample (FC 1%), undrained cyclic triaxial test (CTX), test (4/4). Effective stress-path, stress-strain, excess pore water pressure ratio and strain development plots.

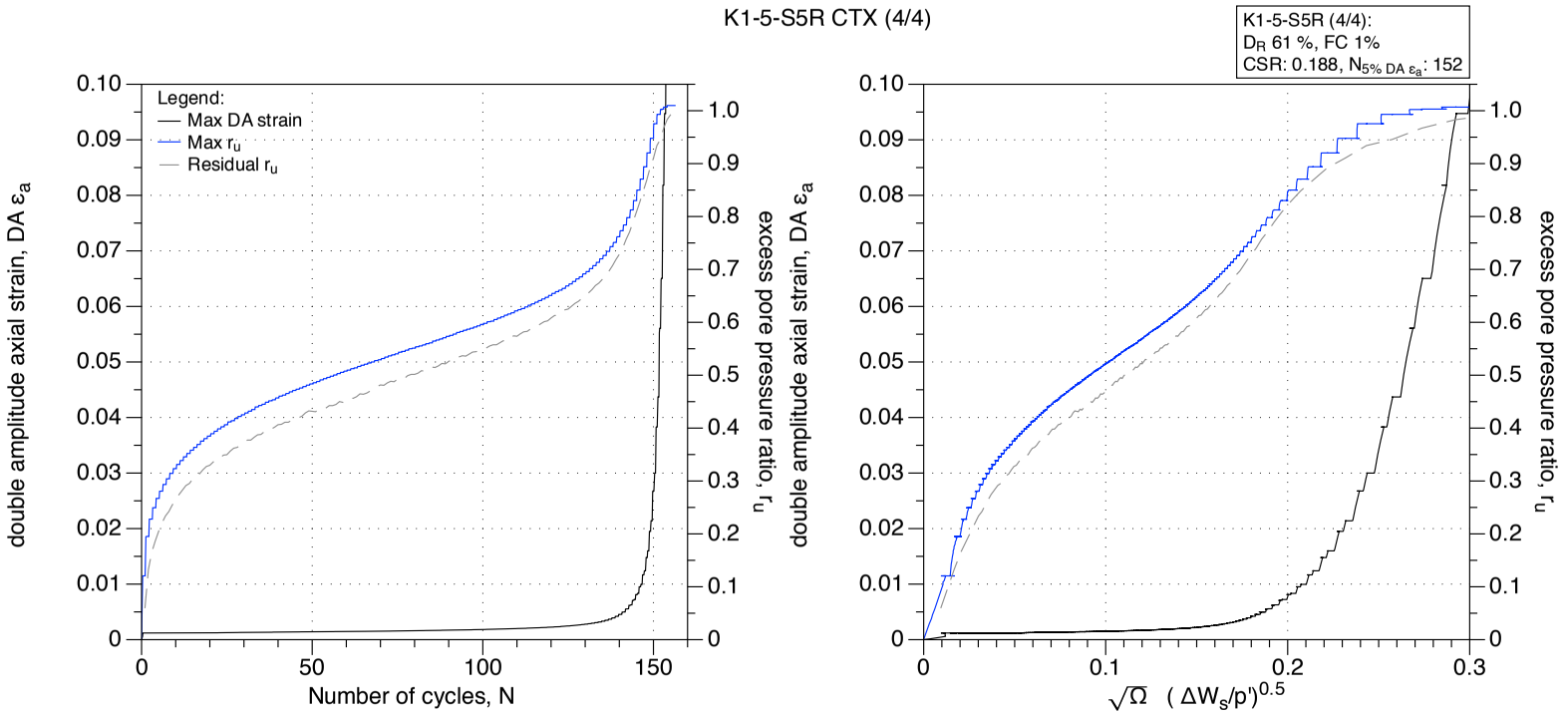

Figure 4.326: K1-5-S5 MT reconstituted sample (FC 1%), undrained cyclic triaxial test (CTX), test (4/4). Development of strain and excess pore water pressure with number of cycles and normalised shear work.

4.5 Undrained stress-dilatancy plot

In developing a similar suite of plots for the undrained monotonic tests, it was desired to plot a similar expression of the soil dilatancy acting during an undrained test. An equivalent *undrained* plastic dilatancy parameter was calculated based on the relationship between drained and undrained response developed by using the well known Martin-Finn-Seed relationship (Martin et al., 1975). They considered a cubic element of saturated sand of unit volume and porosity, n, subjected to a vertical effective stress, σ'_v, and horizontal stress, $\sigma'_h = K_0\sigma'_v$. During drained simple shear loading, a cycle of shear strain, γ, causes an increment in volumetric compaction strain, $\Delta\varepsilon_{vd}$, due to grain slip. During an undrained shear test starting with the same effective stress system, the cycle of shear strain, γ, causes an increase in pore water pressure, Δu. This was shown by Martin et al. (1975) to be related as follows:

$$\Delta u = \frac{\Delta\varepsilon_{vd}}{\frac{1}{K_e} + \frac{n}{K_w}} \tag{4.1}$$

where K_e is the elastic bulk modulus, determined from the elastic shear modulus, G_e for the sand and elastic Poisson's ratio ν_e. Parameter K_w is the bulk modulus of water, assumed to be 2,200 MPa.

During a monotonic undrained triaxial test, excess pore pressure Δu is generated, and this may be used with Equation 4.1 to estimate the equivalent volumetric compaction strain expected from a drained triaxial test. This has been used to represent the *expression* of dilatancy during undrained loading in the accompanying plots for CIU tests. The trend is similar to that observed for drained tests, showing the tendency towards zero dilatancy at critical state, but with much lower magnitude of the estimated values of 'dilatancy'.

Bibliography

Adalsteinsson, D. (2013). *Datagraph 3.1. A simple and powerful graphing program.* Visual Data Tools, Inc., Chapel Hill, NC.

Baldi, G. and Nova, R. (1984). Membrane penetration effects in triaxial testing. *Journal of Geotechnical Engineering*, 110(3):403–420.

Baxter, D. (2000). *Mechanical Behavior of Soil Bentonite Cutoff Walls.* Ph.D. Thesis, Dept. Civil Engineering, Virginia Tech, Blacksburg, VA, USA.

Cho, G.-C., Jake, D., and Santamarina, J. C. (2006). Particle shape effects on packing density, stiffness, and strength: Natural and crushed sands. *Journal of Geotechnical and Geoenvironmental Engineering*, 132(5):591–602.

Chu, J. and Lo, S. C. R. (1993). On the measurement of critical state parameters of dense granular soils. *Geotechnical Testing Journal*, 16(1):27–35.

Cubrinovski, M. and Ishihara, K. (1999). Empirical correlation between SPT N-value and relative density for sandy soils. *Soils and Foundations*, 39(5):67–71.

Cubrinovski, M. and Ishihara, K. (2002). Maximum and minimum void ratio characteristics of sands. *Soils and Foundations*, 42(6):65–78.

Duncan, J. M. and Seed, H. B. (1967). Corrections for strength test data. *Journal of the Soil Mechanics and Foundations Division, ASCE*, 93(5):121–137.

Georgiannou, V. N. (2006). The undrained response of sands with additions of particles of various shapes and sizes. *Géotechnique*, 56(9):639–649.

Henkel, D. and Gilbert, G. (1952). The effect measured of the rubber membrane on the triaxial compression strength of clay samples. *Géotechnique*, 3(1):20–29.

Holoborodko, P. (2013). Smooth noise-robust differentiators. http://www.holoborodko.com/pavel/numerical-methods/numerical-derivative/smooth-low-noise-differentiators/.

Ishihara, K. (1993). The Rankine Lecture: Liquefaction and flow failure during earthquakes. *Géotechnique*, 43(3):351–415.

Jefferies, M. and Davies, M. (1993). Use of CPTu to estimate equivalent SPT N60. *Geotechnical Testing Journal*, 16(4):458–468.

Kramer, S. L., Sivaneswaran, N., and Davis, R. (1990). Analysis of membrane penetration in triaxial test. *Journal of Engineering Mechanics, ASCE*, 116(4):773–789.

La Rochelle, P., Leroueil, S., Trak, B., Blais-Leroux, L., and Tavenas, F. (1988). Observational approach to membrane and area corrections in triaxial tests. In Donaghue, R., Chaney, R., and Silver, M., editors, *Advanced Triaxial Testing of Soil and Rock, ASTM STP 977*, Philadelphia. American Society for Testing and Materials.

Lade, P. V., Liggio, C., and Yamamuro, J. A. (1998). Effects of non-plastic fines on minimum and maximum void ratios of sand. *Geotechnical Testing Journal*, 21(4):336–347.

Martin, G. R., Finn, W. D. L., and Seed, H. B. (1975). Fundamentals of liquefaction under cyclic loading. *American Society of Civil Engineers, Journal of the Geotechnical Engineering Division*, 101(5):423–438.

Rees, S. (2010). *Effects of fines on the undrained behaviour of Christchurch sandy soils*. Ph.D. Thesis, Dept. Civil & Natural Resources Engineering University of Canterbury, Christchurch, New Zealand.

Riemer, M. and Seed, R. B. (1997). Factors affecting apparent position of steady-state line. *Journal of Geotechnical and Geoenvironmental Engineering*, 123(3):281–288.

Riemer, M., Seed, R. B., Nicholson, P. G., and Jong, H. (1990). Steady state testing of loose sands: Limiting minimum density. *Journal of Geotechnical Engineering*, 116(2):332–337.

Robertson, P. K. and Cabal, K. (2012). Guide to cone pentetration testing for geotechnical engineering. Signal Hill, California.

Salgado, R., Mitchell, J. K., and Jamiolkowski, M. (1998). Calibration chamber size effects on penetration resistance in sand. *Journal of Geotechnical and Geoenvironmental Engineering*, 124(9):878–888.

Santamarina, J. C. and Cho, G. (2004). Soil behaviour: The role of particle shape. In Jardine, R. J., Potts, D., and Higgins, K., editors, *Advances in geotechnical engineering: The Skempton conference*, volume 1, pages 604–617, London. Thomas Telford.

Seiken Inc. (2008). *Technical Documents of Triaxial Testing Apparatus (for Dynamic Test & Static Test). Model No. DTC-367.* Seiken Inc., Tokyo, Japan.

Shimobe, S. and Moroto, N. (1995). A new classification chart for sand liquefaction. In *Proceedings, First International Conference on Earthquake Geotechnical Engineering, Tokyo*, volume 1, pages 315–320.

Sladen, J. A., D'Hollander, R. D., and Krahn, J. (1985). Liquefaction of sands, a collapse surface approach. *Canadian Geotechnical Journal*, 22(4):564–578.

Sladen, J. A. and Handford, G. (1987). Potential systematic error in laboratory testing of very loose sands. *Canadian Geotechnical Journal*, 24(3):462–466.

Verdugo, R. (1992). *Characterization of sandy soil behavior under large deformation.* Dr.Eng. Thesis, University of Tokyo.

Verdugo, R. and Ishihara, K. (1996). The steady state of sandy soils. *Soils and Foundations*, 36(2):81–91.

Wijewickreme, D., Sriskandakumar, S., and Byrne, P. (2005). Cyclic loading response of loose air-pluviated Fraser River sand for validation of numerical models simulating centrifuge tests. *Canadian Geotechnical Journal*, 42(2):550–561.

Youd, T. L. (1973). Factors controlling maximum and minimum densities in sands. In *Evaluation of Relative Density and Its Role in Geotechnical Projects Involving Cohesionless Soils, ASTM STP 523*, pages 98–112. American Society for Testing and Materials.

Zlatovic, S. (1994). *Residual strength of silty soils*. Dr.Eng. Thesis, Dept. Civil Engineering, University of Tokyo, Tokyo, Japan.